ISBN 1-56677-045-9

Editors
Hussey
Newman
Mamantov
Ito

MOLTEN SALTS
NINTH INTERNATIONAL SYMPOSIUM

PV 94-13

ISBN 1-56677-045-9

MOLTEN SALTS

NINTH INTERNATIONAL SYMPOSIUM

Edited by

Charles L. Hussey
David S. Newman
Gleb Mamantov
Yasuhiko Ito

The Electrochemical Society
Founded in Philadelphia 1902
Incorporated 1930

PROCEEDINGS OF THE NINTH INTERNATIONAL SYMPOSIUM ON

MOLTEN SALTS

Editors

Charles L. Hussey
University of Mississippi
University, Mississippi

David S. Newman
Bowling Green State University
Bowling Green, Ohio

Gleb Mamantov
University of Tennessee
Knoxville, Tennessee

Yasuhiko Ito
Kyoto University
Kyoto, Japan

PHYSICAL ELECTROCHEMISTRY AND
HIGH TEMPERATURE MATERIALS DIVISIONS

Proceedings Volume 94-13

THE ELECTROCHEMICAL SOCIETY, INC.,
10 South Main St., Pennington, NJ 08534-2896

Published by:

The Electrochemical Society, Inc.
10 South Main Street
Pennington, New Jersey 08534-2896
Telephone (609) 737-1902
Fax (609) 737-2743

Library of Congress Catalog Number: 94-70845

ISBN 1-56677-045-9

Printed in the United States of America

PREFACE

The Ninth International Symposium on Molten Salts was held during the 185th Meeting of the Electrochemical Society in San Francisco, California, May 22-27, 1994. Financial support for this symposium was provided by the Physical Electrochemistry and High Temperature Materials Divisions of the Society and by a generous contribution from the Molten Salt Committee of the Electrochemical Society of Japan. The co-organizers of this symposium were (alphabetically) Charles L. Hussey, University of Mississippi, Yasuhiko Ito, Kyoto University, Gleb Mamantov, University of Tennessee, David S. Newman, Bowling Green State University, and David A. Shores, University of Minnesota.

This symposium was truly international in scope in that participants originated from Belgium, Canada, China, Denmark, France, Germany, Greece, Hungary, India, Italy, Japan, Norway, Poland, Portugal, Slovakia, Russia, Ukraine, the United Kingdom, and the U.S. The unusually large number of papers contributed to this symposium makes it inarguably the largest gathering of molten salt researchers ever witnessed by The Electrochemical Society and attests to the robust world-wide health of the field of molten salt chemistry.

This volume contains 107 of the 119 papers presented during this symposium. These papers cover a diverse range of topics in molten salt chemistry, including batteries and fuel cells, electrochemistry, homogeneous reactions and catalysis, spectroscopy, structure, theory, thermodynamics, and transport properties. The contributions that appear in this volume are grouped into various categories according to the judgement of the editors; however, these groupings are purely artificial because many of these papers encompass several topics and could fit equally well in more than one category.

The senior editor wishes to express his appreciation to the Staff of The Electrochemical Society, especially Mrs. Sarah Kilfoyle and Mr. Brian Rounsavill, for their support and cooperation and to Bobbie J. Clark and William R. Pitner of the University of Mississippi for their assistance in preparing this volume. Financial support for the preparation of this volume was provided by the National Science Foundation.

Charles L. Hussey
The University of Mississippi
May, 1994

GLEB MAMANTOV
1994 Recipient of the Max Bredig Award

The Max Bredig Award was established by the Physical Electrochemistry Division of the Electrochemical Society in 1984 "...to encourage excellence in molten salt chemistry research and to stimulate publication of high quality research papers in the *Journal of the Electrochemical Society*. This encouragement is provided by bringing recognition to scientists who have made outstanding contributions to the field of molten salt chemistry and who have enhanced the scientific stature of the Society by the presentation of well-recognized papers in the *Journal* and at Society meetings..." Previous award winners include Milton Blander (1987), G. Pedro Smith (1990), and Robert A. Osteryoung (1992). This award is financed by the income from the Max Bredig Award Fund established by contributions from ARCO Metals Co. and the Aluminum Corporation of America (ALCOA). It was through Gleb Mamantov's considerable efforts that the Max Bredig Award was established.

Gleb Mamantov was born April 10, 1931 in Karsava, Latvia. His physician parents, Alexander and Helen Mamantov, were natives of St. Petersburg, Russia, who left Russia during the Communist revolution. Latvia and other Baltic states were forcibly annexed by the Soviet Union in 1940, and approximately one year later war broke out between the Soviet Union and Germany. At this time, the Mamantov family narrowly escaped deportation to Siberia by the Soviet government. In 1944, a few months after Gleb graduated from elementary school, the Mamantov family was forced to leave Latvia because the country was once again occupied by the Soviet Union. The family lived in a Displaced Persons Camp in Kleinkotz, Germany, from 1945 to 1949 where Gleb graduated from a Latvian gymnasium located at the camp.

The Mamantov family immigrated to the U. S. in 1949, and Gleb attended Louisiana State University where he completed the B.S. degree (cum laude) in chemistry in 1953, and the M.S. and Ph.D. degrees in electrochemistry in 1953 and 1957, respectively. His masters and doctoral research were directed by the eminent electrochemist, Professor Paul Delahay. From 1957 to 1958, he was employed as a research chemist by E. I. Du Pont de Nemours & Co., Inc. in Niagara Falls, N.Y. From 1958 to 1960, he served on active duty in the U. S. Air Force and was stationed at Edwards AFB, CA. After completing his military service requirement and feeling the urge for a career in academia, Gleb joined Professor J. L. Margrave at the University of Wisconsin as an Instructor and Project Associate from 1960 to 1961. In 1961, he joined the Department of Chemistry of the University of Tennessee as an Assistant Professor, rising to the rank of Professor in 1971. In 1979, he was appointed Head of the Department of Chemistry, a position that he continues to hold. Gleb has served as a consultant for Oak Ridge National Laboratory since 1962 and for Los Alamos National Laboratory since 1987. In 1987, he established a small company called Molten Salt Technology. During the summer of 1991, he was a Visiting Professor at the University of Paris.

Gleb was married to the former Charmaine Bienvenu in 1956. Dr. Charmaine B. Mamantov is also a faculty member at the University of Tennessee. They are the parents of three children, all of whom have pursued professional careers, and they have four grandchildren.

Gleb Mamantov holds membership in several societies and professional organizations, including The Electrochemical Society, American Chemical Society, The American

Association for the Advancement of Science, Sigma Xi, Phi Lambda Upsilon, American Institute of Chemists, Society for Applied Spectroscopy, and the Society of Electroanalytical Chemistry (SEAC). He has received numerous awards and special recognition, including election to Phi Beta Kappa, Phi Kappa Phi, and Omicron Delta Kappa; appointment as a Fellow of both the American Association for the Advancement of Science and the American Institute of Chemists; and selection as a Foreign Member of the Latvian Academy of Sciences. Gleb received the Meggers Award of the Society for Applied Spectroscopy in 1983 and the Charles H. Stone Award of the American Chemical Society Carolina-Piedmont Section in 1989. He was designated as a Distinguished Professor by the University of Tennessee in 1986.

Gleb Mamantov has been very active in The Electrochemical Society, serving as a Physical Electrochemistry Divisional Editor of the *Journal* from 1980 to 1990 and as a member of numerous Society committees. These include the Honors and Awards Committee (1985-88), Chairman of the Carl Wagner Memorial Award Committee (1986-88), and the Ways and Means Committee (1988-89). He has served as co-organizer of several Society sponsored symposia, including the Third International Symposium on Molten Salts held at the Hollywood, FL Meeting (1980), The Joint International Symposium on Molten Salts held at the Honolulu, HI Meeting (1987), and the Ninth International Symposium on Molten Salts held at the San Francisco Meeting (1994). In addition to Society activities, he has been an active participant in numerous Gordon Conferences, serving as Vice-chairman (1985) and Chairman (1987) of the Gordon Conference on Molten Salts and Liquid Metals. In 1986, Gleb was Director of the NATO Advanced Study Institute on Molten Salt Chemistry held in Camerino, Italy.

Gleb Mamantov's research activities can be subdivided into three broad categories. These include the chemistry, electrochemistry, and spectroscopy of haloaluminate molten salts; molten salt batteries (notably the development of the Na/β"-alumina/SCl_3^+ high-voltage cell, which uses $AlCl_3$-NaCl electrolyte); and electrochemical and related studies in molten fluorides. He is the author or coauthor of more than 250 journal articles, symposium proceedings articles, patents, and edited books. Thirty-eight of these articles have appeared in the *Journal of the Electrochemical Society*. Along with J. Braunstein and G. P. Smith, he initiated the six volume series *Advances in Molten Salt Chemistry*, and he edited the monographs *Molten Salts: Characterization and Analysis*, *Characterization of Solutes in Nonaqueous Solvents*, *Molten Salts-An Introduction and Selected Applications* (with R. Marassi), and *Chemistry of Non-Aqueous Solutions: Current Progress* (with A. I. Popov).

Gleb Mamantov is a dedicated and unflagging advocate of the field of molten salt chemistry. It is only fitting that Professor Mamantov receive the Max Bredig Award because he exemplifies the high standards in research and publication set forth for this award.

Charles L. Hussey
The University of Mississippi
May, 1994

TABLE OF CONTENTS

Theory, Calculations, Modeling, and Structure

Thermodynamics and Transport Properties

Spectroscopy

Electrochemistry

Homogeneous Reactions, Kinetics, and Catalysis

Nuclear Fuel Processing and Nuclear Waste Remediation

Batteries and Fuel Cells

FACTS ABOUT THE ELECTROCHEMICAL SOCIETY, INC.

The Electrochemical Society, Inc., is an international, nonprofit, scientific, educational organization founded for the advancement of the theory and practice of electrochemistry, electrothermics, electronics, and allied subjects. The Society was founded in Philadelphia in 1902 and incorporated in 1930. There are currently over 6000 scientists and engineers from more than 60 countries who hold individual membership; the Society is also supported by more than 100 corporations through Patron and Sustaining Memberships.

The Technical activities of the Society are carried on by Divisions and Groups. Local Sections of the Society have been organized in a number of cities and regions.

Major international meetings of the Society are held in the Spring and Fall of each year. At these meetings, the Divisions and Groups hold general sessions and sponsor symposia on specialized subjects.

The Society has an active publications program which includes the following:

JOURNAL OF THE ELECTROCHEMICAL SOCIETY - The JOURNAL is a monthly publication containing technical papers covering basic research and technology of interest in the areas of concern to the Society. Papers submitted for publication are subjected to careful evaluation and review by authorities in the field before acceptance, and high standards are maintained for the technical content of the JOURNAL.

THE ELECTROCHEMICAL SOCIETY INTERFACE - INTERFACE is a quarterly publication containing news, reviews, advertisements, and articles on technical matters of interest to Society Members in a lively, casual format. Also featured in each issue are special pages dedicated to serving the interests of the Society and allowing better communication between Divisions, Groups, and Local Sections.

EXTENDED ABSTRACTS - Extended Abstracts of the technical papers presented at the Spring and Fall Meetings of the Society are published in serialized softbound volumes.

PROCEEDINGS VOLUMES - Papers presented in symposia at Society and Topical Meetings are published from time to time as serialized Proceedings Volumes. These provide up-to-date views of specialized topics and frequently offer comprehensive treatment of rapidly developing areas.

MONOGRAPH VOLUMES - The Society has, for a number of years, sponsored the publication of hardbound Monograph Volumes, which provide authoritative accounts of specific topics in electrochemistry, solid state science, and related disciplines.

DOI: 10.1149/199413.0001PV

A STATISTICAL MECHANICAL THEORY FOR MOLTEN SILICATE SOLUTIONS

Milton Blander and Ira Bloom
Argonne National Laboratory
Argonne, IL 60439-4837

ABSTRACT

A statistical mechanical theory for molten silicates has been deduced that takes into account the silicate structures and the configuration dependence of the free energy of breaking Si-O-Si bridging bonds with O^{2-} ions. Thermodynamic properties of binary solutions can be described in terms of a structural model with four equilibrium constants (K_i) for breaking bridges on silicons already having i broken bonds attached. The theory provides a realistic means to relate structural and thermodynamic data.

INTRODUCTION

Recent work on modeling the solution properties of molten silicates have been based on an *ad hoc* modification of quasichemical theory.[1-10] It can be used to predict the properties of multicomponent silicates from those of the constituent binaries when silica is the only acidic component. However, when another acidic component, such as alumina, is in the molten solution, this approach is not flexible enough to provide this capability. In such cases, one requires *ad hoc* ternary interaction terms in the energy parameters of the theory and empirical predictions of the properties of multicomponent systems can be made from the subsidiary ternaries.[10] Many other silicate solution properties such as sulfide or phosphate capacities can not be treated directly by the quasichemical approach and require separate models to make predictions of these quantities *a priori*. This inflexibility of the quasichemical theory arises because it is not a true model of a silicate solution. The purpose of this paper is to discuss a structural model for silicates that can ultimately incorporate all the above types of thermodynamic properties of silicates in a realistic manner and provide a means for representing and predicting the properties of all multicomponent systems from those of lower order systems.

This structural model is a generalization of a model proposed by Lin and Pelton[11] that is more general than the works of Masson;[12] Gaskell;[13] Fincham and Richardson;[14] Toop and Samis;[15] Frohberg et. al.;[16] Flood and Knapp;[17] Førland;[18] and Niwa and Yokokawa.[19] The Lin-Pelton model incorporated fundamental concepts that were proposed by these workers and reduced to the equations of Flood and Knapp,[17] and of Førland[18] in different ranges of concentration.

The fundamental model starts with the conjectures of Fincham and Richardson.[14] In pure silica, the silica network consists of four coordinated silicons singly connected by bridging nearest-neighbor oxygen atoms, which are thus two-coordinated. Addition of an oxide, MO, to silica cuts a bridging bond as follows:

$$Si\text{-}O\text{-}Si + O^{2-} \rightleftharpoons 2SiO^{-} \qquad (1)$$

or, in shorthand notation:

$$O + O^{2-} \rightleftharpoons 2O^{-} \qquad (2)$$

In the model, it is assumed that the cation of the added oxide binds to the two SiO^{-} ends of the cut bond. Lin and Pelton then calculated the entropy by assuming random mixing of bridges with cut bridges, a concept proposed by Førland.[18] In addition, they incorporate a general form of a proposal by Flood and Knapp,[17] which suggests that the entropy of mixing of basic solutions (high in MO, low in silica) can be calculated by assuming a random distribution of O^{2-} and SiO_4^{4-} anions. As the solution becomes more acidic, the SiO_4^{4-} ions polymerize. Masson[12] showed that the Flory polymer model described such solutions at concentrations less than 50 m/o silica, a concentration above which the Flory model is certainly inadequate because of the formation of three-dimensional and cyclic polymers of bridged silica tetrahedra. The Lin-Pelton model combined all these concepts in a self-consistent manner by assuming random mixing of bridges and cut bridges and also of O^{2-} with the silica tetrahedra.

Although this model was a conceptual generalization and permitted one to describe silicate mixtures at all concentrations, it failed to fit data in binary systems without an *ad hoc* assumption concerning the energy parameter in the theory; this assumption was similar to the one also made later in the modified quasichemical theory, that the energy parameter is a function of composition. In reality, the energy parameter should be a function of the configurations of the bridges and cut bridges about the silicon atoms. By not taking this configuration dependence into account, one loses potentially important advantages of a true theory for silicates, such as the ability to obtain useful structural information from analyses of thermodynamic data, more reasonable entropic terms, and the ability to deduce physically and structurally meaningful values of the energies and free energies of cutting bridge bonds.

Here, the configuration dependence of the energy of cutting a bridging bond is incorporated into a theory for silicates. In the model discussed below, the energy (or free energy) of bridge breaking is a function of the number of broken bridges already attached to the silicon atoms. Since the bridges and cut bridges span two silicon atoms, each "bond" can be distinguished by a two-number index which specifies the number of broken bonds on each of the two silicon atoms connected by the bridge, cut or uncut. Thus, the two types of bridges (cut and uncut) mixed randomly in the Lin-Pelton model become two classes with 10 types of uncut bridges and 10 types of cut bridges.

Partition Function for the Model

The model considers silicates to contain silicon atoms tetrahedrally coordinated by oxygens. In pure SiO_2, these oxygens are considered to be all bridging oxygens connecting two silicons, so that for n_{Si} atoms, the number of bridges, b_{00}, is equal to $2n_{Si}$. The *b* signifies a bridge and the subscript, *00*, signifies that the bridges in question connect two silicons, each with zero cut bridges. At all other concentrations of silica mixed with a basic oxide, MO, there is a distribution of ten types of uncut bridges and the number of bridges of each types are designated b_{ij}, where $i,j = 0,1,2,3$. In addition, there are also ten types of cut bridges with the number of such bridges designated as $c_{i+1,j+1}$, where $i,j = 0,1,2,3$. The bridges and cut bridges form a three-dimensional network of $2n_{Si}$ total species (bridges and cut bridges which mix randomly in the simplest approach considered here). The statistical factor for this is given in Eq. 3.

$$S_1 = \frac{(2n_{Si})!}{\prod_{i=0}^{3}\prod_{j=0}^{3}(b_{ij})!\ \prod_{i=0}^{3}\prod_{j=0}^{3}(c_{i+1,j+1})!} \tag{3}$$

One must be careful in the determination of b_{ij} and c_{ij} to correct for the fact that each bond is counted twice in this notation.

In addition to mixing in the network of bridges, and cut bridges, there is also a statistical factor for the mixing of oxide ions with silicon. In basic solutions, this is equivalent to the simple mixing of O^{2-} with SiO_4^{4-} ions, and in somewhat acidic solutions of $X_{SiO_2} < 0.5$, it is equivalent to the mixing of O^{2-} with polymeric anions, as described by Masson's model based on Flory's polymer theory. This statistical factor, which was generalized by Lin and Pelton to apply for all concentrations, is given by,

$$S_2 = \frac{(n_{Si} + n_{O^{2-}})!}{n_{Si}!\ n_{O^{2-}}!} \tag{4}$$

where n_{Si} is the number of silicons in the melt and $n_{O^{2-}}$ is the number of oxide ions which are free and are not associated with a cut bridge.

One still has to define local partition functions for the relevant entities in the model. The symbols p_{ij} and q_{ij} are defined as the local partition functions for the bridges and the cut bridges, respectively, which span two atoms that have *i* and *j* cut bridges. We define $q_{O^{2-}}$ as the local partition function for the free oxide ion and define the molten silicate mixture as having n_{Si} moles of SiO_2 and n_{MO} moles of the oxide, MO. The moles of "free" oxide is thus given by the following:

$$n_{O^{2-}} = n_{MO} - \sum_i \sum_j c_{ij} \tag{5}$$

where the sum is calculated so that each bond is, in effect, counted once. The total partition function, Q, is therefore given by,

$$Q = \frac{(2n_{Si})!}{\prod_i \prod_j b_{ij}! \prod_i \prod_j c_{i+1,j+1}!} \frac{(n_{Si} + n_{O^{2-}})!}{n_{Si}!\, n_{O^{2-}}!} \prod_i \prod_j p_{ij}^{b_{ij}} \prod_i \prod_j q_{ij}^{c_{i+1,j+1}} q_{O^{2-}}^{n_{O^{2-}}} \tag{6}$$

In order to obtain a usable thermodynamic equation from this partition function, we maximize *ln(Q)* with respect to the variables b_{ij} and $c_{i+1,j+1}$. The results of the calculation are the equilibrium constants for the bridge-breaking reactions in Eqs. 1 and 2, given as follows:

$$K_{i+1,j+1} = \frac{q_{i+1,j+1}}{p_{ij}\, q_{O^{2-}}} = \frac{c_{i+1,j+1}}{b_{ij}\, X_{O^{2-}}} \tag{7}$$

where $X_{O^{2-}} = n_{O^{2-}}/(n_{Si}+n_{O^{2-}})$. Since the ratio $c_{i+1,j+1}/b_{ij}$ is unitless, one may use any self-consistent concentration scale for the uncut bridges and cut bridges. It is not necessary to choose such a scale until we have simplified the equations.

The double summations in some of the expressions (e.g., Eq. 5) and the double subscripts present difficulties in the calculation because there are twenty different species. We can eliminate the double summations and subscripts by performing partial summations and separating the local partition functions for adjacent pairs of silicons (p_{ij} and $q_{i+1,j+1}$) into the more localized partition functions for individual silicons. This reduces the number of terms and simplifies the equations considerably.

If the partition function for the uncut (p_{ij}) and cut (q_{ij}) are solely a function of i and j such that $p_{ij} = p_i p_j$ and $q_{ij} = q_i\, q_j$ (i.e., the bond free energies are additive), and if we perform partial summations of the terms in *ln(Q)* such as $\sum_i \sum_j b_{ij} ln(b_{ij})$ and $\sum_i \sum_j b_{ij} ln(p_{ij})$, we can deduce equilibrium constants K_{i+1} for the formation of a silicon species with $i+1$ cut bonds from one with i cut bonds.

$$K_{i+1} = \frac{q_{i+1}}{p_i\, q_{O^{2-}}^{0.5}} = \frac{(i+1)n_{i+1}}{(4-i)n_i X_{O^{2-}}^{0.5}} \qquad i = 0,1,2,3 \tag{8}$$

where n_i is the number of silicons with *i* cut bonds. In addition, Eq. 5 for $n_{O^{2-}}$ becomes

$$n_{O^{2-}} = n_{MO} - \sum_{i=0}^{4} \frac{in_i}{2} \tag{9}$$

and we can eliminate one of the variables, n_i, with the equation

$$\sum_{i=0}^{4} n_i = n_{Si}$$

Calculations of the partial molar chemical potentials are made by taking a partial derivative of $ln(Q)$ with respect to n_{Si} and n_{MO} to obtain

$$\begin{aligned} \frac{\mu_{SiO_2} - \mu^o_{SiO_2}}{RT} &= \ln a_{SiO_2} = \ln X_{Si} + 2 \ln \frac{b_{00}}{2n_{Si}} \\ &= \ln X_{Si} + 2 \ln \frac{16 n_0^2}{4n_{Si} \Sigma(4-i)n_i} \end{aligned} \tag{10}$$

and

$$\frac{\mu_{MO} - \mu^o_{MO}}{RT} = \ln a_{MO} = \ln X_{O^{2-}} \tag{11}$$

These equations have a physically meaningful interpretation. In Eq. 11, $X_{O^{2-}}$ is the activity of the basic oxide and is also the concentration of "free" oxide ions (not part of a cut bridge bond) that mix with silicons. It is defined as follows:

$$X_{O^{2-}} = \frac{n_{O^{2-}}}{n_{Si} + n_{O^{2-}}} = 1 - X_{Si} \tag{12}$$

The term X_{Si} in Eq. 10 is the concentration of Si in the mixture of Si and O^{2-} and $b_{00}/2n_{Si}$ is the fraction of the total number of bridges that are uncut bridges between two silicons having no cut bridges attached. These are, of course, the only type of bridges present in the standard state of pure silica, so that the properties of these bonds are related to the properties of the standard state. The term $ln\ b_{00}/2n_{Si}$ is multiplied by 2 because there are two bonds per silicon in the melt. The term b_{00} is calculable from knowledge of the parameters n_i, which, in turn, are calculable from the four equilibrium constants, K_{i+1} $(i = 0,1,2,3)$. Conversely, one can deduce these constants from a knowledge of the activities of SiO_2 (or MO) as a function of composition.

DISCUSSION

Equations 8-11 provide the capability for realistically determining the thermodynamic properties of binary molten silicates. Analyses of measurements in terms of the theory can provide values of the four formation constants, k_1, k_2, k_3, k_4, for cutting Si-O-Si bridges. These, in turn provide information on local structures and on the relative stabilities of the different configurations about silicon atoms. In addition, the theory is flexible enough to permit one to describe the solubility of a solute MX (e.g., X is a sulfide, phosphate or carbonate) by simple multiplication of the partition function in Eq. 6 by the factor $q_x^{n_x}(n_{Si}+n_{O^{2-}}+n_x)!/(n_{Si}+n_{O^{2-}})!n_x!$. An analogous, but more complex, procedure can be used to describe solutions containing alumina. This theory has the fundamental capability for a general description of the thermodynamic properties of molten silicates. Some of the assumptions in the theory can be generalized. For example, we have assumed that the distribution of silicon species among the bonds is not preferential, so that all cut bonds have the same probability for being connected to a particular silicon species. One can generalize the theory to take into account steric or other factors which might lead to a preferential distribution of the pairs of silicons connected by bonds. Thus, the probabilities and concentrations ratios such as $b_{11}b_{00}/(b_{01})^2$ could be made higher or lower than calculated by this simple form of the model. At the current stage of development, such complexity is not warranted. In any case, the theory we present should lead to a more realistic representation of silicate structures than prior models, and the results can be compared with structural data (e.g., NMR measurements on glasses).

References

1. M. Blander and A. D. Pelton, "Computer Assisted Analysis of the Thermodynamic Properties of Slags in Coal Combustion Systems," ANL/FE-83-9, Argonne National Laboratory, Argonne, IL (Sept. 1983).

2. A. D. Pelton and M. Blander, Proc. 2nd Intl. Symp. on Metall. Slags and Fluxes, H. A. Fine and D. R. Gaskell, Eds., pp. 281-294, TMS-AIME, Warrendale, PA (1984).

3. M. Blander and A. D. Pelton, Ibid., pp. 295-304.

4. M. Blander and A. D. Pelton, Mineral Matter and Ash in Coal, K. S. Vorres, Ed., Am. Chem. Soc. Symp. Ser. **301** 186-194 (1986).

5. A. D. Pelton and M. Blander, Metall. Trans., **17B**, 805-15 (1986).

6. M. Blander and A. D. Pelton, Geochim. Cosmochim. Acta, **51**, 85-95 (1987).

7. A. D. Pelton and M. Blander, CALPHAD J. **12**, 97-108 (1988).

8. A. D. Pelton, G. Eriksson and M. Blander, Proc. 3rd Intl. Symp. on Metall. Slags and Fluxes, pp. 66-69, Inst. of Metals, London (1989).

9. P. Wu, G. Eriksson, A. D. Pelton, and M. Blander, J. Iron and Steel Inst. of Japan, **33**, 26-35 (1993).

10. G. Eriksson and A. D. Pelton, Metall. Trans., **24B**, 817-825 (1993).

11. P. L. Lin and A. D. Pelton, Metall. Trans., **10B**, 667-675 (1979).

12. C. R. Masson, J. R. Smith and S. G. Whiteway, Can. J. Chem., **48**, 1456-64 (1970); C. R. Masson, Glass 1977, Proc. 11th Intl. Congress on Glass, Vol. 1, pp. 3-41, J. Gotz, Ed., Prague (1977).

13. D. R. Gaskell, Metall. Trans., **8B**, 131-145 (1977).

14. C. J. B. Fincham and F. D. Richardson, Proc. Royal Soc., **223**, 40 (1954).

15. G. W. Toop and C. S. Samis, Trans. TMS-AIME, **224**, 878-87 (1962).

16. G. M. Frohberg, M. L. Kapoor and G. M. Nichotra, Arch. Eisenhuettenwes, **45**, 213-18 (1974).

17. H. Flood and W. J. Knapp, J. Am. Ceram. Soc., **46**, 61 (1963).

18. T. Førland, Fused Salts, B. R. Sundheim, Ed., Chap. 3, McGraw-Hill, NY, (1964).

19. K. Niwa and T. Yokokawa, Trans. Jpn. Inst. Met., **10**, 3-7 (1969).

DOI: 10.1149/199413.0008PV

MOLTEN SULFATE-CARBONATE LIQUIDS IN THE EFFLUENTS OF WOOD COMBUSTION FOR POWER PRODUCTION

M. Blander[1], A. D. Pelton[2], R. Cole[1], J. A. Libera[1], and K. W. Ragland[3]
[1]Argonne National Laboratory, Argonne, IL 60439
[2]Ecole Polytechnique, Montreal, PQ H3C 3A7
[3]University of Wisconsin-Madison, Madison, WI 53706

ABSTRACT

Calculations of the combustion effluents of aspen wood chips indicate that molten and solid $K^+,Ca^{2+}/CO_3^{2-},SO_4^{2-}$ solutions were formed. At 4 atm above 1000°C, a potassium sulfate-rich liquid forms; a corrosive carbonate-rich liquid forms between 875-800°C. These results suggested increasing the temperature range of operation of a gravel bed combustor in a test of a gravel-bed-combustor/gas-turbine system from 800-900°C to 900-1000°C which improved the bed performance considerably. A method deduced for hot gas cleanup could be effective enough to eliminate condensates on the turbine at lower temperatures.

INTRODUCTION

Wood is a renewable fuel that is an alternative to fossil fuels[1-9]; it has much lower contents of sulfur and heavy metals than coal, the ash may be returned to the soil and its' use does not increase atmospheric CO_2. Equilibrium calculations of the inorganic chemistry of the combustion of aspen wood in a gravel-bed-combustor-gas turbine system are presented and discussed with regard to molten salt deposits in the gravel bed and on the turbine[1-2]. These calculations suggest means for avoiding the observed deleterious effects of molten salt deposition in such systems.

CALCULATIONS OF COMBUSTION CHEMISTRY

The calculations were made on the FACT computer program at Ecole Polytechnique in Montreal, which uses the CHEMSAGE[10] computer program for free energy minimization. The FACT system has a large database of more than 6000 solid, liquid, and gaseous species and is flexible enough to allow one to incorporate theoretical equations that describe solid and liquid solutions. Calculations of the chemistry of the relevant ternary reciprocal molten and solid salt systems, $K^+,Ca^{2+}/CO_3^{2-},SO_4^{2-}$, were made possible by incorporating the equations of the Conformal Ionic Solution Theory for this system[11,12] and data deduced from an analysis of the available phase diagrams[13] for the four subsidiary binaries. This procedure, in effect, calculates the stabilities and phase diagrams of the ternary system as well as the activities of the constituents for pertinent ranges of temperatures and pressures. Because there are, apparently, no ternary compounds, the Conformal Ionic Solution theory makes it possible to predict the detailed properties of the ternary system from the known properties of the subsidiary binaries.

The specific wood chosen was aspen, which had been used as fuel in tests of a wood-burning gravel-bed combustor developed at the University of Wisconsin-Madison to power a gas turbine[1-5]. Analysis of the wood showed (in wt %) 85.12 volatiles, 13.66 fixed carbon, and 0.72 ash. The elemental analyses (in wt % on a dry basis) are C-51.57, H-6.24, nitrogen 0.47, sulfur 0.02, and oxygen 39.52. The elemental composition of the ash (in ppm) is Ca-211,700, K-112,500, Mg-35,550, P-11,800, S-7000, Zn-3400, Fe-2600, Mn-1,400, Al-1400, Na-600, B-500 and Cu-300. The wt. % of sulfur (relative to the total weight of wood) from the ash is 0.05, which is about 25% of the relatively low sulfur content of the wood. The elemental analyses of the ash does not add up to 100% because light elements (largely carbon and oxygen) were not included in the analyses.

In order to decrease the complexity of the calculation, we left out three minor elements that play a small role in the degradation of the system performance (Zn, Cu, and Na). The burning of 100 grams of wood was simulated with a large excess of air at temperatures ranging from 700°C to 1150°C. The final gas content of unburned oxygen at 750°C was 4.06 mol %. Table I shows the calculated compositions of the gas phase for constituents present at over 10^{-6} mole fraction at one pressure each for three temperatures (i.e., 750°C, 900°C and 1050°C). Similar calculations were made at 11-13 different temperatures at each of the pressures. The results in Table I illustrate the general trends and provide important clues on methods for eliminating problems in real systems. A significant concentration of potassium is present in the gas phase as KOH molecules. If the total input amount (0.081 g) of potassium was in the 30.69 moles of the gas phase as KOH, it would constitute 6.8×10^{-5} mole fraction. At 1050°C, about 30% and 47% of the potassium precipitated (as sulfates) at 1 atmosphere and at 4 atmosphere, respectively, has precipitated. At 900°C (as we will see later, after sulfates have largely precipitated) only 60% (at 1 atm) and 63% (at 4 atm) of the KOH has formed a sulfate condensate. At 750°C 95% (at 1 atm) and 99% (at 4 atm) of the KOH has precipitated (as sulfate and carbonate). These results and the very low sulfur content of the gas (~ 10^{-9}) provide an important clue in improving the performance of a wood-burning power system. Because the molar ratio of sulfur to potassium in aspen wood is 0.3, there is not enough sulfur (as SO_2) to react with the KOH at high temperatures (e.g., above 900°C), and KOH persists in the gas phase to lower temperatures, where CO_2

reacts with the remaining KOH to form carbonates, which can have a negative impact on the performance of a wood-burning power system.

Table I. **Calculated Gas Compositions (Mole Fraction) at 750, 900, and 1050°C at 1 and 4 Atmospheres. (The total moles of gas were always close to 30.69 moles.)**

		1 atm	4 atm
750°C	N_2	0.71863	0.71869
	CO_2	0.13986	0.13978
	H_2O	0.10085	0.10086
	O_2	0.04064	0.04064
	NO	1.9 x 10^{-5}	1.9 x 10^{-5}
	KOH	3.1 x 10^{-6}	7.4 x 10^{-7}
	NO_2	3.8 x 10^{-7}	7.5 x 10^{-7}
900°C	N_2	0.71857	0.71856
	CO_2	0.13988	0.13988
	H_2O	0.10084	0.10084
	O_2	0.04061	0.04062
	NO	7.4 X 10^{-5}	7.4 X 10^{-5}
	KOH	2.7 X 10^{-5}	2.5 X 10^{-5}
	OH	1.3 X 10^{-6}	8.9 X 10^{-7}
	NO_2	6.1 X 10^{-7}	1.2 X 10^{-6}
1050°C	N_2	0.71848	0.71849
	CO_2	0.13988	0.13988
	H_2O	0.10082	0.10083
	O_2	0.04054	0.04054
	NO	2.1 X 10^{-4}	2.1 X 10^{-4}
	KOH	4.8 X 10^{-5}	3.6 X 10^{-5}
	OH	8.4 X 10^{-6}	5.9 X 10^{-6}
	SO_2	5.3 X 10^{-6}	3.7 X 10^{-7}
	NO_2	8.9 X 10^{-7}	1.7 X 10^{-6}

Most of the solid condensed phases formed at the highest temperatures in the calculations (1150°C). All were unreactive and persisted to temperatures of about 800°C and sometimes 700°C, as low as we went in our calculations, 700°C. These compounds are all benign, so, we will not discuss them here.

The total calculation, also included a calculation of the condensation of a calcium-potassium/carbonate-sulfate assemblage of liquid and solid solutions and solid carbonates (Table II) in equilibrium with the gas phase (Table I) and all the other solid compound phases. The calculation required the analyses of known phase diagrams for such systems,[13] which contain information on both liquid and solid solutions, and the incorporation of fundamental statistical mechanical equations (the Conformal Ionic Solution Theory) for these complex solutions, (defined as "reciprocal salt solutions").[11,12] These equations provide a reliable means for predicting the properties of such solutions with a small amount of phase diagram data[13] and data on the free energies of formation of the compounds formed.[14] Analyses of the four binary phase diagrams led to values of the parameters describing the non-ideality of the subsidiary binary liquid and solid solutions. These parameters and the free energies of formation of $CaCO_3(l)$, $CaSO_4(l)$, $K_2CO_3(l)$, $K_2Ca_2(CO_3)_3$ and $K_2SO_4(l)$ are all one needs to calculate the ternary phase diagram and the activities of all the constituents of the solution phases.

Besides relatively large amounts of carbonate solids, there was a significant amount of liquid both at high temperatures (>1000°C) and at lower temperatures, as well as solid solutions all containing Ca^{+2}, K^+, SO_4^{2-}, and CO_3^{2-}. These liquids and solids contain various amounts of these four ions and have compositions that can be characterized by two of the four cation and anion fractions:

$$X_K = N_K/(N_{Ca} + N_K) = 1 - X_{Ca} \qquad [1]$$

$$X_{CO_3} = N_{CO_3}/(N_{SO_4} + N_{CO_3}) = 1 - X_{SO_4} \qquad [2]$$

where N_i is the number of moles of the designated ions. The total number of moles of the solid or liquid solution, N_T, given in Table II is calculated as follows:

$$N_T = N_{SO_4} + N_{CO_3} = (N_K/2) + N_{Ca} \qquad [3]$$

Examination of Table II reveals that the solid solutions formed are mainly potassium sulfate, with a small amount of calcium and carbonate ions in solid solution. The high-temperature (1000-1025°C) liquid is largely molten potassium sulfate with a relatively small concentration of calcium sulfate, which decreases with decreasing temperature, and even smaller amounts of carbonates. These high-temperature liquids can be avoided by operating the gravel bed at temperatures ≤ 1000°C at 4 atm. However, at 4 atm, molten carbonate liquid also forms at lower temperatures (below 875°C). These liquids are largely mixtures of potassium and calcium carbonates and constitute a major condensate with undesirable physical and corrosive properties in this system.

Table II. Amounts of Carbonate-Sulfate Solids and Liquids Condensed from Combustion Effluents

P(atm)	T°C	Liquid Soln.			Solid Soln.			$CaCO_3$	$K_2Ca_2(CO_3)_3$
		moles	X_K	X_{CO3}	moles	X_K	X_{CO3}	moles	moles
1	1050	4.6×10^{-4}	0.788	0.001	--	--	--	--	--
	1000	6.0×10^{-4}	0.874	0.001	--	--	--	--	--
	975	--	--	--	6.2×10^{-4}	0.989	0.000	--	--
	950	--	--	--	6.2×10^{-4}	0.994	0.000	--	--
	900	--	--	--	6.3×10^{-4}	0.999	0.002	--	--
	850	--	--	--	6.4×10^{-4}	1.000	0.021	--	--
	825	--	--	--	6.6×10^{-4}	1.000	0.061	--	--
	800	--	--	--	7.2×10^{-4}	1.000	0.139	--	--
	775	--	--	--	7.3×10^{-4}	1.000	0.141	--	1.4×10^{-4}
	750	--	--	--	6.5×10^{-4}	1.000	0.049	--	3.3×10^{-4}
	700	--	--	--	6.5×10^{-4}	1.000	0.035	2.5×10^{-3}	3.8×10^{-4}
4	1150	1.8×10^{-4}	0.718	0.004	--	--	--	--	--
	1100	5.4×10^{-4}	0.788	0.004	--	--	--	--	--
	1050	6.1×10^{-4}	0.876	0.004	--	--	--	--	--
	1025	6.1×10^{-4}	0.913	0.005	--	--	--	--	--
	1000	--	--	--	6.2×10^{-4}	0.993	0.001	--	--
	950	--	--	--	6.3×10^{-4}	0.997	0.003	--	--
	900	--	--	--	6.3×10^{-4}	0.998	0.005	--	--
	875	--	--	--	6.8×10^{-4}	1.000	0.089	--	--
	850	3.9×10^{-4}	0.598	0.955	6.7×10^{-4}	1.000	0.090	--	--
	825	1.0×10^{-4}	0.509	0.956	6.1×10^{-4}	0.999	0.048	--	--
	800	--	--	--	6.6×10^{-4}	0.999	0.057	3.1×10^{-4}	3.3×10^{-4}
	750	--	--	--	6.5×10^{-4}	0.999	0.045	2.5×10^{-4}	3.7×10^{-4}
	700	--	--	--	6.5×10^{-4}	1.000	0.035	2.5×10^{-4}	3.9×10^{-4}

APPLICATION TO GRAVEL-BED COMBUSTOR/GAS TURBINE SYSTEM

We applied our calculations to tests of the gravel-bed combustor developed at the University of Wisconsin-Madison to power a gas turbine.[1-5] This combustor burns wood chips in a downdraft mode on top of a refractory MgO gravel bed. The gravel bed holds up the wood chips, facilitates carbon burnout, and holds up some of the ash. The fuel bed was typically about 10 cm deep on top of the gravel. Because of the high downward air flow, the combustion zone in the fuel bed was only 3- to 5-cm thick. The combustor was run with excess air to limit the combustor temperature. An ash layer built up with time at the fuel/gravel interface, and some of the ash passed through the bed to the turbine.

An Allison Model 250 gas turbine (designed to be run at a full power of 300 kW at 1000°C and 7 atm) was directly connected to the combustor and run for 250 hours. In these tests,[2] the turbine inlet temperature was 800-900°C, with some excursions above 1000°C, and the inlet pressure was 4 atm. The average turbine blockage (percentage decrease of flow per unit time for a fixed pressure drop) due to deposits binding the gravel chips was 0.19% per hour, which is excessive for long-term operation. The turbine blade deposits[5] were primarily CaO, MgO, and K_2SO_4, and no carbonates were detected, probably because they precipitated in the relatively cool gravel bed. In other tests, a pressure control valve was used in place of the turbine. These tests established that MgO was a much better bed material than the original acidic Al_2O_3, which probably reacted with the base, KOH. As suggested by our calculations in Table II, we recommended running the bed at higher temperatures (900-1000°C). This change gave considerably less bed deposition than running at 800-900°C.

The major factor for binding the MgO chips together at 800-900°C is likely to be the formation of a carbonate-rich sulfate-carbonate liquid (Table I), which can be present in larger amounts than the solid compounds. For example, at 4 atm and 825°C, the amount of a liquid rich in calcium-potassium carbonate was 1.0×10^{-3} mol whereas, except for CaO (3.06×10^{-3} mol), which is a high-melting, relatively benign solid, the amounts of other solids are low. The formation of an alkali-calcium/carbonate-sulfate liquid is likely to predominate the binding of MgO gravel chips upon crystallization of the liquid. Although the solid compounds can have some influence on degradation of bed performance, that effect is likely to be small relative to the influence of alkali-calcium/carbonate-sulfate liquids. Our calculations indicate that avoidance of regimes of temperatures and pressures were such liquids might form (Table II) appears to be one useful strategy for improving bed performance. For example, at pressures of 1-4 atm, condensation of liquids in the gravel bed could be avoided at about 900-1000°C.

There are some indications that the formation of these corrosive liquid melts anywhere in the system could be avoided. First, we see in Table II that they did not form at 1 atm much below 1000°C. If the gas were sent through a turbine at a fairly high pressure, the adiabatic expansion of the gas would lead to both lower pressures and temperatures. We see in Table II that the temperature range for stability of this carbonate-rich liquid narrows in going down in pressure so that there may be a pathway for the adiabatic expansion of the gas from high pressure to 1 atm, where no liquid condenses. In addition, one might be able to introduce acidic materials (SiO_2, Al_2O_3) to precipitate the potassium as solids which can be physically separated from the gas phase.

DISCUSSION

The original purpose of our investigation was to improve the operation of a gravel-bed wood combustor operating in the vicinity of 4 atm at temperatures of 800-900°C. As can be seen in Table II, a molten carbonate forms in this range of temperatures at that pressure. The formation of a relatively large amount of molten carbonate is likely to be a primary cause for rapid degradation in the performance of the gravel bed. Raising the bed temperatures to a range of 900-1000°C appears to solve the major part of the problem. Tests of this conclusion indicated that molten ash deposition in the gravel bed was greatly reduced when operating at 900-1000°C rather than 800-900°C.

Although raising the temperature solves the problem with the gravel-bed-combustor, the problem could arise again downstream in the turbine. In the expansion through the turbine, the gas would expand from a high temperature and pressure to atmospheric pressure and an intermediate temperature. During this expansion, condensation of a liquid phase as corrosive (and erosive) as the carbonates must be avoided. Even the solid phases (sulfates and carbonates) could pose a significant problem, since solid condensates could erode high-speed turbine rotors. The best method for avoiding condensation in the turbine is hot-gas cleanup, which can be performed by additives that react to form solid condensates that can be separated with cyclones and/or filters. The basic KOH molecule, leads to most of the condensation below 1000°C. Acidic additives such as SiO_2 and Al_2O_3 could react with KOH to form separable solids. For example, a mixture of SiO_2 and Al_2O_3 would be possible reactants which form solid products that are separable by a cyclone and/or filter. Yet another method is suggested by the calculations, which indicate that KOH would react with a higher concentration of added SO_2 to form K_2SO_4. One should be able to reduce the amount of KOH considerably by increasing the partial pressure of SO_2. This can be done by adding a small amount of SO_2 gas (roughly equivalent to the amount of KOH) or a relatively unstable sulfate such as $MgSO_4$ or $CaSO_4$. If the residual pressure of SO_2 is raised from calculated values of the order of 10^{-9} to 10^{-5} mole fraction in the process, the amount of gaseous KOH would decrease by 99% at equilibrium at 1000°C. At lower temperatures, the levels of KOH in the gas would be even lower. If these acidic compounds (Al_2O_3 + SiO_2 or SO_2 or $MgSO_4$ or $CaSO_4$) are added before entry into a cyclone and/or filter system, one might be able to separate the condensing solid sulfates. After separation of solids in a cyclone/filter system, one might react a small amount of unreacted SO_2 with a fixed bed of a basic material or might introduce a basic additive to reduce the SO_2 emissions to levels well below environmental constraints. The disadvantage of the use of SO_2 is that it must be carefully controlled to guarantee conformance with environmental laws. The advantage of gaseous SO_2 is that it would tend to react more completely with bases than solid acidic materials and can more readily be metered and mixed with the combustion effluents. The significance of our calculations is that they provide baseline data which can be combined with chemical, physical, and operational data on a wood-burning-combustor turbine system operating at about 4 atm to define the chemistry and to deduce solutions to problems which arise. In addition, our calculations have provided solutions to problems with a gravel bed combustor and possible solutions to potential problems with turbines caused by condensates.

REFERENCES

1. K. W. Ragland and D. J. Aerts, "100 Hour Test of the Pressurized Woodchip-Fired Gravel Bed Combustor," DOE/CE/40735-3 (August 1992).
2. K. W. Ragland, D. J. Aerts, C. A. Palmer, and S. Waslo, "Evaluation of a Woodchip-Fired Cogeneration System Using a Gravel Bed Combustor," 26th Intersoc. Energy Conversion Eng. Conf. Vol. 5, pp. 444-449 (1991).
3. Purnomo, D. J. Aerts, and K. W. Ragland, "Pressurized Downdraft Combustion of Woodchips," Twenty-Third International Symposium on Combustion, The Combustion Institute, pp. 1025-1032 (1990).
4. C. A. Palmer and K. W. Ragland, "Dynamic Simulation of a Biomass Fired Downdraft Combustor-Gas Turbine," IGTI ASME Cogen-Turbo, Book No. 100333, pp. 165-172 (1992).
5. K. W. Ragland and D. J. Aerts, "Development of a Gravel Bed Combustor for a Solid Fueled Gas Turbine-Phase II," US DOE Report DE/CE40735-2 (1992).
6. "Electric Power Monthly," DOE/EIA-0226(92/07), March 1992 data. July 1992 data.
7. "Waste Wood Fired Plant at Sauder Woodworking," Power and Energy Briefs, Vol. 29, SFT Inc., Toledo, OH (September 1992).
8. K. Sheinkopf, "The Growth of Biomass," Independent Energy, pp. 66-68 (November 1992).
9. "Hepple Announces Canadian Wood-Fired Plant," Cogeneration, 9 (5), 13 (October-November 1992).
10. G. Eriksson and K. Hack, "Chemsage - A Computer Program for the Calculation of Complex Chemical Equilibria," Metall. Trans. 21B, 1013 (1990).
11. M. Blander and S. J. Yosim, "Conformal Ionic Mixtures," J. Chem. Phys. 39, 2610 (1963).
12. M. L. Saboungi and M. Blander, "Topology of Liquidus Phase Diagrams of Charge Asymmetric Systems," J. Am. Ceram. Soc., 58, 1-7 (1975).
13. Phase Diagrams for Ceramists, Vols. II-VII, Amer. Ceramic Soc., Westerville, OH (1969-1989).
14. M. W. Chase et al., JANAF Thermochemical Tables, 3rd Ed., Vols. I and II, Amer. Chem. Soc., Washington, DC (1986).

DOI: 10.1149/199413.0016PV

CORRELATIONS BETWEEN ELECTRONIC POLARIZABILITY AND IONIC COORDINATION FOR LiCl-CsCl

Mamoru Endo, Yuzuru Sato and Tsutomu Yamamura
Department of Metallurgy, Faculty of Engineering
Tohoku University, Sendai, 980 Japan

ABSTRACT

The electronic polarizabilities of LiCl-CsCl binary melts have been determine. The electronic polarizabilities of the binary melts deviate negatively from additivity. To understand the experimental results, the effect of ionic coordination on electronic polarization has been investigated. The semi-empirical equations correlating the electronic polarizability and the coordination number and inter-ionic distance have been developed by using an *ab initio* molecular orbital calculations. Since experimental distribution functions are not available, the inter-ionic distances and coordination numbers of the melts were estimated by using an MD simulation. The electronic polarizabilities of the binary melt have been derived by using the semi-empirical equation obtained from the polarizabilities observed in LiCl and CsCl single melts. The inter-ionic distances and coordination numbers were estimated by using an MD simulation. The estimated electronic polarizabilities deviated negatively from additivity just as the experimental values did.

An alkali halide melt is a typical ionic liquid, and is composed entirely of positively and negatively charged ions. But, it should be noted that the electronic polarization that exists even in such typically ionic melts as the alkali halides may cause a local ionic interaction(1) and may influence the transport properties(2)(3)(4) of the melts. Electronic polarizabilities of ions are important parameters for the investigation of dielectric, photoelastic, thermal and lattice dynamic properties of matter. It has been found that the electronic polarizability of alkali halide single melts has a positive temperature dependence(5)(6). It was thought that the positive temperature dependence was caused by a decrease of the coordination number between an ion and its nearest neighbors with an increase in temperature.

Therefore, the variation of the coordination number on mixing of the salts may affect the electronic polarizability of the constituents. It is therefore of interest to examine the correlation between the electronic polarizability and ionic coordination for the binary melt.

In order to study the mixing effects on the electronic polarizabilities in the binary melts, the coordination number and the inter ionic distance of the binary melts have been investigated by using the molecular dynamics simulation, MD. The correlations between the electronic polarizability and the ionic coordination have been studied by using an *ab initio* molecular orbital calculation. This paper reports the results of the examination done on the LiCl-CsCl binary melts.

Experimental and Calculation Technique

Electronic Polarizability

The electronic polarizability, α, of the melt is determined from the density, ρ, and the refractive index at the infinite wave length, n_∞, by the use of Clausius-Mossotti equation(7),

$$(n_\infty^2 - 1)/(n_\infty^2 + 2) = (4\pi\alpha N\rho)/(3\varepsilon_0 M), \tag{1}$$

where ε_0 is the permitivity of vacuum, N is Avogadro's number and M is the molecular weight. The density was measured by using a manametric method(8) and the refractive index was measured by using a minimum deviation method(9)(10) over the entire composition of the binary melts.

Molecular Dynamics Simulation

The following pair potential, the Born-Mayer Huggins type, was used for the MD calculations,

$$\varphi_{ij} = \frac{z_i z_j}{4\pi\varepsilon_0 r} e^2 + A_{ij}\, b \exp\left(\frac{\sigma_i + \sigma_j - r}{\rho}\right) + \frac{c_{ij}}{r^6} + \frac{d_{ij}}{r^8}, \tag{2}$$

where r is the distance between ions i and j, z_i the ionic charge, e the elementary charge, ε_0 the permitivity of vacuum, the Pauling factor, σ_i ionic radii, ρ softness parameter, and c_{ij} and d_{ij} are dispersion parameters. The parameters for the pair potentials of the mixtures were obtained by an interpolation analogous to the combining rules indicated by Larsen et al(11).

Two hundred anions and 200 cations were contained in basic cells in all cases. The cell sizes are calculated from the experimental densities. After 1,000 steps to allow equilibration, the configurations for the following 20,000 steps were sued for the various calculations of the properties for each compound with 5fs per step under NVT ensemble boundary conditions over the entire composition range of the binary melts.

Molecular Orbital Calculation

The electronic polarizabilities of the F^- ion in various environments were computed by the *ab initio* molecular orbital calculation, HONDA 7.01. In order to understand the effects of the inter-ionic distance and the coordination number on the electronic polarizabilities of isolated ions, the method of ab initio molecular orbital calculation was used. To save time for the calculation and to have qualitative results, F^- ions instead of Cl^- were chosen. The cation's polarizabilities were ignored in the calculation. The polarizabilities were obtained by coupled Hartree-Fock (CHF) theory(12). The anion basis sets were chosen to give good agreement with the experimental polarizability at CHF levels. The crystalline states were simulated by placing F^- ion in the cubic NaCl type and the AnS type lattices of point charges with various spacings.

Results and Discussion

The excess molar volumes observed are plotted against composition for LiCl-CsCl binary melts in Fig. 1. The molar volumes of the melts deviate positively from additivity. This deviation implies a change of coordination number of ions on mixing for the binary melts compared with LiCl and CsCl single melts. The deviations of the electronic polarizabilities from additivity fro the binary melts are plotted in Fig. 2. The deviations are negative over the entire composition range. This negative deviation also implies a change of coordination of ions on mixing compared with LiCl and CsCl single melts, which is similar to the molar volume behavior mentioned above.

The inter-ionic distance and coordination number were determined by the analysis of the pair correlation function obtained in the MD simulation after 20,000 steps with 5fs per step under NVT ensemble boundary conditions. The temperature dependences of the coordination number for Licl and CsCl single melts are shown in Fig. 3. The inter-ionic distance decreases with increasing temperature as seen in Fig. 3. The inter-ionic distances decrease slightly with increasing temperature. Ther inter-ionic distance and coordination number of LiCl-CsCl binary melts at 950K are plotted against composition in Figs. 4 and 5, respectively. The inter-ionic distance and the coordination number obviously change with composition. These results suggest that the inter-ionic distance and the coordination number may be important factors affecting the electronic polarizability of alkali halide melts.

The linear correlation, Eq. (3), between the inter-ionic distance r and the electronic polarizability α of alkali halides was proposed by Wilson and Curtis$^{(13)}$ for the crystalline state.

$$\log \alpha = \log \alpha_0 + k \frac{1}{r^2}, \tag{3}$$

where α_0 is the polarizability of the free ion and k is a constant. On the other hand, in the molten state, the coordination number changes continuously with changes in temperature, as clearly shown in Fig. 3, while that of the crystalline state remains constant. Therefore, to understand the temperature dependence of the electronic polarizability of the melt the coordination number should be also considered as a parameter. To look into the relationships among α, n and r , the electronic polarizability has been calculated by using an MO method for the various n and r taking fluorine ion, F^-, as the reference. The calculated log (α)s are plotted against r^{-2} and n in Figs. 6 and 7, respectively. As previously shown in Fig. 7, there is a linear relation between log (α) and the coordination number was found under conditions of constant ionic-distance. Therefore, it may be reasonable to assume Eq. (4), which is linear in k and r^{-2}.

$$\log \alpha^i = \log \alpha_0^i + k^i \frac{n}{r^2}, \tag{4}$$

Where superscript i refers to LiCl or CsCl and n is the coordination number. The temperature dependence of the electronic polarizabilities observed and the inter-ionic distance and coordination number calculated by using the MD simulations are treated by least square regression analysis based on Eq. (4) for LiCl and CsCl single melts. The electronic polarizability α^{est} if the binary melt were estimated from the electronic polarizabilities of single melts by Eq. (5) on the basis of the additive rule,

$$\alpha^{est} = (1 - x)\,\alpha^{LiCl} + x\,\alpha^{\mathrm{CsCl}} \tag{5}$$

where x is the mole fraction of CsCl.

The deviations of the estimated electronic polarizabilities from additivity for the binary melts are plotted in Fig. 2. The electronic polarizabilities of the binary melts deviate negatively from the additivity values. This behavior agrees with experimental results. Temperature and composition dependences of the electronic polarizabilities in molten salts can be understood in terms of the inter-ionic distance and coordination number.

Summary

The electronic polarizabilities of LiCl-CsCl binary melts have been determined. The negative deviations of the electronic polarizabilities of the melts from the additive values were observed. The inter-ionic distances and coordination numbers for the partial distributions were determined by using MD simulations for the binary melts. The electronic polarizabilities of the anions with various coordination numbers and inter-ionic distances have been calculated by using the MO method. A semi-empirical equation correlating the electronic polarizability, the coordination number and inter-ionic distance has been derived. The electronic polarizabilities of the binary melts were estimated by using this semi-empirical equation which was determined from the experimental coordination number derived from the MD simulation for the binary melts. The estimated electronic polarizabilities deviate negatively from the additive values in a similar manner to the experimental values.

References

(1) S. Zuca, Rev. Roumaine Chim., **23** (1978), 829.

(2) E.R. V. Artsdalen and I.S. Yaffe, J. Phys. Chem., **59** (1955), 188.

(3) O.J. Kleppa and L.S. Hersh, J. Chem. Phys., **42** (1965), 1309.

(4) H. Ohno and K. Furukawa, J. Chem. Soc., *Faraday Trans*. 2, **79** (1983), 463.

(5) M. Endo, T. Hayasaka, Y. Sata, T. Yamamura and T. Ejima, Netsu Bussei, **5** (1991), 6.

(6) M. Endo, A. Tanaka, Y. Sato and T. Yamamura, Netsu Bussei, **6** (1992), 162.

(7) J.O. Hirschfelder, C.F. Curtiss and R.B. Bird, Molecular theory of gases and liquids, (1974), 889.

(8) Y. Sato, K.-i. Kobayashi and T. Ejima, J. Japan. Inst. Metals, **43** (1979), 97.

(9) D. Tentri and J.R. Lerma, Optical Engineering, **29** (1990), 160.

(10) M. Endo, S. Mizuno, T. Mizuno, Y. Sato, T. Yamamura and K. Sugimoto, Netsu Bussei, **7** (1993), 8.

(11) B. Larsen, T. Forland and K. Singer, Mol. Phys., **26** (1973), 1521.

(12) P.W. Fowler and P.A. Madden, Phys. Rev. B, **29** (1984), 1035.

(13) J.N. Wilson and R.M. Curtis, J. Phys. Chem., **74** (1970), 187.

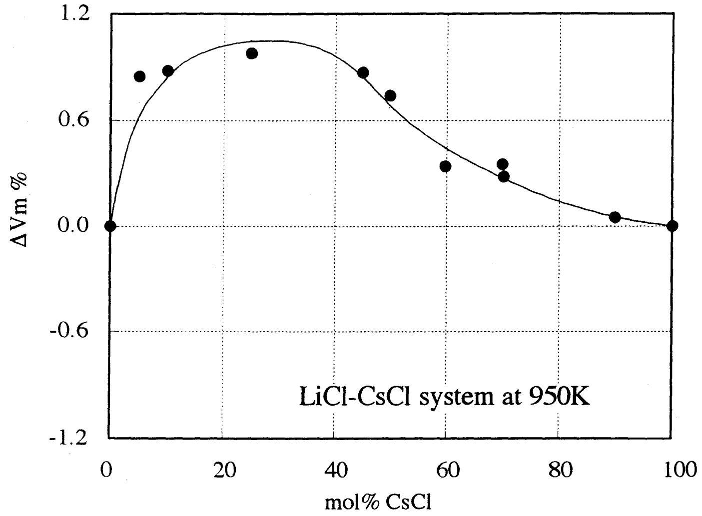

Fig.1 Excess molar volume of LiCl-CsCl binary melt at 950K.

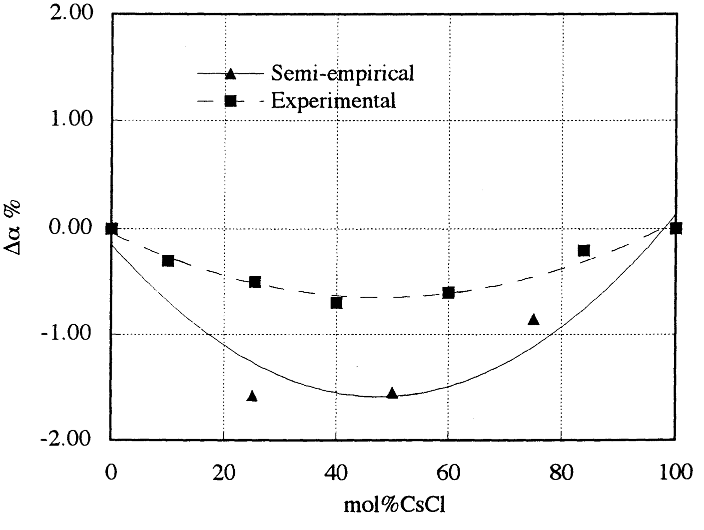

Fig.2 Deviation of electronic polarizability from additive value for LiCl-CsCl binary melt at 950K.

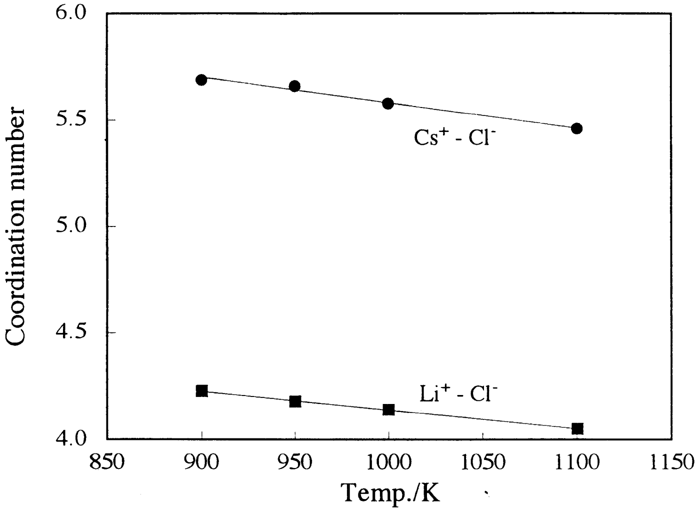

Fig. 3 Temperature dependence of coordination number for LiCl and CsCl single melts at 950K calculated from MD simulation.

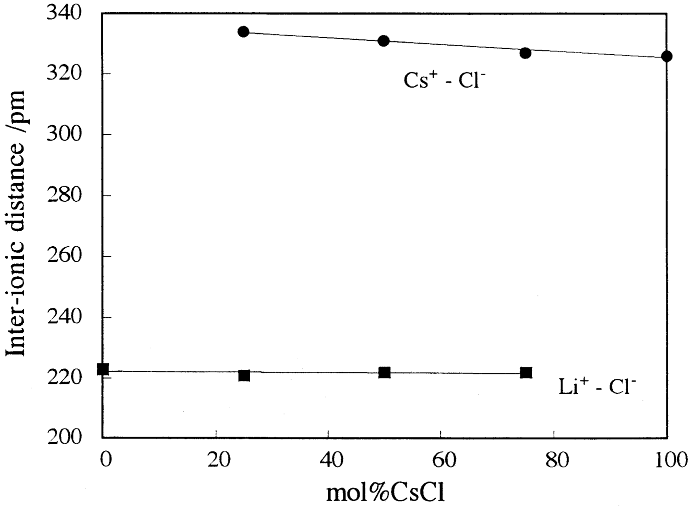

Fig.4 Composition dependence of inter-ionic distance for LiCl-CsCl binary melt at 950K calculated from MD simulation.

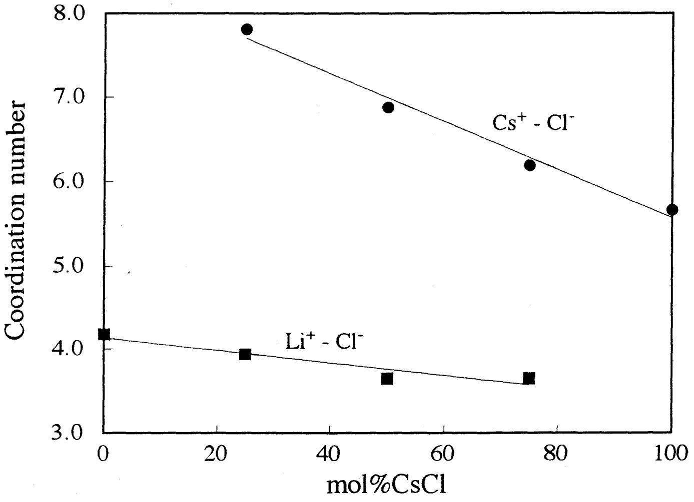

Fig.5 Composition dependence of coordination number for LiCl-CsCl binary melt at 950K calculated from MD simulation.

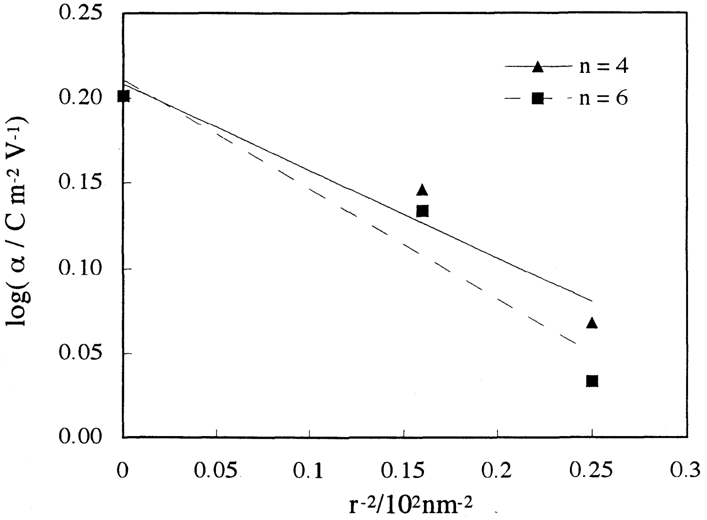

Fig.6 Correlation between electronic polarizability and inter-ionic distance.

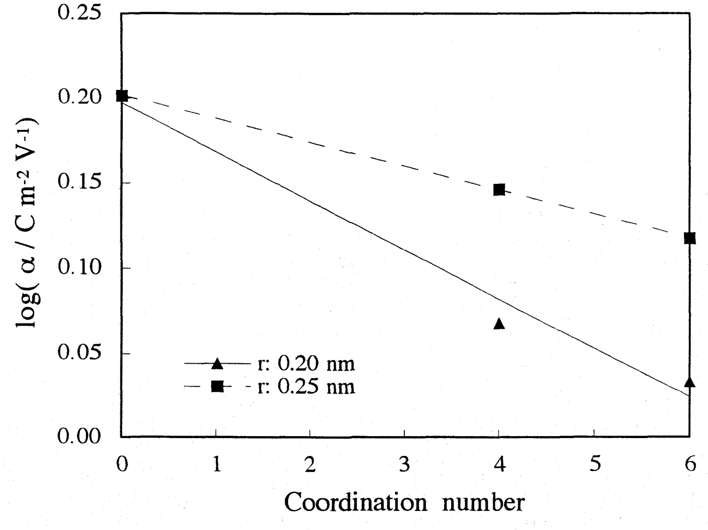

Fig.7 Correlation between electronic polarizability and coordination number for fluoride ion in crystal lattice.

DOI: 10.1149/199413.0026PV

STRUCTURAL MODELLING OF A MOLTEN SALT BY SIMULATED ANNEALING

Jean-Jacques Legendre*, Ludovic Mouron*
and Gérard S. Picard+

Ecole Nationale Supérieure de Chimie de Paris
11, rue Pierre et Marie Curie 75005 PARIS - FRANCE
*Unité de Recherche Modélisation Appliquée
à la Chimie et aux Procédés
Jeune Equipe MEN n°47
+Unité de Recherche Electrochimie Analytique et Appliquée
Unité Associée au CNRS n° 216

ABSTRACT

A new method for limiting structural models during modelling procedures on disordered compounds is desribed. Instead of using the well known periodic boundary, the data derived from neutron diffraction experiments are modified to take into account a spherical limitation of the model. Compared to cubic periodic modelling, this method reduces the computation time and improves model reliability since it introduces no artificial anisotropy. The method has been successfully tested in the structural modelling of molten NaCl.

INTRODUCTION

Until now, the structure of molten salts has been considered to be difficult to obtain. Indeed, as for liquids and amorphous solids, the models are built from experimental data which are mainly derived from diffraction experiments. These experiments use either electromagnetic radiations (X rays) or particles (neutrons). They only provide statistical data about the time and space averaged structure of such disordered objects. Moreover, attempts to obtain the 3D structure has often been considered as useless because most of the physical properties only reflect the average structure. Therefore a statistical description seemed to be sufficient.

Such a description, which is adequate to understand the macroscopic behavior of disordered compounds, is not adapted to the study of chemical reactions in molten salts. In that case it is the short and medium range organization of the molten salt which is of primary importance by strongly influencing the molecules in solution. Therefore, any attempt to model the physicochemical behavior of chemical species in solution has to take into account the structure of the solvent, which has to be known as well as possible. It is the reason why it seemed important to undertake this work in order to obtain a realistic 3D structural model in agreement with the available experimental data.

The structural modelling of disordered compounds is commonly performed by using various techniques based on thermodynamic criteria (Molecular Dynamics or Monte Carlo methods) or on the fit between the model and experimental data. Regardless of the technique, the same method is used for limiting the size of the model: the model is considered to be periodic. However, this limitation induces an artificial anisotropy which degrades the quality of the structural models and increases computation time. We suggest in this paper a new way for bounding the models which improves the quality of the modellings and shortens the calculation time. This new method has been tested in the static modelling of molten NaCl using neutron diffraction data as the experimental basis.

PREPROCESSING OF EXPERIMENTAL DATA

The experimental data which are used in modellings of disordered compounds are derived from the diffracted intensity by standard Fourier Transform processing (1)(2). They are the partial pair distribution functions g++(r), g--(r), g+-(r). The average number of ions located between r and r+dr from a given ion (Nexp(r)) has been chosen as the experimental basis during the optimization process and have been calculated from the experimental partial pair distribution functions. However, these values correspond to unlimited models. Yet, building a structural model that is too large is meaningless since the propagation of order does not exceed 15Å. Therefore, the model has to be limited. Moreover a spatial limitation of the model facilitates modelling operations since it shortens the calculation time. To overcome this problem, periodic boundary conditions have been commonly used to limit the model (3). This choice gives rise to a certain number of problems. The intrinsic anisotropy induced by this type of limitation may influence the geometry of voids in the structural model, thus reducing the quality of the information available from the model. Therefore, we have chosen to limit the model by using the most isotropic limitation: a sphere. Consequently the Nexp had to be corrected with a factor Q which is the self convolution of a 3D slit function with a radius equal to R (4). This correction is isotropic and can be expressed as a function of r/R (R: radius of the model). It is presented in figure 1 and has the following form with x = r/R :

$$Q(x) = 1 - 3x/4 + x^3/16 \qquad [1]$$

MODELLING METHOD

In order to obtain a structural model in agreement with the experimental data, we have chosen simulated annealing as the modelling method. This method belongs to the family of the Monte Carlo methods which are commonly used for optimization, and which have already been used for structural studies on alloys (3), solids (5), surfaces (6) and liquids (7). The main originality of this method is its aptitude not to converge systematically towards the closest local mimima. By this way it is different from classical full deterministic minimization procedures for which the probability of evolution of the modelled system towards states with lower cost function is 1. In the case of simulated annealing this probability depends on a pseudo-temperature with a Boltzmann type relation. This method allows jumps over local minima which are less favorable for the minimization. Therefore it gives deeper minima than purely deterministic methods which only provide the local minimum closest to the starting state.

RESULTS

A model with 396 ions has been built with a good fit with experimental data (98%) (Figure 2). It is limited by a sphere with a radius of 14.4Å which corresponds to the experimental density of molten NaCl (1.55g/cm^3). 10^7 steps have been necessary to obtain a constant value for the cost function. Figure 3 presents a comparison between:

a) the experimental partial pair distribution functions (2),

b) the partial pair distribution functions derived from the present model,

c) the partial pair distribution functions derived from a model generated from a theoretical interionic potential (8). Therefore, this method produces a better fit with experimental data than a theoretical interionic potential for which R=86% up to 10Å. The realism of the correction factor we have used here to take into account the limitation of the model has been checked by determining the local density of a model with 200 ions. Figures 4 clearly show that the local density is relatively constant with the distance to the center of the model and thus is consistent with thermodynamics. If no correction is performed, this density is no longer constant: most of the ions are located near the boundaries of the model since the N(ri)'s corresponding to a high value of r are amplified by the parabolic law:

$$N_{exp+-}(r) = 4\pi D_{-} g_{+-}(r)\, r^2\, \Delta r \qquad [2]$$

N_{exp+-} : Average number of cations located at a distance between r and r+Δr from an anion.
D_{-} : Average number of anions per volume unit.
$g_{+-}(r)$: Partial pair distribution function.

COMPARISON WITH MODELLING USING PERIODIC BOUNDARIES

This method has also been compared with classical methodology using periodic boundaries. As it does not require any artificial repetitions of the model, it takes into account less ions and is therefore less time consuming as it can be seen in figure 5. Moreover, the isotropy of models obtained using spherical or periodic boundaries have been compared. For this purpose, the g(r) have been calculated for each model in two 3Å thick cylindrical slices. For the cubic periodic model, the directions of the slices were 100 and 110. For the spherical model, the slices were perpendicular. As can be seen in figure 6, the spherical models are rather isotropic (the g(r) of the two sections almost coincide), while on the contrary, the cubic models are very anisotropic (the g(r) do not coincide) which is not coherent with the structure of a liquid. These observations give evidence that spherical structural models are much more realistic than periodic models: they do not introduce any artificial anisotropy, which is important even in large cubic models.Therefore, the validity of the structural models previously obtained with a periodic limitation is questionable especially if the geometry of the voids in the models are taken into account for physico-chemical studies.

DISCUSSION

Two very important points have to be emphasized:

1-a model obtained by this method is not unique. Modellings carried out from different initial configurations lead to different models, i.e. models that cannot be superimposed. Notwithstanding, all of these models have common structural features which reflect the common experimental data (6). Therefore, a single model is sufficient for visualizing the main features of molten salt organization.

2- such a model is static even though the experimental data are obtained from moving ions. The diffraction measurements perform a time averaging simultaneously with the space averaging generated by the size of the real sample. If a static model is large enough to simultaneously contain all the main local configurations which appear during the time dependant evolution of the liquid i.e. allowing a good fit with experimental data, then this model is significant.

The main originality of the method we describe here is the way the model is limited. Compared to the periodic limitation of the models, this method produces, with less computation time, more realistic isotropic models of liquids.

REFERENCES

1. J.E. Enderby and S. Biggin in *Advances in Molten Salt Chemistry*, Vol. 5, ed. G. Mamantov, Elsevier (1983) p. 1.

2. S. Biggin and J.E. Enderby, J. Phys. C: Solid State Phys. **15**, 305 (1982).

3. P. C. Gehlen and J.B. Cohen J.B., Phys. Rev. A **139**, 844 (1965).

4. L. Mouron, S. Grandjean, J.J. Legendre and G. Picard to be published in *Computers and Chemistry* (1994).

5. J.J. Legendre and M. Huber, J. Appl. Cryst. **13**, 193 (1980).

6. J.J. Legendre and M. Huber, Surface Science **122**, 137 (1982).

7. R.L. McGreevy and L. Pusztai, Mol. Simul. **1**, 359 (1988).

8. M. Dixon and M.J. Gillan, Phil. Mag. B **43**, 1099 (1981).

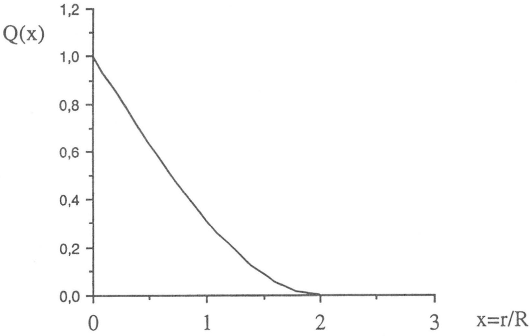

Figure 1: Correction function for a limited spherical model.

Figure 2: 5Å thick slice of a model with 396 ions.

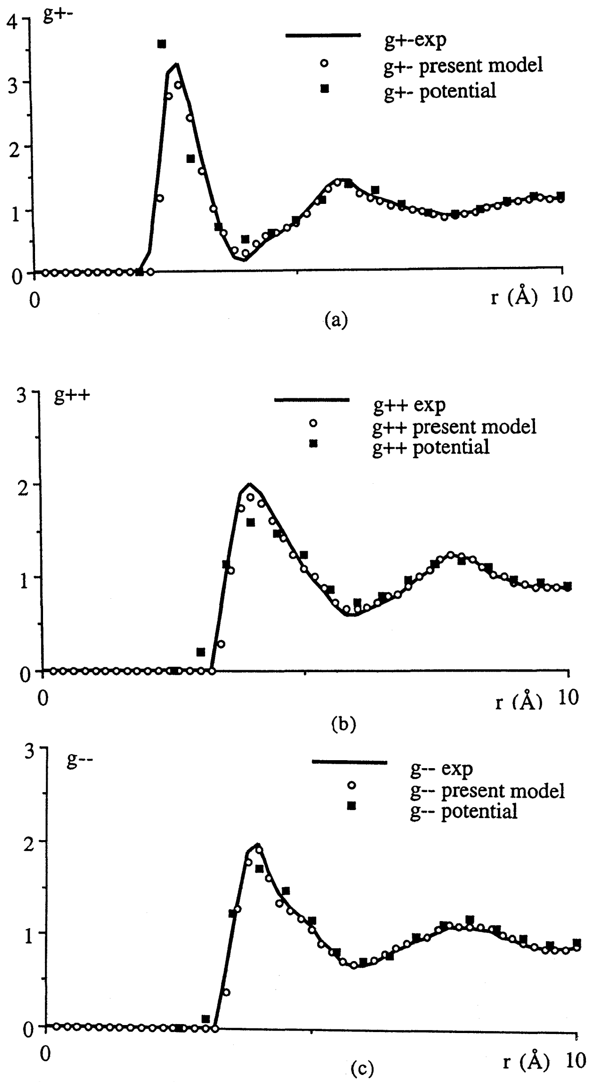

Figures 3(a)(b)(c): Comparison of the partial pair correlation functions derived from the experiment and from models built by a theoretical interionic potential and by the present method. The reliability factor obtained with the present method is 96% which is better than what was obtained with a theoretical potential (86%).

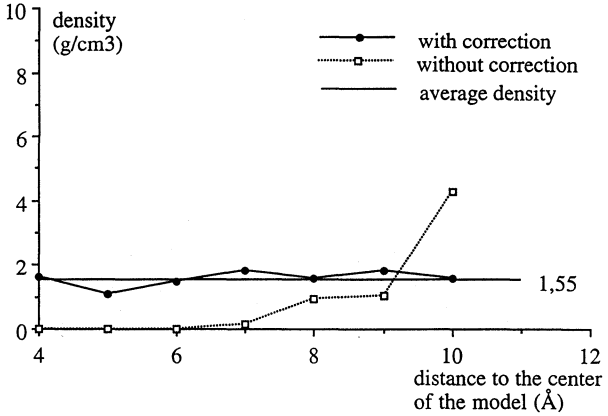

Figure 4: Local density of a model with 200 ions with and without a correction of the N(ri). The model obtained with a correction has a local density which is approximately constant unlike the one obtained without any correction.

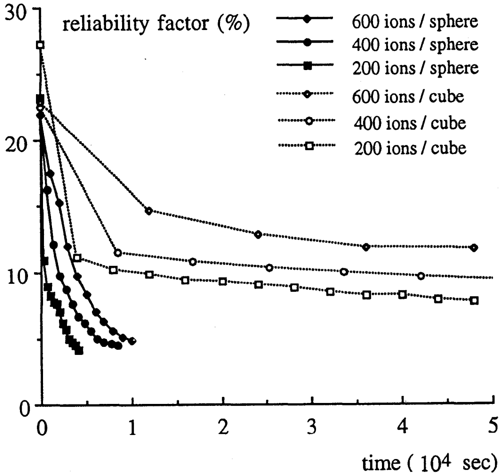

Figure 5: Comparison between spherical and periodic modelling. Computational effort for models of increasing size on a Silicon Graphics Indigo R4000 workstation.

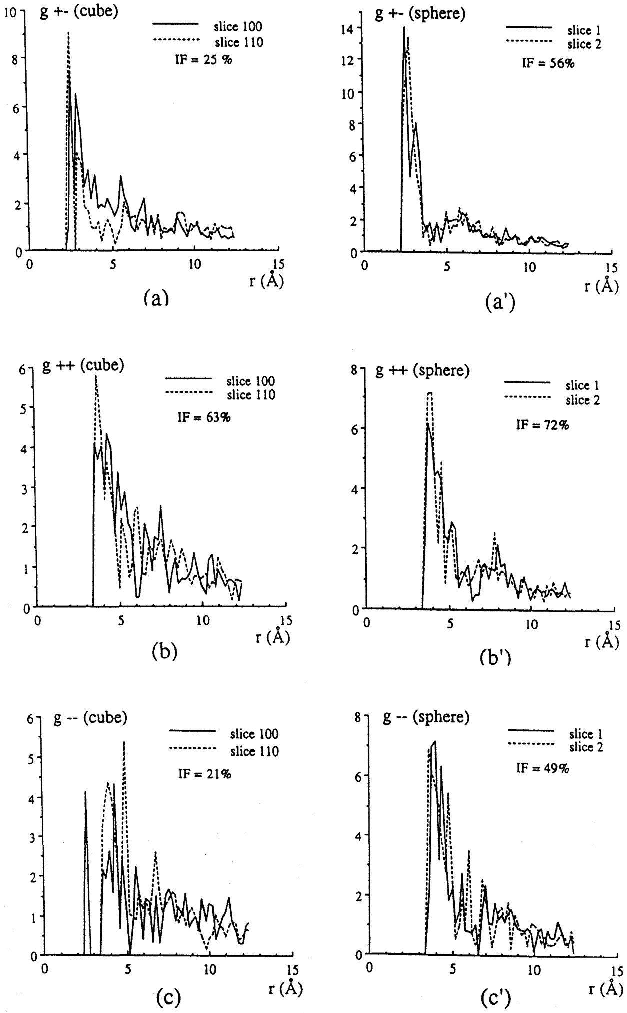

Figures 6: Comparison between a spherical and a cubic periodic model. Each of these figures presents the comparison between the g(r) of two different slices of a model. The slices are perpendicular for the spherical model and they coincide with the 100 and 110 directions for the cubic model. The models contain 400 ions and the slices 68 ions.

DOI: 10.1149/199413.0034PV

BOND ENERGY INVESTIGATIONS FOR ALUMINUM(III)-FLUORIDE COMPLEXES RELATIVE TO CRYOLITIC MELTS. PART I: POTENTIAL ENERGY SURFACE FOR THE DISSOCIATION OF PURE ISOLATED COMPLEXES

Frédéric C. BOUYER, Gérard S. PICARD
Jean-Jacques LEGENDRE+, Sylvie BOUVET* and Yves BERTAUD*

Laboratoire d'Electrochimie Analytique et Appliquée
(Unité associée au C.N.R.S., URA 0216)
+ Laboratoire de Modélisation Appliquée à la Chimie et aux Procédés
(Jeune Equipe du Ministère de l'Education Nationale n°47)

Ecole Nationale Supérieure de Chimie de Paris
11, rue Pierre et Marie Curie - 75231 PARIS Cedex 05 - France

* Pechiney, Centre de Recherche de Voreppe
BP.27 - 38340 Voreppe - France

ABSTRACT

Experimental techniques for structural and dynamics studies are difficult to use in cryolite melts. Therefore a theoretical approach based an quantum chemical calculations (with the formalism of the Density Functional Theory) have been carried out. Results concerning stable structures and Al-F bond dissociations of aluminum(III)-F(-I) complexes are presented. It is shown that energy barriers can be obtained by breaking Al-F chemical bond and the relaxation effetcs on its neighbouring bonds. Potential energy surface relative to bond dissociations is given.

INTRODUCTION

Several experimental techniques, such as X-ray diffractions(1-4), neutron diffusion scattering(5-10), IR and Raman spectroscopies(11-17), are useful for studying structures in molten salts. Due to hard experimental conditions (high working temperatures, corrosiveness, toxicity, ...), some melts are difficult to investigate.

Very few experimental data on structural entities in such melts are available. Only conformational and vibrational studies have been investigated on melts at lower temperature and comparisons with structural species determined in such experimental conditions have been proposed. Therefore theoretical studies have been recently developed(18-25), most often based on quantum chemical computations and molecular dynamics calculations. These techniques can give vibrational spectra and conformational analyses, that are important for chemical aspects and reactivity. In our laboratory, such theoretical simulations are currently in progress, by using these approaches as analytical and predictive tools to be compared with results of experimental methods.

The subject of this paper is to acquire fundamental data on Al(III)-F(-I) complexes required for the study of the molten cryolite structure by molecular dynamics calculations. In fact, for obtaining a realistic model of such a complex melt, dynamics studies should be performed by taking into account the possibility for all complexes to be dissociated or formed. The notion of breaking bonds and bond formation has been advanced(26), and can be a progress for dynamics calculations to have realistic interaction potentials.

Before studying the melts by a dynamics way, we have to establish the structure of species that could be present in molten cryolite. The calculations reported here have been performed in order to simulate dissociation pathways of AlF_6^{3-} and AlF_5^{2-} by loosing one or two fluoride ions.

COMPUTATION ELEMENTS

Approximation levels

Our choice for computational software turned in favour of local density functional (LDF) approach, because of its accuracy in convergence and the computational effort for this method that grows to leading order with the cube of the molecule size. Furthermore the density functional approach has been much used in electronic structure calculations on molecules and solids(27-28). Currently, LDF is becoming an increasingly important method in quantum chemistry, as it leads to much more reliable predictions for large molecules. The power of LDF methods has been demonstrated in numerous applications(29-31).

All theoretical computations were carried out with the DMol software ((32), distributed by Biosym Technologies(33)), for which the mathematical formalism is described elsewhere(32-34). The use of DFT has several advantages. For one, this method employs numerical (in the case of DMol) basis sets obtained by solving the atomic DFT equations numerically; thus the use of the exact DFT atomic orbitals implies that the molecule can be dissociated exactly to its constituents atoms within the DFT context. Because of the quality of these orbitals, basis sets superposition effects are minimized (32), and an excellent description of even weak bonds is possible.

All quantum calculations were done at a local approximation using the UHF (Unrestricted Hartree-Fock) level. The DNP basis sets (double numerical functions, augmented by polarization ones) were chosen. The quality of this type of basis sets is similar to the gaussian 6-31G** sets.

Model for the dissociation processes

The following dissociation pathways have been studied : $AlF_6^{3-} \leftrightarrow AlF_5^{2-} + F^-$, $AlF_5^{2-} \leftrightarrow AlF_4^- + F^-$, $AlF_6^{3-} \leftrightarrow AlF_4^- + 2F^-$, by breaking one Al-F bond for the two first reactions and simultaneously two Al-F bonds in the last dissociation.

In order to describe the reactions in a consistent way, we have to take into account the following effects. The breaking Al-F bond length has to be enhanced for simulating the dissociation mechanism and fixed during each geometry optimization. Furthemore, relaxation effects should be considered for all fluorine atoms that are not fixed during the optimization. So each energy point corresponds to an optimized geometry carried out at these constraint levels.

In this paper, we do not consider the effect of the molten salt environment on Al(III)-F(-I) complexes. This effect will be taken into account in further studies through quantum and molecular dynamics investigations.

RESULTS AND DISCUSSION

The procedure just described is very general and should be applicable to any system. The schemes describe breaking one or two bonds of sixfold- and fivefold-coordinated aluminum complexes. For the reaction involving AlF_5^{2-}, total energies have been modified by adding the total energy of F^- ion, so that all energies in all dissociation pathways can be compared. It is important to mention that we consider the complexes loosing an F^- ion, since the Mulliken and Hirshfeld population analyses give a negative charge on F for relatively large bond length. The bond type is thus ionic and the interaction is an electrostatic one.

The potential energy curves of dissociation pathways by DFT calculations are depicted in figure 1. Some interesting trends emerge from these results. The consistency of all theoretical computations is shown on figure 1 because we find again the energy of a stable conformation, AlF_5^{2-} or AlF_4^-, added to F^- or $2F^-$ energies. Regarding structures through the dissociation mechanism of AlF_5^{2-} into AlF_4^-, we observe that the conformation of AlF_5^{2-} tends towards a distorted tetrahedral geometry due to the presence of the far-off fluoride atom. Analogous remarks can be mentioned considering the dissociation of AlF_6^{3-} into AlF_4^- by stretching two fluoride adjacent ions. However, the reaction: $AlF_6^{3-} \leftrightarrow AlF_4^- + 2F^-$ by stretching two opposite F^- ions shows a square plane geometry for long Al-F bond lengths. On the other hand, concerning the dissociation of AlF_6^{3-} into AlF_5^{2-}, we can point out a distorted octaedral conformation, that could be underline experimentally in the melt.

The energy differences ΔE between the initial stable structures and the transient species are reported in table 1. These results suggest that the dissociation of AlF_6^{3-} into AlF_5^{2-} is more favourable than those of AlF_6^{3-} into AlF_4^- or AlF_5^{2-} into AlF_4^-. The comparison between the energy gaps and $RT \approx 8kJ/mol$ at 1000K suggests that environment effects should occur. In fact, the model used for dissociation schemes does not include molten salt effects, such as F^- exchanges between two complexes and charge effects that could lower the energy barrier of reactions.

CONCLUDING REMARKS

Stable structures of Al(III)-F(-I) complexes have been studied and dissociation schemes have been proposed. In a theoretical point of view, the procedure used is very general and is applicable to any chemical system. The dissociation pathways relative to these complexes have been studied and energy gaps given. LDF calculations of reaction schemes show that $AlF_6^{3-} \leftrightarrow AlF_5^{2-} + F^-$ involves a lower energy barrier than the other dissociations. These studies will be completed by further investigations in order to consider preponderant effect of molten salt environment (charged and solvation effects). It will be the subject of a forthcoming paper.

ACKNOWLEDGEMENTS

The authors thank Pechniney CRV for financially supporting this work. One of the authors, F.B., is grateful to Pechiney and Ademe (Agence de l'Environnement et de la Maîtrise de l'Energie) for providing a doctoral grant.

REFERENCES

1. B. E. Waren in X-Ray diffraction, Addison-Wesley, Reading, Massachusetts (1963).
2. J. E. Enderby in Molten Salt Chemistry, An Introduction and Selected Applications, G. Mamantov and R. Marassi, Editors, p.1-15 (1987).
3. H. Ohno and K. Furukawa, J. Chem. Soc. Faraday Trans. I77, 1981 (1918).
4. H. Ohno, K. Furukawa, K. Igarashi and J. Mochinaga, J. Chem. Soc. Faraday Trans. I78, 1555 (1982).
5. G. Bacon in Neutron Diffraction, Oxford University Press, London (1975).
6. G. L. Squires in Thermal Neutron Scattering, Cambridge University Press, Cambridge, England (1978).
7. Y. Derrien and J. Dupuy, J. Phys. Paris 36, 191 (1975).
8. E. W. J. Mitchell, P. F. J. Poncet and R. J. Stewart, Phil. Mag. 34, 721 (1976).
9. S. Biggin and J. E. Enderby, J. Phys. C 15, L305 (1982).
10. S. Biggin, M. Gay and J. E. Enderby, J. Phys. C 17, 977 (1984).
11. B. Gilbert, G. Mamantov and G. M. Begun, Appl. Spectrosc. 29, 276 (1975).
12. B. Gilbert, G. Mamantov and G. M. Begun, J. Chem. Phys. 62, 950 (1975).
13. E. Rytter and S. K. Ratkje, Acta Chem. Scand A29, n°5, 656 (1975).
14. R. Berg, N. J. Bjerrum, G. N. Papatheodorou and Von Winbusch, Inorg. Nucl. Chem. Letters 16, 201 (1980).
15. M. H. Brooker and G. N. Papatheodorou, in Advances in Molten Salt Chemistry, vol 5, G. Mamantov, Editors, p.26-184, Elservier (1983).
16. J. H. Von Barner, R. W. Berg, N. J. Bjerrum, E. Christensen and F. Rasmussen, in Molten Salt Chemistry and Technology, Materials Science Forum, M. Chemla and D. Devilliers, Editors, vol 73-75, p.279, Trans Tech Publications (1991).
17. E. Rytter, H. A. Oye, S. J. Cyvin, B. N. Cyvin and P. Klæbœ, J. Inorg. Nucl. Chem., 35, 1185 (1973).
18. G. Roullet, J. J. Legendre, D. Filliaudeau and G. Picard, in Molten Salt Forum, C.A.C. Sequeira and G.S. Picard, Editors, p.105-116, Trans Tech Publications (1993/94). S. Grandjean, L. Mouron, J. J. Legendre and G. Picard, in Molten Salt Forum, C.A.C. Sequeira and G.S. Picard, Editors, p.99-104, Trans Tech Publications (1993/94).
19. L. Mouron, S. Grandjean, J. J. Legendre and G. Picard, Computers and Chemistry (1994), in press.
20. M. L. Saboungi, M. Blander and A. Rahman, in Proceedings of the fourth International Symposium on Molten Salts, M. Blander, D.S. Newman, M. L. Saboungi, G. Mamantov, K. Johnson, Editors., vol 84-2, p.1-11 (1984).
21. L. P. Davis, C. J. Dymek, Jr, J. J. P. Stewart, H. P. Clark and W. J. Lauderdale, J. Am. Chem. Soc. 107, 5041 (1985).
22. G. Xie, Z. Qui, C. Xu and N. Chu, Chin. J. Met. Sci. Technol. 5, 426 (1989).

23. H. A. Oye, M. Jagtoyen, T. Oksefjell and J. S. Wilkes, in Molten Salt Chemistry and Technology, Materials Science Forum , M. Chemla and D. Devilliers, Editors, vol 73-75, p.183-190 (1991).
24. M. L. Saboungi, A. Rahman and M. Blander, in Proceedings of the fifth International Symposium on Molten Salts, M. L. Saboungi, D.S. Newman, D. Inman, K. Johnson, Editors., vol 86-1, p.97-108 (1985).
25. L. A. Curtiss and R. Nichols, in Proceedings of the fifth International Symposium on Molten Salts, M. L. Saboungi, D.S. Newman, D. Inman, K. Johnson, Editors., vol 86-1, p.289-295 (1985).
26. R. V. Stanton, D. S. Hartsough and K. M. Merz, J. Phys. Chem., 93, p. 11868 (1993).
27. B. Delley, in Density Functional Methods in Chemistry, J. K. Labanovski and J. W. Andzelm, Editors., p.101-107, Springer-Verlag , New York (1991).
28. A. J. Freeman, S. Tang, S. H. Chou, Y. Ling and B. Delley, in Density Functional Methods in Chemistry, J. K. Labanovski and J. W. Andzelm, Editors., p.61-75, Springer-Verlag, New York (1991).
29. R. O. Jones and O. Gunnarson, Rev. Mod. Phys. 61, p.689 (1989).
30. O. Gunnarson, J. Harris and R. O. Jones, Phys. Rev. B, 29, p. 703 (1984).
31. P. J. Braspenning, R. Zeller, A. Lodder and P. H. Dederichs, Phys. Rev. B, 29, p. 703 (1984).
32. B. Delley, J. Chem. Phys., 92 , p. 508 (1990).
33. DMol, User guide, Biosym Technologies, version 2.3.
34. B. Delley, New. J. Chem. 16, p. 1103 (1992).

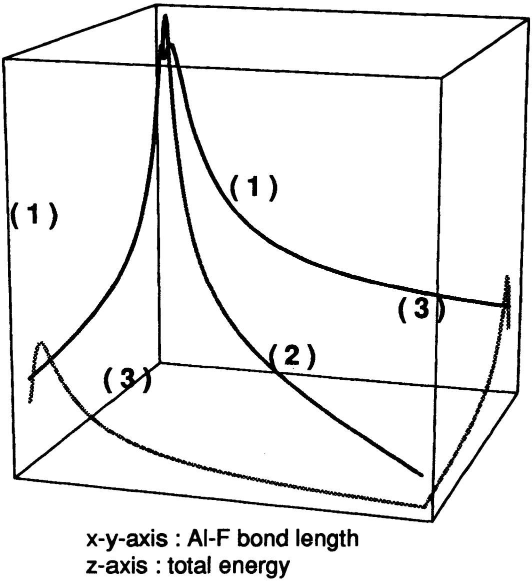

Figure 1 : dissociation energies according to the following dissociations :

(1) $AlF_6^{3-} \leftrightarrow AlF_5^{2-} + F^-$

(2) $AlF_6^{3-} \leftrightarrow AlF_4^- + 2F^-$

(3) $AlF_5^{2-} \leftrightarrow AlF_4^- + F^-$ axial way

(3') $AlF_5^{2-} \leftrightarrow AlF_4^- + F^-$ equatorial way

Reactions	(1)	(2)	(3)	(3')
ΔE (kJ/mol)	35	107.6	121	137.6

Table 1 : energy gaps corresponding to the studied dissociations (see text)

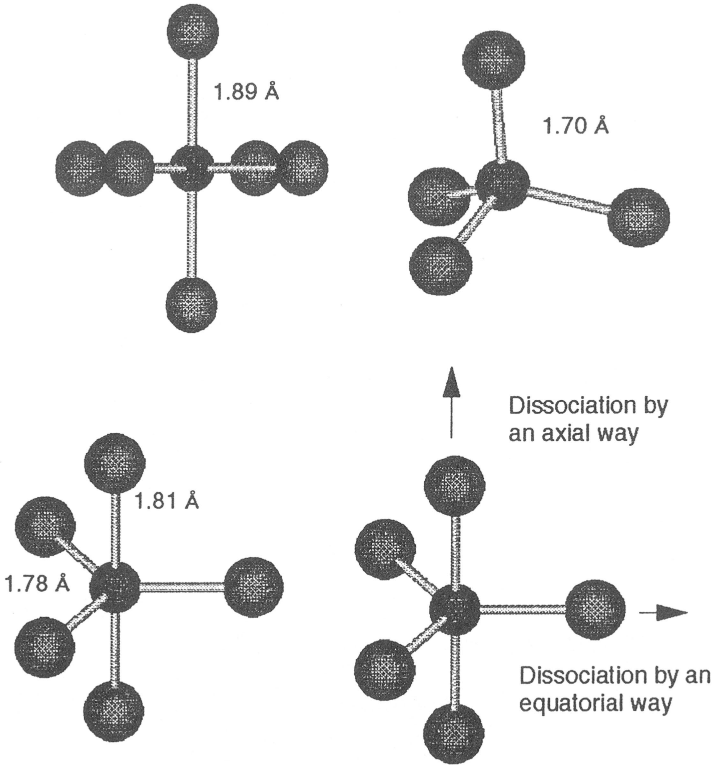

Figure 2 : stable structures of AlF_6^{3-}, AlF_5^{2-} and AlF_4^{-}.

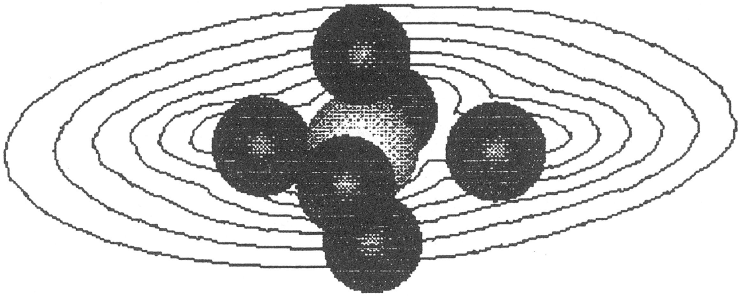

Figure 3 : a typical electron density map : transition structure for dissociation (1) (scaled from 10^{-2} to 10^{-7}).

DOI: 10.1149/199413.0042PV

DYNAMIC PROPERTIES ON AN INTERMEDIATE RANGE SCALE IN GLASSFORMING MOLTEN SALTS

D. Quitmann, A.P. Sokolov[1], A.A. Sokolov[1], A. Kisliuk and E. Rössler[2]

Institut für Experimentalsphysik, Freie Universität Berlin, Arnimallee 14, 14195 Berlin
Germany

[1]Permanent address: Inst. for Automation, Academy of Sciences, Novosibirsk, Russia

[2]Now at: II. Physikalisches Institut, University Bayreuth, Germany

ABSTRACT

A broad distribution of vibrational excitations is found in disordered solids in the frequency range around 1 THz, giving evidence for fluctuations of elastic properties over intermediate range (typically 20...30Å). In the glass-to liquid transition the vibrational motions transform into relaxational motions on the same spatial scale. Coming from the liquid side, the transformation sets in at a temperature well above T_g, and continues smoothly to $T<T_g$. This decrease of relaxational motions explains the pronounced Vogel-Fulcher behaviour of viscosity of fragile glassforming melts, and perhaps also the suppression of crystallization.

1. INTRODUCTION: IRO IN GLASSES

Most non-crystalline materials including molten salts, show an almost crystal-like degree of order on a nearest-neighbour scale, and are homogeneous and isotropic on macroscopic scales. It is on the intermediate range scale, very roughly $10^1...10^3$ Å, where disorder can be detected most clearly, and its effects on transport and other properties are most pronounced. Here we want to address the question how important the atomic (molecular, ionic) dynamics, which happens on this range scale, is in glassforming salt melts. A characteristic feature which is caused by intermediate range order (IRO) is seen in the quasielastic scattering of light (or neutrons) from glasses, viz a typical broad peak in the 1 THz region, often called "boson peak" (bp). Examples can be seen in fig. 1 which shows new Raman data for B_2O_3 and $ZnCl_2$; for SiO_2 see (1), for neutron data on $Ca_2K_3(NO_3)_7$ (2). This spectral feature is also seen in amorphous semiconductors. It is scattering from (inhomogeneously distributed) vibrational excitations. They can be seen in light scattering basically due to loss of q-conservation (3).

An important information which one can derive from the bp is a measure of the spatial range of correlation of elastic properties in the glass, R_c. Several derivations connecting the bp maximum ω_{bp} to R_c have been given (4,5,6). The bp may be seen as caused by localization of strongly scattered acoustic phonons (wavevector $k(\omega)$). At ω_{bp}, the mean free path $l(\omega)$ (7) fulfills the localization criterion $l(\omega_{bp})\cdot k(\omega_{bp})\approx 1$. With

$<\Delta c^2>$ as the mean square fluctuation of sound velocity c, and R_c the correlation length of that fluctuation, one gets

$$R_c \approx \frac{1}{2<\Delta c^2>/c^2} \cdot \frac{c}{\omega_{bp}} \qquad [1]$$

The alternative derivation given in (5), and used in (8), leads to $R_c \approx 0.8\ c_{TA}/\omega_{bp}$. In a selection of glasses, we have found R_c-values of 20...30Å (8). It may be important to point out that a parallel to this elastic IRO may be found in structural studies as well: In amorphous solids, a "first sharp diffraction peak" of the structure factor S(q) from neutron or X-ray measurements is ubiquitous. Its width ΔQ, which reflects the correlation length of some chemical ordering, yields an IRO parameter via $2\pi/\Delta Q$. These values agree for quite a group of glasses with the R_c values obtained from the bp, within 20...50% (8,9). In view of the rough approximations involved, we consider this degree of agreement as an essential confirmation of the basic idea: In disordered solids IRO can be found on a scale of 20-30 Å.

2. THE MELT-GLASS-TRANSITION

In melts of normal (non glassforming) salts the characteristic feature seen in the quasielastic scattering of light or neutrons is the well known broad monotonous decay which happens in the same frequency range as the bp. Its width, which corresponds to the order of 10^{-12}sec, and its intensity behave as a function of temperature as expected for a purely relaxational process.

But when we study glassforming salt melts, signs of the bp appear clearly at a temperature T* well above the glass transition temperature T_g: A hump develops close to where ω_{bp} of the glass is. This may be seen for $ZnCl_2$ and B_2O_3 in fig. 1. As T is lowered towards T_g, the bp vibrational (vib) feature grows at the expense of the relaxational spectral feature (rel); for more examples see (10,11,12,13). We will come back to the shape of the spectrum.

We now put up an hypothesis which, we believe, has important consequences for an understanding and for any formal treatment of the glass transition: Both, the vibrational motions seen in the boson peak (in light or neutron scattering), and the relaxational motions seen in the quasielastic spectrum (in roughly the same frequency range), are motions of essentially the same degrees of freedom.

In support of this hypothesis, we point to several experimental observations [and to possible explanations of these observations.].

1) Upon approaching T_g from above, there is a very smooth transition, which is very similar in all glassforming melts studied so far, between the "vib" spectral shape and the "rel" spectral shape. This transition continues below T_g. Also the depolarization ratio is the same for both spectral features, and it is virtually independent of T. [This suggests a conversion of the same atomic/ionic/molecular coordinates from relaxational to vibrational motion, like in a continuous freezing/melting process. If this process is quantified as a variation of coupling of the vibrations to a fast relaxing bath (14), then the full spectral shape can be very well described, see fig. 2 and (14,10,11,13)].

2) There is a striking parallel (15) between low-temperature specific heat $C_p(T)$ as a function of T and the shape of the Raman-Spectrum in the corresponding frequency region, the rel-part corresponding to the two level system-contribution to C_p, and the vib-part corresponding to the excess vibrational density of states-contribution to C_p. The relative strength of the two contributions is systematically different in systems which are according to (16) strong or fragile glassformers. The point is that this systematics is the same for C_p and for the Raman spectra (15). [A generalized coordinate, and strongly anharmonic potential curve for it, can explain both, the two level systems and the excess density of states, see e.g. (17) Anharmonic potentials induce relaxation, the bp is an excess density of vib states.]

3) The change from vib to rel motions is fully reversible upon T-cycling, as long as crystallization does not occur.[Glass and melt are in a thermodynamic quasi-equilibrium.]

4) Both, vib and rel Raman scattering are observed in disordered condensed matter. [Breakdown of momentum conservation law for light cattering (3) occurs in glass and melt, and thus is to be postulated for any "intermediate" state as well.]

Although the spectrum shape can reasonably well be described, as has often been done, by a sum of two terms, vib and rel spectrum (1,10,11), this should not be considered as counter-evidence to the above hypothesis. Also the treatment of bp explicitly as localized phonons, eq. [1], does not necessarily contradict (17) because in the model (17) one also arrives at $20...10^2$ atoms participating in the motion. - It will be interesting to see results from other spectroscopic techniques for which the relevant frequency range is accessible, like FIR. This will also be important for the question of the coupling coefficient (18).

On the theoretical side, mode coupling theory for the liquid-glass transition (MCT see e.g. (19)) has established in the last years as an important paradigm which allows quantitative analysis of spectral shapes. However, it does not include the bp explicitly, although the bp falls right into the frequency region of "the fast β relaxation" of MCT.

In what follows it will be assumed that the above hypothesis is basically correct, and further conclusions will be derived.

3. A CHARACTERISTIC TEMPERATURE ABOVE T_g

The bp "appears" at a rather sharply defined temperature T*. In the model of Gochiyaev et al. (14) this is the temperature where the renormalized bp frequency $\omega_o^2 = \omega_{bp}^2 - \delta^2$ becomes zero; although no determination exists as yet for a molten salt, this temperature has been determined for molecular glassformers in (14) and recently in OTP, mTCP and glycerol (13). In fig. 3 we show the dependence of the parameter δ of the model (14) on T around T_g for the $GeSBr_2$ glassformer. This parameter δ will now be taken as a measure of the degree of transformation between liquid and glass. In a schematic separation of the spectrum into relaxational plus vibrational part, δ determines the real part. Thus upon cooling the melt from high T, the vib part starts to grow from zero and the real part starts to deminish, at T*. Upon further cooling, the transition (i.e.$\delta(T)$) is smooth, appearently, without any divergence or further anomaly around T_g,, see fig. 3.

The next point is that the temperature T* at which the bp "appears" upon cooling the melt, is at least close to (if not the same as) the temperature, at which the glassforming melt shows other changes of dynamical behaviour: Rotational and translational diffusion constants separate (20); the Debye-Waller factors indicate a break (21) in accord with MCT; viscosity shows the change in temperature dependence which is well known e.g. from the Angell-plot (16). Also in the MCT approach, a most important change of dynamics occurs at a temperature $T_c>T_g$ (19).

We quote from (13) the ratios T^*/T_g and T_c/T_g for three glassformers: 1.9 and 1.7 for glycerol, 1.3 and 1.2 for m-TCP, 1.2 and 1.2 for OTP. It appears to be very clear that these ratios correlate with the fragility. The main difference in dynamics between strong and fragile glassforming melts is the dominant type of motion: for strong sytems it is vibrational, even at T well above T_{melt}, while for fragile ones it is relaxational and the vibrational part comes in only shortly avove T_g (13). This is discussed in detail in ref. (15) and (13).

Connecting the results quoted for diffusion, Debye Waller factor, and viscosity with the hypothesis stated above, we are led to the conclusion that not only the spectral changes, but all the mentioned changes of dynamical properties have their major reason in processes occuring on the IRO spatial scale.

The smooth transition glass ⇔ liquid, seen in the smooth change of δ (fig. 3), is (dis-) appearance of relaxation on the time scale of 10^{-12} sec. Consequences of this change on other effects seen in the glass transition will be illustrated by showing the influence of "rel" and "vib" dynamics in two cases. The tremendous increase of viscosity η towards T_{g+} has been analyzed by Buchenau and Zorn (22) using an ansatz which reminds of the free-volume theory. Modifying it slightly, it reads

$$\eta = \eta_0 \exp\frac{<u^2>_0}{<u^2>_{vib}+<u^2>_{rel}} \qquad [2]$$

Here $<u^2>_{vib}$ is the vibrational mean square displacement, and $<u^2>_{rel}$ its relaxational counterpart; $<u^2>_0$ is a fixed reference value. While Buchenau and Zorn took these values for liquid Se from neutron scattering, we may tentatively use Raman scattering data (using assumptions about the coupling coefficient C(ω) (18)). Such an analysis of the Raman spectra shows, as was just mentioned that in fragile systems $<u^2>_{rel}$ is large compared to $<u^2>_{vib}$, i.e. the rel part is large compared to the bp part. Also it is strongly temperature dependent (because T^*/T_g is relatively small). Let us assume a linear decrease of $<u^2>_{rel}$ between T* and T_g:

$$<u^2>_{rel}=<u^2>_{relTg}+\Delta u^2\cdot\frac{T-T_g}{T^*-T_g};\ T_g\le T\le T^*$$

$$\Delta u^2=<u^2>_{relliq}-<u^2>_{relTg} \qquad [3a,b]$$

Here the indices liq and T_g refer to T>T* and $T=T_g$, respectively. We use $<u^2>_{vib}$ = L·T as a reasonable high T assumption . Now $\Delta u^2/(T^*/T_g-1)$ is large and

$$G=-<u^2>_{relTg}+\Delta u^2/(T^*/Tg-1)>0 \qquad [3c]$$

Then one recovers a Vogel-Fulcher form for η: $\eta = \eta_0 \exp [D/(T-T_0)]$ with

$$D =< u^2 >_0 /(L+H);.T_0 = G/(L+H);.H = \Delta u^2 /(T^*-Tg) \qquad [4]$$

In fragile systems, G and H are large, and the parameter D becomes small, as is known. Above T*, the contribution $<u^2>_{vib}$ is negligible.

It is thus seen how the smooth change from relaxational to vibrational motion between T* and T_g induces the most prominent effect of the glass transition, viz. the extreme increase of η (and thus of the slow or α-relaxation time.) It is hoped that the ansatz eq. [2] can be derived from a feedback or percolation picture. In any case it removes the need for the unphysically large appearent activation energy which η seems to display right above T_g, which is especially surprising since fragile systems usually have no strong inter-bonds.

As the second, short, discussion we would like to show how the vibrational motions stressed here (bp) may fit into the picture of the two-step relaxation (fast β-, followed by slow α-relaxation). There is clear experimental evidence that the α-relaxation splits off from the β-relaxation when the melt is cooled towards T_g; this becomes especially clear in MCT. It means that "part of those relaxations which used to be fast at high T" are becoming slow below some $T>T_g$ (viz at $T<T^*$ or T_c). The fact that the bp appears just where the slow relaxation splits off, does indeed suggest that groups of degrees of freedom couple, cooperate on an IRO scale in such a way that they relax slowly as a whole (α relaxation time) and therefore motions which are "internal" to that group become underdamped, so that one sees them in the boson peak.

4. CRYSTALLIZATION OR GLASS FORMATION?

Finally attention is drawn in fig. 4 to the low frequency Raman spectra of two mixed-cation nitrate melts. One of the melts is a good glass former (CKN), the other crystallizes. The first shows a reduced relaxational part at T_m, compared to the second, and also a very smooth development between T_m and $T_g<T_m$. The comparatively large relaxational intensity in the second system disappears abruptly upon crystallization.

Generalizing this observation, we propose to assume the following reason for the inability to crystallize, which is constitutive for the glassforming melt: The - relative - lack of fast relaxational motions in the glassforming melt may be sufficient to suppress the reordering which would be required for the liquid-to-crystal transformation to take place.

5. SUMMARY

Evidence has been presented and discussed which shows 1) that an important process, or change occuring in the melt above the glass transition temperature T_g, is the transformation between relaxational and vibrational motions on the frequency scale of the order 1 THz; 2) that this transformation begins (upon cooling) at a temperature well above T_g, and continues through T_g smoothly; 3) that this smooth transition is compatible with the Vogel-Fulcher temperature dependence of viscosity; 4) that the said relaxational and vibrational motions happen on an intermediate spatial scale of the order $10^1 \ldots 10^2$ Å.

ACKNOWLEDGEMENTS

One of us (A.A.S.) is obliged to Freie Universität Berlin for its hospitality. This project was supported by German-Israeli-Foundation for Science and Development, and by Deutsche Forschungsgemeinschaft (Sfb 337).

REFERENCES

(1) G. Winterling: Phys. Rev. B12 (75) 2432
(2) W. Knaak, F. Mezei, B. Farago: Europhys. Lett. 7 (88) 529
(3) R. Shuker and R.W. Gammon, Phys. Rev. Lett. 25, (70) 222
(4) J. Martin and W. Brenig, Phys. status solidi B 64 (74) 163
(5) I. Duval, A. Boukenter and B. Champagnon: Phys. Rev. Lett. 56 (86) 2052
(6) W. Schirmacher and M. Wagner: Springer Proc. Phys. 37 (89) 231; Adv. Sol. State Phys. 31 (91) 39
(7) A.K. Raychoudhury: Phys. Rev. B39 (89) 1927
(8) A.P. Sokolov, A. Kisliuk, M. Soltwisch, D. Quitmann: Phys. Rev. Lett 69 (1992) 1540-1543
(9) L. Boerjesson, A.K. Hassan, J. Swensson and L.M. Torrell: Phys. Rev. Lett 70 4027 (93)
(10) M. Krüger, A. Tverjanovich, M. Soltwisch, D. Quitmann: J. Phys. Cond. Matter 5 (1993) 1-10
(11) M. Krüger, M. Soltwisch, I. Petscherizin, D. Quitmann: J. Chem. Phys. 96 (1992) 7352-7363
(12) V.K. Malinowski, V.N. Novikov and A.P. Sokolov: Sov. Phys. Solid State 29 (87) 1990; Solid State Comm. 57 (86) 757; J. Non Cryst. Sol 90 (87) 485
(13) A.P. Sokolov, A. Kudlik, A. Kisliuk. E. Rössler and D. Quitmann: J. Non Cryst. Sol. in the press
(14) V.Z: Gochiyaev, V.K. Malinovsky, V.N. Novikov, A.P. Sokolov, Philos. Mag. B 63 (91) 777
(15) A.P. Sokolov, E. Rössler, A. Kisliuk and D. Quitmann: Phys. Rev. Lett 71 (1993) 2062-2065
(16) C.A. Angell, in Relaxation in Complex Systems, edited by K.L. Ngai and G.B. Wright (NRL Washington, 1984) , p. 3
(17) L. Gil, M.A. Ramos, A. Bringer and U. Buchenau: Phys. Rev. Lett 70 (93) 182
(18) A.P. Sokolov, A. Kisliuk, D. Quitmann, E. Duval: Phys. Rev. B48 (1993) 7692-7695
(19) W. Götze and L. Sjögren: Rep. Prog. Phys. 55 (92) 241
(20) H. Silliscu and E. Bartsch: Disorder Effects on Relaxational Processes, eds. Richter/Blumen, Springer Berlin 1994, p. 55
(21) E. Rössler: Ber. Bunsenges. Phys. Chem. 94 (90) 392
(22) U. Buchenau and R. Zorn, Europhys. Lett 18 (92) 523

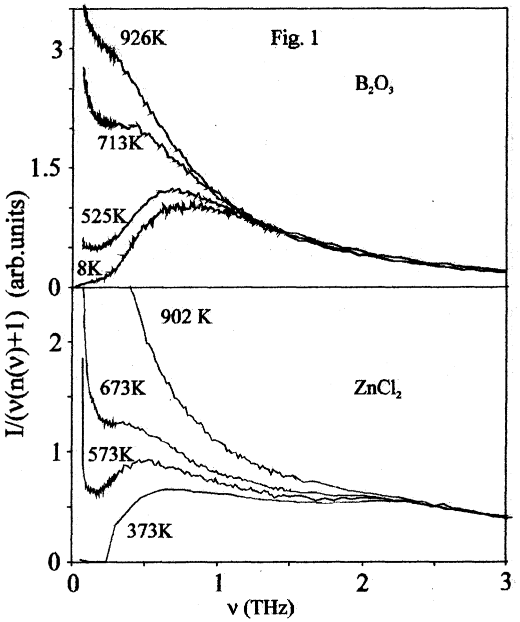

Fig.1: Low frequency Raman spectra of B_2O_3 and $ZnCl_2$. Curves for $T > T_g \sim 525K$ and 400K, respectively, are for the (supercooled) melts. The factor $n(\nu) + 1$, $n(\nu)=[\exp(h\nu/\ k_BT)-1]^{-1}$, is the thermal normalisation for the Stokes side.

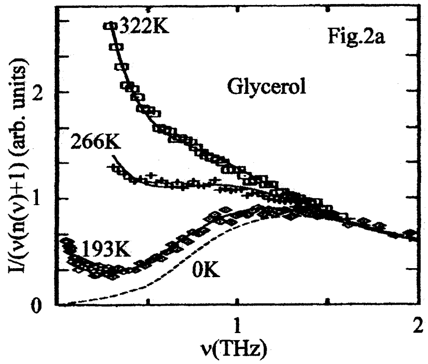

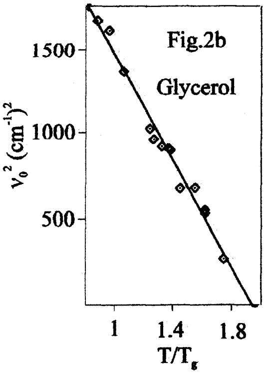

Fig.2a: Normalized low frequency Raman spectra of glycerol, with spectral form given in (14) fitted to the points. T=0 curve is an extrapolation.

Fig.2b: Renormalized bp frequency $\nu_0^2=\nu_{bp}^2-\delta^2$. From(13).

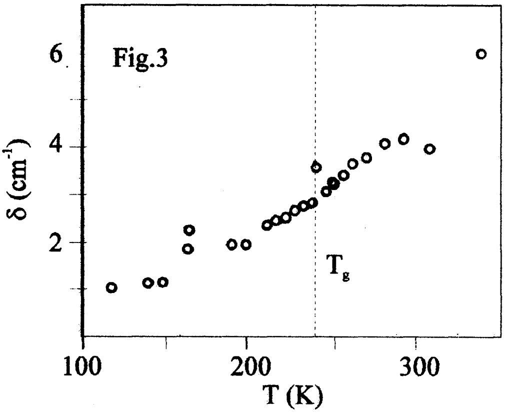

Fig3: Strenght δ of the coupling between bp vibrational states and fast relaxating bath, derived according to (14), for glass former GeSBr$_2$, from (11).

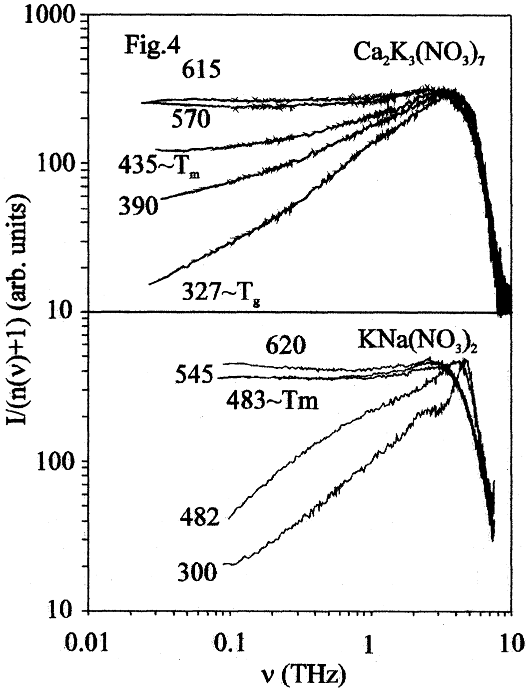

Fig.4: Low frequency Raman spectra for two nitrates melts which do (Ca$_2$K$_3$(NO$_3$)$_7$, top) or not do (KNa(NO$_3$)$_2$, bottom) form glasses. Tm of Ca$_2$K$_3$(NO$_3$)$_7$ was estimated.

DOI: 10.1149/199413.0050PV

Structural Investigations of 1-Ethyl-3-Methylimidazolium Hydrogen Dichloride: Neutron Diffraction Studies of an Ambient-Temperature Molten Salt

Paul C. Trulove, Dustin Haworth, and Richard T. Carlin
The Frank J. Seiler Research Laboratory
Division of Electrochemical Sciences
2354 Vandenberg Drive Suite 2A35
U. S. Air Force Academy, CO 80840-6272

Alan K. Soper
Neutron Science Division
Rutherford Appleton Laboratory
Chilton, Didcot, Oxon, OX11 0QX, UK

Adam J. G. Ellison and David L. Price
Materials Science Division
Argonne National Laboratory
Argonne, IL 60439

ABSTRACT

The structure of 1-ethyl-3-methylimidazolium hydrogen dichloride ($ImHCl_2$) was investigated using neutron diffraction. Structural information was obtained from analysis of diffraction differences resulting from variations in the H-D substitution in the 1-ethyl-3-methylimidazolium cation and in the hydrogen dichloride anion (HCl_2^-). Preliminary data analysis of diffraction differences suggests that HCl_2^- exists as an asymmetric ion in the $ImHCl_2$ molten salt. This asymmetry may result from hydrogen-bonding between HCl_2^- and the 1-ethyl-3-methylimidazolium cation ring hydrogens.

INTRODUCTION

Ambient-temperature chloroaluminate molten salts composed of mixtures of $AlCl_3$ and 1-ethyl-3-methylimidazolium chloride (ImCl) are an important class of aprotic solvents for studying the chemistry of a wide variety of both organic and inorganic solutes (1,2). In addition, these chloroaluminate ionic liquids are promising electrolytes for high energy-density batteries (3,4). The properties of these molten salts are significantly affected by the presence of impurities derived from water contamination. In order to study the effects of water contamination, 1-ethyl-3-methylimidazolium hydrogen dichloride ($ImHCl_2$) was developed as a reagent for the quantitative addition of protons to the chloroaluminate molten salts (5).

$ImHCl_2$ is an ambient-temperature ionic liquid which is simply the equal molar mixture of ImCl and HCl. Mixtures of ImCl and HCl are also liquid at or below ambient-temperature over a wide range of compositions. Recent spectroscopic studies (6) have shown that the anionic speciation in the ImCl:HCl molten salts varies significantly with the relative amounts of ImCl and HCl. When ImCl is in molar excess, the anions present are primarily Cl^- and HCl_2^-. While a molar excess of HCl gives HCl_2^- and $H_2Cl_3^-$ as the primary anions. In the case of a large molar excess of HCl, additional polyanions of the form $Cl(HCl)_n^-$ may be present. When HCl and ImCl are mixed in nearly equal amounts, HCl_2^- is the primary anion (however, small amounts of Cl^- and $H_2Cl_3^-$ may be present); since Im^+ is the sole cationic species, the equal molar mixtures of ImCl and HCl are often referred to as $ImHCl_2$.

The ring hydrogens on the 1-ethyl-3-methylimidazolium cation (Im^+) are known to hydrogen-bond to chloride ion in basic $AlCl_3$:ImCl molten salts (7,8). The existence of anions of the form $Cl(HCl)_n^-$ in the ImCl:HCl molten salts demonstrates the ability of HCl_2^- to act as a hydrogen-bond acceptor. Therefore, it is reasonable to conclude that HCl_2^- may hydrogen bond to the ring hydrogens on Im^+ in ImCl:HCl molten salts. Recent solid state crystallographic studies of low-melting 1-ethyl-3-methlimidazolium salts indicate that Im^+ cations tend to form π-stacks with d-d distances < 4 Å (9). These and other observations suggest significant ordering of the ions in ImCl:HCl molten salts A better understanding of the structure of the ImCl:HCl molten salts would be of considerable aid in understanding their chemical and physical properties, as well as how these properties relate to those of other like low-melting salts (i.e. $AlCl_3$:ImCl). In this manuscript we describe neutron diffraction and infrared studies of the structure of $ImHCl_2$ (the equal molar mixture of ImCl and HCl).

EXPERIMENTAL

Materials. The synthesis and purification of 1-ethyl-3-methylimidazolium chloride (ImCl) and 1-ethyl-3-methylimidazolium-*2,4,5-d_3* chloride (ImCl-d_3) were performed as described elsewhere (7,10-12). The synthesis and purification of 1-ethyl-d_5-3-methyl-d_3-imidazolium chloride (ImCl-d_8h_3) was accomplished by the same method used to prepare ImCl by substituting chloroethane-d_5 (Cambridge Isotope Laboratories, 98% atom D) and 1-methyl-d_3-imidazole for chloroethane and 1-methylimidazole. 1-Ethyl-d_5-3-methyl-d_3-imidazolium-*2,4,5-d_3* chloride (ImCl-d_{11}) was prepared from ImCl-d_8h_3 by a base catalyzed H-D exchange in D_2O; the procedure used was identical to that employed in the preparation of ImCl-d_3 from ImCl (7). The synthesis of 1-methyl-d_3-imidazole was performed in the following manner. Under an inert atmosphere, 30.77 g (0.274 mol) of potassium tert-butoxide (Aldrich) and 34.6 g (0.237 mol) of iodomethane-d_3 (99% D, Aldrich) were added to 18.65 g (0.274 mol) of imidazole (99%, Aldrich) in a 100 mL round bottom flask. (As soon as these reagents were mixed a white precipitate formed.) Tetrahydrofuran was added to this mixture to give a total volume of 50 mL. The flask was then stoppered and allowed to stir at room-temperature for 2 weeks. At the end of two weeks the flask contained a white solid and a clear colorless liquid. The liquid was passed through a filter to remove the white solid (KI). The liquid was then placed on a rotary evaporator to remove the tetrahydrofuran and tert-butyl alcohol (a by product of the reaction); this reduced the original volume by half and yielded a light yellow liquid. The crude 1-methyl-d_3-imidazole was fractionally distilled under vacuum, and then dried by vacuum distillation off of CaH_2. The isolated yield of 1-methyl-d_3-imidazole was ca. 65%.

The hydrogen dichloride (deuterium dichloride) molten salts of the above imidazolium chlorides were prepared by reacting HCl(g) (^{2}HCl(g)) with the appropriate imidazolium chloride (5,12). The stoichiometry of each molten salt was then determined as previously described (12). The molten salts prepared for neutron experiments with their exact stoichiometries are as follows; $ImCl(HCl)_{1.05}$, $ImCl(^2HCl)_{0.82}$, ImCl-$d_3(HCl)_{0.87}$, ImCl-$d_3(^2HCl)_{0.78}$, ImCl-$d_8h_3(HCl)_{0.94}$, ImCl-$d_8h_3(^2HCl)_{1.02}$, ImCl-$d_{11}(HCl)_{0.99}$, and ImCl-$d_{11}(^2HCl)_{1.30}$. The melt samples were nominally equal molar mixtures. Thus, throughout this manuscript we refer to our ImCl:HCl melts generically as $ImHCl_2$.

Procedures. Two separate sets of neutron diffraction experiments were conducted at the Intense Pulsed Neutron Source, Argonne National Laboratory. Both sets of experiments were performed on four samples with differing combinations of H-D substitution. All experiments were done at ambient-temperature (ca. 30 °C). The first set of experiments were performed on the Special Environment Powder Diffractometer. The four samples studied were $ImCl(HCl)_{1.05}$, $ImCl(^2HCl)_{0.82}$, ImCl-$d_3(HCl)_{0.87}$, ImCl-$d_3(^2HCl)_{0.78}$. The incomplete deuteration of the imidazolium cation (i.e. the ethyl and methyl groups were not deuterated) resulted in a large incoherent scattering background. (This problem was essentially eliminated in the second set of diffraction experiments where all the ethyl and methyl groups on the imidazolium cations were fully deuterated.) The sample containers consisted of sealed quartz capillary tubes (1 mm I.D. by 3 mm O.D) lined up across the neutron beam. This sample configuration was less than optimal because most of the neutron beam encountered only quartz.

The second set of diffraction experiments were performed on the Glass, Liquid and Amorphous Material Diffractometer (GLAD). The four samples studied were ImCl-$d_8h_3(HCl)_{0.94}$, ImCl-$d_8h_3(^2HCl)_{1.02}$, ImCl-$d_{11}(HCl)_{0.99}$, and ImCl-$d_{11}(^2HCl)_{1.30}$. The sample containers consisted of 2 mm pathlength quartz UV-vis cells (Wilmad) which had attached a No. 7 Ace-Thred (Ace Glass). The samples were sealed in these cells using a solid No. 7 Teflon plug with a chemraz o-ring.

Infrared spectra were obtained on a Nicolet 510 FT-IR spectrometer. Infrared samples consisted of a single drop of melt sandwiched between two NaCl plates. The NaCl plates were tilted with respect to the incident beam to minimize spectral interference from lagged interferograms. All spectra were acquired at 4 cm^{-1} resolution and were unsmoothed. The absorption axis on the IR spectra in this manuscript were omitted because the cell pathlengths were unknown.

RESULTS AND DISCUSSION

When performing neutron diffraction experiments on compounds containing hydrogen, judicious deuterium substitution can be invaluable in isolating interactions involving hydrogen. This tactic was employed in both sets of neutron experiments. The first set of diffraction experiments were performed under less than ideal conditions. The large incoherent scattering background and the poor sample configuration greatly complicated data collection and analysis. These problems, to a large extent, were eliminated in the second set of diffraction experiments. Unfortunately, at the present time only the data from the first set of diffraction experiments has been fully analyzed. Still, using the diffraction differences resulting from the H-D substitution on this first data set, we were able to extract some interesting information about the $ImHCl_2$ melt structure.

The preliminary analysis of first order differences due to deuteration of HCl_2^- gave two intrastructural peaks. These results indicate that HCl_2^- exists as an asymmetric ion in the $ImHCl_2$ molten salt. This is quite remarkable considering that the HCl_2^- ion in $AlCl_3$:ImCl molten salts is linear with the hydrogen symmetrically placed between the two chlorides (10). Furthermore, to our knowledge, asymmetric HCl_2^- ions have only been observed in the solid-state (13). An asymmetric HCl_2^- implies some type of interaction with an additional species. The samples of $ImHCl_2$ used for these experiments contained small amounts of free Cl^-. As shown in Figure 1A, this free Cl^- could weakly H-bond to the hydrogen in HCl_2^-. This configuration, however, seems unlikely because the low concentration of Cl^- would allow very few of these complexes (Figure 1A) to actually form. A more plausible reason for an asymmetric ion is the formation of a hydrogen-bond between one chloride from the HCl_2^- and a hydrogen on the imidazolium cation ring (Figure 1B). The chlorides in the HCl_2^- ion are capable of acting as hydrogen-bond acceptors as demonstrated by the presence of anions of the type $Cl(HCl)_n^-$ in the ImCl:HCl melts containing excess HCl (6). In addition, the imidazolium ring hydrogens have been shown to strongly hydrogen-bond to Cl^- in $AlCl_3$:ImCl molten salts (7). The analysis of second order differences due to correlations between hydrogens on the imidazolium cation ring and HCl_2^- gave a pronounced peak near $r = 4$ Å. The area for this peak corresponded to 2 - 3 hydrogens about a hydrogen at the origin, suggesting an ordered arrangement in the $ImHCl_2$ melt. The nature of this ordering and the melt anion structure will hopefully be clarified when the second set of neutron diffraction experiments is fully analyzed.

Infrared spectroscopy was employed to further investigate the interaction of the HCl_2^- ion with the imidazolium cation ring hydrogens. Figure 2 shows the infrared spectra of ImCl-d_8h_3(HCl) and ImCl-d_{11}(HCl). Both spectra exhibit bands characteristic of the HCl_2^- ion (11). If HCl_2^- hydrogen-bonds to the imidazolium cation ring hydrogens (Figure 1B), one would expect deuteration of the imidazolium cation ring to affect the infrared spectrum of the HCl_2^- ion. However, simple inspection of the two spectra in Figure 2 shows very little change between the melt with protiums on the ring (Figure 2A) versus the melt with deuteriums on the ring (Figure 2B). The only obvious changes are the isotopic shifts in the imidazolium cation bands (i.e. aromatic C-H stretch shifts from 3100 to 2300 cm^{-1}, ring symmetric stretch shifts from 1570 to 1540 cm^{-1}). Similar observations can be made when comparing the spectra of $^2HCl_2^-$ with and without deuterium on the imidazolium ring (Figure 3).

The lack of gross changes in the hydrogen dichloride spectrum upon deuteration of the imidazolium ring does not preclude the existence of weak hydrogen-bonding interactions. The affect of ring deuteration on the infrared spectrum may be very subtle. It may result in very small shifts in the hydrogen dichloride IR bands, and/or slight changes in the relative intensities of the hydrogen dichloride absorbances. Unfortunately, because of the broad nature of the hydrogen dichloride bands, and the undefined sample pathlength, we are presently unable to observe changes of this nature.

CONCLUSIONS

The preliminary data analysis of diffraction differences resulting from variation in H-D substitution suggest that HCl_2^- exists as an asymmetric ion in the $ImHCl_2$ molten salt. This asymmetric ion may result from hydrogen-bonding of HCl_2^- to the imidazolium cation ring hydrogens. However, infrared measurements fail to confirm the presence of this hydrogen-bonding. It is hoped that complete analysis of the additional neutron diffraction experiments will help clarify the structure of the $ImHCl_2$ molten salt

ACKNOWLEDGMENTS

This work was supported in part by the U. S. Department of Energy, Basic Energy Sciences-Material Sciences, under contract number W-31-109-ENG-38, and by the Air Force Office of Scientific Research.

REFERENCES

1. R. A. Osteryoung, In *Molten Salt Chemistry*; Mamantov, R. Marassi, Editors; p. 329, D. Reidel Publishing, The Netherlands (1987)
2. C. L. Hussey, *Adv. Molten Salt Chem.* **5**, 185 (1983).
3. C. J. Dymeck, J. L. Williams, D. J. Groeger, J. J. Auburn, *J. Electrochem. Soc.* **131**, 2887 (1989).
4. C. J. Dymeck, L. A. King, *J. Electrochem. Soc.* **132**, 1375 (1985).
5. T. A. Zawodzinski, R. A. Osteryoung, *Inorg. Chem.* **27**, 4383 (1988).
6. J. L. E. Campbell, K. E. Johnson, *Inorg. Chem.* **32**, 3809 (1993).
7. K. M. Dieter, C. J. Dymeck, N. E. Heimer, J. W. Rovang, J. S. Wilkes, *J. Am. Chem. Soc.* **110**, 2722 (1988).
8. C. J. Dymeck, J. J. P. Stewart, *Inorg. Chem.* **28**, 1472 (1989).
9. J. S. Wilkes, M. J. Zaworotko, *Supramolecular Chem.* **1**, 191 (1993).

10. P. C. Trulove, R. A. Osteryoung, *Inorg. Chem.* **31**, 3980 (1992).
11. P. C. Trulove, D. K. Sukumaran, R. A. Osteryoung, *J. Phys. Chem.* **98**, 141 (1994).
12. P. C. Trulove, R. A. Osteryoung, *Inorg. Chem.* **91**, 3980 (1992).
13. J. C. Evans, G. Y-S. Lo, *J. Phys. Chem.* **70**, 11 (1966).

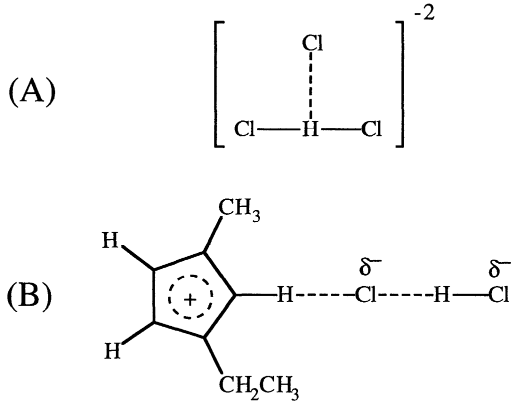

Figure 1. Possible structures for the asymmetric HCl_2^- ion.

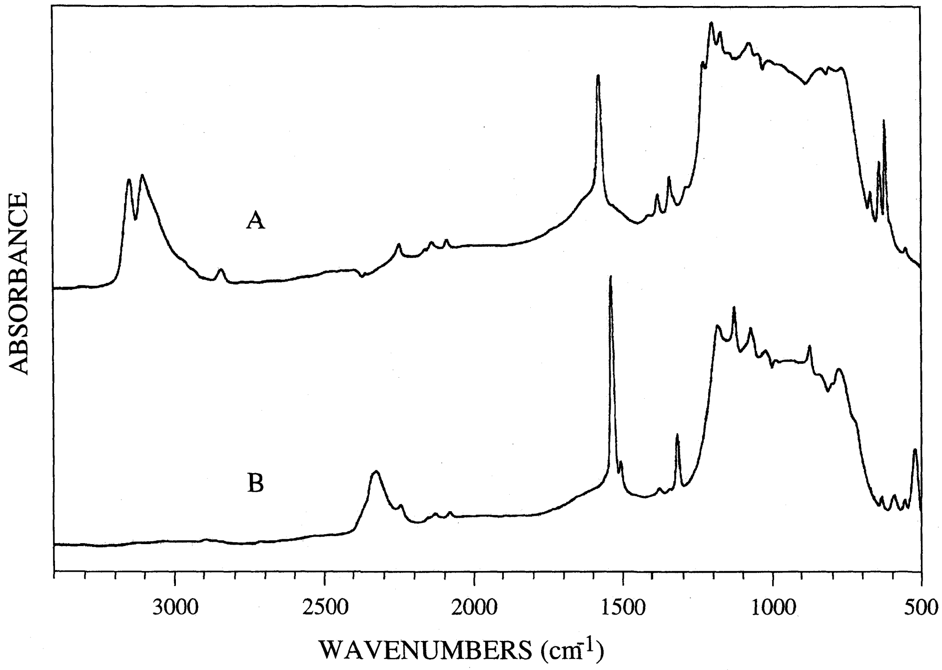

Figure 2. IR absorption spectra of (A) ImCl-d_8h_3(HCl)$_{0.94}$ and (B) ImCl-d_{11}(HCl)$_{0.99}$. Spectra are background subtracted and unsmoothed. Data collected at 25°C.

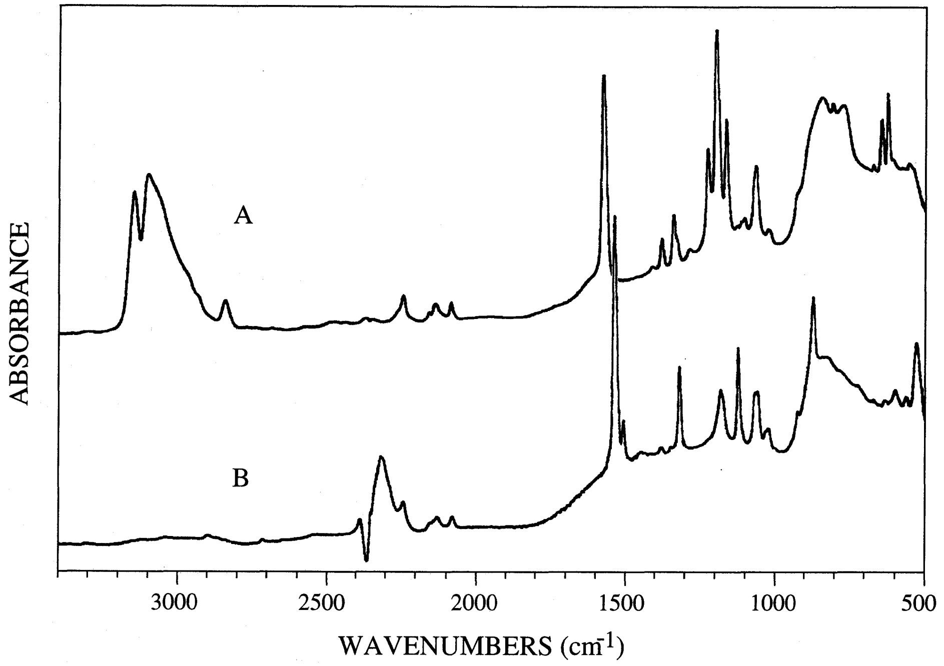

Figure 3. IR absroption spectra of (A) ImCl-d_8h_3(^{2}HCl)$_{1.02}$ and (B) ImCl-d_{11}(^{2}HCl)$_{1.30}$. Spectra are background subtracted and unsmoothed. Data collected at 25°C.

DOI: 10.1149/199413.0058PV

STRUCTURAL INVESTIGATION OF THE PROPOSED SPECIFIC HEAT ANOMALY IN LIQUID $ZnCl_2$

M. Grimsditch,[a] S. Popova[a, b] and D.L. Price[a]

[a]Materials Science Division, Argonne National Laboratory, Argonne, IL 60439
[b]High Pressure Institute, Moscow

ABSTRACT

Liquid $ZnCl_2$ has been investigated up to 700°C using Raman and neutron scattering techniques. The results are critically analyzed for either a confirmation of, or a contradiction to, the interpretation of recent Brillouin scattering experiments which claimed a pronounced maximum in Cp/Cv at 425°C. Our structural results show only minor changes above and below this temperature. The Raman results are interpreted as showing a gradual dissociation of the $ZnCl_2$ network.

INTRODUCTION

In recent years there have been a number of investigations that explore the possibility of the existence of phase transitions in liquids. It is clear that liquids which undergo dissociation as a function of temperature are, at least in a general sense, undergoing a transformation. Whether or not such transformations satisfy the thermodynamical criteria of true phase transitions is the point in question.

One possible candidate for exhibiting such a transformation is $ZnCl_2$. Diffraction studies of the liquid just above the melting point[1,2] indicate a highly connected network structure with well-defined $ZnCl_4$ tetrahedra. Such a structure is consistent with the macroscopic behavior, including the high viscosity above the melting point and also the relatively small latent heat of melting of $ZnCl_2$, compared with other divalent salts on the basis of volume change on melting;[3] the entropy deficit is presumably regained at higher temperatures when the network breaks up into smaller units. Furthermore, recent inelastic neutron scattering experiments[4] on $ZnCl_2$ at 347°C, 30°C above the melting point, show that the energy widths of the scattering function are much less than the Gaussian widths generally exhibited by liquids at high scattering vector Q, even at Q values as high as 10 $Å^{-1}$, indicating unusually strong binding of the ions to the liquid network. This picture is consistent with a peak in the specific heat extracted from a simple two-state model.[5] More recently in a Brillouin scattering investigation of $ZnCl_2$[6] it was reported that the results could be interpreted as providing evidence for a very large anomaly in the ratio of specific heats ($\gamma = C_P/C_V$). The results of this investigation are shown in Fig. 1. The temperature of this maximum (≈ 425°C) is surprising since it lies above the melting temperature of crystalline $ZnCl_2$. Furthermore Cp/Cv reaches a maximum of ≈ 4 which is considered by many to be unrealistically large for any system.

The results shown in Fig. 1 are controversial since they are obtained with the use of simple hydrodynamic theory. It has been shown in similar Brillouin scattering investigations[7,8] that, if the generalized hydrodynamic theory is used, the experimental data can be fit without invoking an anomalous γ. Since both approaches yield excellent fits to the experimental spectra it has not been possible to date to resolve the issue. We note that in the generalized hydrodynamic approach the usual hydrodynamic phenomenological material parameters are *ad hoc.* additionally assumed to be frequency dependent. It is one of these additional parameters which then exhibits anomalous behavior but, since this parameter has no clear microscopic origin, the significance of the anomaly is difficult to interpret.

The purpose of the present investigation was to perform both Raman and neutron scattering experiments to ascertain if there is any evidence for or against the existence of a Cp/Cv anomaly which could be interpreted as a thermodynamic signature of a transformation.

RAMAN SCATTERING RESULTS

Figure 2 shows the temperature dependence of reduced polarized Raman spectra. The spectrum at 700°C has been fitted with three Lorenzians as indicated by the dashed lines : we found that at least three Lorenzians are required to produce a reasonable fit. Such fits show that neither the peak positions, nor line widths show any marked temperature dependence. The relative areas under each peak do however change dramatically with temperature. In Fig. 3 we have plotted the fraction of the total intensity of each one of the three peaks obtained from the fitting procedure. It shows that the peak at around 225 cm^{-1} (307 cm^{-1}) decreases (increases) by a factor of around 3 as temperature is increased, while the one at 253 cm^{-1} remains almost constant.

NEUTRON DIFFRACTION RESULTS

To examine possible structural changes over the temperature region of the anomalous behavior of the Brillouin scattering, neutron diffraction measurements were made at the GLAD facility at IPNS.[9] The sample used was part of the high-purity, anhydrous sample used in the INS measurements, which had previously been shown to have negligible water content.[4] It was contained in three vitreous silica tubes, 3 mm I.D., 4 mm O.D., and mounted in a vanadium furnace on the diffractometer. Diffraction patterns were obtained at 350°C and 500°C and corrected for container and furnace scattering, absorption and multiple scattering using standard procedures. The data were normalized with reference to a 0.635-cm diameter standard vanadium rod. The low-Q regions of the neutron-weighted average structure factors S(Q) are shown in Fig. 4. The most obvious change with temperature is the shift in the position of the "first sharp diffraction peak", which is known to be a signature of intermediate-range order.[10] The peak center moves from 1.04 to 1.01 ± 0.01 Å^{-1} over the temperature interval of the measurement, about a 3% decrease. According to the thermal expansion data discussed below, the volume change over this interval is also about 3%. The measurements of Allen *et al.*[2] found a peak shift of 6% over a somewhat larger temperature interval, 330°C to 600°C, quite consistent with the present results.

Real space distribution functions were obtained by Fourier transformation of S(Q) out to 18.0 Å^{-1}. Gaussian fits, made to the resulting T(r) functions using standard procedures,[11] gave nearest-neighbor Zn-Cl coordination numbers of 4.31 and 4.15 ± 0.2 at 350°C and 500°C, respectively. These values are reasonably consistent with 4.3 ± 0.3 obtained by Biggin and Enderby[1] at 327°C and with 3.93 and 3.67 ± 0.1 obtained by Allen *et al.*[2] at 330°C and 600°C, respectively. The positions of the first two coordination peaks changed negligibly (less than 1%), as did the second-neighbor (Zn-Zn and Cl-Cl) coordination number. This is also consistent with the earlier work. Thus, coordination changes with temperature in the short-range structure appear to be limited to a small decrease in the Zn-Cl coordination, about $2.5.10^{-4}$/°C, comparable in relative magnitude to the decreases in the density and in the scattering vector of the first sharp diffraction peak.

INTERPRETATION OF THE RAMAN RESULTS

There have been two interpretations suggested for the features in the spectra in Fig. 2: (i) they are due to different chemical species[5] of $ZnCl_n$ or (ii) different vibrational symmetry modes[4,12] of $ZnCl_4$. The first model is hard to reconcile with the observation of more than one peak even in the glassy state; the observed temperature dependence of the relative intensities of the various features is hard to reconcile with the second model. We have chosen to interpret our data along the lines of the first model where the three peaks are associated with different coordination states of the Zn atoms viz. $ZnCl_4$, $ZnCl_3$ and $ZnCl_2$. The intensity of each peak is assumed to be proportional to the total number of units with a specific coordination. Assuming that the probability of breaking a Zn-Cl bond, given by exp(-E/kt), is independent of the number of broken bonds, it is straightforward to calculate the number of Zn atoms with zero, one and two broken bonds. If N_0 is the total number of Zn atoms then we have

$$N_1/N_0 = 1/(1 + \exp(-E/kt) + \exp(-2E/kt))$$

$$N_2/N_0 = \exp(-E/kt)/(1 + \exp(-E/kt) + \exp(-2E/kt)) \qquad [1]$$

$$N_3/N_0 = \exp(-2E/kt)/(1 + \exp(-E/kt) + \exp(-2E/kt)).$$

Following Ref. 5 we also write

$$E = \Delta H - T\Delta S. \qquad [2]$$

Fitting the data in Fig. 3 to Eqs. 1 and 2 yields $\Delta H = 4.0 \pm 0.1$ kcal/mol and $\Delta S = 5.7 \pm 0.1$ cal/(mol K). Comfortingly fits to all three data sets yield almost identical values which are also in good agreement with those ($\Delta H = 4.24$ kcal/mol and $\Delta S = 5.86$ cal/(mol K)) extracted in Ref. 5 from volume *vs.* temperature data. The full lines in Fig. 3 are obtained with our values of ΔH and ΔS given above.

The above model leads directly to an expression for the volume expansion. If each bond breaking produces a change in volume ΔV then the total volume of the system is given by

$$V = V_0 + \Delta V(N_2 + 2N_3) \qquad [3]$$

where V_0 is the volume at zero Kelvin. The temperature derivative of this expression yields the thermal expansion α: using our values of ΔH and ΔS we obtain the results given in Fig. 5. Note that since ΔV is not known the absolute value of α is also unknown. However, using the experimental[13] values of α, also plotted (squares) in Fig. 5, allows us to make an estimate of its magnitude. Note that this scaling assumes that all the measured expansion originates from the bond breaking process.

The final step in our analysis comes by recalling the thermodynamic identity

$$(\gamma\text{-}1) = VT\alpha^2 B_S/C_P \qquad [4]$$

where B_S is the adiabatic bulk modulus. Taking $B_S = 10^{11}$ erg/cm^3 and $C_P = 24.1$ cal/(mol K) from Refs. 6 and 14, and since all other parameters are known, allows us to calculate γ: the result is shown in Fig. 6.

CONCLUSIONS

Over the temperature range where previous Brillouin results[6] indicated a maximum in C_P/C_V our neutron and Raman scattering experiments show only small and monotonic changes. However, the change in the relative intensities of the Raman peaks can be interpreted in the framework of a model in which the changes are associated with breaking of Zn-Cl bonds. This model leads directly to an expression for the thermal expansion which in turn allows the ratio C_P/C_V to be calculated: the results are in excellent qualitative agreement with the Brillouin results but there are large uncertainties in the absolute magnitude.

In summary: the results presented here neither confirm nor contradict the existence of an anomaly in C_P/C_V in $ZnCl_2$. In order to resolve this issue it is necessary to await more accurate experimental data on both the specific heat and thermal expansion in this temperature range.

ACKNOWLEDGMENTS

Work supported by the U.S. Department of Energy, BES-Materials Sciences, under contract #W-31-109-ENG-38. The authors wish to thank Dr. A.J.G. Ellison for the furnace configuration at GLAD, and K.J. Volin and the operations staff at IPNS for making the neutron diffraction measurements possible.

REFERENCES

1. S. Biggin and J.E. Enderby, J. Phys. C: Solid State Phys. **14**, 3129-3136 (1981).
2. D.A. Allen, R.A. Howe, N.D. Wood and W.S. Howells, J. Chem. Phys. **94**, 5071-5076 (1991).
3. M.P. Tosi, D.L. Price and M.-L. Saboungi, Annu. Rev. Phys. Chem. **44**, 173-211 (1993).
4. D.L. Price, M.-L. Saboungi, S. Susman, K.J. Volin, and A.C. Wright, J. Phys.: Condens. Matt. **3**, 9835-9842 (1991).
5. C.A. Angell and J. Wong, J. Chem. Phys. **53**, 2053 (1970).
6. M. Grimsditch and N. Rivier, Appl. Phys. Lett. **58**, 2345 (1991).
7. M. Stoltwisch, J. Sukmanowski, D. Quitmann and M. Kuenzler, Mater. Sci. Forum **6**, 571 (1985).
8. M. Stoltwisch, J. Sukmanowski and D. Quitmann, J. Chem. Phys. **86**, 3207 (1987).
9. A.J.G. Ellison, R.K. Crawford, D.G. Montague, K.J. Volin and D.L. Price, J. Neutron Res. 1, 61-70 (1993).
10. S.C. Moss and D.L. Price, in Physics of Disordered Materials, ed. D. Adler, H. Fritzsche and S.R. Ovshinsky (Plenum, NY, 1985), pp. 77-95; D.L. Price, S.C. Moss, R. Reijers, M.-L. Saboungi and S. Susman, J. Phys.: Condens. Matt. 1, 1005-1008 (1989).
11. S. Susman, K.J. Volin, D.G. Montague and D.L. Price, J. Non-Cryst. Solids 125, 168-180 (1990).
12. F.L. Galeener, J.C. Mikkelsen, A.C. Wright, R.N. Sinclair, J.A.E. Desa and J. Wong, J. Non-Cryst. Solids 42, 23- (1980); M.L. Cacciola, S. Magazu, P. Migliardo, F. Aliotta and C. Vasi, Solid State Comm. 57, 513- 1986).
13. J.D. Mackenzie and W.K. Murphy, J. Chem. Phys. **33**, 366 (1960); M. Goldsten and N. Nakonecznyj, Phys. Chem. Glasses **6**, 126 (1965).
14. D. Cubicciotti and H. Eding, J. Chem. Phys. **40**, 978 (1964).

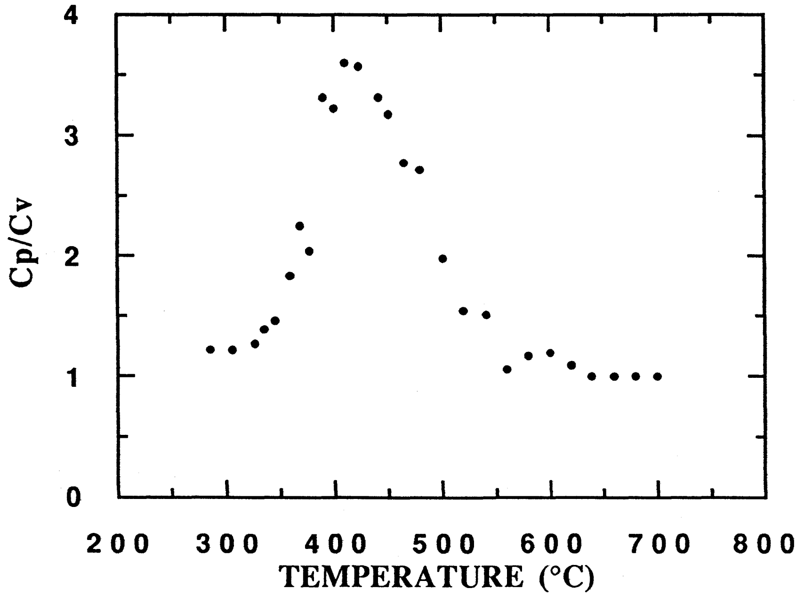

Fig. 1. C_p/C_V anomaly in $ZnCl_2$ obtained from Brillouin scattering experiments (Ref. 6).

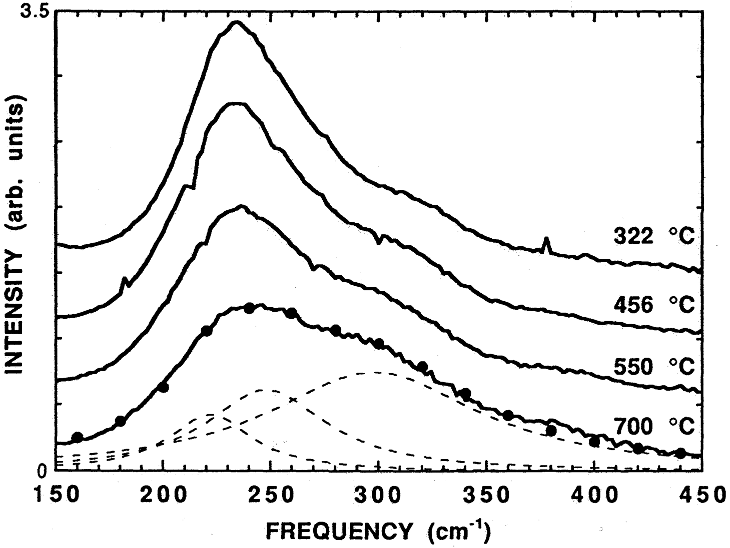

Fig. 2. Representative polarized Raman spectra of $ZnCl_2$ at various temperatures. The dashed lines are three Lorenzians obtained from a fit to the 700°C data. The symbols are the sum of the three Lorenzians.

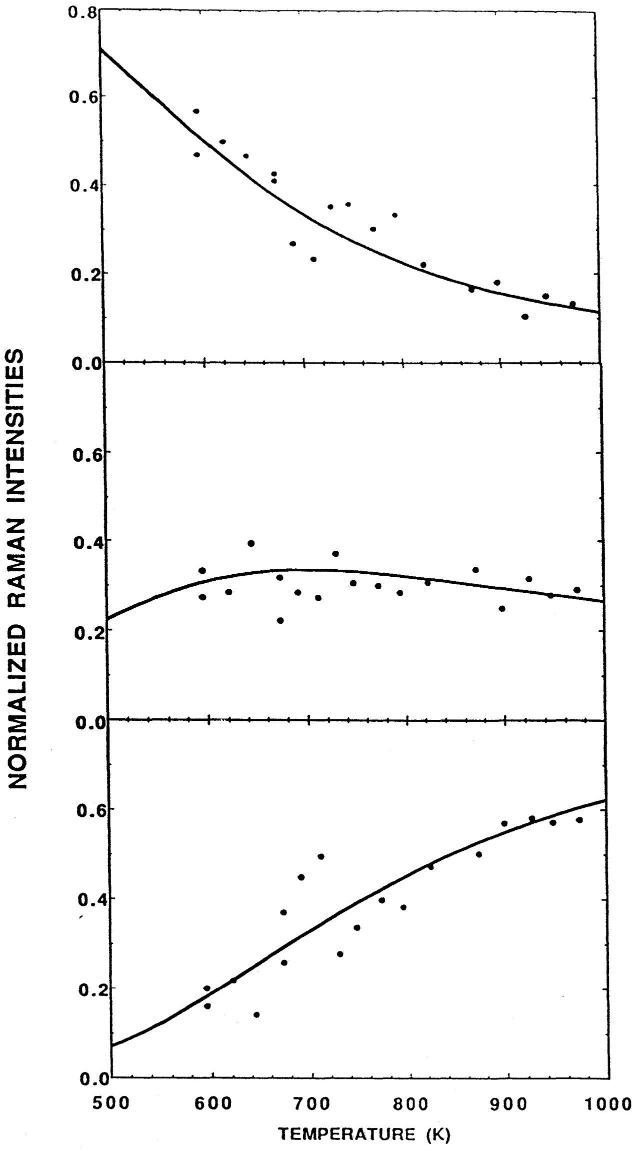

Fig. 3. Fraction of the total intensity under each of the three peaks in Fig. 2. The dots are experimental, the full lines represent Eqs. 1.

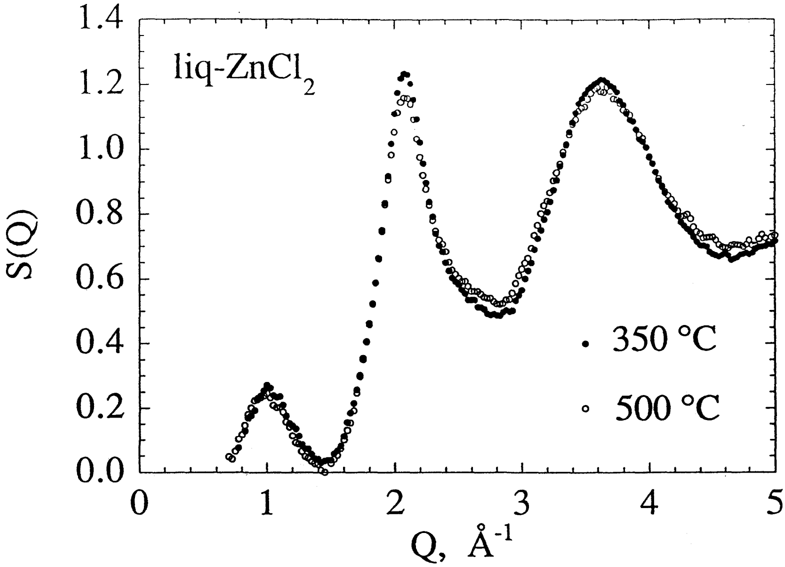

Fig. 4. Neutron weighted average structure factors S(Q) at low scattering vector Q for $ZnCl_2$ at 350°C and 500°C.

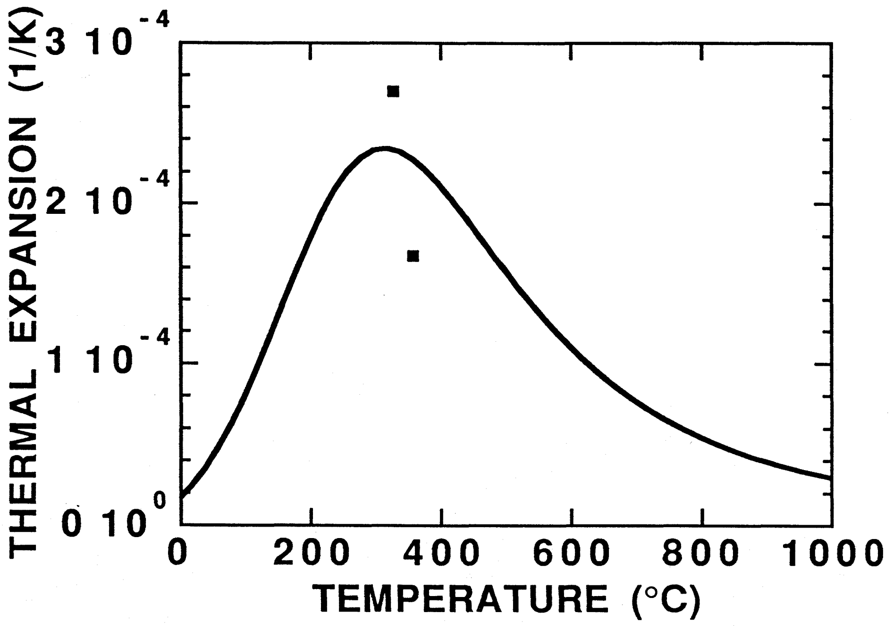

Fig. 5. Thermal expansion of $ZnCl_2$. The full line represents Eq. 3, the squares are experimental values from Ref. 13.

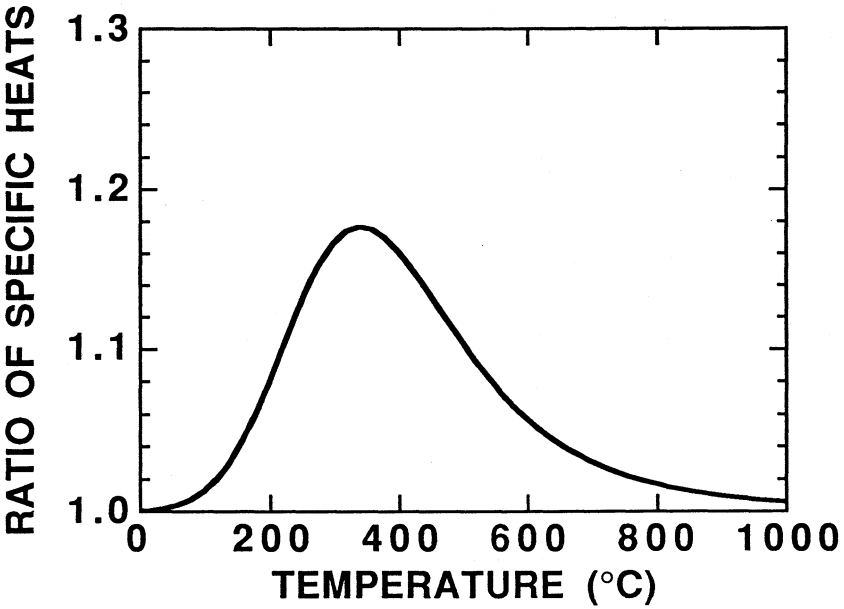

Fig. 6. C_P/C_V calculated using Eq. 4 and the values given in the text.

DOI: 10.1149/199413.0069PV

NEUTRON DIFFRACTION STUDY OF ALUMINUM CHLORIDE IMIDAZOLIUM CHLORIDE MOLTEN SALTS

S. Takahashi,* Marie-Louise Saboungi, K. Suzuya
Argonne National Laboratory
Argonne, IL 60439

N. Koura
Faculty of Science and Technology,
Tokyo University of Science
2641 Yamazaki, Noda 278, Japan

ABSTRACT

The structure of molten mixtures of $(AlCl_3)_x$(1-ethyl-3-methylimidazolium chloride)$_{1-x}$ was investigated by neutron diffraction techniques for x=0.46, 0.50, 0.60 and 0.67. Results derived from earlier *ab initio* molecular orbital (6-31G* basis set) computations for $AlCl_4^-$, $Al_2Cl_7^-$, and EMI^+ were used to calculate the diffraction patterns; the calculated contributions of each species are thus obtained and the overall results are in good agreement with the measurements.

INTRODUCTION

Mixtures of aluminum chloride and 1-ethyl-3-methylimidazolium chloride (EMIC) are technologically relevant room-temperature molten salts.(1,2) To understand their structure, we have initiated a series of studies involving neutron scattering, Raman spectroscopy,(4) ^{27}Al and ^{35}Cl NMR,(4) and ab initio calculations.(4) In this paper, we report results obtained by neutron diffraction measurements.

EXPERIMENTAL

Neutron diffraction studies were carried out to obtain the structure and configuration of the ionic species. The measurements were made on the GLAD instrument at the Intense Pulsed Neutron Source at Argonne National Laboratory. The samples were prepared by mixing highly anhydrous $AlCl_3$ with fully deuterated EMIC in a glove box, where the H_2O and O_2 levels were maintained at less that 2 ppm. The melts were sealed under vacuum in quartz tubes of 1 mm wall thickness and inner diameter of 3 mm. Four compositions, 46, 50, 60 and 67 mol% of $AlCl_3$, were selected. Measurements were made on each sample at room temperature, 298 K, followed by a similar measurement on an empty fused silica container of the same dimension and at the same temperature for purposes of instrument calibration and data normalization; measurements were also carried

---

* Present address: Nisshin Steel Co., Ltd. 7-1, Koya-shinmachi Ichikawa, Chiba, Japan

out on a 0.64 cm diameter vanadium standard and with the spectrometer empty, both at 298 K. The data were analyzed with standard procedures developed at Argonne for glass and liquid diffraction data incorporating simple corrections for multiple scattering and inelasticity effects.

The measured differential cross section per atom $d\sigma_a$ / $d\Omega$ is reduced to the total structure factor $S(Q)$ according to

$$d\sigma_a / d\Omega = \langle\bar{b}\rangle^2[S(Q)-1]+\langle\overline{b^2}\rangle \tag{1}$$

where

$$\langle\bar{b}\rangle = \sum_i x_i \bar{b}_i, \tag{2}$$

and

$$\langle\overline{b^2}\rangle = \sum_i x_i \overline{b_i^2} \tag{3}$$

Here x_i denotes the concentration of the ith component and $\bar{b}_i$ and $\overline{b_i^2}$ are the mean and mean-square scattering amplitudes, respectively, for component i averaged over the nuclear isotopes and spins for that component. In the case of a multicomponent system, $S(Q)$ is, by definition, a weighted sum of partial structure factors, $S_{ij}(Q)$:

$$S(Q) = \sum_{ij} \sqrt{x_i x_j}\, \bar{b}_i \bar{b}_j S_{ij}(Q) / \langle\bar{b}\rangle^2 \tag{4}$$

RESULTS

Fig. 1 shows the structure factors $S(Q)$ as measured for the four solutions. These are rather similar over the range $Q > 5$ Å^{-1}. However, they show differences at relatively low Q, in the range 1-5 Å^{-1}, which must be due to the interactions between the anions Cl_4^-, $Al_2Cl_7^-$, and $AlCl_4^-$, and the cation, EMI^+.

The real space functions complement the reciprocal-space information. The total correlation $T(r)$ and the average pair distribution function $g(r)$ are derived from the function

$$D(r) = \frac{2}{\pi}\int_0^{Q_{max}} Q[S(Q)-1]\sin(Qr)dQ \tag{5}$$

from which it follows that:

$$T(r) = D(r) + 4\pi\rho r \tag{6}$$

and

$$g(r) = 1 + D(r) / 4\pi\rho r \tag{7}$$

The $T(r)$ and $g(r)$ for the four melts are shown in Figs. 2 and 3, respectively. Some information on the interatomic distances can be obtained from these plots. However, it is difficult to make a detailed interpretation because of the complex nature of the systems. The structures of $AlCl_4^-$, $Al_2Cl_7^-$, and EMI^+ were calculated by the *ab initio* molecular orbital (6-31G* basis set) method.(14) The $AlCl_4^-$ anion has a T_d structure with a Al-Cl bond length of 2.17 Å and Cl-Cl bond length of 3.54 Å. The $Al_2Cl_7^-$ anion has a C_2 structure with a bent Al-Cl-Al angle of 123.4 °. The Al-Cl distance in the bridge is 2.32 Å, and that of the terminal group is 2.13 Å. The EMI^+ cation has a structure with C_1 symmetry. which is shown in Fig. 4. The torsion angle of the terminal $-CH_3$, i.e., $H_6C_4N_2$ dihedral angle, of the ethyl group is 73 °. Selected geometrical parameters from the HF/6-31G* structure are listed in Table 1.

The major anions are expected to be $AlCl_4^-$ and Cl^- for the 46 mol%, $AlCl_4^-$ for the 50 mol%, $AlCl_4^-$ and $Al_2Cl_7^-$ for the 60 mol%, and $Al_2Cl_7^-$ for the 67 mol% $AlCl_3$ melt. If correlations between molecular orientations and positions can be neglected, $S(Q)$ takes the form:

$$S(Q) = f_1(Q) + f_2(Q)[S_c(Q) - 1] + 1 - \frac{\langle \bar{b}^2 \rangle}{\langle \bar{b} \rangle^2} \tag{8}$$

where $f_1(Q)$ is an intramolecular form factor, and $f_2(Q)$ and $S_c(Q)$ are an intermolecular form factor and a molecular center structure factor, respectively. For the first three compositions, the intramolecular part (first term in Eq. (8)) of the diffraction patterns were calculated for $AlCl_4^-$ and EMI^+. The results shown in Fig. 5 are in good agreement with the experiments over the range $Q > 3$ Å^{-1}; at lower Q, one would expect the intermolecular part to dominate (second term in Eq. (8)). For the 67 mol% $AlCl_3$ melt, the calculations were carried out for $Al_2Cl_7^-$ and EMI^+ again only for the intramolecular contributions. Fig. 6 shows both measured and calculated $S(Q)$: the calculations represent the measurements surprisingly well.

In conclusion, we have shown that it is possible to derive detailed information by combining experimental techniques probing the atomic structure and *ab initio* calculations of the structure of the main ionic species known to be present in the melts. For $Q > 3$ Å^{-1}, the interpretation that we propose has been validated: it remains to extract information about the interactions between anion and cation by analyzing $S(Q)$ in the range Q =1-3 Å^{-1}.

ACKNOWLEDGMENTS

This work was supported by the U.S. Department of Energy, Basic Energy Science - Materials Science, under Contract No. W-31-109-ENG-38, and by Nisshin Steel Co., Ltd., Japan. We thank the Operations Staff of the Intense Pulsed Neutron Source for making the measurements possible.

REFERENCES

1. J. S. Wilkes, J. A. Levisky, R. A. Wilson, C. L. Hussey, Inorg. Chem., **21**, 1263 (1982).
2. S. Takahashi, I. Saeki, K. Akimoto, J. Surf. Fin. Soc., Japan, **40** (4), 42 (1989).
3. S. Takahashi, L. A. Curtiss, D. Gosztola and M.-L. Saboungi, Proc. Int. Symp. Molt. Salts Chem. and Tech., Electrochem. Soc. Pennington, New Jersey, 1993.
4. S. Takahashi, M.-L. Saboungi, R. J. Klingler, M. J. Chen, J. W. Rathke, J. Chem. Soc. Faraday Trans., **89**, 3591 (1993).

Table 1. EMI^+ geometry calculated by 6-31G* calculations.

Geometry	6-31G*
C_1N_1	1.32
C_1N_2	1.31
N_1C_2	1.38
N_2C_3	1.38
C_2C_3	1.34
N_1C_4	1.47
N_2C_5	1.48
C_5C_6	1.52
$<N_1C_1N_2$	110
$<C_1N_1C_2$	108
$<C_1N_2C_3$	108
$<N_1C_2C_3$	107
$<N_2C_3C_2$	107
$<C_1N_1C_4$	126
$<C_1N_2C_5$	126
$<N_2C_5C_6$	112

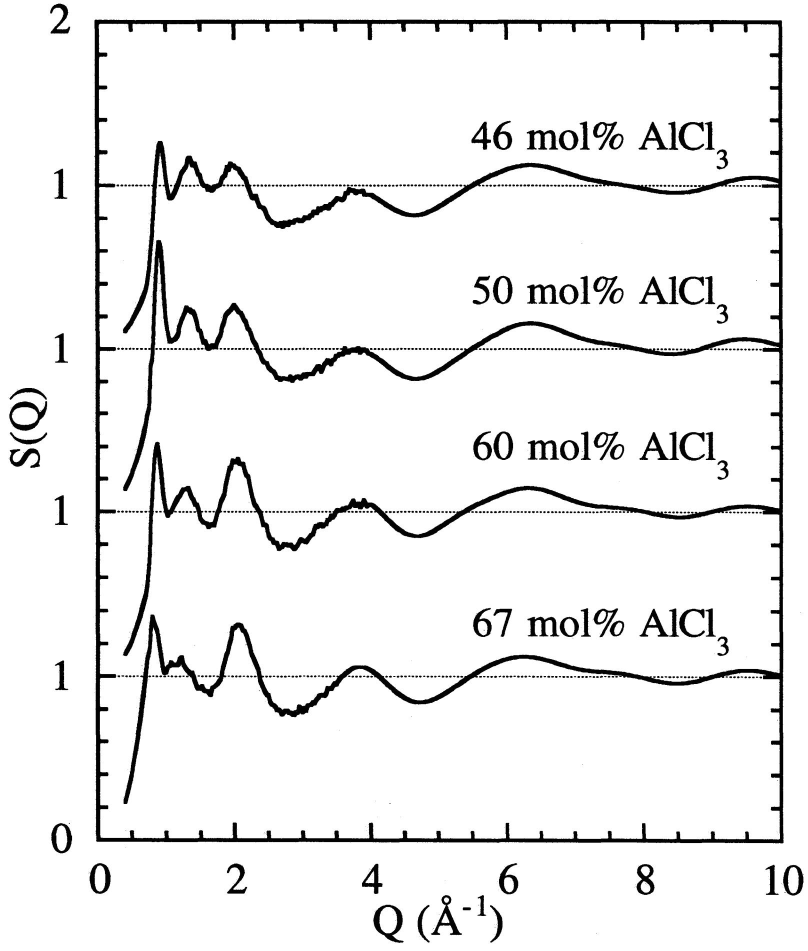

Fig. 1 Structure factors of AlCl$_3$-EMIC.

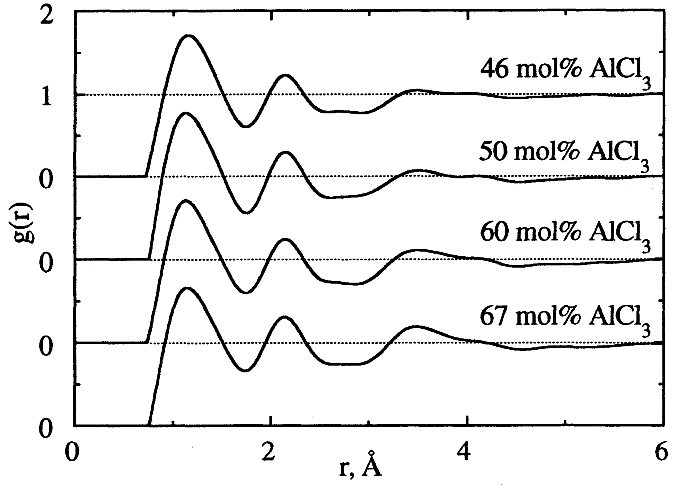

Fig. 2 Pair distribution functions of $AlCl_3$-EMIC.

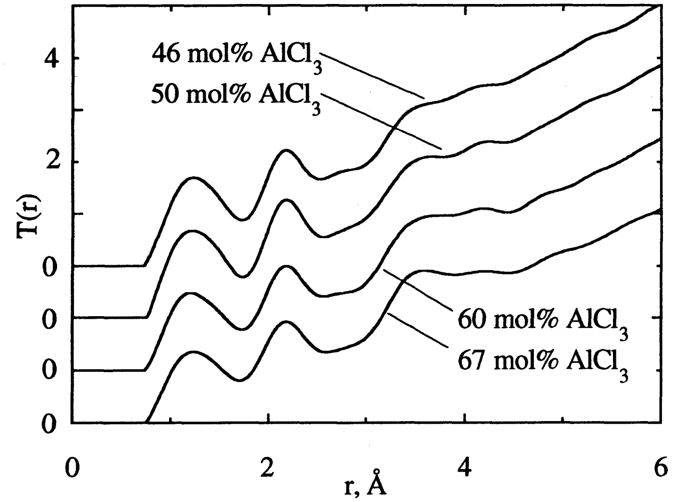

Fig. 3 Total correlation functions of $AlCl_3$-EMIC.

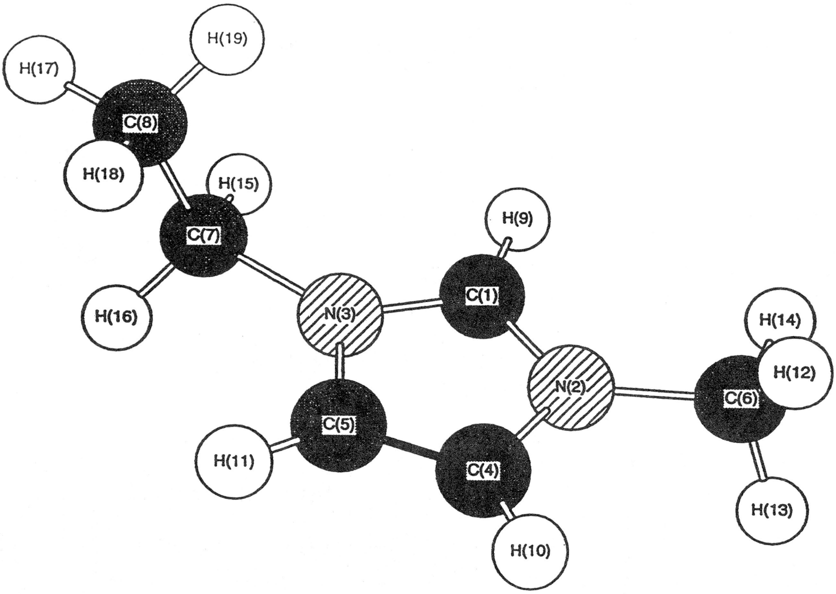

Fig. 4 HF/6-31G* optimized structure for EMI^+ cation.

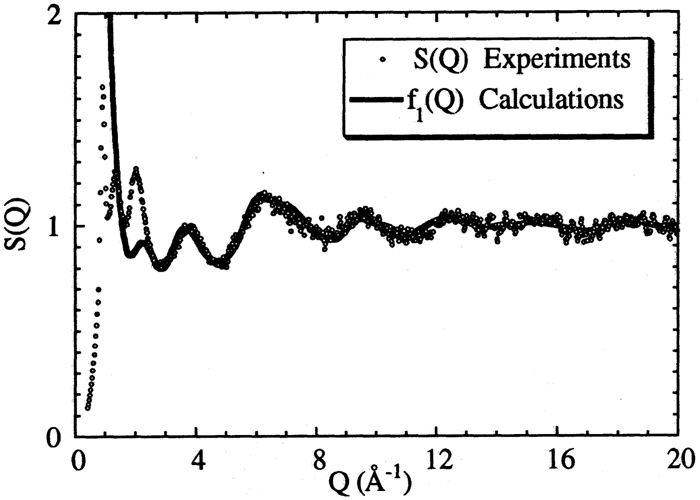

Fig. 5 Structure factors of 50 mol% $AlCl_3$ melt.

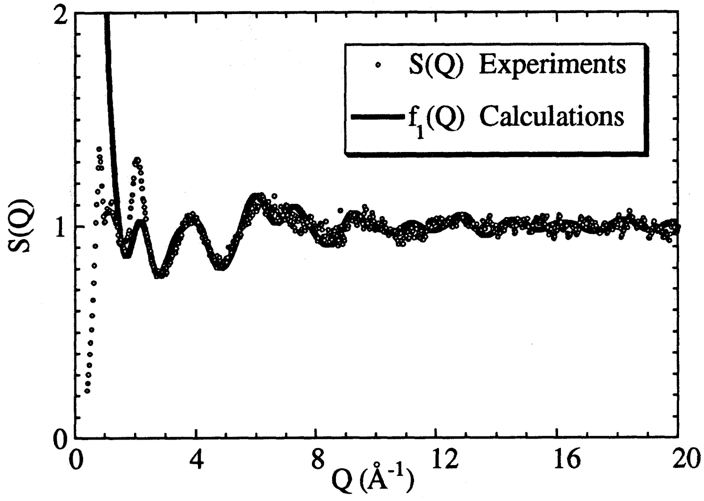

Fig. 6 Structure factors of 67 mol% $AlCl_3$ melt.

DOI: 10.1149/199413.0077PV

X-RAY ABSORPTION STUDY ON SOLID AND MOLTEN ALKALI HALIDES

Andrea Di Cicco, Mario Berrettoni
Dipartimento di Matematica e Fisica, Università degli Studi di Camerino
Via Madonna delle Carceri, 62032 Camerino (MC), Italy

Roberto Marassi, Roberto Tossici
Dipartimento di Chimica, Università degli Studi di Camerino
Via S. Agostino, 62032 Camerino (MC), Italy

Adriano Filipponi
Dipartimento di Fisica - Università degli Studi dell' Aquila
Via Vetoio, 67010 Coppito - L'Aquila, Italy

Abstract

Recent results of a XAS (X-Ray Absorption Spectroscopy) study of solid and molten Br-based alkali halides are presented. The results will be discussed focussing the attention mainly on CsBr. Low-noise high-temperature experiments using synchrotron radiation have been performed by using an original sample preparation techniques and a new furnace. Evidence of signals related to local structure in the liquid phase has been found. Unconventional data-analysis shows a marked reduction of the average metal-Br interionic distance in the liquid with respect to the solid.

I. INTRODUCTION

It is well-known that X-ray Absorption Spectroscopy (XAS) provides local structural information around atoms of selected atomic number by studying the fine structure above core-level excitation thresholds. [1] Quite recently it has been shown that reliable information on amorphous [2] and liquid [3,4] systems can be obtained using an "ab-initio" data-analysis, [5,6] based on the multiple-scattering theory (see for example ref. [7]), that can efficiently substitute standard data-analysis schemes. Moreover, the sensitivity of the technique to three-atom configurations, i.e. to the angle distributions, makes XAS a unique and complementary tool to be associated with X-ray and/or neutron diffraction spectroscopies that are usually employed to derive structural information in disordered systems. In this contribution we present recent results of a XAS study of solid and molten Br-based alkali metal halides. The presentation will be focussed mainly on CsBr. Application of XAS on pure ionic systems such as alkali halides is particularly interesting in order to study details of the local structure that has also been subject of many X-ray and neutron diffraction investigations. [8] New information about three-atom correlations, that can be useful for clarifying the role of three-body terms in ionic bonding (see for example ref. [9]), can be inferred from XAS data . To our knowledge previous XAS investigations on similar systems, using standard schemes for data-analysis, regarded principally RbBr. [10]

II. EXPERIMENTAL

X-ray absorption measurements near the Br K-edge have been performed in transmission mode at LURE (Laboratoire pour L'Utilisation du Rayonnement Electromagnètique) on the D-42 beam-line during dedicated beam-time.

Samples of alkali bromides (LiBr, NaBr, KBr, RbBr, and CsBr, Aldrich chemicals) have been prepared and tested in advance taking care of the severe requirements of thickness and homogeneity needed to perform accurate XAS measurements especially in the liquid phase. Particular care has also been taken to avoid water contamination. Finely ground powder of alkali bromides was dispersed in water-free ethanol or acetone under stirring using an ultrasonic bath. The suspension was left at rest for some time to allow precipitation of the largest particles. Average particle size was in the micrometric range. The same procedure was followed to prepare suspensions of Boron Nitride (BN). The suspensions were decanted and mixed together in such a way to obtain a BN to Metal-Br ratio of about ten to one. The final suspension was then filtered using a Millipore polycarbonate membrane under an inert gas atmosphere. This procedure permits to obtain a random dispersion of particles of Metal-Br powders into the BN matrix. The mixed powders were then dried and pressed at about 7 KBar in an argon filled dry-box (moisture content typically lower than 5 ppm). The final samples were pellets of about 1 cm diameter with thickness of about 1 mm. Thicknesses of the samples were chosen in order to obtain the best signal-to-noise ratio in absorption measurements. Optimization of samples has been performed at the University of Camerino using the XAS laboratory equipment (Centro Interdipartimentale Grandi Apparecchiature).

This original preparation technique has been proved to be successful for high-quality measurements at high temperatures. [11,12]

High-temperature measurements has been performed by using a specially designed furnace. [12] The furnace consisted of a cylindrical glass container, that permits a continuous inspection of the interior, equipped with two Kapton windows mounted on Teflon caps threaded on ACE-glass connectors. Vacuum tightness was ensured by using Vyton O-rings. Vacuum inside the furnace was about 10^{-4} Bar at the highest temperatures. The sample was placed inside a graphite crucible that was heated by electrical current flow. Total thickness of the graphite heater was about 200 μm giving a negligible absorption coefficient at the X-ray photon energies under consideration. The temperature was monitored continuously using a K-type thermocouple placed in direct contact with the sample. Typical temperature control was about 5 ^oC for temperatures less than 1500 ^oC. The crucible was held in place by two 10 mm diameter stainless steel water-cooled cylindrical conductors fixed on a Teflon top cover.

Before taking any measurements each sample was heated in vacuum above 200 ^oC for about 30 minutes to remove any residual moisture from the sample and the crucible.

III. RESULTS AND DISCUSSION

Figure 1 shows normalized near-edge absorption spectra of solid (room temperature, dashed curves) and molten alkali bromides at the Br K-edge. Liquid spectra have been taken at about 830 K (LiBr), 1030 K (NaBr and KBr), 1000 K (RbBr), and 950 K (CsBr). From the figure it is possible to observe the reduction of intensity of the fine structures due to disorder in the liquid phase. The main characteristics of the spectra of the solids are preserved in the liquids showing that local structures of molten and crystalline salts are, as expected, similar. The slight energy shifts of the modulated signals are due to changes in the mean first-neighbor distances.

Figure 2 shows the experimental near-edge structures of CsBr as a function of temperature. Curve (a) is the CsBr near-edge spectrum at room temperature; curve (b) has been recorded at 820 K, about 90 degrees below the melting point ($T_m \approx 909$ K). The reduction of intensity of the near-edge structures is clearly due to the increase of the thermal-disorder. Curve (c) is taken at 880 K, just below the melting point, and shows a slight further decrease in intensity. Finally, upper curve (d), taken at 950 K, shows the remarkable reduction in intensity and the visible shift due to the contraction of the first-neighbor distances associated with the transition to the liquid phase.

A single-scan measurement of the absorption coefficient of liquid CsBr at 950 K is reported in Figure 3. As may be seen, the signal-to-noise ratio is very good (about 10^3-10^4). Although the modulating signal has a rapidly decaying amplitude at high energies, structural oscillations are clearly observed up to about 200 eV in the raw data. In addition to the structural signal, possible many-electron contributions to the atomic background have to be considered. Due to the low intensity of the structural signal, many-electron contributions to the atomic background can be easily detected. The arrows indicate visible slope changes of the atomic background, due to the opening of the [1s3d] and [1s3p] double-electron excitation channels, occurring at about 90 eV and 200 eV above the edge respectively. The dashed straight lines, drawn in Figure 3, help to localize the slope changes. The first slope change, due to the [1s3d] channel, can be easily identified in the raw data. The second weaker slope change, although more difficult to observe in the figure, has to be taken into account in any refined structural data-analysis. The same atomic-like features have been already observed in gas-phase Br_2, HBr, [13] and brominated hydrocarbon molecules [14] as well as in solid RbBr [15,16].

Figure 4 compares the calculated $\chi(k)$, including only the first-neighbor signal (dashed), and the experimental modulating signals $\chi(k)$ derived from CsBr absorption spectra taking into account the contribution of the double-electron excitation channels to the atomic background. [13] $\chi(k)$ signals containing fine structures are shown as a function of the photoelectron wave vector k. The low-frequency first-neighbors signal can explain the main features of the spectra. The average distances have been found R = 3.68 (0.05) Å and R=3.40 (0.07) Å for solid and liquid CsBr respectively. The reduction of the average interionic distances in the liquid with respect to the solid is in agreement with previous determinations by diffraction on alkali chlorides. [8] In the case of the solid, the first-neighbor signal is definitely not sufficient to explain the experimental data that contains a high-frequency component. The presence of high-frequency signals in the spectrum taken at room temperature (lower curve, solid) is related to multiple-scattering contributions typical of the local structure of this salt. High-frequency signals of large amplitude are associated with the linear configurations Br-Cs-Br and Cs-Br-Cs for which the focusing effect takes place. In the liquid phase, the main contribution is certainly due to the first-neighbor two-atom signal. However, a weak high-frequency signal survive especially in the low-energy region. The presence of such signals is also confirmed in other alkali bromides in the near-edge region (see Fig. 1 and Fig. 2). A more detailed analysis of such high-frequency features in alkali halides may shed light on three-body correlations in highly ionic systems.

IV. CONCLUSIONS

Results of the first XAS experiment on molten alkali bromides are reported. The progresses in the experimental set-up have allowed to obtain high-temperature spectra showing a very good signal-to-noise ratio. In particular, a new oven that can handle samples at high temperature in a controlled or vacuum atmosphere has been used. Although the spectra has been recorded for the entire set of metal alkali bromides, data-analysis is presented only for CsBr. A remarkable reduction of the average interionic distance in the liquid phase has been found. Besides the dominating two-atom first-neighbours signal, evidence of higher-frequency signals related to three-atom distribution has been obtained.

ACKNOWLEDGEMENTS

We would like to thank the LURE staff, and in particular Anne Sadoc and Pierre Lagarde. We gratefully thank Franco Bizzarri and Carlo Santoni (Università di Camerino) for their invaluable technical support. This research has been partially financed by the TGE/CEE contract, Consiglio Nazionale delle Ricerche, and MURST (Italy).

REFERENCES

[1] "X-ray Absorption: Principles, Applications, Techniques of EXAFS, SEXAFS and XANES" edited by D. C. Konisberger and R. Prins, John Wiley & sons (1988).

[2] A. Filipponi, A. Di Cicco, M. Benfatto, and C.R. Natoli, Europhys. Lett. **13**, 319 (1990).

[3] A. Di Cicco and A. Filipponi, J. Non-Cryst. Solids **156-158**, 102 (1993).

[4] L. Ottaviano, A. Filipponi, A. Di Cicco, P. Picozzi, and S. Santucci, J. of Non-Cryst. Sol. **156-158**, 112 (1993).

[5] A. Filipponi, A. Di Cicco, T. A. Tyson, and C. R. Natoli, Sol. State Comm. **78**, 265 (1991).

[6] A. Filipponi and A. Di Cicco, Synchrotron Rad. News **6**, 21 (1993).

[7] T. A. Tyson, K. O. Hodgson, C. R. Natoli, and M. Benfatto, Phys. Rev. B **46**, 5997 (1992).

[8] J. E. Enderby and S. Biggin, in " Advance in molten salt chemistry 5", edited by G. Mamantov, pages 1-24, Elsevier (1983).

[9] M. Rovere and M. P. Tosi, Rep. Prog. Phys. **49**, 1001 (1986).

[10] J. F. Jal, J. Dupuy, and A. Sadoc, J. Phys. (Paris) C9 **46**, 107 (1985); J. Phys. (Paris) C8 **47**, 799 (1986).

[11] A. Filipponi, L. Ottaviano, and A. Di Cicco, (submitted).

[12] A. Filipponi and A. Di Cicco, (submitted).

[13] P. D'Angelo, A. Di Cicco, A. Filipponi, and N. V. Pavel, Phys. Rev. A, **47**, 2055 (1993).

[14] E. Burattini, P. D'Angelo, A. Di Cicco, A. Filipponi, and N. V. Pavel, J. Phys. Chem. **97**, 5486 (1993).

[15] G. Li, F. Bridges, and G. S. Brown, Phys. Rev. Lett. **68**, 1609 (1992).

[16] A. I. Frenkel, E. A. Stern, M. Qian, and M. Newville, Phys. Rev. B **48**, 12449 (1993).

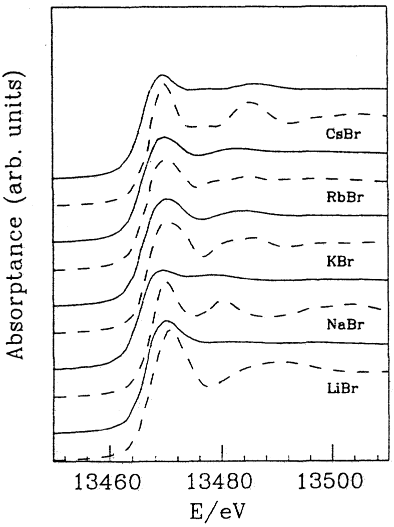

FIG. 1. Near-edge x-ray absorption fine structures near the Br K-edge of solid (dashed line) and liquid (solid line) alkali halides.

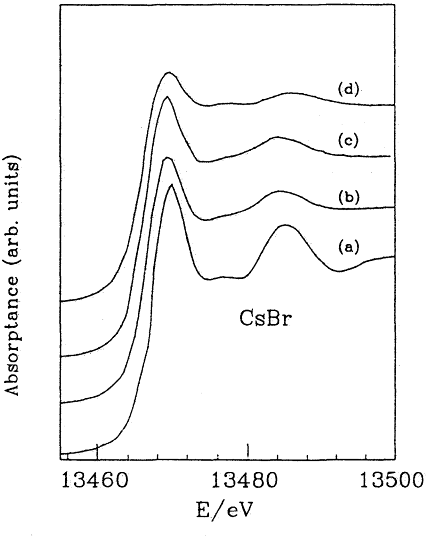

FIG. 2. Near-edge x-ray absorption spectra of CsBr near the Br K-edge shown as a function of temperature. Curve (a), (b) and (c) are the X-ray absorption spectra of crystalline CsBr recorded at 300 K, 820 K and 880 K respectively ($T_m \approx 909$ K). A spectrum of liquid CsBr (d), measured at 950 K, is shown for comparison.

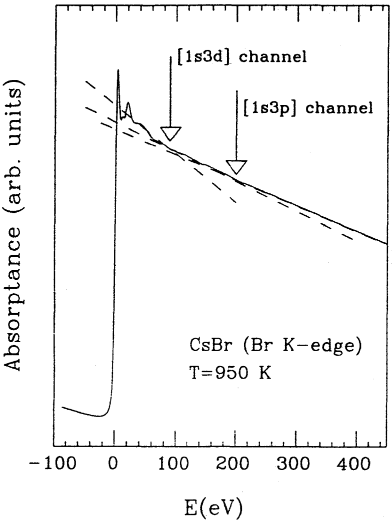

FIG. 3. Extended X-ray absorption spectrum of liquid CsBr recorded in a single-scan measurement. A detectable structural signal extending up to about 200 eV is clearly visible in this low-noise data. The presence of an evident slope change at about 90 eV and of a weaker one at about 200 eV, due to the opening of double-electron excitation channels, can be detected simply looking at the raw data. Dashed lines help to localize the slope changes.

FIG. 4. Experimental structural signals $\chi(k)$ (solid lines) and calculated first-neighbor signals (dashed) shown as a function of the photoelectron wave vector k.

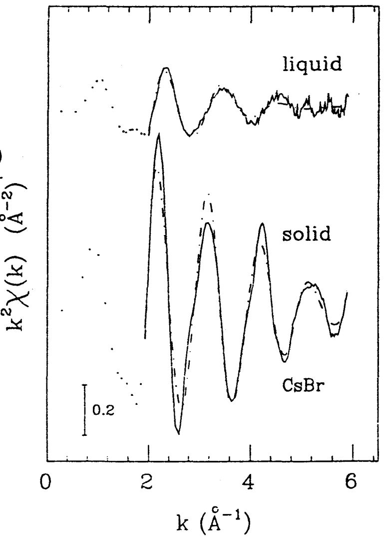

DOI: 10.1149/199413.0083PV

SOME RECENT CONTRIBUTIONS OF MOLTEN SALTS STUDIES TO THE UNDERSTANDING OF VERY CONCENTRATED AQUEOUS SOLUTIONS

Maurice Abraham
Département de Chimie, Université de Montréal, C.P. 6128,
Succ. A, Montréal, Qc, Canada, H3C 3J7

ABSTRACT

Researches in the field of molten salts are beginning to influence the methodological approaches of very concentrated aqueous solutions through results obtained in investigating solutions where molten salts are the solvent and water, the solute. Some equations useful for the study of salt activity in solutions of water in molten salts and the viscosity of such solutions are introduced by means of the BET model, the absolute reaction rate theory and the quantum concept of hole or lacunon. A very simple colligative property based on the viscosity and the electrical conductivity applicable to solutions of water in molten nitrates is also considered.

INTRODUCTION

It appears that experimental and theoretical researches in the field of molten salts and related chemical substances will considerably influence our general scientific perception of electrolyte solutions, perhaps even those containing water as the solvent. The first signs of this evolution are already distinguishable especially when one takes into consideration some important thermodynamic and transport parameters such as the salt activity and the viscosity. Since the subject matter of the present paper is the impact of some molten salts studies on our progress in the field of very concentrated aqueous solutions and, particularly, solutions where the salts are the solvent instead of the solute, we will limit ourselves to the use of concepts which have been successfully applied to molten salts.

WATER AND SALT ACTIVITIES

From recent studies (1), it was concluded that the approach based on the BET model (2) adapted to electrolyte solutions by Stokes and Robinson (3) is most relevant to express the relationship between the activity and the concentration of water in very ionic solutions. As suggested until now by the experimental results, the Anderson parameter (4) can be neglected, and consequently, the Stokes and Robinson equation may be written

$$\frac{a_w\left(1 - x_w\right)}{x_w\left(1 - a_w\right)} = \frac{1}{c\,r} + \frac{c - 1}{c\,r}\,a_w \qquad [1]$$

in which x_W and a_W are respectively the mole fraction and activity of water in the salt-water solution. The parameters c and r are constants expressed by

$$c = \exp\left[-\frac{\left(E - E_L\right)}{R\,T}\right] \qquad [2]$$

and

$$r = \frac{N_{si}}{N_A} \qquad [3]$$

in which E is the molar binding energy of water on sites close to the ions, usually considered to be cations, E_L, the molar binding energy of water in pure water (heat of liquefaction), N_{si}, the number of available sites with the binding energy E for the water molecules, per mole of salt, R, the gas constant, T, the Kelvin temperature and N_A, the Avogadro constant.

From the BET model, the following equation can also be obtained (5), which relates the salt activity, a_s, to the salt mole fraction, x_s

$$\frac{\lambda\left(1 - x_s\right)}{x_s\,(1 - \lambda)} = \frac{r}{c} + \frac{r\,(c - 1)}{c}\,\lambda \qquad [4]$$

where the parameter λ is expressed by

$$\lambda = a_s^{(1/r)} \qquad [5]$$

The parameters r and c in Eqs. [4] and [5] are the same as in Eq. [1].

Equation [4] gives the salt activity in a solution of water in a single salt or in a mixture of salts whose composition is kept constant so that it behaves like a single salt. Equation [4] does not give the activity of an individual salt in a solution containing several salts. In spite of this limitation, Eqs. [1] and [4] could have interesting applications in estimating orders of magnitude of useful thermodynamic parameters if additivity rules applicable to the BET constants, observed in some nitrate-water mixtures (5-7) are confirmed in the future for other salt-water solutions. The validity range of the BET model seems to be $0 < x_w < 0.5\text{-}0.7$, depending upon the nature of the salts (8).

As typical examples, the curves a_s and a_w vs x_w in Fig. 1 are defined by Eqs. [1] and [4] applied to three nitrate-water systems using values of c and r determined from water vapor pressure measurements (1,9).

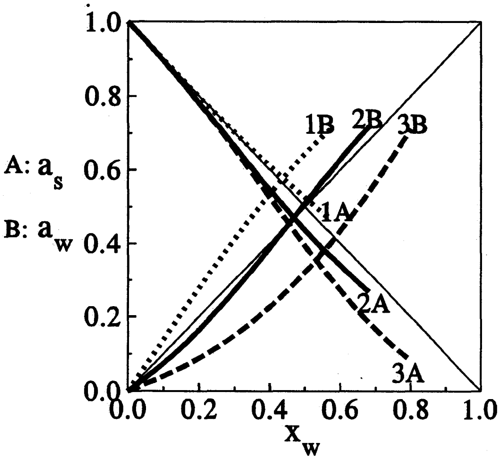

FIGURE 1
The salt activity a_s and water activity a_w as functions of the water mole fraction x_w, at 372 K.

1: $[0.515AgNO_3 - 0.485TlNO_3] + H_2O$

2: $[0.476AgNO_3 - 0.449TlNO_3 - 0.075Cd(NO_3)_2] + H_2O$

3: $[0.467TlNO_3 - 0.214CsNO_3 - 0.319Cd(NO_3)_2] + H_2O$

For the system containing only Ag^+ and Tl^+ cations, a_s and a_w exhibit positive deviations from Raoult's law. In contrast, negative deviations of a_s and a_w from Raoult's law are observed in the case of the system containing a high concentration in Cd^{2+} which have a strong hydrating power. For the system containing a relatively low concentration in Cd^{2+}, the curve a_w vs x_w shows positive and negative deviations from Raoult's law, in connection with the simultaneous presence of weakly and strongly hydrated cations whereas such a crossover point does not exist for its curve a_s vs x_s. It has to be noticed that in the limit of vanishing water mole fraction the Raoult's straight line is tangent to the curves defined by Eq. [4] in a satisfactory manner. Moreover, in the case of the system containing only Ag^+ and Tl^+ cations, a_s is practically equal to x_s over a relatively large salt mole fraction range, $\sim 0.7 < x_s < 1$.

VISCOSITY

With regard to this property, the absolute reaction rate theory (10,11) and the quantum concept of hole (12,13) can be fruitful, although other theories are used when cooperative phenomena have to be taken into account (14). With the quantum concept of hole, one considers that a hole in a liquid exhibits, in connection with its surroundings, wavelike properties. A frequency ν and a quantum of energy $h\nu$, h being the Planck constant, are associated to the hole. The moving hole together with the induced perturbation of the surrounding quasi-lattice is called the lacunon or fluctuating hole. Considering a simple liquid in which a state of equilibrium exists between the lacunons and the flow units, we have the following expression

$$\frac{N^{\star}}{N} = K \tag{6}$$

where K is the equilibrium constant, $N^{\star}$ and N respectively the number of lacunons and the number of flow units in the molar volume of liquid.

The constant K is related to a standard free energy, taken as the molar free energy of activation for the viscous flow, $\Delta G_{\eta}^{\star}$, in the Eyring equation

$$\Delta G_{\eta}^{\star} = - R\,T \ln K \tag{7}$$

The Eyring equation may be written in the form

$$\phi = \frac{1}{\eta} = \frac{v}{h} \exp\left(- \frac{\Delta G_{\eta}^{\star}}{R\,T} \right) \tag{8}$$

where ϕ is the fluidity, η, the viscosity and v, the volume of a hole considered to be close to that of a flow unit.

From Eqs. [6], [7] and [8]:

$$\phi = \frac{v}{h} \frac{N^{\star}}{N} \tag{9}$$

The product ($vN^{\star}$) is the volume of the fluctuating holes or lacunons. One would expect that increased free volume would make easier lacunon formation. Then, assuming that the volume of the lacunons is proportional to the free volume, one may write

$$v\,N^{\star} = \gamma\, V_f \tag{10}$$

where V_f is the molar free volume and γ is a proportionality constant.

The molar free volume itself is given by

$$V_f = V - V_\phi \qquad [11]$$

where V is the molar volume and V_ϕ, the intrinsic molar volume.

From Eqs. [9], [10] and [11]

$$\phi = \frac{\gamma}{h\,N}\left(V - V_\phi\right) \qquad [12]$$

In the case of a simple liquid where the flow units are the molecules themselves, N is the Avogadro constant N_A and Eq. [12] becomes

$$\phi = \frac{\gamma}{h\,N_A}\left(V - V_\phi\right) \qquad [13]$$

If γ is a constant within a given temperature range, Eq. [12], or [13], expresses a linear relationship between the fluidity and the molar volume. The mathematical form of this equation is analogous to that of an equation proposed by Batchinski (15). This equation has been written in various forms (15-17) equivalent to the following

$$\phi = B_\phi\left(V - V_\phi\right) \qquad [14]$$

where V_ϕ and B_ϕ are two empirical constants valid over a given temperature range.

It has to be noticed that the Batchinski equation was proposed at a time when, in fact, quantum arguments could not be recognized as they are now in the absolute reaction rate theory and the quantum concept of hole.

Results obtained by application of Eq. [13] to nitrate-water systems are shown in Figs. 2, 3 and 4, using average values of the molar volume expressed by

$$V = \frac{x_s \sum_i X_i M_i + x_w M_w}{\rho} \qquad [15]$$

where M_i is the molecular weight of the salt i, M_w, the water molecular weight, X_i, the mole fraction of the salt i in the anhydrous salt system whose composition is kept constant, ρ, the density of the salt-water system. N is taken to be equal to N_A, assuming the flow units to be H_2O molecules and salt entities such as

$\left(Tl^+, NO_3^-\right)$, $\left(Cd^{2+}, 2\ NO_3^-\right)$, etc...

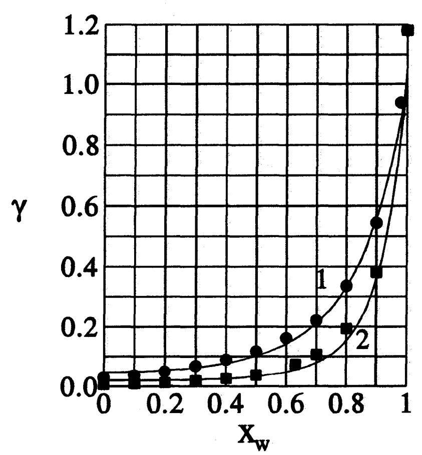

FIGURE 2

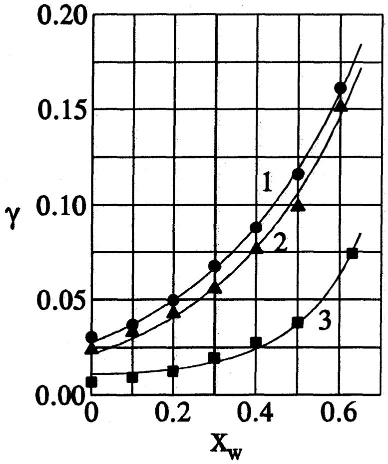

FIGURE 3

FIGURE 2: γ as function of the water mole fraction x_w, at 372 K.
1: $[0.515AgNO_3 - 0.485TlNO_3] + H_2O$
2: $[0.467TlNO_3 - 0.214CsNO_3 - 0.319Cd(NO_3)_2] + H_2O$

FIGURE 3: γ as function of the water mole fraction x_w, at 372 K.
1: $[0.515AgNO_3 - 0.485TlNO_3] + H_2O$
2: $[0.464AgNO_3 - 0.436TlNO_3 - 0.100Cd(NO_3)_2] + H_2O$
3: $[0.467TlNO_3 - 0.214CsNO_3 - 0.319Cd(NO_3)_2] + H_2O$

As may be seen in Fig. 2, the curves $\gamma = f(x_w)$ for two different nitrate-water systems converge and cut the γ-axis at about $\gamma = 1$ for pure water. The curve of the system in which $X(Cd(NO_3)_2) = 0.319$ is situated below that of the system containing only monovalent cations. Over the concentration range $0 < x_w < \sim 0.7$, an enlarged view of the curves $\gamma = f(x_w)$ for three systems, provided by Fig. 3, shows clearly the effect of the addition of the Cd^{2+} cation on the values of γ, even in the case of the system in which $X(Cd(NO_3)_2) = 0.100$. This latter curve is close to that of the system which does not contain divalent cations and in an appropriate lower position. Addition of divalent cations to monovalent ones increases electrostatic interactions and consequently reduces hole formation.

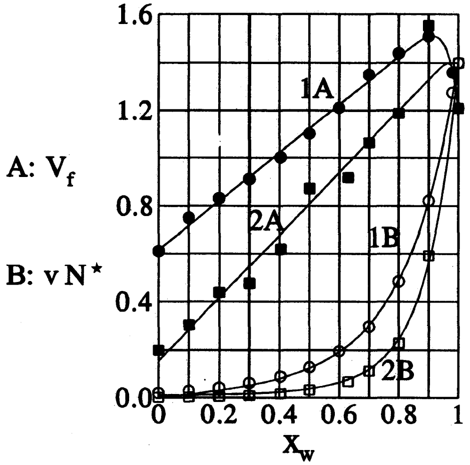

FIGURE 4

The molar volume of the lacunons (vN*) and the molar free volume V_f as functions of the water mole fraction x_w, at 372 K.

1: $[0.515AgNO_3 - 0.485TlNO_3] + H_2O$

2: $[0.467TlNO_3 - 0.214CsNO_3 - 0.319Cd(NO_3)_2] + H_2O$

Unit of vN* and V_f : $cm^3\ mol^{-1}$

Figure 4 gives the orders of magnitude of the molar volume of the lacunons (vN*) and the molar free volume V_f as functions of x_w, for the two same systems as in Fig. 2. Comparison of these two figures points to the similarity of the curves $\gamma = f(x_w)$ and $(vN^*) = f(x_w)$, in connection with the fact that V_f is quasi linear over a large concentration range. It also leads to the conclusion that the lacunons involved in the viscous flow process of the molten nitrates would represent a small part of the free volume contrary to water where practically all the free volume would appear in the form of lacunons.

VISCOSITY AND ELECTRICAL CONDUCTIVITY

In the course of investigations of solutions of water in molten nitrates [1,18], the following simple relation which contains no empirical constants, was found between the viscosity η and the electrical conductivity χ

$$\eta\ \chi = \eta_s\ \chi_s\ x_s \qquad [16]$$

where η_s and χ_s are respectively the viscosity and the electrical conductivity of the pure salt. This equation is valid accurately for $0.2 < x_s < 1$. Illustration of Eq. [16] is given in Fig. 5

More experiments are required at high temperature and high water vapor pressure with other salts than fused nitrates to determine the extent to which this new colligative property based on transport phenomena is feasible.

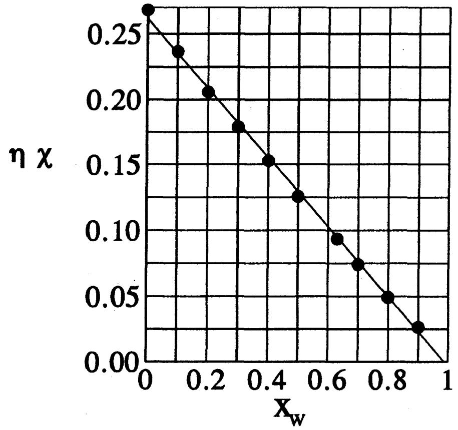

FIGURE 5

The product $\eta\ \chi$ as function of the water mole fraction x_w, for the system $[0.467TlNO_3 - 0.214CsNO_3 - 0.319Cd(NO_3)_2] + H_2O$, at 372K

Unit of $\eta\ \chi$: $C^2\ m^{-4}$

REFERENCES

1. M.-C. Trudelle-Abraham, Ph.D. Thesis, Université de Montréal (1987).
2. S. Brunauer, P.H. Emmet and E. Teller, *J. Am. Chem. Soc.*, **60**, 309 (1938).
3. R. H. Stokes and R. A. Robinson, *J. Am. Chem. Soc.*, **70**, 1870 (1948).
4. R. B. Anderson, *J. Am. Chem. Soc.*, **68**, 686 (1946).
5. M. Abraham, *J. Chim. Phys.*, **78**, 57 (1981).
6. J. M. Sangster, M.-C. Abraham and M. Abraham, *Can. J. Chem.*, **56**, 348 (1978).
7. M. Abraham, *Electrochim. Acta*, **26**, 1397 (1981).
8. H. Braunstein and J. Braunstein, *J. Chem. Thermodynamics*, **3**, 419 (1971).
9. M. Abraham, M.-C. Abraham, I. Ziogas and Z. Kodejš, *J. Am. Chem. Soc.*, **115**, 4300 (1993).
10. H. Eyring, *J. Chem. Phys.*, **4**, 283 (1936).
11. S. Glasstone, K. J. Laidler and H. Eyring, *The Theory of Rate Processes*, Mc Graw Hill, New York (1941).
12. M. Abraham and M.-C. Abraham, *Electrochim. Acta*, **33**, 967 (1988).
13. M. Abraham and M.-C. Abraham, *J. Phys. Chem.*, **94**, 900 (1990).
14. M. Spiro and F. King, *Ionic Liquids*,Chapter 5, D. Inman and D. Lovering Eds., Plenum Press, New York (1981).
15. A. J. Batchinski, Z. Physik. Chem., **84**, 643 (1913).
16. R. P. Chhabra and R. J. Hunter, Rheol. Acta, **20**, 203 (1981).
17. M. Abraham and M.-C. Abraham, *Electrochim. Acta*, **32**, 1475 (1987).
18. M. Abraham and M.-C. Abraham, *Electrochim. Acta*, **31**, 821 (1986).

DOI: 10.1149/199413.0091PV

CALORIMETRIC INVESTIGATION OF THE PrCl3-MCl MELTS AND OF THE M_3PrCl_6 COMPOUNDS(M = Li, Na, K, Rb, Cs)

M. Gaune-Escard, L. Rycerz*, W. Szczepaniak*, A. Bogacz*

IUSTI, UA 1168 CNRS, Université de Provence,
Centre de St Jérôme, av. Escadrille Normandie Niemen,
13397 Marseille Cédex 20 (France).

*Institute of Inorganic Chemistry and Metallurgy of Rare Elements,
Technical University, Wybrzeze St. Wyspianskiego 27,
50 370 Wroclaw (Poland).

ABSTRACT

The present work is a part of the thermodynamic research performed on the $LnCl_3$ - MCl systems (Ln - lanthanide, M - alkali metal). The molar enthalpies of mixing in the NaCl-$PrCl_3$ and KCl-$PrCl_3$ liquid binary systems were measured at the temperature 1122 K by direct calorimetry in the whole composition range . In both systems the enthalpies of mixing values are negative with a minimum value at $xPrCl_3 \approx 0.4$. We also determined the enthalpies of mixing of the MCl-$PrCl_3$ melts (M = Li, Na, K, Rb, Cs)at the composition $xPrCl_3 = 0.25$ i.e. the enthalpies of the reaction :

$$3\ MCl(l) + PrCl_3(l) = M_3PrCl_6(l)$$

These values are very similar to those of the systems MCl - $LnCl_3$ (Ln = La, Ce, Nd) previously investigated.

DSC experiments were also performed in order to measure the temperatures and enthalpies of phase transition in the K_3PrCl_6, Rb_3PrCl_6 and Cs_3PrCl_6 definite compounds.

INTRODUCTION

This work is a part of a general research program on the thermodynamic properties and electrical conductivity of the MCl-$LnCl_3$ liquid mixtures (M = Li, Na, K, Rb, Cs ; Ln = La, Ce, Pr, Nd) (1,2) and of the solid and liquid definite compounds M_3LnX_6 , which only exist for the heaviest akali metals (M = K, Rb, Cs).

We report here the experimental enthalpies of mixing of the NaCl-$PrCl_3$ and

KCl-$PrCl_3$ liquid systems. A comparison with the analogous $LaCl_3$- (3), $CeCl_3$-(4), $NdCl_3$- based mixtures (2) is also presented

Furthermore the enthalpies of formation for all the liquid $PrCl_3$-MCl melts (M = Li, Na, K, Rb, Cs) at the composition $xPrCl_3=0.25$ were determined.

The molar enthalpy and entropy of phase transition of the K_3PrCl_6, Rb_3PrCl_6 and Cs_3PrCl_6 compounds were obtained by Differential Scanning Calorimetry.

EXPERIMENTAL

A. Chemicals

$PrCl_3$ was synthesized from Pr_4O_{11}(99.9 %) produced by Hydromet Co. (Kowary, Poland). The main steps of this synthesis are the same as for $NdCl_3$ preparation and have been described in detail previously (2) : $PrCl_3$ obtained after successive distillations, was of high grade (min. 99.9 %).

The MCl alkali chlorides (M = Li, Na, K, Rb, Cs) were Merck Suprapur reagents (min. 99.9 %). Before their use in the calorimeter the alkali chlorides were purified and treated by progressive heating up to fusion under gaseous HCl atmosphere. Excess HCl was removed from the melt by argon. They were kept in the glove-box.

The M_3LnCl_6 compounds were prepared from the MCl and $PrCl_3$ chlorides which were weighed in the molar ratio 3:1 . All the mixtures were prepared in a glove-box filled with purified and water-free argon. Though a small amount of sample was used for the DSC experiments (300-500 mg), about 10g of each compound was synthesized in order to avoid deviation from stoichiometry. The stoichiometric mixtures of chlorides were melted in vacuum-sealed quartz ampoules in an electric furnace. The melts were homogeneized by shaking and solidified. These samples were ground in an agate mortar in a glove-box.

B. Procedures.

The mixing experiments were all of the simple liquid-liquid type under argon at atomopheric pressure. The calorimetric apparatus, a Calvet-type high temperature microcalorimeter, the mixing devices used and the experimental methods adopted have all been described in some detail elsewhere (5) . Mixing of the two salts was obtained by the break-off ampoule technique .

Calibration of the calorimeter was performed with NIST a-alumina (6) ; known amounts of alumina were dropped directly in the melt. Integration of the surface of thermograms was made automatically by computer. The experimental uncertainty on calibration is about 3% ; the experimental uncertainty on enthalpy of mixing data is estimated to be 6% since they are obtained from independent experiments.

The Differential Scanning Calorimeter (DSC 121, Setaram) used for the determination of the temperature and enthalpy of phase transitions and the experimental procedure have been described in detail elsewhere (5).

The experimental quartz cells, 7mm diameter and 15 mm long, were filled with the required amount of sample and sealed under reduced pressure of argon. The DSC experiments were conducted at the heating or cooling rate 1-5 K/mn. The experimental error on the enthalpy measurements was 2% to 4%, according to the nature of the sample and the magnitude of the thermic effect.

RESULTS

Calorimetric mixing experiments were carried out at 1122 K for the systems NaCl-$PrCl_3$ and KCl-$PrCl_3$.

A. Enthalpy of mixing

The experimental enthalpies of mixing $\Delta_{mix}H_m$ are plotted against composition in Figures 1. In evaluating the results of our measurements, all experimental uncertain data were disgarded when evaporation or poor homogeneity of the melt during mixing were noticed ; furthermore, in order to improvee the overall accuracy , some experimental points were obtained as the average value of several runs.

Several experiments were also conducted in order to determine accurately the enthalpy of formation at $xPrCl_3 = 0.25$ for all the MCl-$PrCl_3$ systems (M = Li, Na, K, Rb, Cs), e.g. the enthalpy variation related to the reactions :

$$3\ MCl\ (l) + PrCl_3\ (l) \rightarrow "M_3PrCl_6"\ (l).$$

The notation "M_3PrCl_6 " was adopted since there is no compound of the type M_3PrCl_6 with LiCl and NaCl .

The experimental values are reported in Table 1. The same table also includes analogous values obtained for the mixtures of alkali chlorides with $CeCl_3$(4) , $LaCl_3$ (3) and $NdCl_3$ (2). The values of ionic radii used are also indicated (7) in Table 1.

B. Entropies of phase transition

The values of enthalpies of phase transition for the M_3PrCl_6 compounds , obtained from DSC heating and cooling curves, were almost the same ; the difference between them was no more than 2%. Supercooling was observed in several measurements. The results obtained are listed in Table 2.The values of the temperatures and enthalpies of phase transition given in this work were determined from the heating curves. The few literature data are also listed for comparison.

Table 1 : Molar enthalpy of formation $\Delta_f H_m(M_3LnCl_6, l, T)$ / (kJ.mol^{-1}) of the liquid mixtures according to the reaction : 3 MCl (l) + $LnCl_3$ = "M_3LnCl_6"(l) (M = Li, Na, K, Rb, Cs ; Ln = La, Ce, Pr, Nd).

	ΔfHm / kJ.mol-1	ΔfHm / kJ.mol-1	ΔfHm / kJ.mol-1	ΔfHm / kJ.mol-1	r(M^+)[5] / pm
MCl	$LaCl_3$ [1] 1173 K	$CeCl_3$ [2] 1118 K	$NdCl_3$[3] 1122 K	$PrCl_3$[4] 1122 K	
LiCl	-6.7	-5.8	-6.9 (1065 K)	-6.1	74
NaCl	-27.6	-26.7	-24.8	-25.0	102
KCl	-52.0	-55,7	-55.2 (1065 K)	-55.9	138
RbCl	-65.7	-68.2	-68.8	-66.4	149
CsCl	-83.7	-80.8	-80.8	-80.4	170

[1] calculated from Ref.(3)
[2] calculated from Ref. (4)
[3] from Ref. (2)
[4] this work
[5] from Ref. (7)

Table 2 : Temperatures and molar entropies of phase transition of the M_3PrCl_6 compounds

Compound	T_f / K	T_{trs} / K	T_{fus} / K	$\Delta_f H_m$ / kJ/mol	$\Delta_{trs} H_m$ / kJ/mol	$\Delta_{fus} H_m$ / kJ/mol	Reference
K_3PrCl_6	768	-	944	52.6	-	48.9	this work
	762	-	945	-	-	-	[14]
	-	-	1048	-	-	106.6	[18]
	-	-	938	-	-	84.0	[17]
	-	723	931	-	-	-	[19]
	-	-	948	-	-	-	[9]
	-	-	963	-	-	-	[11]
Rb_3PrCl_6	-	396			1.0		this work
	-	658	1037	-	6.6	54.0	this work
	598	659	1040	-	-	-	[14]
Cs_3PrCl_6	-	676	1093	-	7.6	61.1	this work
	-	677	1093	-	-	-	[14]

DISCUSSION

The melts investigated on the whole composition range, namely NaCl-$PrCl_3$ and KCl-$PrCl_3$ are characterized by negative enthalpies of mixing . The composition dependence of the interaction parameter λ :

$$\lambda = \Delta_{mix}H_m \,/\, xMCl \,.\, xPrCl_3$$

is representative of the energetic asymmetry in these melts.For both systems, the minimum of the enthalpy of mixing is shifted toward alkali chloride rich-composition and is located in the vicinity of $xPrCl_3 \approx 0.4$.

These results are almost identical , within the experimental uncertainty, to those found previously for the NaCl-$NdCl_3$ and KCl-$NdCl_3$ molten salt mixtures (2). They are also very similar to those obtained by Papatheodorou and Kleppa (3) and Papatheodorou and Østvold (4) for the analogous mixtures MCl-$CeCl_3$ and MCl-$LaCl_3$. This finding is not surprising because of the great similarity between the physicochemical properties of $LaCl_3$, $CeCl_3$, $PrCl_3$ and $NdCl_3$.

On the other hand, our results were compared to those obtained for the KCl-$PrCl_3$ mixture by Savin et al. (8) . The comparison is reported in Figure 1 : the enthalpy values obtained indirectly at 3 compositions by the drop method differ by 10-15% from ours.

The composition dependence of the interaction parameter λ for NaCl-$PrCl_3$ is close to linear. For the KCl-$PrCl_3$ system the composition dependence of λ is somewhat more complicated : a broad minimum appears to exist at $xPrCl_3 \approx 0.2$ - 0.3 ; the relative changes of l are smaller in the alkali chloride-rich than in the praseodymium chloride-rich region. Similar variations of l were also observed for the corresponding MCl-$LaCl_3$, MCl-$CeCl_3$ and MCl-$NdCl_3$ mixtures ; for all the KCl-$LnCl_3$ the minimum of l was attributed to the formation of $LnCl_6^{3-}$ complexes in the alkali chloride-rich mixtures.

Some similarities too can be observed for the entropy of fusion of these compounds.

The systems under investigation all exhibit different compounds in the solid state.

In NaCl-$PrCl_3$, Novikov et al. (9) and Shevtsova et al.(10) did not report any compound ; this fact was confirmed by Desyatnik et al. (11). On the other hand, Mochinaga et al. (12-13) found the $3PrCl_3{\bullet}NaCl$ wich melts incongruently at 860 K. Also Seifert et al. (14) reported only the $Na_3Pr_5Cl_{18}$ compound with an incongruent melting at about 873 K.

Two or three compounds have been found in the KCl-$PrCl_3$ mixture :

3KCl•2$PrCl_3$ which melts incongruently at 888 K (9)

2KCl•$PrCl_3$ which melts incongruently at 893 K (9), 898 K (11), 890 K (14)

K_3PrCl_6 which melts congruently at 948 K (9), 963 K (11), 945 K (14)

According to (14), solid K_3PrCl_6 only exists from 762 K (formation) up to 945 K (melting) .

In spite of the above contradictions, the phase diagrams of the NaCl-$PrCl_3$ and KCl-$PrCl_3$ exhibit many similarities with the analogous NaCl-$NdCl_3$ and KCl-$NdCl_3$.

$PrCl_3$ and $NdCl_3$ are probably associated in the liquid state (15) and the values of the equivalent electrical conductivity, at a fixed temperature, are very similar (16).

There is no literature data of enthalpy with the exception of the fusion enthalpy of K_3PrCl_6 (17, 18), the value of which, however, differs significantly from ours.

The K_3PrCl_6 compound is formed at the temperature 768 K with the enthalpy 52.6 kJ.mol-1. The formation temperature is in good agreement with the one reported by Seifert et al. (14) and differs significantly from the temperature given by Morozov et al. (19) as the temperature of transition (723 K). Similarly, as for the other compounds formed at high temperature, a supercooling effect of about 32 K was observed.

For the Rb_3PrCl_6 compound the transition at 658 K and melting at 1037 K were found in good agreement with literature (14). No supercooling was observed. The formation of this compound reported by Seifert et al. (14) at 598 K was not found. Instead, the transition at 396 K with the enthalpy 1.0 kJ.mol-1 was observed. This indicate that Rb_3PrCl_6 may exist at ambient temperature.

The Cs_3PrCl_6 compound, stable at ambient temperature, undergoes a solid state transition at 676 K and fusion at 1093 K. These results are identical to those reported by Seifert et al. (14).

These results show that the systems under investigation behave like the analogous mixtures with $NdCl_3$. Figure 2, which displays the dependence of the enthalpy of formation $\Delta_f H_m((M_3LnCl_6, l, T)$ on ionic radius of the alkali metal $r(M^+)$ clearly indicates that the same behavior can be observed with other lantanide chloride systems like $LaCl_3$-MCl and $CeCl_3$-MCl.

The enthalpy of formation changes linearly with the ionic radius of the alkali metal and is almost the same, within the experimental uncertainty, for the four series of mixtures.

REFERENCES

1. M. Gaune-Escard, A. Bogacz, L. Rycerz, W. Szczepaniak, Materials Science Forum, vol. 73-75 (1991) 61.

2. M. Gaune-Escard, A. Bogacz, L. Rycerz, W. Szczepaniak (To be published).

3. G. N. Papatheodorou, T. Østvold, J. Phys. Chem., 78 (1974) 181.

4. G. N. Papatheodorou, O. J. Kleppa, J. Phys. Chem., 78 (1974) 178.

5. M. Gaune-Escard, "Molten Salt Techniques", R. Gale, D. G. Lovering, Ed., Plenum Press, New York, London, (1991), Chap. 5.

6. K. K. Kelley , United States Department of the Interior, Bureau of Mines, Bull. 476, (1949).

7. A. G. Sharpe, "Inorganic Chemistry, Longman, New York (1986) pp. 146 and 659.

8. V. D. Savin, N. P. Mikhailova, V.A. Morozova, Russ. J. Phys. Chem., 53 (1979) 797

9. .G. N. Novikov, A. K. Baev, Z. Neorg. Khim., 6 (1961) 2610

10. Z. N. Shevtsova, E. N. Korzina, B.G. Korshunov, Z. Neorg. Khim., 7 (1962) 2596.

11. V. N. Desyatnik, I. I. Trifonov, T. A. Pobirchenko, G. A. Lebedev, Izv. Vyss. Ucheb. Zaved., Tsvetn. Met., 1 (1987) 124.

12. J. Mochinaga, H. Othani, K. Igarashi, Denki Kagaku, 49 (1981) 19.

13. T. Hattori, H. Ikezawa, R. Hirano, J. Mochinaga, J. Chem. Soc. Jpn., 6 (1982) 952.

14) H.J. Seifert, J. Sandrock, J. Uebach, Z. Anorg. Chem., 555 (1987) 143

15. J. Mochinaga, Y. Iwadate, K. Fukushima, Materials Science Forum, 73-75 (1991) 61.

16. J. Mochinaga, Y.Iwadate, K. Igarashi, J. Electrochem. Soc. 138 (1991) 3588.

17. T. Hattori, K. Igarashi,.J. Mochinaga, Bull. Chem. Soc. Jpn., 54 (1981) 1883.

18. R. Blachnik, A. Schneider, Monatsh. Chem., 102 (1971) 1337.

19. Sun In-Chzu, I.S. Morozov, Zh. Neorg. Khim., 3 (1958) 1914.

Key words :

Enthalpy of mixing, Entropy, Phase transition.

FIGURES

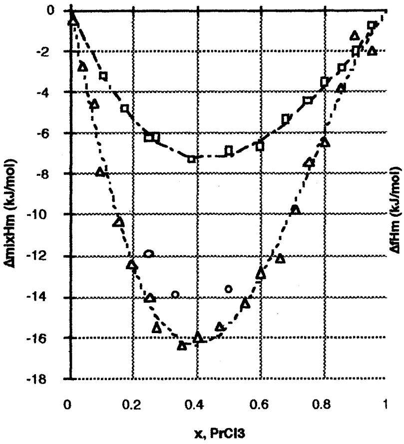

Fig.1 : Enthalpy of mixing (kJ/mol)
NaCl-$PrCl_3$: □ (this work)
KCl-$PrCl_3$: ∧ (this work)
○ (8)

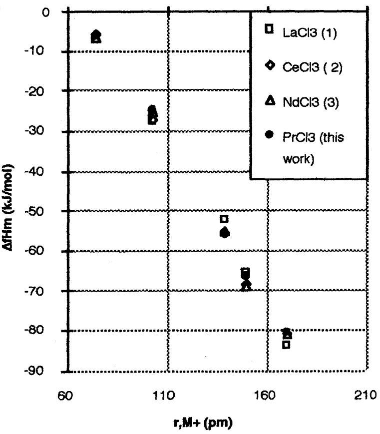

Fig. 2 : Dependence of the molar enthalpy of formation $\Delta_f H_m$(kJ/mol) of the liquid mixtures M_3LnCl_6 on the alkali metal ionic radius .

DOI: 10.1149/199413.0099PV

MIXING ENTHALPY AND STRUCTURE OF THE MOLTEN NaCl-$DyCl_3$ SYSTEM

Ryuzo Takagi[a], Leszek Rycerz[b] and Marcelle Gaune-Escard[c]

[a]Research Laboratory for Nuclear Reactors, Tokyo Institute of
Technology, 2-12-1, Ookayama, Meguro-ku, Tokyo 152, Japan

[b]Institute of Inorganic Chemistry and Metallurgy of Rare Elements,
Technical University, Wybrzeze St. Wyspianskiego 27,
50 370 Wroclaw (Poland).

[c]IUSTI, UA 1168 CNRS, Université de Provence,
Centre de St Jérôme, av. Escadrille Normandie Niemen,
13397 Marseille Cédex 20 (France).

ABSTRACT

The enthalpy of mixing $\Delta_{mix}H_m$ of the NaCl-$DyCl_3$ system was measured at 1100K by direct calorimetry in the whole composition range . The enthalpies of mixing values are negative with a minimum value at $xDyCl_3 \approx 0.4$.

Isothermal molecular dynamics (MD) simulations of the molten $DyCl_3$ and NaCl-$DyCl_3$ systems were carried out to calculate the mixing enthalpy, and then the structure in these systemswas investigated.

In the simulated systems the coordination number of the Cl^{-1} ions around the Dy^{3+} ion is 6. The complex ions $Dy_2Cl_{11}{}^{5-}$ and $Dy_3Cl_{16}{}^{7-}$ were observed as well as $DyCl_6{}^{3-}$. Although most of these polymers share apex Cl^- ions, an edge sharing polymers were found around $x_{DyCl3} \approx 0.4$.

INTRODUCTION

Spent metallic fuels in fast nuclear reactors contain significant amount of fissile lanthanide elements. In the Integral Fast Reactor (IFR) program proposed by Argonne National Laboratory in the United States, fissile lanthanide elements as well as other elements are transferred into a molten salt (an eutectic mixture of LiCl and KCl) by anodic dissolution since a spent metallic fuel acts as an anode (1).

Depending on standard decomposition potentials, some elements among those elements transferred from the anode to the melt may be recovered by electrolysis. As well known, a decomposition potential (E) is determined by the Nernst equation :

$$E = E_o + RT/nF \ln(a_{Mn+} / a_M) \qquad [1]$$

where E_o, R, T, F, n, a_{Mn+} and a_M are the standard decomposition potential, the gas constant, temperature, the Faraday constant, an electron transfer number and activities of an ion M^{n+} and a product M. The activity coefficient ($\gamma_i = a_i/x_i$) of a component i is related to the mixing enthalpy as follows :

$$RT \quad Ing_i = \Delta_{mix}G^{xs}{}_{m,i} = \Delta_{mix}H_{m,i} - T \quad \Delta_{mix}S^{xs}{}_{m,i} \qquad (2)$$

where $\Delta_{mix}G^{xs}{}_{m,i}$, $\Delta_{mix}H_{m,i}$ and $\Delta_{mix}S^{xs}{}_{m,i}$ are the partial molar excess Gibbs free energy, mixing enthalpy and excess entropy of the component i.

The thermodynamic properties and the phase diagrams of lanthanide halides in molten alkali chloride solvents show that the lanthanide ions are much stabilized (2-11), i.e. that their activities become much smaller than in their pure melts. The structure of structure of the molten lanthanide halides or of halides containing a trivalent cation is not accurately known so far since most structural investigations, by X-ray or neutron diffraction, were performed on monovalent and divalent molten salts (12-15).

Although structure of the molten lanthanide halides and their mixtures have been scarcely revealed, Mochinaga et al. (16) suggested complexes more complicated than MX_6^{3-} (M: lanthanide ion and X: halide ion) which is determined by X-ray diffraction.

In the present work the mixing enthalpy of the molten NaCI-$DyCI_3$ system was measured by direct calorimetry and the stabilization of the Dy^{3+} ion in this system was interpreted in terms of complexes by molecular dynamics (MD) simulation.

EXPERIMENTAL

Mixing enthalpy at 1100K was measured in the molten NaCI-$DyCI_3$ system by direct calorimetry.

A. Chemicals

$DyCl_3$ was synthesized from Dy_4O_{11}(99.9 %) produced by Hydromet Co. (Kowary, Poland). The main steps of this synthesis are the same as for $NdCl_3$ preparation and have been described in detail previously (17) : $DyCl_3$ obtained after successive distillations, was of high grade (min. 99.9 %).

NaCl was a Merck Suprapur reagent (min. 99.9 %). Before its use in the calorimeter it was purified and treated by progressive heating up to fusion under gaseous HCl atmosphere. Excess HCl was removed from the melt by argon.

All the salts were kept and handled in the glove-box.

B. Procedures.

The mixing experiments were all of the simple liquid-liquid type under argon at atomopheric pressure. The calorimetric apparatus, a Calvet-type high temperature microcalorimeter, the mixing devices used and the experimental methods adopted have all been described in some detail elsewhere (18) . Mixing of the two salts was obtained by the break-off ampoule technique .

Calibration of the calorimeter was performed with NIST α-alumina (19) ; known amounts of alumina were dropped directly in the melt. Integration of the surface of thermograms was made automatically by computer. The experimental uncertainty on calibration is about 3% ; the experimental uncertainty on enthalpy of mixing data is estimated to be 6% since they are obtained from independent experiments.

COMPUTATION

In order to carry out MD simulations, the following pair potential (uij) between ions i and j was employed.

$$u_{ij}(r) = z_i\, z_j\, e^2 / 4\pi\, \varepsilon_0\, r + b\, A_{ij} \exp[(r_i^\circ + r_j^\circ - r) / \rho] \qquad [3]$$

where r, z, e, ε_0 , b, A, r° and ρ are the separation distance between ions i and j, the valence number, the elementary charge of electron, the dielectric constant of vacuum, the pre-exponential term, the Pauling factor, an ionic radius and a softness parameter, respectively. Since the values of r° and ρ of Dy^{3+} ion are not available, they were adjusted to reproduce experimental structure factors (20) of the molten $DyCl_3$ and the molten $NaCl\text{-}DyCl_3$ systems. In order to compare the experimental and computational structure factors, MD simulations of two systems were carried out, i. e., one is for the pure molten $DyCl_3$ at 973K and the other one for the equimolar $NaCl\text{-}DyCl_3$ system at 743K The basic cells contained 108 Dy and 324 Cl ions for the pure $DyCl_3$, and 80 Dy, 80 Na and 320 Cl ions for the $NaCl\text{-}DyCl_3$ (50/50 mol%) mixture. The softness parameter ρ for NaCl is given by Fumi and Tosi (21) and ρ in the mixture was evaluated according to Larsen and Forland (22). The simulated systems were well annealed (more than 10 time steps : Δt = 0.5fs) by the Velret method, then the isothermal MD simulation proposed by Nose (20) was adopted. The structure factors were estimated in the basic cells by the Debye equation.

$$Qi(Q) = \Sigma\Sigma f_i f_j \sin(Q r_{ij}) / r_{ij} \qquad [4]$$

where Q and f_i are the wave number and the atomic structure factor of a component i, respectively.

Then we made MD simulations at 1100K to obtain the enthalpy of mixing in this system. Potential energy Φ was estimated according to Eq. [1], where the Coulomb energy was evaluated by the Ewald method, and the internal energy U was calculated by

$$U = \Phi + E_k \qquad [5]$$

where E_k is the kinetic energy. Although one can obtain enthalpy by

$$H = U + pV \qquad [6]$$

where p and V are pressure and molar volume, respectively, it is usually difficult to estimate p, because p is small and results from the difference between two large quantities (coulombic and repulsive). In condensed phases pV is so small that it can be neglected: in this work pV is less than 0.1 kJ/mol. Accordingly, in this work the enthalpy was assimilated to internal energy.

RESULTS

Figure 1 shows the molar mixing enthalpy $\Delta_{mix}H_m$ measured by calorimetry. The interaction parameter, λ, defined by

$$\Delta_{mix}H_m = -l\ x_{DyCl3} \cdot (1 - x_{DyCl3}) \qquad [7]$$

is obtained by least square fitting of calorimetric data (in kJ/mol):

$$\lambda = 48.74\, x_{DyCl3}{}^3 - 20.90\, x_{DyCl3}{}^2 - 62.92\, x_{DyCl3} + 56.44 \qquad [8]$$

The solid line in Fig. 1 indicates the mixing enthalpy estimated with Eqs. [7] and [8].

Figures 2a and 2b are the experimental and computational structure factors for the molten systems $DyCl_3$ and NaCl-$DyCl_3$ (50/50 mol%), respectively. We concluded that the adjusted parameter ($r^{o}{}_{Dy}$ = 0.173 nm and r = 0.025 nm) give reasonable agreement between experimental and computational structure factors.

The mixing enthalpy in the simulated system was calculated by the following equation and depicted in Fig3.

$$\Delta_{mix}H_m = H_m(x_{NaCl}, x_{DyCl3}) - x_{NaCl} \cdot H_m(NaCl) - x_{DyCl3} \cdot H_m(DyCl_3) \qquad [9]$$

where $H_m(NaCl)$ and $H_m(DyCl_3)$ are the enthalpies of the pure components.

DISCUSSION

Although there are some discrepancies between Fig. 1 and Fig. 3 as follows, an interaction around x_{DyCl3}= 0.35 is realized by the MD simulation.

i) In Fig. 3, one can see two peaks at x_{DyCl3} = 0.35 and x_{DyCl3} = 0.50, while in Fig. 1, one peak at x_{DyCl3} = 0.30 and one shoulder around x_{DyCl3} = 0.80 are observed. The peak implies a preferential interaction between ions. In this MD simulation, only ionic sizes and charges are taken into account. An orientational interaction of orbital electrons can not be included. Then the peaks shown in Fig. 3 correspond to a geometrical preferential arrangement.

ii) The magnitude of the enthalpy of mixing in the simulated system is about 4 times larger than that in the experimental system. The pair potential given by Eq. (1) excludes dispersion terms, which may affect the repulsion parameter ρ.

Then in this work we try to interpret the interaction at x_{DyCl3} = 0.35 by the MD simulation.

The pair correlation functions between Dy and Cl are depicted in Figs. 4a, 4b and 4c for the systems with x_{DyCl3} = 1.0 and 0.2. While interaction distance between Cl-Cl does not significantly depend on composition, interaction distance between Dy and Cl increases with an increase of x_{DyCl3}, and that betveen Dy and Dy drastically increases at x_{DyCl3} = 0.4. An increase in separation distance between opposite sign ions will bring increase of the internal energy and vice versa. In all compositions, a coordination number of Cl^- ions around Dy^{3+} ion is 6. As shown in Fig. 4b, the first peak of g_{DyCl} is isolated, which means that the complex $DyCl_6^{3-}$ is rigid. Figure 4a shows that the first interaction between Dy and Dy is extinct at 0.58 nm. When separation distance between any two Dy^{3+} ions selected arbitrarily in a group of Dy^{3+} ions is within this extinction distance, we considered a group of these Dy^{3+} ions as a complex. Most Dy ions exist as $DyCl_6^{3-}$ and most polymers as Dy_nCl_{5n+1} (n = 2 or 3). Polymers which are different from Dy_nCl_{5n+1} appear between x_{DyCl3} =0. 1 and 0.6. For example, stereoscopic views of $Dy_2Cl_{10}^{4-}$ and $Dy_3Cl_{15}^{6-}$ are depicted in Figs. 6a and 6b, respectively.

We observed a small hump before the first main peak of g_{DyDy}, as shown in Fig. 5. This peak is remarkable at x_{DyCl3} = 0.4 and corresponds to a separation distance between Dy and Dy in the edge shared complex which is shown in Fig. 6a. Formation of this kind of complex decreases the enthalpy. Thus we should find the minimum of the of the mixing enthalpy at x_{DyCl3} = 0.4 instead of x_{DyCl3} = 0.35. Although we repeated the MD simulation with a different initial configuration at x_{DyCl3} = 0.4, we failed to obtain the minimum of the mixing enthalpy at x_{DyCl3} = 0.4. It is difficult to say what shifts the minimum of the mixing enthalpy at present. However, it may be concluded that the decrease of interaction distance between opposite sign ions with decrease of x_{DyCl3} and appearance of the edge sharing complexes decreases the mixing enthalpy.

The partial molar mixing enthalpy of $DyCl_3$ in the molten NaCl-$DyCl_3$ can be estimated by the following equation.

$$\Delta_{mix}H_{m,DyCl3} = \Delta_{mix}H_m + (1 - x_{DyCl3})\,[d\Delta_{mix}H_m/dx_{DyCl3}] \qquad [10]$$

Then at the limit x_{DyCl3} ->0, we obtain $\Delta_{mix}H_{m,DyCl3}$ = -56.44 kJ mol^{-1}, which means that the Dy^{3+} ion is stabilized in the dilute solution of $DyCl_3$.

CONCLUSION

Mixing enthalpy in the molten NaCl-$DyCl_3$ system was measured at 1100 K by calorimetry. As shown in Fig. 1, the molar mixing enthalpy of this system has a minimum at $x_{DyCl3} = 0.3$. Isothermal MD simulation of this system was carried out to estimate this mixing enthalpy. Although the experimental and computational mixing enthalpies show some discrepancies, they have minimums around x_{DyCl3} = 0.3. This minimum is attributed to formation of the edge sharing polymers.

REFERENCES

1. Y. I. Chang, C. Walters, J. E. Battles, D. R. Pedersen, D. C. Wade, M. J. Lineberry, Integral Fast Reactor Program Summary Report FY 1985-FY 1989, ANL-IFR-125 (1990).
2. M. Gaune-Escard, A. Bogacz, L. Rycerz, W. Szczepaniak (in print J. Alloys & Compounds).
3. M. Gaune-Escard, A. Bogacz, L. Rycerz, W. Szczepaniak (To be published).
4. G. N. Papatheodorou, T. Østvold, J. Phys. Chem., 78 (1974) 181.
5. G. N. Papatheodorou, O. J. Kleppa, J. Phys. Chem., 78 (1974) 178.
6. V. D. Savin, N. P. Mikhailova, V.A. Morozova, Russ. J. Phys. Chem., 53 (1979) 797
7. .G. N. Novikov, A. K. Baev, Z. Neorg. Khim., 6 (1961) 2610
8. Z. N. Shevtsova, E. N. Korzina, B.G. Korshunov, Z. Neorg. Khim., 7 (1962) 2596.
9. V. N. Desyatnik, I. I. Trifonov, T. A. Pobirchenko, G. A. Lebedev, Izv. Vyss. Ucheb. Zaved., Tsvetn. Met., 1 (1987) 124.
10. H.J. Seifert, J. Sandrock, J. Uebach, Z. Anorg. Chem., 555 (1987) 143

11. R. Blachnik, A. Schneider, Monatsh. Chem., 102 (1971) 1337.

12. J. E. Enderby, D. M. North P. A. Egelstaff, Phil. Mag. 14, 961 (1966).

13. J. E. Enderby and S. Biggins in “Advances in Molten Salt Chemistry”, vol. 5, ed. G. Mamantov, p. 1, Elsevier (1983).

14. N. D. Wood, R. A. Howe, R. J. Newport, J. Faber, J. Phys. C : Solid State Physics 21, 669 (1988)

15. N. D. Wood, R. A. Howe, J. Phys. C : Solid State Physics 21, 3177 (1988)

16. J. Mochinaga, Y. Iwadate, T. Fukushima, private communication.

17. M. Gaune-Escard, A. Bogacz, L. Rycerz, W. Szczepaniak, Materials Science Forum, vol. 73-75 (1991) 61.

18. M. Gaune-Escard, "Molten Salt Techniques", R. Gale, D. G. Lovering, Ed., Plenum Press, New York, London, (1991), Chap. 5.

19. K. K. Kelley , United States Department of the Interior, Bureau of Mines, Bull. 476, (1949).

20. S. Nose, Mol. Phys., 52, 255 (1984).

21. F. G. Tosi, M. P. Tosi, J. Phys. Chem. Solids, 25, 31 (1964).

22. B. Larsen, T. Førland, Mol. Phys., 26, 1521 (1973).

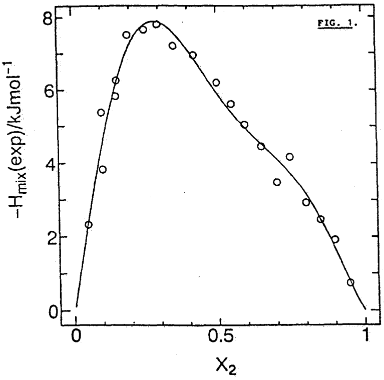
FIG. 1.

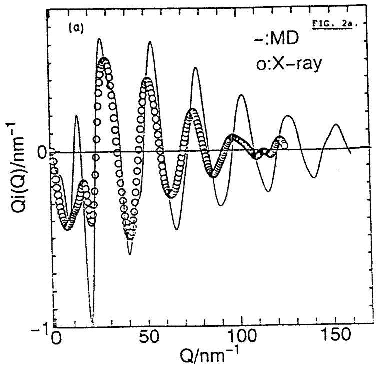
FIG. 2a.

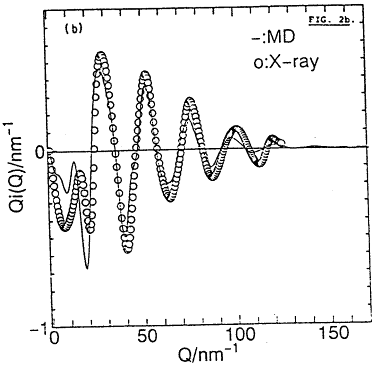
FIG. 2b.

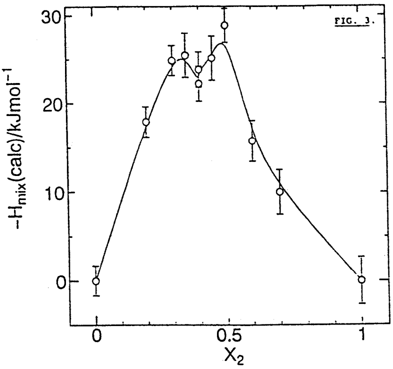
FIG. 3.

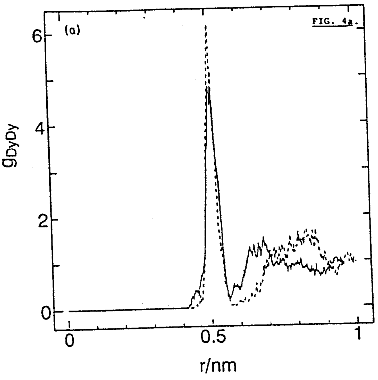
FIG. 4a.

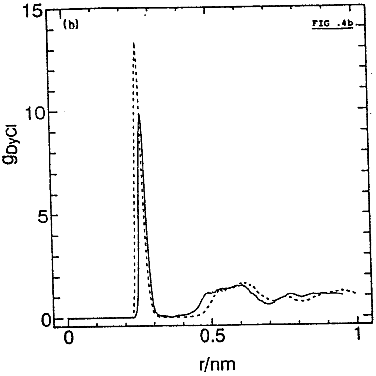
FIG .4b

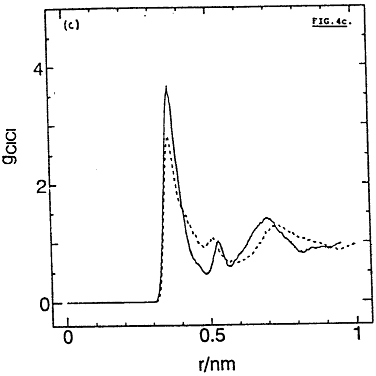
FIG.4c.

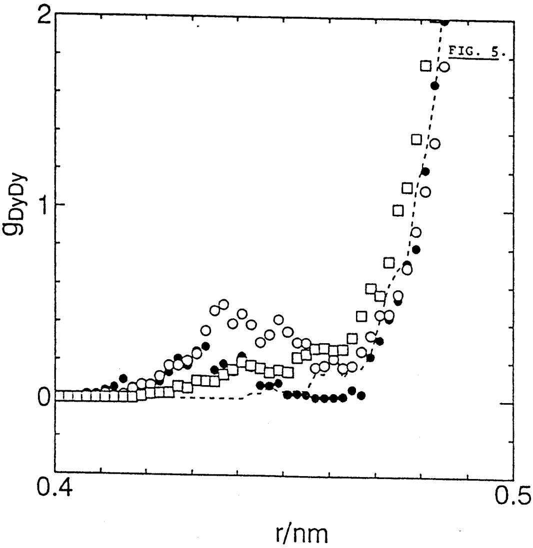

FIG. 5.

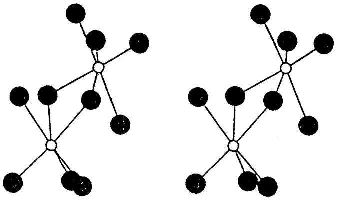

FIG. 6 (a)

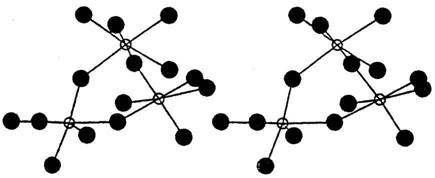

FIG. 6 (b)

DOI: 10.1149/199413.0108PV

THERMODYNAMIC ANALYSIS OF THE MOLTEN SYSTEM $KF - KCl - KBF_4 - K_2TiF_6$

V. Daněk, M. Chrenková, A. Silný,
O. Patarák, D. K. Nguyen

Institute of Inorganic Chemistry, Slovak Academy of Sciences
Dúbravská cesta 9, 842 36 Bratislava, Slovakia

ABSTRACT

Complex physicochemical and thermodynamic study of the melts of the system $KF - KCl - KBF_4 - K_2TiF_6$ have been performed. Significant deviations from ideal behaviour due to the interactions between component were found. The following chemical reactions were confirmed to take place in the melt

$$BF_4^- + n\,Cl^- = [BF_{4-n}Cl_n]^- + n\,F^-$$

$$KBF_4(l) + K_2TiF_6(l) = K_3TiF_7(l) + BF_3(g)$$

$$K_2TiF_6(l) + KF(l) = K_3TiF_7(l)$$

$$K_2TiF_6(l) + KCl(l) = K_3TiF_6Cl(l)$$

Negative deviations from the ideal viscosity behaviour were found in the binary system $KF - KBF_4$ probably due to the break of the B-F-B bridges caused by the excess of F^- or Cl^- ions.

INTRODUCTION

The melts of the system $KF - KCl - KBF_4 - K_2TiF_6$ seem to be very suitable electrolytes for the electrochemical synthesis of TiB_2, especially when coherent coatings on metallic bases have to be prepared [1]. The knowledge of the structure of these electrolytes is needed for the understanding of the mechanism of the electrochemical process. The interaction of components and the chemical reactions taking place in the melt affect the ionic composition, determining the kind of the electroactive species. The suitable choice of the electrolyte composition may suppress the formation of volatile compounds which leads to undesirable exhalation and lowers the efficiency of the process.

The aim of the study was to determine some physicochemical properties, like phase equilibria, density, electrical conductivity and viscosity of the electrolyte and to elucidate the structure, i.e. the actual ionic composition of the melts using the complex thermodynamic and physicochemical analysis of the melts as well as the complementary X-ray diffraction and spectroscopic analyses of quenched melts.

EXPERIMENTAL

The temperature of the primary crystallization was measured using the thermal analysis method recording the cooling and heating curves of the studied samples. A computer-controlled automatic thermal analysis device with a subsequent statistical processing of the output data was used. The reproducibility of the temperature of primary crystallization measurement was ± 2 K.

The density of the investigated melts was measured using the Archimedean method. The platinum sphere with the diameter of 20 mm, suspended using the platinum wire on the automatic analytical balance, was used as measuring body. The experimental error of the density measurement was less than ± 0.4 %.

The conductivity measurement was realized using the four-electrode method. In this method the potential gradient of the electrical field of known intensity created using one couple of electrodes is measured by means of the another couple of electrodes. The measurement is realized at two depths of immersion of the electrodes. The experimental error in the conductivity measurement did not exceed ± 1 %.

The torsion pendulum method was used for the viscosity measurement. The platinum cylinder with the diameter of 15 mm and the height of 20 mm was used as the measuring body. The oscillations of the pendulum system were followed by means of two fixed phototransistors, placed in the path of a light beam reflected from a mirror attached to the pendulum. The experimental error in the viscosity measurement did not exceed ± 1 %.

The actual composition of the investigated melts was elucidated on the basis of the thermodynamic calculation, the X-ray powder difraction analysis, and the IR spectroscopic measurement of the quenched samples. Infrared spectra were measured using a Perkin-Elmer 983G spectrometer. The mid infrared spectra were recorded at 300 K as a KBr pellets or mulled in Nujol. To record the weak infrared bands in the 600-900 cm^{-1} region, 0.5 mm thick pellets were pressed from pure materials.

RESULTS AND DISCUSSION

The study of the system KF - KCl - KBF_4 - K_2TiF_6 was realized in succesive steps examining important properties of the individual ternary subsystems.

Subsystem KF - KCl - KBF_4

The phase diagram of the ternary system KF - KCl - KBF_4 was measured in [2]. The system is a simple eutectic one with the coordinates of the eutectic point of 61.4 mole % KBF_4, 19.4 mole % KF, 19.2 mole % KCl and the temperature of the eutectic crystallization of 422 °C. For the calculation of the activity of components in the ternary system the following relation was considered for the dependence of the excess molar Gibbs energy on composition

$$\Delta G(ex) = \sum_{i \neq j}^{3} \sum_{n=1}^{5} A_{ijn} x_i x_j^n + B x_1 x_2 x_3 + \sum_{i \neq j < k}^{3} C_i x_i^2 x_j x_k \qquad (1)$$

The calculated excess molar Gibbs energy of mixing of the molten system KF - KCl - KBF_4 is shown in Fig. 1.

The density of the system KF - KCl - KBF_4 was measured in [3]. On the basis of the experimental data the molar and excess molar volumes were calculated. The concentration dependence of the molar volume was described by the eqn.

$$V = \sum_{i=1}^{3} A_i x_i + \sum_{i \neq j}^{3} x_i x_j (B_{ij} + C_{ij} x_j) + D x_1 x_2 x_3 \qquad (2)$$

The excess molar volume of the system KF - KCl - KBF_4, which represents the sum of the second and third terms of eqn (2), is shown in Fig. 2. The low excess molar volumes indicate that the investigated system differs only slightly from the ideal behaviour.

The electric conductivity of the system was measured in [4]. Similar equation like for the molar volume was used for the description of the molar conductivity of the system KF - KCl - KBF_4. The excess molar conductivity of the studied system is shown in Fig. 3. Considerable negative deviations from additivity have been found in the KF - KBF_4 boundary system, while in the systems KF - KCl and KCl - KBF_4 only little negative deviations from the additive course may be observed.

The viscosity of the system KF - KCl - KBF_4 was measured in [5]. The additivity of the logarithm of viscosity was adopted for the ideal viscosity behaviour of the mixtures. For real solutions we can then write

$$\eta = \eta_1^{x1} \eta_2^{x2} \eta_3^{x3} + \sum_{i \neq j}^{3} x_i x_j \sum_{n=0}^{k} A_{nij} x_j^n + B x_1^l x_2^m x_3^n \qquad (3)$$

The excess viscosity of the ternary system KF - KCl - KBF_4 defined in such a way is shown in Fig. 4. Negative deviations from the ideal behaviour were observed in all three binaries as well as in the ternary system.

From the physicochemical analysis of this system it follows, that a significant ternary interaction of all components takes place. With regard to the fact, that the investigated system has a common cation, the observed deviations from the ideal behaviour must be a consequence of the anionic interaction. The exchange of the fluoride atoms in the BF_4^- tetrahedron by chloride ones according to the general scheme

$$BF_4^- + n\ Cl^- = [BF_{4-n}Cl_n]^- + F^- \qquad (4)$$

and the possible presence of the $[BF_{4-n}Cl_n]^-$ and F^- anions seems to be the most probable interaction of all three anions. As follows from the course of all the excess functions of the investigated system (Figs. 1 - 4), the maximum interaction effect is localized near the KF - KBF_4 boundary. The negative deviations from the ideal viscosity behaviour found in the binary KF - KBF_4 and in the ternary systems are probably due to the breaks of the B-F-B bridges caused by the excess of F^- and/or Cl^- ions.

The anionic interaction according to eqn (4) was confirmed by means of the IR spectroscopy study. The IR spectra of KBF_4 and of the quenched molten KBF_4 - KCl (1:1 mole ratio) mixture are shown in Fig. 5. Significant differences have been observed in the 600-900 cm^{-1} region. It can be seen that the KBF_4 - KCl mixture produces beside $\nu(1)$ vibration, which corresponds to BF_4^- anion, two additional peaks at 760 and 796 cm^{-1} with a shoulder at 770 cm^{-1}. It may be assumed, that this peaks arise due to the different (B-F) and (B-Cl) valence vibrations in $[BF_{4-n}Cl_n]^-$ anions. However, the type of the mixed anion might not be determined either by the physicochemical analysis or by the spectroscopic method.

Subsystem KF - KCl - K_2TiF_6

The phase diagram of the system KF - KCl - K_2TiF_6 has been studied in [6]. Two congruently melting compounds, K_3TiF_7 and K_3TiF_6Cl, are formed in the system. However, considering the relatively low symmetry and high energetic state of the TiF_7^{3-} and TiF_6Cl^{3-} complex anions, a high degree of their thermal dissociation was expected. This assumption was confirmed by two different methods based on the thermodynamic analysis of the phase equilibria and of the volume properties of the investigated melts [7, 8].

The degree of thermal dissociation of K_3TiF_6 calculated from the phase diagram, α_o = 0.64, agrees well with the values calculated on the basis of the density data α_o(1000K) = 0.6 and α_o(1100K) = 0.7. The corresponding data for K_3TiF_6Cl are α_o = 0.78 from the phase diagram and α_o(1000K) = 0.72 and α_o(1100K) = 0.81 from the density data. Based on the temperature dependence of the equilibrium dissociation constant the values of dissociation enthalpies ΔH^0(dis, K_3TiF_7) = 52.4 kJ mol^{-1} and ΔH^0(dis,K_3TiF_6Cl) = 46.6 kJ mol^{-1} have been calculated, which is in both cases a major part of the enthalpy of fusion ΔH(f,K_3TiF_7) = 56.0 kJ mol^{-1}, ΔH(f,K_3TiF_6Cl) = 52.9 kJ mol^{-1} [8]. Positive excess molar volumes refering to the formation of bigger species were really found in the KF - K_2TiF_6 system (Fig. 6).

Subsystem KF - KBF_4 - K_2TiF_6

The density and viscosity of the melts of the system KF - KBF_4 - K_2TiF_6 has been measured in [9, 10]. The concentration dependence of the molar volume was described by eqn (2). The excess molar volume of this system is shown in Fig. 7. From the figure it follows, that this system deviates only little from ideal behaviour. Maximum deviation from the additivity is in the binary system KBF_4 - K_2TiF_6. At lover concentration of K_2TiF_6 this system shows positive deviation from ideal mixing, while at higher concentration of K_2TiF_6 the deviation from ideality is negative. This can be explained by means of the values of the partial molar volumes of KBF_4 and K_2TiF_6 in dilute solutions at 1100 K. The partial molar volume of K_2TiF_6 for x(KBF_4)->1, 129.12 cm^3 mol^{-1}, is higher than the molar volume of pure K_2TiF_6 (114.57 cm^3 mol^{-1}), which indicates the formation of bigger complex ions, e.g. TiF_7^{3-}. On the other hand the partial molar volume of KBF_4 for x(K_2TiF_6)->1 is 68.24 cm^3 mol^{-1}. This value is lower than the molar volume of pure KBF_4 (75.37 cm^3 mol^{-1}). The reason for this lowering may be the decomposition of KBF_4 and escape from the melt of gaseous BF_3, which was actually observed.

In the binary systems KF - K_2TiF_6 and KBF_4 - K_2TiF_6 positive deviation from the ideal viscosity behaviour (c.f. eqn (3)) was found obviously due to the formation of larger TiF_7^{3-} anions (Fig. 8).

On the basis of the given findings the following possible chemical reactions may be considered to take place in the ternary system KF - KBF_4 - K_2TiF_6

$$KBF_4(l) + K_2TiF_6(l) = K_3TiF_7(l) + BF_3(g) \qquad (5)$$

$$K_3TiF_7(l) = K_2TiF_6(l) + KF(l) \qquad (6)$$

The Gibbs energy of eqn (6), $\Delta_r G^o = 0.963$ kJ mol^{-1}, was calculated from the equilibrium constant of the dissociation reaction of K_2TiF_6 given in [8]. The Gibbs energy of reaction (5), calculated from the literature data [11] and the Gibbs energy of reaction (6) is $\Delta_r G^o = 10.71$ kJ mol^{-1}. The relatively low positive value of the reaction Gibbs energy, as well as the observed escape of gaseous BF_3, indicate the probability of reaction (5) in the melt. The presence of the assumed reaction was confirmed also by means of the theoretical calculation of the density of the system KF - KBF_4 - K_2TiF_6. The agreement between the calculated and experimental density values lies within the 1 % error.

CONCLUDING REMARKS

All the chemical reactions taking place in the investigated system are controlled by temperature and composition of the melt. This may be of importance in the study of the electrochemical processes in the electrodeposition of TiB_2 from these melts. At low concentration of K_2TiF_6 the formation of the additive compounds is strongly favoured so that beside TiF_6^{2-} also the presence of the ionic species TiF_7^{3-} and/or TiF_6Cl^{3-} must be considered. Also the formation of gaseous BF_3 may be supressed by suitable choice of the temperature and the composition of the electrolyte.

REFERENCES

1. K. Matiašovský, K. Grjotheim, and M. Makyta, Metall 42, 1192 (1988).
2. O. Patarák and V. Daněk, Chem. Papers 46, 2 (1992).
3. M. Chrenková and V. Daněk, Chem. Papers 45, 213 (1991).
4. M. Chrenková, M. Hura, and V. Daněk, Chem. Papers 45, 739 (1991).
5. V. Daněk and D. K. Nguyen, to be published.
6. R. V. Chernov and P. M. Ermolenko, Zh. Neorg. Khim. 18, 1372 (1973).
7. V. Daněk, J. Šiška, and K. Matiašovský, Chem. Papers 42, 753 (1988).
8. V. Daněk and K. Matiašovský, Z. anorg. allg. Chem. 570, 184 (1989).
9. M. Chrenková, V. Daněk, and D. K. Nguyen, to be published.
10. A. Silný, V. Daněk, and D. K. Nguyen, to be published.
11. D. P. Stuhl and H. Prophet, JANAF Thermochemical Tables, 2nd Edition. NSRDS, Nat. Bur. Stand., Washington 1971.

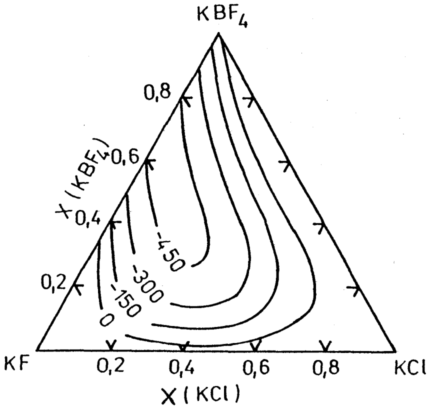

Fig. 1. Excess molar Gibbs energy of the molten system KF-KCl-KBF$_4$ (J mol^{-1}).

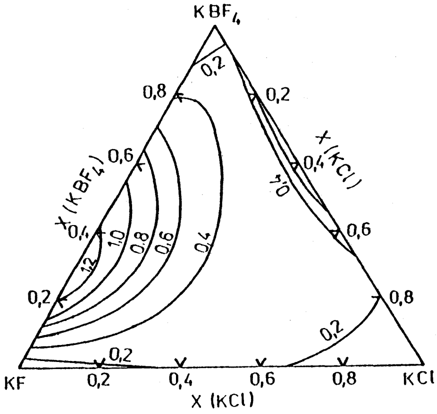

Fig. 2. Excess molar volume of the system KF-KCl-KBF$_4$ at the temperature of 1100 K (cm^3 mol^{-1}).

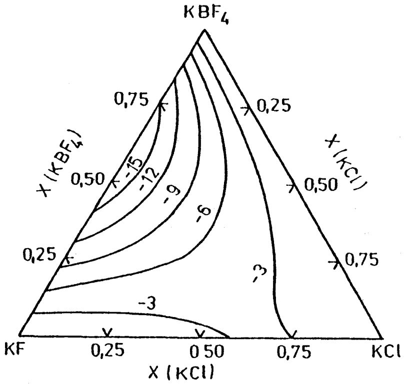

Fig. 3. Ecxess molar conductivity of the system KF-KCl-KBF$_4$ at the temperature of 1100 K (S cm^2 mol^{-1}).

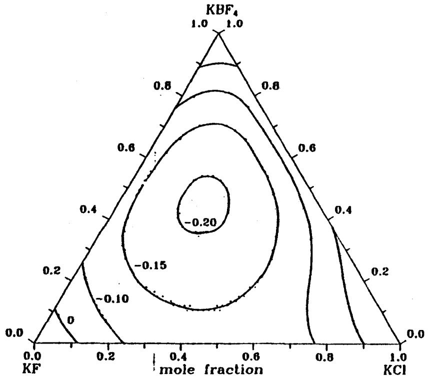

Fig. 4. Excess viscosity of the system KF-KCl-KBF$_4$ at the temperature of 1100 K (mPa s).

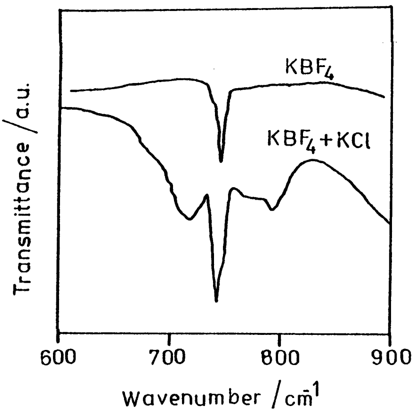

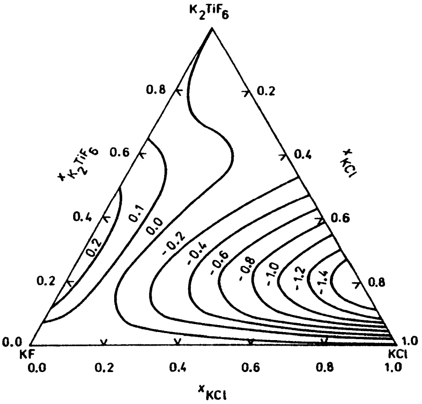

Fig. 5. IR spectra of KBF_4 and of the quenched molten KBF_4-KCl mixture.

Fig. 6. Excess molar volume of the system KF-KCl-K_2TiF_6 at the temperature of 1100 K (cm^3 mol^{-1}).

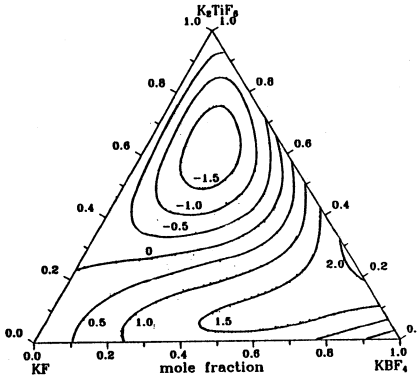

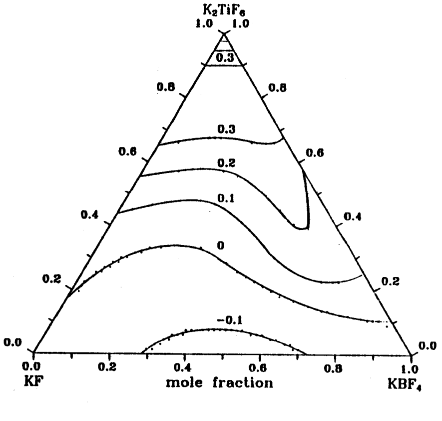

Fig. 7. Excess molar volume of the system KF-KBF_4-K_2TiF_6 at the temperature of 1100 K (cm^3 mol^{-1}).

Fig. 8. Excess viscosity of the system KF-KBF_4-K_2TiF_6 at the temperature of 1100 K (mPa s).

DOI: 10.1149/199413.0116PV

Calculations of Phase Equilibria in the Ternary Molten Salt System AlF_3-BaF_2-NaF.

M. Gaune-Escard[a], G. Hatem[a], P. Peretz[a], M. Hoch[b]

a.Institut Universitaire des Systèmes Thermiques Industriels,
Université de Provence, Centre de Saint Jérôme, Avenue Escadrille
Normandie Niemen, 13397 Marseille Cedex 20, France.

b. Department of Materials Science and Engineering, University of
Cincinnati, 497 Rhodes Hall, Cincinnati, Ohio 45221-0012, USA

ABSTRACT

As a first step to calculate the quaternary system Al, Ba, Na//Cl,F, we calculated certain pseudo binary sections of the ternary system AlF_3-BaF_2-NaF, as was done previously with the BaF_2-NaF-ZrF_4 system. We obtained lower melting points involving cryolite Na_3AlF_6, than are obtained with the additions of CaF_2 or other fluorides or chlorides because in the BaF_2-AlF_3 binary the liquid, at the lowest temperature (in all systems around 880 °C) in equilibrium with solid AlF_3, has a composition richer in AlF_3 than in the other systems, indicating a strong interaction between AlF_3 and BaF_2. The available experimental data on the ternary system AlF_3-BaF_2-NaF are not consistent.

We first evaluated the binary phase diagrams AlF_3-BaF_2, AlF_3-NaF, and BaF_2-NaF. The thermodynamic data deduced from the phase diagrams agrees very well with the data measured by conventional means. We used the same solution model as previously, but a more correct method for C_p(L-s) the difference in heat capacity between liquid and solid was used.

INTRODUCTION

Molten salt mixtures involving chlorides and fluorides of aluminum, barium and sodium are used for electrolytic production and purification (Gadeau's bath) of aluminium .Basic knowledge of the thermodynamics of this quaternary reciprocal mixture Al, Ba, Na // Cl, F is needed to improve the industrial processes and to palliate some drawbacks. As a first step to calculate the quaternary system AlF_3-BaF_2-NaF-NaCl (also $AlCl_3$ and $BaCl_2$), we calculated certain pseudo binary sections of the ternary system AlF_3-BaF_2-NaF, as was done previously with the BaF_2-NaF-ZrF_4 system (1,2). The available experimental data on the ternary system AlF_3-BaF_2-NaF and also on the three limiting binary systems are not consistent. One major difficulty, from the point of view of predictive phase equilibrium calculations, lies in the fact that experimental thermodynamic data are not available for AlF_3 at high temperature since this salt sublimates under normal conditions.

We obtained lower melting points involving cryolite Na_3AlF_6, than are obtained with the additions of CaF_2 or other fluorides or chlorides because in the BaF_2-AlF_3 binary the liquid, at the lowest temperature (in all systems around 880 °C) in equilibrium with solid AlF_3, has a composition richer in AlF_3 than in the other systems, indicating a strong interaction between AlF_3 and BaF_2.Furthermore no congruently melting compound exists in CaF_2-AlF_3 while one does in BaF_2-AlF_3 yielding more negative values of the interaction parameter.

We first give a short description of the Hoch-Arpshofen (3,4) solution model and of the model to calculate C_p(L-s), the difference in heat capacity between liquid and solid (5-7).We report the experimental thermodynamic data obtained in the present work by isothermal solution calorimetry at high temperature (enthalpies of mixing) and by differential scanning calorimetry (equilibrium temperatures).

THE HOCH-ARPSHOFEN MODEL

In an earlier paper Hoch and Arpshofen (3) derived a model for binary solutions. In a subsequent paper Hoch (4) derived the model for ternary, quaternary, and larger systems. The binary model is merely a special case of the ternary model. The model is an extension of Guggenheim's (8) treatment of solutions, combined with an adaptation of Pauling's (9) ideas of the metallic bond.

In a multicomponent system with the components A,B,C,D, etc. and their mole-fractions x,y,z,u, etc. the effect of the mixing function Fm (Hm, enthalpy of mixing, Sm_{ex}, excess entropy of mixing) of the binary system A-B (mole-fraction x and y) in the multicomponent is

$$Fm = Wnx[1 - (1-y)^{\{n-1\}}] \qquad (1)$$

W is the interaction parameter and n is an integer (2,3,4, etc). The term x is the mole-fraction of the component so that in Equation (1) Fm is maximum (positive or negative) at $x \geq 0.5$.

The excess Gibbs energy of mixing, Gm^{ex}, is a combination of Hm and Sm^{ex}. Equation (1) can be applied to Gm^{ex} only if Sm^{ex} has the same n and x as Hm, or if Sm^{ex} is zero.

Equation (1) also applies to binary systems: In a binary system

$$x + y = 1 \qquad (2)$$

In our nomenclature 6,(Na_2SO_4) means that n is equal to 6, and x is Na_2SO_4. Wh shows that the interaction parameter was calculated from enthalpy values, Wg from Gibbs energy values, and Ws from entropy values.

The model was applied earlier to various binary and ternary systems ; the method of evaluation of binary phase diagrams was also shown (10-11). To describe solid compounds that are very stable and have a wide homogeneity range, we use the Schottky-Wagner model (12) combined with activity coefficients derived by dividing the binary system into two binaries A-AB and AB-B. We refer the reader to the above publications for derivation of the model and the method of application.

The interaction parameters are designated depending on what experimental data they were calculated from: Wh from Hm enthalpy of mixing, Ws from Sm^{ex}, excess entropy of mixing, and Wg from Gm^{ex}, excess Gibbs energy of mixing.

In all of our calculations the thermodynamic quantities are divided by R, the gas constant. Thus the enthalpy H and the Gibbs energy G are expressed in kK (kiloKelvin); the entropy S and the heat capacity Cp are dimensionless.

Difference in heat capacity between liquid and solid Cp(L-s).

The Gibbs energy of fusion G(L-s) at temperatures below and above the melting point, and thus the calculated phase diagram is greatly influenced by the difference in heat capacity between liquid and solid C_p(L-s).

If one assumes that the heat capacity of the liquid is constant, or decreases with increasing temperature, and the heat capacity of the solid increases with increasing temperature, each solid will have a glass transition and a jelly transition temperature, at which the entropy of the liquid becomes less than that of the solid. We applied our method to describe the Al-Ca and Ca-Pb phase diagrams (13). The equation for G(L-s) showed that in the Al-Ca phase diagram on the Ca side a repulsive term had to be included in the thermodynamic description.

RESULTS

We are interested in the ternary AlF_3-BaF_2-NaF phase diagram; thus we are using mostly binary phase diagrams. First, we have to obtain the enthalpy and temperature of fusion of AlF_3. These data cannot be obtained experimentally since AlF_3 sublimates.They have been estimated from the values reported by Kubaschewski and Alcock (14) for the analogous compounds CeF_3, LaF_3, NdF_3 and PuF_3 . We obtain an entropy of fusion $S_{fus}/R = 3.431$ and a temperature of fusion T_{fus} = 1433°C . With this temperature T_{glass}, the glass transition is 660°C , which is just below 695°C , the lowest temperature where liquid AlF_3 is present in the binary AlF_3-NaF binary system (15).

• Binary systems:

BaF_2-NaF: This is a simple eutectic system according to Bukhalova et al (16) with the eutectic point at 37 mol% BaF_2 and 812°C . Within the uncertainties of the enthalpies of fusion (Kubaschewski and Alcock (14)), the liquid in this system is ideal. Hong and Kleppa (17) measured the enthalpy of mixing at 1081°C and $0 < x,BaF_2 < 0.6$. From their data we deduced a sligthly negative interaction parameter, W = 0.174 ± 0.01 kJ/mol, while the one deduced from the phase diagram is W = 0.112 kJ/mol.

AlF_3-NaF: Holm (18) measured the enthalpy of mixing at 1012°C in the binary system NaF-Na_3AlF_6, Hong and Kleppa measured the enthalpy of mixing of NaF-AlF_3(s) at 1025°C (19) and of Na_3AlF_6-AlF_3(s) at 1025°C (20). Using regression analysis on the data of Hong and Kleppa (19, 20) and Holm (18), we deduced an enthalpy of fusion of 95.2 ± 1.54 kJ/mol and calculated the interaction parameter W = -33.4 ± 0.70 kJ/mol, and plotted the experimental data together with the interaction parameter obtained from the phase diagram in Figure 1. The agreement is excellent.

Using the phase diagrams given by Kvande (15), Ginsberg et al. (21) and Kuxmann et al. (22) we deduced a temperature of fusion T_{fus} = 1541 °C (the AlF_3 liquidus line was used to calculate $G_{fus} = G^0{}_L - G^0{}_s = - RT \ln x - Fm(x)$

using the G_{fus} equation in (6-7) and the value W determined above we obtained the melting temperature).

From these data, G_{fus} and T_{fus}, coupled with the phase diagram a final value of the interaction parameter was obtained W = -36.4 ± 2.4 kJ/mol.The enthalpies of formation of Na_3AlF_6 and $Na_5Al_3F_{14}$ were also evaluated (Hform (s+s->s) = -35.00±2.82 kJ/mol (1/4 Na_3AlF_6) and -12.22±5.23 kJ/mol (1/8 $Na_5Al_3F_{14}$) . The values are more negative than the values given by Kubaschewski and Alcock (14) and Kubaschewski et al.(23). We are dealing with phase diagrams, thus the enthalpy of formation given for $Na_5Al_3F_{14}$ is 1/8($Na_5Al_3F_{14}$).

AlF_3-BaF_2: Two phase diagrams are available, by Schultz et al (24) and de Kozak et al (25). The difference between the two is small, mainly at what composition is the congruently melting compound: $Ba_3Al_2F_{12}$ (24) and $Ba_5Al_3F_{19}$ (25), and Schultz et al (24) show more incongurently melting compounds than de Kozak et al (25). The latter diagram, however, seems more accurate since the compounds have been evidenced from several experimental techniques including neutron diffraction.We calculated the interaction parameter in the liquid (w = -62.94±1.25 kJ/mol) and the enthalpies of formation of the compounds $BaAlF_5$ and

$Ba_5Al_3F_{19}$ using both phase diagrams (Hform (s+s->s) = -19.95±4.07 kJ/mol (1/2 $BaAlF_5$) and -23.36±3.74 kJ/mol (1/8 $Ba_5Al_3F_{19}$). The AlF_3 liquidus was calculated.

Other MeF_2-AlF_3 systems: Holm (26) determined the CaF_2-AlF_3 phase diagram. We calculated from it the interaction parameter in the liquid, and the enthalpy of formation of $CaAlF_5$. The values are much less negative than in the BaF_2-AlF_3 cases discussed above.

The results show the lowest temperature and composition of the AlF_3 liquidus in various experimental binary systems. This clearly indicates that CaF_2 reacts much less with AlF_3 than does BaF_2.

Ternary AlF_3-BaF_2-NaF system

From all the binary data, it was possible to make calculations of phase equilibria in the ternary system.The results reported in the present work deal with the quasi binary section BaF_2-Na_3AlF_6 and the sections Na_3AlF_6-$Ba_5Al_3F_{19}$ and Na_3AlF_6-$BaAlF_5$.

BaF_2-Na_3AlF_6 : Two kinds of calculations were performed :

i) the values of the interaction parameters W and of the thermodynamic quantities (fusion, formation) of the existing phases in the binary systems were used : the phase diagram calculated is displayed in Figure 2 and exhibits an eutectic at 820 °C and x(1/4 Na_3AlF_6) = 0.58.

ii) the value of the interaction parameter W is obtained, in this case, from our calorimetric enthalpy-of-mixing data (27) and the litterature thermodynamic data for Na_3AlF_6 (28). With the simple approximation $G_{fus} = S_{fus} (T - T^0)$, we obtained the eutectic composition x(1/4 Na_3AlF_6) = 0.58 at the temperature 837 °C.

The results of both sets of calculations are in excellent agreement. They were compared to the experimental eutectic composition and temperature (29) : the results of the same paper are contradictory since the following values can be read either in the paper or in the related graph x(1/4 Na_3AlF_6) = 0.59 ; T = 822°C and x(1/4 Na_3AlF_6) = 0.53 ; T = 818°C, respectively.

In order to check the results of our calculations and also the experimental eutectic coordinates, we performed differential scanning calorimetry experiments experiments. The experimental technique was described in detail elsewhere (30). The mixture with the composition x(1/4 Na_3AlF_6) = 0.65 had the melting temperature 831 °C which is intermediate between the calculated values.Further experiments, however, have to be carried out at other compositions to determine more accurately the eutectic composition.

Na_3AlF_6-$Ba_5Al_3F_{19}$: The phase diagram of this system has been calculated based on the results of de Kozak (25).A minimum temperature T = 775 °C was

found at the composition x(1/4 Na_3AlF_6) = 0.472 as indicated in Figure 3.

Na_3AlF_6-$BaAlF_5$: The phase diagram of this system has been calculated based on the results of de Kozak (25).A minimum temperature T = 677 °C was found at the composition x(1/4 Na_3AlF_6) = 0.419 as indicated in Figure 4.

CONCLUSION

The present paper is a first step to calculate the quaternary system AlF_3-BaF_2- NaF-NaCl or other related systems containing chlorides and fluorides of aluminum, barium and sodium.It illustrates how it is possible to solve by calculation and a few selected experiments a fundamental problem with potential industrial interest. A similar procedure can be extended to more complex systems, e.g. with a larger number of components like AlF_3-Al_2O_3-BaF_2-NaF-NaCl for instance, or to other problems in different fields.

REFERENCES

1. G. Hatem, K. Mahmoud, M. Gaune-Escard, and M. Hoch, High Temperature Science, 31 159-179 (1991).
2. G. Hatem, M. Gaune-Escard, and M. Hoch, J. Non-Cryst. Solids 161 91-97 (1993)
3. M. Hoch and I. Arpshofen, Z. Metallkde 75 23-29 (1984)
4. M. Hoch, Calphad 11 219-24 (1987)
5. M. Hoch, High Temperatures-High Pressures, 24 87-96 (1992)
6. M. Hoch, Met. Trans. 23B 309-315 (1993)
7. M. Hoch, Z. Metallkde 83 820-823 (1992)
8. E.A. Guggenheim, Mixtures, Clarendon Press, Oxford (1952)
9. L. Pauling, The Nature of the Chemical Bond, Third Edition,Cornell University Press, Ithaca, New York (1960).
10. M. Hoch, Calphad 11 225-36 (1987)
11. M. Hoch, Calphad 12 45-58 (1988)

12. C. Wagner, Thermodynamics of Alloys, Addison Wesley Publishing Co, Inc. Reading, MA (1952)

13. M. Hoch, J. Chim. Phys 90 201-208 (1993)

14. O.Kubaschewski and C.B.Alcock, Metallurgical Thermochemistry,Fifth Edition, Pergamon Press, NY, 1976.

15. H. Kvande, High Temp-High Press 15 51-62 (1983)

16. G.A. Bukhalova, V.T. Berezhnaya and and A.G. Bergman Zh. Neorg. Khim. 6 (10) 2359 (1961)

17. K.C. Hong and O.J. Kleppa, J. Phys. Chem. 82 1596-1603 (1978)

18. J.L. Holm, High Temp. Science. 6 16-36 (1974)

19. K.C. Hong and O.J. Kleppa, J. Phys. Chem. 82 176-181 (1978)

20. K.C. Hong and O.J. Kleppa, High Temp. Science. 8 299-307 (1976)

21. H. Ginsberg, K. Wefers, Erzmetall., 20, 156, (1967)

22. U. Kuxmann, U. Tillesen, Erzmetall., 20, 147, (1967)

23. O. Kubaschewski, C.B. Alcock and P.J. Spencer, Materials Thermochemistry, Sixth Edition, Pergamon Press, NY, (1992).

24. A.H. Schultz, B. Bieker and J. Krogh-Moe, Acta Chem. Scand. 26 2623-2630 (1972).

25. A. de Kozak, M. Samouël, J. Renaudin and G. Ferey, Z. anorg. allg. Chem 613 98-104 (1992).

26. J.L. Holm, Acta Chem. Scand. 19 1512-14 (1965).

27. P. Peretz, M. Gaune-Escard, G. Hatem (to be published).

28. JANAF "Thermochemical Tables" 2th edition NSRDS-NBS 37, Washington (1971).

29. M.A. Kubakin, A.N. Sunin and L.I. Talanova Russ. J. Inorg. Chem. (English Trans) 17 1459-61 (1972).

30. M. Gaune-Escard, in "Molten Salt Techniques", R. Gale, D. G. Lovering, Ed., Plenum Press, New York, London, (1991), Chap. 5.

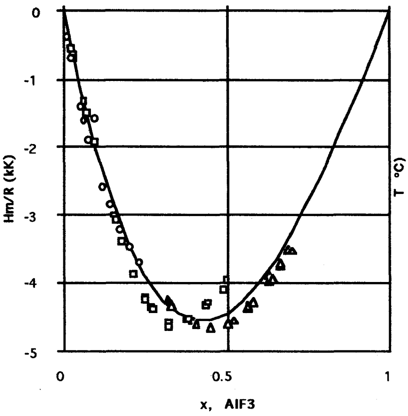

Fig.1 : Enthalpy of mixing in $NaF-AlF_3$
○ (19) □ (20) ∧ (18) ___ Hoch model

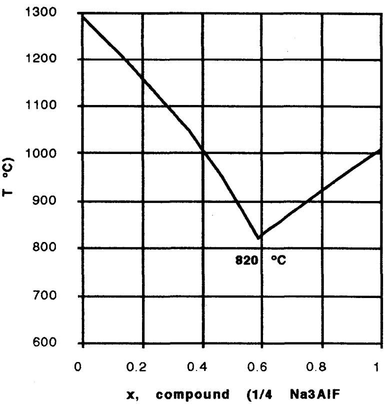

Fig.2: Calculated phase diagram of BaF_2-Na_3AlF_6

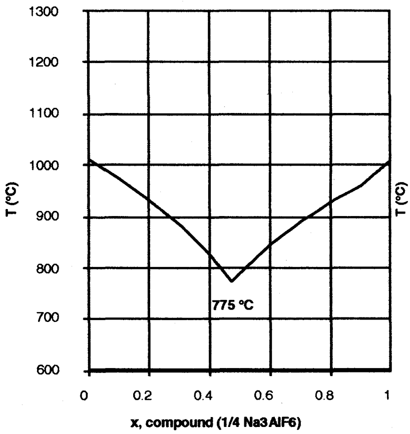

Fig.3: Calculated phase diagram of $Ba_5Al_3F_{19}$-Na_3AlF_6

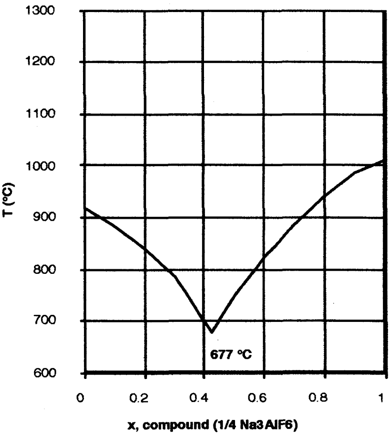

Fig.4: Calculated phase diagram of $BaAlF_5$-Na_3AlF_6.

DOI: 10.1149/199413.0124PV

CONDUCTIVITY, NMR, THERMAL MEASUREMENTS AND PHASE DIAGRAM OF THE $K_2S_2O_7$-$KHSO_4$ SYSTEM

K. M.Eriksen[a], R. Fehrmann[a], G. Hatem[b], M. Gaune-Escard[b],
O. B. Lapina[c] and V. M. Mastikhin[c]

a. Chemistry Department A, Technical University of Denmark
Lyngby, Denmark

b.Institut Universitaire des Systèmes Thermiques Industriels,
Université de Provence, Centre de Saint Jérôme, Avenue Escadrille
Normandie Niemen,
13397 Marseille Cedex 20, France.

c. Boreskov Insitute of Catalysis, Novosibirsk, Russia

ABSTRACT

The phase diagram of the catalytically important $K_2S_2O_7$-$KHSO_4$ solvent system has been investigated by means of electrochemical, thermal and spectroscopic methods. A peritectic seems to be present around x_{KHSO4} = 0.4 and an eutectic at around x_{KHSO4} = 0.9 with the temperatures of fusion around 320°C and 205°C, respectively. However, a maximum at x_{KHSO4} = 0.5 cannot be ruled out at present. Thus a compound is most probably formed in the range x_{KHSO4} = 0-0.5.Further measurements are in progress.

INTRODUCTION

The molten salt-gas system $K_2S_2O_7/KHSO_4/V_2O_5$ - $SO_2/O_2/SO_3/CO_2/H_2O/N_2$ at around 400°C is considered as a realistic model of the catalyst used for the oxidation of SO_2 to SO_3 by O_2 in a novel "wet" process developed for the purification of flue gases. The chemistry of the "dry" system,i.e. $K_2S_2O_7/V_2O_5$ - $SO_2/O_2/SO_3/N_2$ reflecting the traditional sulfuric acid catalyst has previously been explored in detail by us (1), (2), (3), (4). In both catalytic processes, the active component is the vanadium complexes formed in the molten $K_2S_2O_7$ or in the molten $K_2S_2O_7$-$KHSO_4$ system, respectively. Thus detailed information about the molten $K_2S_2O_7$-$KHSO_4$ solvent including the species formed, their structure, the equilibria governing the melt and fundamental physicochemical data sems important for the understanding of the working catalyst for flue gas cleaning. Such investigations are undertaken by us or will be carried

out by means of spectroscopic, thermal and electrochemical methods. Previous (5) Raman- and NIR-spectroscopic investigations on the molten $K_2S_2O_7$-$KHSO_4$ have shown that the dominant species present most probably are $S_2O_7^{2-}$, HSO_4^- and H_2O. The H_2O molecules seem strongly associated by hydrogen bonds to the other species of the melt, even at 450°C. Therefore the vapor pressure of H_2O seems surprisingly low even at these high temperatures. Nevertheless it appears to control the position of the water sensitive equilibrium
$2\ HSO_4^- <-> S_2O_7^{2-} + H_2O$ in the melt. Our ongoing investigations will hopefully throw more light on these matters.

The work presented here concerns a re-investigation of the equilibrium phase diagram of the binary system $K_2S_2O_7$-$KHSO_4$. Our work has proven to show large discrepancies from the only diagram previously published, almost sixty years ago (6) .Knowledge of this phase diagram may be useful for the design of new low-melting catalysts which are able to operate in the desired temperature range below 400°C.

Three different methods of investigations have been applied for this study, i.e. electrical conductivity, Differential Thermal Analysis (DTA) and ^{39}K NMR at temperatures up to 500°C.

EXPERIMENTAL

Chemicals

The hygroscopic $K_2S_2O_7$ used was obtained by thermal decomposition of $K_2S_2O_8$ (Merck, p.a.) and kept in sealed ampules until used in the dry-box.

The $KHSO_4$ used for additions (Merck, Suprapur, 99 %) was dried at 110 °C and stored in the dry-box.

Conductivity measurements

The borosilicate glass cell (Figure 1) with gold electrodes used for measuring the electrical conductivity has been described in detail previously (7). The cell was filled in the dry-box, sealed and placed in the measuring furnace regulated to within ± 0.1 °C, as earlier described (8). All additions to the cell were made in the dry-box by cutting the stem open and thereafter resealing it again. The conductivity was measured by a Radiometer CDM-83 conductivity meter.

Thermal investigations

Differential Thermal Analysis (DTA) was made on samples of about 3 g in sealed ampules of borosilicate glass.The temperature was recorded with a Pt/Pt-10%Rh within ± 1°C and checked in a separate experiment with the melting of lead.

With this technique the heating rate was low, i.e. 2 °C/mn leading to a very good separation of the thermal effects occurring at close temperatures (9).

NMR measurements

The ^{39}K NMR spectra were measured on a Bruker MSL-400 spectrometer at 18.67 MHz and 50 μs pulse width with a delay of 0.15 s between the pulses in a 50 KHz frequency range. The measurements were performed by use of a home-made high temperature probe head. The chemical shifts were referred relatively to saturated solutions of KCl in water. The samples of around 3g were contained in sealed quartz ampules.

RESULTS AND DISCUSSION

The conductivity of the solid and molten mixtures of the binary system $K_2S_2O_7$-$KHSO_4$ was measured at 12 different compositions in the mole fraction range x_{KHSO4} = 0-0.9. The measured conductivities are plotted as -lnκ vs. 1/T in Figure 2 for some selected compositions. As found very recently (10), (11) for the $M_2S_2O_7$-V_2O_5 systems (M = Cs or 80% K + 20% Na), a marked change of the conductivity is found at the phase transition temperature. This is in accordance with the equation :

$$\kappa = A(\kappa)\, e^{-E(\kappa)/RT} \qquad (1)$$

relating the conductivity κ to the activation energy E(κ) for ionic migration and to the temperature. Thus plots of -ln κ vs. 1/T will give rise to straight lines of different slopes in the liquid and in the solid region since especially E(κ) will be different for the two regions. In the intermediate solid+liquid region the curve will deviate from these two lines.

However, for the mixtures rich in $KHSO_4$ the transition from the two phase solid+liquid region to the liquid region does not give rise to a marked change since the conductivity of the liquid does not change much with the composition in that part of the binary system.Thus no liquidus temperature could be found for x_{KHSO4} = 0.8 and for x_{KHSO4} = 0.9 only one transition is observed indicating that the eutectic mixture is close to this composition. Contrary to this the solid to solid+liquid transition was very marked in all cases but unfortunately the temperature was not lowered sufficiently to observe this transition in the K_2SO_7-rich region, i.e. x_{KHSO4} = 0- 0.4.

Supplementary DTA measurements have been carried out, especially at relatively high contents of $KHSO_4$. As can be seen from the phase diagram in Figure 5, the liquidus temperatures and the low temperature transitions around 200°C agree well with the conductivity measurements.

The ^{39}K NMR spectra of a sample with the composition $x_{KHSO4} = 0.7$ measured in the temperature range 195-355 °C are shown in Figure 3. Below around 200°C, no signal is seen, presumably due to line broadening in the solid state. In the range 200-300°C a rather sharp line appears at -18.8 ppm with a gradually increased intensity up to around 300°C as can be seen in Figure 4. Thereafter the intensity remains constant indicating that the sample is completely molten. In the two phase region the chemical shift is independent of the temperature. Thus the mobility of K^+ seems high and the association with the anions appears low independent of the large composition variation of the melt in this region. The observed transition temperatures agree well with the those obtained from the other methods , as can be seen in Figure 5.

The phase diagram depicted in Figure 5 shows considerable variations from the diagram of Hagisawa and Takai (6) obtained from differential thermal analysis only.

Our measurements point to the presence of a peritectic around $x_{KHSO4} = 0.4$. Thus a compound should be formed at lower mole fractions. Alternatively the measurements cannot at the present time rule out a maximum at $x_{KHSO4} = 0.5$ in the phase diagram corresponding to the formation of a 1:1 compound. However supplementary measurements and X-ray investigations of isolated solids may lead to a conclusion. The diagram indicates the presence of an eutectic at $x_{KHSO4} = 0.9$ with a temperature of fusion of around 205°C. The temperatures of fusion of the pure components are found to be 420°C and 212°C, respectively for $K_2S_2O_7$ and $KHSO_4$, in accordance with the literature. The transition for $x_{KHSO4} = 0.25$ at 320 °C and for $x_{KHSO4} = 0.10$ at 337 °C are attributed to the fusion of the peritectic and the $\alpha \rightarrow \beta$ transition in solid $K_2S_2O_7$ (12), respectively.

If a compound is formed at $x_{KHSO4} = 0.5$, the low temperature transitions at lower mole fractions of $KHSO_4$ should be attributed to solid-solid transitions rather than to the fusion of the eutectic. As far as we know, no compound between the two components has previously been reported in the literature.

ACKNOWLEDGMENTS

This investigation has been supported by the EEC programs Human Capital and Mobility (contract N° ERBCHBGCT 92029) and Brite Euram II (contract N° BRE2.CT93.0447). Further support is acknowledged from the Danish Natural Science Foundation and the French Ministery of Foreign Affairs.

Key words :
SO_2-oxidation, Flue gas cleaning, Wet sulfuric acid process.

REFERENCES

1. G. E. Folkmann, G. Hatem, R. Fehrmann, M. Gaune-Escard, N. J. Bjerrum, Inorg. Chem., 32, 1559 (1993).

2. K. Nielsen, R. Fehrmann, K. M. Eriksen, Inorg. Chem., 23, 4714 (1993).

3. S. Boghosian, R. Fehrmann, N. J. Bjerrum, G. N. Papatheodorou, J. Catal., 119, 121 (1989).

4. B. S. Bal'zhinimaev , A. A. Ivanov, O. B. Lapina, V. M. Mastikhin, K. I. Zamaraev, Faraday Discuss. Chem. Soc., 87, 133 (1989).

5. R. Fehrmann, N. H. Hansen, N. J. Bjerrum, Inorg. Chem., 22, 4009 (1983).

6. T. Hagisawa, T. Takai, Sci. Papers Inst. Phys. Chem. Soc., 31, 677 (1937).

7. G. Hatem, R. Fehrmann, M. Gaune-Escard, N. J. Bjerrum, Inorg. Chem., 26, 195 (1987).

8. H.A. Andreasen, N. J. Bjerrum, C. E. Fokerskov, Rev. Sci. Instrum. 48, 1340 (1977).

9. M. Gaune-Escard, in "Molten Salt Techniques", R. Gale, D. G. Lovering, Ed., Plenum Press, New York, London, (1991), Chap. 5.

10. G. E. Folkmann, G. Hatem, R. Fehrmann, M. Gaune-Escard, N. J. Bjerrum, Inorg. Chem.,30, 4057 (1991).

11. D. A. Karydis, S. Boghosian, R. Fehrmann,, J. Catal., (1994, accepted for publication).

12. B. J. Meehan, S. A. Tariq, J. O. Hill, J. Thermal Anal., 12, 235 (1977).

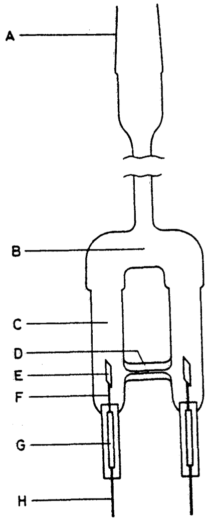

Figure 1. Conductivity cell of borosilicate glass :
A, standard taper joint with stem ;
B, melt resrvoir ;
C, cell compartment ;
D, capillary tube ;
E, gold electrode plate ;
F, gold wire ;
G, glass sealed gold foil ;
H, gold wire.

Figure 2 . Phase transitions in the $K_2S_2O_7$-$KHSO_4$ system obtained from measurements of the conductivity, κ, for the compositions x_{KHSO4} : 0.0000 (A) ; 0.1002 (B) ; 0.1997 (C) ; 0.3003 (D).

For clarity the data (except for the pure melt) are offset on the ordinate by the specified values.

Open circles indicate subcooling. The arrows indicate the liquidus temperature.

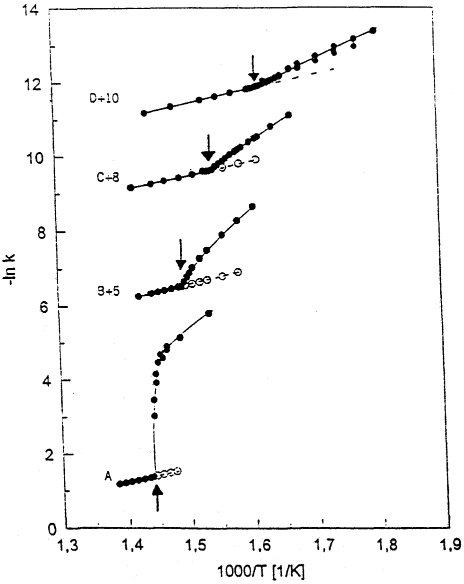

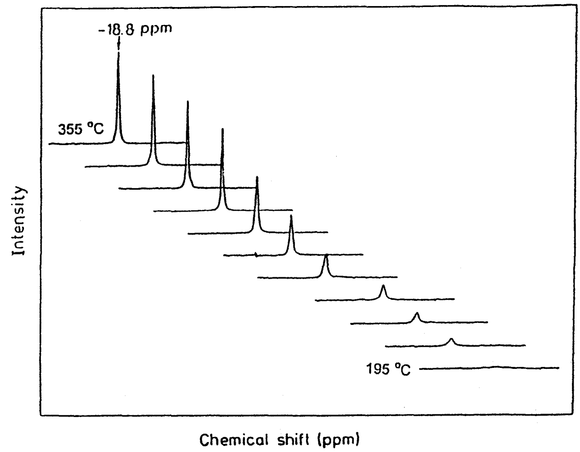

Figure 3. ^{39}K NMR spectra of the $K_2S_2O_7$-$KHSO_4$ system for $x_{KHSO4} = 0.7$ in the temperature range 195-355 °C. The chemical shift of the signal is -18.8 ppm in all spectra.

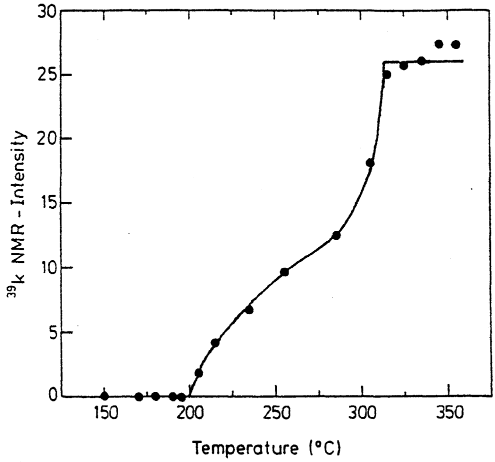

Figure 4. The NMR line intensity obtained as the integrated signal at -18.8 ppm in the ^{39}K NMR spectra for $x_{KHSO4} = 0.7$ at 150-355 °C.

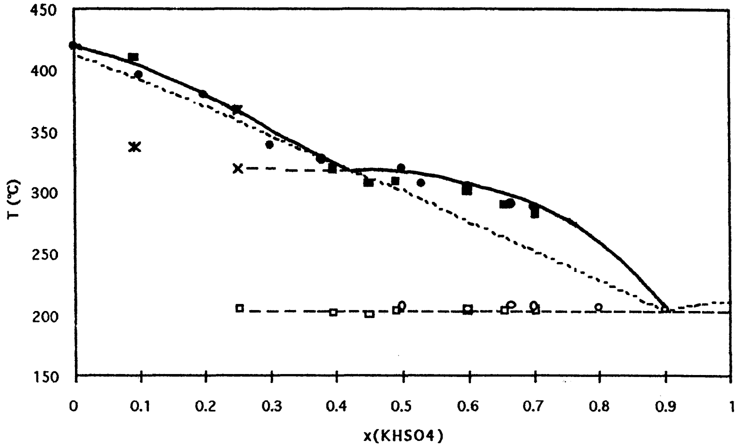

Figure 5: Phase diagram of the $K_2S_2O_7$-$KHSO_4$ system.
■, □, x, ∗ DTA ; ●, ○ electrical conductivity
Dashed liquidus curve is from ref. (6).

DOI: 10.1149/199413.0132PV

Phase Equilibria and Structures in the Sodium Chloride + 1-Methyl-3-ethylimidazolium Chloride + Aluminum Chloride System

Do Ren Chang
Chemistry Department, Averett College
Danville, VA 24541

Anselmo M. Elias
Department of Chemistry, University of Lisbon
1700 Lisbon, Portugal

Richard T. Carlin and John S. Wilkes
The Frank J. Seiler Research Laboratory
US Air Force Academy, CO 80840

ABSTRACT

The melting points of the aluminum chloride + sodium chloride + 1-methyl-3-ethylimidazolium chloride system were determined by differential scanning calorimetry and by visual observation in a capillary tube. Also, the melting points of the sodium chloride + 1-methyl-3-ethylimidazolium chloride binary system were measured to establish the third side of the ternary diagram. A large portion of the ternary phase diagram has the solid-liquid transition below room temperature. The compositions with $AlCl_3$ mole fraction of 1/2 is particularly interesting, because they are Lewis neutral mixtures. One composition along that line is a syntectic point, where the compound $Na(MEI)(AlCl_4)_2$ is indicated. The salt was crystallized and the structure determined by x-ray diffraction. The packing of the ions is composed of a sodium tetrachloroaluminate anionic network separated by layers of 1-methyl-3-ethylimidazolium cations.

INTRODUCTION

Room-temperature chloroaluminate molten salts composed of 1-methyl-3-ethylimidazolium chloride (MEIC) and aluminum chloride have proven to be versatile solvents for electrochemistry, spectroscopy, and reaction chemistry (1). More recently, ternary melts produced by adding an alkali metal chloride (MCl) to melts with $N > 0.5$ (termed an acidic melts), where N is the mole fraction of $AlCl_3$, are being evaluated for battery applications (2-7). In the preparation of these ternary melts, the alkali metal chloride neutralizes the Lewis-acidic $Al_2Cl_7^-$ ions to form $AlCl_4^-$ ions and, at the same time, introduces alkali metal cations into the melt. Because MCl is not soluble in the resulting neutralized melt, the addition of excess MCl to the binary acidic melt produces a neutral ternary melt of composition $AlCl_3$-MEIC-MCl where the moles of $AlCl_3$ equal the total moles of MEIC and MCl. Tetrachloroaluminate is the predominant anion in the neutral melts, and only negligible quantities of $Al_2Cl_7^-$ and Cl^- ions are produced by the reaction

$$2\ AlCl_4^- = Al_2Cl_7^- + Cl^- \qquad K_{eq} = 6 \times 10^{-18} \text{ at } 40\ ^{o}C. \quad (1)$$

When chloride ions are introduced into the melt by physical, chMEICal, or electrochMEICal means, solid alkali metal chloride precipitates from the neutral ternary melt. Also, when excess MCl is present as a solid phase, $Al_2Cl_7^-$ ions introduced into the melt are removed by conversion to $AlCl_4^-$. Thus, the melt is maintained at a neutral composition and is termed a buffered neutral melt (7).

The physical properties of the binary $AlCl_3$-MEIC ionic liquids have been thoroughly investigated (8), and the local ion-ion interactions, in particular hydrogen-bonding, have been used to explain trends in conductivities and viscosities (9-13). Although a number of $AlCl_3$-MEIC-NaCl ternary melt physical properties have been determined (14), the phase diagram of the ternary melt system has not been reported.

We present here the phase diagram of the $AlCl_3$-MEIC-NaCl ternary system. The compositions of that ternary having N = 0.5 are the neutral buffered melts. At the 0.5:0.25:0.25 composition in the $AlCl_3$-MEIC-NaCl phase diagram, the congruently melting compound $(MEI)(Na)(AlCl_4)_2$ is found. We have grown crystals of this compound and report here a single crystal structure analysis of this unusual mixed organic-inorganic tetrachloroaluminate salt.

EXPERIMENTAL

The preparation of MEIC is reported elsewhere (15). High purity, anhydrous NaCl was obtained from Aldrich and used without further purification. Salts used for determining the phase diagram were made by preparing the binary mixtures A, C, E, G, I, K, W, X, Y, and Z shown in Figure 1. Additions of the appropriate third component were added to attain the desired ternary composition. The mixtures were fused, cooled to room temperature, and the solid samples were ground in a mortar and pestle. All operations were conducted under anhydrous helium gas atmosphere in a glove box.

Melting points were determined using a Perkin Elmer Model 7 DSC with stainless steel sample pans, or visually in sealed glass capillary tubes.

Crystals of $Na(MEI)(AlCl_4)_2$ were grown by a seed method using slow rotation of a seed touching the surface of the melt (16, 17). The melt for crystal growth was prepared by mixing $AlCl_3$ and MEIC to N = 0.667 and then adding NaCl in a stoichiometric amount corresponding to the amount of $Al_2Cl_7^-$. The crystalline product obtained was colorless and formed crystals suitable for single crystal X-ray diffraction analysis. The sample was placed in a glass capsule and sealed under He and sent to Molecular Structure Corporation for single crystal analysis. All handling and preparation of the crystals was performed inside a glove box under a dry helium atmosphere.

For structural analysis, a colorless irregularly cut crystal of $Na(MEI)(AlCl_4)_2$ having approximate dimensions of 0.700 x 0.450 x 0.350 mm was mounted on a glass fiber. Data collection was performed at -120 ±1°C on a Rigaku AFC6R Diffractometer with a graphite monochromated MoKα radiation and a 12 kw rotating anode generator. All calculations were performed with the TEXSCAN crystallographic software package from Molecular Structure Corporation. Final cell constants and an orientation matrix for data collection were obtained from a least-squares refinement of 25 carefully centered reflections in the range $21.94 < 2\theta < 26.73^\circ$. The crystal was found to have a triclinic cell with the dimensions given in Table I. Based on statistical analysis of the intensity distribution, the space group was determined to be $P\bar{1}$. The structure was solved by direct methods. All non-hydrogen atoms were refined with anisotropic thermal parameters. The three hydrogen atoms on the ring carbons were located and refined with isotropic thermal parameters. Space limitations prevent the listing of final positional and isotropic parameters for all atoms and the anisotropic thermal parameters for non-hydrogen atoms. The position of the hydrogen atoms on the methyl and ethyl groups were calculated and are given in the supplemental material. Final full-matrix least-squares refinement on 185 parameters using 2713 observed reflections ($I > 3.00\ \sigma(I)$) yielded residuals of $R = 0.037$ and $R_w = 0.045$. Additional details of the structure solution and refinement will be published at later date.

RESULTS AND DISCUSSION

Phase Diagram.

The melting points of the $AlCl_3$-MEIC-NaCl salts are depicted in Figure 2 as contours on a ternary composition diagram. A large area of the diagram has relatively low melting points. The cross-hatched region was not investigated, since there was evidence of thermal decomposition during preparation of samples having those compositions. The compositions at $N = 0.5$ (line M-N in Fig. 1) are particularly interesting since those are the buffered neutral melts. At the 0.5:0.25:0.25 $AlCl_3$-MEIC-NaCl composition there is a syntectic point that melts congruently at 36.7 °C. This indicates a compound of formula $Na(MEI)(AlCl_4)_2$.

$Na(MEI)(AlCl_4)_2$ Structure.

The formula unit is shown in Figure 3 and exhibits no unusual structural features. Table I contains the crystallographic properties of the compound.

Table I. Crystal Data for $Na(MEI)(AlCl_4)_2$

Formula	$C_6H_{11}Al_2Cl_8N_2Na$
f.w.	471.74
a/Å	10.321(4)
b/Å	10.895(3)
c/Å	9.284(4)
V/Å^3	984.7(6)
$\alpha/^\circ$	98.31(2)
$\beta/^\circ$	100.83(4)
$\gamma/^\circ$	101.95(3)
Z	2
t/°C	-120±1
$d_{cal}/(g\ cm^{-3})$	1.591
space group	$P\bar{1}$
$\mu(MoK\alpha)/cm^{-1}$	25.00
R	0.037
R_w	0.045

The crystal packing shown in Figure 4, reveals that sodium ions form a chain along the *a*-axis which resides in a channel created by the $AlCl_4^-$ ions. This is more clearly seen in Figure 5 where only the sodium and chlorine atoms are drawn; the chlorines have been connected to each other, forming empty tetrahedra, and to the sodium ions. The sodium atoms form a zig-zag chain with an average Na-Cl distance of 3.04 Å and standard deviation of 0.19 Å. The organic cations fill the regions between the $[(Na)(AlCl_4)_2]_n^{n-}$ columns. A detailed analysis of sodium-chlorine and sodium-aluminum distances and geometries showed that Na^+ is closer to the tetrachloroaluminate anions than in the structure of $NaAlCl_4$. Apparently the large organic imidazolium cations relax the structure and allow more efficient packing of the inorganic part of the compound.

REFERENCES

1. R. A. Osteryoung, in Molten Salt Chemistry; G. Mamantov and R. Marassi, Editors, p. 329, Reidel, Dordrecht, The Netherlands, (1987).
2. C. Scordilis-Kelley and R. T. Carlin, J. Electrochem. Soc., 140, 1606 (1993).
3. Y. S Fung, and S. M Chau, J. Appl. Electrochem., 23, 346 (1993).
4. T. L. Riechel and J. S. Wilkes, J. Electrochem. Soc., 139, 977 (1992).
5. C. Scordilis-Kelley, J. Fuller, R. T Carlin and J. S. Wilkes, J. Electrochem. Soc., 139, 694 (1992).
6. C. L. Yu, J. Winnick and P.A. Kohl, J. Electrochem. Soc., 138, 339 (1991).
7. T. J. Melton, J. Joyce, J. T. Maloy, J. A. Boon, and J. S. Wilkes, J. Electrochem. Soc., 137, 3865 (1990).
8. A. A. Fannin, Jr., D. A. Floreani, L. A. King, J. S. Landers, B. J. Piersma, D. J. Stech, R. L. Vaughn, J. S. Wilkes, and J. L. Williams, J. Phys. Chem., 88, 2614 (1984).
9. C. J. Dymek, Jr., D. A. Grossie, A. V. Fratini and W. W. Adams, J. Mol. Struct., 213, 25 (1989).
10. C. J. Dymek, Jr., J. J. P Stewart, Inorg. Chem., 28, 1472 (1989).
11. K. M. Dieter, C. J. Dymek, Jr., N. D. Heimer, J. W. Rovang, and J. S. Wilkes, J. Am. Chem. Soc., 110, 2722 (1988).
12. A. A. Fannin, Jr., L. A. King, J. A. Levisky and J. S Wilkes, J. Phys. Chem., 88, 2609 (1984).
13. S. Tait and R. A. Osteryoung, Inorg. Chem., 23, 4352 (1984).
14. A. M. Elias and J. S. Wilkes, J. Chem. and Eng. Data (in press).

15. J. S. Wilkes, J. A. Levisky, R. A. Wilson, C. L. Hussey, Inorg. Chem., 21, 1263 (1982).

16. D. Elwell and H. J. Sheel, Crystal Growth from High-temperature, p. 138, Academic Press, London, 1975.

17. D. Elwell, in Crystal Growth, R. Pamplin, Editor, p. 185, Pergamon, New York, 1975.

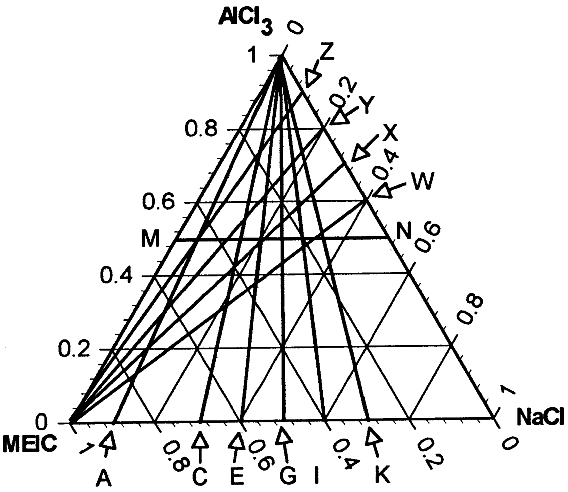

Figure 1. Compositions used in experimental procedure.

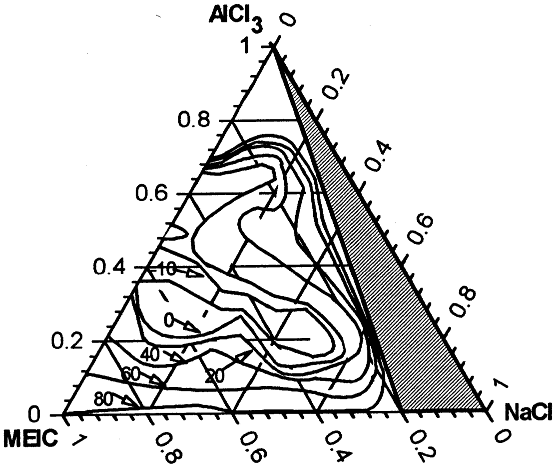

Figure 2. Melting point contours.

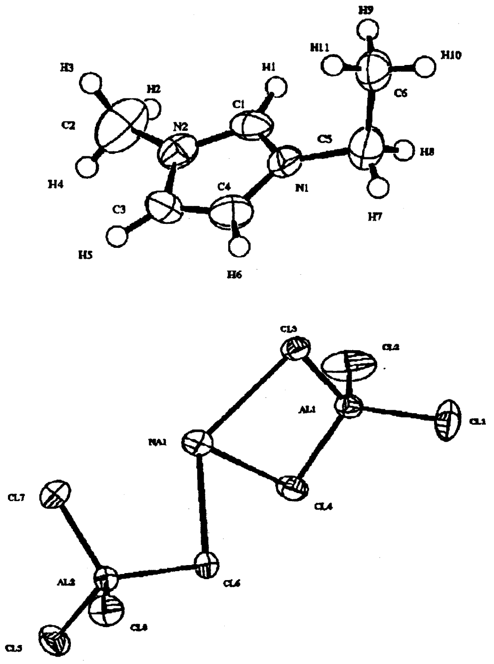

Figure 3. Crystal structure of Na(MEI)(AlCl$_4$)$_2$.

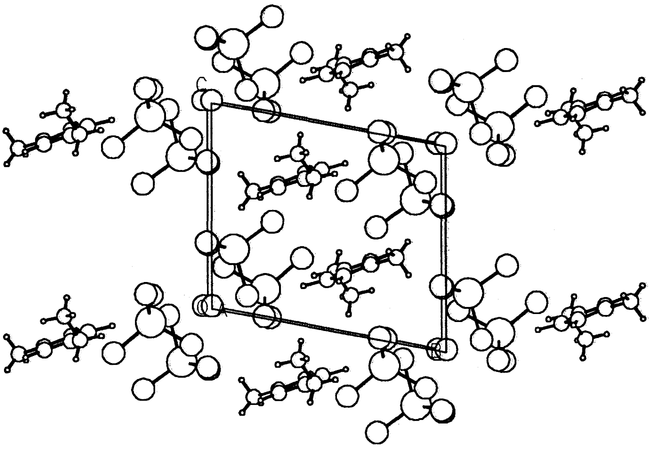

Figure 4. Crystal packing of $Na(MEI)(AlCl_4)_2$.

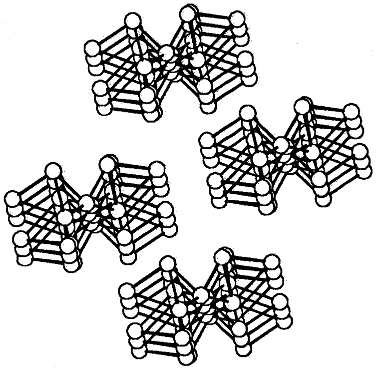

Figure 5. Inorganic portion of the packing of $Na(MEI)(AlCl_4)_2$.

DOI: 10.1149/199413.0141PV

Phase Relationships of the La-Ba-Cu-O System

H. Kojima, M. Kameda, H. Tanabe, and I. Tanaka
Institute of Inorganic Synthesis, Faculty of Engineering
Yamanashi University
7 Miyamae, Kofu, 400, Japan

ABSTRACT

The phase behavior of the ternary system La_2O_3-BaO-CuO (LBCO) has been studied. The liquidus temperature and the stable regions of primary phases have been determined over selected composition ranges by TG-DTA and a Slow Cooling Floating Zone Method (SCFZ). An EPMA has been employed to analyze the quenched sample by the SCFZ method. It has been shown that the distribution coefficients, k, of Ba ion into the solid LBCO crystals are approximately 0.12-0.20. However, when the concentration of Ba in the liquid is greater than x = 1.0 of mole fraction, other phases like 101 and 212 are easily formed.

INTRODUCTION

$La_{2-x}Ba_xCuO_4$ (LBCO) is a p-type superconducting material which is formed by substitute Ba for La ion in La_2CuO_4 (LCO). LBCO shows superconducting behavior in the range of Ba concentration $0.06 \leq x \leq 0.3$ and a local minimum near $x=0.125$. Also, this material shows metallic behavior over $x>0.3$. These data were found by using sintered materials. However, these materials have anisotropic properties, so it is desirable to measure the physical properties by using single crystals of LBCO. The phase relations of the La-Ba-Cu-O system, which will be necessary to grow the LBCO single crystals by using the Traveling Solvent Floating Zone Method (TSFZ), will be made clear in this study.

EXPERIMENTAL

Phase relationships were determined by using a Slow Cooling Floating Zone Method (SCFZ) and thermal differential analysis (TG-DTA). Stoichiometric amounts of La_2O_3BaO and CuO were mixed in ethanol, dried and calcined at 900~950°C for 24 hours in air. The preheated powder was formed into a cylindrical shape 6 mm in diameter by 70mm in length, sintered at 1280°C for 12~20 hrs in oxygen, and then used as the feed rod for the SCFZ method. The apparatus for the SCFZ method was an infrared heating furnace with a 1.5 kw halogen lamp as the heat source. The composition of the solid before melting was analyzed by an electron probe microanalyzer (EPMA).

The growth of LBCO single crystals was performed by using the TSFZ method in order to be sure of the phase relations. The apparatus for single crystal growth was a single ellipsoidal infrared heating furnace with a 1.5 kw halogen lamp as the heat source. The growth conditions were as follows: the solvent composition was 78-85 mol.% CuO, the oxygen gas pressure was 2 atmospherics and the growth rate was 1mm/hr.

RESULTS

The composition of the liquids in equilibrium with solid LCO is 75-89 mol.% CuO according to the phase diagram of the La_2O_3-CuO system (1). It was reported that the suitable solvent composition was 78-80 mol.% CuO for growing single crystals of $La_{2-x}Sr_xCuO_4$ (LSCO) (1). In this study, the same composition has been used.

The samples, whose Ba concentration was changing in the solvent, were analyzed by a TG-DTA method. These results are shown in Fig. 1. In the case where the Ba concentration was $x=0.075$ and 78 mol.% CuO, two endothermic peaks and a weight loss were observed at 1000°C while heating the sample to 1400°C. In the cooling stage, three exothermic peaks were observed at 1300°C, 1010°C and 1000°C and the weight increased at 1300°C and 1010°C. The weight decrease during heating may be due to the decomposition of CuO to Cu_2O or the vaporization of Cu_2O. The exothermic peak, which seemed to be a primary deposition, was observed to divide into two peaks in the Ba concentration range $x=0.1$-0.3. Variations in peak intensity and deposition temperature are also observed over the same concentration range. The maximum deposition temperature reached was 1310°C at a Ba concentration of $x=0.25$. However, the peaks corresponding to the primary deposition of LBCO did not appear at a Ba concentration $x\leq0.6$. The reason why the peaks for primary deposition became very weak seems to be that other phases besides LBCO such as $La_{2-x}Ba_xCu_2O_5$ (101 phase) and $La_{2-x}Ba_{1+x}Cu_2O_5$ (212 phase) precipitate.

Fig. 2 shows the change in concentration of the Ba ion in the solid LBCO vs. that of the solvent, which was determined by EPMA analysis of the samples solidified by the SCFZ method. These results suggest that the effective distribution coefficient (k) of Ba into solid LBCO is less than unity and will be $0.12\leq k\leq0.2$ at the concentration of Ba $0\leq x\leq1.0$.

Fig. 3 shows the effective distribution coefficient (k) of Ba ion vs. the concentration of Ba in the 214 phase. In this case, the composition of Ba in the solvent phase was $x=1.0$, and Ba concentration in the solid LBCO was 0.124. However, if the concentration of Ba in the solvent phase increased to more than $x=1.0$, other phases like the 101 and 212 phases will be easily precipitated.

In the crystal growth experiments, the Ba concentration in the feeding materials were from $x=0.1$ to 0.2. However, the Ba concentrations in the grown crystals were $x=0.06$~0.1 even if solvents of high Ba concentration were used. Table 1 shows the composition of grown single crystals and the solvents used. These results agree with the results from the phase relations mentioned above.

The sizes of the grown crystals were about 60mm in length and 5mm in diameter. Crystals were black colored and lusterless. Characterization was carried out by using a Laue back diffraction X-ray camera which revealed the single crystal structure. The superconductivity of the grown crystals measured by a SQUID shows that the Tc onset is 24K.

ACKNOWLEDGMENTS

This work was partly supported by a Grant-in-Aid for Scientific Research on Priority Areas, "Science of High Tc Superconductivity" given by Ministry of Education, Science and Culture, Japan.

REFERENCES

1. I. Tanaka, K. Yamane and H. Kojima, J. Crystal Growth **96**, 711 (1989).

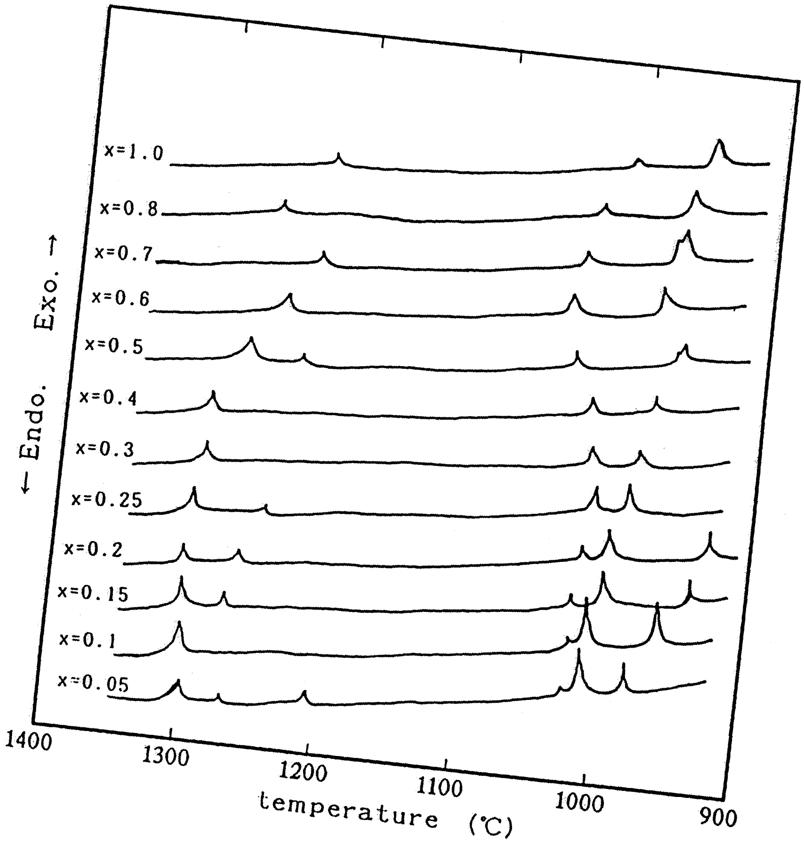

Fig. 1 DTA Curves of $La_{2-x}Ba_x CuO_4$ $(0.0<x\leqq 1.0)$

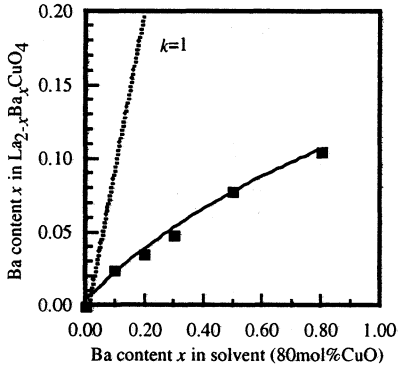

Fig. 2 Relation of Ba content x between solvents (80mol%CuO) and $La_{2-x}Ba_xCuO_4$.

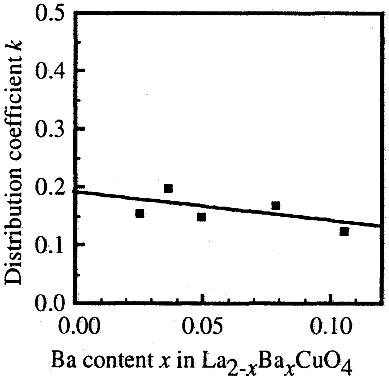

Fig. 3 Effective distribution coefficient k of Ba into La_2CuO_4.

Table 1 Composition of $La_{2-x}Ba_xCuO_4$ grown crystals

Feeds	Solvents	Crystals
0.100	0.300	0.060(2)
0.100	0.800	0.060(2)
0.160	0.700	0.079(4)
0.160	0.800	0.101(5)
0.200	0.800	0.105(3)

DOI: 10.1149/199413.0146PV

EXPERIMENTAL DETERMINATION OF VAPOR PRESSURES OF KCl

S. Wang and R. G. Reddy

Department of Chemical & Metallurgical Engineering
University of Nevada, Reno
Reno, NV 89557

SYNOPSIS

The vapor pressures of KCl are measured in the temperature range of 873 to 1250K using transpiration technique. In the system, the variation of vapor pressure of solid KCl with temperature is determined as $\ln P(\text{atm}) = -14477.868/T - 10.45 \ln T + 80.53$ and that of liquid KCl as $\ln P(\text{atm}) = 326265.24/T + 283.41 \ln T - 2286.24$. The melting point and the boiling point of KCl were determined as 1047K and 1445K, respectively.

INTRODUCTION

Several investigations were made on the determination of vapor pressures and thermodynamic relationships of the KCl(1-3). The work of Fiock and Rodebush(4) on KCl did not clearly delineate the boundaries of the phase region. The plateau vapor pressures were not thoroughly defined and were considerably displaced in pressure compared to those from the work of Kangro and Wieking(5). These latter authors concentrated their studies primarily from 1133 to 1263K in the pressure range of 2.5 to 25 mmHg. No data were determined to outline the regions of primary solid phase. Also the establishment of the plateau vapor pressure was rather limited in scope. In neither work was a treatment conducted of Gibbs energy of solutions of potassium compound in the single-phase regions and the integral thermodynamic quantities of mixing throughout the system. Therefore, an experimental study is undertaken to determine the complete equilibrium relationships and thermodynamic data for the KCl system, and a KCl equilibrium diagram is constructed.

EXPERIMENTAL

There are several methods that are widely used in the measurement of vapor pressures, such as dynamic method(6), static method(7,8) and other general methods(9,10). In this study, the transpiration technique (or gas-saturation method)(11) is employed for determining the vapor pressures of KCl in one component system. A measured volume of inert gas is saturated by passing it through the liquid at a definite temperature. The quantity of liquid vaporized is obtained from the loss in weight of the liquid, or by removal of the vapor from the gas stream in weighed absorbing tubes. Assuming Dalton's law of partial pressures and the ideal-gas law, the partial pressure of the vapor, p, is calculated by the formula

$$P = \frac{g}{M\,V}\,R\,T \qquad [1]$$

where R = gas constant, T = absolute temperature, and v = total volume of gas (including inert gas vapor) containing g grams of vapor of molecular weight M. When both components of a solution, however, are volatile, it is necessary to have a suitable physical and chemical methods for analyzing the condensed vapor.

The overall view of the experimental set-up is shown in Figure 1. It consists of passing a stream of inert carrier gas at a known rate over a condensed sample of interest. The flow rate is maintained such that equilibrium saturation is established between the condensed and vapor phases. The carrier gas stream is saturated with the vapor from the sample and transported from the reaction chamber downstream to a condenser system. The vapor pressure is then calculated by using the following relationship for partial pressure:

$$P_i = \frac{m_i}{m_t + m_f}\,P_T \qquad [2]$$

where m_i is the moles of vapor species i, m_t is the total moles of vapor species, m_f is moles of carrier gas, p_i is the partial pressure of vapor species i and P_T is the total pressure in the system.

The purified salts are loaded into high purity graphite sample boats under the protective atmosphere of a dry box and then transferred to the transpiration apparatus in an atmosphere of dry argon gas. The pure chloride salts are used as reference salts. Several sample boats such as silica, nickel and iron were unsuccessful as a container material. The furnaces are preheated to the desired set temperature and the sample carrier tube inserted into the reactor tube under a flow of the carrier gas. The temperature of the melt is measured using the Pt-13%Rh+Pt thermocouple. After the predetermined equilibration time of 4 hours, the sample boat is withdrawn and cooled to the room temperature under the argon gas. The condenser assembly is removed and the deposited material is dissolved in the striping solution. The striping solution is then analyzed by Ion Chromatograph. X-ray analysis of the condensed material is also made to identify the vapor species present in the gas phase.

RESULTS AND DISCUSSION

Vapor pressure of KCl

The vapor pressures of pure KCl are determined in the temperature range of 873 to 1300K. The results are presented in Figure 2. The experimentally determined values of vapor pressure of KCl (broken lines) are in very good agreement with the Kangro et al.'s data(5).

Thermodynamic consideration

In the thermodynamic consideration, the Clausius-Clapeyron equation

$$d \ln P = \frac{\Delta H}{R\, T^2}\, dT \qquad [3]$$

can be employed[(12)]. When ΔC_p for the evaporation or sublimation is not zero, but independent of temperature, ΔH_T is given as

$$\Delta H_T = \Delta H_{298} + \Delta C_p\ (T-298) = (\Delta H_{298} - 298\ \Delta C_p) + \Delta C_p + T \qquad [4]$$

in which case integration of Eq.(3) gives

$$\ln P = \frac{298\ \Delta C_p - \Delta H_{298}}{R}\ \frac{1}{T} + \frac{\Delta C_p}{R} \ln T + constant \qquad [5]$$

which is normally expressed in the form

$$\ln P = \frac{A}{T} + B \ln T + C \qquad [6]$$

Where A, B and C are constants. They can be calculated by selecting the experimental data of vapor pressures at different temperatures. In this study, the vapor pressure of solid potassium chloride with temperature is determined as

$$\ln P(atm) = -\frac{14477.868}{T} - 10.45 \ln T + 80.35 \qquad [7]$$

and the vapor pressure of liquid potassium chloride with temperature is determined as

$$\ln P(atm) = \frac{326265.24}{T} + 283.41 \ln T - 2286.24 \qquad [8]$$

Liquid-vapor and solid-vapor equilibria

The normal boiling temperature T_b of KCl can be defined as that temperature at which the vapor pressure of the liquid equals 1 atm. Therefore, from the liquid-vapor equilibrium equation (6),

$$\ln P(atm) = 0 \ at\ T = T_b$$

Thus

$$-\frac{326265.24}{T}+2286.24=283.41\ln T \qquad [9]$$

and plots of each side of this equation, against T, intersect at T = 1445K = T_b.

The liquid and solid vapor-pressure curves intersect at the triple point, at which temperature T_{rp}, solid, liquid, and vapor at P_{tp} are in equilibrium. Therefore at T = T_{rp}

$$\frac{326265.24}{T}+283.41lnT-2286.24=\frac{-14477.87}{T}-10.45lnT+80.53$$

or

$$-\frac{1159.5424}{T}+8.0541=\ln T \qquad [10]$$

Plots of each side of the above equation, against T, intersect at T = 1047K = T_{rp}. Triple point is a zero-dimensional region of three-phase stability. When the lines and points are projected into a T-P plane, the pressure-temperature equilibrium diagram is obtained.

Solid-Liquid Equilibrium

If a solid is under a pressure P, different from 1 atm, its melting temperature will change by an amount dT that can be calculated from:

$$\frac{dP}{dT}=\frac{\Delta H_f}{T\,\Delta V_f} \qquad [11]$$

where ΔH_f is the enthalpy of fusion, and ΔV_f is the volume change. The volume of one mole of KCl (solid) is 37.57 cm^3, and the volume of one mole of KCl (liquid) is 45.94 cm^3(13). Consequently:

$$\Delta V_f=V_l-V_s=8.367\ cm^3/mol \qquad [12]$$

In order to operate in compatible units, the volume change must be expressed in cal/mol atm. One cal/atm. represents 41.3 cm^3; therefore:

$$\Delta V_f=\frac{8.367}{41.3}=0.2026\ cal/mol.atm. \qquad [13]$$

and thus:

$$\frac{dP}{dT}=\frac{6251}{1045\times0.2026}=29.52\ atm/K \qquad [14]$$

This means that a container with KCl at 1^0C will have to resist a pressure of 30 atmospheres. Figure 3 represents the solid-liquid, solid-vapor and liquid-vapor equilibria in the vicinity of the triple point. From the figure, we can see that the lines OA, OB, and OC divide KCl into three distinct areas within each of which only one phase is stable. Within these areas the pressure exerted on the phase and the temperature of the phase can be independently varied without upsetting the one-phase equilibrium.

Gibbs energy and properties of the phase

The total Gibbs energy of phase change in the pure KCl system can be calculated by the equation(14)

$$\Delta G^0_{phase\ change} = R\ T\ \ln\ P_{e,\ KCl} \qquad [15]$$

where $P_{e,\ KCl}$ is the equilibrium partial pressure of KCl. The relationship between Gibbs energy of phase change and the temperature is shown in Figure 4. From the figure, there is a Gibbs energy surface such as this for each phase - the vapor phase, the liquid phase, and one solid phase in KCl system. They intersect each other, and that portion of each surface which is lowest of all surfaces in the region gives the T-P range in which the corresponding phase is stable. It also shows that the KCl system has one possible solid phase.

CONCLUSIONS

From this thermodynamic study, the following conclusions can be made:

1. The vapor pressure of KCl measured in this study increased lightly from 0.83 to 1.80 mmHg at low temperature range (873 - 1023K); but at high temperature range (1180 - 1250K), it increased sharply from 4.79 to 11.10 mmHg.
2. The vapor pressure of solid potassium chloride with temperature is determined as $\ln P(atm) = -14477.87/T - 10.45 \ln T + 80.53$; and the vapor pressure of liquid potassium chloride with temperature is determined as $\ln P(atm) = 326265.24/T + 283.41 \ln T - 2286.2$ in KCl system.
3. From the equilibrium diagram of KCl, the melting point is determined as 1047K and boiling point is determined as 1445K at 1 atm.
4. A free energy surface of KCl is determined by the relationship between free energy of phase change with temperature and vapor pressure.

ACKNOWLEDGEMENTS

The authors are pleased to acknowledge the financial support of this research by Gas Research Institute and Arthur D. Little, Inc. U.S.A.. Thanks are also due to Drs. A. Lingras and S. Malhotra for their useful criticism and suggestions.

REFERENCE

1. L.B. Pankratz, Thermodynamic Properties of Halides, Bulletin/United States Department of the Interior, Bureau of Mines; 674, pp. 352.
2. D.R. Stull and H. Prophet, JANAF Thermochemical Tables, 2nd ed., NSRDS-NBS37, U.S. Department of Commerce, Wanshington, D.C., 1971.
3. E.M. Levin, C.R. Robbins and H.F. McMurdie, Phase Diagrams for Ceramists, The Amirican Ceramic Society,INC., 1964, pp 376-377.
4. E.F. Fiock and W.H. Rodebush, J. Amer. chem. Soc. 48 (1926) 3522.
5. W. Kangro and W. Weiking, Z. Phys. Chem., 1938, 138A, pp.199.
6. G. DE Maria and V. Piacente, The Journal of Chemical Thermodynamics, Vol. 6, No.1, 1974, pp.1.
7. R.A. Rapp, Physicochemical Measurements in Metals Research, Vol. IV, Part 1, 1970, pp. 21-195.
8. J. OM. Pockris, et al, Physicochemical Measurements at High Temperatures, 1959, pp. 225-246.
9. J. Moriyama, T. Oishi, K. Ogino, and A. Egami. Proc. 4th Internat. Conf. Therm. Anal., Budapest, v. 3, 1974, pp. 867-872.
10. D. Hodouin, Metall. Trans. B, v. 6B, 1975, pp. 223-228.
11. C. Rampacek, W.A. and P.T. Waddleton, U.S. Bureau of Mines Report of Investigations 5501, 1959.
12. M.C. Nutt, Principles of Modern Metallurgy, 1984, PP.52.
13. G.J. Janz, et al, National Standard Reference Data System: Molten Salts, PB-295406, Apr. 1979.
14. M.J. Perona, J. Chem. Educa., Vol.56, 1979, pp 726-727.

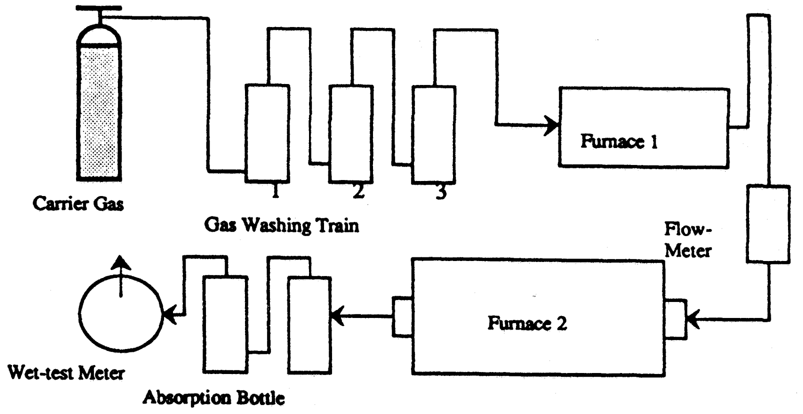

Figure 1: Transpration experimental setup

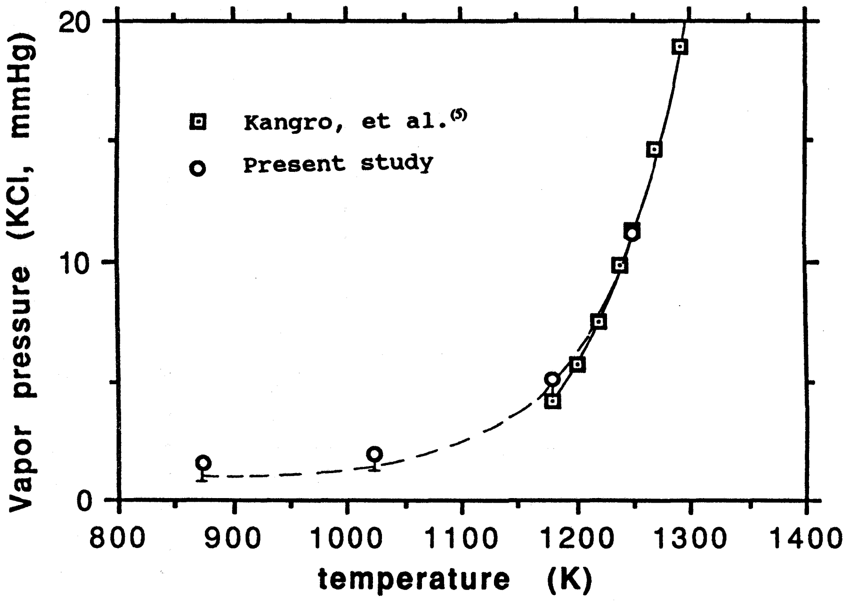

Figure 2. Vapor pressure of KCl as a function of temperature

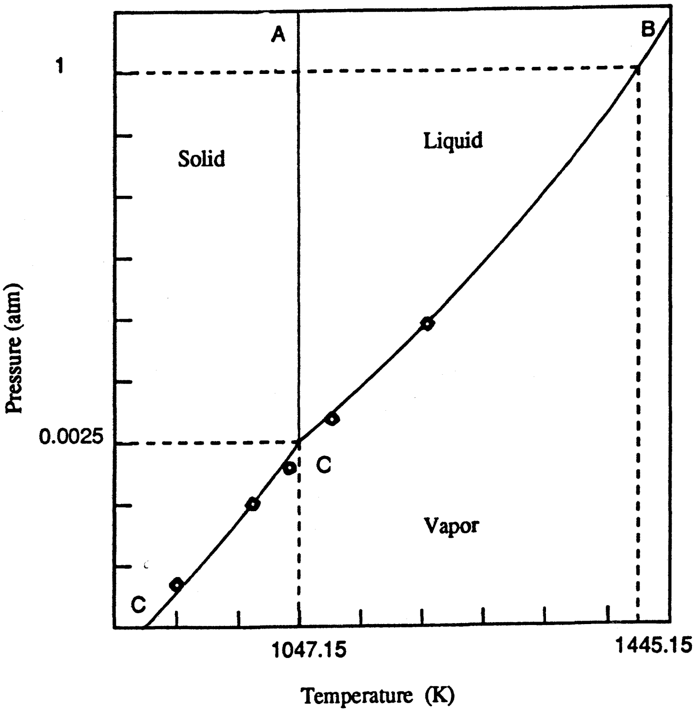

Figure 3: Schematic representation of part of KCl phase diagram

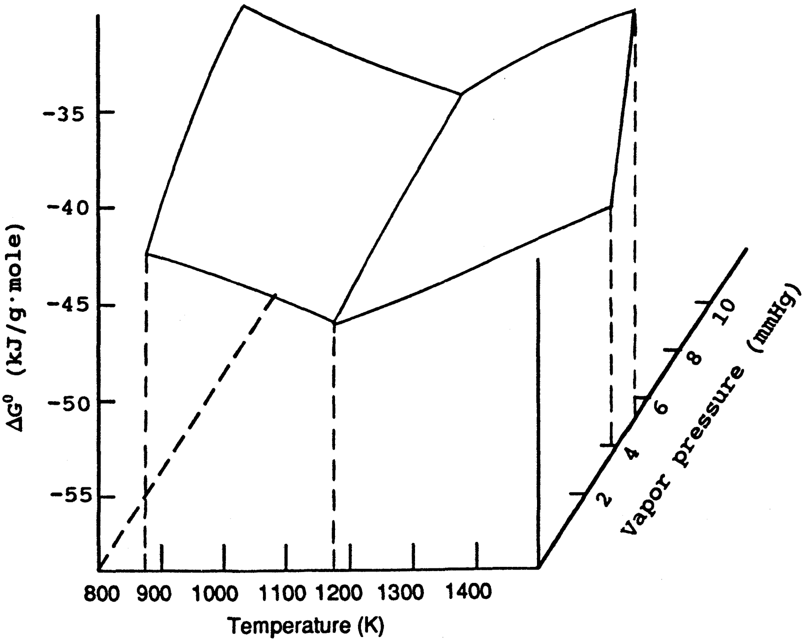

Figure 4: The relationship of G -P-T for KCl at 873 to 1250 K

DOI: 10.1149/199413.0156PV

CALCIUM SOLUBILITY IN MOLTEN CALCIUM CHLORIDE

J. M. Matta Machado Paixão* and R. Combes**

* Superintendência de Tecnologia da Companhia Vale do Rio Doce,
Rua São Paulo, 351, 30.170-130, Belo Horizonte, MG, Brazil.
** Institut Galilée, Université de Paris-Nord, Avenue J.B. Clément,
F-93.430 Villetaneuse, France

ABSTRACT

In order to develop a new process for a direct titanium powder production in a molten calcium chloride media, calcium solubility and calcium diffusion coefficient has been determined in this melt at temperatures ranging from 850° to 900°C.

The corresponding results are compared to those of the litterature, which show rather large discrepancies. Nevertheless, a fair agreement is obtained with the latest studies.

INTRODUCTION

Metal solubility in its molten chloride is a phenomenom which has called chemists attention for a large period of almost 200 years (1-4). The case of Ca in molten $CaCl_2$ seems the more stricking, but reliable descriptions had to wait until the second part of the 20th century. For example, in 1949, Cubicciotti and his co-workers (5) claimed a Ca solubility value in its molten chloride as high as 16 moles%, obtained by determinations on Ca-$CaCl_2$ liquidus curves.

Ten years later, Peterson and coll. (6) obtained much lower values (S_{Ca} = 3,8 moles%) and explained that such a difference can be ascribed to the unavoidable pollution by oxygen and water of $CaCl_2$ and the very reactive calcium metal.

Phase diagrams of Ca-$CaCl_2$ system have partially been determined par various authors, with different techniques, such as chemical analysis, in Dworkin's (7) and Sharma's (8) works, vapor pressure measurements, in Van Westenburg's work (9), and electrochemical determinations, in Dosaj's one (10).

According to Sanchez et Monier (11), results may differ as they are obtained by static or dynamic methods, due to the relatively long time necessary to reach equilibrium. These authors have determined the whole Ca-crucial phase diagram by differential thermal analysis (DTA).

Very recently, Axler et DePoorter (12) have measured the calcium solubility by using $CaCl_2$ and Ca, as pure as 99,995%.

As shown in table I, the set of results obtained from the above mentionned studies, exhibits rather large discrepancies in calcium solubilities values in molten $CaCl_2$.

In the frame of an industrial program aimed to the development of a new process for titanium powder production, direct reduction of $TiCl_4$ by calcium dissolved in molten calcium chloride has been studied extensively. In order to avoid any doubt on a parameter which plays a crucial part on the reduction process in this melt, new solubility values have been determined, by taking, for analysis, melt samples, previously saturated in Ca by agitating an excess of liquid Ca in molten $CaCl_2$ at a given temperature.

TABLE I : Ca solubility values in molten $CaCl_2$

Comparison of results				
T (°C)	Ca Solubility in Moles %	Authors	Date	Ref
900	16.00	Cubicciotti and coll.	1949	5
900	3.80	Peterson and coll.	1959	6
855	2.95	Dworkin and coll.	1961	7
860.5	3.57	Van Westenburg	1964	8
800	2.14	Sharma	1970	9
830	2.45			
850	2.75			
900	3.26			
925	3.47			
940	3.60			
805	2.73	Dosaj, Morris and coll.	1975	10
855	3.02			
905	3.98			
826.5	5.00	Sanchez and Monnier	1979	11
850	2.80	Axler and DePoorter	1991	12
900	3.70			

EXPERIMENTAL

The experimental device used to perform these solubility values determinations is represented in figure 1, and is composed of:
- an electric furnace and its regulation device,
- a refractory stainless steel reactor,
- a 316 L steel crucible, containing the melt inside the reactor,

- a refractory stainless steel agitator,
- two thermocouples,
- a 316 L steel vessel, for metal calcium feed.

In a first step, a quantity of 5 Kg of $CaCl_2$, is dehydrated by heating and melting under a chlorine flow, according to a procedure recommended by White (13) and Combes and coll. (14). After the removal of the air in the reactor by a vacuum pump, argon gas is injected to maintain an inert atmosphere. In the next step, a large excess of Ca, in relation to its expected solubility according to the more reliable values mentionned in the litterature is added to the melt.

Then, a regular and slow agitation is maintained, in order to provide an homogeneous solution, without making an emulsion of calcium in its salt. Melt samples are taken at regular time intervals, by means of a refractory stainless steel tube, in contact with the crucible bottom. These samples are solidified and cooled down in air proof vessels and are dissolved in freshly boiled distilled water. Their calcium content is determined by hydrogen evolution, according to a classical analytical method (15). The corresponding results are checked against those obtained by an acid titration, in order to be sure that none, or negligeable amount of calcium oxide, is present.

RESULTS

These determinations, performed at three different temperatures, provided the calcium solubility values collected in table II.

In figure 2, the mole fractions of soluble Ca, are plotted against time for experiment n°1, and give a fair idea on the kinetics of the melt saturation in calcium.

TABLE II: Calcium solubility values

	Experiment 1		Experiment 2		Experiment 3	
	m (g)	mole	m (g)	mole	m (g)	mole
$CaCl_2$	5000	45.05	5000	45.05	5000	45.05
Ca	150	3.74	150	3.74	150	3.74
T (°C)	870		900		850	
Number of samples	5		2		1	
Duration (min)	Moles% Ca					
7	1.73		-		-	
14	2.19		-		-	
19	2.27		-		-	
25	2.35		2.67		-	
60	2.37		2.67		2.27	

DISCUSSION

Two kinds of interpretations can be obtained from these results: the first one is related to the kinetics of dissolution, and the second one is related to the solubility value itself and its comparison to previous ones.

As shown in figure 2, it is possible to assume that Ca saturation in this melt is obtained fairly rapidly (around 20 minutes). This is confirmed by the equal solubility values obtained in experiment 2, respectively after 25 and 60 minutes.

Moreover, the kind of curve obtained suggests a Ca diffusion in this melt, obeying to the Fick's law :

$$V\frac{dX}{dt} = -\frac{DS}{d}X \qquad [1]$$

where :
$X = C^\circ - C$, is equal to the difference between Ca concentration at saturation (C°) and its value at a time t,
D is the Ca diffusion coefficient,
V is the melt volume,
S is the Ca diffusion surface in the melt,
d is the diffusion layer thickness.

By integrating equation [1] from 0 to t

$$\int_0^t \frac{dX}{X} = \int_0^t -\frac{DS}{Vd}dt$$

one obtains :

$$\ln\frac{C^\bullet - C}{C^\bullet} = -\frac{DS}{Vd}t \qquad [2]$$

as, $X = C^\circ$, when $t = 0$.

By plotting the values of $\ln\frac{C^{\bullet}-C}{C^{\bullet}}$, obtained in experiment 1, versus time, a line, of slope 3.0 10^{-3} sec^{-1}, can be fitted by the least squares method, as shown in figure 3.

From this result, D can be calculated numerically, by using the following experimental data :
S = 150 cm^2, cross-section of the reaction crucible,
V = 2500 cm^3, melt volume,
d has been taken from Chemla's and Lantelme's work (16) and assumed to be equal to 5 10^{-3} cm,

$$D = 2.5\ 10^{-4}\ cm^2\ s^{-1}.$$

This value, which is of the same order of magnitude as Na^+ one in NaCl (18) at 838 °C (10^{-4} cm^2 s^{-1}), is relatively high, but can be explained by the fact that soluble Ca is nothing more than the solvated electron.

The second kind of interpretation is related to the Ca solubility values obtained in this work. They vary from 2.27 to 2.67 moles% at 850 and 900°C respectively, and can be compared to those of Sharma, Dosaj and Axler in a close range of temperature: 800-940°C. All these values have been plotted against the reciprocal of absolute temperature in figure 4. Though a fairly comparable behaviour versus 1/T be observed, the solubility values obtained by the above mentionned authors are 20 to 30% higher than this work's ones: a difference which can be ascribed to the possible pollution of calcium by its oxide in the previous works.

ACKNOWLEDGMENTS

The authors want to express their gratitude to the brazilian company CVRD which provided the financial support and to the french company EXTRAMET, in which the experimental work has been performed.

REFERENCES

1. Davy, Trans. Roy. Soc. (London), 97, 1 (1807).

2. Bunsen, Kirchhoff, Pogg. Ann., 113, 364 (1861).

3. Stockem, Z. Angew. Chim., 17, 341 (1904).

4. Guntz, Benoit, Bull. Soc. Chim., 35(4), 709 (1924).

5. D. D. Cubicciotti, C. D. Thurmond, J. Amer. Chem. Soc, 71, 2149 (1949).

6. D. T. Peterson, J. A. Hinkenbein, J. Phys. Chem., 63, 1360 (1959).

7. A. S. Dworkin, H. R. Bronstein, M. A. Bredig, Discussions Faraday Soc., 32, 188 (1961).

8. R. A. Sharma, The Journal of Physical Chemistry, 74, 22, 3896 (1970).

9. J. A. Van Westenburg, Dissertation Abstracts, 25 (2), 1129 (1964).

10. V. Dosaj, C. Aksaranan, D. R. Morris, J. Chem. Soc., Faraday Trans., I, 71, 1083 (1975).

11. J. A. Sanchez, R. Monnier, Rev. Int. Hautes Tempér. Réfract., 16, 5 (1979).

12. K. M. Axler, G. L. DePoorter, "Molten Salt Chemistry and Technology", p. 19 Ed. M. Chemla and D. Devilliers, (1991).

13. S. White, in "Ionic Liquids", Plenum Press, New-York, (1981)

14. R. Combes, B. Trémillon, F. de Andrade, M. Lopes, A. Ferreira, Anal. Letters, 15, p. A20 (1982).

15. G. Charlot, "Chimie Analytique Quantitative", 6ème édition, Paris, Masson, (1974).

16. D. Damianacos, F. Lantelme, M. Chemla, Electrochim. Acta, 28, 217 (1983).

17. E. Janz, "Molten Salts Handbook", Academic Press, New York, (1967)

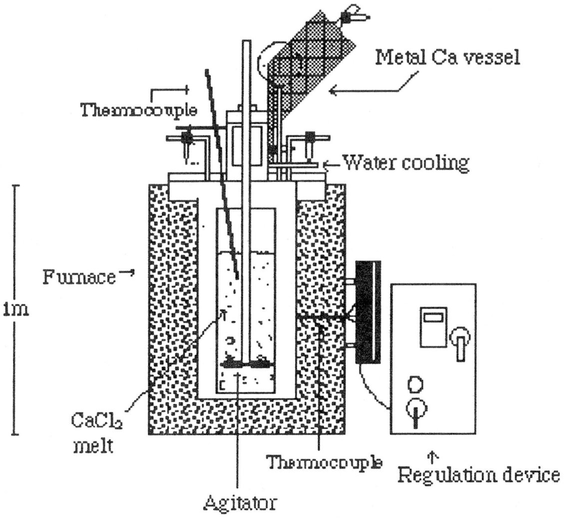

Figure 1: Experimental device used in order to perform Ca solubility determinations in molten $CaCl_2$

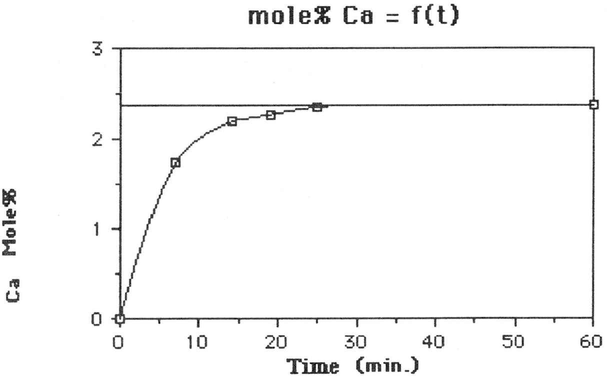

Figure 2 :Mole fractions of soluble Ca versus time, for experiment n°1, at t = 870 °C

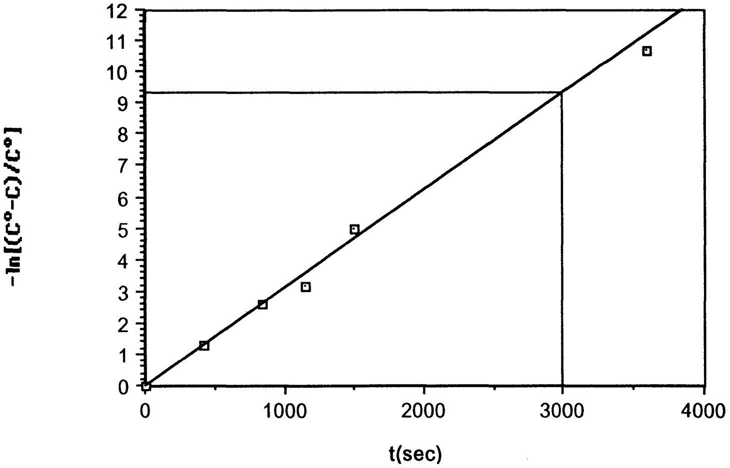

Figure 3 : $\ln\frac{C^{\bullet}-C}{C^{\bullet}}$ values versus time in experiment 1 at 870 °C

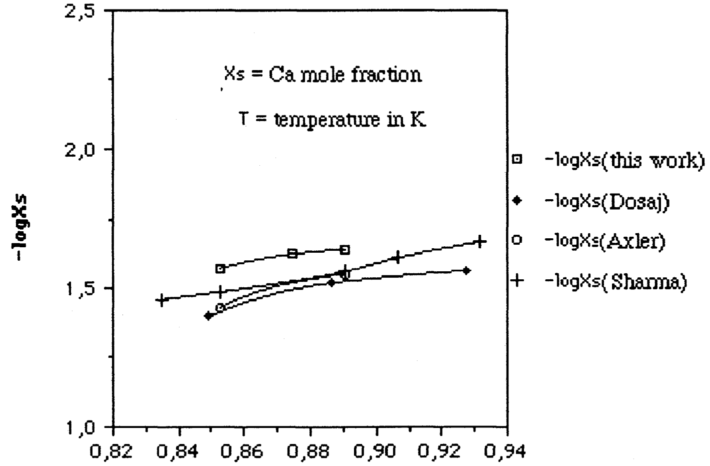

Figure 4 : Logarithm of Ca solubility values (mole fractions), versus the reciprocal of the absolute temperature T.

DOI: 10.1149/199413.0164PV

DISSOLVED STATES OF DIVALENT METAL CHLORIDES IN $AlCl_3$-NaCl MELTS

T. Ishikawa, T. Sasaki, S. Konda and M. Noguchi

Faculty of Engineering, Hokkaido University,
Sapporo 060, Japan

ABSTRACT

Solubilities of the divalent metal chlorides, $MnCl_2$, $MgCl_2$, $CdCl_2$, $CoCl_2$ and $PbCl_2$, in binary chloride melts ($AlCl_3$ + NaCl) were measured in the concentration range from 55 to 59 mol% of $AlCl_3$ at 200°C. The equilibrium constants for dissolution were derived as a function of solubilities and the mole fraction of $AlCl_3$ on the assumption of the dissolution reaction being $Al_2Cl_7^- + 1/2MeCl_2(s) = 1/2Me^{2+} + 2AlCl_4^-$.
The equilibrium constants calculated from experimental results suggest that divalent metal chlorides dissolve in the melts as free Me^{2+} cations forming complex anions.

INTRODUCTION

Many experimental studies on electrowinning and electrorefining of aluminum from chloride melts containing over 50 mol% of $AlCl_3$ have been carried out because the melting points of the melts are low as about 150°C and it may possible to work at a relatively low temperature. But there are difficulties, as the deposits easily grow in a dendritic and/or sponge-like fashion. Recently, it was reported that smooth deposition could be attained by addition of $MnCl_2$ to the melts as noted from the viewpoint of surface treatments for steel.(1) But the factors affecting the morphology of the deposits have not been elucidated yet mainly because of a lack of information on the dissolved states of the chlorides in the melts.

The objectives of this work were, first, to determine solubilities of several divalent metal chlorides ($MeCl_2$) in binary $AlCl_3$ - NaCl melts and next, to elucidate the dissolved states of the chlorides by means of estimations of equilibrium constants of dissolutions of the chlorides under the assumption of equilibrium equations.

EXPERIMENTAL

All chlorides for the solvent were thoroughly purified before usage. The equipment for purification of $AlCl_3$ is depicted in Fig.1. Crude $AlCl_3$ (usually yellow) in a hopper was supplied to a boiler containing a small amount of NaCl by a rotary feeder with desired constant speeds and melted to form a low-temperature binary melt. Part of the $AlCl_3$

beyond the equilibrium concentration in the melts at the prescribed temperature sublimated, leaving impurities with low vapor pressure. The vapor of Al_2Cl_6 carried by Ar gas was solidified as fine particles in a cooling zone and collected in a flask. These purified particles were kept under evacuated conditions.

The purification equipment for the binary mixture of $AlCl_3$ - NaCl is shown in Fig. 2. The mixtures with prescribed concentrations of $AlCl_3$ and NaCl (about 2 kg) were melted in a glass vessel and chips of high-purity Al were added for purification of the melts by reducing water and so on. As shown in the figure, the lower part of the vessel with a small diameter was heated in an electric furnace at 250 - 300°C while the upper part of the vessel with a large diameter was open to the atmosphere and was left to cool. The temperature differences between upper and lower parts of the melts induced a thermal convection and mixing of the melts by this convection led to elevation of the rate of purification. After two- or three-day purification, the melts were filtrated with a sintered glass to remove suspended aluminum particulates and kept in flasks under vacuum. Three kinds of melts were prepared in this manner. $AlCl_3$ concentrations of 55.2, 57.3 and 59.1 mol% in these melts were determined, by the usual chelate titration method. The sample chlorides, $MnCl_2$, $MgCl_2$, $CdCl_2$ and $PbCl_2$, were preliminarily prepared as rods 6 mm in diameter by melting and solidifying followed by drying under evacuated conditions. A $CoCl_2$ rod was similarly prepared except for drying and melting under an Ar atmosphere.

For solubility tests, 15 g of binary mixtures ($AlCl_3$ and NaCl) of containing 55-59 mol% $AlCl_3$ were introduced into a glass ampoule together with a large excess of the divalent metal chloride samples. The ampoule is presented in Fig. 3. The salts were melted under vacuum and the ampoules were also sealed under vacuum. The ampoule was set in an oven equipped with a vibration system as shown in Fig. 4. The vibration equipment could, at once, give six ampoules a tilt motion of inclination of 30 degrees and frequency of 60 times a minute. This vibration promoted dissolution of the salts and the experiments were carried out for various periods up to 20 hours at 200°C. After a vibration for the prescribed period the ampoules were allowed to stand perpendicularly for 30 minutes to settle undissolved divalent samples in the bottom, after which they were inclined carefully to transfer the supernatant liquid to the stems of sampling spaces. The sample holder made it possible to carry out the course of sampling procedures mentioned above in the oven. After precise scaling the samples were dissolved into distilled water for analysis and the solubilities of the divalent metal chlorides were determined. The sample containing $PbCl_2$ was dissolved in 2 N HCl and analyzed through the same procedure.

RESULTS AND DISCUSSION

In alkali metal chloride, XCl(X = Na or K) - $AlCl_3$ melts the equilibrium of the chemical reaction between $AlCl_3$ and XCl [1] shifts very much to right,

$$AlCl_3 + XCl = X^+ + AlCl_4^- \qquad [1]$$

The excess $AlCl_3$ on the left hand side of Eq.[1] reacts with $AlCl_4^-$ to produce $Al_2Cl_7^-$ as follows,

$$AlCl_3 + AlCl_4^- = Al_2Cl_7^- \qquad [2]$$

The equilibrium of this reaction also shifts to the extreme right, and this indicates that the system is almost entirely composed of X^+, $AlCl_4^-$, and $Al_2Cl_7^-$; the amount of Cl^- is very small.(2)

The divalent metal chlorides ($MeCl_2$) under investigation are assumed to react with $Al_2Cl_7^-$ and dissolve as follows,

$$\frac{1}{2}MeCl_2 + Al_2Cl_7^- = \frac{1}{2}Me^{2+} + 2AlCl_4^- \qquad [3]$$

The equilibrium constant (K) for this reaction is given as

$$K = \frac{\left[Me^{2+}\right]^{\frac{1}{2}} \cdot \left[AlCl_4^-\right]^2}{\left[Al_2Cl_7^-\right]} \qquad [4]$$

where [ ] represents the mole fraction in the melts.

Consider the solubility of $MeCl_2$ is Q moles in one mole solvent ($AlCl_3$ + XCl), then the K value is given as follows,

$$K = \frac{Q^{\frac{1}{2}}(2-3\alpha+4Q)^2}{(2\alpha-1-2Q)} \cdot \frac{1}{(2-2\alpha+3Q)^{\frac{3}{2}}} \qquad [5]$$

where α is a mole fraction of $AlCl_3$ in the solvent. In this equation the last term on the right is added to convert amounts of ionic components expressed by mole numbers to mole fractions. By measuring the solubility of $MeCl_2$ we can estimate K from the equation.

The results of solubility tests on the divalent samples of $CdCl_2$ and $CoCl_2$ are shown in Fig. 5. The numbers of moles dissolved per one mole of the solvent melt are presented with vibrating time in the oven at 200°C. For each case, numbers of dissolved moles increased with the mole fraction of $AlCl_3$ in the solvent melt. Nearly constant values, regarded as saturated solubility, were obtained in the range of 5 hours to 20 hours.

The relation between solubilities of various divalent chlorides and the mole fraction of $AlCl_3$ at 200℃ is presented in Fig.6. The solubilities of all chlorides increase with the concentration of $AlCl_3$. The dotted line in the figure indicates the maximum amount of dissolution of the chlorides under the assumption that the chlorides react with all $Al_2Cl_7^-$ in the melts.

Next, the equilibrium constants of $MeCl_2$ were calculated from the solubility data in Fig.6 and plotted against the $AlCl_3$ concentrations in Fig.7. The calculated values remained constant within the experimental concentration ranges of $AlCl_3$, as shown in the figure. This suggests that the added divalent metal chlorides react with $Al_2Cl_7^-$ and dissolve in the melts as a Me^{2+} cation and a complex anion.

CONCLUSIONS

Solubilities of five kinds of divalent metal chlorides in $AlCl_3$ + NaCl melts were examined by using a special oven with a vibration system. The divalent metal chlorides were saturated within 5 hours and the solubilities were determined in the concentration range from 55 to 59 mol% of $AlCl_3$ at 200℃. The equilibrium constants for dissolution derived on the assumption that the divalent metal chlorides dissolved in the reaction with $Al_2Cl_7^-$ complex showed constant values on the basis of the solubility data in the entire experimental concentration range of $AlCl_3$.

This leads the conclusion that the dissolution reaction is expressed as

$$1/2MeCl_2(s) + Al_2Cl_7^- = 1/2Me^{2+} + 2AlCl_4^- .$$

REFERENCES

1 J. Uchida, T. Tsuda, Y. Yamamoto, H. Seto, M. Abe, A. Shibuya, *J. Iron and Steel Inst. Japan*, **77**, 931(1991).
2 T. Sato, T. Ishikawa and R. Midorikawa, *DENKI KAGAKU*, **41**, 123(1973).

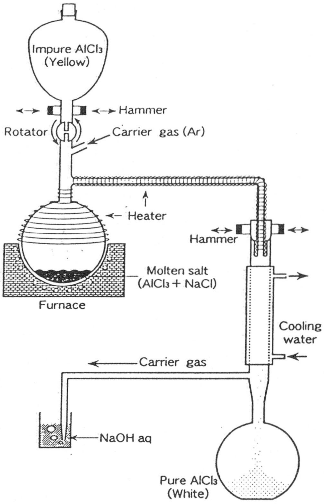

Fig. 1. Equipment for purification of $AlCl_3$.

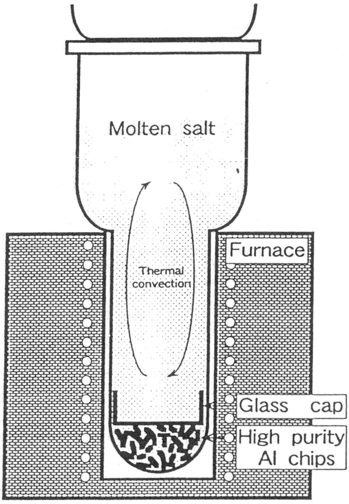

Fig. 2. Equipment for purification of solvent ($AlCl_3$ + NaCl).

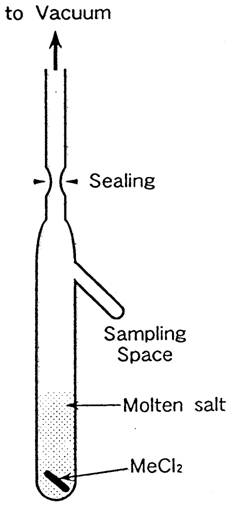

Fig. 3. Ampoule for solubility tests.

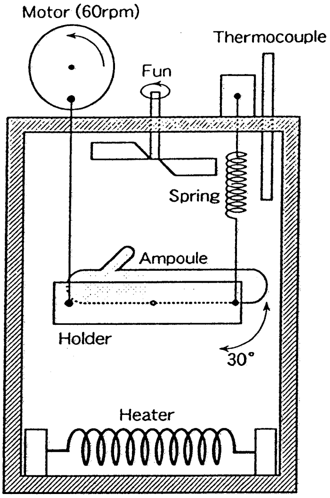

Fig. 4. Schematic diagram of the oven and vibration equipment for solubility tests.

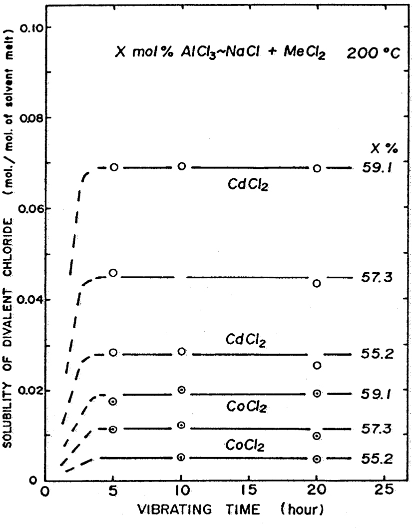

Fig. 5. Time variations in the amounts of dissolved $CdCl_2$ and $CoCl_2$ in one-mole solvent melts of different concentrations of $AlCl_3$ at 200 °C.

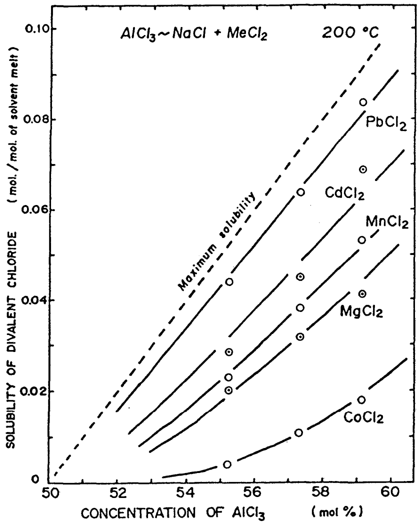

Fig. 6. Relation between the solubility of divalent metal chlorides and the $AlCl_3$ concentrations at 200 °C.

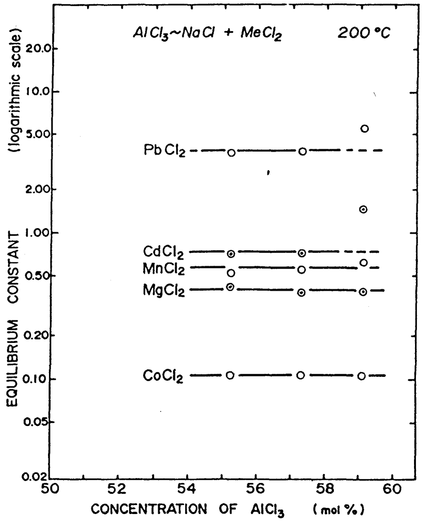

Fig. 7. Relation between the equilibrium constants for dissolution and the $AlCl_3$ concentrations at 200 °C.

DOI: 10.1149/199413.0171PV

SOLUBILITY OF CeO_2 IN MOLTEN Na_2SO_4-10 mol% $NaVO_3$ SALT SOLUTION AT 900°C

Y.S. Zhang and Robert A. Rapp

Department of Materials Science and Engineering
The Ohio State University, Columbus, Ohio 43210

ABSTRACT

The solubility of CeO_2 was measured as a function of melt basicity in a Na_2SO_4-10 mol% $NaVO_3$ solution at 900°C and 1 atm oxygen. The results indicate that CeO_2 dissolves in the salt solution either as a basic or as an acidic solute. The dissolution reactions were derived from the dependence of the solubility on solvent basicity. A comparison of the CeO_2 solubility in Na_2SO_4-10 mol% $NaVO_3$ with the solubilities in both pure Na_2SO_4 and in Na_2SO_4-30 mol% $NaVO_3$ is made. The results agree quantitatively with a theory based on the "common component effect".

KEYWORDS hot corrosion, vanadate, dissolution

INTRODUCTION

Vanadium, sodium and sulfur are common impurities in low-grade fossil fuels. As "clean" fuel resources diminish, these low-grade fuels come into use in engines. The condensation of combustion products of such fuels leads to molten salt deposits containing vanadium, such as $NaVO_3$ and V_2O_5, in addition to sulfates (1). These deposits are known to be very corrosive to high temperature materials and coatings in combustion systems (2). For example, although Y_2O_3-stabilized ZrO_2 thermal barrier coatings offer a good match in thermal expansion coefficient and generally exhibit chemical stability when in contact with a thin film of fused sulfate deposit, the coatings have been found to destabilize as the Y_2O_3 is leached from the ceramic by a Na_2SO_4-$NaVO_3$ deposit in an $O_2/SO_2/SO_3$ gas atmosphere (3,4). The chemical stabilities of various oxides, such as Y_2O_3, CeO_2, HfO_2, In_2O_3, Sc_2O_3 and ZrO_2, in V_2O_5 and vanadate or sulfate fused salt solutions have been studied by Jones et al. (5-9).

As a knowledge of metal oxide solubilities in molten salt solutions is of great importance in evaluating the hot corrosion resistance of these materials, the solubilities of CeO_2, HfO_2 and Y_2O_3 in Na_2SO_4-30 mol% $NaVO_3$ solution were measured as a function of solvent basicity at 900°C and 1 atm oxygen (10). For comparison, the solubility of CeO_2 in pure fused Na_2SO_4 was also determined. Assuming an ideal solution for the Na_2SO_4-30 mol% $NaVO_3$ system, Hwang and Rapp (11) derived the equilibrium distribution of vanadate derivatives, which leads to a theoretical prediction for the dependence of oxide solubilities on salt composition. Following the results of references (10) and (11), in the present study, the solubility of CeO_2 was measured in a Na_2SO_4-10 mol% $NaVO_3$ salt solution as a function of melt basicity at 900°C and 1 atm oxygen. A comparison of the CeO_2 solubility in Na_2SO_4-10 mol% $NaVO_3$ with the solubilities in both pure Na_2SO_4 and in Na_2SO_4-30 mol% $NaVO_3$ is made, and the prediction made by Hwang and Rapp is evaluated.

EXPERIMENTAL PROCEDURES

The chemicals used in this study were 99.9% pure CeO_2 powder, 99% $NaVO_3$ powder and reagent grade Na_2SO_4. The $NaVO_3$ was dehydrated at 400°C for 8 hrs. The CeO_2 and Na_2SO_4 were dried at ~110°C in an oven for at least 4 hrs before use. For each experiment, ~1.5 g CeO_2 powder was charged into an alumina crucible with ~20 g of salt mixture of Na_2SO_4-10 mol% $NaVO_3$. The chemicals were further dried at 400°C overnight before heating the system to 900°C. Na_2O_2 was added, or catalyzed O_2-SO_2 mixed gas with different compositions was introduced, to the system to adjust the melt basicity in the range of $-13.0 \le \log a_{Na2O} \le -7.8$.

The electrochemical reference electrodes used previously (10,12) were employed in the present study to monitor the melt basicity and oxygen activity. A sodium sensor consisted of a piece of silver wire contacting a Na_2SO_4-10 mol% Ag_2SO_4 salt solution contained in a fused SiO_2 (GE 214) tube, which is a good Na^+ conductor at high temperature. The SiO_2 tube was sealed at the top with alumina-base Ceramabond, and a platinum wire spot-welded to the silver wire was used as a lead wire. The other reference electrode, an oxygen probe, was composed of a Y_2O_3-stabilized ZrO_2 tube with porous platinum paste painted inside the closed-end bottom. A platinum wire again served as the lead wire. Another platinum wire contacting the fused Na_2SO_4-$NaVO_3$ salt solution was used as the working electrode. According to thermodynamic calculations (12), the melt basicity for 900°C was derived from the voltage measured between the two reference electrodes:

$$E(V) = 1.468 + 0.116 \log a_{Na_2O} \tag{1}$$

The oxygen pressure in the melt was determined by the voltage measured between the platinum working electrode and the oxygen probe:

$$E(V) = 0.039 + 0.0582 \log P_{O_2} \qquad \textbf{(2)}$$

Two days after the system reached the internal equilibration at which the oxygen pressure was 1 atm and the melt basicity remained almost constant, samples were taken by quenching small amounts of salt onto a cool alumina rod. The samples of ~0.5g each were put into polyethylene vials which had been cleaned in methanol, dried and weighed. The vials containing the salt samples were weighed to an accuracy of 0.1 mg, and then kept in a desiccator.

The cerium concentrations in the frozen salt samples were determined by neutron activation analysis (NAA) in the Central Irradiation Facility of the Ohio State University Research Reactor. During the irradiation, the target nuclei of Ce-140 absorb thermal neutrons to form Ce-141. The activated Ce-141 nuclei undergo beta decay with the formation of Pr-141 nuclei, which decay further to the ground state by gamma ray emission. The gamma ray emission occurs at 145.43 Kev with a half-time of 33 days for Pr-141. These gamma rays were detected and analyzed with a gamma ray spectrometer.

A series of standard samples with known Ce concentrations was prepared by homogeneously mixing fine Na_2SO_4-10 mol% $NaVO_3$ salts with CeO_2 powder. The standard samples and the salt samples obtained from solubility experiments were irradiated in the same batch to insure the same irradiation condition.

RESULTS AND DISCUSSION

From the gamma emission for each sample detected and recorded with the gamma ray spectrometer, the specific Ce-141 activities were calculated. The relationship between the specific Ce-141 activities and the Ce concentrations for the standard samples is shown in Fig. 1, which indicates that the specific Ce-141 activities are proportional to the Ce concentrations in the samples, as expected.

Compared to the Ce standards, the Ce concentrations in the salt samples from the solubility experiments were calculated and plotted as a function of melt basicity in Fig. 2. Each datum point in Fig. 2 represents the measured solubility value for a sample from a separate experiment. In Fig. 2, the solubility minimum for CeO_2 in Na_2SO_4-10 mol% $NaVO_3$ at 900°C occurs at $-\log a_{Na2O} = -10.1$ with a concentration of ~18 ppm of Ce by weight in the salt solution.

For the basic dissolution of CeO_2, the dependence of the solubility on melt basicity is consistent with the dissolution reaction

$$CeO_2 + Na_2O = Na_2CeO_3 \tag{3}$$

For excess CeO_2, with a henrian proportionality between the activity of Na_2CeO_3 and its concentration in dilute solutions:

$$\frac{\partial(\log a_{Na_2CeO_3})}{\partial(-\log a_{Na_2O})} = -1 \tag{4}$$

For the acidic dissolution of CeO_2, as discussed in the previous paper (10), the dependence of the solubility upon melt basicity is in agreement with the following dominant dissolution reaction:

$$3CeO_2 + 4NaVO_3 = Ce_3(VO_4)_4 + 2Na_2O \tag{5}$$

For excess CeO_2,

$$\frac{\partial(\log a_{Ce(VO_4)_{1.33}})}{\partial(-\log a_{Na_2O})} = \frac{2}{3} \tag{6}$$

A comparison of the CeO_2 solubility in Na_2SO_4-10 mol% $NaVO_3$ with the solubilities in both pure Na_2SO_4 and in Na_2SO_4-30 mol% $NaVO_3$ is made and presented in Fig. 3 (10). The effect of the vanadate anion in stabilizing the acidic solute is obvious, raising the solubility of CeO_2 by orders of magnitude. The higher the vanadate anion concentration in the salt solution, the more significant is the observed effect.

The results clearly indicate that the acidic solute of CeO_2 in the Na_2SO_4-$NaVO_3$ solution is cerium orthovanadate, $Ce_3(VO_4)_4$, instead of cerium sulfate, $Ce(SO_4)_2$, as in a pure Na_2SO_4 melt. This results because the strong acid component V_2O_5 in the salt solution and its derivatives exhibit higher reactivities with oxide ions than SO_3 present in the system.

$$NaVO_3 + Na_2O = Na_3VO_4 \tag{7}$$

Thus, according to equation (5) the metavanadate ion reacts with CeO_2, leading to the acidic dissolution of the oxide with the formation of the orthovanadate anion. According to the thermodynamic calculations made by Hwang and Rapp (11), $NaVO_3$ is the dominant component containing vanadium and its concentration, or activity, is almost constant in the range of melt basicity concerned in both the previous study (10) and this study, $-9.4 \leq \log a_{Na2O} \leq -13.4$, that is, the range for the acidic dissolution of CeO_2. Equations (5) and (7) provide an explanation for the dependence of the acidic solubility of CeO_2 upon solvent basicity, as obtained from the experiments.

The experimentally measured solubilities of CeO_2 in Na_2SO_4-10 mol% $NaVO_3$ are compared to the theoretical predictions (11) in Fig. 5. The two curves for the acidic solubilities are almost the same, but a small deviation for the basic solubilities is observed. This deviation may arise from the difference in activity coefficient for the basic solute in the Na_2SO_4-$NaVO_3$ solutions with different compositions. In general, the measured solubilities of CeO_2 in Na_2SO_4-10 mol% $NaVO_3$ at 900°C are consistent with the values predicted on the basis of an ideal solution.

The oxide solubility measurements, particularly the comparison of CeO_2 solubilities in pure Na_2SO_4 and in Na_2SO_4-$NaVO_3$ salt solutions, reinforces the previously described (10) revision to the mechanism of alloy hot corrosion by acidic fluxing postulated by Goebel et al.(13). That model suggested that a strong acid oxide, such as V_2O_5, MoO_3 or WO_3 present in sulfate melts, would complex with oxygen anions, thus increasing the melt acidity, namely P_{SO3}. As a result, a protective oxide would experience an increase in its acidic dissolution, and the alloy would undergo severe hot corrosion. That model is based on the assumption that the solubility curve for the oxide remains the same for the pure and mixed sulfate solutions, and that the vanadate causes a significant increase in melt acidity. Although such an analogous explanation is generally valid for aqueous solutions, it is not the case for molten sulfate-vanadate salt solutions.

In spite of the fact that the oxygen anions are indeed strongly complexed to form vanadate anions, the effect is not to reduce the melt basicity, but to increase it. For example, at 900°C, a melt buffered by equal activities of $NaVO_3$ and Na_3VO_4 assumes a calculated log a_{Na2O} value of -8.17. Equal activities of V_2O_5 and $NaVO_3$ occur at a calculated value of -15.33 for log a_{Na2O}. However, a pure Na_2SO_4 melt equilibrated with 10^{-3} atm SO_3 is a very acidic salt with a calculated log a_{Na2O} = -14.36. In the experimental range of melt basicity, the principal solvent anion of vanadium is the metavanadate, VO_3^-, and therefore the oxide ions supplied by oxide dissolution are consumed in forming the orthovanadate anions, VO_4^{3-}. Since the cerium solute is incidental to the vanadate reaction, the presence of $NaVO_3$ in Na_2SO_4 melt would greatly increase the acidic solubility of any oxide. However, the solvent solution is not made more acidic than pure Na_2SO_4, but more basic. From the previous (10) and the present studies, the solubility minimum for CeO_2 at 900°C lies at log a_{Na2O} = -11.7 for pure Na_2SO_4, -10.1 for Na_2SO_4-10 mol% $NaVO_3$, and -9.4 for Na_2SO_4-30 mol% $NaVO_3$, respectively. These results agree quantitatively with the theory of Hwang and Rapp (11) based on an ideal solution for the solutes.

In their study, Jones et al. (7) observed an increase in the reactivity for the oxides Y_2O_3, CeO_2 and ZrO_2 with salt solutions in the order of V_2O_5 > $NaVO_3$ > Na_3VO_4, i.e. with increasing salt acidity. Seiersten and Kofstad (14) studied the hot corrosion of MCrAlY coatings on Inconel 600 alloy by $NaVO_3$-V_2O_5 salt solutions at 650-800°C and found that the corrosion rate increased with increasing V_2O_5 content. In an investigation of the leaching of Y_2O_3 from yttria-stabilized zirconia by Na_2SO_4-$NaVO_3$ melts at 900°C, Nagelberg (3) reported that the parabolic rate constant for the hot corrosion attack was proportional to the SO_3 pressure and the square of $NaVO_3$ concentration. In the measurement of thin film salt chemistry during hot corrosion of preoxidized nickel, Otsuka and Rapp (15) noticed that $NaVO_3$ added to Na_2SO_4 enhanced the onset of hot corrosion and substrate sulfidation. The solubility measurements reported here as well as in the previous paper (10) are consistent with all these results and observations.

CONCLUSIONS

From the experimental results and discussion above, the following conclusions can be drawn.

1. The oxide CeO_2 dissolves in Na_2SO_4-10 mol% $NaVO_3$ salt solution at 900°C either as a basic solute, Na_2CeO_3, or as an acidic solute, $Ce_3(VO_4)_4$, with a solubility minimum occurring at $\log a_{Na2O} = -10.1$.

2. The CeO_2 solubilities experimentally determined are consistent with the theoretically predicted dependence of the oxide solubility upon the $NaVO_3$ content in the Na_2SO_4-$NaVO_3$ salt solutions. Even a small vanadate concentration raises the acid solubility of any oxide significantly.

3. The solubility measurements show that solutions of the salts of strong acids with a Na_2SO_4 solvent provide higher acidic solubilities for all oxides. The mixed salt solutions are generally buffered to higher values of basicity. The results agree quantitatively with a theory based on the "common component effect". The sodium oxide activity is tied to both CeO_2 dissolution and to equilibria among vanadate species, so these equilibria are interdependent.

ACKNOWLEDGEMENTS

The assistance of J.W. Talnagi in the neutron activation analysis is greatly acknowledged. This research was supported by the Office of Naval Research on project N00014-92-J-1229 (J. Sedriks, project monitor).

REFERENCES

1. K.L. Luthra and H.S. Spacil, J. Electrochem. Soc., **129**, 649 (1982).
2. J. Stringer, Mater. Sci. Tech., **3**, 482 (1987).
3. A.S. Nagelberg, J. Electrochem. Soc., **132**, 2502 (1985).
4. J.C. Hamilton and A.S. Nagelberg, J. Amer. Ceram. Soc., **67**, 686 (1984).
5. R.L. Jones, D.B. Nordman and S.T. Gadomski, Met. Trans., **16A**, 303 (1985).
6. R.L. Jones, S.R. Jones and C.E. Williams, J. Electrochem. Soc., **132**, 1499 (1985).
7. R.L. Jones, C.E. Williams and S.R. Jones, J. Electrochem. Soc., **133**, 227 (1986).
8. R.L. Jones and D. Mess, J. Amer. Ceram. Soc., **75**, 1818 (1992).
9. R.L. Jones, High Temp. Tech., **6**, 187 (1988).
10. Y.S. Zhang and R.A. Rapp, Corrosion, **43**, 348 (1987).
11. Y.S. Hwang and R.A. Rapp, Corrosion, **45**, 933 (1989).
12. C.O. Park and R.A. Rapp, J. Electrochem. Soc., **133**, 1636 (1986).
13. J.K. Goebel, F.S. Pettit and G.W. Goward, Met. Trans., **4**, 261 (1973).
14. M. Seiersten and P. Kofstad, Mater. Sci. Tech., **3**, 576 (1987).
15. N. Otsuka and R.A. Rapp, J. Electrochem. Soc., **137**, 53 (1990).

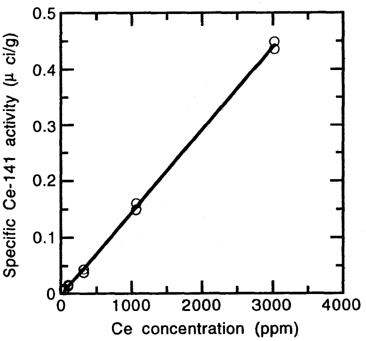

Figure 1 Specific Ce-141 activity vs. Ce concentration for standard samples

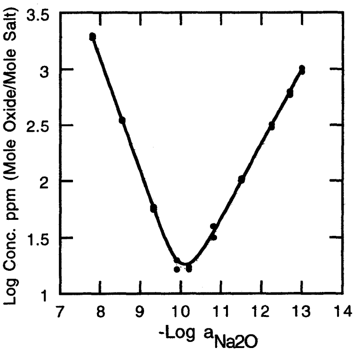

Figure 2 Solubility of CeO_2 in Na_2SO_4-10 mol% $NaVO_3$ at 900°C and 1 atm O_2

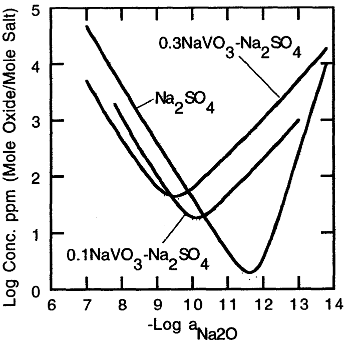

Figure 3 Measured solubilities of CeO_2 in fused salts at 900°C

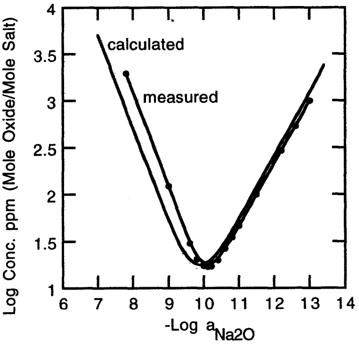

Figure 4 Measured and calculated solubilties of CeO_2 in Na_2SO_4-10 mol% $NaVO_3$ at 900°C

DOI: 10.1149/199413.0179PV

SOME PHYSICOCHEMICAL CHARACTERISTICS OF MOLTEN SALTS DERIVED FROM TRIMETHYLSULFONIUM BROMIDE.

M. Ma†, and K.E. Johnson

Department of Chemistry, University of Regina,
Regina, Saskatchewan, Canada, S4S 0A2.

ABSTRACT

Ambient temperature melts were derived from trimethylsulfonium bromide (TMSuBr) and $AlBr_3$, $AlCl_3$ or HBr. The aluminum halide melts have low wavelength uv cutoffs and single band ^1H-NMR spectra. There is excellent evidence from ^1H-NMR and IR spectra for the formation of HBr_2^- and $H_2Br_3^-$ in the TMSuBr:HX systems. Conductivity and viscosity data indicate stronger $TMSu^+$ - anion interactions than those between substituted imidazolium and halide anions. A Grotthus mechanism may operate for conduction in TMSuBr:HBr melts.

Key words: Conductivity, NMR, and IR

INTRODUCTION

Although a variety of organic salts can be mixed with the appropriate aluminum halide to produce haloaluminate melts that are liquid at or below ambient temperature, most work in the field has involved two systems: $AlCl_3$:1-butylpryridinium chloride ($AlCl_3$:BPC) and $AlCl_3$:1-ethyl-3-methyl-1H-imidazolium chloride ($AlCl_3$:ImCl). Liquids are obtained for $AlCl_3$ mole fractions ranging from 0.37 to 0.67 for the former and 0.33 to 0.67 for the latter. Potentiometry suggests that acid-base properties of these melts are governed by tetrachloroaluminate dissociation with $K_{eq} \cong 10^{-17}$ at 40°C. Some formation of $Al_3Cl_{10}^-$ may be important at high (> 64 mol %) $AlCl_3$ mole fractions. The anion-cation interactions that take place in ambient temperature melts have been studied by NMR spectroscopy (1-3). In basic melts the organic cations interact strongly with halide ions apparently through hydrogen bond formation; in particular all three Im^+ ring protons interact (4-7) with Cl^-. In acidic melts (excess $AlCl_3$ over Cl^-) little interaction seems to occur (1-3).

---

† Department of Chemistry, University of Alberta, Edmonton, Canada, T6G 2G2.

ampoules awaiting use. Anhydrous aluminum bromide (Fluka, >98%) was vacuum sublimed thrice at ~ 130°C. The purified crystals were colorless.

$AlCl_3$:ImCl (2:1), $AlCl_3$:TMSuBr (2:1) and $AlBr_3$:TMSuBr (2:1) acidic melts were prepared by adding the aluminum halide slowly to the second salt with continuous stirring. The three melts were colorless, pale yellow turning yellow in days, and colorless turning pale yellow in days, respectively. Reactions with TMSuBr were much less exothermic than that with ImCl.

TMSuHBr_2 was prepared at room temperature by passing HBr through a needle (26 G or 22 G) over weighed amounts of TMSuBr crystals in a 10 mL serum bottle or in a 30 mL Barnes dropping bottle fitted with a septum. The speed of the reaction depended on the HBr pressure, being very slow at 1 atm. Consequently, melts of composition TMSu Br$(HBr)_n$ ($1.00 < n < 1.15$) were prepared by applying HBr at a few atm for several minutes and then pumping HBr out of the melts until the required mole ratio was achieved as indicated by gravimetry. Melts with $1.15 < n_{HBr} < 1.40$ were prepared directly. All melts were pale yellow. They were transferred to the drybox ready for physical measurements. For melts with $n_{HBr} > 1.25$, the HBr partial pressures above them were quite high so that the melts had to be transferred to appropriate measuring bottles through cannulation using a Teflon tubing cannula and a syringe. For NMR measurements only, melts with $n_{HBr} > 1.40$ were prepared *in situ* in NMR tubes with rubber septa secured by Parafilm and n values were determined gravimetrically. Small needles (26 G) were required to eliminate leaks.

Physical Measurements

Densities of $AlCl_3$:TMSuBr and $AlBr_3$:TMSuBr melts were measured at 25°C with either 5 mL or 10 mL volumetric flasks which had been calibrated with distilled water at 25 ± 0.2°C. Densities of TMSuBr$(HBr)_n$ ($1.00 < n < 1.40$) were measured at 25°C using 2.5 mL dilatometric tubes calibrated with distilled water. A reference mark was etched midway up the 2.5 mm bore stem. Once melts were loaded to the mark they were capped with septa to minimize HBr loss.

Viscosities of melts were measured using Cannon-Fenske viscometers (sizes 50, 100, 150 and 300) which had been calibrated with aqueous glycerol (Fisher ACS) solutions (16, 17). A paraffin oil bath with a submerged heater and an Omega 871 digital thermometer were used in temperature control. Viscometers were calibrated by an overlapping technique: distilled water was the primary standard (sizes 50 and 100), 50% aqueous glycerol (sizes 50, 100 and 150) and 85% aqueous glycerol (sizes 150 and 300) the secondary standards. The densities of 50% and 85% glycerol were measured with a 10 mL dilatometer and their viscosities agreed with Sheely's (16) table. Before each measurement the viscometer loaded with melt was immersed in the bath for 10 min; the melt was then drawn (or forced) up by vacuum (or pressure) to 5-10 mm above the upper mark. A minimum flow time of 120 s was required. To minimize HBr loss from TMSuBr(HBr) melts, the ends of the viscometer were capped with rubber septa and connected with Teflon tubing to equalize pressures.

Conductances of $AlBr_3$:TMSuBr and $AlCl_3$:TmSuBr were measured with an Orion Model 160 conductivity meter with an Orion 016010 conductance cell which has four glass carbon electrodes and a temperature sensor. The conductances were frequency independent and the cell constant was 0.609 cm^{-1} (confirmed with 0.1 demal aqueous KCl). Melts were contained in a small glass cylinder and two O-rings were mounted between the cell and the cylinder to get an airtight seal. Conductances of TMSuBr$(HBr)_n$ melts were measured with a YSI Model 31 conductivity bridge (Yellow Springs) at 1 KHz. This cell was made by attaching two Pt electrodes on opposite sides of a glass block attached to a glass tube bearing the separated leads; the tube in turn was placed in a melt container drawn from a 50 mL buret fragment and tube and container sealed by a nut with Teflon and silicone rubber bushings. The cell was calibrated at 25 ± 0.2°C with 0.1 demal aqueous KCl (18) and the cell constant was 2.26 cm^{-1} ± 1%. The container was immersed in an oil bath such that the melt surface was 3 cm below the oil surface.

^{1}H NMR spectra were obtained with a Bruker AC-200 NMR spectrometer. 3-(Trimethylsilyl)-1-propanesulfonic acid, sodium salt (Thompson-Packard) dissolved in dimethyl sulfoxide - d_6 was sealed into melting point capillaries and then inserted into 5-mm NMR tubes as an external standard (at 0.49 ppm vs. TMS in $CDCl_3$). NMR tubes were filled with melt in the drybox, capped, and sealed with Parafilm before transfer to the spectrometer.

UV-Visible spectra were measured with a Hewlett-Packard Model 8452A diode array spectrophotometer.

Infrared spectra of TmSuBr$(HBr)_n$ were recorded with a Perkin-Elmer Model 1600 FT-IR spectrophotometer. One or two drops of melt were sandwiched between the two films cut off from a polyethylene sampling bag which, in turn was placed between two KBr windows: the film thickness was adjusted by gently pressing the upper window (11).

Cyclic voltammograms were obtained with a BAS Model 100A electrochemical analyzer (Bioanalytical Systems) and recorded with a Hewlett-Packard 7475A plotter. A glassy carbon disk (0.071 cm^2) served as working electrode, a coiled Al wire (Aldrich, 99.999%) as counter electrode and an Al wire, immersed in the 2:1 AlX_3:TMSuBr melt in a compartment separated by a fine porosity glass frit, served as reference electrode.

Elemental analyses were performed on a Perkin-Elmer Model 2400 CHN analyzer.

Weighing and material transfers involving AlX_3 systems were performed in a drybox under a purified nitrogen atmosphere. Stored materials were capped, sealed with Parafilm and wrapped with Al foil.

RESULTS AND DISCUSSION

Recrystallized and dried TMSuBr gave satisfactory C and H analyses and, moreover, showed little deterioration after exposure to the laboratory atmosphere (purified salt: C = 22.71%, H = 5.74%, H/C = 3.01; exposed salt: C = 23.19%, H = 5.87%, H/C = 3.02; theoretical: C = 22.94%, H= 5.77%). The reactions of TMSuBr with aluminum halides are much less exothethermic than those of ImCl. These two factors favor the preparation and use of TMSuBr derivatives over those of ImCl.

$AlCl_3$:TMSuBr and $AlBr_3$:TMSuBr are liquid at ambient temperature for AlX_3:TMSuBr mole ratios close to 2:1. They show a range > 40°C between freezing and melting temperatures. For the HBr:TMSuBr systems, liquids are found for HBr:TMSuBr ratios > 1.00 and the melting and freezing temperatures differ by ~ 20°C.

Density (ρ), viscosity (η) and conductance (κ) data for the melts studied are compared with literature values for other ambient temperature melts in Table 1. The specific conductance of 2:1 $AlBr_3$:TMSuBr showed a linear dependence on temperature. (t, °C) over the range 25-60°C viz.

$$K = 0.303 + 0.0455\,t \quad \text{(corr. coeff. 0.9998)} \qquad [2]$$

Melts derived from trimethylsulfonium and aluminum halides were the least conducting and most viscous (data for $AlBr_3$:EPB are approximate) among those listed, suggesting a stronger cation-anion interaction than in the other acidic chloroaluminates. The TMSuBr:(HBr)*n* melts possess viscosities similar to that of 2:1 $AlCl_3$:ImCl but conductances up to 4 times greater. Within the TMSuBr:(HBr)*n* system the viscosity variation is more extreme (notice that by n > 1.24 we have the most fluid of the quoted systems). Comparing 2:1 $AlBr_3$:TMSuBr and 1:1 HBr:TMSuBr we see that a change from $Al_2Br_7^-$ to HBr_2^- brings about a 7-fold viscosity decrease but a 24-fold conductance increase. This viscosity change may be ascribed to ion size but the conductance change suggests that a Grotthus mechanism of Br^- exchange may be facilitating conduction in a manner similar to that suggested for molten polyiodides by Stegemann, *et al* (23).

$$[Br\text{-}H\text{-}Br]^- + HBr \Leftrightarrow Br\text{-}H + [Br\text{-}H\text{-}Br]^- \qquad [3]$$

The electrochemical windows for TMSuBr:$AlCl_3$ and TMSuBr:$AlBr_3$ melts are 1.9 v. and 1.8 v., respectively ($Al_2Br_7^-$ is easier to oxidize than $Al_2Br_6Cl^-$). The UV-visible spectra of 2:1 $AlCl_3$:ImCl, $AlBr_3$:TMSuBr and $AlCl_3$:TMSuBr obtained with a 1 mm cell show UV-cutoffs (absorbance = 1) of 242, 228 and 210 nm, respectively. Thus, bands such as the B band of benzene (λ_{max} = 256 nm) should be completely viewable in the TMSu-based melts.

The ^1H-NMR spectra of 2:1 AlX_3:TMSuBr melts show the simple $TMSu^+$ methyl proton band flanked by two spinning side-bands and two ^1H-^{13}C coupling bands (J = 146 Hz). These bands are shifted 0.38 ppm upfield in the $AlBr_3$ melt compared to the $AlCl_3$ melt. This means a much greater scope for studying ^1H-containing solutes exists in TMSuBr-based melts than in $AlCl_3$:ImCl systems (5 distinct solvent bands). Typical ^1H-NMR spectra of HBr-TMSuBr melts consist of a larger singlet at ~2.18 ppm, attributable to the methyl protons of $TMSu^+$ and a singlet at lower field arising from the added HBr. Since the ^1H signal in $CHCl_2CHCl_2$ occurs at -2.73 ppm vs. TMS for HBr and at 10.2 ppm for HBr_2^- (24) we conclude that the HBr_2^- formation reaction is not complete in the 1:1 mixture with a shift of 8.1 ppm vs. TMS. This situation is not found in ImCl:HCl melts (10). As the HBr:TMSuBr mole ratio is increased, the $TMSu^+$ signal is unchanged but the lower field signal intensifies and shifts upfield reaching 4.18 ppm at a ratio of 2:1. This type of behavior is observed for HCl:ImCl melts and is readily explained in terms of $H_2Cl_3^-$ formation (9). We suggest that the $H_2Br_3^-$ formation reaction is occurring at higher HBr concentrations in the HBr:TMSuBr system.

Figure 1 depicts the IR spectrum of 1:1 HBr:TMSuBr. The sharp bands at 3000 and 1435 cm^{-1} can be assigned to the methyl C-H stretching and bending vibrations (8) while the broad bands at 1350 cm^{-1} and 780 to 1050 cm^{-1} can be assigned by comparison with the spectrum of tetrabutylammonium hydrogen dibromide to ν_2, the degenerate bending mode and combinations of ν_3 and ν_1, the antisymmetric and symmetric stretching modes, of HBr_2^- (25, 26). The broad absorption between 1500 and 2200 cm^{-1} and the weak band at 2500 cm^{-1} are not found for $(R_4N)(HBr_2)$ (25) nor TMSuCl (8) and therefore, must be due to HBr or $H_2Br_3^-$. Comparison with spectral data for $H_2Cl_3^-$ (11) which has a broad absorption centred about 2000 cm^{-1} and HBr gas (27) with absorption at 2650 cm^{-1} leads to the assignment of the 1500-2200 cm^{-1} band(s) to $H_2Br_3^-$ and the weak 2200 cm^{-1} band to HBr.

The overall implication of the NMR and IR data is that stepwise $Br(HBr)_n^-$ formation proceeds less readily than stepwise $Cl(HCl)_n^-$ formation and the controlling equilibrium lies less to the right than its chloride counterpart (eqn. [1]). Thus, ostensibly stoichiometric $TMSuHBr_2$ contains detectable quantities of HBr_2^-, $H_2Br_3^-$ and HBr and HBr_2^- and $H_2Br_3^-$ require significant HBr pressure for their formation and endurance.

In conclusion, TMSuBr readily forms salts with aluminum halides which are liquid at ambient temperature in the more Lewis acidic composition range and, although somewhat viscous, are promising solvents in terms of their spectroscopic and electrochemical windows. Reaction of TMSuBr with HBr can produce HBr_2^- and $H_2Br_3^-$ ions but less readily than does ImCl + HCl yield the chloride species. $TMSuHBr_2$ could be used as an HBr source, but it does include Br-, $H_2Br_3^-$ and free HBr as well as HBr_2^-.

REFERENCES

1. J.S. Wikes, J.S. Frye and G.F. Reynolds, *Inorg. Chem.* 22, 3870 (1983)
2. A.A. Fannin, Jr., L.A. King, J.A. Levisky and J.S. Wilkes, *J. Phys. Chem.* 88, 2609 (1984)
3. J.S. Wilkes, C.L. Hussey and J.R. Sanders, *Polyhedron* 5, 1567 (1986)
4. A.K. Abdul-Sada, A.M. Greenway, P.B. Hitchcock, T.J. Mohammed, K.R. Seddon and J.A. Zora, *Chem. Comm.* 1753 (1986)
5. C.J. Dymek, Jr., D.A. Grossie, A.V. Fretini and W.W. Adams, *J. Mol. Struct.* 213, 25 (1989)
6. S. Tait and R.A. Osteryoung, *Inorg. Chem.* 23, 4352 (1984)
7. A.G. Avent, P.A. Chaloner, M.P. Day, K.R. Seddon and T.Welton, Proc. VIIth Internat. Symp. Molten Salts, ed. C.L. Hussey, S.N. Flengas, J.S. Wilkes and Y. Ito, ECS, Pennington, N. J. 98 (1989)
8. S.D. Jones and G.E. Blomgren, *ibid.* 273 (1989).
9. J.L.E. Campbell and K.E. Johnson, *Inorg. Chem.* 32, 3809 (1993)
10. T.A. Zawodzinski, Jr., and R.A. Osteryoung, *Inorg. Chem.* 27, 4383 (1988)
11. J.L. E. Campbell, K.E. Johnson and J.R. Torkelson, Submitted for publication.
12. F. Kaufler and E. Kunz, *Ber.* 42, 2482 (1909)
13. D.G. Tuck, *Progr. Inorg. Chem.*, ed. F.A. Cotton, Wiley, New York 9, 161 (1968)
14. J. Emsley, *Chem. Soc. Rev.* 9, 91 (1980)
15. M. Schmeisser, *Handbook Prep. Inorg. Chem.*, 2nd Ed., ed. G. Brauer, Academic Press, N.Y. 1, 282 (1961)
16. M.L. Sheely, *Ind. Eng. Chem.* 24, 1060 (1932)
17. J.B. Segur and H.E. Oberstar, *Ind. Eng. Chem.* 43, 2117 (1951)
18. G. Jones and B.C. Bradshaw, *J. Amer. Chem. Soc.* 55, 1780 (1933)
19. R.A. Carpio. L.A. King, R.E. Lindstrom, J.C. Nardi and C.L. Hussey, J. *Electrochem. Soc.* 126, 1644 (1979)
20. A.A. Fannin, Jr., D.A. Floreani, L.A. King, J.S. Landers, B.J. Piersma, D.J. Stech, R.L. Vaughn, J.S. Wilkes and J.L. Williams, *J. Phys. Chem.* 88, 2614 (1984)
21. J. Robinson, R.C. Bugle, H.L. Chum, D. Koran and R.A. Osteryoung, *J. Amer. Chem. Soc.* 101, 3776 (1979)
22. J.R. Sanders, E.H. Ward and C.L. Hussey, *J. Electrochem. Soc.* 133, 325 (1986)
23. H. Stegemann, A. Rohde, A. Reiche, A. Schnittke and H. Fullbier, *Electrochim. Acta* 37, 379 (1992)
24. F.Y. Fujiwara and J.S. Martin, *J. Chem. Phys.* 56, 4091 (1972)
25. J.C. Evans and G.Y-S. Lo, *J. Phys. Chem.* 71, 3942 (1967)
26. *idem, ibid.*, 73, 448 (1969)
27. *American Institute of Physics Handbook*, ed. D.E. Gray, McGraw Hill, New York (1972)

Table I. Physical Properties of Melts at 25°C

Acid	Base	Ratio	ρ g cm^{-3}	V$_M$ mL mole^{-1}	κ mS cm^{-1}	η cP	T$_m$ °C	T$_f$ °C	Ref.
$AlCl_3$	EPBr†	2	1.52	299	8.43	22.5			25
$AlCl_3$	ImCl	2	1.39	297	14.7	13.5			26
$AlCl_3$	TMSuCl	2	1.40	271	5.5	39.3			14
$AlCl_3$	TMSuBr	2	1.59	266	4.21	54.9	5	-45	
$AlBr_3$	EPBr	2	2.20	328		~50			27
$AlBr_3$	ImBr	2	2.22	326	5.6	31			28
$AlBr_3$	TMSuBr	2	2.40	288	1.44	138	37	-5	
$AlBr_3$	TMSuBr*	2	2.38	290	2.59	50			
HBr	TMSuBr	1.00	1.74	137	34	20.5	27	10	
HBr	TMSuBr	1.15	1.76	142	43	15.3	25	2	
HBr	TMSuBr	1.24	1.77	145	48	12.4	22	0	
HBr	TMSuBr	1.32	1.78	148	54	10.2	20	-3	
HBr	TMSuBr	1.38	1.79	150	56	8.3	18	-10	

* at 50°C † EP ≡ 1-ethylpyridinium V$_M$ is an average molar volume

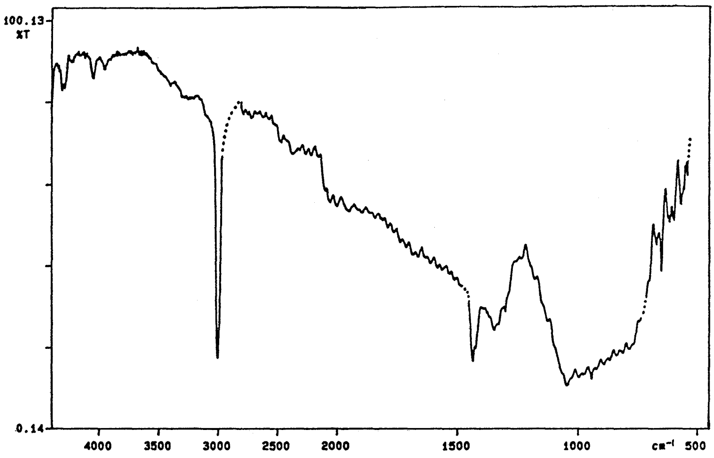

Figure 1. IR spectrum of 1:1 HBr:TMSuBr melt at 23°C.

DOI: 10.1149/199413.0187PV

ELECTRONIC TRANSPORT PROPERTIES OF THE MOLTEN–ALLOY SYSTEMS Na–Pb AND Rb–Au

K. Funke and J. Kellers

Institut für Physikalische Chemie
der Westfälischen Wilhelms–Universität
Schlossplatz 4/7, 48149 Münster, Germany

ABSTRACT

Conductivity and Hall–effect measurements have been performed in the molten-alloy systems Na–Pb and Rb–Au. Concentration dependent carrier densities and mobilities have thus been derived. In Na–Pb the composition dependent carrier density reflects the formation of aggregates Na_4Pb and $(NaPb)^+$ in the melt. This is in agreement with the thermodynamic factor and the excess stability function which have maxima close to sodium mole fractions of 0.5 and 0.8. In Rb–Au the localization of electrons is even more pronounced than in Na–Pb. For Rb–rich compositions the electronic mobility is found to decay exponentially with increasing content of gold. Applicability and limitations of the nearly-free–electron model are being discussed.

INTRODUCTION

The molten alloy systems Na–Pb and Rb–Au are both known for their metal/non-metal transitions.

In molten Na–Pb, consecutive transitions metal → semiconductor → metal are observed with increasing sodium mole fraction, x_{Na}. The semiconducting regime extends from about $x_{Na} = 0.7$ to almost $x_{Na} = 0.9$. In this composition range, the electrical conductivity attains a minimum, while its temperature coefficient is positive, see below [1]. The effect results from an electronic localization around $x_{Na} = 0.8$ due to the formation of neutral Na_4Pb aggregates in the melt [2].

Like molten Cs–Au, molten Rb–Au is one of the rare examples displaying consecutive metal → ionic conductor → metal transitions with varying composition [3]. At the stoichiometric point, $x_{Au} = 0.5$, the electrons are completely localized, and the melt only consists of cations Cs^+ and anions Au^-.

This paper aims at a more detailed analysis of the metal/non–metal transitions in molten Na–Pb and molten Rb–Au. This is achieved by monitoring the variations of carrier density and carrier mobility individually, while changing the composition. The experimental techniques applied in this study are measurements of the electrical conductivity and the Hall coefficient. In molten Na–Pb the occurrence of ordering processes at both $x_{Na} \approx 0.5$ and $x_{Na} \approx 0.8$ is clearly reflected by the composition dependent carrier density. – In the Rb–Au system, where our measurements were restricted to $x_{Au} < 0.32$, the most remarkable feature is the way the electronic mobility is found to vary as a function of x_{Au}.

EXPERIMENTAL

In both molten alloy systems, Hall voltages have been measured by use of the double ac cross modulation technique [4–6]. The currents in the sample and in the induction coils of the electromagnet had frequencies of 205 Hz and 40 Hz, respectively. The Hall voltage was measured at the sum frequency of 245 Hz, by means of a lock–in amplifier whose reference signal was generated by an electronic mixer. At the same time, the electrical conductivity was determined from the voltage drop along the sample, measured by a lock–in amplifier operated at 205 Hz. Our experimental set–up reproducibly detects Hall voltages of the order of 10 nV. This implies the feasibility of routine measurements of Hall coefficients of the order of 10^{-10} m^3 $(As)^{-1}$. The precision of our Hall and conductivity data is essentially limited by uncertainties in determining the thickness of the sample film ($\approx$ 0.5 mm). Systematic errors due to this effect are expected to amount to about 10 %.

The sample cells were made of "Duran" glass, which was found to be surprisingly stable even with regard to Rb–Au melts at temperatures above 500 °C. The cells were rectangularly shaped, providing a sample volume of 20 mm x 5 mm x 0.5 mm. Fused–in platinum leads served as electrical contacts.

The samples were prepared from 99.995 % purity lead (Aldrich), 99.95 % purity sodium (Aldrich), 99.999 % purity gold (Aldrich), and rubidium (Merck, purity not specified). All preparation steps were performed in a specially designed glove–box which guarantees a constantly pure argon atmosphere contaminated by less than 1 ppm of oxygen and water.

In the case of the Na–Pb system, the technique of Coulometric titration was applied in order to change the composition of the sample in a well–defined manner [7]. The sample was part of an electrochemical cell, V2A|Na|Na–β"–alumina|Na–Pb|V2A. In situ measurements of the emf of this cell provided the possibility of monitoring the sodium activity, a_{Na}, as a function of x_{Na}.

THE SODIUM – LEAD SYSTEM

Fig. 1 is a plot of the electronic conductivity, σ, and resistivity, ρ, of molten Na–Pb at 405 °C and 450 °C. The conductivity has a minimum at $x_{Na} \approx 0.8$, while its temperature coefficient is positive. In Fig. 2 we present the Hall coefficient, R_H, of molten Na–Pb at 450 °C. Like ρ, $|R_H|$ displays a pronounced maximum at $x_{Na} \approx 0.8$, corresponding to a minimum in the number density of conduction electrons.

In molten metals and alloys, the predictions of the nearly–free–electron (NFE) model are usually well fulfilled, and the energy dependence of the electronic relaxation time need not be considered [8]. In this case, R_H can simply be identified with the negative inverse product of the elementary charge, e, and the number density of nearly free electrons, n. Moreover, one can also identify the Hall mobility, σR_H, and the electronic drift mobility, u. The Fermi wavevector, k_F, and the mean free path of the electrons, $\bar{\ell}$, are now easily derived via $k_F = (3\pi^2 n)^{1/3}$ and $\bar{\ell} = -\hbar k_F u/e$. The dimensionless product, $k_F \cdot \bar{\ell}$, is of particular interest. For the NFE model to be applicable, $k_F \cdot \bar{\ell}$ should be considerably larger than one. The plot of Fig. 3 shows that in molten Na–Pb alloys $k_F \cdot \bar{\ell}$ varies very little for $0.0 \leq x_{Na} \leq 0.9$, staying between 7 and 5. However, $k_F \cdot \bar{\ell}$ is found to increase rapidly as x_{Na} exceeds 0.9. On the basis of Fig. 3, we expect the NFE model to

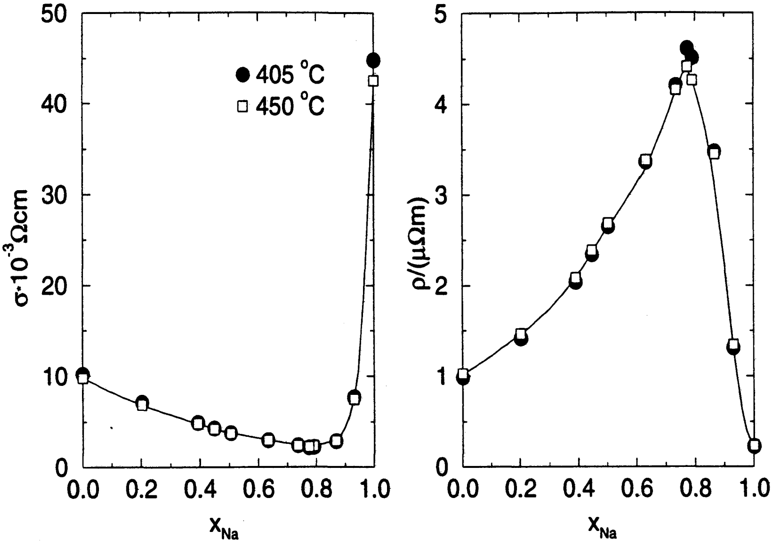

Fig. 1. Composition dependent conductivity and resistivity of molten Na–Pb alloys at 678 K and 723 K.

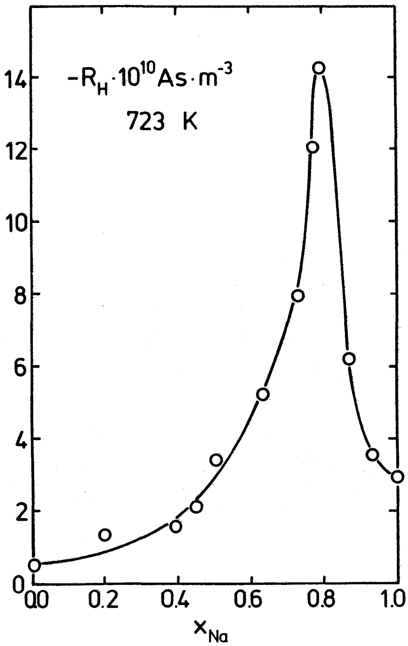

Fig. 2. Composition dependent Hall coefficient of molten Na–Pb alloys at 723 K.

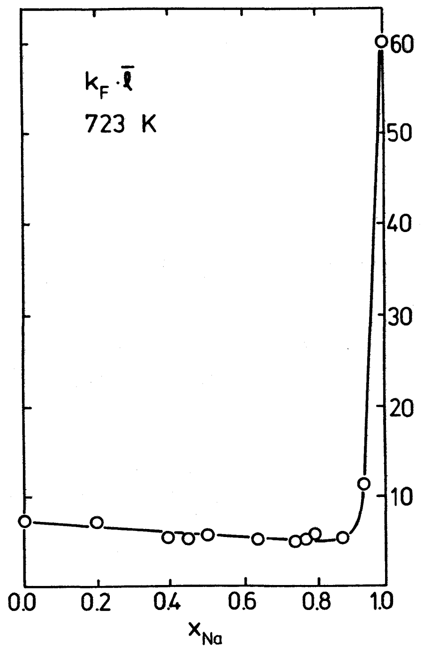

Fig. 3. Composition dependent product $k_F \cdot \bar{l}$ of molten Na–Pb alloys at 723 K.

be valid for molten Na–Pb at all compositions.

We now consider the average number of nearly free electrons per atom,

$$\bar{z} = n/(N/V) = -(eR_H N/V)^{-1} . \tag{1}$$

Here N/V denotes the number density of the atoms in the melt. Values for N/V have been taken from ref. [9].

Fig. 4 is a plot of our results for $\bar{z}(x_{Na})$ at 450 °C. For comparison, the straight line

$$\bar{z}_{ideal}(x_{Na}) = x_{Na} + 4x_{Pb} = 4 - 3x_{Na} \tag{2}$$

is also shown in the figure. Here, the ideal mixture is assumed to consist of Na^+ and Pb^{4+} ions exclusively, plus nearly free electrons. The actual shape of $\bar{z}(x_{Na})$, and in particular its minimum at $x_{Na} \approx 0.8$ and its change of slope at $x_{Na} \approx 0.5$ are nicely reproduced by a solid line in Fig. 4. This line has been obtained from a simple model, which will be briefly outlined in the following.

In our in–situ measurements of the sodium activity, $a_{Na}(x_{Na})$, we could well reproduce the data given earlier by Saboungi et al. [2]. Our results are, therefore, also consistent with the excess stability, $ES(x_{Na})$, derived in ref. [2] according to

$$ES = (\partial \ell n a_i / \partial \ell n x_i - 1) RT / (x_i(1-x_i)), \tag{3}$$

where i denotes either Na or Pb. Like the thermodynamic factor, $\partial \ell n a_i / \partial \ell n x_i$, this function [10] displays maxima at compositions corresponding to the formation of aggregates in the melt. Well pronounced peaks indicate the existence of rather long–lived aggregates or compounds. In the case of molten Na–Pb, ES has a sharp peak at $x_{Na} \approx 0.8$ and a much broader maximum at $x_{Na} \approx 0.5$, see Fig. 5. Evidently, the peaks indicate the formation of rather stable aggregates Na_4Pb and of less stable pairs NaPb, respectively.

Treating the melt as a system consisting of ions Na^+ and Pb^{4+} and of aggregates NaPb and Na_4Pb we now introduce the respective mole fractions, which add up to one:

$$y_{Na} + y_{Pb} + y_1 + y_4 = 1 . \tag{4}$$

In a simple law–of–mass–action ansatz we have

$$y_4 = C \cdot y_{Na}^4 \cdot y_{Pb} \quad \text{and} \quad y_1 = D \cdot y_{Na} \cdot y_{Pb} . \tag{5a,b}$$

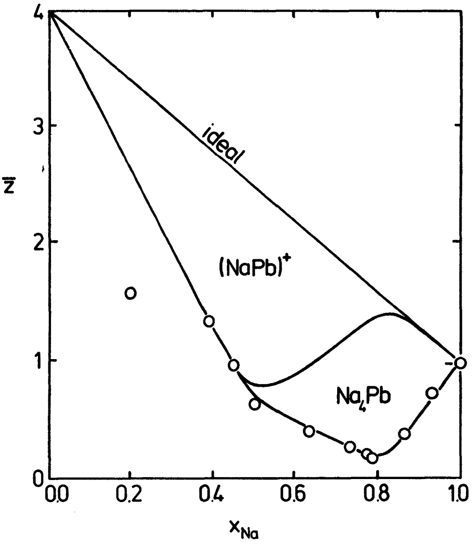

Fig. 4. Composition dependent average number of nearly free electrons in molten Na–Pb alloys. For the solid lines, see text.

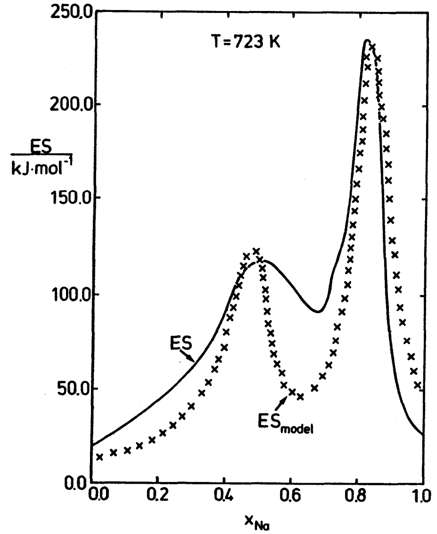

Fig. 5. Excess stability functions ES and ES_{model} for molten Na–Pb, see text.

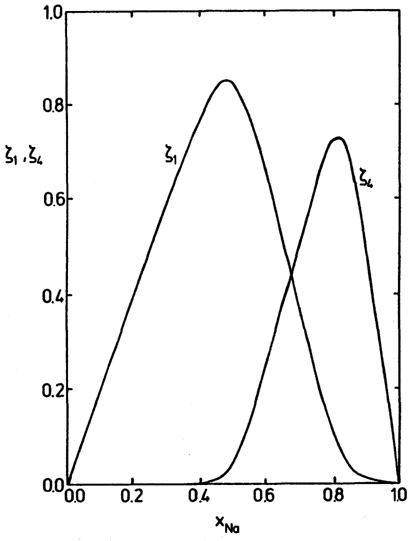

Fig. 6. Fractions of atoms in NaPb and Na_4Pb aggregates, see text.

The overall sodium mole fraction is, then,

$$x_{Na} = (y_{Na} + y_1 + 4y_4) \;/(1 + y_1 + 4y_4)\,. \tag{6}$$

If C and D are fixed, then the four equations (4), (5a,b) and (6) yield the four y_i for any given x_{Na}. Also, the fractions, ζ_i, of atoms present as Na^+ or Pb^{4+} or in NaPb or Na_4Pb aggregates can now be given. In particular, we have

$$\zeta_1 = 2y_1 \;/(1 + y_1 + 4y_4) \text{ and} \tag{7a}$$

$$\zeta_4 = 5y_4 \;/(1 + y_1 + 4y_4)\,. \tag{7b}$$

While Na_4Pb is a neutral entity, a pair of NaPb is probably positively charged: $(NaPb)^{\xi+}$. Therefore, $\bar{z}(x_{Na})$ can now be written as

$$\bar{z}\,(x_{Na}) = \zeta_{Na} + 4\zeta_{Pb} + \xi\cdot\zeta_1/2 \;, \tag{8a}$$

while

$$\bar{z}_{ideal}(x_{Na}) = \zeta_{Na} + 4\zeta_{Pb} + 5\zeta_1/2 + 8\zeta_4/5\,. \tag{8b}$$

The difference, $\bar{z}_{ideal} - \bar{z}$, thus consists of two parts:

$$\bar{z}_{ideal}(x_{Na}) - \bar{z}(x_{Na}) = (5-\xi)\zeta_1 \,/2 + 8\zeta_4/5. \tag{8c}$$

In Fig. 4, the solid line for $\bar{z}(x_{Na})$ has been obtained from Eq. (8a). The two contributions to $\bar{z}_{ideal} - \bar{z}$, as given by Eq. (8c), are also indicated. The parameter values are C = 2000, D = 70, $\xi = 1$.

However, this set of parameter values has not been derived from a direct fit to our $\bar{z}(x_{Na})$ data. Rather, the function $ES(x_{Na})$ has first been considered. Following an ansatz which has been frequently made, e.g. by Carl Wagner [11], we try to explain a_{Na} and a_{Pb} in the two–component notation by comparing them with model activities which are in turn identified with y_{Na} and y_{Pb} in our four–component notation. These model activities automatically fulfil the Gibbs–Duhem relation. Using y_{Na} for a_{Na} in Eq. (3) we obtain the model function ES_{model} included in Fig. 5, if we put C = 2000, D = 70. Note that the heights of the two maxima and the width of the maximum at $x_{Na} \approx$

0.8 are well reproduced by ES_{model}. However, the model peak at $x_{Na} \approx 0.5$ is by far too narrow. Clearly, stability and stoichiometry of the NaPb pairs have been overestimated in the model ansatz. On the other hand, the function required for the construction of $\bar{z}(x_{Na})$ is not $ES(x_{Na})$, but essentially $\zeta_1(x_{Na})$. Even when derived from our model ansatz, the distribution $\zeta_1(x_{Na})$ turns out to be rather broad on the x_{Na} scale, quite in contrast to the pronounced maximum of ES_{model}. In comparison to ES_{model}, height and shape of $\zeta_1(x_{Na})$ are, moreover, rather insensitive to variations of C and D. We, therefore, assume that $\zeta_1(x_{Na})$ as plotted in Fig. 6 is well suited for an interpretation of $\bar{z}(x_{Na})$ by means of Eq. (8a). In doing so we find that ξ has to be chosen to be one in order to reproduce the experimental data of Fig. 4. As the agreement between ES and ES_{model} is deteriorated if larger entities Na_xPb_x are assumed to be present in the melt, we conclude that the aggregates mainly formed at $x_{Na} \approx 0.5$ are $(NaPb)^+$ ions.

THE RUBIDIUM – GOLD SYSTEM

The conductivities and Hall coefficients obtained for the molten alloy system Rb–Au are plotted in Fig. 7. Along with the Hall data we also present the variation of R_H (at 774 K) that has to be expected on the basis of the NFE model, according to

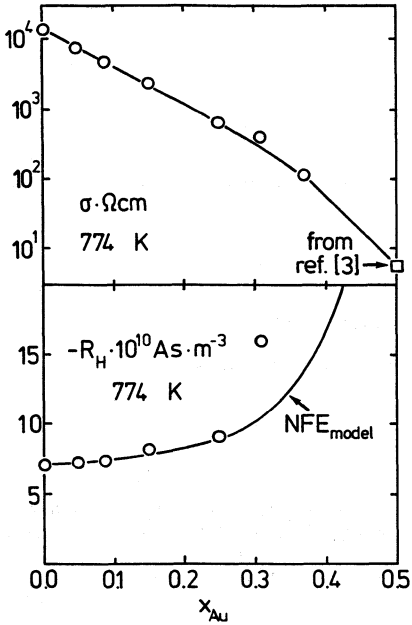

Fig. 7. Composition dependent conductivity and Hall coefficient of molten Rb–Au alloys at 774 K.

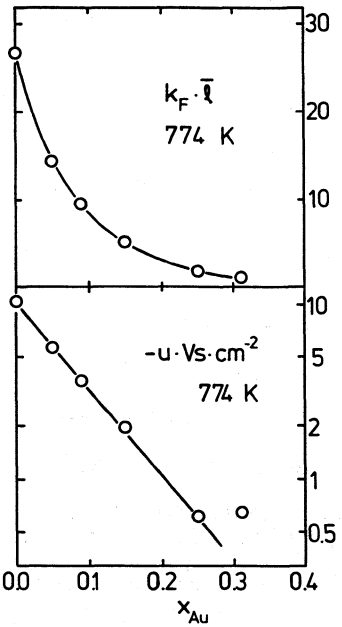

Fig. 8. Composition dependent product $k_F \cdot l$ and Hall mobility of molten Rb–Au alloys at 774 K.

$$-R_H(\mathrm{NFE}) = ((1-2x_{Au})eN/V)^{-1} . \qquad (9)$$

In Eq. (9), $1-2x_{Au}$ is the average number of nearly free electrons per atom. Here we have assumed that in a melt with $x_{Au}<0.5$ all gold atoms are turned into Au^- anions. The N/V data have been taken from ref. [12].

Evidently, the NFE model is able to reproduce the Hall data very well up to x_{Au} = 0.25, but no further. This result is not unexpected as the product $k_F \cdot \bar{l}$, determined by means of the relations given in the preceding section, is now very close to one, indicating the obvious breakdown of the NFE model.

Fig. 8 is a plot of $k_F \cdot \bar{l}$ and of the Hall mobility. Within the NFE regime, i.e. up to about x_{Au}= 0.25, the mobility and the mean free path are both found to be well described by expressions decaying exponentially with increasing x_{Au}. This result is considered particularly interesting. However, its physical interpretation requires a more detailed theoretical treatment than can be given in this paper.

ACKNOWLEDGEMENT

The authors profited from discussions with and advice given by H. Schmalzried, M.–L. Saboungi, and D.L. Price. One of us (J.K.) gratefully acknowledges a fellowship granted by the Fonds der Chemischen Industrie.

REFERENCES

1. See, e.g., S.Tamaki, Z.Phys.Chem. Neue Folge 156 (1988) 537.
2. M.–L.Saboungi, S.J.Herron and R.Kumar, Ber.Bunsenges.Phys.Chem.89 (1985) 375.
3. N.Nicoloso, R.W.Schmutzler and F.Hensel, Ber.Bunsenges.Phys.Chem.82 (1978) 621.
4. B.R. Russell and C.Wahling, Rev.Sci.Inst.21 (1950) 1028.
5. H.L.McKinzie and D.S.Tannhauser,J.Appl.Phys. 40 (1969) 4954.
6. G.Bödecker, Thesis, Göttingen 1979.
7. C.Wagner, J.Chem.Phys. 21 (1953) 1819.
8. L.E. Ballentine, "The Hall Effect in Liquid Metals", in "The Hall Effect and Its Applications", C.L. Chien and C.R. Westgate eds., Plenum Press, New York 1980.
9. H.Ruppersberg and J.Jost, Thermochim. Acta 151 (1989) 187.
10. L.S.Darken, Trans. AIME 239 (1967) 60.
11. B.R.Ilscher and C.Wagner, Acta Met. 6 (1958) 712.
12. A. Kempf, Ph. D. Thesis, Marburg 1981.

DOI: 10.1149/199413.0195PV

THE CONTRIBUTIONS OF THERMAL RADIATION AND THERMAL CONDUCTIVITY TO THE HEAT TRANSPORT IN THE SLAG 40% CAO - 40% SIO_2 - 20% AL_2O_3

T. EL GAMMAL*, E. WOSCH**, X. LI***

* PROF. DR.-ING., DEPT. FERROUS METALLURGY,
TECHNICAL UNIVERSITY (RWTH) AACHEN, GERMANY
** DR. RER.NAT., DEPT. FERROUS METALLURGY,
TECHNICAL UNIVERSITY (RWTH) AACHEN, GERMANY
*** DR.-ING., FORMERLY ASSISTANT, DEPT. FERROUS METALLURGY,
TECHNICAL UNIVERSITY (RWTH) AACHEN, GERMANY

ABSTRACT

Measurements of phonon and photon conductivity have been carried out on metallurgical slags of the system CaO - SiO_2 - Al_2O_3. The results show that the values for photon conductivity lie considerably higher than those of phonon conductivity, indicating that the main energy transport in the slag takes place by radiation. This has been confirmed for other slags. Both photon and phonon conductivity show increased values within the melting range, which may be accounted for by the solid/liquid transformation.

INTRODUCTION

In metallurgical process technology a knowledge of the thermal properties of slags is of prime importance. The surface finish of continuous cast steel slabs, for example, is dependent on the heat transfer between mould and strand, which in turn is determined by the heat conductivity of the intermediate slag layer. Likewise, the Electroslag Remelting Process (ESR) and the recuperation of heat from slags are greatly influenced by the thermal conductivity of metallurgical slags.

Many investigations have already been carried out on the heat transport in metallurgical slags and a number of theoretical models put forward (1-5). However, new aspects come to light when novel measuring methods are applied, as in the measurement of photon conductivity, which is presented here and compared with the conventional phonon conductivity measurement.

EXPERIMENTAL

a) Measurement of phonon (conventional) conductivity

For this determination the instationary hot wire method was used. This is shown in principle in Fig. 1. The crucible {1} containing the slag sample {2} is initially brought up to temperature in a Tammann furnace and then carefully heated further by means of a centrally located, current carrying tungsten wire {5}.

The temperature profile in the slag is measured by a Pt/PtRh/8 thermocouple {8}, adjacent to the heat source, and is recorded as a function of time. To satisfy the theoretical requirements of an infinitely extending temperature field and a linear heat source, a large testing space (60 mm diam.) together with a long thin heat wire (0.35 mm diam.) were selected. The calculation of the heat conductivity followed from the relevant equation for linear heat sources (6). The expression d T/d ln(t) was evaluated using the method of linear regression.

$$k_{cond} = \frac{C \cdot q_e \cdot d\ln(t)}{4\pi \cdot dT} \qquad [1]$$

with k_{cond} = thermal conductivity (phonon conductivity) [W/(m·K)]
q_e = electrical/thermal power per unit length of wire over the measuring distance [W/m]
C = correction factor for heat losses in axial direction of the wire
T = measured temperature [K]
t = time [sec]

b) Measurement of the photon conductivity

The determination of photon conductivity was based on a method proposed by Keene and Quinn for measuring the emissivity of slags (7), and further developed here for measuring photon conductivity. The principle involves the simultaneous spectroscopic determination of the real and imaginary terms of the complex refractive index (9) of slags between 800°C and 1600°C and within the wavelength range of 550 nm to 850 nm (this being restricted by the apparatus available). Fig. 2 shows a sketch of the apparatus. The sample graphite crucible {1} was provided with a stepped insert to receive two reference emitters (black body radiators), a molybdenum disc as radiation reflector and a cover. Three apertures in the cover permitted the passage of three ray bundles:

- slag emission above the molybdenum disc
- slag emission plus reference emitter
- emission of the reference emitter

With the aid of an optical bank these three ray bundles are focused onto the entry slit of a monochromator {2} and their spectrum registered at the particular temperature. To eliminate as fas as possible the background emission of the Tammann furnace {3}, two additional sites of the crucible cover were spectroscopically observed. After subtraction of the background emission and the setting up of the relationships between the ray bundle intensities at each wave-length, the complex refractive index can be calculated as a function of wavelength.

$$n_C = n_R - i \cdot n_I = \left(\frac{c}{v}\right) - i \cdot \left(\frac{\kappa \cdot \lambda}{4\pi}\right) \qquad [2]$$

with n_R = real term of the complex refractive index
n_I = imaginary term of the complex refractive index
c = velocity of light in vacuo = $2.99792 \cdot 10^8$ m/sec
v = velocity of light in the slag
κ = absorption coefficient [m^{-1}]
λ = wave length [m]

The quantity n_C contains not only information about the absorption coefficients and the reflection, emission and transmission powers of a substance, but also provides the link with fundamental electrical data, the dielectric constants and the electrical conductivity. With the aid of the complex refractive index, all optical material constants of slags may be expressed, including the photon conductivity. The relation between radiation flow and temperature gradient during radiation transport in hot media was originally investigated by Rosseland (8), and the approximation named after him for photon conductivity (k_{rad}), in terms of the complex refractive index, is written as

$$k_{rad} = \frac{4\sigma}{3\pi} \cdot \left\langle \frac{n_R{}^2}{n_I/\lambda} \right\rangle \cdot T^3 \qquad [3]$$

As n_R and n_I are wavelength dependent, the expression inside brackets must be averaged over the wavelength.

RESULTS

A comparison of the two conductivities, phonon and photon, is shown in fig. 3 for a slag of composition 40% CaO - 40% SiO_2 - 20% Al_2O_3 as a function of temperature. To enable both conductivities to be included in the same graph, a logarithmic scale has been applied, which, in part, is responsible for the apparent wide scatter of the phonon values.

It is evident that, the photon conductivity is considerably higher than the phonon conductivity, the ratio k_{rad} to k_{cond} being, on average, 20 to 1. Such high values for photon conductivity have also been found for other compositions of the $CaO-SiO_2-Al_2O_3$ system (9). In general, slags at high temperatures exhibit similar conductivity behaviour to glass. In the case of a time independent or stationary temperature field in the slag, the 1st Fourier heat theorem may be applied to the transported energy flux density in the x-direction, namely

$$Q = -k \cdot \frac{dT}{dx} \qquad [4]$$

with Q = heat flux or heat flux density [W/m^2]
k = heat conductivity or coefficient of heat conductivity [W/m·K]
T = Temperature [K]

If several mechanisms (as heat conductivity and heat radiation) contribute to the heat transfer, the heat conductivity expressed in the 1st Fourier heat theorem may be written as a simple sum, but only where there is strong interaction between the individual transfer mechanisms i.e alternating heat conduction and radiation, as in the case of slags.

Not only in their additive behaviour in energy transport is there similarity between the two conductivities, but also with respect to the phenomena exhibited in the melting range of the $40\%CaO-40\%SiO_2-20\%Al_2O_3$ slag. Both show a discontinuity or conductivity peak. In fig. 4 the measured k_{rad} and k_{cond} curves are plotted for the temperature range 1200°C - 1500°C, the differential scaling of the ordinate axis being a consequence of the considerably higher absolute values of the photon conductivity.

There is a striking difference in the absolute widths and heights of the two peaks. The k_{rad} discontinuity is high and narrow (amplitude 40W/(mK), FWHM 15K) whereas the k_{cond} discontinuity is flat and wide (amplitude 1.5W/(mK), FWHM 100K). The photon peak can be described approximately by a Gauß profile with a maximum at 1360°C, but the phonon peak is asymmetric with a maximum at 1335°C.

The occurrence of these peaks may be ascribed to a phase change in the slag $40\%CaO-40\%SiO_2-20\%Al_2O_3$ in passing from solid to liquid state. This phase change, which occurs at 1355°C, absorbs energy and thus reduces the transported heat flux density. Here the 1st Fourier heat theorem (equation 4), relating transported heat flux density, heat conductivity and temperature gradient, no longer applies. The relevant DTA (Differential Thermal Analysis) curve dips below the equilibrium line (endothermic process). This means that, for the same time interval t, the temperature rise dT is less than equilibrium, which in equation [1] is indicative of a higher heat conductivity. The converse applies for an exothermic process. A simple relationship can be obtained between the peak surface, the specific heat of fusion and the mean specific heat $\langle c_p \rangle$ by deriving the following expression from the 2nd Fourier heat theorem:

$$\int_{peak} \left(\frac{k_{cond}^{peak}}{<k_{cond}>} - 1 \right) dT = \frac{h}{<c_p>} \qquad [5]$$

in which the mean specific heat is given by $<c_p>=(c_p{}^s+c_p{}^l)/2$. k<cond> describes the conductivity underlying the peak i.e. without the peak and h is the specific heat of fusion.

According to a model put forward by K.C. Mills and B.T. Keene (10), $c_p{}^s$ and $c_p{}^l$, as well as the latent heat, can be calculated for the slag 40%CaO-40%SiO_2-20%Al_2O_3, giving $c_p{}^s$(1355°C)=1.20 J/(g·K), $c_p{}^l$=1.44 J/(g·K) and h=496.9 J/g. The mean value $<c_p>$ in the region of the phase change is then 1.32 J/(g·K). The integral in equation [5] represents a value of (388 ± 29) K, which yields a value for h, the latent heat, of (512 ± 38) J/g. Within the limits of accuracy for graphical integration, this gives excellent agreement with the value h=496.9 J/g of Mills and Keene.

The phase change solid/liquid is also responsible for the photon peak. The principal factors in the photon conductivity are the real and imaginary terms of the refractive index, the mean values of which are shown in fig. 5 for the melting region of the slag 40%CaO-40%SiO_2-20%Al_2O_3.

The real term remains practically constant in the region 1325°C - 1455°C, but the imaginary term shows a clear minimum. In the calculation of the photon conductivity as in equation [3], the imaginary term of the refractive index is in the numerator, leading to an increased value for k_{rad} in the melting region. It is noteworthy that N. Neuroth (11) found in the melting region of window glass a minimum in the absorption coefficient, which, according to equation [2], is proportional to the imaginary term of the refractive index.

CONCLUSIONS

With the aid of two different measuring methods, the instationary hot-wire method and optical spectroscopy, the phonon and photon conductivity of slags could be measured. Of importance is that the instationary wire method can only register the contribution to heat conductivity made by atomic vibrations (phonon conductivity). This is evident from the fact that, with the instationary hot-wire method, temperature is recorded by thermocouples, which are insensitive to radiant heat. Furthermore, the measurement of heat conductivity is based on the recording of temperature differences of the order of less than 1°C in a temperature medium of 1000-1500°C, i.e. $\Delta T/T \approx 10^{-3}$. According to the Stefan-Boltzmann-Law, the radiation flux Φ is proportional to T^4, so that $\Delta\Phi/\Phi \approx 4 \cdot 10^{-3}$. Thermocouples cannot detect these relatively minute changes in Φ, as they are ineffective radiation detectors.

Photon and phonon conductivity of the slag 40%CaO-40%SiO_2-20%Al_2O_3 in the temperature and wavelength range under consideration are related to one another by the ratio of 20:1. Even if this ratio is reduced to 10 or 5:1 for slags of other chemical composition, the fact remains that, as long suspected, that heat transport within a slag layer is largely determined by the heat radiation.

Both photon and phonon conductivity show increased values within the melting range, which may be accounted for by the solid/liquid transformation. The phonon peak can be directly related to the latent heat of transformation, whereas the photon peak is a result of a drastic reduction in the absorption coefficients of the slag.

An extension of the measurable wavelength range of the spectrscopic equipment into the IR-region up to approx. 4.5μm would be great value, as the temperatures that most concern the metallurgist lie between 1000°C and 1700°C. The main portion of radiant heat is to be found in this wavelength range.

ACKNOWLEDGEMENT

The authors would like to thank the Deutsche Forschungsgemeinschaft (DFG) for funding this work.

REFERENCES

1. Ohta, H.; Waseda, Y: Shiraishi, Y.: 2nd International Symp. on Metallurgical Slags and Fluxes, No. 1984, p.863-873.
2. Susa, M.; Nagata, K.; Goto, K.S.: TJIM, Vol. 19 (1988), No. 2, p. 133-142.
3. El Gammal, T.; Li, X.: The effect of Possible Phase Changes on the Heat Conduction of Slags, [in:] Molten Salt Chemistry and Technology, [eds.:]Chemla, M. and Devilliers, D., Mater. Sci. Forum 73-75 (1991), p. 37-44.
4. Mills, K.C.: 3rd Int. Conference on Molten Slags and Fluxes, June 1988, p. 229.
5. El Gammal, T.; Jofre Sanchez de Loria, S.J.: Steel Research No. 12 (1986), p. 620-625.
6. Carlslaw, H.S.; Jaeger, T.C.: Conduction of Heat it Solids p.193, Oxford, Clarendon Press 1973 (2nd ed.).
7. Keene, B.J.; Quinn, T.J.: An apparatus to determine total normal emissivity of opaque and diathermanous liquids at high temperatures, 1979 High Temp. - High Pressures, (11), p. 693-702.
8. Rosseland, S.: Astrophysik und Atom-Theoretische Grundlagen, Springer Verlag, Berlin, (1931).
9. El Gammal, T.; Wosch, E.: Photon conductivity of metallurgical slags of the three component system CaO-SiO_2-Al_2O_3, Steel Research No. 10 (1993), p. 501-504.
10. Mills, K.C.; Keene, B.J.: Physiochemical Properties of BOS Slags, DMA Report D/509, October 1985, chap.10.
11. Neuroth, N.: Der Einfluß der Temperatur auf die spektrale Absorption von Gläsern im Ultraroten, Glastechn. Ber., 25, Heft 8, 1952, p. 242.

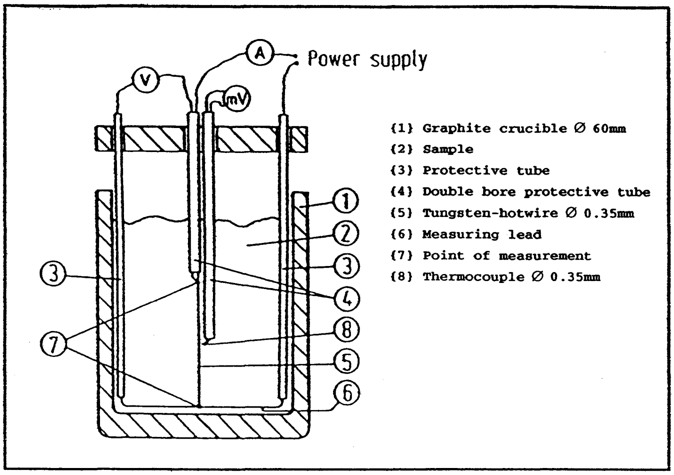

Fig. 1 Experimental set-up for the hotwire method

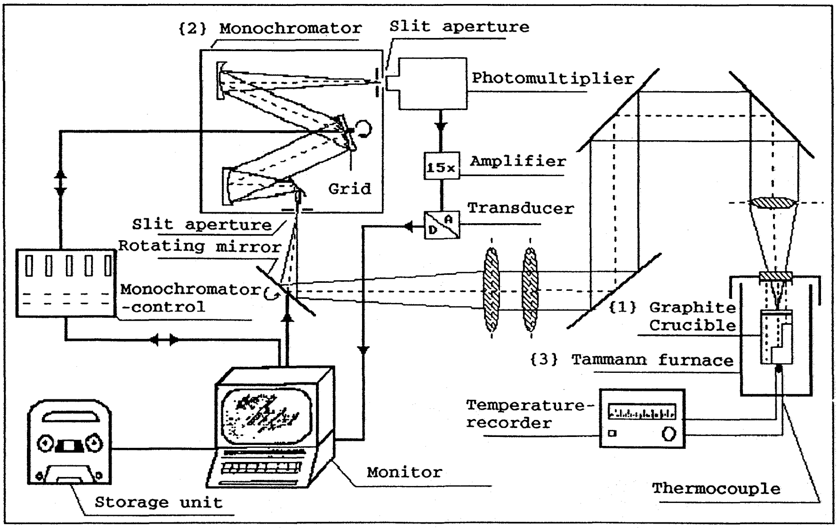

Fig. 2 Experimental set-up for measuring the photon conductivity of metallurgical slags

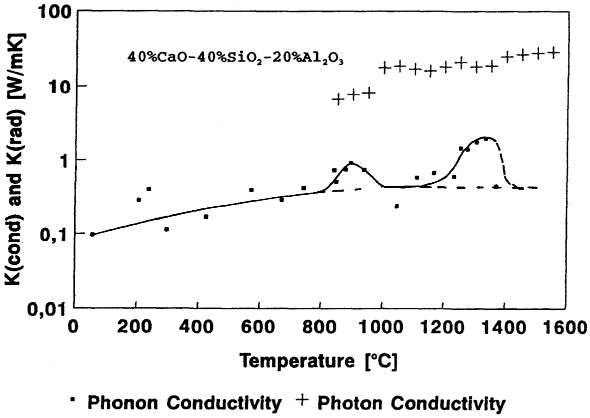

Fig. 3 General comparison of the measured phonon conductivity (lower values) with photon conductivity (upper values)

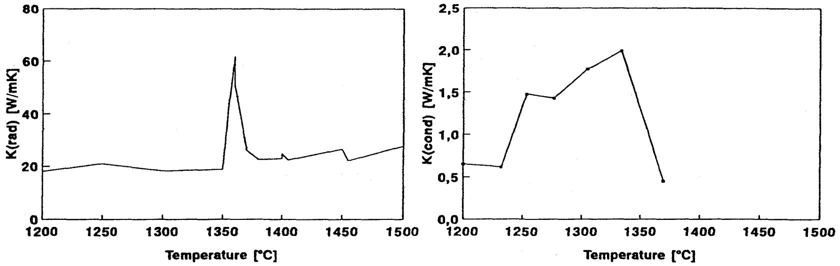

Fig. 4 Measured photon (left) and phonon (right) conductivity near the melting range for the slag $40\%CaO-40\%SiO_2-20\%Al_2O_3$

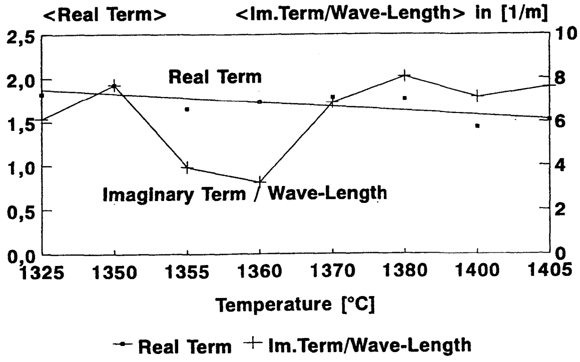

Fig. 5 Mean values of the real term (straight line) and the quotient of imaginary term / wave-lenght of the refractive index

DOI: 10.1149/199413.0203PV

THE ELECTRICAL CONDUCTIVITY OF SOLID/MELT COEXISITING SYSTEMS

Shigehito Deki,Masako Taira, Masako Takase,
*Akihiko Kajinami, Yukio Kanaji and Minoru Mizuhata**

Department of Chemical Science & Engineering,
Faculty of Engineering, Kobe University
Rokkodai-cho, Nada-ku, Kobe 657, Japan

*Department of Energy & Enviroment,
Osaka National Research Institute, AIST
1-8-31, Midorigaoka, Ikeda, Osaka 563, Japan

ABSTRUCT

The electrical conductivity and its temperature dependence were investigated for α-Al_2O_3 powder / molten KNO_3 coexisting system by ac impedance method with LF impedance analyzer. The electrical conductivity of the system decreased with increasing of the volume fraction of the solid phase following Archie' s equation. The activation energy of the electrical conductivity, $\Delta E_{a,}$ determined from the temperature dependence by using Arrhenius equation, was correlated with an apparent average thickness of the melt phase on the surface of the α-Al_2O_3 particle, and it suggested that the nature of the melt changes in the vicinal liquid layer on the solid phase owing to the interaction between the melt and the solid surface.

INTRODUCTION

Molten salt / powder coexisting system is a very important and attractive system not only in the applied field of molten salt chemistry such as a metal refining process or a fuel cell technology, but also general technology such as a crystal growth, composite materials or liquid-phase sintering process of ceramics and powder metallurgy. Recently, it is also suggested that molten salts inserted in Al_2O_3 powders can be used as one of solid electrolytes.

Regarding with the interfacial phenomena in the solid/liquid coexisting systems, many researches have been done. However, most of them were dealt with systems ranging in the low concentration of solid phase, which are called a suspension or colloidal solution. Whereas, few resaerches on the system ranging in the higher concentration of solid phase, which is called a paste, have been done.

We have already reported that in coexisting systems of the aqueous electrolyte solution and inorganic powders, the physicochemical properties of the liquid phase near the solid phase is different from those of bulk.[1-5]

In the present paper, molten KNO_3 was used as a liquid phase and α-Al_2O_3 powder was used as a solid phase. For this system, electrical conductivity was measured by the ac impedance method and melting behavior of KNO_3 was investigated with a differential scanning calorimeter.

EXPERIMENTAL

Various kinds of high-purity α-Al_2O_3 powder for the ceramics, which were supplied by Showa Denko Co.Ltd. and had various specific surface areas of 1.08 - 17.7 m^2/g, was used. The α-Al_2O_3 powder, after annealed at 1000°C in the air for 3hr, and solid KNO_3 were mixed thoroughly in an agate mortar under N_2 gas atmosphere and molded into a tablet with a diameter of 20mm under the pressure of 52 MPa for 30 min. Then the tablet was annealed again at 400°C in N_2 gas flow for 3hr, so that KNO_3 in the tablet melted and wetted well the surface of α-Al_2O_3 particles.

After molding, the ac impedance for the composite samples with various melt contents was measured in the frequency range from 5Hz to 13 MHz with a Hewlett-Packard 4192A LF impedance analyzer at 160-440°C in N_2 atmosphere.

The sample tablet was set in an alumina ceramic inner cell, and was put closely in Pt electrodes with diameters of 10mmφ. The inner cell was held in a quartz glass tube in which N_2 gas was flowed, and the silica glass tube was kept in a furnace to be temperature-controlled. (Fig.1)

The resistance was determined from Z' value at the intercept of the semicircular arc to Z'-axis on the complex impedance plane and the electrical conductivity of the tablet sample was calculated from the resistance, sample thickness and the area of the electrode.

X-ray diffraction measurement was applied to make sure of the composition for the tablet after annealed. The colorimetry was applied to determine the solubility of α-Al_2O_3 powder in molten KNO_3. After annealed, the tablet was dispersed in distilled water and the salt was dissolved into the water and separated from the α-Al_2O_3 powder with a filter. Ferron(8-hydroxy-7-iodoquinoline-5-sulfonic acid) and pH buffer solution were added to this filtrate. The absorbance measurement was carried out with a UV/VIS spectrophotometer.

DTA-TG and DSC were applied to investigate the decomposing and melting behavior for KNO_3 coexisting with the alumina powder in the tablet. The measurement was carried out under N_2 gas flow.

RESULTS AND DISCUSSION

SEM observation was applied in order to investigate the change of the surface morphology of the alumina particles due to some reactions with the melt during the temperature raising. The cross section of tablet before and after annealing was observed with SEM. The change in the morphology of α-Al_2O_3 particles after annealing was not observed.

The X-ray diffraction patterns measured for composite samples were only assigned to α-Al_2O_3 and KNO_3, and none of eutectic mixtures or reaction product were not detected. (Fig.2)

The solubility of the α-Al_2O_3 powder into molten KNO_3 was measured for the fine α-Al_2O_3 powder whose specific surface area of 17.7m^2/g was the largest in the applied alumina. As a result, *ca.* 150 μg of Al^{3+} in 1g of molten KNO_3 was detected. As the solubility of α-Al_2O_3 powder for the melt was so small, the contribution of the dissolved alumina to the electrical conductivity as a carrier might be neglected

As a above mentioned result, α-Al_2O_3 powder and molten KNO_3 were less reactive in the measuring temperature region and each sample was treated as a mixture of α-Al_2O_3 powder and molten KNO_3.

The complex impedance plots varied with the temperature. At higher temperature the complex impedance plots showed a linear locus, which indicated a typical Warburg impedance. It is recognized that the resistance of the composite decreased with melting of KNO_3. At the lower temperature, the complex impedance plots showed a semi-circular arc in the high frequency range. It is presumed that KNO_3 gradually froze and the resistance of the composite increased rapidly. At the lower temperature region, the complex impedance plots showed only the semi-circular arc. However, most arcs were slightly deformed and it showed that those complex impedance plots consisted of two kinds of semi-circular arcs. Such impedance plots often can be seen for solid electrolyte systems, and suggests that two different types of capacitance and resistance are contained in the equivalent circuit for these systems. And also, it indicates that the nature of molten KNO_3 near solid surface is different from that in the bulk of liquid phase.

The deflection point , Tt, corresponding to the phase transition of KNO_3 was observed on a temperature dependence of the electrical conductivity. In the higher temperature region, the plots of log σ *vs.* 1/T showed a linear relationship, and the activation energy of the electrical conductivity was calculated from the gradient of the linear part of the plot by use of the Arrehenius equation.

The temperature hysteresis of the electrical conductivity on heating and cooling was observed. Those showed a tendency that the electrical conductivity on cooling is higher than that on heating. As a repetition of heating and cooling, the difference of the electrical conductivity decreased and the activation energy for the electrical conductivity became constant. It is assumed that the packing of KNO_3 and alumina particles came to be equilibrated through the repetition of melting and solidification, and a conductive path was settled in the tablet. Whereas, the hysteresis shows the tendency that the transition temperature, T_t, for the electrical conductivity on cooling is higher than that on heating. The temperature dependencies of the electrical conductivity for various kinds of α-Al_2O_3 powders were measured. The coexisting system of which the specific surface area was the smallest, the electrical conductivity increased with the increase of the melt content. (Fig.3, Fig. 4) However, the activation energy in the temperature region above the transition temperature, and the transition temperature did not vary with the melt content. Besides the electrical conductivity in the temperature region below the transition temperature hardly varied. While, as the increase of the surface area, the activation energy increased and the transition temperature decreased with the increase of the melt content. (Fig. 5, Fig. 6)

The activation energy increased rapidly at a certain melt content. This behavior was observed evidently for the system containing the powder with the large surface area. However, the change of the activation energy became not so clear with the decrease of the specific surface area. This tendency was also observed for the transition temperature, also.

It is assumed that these results is correlative with a thickness of the molten salt existing near the surface of α-Al_2O_3 powder. Here, the apparent average thickness was defined as follows.

$$[\text{apparent average thickness}] = \frac{[\text{total volume of molten salt}]}{[\text{total surface area of } \alpha\text{-}Al_2O_3]}$$

This value has a length dimension and means, as a parameter, a distance from the surface of the solid phase. Therefore, it can be known that how far the influence of the solid surface extends to the melt phase. The variations of the activation energy and the transition temperature for electrical conductivity with the apparent average thickness showed good correlative. The value of the activation energy decreased and the value of the transition temperature increased with the thickness up to *ca.* 5-10nm. As a result, it is suggested that the ion interaction of KNO_3 is affected in the range of *ca.* 5-10nm as the apparent average thickness from the surface of solid phase, owing to the interaction between ionic species in the melt and the surface of α-Al_2O_3 powder. (Fig. 7, Fig. 8)

REFERENCES

1. S. Deki, M. Mizuhata, K. Nakamura, A. Kajinami and Y. Kanaji *J. Electrochem. Soc.,* **139**(6), 1544(1992)

2 S. Deki, M. Mizuhata, S. Nakamura, K. Nakamura, A. Kajinami and Y. Kanaji *J. Electrochem. Soc.,* **139**(4), 996(1992)

3. S. Deki, M. Mizuhata, S. Nakamura, A. Kajinami and Y. Kanaji *J. Chem. Soc., Faraday Trans.,* **89**(20), 3805(1993)

4. S. Deki, M. Mizuhata, A. Kajinami and Y. Kanaji *J. Chem. Soc., Faraday Trans.,* **89**(20), 3811(1993)

5. S. Deki, M. Mizuhata, S. Nakamura, K. Nakamura, A. Kajinami and Y. Kanaji *J. Colloid Interface Sci.,* **159**, 444(1993)

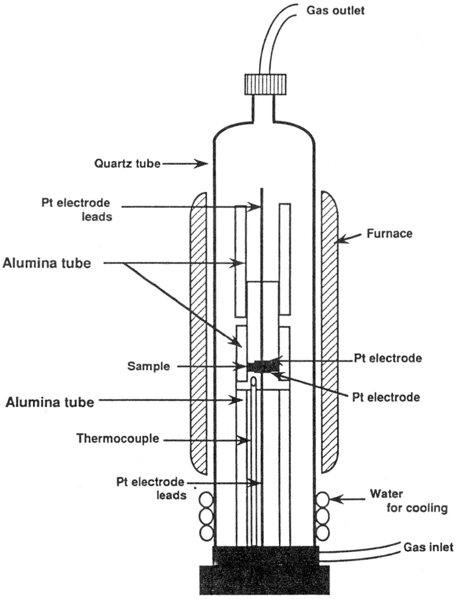

Fig. 1. Apparatus for electric conductivity measurements.

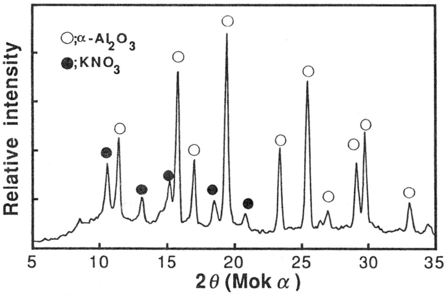

Fig. 2. X-ray diffraction pattern of α-Al_2O_3(17.7m^2/g) powder / KNO_3 coexisting system.
Melt content ; 35vol%.

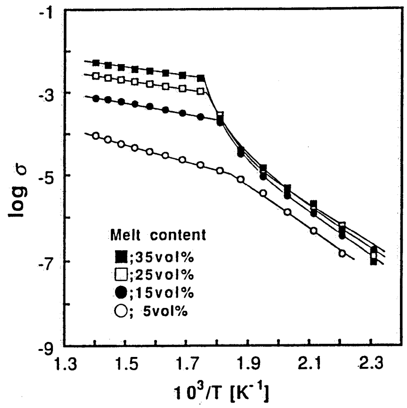

Fig. 3. Temperature dependence of the electrical conductivity for various kinds of α-Al_2O_3(17.7m^2/g) powder / KNO_3 coexisting system.

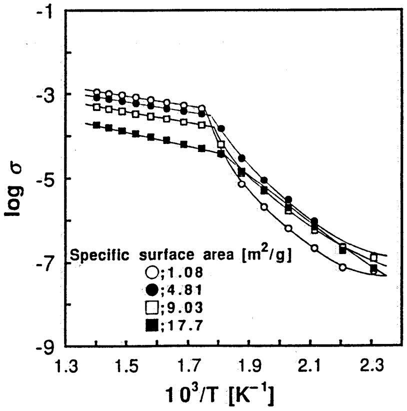

Fig. 4. Temperature dependence of the electrical conductivity for various kinds of α-Al_2O_3 powders / KNO_3 coexisting system.
Melt content ; 10vol%.

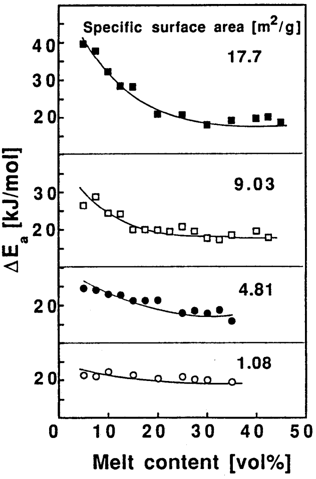

Fig. 5. Variations of ΔE_a with the melt content for various kinds of α-Al_2O_3 powders / KNO_3 coexisting systems.

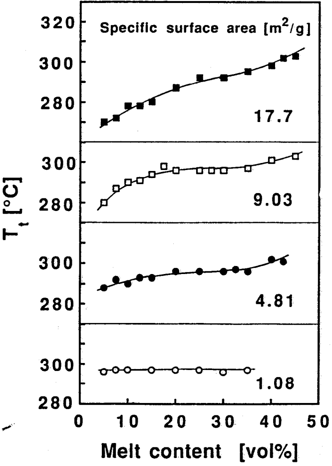

Fig. 6. Variations of the transition temperature for the electrical conductivity with the melt content for various kinds of α-Al_2O_3 powders / KNO_3 coexisting systems.

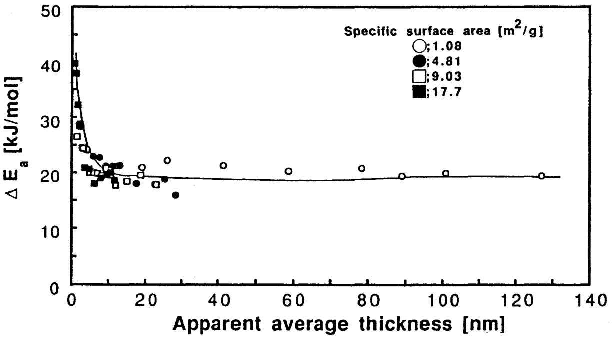

Fig. 7. Variation of ΔE_a with the apparent average thickness of the liquid layer for various kinds of α-Al_2O_3 powders / KNO_3 melt coexisting systems.

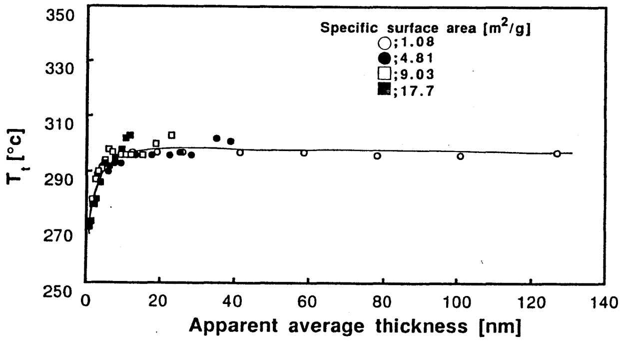

Fig. 8. Variation of the transition temperature for the electrical conductivity with the apparent average thickness of the liquid layer for various kinds of α-Al_2O_3 powders / KNO_3 melt coexisting systems.

DOI: 10.1149/199413.0211PV

Electrical Conductance of Molten Halides

A. A. Red'kin

Institute of High Temperature Electrochemistry
Ural Branch of Russian Academy of Sciences,
620219 S.Kovalevskaya 20, Ekaterinburg, Russia

ABSTRACT

A review of molten halides electrical conductance data is given with special emphasis on new approach to systematisaton of those data. The old ideas about connection of salt's conductivity with the place of element in periodic table are also used in this approach. All salts and mixtures are divided into two groups: ideal and non-ideal. It allow specific conductance of many salts and mixtures to be calculated through molar volume.

IDEAL SALTS AND MIXTURES

Many years ago Biltz and Klemm proposed next classification of molten chlorides according their electrical conductivity using Mendeleev's periodical table (1).

LiCl	$BeCl_2$	BCl_3	CCl_4		
NaCl	$MgCl_2$	$AlCl_3$	$SiCl_4$	PCl_5	
KCl	$CaCl_2$	$ScCl_3$	$TiCl_4$	VCl_5	
RbCl	$SrCl_2$	VCl_3	$ZrCl_4$	$NbCl_5$	$MoCl_5$
CsCl	$BaCl_2$	$LaCl_3$	$HfCl_4$	$TaCl_5$	WCl_6
			$ThCl_4$		UCl_4

The line divides ideal and non-ideal salts. Ideal salts are good ionic conductors in molten state, non-ideal ones are mostly molecular compounds with poor conductivity. The relations recently obtained partly confirm such classification(2). There are a group of molten chlorides with some ideal electrical conductivity described by next equation:

$$\varkappa = A\cdot\exp\ (-B-D/V)/T)\cdot\exp(C/V) \qquad [1]$$

where

$\varkappa$ - specific conductance, $om^{-1}cm^{-1}$
V - molar volume, cm^3/mol
T - temperature, K
A, B, C, D - empirical coefficients

It is valid for a molten chlorides of Li, Na, K, Rb, Cs, La and Fe(2)with Mn(2) also. The equation is valid for alkaline earth chlorides (Ca, Sr, Ba) with coefficient 1.14. Hence this equation is valid for most of molten chlorides described as ideal ionic salts by Biltz and Klemm, but the dividing line must be slightly changed:

LiCl	$BeCl_2$	BCl_3	CCl_4		
NaCl	$MgCl_2$	$AlCl_3$	$SiCl_4$	PCl_5	
KCl	$CaCl_2$	$ScCl_3$	$TiCl_4$	VCl_5	
RbCl	$SrCl_2$	VCl_3	$ZrCl_4$	$NbCl_5$	$MoCl_5$
CsCl	$BaCl_2$	$LaCl_3$	$HfCl_4$	$TaCl_5$	WCl_6
			$ThCl_4$		UCl_4

Now it is possible to create new classification of molten chlorides on the base of previous ones.

A) Ideal ionic salts. It is good conducting melts. At substitution of some cation to other specific conductance in this group varies according inter-ion distance (1/V) change. It means that all these melts (pure salts and mixtures) have close structure frame.

B. Molecular and ionic-molecular salts. It is non-conducting and badly conducting melts.

LiCl	$BeCl_2$	BCl_3	CCl_4		
NaCl	$MgCl_2$	$AlCl_3$	$SiCl_4$	PCl_5	
KCl	$CaCl_2$	$ScCl_3$	$TiCl_4$	VCl_5	
RbCl	$SrCl_2$	VCl_3	$ZrCl_4$	$NbCl_5$	$MoCl_5$
CsCl	$BaCl_2$	$LaCl_3$	$HfCl_4$	$TaCl_5$	WCl_6
			$ThCl_4$		UCl_4
			$MnCl_2$	$FeCl_2$	?

Let's consider a mixtures. If at mixing a salts show additive change of a molar volume and low enthalpy of mixing we can say about ideal mixture. For example such systems as LiCl-NaCl, KCl-NaCl, RbCl-CsCl, $LiCl-LaCl_3$ NaCl-LaCl $LiCl-FeCl_2$, $NaCl-FeCl_2$ meet these conditions and poses ideal conductivity. In case of alkaline earth chlorides mixtures with other ideal chlorides the equation is:

$$\varkappa = A\cdot\exp\ (-B-D/V)/T)\cdot\exp(C/V)\cdot\exp(0.135\cdot N) \qquad [2]$$

Where N - molar faction of alkaline earth chloride

It is valid for mixtures: $LiCl-MeCl_2$ (Me= Ca,Sr,Ba) and $NaCl-MeCl_2$(Me= Ca,Sr,Ba).
The picture is the same for other halides. The empirical coefficients A,B,C,D of equation 1 for fluorides, chlorides, bromides and iodides are shown below

	A	B	C	D	Temp. int.
Fluorides*	5.56	1199	26.2	9551	1000-1400K
Chlorides	4.90	2747	53.7	33724	800-1200K
Bromides	9.63	4041	31.6	93107	800-1200K
Iodides	7.69	4400	59.8	123145	800-1200K
Fluorides(2)	1.83	2617	137.9	14003	1000-1400K

*-except LiF

It is valid for alkali and La halides. When molar volume is less 20 cm^3/mol the dependence $\ln\varkappa$ - 1/V (T=const) become non-linear for fluorides. The equation is of a next type to take into consideration LiF:

$$\varkappa = A\cdot\exp\cdot(-(B-D/V)/T)\cdot\exp(C/V^2) \qquad [3]$$

NON-IDEAL MIXTURES OF IDEAL SALTS

When using eq. 1 for non-ideal (or interacting) systems a calculated results are higher then experimental ones. It can be explained by chemical bond structure change and a ion mobility reduction. The value of the interaction can be evaluated through a thermodynamic parameters such as enthalpy of mixing.

Let's compare the deviations of calculated values of specific conductance from experimental ones for some non-ideal mixtures with enthalpy of mixing for those systems. It is shown on the example of $CsCl-LaCl_3$ on fig. 1 Thermodynamic data are taken from [3], specific conductance and density from (4,5). The general form of such correlation between $\Delta\varkappa$ and ΔH is:

$$\Delta\varkappa = \Delta H \cdot (E - F*N) \qquad [4]$$

where ΔH - enthalpy of mixing
N- molar faction of more heavy salt
E, F - empirical coefficients

For molten chlorides:

$$\Delta\varkappa = \Delta H \cdot (3.74 - 3.52*N) \cdot 10^{-5} \quad \Delta H,\ J/mol \qquad [5]$$

Hence for molten chlorides the general equation is:

$$\varkappa = 4.9 \cdot \exp(-(2747 - 33724/V)/T) \cdot \exp(53.7/V) + \Delta H \cdot (3.74 - 3.52*N)*10^{-5} \qquad [6]$$

It is valid for all alkali chlorides mixtures and also a mixtures of alkali chlorides with La, Fe(2), Mn(2) chlorides. The comparison of calculated and experimental values for some chloride systems are presented in table 1

Table 1. Experimental and calculated on eq.5 specific conductance values.

$CsCl-FeCl_2$ at 1100K.			LiCl-CsCl at 943K		
N2	$\varkappa$exp (6)	$\varkappa$calc	N2	$\varkappa$exp (8)	$\varkappa$calc
0.00	1.48	1.48	0.00	6.06	5.96
0.32	1.06	0.96	0.20	3.37	3.12
0.50	1.08	1.11	0.40	2.06	2.12
0.61	1.25	1.28	0.62	1.70	1.68
0.75	1.49	1.49	0.80	1.25	1.34
1.00	1.79	1.79	1.00	1.19	1.17

Thermodynamic data are taken from articles (9,10), density from (7,8). Sufficient difference between calculated and experimental data takes place for $KCl-LaCl_3$ mixture(fig.2) but the character of this difference maybe shows the dispersion of experimental data.
The coefficients of equation 4 can be obtained for other halides also.

Conclusions

Change of any molten salt parameter takes place according objective laws of nature and can be connected with changing of other parameters for some ideal systems.

Molar volume can be chosen as primary property. Empirical relations allow all other ones to be calculated from molar volume. When we deal with non-ideal systems thermodynamic data are needed.

References

1. W. Biltz W.Klemm. Z. Phys. Chem. 110,318 (1924)

2. A.A. Red"kin, Rasplavy 3,111 (1989)

3. G.N. Papatheodorou, O.J. Cleppa, J.Phys.Chem,78,181(1974)

4. M.V Smirnov, V.P. Stepanov. Collection of works of Institute of Electrocemistry of Ural Branch of USSR Academy of Sciences. Sverdlovsk, 14 ,58(1970)

5. M.V. Smirnov, V.A. Khokhlov, Journal of Applied Chemistry,43,302 (1970)(Russ.)

6. A.A. Red"kin, M.V. Smirnov V.A Khokhlov, Deposited Doc. VINITI No 3286-85 (1985)

7. A.A. Red"kin, M.V. Smirnov, V.A Khokhlov I.A. Sherstobitova, Deposited Doc.,VINITI, No 3286-85(1985).

8. G.Janz et al. J.Phys.Chem. Ref.Data.Molten salts: 4, part 2: Chlorides and mixtures. 1975

9. G.N. Papatheodorou, O.J. Cleppa, J.Inorg. and Nucl. Chem., 33, 1249 (1971)

10 L.S. Hersh, O.J. Cleppa, J. Chem. Phys. 42, 1309 (1965)

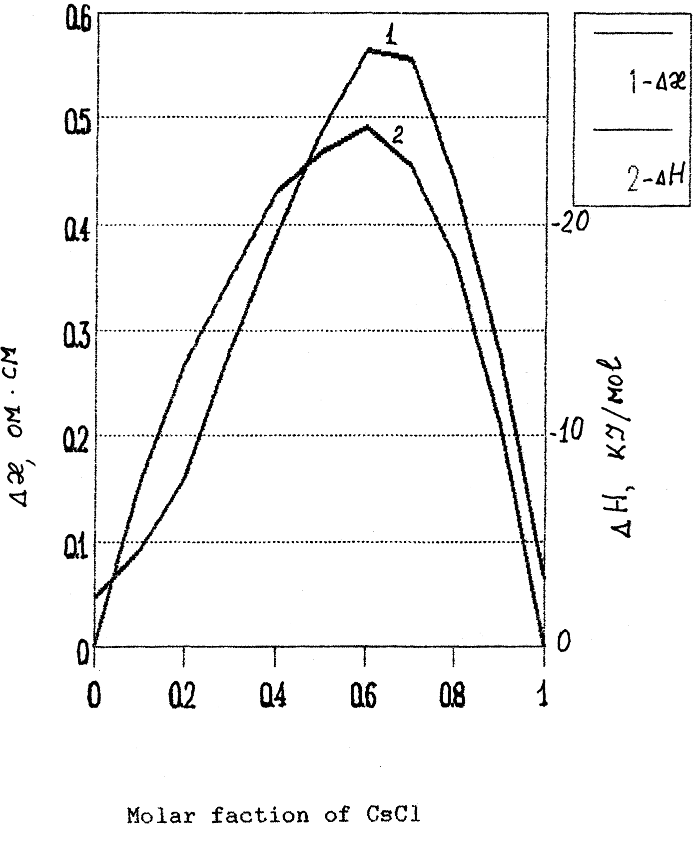

Fig. 1. The correlation between enthalpy of mixing and Δϰ for CsCl-LaCl$_3$

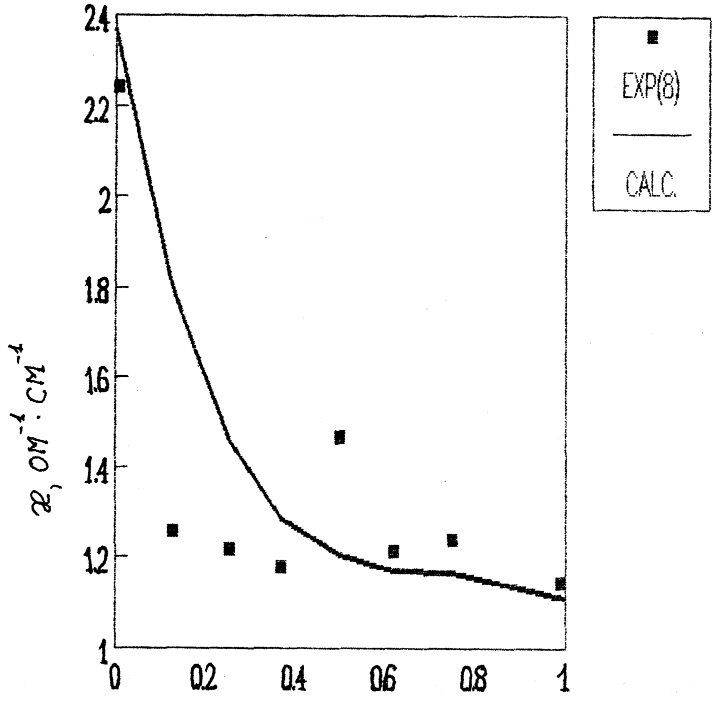

Molar faction of $LaCl_3$

Fig. 2. The comparison of experimental and calculated data for $KCl-LaCl_3$

DOI: 10.1149/199413.0218PV

RAMAN SPECTROSCOPY OF ROOM TEMPERATURE ORGANOCHLOROALUMINATE MOLTEN SALTS.

B. Gilbert and J-P. Pauly
Université de Liège, Laboratoire de Chimie Analytique B6
Sart Tilman, B-4000 Liège, Belgium
Y. Chauvin and F. Di Marco-Van Tiggelen
Institut Français du Pétrole
BP 311, 92506 Rueil-Malmaison, France

ABSTRACT

Organochloroaluminate salts based on mixtures of $(Ethyl)_nAlCl_{(3-n)}$ (n=1 to 3) with 1-methyl-3-butyl-imidazolium chloride (BMIC) are liquid near room temperature in a very large composition range. In the case of mixtures made with $(Et_2AlCl)_2$ and $(Et_3Al)_2$ demixion occurs above 0.75 mole fraction of the organoaluminium. The structural properties of all these mixtures have been studied by Raman spectroscopy and compared with the ones of classical chloroaluminate melts. They form mono and polynuclear anions and a whole new family of species has been identified. It was also found that the tendency to polymerize decreases with the increase of ethyl groups number. Because of the complexity of the spectra, the existence and the stoichiometry of the various species have been confirmed by a quantitative study of the bands intensity variation as a function of the composition.

INTRODUCTION

Mixtures of aluminium trichloride with organic chlorides have been shown to form liquids at room temperature over wide composition ranges (1-5). Recently, organic derivatives of aluminium trichloride have called the attention as presenting particularly interesting properties. For instance, ethylaluminium dichloride $(EtAlCl_2)_2$ is a good reducing reagent capable of removing the proton impurities present in the room temperature chloroaluminate melts (6). Secondly, by mixing the organoaluminium chloride with an alkylpyridinium chloride or alkylimidazolium chloride, new molten salts are formed, also liquid at room temperature (7). These systems have been proved as very good solvents for the catalytic dimerization of propene into hexenes isomers by nickel complexes (8).

As it is the case for all chloroaluminate systems, the acid-base properties of the new mixtures are expected to be very depending on the composition, i.e. on the structure of the solvent. Initial structural studies have been made on the $EtAlCl_2$ - 1-butyl-3 methylimidazolium chloride (BMIC) mixtures. From Raman spectrometry, it was first proposed that monomer, dimer and trimer anions, analogous to those found in the usual chloroaluminates, are formed in the liquid (7). A recent study from ^{27}Al NMR concluded also to the formation of anions but these anions are in equilibrium with an excess of $EtAlCl_2$ dimer, even in an equimolar composition mixture (9). This latter interpretation however is not in agreement with the Raman data neither with the recent measurements of the aluminium electronegativity by ^1H NMR (10).

Finally, these molten salts are good solvents for inorganic salts but do not dissolve hydrocarbons. They are consequently good candidates for a two-phase catalysis process where one can take advantage of the solubility of an organometallic catalyst and the insolubility of the products of the catalytic reaction. These products can then be extracted on a continuous basis. However, it has been known for a long time that contacting alkylaluminium chloride compounds with bases such as alkali metal halides (11) or ethers (12) results in disproportionation of the alkylaluminium into compounds containing more and less chloride. Similarly, due to the total miscibility of the chloroethylaluminium compounds and hydrocarbons, disproportionation could be expected when a molten salt based on dialkylimidazolium chloride and alkylaluminium chloride is contacted with an hydrocarbon. It is then very important to be able to characterize all the species involved in this process.

This paper describes the Raman spectra of mixtures made of $(Ethyl)_nAlCl_{(3-n)}$ (n=0 to 3) mixed with BMIC as a function of their composition. The mixed salts formed with Al_2Cl_6 and $(EtAlCl_2)_2$ or $(EtAlCl_2)_2$ and $(Et_2AlCl)_2$ are also considered.

EXPERIMENTAL

All chemical manipulations were conducted in a glove box with a water and oxygen content below one ppm. The organic chlorides have been prepared as described previously (7). The 1-butyl-3-methylimidazolium chloride has been chosen instead of the more commonly used 1-ethyl-3-methylimidazolium chloride because its synthesis involves less hazard. The resulting solid is recrystallized from an acetonitrile-toluene mixture. Aluminium chloride was sublimed twice, first on aluminium powder and sodium chloride, then on sodium chloride. $(EtAlCl_2)_2$, $(Et_2AlCl)_2$ and $(Et_3Al)_2$ (Schering A.G.) were distilled in a vacuum tight apparatus before use.

The molten mixtures were prepared by weighing the required amounts of BMIC and the aluminium compound in a dry box. Upon mixing, the solids melt and a strongly exothermic reaction occurs. Only small amounts of melts were then prepared at one time (0.5-1 g) resulting in colorless solutions, stable for months.

The melts were placed into 1 cm square glass tubing cells which were sealed or closed with vacuum-tight grease free fittings. If necessary, the spectra of the melts could be recorded at higher temperature with a furnace similar to the one already described (13) but provided with a much better temperature controller (± 0.2 °C). The spectra were recorded with a modified Cary 81 spectrometer interfaced to a computer allowing fast recording rates and full data treatment (13). Slit widths from 2 to 4 cm^{-1} and a time constant of 0.1 sec. were used depending on the bands intensities. No smoothing was applied to any of the spectra.

RESULTS AND DISCUSSION

When a pyridinium or imidazolium chloride is mixed with $AlCl_3$, it has been shown that the well-known $AlCl_4^-$ and $Al_2Cl_7^-$ anions are formed in equilibrium and their relative proportion depends on the melt composition (3). The Raman spectra of such mixtures are quite difficult to obtain because of fluorescence originating from organic impurities. However, by improving the purification of the starting materials, it is now possible to record good quality spectra on such systems. Fig. 1 shows the Raman spectrum of $Al_2Cl_7^-$ which has never been published in details. In this spectrum, eleven bands (noted by a capital letter) can be assigned to $Al_2Cl_7^-$, the other belonging either to the organic cation or to some $AlCl_4^-$. Because only six bands are expected for a linear molecule (of D_{3d} symmetry), this result confirms that the anion must be bent, as already suggested (14). However, a non-linear molecule (symmetry C_s) is expected to present 21 Raman active modes and ten lines are then too weak or hidden by others. This emphasizes the difficulty of deducing a symmetry for a molecule simply by counting the number of experimental bands with their polarization state.

During our study of $EtAlCl_2$ -BMIC mixtures, we have shown that another technique can be applied to deduce the stoichiometry of species in equilibrium (7). It involves the quantitative measurement of the intensity ratios of two bands, each characteristic of one species, as a function of the mixture composition. In the present case, this ratio has been measured for the 349 cm^{-1} band of $AlCl_4^-$ and the 307 cm^{-1} band of $Al_2Cl_7^-$ at various melt compositions (Fig.2). If the model is correct, this ratio should be proportional to the ratio of the amounts of concerned species:

$$R = \frac{I_{307}}{I_{349}} = K \frac{[Al_2Cl_7^-]}{[AlCl_4^-]}$$

The ratios [$Al_2Cl_7^-$]/[$AlCl_4^-$] is readily calculated from the assumed stoichiometry and mass balance consideration. Fig. 3 shows a plot of the measured intensity ratios versus the respective calculated concentration ratios. A straight line is observed indicating that the model is indeed correct. In addition, the slope of that line represents the ratio of the scattering efficiencies of the species of concern. Here, the experimental ratio is 0.87 ± 0.02, which means that the main vibration of $Al_2Cl_7^-$ scatters less per mole than the corresponding one of $AlCl_4^-$.

In the case of $EtAlCl_2$-BMIC mixtures, a straight line was also observed in similar conditions, indicating that the reaction $EtAlCl_3^- + EtAlCl_2 \rightarrow Et_2AlCl_5^-$ is quantitative, at least up to a composition of 0.66 (expressed in mole fraction N) (7). It should be noted that this latter result and the recent aluminium electronegativity measurements (10) do not agree with the work of Keller et al. (9) where it is proposed that $EtAlCl_2$ dimer exists as major species even in a 1:1 melt. From our measurements, a 1:1 or more basic mixture never showed any of the very characteristic $(EtAlCl_2)_2$ bands. Fig. 4 shows that these two spectra are clearly distinct.

Because of their possible interest in the two-phase catalysis, the Et_2AlCl-BMIC and Et_3Al-BMIC mixtures which are also liquid at room temperature have been investigated as well. The spectra of 1:1 mixtures were found totally different than the ones of corresponding pure ethylaluminium compound (Fig.5 and 6). In addition, if the amount of BMIC is further increased, the main spectrum stays unchanged, only the intensity of the BMI^+ cation bands increases. We have then assumed that the $AlCl_4^-$ equivalent species are formed, i.e. $Et_2AlCl_2^-$ and Et_3AlCl^- respectively. These species are characterized by their main band at 366 and 492 cm^{-1} respectively.

When Et_2AlCl is added to a 1:1 Et_2AlCl-BMIC mixture, the bands assigned to $Et_2AlCl_2^-$ are progressively replaced by another distinct spectrum which is not the one of Et_2AlCl (Fig. 7). By analogy to the behaviour of the other above systems, this new species has been assumed as $(Et_2AlCl)_2Cl^-$; it exhibits one major band at 410 cm^{-1} and a weaker one at 366. In this case, the 366 cm^{-1} band of $(Et_2AlCl)_2Cl^-$ overlaps with the intense band of $Et_2AlCl_2^-$. However, because the spectrum of $Et_2AlCl_2^-$ can be obtained alone, it can be easily quantitatively subtracted from each spectrum of Fig. 7. The intensity ratio of all the resulting bands stays constant at any composition up to N= 0.67, a proof of the existence of only one additional species. The same quantitative procedure described above for $Al_2Cl_7^-$ has then been applied to the intensity ratios of the 410 cm^{-1} band of the hypothetical $(Et_2AlCl)_2Cl^-$ over the 366 cm^{-1} band of $Et_2AlCl_2^-$. A straight line is obtained between these ratios and the calculated amounts of species showing that the following reaction should occur:

$$(Et_2AlCl)Cl^- + Et_2AlCl \rightarrow (Et_2AlCl)_2Cl^-$$

Upon addition of Et_3Al to a 1:1 Et_3Al-BMIC mixture, the shape of the Et_3AlCl^- spectrum does not change very much except that the main 493 cm^{-1} band intensity seems to increase. In order to solve this problem, we have added to each investigated mixture an internal intensity standard. This standard must be miscible, inert and should not exhibit any band in the region of interest. We then chose to refer all intensity measurements to the intensity of the 992 cm^{-1} band of C_6H_6 whose concentration was kept constant in each mixture. Examples of such spectra are shown in Fig.8 where it can be seen that the 493 cm^{-1} band intensity increases regularly with the Et_3Al addition. We then proposed that this band is made of two components: one is the Et_3AlCl^- which decreases progressively and is replaced by the bridged $(Et_3Al)_2Cl^-$. Again, the intensity ratios of the two components, obtained by computer, were found directly proportional to the expected amounts calculated from the reaction:

$$(Et_3Al)Cl^- + Et_3Al \rightarrow (Et_3Al)_2Cl^-$$

The above considerations are valid for compositions up to N=0.66. Above 0.66, it has been shown that the $AlCl_3$ based mixtures contain, in addition to $AlCl_4^-$ and $Al_2Cl_7^-$, $Al_3Cl_{10}^-$ trimers. The composition range where the mixture stays liquid is however very limited (15-17). In the $EtAlCl_2$-BMIC mixtures, trimers are also formed but they are rapidly replaced by $(EtAlCl_2)_2$ which is miscible all the way up to pure $(EtAlCl_2)_2$ (7).

For the Et_2AlCl-BMIC and Et_3Al-BMIC mixtures where N>0.66, the spectra can be interpreted respectively as mixtures of $(Et_2AlCl)_2Cl^-$ or $(Et_3Al)_2Cl^-$ with $(Et_2AlCl)_2$ or $(Et_3Al)_2$. No trimer was found and demixion occurs at N=0.8 (Et_2AlCl) or N=0.75 (Et_3Al). The demixed phase is made of the corresponding pure ethylaluminium.

All these experiments have allowed to measure the scattering efficiencies within each couple $(Ethyl)_nAlCl_{(3-n)}Cl^-$ / $((Ethyl)_nAlCl_{(3-n)})_2Cl^-$ (n=0 to 3). In order to determine the concentration of any such species involved in a reaction, it is necessary to measure the scattering efficiencies of the various couples versus each other. In this purpose, we have prepared mixed salts formed from Al_2Cl_6 and $(EtAlCl_2)_2$ or $(EtAlCl_2)_2$ and $(Et_2AlCl)_2$. Fig.9 shows the spectrum obtained by mixing a 0.5:0.5:1 $AlCl_3$-$EtAlCl_2$-BMIC mixture (spectrum A). This spectrum exhibits only the characteristic bands of $AlCl_4^-$ and $EtAlCl_3^-$ and no other species is observed. Consequently, the number of mole of each species must be the same and the ratio of scattering coefficients is simply the ratio of the heights of the respective ν_1 major bands. A similar experiment has been made with a 0.5:0.5:1 $EtAlCl_2$-Et_2AlCl-BMIC mixture to measure the relative scattering coefficients between $EtAlCl_3^-$ and $Et_2AlCl_2^-$. Finally, all the scattering coefficients have been expressed versus a common reference, the ν_1 $AlCl_4^-$ band.

To complete this study, we have recorded the spectra of mixed acidic systems. First, an equimolar $EtAlCl_2$ and Et_2AlCl mixture of global Lewis acid composition N=0.66 exhibits a spectrum of its own (characterized by a main band at 366 cm^{-1}, Fig.10 A) which corresponds most probably to the mixed dimer $(EtAlCl_2)(Et_2AlCl)Cl^-$. If this spectrum ressembles the one of $Et_2AlCl_2^-$, the confusion is not possible because several strong bands are present which do not belong to any known species up to now. Secondly, the equivalent mixture made from $AlCl_3$ and $EtAlCl_2$ is more complex (Fig. 10 B). From a detailed analysis of this figure, one can indeed recognize the main bands of $Al_2Cl_7^-$ (307 cm^{-1}) and of $(EtAlCl_2)_2^-$ (349 cm^{-1}). By subtracting these two spectra from the original, a third spectrum is left (main band at 333 cm^{-1}) which belongs to the mixed dimer $(AlCl_3)(EtAlCl_2)Cl^-$. Hence, this dimer is not totally stable and dissociates through the following reaction:

$$2\,(AlCl_3)(EtAlCl_2)Cl^- \rightleftharpoons Al_2Cl_7^- + (EtAlCl_2)_2^-$$

which also means that the association of $EtAlCl_2$ with $AlCl_3$ is not as strong as with Et_2AlCl.

As general conclusion, if our interpretations are correct, the ethylaluminium derivatives mixed with an organic chloride form a new class of ionic mixtures with a behaviour very similar to the one of regular chloroaluminates. All the identified species have been collected in table I as a function of the composition. In addition, it is now possible by Raman spectroscopy to identify and quantify any of the reaction products involved in an industrial process based on these melts. Because of the overlap of some of the major bands, this identification and quantification can be made safely by considering the full spectrum of one given species and not the main bands only.

REFERENCES

1. F.H. Hurley and T.P. Wier, J. Electrochem. Soc., 98, 203 (1951).
2. C.L. Hussey, in Advances in Molten Salt Chemistry, Vol 5, ed. G. Mamantov, Elsevier, p.185 (1983) .
3. R.J. Gale, B. Gilbert and R.A. Osteryoung, Inorg. Chem., 17, 2728. (1978).
4. J. Robinson and R.A. Osteryoung, J. Am. Chem. Soc., 101, 323 (1979).
5. J.S. Wilkes, J.A. Levisky, R.A. Wilson and C.L. Hussey, Inorg. Chem., 21, 1263 (1982) 6. T.A. Zawodzinski, R.T. Carlin and R.A. Osteryoung, Anal. Chem., 59, 2639 (1987)
7. B. Gilbert, Y. Chauvin and I. Guibard, Vib. Spectrosc. 1, 299, (1991)
8. Y. Chauvin, B. Gilbert, I. Guibard, J. Chem. Soc. Chem. Commun., 1715 (1990); Olivier H., Chauvin Y., Hirschauer A., San Francisco A.C.S. Meeting, April 5-10, (1992); Division of Petroleum Chemistry, Preprint Vol. 37, N°3, 780-785.
9. C.E. Keller, W.R. Carper and B.J. Piersma, Inorg. Chim. Acta, 209, 239 (1993)
10. Y. Chauvin, F. Di Marco-Van tiggelen and H. Olivier, J. Chem. Soc. Dalton Trans. 1009 (1993).
11. K. Ziegler, Organoaluminium Compounds in Organo-metallic Chemistry, Reinhold Publishing Co., New York,p 194, 269 (1960).
12. H. Lehmkuhl, Angew. Chem. Internat. Ed., 3, 107 (1964).
13. B. Gilbert and T. Materne, Appl. Spectr., 44, 299 (1990).
14. R.J. Gale and R.A. Osteryoung, Inorg. Chem.,19, 2240 (1980)
15. G. Torsi, G. Mamantov and G.M. Begun, Inorg. Nucl. Chem. Letters 6, 553 (1970)
16. C.J. Dymek jr., J.S. Wilkes, M.A. Einarsrud, H.A. Øye, Polyhedron ,7,1139 (1988)
17. A.K. Abdul-Sada, A.M. Greenway, K.R. Seddon and T. Welton, Org. Mass Spectrometry 24, 917 (1989)

Table I: ***Species identified from the Raman spectra***

EADC = $EtAlCl_2$; DEAC = Et_2AlCl; TEA= Et_3Al

Cl^- $AlCl_4^-$	$AlCl_4^-$ $Al_2Cl_7^-$	$Al_2Cl_7^-$ $Al_3Cl_{10}^-$		*MIXED SPECIES*
Cl^- $(EADC)Cl^-$	$(EADC)Cl^-$ $(EADC)_2Cl^-$	$(EADC)_2Cl^-$ $(EADC)_3Cl^-$	$(EADC)_3Cl^-$	$(AlCl_3)(EADC)Cl^-$
Cl^- $(DEAC)Cl^-$	$(DEAC)Cl^-$ $(DEAC)_2Cl^-$	$(DEAC)_2Cl^-$ DEAC	$(DEAC)_2Cl^-$ DEAC	$(EADC)(DEAC)Cl^-$
Cl^- $(TEA)Cl^-$	$(TEA)Cl^-$ $(TEA)_2Cl^-$	$(TEA)_2Cl^-$ TEA		(EADC)(DEAC)

0 0.50 0.67 0.75 1

Mole fraction of $(Ethyl)_nAlCl_{(3-n)}$ (n=0 to 3)

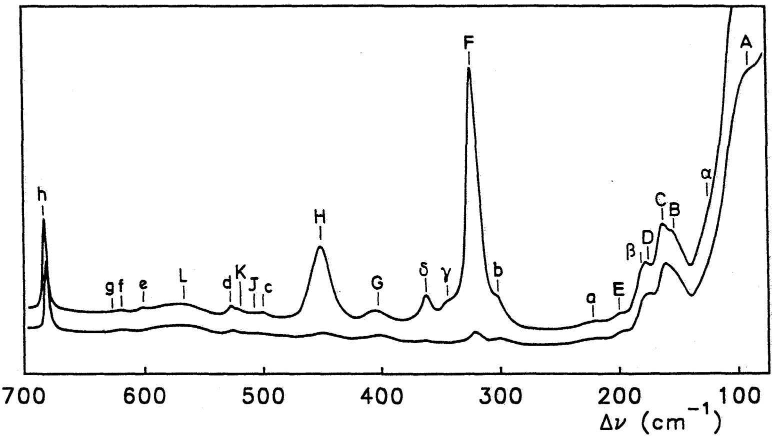

Fig. 1: Raman spectrum of the $Al_2Cl_7^-$ anion; capital letters: $Al_2Cl_7^-$; lowercase letters: organic cation (butyl pyridinium); greek letters: $AlCl_4^-$ and $Al_3Cl_{10}^-$.

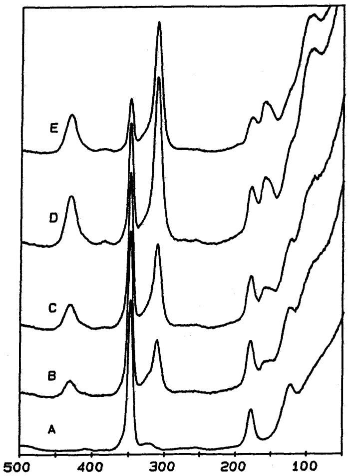

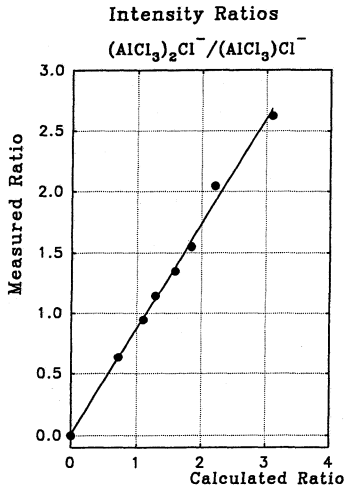

Fig.2: Raman spectra of $AlCl_3$-BMIC mixtures at various compositions N = respectively A: 0.475; B: 0.56; C: 0.582; D: 0.617; E: 0.639

Fig.3: Plot of the I_{307}/I_{349} ratio as a function of the $Al_2Cl_7^-/AlCl_4^-$ calculated ratio.

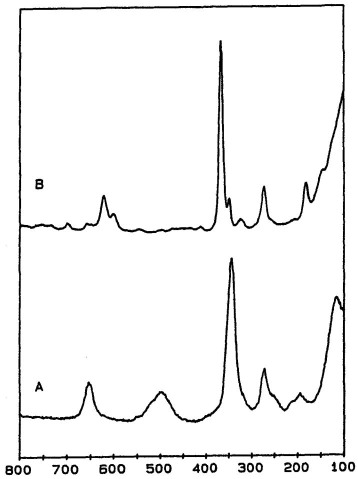

Fig.4: Raman spectra of A: pure $(EtAlCl_2)_2$
B: $EtAlCl_2$-BMIC 1:1 mixture

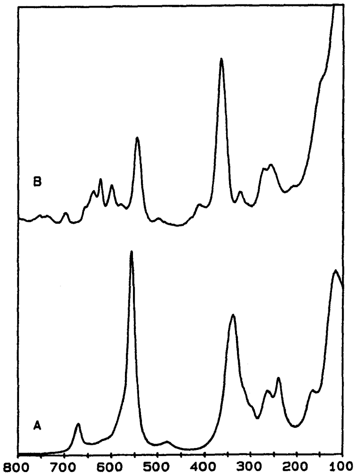

Fig.5: Raman spectra of A: pure $(Et_2AlCl)_2$
B: Et_2AlCl-BMIC 1:1 mixture

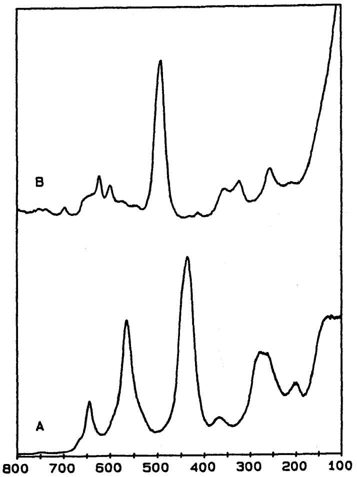

Fig.6: Raman spectra of A: pure $(Et_3Al)_2$
B: Et_3Al-BMIC 1:1 mixture

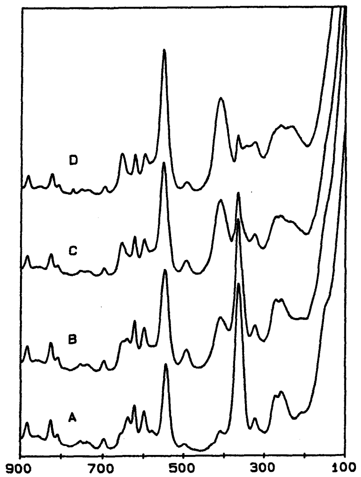

Fig.7: Raman spectra of Et_2AlC-BMIC mixtures at various compositions
N = respectively: A: 0.495; B: 0.572;
C: 0.631; D: 0.675

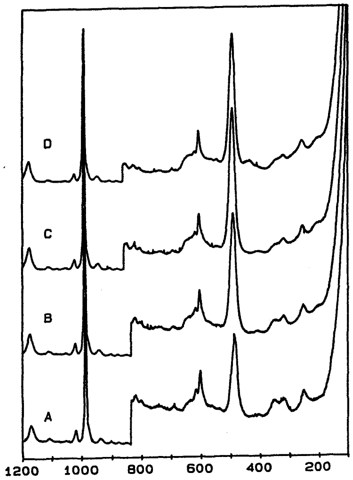

Fig.8: Raman spectra of Et_3Al-BMIC mixtures
with C_6H_6 as internal intensity standard:
N = : A: 0.5; B: 0.588; C: 0.649; D: 0.708
From 800 cm^{-1},the sensitivity is reduced 5 times

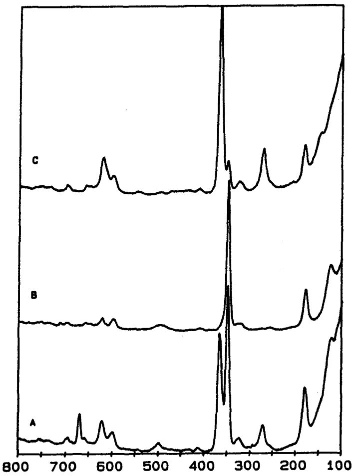

Fig.9: Raman spectra of:
A: $AlCl_3$-$EtAlCl_2$-BMIC 0.5:0.5:1
B: $EtAlCl_2$-BMIC 1:1
C: $AlCl_3$-BMIC 1:1

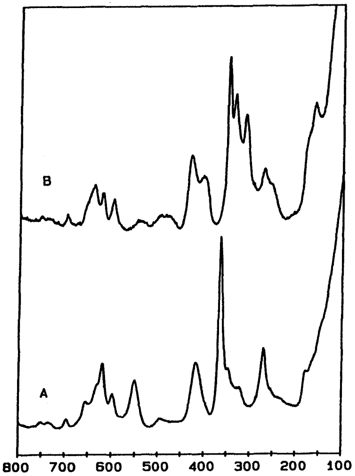

Fig. 10 Raman spectra of:
A: $EtAlCl_2$-Et_2AlCl-BMIC 1:1:1 mixture
B: $AlCl_3$-$EtAlCl_2$-BMIC 1:1:1 mixture

DOI: 10.1149/199413.0227PV

Raman Studies of Species Formation in Solid and Liquid Phases from Molten Salt Mixtures

M. H. Brooker, J. Johnson, A. Shabana and J. Wang

Chemistry Department
Memorial University of Newfoundland
Canada, A1B 3X7

ABSTRACT

Raman spectra have been obtain for alkali metal chloride mixtures with magnesium, manganese, zinc, cadmium and lead chlorides both as liquids and solids over a wide range of temperatures. Although the discrete ions $CdCl_4^{2-}$ and $CdCl_6^{4-}$ were identified in the solids Cs_2CdCl_4 and K_4CdCl_6 the molten salt appeared to retain an average tetrahedral coordination at all compositions. Evidence is presented for a two species equilibrium in the magnesium system ($MCl_4^{2-} \rightleftarrows M_2Cl_7^{3-}$) but the chloride exchange process is too fast to detect similar species in the other melts. The similarity of the spectrum of solid Na_3AlF_6 to that of the molten phase indicated that fusion occurred with retention of octahedral coordination. The need for excellent depolarization data and normalization factors to account for temperature and frequency dependence of Raman intensity will be emphasized.

INTRODUCTION

Raman spectroscopy is being used to characterize species formed in molten salt mixtures and to follow the liquid-solid and solid-solid phase equilibria that result from cooling the melts. The presence or absence of discrete molecular ion species in molten salts can often be deduced from Raman spectra but the assignment gains considerable credibility if the the discrete molecular ion can be isolated in a crystal structure(1,2). A major goal of the work is to establish Raman spectroscopy as an analytical tool in the measurement of equilibrium concentrations in molten media.

Raman spectroscopy has gained acceptance as a reliable technique for the identification of discrete species in molten salts and there have been attempts to develop Raman intensity methods for quantitative or at least semi-quantitative analysis. However, it must be emphasized that the actual quantity measured in the Raman experiment, the scattering cross section, $\partial\sigma/\partial\Omega$ has both temperature and frequency dependent factors that are especially important in the low wavenumber region of the spectrum at the high sample temperature normally employed for molten salts(1-4). Raman bands measured in the scattering cross section spectrum have an intrinsic asymmetry on the low wavenumber side that must not be confused with a new component or new species. Even relative intensities of two separate bands are temperature dependent. Several groups have recommended the use of a normalized or reduced intensity, $R(\omega)$ to create a spectrum that is directly proportional to the intrinsic Raman scattering activity. Within the double harmonic approximation the use of the $R(\omega)$ spectrum removes a temperature and frequency dependent band asymmetry and permits comparison of spectra obtained at different temperatures(3,4). Comparison of Raman spectra with and without the normalization factors has emphasized the need for these factors prior to detailed bandshape analysis. Furthermore, depolarization measurements permit the separation of Raman intensity into isotropic and anisotropic components. Deconvolution procedures to resolve overlapped bands are best performed on the isotropic intensity.

Raman spectroscopy is a very fast process and that is one of its advantages. Even collision encounters that last for only a few picoseconds may be sticky enough for an ion-pair to vibrate several times and give rise to Raman intensity. However this property also presents the problem of how to account for the Raman intensity in terms of a species with a defined geometry or symmetry. Environmental broadening and possible exchange broadening may result in a broad symmetric Raman band that by itself cannot provide information on species geometry or even coordination number. The molten alkali metal halides and their mixtures represent the extreme example of Raman scattering at the detection limit(5,6). Polarized Raman intensity indicates the presence of a symmetric stretching mode of some entity but the concept of a species with a defined geometry has little meaning. Interpretations based on lattice models can be misleading because they tend to under-emphasize the dynamic properties and infer too much order.

EXPERIMENTAL

Raman spectra were measured with a Coderg PHO Raman spectrophotometer. The 514.5nm (500 mW, green) and 488.0nm (500mW, blue) line of a Control laser model 52 system were used to excite the sample. Plasma lines were removed with a narrow band-pass interference filter. Peak positions were calibrated against laser plasma lines. The slit widths were set at 2.0 cm^{-1} . Raman spectra from chlorides were obtained for samples in quartz glass tubes with 6 mm id. Fluoride sample were held in a graphite windowless cell which was sealed in a quartz tube. The tube walls were masked to reduce reflection and Raman scattering from the glass. Spectra were recorded for samples in a furnace with the temperature at the sample regulated to ±5 K. Raman spectra from the molten salts were obtained for $I_{||}$ and $I_{\perp}$ polarizations for orientations x(zz)y and x(zx)y. Polarization of the incident beam was controlled by a half-wave plate and the 90° scattered light was analyzed with Polaroid films which accepted parallel or perpendicular polarized light. A quarter wave-plate before the entrance slit served to compensate for grating polarization preference.

The Raman scattered light was detected with a PMT cooled to 250 K. Digital data files were created by integration of the photon counts with a home-built box-car averager interfaced to the Memorial University VAX 8800 computer. At least five identical sets of data were collected for each spectrum. Spectra were signal averaged and smoothed once with a three point Savitsky- Golay smoothing function. A baseline program was applied which corrected the measured intensity for the fourth power frequency factor and then set the lowest data point to zero and the highest data point to 999 on a relative intensity scale. This form of the data is defined as our $I(\omega)$ spectrum which should be independent of excitation frequency. The same baseline program was applied with the option to correct for the fourth power scattering factor, the temperature factor, $B = [1-\exp(-hc\,\omega/kT)]$ and the frequency factor, ω, to give the reduced or $R(\omega)$ spectrum which is directly proportional to a point by point relative scattering activity, $S_Q(\omega)$ in terms of mass weighted normal coordinates, Q , in the double harmonic approximation. $R_Q(\omega)$ is the form of the Raman spectrum that most closely approaches the vibrational density of states (1,3,4). The relationship between the $I(\omega)$ and $R_Q(\omega)$ forms of the spectra is given by Eq. 1.

$$S_Q(\omega) \propto R_Q(\omega) = I(\omega) \bullet \omega \bullet B \tag{1.}$$

It is our preference to plot the spectrum in the $R_Q(\omega)$ form because the Bose-Einstein factor removes the state dependent temperature factor of the excited state transitions and leaves the effect that is due to concentration changes.

DISCUSSION

In molten solutions of divalent metal chlorides with excess alkali metal chloride(mol ratio ACl to MCl_2 of 2 or more) there is strong evidence from the Raman spectra for the presence of MCl_4^{2-} ions. The characteristic four band spectrum was observed for molten mixtures of CsCl and $MgCl_2$, $MnCl_2$, $ZnCl_2$, $CdCl_2$, $PbCl_2$(Table 1). The frequency of the polarized ν_1 band has a value that reflects the magnitude of the force constant for the M-Cl bond since the symmetric stretching motion of the tetrahedron does not involve motion of the metal. On the other hand both ν_3 and ν_4 will have a large mass dependence. It can be seen(Table 1.) that the ν_3 band decreased with increased mass of M and becomes almost coincident with ν_1 for manganese, zinc and cadmium and less than ν_1 for lead. For a similar reason the ν_4 tends to shift into accidental coincidence with ν_2 for the heavier cations.

Table 1. Peak maxima and halfwidths(parenthses) in cm^{-1} for MCl_4^{2-} ions.

$MgCl_4^{2-}$	$MnCl_4^{2-}$	$ZnCl_4^{2-}$	$CdCl_4^{2-}$	$PbCl_4^{2-}$	assignment
$MgCl_2$ in 4CsCl	$MnCl_2$ in 3CsCl	$ZnCl_2$ in 2CsCl	$CdCl_2$ in 3CsCl	$PbCl_2$ in 3CsCl	
840 K	844 K	925 K	780 K	835 K	
110(50)			100(58)		ν_2 (E)
	123(80)	128(61)		118(98)	ν_2(E) + ν_4(F)
147(32)			134(71)		ν_4 (F)
251(23)	255(37)	280(45)	261(34)	235(55)	ν_1 (A)
350(100)	268(88)	285(80)	256(76)	217(109)	ν_3 (F)

Raman spectra measured for alkali metal chloride mixtures with magnesium chloride exhibited two symmetric stretching bands which can be interpreted in terms of a two species equilibrium ($MgCl_4^{2-}$ and $Mg_2Cl_7^{3-}$). For instance the Raman spectra of the 1:1 mixture of CsCl and $MgCl_2$ clearly show the presence of two bands at about 225 and 250 cm^{-1}(Fig. 1). Curve analysis routines applied to the $R(\omega)_{iso}$ spectrum(Fig. 2) indicated a third band was necessary at 295 cm^{-1} to achieve the good fit. The intensity of bands at 225 and 295 cm^{-1} increased by the same proportion with the increase in the ratio of $MgCl_2$ to CsCl and were assigned to the two symmetric stretching modes of the $Mg_2Cl_7^{3-}$ polynuclear species. Similar three band spectra were measured for mixtures of $MgCl_2$ with RbCl and KCl but the halfwidths of the component bands were greater for the smaller cations and the band overlap was more severe. For mixtures of $MgCl_2$ with NaCl and LiCl it was no longer possible to identify separate components. Raman spectra from molten alkali metal mixtures with cadmium, manganese zinc and lead chloride melts did not show evidence for two bands in the symmetric stretching region for any mixtures. The Raman spectrum of the 1:1 CsCl + $MnCl_2$ melt(Fig. 3) gave only a single maximum and could be curve-fit to a single component. The peak maxima for the molten mixtures with manganese, zinc, cadmium and lead remained near the values for the MCl_4^{2-} of the melts with excess chloride which suggests that these metal ions retained an average tetrahedral coordination over the complete composition range. Retention of tetrahedral coordination would require chloride bridges similar to that proposed for the $Mg_2Cl_7^{3-}$ species. It would appear that for chloride melts which contain manganese, zinc, cadmium and lead the environmental and exchange broadening resulted in a single average symmetric stretching band from which unequivocal inferences about the geometry were not possible.

Assignments have been assisted by identification of characteristic bands due to the discrete tetrahedral and octahedral ions in crystals. It was possible to identify discrete MCl_4^{2-} ions in Cs_2MgCl_4, Cs_2MnCl_4, Cs_2ZnCl_4 and a high temperature form of solid Cs_2CdCl_4. It was possible to identify discrete MCl_6^{4-} ions in solid K_4CdCl_6 and K_4PbCl_6.

Raman spectra are presented for solid Na_3AlF_6 at temperatures over the phase transition(845 K) at which temperature the peak maximum of the intense band near 550 cm^{-1} increased suddenly by 2 cm^{-1}(Fig. 4). Raman spectra(Fig. 5) for molten Na_3AlF_6 are dominated by an intense, broad polarized band centered at 556 cm^{-1}. Curve resolution of the band in the $R(\omega)_{iso}$ spectrum was achieved with a two band fit for bands at 550 and 622 cm^{-1}. The $R(\omega)_{iso}$ spectrum has the advantage of a natural flat baseline because the overlap with $\nu_2 + \nu_5$ and the thermal background increase present in $R_{||}$ have been removed from the $R(\omega)_{iso}$ spectrum. The similarity of the Raman spectra of solid and molten cryolite indicated that the octahedral AlF_6^{3-} ion present in the solid was retained into the melt although the presence of a band at 622 cm^{-1} due to AlF_4^- indicated some dissociation. The large halfwidth of the band due to AlF_6^{3-} indicates considerable environmental broadening perhaps with a contribution due to fast ligand exchange. A broad polarized intensity with a maximum at about 200 cm^{-1} was assigned to interactions between sodium and fluoride ions much like those which gives rise to polarized intensity in the pure alkali metal chloride melts. The temperature and frequency dependent normalization factors for Raman intensity were found to be important even to 600 cm^{-1} for molten cryolite at 1300 K. There was no evidence to justify the deconvolution of the broad polarized band into three components as has been proposed(7). The original interpretation(8) of for the spectrum of cryolites is supported by the present work.

ACKNOWLEDGMENTS

The work was supported by a Research Grants from the Natural Science and Engineering Research Council of Canada.

REFERENCES

1. M. H. Brooker and G. N. Papatheodorou, in "Advances in Molten Salt Chemistry, edited by G. Mamantov, (Elsevier, Amsterdam,1983) Vol.5.
2. M. H. Brooker and J. Wang, J. Raman Spectrosc. **23**, 471 (1992)
3. M. H. Brooker, O. Faurskov Nielsen and E. Praestgaard, J. Raman Spectrosc. **19**, 71 (1988).
4. W. F. Murphy, M. H. Brooker, O. Faurskov Nielsen, E. Praestgaard and J. E. Bertie, J. Raman Spectrosc. **20**, 695 (1989).
5. E. W. J. Mitchell and C. Raptis, J. Phys. C, **16**, 2973 (1983).
6. W. Rudolph and M. H. Brooker, these proceedings.
7. B. Gilbert, G. Mamantov and G. M. Begun, J. Phys. Chem. **62**, 950 (1975).
8. B. Gilbert and T. Materne, Appl. Spectrosc.**44** 299 (1990).

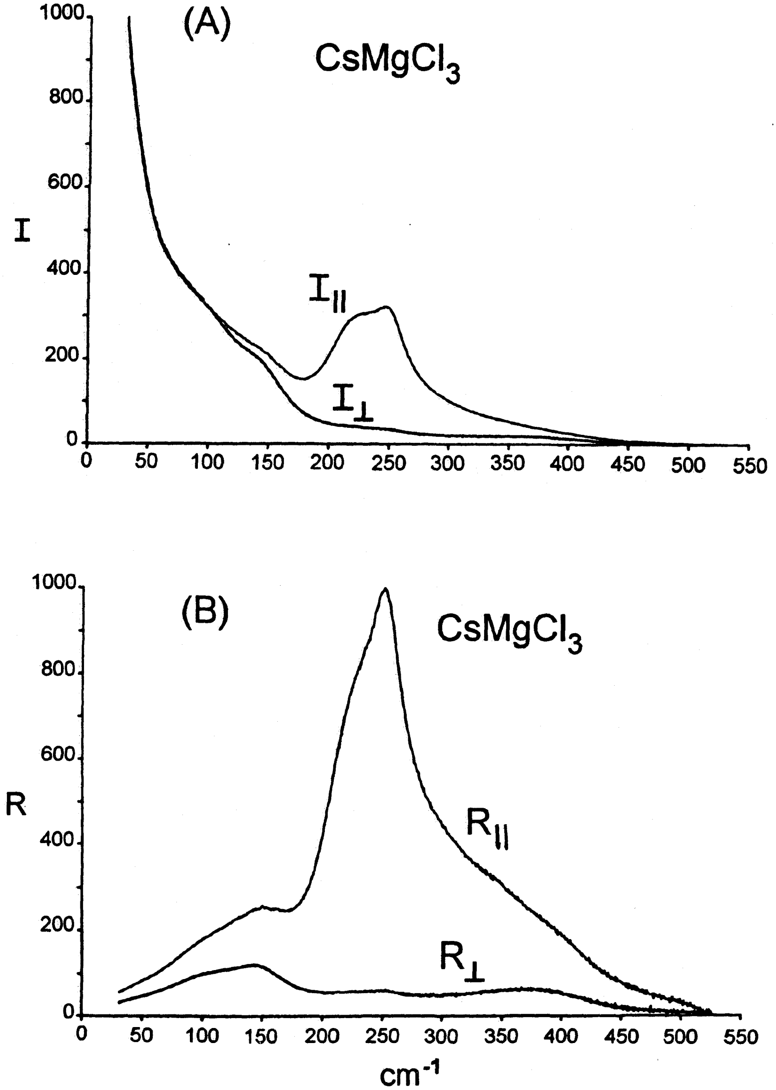

Fig. 1
Raman spectra from the molten mixture of CsCl + MgCl$_2$ at 896 K in the regular I(ω) format (A) and the normalized R(ω) format (B).

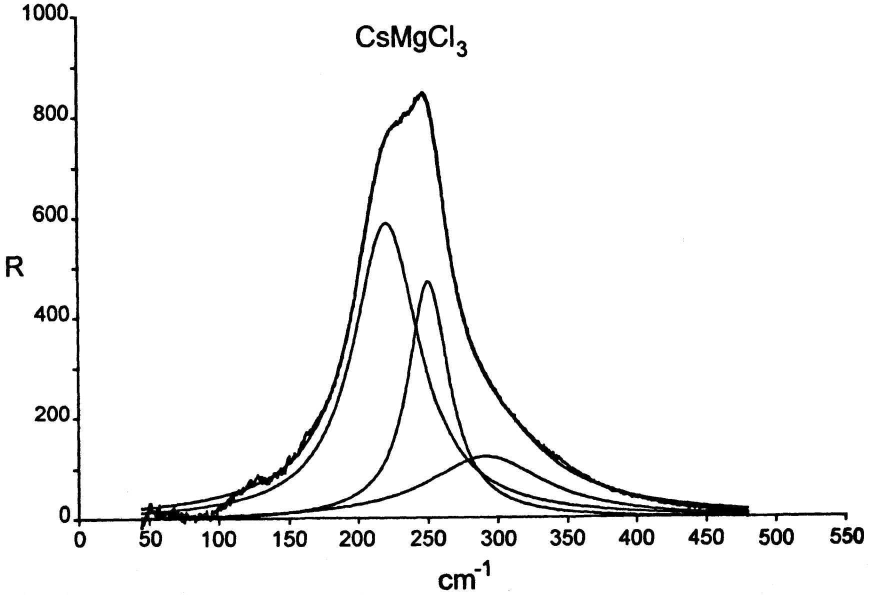

Fig. 2
Raman spectrum of $R(\omega)_{iso}$ created from $R(\omega)_{||} - 4/3\, R(\omega)_{\perp}$ from Fig. 1B. The curve resolved components are shown.

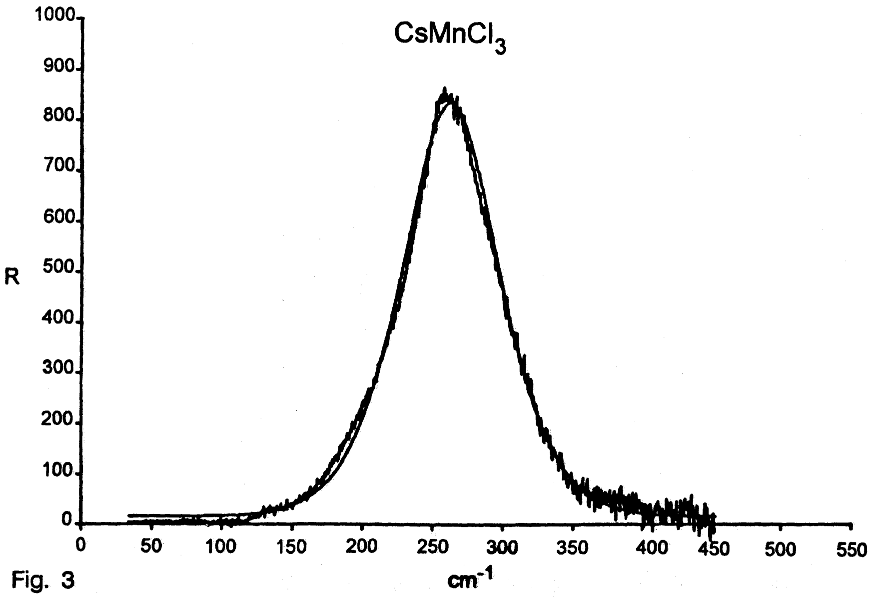

Fig. 3
Raman spectrum of the $R(\omega)_{iso}$ spectrum from the molten mixture of CsCl + $MnCl_2$ at 916 K. The best fit was achieved with a single band.

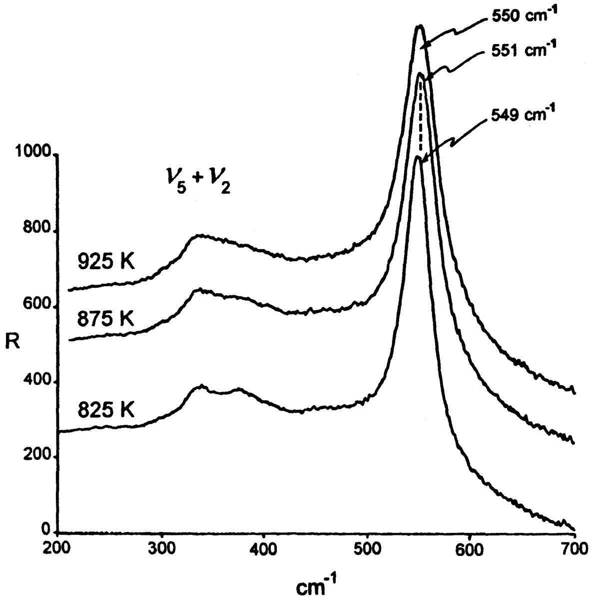

Fig. 4
Raman spectrum of Na_3AlF_6 over the temperature range of the phase transition at 845 K.

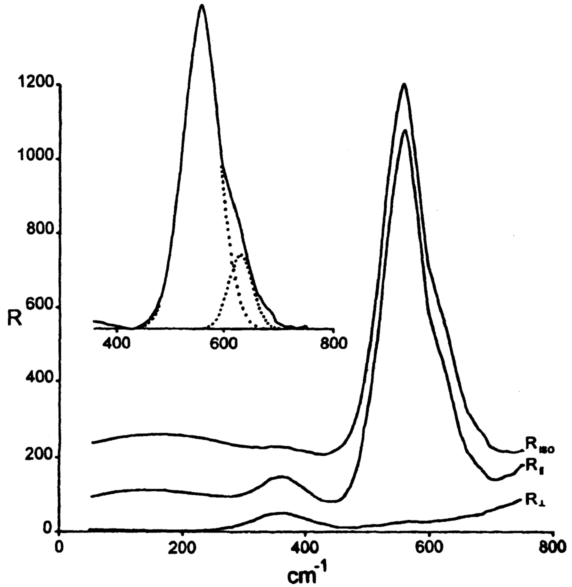

Fig. 5
Raman spectrum in the $R(\omega)$ format of molten Na_3AlF_6 at 1300 K. The insert illustrates the curve resolution of the $R(\omega)_{iso}$ band centred at 556 cm^{-1} into two gaussian components.

DOI: 10.1149/199413.0235PV

Raman Studies of Lithium Coordination in Molten and Aqueous Environments

Wolfram Rudolph, and Murray H. Brooker

Chemistry Department
Memorial University of Newfoundland
Canada, A1B 3X7

ABSTRACT

Raman spectra have been obtain for alkali metal chloride melts and for very concentrated solutions of alkali metal chlorides and perchlorates. The frequency maximum and the intensity of Raman scattered light from molten alkali metal chlorides decreased from lithium to cesium. In very concentrated solutions of lithium chloride a weak polarized band at about 380 cm^{-1} was assigned to an inner-sphere $LiCl(H_2O)_n$ where n is probably three. In more dilute aqueous lithium chloride and perchlorate a polarized band at 255 cm^{-1} has been assigned to the Li-O symmetric stretching motion of $Li(H_2O)_4^+$. The need for excellent depolarization data and normalization factors to account for temperature and frequency dependence of Raman intensity will be emphasized.

INTRODUCTION

The structure and dynamics of the coordination sphere of lithium ion in molten salts and in aqueous solution has been the subject of considerable research(1-7). Light scattering(1), inelastic neutron scattering(2,3) and theoretical calculations(4) for molten alkali metal halide salts indicated a tendency for local ordering of halide ions in the lithium coordination sphere. Diffusion of Lithium ion is accompanied by the halide ion atmosphere(6). Similar studies of concentrated aqueous solution of lithium salts by X-Ray(5), neutron diffraction(3) and Raman(7) methods indicated a moderately well define hydration sphere for lithium. A coordination number of about four has been inferred for lithium ion in both the molten and aqueous phases although penetration of lithium ion into the coordination sphere of a neighbour lithium suggests a short lifetime of a coordinated ligand.

Raman spectroscopy has been employed to study structural arrangements and species concentration in electrolytes in the solid, molten and aqueous phases(6,7). Spectroscopic data such as: the number of bands, the frequency of band maxima, infrared and Raman activities and intensities, polarization characteristics and spectral profiles, provide information about the dynamic microscopic local structure. In particular, Raman intensity measurements probe the very nature of the chemical bond by virtue of the fact that the band intensity is proportional to the square of the polarizability derivative with respect to the change in the normal coordinate, Q associated with the normal mode$[\delta\alpha/\delta Q]$(6,7). Since bond polarizability, α is a function of electron density it is possible to relate the Raman intensity to the electron density. In the hard-sphere model ionic liquids do not generate Raman intensity. The question arises as to whether or not the mutual polarization(8) of the alkali metal ion and the coordinated halide or water ligand is sufficient to give rise to detectable Raman intensity.

It must be emphasized that the actual quantity measured in the Raman experiment, the scattering cross section, $\partial\sigma/\partial\Omega$ has both temperature and frequency dependent factors that are especially important in the low wavenumber region of the spectrum at the high sample temperature normally employed for molten salts. The use of a normalized or reduced intensity, $R(\omega)$ to create a spectrum that is directly proportional to the intrinsic Raman scattering activity is essential for measurements in the low wavenumber region(6,7,9). Within the double harmonic approximation the use of the $R(\omega)$ spectrum removes a temperature and frequency dependent band asymmetry and permits comparison of spectra obtained at different temperatures(9). Furthermore it is essential to carefully measure light scattered in both the parallel, $R_{\parallel}$ and perpendicular, $R_{\perp}$ orientations in order to detect weak isotropic intensity R_{iso} due the symmetric motions.

Raman spectroscopy is a fast process. Collision encounters that last for only a few picoseconds will be sticky enough for an ion-pair to vibrate several times and give rise to Raman intensity. However this property also presents the problem of how to account for the Raman intensity in terms of a species with a defined geometry or symmetry. Environmental broadening and possible exchange broadening may result in a broad symmetric Raman band that by itself cannot provide information on species geometry or even coordination number. Raman intensity in the isotropic spectrum can be attributed to a symmetric stretching mode of some entity but the concept of a species with a defined geometry has little meaning. Interpretations based on lattice models can be misleading because they tend to under-emphasize the dynamic properties and infer too much order.

EXPERIMENTAL

Raman spectra were measured with a Coderg PHO Raman spectrophotometer. The 514.5nm (500 mW, green) and 488.0nm (500mW, blue) line of a Control laser model 52 system were used to excite the sample. Plasma lines were removed with a narrow band-pass interference filter. Peak positions were calibrated against laser plasma lines. The slit widths were set at 2.0 cm^{-1} . Raman spectra were obtained for samples in quartz containers with 6 to 10 mm paths. The container walls were masked to reduce reflection and Raman scattering from the glass. Spectra of solutions were were recorded for samples at 25 °C and there was no evidence to indicated local laser heating. Spectra of the melts were obtained in a in furnace with temperature regulated to ± 5 K. Raman spectra obtained for $I_{\parallel}$ and $I_{\perp}$ polarizations for orientations x(zz)y and x(zx)y. Polarization of the incident beam was controlled by a half-wave plate and the 90° scattered light was analyzed with Polaroid films which accepted parallel or perpendicular polarized light. A quarter wave-plate before the entrance slit served to compensate for grating polarization preference.

The Raman scattered light was detected with a PMT cooled to 250 K. Analogue spectra were output on a strip-chart recorder. Digital data files were created by integration of the photon counts with a home-built box-car averager interfaced to the Memorial University VAX 8800 computer. In the present case either two data points were collected per wavenumber. At least five identical sets of data were collected for each spectrum. Spectra were signal averaged and smoothed once with a three point Savitsky- Golay smoothing function. A baseline program was applied which corrected the measured intensity for the fourth power frequency factor and then set the lowest data point to zero and the highest data point to 999 on a relative intensity scale. This form of the data is defined as our $I(\omega)$ spectrum which should be independent of excitation frequency. The same baseline program was applied with the option to correct for the fourth power scattering factor, the temperature factor, $B = [1-\exp(-hc\,\omega/kT)]$ and the frequency factor, ω, to give the reduced or $R(\omega)$ spectrum which is directly proportional to a point by point relative scattering activity, $S_Q(\omega)$ in terms of mass weighted normal coordinates, Q , in the double harmonic approximation. $R_Q(\omega)$ is the form of the Raman spectrum that most closely approaches the vibrational density of states (6-9). The relationship between the $I(\omega)$ and $R_Q(\omega)$ forms of the spectra is given by Eq. 1.

$$S_Q(\omega) \propto R_Q(\omega) = I(\omega) \bullet \omega \bullet B \qquad 1.$$

It is our preference to plot the spectrum in the $R_Q(\omega)$ form because the Bose-Einstein factor removes the state dependent temperature factor of the excited state transitions and leaves the effect that is due to concentration changes.

Sample were prepared from recrystallized and carefully dried reagent salts. Aqueous samples of LiCl, LiBr and $LiClO_4$ were prepared by weight with to give solutions with known mole ratios of water to salt, R, which were confirmed with density measurements.

RESULTS and DISCUSSION

In a very concentrated solution of lithium chloride(R = 3) a weak, polarized Raman band at about 380 cm^{-1} has been assigned previously(7) to the Li-O motion of the hydrated lithium ion, $Li(H_2O)_4^+$. However the present studies have shown that this band is more likely due to the Li-Cl motion of the inner-sphere ion-pair $LiCl(H_2O)_n$ where n is probably three. The Raman spectra from an aqueous solution of LiCl with R = 2.8(Fig. 1) clearly show the band at 380 cm^{-1} for the R_{iso} spectrum. Raman bands due to the hydrogen-bonded motions of water have also been identified at about 50, 200 and from 300 to 900 cm^{-1}(7). Additional studies with LiCl in D_2O indicated that the band was insensitive to deuterium substitution while the Raman spectra from an aqueous LiBr solution with R = 2.7 showed that a similar band was shifted to 340 cm^{-1}. It appears that for very concentrated solutions of LiCl and LiBr the anion penetrates the coordination sphere of Li^+ to give an inner-sphere ion-pair with characteristic Raman bands for the Cl^- and Br^- at 380 and 340 cm^{-1}. These Raman bands provide a potential probe for more quantitative studies of ion-pair formation. Furthermore, in more dilute aqueous LiCl, LiBr and $LiClO_4$ a polarized band at 255 cm^{-1} has now been detected and assigned to the Li-O symmetric stretching mode of $Li(H_2O)_4{}^+$. Raman spectra (Fig. 2) for aqueous LiCl with R = 6.9 and for $LiClO_4$ with R = 10.5 both show the polarized band at about 255 cm^{-1} with halfwidth of about 60 cm^{-1}. The band is accentuated in aqueous $LiClO_4$ because the $ClO_4{}^-$ disrupts the hydrogen-bond structure of water and causes a decrease in the relative intensity of the band due to the O-H•••O stretching mode at about 200 cm^{-1}. Bands due to the M-O stretching modes of aqueous divalent and trivalent cations have been reported(7) but the present work represents the first definitive result for a univalent cation.

Light scattering studies from molten alkali metal halides and there mixtures indicate significant Raman intensity in the 20 to 500 cm^{-1} region. The scattered light is highly polarized and appears to arise from short-range, short-lived ion-pairs or aggregates which do not have well defined geometries on the ps time scale of the measurement. For the alkali metal halides the peak maxima and halfwidths in the $R(\omega)$ format are both anion and cation dependent. The wavenumber values for the peak maxima and halfwidths(parentheses) for the chlorides are: LiCl at 990 K, 310(350); NaCl at 1140 K, 215(260); KCl at 1110 K, 167(180); RbCl at 1090 K, 136(150); CsCl at 960 K, 118(130). The fact that the wavenumber values are reduced by about 0.7 for the molten alkali metal bromides suggests a mode of vibration which involves relative vibrational motion of both the anion and the cation and precludes the symmetric stretching mode of a species of symmetry as high as tetrahedral or octahedral.

Raman spectra of molten mixtures of LiCl with CsCl and KCl gave Raman spectra which gave rise bands which had characteristic intensity in regions which corresponded to that for each of the separate components. For instance in the mixtures of CsCl with LiCl there were two maxima in the spectra at about 420 and 120 cm^{-1} corresponded to the separate maxima in pure LiCl and pure CsCl. Raman spectra for the isotropic intensity for pure LiCl and for the LiCl + 5 CsCl mixture(Fig. 3) illustrate these features. In molten LiCl the Raman intensity is highly polarized and very broad with peak maximum about 310 cm^{-1} and halfwidth of 350 cm^{-1}. The large halfwidth reflects the wide range of environments associated with the Li-Cl vibrational motions of the ion aggregates. For the CsCl mixture with LiCl the peak maximum of the LiCl band shifted to about 420 cm^{-1} and the halfwidth decreased to about 140 cm^{-1}. Polarized intensity due to CsCl was observed at about 120 cm^{-1}. Addition of CsCl has the effect of reducing the range of environments for the Li-Cl vibrations because the more massive Cs^{+} counter ions present a more static environment.

The present Raman studies have demonstrated that intensity due to the Li-Cl vibrational motions may be identified in very concentrated aqueous solutions and the molten salts. Raman studies of aqueous lithium halide solutions under hydrothermal conditions should prove interesting.

ACKNOWLEDGMENTS

The work was supported by a Research Grants from the Natural Science and Engineering Research Council of Canada and a Deutscher Akademischer Austauschdienst Fellowship(WR).

References:

1. E. W. J. Mitchell and C. Raptis, J. Phys. C, **16**, 2973 (1983).
2. L. Pusztai and R. L. McGreevy, J. Phys. Condens. Matter, **1**, 2369 (1989).
3. J. E. Enderby, Pure Appl. Chem. **57**, 1025 (1985).
4. P. A. Madden and K. F. O'Sullivan, J. Chem. Phys. **95**, 1980 (1991).
5. K. Yamanaka, M. Yamagami, T. Takamuka, T. Yamaguchi and H. Waikita, J. Phys. Chem. **97**, 10835 (1993).
6. M. H. Brooker and G. N. Papatheodorou, in Advances in Molten Salt Chemistry, Vol. 5, G. Mamantov(ed), Elsevier, Amsterdam,1983, pp 27-165.
7. M.H. Brooker, Raman Spectroscopic Measurements of Ion Hydration, in Chemical Physics of Solvation, Part B, R.R. Dogonadze, E. Kalman, A.A. Kornyshev and J. Ulstrup (eds.) Elsevier, Amsterdam, 1986, pp 119-184.
8. M.H. Brooker and M.A., Bredig, J. Chem. Phys., **58**, 5319-21 (1973).
9. W. F. Murphy, M. H. Brooker, O. F. Nielsen, E. Praestgaard and J. E. Bertie, J. Raman Spectrosc. **20**, 695 (1989).

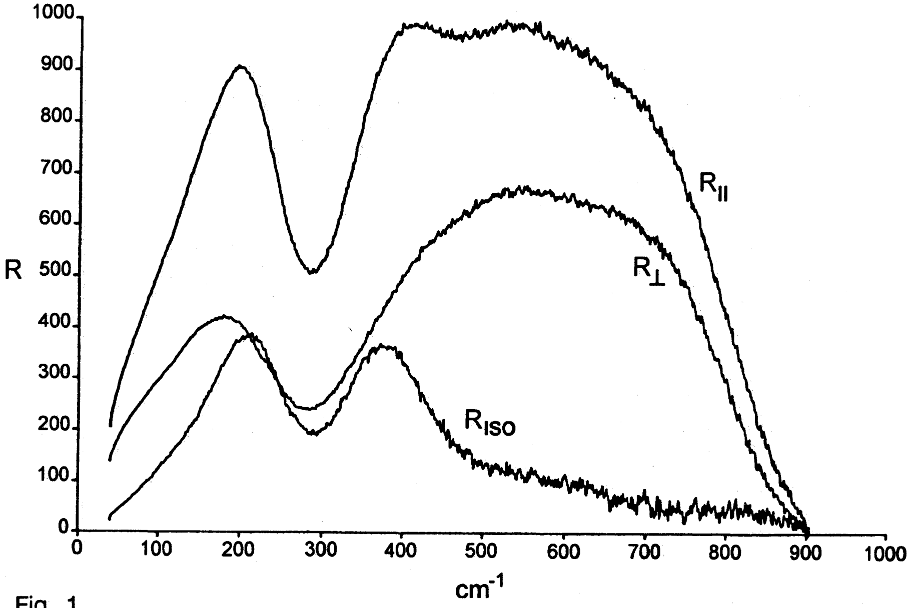

Fig. 1.
Raman spectra in the R(ω) format for saturated LiCl(R = 2.8) at 25 °C.

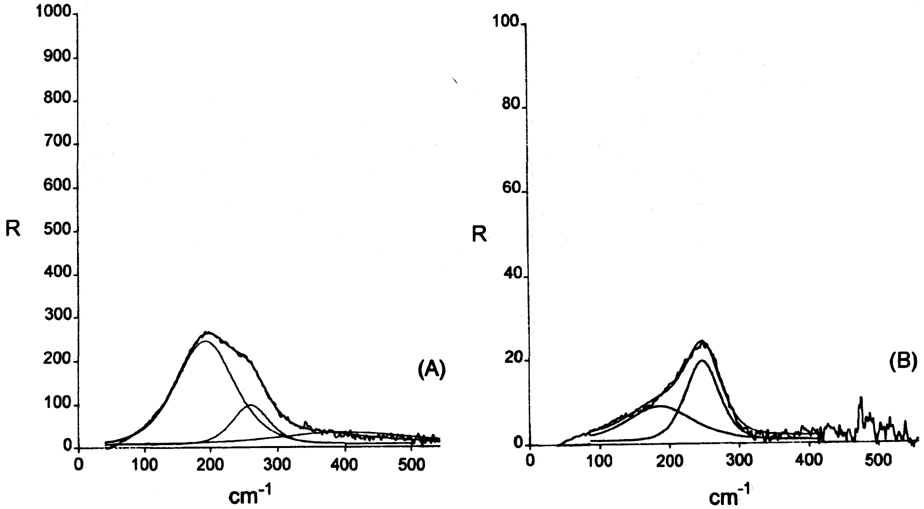

Fig. 2.
Raman spectra of R_{iso} for aqueous LiCl (R = 6.9) (A) and aqueous $LiClO_4$ (R = 10.5) (B). The best fit curve resolved components are indicated.

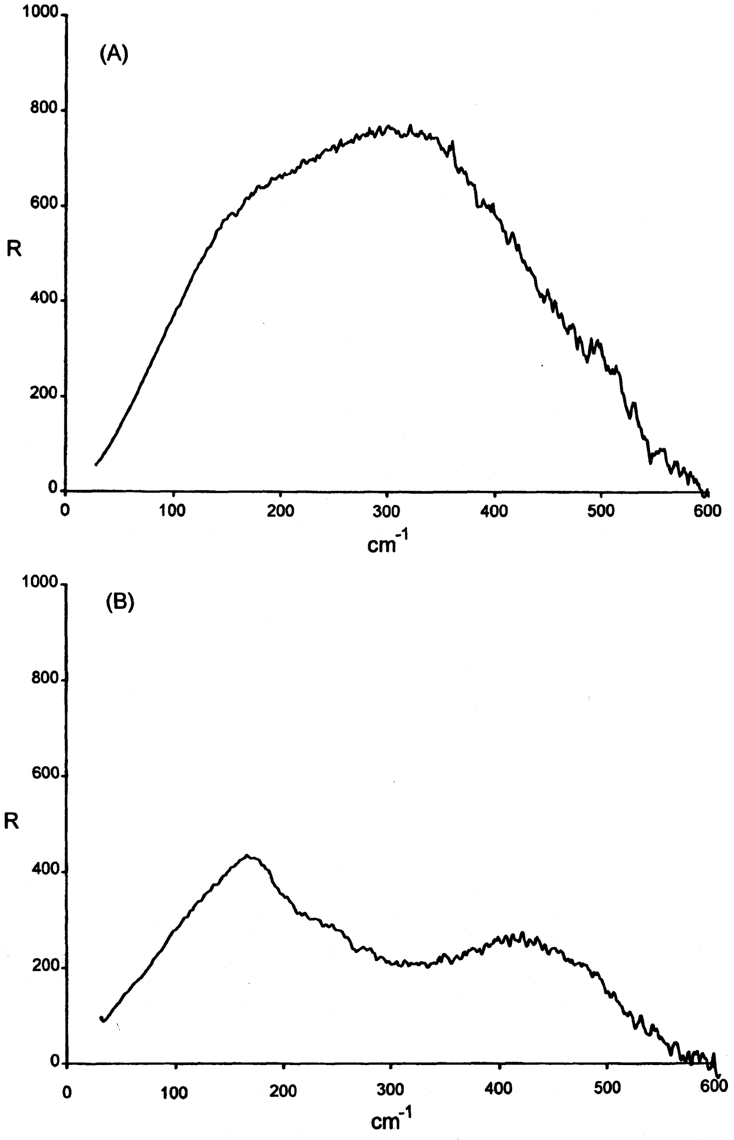

Fig. 3.
Raman spectrum for the R_{iso} component of molten LiCl at 990 K (A) and the molten mixture of LiCl in 5 CsCl at 875 K (B).

DOI: 10.1149/199413.0242PV

CHANGES OF VIBRATIONAL MODES UPON MELTING $CsHgCl_3$, Cs_2HgCl_4 AND Cs_3HgCl_5 SOLIDS AND RAMAN SPECTRA OF $HgCl_2$-ACl (A=Li,Na,K,Cs) MOLTEN SALT MIXTURES

G.A. Voyiatzis and Ṡ. Boghosian

Department of Chemical Engineering, University of Patras and
Institute of Chemical Engineering and High Temperature Chemical Processes
P.O. Box 1414, GR-265 00 Patras, GREECE

ABSTRACT

Spectra of polycrystalline $CsHgCl_3$, Cs_2HgCl_4 and Cs_3HgCl_5 have been measured from LN_2 to temperatures above melting. The Raman spectra for the Cs_3HgCl_5 solid are in aggrement with the discrete tetrahedral $HgCl_4^{2-}$ species present in crystal structure. The spectral changes occurring on melting Cs_2HgCl_4 and Cs_3HgCl_5 suggest the retention of the $HgCl_4^{2-}$ tetrahedral configurations. Upon melting $CsHgCl_3$, the coordination of Hg in the crystal changes and melt microstructure is better characterized by a planar $HgCl_3^-$ type complex formation. The Raman spectra of molten $HgCl_2$-ACl (A=Li,Na,K,Cs) mixtures have been also measured at different compositions and temperatures up to 973 K. At high alkali halide concentration range, the $HgCl_4^{2-}$ and $HgCl_3^-$ configurations seem to be stabilized by the Cs^+, K^+ and Na^+, Li^+ ions respectively.

INTRODUCTION

The formation of complex ions in charge-unsymmetrical binary molten salt systems MCl_2-ACl (M=Be,Mg,Mn,Fe,Ni & A=Li...Cs) has been extensively investigated by spectroscopic (1) and thermodynamic (2) methods. The examination of the vibrational spectra of MCl_2-ACl mixtures in the molten state has revealed that several spectral changes occur which depend on composition and/or on substituting the alkali metal cation from Li to Cs. For mixtures rich in ACl both spectroscopic and thermodynamic measurements indicate that the MCl_4^{2-} tetrahedra are the predominant "complex-ion" species. Raman spectroscopy has been already used to identify and characterize solid compounds formed in the binary system and to study the changes of vibrational frequencies upon melting (1,3).

In the present work, Raman spectroscopy is used (a) for determining the changes of vibrational modes occurring upon melting $CsHgCl_3$, Cs_2HgCl_4 and Cs_3HgCl_5 solids

(b) for correlating the solid and liquid structures and (c) for characterizing the melt microstructure of the $HgCl_2$-ACl (A=Li,Na,K,Cs) molten salt mixtures.

EXPERIMENTAL

Mercury (II) chloride (Merck Chemical Co.) was purified by several sublimations in Pyrex tubes at a small temperature gradient around its melting point. CsCl (Cerac Pure Inc.) was repeatedly sublimed in high dynamic vacuum, while LiCl (Alpha) was cleaned by bubbling gaseous HCl through the melt and then filtering under N_2 atmosphere. NaCl and KCl (Merck Chemical Co.) were further purified by recrystallization.The anhydrous materials were handled in Pyrex tubes sealed in vacuum or in a N_2-atmosphere drybox with a water vapor content of less than 1 ppm.

Raman cells were made of fused-silica tubing: 3 mm i.d., 4 mm o.d. and 30 mm length. All cells were thoroughly cleaned, baked out to red-heat, and degassed by evacuation while hot. The total amount of chemicals added to the cells was approximately 180 mg. Samples of $CsHgCl_3$, Cs_2HgCl_4, Cs_3HgCl_5 and all $HgCl_2$-ACl mixtures were prepared by mixing and heating together the appropriate amounts of the corresponding starting materials.

Raman spectra were recorded on a Spex 1403 double monochromator equipped with high-temperature cell device as described elsewhere (4).

RESULTS AND DISCUSSION

$CsHgCl_3$: solid and melt.

A number of crystal structures, some of which are polymorphic modifications, have been reported for the $CsCl/HgCl_2$ (1/1) compound (5,6). Zvonkova et al. have proposed (5) a deformed perovskite structure for $CsHgCl_3$ in which Hg has 2 Cl neighbors at 2.29 Å and 4 Cl at 2.70 Å, an eventually deformed octahedral configuration. In Fig. 1 the Raman spectra of polycrystalline $CsHgCl_3$ from LN_2 to the premelting temperature of 523 K are shown. A number of Raman peaks are clearly visible and the strong band situated at 231 cm^{-1} (at 77 K) is attributed to Hg-Cl symmetrical stretching mode. The appearance of these bands excludes an ideal perovskite structure for $CsHgCl_3$ for which no Raman activity is expected.

The Hg-Cl stretching frequency of pure polycrystalline $HgCl_2$ has been reported (7) at ~319 cm^{-1} (at 77 K) and is attributed to the presence of $HgCl_2$ molecules in the lattice. The remarkable red shift (of ~ 90 cm^{-1}) of the Hg-Cl stretching frequency observed on going from $HgCl_2$ to $CsHgCl_3$ certainly indicates an increase in the coordination number of Hg, accounting most probably for an octahedral configuration around Hg in the $CsHgCl_3$ crystal. Thus, the interpretation of the vibrational spectra of $CsHgCl_3$, in terms of a molecular or quasi-molecular $HgCl_2$ unit (8), seems to be incomplete. Furthermore with increasing temperature there is a slight blue shift of the Hg-Cl stretching frequency from

231 at LN_2 to 245 cm^{-1} at 523 K and a corresponding half width broadening, which imply that no phase transitions exist in this temperature range.

The Raman spectra of molten $CsHgCl_3$ is shown on the top of Fig. 1 at 723 K. The main feature of the spectra is a strong polarized band at 275 cm^{-1} which lies between the 319 and 231 cm^{-1} frequencies of the $HgCl_2$ and $CsHgCl_3$ solids correspondingly. These observations indicate that upon melting $CsHgCl_3$ a new mercury "complex" is formed with coordination number higher than that in $HgCl_2$ (s) (i.e. 2) but lower than that in $CsHgCl_3$(s) (i.e. 6). The strong polarized band observed in the Raman spectrum of KCl/HgCl (1/1) binary melt by Janz and James (9) at 282 cm^{-1} has been attributed to the symmetric stretching vibration of a planar $HgCl_3^-$ complex. Most probably the 275 cm^{-1} band in molten $CsHgCl_3$ is due to the same species.

Cs_2HgCl_4: solid and melt.

The crystal structure of Cs_2HgCl_4 is orthorhombic and isomorphous to β-K_2SO_4 (10). Slightly distorted tetrahedra $HgCl_4^{2-}$ are present with one short (2.386 Å) and 3 longer (~2.455 Å) Hg-Cl distances.

Figure 2 shows the Raman spectra of polycrystalline Cs_2HgCl_4 from 300 to 663 K. The similarities of the four line spectrum of Cs_2HgCl_4 solid at 300 K with the corresponding high temperature spectra of solid and liquid (Fig. 2) indicate a retention of the Hg coordination of the solid structure in the melt and leave little doubt about the assignments of these peaks to four lines expected for the tetrahedral $HgCl_4^{2-}$. With increasing temperature all Raman bands shift to the red - the ν_1 from 275 cm^{-1} at 300 K is shifted to 269 cm^{-1} at 803 K - with a corresponding half width broadening.

The high frequency Raman band of the solid at ~275 cm^{-1} (300 K) is attributed to the Hg-Cl vibrational frequency of the ν_1 symmetrical stretch of $HgCl_4^{2-}$ tetrahedra, the ν_3 being lower at 251 cm^{-1}. Such sequence of the ν_1 and ν_3 frequencies has been also reported before (11) for $HgCl_4^{2-}$ in the $(Me_4N)_2$ $HgCl_4$ solid.

Cs_3HgCl_5: solid and melt.

An orthorhombic structure, with space group P_{nma} (Z=4), has been reported (12) for the Cs_3HgCl_5 crystal. The structure consists of Cs^+, Cl^- and distorted $[HgCl_4]^{2-}$ tetrahedral ions.

The Raman spectra of polycrystalline Cs_3HgCl_5 at 77 and 298 K (Fig. 3) are in good agreement with factor group analysis based on the space group P_{nma} (D_{2h}^{16}) for the corresponding crystal. The similarity of the spectra for the high temperature solid (623 K) and melt (773 K) suggests that the vibrational modes of the $HgCl_4^{2-}$ tetrahedral species in the Cs_3HgCl_5 solid are retained in the liquid.

$HgCl_2$-ACl (A=Li,Na,K,Cs): molten salt mixtures

Table I lists the main Raman frequencies observed in the $HgCl_2$-ACl (A=Li,Na,K,Cs) liquid mixtures at different representative compositions and temperatures. In Fig. 4 the Raman spectra of $HgCl_2$-CsCl liquid mixtures are shown at 873 K. The spectra of pure $HgCl_2$ melt was recently interpreted (7) in terms of a molecular liquid involving linear triatomic $HgCl_2$ type molecules and strong intermolecular forces. Progressive additions of CsCl, that is dissolving an ionic to a molecular liquid, give rise to an increase in the half width and a red shift of the ~310 cm^{-1} polarized band of pure $HgCl_2$ to 276 and 265 cm^{-1} for x_{HgCl_2}=0.5 and 0.33 respectively. The low frequency depolarized "Rayleigh" wing of the $HgCl_2$-CsCl liquid mixtures possess a shoulder band in melts rich in either CsCl or $HgCl_2$. For intermediate composition x_{HgCl_2} =0.5 no shoulder band was observed. At compositions $x_{HgCl_2} \leq 0.33$, the Raman peak positions are relatively constant, their intensities are proportional to the $HgCl_2$ mole fraction and the half width of the polarized band is narrower than that of the intermediate compositions. This implies that the predominant species in the CsCl rich region is the $HgCl_4^{2-}$ and confirms our conclusions concerning the Cs_2HgCl_4 and Cs_3HgCl_5 solids and melts.

Table I: Main Raman Frequencies in cm^{-1} observed in the $HgCl_2$-ACl (A=Li,Na,K,Cs) liquid mixtures at different compositions and temperatures.

A	x_{HgCl_2}=0.5		x_{HgCl_2}=0.33		x_{HgCl_2}=0.25	
		T (K)		*T (K)*		*T (K)*
Li	294	*873*	289	*873*	282	*873*
Na	286	*923*	281	*923*	279	*973*
K	281	*513*	273	*923*	271	*973*
Cs	276	*873*	265	*873*	262	*873*

Figure 5 shows the Raman spectra of $HgCl_2$/ACl (1/3) (A=Li,Na,K,Cs) liquid mixtures. The spectral features of the potassium and cesium systems are similar and confirm the presence of $HgCl_4^{2-}$ species as suggested by Janz (9). The mixtures with LiCl and NaCl are characterized by a broad polarized Raman shoulder and the lack of the low frequency depolarized "Rayleigh" wing. The resemblance of the above characteristics to the Raman spectrum of $CsHgCl_3$ melt suggest that the $HgCl_3^-$ configurations are most probably stabilized in mixtures rich in NaCl or LiCl.

CONCLUSIONS

a) Upon melting $CsHgCl_3$, the octahedral configuration of the Hg in crystal changes and the melt microstructure is better characterized by a planar $HgCl_3^-$ type complex.
b) The Cs_2HgCl_4 and Cs_3HgCl_5 solid compounds melt with retention of the tetrahedral, $HgCl_4^{2-}$, configurations of the crystals.
c) In $HgCl_2$-ACl (A=Li, Na, K, Cs) molten salt mixtures, at high alkali halide concentration range, the $HgCl_4^{2-}$ and $HgCl_3^-$ configurations seem to be stabilized by the Cs^+, K^+ and Na^+, Li^+ ions respectively.

ACKNOWLEDGEMENTS

The authors wish to thank Professor G.N. Papatheodorou for helpful discussions during the investigation and valuable comments on the manuscript and Mr. G.C. Carountzos for his help in the preparation of $HgCl_2$-ACl (A=Li, Na, K) Raman cells.

REFERENCES

1. M. Brooker and G.N. Papatheodorou in *Advances in Molten Salt Chemistry,*Vol. 5, ed. G. Mamantov , Elsevier (1983) p. 27.
2. G.N. Papatheodorou in *Comprehensive Treatise of Electrochemistry*, Vol. 5, ed. B.F. Conway, Plenum Press (1983) p. 339.
3. M.H. Brooker and C.-H. Huang, Can. J. Chem. **58**, 168 (1980).
4. G.A. Voyiatzis and G.N. Papatheodorou, Inorg. Chem **31**, 1945 (1992).
5. Z.V. Zvonkova, .V.V. Samodurova and L.G. Vorontsova, Dokl.Akad. Nauk SSSR **102**, 115 (1955).
6. H.F. McMurdie, J. de Groot, M. Morris and H.E. Swanson, J. Res. Nat. Bur. Stand. Sect. A **73A**, 621 (1969).
7. G.A. Voyiatzis and G.N. Papatheodorou, Ber. Bunsenges. Phys. Chem. **98**, xxxx (1994).
8. J.T.R. Dunsmuir and A. P. Plane, J. Inorg. Nuclear Chem., **33**,4361 (1971).
9. G. J. Janz and D.W. James, J. Chem. Phys., **38**, 905 (1962).
10. S.A. Linde, A.Ya. Mikhailova, V.I. Pakhomov, V.V. Kirilenko and V.G. Slul'ga, Koord. Khim. **9**, 998 (1983).
11. G.B. Deacon, J.H.S Green and W. Kynaston, Aust. J. Chem. **19**, 1603 (1966).
12. W. Clegg, M.L. Brown and L.J.A. Wilson, Acta Cryst. **B32**, 2905 (1976).

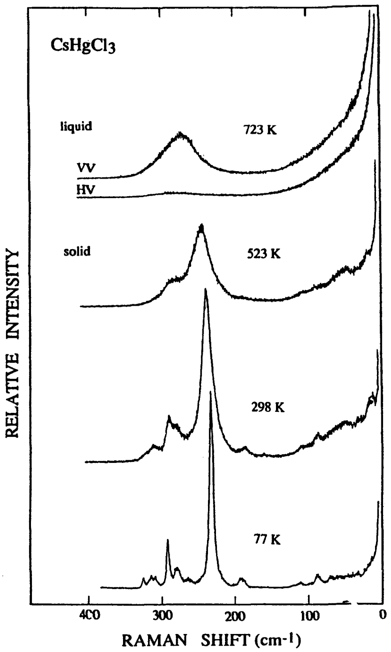

Fig.1 : Raman spectra of polycrystalline and liquid $CsHgCl_3$: λ_0=514.5 nm, laser power (P) ~ 50mW, Spectral Slit Width (SSW) ~ 2 cm^{-1}, time constant (τ) =0.1 s, Scan Rate (SR) = 0.5 $cm^{-1}s^{-1}$.

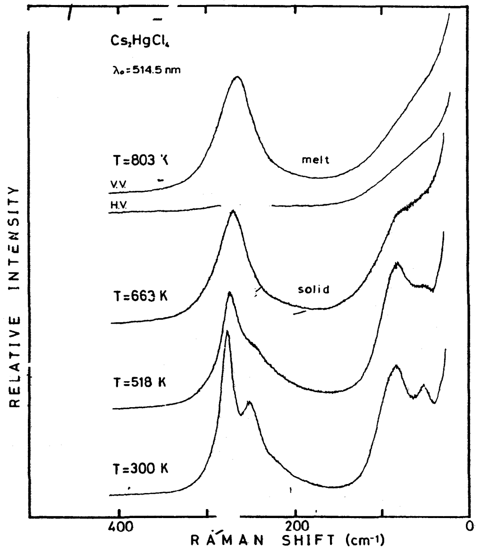

Fig. 2. Raman spectra of polycrystalline and liquid Cs_2HgCl_4. Spectra conditions as in Fig. 1.

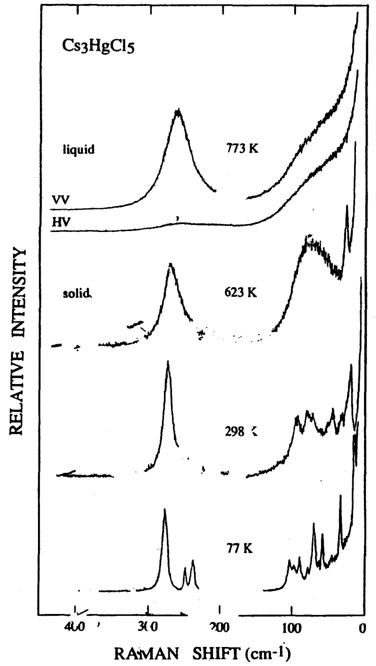

Fig.3 : Raman spectra of polycrystalline and liquid Cs_3HgCl_5. Spectra conditions as in Fig. 1.

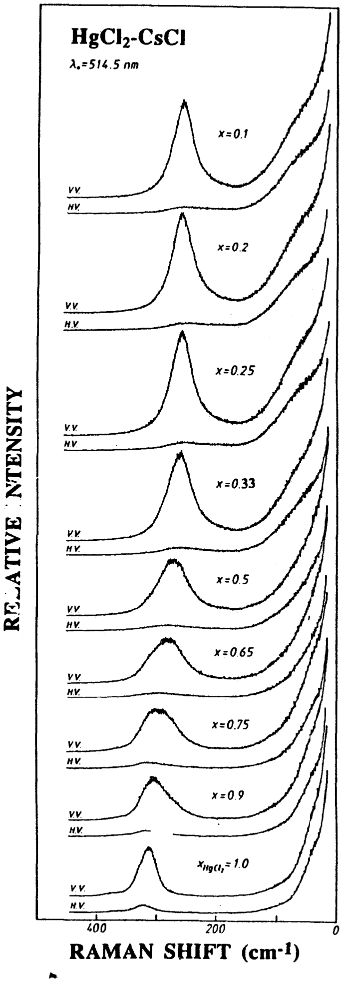

Fig.4 : Raman spectra of $HgCl_2$-CsCl liquid mixtures at 873 K. Spectra conditions as in Fig. 1.

Fig.5 : Raman spectra of 25% $HgCl_2$-75% ACl (A=Li, Na, K, Cs) liquid mixtures at ~873 (A=Li, Cs) and ~ 973 K (A=Na, K). Spectra conditions as in Fig. 1.

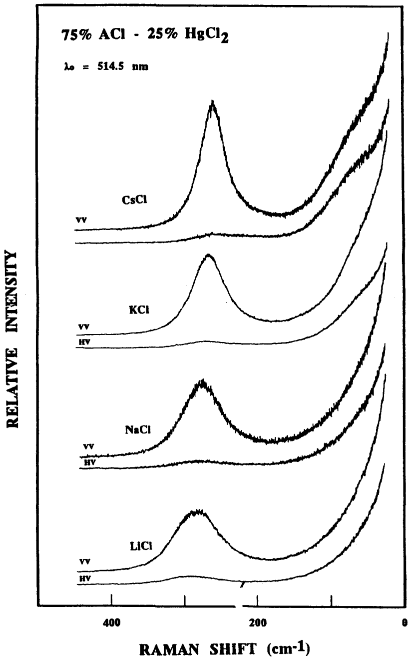

DOI: 10.1149/199413.0250PV

An Investigation of the Depolarization Ratio of NO_3^- and NO_2^- Anions in KNO_3-$NaNO_2$/KNO_2-$NaNO_3$ Reciprocal Molten Salt Systems by Raman Scattering

Licheng Yan*, Wencong Lu, Jianhui Fang, Jinxiu Yang and Ju Yang

Department of Chemistry
Shanghai University of Science and Technology
Shanghai, P.P. China (201800)

Nianyi Chen

Shanghai Institute of Metallurgy, Academia
Shanghai, P.R. China

ABSTRACT

Raman scattering was used to investigate the micro-environment of some complex ions (such as NO_3^-) in molten salt solutions. From the Raman spectra, the depolarization ratio of NO_3^- and NO_2^- anions in several KNO_3-$NaNO_2$/KNO_2-$NaNO_3$ reciprocal molten salt systems was studied. It was found that the concentration of NO_3^- ions had the greatest impact on the frequency peaks, ν_1, of NO_3^- in the K^+, Na^+//NO_2^-, NO_3^- system. Also, the depolarization ratio of the NO_2^- anion was affected more significantly than that of NO_3^- in the systems that contained only a single cation (Na^+ or K^+). These results can be explained by molecular dynamics based on a Monte Carlo simulation.

INTRODUCTION

The use of a Raman spectrometer system to detect and analyze ions in molten salt solutions under micro-environmental conditions could be extremely helpful for both theory and model development. Yan etc., used this method to investigate the peak shape of some complex ions (such as NO_3^-) in the KNO_3-$NaNO_2$ molten salt system and found the results could be explained by a computerized Monte Carlo simulation (1). The Raman spectra of the KNO_3-$NaNO_2$ molten salt system has also been published by Akhtyrskii (2), but the available information is still not sufficient for the investigation of the local structure of this system. On the other hand, methods based on Monte Carlo simulations have been successfully used to investigate the local structures of some molten salt solutions (3,4). Therefor, the use of Raman scattering methods together with the computerized Monte Carlo simulation will be able to provide both experimental and theoretical approaches to the micro-environment of ions in molten salt systems.

One of the most useful physical parameters for this Raman scattering method is the ratio of depolarization (or depolarization ratio), which reveals information about molecular structure. The ratio of depolarization is defined as follows:

$$\text{The ratio of depolarization:} \quad \Delta = I_z/I_x \qquad (1)$$

Where I_z is the scattering light intensity along the z axis and I_x is the scattering light intensity along the x axis. The relationship between this depolarization ratio and the g-factor is as follows:

$$g = (n-1)/2nN * [(45\,\Delta) / (6 - 7\,\Delta)]^{1/2} \qquad (2)$$

In Eq. [2], where $(n-1) = 2\pi N\alpha$, n is the index of refraction, N is the number of molecules and α is the rate of polarization. Therefore, the ratio of depolarization has a direct bearing on the g-factor. By knowing the ratio of depolarization of those ions in a molten salt system, we will be able to obtain some important information regarding the molecular micro-environment.

In this work, the Raman spectrometer was used to investigate the frequency peak, ν_1, of NO_3^- and NO_2^- anions in the KNO_3-$NaNO_2$/KNO_2-$NaNO_3$ molten salt solution. The depolarization ratio of these anions obtained by Raman scattering was examined by varying the molten salt composition and system temperature. These results will then be explained by Monte Carlo simulation.

EXPERIMENTAL

The Laser Raman spectrometer system was purchased from SPEX RAMALOG. It was equipped with a 1403 double monochromator and had a 514.5 nm excitation radiation. The power supply for the laser was 400 mW. The spectral resolution associated with the slit width was 4 cm^{-1}. The sample cell used in these experiments was made in-house and could be potentially heated up to 800°C. All the chemicals used in these experiments were the purist grade available. The molten salt solutions were prepared by dehydrating the proper chemicals under vacuum over night and then heating them above their melting points.

RESULTS AND DISCUSSION

The depolarization ratio of the v_1 peak of NO_3^- and NO_2^- ions in K^+, $Na^+//NO_3^-$, NO_2^- reciprocal molten salt systems has been examined by varying both system temperature and molten salt composition. First, the relationship between the depolarization ratio and system temperature was studied in several different molten salt compositions. In the system which was composed of 60% $NaNO_3$ and 40% KNO_2, little change was observed for the depolarization ratio of both NO_3^- and NO_2^- anions under temperatures ranging from 200°C to 400°C. The same results were also obtained from another molten salt system which was composed of 60% KNO_3 and 40% $NaNO_2$. These results imply that the system temperature has almost no effect on the molecular parity of these systems.

We then examined the relationship between the molten salt composition and the ratio of depolarization isothermally of 350°C. For both $NaNO_3$-KNO_2 and KNO_3-$NaNO_2$ systems, the ratios of the depolarization of the NO_3^- anion were obtained and the results are shown in Figure 1. It was found that the depolarization ratio of NO_3^- anion in pure $NaNO_3$ solution was greater than in pure KNO_3. From our view-point of molecular dynamics based on a Monte Carlo simulation, in this nitrate molten salt system, the cation with larger z/r (charge-radius ratio) would be more likely to be distributed on the same plane as the NO_3^- anion (which is trigonal planar). The cation with smaller z/r ratio would be distributed on each side of a NO_3^- plane. In this K^+, Na^+/NO_3^- system, the z/r ratio of Na^+ is greater than that of K^+, so that the Na^+ cation would stay in the same plane as the NO_3^- anion, and this results in the flat electronic cloud distribution which leads to a larger parity difference. The same theoretical approach could be used to explain the fact that the increase in the $NaNO_2$ concentration in the KNO_3-$NaNO_2$ molten salt solution would result in an increase in the depolarization ratio of the NO_3^- anion. The molten salt system KNO_2-$NaNO_3$ was also examined. However, a minimum value of the depolarization ratio of the NO_3^- anion was observed at a particular composition (50% KNO_2 + 50% $NaNO_3$) and this could be related to the formation of some anionic aggregates of NO_3^- and NO_2^- within the system.

The molten salt systems with only a single cation or anion were also examined. For the single anion system, the depolarization ratios of both NO_3^- and NO_2^- anions in K^+, Na^+ // NO_3^- and K^+, Na^+ // NO_2^- systems have shown little or no change with different molten salt compositions and system temperature. In the mean time, two molten salt systems with a single cation (K^+ //NO_2^-, NO_3^- and Na^+ // NO_2^-, NO_3^-) were also studied. The depolarization ratios of NO_3^- and NO_2^- obtained for the Na^+ // NO_2^-, NO_3^- system are shown in Figure 2. It is easy to see that in Figure 2a, the change of molten salt composition has a much greater impact on the depolarization ratio of NO_2^- than that of NO_3^-. And by setting the molten salt composition to a certain point (40% $NaNO_3$ and 60% $NaNO_2$ as shown in Figure 2b), the relationship between system temperature and depolarization ratio was studied. It was found that the change of temperature has much more influence on the ratio of depolarization of NO_2^- than that of NO_3^- (Figure 2b). Also, very similar results have been obtained in the systems with only K^+ cation present. These phenomena can be related to the structures of NO_3^- and NO_2^-. As we mentioned before, the electron cloud of the NO_3^- is distributed uniformly triangular. This type of electron distribution is smoother and more stable, and it will not be easily changed as the result of differences in micro-environment. It will therefor have a relatively smaller parity and thus result in a more stable depolarization ratio than the NO_2^-.

CONCLUSIONS

This study examined the ratio of depolarization of both NO_3^- and NO_2^- ions in several Na^+, K^+ // NO_2^-, NO_3^- reciprocal molten salt solutions. By varying both system temperature and molten salt composition, we have found that the depolarization ratio of NO_3^- was affected significantly by changing molten salt composition. It has also been shown that in the systems where there was only a single cation present (K^+ or Na^+), the depolarization ratio of NO_2^- was affected more significantly than that of NO_3^-. All these observations have been explained well by Monte Carlo simulations.

ACKNOWLEDGMENTS

We thank National Nature Foundation of China for the funding. We also thank our university for supporting this research work.

REFERENCES

(1). L. Yan, Y. Wang, J. Yang, L. Yu, G. Ma and N. Chen, Acta Metallurgica Sinica, **1988**, 1, 72.

(2). I. T. D. Akhtyrskii, Ukr. Khim Zhur, **1974**, 40, 1208.

(3). N. Chen, N. Jiang, T. Li, Proceedings of the First International Symposium on Molten Salt Chemistry and Technology, Kyoto, Japan, **1983**, 349.

(4). C. Xu, N. Chen, N. Jiang, Q. Li, S. Sen, Acta Metallurgica Sinica, **1986**, 22, B68.

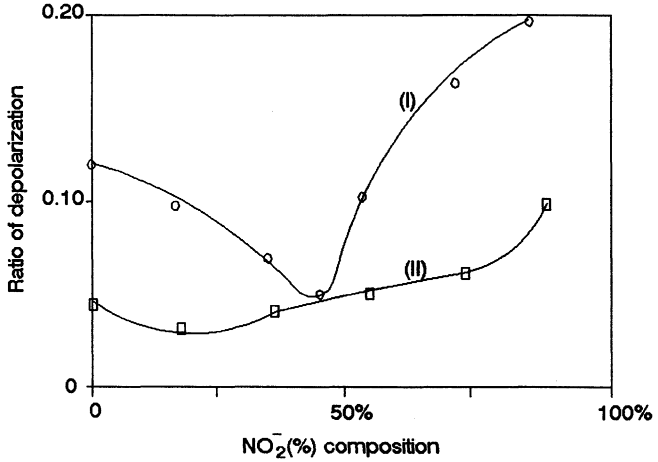

Figure 1. The depolarization ratio of NO_3^- by Raman scattering in (I) $NaNO_3$-KNO_2 and (II) $NaNO_2$-KNO_3 systems

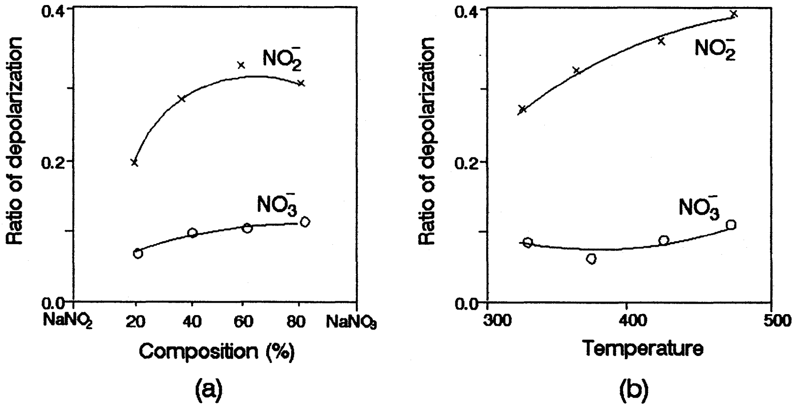

Figure 2. The depolarization ratio of NO_3^- and NO_2^- anions in $NaNO_3$-$NaNO_2$ systems

DOI: 10.1149/199413.0256PV

MATRIX ISOLATION STUDIES ON THE VAPORISATION OF ALKALI-METAL RUTHENATES

J. S. Ogden, T. N. Day, and R. A. Gomme

Department of Chemistry, University of Southampton,
Southampton. SO9 5NH. U.K.

ABSTRACT

The vaporisation of the salts M_2RuO_4 ($M=K$, Rb, Cs) has been investigated by classical analytical methods, and by matrix isolation i.r. spectroscopy. For all three systems, the principal ternary vapor species is identified as $MRuO_3$, and a planar (C_{2v}) structure is proposed based on a detailed vibrational analysis involving both ruthenium and oxygen isotopic structure. Subsequent analysis of the solid sublimate, however, revealed that a disproportionation of this Ru(V) species occurs to form RuO_2 and ruthenate(VI) ($RuO_4^{=}$).

INTRODUCTION

There is considerable current interest in the chemistry of ruthenium and its compounds, generated in part by the need to understand and predict the speciation of this element if released inadvertently from nuclear reactors. In particular, considerable attention has been focussed on high temperature species, and data are now available for the four binary molecular oxide species RuO, RuO_2, RuO_3, and RuO_4 (1-5). However, although alkali metal ruthenates and perruthenates are well known in the solid state, there appears to be only one account describing possible ternary species which might be present in the high temperature vapors above these systems. This paper, by Cordfunke et al.(6), is concerned with transpiration studies on cesium ruthenate(VI) in oxygen atmospheres, and concludes, on the basis of analytical data on the sublimate, that the ternary species present in the vapor is molecular Cs_2RuO_4.

The combination of matrix isolation and i.r. spectroscopy has led to the identification and subsequent characterisation of numerous high temperature chemical species, and using this strategy we have studied the vaporisation of several alkali-metal ruthenate(VII) and ruthenate (VI) salts M_xRuO_4, where M = K. Rb, and Cs, and x = 1 or 2. Here, we outline the most significant conclusions arising from our experiments on the ruthenate(VI) systems: a more detailed account of this work will be presented elsewhere (7).

EXPERIMENTAL

The samples of alkali-metal ruthenate(VI) used in this work were prepared by heating well-ground mixtures of the alkali metal carbonate and ruthenium dioxide (M : Ru = 2 : 1) in an alumina crucible according to the recipe described by Fischer and Hoppe (8). All the products were dark green in colour, and their identity was confirmed by powder XRD and elemental analysis for M (flame photometry). ^{18}O enrichment was effected by isotopic exchange with $H_2{}^{18}O$.

The principal features of our matrix isolation apparatus have been described elsewhere (9). In these present studies, ruthenate samples were vaporised from silica sample holders at temperatures in the range 800 - 1000 ^{0}C, and condensed at ca. 12 K with high purity nitrogen or argon (99.999%, BOC). Deposition times were typically ca. 1 hr., and i.r. spectra were recorded using Perkin-Elmer 983G or Biorad FTS-65A instruments. During deposition, there was a significant build-up of sublimate on the off-axis walls of the sample tube, and this was subsequently recovered and analysed both qualitatively and quantitatively by flame photometry (M), electronic spectroscopy (Ru), and powder XRD.

RESULTS AND DISCUSSION

Figure 1a shows part of a typical argon matrix spectrum obtained from the vaporisation of Cs_2RuO_4 at ca. 800 ^{0}C. The three bands denoted **A** at 905, 839, and 745 cm^{-1} maintained a constant intensity ratio over a wide range of experiments, and are assigned to a single species. The weaker feature **B** at 792 cm^{-1} exhibits a variable relative intensity, and its assignment is discussed elsewhere (7). In nitrogen matrices, the bands denoted **A** appear at 907, 849, and 752 cm^{-1}.

Figure 1b shows the corresponding argon matrix spectrum obtained from a sample of 18-oxygen enriched Cs_2RuO_4. The bands at 905 and 839 cm^{-1} now appear as doublets, with accompanying features at 863 and 822 cm^{-1} respectively, whilst the 752 cm^{-1} feature forms part of a well-defined triplet. 18-oxygen enrichment studies were also carried out on the potassium salt, and Table I summarises all the frequencies obtained.

Figure 2 shows a typical nitrogen matrix spectrum of the bands due to **A** under higher resolution. The structure present on the highest frequency feature at ca. 907 cm^{-1} is due to the presence of naturally occurring ruthenium isotopes (96, 5.5%; 98, 1.9%; 99, 12.7%; 100, 12.6%; 101, 17.1%; 102, 31.6%; 104, 18.6%), and similar structure is partially resolved on the lowest frequency band at ca. 752 cm^{-1}. Similar structure was also observed for the rubidium and potassium salts in nitrogen matrices, and Table II summarises the data obtained. No ruthenium structure could be resolved for the central band at ca. 850 cm^{-1}.

Spectral Interpretation

The presence of clearly resolved ruthenium isotope structure on the highest frequency band shows that species A is likely to contain one atom of ruthenium. The doublet observed on ^{18}O enrichment (Figure 1b) indicates that this mode involves the motion of essentially one oxygen atom, and its relatively high frequency identifies it as a terminal mode. In contrast, the band at ca. 745 cm^{-1} clearly involves the motion of two equivalent oxygen atoms, which almost certainly occupy bridging positions in view of the comparatively low frequency.

We therefore propose that species A is $CsRuO_3$, and that it exhibits the structure shown in Figure 3. From the above discussion, both planar (C_{2v}) and non-planar (C_s) structures would be qualitatively consistent with the observed isotope patterns, but we favor the planar model on the basis of a quantitative study of the isotope shifts. The vibrational analysis we adopt is based on our previous characterisation of the molecular KNO_3, $NaPO_3$, and $CsAsO_3$, all of which have been shown (9) to adopt the planar bidentate structure proposed in Figure 3.

Using a "stretch-only" force field, and a bond-dipole model for i.r band intensities (9), this analysis satisfactorily reproduces not only the positions of all the ruthenium and oxygen isotopic species observed, but also the relative intensities of the three basic fundamentals. Figure 1c and Table I compare our observed and calculated spectra in the ^{18}O enrichment studies, whilst Table II summarises the observed and calculated ruthenium isotopic data.

Analysis of sublimate

The sublimate present on the off-axis walls of the sample holder was analysed by powder XRD, u.v./vis. spectroscopy and flame photometry. XRD showed that both RuO_2 and ruthenate(VI) were present, and u.v./vis was consistent with an equal distribution of Ru between these forms. The proportion of alkali-metal present was consistent with an overall stoichiometry $MRuO_3$. These analytical results are therefore consistent with vapor transport via a ternary $MRuO_3$ species, which disproportionates to Ru(IV) and Ru(VI) on condensation.

CONCLUDING REMARKS

These experiments clearly demonstrate that under our vaporisation conditions, the principal ternary species in these M/Ru/O systems is $MRuO_3$. This is in contrast to the results recently reported by Cordfunke et al (6), who deduced that the ternary species present in their transpiration studies is molecular Cs_2RuO_4. Evidently the higher oxygen partial pressures in these latter studies were sufficient to suppress the change in oxidation state from Ru(VI) to Ru(V), which appears to take place under high vacuum. Further experiments are in progress to identify the low frequency modes for molecular M/Ru/O ternary species in order to estimate thermodynamic properties.

ACKNOWLEDGEMENTS

We gratefully acknowledge the financial support of AEA Technology, Winfrith, U.K., and the EEC for this work, and also wish to thank Dr. B. R. Bowsher and Dr. A. L. Nichols for helpful discussions.

REFERENCES

1. A. B. Nikokskii and A. N. Ryabov, Russ. J. Inorg. Chem., **10**, 1, (1965)
2. J. G. Dillard and R. W. Kiser, J. Phys. Chem., **69**, 3893, (1965)
3. H. Schafer, A. Tebben and W. Gerhardt, Z. Anorg. Allg. Chem., **321**, 41, (1961).
4. F. Koniger and A. Muller, J. Mol. Spectrosc., **65**, 339, (1972).
5. J. G. Kay, D. W. Green, K. Duca and G. L. Zimmerman, J. Mol. Spectrosc., **138**, 49, (1989).
6. E. H. P. Cordfunke, R. J. M. Konings, and S. R. M. Meyssen, J. Chem. Thermodyn., **24**, 724, (1992).
7. J. S. Ogden, T. N. Day, and R. A. Gomme, (to be published).
8. D. Fischer and R. Hoppe, Z. Anorg. Allg. Chem., **591**, 87, (1990)
9. I. R. Beattie, J. S. Ogden, and D. D. Price, J. Chem. Soc. Dalton, 1460, (1979). S. N. Jenny and J. S. Ogden, ibid, 1465 (1979). J. S. Ogden, T. J. Sibley, and S. J. Williams, ibid, 851, (1983).

Table I Observed and calculated infrared band positions for 18-oxygen enriched $MRuO_3$ species isolated in argon matrices.

	$CsRu^{16.18}O_3$		$KRu^{16,18}O_3$	
Assignments	Observed bands	Calculated bands†	Observed bands	Calculated bands†
A_1 (C_{2v}) $M_x{}^{16}ORu^{16}O_2$	905.6	905.6	907.9	907.9
A' (C_s) $M_x{}^{16}ORu^{18}O^{16}O$		905.6		907.8
A_1 (C_{2v}) $M_x{}^{16}ORu^{18}O_2$		905.6		907.8
A_1 (C_{2v}) $M_x{}^{18}ORu^{16}O_2$	863.4	863.4	865.3	866.8
A' (C_s) $M_x{}^{18}ORu^{18}O^{16}O$		862.4		865.3
A_1 (C_{2v}) $M_x{}^{18}ORu^{18}O_2$		861.9		864.5
A_1 (C_{2v}) $M_x{}^{16}ORu^{16}O_2$	839.6	839.6	839.7	839.7
A_1 (C_{2v}) $M_x{}^{18}ORu^{16}O_2$	837.3	836.6		835.4
A' (C_s) $M_x{}^{16}ORu^{18}O^{16}O$	821.8	822.3	821.7	822.7
A' (C_s) $M_x{}^{18}ORu^{18}O^{16}O$		820.2	819.2	819.8
A_1 (C_{2v}) $M_x{}^{16}ORu^{18}O_2$		796.8		797.3
A_1 (C_{2v}) $M_x{}^{18}ORu^{18}O_2$		795.2		795.2
B_1 (C_{2v}) $M_x{}^{16}ORu^{16}O_2$	744.9	744.9	746.6	746.6
B_1 (C_{2v}) $M_x{}^{18}ORu^{16}O_2$		744.9		746.6
A' (C_s) $M_x{}^{16}ORu^{18}O^{16}O$	722.8	722.8	724.7	724.8
A' (C_s) $M_x{}^{18}ORu^{18}O^{16}O$		722.8		724.2
B_1 (C_{2v}) $M_x{}^{16}ORu^{18}O_2$	709.2	708.9	711.5	710.2
B_1 (C_{2v}) $M_x{}^{18}ORu^{18}O_2$		708.9		710.2

† Force constants and geometries used for calculations:-

$CsRuO_3$: $f_R = 6.76$ mdyneÅ^{-1}, $f_r = 5.19$ mdyneÅ^{-1}, $f_{Rr} = 0.51$ mdyneÅ^{-1}, $f_{rr} = 0.76$ mdyneÅ^{-1}; $\alpha = 98°$, $\beta = 131°$

$KRuO_3$: $f_R = 6.79$ mdyneÅ^{-1}, $f_r = 5.20$ mdyneÅ^{-1}. $f_{Rr} = 0.50$ mdyneÅ^{-1}, $f_{rr} = 0.70$ mdyneÅ^{-1}; $\alpha = 94°$, $\beta = 133°$

Table II Observed and calculated ruthenium isotope structure for $MRuO_3$ species isolated in nitrogen matrices.

	$CsRuO_3$		$RbRuO_3$		$KRuO_3$	
Assignments	Obs. bands*	Calc. bands†	Obs. bands*	Calc. bands†	Obs. Bands*	Calc. bands†
A_1 terminal						
^{104}Ru	906.1	906.0	906.7	906.7	907.2	907.1
^{102}Ru	907.4	907.3	907.9	907.9	908.4	908.4
^{101}Ru	907.9	908.0	-	908.5	-	909.1
^{100}Ru	908.5	908.7	-	909.2	-	909.8
^{99}Ru	909.3	909.4	909.7	909.8	-	910.6
^{98}Ru	910.0	910.1	-	910.5	-	910.6
^{96}Ru	911.5	911.6	912.0	912.0	-	912.9
A_1 bridge						
^{104}Ru	-	848.2	-	848.3	-	847.2
^{102}Ru	848.8	848.8	849.1	849.1	847.8	847.8
^{101}Ru	-	849.1	-	849.5	-	848.1
^{100}Ru	-	849.5	-	849.9	-	848.4
^{99}Ru	-	849.8	-	850.3	-	848.8
^{98}Ru	-	850.1	-	850.6	-	849.1
^{96}Ru	-	850.7	-	851.4	-	849.7
B_1 bridge						
^{104}Ru	750.7	750.8	752.4	752.2	751.8	751.7
^{102}Ru	751.9	751.9	753.3	753.3	752.7	752.7
^{101}Ru	752.5	752.5	753.7	753.9	-	753.2
^{100}Ru	753.0	753.0	754.5	754.4	-	753.8
^{99}Ru	753.4	753.6	-	755.0	-	754.3
^{98}Ru	754.4	754.2	755.4	755.6	-	754.9
^{96}Ru	755.0	755.4	756.5	756.7	755.9	756.1

* Resolution = 0.6 cm^{-1}, frequency precision = ± 0.1 cm^{-1}

† Force constants and geometries used for calculations

$CsRuO_3$: $f_R = 6.79$ mdyneÅ^{-1}, $f_r = 5.30$ mdyneÅ^{-1}, $f_{Rr} = 0.51$ mdyneÅ^{-1}, $f_{rr} = 0.78$ mdyneÅ^{-1};
$\alpha = 98°$, $\beta = 131°$

$RbRuO_3$: $f_R = 6.82$ mdyneÅ^{-1}, $f_r = 5.31$ mdyneÅ^{-1}, $f_{Rr} = 0.55$ mdyneÅ^{-1}, $f_{rr} = 0.74$ mdyneÅ^{-1};
$\alpha = 96°$, $\beta = 132°$

$KRuO_3$: $f_R = 6.80$ mdyneÅ^{-1}, $f_r = 5.30$ mdyneÅ^{-1}. $f_{Rr} = 0.50$ mdyneÅ^{-1}, $f_{rr} = 0.72$ mdyneÅ^{-1};
$\alpha = 94°$, $\beta = 133°$

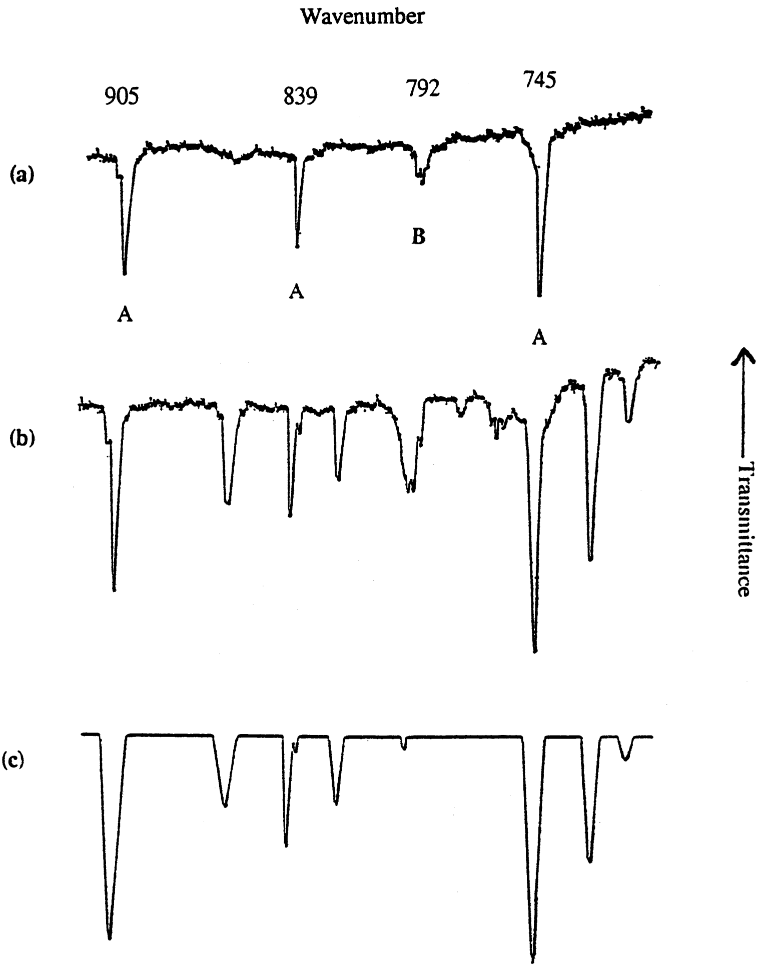

Figure 1 Argon matrix IR spectrum obtained from Cs_2RuO_4 vaporisation

(a) Survey spectrum of Ru-O stretching region, showing bands assigned to species **A** and **B**.
(b) The same spectral region, with ca. 25% ^{18}O enrichment.
(c) Calculated spectrum, assuming **A** to be $CsRuO_3$ (C_{2v}).

Figure 2 Nitrogen matrix IR spectra of species above above Cs_2RuO_4, showing Ru isotope structure.

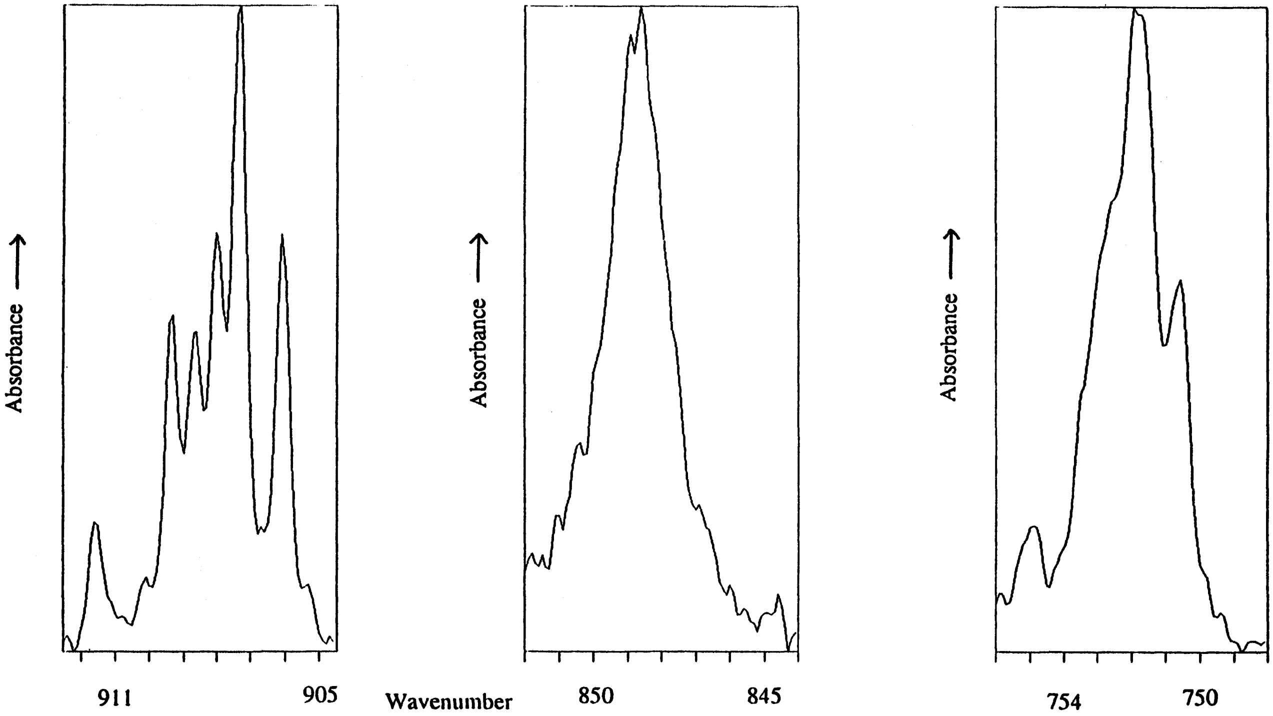

Figure 3 Proposed Structure for Molecular $CsRuO_3$

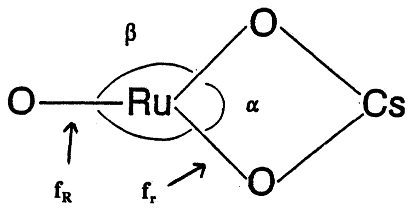

DOI: 10.1149/199413.0265PV

RELAXATION IN NITRATE MELTS

A.Kisliuk, S.Loheider, A.P.Sokolov*, M.Soltwisch and D.Quitmann

Institut für Experimentalphysik, Freie Universität Berlin
Arnimallee 14, D-14195 Berlin, Germany

A.Voronel, and E.Shasha

R.and B. Sackler School of Physics and Astronomy, Tel-Aviv University
Ramat-Aviv, Israel
* Permanent address: Institute of Automation & Electrometry, Russian Academy of Sciences, Novosibirsk, 630090, Russia.

ABSTRACT

We have performed Raman and Brillouin scattering experiments on almost ideal salt melt mixture $KNa(NO_3)_2$. The Raman spectrum of the breathing mode of NO_3 ion was measured in order to obtain rotational line width. The results were analyzed together with literature data on other nitrate systems. All rotational line widths are compared with inverse relaxation times obtained from shear viscosity ($\omega \to 0$) measurements (1). It is found that the rotational line width of the NO_3 group is proportional to inverse relaxation time obtained from the static shear viscosity data. Within accuracy of ±15% the proportionality coefficient is the same for all nitrates systems except $Ca_2K_3(NO_3)_7$. Results of Brillouin measurements were compared with ultrasound measurements in order to estimate the bulk relaxation time. The bulk relaxation time was found in agreement with literature for pure alkali melts. Contrary to the shear relaxation time, it depends strongly on the cation volume.

INTRODUCTION

The shear and bulk viscosities η_s, η_v and their relaxation times τ_s, τ_v are pivotal in the study and understanding of glass transition phenomena. Both η_s and η_v are temperature and frequency dependent. The frequency dependence is most pronounced for both viscosities around the frequency $\omega \approx 1/\tau$ and temperature dependence for fragile glass systems is most pronounced around $T \approx T_g$. Therefore, in order to obtain meaningful information about systems with large viscosity changes, measurements have to be done in wide enough temperature and frequency intervals. Such a wide range study is possible by combining results from Raman and Brillouin spectroscopy, ultrasound and static (low frequency) viscosity measurements.

In the present work we tried to connect results of all these methods. For this first attempt we have chosen alkali nitrates which do not form glasses with one exception.

In order to increase the viscosity changes within the liquid phase, KNO_3-$NaNO_3$ mixture is included. This mixture has low viscosity at high temperature, while in the eutectic point (lowest temperature before crystallization) it has relatively high viscosity about 6 cp. Most physical properties of the components are very similar. Most physical properties of the mixture are also similar i.e. averages of properties of both components. Therefore it is possible to regard this mixture as ideal but with much lower melting point.

EXPERIMENTAL

Both salts, KNO_3 and $NaNO_3$ (Alpha, Karlsruhe) were mixed 1:1 in a glove-box under argon atmosphere, then slowly heated under vacuum up to 400 °C, filtrated through a quartz filter into a cylindrical ampoule of 2.3 cm diameter and sealed. An optical furnace with resistive heating and with four quartz windows was used in both experiments. The temperature in the furnace was computer controlled with stability and accuracy better than ±0.3 K.

Brillouin spectra were measured at VO and HO polarization in right-angle geometry, with finesse about 50, using a Burleigh RC-110 3-pass Fabry-Perot interferometer, by a procedure essentially as described in (2).

In order to evaluate the damping of the observed hypersound longitudinal waves the Brillouin spectra were fitted as described in (3) including the convolution of theoretical function with experimental apparatus profile that was taken from elastic scattering.

In the Raman experiment the same right angle geometry was used to measure polarized VV and depolarized HV scattering of the 1050 cm^{-1} mode for the KNO_3-$NaNO_3$ melt. We used a Jobin-Yvon U-1000 double monochromator with spectral width set to 0.5 cm^{-1}. In Raman and Brillouin experiments we used the 514.5 nm line of an Ar ion laser in multi mode and in single respectively.

The intensity of the isotropic part can be estimated from polarized and depolarized intensity in frequency domain by the following equation:

$$I_{ISO}(\omega)=I_{VV}(\omega) - 4/3\ I_{HV}(\omega) \qquad [1]$$

where I_{ISO} is the isotropic intensity, I_{VV} and I_{HV} are polarized and depolarized intensities, respectively and ω is the frequency. The value of I_{HV} is much smaller than I_{VV} value in the 1050 cm^{-1} line. It allowed us to neglect the contribution of I_{HV} value to isotropic intensity in equation [1]. The line width of isotropic intensity become equal under these conditions to the line width of polarized intensity.

The line width of depolarized intensity consists of isotropic and rotational parts. Rotational part can be estimated by deconvolution of depolarized with isotropic intensities (4,5,6). We assume that the shape of intensities I_{VV} and I_{HV} line is a simple Lorentzian. In this case rotational line widths could be estimated by a subtracting the isotropic from the depolarized width instead of deconvolution procedure:

$$\Gamma_r = \Gamma_{VH} - \Gamma_{VV} \qquad [2]$$

where Γ_r, Γ_{VH}, Γ_{VV} are line widths of rotational part, depolarized part and polarized part respectively.

To obtain the line widths Γ_{VH} and Γ_{VV} from the Raman spectra, the 1050 cm^{-1} line was integrated and then divided by the maximum value for both VV and HV polarizations. A coefficient $2/\pi$ was used to transform triangular approximation in to Lorentzian approximation.

The value of rotational line width Γ_r was calculated in references (5,6) for molten nitrates $NaNO_3$ and the mixture of $LiNO_3$ with $RbNO_3$ for different concentration and temperatures. The value of rotational line width was calculated in references (4) for NH_4NO3, $NaNO_3$ and $LiNO_3$ in water for different concentrations. The values of line widths of Γ_{VH} and Γ_{VV} were obtained for $Ca_2K_3(NO_3)_7$ from references (7). The Γ_r for $Ca_2K_3(NO_3)_7$ and for $KNa(NO_3)_2$ was calculated according to eq.[2].

All line widths Γ are full widths at half height in Lorentzian approximation, measured in cm^{-1}.

RESULTS AND DISCUSSION

Raman Scattering Measurements

The rotational line width Γ_r obtained from Raman scattering measurements in the way described above, may be interpreted as the decay rate of rotation of the NO_3 group, yielding the characteristic time τ_r. In earlier investigations (4,8) this characteristic time was connected with static shear viscosity η_s in the following way

$$\tau_r = C\eta_s + \tau_r^\circ \qquad [3]$$

where $\tau_r = 1/(\pi\Gamma_r)$ was derived from the rotational line width and τ_r° is the zero viscosity intercept. The slope C may be predicted by a hydrodynamic model. This calculation was performed in (4) to analyze slope C for aqueous nitrate solutions which had different viscosities. The slope C was found 2 ps/cp for NH_4NO_3 and 1.5 ps/cp for $NaNO_3$ in water.

However, for the $LiNO_3$ solution rotational relaxation time (τ_r) could not be estimated by eq.[3]. It was found (4) that the rotational relaxation time is a non linear function of viscosity in $LiNO_3$ solutions. Slope C was found to be about 1.5(ps/cp) for low viscosity and 1(ps/cp) for high viscosity.

Simple summation of times of decay was used in previous papers (4,8) to describe a relationship between rotational relaxation time and shear viscosity. In the present work we use a different way to connect the rotational line width with static viscosity. We assume that some viscosity independent relaxation process contribution to Γ_r has to be taken into account. With this assumption we have to compare between Γ_r and inverse relaxation time obtained from shear viscosity, see eq.[6] bellow.

Stokes-Einstein ratio establishes a connection between a shear viscosity η_s and relaxation time τ_s for a given temperature T

$$\eta_s = k_B T \tau_s / V \qquad [4]$$

where V may be interpreted as an effective volume and k_B is the Boltzmans constant. Below we will compare the inverse relaxation time obtained from the low frequency shear viscosity with rotational line width that correspond to a measurement of viscosity at high frequency. For the inverse relaxation time per unit volume we used the symbol G. The unit of volume was chosen $Å^3$ (the natural volume in molecular scale). Using eq.[4], $G= (\tau_s / V)^{-1}$ was calculated by the following equation:

$$G = 0.46T/\eta_s \qquad [5]$$

The numerical coefficient in this equation has units ($Å^3$ cm^{-1} cp / K). We use inverse cm^{-1} scale in order to present G ($Å^3$ cm^{-1}) and Γ_r in similar units.

Viscosity and temperature was substituted in eq.[5] for various nitrate melts and solutions in order to calculate G. The static shear viscosity data for salt melts were taken from (1). They were extrapolated or interpolated to the temperatures at which Γ_r was measured. This was done for every rotational line width (Γ_r). All Γ_r had been calculated from Raman data by one of the methods described above .

In order to test the correlation between Γ_r and G, Γ_r values were plotted against G values calculated by eq.[5] see figures 1, 2 and 3. A clear linear dependence between Γ_r and G is found for melts and water solutions.

A regression analysis was used to find the parameters (Γ_∞, V) that define linear dependence for different nitrate systems. These parameters are summarized in tables I and II. They were calculated by the following equation:

$$\Gamma_r = \Gamma_\infty + G / V \qquad [6]$$

where Γ_∞ is a rotational line width for infinite viscosity, and V is an effective volume.

We found that Γ_r depends linearly on G also for $Ca_2K_3(NO_3)_7$ which is a well known glassformer, up to viscosity about 650 cp. The parameters of eq.[6] in this region are $V = 13.8Å^3$ and $\Gamma_\infty = 0.65$ cm^{-1}, see table I. Other systems crystallize already when they have viscosity much lower than 650 cp.

However for $Ca_2K_3(NO_3)_7$ at viscosity larger then 650cp, the difference between Γ_{VH} and Γ_{VV} becomes very small. This circumstance makes an estimation of Γ_r by eq.[2] difficult.

We compared relaxation times of $Ca_2K_3(NO_3)_7$ obtained by different methods. In first case we calculated relaxation time ($\tau_{s\eta}$) estimated from shear viscosity up to viscosity 650 cp or down to corresponding temperature 420 K.

$$\tau_{s\eta} = V\eta_s / (k_B T) \qquad [7]$$

where $V=13.8Å^3$ from table I. We also calculate relaxation time (τ_{sr}) from rotational line width Γ_r.

$$\tau_{sr} = 1/(\pi(\Gamma_r - \Gamma_\infty)) \qquad [8]$$

where Γ_∞=0.65cm^{-1} from table I. These relaxation times $\tau_{s\eta}$ and τ_{sr} were plotted against inverse temperature together with relaxation times obtained from central line widths from reference (9) see fig.4.

Brillouin Scattering Measurements

Our Brillouin scattering measurements showed that the properties (line width of longitudinal waves and hypersound velocity) of $KNa(NO_3)_2$ melt were averages of the properties of the pure components KNO_3, $NaNO_3$. The relaxation time of bulk viscosity we obtained from our measurements and ultrasound measurements (10) by the method described in (11).

The bulk viscosity was found to be proportional to the cation volume as in pure components (12) see fg.5.

CONCLUSIONS

We found here that shear viscosity is essentially cation independent in all investigated systems of alkali nitrate melts and water solutions. The bulk viscosity depends linearly on the size of cation as was found in (12). In this sense bulk and shear relaxation time of alkali nitrate melts have qualitatively different behavior. We suppose that the shear viscosity depends mainly on rotational properties of the NO_3 group

The correlation between the low frequency shear viscosity and orientation relaxation times described well by the simple ratio eq.[4]. The effective volume may be connected with a volume of the $(NO_3)^-$ group for alkali nitrate melts and their water solutions.

The relaxation time calculated by our method is in good agreement with relaxation time calculated from width of central line, in the glass forming system $Ca_2K_3(NO_3)_7$.

ACKNOWLEDGMENTS

The project was supported by German-Israeli - Foundation (GIF) for Science and Development, and by Deutsche Forschungsgemeinschaft (SFb 337).

REFERENCES

1. G.J.Janz, U.Krebs, H.F. Siegenthaler, and R.P.T Tomkins, J.Phys.Chem. Ref. Data, 1,3 (1972).
2. A.Kisliuk, A.Kudlik, J. Sukmanowski, S.Loheider, M.Soltwisch, and D.Quitmann, J.Phys.Condens.Matter,3,9831, (1991).
3. S.Loheider, G.Vögler, I.Petscherizin, M. Soltwisch, and D.Quitmann J.Chem.Phys.93, 5436, (1990) J.Phys.Condens.Matter 3, 9831 (1991).
4. T. Katõ, J.Umemura, T. Takenaka, Molec. Phys. 36, 3, 621 (1978).
5. T. Katõ, T.Takenaka, Molec. Phys. 54, 6, 621 (1985).
6. T.Katõ, T.Takenaka, J.Chem.Phys 84, 6, 3405 (1986).
7. J.R. Clarke and S.Miller, Chem.Phys.Lett. 13, 2, 97, (1972)

8. Bauer D.R., Brauman, J.I., and Pecora, R.J. Am. Chem. Soc., 96, 22, 6840 (1974).
9. G.Li, W.M Du, A.Sakai, and H. Z. Cummins Phys.Rev. A 45, 3867 (1992)
10. W.Fuchs and J.Richter, Z.Naturforsch. 39,a ,1279 (1984)
11. L.Torell, Thesis, Göteborg (1975).
12. R.W. Higgs and T.A. Litovitz, J. Acoust.Soc.Am. 32, 1108, (1960).

	AQUEOUS SOLUTIONS			MELT		
	NH_4	Li	Na	Na	KNa	Ca_2K_3
V ($Å^3$)	25	25	22	25	24	14
Γ_∞	0	1.0	0.2	1.5	1.3	0.65

Table I. Result of the regression analysis applied on the data plotted in fig.1 and fiig.2. The slopes 1/V are very close for all systems except $Ca_2K_3(NO_3)_7$.

c(Li)	1.0	0.8	0.65	0.5	0.33	0.2	0.0
V ($Å^3$)	22	24	18	18	20	21	17
Γ_∞	1.2	3.6	2.3	2.8	3.5	4.7	4.8

Table II. Result of the regression analysis applied on the data plotted in fig.3. The slopes are still similar but Γ_∞ are different for different concentrations.

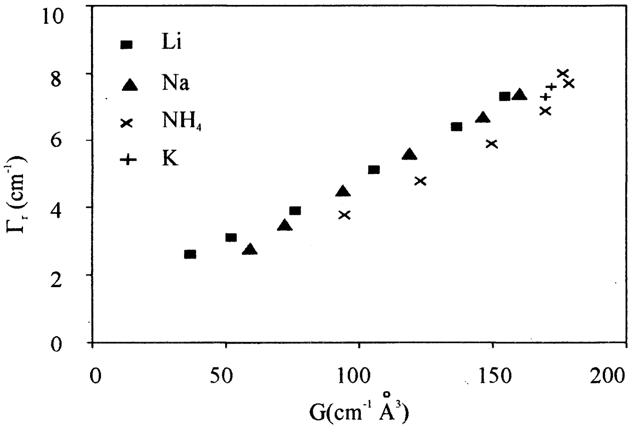

Fig.1 Rotational line width Γ_r from Raman spectra plotted against G (inverse relaxation time per unit volume) obtained from shear viscosity (eq.[5]) for water solutions of different nitrates from reference (3). All points are measured at temperature T=302K. The change in viscosity appears only due to changes in concentration. All solutions show a linear behavior.

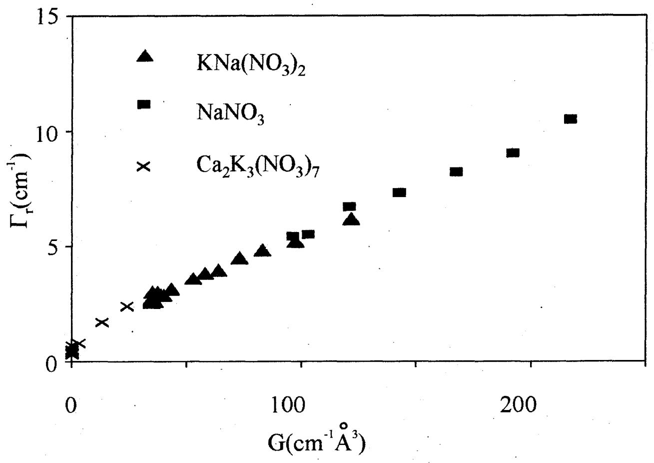

Fig.2 Rotational line width Γ_r from Raman spectra plotted against G (inverse relaxation time per unit volume) obtained from shear viscosity (eq.[5]) for different nitrate melts at different temperature. (See references (1,5,6,7) and ▲ - our data).

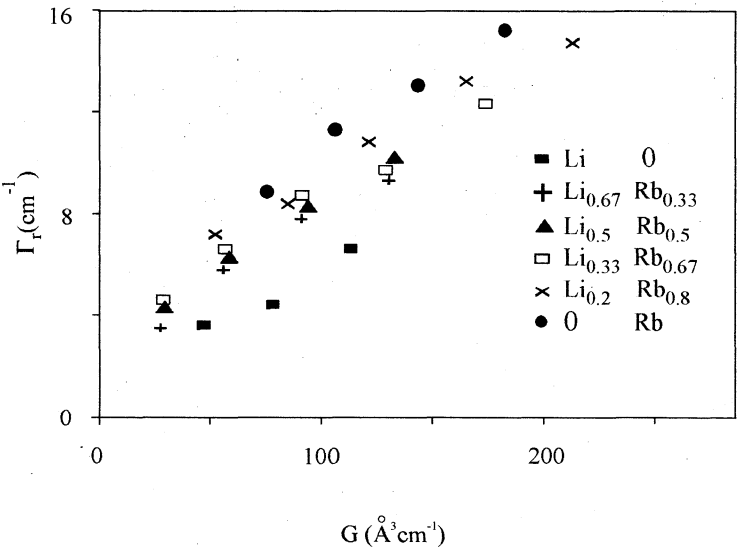

Fig.3 Rotational line width Γ_r from Raman spectra plotted against G obtained from shear viscosity (eq.[5]) for Li-Rb nitrates for different concentrations of Rb. Linear behavior is followed well, but Γ_∞ vary with concentration. (See references (1,6)).

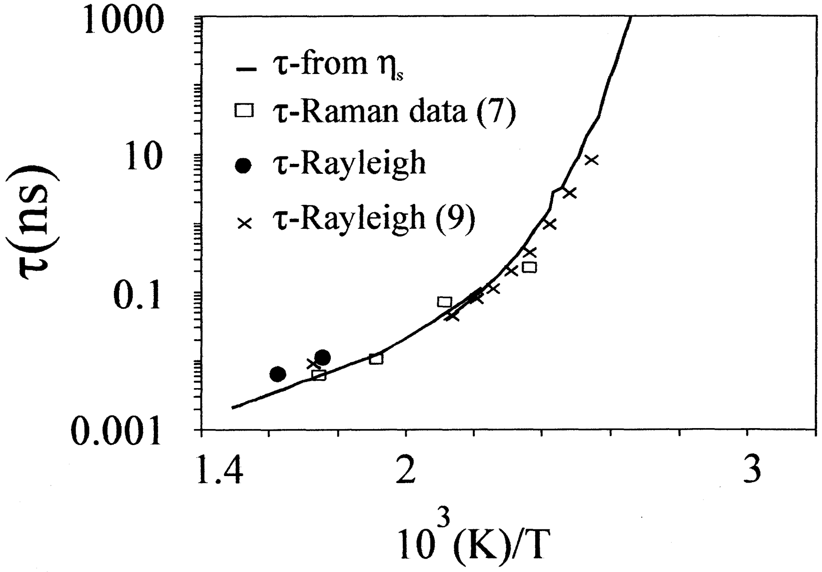

Fig.4 The relaxation times obtained in different ways, plotted against the inverse temperature for $Ca_2K_3(NO_3)_7$. Relaxation times obtained from shear viscosity data with effective volume from table I; rotational relaxation times obtained from (7), and from central (Raylegh) line (9) and this work.

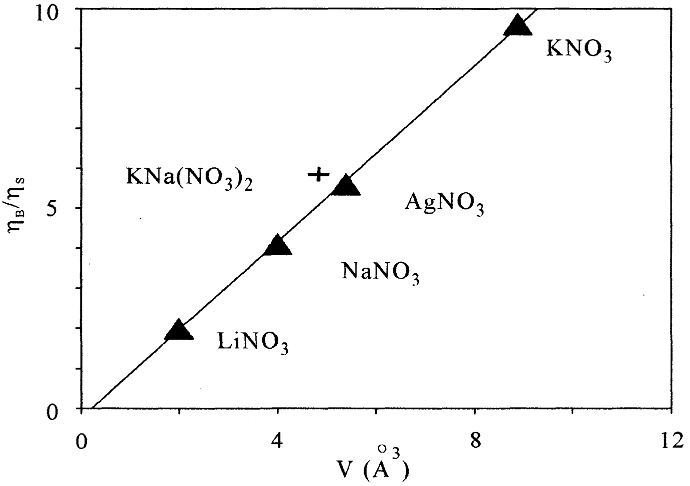

Fig.5 Ratio of bulk to shear viscosities as a function of the cationic volume V for alkali nitrates and silver (10,12). All pure melts are measured at a temperature 40 K above the respective melting points. The KNa(NO$_3$)$_2$ mixture was measured at 140K above its melting point.

DOI: 10.1149/199413.0276PV

OXYGEN BRIDGED ADDUCT COMPOUNDS OF PHOSPHORYL CHLORIDE WITH METAL TRICHLORIDES AND PENTACHLORIDES

S. Boghosian, G. Zissi and G. A. Voyiatzis

Institute of Chemical Engineering and High Temperature Chemical Processes
and
Department of Chemical Engineering, University of Patras,
P.O. Box 1414, GR-26500 Patras, GREECE

ABSTRACT

Raman spectroscopy is used for studying the structural properties of $POCl_3{\cdot}MCl_5$(M=Nb, Ta) molecular complexes in the solid, liquid and gaseous state at temperatures up to 800 K. It is shown that complexing occurs through the formation of P-O-M bridges. The spectra are interpreted in terms of a C_s configuration consisting of a "MCl_5O" octahedron sharing a corner with a "$OPCl_3$" tetrahedron for the $POCl_3{\cdot}NbCl_5$ and $POCl_3{\cdot}TaCl_5$ liquid and vapor complexes. The structural and vibrational properties of a series of $POCl_3{\cdot}MCl_x$(M=Al, Ga, Fe, Zr and Hf) vapor complexes with C_{3v} (involving straight P-O-M bridges) or C_s (involving bent P-O-M bridges) symmetries are discussed. The energies of the $M \leftarrow L$ charge-transfer transitions in the electronic absorption spectra of the $POCl_3{\cdot}FeCl_3$ vapor complex indicate that bonding occurs with the formation of a P-O-Fe bridge. Partial ionization in the liquid and solid phases of the $POCl_3$-$FeCl_3$ and in the solid phase of the $POCl_3$-$AlCl_3$ systems is shown to occur below 450 K.

INTRODUCTION

Phosphoryl chloride is known to act as donor molecule towards other inorganic metal halides by forming a wide range of liquid complex compounds with low melting points. However, although a detailed summary of the chemistry of such compounds is available (1), not much work has been directed towards the determination of structural characteristics in the liquid and vapor state. In contrary, the vibrational and structural properties of a large number of liquid and vapor complexes where $AlCl_3$, $GaCl_3$, $InCl_3$ and $FeCl_3$ act as complex forming agents have been established (2,3).

The aim of the present work is the characterization by Raman spectroscopy of the liquid and vapor complexes formed between $POCl_3$ and *i)* The pentachlorides of Nb and Ta and *ii)* The "acidic" trichloride of Fe. The complexes are investigated also in the solid state in order to clarify in which form they occur (molecular, glassy or ionic).

Furthermore, the nature of the known complexes formed in the $POCl_3$-$AlCl_3$ system (4) is examined in the solid state for comparison with the P-O-Fe system and a summary of certain structural and vibrational properties of $POCl_3 \cdot MCl_x$ (M= Al (4), Ga (4), Fe, Zr (5), Hf (5), Nb and Ta) vapor complexes is presented.

EXPERIMENTAL

High purity anhydrous $NbCl_5$, $TaCl_5$, $FeCl_3$ and $AlCl_3$ were prepared from the corresponding Cerac/Pure Inc. reagents by repeated slow sublimations in fused silica tubes under vacuum. All handling of chemicals took place in a nitrogen-filled glove-box with a water vapor content of less than 1 ppm. Liquid $POCl_3$ was purchased from Fluka.

The Raman (optical) cells containing the melt mixtures consisted of fused silica tubing (4±0.1 mm o.d. and 2±0.1 mm i.d., ~3 cm long). In case of cells containing vapor mixtures, silica tubing with 20±0.2 mm o.d, 18±0.2 mm i.d. was used. Preweighed amounts of salts were transferred into clean, dry, flamed and degassed optical cells of known volume. The cells were afterwards attached to an all-glass vacuum line where a container with $POCl_3$ was also connected. Phosphoryl chloride was then allowed to vaporize and occupy a confined bulb of known volume and it was afterwards transferred by distillation and condensed in the bottom of the optical cell which was immersed in liquid nitrogen. The optical cell was then sealed under vacuum, the salt mixtures were reacted inside a side tube (6±0.1 mm o.d., 4±0.1 mm i.d.), vapor transported into the main cell compartment and finally the side tube was sealed off. In this way a high degree of sample purity could be achieved. The ideal gas pressure, P^0, of each undissociated and unreacted compound could be calculated from the number of moles added to the cell.

Raman spectra were excited with the 514.5 and 488.0 nm lines of a 4W Spectra Physics Ar^+ laser and the 647.1 and 676.4 nm lines of a Spectra Physics Kr^+ laser. The scattered light was collected at an angle of 90° (vertical scattering plane) and analyzed with a Spex 1403, 0.85 m double monochromator equipped with a -20°C cooled RCA photomultiplier and EG&G/ORTEC rate meter and photon counting electronics. The optical furnace for obtaining the high-temperature Raman spectra was similar to that described in detail elsewhere (6).

RESULTS AND DISCUSSION

Raman Spectra of $POCl_3$-MCl_5(M=Nb, Ta) Vapors and Liquids

Figure 1 shows representative vapor Raman spectra obtained for $POCl_3$(g) and $TaCl_5$(g) at 600 K and for a $POCl_3$-$TaCl_5$ vapor mixture at 600 and 700 K. The spectra of the vapor mixtures consist of superpositions of bands due to the pure gaseous components plus five new polarized bands at wavenumbers listed in Table I, which are attributed to a vapor complex. Complex band intensities are decreasing with increasing temperature, probably due to thermal decomposition. Several bands due to the vapor complex might have been obscured by $POCl_3$(g) and $TaCl_5$(g) bands, which dominate the spectra. The vapor Raman spectra obtained for the $POCl_3$(g)-$NbCl_5$(g) system exhibited similar general features. Three weak polarized bands were assigned to a vapor complex (see Table I for wavenumbers). It is noteworthy that in the course of the experiments when the blue to green Ar^+ laser lines were used to excite the spectra, a photodissociation of the colored vapors occurred due to light absorption. Therefore, the use of the rotating cell technique (7) was necessary for preventing this phenomenon.

More information about the number of bands due to the complexes can be obtained by considering the spectra of the liquids. Figure 2 shows Raman spectra obtained from $POCl_3$(l), Ta_2Cl_{10}(l) and three different $TaCl_5$-$POCl_3$(l) mixtures at 220°C. The spectral data clearly indicate that the complex species is the 1:1 $POCl_3 \cdot TaCl_5$ (m.p. ~190°C). All 12 bands observed in the spectrum of the 1:1 mixture are assigned to the $POCl_3 \cdot TaCl_5$(l) complex (see Table I for wavenumbers and polarization characteristics). Similar spectra were recorded for the $NbCl_5$-$POCl_3$(l) system, where again no bands due to $POCl_3$(l) or $NbCl_5$(l)/Nb_2Cl_{10}(l) were observed in the spectra of the 1:1 mixture. The wavenumbers and polarization characteristics of 13 bands due to the $POCl_3 \cdot NbCl_5$ complex (m.p. ~170°C) are listed in Table I. Formation of ionic $POCl_2^+MCl_6^-$ liquid compounds can be excluded because of the absence of the characteristic $NbCl_6^-$ and $TaCl_6^-$ bands (3).

Table I. Raman spectral data (cm^{-1}) of $POCl_3 \cdot NbCl_5$ and $POCl_3 \cdot TaCl_5$ liquid and vapor complexes[a].

$POCl_3 \cdot NbCl_5$(l) 500 K	$POCl_3 \cdot NbCl_5$(g) 600 K	$POCl_3 \cdot TaCl_5$(l) 500 K	$POCl_3 \cdot TaCl_5$(g) 600 K	Assgn
90 vw,dp		88 w,dp		
144 s,dp				
155 s,p		144 s,p	142 w,p	
169 m,dp		160 m,dp		
189 w,dp		185 m,dp		
211 w,dp		210 w,dp		
298 m,dp		304 m,dp		
358 s,p	360 vw,p	360 s,p	362 w,p	$(\nu_{M-Cl})_{br}$
399 vs,p		402 vs,p		$(\nu_{M-Cl})_t$
524 s,p	520 vw,p	529 s,p	515 w,p	ν_{P-Cl}
636 vw,dp		642 vw,dp		
1210 vw, p		1200 w,p	1225 vw,p(?)	
1256 vw,p	1265 vw,p	1260 vw,p	1268 vw,p	ν_{P-O}

[a] Abbreviations: s=strong, m=medium, w=weak, v=very, p=polarized, dp=depolarized

It appears that the positions of bands assigned as due to the vapor complexes in the spectra of $POCl_3$-MCl_5(M= Ta, Nb) vapors are very close to the positions of the most prominent bands of the $POCl_3{\cdot}MCl_5(l)$ complexes, a fact indicating that the predominant vapor complex species are the 1:1 $POCl_3{\cdot}MCl_5(g)$ (M=Ta, Nb) molecules. This is in agreement with what it has been established for the case of $POCl_3{\cdot}MCl_3$ [M= Al, Ga (4), Fe (8)] and $POCl_3{\cdot}MCl_4$ [M= Zr, Hf(5)] gaseous compounds. The stability of the vapor complexes is decreasing in the order: Al ⟩ Ga, Fe ⟩ Zr, Hf ⟩ Nb, Ta.

Table II lists the principal stretching frequencies for the studied $POCl_3{\cdot}MCl_x$ (x=3, 4 and 5) vapor complexes. It is noteworthy that in all cases studied, the $\nu_{P\text{-}O}$ and $\nu_{M\text{-}Cl}$ stretching frequencies were red-shifted relative to the corresponding bands of the free $POCl_3(g)$ and the free metal chlorides, while on the other hand the $\nu_{P\text{-}Cl}$ stretching frequencies were blue-shifted relative to the corresponding band of $POCl_3(g)$. These shifts are compatible with the formation of P-O-M bridging bonds, which are expected to weaken the P-O and M-Cl bonds and strengthen the P-Cl bonds.

Table II. Principal stretching frequencies (in cm^{-1}) in $POCl_3{\cdot}MCl_x$ vapor complexes

	$\nu_{M\text{-}Cl}$,cm^{-1}		$\nu_{P\text{-}Cl}$,cm^{-1}	$\nu_{P\text{-}O}$,cm^{-1}	Ref.
$POCl_3(g)$			478.5	1319	
$AlCl_3(g)$	377				
$POCl_3{\cdot}AlCl_3(g)$		313	537	1231	4
$GaCl_3(g)$	381				
$POCl_3{\cdot}GaCl_3(g)$		366	513	1220	4
$FeCl_3(g)$	370				
$POCl_3{\cdot}FeCl_3(g)$		362	530	1200	8
$ZrCl_4(g)$	377				
$POCl_3{\cdot}ZrCl_4(g)$		-	508	-	5
$HfCl_4(g)$	381				
$POCl_3{\cdot}HfCl_4(g)$		347	512	1263	5
$NbCl_5(g)$	393				
$POCl_3{\cdot}NbCl_5(g)$		360	520	1265	this work
$TaCl_5(g)$	406				
$POCl_3{\cdot}TaCl_5(g)$		362	515	1268	this work

The bonding in the vapor and liquid adduct $POCl_3{\cdot}MCl_5$ complexes occurs by coordination of he oxygen with the metal atom, leading presumably to a Cl_3POMCl_5 configuration with C_s symmetry (Cl_3PO tetrahedron sharing corner with $OMCl_5$ octahedron) giving rise to coordination numbers of 6 and 4 for M(Nb,Ta) and P, respectively (3).

Electronic Absorption Spectra of $POCl_3$-$FeCl_3$ Vapors

The type of bonding and M-Cl interaction in the $POCl_3{\cdot}FeCl_3$ vapor complex can be studied exclusively by means of UV/VIS spectrophotometry by measuring the energies of the ligand-to-metal (M←L) charge transfer transitions. However, considering the gaseous equilibrium:

$$POCl_3(g) + 1/2Fe_2Cl_6(g) \rightleftharpoons POCl_3 \cdot FeCl_3(g)$$

a sufficiently large excess of phosphoryl chloride ($P^{0}_{P,600\ K} = 2.5 - 6.75$ atm) had to be present in order to consider that the contribution of the iron chloride sample (small enough to vaporize completely) to the absorbance in the homogeneous gas region was negligible. Thus in such a case it can be assumed that all the iron in the cell is in the form of $POCl_3 \cdot FeCl_3(g)$ and the molar absorptivities of this species can be determined (9). Figure 3 shows that the appearance of the $POCl_3 \cdot FeCl_3(g)$ spectrum [curve (a)] is different from that of $Fe_2Cl_6(g)$ [curve(b)]. The wing of the band at the far UV range is due to a forbidden ($n \rightarrow \pi^*$) transition from a non-bonding oxygen orbital to the antibonding molecular orbital of the P-O bond (10). It turned out, however, that a third charge transfer band of the $POCl_3 \cdot FeCl_3$ vapor complex is obscured from he strong $POCl_3(g)$ absorption band [spectrum (a)]. This is illustrated in spectrum (c), Fig. 3, which is obtained from a gaseous sample in equilibrium with a condensed phase ($POCl_3 \cdot FeCl_3(l)$ + "$FeCl_3(l)$"?) in a cell with no excess $POCl_3$ at 490 K. The contribution of gaseous Fe_2Cl_6 is subtracted from spectrum (c), which can thus be assigned to $POCl_3 \cdot FeCl_3(g)$. It appears from Figure 3 that the positions of the charge transfer bands' maxima move to higher energies on going from $Fe_2Cl_6(g)$ to $POCl_3 \cdot FeCl_3(g)$. This is exactly what it should be expected from the alteration of the chloride ligands' environment caused by the formation of a P-O-Fe bridge. The electron donating ability of the chloride ligands decreases since their electronic density is pulled away and the M←L charge transfer is hindered and occurs at higher energies. Thus weak covalent bonding is implied for the Fe-Cl interaction in the $POCl_3 \cdot FeCl_3(g)$ molecule in agreement with the results of the Raman spectroscopic investigation (see Table II and refs. 8,9).

Partial Ionization of $POCl_3$-$FeCl_3$ and $POCl_3$-$AlCl_3$ solid complexes

It has been established that the $POCl_3$-$AlCl_3$ molten mixtures are molecular liquids consisting of $POCl_3 \cdot AlCl_3(l)$, $POCl_3 \cdot (AlCl_3)_2(l)$, $Al_2Cl_6(l)$ and $POCl_3(l)$ at temperatures above their melting points (4, 11). Furthermore, while the molecular nature of the $POCl_3$-$FeCl_3$ molten mixtures can be considered established at T⟩500 K (8), a study of the temperature dependence of their Raman spectra indicates that below 450 K, and as temperature is gradually decreased, a partial self-ionization of the liquid occurs, which is more pronounced in the $POCl_3$-rich mixtures (e.g. for a P/Fe ratio of 2/1) (8). By lowering the temperature from 525 to 425 K three new bands appeared at 114, 332 and 520 cm^{-1} that became progressively stronger on going from 425 to 360 K and attained their maximum intensities in the solid state at liquid nitrogen temperature (9). The bands at 114 and 332 cm^{-1} are assigned to $FeCl_4^-$, while the band at 520 cm^{-1} is more difficult to assign. In view of the 525 cm^{-1} value reported for the $v_{P\text{-}Cl}$ mode of $PFCl_2$ (12) one could assign the 520 cm^{-1} band to the $v_{P\text{-}Cl}$ mode of $POCl_2^+$.

The molecular nature of the $POCl_3 \cdot AlCl_3(l)$ complex (4) is not retained in the solid state. A very prominent band at 352 cm^{-1}, which is attributed to $AlCl_4^-$ appears in the crystal Raman spectra from 2:1 and 1:1 $POCl_3$-$AlCl_3$ mixtures (see Figure 4). However the strong feature at 549 with a shoulder at 535 cm^{-1} observed for the crystalline phase from the 2:1 mixture is not observed in the 1:1 solid. The 1:1 ionic compound is probably the $[Al(POCl_3)_4][AlCl_4]_3$, for which a X-ray powder diagram is reported (13). While freezing a 2:1 mixture, gas bubbles are evolved which are believed to be $POCl_3$. This is further justified from the close resemblance of the spectra of the solids from the 2:1 and 3:2 mixtures, indicating that the same ionic compound is formed, which is believed to be the $[Al(POCl_3)_6][AlCl_4]_3$ in agreement with ref.11, with the 535-549 cm^{-1} band assigned to the Al-O stretching mode of $[Al(POCl_3)_6]^{3+}$, in analogy with the 526 cm^{-1} $\nu_1(A_{1g})$ Al-O band of $[Al(OH_2)_6]$ (14).

ACKNOWLEDGMENT

The authors are indebted to Professor G. N. Papatheodorou for helpful discussions and valuable comments during the course of the investigation

REFERENCES

1. R. H. Tomlinson, in Mellor's Comprehensive Treatise on Inorganic and Theoretical Chemistry, Vol. 8, Supplement 3, p. 496. Longmans, London (1971).
2. G. N. Papatheodorou, in Current Topics in Materials Science, E. Kaldis, Editor, Vol. 10, p.251,North Holland Pub. Co., New York (1982).
3. M. Brooker and G. N. Papatheodorou, in Advances in Molten Salt Chemistry, G. Mamantov, Editor, Vol. 5, p. 27. Elsevier, New York (1983).
4. S. Boghosian, D. A. Karydis and G. A. Voyiatzis, Polyhedron, 12, 771 (1993).
5. S. Boghosian, G.N. Papatheodorou, R.W. Berg and N.J. Bjerrum, Polyhedron, 5, 1393 (1986).
6. G. N. Papatheodorou, in Proceedings of the 10th Materials Research Symposium on Characterization of High Temperature Vapors and Gases, J. W. Hastie, Editor, NBS Publication 561, p.647, National Bureau of Standards, Washington, DC (1979).
7. L. Nalbandian and G. N. Papatheodorou, High Temp. Sci., 28, 49 (1990).
8. G. A. Voyiatzis and S. Boghosian, in Molten salt Chemistry and Technology/1993, M.L. Saboungi and S. Kojima, Editors, PV 93-9, p. 14, The Electrochemical Society Softbound Proceedings Series, Pennington, NJ (1993).
9. S. Boghosian, G. A. Voyiatzis and G. N. Papatheodorou, to be submitted for publication.
10. M. Halmann, J.Chem.Soc., 2853 (1963).
11. F. Birkeneder, R. W. Berg and N. J. Bjerrum, Acta Chem.Scand., 47, 344 (1993).
12. K. Nakamoto, Infrared and Raman Spectra of Inorganic and Coordination Compounds, p. 122, Wiley Interscience, New York (1986).
13. V. Gutmann and M. Baaz, Monatsh.Chem., 90, 729 (1959).
14. M. H. Brooker, in The Chemical Physics of Solvation, R. R. Dogodnadze, Editor, Vol. 38 B, p. 119, Elsevier, Amsterdam 1986.

Fig. 1. Raman spectra of $POCl_3$-$TaCl_5$ vapors. $P^0_{POCl_3,\ 600\ K} = 2$ atm, $P^0_{TaCl_5,\ 600\ K} = 0.5$ atm. Bands due to the complex are marked by "C". $\lambda_0 = 488.0$ nm, w=320 mw, ssw=6 cm^{-1}, $\tau = 0.5$ s, ss= 18 cm^{-1} min^{-1}

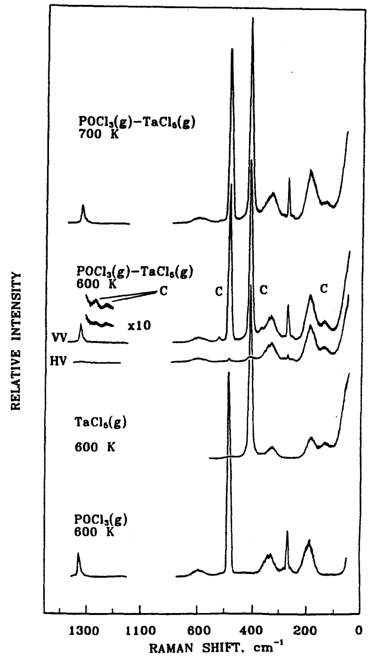

Fig. 2. Concentration dependence of Raman spectra of $POCl_3$-$TaCl_5$ molten mixtures. $\lambda_0 = 488.0$ nm, w=15 mw, ssw=3.5 cm^{-1}, $\tau = 0.1$ s, ss= 60 cm^{-1} min^{-1}.

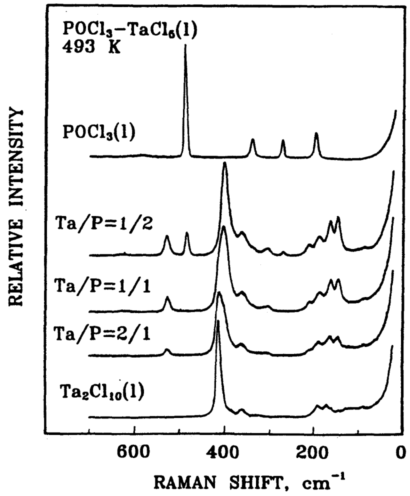

Fig. 3. Molar absorptivities of $POCl_3{\cdot}FeCl_3(g)$ in equilibrium with $POCl_3(g)$ ($P^0_{POCl_3,\,600\,K}$= 4.5 atm) at 550 K [curve (a)] and $Fe_2Cl_6(g)$ at 500 K [curve (b)]. To the bottom [curve (c)] the spectrum of $POCl_3{\cdot}FeCl_3(g)$ is shown in arbitrary intensity units.

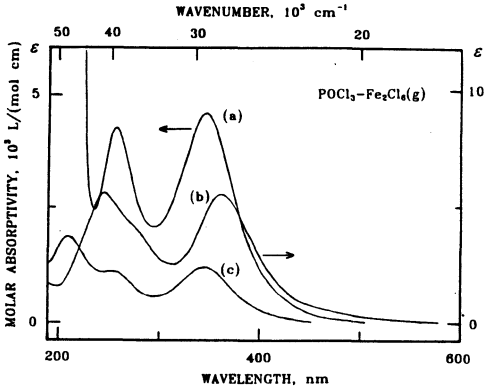

Fig. 4. Raman spectra of $POCl_3{\cdot}AlCl_3(l)$ at 500 K and solids from 1:1 and 2:1 $POCl_3$-$AlCl_3$ mixtures at room temperature. λ_0=488.0 nm, w=15 mw, ssw$\approx$3.5 cm^{-1}, τ= 0.1 s, ss= 60 cm^{-1} min^{-1}.

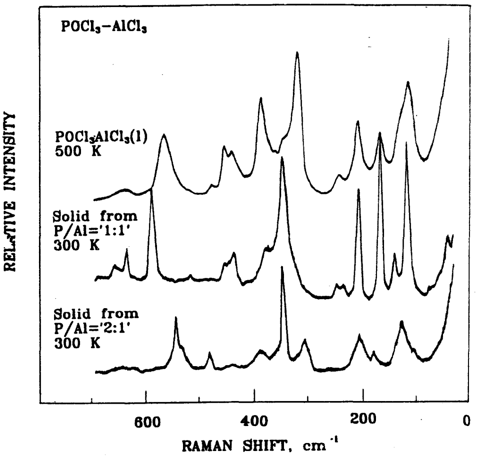

DOI: 10.1149/199413.0284PV

RAMAN SCATTERING FROM ALKALI METAL HALIDE MELT MIXTURES: COMPOSITION AND TEMPERATURE EFFECTS

S.G. Kalogrianitis, T.G. Mihopoulos, E.A. Pavlatou and
G.N. Papatheodorou

Department of Chemical Engineering, University of Patras and
Institute of Chemical Engineering and High Temperature
Chemical Processes
P.O.Box 1414, GR-26500, Patras, GREECE

ABSTRACT

Reduced isotropic and anisotropic Raman spectra were measured for a series of molten alkali metal halides and their mixtures. The systems involving CsX and LiX (X=Cl, Br, I) were investigated at different temperatures and compositions. The spectra of the common anion mixtures show two bands which appear to be a superposition of the bands of the component salts. Similar is the spectral behavior of the common cation salts. The data are interpreted in terms of the fluctuations of the X^- and Cs^+ polarizabilities induced by short range ionic interactions. The Li-X pair interactions appear to be important in determining the scattered light intensity and its temperature variation.

INTRODUCTION

Over the past decade the Raman (or Rayleigh wing) light scattering spectra of molten alkali halides have been systematically studied. A series of experimental measurements have been reported by Raptis et all (1-3) and theoretical and computer simulation studies have been reported by Madden et all (4-5). An exponential decay like spectrum is obtained having shoulder like bands and showing a tail that in certain cases covers frequencies $\omega > 600\ cm^{-1}$.

The origin of the spectra is due to fluctuations of the polarizability density in the medium, induced by ionic interactions. The interaction-induced polarizability model (4-5) argues that several physical processes may contribute to the fluctuations of the total polarizability. Asymptotic contributions, due to the field, created by other ions outside the electronic cloud of the ion and short range contributions which result from interactions between nearest neighboring ions, give rise to the features seen in the spectra. The temperature dependence studies of the Raman scattering spectra of alkali metal halides are very limited. In a recent study (1) the CsCl spectra have been measured in the temperature range 945-1245 K. The integrated intensity corrected for the Bose thermal factor was found to increase slightly with increasing temperature. This excess scattering was attributed to second order summation or difference bands arising from a quasi-harmonic oscillator type model. No drastic changes in the depolarization ratio spectra were observed with temperature variation.

The purpose of the present study is to study the temperature dependence of the alkali metal halide melts. Due to experimental difficulties, arising mainly from the slight attack of the fused silica containers by the melts at temperatures close to 700 °C, the studies are limited to a narrow temperature range above the melting points of these salts. The range, however, can be expanded to lower temperatures by studying mixtures of alkali halide melts. Thus, apart from temperature, the composition dependence of the light scattering spectra of mixed alkali halide melts is also investigated. Spectra of the following systems have been measured at different temperatures and compositions:

I. single salts : CsX, LiX (X=Cl, Br, I)
II. common anion mixtures : CsX-LiX (X=Cl, Br, I)
III. common cation mixtures : ACl-ABr, ACl-AI, ABr-AI (A=Cs, Li)

The data presented here are discussed in terms of the influence of the different ions and of the temperature to the physical processes that contribute to the fluctuations of the total polarizability and give rise to the observed spectra.

EXPERIMENTAL

High purity chemicals purchased from Merck Chemical Co. or Cerac Pure Inc. were used as starting materials. The alkali metal chloride and bromide salts were furthur purified by bubbling gaseous HCl or HBr through the corresponding melt and then filtering under nitrogen atmosphere. The alkali metal iodide salts were dried under vacuum by slowly raising the temperature up to 300 °C. Finally all the above purified salts were sublimed (or distilled) under high vacuum at temperatures up to 800 °C. All operations with the purified chemicals were carried out in a glove box (<1 ppm H_2O) and/or in sealed fused silica containers.

Fused silica tubes of constant diameter (OD=6mm, ID=4mm) were used for making the Raman cells. About 0.02 moles of the clean and anhydrous chemicals were transferred into the cells and sealed under vacuum. The cell was 2-3 cm long and the melt occupied about half of its volume.

The Raman spectroscopic system and techniques for measuring relative Raman intensities from samples in different cells and at different temperatures were the same as before (6-7). The optics and the Hartman diagram of the entrance slit were adjusted so that only scattered radiation coming from ~1.5 mm across the laser beam, inside the Raman cell, was collected and entered into the monochromator. This eliminated stray light scattering from the wall of the silica containers.

The spectrometer was interfaced with a P.C. for recording the spectra, for calculating the reduced intensity and the depolarization ratios and for statistically smoothing the spectra.

RESULTS AND DISCUSSION

In the liquid phase, the Raman spectra measured for any combination of polarization of the incident and scattered radiation can be expressed in terms of the isotropic ($I_{ISO}(\omega)$) and anisotropic ($I_{ANISO}(\omega)$) spectra. Thus, by measuring the VV and HV Raman intensities we can express:

$$I_{ISO}(\omega) = I_{VV}(\omega) - \frac{4}{3} I_{HV}(\omega) \; ; \; I_{ANISO}(\omega) = I_{HV}(\omega) \qquad [1]$$

The reduced Raman intensity $R_{XY}(\omega)$ is related (8) to the measured intensity $I_{XY}(\omega)$:

$$R_{XY}(\omega) = I_{XY}(\omega)\ \omega\ (\omega_o-\omega)^{-4}\,[n(\omega)+1]^{-1} \qquad [2]$$

where ω_o is the excitation laser frequency and $n(\omega)+1=\left[\exp\frac{h\omega c}{RT}-1\right]^{-1}+1$ is the Boltzmann thermal population factor. Reduced isotropic $[R_{ISO}(\omega)]$ and reduced anisotropic $[R_{ANISO}(\omega)]$ spectra can be also calculated from equations 1 and 2.

From the over 30 Raman cells prepared and the over 400 spectra collected at different polarizations, compositions and temperatures, a small collection of spectra are presented here. The discussion and conclusions cover all the systems studied.

Figure 1 shows representative spectra obtained for the LiCl-CsCl eutectic. The $I_{ISO}(\omega)$ and $I_{ANISO}(\omega)$ representations of the spectra are shown. All system studied in this work show in the $I_{ISO}(\omega)$ and $I_{ANISO}(\omega)$ spectra three main regions: (I) a narrow exponentially decaying region close to the Rayleigh line at frequencies $\omega<50\ cm^{-1}$, (II) a middle region which depending on the system, covers frequencies up to 200 cm^{-1} (i.e. CsI) to up to 500 cm^{-1} (i.e. LiCl) and (III) an end exponentially decaying tail that extends the middle region by 200 to 300 cm^{-1}. The scattering from region I overlaps with stray light scattering (arising from impurities, dust, container etc) and is very sensitive to the thermal population factor $[n(\omega)+1]$. This region involves uncertainties in determining accurately its shape and characteristics and is not considered and discussed here. In the $R(\omega)$ representation of the spectra, region I is practically suppressed. Regions II and III show in "general" two shoulder bands in the $I(\omega)$ spectra which are well resolved in the $R(\omega)$ spectra (see insert Fig. 1). Our presentation of results and discussions is focussed on these two last regions of the spectra.

I. Single Salts: LiX, CsX (X=Cl, Br, I).

The isotropic and anisotropic spectra of all six single salts are shown in Fig. 2 and are in good agreement with the spectra (HV) reported by Raptis et all (1-3). There are, however, some features that are more pronounced in our spectra as follows:

i. For the LiX systems both the $R_{ISO}(\omega)$ and $R_{ANISO}(\omega)$ show two bands for each halide system. The relative intensities $R_{ISO}(\omega) > R_{ANISO}(\omega)$ confirm the high depolarization ratio reported before (1-3).

ii. The CsX systems possess only one band with low depolarization ratio and with comparable $R_{ISO}(\omega)$ and $R_{ANISO}(\omega)$ intensities.

iii. For both systems, LiX and CsX, the frequency at the maximum of $R_{ISO}(\omega)$ is shifted to higher energies relative to the corresponding frequency of $R_{ANISO}(\omega)$.

It has been pointed out by Raptis (1) that the maximum frequency, v_{max}, of the main band in the $R_{HV}(\omega)$ spectra is close to the Debye frequency, v_D, of the corresponding solid. In the theoretical description of Madden and O'Sullivan (4), the light scattering spectra of the alkali metal halide melts are expected to have contributions from longitudinal (L.O., L.A. type) and transverse (T.O., T.A. type) charge current and density modes. Such modes appear predominantly in the anisotropic spectra (HV) and may be associated with the two bands shown in the $R_{ANISO}(\omega)$ of the LiX salts. The small cation mass and high ion density in each LiX melt give rise to a high ω_{LO} frequency, which is separated from modes in the the low frequency region (Fig. 2). It appears, that for the CsX salts all these modes are compressed to lower frequencies and thus, only one band is seen in the spectra (Fig. 2).

The isotropic light scattering $I_{ISO}(\omega)$ (or $R_{ISO}(\omega)$) is dominated by short range contributions to the polarizability (overlap effects) and reflects spherically symmetric distortions of the ion. The $R_{ISO}(\omega)$ spectra in Fig. 2 show much higher intensities for the LiX relative to the CsX systems, which imply stronger overlap effects in the lithium than in the cesium systems. On the other hand, the frequency shift of ν_{max} from $R_{ANISO}(\omega)$ to $R_{ISO}(\omega)$ (Fig. 2) is probably an indication that the contribution of the short range interactions to the spectra is at higher energies than the contributions due to field gradients.

II. Common anion mixtures: LiX-CsX (X=Cl, Br, I).

Representative spectra of several common anion mixtures are shown in Figs. 1, 3 and 4. Both composition and temperature effects have been measured. From the data presented, as well as, from similar measurements for the bromide systems we may note the following:

α. The $R_{ISO}(\omega)$ and $R_{ANISO}(\omega)$ spectra of the mixture show in general two main bands with frequencies shifted relative to the band frequencies of the pure components. For the isotropic spectra a "blue" shift is seen for both bands while for the anisotropic spectra the shifts, especially in the CsX region, are rather small.

β. The overall intensity of $R_{ISO}(\omega)$ and $R_{ANISO}(\omega)$ of the mixture is lower than the corresponding intensity obtained by superimposing and adding proportionally the intensities of the pure components (e.g. dotted lines in Fig.3).

γ. With increasing temperature the $R_{ISO}(\omega)$ intensity of the mixture increases drastically in the high frequency region (the LiX region), but very small changes occur in the low frequency region (the CsX region). The temperature effect in the anisotropic spectra is small relative the $R_{ISO}(\omega)$ and rather uniform in the overall frequency region (e.g. Fig. 1 and 4).

In glassy materials the low frequency $R_{ANISO}(\omega)$ spectra (eq. 2) have been associated and used to produce an effective vibrational density of states, VDOS (8). The use of $R(\omega)$ for liquids is not entirely appropriate since, in contrast to the glasses, the atoms (ions) in the liquid diffuse more rapidly and thus there is lack of long living equilibrium positions. It appears however, that at least for viscous liquids [e.g. $ZnCl_2$ (9)], a correlation exists between $R_{ANISO}(\omega)$ and VDOS. Furthermore, the $R(\omega)$ spectra of many glasses and liquids are similar with the low frequency (L.F.) I.R. spectra (10, 11). For molecular melts the L.F.-$R_{ANISO}(\omega)$ spectra have been attributed to reorientational/rotatory modes (11, 12), while for ionic glasses and melts the L.F. region of both the I.R. and $R(\omega)$ spectra are associated with cation-site modes (10, 13). Studies of a series of glasses (10, 13) containing metal cations of different sizes and charges, have argued that a "cage" like structure is formed around each cation. Within this cage, the cation-site interaction gives rise to a distribution of low frequency modes appearing in both the I.R. and $R(\omega)$ spectra as a broad band having a characteristic ν_{max} for each cation. This characteristic frequency is present in the common anion spectra of both the single salts and the mixtures with different cations.

As pointed out above (α) the reduced Raman spectra of melt mixtures and components appear to have a characteristic frequency for each alkali halide cation. It seems that the "cation frequencies" measured in the single salts CsX and LiX are close to the frequencies of the two bands in the melt mixture. The "blue shift" (α) and the non additivity (β) of the spectra can be justified on the bases of the interaction-induced polarizability model. For pure LiX, the short range polarization interactions are responsible for changing the anion polarizabilities and give the predominant contribution to R_{ISO} (ω). The high polarizing power ($1/r^+$) of the "hard" (low polarizability) Li^+ cation facilitates electronic overlap with the "soft" X^- anion and the formation of short living Li-X pairs. Due to their small size, the Li^+ cations have high mobility and create a rather uniform (symmetric) field around each anion. Thus, breathing-like fluctuations of the anion polarizability may occur that scatter the light isotropically. In the pure CsX melts the ionic sizes and polarizabilities of the ions are not as dissimilar as in LiX and scattering may occur from polarizability fluctuations of both the anion (X^-) and the cation (Cs^+). In the CsX-LiX mixture each anion is "statistically" surrounded by cations and although electron overlap between Li^+ and X^- may occur, the field is less symmetric due to the presence of Cs^+ and thus,the intensity of the isotropically scattered light is less than that expected by adding the contributions of the pure individual salts (this accounts for (β)). Furthermore, as we go from pure LiCl to the mixture the second nearest neighbors of Li^+ change from Li^+ to Cs^+. This facilitates the Li-X "pair" overlap and the Li^+ cation "cage frequency" shifts to the "blue". In turn, the Cs^+ cation has as nearest neighbor a "harder" anion whose electron density has been pulled away by the Li-X overlap. In other words on going from pure CsX melts to the melt mixtures the Cs^+ cation cage frequency will follow the blue shift trends of Fig. 2, where a decrease in the softness of the anion (I → Cl) increases the ν_{max} frequency ($70 \rightarrow 130$ cm^{-1}). These arguments account for the above observation (β).

Finally the drastic temperature effect on the intensity of the isotropic spectra in the Li^+ frequency region (γ) can be attributed to the mobility of the Li^+, which with increasing temperature tends to create a more symmetric field around the anion and thus, facilitates the breathing-like fluctuation of the polarizability. The shift of the ν_{max} to higher energies with increasing temperature, probably indicates an increasing overlap in the Li-X pair and is in accordance with early studies on covalency effects in melts (14). It is noteworthy, that for molecular melts the temperature effect on the L.F. R(ω) spectra is opposite (12) to that observed for these ionic CsX-LiX systems.

III. Common cation mixtures: ACl-ABr, ACl-AI, ABr-AI (A=Li, Cs)

Representative spectra of the common cation systems are given in Fig. 6 for the LiCl-LiI eutectic. From the data obtained for all six systems at different compositions and temperatures, a series of observations can be made, which to a large extend, are similar to those for the common anion systems. The behavior is similar but the effects are less pronounced. The "cage frequencies" of the individual salts are transferred into the mixture (Fig. 6) but due to comparable band intensities their resolution is not well defined. For the common Li^+ systems the R_{ISO} (ω) intensity increases with increasing temperatures while, as expected, the common Cs^+ systems are invariant to temperature.

The data for the common cation systems confirm the interpretation given above for the common anion systems and support the view, that the predominant ion-induced polarizability fluctuations are due to short range interactions.

CONCLUSIONS

The isotropic and anisotropic Raman scattering from alkali metal halide mixtures involving the LiX and CsX (X=Cl, Br, I) salts, arises from a superposition of contributions from the individual ions in the pure components. Polarizability fluctuations of both the anion(s) X^- and the highly polarizable Cs^+ cation contribute to the light scattering intensity. The origin of the isotropic scattering spectra is mainly due to short range ion-induced polarizability fluctuations. Electron overlap interaction betwen the anion and the surrounding Li^+ cations induces a rather symmetric field, which contributes to the breathing-like fluctuations of the anion polarizability and gives rise to strong isotropic Raman scattering intensity. The Li-X pair interactions are also important in determining the temperature variation of the isotropic intensity.

REFERENCES

1. C. Raptis and R.L. McGreevy, J. Phys. Condens. Matter 4 5471 (1992) and references therein.
2. C. Raptis and E.W.J. Mitchell, J. Phys. C.:Solid State Phys. 20 4513 (1987).
3. E.W.J. Mitchell and C. Raptis, J. Phys. C.: Solid State Phys. 16 2973 (1983).
4. P.A. Madden and K.F. O'Sullivan, J. Chem. Phys. 95 1980 (1991).
5. P.A. Madden, K.F. O'Sullivan, J.A. Board and P.W. Fowler, J. Chem. Phys. 94 918 (1991) and references therein.
6. G.N. Papatheodorou, J. Chem. Phys. 66 2893 (1977).
7. S. Boghosian and G.N. Papatheodorou, J. Phys. Chem. 93 415 (1989).
8. R. Shuker and R.W. Gammon, Phys. Rev. Lett. 25 112 (1970).
9. E.A. Pavlatou, Proceedings of the "International Symposium on Glass Science and Technology-1993" in press.
10. C.D. Chryssikos, E.I. Kamitsos, A.P. Patsis, M.S. Bitsis and M.A. Karakassides, J. Non-Cryst. Solids 126 42 (1990) and references therein.
11. M. Brooker and G.N. Papatheodorou in "Advances in Molten Salt Chemistry", G. Mamantov and C.B. Mamantov, Eds Vol.5, p.27, Elsevier (1983).
12. G.A. Voyiatzis and G.N. Papatheodorou, Ber. Bunsenges. Phys. Chem. 98 xxxx (1994).
13. B.N. Nelson and G.J. Exarchos, J. Chem. Phys. 71 2439 (1979) and references therein.
14. G.N. Papatheodorou and O.J. Kleppa, J. Inorg. Nucl. Chem. 33 1249 (1971) and references therein.

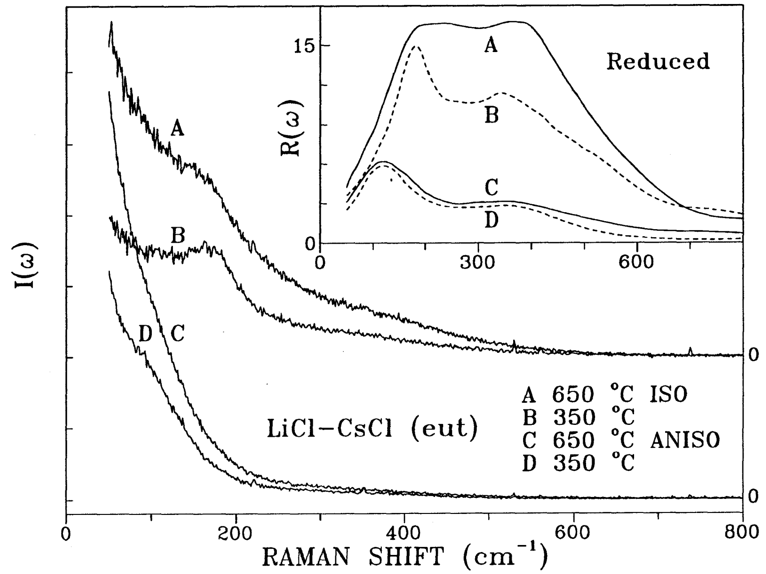

Fig. 1: Temperature dependence of the Raman spectra of the LiCl-CsCl eutectic mixture. The R(ω) ordinate values (insert) are arbitrary but in scale with the R(ω) values in Figs. 2-5.

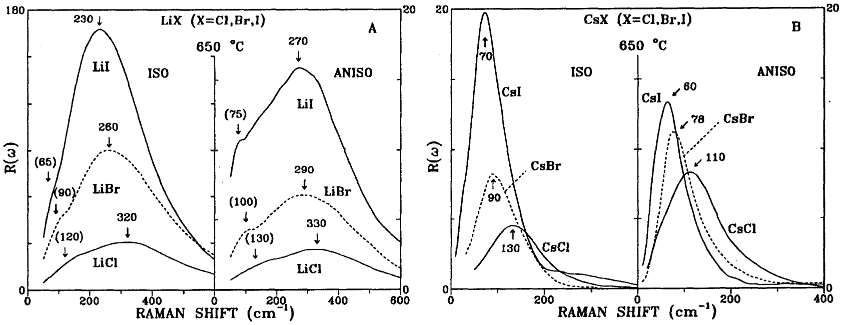

Fig. 2: Reduced Raman spectra of LiX (A) and CsX (B) melts at 650 °C. Note differences in ordinate scales.

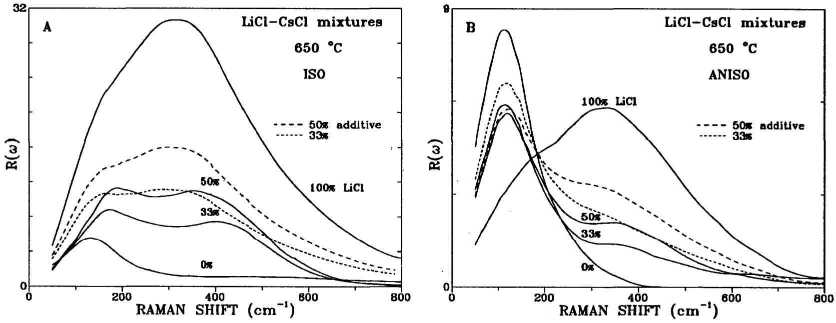

Fig. 3: Composition dependence of the reduced Raman spectra of the LiCl-CsCl mixtures. Note differences in ordinate scales between the isotropic (A) and anisotropic (B) spectra.

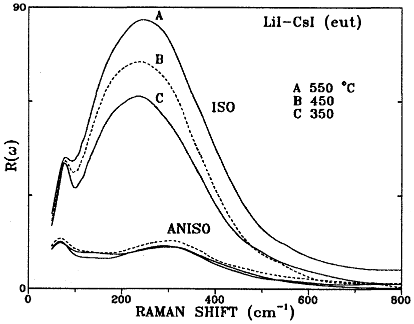

Fig. 4: Temperature dependence of the reduced Raman spectra of the LiI-CsI eutectic mixture.

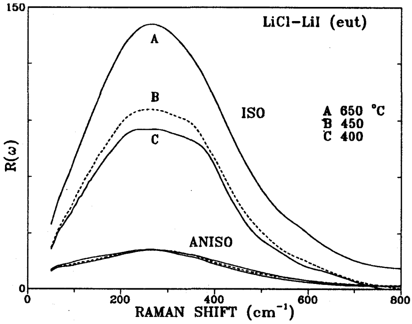

Fig. 5: Temperature dependence of the reduced Raman spectra of the LiCl-LiI eutectic mixture.

DOI: 10.1149/199413.0292PV

RAMAN SPECTROSCOPY: A QUANTITATIVE TOOL FOR THE STUDY OF DOPED ZIRCONIAS' PHASE TRANSFORMATION CAUSED BY MOLTEN FLUORIDES

C. G. Kontoyannis, M. Orkoula, V. Dracopoulos and G. Carountzos

Institute of Chemical Engineering and High Temperature Chemical Processes
and
Department of Pharmacy, University of Patras
P.O. Box 1414, GR 26 500 Patras, GREECE

ABSTRACT

Fully stabilized zirconias (FSZ) were prepared by using CaO, MgO, Y_2O_3, Yb_2O_3, Gd_2O_3 and Nd_2O_3 as dopants. The sintered ceramics were immersed in molten fluorides. Raman spectroscopy was used succesfully in order to probe quantitatively the cubic-to-monoclinic transformation (corrosion) caused in the crystal structure of FSZ from the molten fluorides. For this purpose spectra of mixtures of known quantities of FSZ with monoclinic phase were obtained and a calibration curve was established. The curve was found to be a straight line in a plot of the Raman intensity ratio of the 177 versus the 617 cm^{-1} band against the inverse monoclinic molar fraction. The ceramic with the best performance against corrosion was zirconia with 8 mol % Yb_2O_3 fired at 1600 °C for 2 hours.

INTRODUCTION

The crystal structure of zirconia, one of the best corrosion resistant and refractory materials, is known to change from monoclinic to tetragonal and then to cubic at 1150 and 2200 °C respectively. Small additions of oxides such as MgO, CaO, Y_2O_3 e.t.c. have been used to lower the two transition temperatures and thus act as stabilizers for the tetragonal and the cubic phase (fully stabilized, FSZ). Stabilized zirconia systems have improved mechanical properties with respect to fracture strength and resistance to thermal shock. They are known also to exhibit high ionic conductivity and are used as oxygen/oxide sensors.

Raman spectroscopy has been used in order to study the transformations of pure zirconia and of tetragonal and cubic phase (1,2) during heating and cooling cycle. The transitions from stabilized zirconia's phase to monoclinic after the exposure of the ceramics in the environment of corrosive media have been also investigated (3,4). No quantitative determination for the cubic-to-monoclinic transformation by Raman spectroscopy is known. The reason is that the spectra of the disordered cubic phase exhibit only a broad continuum decreasing in intensity with increasing frequency and contain few bands with poorly defined maxima.

In the present work Raman spectroscopy was used successfully for determining the percentage of the cubic and monoclinic phase in a zirconia ceramic. For this purpose a calibration curve was obtained by mixing known quantities of doped zirconia powders having cubic crystal structure and pure monoclinic zirconia. The derived calibration curve was then used in order to establish in a quantitative way the resistance ability, regarding the phase transformation, of sintered FSZ after their immersion in molten fluorides. For this purpose different sintering conditions were aplied and the CaO, MgO, Y_2O_3, Yb_2O_3, Gd_2O_3 and Nd_2O_3 were used as dopants in order to find the best conditions and materials for FSZ to be used in molten fluorides bath.

EXPERIMENTAL PROCEDURE

1. Preparation of Pellets for the Calibration Curve

Monoclinic zirconia powder from "Tosoh" and ZrO_2 powder fully stabilized with 8 mol % Y_2O_3 from "Tosoh" and "Zirconia Sales" were used. Mixtures in the correct stoichiometric ratios were prepared, by mixing the powders in a marble mortar, so that the complete range from 0 to 100 mole % of cubic phase could be obtained. In order to avoid the occurrence of a fluorescence signal in the as received material, arising from the presence of some organic impurities, the mixed powders were fired at 1000 °C in the presence of oxygen for two hours. Pellets were prepared from the mixtures by applying a 70 kN pressure. The homogeneity of the pellets was verify by obtaining several spectra for each pellet from different points on the surface.

2. Identification of Phases (Raman Spectroscopy)

Raman spectra were excited with the 488-nm line of a 4 W Spectra Physics argon laser. The plasma lines were removed from the laser beam by using a small monochromator as filter. A cylindrical lens, with 5″ focal length, was used to focus the laser line on the sample giving a probed area of approximately 1 mm^2. The scattered light was collected at an angle of 90° and analyzed with a SPEX 1403, 0.85-m double monochromator equipped with a -20 °C cooled RCA photomultiplier and EG&G/ORTEC photon-counting and amplifier electronics. The power of the incident laser beam was about 100 mW at sample's surface. Typical spectral width and time constant were 1 cm^{-1} and 0.3 s respectively. The system was also interfaced with computer and the spectra were recorded on X-T recorder's paper and simultaneously were digitized and stored in diskettes. For the necessary calculations a home-made Fortran program was used. The spectra were excited at room temperature

3. Sintered Fully Stabilized Zirconias Preparation

The zirconia fully stabilized powders used were either purchased from the Zirconia Sales and Tosoh or were prepared by using the co-precipitation method. The powders were uniaxially pressed at 300 MPa. The compacts were sintered in open air for 2-5 h at temperatures ranging from 1200 to 1700 °C. The sintered specimens were in the form of cubes (1 x 1 x 1 cm). The samples exhibiting the presence of the monoclinic phase after the sintering were rejected. The percentage of the stabilizer used was the minimum required for a FSZ. All ceramics samples were prepared by CERECO SA (P.O. Box 146, GR 34100 Chalkis, Greece). The sintered ceramics as well as the stabilizer's percentage, the firing conditions and the physical characteristics (density and pore size) are in Table I.

Table I. Method of Preparation and Physical Properties of Stabilized Zirconias

MOL % OF STABILIZER	FIRING CONDITION	POROSITY (%)	DENSITY (g/cm^3)
15 CaO	1600 °C, 2h	0.70	5.03
8 Gd_2O_3	1650 °C, 5h	0.15	5.88
15 MgO	1700 °C, 2h	0.11	5.42
15 Nd_2O_3	1600 °C, 2h	0.18	5.48
8 Y_2O_3	1550 °C, 5h	0.15	5.99
8 Yb_2O_3	1600 °C, 2h	0.14	5.78

4. Corrosion Tests

Fluoride salts were purchased from Merck (p.a. grade) and were purified further by melt crystallization. A LiF, NaF, KF eutectic (FLINAK) was prepared by mixing the recrystallized compounds in a glove-box. A home-made oven with three heating zones and programmable heating controller and two programmable "Scandiaonven" furnaces were used. All furnaces were equipped with a Ni tube core and were modified in order to accommodate the need for vacuum and/or inert atmosphere. Each of the ceramics was immersed into 50 g of molten FLINAK for a maximum of 15 hours at 700 °C under argon atmosphere. Vitreous carbon crucibles (Le Carbone - Lorraine) were chosen as containers for the FLINAK. The solidified FLINAK was removed mechanically after submerging the samples into water for 48 hours.

RESULTS AND DISCUSSION

1. Deriving the Calibration Curve

The spectrum of the pure monoclinic zirconia powder (Fig. 1.E) exhibits 16 out of the 18 theoretical predicted bands (5,6). Assuming a fluorite structure for ZrO_2 in the cubic phase one should expect only one Raman active frequency but the spectra for doped zirconia's cubic structure are characterized with a broad band in the area of 617 cm^{-1} together with a high "background" profile (Figure 1.A). The absence of sharp well defined peak has been attributed to the structural disorder associated with the oxygen sublattice (7). In contrast, the bands of the well ordered monoclinic phase are sharp and intense.

In order to correlate the appearance of a zirconia ceramic spectrum with the percentage of the cubic and the monoclinic phase present, a number of pellets were prepared from powder mixtures with known phase percentage. Two sets of pellets were used with cubic phase powder from different manufacturer ("Zirconia Sales" and "Tosoh") in order to test if the calibration curve is "universal" or depends on powders' characteristics.

Our objective was to find an easy and reliable method for calculating each phase's percentage, and thus we used the peak and not the integrated intensities of the bands. The differences in the measured intensities of the different spectra made apparent that only relative factors within each spectrum e.g. ratio of intensities, could be used.

The 177 cm^{-1} band of the monoclinic phase was chosen for the quantitative study since it exhibits very strong intensity even in the spectra excited from pellets having small percentage of the monoclinic phase (Fig. 1.B). On the other hand the spectra of Fig. 1 suggest that the only criteria in the estimation of the cubic's phase percentage was the cubic's broad band, which unfortunately overlaps with a monoclinic peak, at 617 cm^{-1}.

The intensity of a Raman line depends on a number of factors including incident laser power, frequency of the scattered radiation, absorptivity of the materials involved in the scattering, and the response of the detection system. Thus, the measured Raman intensity, $I(\nu)$, can be represented (8) as:

$$I(\nu)=I_0K(\nu)C \qquad [1]$$

where I_0 is the intensity of the excitation laser line, ν is the Raman shift, $K(\nu)$ is a factor which includes the frequency dependent terms: the overall spectrophotometer response, the self-absorption of the medium and the molecular scattering properties. C is the concentration of the Raman active species.

As it was mentioned previously, in the pellet's spectra an overlap of a monoclinic and the cubic peak exists at 617 cm^{-1}. Therefore, the intensity at this wavenumber is the sum of the intensities of the monoclinic, $I_0 K_m^{617} \chi_m$, and the cubic phase, $I_0 K_c^{617} (1-\chi)$. Where χ is the monoclinic's phase molar fraction in a pellet. The superscript of the K is the Raman shift of the peak while the subscript represents the phase, m for monoclinic and c for cubic. A ratio of the intensity of the 617 cm^{-1} band to the intensity of the 177 cm^{-1} peak will yield:

$$\frac{I^{617}}{I_m^{177}}=\frac{K_c^{617}}{K_m^{177}}\frac{1}{x_m}+\frac{K_m^{617}-K_c^{617}}{K_m^{177}} \qquad [2]$$

Where I^{617} and I_m^{177} represent the measured intensity of the 617 cm^{-1} band and the intensity of the monoclinic's phase peak at 177 cm^{-1} respectively. K_m^{177} is the frequency dependent constant for the 177 cm^{-1} monoclinic phase peak .

The plot of the intensity ratio of I^{617} to I_m^{177} versus the χ_m^{-1} is in Fig. 2. For convenience the scale for x-axis is logarithmic. The value of the I^{617} was obtained by subtracting from the total measured intensity at 617 cm^{-1} the "background" intensity of the 800 cm^{-1}. The exact wavenumber corresponding to the maximum intensity of the peak was determined by a computer-aided (c.a) search, of the digitized spectra, between the 610 and 620 cm^{-1}. The 800 cm^{-1} was arbitrary chosen as the spectral point where the "background" level is zero since at this wavenumber the intensity of all the pellet's spectra reaches a constant value.

The wavenumber of the monoclinic peak (177 cm^{-1}) was c.a searched between the 170 and 182 cm^{-1} and its intensity, I_m^{177}, was calculated by subtracting the "background" for the 177 cm^{-1}. The "background" was defined as the line passing through the two data points, one on each side of the peak, with the lowest intensity value. The data points specifying the monoclinic's peak "background" line were located by searching for the lowest intensity data point between the 145 to 170 cm^{-1} and 182 to 210 cm^{-1} respectively.

In order to avoid problems arising from random spectral noise, the intensity values used were averaged with the intensities of the neighboring data points. Several Raman spectra were recorded for each composition and the data in the plot (Fig. 2) are the mean values of the real data. No difference was observed between the data obtained from pellets made from "Tosoh's" and "Zirconia Sales'" cubic powder. Therefore the method is independent of powders' origin and can be applied to any doped zirconia ceramic undergoing a cubic to monoclinic transformation. A linear regression on all data yields the following equation:

$$\frac{I^{617}}{I_m^{177}}=\frac{1}{x_m}0.11+0.26 \qquad [3]$$

The correlation coefficient was 0.9995 while the standard errors for the slope and the intercept were $\pm 6.4 \times 10^{-3}$ and $\pm 2.1 \times 10^{-2}$ respectively.

2. Dependence of FSZ Endurance in Fluorides Melts on Stabilizer's Cation

The FSZ ceramics of the Table I were immersed in FLINAK for 15 h and at 700 °C. Raman spectroscopy was applied in order to measure the extent of crystal's structure transformation which was caused by FLINAK and the spectra were obtained, at room temperature, from samples' surface before and after the treatment. The use of Raman spectroscopy as an analytical tool for the cubic-to-monoclinic transformation was based on the intensities of the 617 and 177 cm^{-1} bands which were measured as was described previously. The monoclinic's phase molar fraction was obtained by using the calibration curve given by equation [3].

There is a profound dependence of ceramics' endurance in fluoride melts on on stabilizer's cation size and charge. As a measure of size's and charge's influence the value of Q^+/r^+ was determined, where Q^+ represents the ion's charge and r^+ the ionic radius. In Fig. 3 the Q^+/r^+ for the different dopant cations are plotted against their respective monoclinic molar fraction values which were calculated from equation [3]. A linear relationship between Q^+/r^+ values and corrosion exists. Thus the Yb^{3+} having the largest Q^+/r^+ value, 5.60×10^{-9} Cb m^{-1}, is also the more resistant stabilizer. Zr^{4+} is not expected to react with fluorides since its Q^+/r^+ value, 8.1×10^{-9} Cb m^{-1}, is by far the largest among those presented in Fig. 3.

CONCLUSIONS

A calibration curve for calculating the percentage of zirconia's cubic and monoclinic phase when both are present in a ceramic, by Raman spectroscopy, was developed. A plot of the Raman intensity ratio of the 617 cm^{-1} band to the 177 cm^{-1} monoclinic peak against the inverse monoclinic's phase molar fraction found to yield a straight line. The intensity of the monoclinic peak was calculated by subtracting the "background". In contrast, the intensity for the 617 cm^{-1} which is attributed to both phases was determined including the "background".

The calibration curve was applied on Raman spectra obtained from zirconias which were stabilized with either CaO, MgO, Y_2O_3, Yb_2O_3, Gd_2O_3 or Nd_2O_3, after their immersion in molten FLINAK. The quantitative results revealed a dependence between the stabilizer's cation size and charge and the resistance of the FSZ to the phase transformation caused from molten fluorides. Thus the zirconia having as dopant Yb_2O_3 (largest cation size to charge ratio) is also the more resistant.

ACKNOWLEDGMENTS

The authors are indebted to Prof. G.N. Papatheodorou for helpful suggestions and for providing the experimental facilities. We thank Dr. Stournaras and Dr. Tsetsekou of CERECO for providing the sintered fully stabilized zirconia ceramics.

REFERENCES

1. C.M. Phillippi and K.S. Mazdiyasni, J. Amer. Ceram. Soc., **54** 254-258 (1971).

2. D. K. Veirs, G.M. Rosenblatt, R.H. Dauskardt and R.O. Ritchie, Microbeam Analysis, **23** 179-181 (1988).

3. J.C. Hamilton and A.S. Nagelberg, J. Am. Ceram. Soc., **67** [10] 686-690 (1984).

4. C.G. Kontoyannis and N. Tziafos, in Proceedings of the Eighth International Symposium on Molten Salts, R.J. Gale, G. Blomgren and H. Kojima, Editors, PV 92-16, p.103. The Electrochemical Society Softbound Series, Pennington, NJ (1992).

5. A. Feinberg and C. Perry, J. Phys. Chem. Solids, **42** 513-518 (1981).

6. E. Anastasssakis, B. Papanicolaou and I. M. Asher, J. Phys. Chem. Solids, **36** 667-676 (1974).

7. C. Perry, D. Liu and R. Ingel, J. Am. Ceram. Soc., **68** [8] C-184 - C-187 (1985).

8. D. Strommen and K. Nakamoto, Laboratory Raman Spectroscopy, pp. 71-75, Wiley Interscience, New York, 1984.

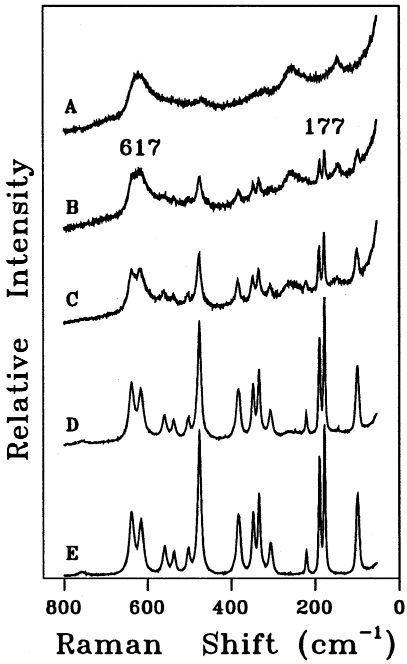

Figure 1: Raman spectra of pellets prepared from A: ZrO_2- 8 mol % Y_2O_3 (cubic phase); B: mixture of 10 % pure ZrO_2 (monoclinic phase) with 90 % cubic phase; C: mixture of 25 % monoclinic phase with 75 % cubic phase; D: mixture of 70 % monoclinic phase with 30 % cubic phase; E: pure ZrO_2 (monoclinic phase) Spectra were excited at 20 °C; λ_0=488.0 nm; spectral slit width, 1 cm^{-1}.

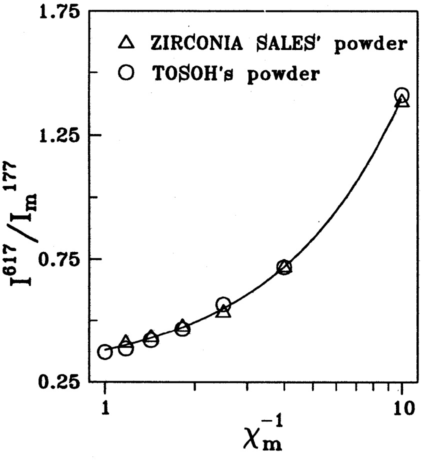

Figure 2. I^{617}/I_m^{177} vs. χ_m^{-1}.

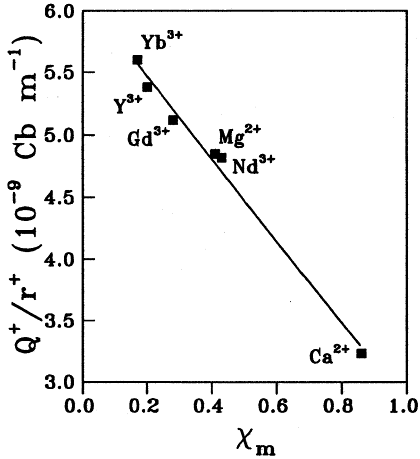

Figure 3: Q^+/r^+ vs. χ_m.

DOI: 10.1149/199413.0300PV

RAYLEIGH-BRILLOUIN SCATTERING OF $ZnCl_2$-MCl(M: Na, K AND Cs) BINARY MELTS

Hongmin Zhu, Yuzuru Sato and Tsutomu Yamamura
Department of Metallurgy, Tohoku University
Aramaki-Aza-Aoba, Sendai, Japan

ABSTRACT

Rayleigh-Brillouin scattering experiment has been carried out for $ZnCl_2$ -NaCl, $ZnCl_2$-KCl and $ZnCl_2$ $ZnCl_2$-CsCl binary melts. The complete profiles of Rayleigh-Brillouin spectra were obtained for each binary melt, and at temperatures ranging from 550 to 1000K. The remarkable change in the shape of the spectrum with the variations in temperature and composition has been observed and has been concluded to be due to a structural relaxation in the melts. A dispersion of sound wave propagation was observed in the melts at the hypersonic region. The spectra have been analyzed by the viscoelastic theory with the assumption of the single relaxation. The relaxation time and the velocities at limiting low frequency and high frequency were determined as functions of temperature and of alkali chloride composition.

INTRODUCTION

Among molten salts, zinc chloride melt is unusual for its high viscosity(1) and low electrical conductivity(2) at temperatures near the melting point. This is due to the presence of the network structure in the melt[(3), (4)]. However , as temperature increases the network structure breaks, and the degree of the polymerization becomes lower. The network structure also breaks with an addition of basic salts, such as alkali metal halides. Such structural change in the melt would result in a variation of viscoelastic properties, especially the structural relaxation behavior[(5~7)].

In case of highly viscous liquids the structural relaxation plays an important role in the Rayleigh-Brillouin spectrum(8). In viscous liquids, a considerable frequency dispersion as well as a broadening of the linewidth of the Brillouin doublet are known to occur. One also finds significantly more intensity distribution in the region between the unshifted Rayleigh and Brillouin peaks than that found in a simple liquid. This is due to the structural relaxation in the melt as described by Lin and Wang(8). Therefore, it is important to obtain the full spectrum of Rayleigh-Brillouin scattering, and one can get useful information about the structural relaxation from the spectrum.

As described in our previous paper(9), the complete profiles of Rayleigh-Brillouin spectra in molten $ZnCl_2$ were obtained by the use of the carefully purified sample. The spectra were successfully analyzed by the viscoelastic theory. In the present study, a series of zinc chloride and alkali chloride binary melts, $ZnCl_2$-NaCl, $ZnCl_2$-KCl and $ZnCl_2$-CsCl, were investigated by Rayleigh-Brillouin scattering experiments. The complete spectra of these binary melts have been obtained at the temperatures ranging from 550 to 1000K. The spectra have been analyzed by a single relaxation theory. The effect of the addition of alkali chlorides on the relaxation in the melts has been determined.

EXPERIMENTAL

The experimental arrangement used for the Rayleigh-Brillouin scattering in $ZnCl_2$ -

MCl binary melts is similar to that used previously in this laboratory(9). The light source was a He-Ne gas laser operating in single mode at a wavelength of 632.8 nm. The light scattered was analyzed by a pressure scanned Fabry-Perot interferometer. The measurements were done at scattering angles of 90° and at temperatures ranging from 550 to 1000K. The profiles were monitored by a X-Y recorder, and were also recorded digitally by a personal computer for the detailed analysis of the spectra. The measuring time was about 15 minutes per spectrum. The measurement of spectrum was repeated for more than two times at the same temperature, and the average of these profiles was used for analysis of the spectrum.

In the Rayleigh-Brillouin scattering experiment, the inclusions contained in the sample liquid may cause the spikes in the spectrum around zero shift frequency(9). Therefore, the sample was carefully purified so as to avoid the light reflecting inclusions. Each sample of the binary systems was purified by HCl bubbling, filtration and distillation. By the use of those purified samples the complete spectra of Rayleigh-Brillouin scattering were obtained.

RESULTS AND DISCUSSION

Typical profiles obtained in $ZnCl_2$-KCl binary melts at different compositions at 577 and 778K are shown in Figs. 1 and 2. As shown in these figures, the shape of the spectrum changes remarkably with the variation in temperature, as well as with the variation in alkali chloride composition of the melts.

The frequency shift between the Brillouin peaks and the Rayleigh peak, $\Delta\nu_B$ can be expressed by the following equation

$$\Delta\nu_B = 2\nu_i n \ (V/c)\sin(\theta/2) \qquad (1)$$

where ν_i is the frequency of the incident light and c is the light velocity. The velocity of longitudinal sound wave V can be determined from Brillouin shift and scattering angle θ. The attenuation of the sound wave α can be determined from the linewidth of the Brillouin peak by the following equation,

$$\alpha = \delta\nu_B/V \qquad (2)$$

where $\delta\nu_B$ is the half-width of the Brillouin peak.

Using the refractive index data of literature(10), we can derive the velocity and attenuation of hypersound at various temperatures and compositions from the frequency shift and half-width of the Brillouin peaks. As shown in Figs.1 and 2, the Brillouin peaks broaden significantly and overlap with the central line at certain temperatures. The spectrum is separated into three Lorentzian lines by the use of the least squares method to obtain the frequency shift and linewidth. In the calculation of attenuation, the linewidth of the apparatus profile was excluded from the observed Brillouin lines. The results of velocity and attenuation in $ZnCl_2$-NaCl binary melts are plotted in Figs.3 and 4 as a function of temperature. In Fig.4 the values are shown as the attenuation per wave length, λ. The values near the maximum are only approximate because of the overlapping of the peaks.

As shown in Figs.3 and 4, the hypersonic velocity has a negative linear temperature dependence at the higher temperature region for the binary melts at all compositions measured. As the temperature decreases, the velocity increases rapidly at a lower temperature region. At the corresponding temperature region, the attenuation shows the maximum. These results indicate that the dispersion of hypersonic wave occurs at those temperature region. The temperature region where the dispersion occurs goes to a lower one as the composition of alkali chlorides increases.

As has been described above, the analysis of Brillouin peak shift and linewidth is only approximate. For the detailed discussion, the full spectrum should be analyzed. In this work all the spectra obtained were analyzed fully by the viscoelastic theory [(5), (11)]. The viscoelastic theory (12) gives the spectral distribution function S(q,ω) as follows.

$$S(q,\omega) = (1 - \frac{1}{\gamma})\frac{2(\lambda q^2/\rho_0 C_p)}{(\lambda q^2/\rho_0 C_p)^2 + \omega^2} + (\frac{2M_0}{\gamma})\frac{\eta(\omega) + \eta_0}{\{\omega[\eta(\omega) + \eta_0]\}^2 + \{\rho_0\omega^2/q^2 - M(\omega)\}^2} \quad (3)$$

where q is the shift in wave vector, ω is the shift in angular frequency of the scattered light, λ is the thermal conductivity, ρ_0 is the density, C_p is the heat capacity at constant pressure, M(ω) is the longitudinal storage modulus, M_0 is the low-frequency storage modulus, η(ω) is the longitudinal viscosity and η_0 is the nonrelaxing part of the viscosity. For single relaxation behavior, following relations hold,

$$\eta(\omega) = \rho_0(V_\infty^2 - V_0^2)\tau/(1 + \omega^2\tau^2) \quad (4)$$

$$M(\omega) = \rho_0(V_0^2 + V_\infty^2\omega^2\tau^2)/(1 + \omega^2\tau^2) \quad (5)$$

where τ is relaxation time, V_0 and V_∞ are velocities at limiting low and high frequencies, respectively. The analysis of the spectra was a least-squares fitting procedures on the relaxation time and velocities at limiting low and high frequencies. In Figs.1 and 2, the solid lines represent the profiles calculated by the viscoelastic theory with the best fitting parameters and with the convolution by the apparatus profile. As shown in the figures, the description of the spectrum is very excellent at each temperature and composition.

The results of V_0 and V_∞ determined by the fitting for the $ZnCl_2$-NaCl binary melts are shown as functions of temperature in Fig.5. The velocity at limiting low frequency V_0 decreases linearly with increasing temperature for each binary melt, and increases with increasing NaCl composition if compared at the same temperature. The value of V_0 agrees within 50m s^{-1} with the ultrasonic velocity measured by the pulse transmission method(6). The velocity at limiting high frequency exhibits discontinuous slope change. This behavior might be considered to be due to the glass transition, as described by Dreyfus et al.(13) and Tao et al.(14).

The temperature dependence of relaxation time for $ZnCl_2$-NaCl and $ZnCl_2$-KCl binary melts of various compositions are plotted logarithmically against the inverse temperature in Figs.6 and 7. The relaxation time decreases with increasing the composition of alkali chlorides. The value of τ decreases over one order from pure $ZnCl_2$ to 40% alkali chlorides. As shown in Figs.6 and 7, the plots are essentially linear, indicating that the relaxation time τ obeys the Arrhenius relation.

The remarkable variation of relaxation time indicates the structure variation of the melt with temperature and composition changes. It has been considered that $ZnCl_2$ melt consists of polymeric $(ZnCl_2)_n$ species of various sizes[(15), (16)]. These species are made up of $ZnCl_4$ tetrahedra bridged at the corners to give three dimensional networks. With the addition of chloride ion donors such as alkali chlorides and increasing temperature the degree of polymerization lowers. Due to the presence of the large sized polymeric species at the lower temperatures and low alkali chloride composition, the response of the melt is expected to be very slow. This is the reason for the relaxation time being long at the lower temperatures and low MCl composition melts. The response rate increases with increasing temperature and alkali composition because the degree of polymerization decreases. Therefore the relaxation time decreases with increasing temperature and with the addition of an alkali chloride.

Using the values of τ, V_0, V_∞ and γ determined by the least squares fitting, the theoretical spectra can be given by eqs.3~5. In Fig.8, the Brillouin spectra of $ZnCl_2$-KCl binary melts at various compositions are compared at $q=22\times10^6$ m^{-1} ($\theta\approx90°$), and at *T*=

600, 800 and 1000K. In this figure, only Brillouin components (adiabatic component) which are the main part of Rayleigh-Brillouin spectrum in present system, are shown. As shown in the figure, the spectral shape is remarkably sensitive to the variations in temperature and MCl composition. This behavior of spectral shape is due to the structural relaxation in the melts(8). In pure $ZnCl_2$ melt, at high temperatures (~1000K), the relaxation rate is faster than the frequency of the hypersonic wave in each binary melts. In this case, the structural relaxation contributes mainly to the Brillouin doublet, and the spectrum has the shape similar to those observed in non-relaxing liquids. At the intermediate temperatures(~800K) when the relaxation rate is of the order of ω_s (the frequency of hypersound), the linewidth of the Brillouin doublet shows the maximum and the hypersonic velocity shows a considerable dispersion. Thus the relaxation contributes significantly to the intensity of the Brillouin doublet as well as the intensity in the region between the central line and the Brillouin doublet. At low temperatures (~600K), on the other hand, the relaxation rate is slow compared to the hypersonic frequency and the relaxation mode manifests itself as a central line. The relaxation rate increases with the addition of MCl, thus the structural central peak becomes weaker and broader. When the composition of MCl increases to 40%, then the central peak becomes a negligible one.

SUMMARY

The complete profiles of Rayleigh-Brillouin spectra have been obtained for $ZnCl_2$ -NaCl, $ZnCl_2$ -KCl and $ZnCl_2$ $ZnCl_2$-CsCl binary melts by the use of carefully purified samples. The remarkable change in the shape of the spectrum with the variations in temperature and composition has been observed and has been concluded to be due to a structural relaxation in the melts. The spectra have been well analyzed by the viscoelastic theory with the assumption of the single relaxation.

REFERENCE

(1) T.Ejima, T.Yoko and K.Nakashima: J.Jpn.Inst. Metals, **41**(1977), 86.
(2) J.O'M.Bockris, E.H.Crook, H.Bloom and N.E.Richards: Proc.Roy.Soc. (London) **A255**(1960), 558.
(3) M.Itoh, K.Sakai and T.Nakamura: Inorg.Chem., **21**(1982), 3552.
(4) D.A.Allen, R.A.Howe and N.D.Wood: J.Chem.Phys., **94**(1991), 5071.
(5) H.Zhu, Y.Sato, T,Yamamura and T.Ejima, “Proceedings of 11th International Symposium on Molten Salts”, (1990),152.
(6) T.Yoko, M.Nakano and T.Ejima, J.Jpn.Inst. Metals, **44**(1980), 508.
(7) T.Yoko, M.Nakano and T.Ejima, J.Jpn.Inst. Metals, **44**(1980), 516.
(8) Y.H.Lin and C.H.Wang, J.Chem.Phys., **70**(1979), 681.
(9) H.Zhu, Y.Sato, T.Yamamura and K.Sugimoto, Ber. Bunsenges.Phys.Chem., **93**(1993), 583.
(10) T.Yamamura, S.Mizuno, T.Nito, M.Endo, Y.Sato and T.Ejima, J.Jpn.Inst. Metals, **56**(1992), 889.
(11) M.Soltwisch, J.Sukmanowski and D.Quitman, J. Chem. Phys., **86**(1987), 3207.
(12) C.J.Montrose, V.A.Solovyev and T.A.Litovitz, J. Acoust. Soc.Am., **43**(1968), 117.
(13) C.Dreyfus, M.J.Lebon, H.Z.Cummins, J.Toulouse, B.Bonello and R.M.Pick, Phys.Rev.Lett. **69**(1992), 3666.
(14) N.J.Tao, G.Li and H.Z.Cummins, Phys.Rev. B **43**(1991), 5815.
(15) J.R.Moyer, J.C.Evans and G.Y.Lo, J. Electrochem. Soc. **113**(1966), 158.
(16) M.Itoh, K.Sakai and T.Nakamura, Inorg. Chem., **21**(1982), 3552.

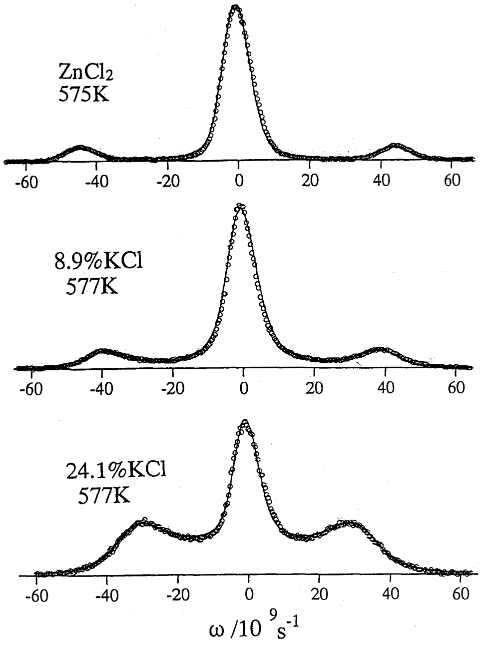

Fig.1 Brillouin spectra of $ZnCl_2$-KCl binary melts around 577K.

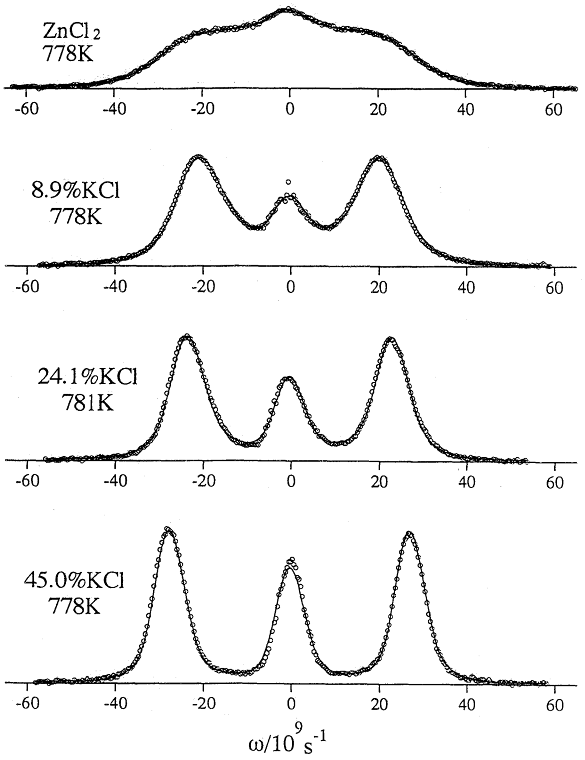

Fig.2 Brillouin spectra of $ZnCl_2$-KCl binary melts around 778K.

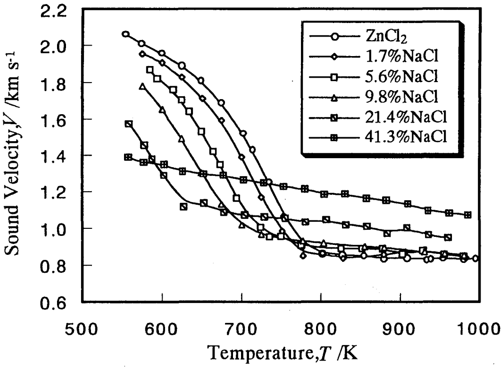

Fig.3 Hypersonic velocity in $ZnCl_2$-NaCl binary melts.

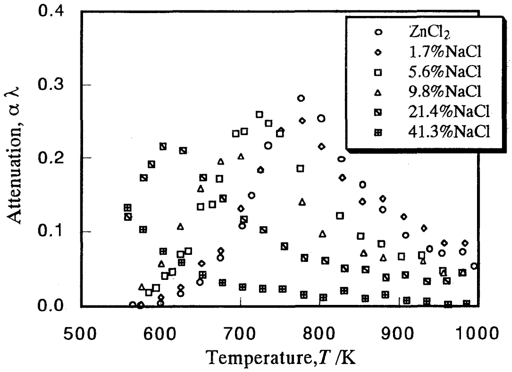

Fig.4 Hypersonic attenuation in $ZnCl_2$-NaCl binary melts.

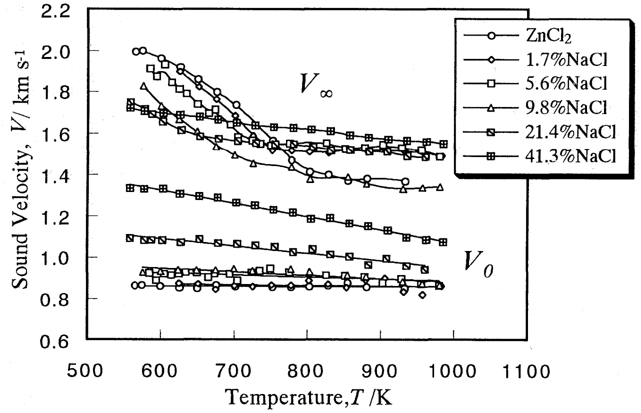

Fig.5 Temperature dependence of V_0 and V_∞ for $ZnCl_2$-NaCl binary melts.

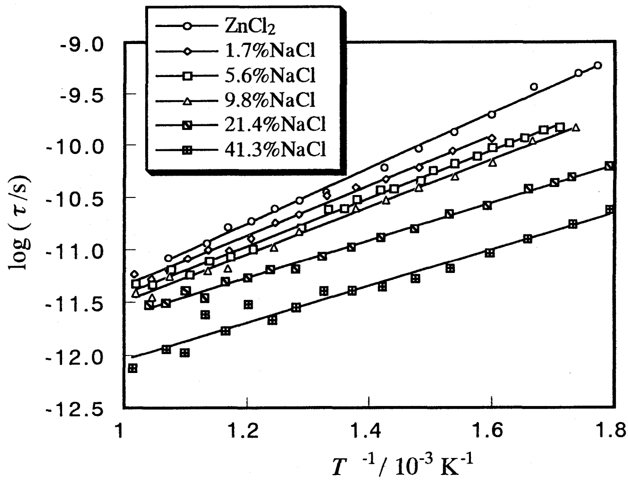

Fig.6 Relaxation time of $ZnCl_2$-NaCl binary melts.

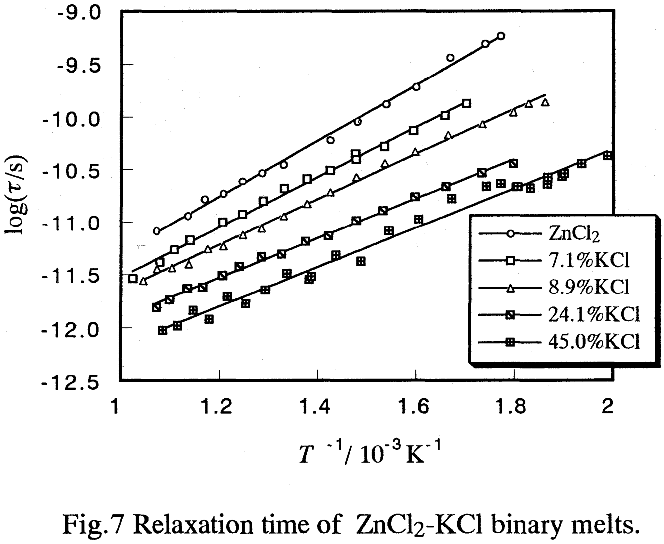

Fig.7 Relaxation time of $ZnCl_2$-KCl binary melts.

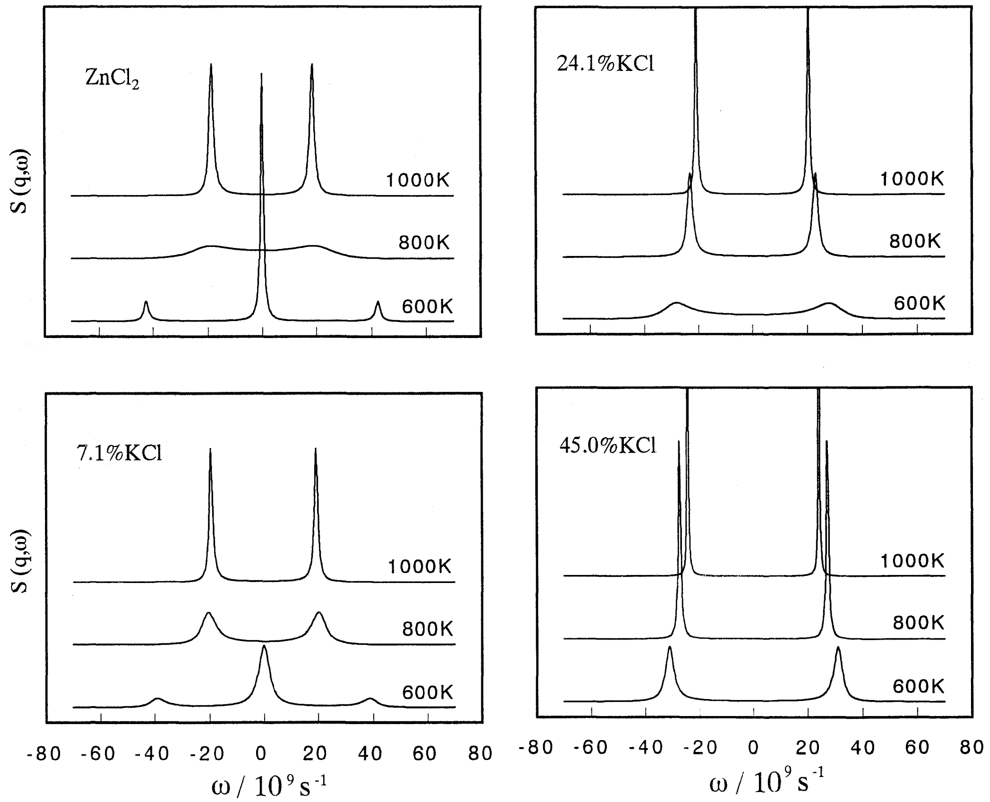

Fig.8 Comparison of theoretical Brillouin spectra of ZnCl2-KCl binary melts, at T=600, 800 and 1000K, and q=22X10^6 m^{-1}.

DOI: 10.1149/199413.0308PV

VISIBLE AND NEAR-IR SPECTROSCOPIC STUDIES OF UCl_4 IN A BASIC AMBIENT TEMPERATURE MELT: THE OBSERVATION OF A POSSIBLE GEOMETRIC DISTORTED UCl_6^{2-} SPECIES AND THE EVIDENCE FOR THE HYDROGEN-BOND IN THE MELT

Sheng Dai, L.M. Toth, G.D. Del Cul and D.H. Metcalf
Chemical Technology Division, Oak Ridge National Laboratory, Oak Ridge, TN 37831-6181, USA

ABSTRACT

The visible and NIR spectra of UCl_6^{2-} in a basic ambient temperature melt composed of mixture of $AlCl_3$ and 1-ethyl-3-methyl-imidazolium chloride(EMIC) have been investigated. Both temperature-dependence of the total intensity of the band at 2000 nm and its vibronic pattern indicate that the transitions in this range are induced by a static strong hydrogen-bonding of UCl_6^{2-} with the EMI cation.

INTRODUCTION

Extensive studies have been made of the absorption spectra of dilute solutions of uranium(IV) tetrachloride in high temperature molten halide salts(1-2). These studies provide information on the coordination number of the uranium complex species. However, the high temperature employed in such studies can induce the broadening of the spectra, making the assignment difficult. This prompted us to use ambient temperature chloride melts to study such systems. The ambient temperature melt we used is composed of the mixture of aluminum chloride and 1-ethyl-3-methyl-imidazolium chloride(EMIC). This melt exhibits widely varying Lewis acid-base properties depending on its composition and is known to produce the best resolved and most reliable spectra ever recorded for metal halides at room temperature(3).

There are some controversy over the role of the organic cation(EMI)in this melt system(4-5). Based on their IR measurement, Osteryoung et al(4) have proposed that two-species ion-pair interactions occur in the basic melt, possibly involving distortion of the imidazolium ring with a hydrogen-bond between the hydrogen on the C(2) carbon atom of the ring and anions. In contrast, Wilkes et al(5) suggested that the ionic liquid consists of oligomeric chains held together by ion-ion interactions, each cation being associated with two anions , one above and one below the plane of the imidazolium ring. They explicitly stated that no hydrogen-bonding is possible in this system. It has been known that the f-f transitions of uranium(IV) hexachloride complex are very sensitive to the hydrogen bond(6). The objective of the present work is to use UCl_4 to probe the possible hydrogen-bonding interactions in the $AlCl_3$-EMIC melt. Although some electrochemistry work of UCl_4 in this ambient temperature melt has been done(7), no detailed visible and near IR spectroscopic analysis has been reported.

EXPERIMENTAL

The preparation and purification of uranium tetrachloride and uranium oxychloride have been reported previously(8). The UCl_4 was purified by loading the nominally pure starting material in a silica tube and pumping it down to ~20μ Hg at 650°C to remove any moisture or HCl. The tube was then sealed and UCl_4 was sublimed from one end of the tube to the other at 510°C. The $UOCl_2$ was prepared by the reaction of stoichiometric amounts of UCl_4 and Sb_2O_3 at 150°C in a tube furnace for a period of 5 h. The procedure for the purification of $AlCl_3$ has been described previously(9). The EMIC was supplied by Dr. P. Zingg(Chemistry Division, Oak Ridge National Laboratory), which was synthesized according to the procedure of Smith et al(10). All molten salt solutions were prepared under helium atmosphere in a drybox of <1 ppm moisture.

Visible and near-IR spectra were measured by a Cary 14 scanning spectrophotometer converted by On-Line Instrument Systems(OLIS) for data acquisition and analysis by a IBM-AT computer. Samples were loaded into a quartz cuvette(1 cm pathlength) with a threaded glass cap. Absorption spectra were measured from 2200 nm to 400 nm as a function of temperature.

RESULTS AND DISCUSSIONS

Figure 1 gives the recorded UV-visible spectrum of UCl_4 in a basic melt($AlCl_3$:EMIC=40:60). A basic melt is defined to contain a molar excess of the organic salt relative to $AlCl_3$ while an acidic melt contains a molar excess of $AlCl_3$ relative to the organic salt. The excess chloride ion in basic melts can act as a Lewis base. As seen from the figure, it consists of many peaks with the most intense ones(triplet) around 2000 nm. The similarity between the general spectral pattern of this spectrum and those recorded for UCl_4 in high temperature $AlCl_3$-KCl melts and $(Et_4N)_2UCl_6$ in non-aqueous organic solvents(2) strongly indicates that the same species is involved in both systems. Morrey(2) assigned the complex species in basic $AlCl_3$-containing melts to UCl_6^{2-} species based on the comparison of the UV-visible spectrum in the melt with that of authentic UCl_6^{2-} species in a solid host matrix, namely Cs_2UCl_6. Compared with the spectra obtained in high temperature melts, the spectrum of UCl_6^{2-} in our room temperature melt has much higher resolution. The band around 2000 nm in our spectrum consists of three peaks instead of a broad band such as those measured in the basic KCl-$AlCl_3$ melt.

It is well known that visible and NIR absorption spectra of uranium(IV) complexes result from the f-f transition. Since the f-f electronic transitions are electronically forbidden, the observed bands arise from the relaxation of the selection rule via either a static or a vibronic interaction. One of the characteristics for a band induced vibronically is that its total intensity is temperature dependent. The intensity of a band, f_i, at temperature T induced by coupling with the ith normal mode of energy hv_i is given by(11-12)

$$f_{iT}=f_{i0}\frac{[1+exp(-hv_i/kT)]}{[1-exp(-hv_i/kT)]}$$

where f_{i0} is the zero-point intensity and k is the Boltzmann constant. The above equation can be rearranged to give the well-known "$\coth^{-1}$ rule" for the variation of vibronically induced intensity as a function of temperature:

$$coth^{-1}\frac{f_{iT}}{f_{i0}}=hv_i/2kT.$$

The qualitative prediction of this rule is that the total intensity increases with temperature. Figure 2 gives the NIR band at 2000 nm as a function of temperature. Because of its high intensity and separation from the other bands, the following observation regarding the temperature dependence of this band will be used to establish the nature of the interaction.

This band can be attributed to the electronic transition from ground state Γ_1 of $^3H_4$ to the excited state Γ_3 of $^3F_2(2)$. It is clear from the figure that the total intensity decreases with temperature rather than increase. The absence of such a temperature dependence implies that the transition is allowed by a static rather than a vibronic mechanism. This assertion is also consistent with the vibrational pattern of the band. In contrast to the observation by Morrey that the band is composed of two peaks, three peaks are found for our band. The peak at the low energy side of the band can be assigned as a transition from a ground vibronic state j+1 to an excited vibronic state j. Similarly, the peak at the larger energy side of the band is attributed to the transition from j to j-1. The central peak corresponds to the j→j transition. This transition is usually forbidden for octahedral UCl_6^{2-} complex as observed in the spectra reported by Morrey(2), where the central peak is totally missing. The observation of this peak in our UCl_6^{2-} spectra strongly indicates that the distortion of geometry from the O_h symmetry by the solvent medium. Ryan(6) has demonstrated that the relaxation of the selection rule can be induced by the strong solvent and solute interaction, i.e. hydrogen bonding. The stronger the interaction is, the more intense this peak becomes. The fact that this peak is strongest in our room temperature spectrum suggests a very strong hydrogen bonding between UCl_6^{2-} and solvent EMI.

The dissolution of $UOCl_2$ into the same basic melt gives rise to the same spectra as those from UCl_4. This strongly indicates that the uranium oxychloride complex is not stable in the melt. This implies that the oxygen ligand is transferred from the uranium oxychloride complex to the aluminum chloride complex, forming aluminum oxychloride species. Therefore, the affinity of $AlCl_4^-$ to O^{2-} is larger than that of UCl_6^{2-}. A further support for this assertion is the fact that the addition of Li_2CO_3 into the melt containing UCl_6^{2-} does not result any changes in the spectra, where, otherwise, uranium oxychloride is expected.

CONCLUSIONS

The visible and NIR spectra of UCl_4 dissolved into the basic ambient temperature melt have been investigated. Both temperature-dependence of the total intensity of the band at 2000 nm and its vibrational pattern reveal that the transition results from a static strong hydrogen-bonding of UCl_6^{2-} with the EMI cation.

ACKNOWLEDGMENT

This work was performed under the auspices of U.S. Department of Energy, Office of Basic Energy Sciences, under contract DE-AC05-84OR21400 with Martin Marietta Energy Systems, Inc..

REFERENCES

1. D.M. Gruen and R.L. McBeth, *J. Inorg. Nucl. Chem.*, **1959**, *9*, 290.
2. J.R. Morrey, *Inorg. Chem.*, **1963**, *2*, 163.
3. C.C. Hussey, *Adv. Molten Salt Chem.*, **1983**, *5*, 185.
4. S. Tait and R.A. Osteryoung, *Inorg. Chem.*, **1984**, *23*, 4352.
5. A.A. Fannin, L.A. King, J.A. Levisky and J.S. Wilkes, *J. Phys. Chem.*, **1984**, *88*, 2609.
6. J.L. Ryan, *Inorg. Chem.*, **1964**, *3*, 211.
7. C.J. Anderson, M.R. Deakin, G.R. Choppin, W.D'Olieslager, L. Heerman and D.J. Pruett, *Inorg. Chem.*, **1991**, *30*, 4013.
8. L.M. Toth, L.K. Felker, R.D. Hunt, R.R. Brunson, and S.L. Loghry, *Separation Science and Technology*, **1993**, *28*, 781.
9. R. Marassi, J.Q. Chambers, G. Mamantov, *J. Electroanal. Chem. Interfacial Electrochem.*; **1976**, *69*, 345.
10. G.P. Smith, A.S. Dworkin, R.M. Pagni and S.P. Zingg, *J. Am. Chem. Soc.*, **1989**, *111*, 525.
11. A.D. Liehr and C.J. Ballhausen, *Phys. Rev.*, **1957**, *106*, 1161.
12. M. A. Hitchman in *Transition Metal Chemistry*, eds. G.A. Melson and B.N. Figgis, 1985, vol 9.

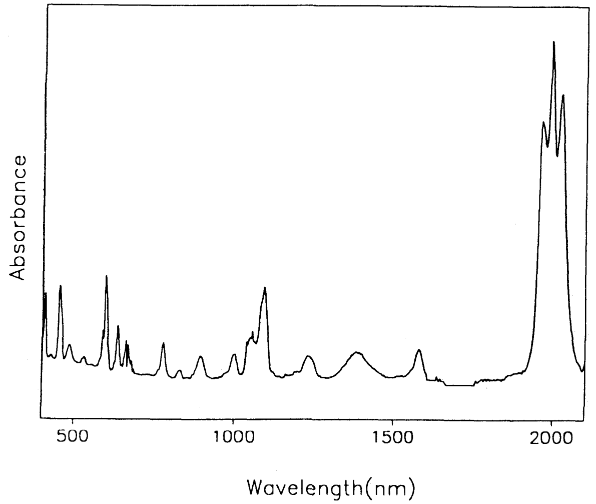

Figure 1. UV-visible and near-IR absorption spectrum of UCl_6^{2-} in the ambient temperature melt.

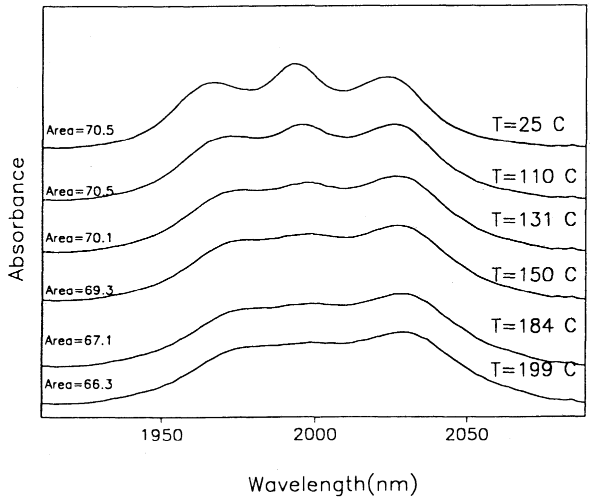

Figure 2. Variation of the absorption band around 2000 nm from UCl_6^{2-} with temperature.

DOI: 10.1149/199413.0313PV

VIBRATIONAL AND ^{31}P NMR STUDIES OF MOLTEN PHOSPHORIC ACID AND HIGHLY CONCENTRATED AQUEOUS SOLUTIONS

Wolfram Rudolph†

Chemistry Department
Memorial University of Newfoundland
St. John's, Newfoundland, Canada AIB 3X7

ABSTRACT

Highly concentrated phosphoric and deutero phosphoric acid solutions and the anhydrous melt were investigated by Raman and i.r. spectroscopy. Intermolecular coupling effects due to strong H-bonds between neighbouring acid molecules in the melt and in highly concentrated solutions cause lowering of the C_{3v} symmetry. The formation of pyrophosphoric acid in the freshly fused acid melt was observed by ^{31}P NMR as a function of time at different temperatures. Thermodynamic and kinetic parameters for this interconversion reaction were determined.

INTRODUCTION

Phosphoric acid has been investigated by Raman and infrared spectroscopy many times (see [1] and the references therein). Most of the Raman measurements were done before the laser was introduced as a light source, so that many spectroscopic details remained unnoticed. Therefore structural conclusions concerning the symmetry of the PO_4 skeleton were inconsistent. Because of the great industrial, synthetic and physiological importance of phosphoric acid a reinvestigation anhydrous phosphoric acid and highly concentrated phosphoric and deutero-phosphoric acid solutions by Raman and infrared spectroscopy is warranted. Furthermore the necessity of careful measurements of scattered light in the parallel and perpendicular orientations in order to detect weak isotropic intensities (also for some examples in R-format) due to the symmetric motions is shown. The formation of pyrophosphoric acid in the anhydrous phosphoric acid melt was measured by ^{31}P NMR spectroscopy as a function of time at several temperatures.

Anhydrous crystalline phosphoric acid is a white solid and melts at 42.3°C. Pure phosphoric acid crystallizes rather slowly and it is easy to form a supercooled phosphoric acid melt at room temperature [2]. Raman and infrared spectroscopy was used to obtain structural information of the anhydrous phosphoric acid melt. The overall picture from our vibrational spectroscopic studies is, that the phosphoric acid forms a

---

† Permanent address: TU Dresden, Universitaetsklinikum "Carl Gustav Carus", 0-8019 Dresden, Fetscherstr. 74, Germany

complicated network of very short, strong H-bonds between the phosphoryl oxygen (P=O) and the POH groups. The strength of the H-bonds is comparable to those which are formed in the crystal [9,10] as shown by comparison of the Raman spectra of the melt and a crystalline powder at room temperature as seen in Figure 1. In contrast to the dilute solution where the phosphoric acid possesses C_{3v} symmetry [3,4], the symmetry in the melt is reduced by strong intermolecular coupling of neighbouring H-bonded acid molecules. This effect is shown by the difference between $I_{\parallel}$ and $I_{\perp}$ peak maxima in the Raman effect and additionally between the $I_{\parallel}$ peak maximum and the infrared band position of the P=O and $P(OH)_3$ groups in the melt. This effect of intermolecular coupling of neighbouring H-bonded acids in melts was also observed in anhydrous H_2SeO_4 [11] and H_2SO_4 [12]. For the molten phosphoric acid the following frequencies were found: (ν_S $P(OH)_3$ ($I_{\parallel}$): 915 cm^{-1} ($\Gamma_{1/2}$ = 29 cm^{-1}); ν_S $P(OH)_3$ ($I_{\perp}$): 896 cm^{-1} ν_S $(POH)_3$ (i.r.) = 895 cm^{-1}) $\nu P=O$ ($I_{\parallel}$): 1100 cm^{-1} $\nu P=O$ ($I_{\perp}$): 1125 cm^{-1} $\nu P=O$ (i.r.): 1135 cm^{-1}.

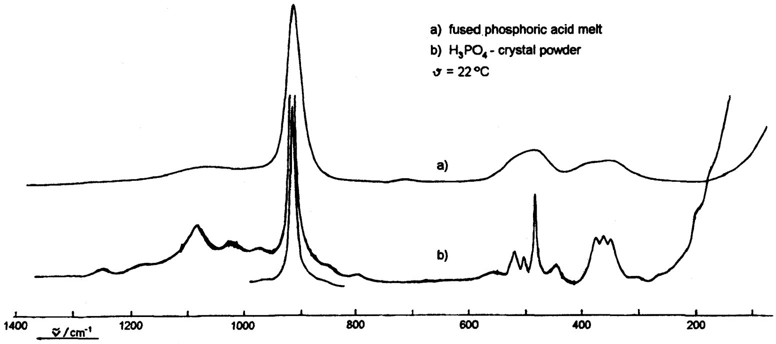

Figure 1: Comparison of the $I_{\parallel}$ Raman spectrum of a cooled anhydrous phosphoric acid melt (a) and the Raman spectrum of H_3PO_4-crystal powder (b) between 100 and 1400 cm^{-1} at 22°C.

In highly concentrated phosphoric acid solutions the acid still forms H-bonded species. This is indicated by the fact, that the intermolecular coupling of neighbouring acid molecules still remains as seen in Figure 2 for a 14.5 M H_3PO_4 and in Figure 3 for a 11.47 M D_3PO_4 solution.

Freshly fused anhydrous phosphoric acid exhibits an appreciable ionic conductivity, which suggests autoprotolysis [13] according to eq. (1).

$$2H_3PO_4 \rightleftarrows H_4PO_4^+ + H_2PO_4^- \qquad (1)$$

Simultaneously, phosphoric acid interconverts into pyrophosphoric acid but in a more sluggish reaction according to eq. (2).

$$2H_3PO_4 \rightleftarrows H_4P_2O_7 + H_2O \qquad (2)$$

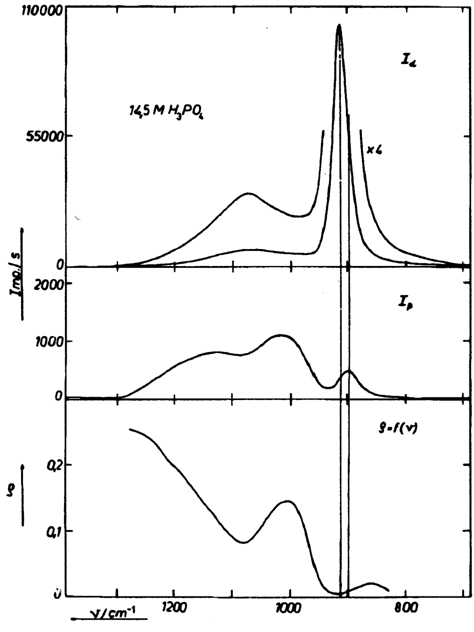

Figure 2: I_α and I_β Raman spectrum of a 14.5 M H_3PO_4 solution (H_3PO_4:H_2O = 1:1) and $\rho = f(\nu)$ between 700 and 1400 cm^{-1}.

After approximately 2 h at 22°C in the Raman spectrum of a freshly fused anhydrous phosphoric acid melt a polarized band at 720 cm^{-1} is detectable (See Fig. 1). This band, ν_S P-O-P, represents the amount of pyrophosphoric acid (approximately 1 mol % formed 2 hours after fusing the melt). This interconversion of orthophosphoric acid to pyrophosphoric acid (see eq. (2)) was followed by ^{31}P NMR measurements between 43.5°C and 74°C. Kinetic and thermodynamic data of this interconversion reaction were obtained [5] at four temperatures. The concentration quotient Q_C for reaction (2) was calculated by eq. (3).

$$Q_C = \frac{[H_4P_2O_7][H_2O]}{[H_3PO_4]^2} \tag{3}$$

The following Q_C-values were obtained: at 43.5°C (0.00142); at 50°C (0.00192); at 60°C (0.00248) and at 74°C (0.00337). The enthalpy of the pyrophosphoric acid formation was calculated to be $\Delta H_R^0 = 26 \pm 1$ KJ·mol^{-1}.

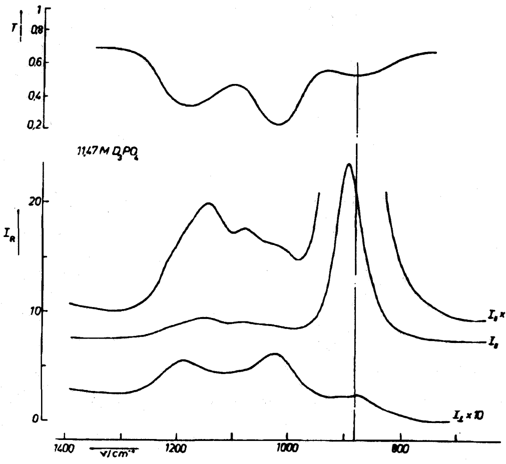

Figure 3: $I_\parallel$ and $I_\perp$ Raman spectrum and the i.r. spectrum of a 11.47 M deutero phosphoric acid (D_3PO_4:D_2O = 1:2) between 750 and 1420 cm^{-1}.

For the interconversion reaction (see eq. (2)) the second order rate law can be written:

$$rate \ = \ k_2[H_3PO_4]^2 - k_{-2}[H_4P_2O_7][H_2O] \qquad (4)$$

The following rate constants were found: 43.5°C: k_2 = 0.636 10^{-4} mol $\%^{-1}\cdot min^{-1}$; k_{-2} = 4.49 10^{-2} mol $\%^{-1}\cdot min^{-1}$; 50°C: k_2 = 2.24 10^{-4} mol $\%^{-1}\cdot min^{-1}$; k_{-2} = 1.166 10^{-1} mol $\%^{-1}\cdot min^{-1}$; 60°C: k_2 = 7.36 10^{-4} mol $\%^{-1}\cdot min^{-1}$; k_{-2} = 2.97 10^{-1} mol $\%^{-1}\cdot min^{-1}$; 74°C: k_2 = 24.72 10^{-4} mol $\%^{-1}\cdot min^{-1}$; k_{-2} = 7.340 10^{-1} mol $\%^{-1}\cdot min^{-1}$.

Raman spectroscopy has gained acceptance as a reliable technique for the identification of discrete species in molten salts and there have been attempts to develop Raman intensity methods for quantitative or at least semi-quantitative analysis. It must be emphasized that the actual quantity measured in the Raman experiment, the scattering cross section, $\partial\alpha/\partial\Omega$ has both temperature and frequency dependent factors that are especially important in the low wavenumber region of the spectrum at the high sample temperature normally employed for molten salts. The use of a normalized or reduced intensity, $R(\omega)$ to create a spectrum that is directly proportional to the intrinsic Raman scattering activity is essential for measurements in the low wavenumber region (6-8). Within the double harmonic approximation the use of the $R(\omega)$ spectrum removes a temperature and frequency dependent band asymmetry and permits comparison of spectra obtained at different temperatures (8). Furthermore it is essential to carefully measure light scattered in both the parallel, $R_{\parallel}$ and perpendicular, $R_{\perp}$ orientations in order to detect weak isotropic intensity R_{iso} due the symmetric motions.

Experimental

Raman spectra were recorded using standard experimental equipment [1], including an ILA 120 argon ion laser, GDM 1000 double monochromator and d.c. amplification. $I_{\parallel}$ and $I_{\perp}$ spectra are proportional to $45\overline{\alpha}'^2 + 4\beta'^2$ and $3\beta'^2$ respectively. The precision of frequencies is ± 1 cm^{-1}. All measurements refer to room temperature (295±2 K). Some Raman spectra were also measured in R format with a Coderg PHO Raman spectrometer at Memorial University, NF. Infrared spectra were obtained using a FT-IR spectrometer. The ^{31}P NMR-spectra were measured with a Bruker FT-spectrometer WH-90 DS at 36.44 MHz. The chemical shifts are related to 85% H_3PO_4 as an external standard. DMSO was used as an external lock. The phosphoric acid and deuterated phosphoric acid solutions and the anhydrous phosphoric acid were prepared as described elsewhere [1].

ACKNOWLEDGEMENTS

The assistance of a fellowship granted by the DAAD (Deutscher Akademischer Austauschdienst) to W.R. is gratefully acknowledged. W.R. thanks also Prof. Dr. M.H. Brooker (MUN, Dept. of Chemistry) for helpful discussions and for the use of the Raman spectrometer.

REFERENCES

1. W. Rudolph, thesis, TU Dresden, 1986.
2. J.R. Van Wazer, "Phosphorus and its Compounds", Vol. I, Instescience, New York 1958.
3. W. Rudolph and W.E. Steger, Z. Phys. Chem. 172, 49 (1991).
4. W. Rudolph and W.E. Steger, Z. Phys. Chem. 176, 185 (1992).
5. W. Rudolph, unpublished work.
6. M.H. Brooker and G.N. Papatheodorou, in "Advances in Molten Salt Chemistry", edited by G. Mamantov, (Elsevier, Amsterdam, 1983) Vol. 5, pp 27-165.
7. M.H. Brooker, O. Faurskov Nielsen and E. Praestgaard, J. Raman Spectrosc. 19, 71 (1988).
8. W.F. Murphy, M.H. Brooker, O. Faurskov Nielsen, E. Praestgaard and J.E. Bertie, J. Raman Spectrosc. 20, 695 (1989).
9. J.P. Smith, W.E. Brown and J.R. Lehr, J. Am. Chem. Soc. 77 (1955) 2728.
10. S. Furberg, Acta Chem. Scand. 9 (1955) 1557.
11. G.E. Walrafen, J. Chem. Phys. 39 (1963) 1479.
12. A. Goypiron, J. de Villepin and A. Novak, J. Chim. Phys., 75 (1978) 889.
13. R.A. Munson, J. Phys. Chem. 68 (1964) 3374.

DOI: 10.1149/199413.0318PV

^{27}Al NUCLEAR QUADRUPOLE COUPLING CONSTANTS IN ETHYLALUMINUM DICHLORIDE MELTS

W. Robert Carper and Charles E. Keller
Department of Chemistry, Wichita State University
Wichita, Kansas 67260-0051

and

Bernard J. Piersma
Department of Chemistry, Houghton College
Houghton, New York 14744

^{27}Al relaxation data of the room temperature melt, LiCl-ethylaluminum dichloride(1:2 mole ratio, f.p. ≈ 178K), is analyzed by a unique mathematical solution of the relaxation equations for T_1 and T_2. In this melt, the broad(short T^Q) ^{27}Al peak at 128.5 ppm($EtAlCl_2$ dimer) has been completely replaced by a single narrow(long T^Q) peak at 100.5 ppm, similar to those narrow peaks observed for $AlCl_4^-$(103 ppm) and $EtAlCl_3^-$ (102 ppm). The quadrupolar relaxation rates($R^Q = 1/T^Q$) of this peak(100.5 ppm) are used to determine correlation times. These correlation times are used to calculate QCC values for ^{27}Al in ethylaluminum dichloride.

INTRODUCTION

NMR relaxation methods have been used to study the interactions between both ionic and neutral species in room temperature chloroaluminate melts(1-6). A recent addition to these melts is ethylaluminum dichloride ($EtAlCl_2$) which melts at approx. 32°C. The combination of $EtAlCl_2$ and either 1-butyl-3-methylimidazolium chloride or 1-ethyl-3-methylimidazolium chloride(ImCl) produces a melt that is liquid over a wide range of temperatures and melt compositions(4-7).

The ^{27}Al NMR of neat $EtAlCl_2$ consists of a broad peak at 129 ppm relative to external standard $Al(H_2O)_6^{3+}$(4,5). This peak is assigned to the dimer of $EtAlCl_2$, consistent with this species ability to form C_{2H} dimers and the fact that other dimers of alkylaluminum compounds have similar chemical shifts(4-6,8-10). A chemical shift value of 140 ppm has been reported for dimeric $EtAlCl_2$ in deuterated toluene at 300K(11). In room temperature melts containing ImCl and $EtAlCl_2$, a sharp(long T_1) peak is observed at 102 ppm in addition to the broad $(EtAlCl_2)_2$ peak centered at 129 ppm(4,6). The sharp peak at 102 ppm is that of $EtAlCl_3^-$ as evidenced by its similarity to the ^{27}Al peak for $AlCl_4^-$ at 103 ppm(6), both in terms of relaxation time(symmetry) and chemical shift(coordination number)(10). A similar ^{27}Al peak is observed at 101 ppm in LiCl-$EtAlCl_2$ solutions(5).

A very sensitive indication of molecular and/or ionic symmetry is the value of the Nuclear quadrupole coupling constant(QCC) which approaches zero as cubic symmetry about the quadrupole nucleus is realized. Knowledge of Nuclear quadrupole coupling constants(QCC) in the liquid state can therefore provide much useful information concerning a particular nucleus and its surrounding ligands(12). At present, the only simple approach for liquids involves using the Dual Spin Probe(NMR relaxation) method(2,3,13) in which a quadrupolar relaxing nucleus is adjacent to a dipolar relaxing nucleus such as ^{13}C. Assuming identical correlation times, isotropic motion and the condition of extreme narrowing($\omega^2\tau_c^2 << 1$, where $\omega = 2\pi\nu$ and τ_c = the effective correlation time), one can then relate the quadrupolar relaxation rate, $R_1^Q(= 1/T^Q)$, to the dipolar relaxation rate, $R_1^{dipolar}$. This method has been used to obtain values for ^{23}Na and ^{27}Al quadrupole coupling constants in several cases including room temperature melts(2,3). While this approach is reasonable for non-viscous solutions, it appears questionable for particular room temperature melts(acidic chloroaluminate melts) or other solutions of high viscosity where the condition of extreme narrowing($\omega^2\tau_c^2 << 1$) is unlikely to be met. If this is the situation, then another method must be devised to determine the correlation time, τ_c, for highly viscous solutions. One alternative involves the use of sub-ambient measurements such as those reported recently for melt systems based on ethylaluminum dichloride($EtAlCl_2$)(6). However, there is another possible solution to this problem as follows. To determine an accurate value for τ_c, one may use the following equations(14) for R_1^Q and R_2^Q:

$$R_1^Q = [(3\pi^2/100)(1 + \eta^2/3)][(2I+3)/I^2(2I-1)](QCC)^2 [(2\tau_c/1+ \omega^2\tau_c^2) + (8\tau_c/1+ 4\omega^2\tau_c^2)] \quad [1]$$

$$R_2^Q = [(3\pi^2/200)(1 + \eta^2/3)][(2I+3)/I^2(2I-1)](QCC)^2[6\tau_c + (10\tau_c/1+ \omega^2\tau_c^2) + (4\tau_c/1+ 4\omega^2\tau_c^2)] \quad [2]$$

where η is an asymmetry parameter which accounts for deviation from axial symmetry ($\eta = 0$ for $AlCl_3$).

In the case where one is outside the region of extreme narrowing, $R_2^Q > R_1^Q$, and eqs [1] and [2] can be combined(15) to form:

$$R_1^Q /2R_2^Q = [(1/1+ \omega^2\tau_c^2) + (4/1+ 4\omega^2\tau_c^2)]/[3 + (5/1+ \omega^2\tau_c^2) + (2/1+ 4\omega^2\tau_c^2)] \quad [3]$$

Solving eq [3] for $\omega\tau_c$, one obtains:

$$\omega^4\tau_c^4 + [3.0833 - 0.6667(2R_2^Q/R_1^Q)]\omega^2\tau_c^2 - 0.4167(2R_2^Q/R_1^Q) + 0.8333 = 0 \qquad [4]$$

The solutions of the above quartic include a single value for the effective correlation time, τ_c, when $R_2 > R_1$, whereas only complex roots are obtained when $R_2 < R_1$. A similar equation can be derived for other cases(dipolar relaxation) if accurate correlation times are of significance to the investigator.

EXPERIMENTAL

^{27}Al NMR spectra were recorded at 78.15 MHz and temperatures calibrated against methanol or ethylene glycol. Pulse widths are typically 6-8 μs and T_1^Q's were measured by the inversion recovery method(180°-τ-90°-T) with $T > 10T_1$. At least 12 delay times (τ) were used and relaxation times (in duplicate or triplicate) were obtained from a three parameter exponential fit of magnetization as a function of T. There was no evidence of any non-exponential behavior. Transverse(spin-spin) relaxation times, T_2, were determined from half-height peak widths ($=1/\pi{}^*T_2$, where ${}^*T_2 = T_2$). The relatively narrow ^{27}Al linewidths made T_2 measurements less subject to signal acquisition problems as carefully outlined in (16). All chemical shift measurements are relative to $Al(H_2O)_6^{3+}$.

RESULTS AND DISCUSSION

We have recently obtained ^{27}Al relaxation data on the room temperature melt, LiCl-ethylaluminum dichloride(1:2 mole ratio, f.p. ≈ 178K)(6,7). In this melt, the broad(short T^Q) ^{27}Al peak at 128.5 ppm($EtAlCl_2$ dimer) has been completely replaced by a single narrow(long T^Q) peak at 100.5 ppm, similar to those narrow peaks observed for $AlCl_4^-$ (103 ppm) and $EtAlCl_3^-$(102 ppm)(8). The quadrupolar relaxation rates($R^Q = 1/T^Q$)(9) of this peak(100.5 ppm - see Fig. 1) are not equal (Unlike $EtAlCl_2$, whose ^{27}Al T_1's and T_2's were identical at 78.15 MHz over the same temperature range) and are used(eq [4]) to determine correlation times from -12.5 to 65°C as shown in Fig. 2. The correlation times are(theoretically) the time required for the nuclei in question to rotate through a distance of one radian. Thus the faster the rotation, the shorter the correlation time. The existence of a correlation time maximum well above the freezing point of this melt suggests that the melt is going through a particular type of liquid structural change(phase transition, etc.) Additional support for this concept follows from the calculated values of the nuclear quadrupole coupling constants (QCC's).

As a numerical check, the existence of a R_1 maximum at 20°C(Fig. 1) allows the exact solution of eq [1] at the maximum where $\omega\tau_C = 0.6157$. The resulting QCC value(assuming that $\eta = 0$) is 3.71 MHz which agrees with the value of 3.70 MHz calculated from eq [4]. The R_1 maximum(T_1 minimum) at 20°C is considerably above this solution's f.p.(≈ 178K) and is similar to glass-like transition regions observed for other melts(6).

The ^{27}Al correlation times for the ethylaluminum dichloride in Fig. 2 are used to calculate QCC values using eq [1], assuming that $\eta = 0$, as is the case for solid $AlCl_3$(17). These QCC values are also shown in Fig. 2 and indicate a gradual increase from 3.20 to 3.83 MHz between 65 and 10°C. From 10 to -12.5°C, there is a steady decrease in the QCC values. These two observations are consistent with a complex structure that: (1) changes only slightly at the higher temperatures(one would expect a small increase in QCC as the temperature rises due to increased mobility of the ethyl groups at the higher temperatures), and (2) approaches a more cubic(tetrahedral) structure as the temperature is lowered. There is no particular physical or mathematical requirement that correlation times and QCC values have a maximum at the exact same temperature. This may be explained in terms of several dynamic processes being involved in the structural changes of $EtAlCl_2$ as it approaches a glassy or crystalline state.

Finally one may compare the QCC results which have a maximum of 3.83 MHz and vary between 3.20 and 2.20 MHz to other similar aluminum containing compounds. Other ^{27}Al QCC values include 0.471 MHz for solid $AlCl_3$(17), 0.909 MHz for $EtAlCl_3^-$ (6,18), 0.821 MHz for $AlCl_4^-$(6), and 9.39 MHz for the $EtAlCl_2$ dimer(6,18). It is apparent that the insertion of LiCl into the $EtAlCl_2$ dimer solution has altered the C_{2H} symmetry of dimeric $EtAlCl_2$(8) and produced a species of higher symmetry.

REFERENCES

1. W. R. Carper, J. L. Pflug, A. M. Elias and J. S. Wilkes, J. S., *J. Phys. Chem.* **96**, 3828(1992).
2. W. R. Carper, J. L. Pflug and J. S. Wilkes, *Inorg. Chim. Acta* **193**, 201(1992).
3. W. R. Carper, J. L. Pflug and J. S. Wilkes, *Inorg. Chim. Acta* **202**, 89(1992).
4. P. A. Shaw, W. R. Carper, C. E. Keller and J. S. Wilkes, *Bull Magn.Reson.* **14**, 92(1992).
5. C. E. Keller, W. R. Carper and B. J. Piersma., *Inorg. Chim. Acta* **209**, 239(1993).
6. C. E. Keller and W. R. Carper, *Inorg. Chim. Acta* **210**, 203(1993).

7. B. Gilbert, Y. Chauvin and I. Guibard, *Vib. Spectrosc.* **1**, 299(1991).
8. J. Weidlein, *J. Organometal. Chem.* **17**, 213(1969).
9. O. Yamamoto, K. Hayamizu and M. Yanigisawa, *J. Organometal. Chem.* **73**, 17(1974).
10. R. Benn and A. Rufinska, *Angew. Chem. Int. Ed. Eng.* **25**, 861(1986).
11. R. Benn, A. Rufinska, H. Lehmkuhl, E. Janssen and C. Kruger, *Angew. Chem. Int. Ed. Eng.* **22**, 779(1983).
12. J. W. Akitt and W. S. McDonald, *J. Magn. Reson.* **58**, 401(1984).
13. J. J. Dechter, U. Henriksson, J. Kowalewski and A.-C. Nilsson, *J. Magn. Reson.* **48**, 503(1982).
14. (a) T. C. Farrar and E. D. Becker, "Pulse and Fourier Transform NMR", Academic Press, New York, (1971). (b) A. Abragam, "The Principles of Nuclear Magnetism", Clarendon, Oxford, (1961). (c) H. W. Spiess, in "NMR Basic Principles and Progress", P. Diehl, E. Fluck and R. Kosfeld, Editors., Springer-Verlag, Berlin, **15**, 55(1978). (d) R. G. Kidd, in "NMR of Newly Accessible Nuclei", P. Laszlo, Editor, Academic Press, New York, **1**, 103(1983).
15. J. D. Decatur and T. C. Farrar, *J. Phys. Chem.* **94**, 7391(1990).
16. J. W. Akitt, in "Progress in NMR Spectroscopy", J. W. Emsley, J. Feeney and L. H. Sutcliffe, Editors., Academic Press, New York, **21**, 1(1989).
17. P. A. Casabella and N. C. Miller, *J. Chem. Phys.* **40**, 1363(1964).
18. The original values of 5.01 MHz($EtAlCl_2$ dimer) and 0.486 MHz($EtAlCl_3^-$) were calculated assuming that $\omega\tau_c = 1$.

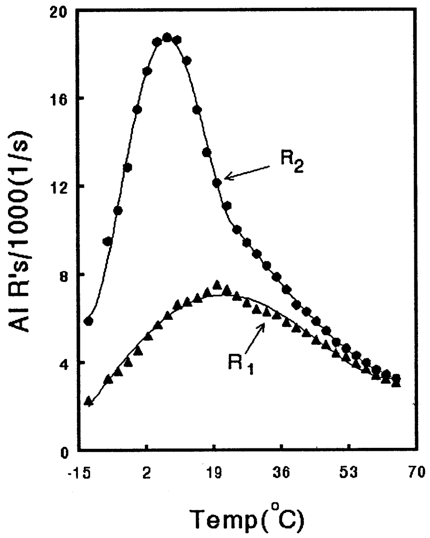

Figure 1. ^{27}Al quadrupole relaxation rates(R_1^Q/1000 and R_2^Q/1000 in s^{-1}) vs temp(°C) from eq [4] vs temp(°C).

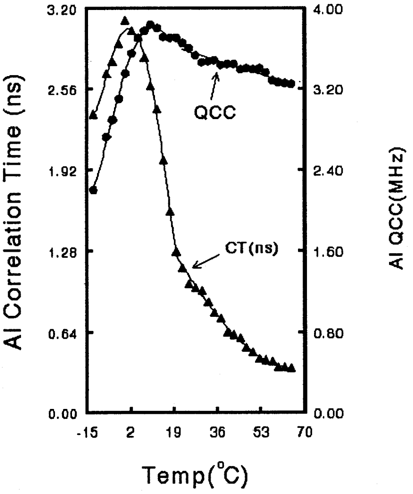

Figure 2. Nuclear quadrupole coupling constants, QCC's, (MHz) and effective correlation times, τ_c's(ns), for 1:2 LiCl:EtAlCl$_2$

DOI: 10.1149/199413.0324PV

CF_3COONa - CH_2FCONH_2 MOLTEN MIXTURES : A MICROHETEROGENEOUS SYSTEM

G.Berchiesi, G.Vitali and F.Farhat
Dipartimento di Scienze Chimiche, 62032 Camerino
Italy

ABSTRACT

The longitudinal relaxation time of the nuclear magnetic momentum was measured on ^{19}F nuclei of both amide and salt in order to prove the microheterogeneous nature of the molten mixtures composed of salt and amide.

INTRODUCTION

Amide-salt mixtures (in a composition range around the eutectic point) show a peculiar behavior. Firstly, owing to the high viscosity, they seem an oily or paste-type system. Secondly, they supercool easily, and for this reason in certain cases crystallization does not occur and the supercooled system remains liquid indefinitely (1-4) till the glass transition temperature.

In the concentration range where this behavior is evident, the salt is practically undissociated. These peculiarities disappear with increasing chain length of the amide. Viscoelastic relaxation occurs in the ultrasonic range, showing a shift towards higher frequencies compared to the Maxwell body relaxation. Ultrasonic relaxation shows a strong relaxation phenomenon, which may be ascribed to a structural process (5), or to an equilibrium of the amide, present in different aggregates (6). Moreover, the dielectric constant is very high, reaching the value of 10^6, (7,8).

These peculiarities may be explained only on the basis of a polymeric structure. Recently we have invoked a micellar dispersion of salt in amorphous amide as a model to explain the peculiar behavior of these mixtures (8).

RESULTS

In order to prove the microheterogeneity of the mixtures, we have measured the longitudinal relaxation time (T_1) of the nuclear magnetic momentum of fluorine nuclei in a mixture of CH_2FCONH_2 and CF_3COONa.

Since T_1 is dependent on the local magnetic field caused by the molecule tumbling, it may represent a tool for discovering local heterogeneity in the molecular assembly. In Figure 1, T_1 is shown for the fluorine nuclei of amide and salt, respectively.

DISCUSSION

It is evident (Fig. 1) that the longitudinal relaxation time of nuclear magnetic momentum for Fluorine nuclei in the salt and Fluorine in the amide is very different :

$$T_{1salt} \approx 7\ T_{1amide}.$$

We believe that this is a proof of the heterogeneity of the amide-electrolyte mixtures, which show supercooling phenomena. Salt aggregates probably have a rigid structure and are dispersed in an amorphous organization of amide molecules (less rigid). The importance of this structure has been emphasized in previous publications (8,9).

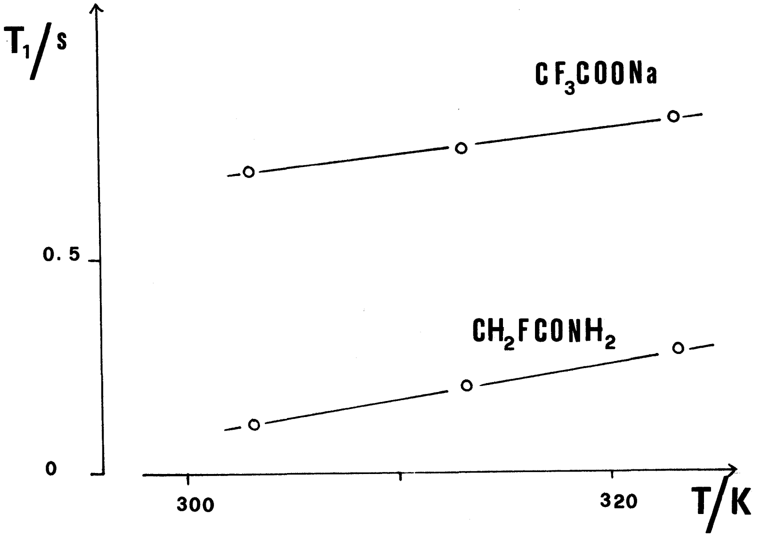

REFERENCES

1 F.Castellani, G.Berchiesi,F.Pucciarelli, V.Bartocci, J.Chem.Eng.Data, **26**, 150 (1981).
2 G.Berchiesi, G.Gioia Lobbia, V.Bartocci, G.Vitali, Thermochim.Acta, **70**, 317 (1983).
3 G.Gioia Lobbia, G.Berchiesi, Thermochim.Acta, **74**, 251 (1984).
4 G.Berchiesi, G.Gioia Lobbia, M.A.Berchiesi, G.Vitali, J.Thermal Anal. **29**, 729 (1984).
5 R.Plowiec, A.Amico, G.Berchiesi, J.Chem.Soc.Faraday Trans.2, **81**, 217 (1985).
6 G.Berchiesi, M.De Angelis, G.Rafaiani, G.Vitali, J.Molecular Liquids **51**, 11 (1992).
7 A.Amico, G.Berchiesi, C.Cametti, A.Di Biasio, J.Chem.Soc.Faraday Trans.2, **83**, 619 (1987).
8 G.Berchiesi, F.Farhat, M.De Angelis, S.Barocci, J.Molecular Liquids, **54**, 103 (1992).
9 G.Berchiesi, F.Farhat, G.Vitali, Materials Science Forum, **126-128**, 367-370 (1993).

DOI: 10.1149/199413.0326PV

THE RELATIONSHIP OF THE HNMR SPECTRA OF BINARY SOLUTIONS OF METHYLPYRIDINIUM HALIDES TO THE MELT'S STRUCTURE

David S. Newman and Mary Potter

Department of Chemistry
Bowling Green State University
Bowling Green , OH 43403

Frank Parker
Department of Chemistry
University of Michigan
Ann Arbor, MI 48109

ABSTRACT

The HNMR spectra of binary mixtures of 4-methylpyridinium chloride and 4-methylpyridinium iodide were measured as a function of temperature and composition over the entire composition range. Correlations were made between these spectra and thermodynamic and transport properties of the melts. The effect of hydrogen bonding on the melt's properties was assessed and a four species model was proposed to account for these properties. A pronounced "mixed ion" effect was observed in the NMR spectra, but was barely discernible in the transport properties and completely absent in the thermodynamic properties.

INTRODUCTION

Hypotheses about ion transport mechanisms, ionic and molecular interactions, and the nature of complex species thought to exist in molten salt solutions, often have been tested by examining macroscopic properties of binary mixtures with a common ion. In effect, the common ion serves as a reference in much the same way water serves as a reference in aqueous solutions so that isothermal deviations from ideality as a function of changing composition are attributed to interactions between the components of the mixture. Although defining a reference is necessary for macroscopic measurements to be at all useful, fixing a reference may inherently mask microscopic or molecular contributions to the property measured. This is especially true in the case of partial molar volumes where the reference is the molar volume of each of the pure components. Moreover, since it is formally impossible to obtain molecular information from thermodynamic measurements, it is necessary to accompany the thermodynamic or transport property measurement with a microscopic measurement to establish the microscopic origin of that property unambiguously or, often enough, to avoid missing a significant interaction altogether because of the mutually canceling out of two equal but opposite macroscopic effects. Because of the comparatively long relaxation times involved and the temperature range over which the mixture is liquid, the technique of choice for many molten organic salt solutions is NMR spectroscopy.

We therefore measured the HNMR spectra of binary solutions of 4-methylpyridinium chloride (4-mepyrCl) and 4-methylpyridinium iodide (4-mepyrI) as a function of temperature and as a function of composition over the entire composition range. The mixtures contain identical cations, but a different anion and 4-mepyrCl is capable of hydrogen bonding whereas 4-mepyrI is not. (1) We expected that the hydrogen bonding would cause significant deviations from ideality. We then compared these data with previously measured conductivities, viscosities and partial molar volumes (2,3,4) of the same solutions and constructed a detailed microscopic model of the melt. These data were also used to determine if a mixed univalent anion effect exists in these organic melts that is similar to the "mixed univalent cation effect" in inorganic melts discussed by Moynihan in 1979 (5).

EXPERIMENTAL DETAILS

The 4-mepyrCl and 4-mepyrI were each synthesized by bubbling anhydrous HCl mixed with dry nitrogen gas or anhydrous HI mixed with dry nitrogen gas through 4-methylpyridine that had been distilled over BaO. White crystalline methylpyridinium salts appeared after about one minute. Reaction vessels were wrapped with aluminum foil to exclude light so as to prevent photochemical reactions from occurring.
Details of the recrystallization ,washing, filtration and drying procedures can be found elsewhere (6).

The melting point of the 4-mepyrI salt was 444K and that of the 4-mepyrCl salt was 441K The iodide's melting point agreed exactly with our previously published value (2) and the chloride's melting point was 0.5 degrees higher than our earlier literature value. (7) Chemical analyses of the final products gave their exact stoichiometry to three significant figures. Upon melting, the 4-mepyrCl remained water clear and after approximately 10 hrs at 473K showed no discernible decomposition. The 4-mepyrI turned yellow upon melting, but the yellow color disappeared and the salt returned to its white crystalline state upon freezing . Chemical analysis indicated the salt decomposed approximately 2% after 10 hrs at 473K. This amount of decomposition was considered negligible since no experiment lasted more than two hours and most experiments were conducted in the 430K - 460K range.

The NMR measurements of the melts were made with the variable temperature probe of a Brucker DZH 360/50 spectrometer. An external standard of DMSO was used and the temperature setting of the machine was calibrated with ethylene glycol.

RESULTS

The HNMR spectra of the binary mixtures were obtained isothermally and, for the $X_{Cl} = 0.3$ and the $X_{Cl} = 0.5$ compositions, as a function of temperature between 425 and 440 K. The upper temperature range accessible to the instrument was only about 445 K, with 440 K being the temperature at which most of the spectra were obtained. The spectrum of the pure iodide melt was obtained at its melting point of approximately 444 K. The spectra of the $X_{Cl} = 0.3$ and the 0.5 melts changed their chemical shifts a negligible amount over the fairly narrow temperature range investigated . For instance, at $X = 0.5$, $\delta_{N\text{-}H} =$ 16.84 ppm at 430K and 16.91 ppm at 440K so that a temperature difference of $\pm$ 5 ^{o}C at any composition is insignificant as far as the chemical shift is concerned. For illustrative purposes, the spectrum obtained at 440K for $X_{Cl} = 0.4$ is shown in Fig. 1 relative to the external standard of DMSO. In order to correct DMSO data to TMS data, 2.49 ppm is added to the DMSO chemical shift.

Fig. 2 A shows the chemical shift, δ, as a function of composition for the nitrogenic proton and Fig. 3 shows the chemical shifts of the 4-methyl protons, the α protons, and the β protons as a function of composition at 440K. In these figures, the chemical shifts have been corrected to the more familiar TMS standard. It is obvious from these data that between $X_{Cl} = 0.4$ and $X_{Cl} = 0.8$ there is a large positive deviation from ideality in the chemical shifts as a function of composition, ideality being the tie line between the pure iodide and the pure chloride melts. The protons are all considerably more acidic (farther down field or more deshielded) than the weighted average of the two pure components.

DISCUSSION

Errors and Comparison With Earlier Work. The temperature of the NMR machine was controlled to ± 2 °C, but the spectra were relatively insensitive to small temperature changes so this variation was considered negligible. The chemical shifts between different samples at any nominal temperature and composition differed by about ± 0. 05 ppm which is therefore considered as the random error in the chemical shift measurements. The chemical shifts of the 4-mepyrI melt were within ± 0.1 ppm of those reported by Newman and Stevens (1) . The present results are considered slightly more accurate because of improvements in instrumentation and technique.

Several years ago, Angell and Shuppert measured the HNMR spectra of binary mixtures of molten pyridinium chlorides and strong Lewis acids (8,9). Table I lists the chemical shifts of the nitrogenic protons taken from their work together with the chemical shifts of the nitrogenic protons in the pure 4-mepyrCl melt and the 70% 4-mepyrI melt taken from our study, all corrected to TMS. It is obvious from these data that $\delta_{N\text{-}H}$ for each of the three different pyridinium chlorides are within 0.2 ppm of each other, which means the methyl group has little influence on this chemical shift, but also helps confirm the validity of the three measurements. The most striking feature of the data in Table I, is that in the four pyridinium binaries, the chemical shift is inversely proportional to the Lewis acidity of the second component; the stronger the Lewis acid, the closer the N-H proton is to the theoretical or, stating it differently, the smaller the chemical shift. The reason for this δ_H dependence on Lewis acidity is that the stronger the Lewis acid, the more successfully it competes with the nitrogenic proton for the deshielding Cl^- ion. In a melt which is 70 mol% $AlCl_3$, the pyridinium ion can be considered virtually "free", because nearly all of the Cl^- ions are tied up in $Al_2Cl_7^-$ ions or $AlCl_4^-$ ions. $AlCl_3$ is a stronger Lewis acid than $ZnCl_2$, which in turn is a stronger Lewis acid than HCl (HCl is a strong Bronsted acid, but a relatively weak Lewis acid). 4-mepyrI is the weakest Lewis acid of the four and therefore, the chemical shift of its nitrogenic proton in the 70 mol% binary is the farthest down field of the four.

Mixed Ion Effect The isothermal composition dependence of the density, ρ , was used to obtain the excess molar volume, V_m^E. This quantity is given by the equation

$$V_m^E = \Delta_{mix}V_m - \Delta_{mix}V_m^{ideal} \qquad [1]$$

where $\Delta_{mix}V_m$ is the molar volume of mixing and $\Delta_{mix}V_m^{ideal}$ is the ideal molar volume of mixing. The molar volume of mixing is given by the equation

$$\Delta_{mix}V_m = \{[(1\text{-}x)M_{Cl} + xM_I]/\rho_m\} - [(1\text{-}x)M_{Cl}/\rho_{Cl}] - xM_I/\rho_I \qquad [2]$$

where the M_i are the molecular weights and the ρ_i are the densities of the mixture, chloride, and iodide melts, respectively.(2,4)

Since $\Delta_{mix}V_m^{ideal} = 0$, $V_m^E = \Delta_{mix}V_m$.. At all temperatures investigated, within experimental error, $V_m^E = 0$. This means that the solutions appear to be behaving ideally with regard to this mixing function and no mixed ion effect is observed. Fig. 4 shows the molar conductance of several binary mixtures as a function of composition and Fig. 5 shows the viscosity as a function of composition for the same melts. Here it is clear that there is a small, but distinct, negative deviation from additivity at the lower temperatures which diminishes as the temperature is raised. With respect to the transport properties then, there does seem to be a small mixed ion effect at the lower temperatures. There is also a large positive deviation from additivity in the chemical shift isotherms which means that at the molecular level the mixtures are anything but ideal.

This implies there is a mixed univalent *anion* effect in this binary mixture of organic salts which is similar to the mixed univalent *cation* effect bound in binary mixtures of inorganic salts (5) and what appears to be a mixed *divalent* cation effect found by Kim and Sadoway (10) in several alkaline earth fluoride mixtures. We therefore suggest the mixed ion effect may be quite general. It is certainly not limited to univalent cations. The mixed ion effect can now be generalized to include *deviations from additivity in isotherms of various properties as a function of composition as one ion is substituted for another ion in a glass or melt.* Macroscopically, whether or not a mixed ion effect is observed depends on the magnitude of the effect, the precision of the experiment, and whether or not there are mutually canceling out effects. On a microscopic level, e.g. ^{1}HNMR spectrometry or FTIR spectroscopy, the effect can always be observed, in principle.

The reasons why the mixed ion effect on the transport properties diminishes with increasing temperature at all compositions are that the configurational entropy increases with increasing temperature, which means, among other things, that the local relaxation times are shorter relative to the site to site jump times. This results in a more idealized fluid in which the transport isotherms are linear functions of the composition. In other words, as thermal energy increases relative to the chemical potential, concentrations of weakly associated species are reduced and since it is these weakly associated complexes that causes the deviations from additivity in the transport property, the magnitude of the mixed ion effect necessarily diminishes. With regard to the thermodynamic property, the apparent ideality of the mixing function, $V_m^E = 0$, is caused by compensating forces, or phenomena that cancel each other, because complexation is certainly occurring, as indicated by the ^{1}HNMR spectra. What must be happening then, is that the reduction in volume caused by increased ion pair formation is accompanied by just enough expansion due to local relaxation for V_m^E to be zero, within experimental error.

Modeling The 4-MepyrCl - 4-MepyrI Binary Mixtures. In order to explain the large deviation from ideality in the chemical shifts of the N-H proton and the ring protons as a function of composition, while simultaneously accounting for the ideality in the mixing function and the small, but distinct, mixed ion effect in the transport properties, we propose the following model. We assume there are four possible species in the mixture and that at any composition but the pure 4-mepyrI, there is an equilibrium between at least two of them. The four species are shown in Fig. 6.

The species present in the neat chloride melt are **A** in equilibrium with **B**. The reasons for postulating the existence of a neutral species in this melt are that the Λ_m of 4-mepyrCl is 6.61 $cm^2\Omega^{-1}mol^{-1}$ at 425K whereas the Λ_m for N-methylpyridinium chloride (N-mepyrCl) is 10.5 $cm^2\Omega^{-1}mol^{-1}$ at the same temperature (11,12). Since both molecules have virtually the same dimensions, but N-mepyrCl cannot hydrogen bond, the lower equivalent conductance must be attributed almost exclusively to hydrogen bonding between the 4-mepyr$^+$ ion and the Cl$^-$ ion to form an associated species. To sharpen this argument, the equivalent conductance of 4-mepyrI is 7.97 cm$^2\Omega^{-1}$mol^{-1} and the equivalent conductance of N-mepyrI is 8.16 cm$^2\Omega^{-1}$mol^{-1}, a difference just barely exceeding the experimental error in the measurement(2). In neither of these two melts does hydrogen bonding occur.

The reason for postulating the existence of the associated monomer in this melt rather than the charged dimeric chloride similar to that proposed by Shuppert and Angell (8) (similar to species C in Fig. 7) is that while this species would also be expected to lower the conductivity relative to that of N-mepyrCl, it would be expected to *raise* the viscosity. However, the viscosity of 4-mepyrCl is considerable less than the viscosity of N-mepyrCl (3.05 cp vs 6.42 cp at 425K) (11). Therefore, the dimeric species cannot be a major contributor to the structure of the neat melt. The fact that the relative viscosity difference, $(\eta_{\mathrm{NmepyrCl}} - \eta_{\mathrm{4mepyrCl}})/\eta_{\mathrm{NmepyrCl}} = 0.52$, and the relative conductance difference $(\Lambda_{\mathrm{NmepyrCl}} - \Lambda_{\mathrm{4mepyrCl}})/\Lambda_{\mathrm{NmepyrCl}} = 0.37$, differ in the same "anti-Walden's rule" sense is also the expected consequence of our model because a neutral species acts as a kind of "lubricant" causing a breakdown, or relaxation, in the symmetry of Coulombic forces. This relaxation caused by molecular contraction along the line of centers during the formation of the neutral ion pair causes a concomitant local expansion which would be expected to reduce the viscosity while at the same time reducing the conductivity since there are fewer charges per unit volume. The reason for postulating the eventual formation of a dimeric species as X_I increases, is that it is necessary to account for the fact that the maximum chemical shift deviation occurs at $X_I = 0.6$ rather than at $X_I = 0.5$ or lower, where it would occur if only the associated monomer, **B**, were forming.

The relative molar conductance is, to a good first approximation, a direct measure of the fraction of the 4-mepyrCl melt that is dissociated at any instant. For example, if the relative molar conductance was unity, the 4-mepyrCl melt would be completely dissociated. Therefore, the percent associated is given by the equation:

$$\%\textbf{4-mepyrCl associated} = (1 - \Lambda_{\textbf{4-mepyr}}/\Lambda_{\textbf{N-mepyrCl}})\mathbf{100} = \mathbf{37\%} \qquad [3]$$

which means that in the pure chloride melt, the mole fraction of associated species, **B**, is 0.37 and the mole fraction of dissociated species, **A**, is 0.63.

As the formal mole fraction of 4-mepyrI (X_I) increases from 0 to 1, there is an initial increase in the concentration of 4-mepyr$^+$ ions because 4-mepyrI does not hydrogen bond. According to Le Chatelier's Principle, an increase in [4-mepyr$^+$] has the effect of driving the equilibrium between **A** and **B** to the right, thereby increasing [**B**] and ultimately decreasing [**A**]. A third species , **D**, is, of course, being added which has the additional consequence that I$^-$ ions are becoming more numerous while inherently more mobile Cl$^-$ ions are having their motion restricted by being associated with 4-mepyr$^+$ ions in neutral complexes. This would be expected to initially cause a small negative deviation from additivity in conductivity because slower I$^-$ ions are not simply being substituted for faster Cl$^-$ ions, neutral species are also being formed. The mole fraction of **D** then, is always equal to the formal mole fraction, X_I. As X_I continues to increase, [**A**] decreases and [**B**] increases until all of **A** is gone. At this mole fraction, a new dimeric species, **C**, begins to form again because of LeChatelier's principle and because the Lewis acid, 4-mepyr$^+$ considers **B** to be a stronger Lewis base than I$^-$.

The mole fractions of each species present in the melt are listed in Table I I. The calculations were made by assuming that in the pure chloride melt, ($X_I = 0$) $X_B = 0.37$ and $X_A = 0.63$, (Eq [4]), and then simply increasing X_I from 0 to 1. For example, at $X_I = X_D = 0.2$, ($X_{Cl} = 0.8$), $X_B = (0.37 \times 0.8) + 0.2 = 0.496$, $X_A = 0.8 - 0.496 = 0.304$. ($X_{total} = X_D + X_B + X_A = 1$) . The largest mole fraction of **B,** 0.613, appears at $X_D = 0.387$. At this mole fraction, all of the dissociated 4-mepyrCl is gone and C is just beginning to form.

The mole fractions in Table I, together with the assumption that each species' contribution to the melt's measured chemical shift of the nitrogenic proton is additive, can be used to calculate these shifts. That is, for the purpose of modeling the system, the simplifying assumption that at any instant each species present in the melt exists independently of the others so that the product of the chemical shift of this species and its mole fraction equals the chemical shift of the mixture :

$$\delta_{mixt} = \Sigma(\delta_i X_i) \qquad [4]$$

These calculated shifts will then be compared to the measured shifts in order to further support the four species model. Using Eq. [4], two equations for two different mole fractions of 4-mepyrCl were solved simultaneously to calculate the chemical shifts of the nitrogenic protons of **A** and **B.** For example, at $X_I = 0$, $0.376(\delta_B) + 0.630(\delta_A) = 17.31$ ppm and at $X_I = 0.3$, $0.559(\delta_B) + 0.141(\delta_A) + 0.3(14.51 \text{ ppm}) = 16.85$ ppm. Solving these two equations simultaneously yields a value of 16.9 ppm for the chemical shift of pure **A,** were it to exist independently and a value of 18.08 for the chemical shift of pure **B** if it were to exist independently. The chemical shift of the pure dimer, **C,** has a value of 17.49 ppm which is obtained by making the simple assumption that the nitrogenic proton of the dimer is half way between the chemical shift of **A**'s nitrogenic proton and **B**'s nitrogenic proton. The chemical shift of the nitrogenic proton in **D** is 14.51 ppm. Using these chemical shifts and Eq. [4], the chemical shifts of the nitrogenic proton were calculated for each formal X_I and plotted against the formal mole fraction, X_I, in Fig. 2B. The rather remarkable coincidence of the two curves, one empirically measured and the other calculated, lends some measure of confidence to our model and lends additional support for the existence of **C.** At $X_I = 0.7$, X_B is calculated to be zero and δ_C multiplied by its mole fraction plus δ_D times its mole fraction gives the measured chemical shift of the binary within experimental error.

Effect of Hydrogen Bonding. Based on our discussion of the mixed ion effect and our model of the binary mixture, we can say with some degree of assurance that H-bonding between the pyridinium ion and the Cl$^-$ actually *reduces* the mixed ion effect on the transport properties and molar volumes in the binary melts, but increases the mixed ion effect on the proton chemical shifts of the melts. That is, a larger deviation from ideality would be expected in the thermodynamic and transport properties in a mixture of N-mepyrCl and N-mepyrI where no H-bonding can occur, but a smaller deviation in the proton chemical shifts. In addition, H-bonding *reduces* the melt's viscosity, an effect exactly opposite to what is generally observed in molecular liquids, such as water or ammonia, where H-bonding increases the viscosity. We suggest that this too may be general: namely that in molten salts H-bonding decreases viscosity where as in molecular liquids H-bonding increases viscosity. A decrease in bulk volume due to contraction of a molecule along its line of centers, >N-H-Cl, which might have been expected to accompany the viscosity decrease, was not observed. We think this is due to the introduction of an element of asymmetry into the Coulombic field by the neutral species which has a long enough life time for the melt to locally expand just enough to offset the contraction.

Chemical Shifts of the Ring and Methyl Protons. The hydrogen bonding between the Cl^- ion and the 4-mepyr$^+$ ion affects the ring and methyl protons as well as the N-H. These protons become more acidic or deshielded with increasing 4-mepyr$^+$ - Cl^- association because this association reduces the polarization of the π electrons (2, 9). The less polarized, or the more "benzene-like", the ring current, the more it deshields. In addition to our results confirming those of Shuppert and Angell with regard to ring protons, they lend additional support to our model. The associated species **B** and the dimeric ion, **C**, have much less polarized, or distorted, ring currents than do dissociated species **A** and **D**. Consequently, the ring and methyl protons in **B** and **C** will be more acidic or down field than in **A** or **D**. In particular, the greater the relative concentration of **B**, the greater the deviation from ideality. In our model, the total mole fraction of **B** is 0.496 at $X_I = 0.2$, 0.559 at $X_I = 0.3$, 0.613 at $X_I = 0.387$, 0.6 at $X_I = 0.4$, 0.436 at $X_I = 0.5$, and 0.292 at $X_I = 0.6$. It then drops sharply to 0 at $X_I = 0.7$ which very much parallels the chemical shift vs. composition behavior of the ring and methyl protons.

Additional evidence that our suggestions with regard to the ring protons are probably correct is that the least acidic or most shielded ring protons are in pure **D** where no association occurs and the ring current is the most distorted.

CONCLUSION

We have used HNMR spectroscopy to discover intermolecular interactions in binary melts that would have gone unnoticed had molar volumes or transport properties been used exclusively. We have correlated these HNMR spectra with equivalent conductance, viscosity and molar volume and constructed a model of these binary melts in which a completely neutral monomeric chloride species (Fig. 6, **B**) and a dimeric chloride ion, (Fig.6, **C**) form in the melt. Both of these species have a long enough lifetime to affect the HNMR spectrum. We have found that the phenomenon referred to as the mixed univalent ion effect is neither restricted to cations nor to univalent ions, but is probably quite general in nature. We further suggest that hydrogen bonding generally *reduces* the mixed ion effect on macroscopic properties and that hydrogen bonding generally *reduces* viscosity in ionic melts.

LIST OF REFERENCES

1. N. Goldstein, J.L. Ragle, *J. Chem. Phys.*, **70**, 5072(1979)

2. D.S. Newman, R.M. Stevens, *J. Electrochem. Soc,* **131**, 1275(1984)

3. D.S. Newman, R.R. Rhinebarger, D. Siconolfi, O.A. Banjoko, *J. Electrochem. Soc.* **128**, 2331(1981)

4. D.S. Newman, L . Fang, R. Davy, P. Endres, A.R. Ebert, S.L. Gatton, " The Proceedings of the Fifth International Symposium on Moltern Salts", M-L. Saboungi, D.S. Newman, K. Johnson, D. Inman, Editors, PV 86-1, p 522-530, The

Electrochemical Society Softbound Proceedings Series, Pennington, NJ (1986)

5. C.T. Moynihan, *J. Electrochem. Soc,* **126,** 2144(1979)
6. Mary Potter, MS Thesis, Bowling Green State University, Bowling Green, OH (1992) . Leuh Fang, MS Thesis, Bowling Green State University, Bowling Green, OH (1981) .
7. D.S. Newman, D.P. Morgan, R.T. Tillack, *J. Chem. Eng. Data,* **21**, 279(1976)
8. C.A. Angell, J.W. Shuppert, *J. Phys. Chem.* **84,** 538(1980)
9. J.W. Shuppert , C.A. Angell, *J.Chem. Phys.* **67**, 3050(1977)
10. K. B. Kim, D.R. Sadoway, *J. Electrochem. Soc,* **139,** 2128(1992)
11. D.S. Newman, R.T. Tillack, D.P. Morgan, W-C. Wan, *J. Electrochem. Soc.* **124,** 856 (1977)
12. R.A. Carpio, L.A. King, R.E. Linstrom, J.C. Nardi, C.L. Hussey, *J. Electrochem. Soc.* **126,** 1644 (1979)

Table I

Chemical Shifts of the N-H proton in melts containing pyridinium salts, all corrected to TMS.

Species	δ_{N-H}
pyridinium chloride	17.2
2-methylpyridinium chloride	17.1
4-methylpyridinium chloride	17.3
4-mepyrCl in 70 mol% 4-mepyrI	15.5
pyrCl in 70 mol% HCl	15.3
pyrCl in 70 mol% $ZnCl_2$	13.3
pyrCl in 70 mol% $AlCl_3$	12.8
$pyrH^+$, theoretical	12.7

Table II

The Mole Fraction of each model species present in binary mixtures of 4- methylpyridinium chloride and 4-methylpyridinium iodide

X_{Cl}	X_A	X_B	X_C	X_D
1.00	0.630	0.370	0.00	0.00
0.900	0.467	0.433	0.00	0.10
0.800	0.304	0.496	0.00	0.20
0.700	0.141	0.559	0.00	0.30
0.613	0.00	0.613	0.00	0.387
0.600	0.00	0.587	0.013	0.400
0.50	0.00	0.436	0.127	0.436
0.400	0.00	0.292	0.217	0.492
0.300	0.00	0.00	0.30	0.70
0.20	0.00	0.00	0.20	0.80
0.100	0.00	0.00	0.10	0.90
0.00	0.00	0.00	0.00	1.00

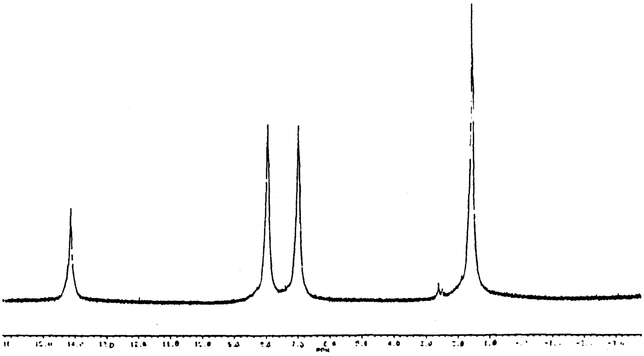

Fig. 1 HNMR spectrum of X_{Cl} = 0.4 vs DMSO

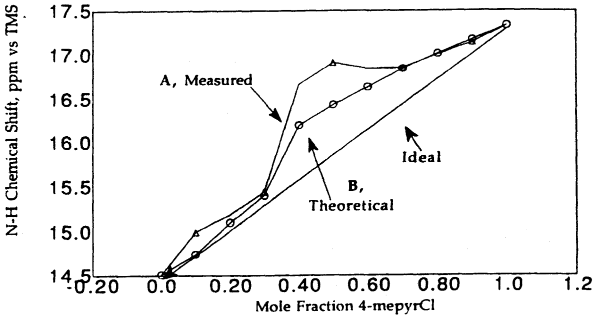

Fig. 2 A. Measured N-H chemical shifs as a function of composition
B. Theoretical N-H chemical shifts as a function of composition

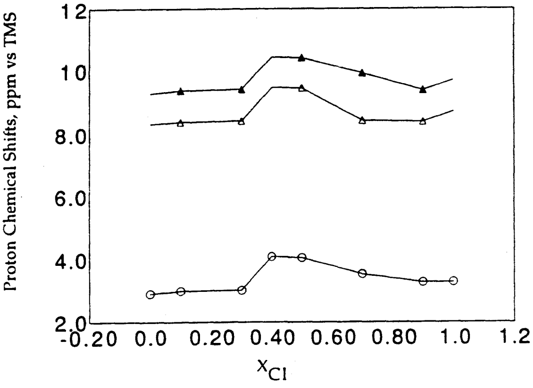

Fig. 3 ▲ ∝ proton chemical shifts
Δ ß proton chemical shifts
o CH_3 proton chemical shifts

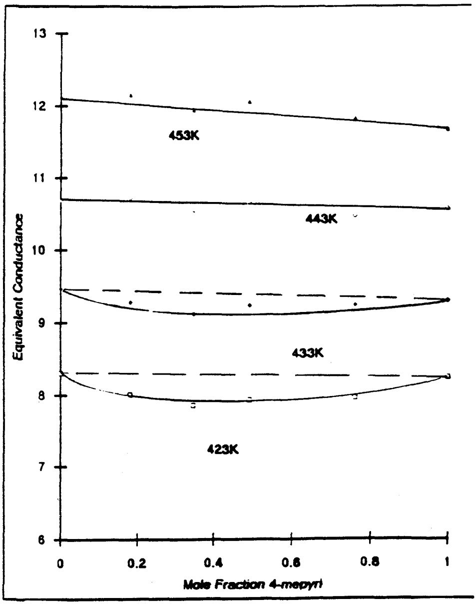

Fig. 4 Molar conductivites of binary mixtures

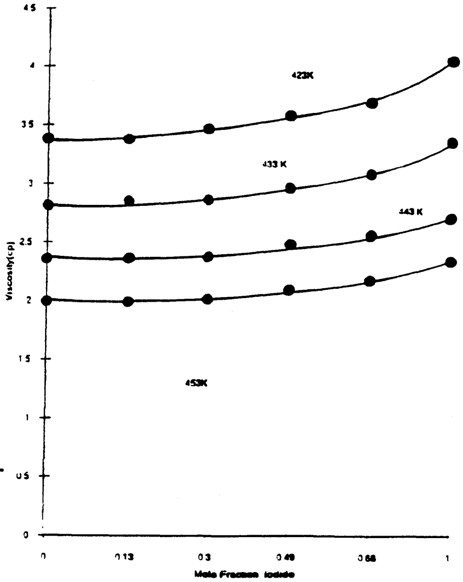

Fig. 5 Viscosities of binary mixtures

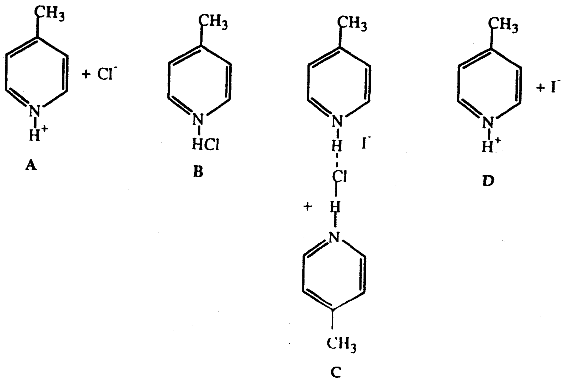

Fig. 6, Four species present in the Binary Mixtures

DOI: 10.1149/199413.0336PV

ROESY NMR OF BASIC AMBIENT-TEMPERATURE CHLOROALUMINATE IONIC LIQUIDS

Robert A. Mantz, Robert A. Osteryoung
Department of Chemistry
North Carolina State University
Raleigh, NC 27695-8204

Paul C. Trulove, Richard T. Carlin
The Frank J. Seiler Research Laboratory
Division of Electrochemical Sciences
2354 Vandenburg Drive Suite 2A35
U. S. Air Force Academy, CO 80840-6272

Hanna Sierzputowska-Gracz
Department of Biochemistry
North Carolina State University
Raleigh, NC 27695-7622

ABSTRACT

Basic $AlCl_3$:ImCl melts prepared with a molar excess of ImCl exhibit a much higher viscosity than their acidic counterparts. This viscosity increase suggests a structure-making interaction in the basic melts is absent in the acidic melts. Two-dimensional NMR ROESY experiments have been used to determine intermolecular distances between the ImCl cations in basic $AlCl_3$:ImCl melts. We have found evidence of intermolecular Nuclear Overhauser Effect (NOE) transfer between ImCl molecules. This further demonstrates the existence of intermolecular interactions in basic $AlCl_3$:ImCl melts.

INTRODUCTION

Chloroaluminate ionic liquids are prepared by mixing, 1-ethyl-3-methylimidazolium chloride (ImCl, Figure 1) and aluminum chloride ($AlCl_3$). The two solids react over a wide range of stoichiometries to yield room-temperature molten salts (1). The melts are defined as acidic, basic, or neutral, if the mole ratio of $AlCl_3$ to ImCl is greater than, less than, or equal to unity. Basic melts exhibit a much higher viscosity than their acidic counterparts. The viscosity at 25 °C of a 1:1 neutral melt is 17.8 cp while that for a 0.4:1 melt is 412 cp (2). This viscosity increase suggests a structure-making interaction is present in the basic melts that is absent in the acidic melts.

The presence of local structure in basic chloroaluminate ionic liquids has been suggested by several researchers (3-5). Infrared measurements in our laboratory have shown strong cation-anion interactions in the basic melts. In addition data from the C-H stretching region of the infrared spectrum indicated possible hydrogen bonding between Cl^- and H-2 of the imidazole ring (3). Dymek and co-workers combined crystallographic and infrared data, with theoretical calculations to investigate the local structure present in the basic $AlCl_3$:ImCl melts. They found that the crystal structure of ImCl consists of stacks of imidazolium cations with chloride ions interspersed between the stacks such that they are hydrogen bonded to a ring hydrogen on three different imidazolium cations. They also found that the C-H stretching region in the infrared spectrum of ImCl remained essentially unchanged in going from a solid to a chloroaluminate ionic liquid. They concluded that the same bonding and structure present in ImCl(s) are present in basic $AlCl_3$:ImCl melts (5). Furthermore, they were able to accurately predict the C-H stretches in the infrared spectrum by employing a model based on the ImCl crystal structure (6).

In this manuscript we expand on the research described above using two-dimensional NMR ROESY experiments to investigate the structural interactions of the imidazolium cation in basic room-temperature chloroaluminate molten salts.

EXPERIMENTAL

Chloroaluminate melts were prepared by weighing and slowly mixing the components in helium or nitrogen containing VAC Atmospheres dry boxes maintained with less than 5 ppm water and oxygen. Bruker AC 300, Bruker AMX 300, and GE Omega 500 NMR spectrometers were utilized to obtain spectra.

ROESY Two-Dimensional NMR Experiments

ROESY experiments were conducted on basic chloroaluminate melts. Samples were prepared for spectroscopy using two types of NMR tubes. Melts containing ImCl were placed in the inner tube of a Wilmad 520-3 coaxial tube. The tube was then flame sealed. The melt containing ImCl-d_{11} was filtered using a 0.45 Å Gelmen PTFE syringe filter. This sample was then placed in the inner tube of a Wilmad 516-CC-5 coaxial tube which was flame sealed. To obtain NMR spectra, deuterated solvent was placed between the two tubes to maintain lock and to facilitate shimming.

ROESY experiments were run at 20 °C with a static sample. 256 increments of 32 acquisitions comprised each experiment with a delay time of 5 to 7 seconds for relaxation. The ROESY pulse sequence utilized a 16 step phase cycle. The 90° pulse width was 26 µsec and a 134 µsec 90° pulse was used for the spinlock. The 134 µsec pulse corresponds to a 2 kHz spin lock field. Spinlock times were varied between 100 and 350 msec to maximize the NOE transfer.

T1 Determination

Proton T1 relaxation times were determined for the 0.5:1 ImCl:$AlCl_3$ melt on a Bruker AC 300 MHz spectrometer. The inversion recovery pulse sequence was used with an 8.5

µsec 90° pulse width. Thirty increments varying between 50 msec and 2 sec were used as the variable delay separating the 90° and the 180° pulses. The range of T1 values were determined to vary between 766 msec for H-6 and 1.66 sec for H-4.

Materials

The synthesis and purification of 1-ethyl-3-methylimidazolium chloride (ImCl), 1-ethyl-3-methylimidazolium-*2,4,5*-d_3 chloride (ImCl-d_3), and Aluminum Chloride were performed as described elsewhere (4,7-9). The synthesis and purification of 1-ethyl-d_5-3-methyl-d_3-imidazolium chloride (ImCl-d_8h_3) were identical to that of ImCl with the exception that 1-methyl-d_3-imidazole and chloroethane-d_5 (Cambridge Isotope Laboratories, 98% atom D) were substituted for 1-methylimidazole and chloroethane, respectively. 1-ethyl-d_5-3-methyl-d_3-imidazolium-*2,4,5*-d_3 chloride (ImCl-d_{11}) was prepared from ImCl-d_8h_3 by a base catalyzed H-D exchange in D_2O; the procedure used was identical to that employed in the preparation of ImCl-d_3 from ImCl. The synthesis of 1-methyl-d_3-imidazole was performed in the following manner. Under an inert atmosphere, 30.77 g (0.274 mol) potassium tert-butoxide (Aldrich) and 34.6 g (0.237 mol) of iodomethane-d_3 (99% D, Aldrich) were added to 18.65 g (0.274 mol) of imidazole (99%, Aldrich) in a 100 mL round bottom flask. (As soon as these reagents were mixed a white precipitate began forming.) Tetrahydrofuran was added to this mixture to give a total volume of 50 mL. The flask was then stoppered and allowed to stir at room-temperature for 2 weeks. At the end of two weeks the flask contained a white solid and a clear colorless liquid. The liquid was passed through a filter to remove the white solid (KI). The liquid was then placed on a rotary evaporator to remove the majority of the tetrahydrofuran and tert-butyl alcohol; this reduced the original volume by half and gave a light yellow viscous liquid. The crude 1-methyl-d_3-imidazole was then fractionally distilled under vacuum. Finally, the wet 1-methyl-d_3-imidazole was dried by vacuum distillation off of CaH_2. The isolated yield of 1-methyl-d_3-imidazole was ca. 65%.

RESULTS AND DISCUSSION

Internuclear distances can be determined using the Nuclear Overhauser Effect (NOE). Simply described, NOE is the dipole-dipole interaction through space between two nuclei. This manifests itself when a single resonance in a spectrum is irradiated and the intensities of other resonances are changed. The dependence of the NOE on the internuclear distance (r_{AB}) is given by:

$$1/\eta_A(B) = K(r_{AB})^6 \qquad [1]$$

$\eta_A(B)$ is the NOE enhancement at nucleus A due to the saturation of spin B. K is a constant which includes the effects of molecular tumbling and alternative relaxation pathways; normally, the value of K is difficult to determine. The ratio between the NOE's is proportional to the ratios of the distances. Therefore, if an internuclear distance is known, the NOE enhancements can be compared to determine the unknown internuclear distance.

$$(r_{CD})^6\left(\frac{\eta_{C(D)}}{\eta_{A(B)}}\right) = (r_{AB})^6 \qquad [2]$$

This equation assumes K is the same for both NOE enhancements. This assumption is valid when similar molecules are being compared under identical conditions and the extreme narrowing limit condition is met (10). However, in basic melts the extreme narrowing limit condition is not met due to the high viscosity. To overcome this, Rotating Frame Nuclear Overhauser Enhancement Spectroscopy (ROESY) can be used (11,12). The ROESY experiment is conducted in such a way that the nuclei are always in the extreme narrowing condition. ROESY measures the transient NOE instead of equilibrium NOE. The build up of Intensity (I) of NOE cross-peaks (dI/dt) is proportional to the internuclear distance and can be substituted into equation 2 for NOE enhancement (η) to yield:

$$(r_{CD})^6\left(\frac{dI/dt_{CD}}{dI/dt_{AB}}\right) = (r_{AB})^6 \qquad [3]$$

The rate of NOE build up is determined by varying the mixing time and determining the resulting change in volume of the two-dimensional cross-peak. The volume of the cross-peaks is inversely proportional to the internuclear distance to the sixth power.

As shown in Figure 2, proton NMR of basic chloroaluminate molten salts yields well resolved one-dimensional spectra corresponding to the protons of the 1-ethyl-3-methylimidazolium chloride. In Figure 3, cross-peaks due to NOE transfer are present. NOE cross-peaks are not normally observed for internuclear distances beyond 4 Å because of the r^{-6} dependence (13). The ROESY spectrum (Figure 3) shows cross-peaks which are clearly due to intramolecular interactions (i.e. between H-6 and H-7). In addition, there are cross-peaks in Figure 3, which are due to intermolecular interactions. For example, H-2, which is separated across the imidazole ring from H-4 and H-5 by 4.3 Å, still shows cross-peaks to both H-4 and H-5, thus indicating some type of intermolecular interaction. In addition, although H-4 and H-7 are separated by 5.2 Å, and H-5 and H-8 are separated by a similar distance, they both still show significant NOE interactions. This further demonstrates the existence of intermolecular interactions in basic $AlCl_3$:ImCl melts.

CONCLUSIONS

Evidence of intermolecular NOE transfer for basic ambient-temperature chloroaluminate melts has been presented. The intermolecular NOE transfer demonstrates the existence of intermolecular interactions in the basic melts. Further research is underway to quantify the average intermolecular distances between 1-ethyl-3-methylimidazolium chloride rings in melts of varying composition.

ACKNOWLEDGMENTS

This work was supported in part by the Air Force Office of Scientific Research.

REFERENCES

1. C. L. Hussey, *Pure Appl. Chem.*, 60, 1963 (1988).
2. A. A. Fannin, D. A. Floreani, D. A. King, J. S. Landers, B. J. Piersma, D. J. Stech, R. L. Vaughn, J. S. Wilkes, J. L. Williams, *J. Phys. Chem.*, 88, 2614 (1984).
3. S. Tait, R. A. Osteryoung, *Inorg. Chem.*, 23, 4352 (1984).
4. K. M. Dieter, C. J. Dymek, N. E. Heimer, J. W. Rovang, J. S. Wilkes, *J. Am. Chem. Soc.*, 110, 2722 (1988).
5. C. J. Dymek, D. A. Grossie, A. V. Fratini, W. W. Adams, *J. Mol. Struc.*, 213, 25 (1989).
6. C. J. Dymek, J. J. Stewart, *Inorg. Chem.*, 28, 1472 (1989).
7. P. C. Trulove, R. A. Osteryoung, *Inorg. Chem.*, 91, 3980 (1992).
8. P. C. Trulove, D. K. Sukumaran, R. A. Osteryoung, *J. Phys. Chem.*, 98, 141 (1994).
9. R. J. Gale, R. A. Osteryoung in *Molten Salt Techniques*, Eds. D. G. Lovering and R. J. Gale, Plenum, New York (1983) p. 55.
10. A. E. Derome in *Modern NMR Techniques for Chemistry Research*, Pergamon (1987) Chapters 5 and 6.
11. A. Bax, D. J. Davis, *J. Mag. Res.*, 63, 207 (1985).
12. H. Kessler, M. Gehrke, Griesinger, *Angew. Chem. Int. Ed. Engl.*, 27, 490 (1988).
13. R. A. Bell, J. K. Saunders, *Can J. Chem.*, 48, 1114 (1970).

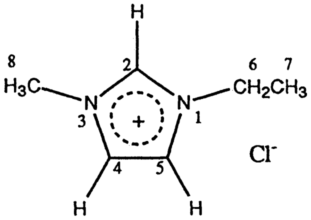

Figure 1. Structure and numbering of 1-ethyl-3-methylimidazolium chloride (ImCl).

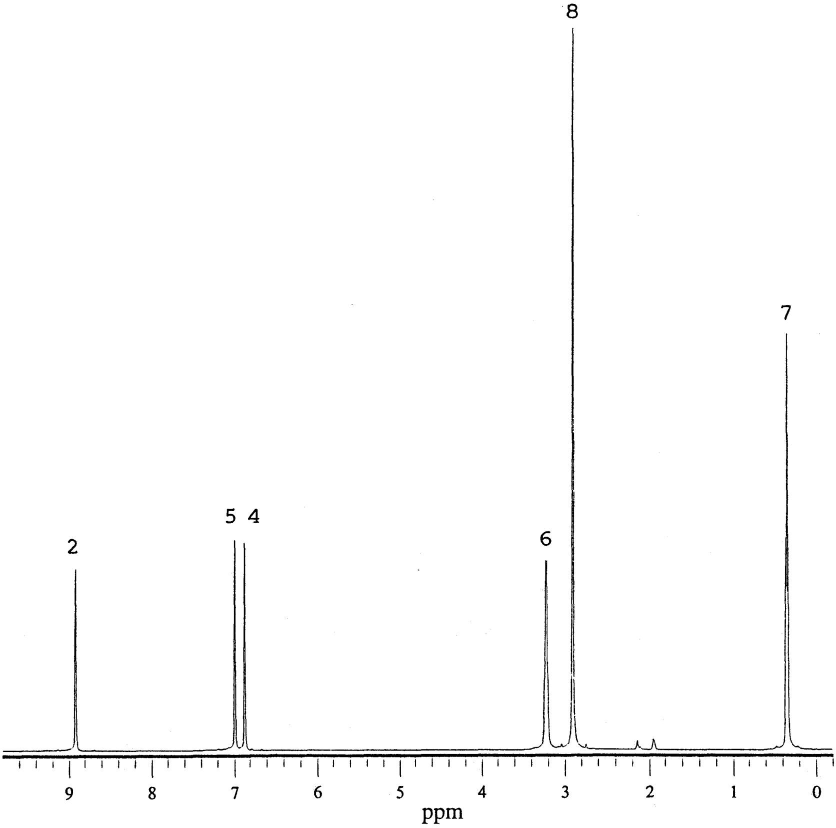

Figure 2. NMR Spectrum of 0.5:1 Melt

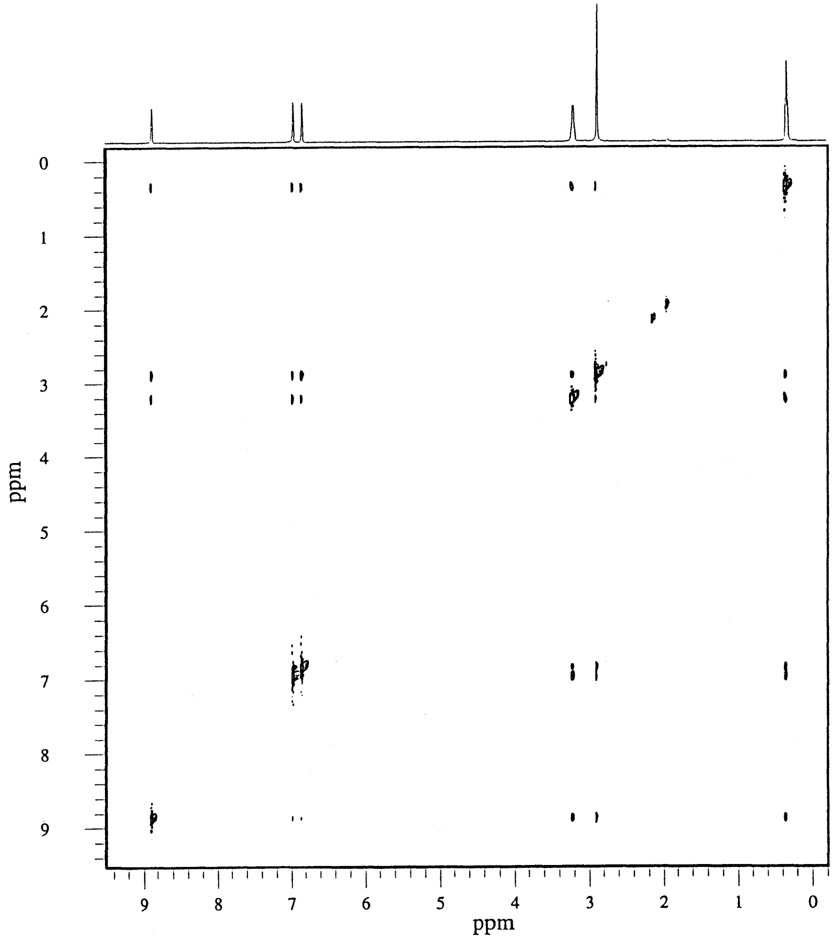

Figure 3. Two-Dimensional ROESY NMR Spectrum

DOI: 10.1149/199413.0343PV

AC IMPEDANCE SPECTROSCOPY AT AN ULTRAMICROELECTRODE IN MOLTEN SALTS

Przemyslaw Los* and Peter G. Bruce, Centre for Electrochemical and
Materials Sciences (CEMS), University of St. Andrews, Department of
Chemistry, St. Andrews, KY16 9ST, Scotland

ABSTRACT

By combining ac impedance spectroscopy with ultramicroelectrodes a powerful electrochemical tool becomes available with which to probe the nature of electrode processes in molten salts. We have shown that ac impedances up to 100 MOhm can be measured at microelectrodes within the range 0.1 Hz to 5 kHz and accurate parameters for all the electrochemical processes, be they Faradaic or non-Faradaic, measured. Simulation have been have been carried out for two working electrodes one a disc of radius 1mm and the other a microdisc of radius 1 µm using typical parameters of redox couples in molten eutectic LiCl-KCl. Experimental measurements of cathodic reduction of Cd^{2+} in molten eutectic LiCl-KCl at ultramicroelectrodes is underway.

INTRODUCTION

Electrochemical investigations in molten salts call for new experimental methods. It is well established that the electrode reactions in molten salts can be very fast and their rate constants k_s may then be difficult to measure using conventional methods developed for aqueous and non-aqueous solutions. Ultramicroelectrodes the dimensions of which are typically a few microns, have properties which are useful for electrochemical studies in molten salts. The rate of mass transfer to and from the electrode is increased due to the spherical nature of the diffusion compared with semi-infinite linear diffusion to electrodes of normal dimensions. Also the iR drop and double-layer charging currents are reduced (1-4).

By combining ac impedance spectroscopy with microelectrodes a powerful electrochemical tool becomes available with which to probe the nature of electrode processes in molten salts, particularly the mechanism and kinetics of fast heterogeneous electrode reactions (5). The analysis of the diffusion process to

---

* On leave from Department of Pharmacy, School of Medicine, 50-139 Wroclaw, Poland

a microdisk has been given by Fleischmann and Pons (2, 6).

The appropriate equivalent circuit is presented in Fig. 1, where R_u is the uncompensated solution resistance, C_{dl} the double-layer capacitance, R_{ct} the charge transfer resistance and M the diffusional impedance. The real and imaginary components of the microdisk diffusional impedance can be represented by the following equations (2, 6):

$$Z' = (4RT/\pi n^2F^2D^{1/2}\omega^{1/2}a^2c)\ \Phi_4\ (a^2\omega/D) \qquad [1]$$

$$Z'' = (4RT/\pi n^2F^2D^{1/2}\omega^{1/2}a^2c)\ \Phi_5\ (a^2\omega/D) \qquad [2]$$

where Φ_4 and Φ_5 are functions of the non-dimensional frequency $a^2\omega/D$, the symbols R, T, F and n have their usual meanings and D is the diffusion coefficient, a is the radius of the microdisk and ω is the angular frequency. Whereas the diffusional impedance at normal electrodes is a function of the angular frequency ω ($=2\pi f$), in the case of microelectrodes it is a function of the dimensionless parameter ($a^2\omega/D$) and as a consequence the radius of the microelectrode becomes a kinetic parameter of the electrochemical system under investigation. This is true for any electrochemical measurement, as a consequence the highest measurable value of k_s can be estimated from the equation (7):

$$(k_sa/D) \cong 10 \qquad [3]$$

Analysis of equations [2] and [3] reveals that at high frequencies M resembles a Warburg impedance and at low frequencies a steady-state mass transport limit is obtained due to the spherical diffusion field. Thus it is possible to represent the diffusional impedance to the microdisk, M, in Fig. 1 as a parallel combination of a Warburg impedance Z_w and non-linear resistance R_{nl} (5, 8-11). The same equivalent circuit is used for the impedance of the hemispherical electrode. This is only an approximation at intermediate frequencies in the case of a microdisk, however it is sufficiently accurate (exact at low and high frequencies) to be useful in analysis of experimental results. The parallel combination is a rigorous solution for a hemispherical microelectrodes.

RESULTS AND DISCUSSION

In our laboratory ac impedance measurements have been carried out on several different redox couples in aqueous, non-aqueous and polymer electrolytes (5, 10, 11). In the present work the reduction of Cd^{2+} to Cd^0 in a LiCl-KCl eutectic melt is considered at a platinum microdisk. Ac impedance measurements have been used in the past to investigate the reduction of metal ions in molten LiCl-KCl at small platinum electrodes (12-14) and, as expected, relatively high values of the standard rate constants (0.686 cm/s for the reaction $Cd^{2+} + 2e = Cd$) were found at 720 K. It is worth noting that using relaxation and ac impedance methods Kisza and Kazmierczak (15) obtained k_s values in the same order of magnitude for Sn, Pb, Zn and Bi metals immersed in their pure molten chlorides at 800 K. Ac impedance plots for a microelectrode of radius 1 µm based on the equivalent circuit shown in Fig. 1 were simulated using values for the diffusion coefficent and double-layer capacitance similar to these measured experimentally by Laitinen et al. (12-14), Fig. 2. In Fig. 3 we present simulated complex impedance plots at a disk electrode of normal dimension (radius 1mm) using the identical electrochemical parameters to those in Fig. 2. Comparing Figs. 2 and 3 it is evident that for rate constants in excess of 0.5 cm/s only the diffusional impedance is observed at a normal electrode making extraction of k_s impossible. In contrast the electrode kinetics make a significant contribution to the impedance at an ultramicroelectrode, Fig. 2.

Our measurement system consisted of a Solartron Frequency Response Analyser 1255 and current preamplifier EG&G model 181 (bandwidth 10 kHz at a sensivity of 10^{-7} A V^{-1}) (5, 8-10). We have shown that ac impedance of up to 100 MΩ can be reliably measured within the range 0.1 Hz to 5 kHz, and accurate parameters for all the electrochemical processes, be they Faradaic or non-Faradaic, can be measured. By employing microelectrodes only a two electrode system is required, with e.g. a platinum grid counter electrode serving as reference or quasi-reference. In this way one can avoid many difficulties related to mesurements in molten salt systems (16-18).

REFERENCES

1. M. I. Montenegro, M.A. Queiros and J. L. Daschbach (Ed.), Microelectrodes: Theory and Applications, NATO ASI Series E: Applied Sciences, Vol.197, Kluwer Academic Publishers, Dordrecht, 1991.

2. M. Fleischmann, S. Pons, D.R. Rolison and P. P. Schmidt (Ed.), Ultramicroelectrodes, Datatech Systems, Inc., Morganton, NC, 1987.

3. B. R. Scharifker, Microelectrode techniques in Electrochemistry, Modern Aspects of Electrochemistry, No. 22, J. O'M. Bockris et al, Ed., Plenum Press, New York, 1992.

4. R. M. Wightman and D. O. Wipf, Voltammetry at Ultramicroelectrodes, A. J. Bard, Ed., Electroanalytical Chemistry, Vol. 15, Marcel Dekker, New York, 1988.

5. P. G. Bruce, A. Lisowska-Oleksiak, P. Los and C. A. Vincent, J. Electroanal. Chem., in press.

6. M. Fleischmann and S. Pons, J. Electroanal. Chem., 250, 277 (1988).

7. A. J. Bard et al., J. Phys. Chem., 97, 7147 (1993).

8. A. Baranski, J. Electroanal. Chem., 300, 309 (1991).

9. K. Winkler and A. Baranski, J. Electroanal. Chem., 346, 197 (1993).

10. P. G. Bruce, P. Los, D. Stewart and C. A. Vincent, in preparation.

11. P. G. Bruce, P. Los, D. Stewart and C. A. Vincent, in preparation.

12. H. A. Laitinen and R. A. Osteryoung, J. Electrochem. Soc., 102, 598 (1955).

13. H. A. Laitinen and H. C. Gaur, J. Electrochem. Soc., 104, 730 (1957).

14. H. A. Laitinen and W. S. Ferguson, Anal. Chem., 29, 4 (1957).

15. A. Kisza and J. Kazmierczak, Collect. Czech. Chem. Commun., 57, 1015 (1992).

16. P. Los, J. Josiak and K. Kowalczewska, Bull. Electrochem., 8, 288 (1992).

17. P. Los, J. Josiak and K. Kazmierczak, Pol. J. Chem., 65, 763 (1991).

18. P. Los and J. Josiak, Bull. Electrochem., 11, 829 (1989).

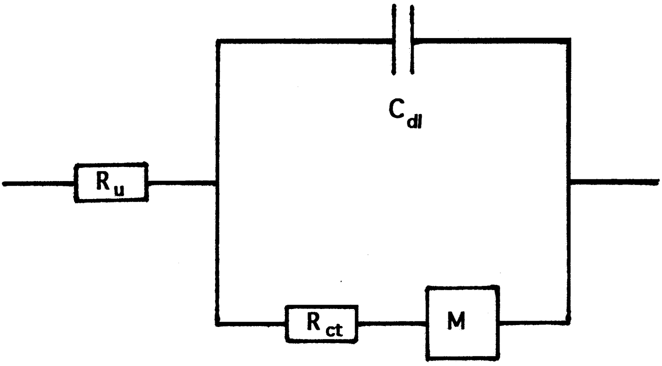

Figure 1. Equivalent circuit for the disk microelectrode.

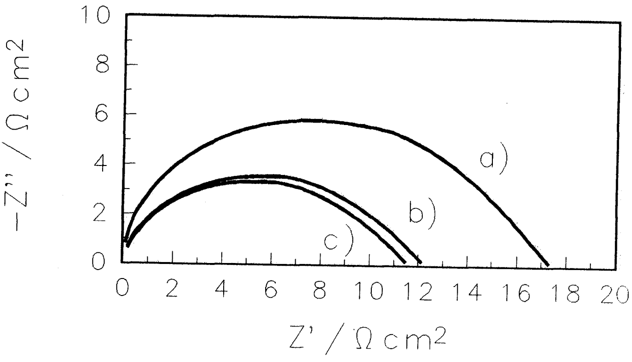

Figure 2. Simulated Nyquist graphs calculated using Fleischmann and Pons (2, 6) equivalent circuit from Fig. 1. The following simulation parameters were chosen: T = 723 K, bulk concentration of the redox couple c = 0.001 mol/dm^3, double-layer capacitance C_{dl} = 20 μF/cm^2, disk electrode radius a = 1 μm, diffusion coefficient D = 10^{-5} cm^2/s, frequency range 0.1 Hz to 10 kHz and standard rate constants k_s equal a) 0.1 cm/s, b) 0.5 cm/s and c) 1 cm/s, respectively.

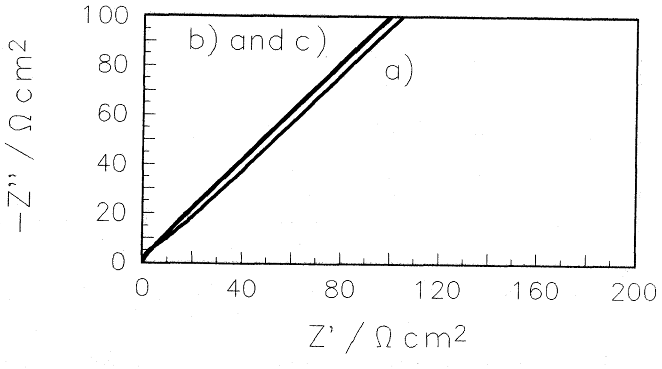

Figure 3. Simulated Nyquist graphs for the disk radius a = 1 mm and other parameters the same as in Fig. 2.

DOI: 10.1149/199413.0350PV

IMPEDANCE OF ELECTRODE-OXIDE MELTS CONTAINING IRON OXIDE

Toshio Yokokawa and Takuya Nakanishi
Department of Chemistry, Faculty of Science,
Hokkaido University, Sapporo 060, Japan

ABSTRACT

In view of the abnormal redox voltammogram of iron oxide melts, the impedance method was applied. As far as the measured quantities are concerned, many extraordinary phenomena were observed. If the iron concent is lower than 2 mole % Fe_3O_4; it was proved that the reaction of $1/2O_2 + 2e = O^{2-}$ is not electrochemically reversible even above 1100K.

INTRODUCTION

Redox equilibria in molten oxide mixtures like silicates and borates are very important in metal refining as well as in high temperature corrosion. For iron oxides in silicate melts, this is especially true for the additional reason that iron oxide is one of the most important components of magma. Thus, iron (III) oxide is an acid and a network former just like Al_2O_3, while iron (II) oxide is a base that altars the silicate network. Depending on the oxygen potential and the basicity of the melt, the liquidus temperature and chemical behavior of magma show dramatic changes.

In a series of redox studies1-5), when we came to the iron containing system, we found that neither the ordinary LSV nor pulse voltammetry worked well 6). Therefore we employed an impedance method to investigate more carefully why that system is so unusual. It has been suggested that electronic conduction by way of the Fe^{2+} -Fe^{3+} pair contributes in various ways. The impedance method has been applied to metallurgical slags to some extent. However, the influence of redox reactions on the impedance at particular potentials had not been investigated and the origin of the current near zero potential had not been carefully considered. In this paper we will report the results of our methodology as it applies to iron oxide containing borates.

EXPERIMENTAL

Use was made of a two electrode arrangement. The working electrode was made of platinum wire, one mm in diameter, immersed in the melt and the counter electrode was a platinum crucible, as shown in Fig. 1. Because of the wide surface area of the latter, it can actually be considered as the reference electrode. Potentials of various values were superimposed by an ac signal of 10 to 25mv and 0.01 to 3400 Hz and the impedance was analyzed in the usual way as a function of the gaseous atmosphere, immersed depth and iron oxide content. The peripheral line of metal-gas-melt coexistence contributes to admittance differently than the immersed melt-electrode interface. Therefore, the dependence of the admittance on the immersion depth will disclose the contribution of the peripheral line extrapolated to zero depth or "just in contact". Throughout this experiment, the solvent was $Na_2O{\bullet}2B_2O_3$. The gaseous atmosphere was either air, oxygen or Ar at 1 atm. When Fe_3O_4 was used as the source of iron oxide, the melts were prepared from an equi-molar mixture of FeO and Fe_2O_3 and melted in an Ar atmosphere.

RESULTS

Fig. 2 shows a Cole-Cole plot of the solvent and three melts with increasing Fe_2O_2 content at the immersed depth of 5 mm. When the melt is free of iron oxide, the curve is an ordinary one for a chemical reaction and the Warburg impedance is in parallel with the double layer capacitance. It indicates that the electrode reaction

$$1/2\ O_2 + 2e = O^{2-} \qquad (1)$$

behaves like a redox reaction with an appreciable activation energy. In contrast with ordinary reactions at high temperature, O-O bond scission seems irreversible. At the same time O^{2-} ion is not fully available at the surface as a solvent component, but is supplied by diffusion, probably by way of $-BO^-$ or BO^-_4,

$$2\ -BO^- = B\text{-}O\text{-}B + O^{2-} \qquad (2)$$

As soon as iron oxide is added, the Cole-Cole plot changes in to a nearly straight line indicating diffusion control of impedance, and decreases with the solute content. Fig. 3 shows a Bode plot of the same systems. Log Z decreases with decreasing iron content except for the high frequency range, which means the bulk impedance does not change and Na^+ seems to carry, essentially, the whole current.

The effect of a dc potential on log Z is shown in Fig. 4. The impedance depends very much on the potential, especially at lower frequencies. The phase differences between the voltage and current wave of the same systems are shown in Fig. 5. While the phase difference shows a maximum at zero potential, it became 45° and constant at 600mv. This means a non-zero reaction resistance controls the current at zero potential, although the Warburg impedance predominates at the lower potential.

Finally, Figs. 6 and 7 show the effect of the immersion depth on the impedance and admittance respectively. The impedance in an O_2 atmosphere is quite similar to that shown in Fig. 2, while in the Ar atmosphere it became a straight line with a slope of 45°. Since the admittance is additive, we can get the contribution from the meniscus part as the residue at zero depth, as shown in Fig. 7.

DISCUSSION

Effect of iron oxide

It has been concluded that, in the absence of any solute undergoing a redox reaction, the electrode process near zero potential at an inert electrode is reaction (1). The curve of the iron free system in Fig. 2 is not strictly hemicircular, but clearly indicates an irreversible reaction coming into play in this range. When iron oxide was added, the Cole-Cole plot gave a nearly straight line even at high frequency, although the redox reaction should not be important and iron is in the Fe(III) state. This is also reflected in the Bode plot. Thus, the log Z vs log f plot does not show any change. When Warburg impedance is important, it should be a straight line with a slope of 1/2.

Effect of the dc potential

It is known that an ac shows a maximum at $E_{1/2}$ because the redox content ratio [ox]/[red] approaches 1 at the potential. In Fig. 4, at the left end of the low frequency limit, such a minimum is observed at around -600mv, which seems just to be the $E_{1/2}$ of the Fe(III)/Fe(II) pair. The plot of log Z versus log f also approaches a straight line of slope =1/2.

Fig. 5 is more evidence for what we think is the main reaction at each dc potential. At zero voltage, the phase difference shows a maximum, indicating the process is limited by a chemical reaction, while a flat line of 45 degree at -600mv is just what we would expect for Warburg impedance.

Effect of the immersed depth of the working electrode

Figs. 6 and 7 show that even in an O_2 atmosphere, the impedance decreases with increasing depth. In an Ar atmosphere, only the Warburg impedance governs the process and it too decreases with depth. When the admittance is separated into the real and imaginary parts, the relative contribution of the imaginary part dominates the frequency. This is natural because reaction (1) does not keep up at high frequency.

REFERENCES

1) T. Yokokawa, *Canad. Mettall. Quarterly*, **20**, 21 (1981).
2) A. Sasahiro and T. Yokokawa, *Electrochimica Acta*, **29**, 533 (1984).
3) A. Sasahiro and T. Yokokawa, *Electrochimica Acta*, **30**, 441 (1985).
4) A. Sasahiro, K. Kawamura, M. Shimizu, N. Takada, M. Hongo, and T. Yokokawa, *J. Electrochem. Soc.*, **136**, 1861 (1989).
5) K. Suzumura, K. Kawamura, and T. Yokokawa, *J. Chem. Soc. Faraday Trans*, **87**, 307 (1991).
6) T. Yokokawa, K. Kawamura, T. Miyaki, and A. Furuta, Proc. Int'l Symo. Molten Salt Chem. Tech., Hawaii, P284 (1983).

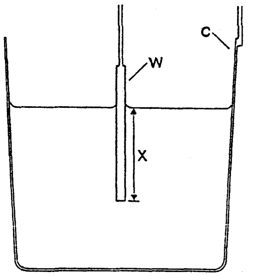

Fig.1 Cell construction.

w : working electrode (Pt wire)
c : counter electrode (Pt crucible)
x : immersed length

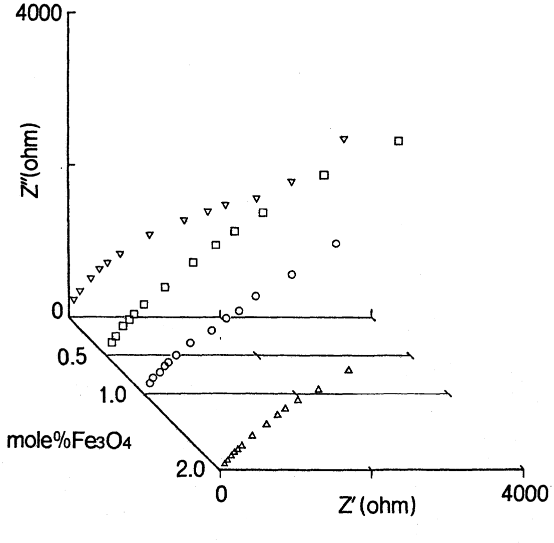

Fig.2 Cole-Cole plot of the systems $Na_2O \cdot 2B_2O_3$ + x mole%Fe_3O_4(x : 0.0 to 2.0) at 5mm depth in O_2 atmosphere at 1123K.

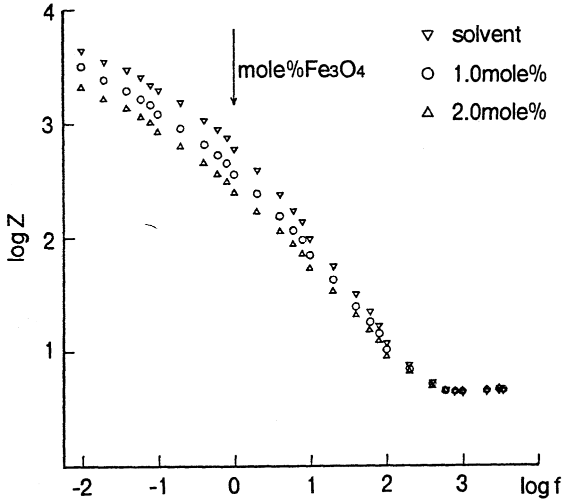

Fig.3 Bode plot of the same systems as shown in Fig.2.

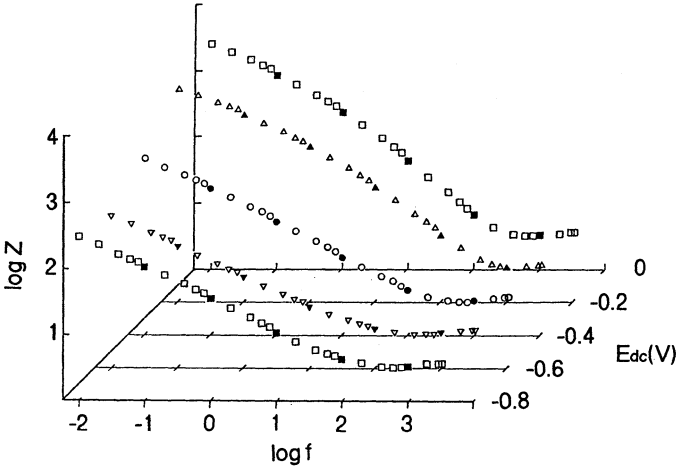

Fig.4 Dependence of log Z on the direct potential at 10mm depth in O_2 atmosphere at 1123K. System: $Na_2O \cdot 2B_2O_3$ + 0.5mole%Fe_3O_4.

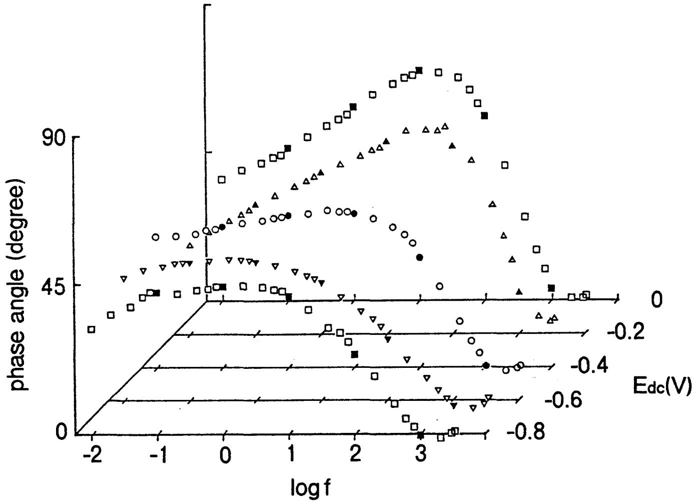

Fig.5 Phase difference between the voltage and current waves as a function of the direct potential, 10mm depth in O_2 atmosphere at 1123K. System: $Na_2O \cdot 2B_2O_3 + 0.5$mole%$Fe_3O_4$.

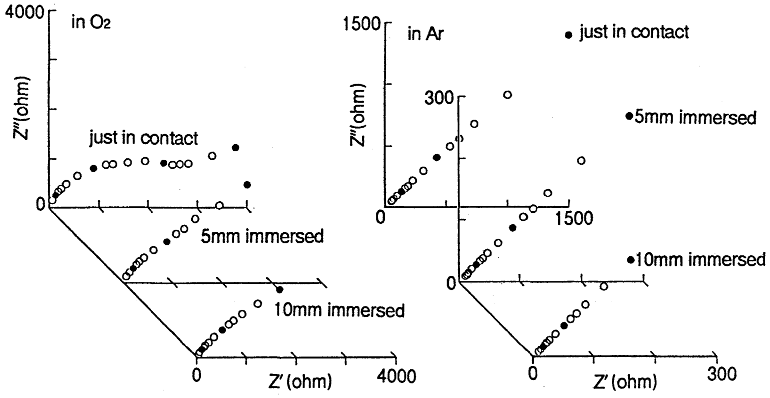

Fig.6 The effect of the depth of the working electrode at O_2 atmosphere(left) and Ar atmosphere(right) at 1123K. System: $Na_2O \cdot 2B_2O_3 + 1.0$mole%$Fe_3O_4$.

(a) O_2 atmosphere

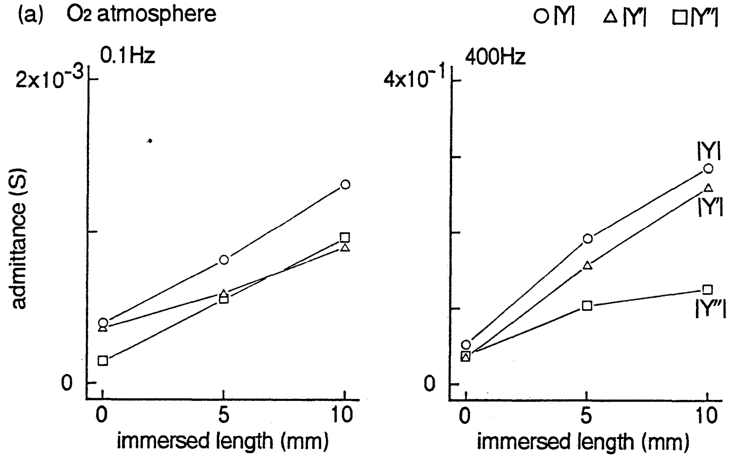

(b) Ar atmosphere

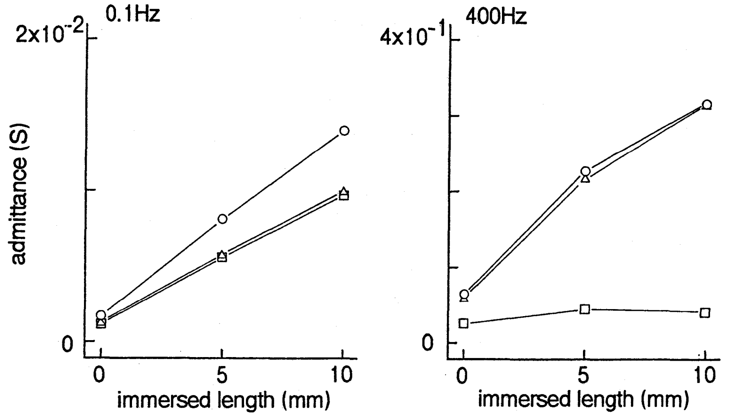

Fig.7 Admittance as a function of depth of the immersed electrode, depicting the contribution of the metal-gas-liquid coexisting periphery as the residual at zero at 1.0mole%Fe_3O_4. (a) O_2 atmosphere (b) Ar atmosphere

DOI: 10.1149/199413.0357PV

EFFECT OF ILLUMINATION ON THE ELECTROCHEMICAL REDUCTION OF SO2 FROM MOLTEN AMIDE - METALLIC AND SEMICONDUCTOR ELECTRODES

R.Narayan* and Varughese Mathew
Chemistry Department, IIT Madras 600 036

ABSTRACT

The reduction of SO_2 is a one electron process at themercury,glassy carbon and dichalgogenide semiconductor electrodes but a two electron process at the platinum electrode. Illumination of the electrode solution interface is found to enhance the cathodic peak currents at all electrodes except with platinum. The peak potentials are not much affected. The enhancement depends on the intensity of illumination. No enhancement is observed with a rotating glassy carbon electrode. The observations are explained based on photochemical effect on the one electron product of reduction, $SO_2^{\bullet -}$, leading to a regeneration of SO_2. SO_2^{--} does not undergo such effects. The observation is made in molten acetamide at 85°C and in a ternary mixture of acetamide, urea and a nitrate at 25°C.

INTRODUCTION

Molten acetamide and ternary mixtures of nitrate, urea and acetamide have been shown to be very useful solvents for electrochemical studies [1]. The ternary mixture is a room temperature molten solvent and stable over a wide range of temperatures [1]. The reduction of SO_2 dissolved in the melt was taken up for a detailed investigation as a part of our ongoing programme. SO_2 is soluble to the extent of 1.2 M at room temperatures. The electrochemical reduction is a one electron process followed by rapid dimerisation of the $SO_2^{\bullet -}$ to $S_2O_4^{--}$ [2] at most electrodes. The reduction is a two electron process at the platinum electrode [3]. The currents obtained with the n-type semiconducting dichalcogenide [4] were found to double on illumination with a halogen lamp. Earlier studies with oxygen and quinones [5] had not shown such an increase of photocurrent. The reduction of the species occurs by the transfer of the electrons, which are the majority carriers of the n-type semiconductors. A large increase in the number of electrons is not expected by illumination. The photoeffect is probably due to a solution species and hence experiments were conducted with illuminated metallic electrodes. The results are described and discussed below.

EXPERIMENTAL

Details may be found in our earlier papers [3-6]. SO_2 was generated from bisulfite and passed into the experimental cell. A 12V/100 W halogen lamp was used to illuminate the electrode. An optical window was fused on to the double walled cell for this purpose. Cyclic voltammetry with the g.c.e. and rotating electrode experiments were carried out. All potentials are quoted with respect to the $Ag/AgCl.Cl^-$ satd. in the melt, electrode.

RESULTS AND DISCUSSION

The variations for the reduction of SO_2 at the g.c.e. under dark and illuminated conditions are shown in fig 1. Illumination nearly doubles the current while the cathodic peak potential is shifted by about + 0.02V. This current enhancement is observed for all sweep rates. The anodic peak currents which are due to the oxidation of dithionite are also increased. Dithionite is formed by dimerisation of the one electron reduction product $SO_2^{\cdot-}$. The magnitude of the photocurrent is dependent on the intensity of illumination and is negligible when the electrode is turned away from the window.

Photoeffects are not expected with metal surfaces and hence the observed increase of currents may be associated with some photo generated species in solution. The rotating electrode experiments confirm this inference (Fig 2). The photocurrent decreases with increase of rotation rates and becomes zero at a rotation rate depending on the melt used. This rotation rate is 1750 rpm for the ternary amide containing ammonium nitrate (AN melt), 3600 rpm for the melt containing lithium nitrate (LN melt) and 750 rpm in molten acetamide (AA melt). These values run parallel with the viscosities of the respective solvents. The species responsible for the photoeffect is electrochemically generated but thrown away from the interface rapidly with increasing rates protection.

Since no such effects have been observed with other depolarisers such as oxygen, quinones, dithionite, the effects are to be associated with electrogenerated $SO_2^{\cdot-}$, the product of reduction of SO_2. If the solution is illuminated for a time interval and switched off prior to the cathodic sweep, no photocurrents are observed. This is true even when a xenon lamp is used for illumination.

The photoeffect is explained based on the following sequences of reactions.

$$SO_2 + e \dashrightarrow SO_2^{\cdot -} \quad .... \quad (1)$$

$$SO_2^{\cdot -} + h\nu \dashrightarrow SO_2^{\cdot -*} \quad .... \quad (2)$$

$$SO_2^{\cdot -*} + X \dashrightarrow SO_2 + X^{-} .... \quad (3)$$

The excited $SO_2^{\cdot --*}$ radical anion transfers an electron to a species X in solution and regenerates SO_2 in the interface. This SO_2 undergoes reduction and the cycle continues. The formation of $SO_2^{\cdot --}$ and reduction of regenerated SO_2 can occur only when sufficient potential is applied.

A similar mechanism has been suggested for the observations of photocurrents in the reduction of pyrene from acetonitrile solutions, using mercury electrodes [7]. Walter and Compton suggested that the pyrene radical anion is excited by light and subsequently transfers an electron to another unexcited pyrene radical anion to form a dianion and also regenerate a pyrene. They observed that the photocurrent increase was a maximum when light of wavelength 580 nm was incident and this corresponded to the λ_{max} of pyrene radical.

Experiments with a monochrometor shows that maximum photoeffect in SO_2 reduction is obtained with light of wavelength 430-440 nm. λ_{max} of $SO_2^{\cdot --}$ and λ_{max} of dithionite in aqueouos solution are 365 nm and 317 nm respectively. The λ_{max} of dithionite in molten amide is found to be 358 nm. Extrapolating the observations in aqueous media the λ_{max} of $SO_2^{\cdot -}$ may be expected to be around 410 nm.

Additional evidences for the proposed mechanism are 1) The I_p-$v^{1/2}$ plots (fig 3) show positive deviations at low sweep rates and negative deviations at high sweep rates under illuminated conditions. The reduction peak is observed to become a plateau at low sweep rates under illuminated conditions. These are characteristics of a catalytic process regenerating the depolariser [8]. 2) No photocurrents are observed when platinum electrodes are used. The reduction has been shown to be a two electron process [3]. SO_2^{--} and not $SO_2^{\cdot --}$ is the species generated. High photocurrents are observed with mercury n-WSe_2, n-$MoSe_2$ and n-MoS_2 electrodes. The reduction is a one electron process at these electrodes. 3) The anodic oxidation peak is found to be present at all sweep rates as in dark conditions and i_p^a/i_p^c rates is the same under both conditions. The anodic peak is due to the oxidation of dithionite, which is formeod by dimerisation of SO_2^{--} radical [2]. Illumination has no effect on the anodic oxidation of dithionite. In an experiment with pure dithionite in solution, the electrode is illuminated and anodic sweep is started from -0.5V. An anodic peak with a peak current equal that observed under dark condition is observed. The increase in the anodic peak of fig (1) is due to the fact that the $SO_2^{\bullet-}$ radical production (I_{pc}) is increased by illumination and hence more of the dimerisation product is also produced.

CONCLUSION

Photocurrents are observed in the reduction of SO_2 at metallic electrodes, only when the reduction is a one electron process producing the $SO_2^{\bullet-}$ radical anion. The radical can be photoexcited and can transfer an electron to a solutioon species while regenerating the original depolariser in the interface.

REFERENCES

1. R.Narayan and K.L.N.Phani in Molten Salt Techniques, Vol IV, ed. D.Lovering and R.Gale, Plenum, NY (1991)

2. V.Mathews and R.Narayan, J.Electroanal.Chem. (1993) (in print)

3. V.Mathews and R.Narayan, Bulletin of Electrochemistry (1993) (in press)

4. V.Mathews and R.Narayan, Molten Salt Forum, 1,2, 397, (1994)

5. S.Sampath and R.Narayan, J.Electroanal.Chem., 33, 273, (1992)

6. S.Sampath, Ph.D Thesis, Indian Institute of Technology, Madras (1991)

7. A.G.Waller and R.G.Compton, Electrochim.Acta 35, 1837, (1990)

8. R.Greef, R.Peat, L.M.Peter and D.Pletcher and J.Robinson, Instrumental methods in electrochemistry, pp.198, Ellis Horwood, John Wiley, London (1985)

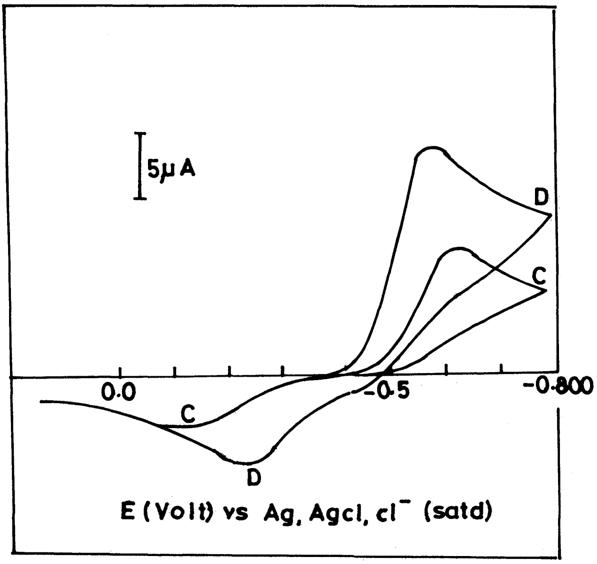

Fig. 1: CVM of SO_2 in AN melt. (25°C), ($V = 0.04 V S^{-1}$)
$C_{SO_2} = 2.2 \times 10^{-3}$ M. Area of the electrode = $0.07 cm^2$
C = dark; D= illuminated: Halogen lamp = 100W/12V DC, 25°C

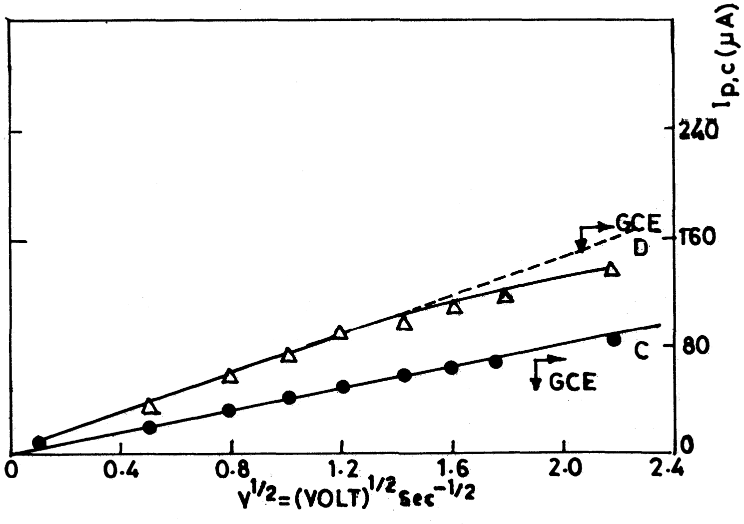

Fig. 2: $I_{P_1 C}$ vs $V^{1/2}$ for SO_2 reduction in the AN melt at 25°C
GCE ($0.07 cm^2$) $SO_2 = 2.5 \times 10^{-3} ML^{-1}$.
C – dark, D – illuminated.

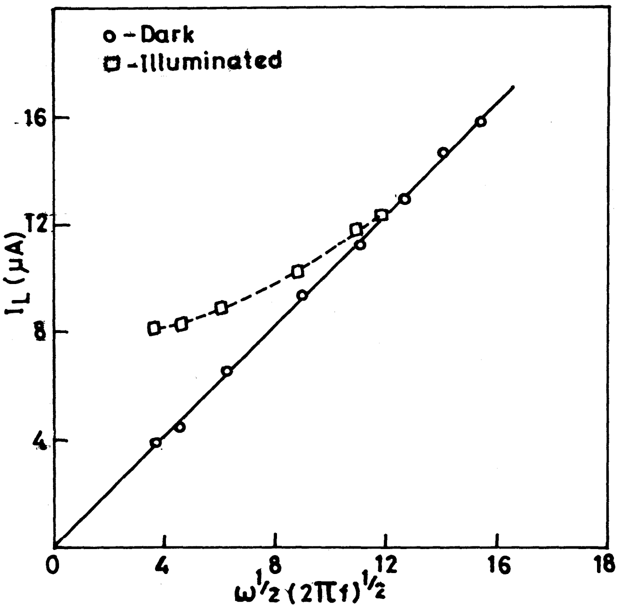

Fig. 3 : I_L vs $\omega^{1/2}$ plots for the reduction of SO_2 in ANmelt at GCE ($0.049 cm^2$) ($C_{SO_2} = 2.5 \times 10^{-3}$ ML^{-1})

DOI: 10.1149/199413.0363PV

MEMBRANE POTENTIALS ACROSS MACOR IN MIXTURES OF MOLTEN BROMIDES

M.L. Orfield

University of Wisconsin-Stout
Menomonie, Wisconsin 54751

ABSTRACT

Potentials generated across a Macor membrane in molten NaBr-KBr mixtures were measured. The composition of a melt on one side of the membrane was fixed and the other allowed to vary systematically in the conducted cations. Measurements were made with mixtures of Na-Br-KBr and LiBr-KBr. The best $K^{POT}_{Na\text{-}K}$ and $K^{POT}_{Li\text{-}K}$ were calculated for the systems from the data points. The measured membrane potentials were plotted as a function of the activity of one of the ions in the indicator melt and compared with a curve of the theoretical potentials .

INTRODUCTION

Many ceramics conduct ionically in molten salt solutions at high temperatures. However most are not exclusive conductors of a single ion. For example mullite conducts Na^+, K^+, and Li^+ ions (1). Such mixed conduction is believed to occur via a glassy phase in the ceramic.

When this type of ceramic forms a separator in an electrochemical cell a membrane potential is generated across the conductor. This potential is predicted by the equation:

$$E_{mem} = RT/F \ln\left(\frac{a(N^+)_I + K^{POT}_{NM}\ a(M^+)_I}{a(N^+)_O + K^{POT}_{NM}\ a(M^+)_O.}\right) \qquad (1)$$

where the E_{mem} is the potential generated, R,T, F, are the gas constant, the temperature, and Faraday's constant , $a(N^+)_I$ and $a(N^+)_O$ are the activities of the conducted ion N^+ on either side of the membrane, and $a(M^+)_I$ and $a(M^+)_O$ are the activities of the second conducted ion M^+ on either side of the membrane. K_{NM}^{POT} is the potential selectivity coefficient which is a measure of the preference of the membrane for M^+ over N^+ as a means of moving ionic current (2). For example, if the potential selectivity coefficient for a mixture of NaBr-KBr, $K_{Na\text{-}K}^{POT}$, is less than 1, a preference for Na^+ conduction by the membrane is indicated. If the value is small enough the membrane becomes effectively an exclusive conductor of Na^+.

The relationship between the value of potential selectivity coefficient and the composition of a membrane has been established for glasses in aqueous solutions (3). It may hold as well for ceramic membranes in molten salts. This investigation proposes to examine that relationship beginning with Macor. Macor is a machinable glass ceramic produced by Corning and containing approximately 60% crystalline and 40% glassy phases. It is approximately 47% SiO_2, 8.5% B_2O_3, 16.7% Al_2O_3, 14.5% MgO, 9.5% K_2O, and 6.3 fluoride by weight. This material was selected because it is commercially available and is replicated by other manufacturers with only slight modifications in composition. In addition glass ceramics have good resistance to high temperatures and have been shown in this work to resist degradation in molten salts.

EXPERIMENTAL

A diagram of the experimental apparatus depicted in Figure 1. It and the experimental procedure are fully described in (1). A large mullite tube contained the experimental system. Dry argon flowed throughout the system at all times during the experiments. One gas inlet was directed through the reference melt and the other into the indicator melt. A silver crucible contained the indicator melt ,which was changed for each experiment, and the reference melt of constant composition . The Macor was purchased as a rod 2.54 cm. in diameter and 7.62 cm. in length. The rod was machined to form a tube with one end closed and a wall width of either 0.3175 or 0.1587 cm. This tube held the reference melt and the wall of the tube became the membrane determining the potential of the cell.

The cell may be described,

M^1Br(mol %=X), M^2Br(mol%=100-X-Y)), AgBr(mol%=Y)|Ag |**Macor**|
M^1Br (ref = 10 mol%), M^2Br(ref= 85mol%), AgBr(ref= 5mol%)|Ag

where M^1Br and M^2Br define either the combination, NaBr-KBr or NaBr-LiBr, the mole fractions X and Y vary from 10-90%, ref stands for the reference melt composition. Both electrodes were silver wire.

The indicator melt, the Macor tube containing the reference melt and the electrodes were sealed into the mullite chamber and the temperature of the system raised to 760°C. Equilibration of the temperature required approximately 1-2 hour. After this time the electrodes were lowered into the melts and readings were taken every minute until a stable potential was reached.

To insure that the membrane potential was equal to the measured cell potential the contribution to the potential from the electrodes was fixed at 0.00 volts. Both electrodes were the same silver wire and the mole fraction of AgBr was adjusted in the indicator melt to make the activity of AgBr in that melt the same as in the reference melt. Activities of AgBr in each indicator melt were determined using the equation (4),

$$RT \ln\gamma_x = k_{12}N_1N_2 + (k_{x1}N_xN_1 + k_{x2}N_xN_2)(N_1 + N_2) \qquad (2)$$

for a ternary solution where x indicates AgBr and 1 and 2 the alkali metal bromide components of the mixture, γ_x is the activity coeficient of AgBr, and k is the interaction coefficient of the pair of components indicated by the subscript. Activity coefficients for each system of alkali metal bromides were calculated with the same equation using appropriate interaction coefficients (5-9).

RESULTS AND DISCUSSION

The Macor membrane resisted degradation in the molten salts very well. It lasted, on average several weeks longer than did mullite in earlier experiments. The resistance of the Macor membrane to degradation may be explained by its microstructure and the nature of failure in such membranes. Earlier work with a mullite membrane indicated that failure usually occurs through crack propagation begun through a corrosion process. In the Macor membrane the mica crystalline phase, which makes the ceramic machinable with ordinary tool steel, inhibits crack growth

The measured membrane potentials for NaBr-KBr melts are plotted as a function of the activity of Na^+ in the indicator melt in Fig. 2. K^{POT}_{Na-K}, values were calculated for each measurement using equation 1 and the measured membrane potentials. They are shown as a function of the activity of the Na^+ ion in the melt in Fig 3. The K^{POT}_{Na-K}, is clearly a constant within reasonable experimental error indicating that the membrane potentials may be predicted by equation 1. Values of K^{POT}_{Na-K} are shown in Fig. 3 for two membranes, one 0.3175 cm and the other, 0.1587 cm thick. As expected in these early experiments the thickness of the membrane had no effect on the potential selectivity coefficient. It did however significantly affect the time required for the system to come to equilibrium. With the 0.125 cm membrane the system required approximately 2.5 hours, but with the 0.0637 cm membrane 1.5 hours was required.

The best value, $K^{POT}_{Na\text{-}K} = 0.452$, was calculated using a commercial curve fitting program. This value was substitued into equation 1 to generate the theoretical potential line shown in Fig. 2. The experimental values agree quite well with this theoretical line making the calculation of membrane potentials with this $K^{POT}_{Na\text{-}K}$ a practical matter.

The value of $K^{POT}_{Na\text{-}K} = 0.452$. indicates that the membrane has a slight preference for conducting Na^+ over K^+ ions ($K^{POT}_{Na\text{-}K}$, <1) although the size of this number suggests that both ions are easily conducted. This result contrasts with the $K^{POT}_{Na\text{-}K}$, found for mullite (1) which indicated a greater preference for Na^+ ($K^{POT}_{Na\text{-}K} = 0.048$). Unlike the mullite the assumption of exclusivity of conduction across a Macor membrane at any activity of K^+ in a mixed melt would lead to serious error in the calculation of a membrane potential.

The experimental potentials were also plotted in Fig. 4 using a modification of equation 1 proposed by Eisenman et al. (10),

$$E_{mem} = RT/nF \ln\left(\frac{(a(Na^+)_l)^{1/n} + (K^{POT}_{Na\text{-}K}\ a(K^+)_l\ )^{1/n}}{a(Na^+)_{ref}\ )^{1/n} + (K^{POT}_{Na\text{-}K}\ a(K^+)_{ref})^{1/n}} \right) \qquad (3)$$

where n is a correction for the nonideality of sites on the surface of the membrane. $K^{POT}_{Na\text{-}K}$ and n were calculated to best fit the data ($K^{POT}_{Na\text{-}K} = 0.428$, $n = 1.077$) and were used to generate the theoretical line in Fig. 4. The results indicate that this modification does not improve the fit of the experimental data to the theoretical curve, suggesting that relationship does not depend on the ideality of surface exchange sites on the membrane.

The measured membrane potentials for KBr-LiBr melts are plotted in Fig.5. Using the same method as that for NaBr-KBr melts the best value of $K^{POT}_{Li\text{-}K} = 0.1178$ was calculated and used to generate the theoretical line shown in Fig. 5. Agreement between the measured and theoretical potentials. is less than in the Na-K system. The measured potentials are plotted again in Fig. 6 with a theoretical curve generated from equation 3 and $K^{POT}_{Li\text{-}K} = 0.2265$ and $n = 0.5954$. Using the Eisenman modification of equation 1 improves the correlation between experimental data and theoretical but the agreement is still not as good as that found for the Na-K system. Since the measured cell potentials were reproducible, and since a very similar problem was observed with the mullite membrane in the Li-K system the error may be due to factors other than experimental procedure. The interaction coefficients and calculated activity coefficients indicate that this system is much more removed from the ideal than is the Na-K system. Any error in the interaction coefficients would lead to a just such systematic error as appears in the experimental data.

In this system the $K_{Li\text{-}K}^{POT}$ indicates the membrane shows a preference for the conduction of Li^+ over K^+ this preference being greater , $K_{Li\text{-}K}^{POT} < K_{Na\text{-}K}^{POT}$, than that for Na^+ over K^+. Overall the mullite conducted Na^+ to a greater extent than Li^+ and Li^+ to a greater extent than K^+. In the Macor system, even without the results from the third system, the likely preferred order of conduction will be $Li^+ > Na^+ > K^+$. It seems reasonable to assume that the difference in transport numbers is due to the difference in the composition of the conducting phases. Additional work is planned with different glass ceramics to examine this idea further.

SUMMARY

The potentials measured across Macor in molten NaBr-KBr and LiBr-KBr solutions are predicted quite well by equation 1. Use of Eisenman's modification of equation 1 does not improve the correlation of data with theory in the Na-K system, but does improve the agreement for the Li-K system. The value of the potential selectivity coefficients suggests a tentative ranking of conductivity, $Li^+ > Na^+ > K^+$ for a Macor membrane · Again this order is different from that observed for a mullite membrane suggesting that the composition of the glassy phase is likely different as well.

REFERENCES

1. M. Orfield, J. Electrochemical Soc., 138, 2348, (1990).

2. B.P. Nicolski, Zh. Fiz. Khim., 10, 495, (1937).

3. G. Eisenman in "Glass Electrodes for Hydrogen and Other Cations", G. Eisenman Ed., Chapt. 5, Marcell Dekker Inc., New York, (1966).

4. J. Lumsden, "Thermodynamics of Molten Salt Mixtures," p.96, Academic Press Inc., London (1966).

5. E. Aukrust, B. Bjorge, H. Flood, and T. Forland, Ann. N.Y. Acad. Sci., 79, 830, (1960).

6. E.J. Salstrom, and J.H. Hildebrand, J. Am. Chem. Soc.., 52, 4650, (1930).

7. E.J. Salstrom, ibid. 53, 1794, (1931).

8. E.J. Salstrom, ibid., 53, 3385, (1931).

9. L.S. Hersh, and O.J. Kleppa, J. Chem. Phys., 42, 1309, (1965).

10. G. Eisenman, in "Advances in Analytical Chemistry and Instrumentation," Vol. 4, C.N. Reilly, Editor , Interscience Publishers, New York, (1965).

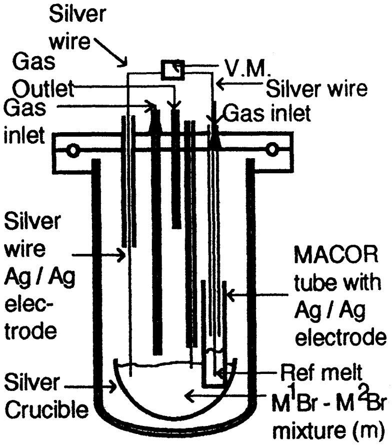

Fig 1: Diagram of Experimental Apparatus.

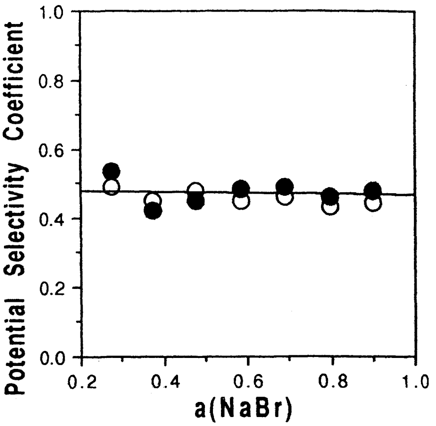

Fig 3: Potentials selectiviy coefficients calculated from measured cell potentialss as a function of activity NaBr where O = 0.317 cm. and O=0.159 cm.

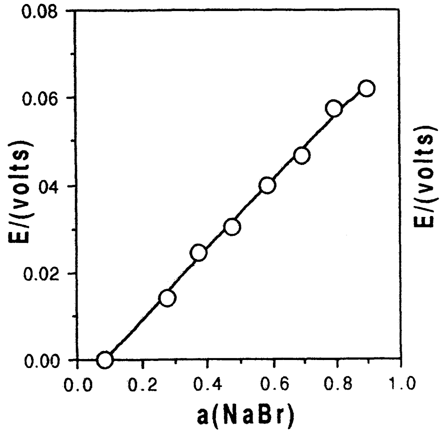

Fig. 2: Membrane potentials as a function of activity NaBr where O = measured potentials and — = theoretical potentials when $K^{POT}_{Na\text{-}K}$ =0.452

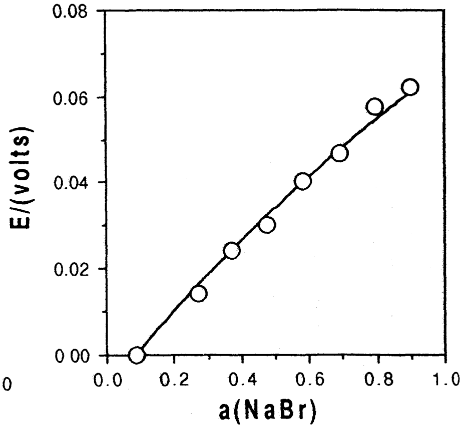

Fig 4: Membrane potentials as a function of activity NaBr where O = measured potentials and — = theroretical potentials when $K^{POT}_{Na\text{-}K}$ = 0.428 and n = 1.077.

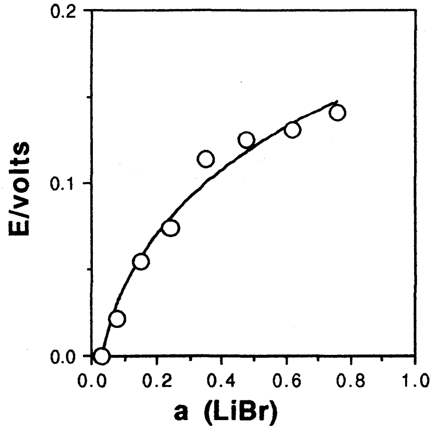

Fig 5: Membrane potentials as a function of activity LiBr where O = measured potentials and — = theoretical potentials when K_{Li-K}^{POT} = 0.1178.

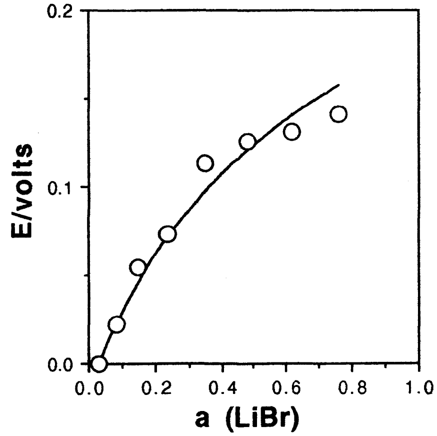

Fig 6: Membrane potentials as a function of activity LiBr where O = measured potentials and — = theoretical potentials when K_{Li-K}^{POT} .= 0.2264 and n = 0.5954.

DOI: 10.1149/199413.0371PV

GRAPHITE AS MEMBRANE IN A REFERENCE ELECTRODE FOR MOLTEN FLUORIDES BETWEEN 650 AND 800 °C

Christos G. Kontoyannis, Stelios Antoniadis and Christina Samara

Institute of Chemical Engineering and High Temperature Chemical Processes
and
Department of Pharmacy, University of Patras
P.O. Box 1414, GR 26 500 Patras, GREECE

ABSTRACT

A reference electrode for use in fluorides melts has been developed and tested. It consists of a nickel wire immersed in a solution of nickel fluoride in LiF-NaF-KF (FLINAK) eutectic. The electrode was contained in a one-end-open graphite cylinder with wall thickness of 1 mm. The exterior was coated with pyrolytic boron nitride (PBN), for electrical insulation, except from cylinder's bottom. The EMF between two electrodes was stabilized within 3 hours after the immersion in the bath and a Nernstian response with temperature was observed. The electrode was found to be stable for more than 30 hours and could be reused with reproducible results. No potential shift was observed in cyclic voltammograms which were obtained, with a lapse of 24 hours, from FLINAK with 0.1 mol % K_2NbF_7 having as reference the described electrode.

INTRODUCTION

Systematic electrochemical studies of molten fluoride systems, specially in the temperature range of 600 to 850 °C, are difficult to be conducted because of the problems encountered in selecting a reference electrode having all the desired characteristics i.e stability, durability, reversibility, reproducibility and fast response. The commonly used reference electrodes in fluoride melts are:

a) The nickel-nickel fluoride reference electrode contained in a thin-walled boron nitride (BN) envelope. The electrode was developed for potential measurements in molten LiF-NaF-KF [42-11.5-46.5 mole %](FLINAK) at a working temperature of 500 -550 °C (1,2). Boron nitride is slowly impregnated by the melt to provide ionic contact. The wetting occurs in about 6 hours (3) in molten FLINAK. At higher temperatures the BN appears to deteriorate permitting mixing of the melts. Furthermore the boron nitride tube contained a boric oxide binder that dissolved contaminated the electrolyte, and changed the electrode potential.

b) The nickel-nickel fluoride reference electrode system exhibiting a membrane from a single crystal lanthanum trifluoride (4,5). Because of the solubility of the LaF_3 in the fluorides melts a nickel frit with fine porosity was used in order to protect the crystal. The system was tested for temperatures up to 600 °C. On the other hand the single crystal LaF_3 is expensive, the assembling of the electrode is more complicated while the crystal cracks after few experiments.

c) The Ni-NiO reference electrode of the third kind with a nickel wire immersed in molten $2LiF-BeF_2$ with excess NiO and BeO and contained in silica tube (6). The electrode has been tested up to 700 °C.

d) The dynamic $Li,K/Li^+,K^+$ reference electrode (7). The thermodynamic explanation for the potential of this reference electrode is unclear while the preparation by a constant current electrolysis before the potential measurement is cumbersome.

From the electrodes described above it is apparent that there is a need for an easy-to-made, durable and having shorter wetting period reference electrode to be used from 700 to 800 °C in fluoride melts. The aim of this work was to develop and quantitatively test such an electrode by using graphite as membrane. The Ni/Ni(II) couple was chosen because its suitability as a reference electrode in molten fluorides has be proven previously (1-5).

EXPERIMENTAL

Chemicals

- LiF; NaF; KF: Merck p.a. grade. The fluoride salts were purified further by melt crystallization. FLINAK was prepared by mixing the recrystallized compounds in a glove-box.
-K_2NbF_7: Johnson Matthey Electronics.
-Vitreous carbon crucibles: Le Carbone - Lorraine.
- AgF: Aldrich, 99.9+% purity.
-Ni wire: Alfa, 99.99 % purity.
-Ag wire: Alfa, 99.999 % purity.
-Boron Nitride: Carborundum, Combat HP grade.
-NiF_2: Cerac, 99.5 % purity.
- Al_2O_3 tubes: Friedrichsfeld.
-Graphite: Ringsdorff, grade EK-90.

Reference Electrode

The electrode was contained in a one-end-open graphite (grade EK-90, Ringsdorff) cylinder with wall thickness of 1 mm and outside diameter 8 mm. The graphite was isostatic molded and the total open porosity was 14 %. The pore size was 1.5 μm. Permeability for air was 17 x 10^{-2} cm^2/sec. The exterior was coated by using CVD with pyrolytic boron nitride (PBN) for electrical insulation. The PBN layer had no porosity. No PBN layer was coated on the surface of electrode's bottom. The wall thickness in the bottom was 2 mm.

The electrode was isolated from the furnace's environment with a cover constructed from BN. Electrical insulation for the metal leads of the electrodes was accomplished by enclosing them in alumina tubes. The alumina tube, the BN cover and the graphite body were held together with the help of BN screws (Fig. 1).

The graphite prior to the filling was immersed in a ultrasonic bath for two hours and then washed with deionized water. In electrode's interior Ni or Ag wire was used in contact with FLINAK and the lead's fluoride salt. Typical resistance of such an electrode is of the order of 2 K ohm over the range 700 - 800 °C.

Instrumentation

A home-made oven with three heating zones and programmable heating controller was used. The furnace was equipped with a Ni tube core and vacuum and/or inert atmosphere could be established in the interior. Al_2O_3 radiation shields were used. Temperature of the bath was measured with an Inconel sheathed Chromel-Alumel thermocouple housed in a closed end alumina tube (Fig. 2).

An EG&G potensiostat/galvanostat (Model 173) equipped with the model 178 electrometer probe was used for the emf measurements and the application of the desired voltage in the reference electrodes. For the cyclic voltammogram a home-made variable voltage ramp generator was utilised in conjunction with the potensiostat. The data were recorded in an IBM compatible personal computer an SMM 818 data acquisition card.

RESULTS AND DISCUSSION

The Ni^{2+}/Ni^0 couple in fluoride salts it is known to exhibit a Nernstian behavior (1-5) but is strongly oxidizing when high concentrations of Ni^{2+} are used. Diffusion of dissolved NiF_2 out of the reference electrode could cause oxidation of the materials in the outer half-cell. As an alternative to Ni^{2+}/Ni^0 the Ag^+/Ag^0 couple was also tested. The characteristics of the reference electrode were acquired by measuring the deviation of the potential difference between identical designs (stability, reproducibility) or between electrodes having different concentrations of NiF_2 or AgF (Nernstian response). Reversibility was tested by superimposing a potential difference on the EMF of two identical electrodes. The reliability was verified by observing the potential difference with time of the reduction and oxidation waves of cyclic voltammograms of K_2NbF_7 in a cell having the proposed reference electrode.

Stability and Reproducibility

Reference electrodes having either Ni/NiF_2 (1 mol % in FLINAK) or Ag/AgF (1 mol % in FLINAK) were immersed in the alkali fluoride eutectic at 700 °C. The EMF was stabilized in a period of 3 hours after their immersion in the molten bath. The wetting period was almost half of what has been reported elsewhere (3). EMF remained virtually unchanged (± 2 mV) for more than 30 hours. The same electrodes were cleaned, refilled and re-immersed again in the FLINAK eutectic. The wetting period was again approximately 3 hours (Fig. 3). As can be seen in Fig. 3 no significant difference in behavior was observed between electrodes having either the Ni/Ni(II) or the Ag/Ag(I) couple.

Nernstian Response

The EMF values between two electrodes having different molar fraction of NiF_2, $x_1=0.002$ and $x_2= 0.001$ were recorded at different temperatures. The experimental as well as the theoretical emf values expected from Nernst equation for the cell:

$Ni/Ni^{2+}(x_1=0.002)/Graphite/FLINAK/Graphite/Ni^{2+}(x_2=0.001)/Ni$

are presented in Table I.

Table I: EMF Values Between Two Reference Electrodes with $[Ni^{2+}]_1/[Ni^{2+}]_2=2$

Temperature °C	Theoretical[1] (mV)	Experimental (mV)
680	27.4	27.6
710	28.3	28.9
730	28.9	29.3
790	30.6	31.1

(1). Assuming that the activity coefficient of Ni^{2+} in both electrodes are equal to 1.

The experimental values of Table I indicate that the electrodes exhibit a Nernstian behavior since the difference from the theoretical values are negligible and therefore the junction potential is insignificant.

Reversibility

On the EMF of two identical electrodes filled 1 mol % AgF, a ± 1 V and ± 0.5 V were superimposed for 60 and 30 s respectively. The response with time is represented in Fig. 4. The potential difference decays to a stable value within 5 minutes.

Potential Shift

Cyclic voltammograms of 0.1 mol % K_2NbF_7 in FLINAK at 700 °C were obtained over a period of 24 hours. A Pt working electrode (0.5 mm diameter), a Ni/NiF_2 (0.1 mol %)/graphite membrane reference electrode and the glassy carbon crucible as the counter electrode (exposed area 30 cm^2) were used. A Pt lead was utilised to establish the current flow to the crucible. No shift of the reduction-oxidation waves against the reference electrode was observed with time (Fig. 5). The explanation for the reduction and oxidation waves of NbF_7^{2-} has been reported elsewhere (8-9).

CONCLUSIONS

A rather inexpensive and easy to made Ni/Ni(II) reference electrode contained in an one-end-open PBN covered graphite cylinder, except from the electrode's bottom has been constructed. No PBN layer was coated on cylinder's surface bottom. Electrode's potential stabilizes within 3 hours while EMF remains stable for more than 30 hours. The electrode can be reused with no loss of its stability and exhibits a Nernstian response with temperature up to 800 °C. The EMF after an application of ±1 V perturbation decays to a stable value within 5 minutes. The reference electrode was used in cyclic voltammograms of 0.1 mol % K_2NbF_7 in FLINAK. No potential shift was observed in the reduction and oxidation waves indicating the stability of the electrode.

ACKNOWLEDGMENTS

The authors are indebted to Professor G.N. Papatheodorou for helpful suggestions and for providing the experimental facilities. We would like to express our thanks to Professor N.J. Bjerrum of DTH for valuable discussions on the electrochemistry of the fluoride melts.

REFERENCES

1. H. W. Jenkins, G. Mamantov and D. L. Manning, J. Electroanal. Chem., **19**385 (1968).

2. H. W. Jenkins, G. Mamantov and D. L. Manning, J. Electrochem. Soc., **117** 183 (1970).

3. P. Taxil and Zhiyu Qiao, J. Chim. Phys., **82** 83 (1985).

4. H. R. Bronstein and D. L. Manning, J. Electrochem. Soc., **119** 125 (1972).

5. F. R. Clayton, G. Mamantov and D. L. Manning, High Temperature Science, **5** 358 (1973).

6. B.F. Hitch and C.F. Baes, J. Inorg. Nucl. Chem., **34** 163 (1972).

7. K. Ema, Y. Ito, T. Takenaka and J. Oishi, Electrochimica Acta, **32** 1537 (1987).

8. P. Los and J. Josiak, B. Electrochem. **5** 829 (1989).

9. J.H. Barner, E. Christensen and N.J. Bjerrum, in "Molten Salt Chemistry and Technology", M.L. Saboungi and S. Kojima, eds., The Electrochemical Society Proceedings Series, Pennington, NJ, Vol. PV 93-9, 1993.

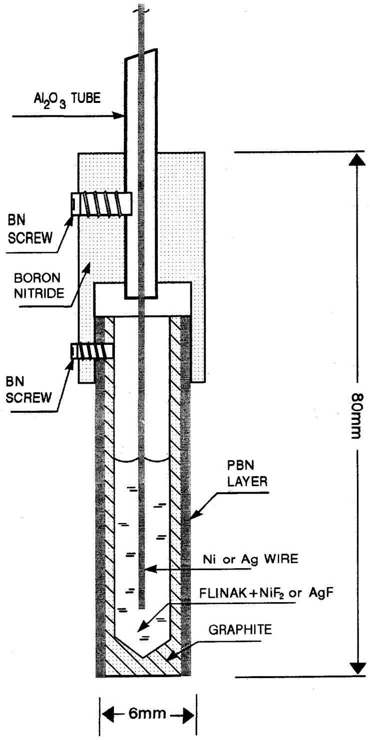

Figure 1. Reference Electrode.

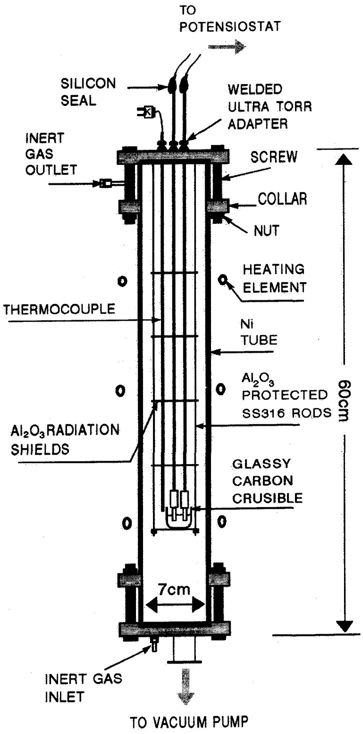

Figure 2. Furnace's schematic during an EMF measurement.

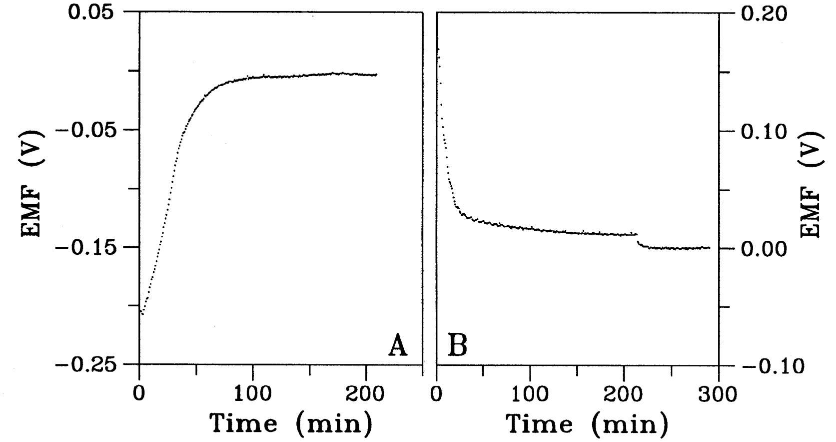

Figure 3. A: EMF vs. time between two electrodes with Ni/NiF$_2$ (1 mol % in FLINAK); B: EMF vs. time between two electrodes with Ag/AgF (1 mol % in FLINAK).

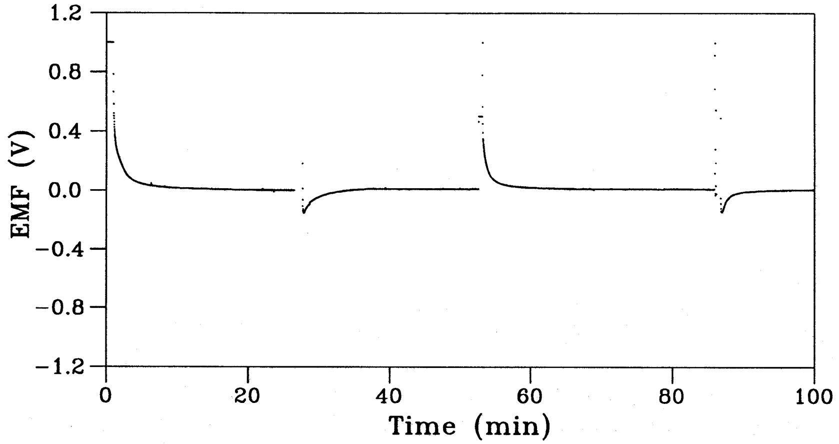

Figure 4.EMF vs. time between two electrodes with Ag/AgF (1 mol % in FLINAK). A ± 1 V and ± 0.5 V were superimposed for 60 and 30 s respectively on the EMF.

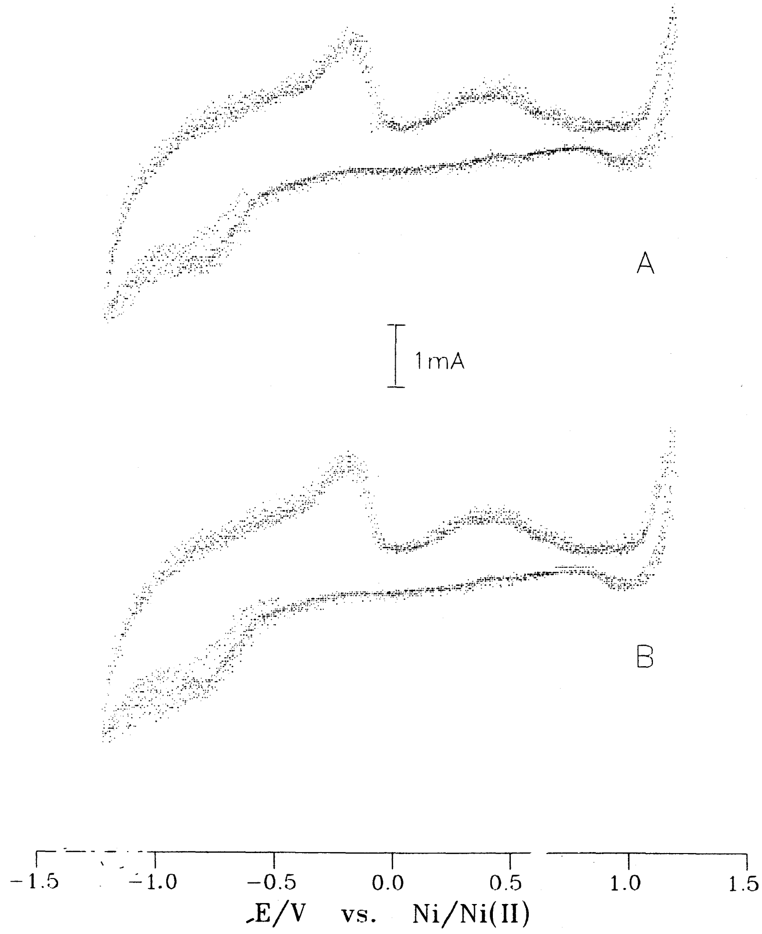

Figure 5. Voltammograms of 0.1 mol % K_2NbF_7 in FLINAK at 700°C obtained with a Pt working electrode (0.5 mm diameter), Ni/NiF_2 (0.1 mol %)/graphite membrane reference electrode and glassy carbon counter electrode. Scan rate 0.4 V s^{-1} Scan ± 1250 mV Voltammograms A and B were recorded 12 and 24 hours respectively after the immersion of the electrodes in the melt.

DOI: 10.1149/199413.0379PV

SYNTHESIS OF HIGHLY FLUORINATED GRAPHITE IN ANHYDROUS LIQUID HYDROGEN FLUORIDE

Tsuyoshi Nakajima and Michiyuki Namba
Division of Polymer Chemistry,
Graduate School of Engineering,
Kyoto University,
Sakyo-ku, Kyoto, 606, Japan

ABSTRACT

Fluorine intercalation in graphite was studied in anhydrous liquid hydrogen fluoride containing a small amount of MoF_6 or SbF_5. The products were stage 1 compounds with compositions of $C_{2.0}F$ to $C_{2.4}F$. The c-axis repeat distances of 5.2Å to 6.6Å were observed, indicating the formation of stage 1 C_xF. The in-plane lattice parameter a_0 was increased to 2.470~2.474Å due to the formation of C-F semi-covalent bonding. The C_{1s} XPS peaks were observed at 287.7~288.0eV and 284.6eV which indicate the carbon atoms semi-covalently bonded to fluorine and those unbound to fluorine, respectivery. IR absorption spectrum also shows a strong absorption for C-F stretching vibration at $1120cm^{-1}$.

INTRODUCTION

Electrochemical intercalation of fluorine in graphite in molten KF•2HF at 100°C yielded stage 7 to 3 compounds (1,2). The importance of fluorine-graphite intercalation compound in electrolytic production of elemental fluorine was shown by the electrochemical study (1,3) and its physical properties (4). Fluorine intercalation is thermodynamically favorable in anhydrous liquid HF than in molten KF•2HF. In this study, fluorine-graphite intercalation compound C_xF was synthesized in anhydrous liquid HF containing a small amount of MoF_6 or SbF_5 and the products were characterized by X-ray diffractometry, XPS, IR absorption spectroscopy and so on.

EXPERIMENTAL

Chemicals

Host graphite is Madagascar natural graphite powder (<37μm). Fluorine gas (F_2:99.4~99.7%, N_2:0.3~0.6%, HF<0.01%) and HF (purity>99%) were supplied by Daikin Kogyo Co. Ltd. MoF_6 was supplied by Central Glass Co. Ltd. and SbF_5 was a commercial one (Aldrich Chemical Co., Inc.).

Synthetic method

Anhydrous liquid HF (AHF) transferred from the cylinder to Teflon PFA tube was dehydrated by bubbling fluorine gas into AHF cooled by ice bath for 6-12 hrs. The purified AHF was further transferred to Teflon PFA tube reactor containing graphite powder and a small amount of MoF_6 or SbF_5 by distillation. Fluorine gas was then bubbled into AHF for 1 to 4 days at 8-25°C. During this operation, AHF was gradually removed from the reactor with fluorine gas. After removal of AHF, fluorine gas was allowed to flow over graphite for 1 to 2 days.

Characterization of the products

The composition of the product was determined by elemental analysis of carbon and fluorine. The stage number and lattice parameter a_0 were determined by X-Ray powder diffraction (Debye-Scherrer method). Carbon-fluorine bonding was evaluated by XPS, IR absorption spectroscopy and Raman spectroscopy.

RESULTS AND DISCUSSION

Effect of Lewis acid addition to AHF

A small amount of MoF_6 or SbF_5 as an oxidizer of graphite was added to AHF to facilitate the fluorine intercalation. Fig. 1 shows the in-plane lattice parameter a_0 as a function of added MoF_6 or SbF_5. It is known that a_0 value increases with increasing fluorine content in highly fluorinated graphite ($2 \leq X \leq 3$ in C_xF) as shown in Fig. 2 (5-7). The a_0 value increased with increasing MoF_6/C or SbF_5/C ratio, reaching the maximum at $MoF_6/C = 0.004$~0.005. Further increase of MoF_6 or SbF_5 reduced the a_0 value. The maximum a_0 value was 2.474Å which was observed for a sample prepared with $MoF_6/C = 0.004$ at 8°C. MoF_6 was more effective than SbF_5. Since SbF_5 is a more stronger Lewis acid than MoF_6, SbF_5 would act as a Lewis acid against HF, giving SbF_6^- and H_2F^+. For this reason, SbF_5 does not seem suitable as an oxidizer of graphite. Furthermore it has been also shown that the lower temperature is thermodynamically preferable.

Composition and structure

At the beginning of the reaction, stage 1 C_xHF_2 is rapidly formed and cointercalated HF molecules are gradually desolvated with removal of AHF and further flow of fluorine gas (6-8).

The products obtained in this study were stage 1 compounds with compositions of $C_{2.0}F$ to $C_{2.4}F$ as given in Table 1. Their c-axis repeat distances (I_c values) were in the range of 5.2Å to 6.6Å. The larger I_c values than 6Å were

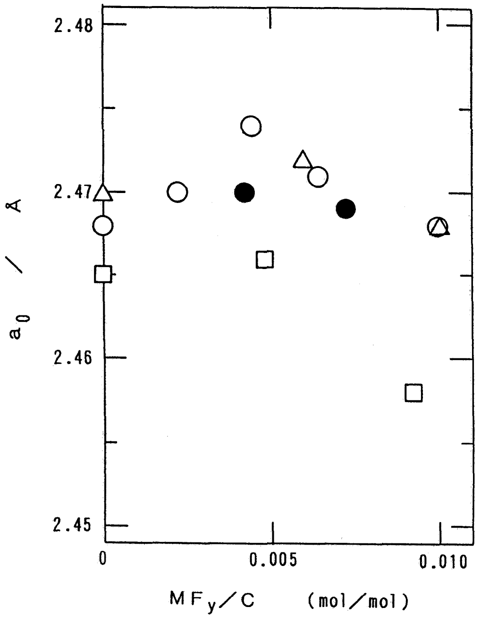

Fig.1 Dependence of lattice parameter a_0 on MF_y/C and temperature.
MF_y, ○:moF_6, ●:SbF_5.
Temperature, ○ and ●:8°C, △:18°C,
□:25°C.

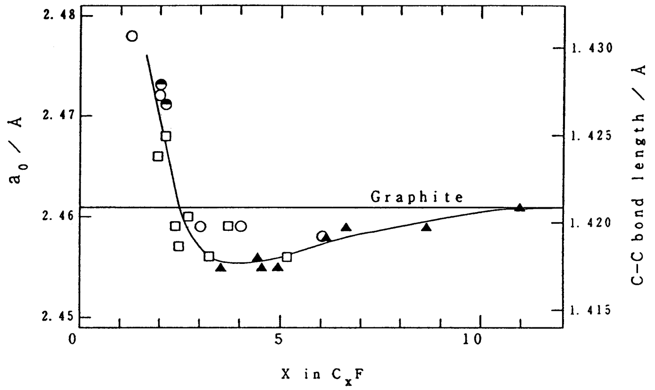

Fig. 2 C-C bond length and lattice parameter a_0 of host graphite as a function of composition of C_xF.

▲ : Ref. 5

◓ : This work

□ : Ref. 6

○ : Ref. 7

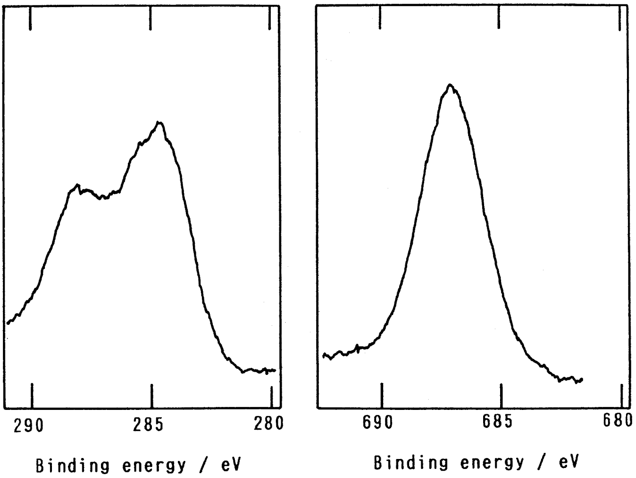

Fig.3 XPS spectra of $C_{2.0}F$ with a_0=2.473 A.

Table 1 Composition and X-ray data of stage 1 C_xF samples prepared in anhydrous liquid HF

Sample	Composition	a_0 / Å	I_c / Å	Intensity[a)]
1[b)]	$C_{2.0}F$	2.473	6.60 6.06	vs s
2[c)]	$C_{2.0}F$	2.473	6.19	s
3[c)]	$C_{2.3}F$	2.472	6.28 5.87	s vs
4[d)]	$C_{2.1}F$	2.471	6.01	s
5[c)]	$C_{2.3}F$	2.471	6.41 5.99	vs s
6[c)]	$C_{2.4}F$	2.470	6.14 5.37	vs s
7[e)]	$C_{2.0}F$	2.468	6.56 5.19	s w

a)Intensity of X-ray diffraction peak, s:strong, w:weak, v:very, b)F_2 flow for 5 days after removal of anhydrous liquid HF, c) F_2 flow for 1 day after removal of anhydrous liquid HF, d)F_2 flow for 3 days after removal of anhydrous liquid HF, e)Fluorination procedure c) was repeated 4 times.

often observed, indicating the cointercalation of HF molecules. The large I_c values were somewhat decreased by pumping or drying in silica gel.

The lattice parameter a_0 and C-C bond length of host graphite decrease with increasing fluorine content in the region where the ionic nature is dominant in C-F bonding, however they increase at stage 1 due to the formation of semi-covalent C-F bonding as shown in Fig. 2. The a_0 values of C_xFs obtained in this study were in the range of 2.468Å to 2.474Å which are larger than that of graphite itself, 2.461Å.

Carbon-fluorine bonding

The C_{1s} XPS spectrum has two peaks at 287.7~288.0eV and 284.6eV as shown in Fig. 3. The former clearly indicates the carbon atoms semi-covalently bonded to fluorine atoms, and the latter those unbound to fluorine. The F_{1s} peaks appeared at 687.0~687.1eV, which are larger values than those for fluoide ions. These binding energies were shiftd to higher values with increasing lattice paramater a_0.

The IR absorption spectrum showed two absorptions at 1120cm^{-1} and 1240cm^{-1}. The former indicates the stretching vibration of C-F bond and the latter corresponds to surface CF_2 groups with covalent bonding.

The Raman spectrum gave two peaks at 1340cm^{-1} and 1590cm^{-1}. The former indicates the disorder of host graphite and the latter the E_{2g} mode of host graphite.

REFERENCES

1. T. Nakajima, T. Ogawa and N. Watanabe, J. Electrochem. Soc., 134, 8 (1987).
2. T. Nakajima, M. Namba and Y. Kawabata, Denki Kagaku, 61, 738 (1993).
3. T. Nakajima, T. Ogawa and N. Watanabe, J. Fluorine Chem., 40, 407 (1988).
4. T. Nakajima and M. Touma, J. Fluorine Chem., 57, 83 (1992).
5. T. Nakajima, M. Molinier and M. Motoyama, Carbon, 29, 429 (1991).
6. T. Mallouk and N. Bartlett, J. Chem. Soc., Chem. Commun., 103 (1983).
7. R. Hagiwara, M. Lerner and N. Bartlett, J. Chem. Soc., Chem. Commun., 573 (1989).
8. H. Takenaka, M. Kawaguchi, M. Lerner and N. Bartlett, J. Chem. Soc., Chem. Commun., 1431 (1987).

DOI: 10.1149/199413.0385PV

ANODIC OVERVOLTAGE ON GRAPHITE IN Li_2O-LiF-CaF_2 MELTS

R.G. Reddy , A.R. Narayan and P.T. Velu
Department of Chemical and Metallurgical Engineering
University of Nevada , Reno , NV , 89557

ABSTRACT

The anodic overvoltage on graphite anode during electrolysis of Li_2O in $4LiF.CaF_2$ melts at 1093 K was measured. A steady state current voltage method was used. The experimental results of plots, anodic overvoltage as a function of log current density, showed a straight line relationship, $\eta = 1.32 + 0.84 \log i$. A two electron controlled charge transfer reaction between the complex oxyfluoride and the graphite anode is proposed. The limiting current density in the melt is determined to be 0.55 A/cm^2.

INTRODUCTION

In our earlier paper[1], the anode reaction mechanisms of Al-Li alloys and fluoride melts was reported. It was concluded that the existence of the limiting current phenomenon was due to the absorption of CO on the anode surface. Very few studies were made on the determination of the anode overvoltage and its effect on the efficiency of high temperature molten salt electrolysis[1-3]. In this paper, the anodic overvoltage on graphite during the electrolysis of Al-Li alloys in Li_2O-LiF-CaF_2 melts at 1093 K is discussed. From the experimental data, Tafel constants, limiting current density and the complex oxyfluoride species in the melt were deduced.

EXPERIMENTAL METHOD

The experimental set-up, materials used and the conditions of measurements used in this study were described elsewhere[1] and only a brief description is presented here.

The experimental set-up is shown in Figure 1. The materials used were calcium fluoride (99.9% purity), lithium fluoride (99.9% purity) and lithium oxide (99.8 % purity). The apparatus used consisted of a 11.5 cm diameter stainless steel chamber and was heated by a kanthal wire-wound resistance furnace. The 75 gm dry mixture of $4LiF.CaF_2$ stoichiometric proportion was melted at 1073 K under argon gas atmosphere for one hour in a graphite crucible. Lithium oxide (Li_2O), 20 wt% of electrolyte mixture was added to the liquid melt. The melt was stirred with argon gas at a rate of 60 to 80 cm^3/min. The temperature of the melt was measured by chromel-alumel thermocouple.

A graphite anode and graphite reference electrode was used for the overvoltage measurements. The voltage between the electrodes was measured by a multimeter with an internal resistance of 100 M-ohm and the current was measured by the potential drop across a standard resistance with a multimeter. The anodic polarization curve was obtained by increasing the applied current in small steps and holding the current at each step to obtain a steady potential. The current was found to be steady with a scatter of 0.01 ampere.

The solidified samples were ground to less than 100 mesh size in alundam vial and the homogenized mixture powder analyzed for the Ca, Li, F and O. X-ray diffraction studies were also performed on the solidified melt samples.

RESULTS AND DISCUSSION

The experiments were done in $4LiF.CaF_2$ melt saturated with Li_2O. Figure 2 shows the plot of measured overpotential η Vs log current density, Tafel relationship, linear dependence of overvoltage with log current density. A linear dependence of η Vs log i was observed upto 0.50 A/cm^2 and a limiting current phenomenon was observed between 0.50 and 0.71 A/cm^2, where the line deviated from the straight line. On further increasing the current density, abrupt changes were observed with a small change in current density. From the Tafel region, the following equation was obtained.

$$\eta = 1.32 + 0.84 \log i \qquad (1)$$

Experimental data was analyzed by considering an anode reaction mechanism consisting of the following two steps[1]:

I. Reaction between oxygen-carrying complex and anode, with the transfer of two electrons:

$$LiO_xF^{-2} + C(gr) = LiF + CO_x(g) + 2e^- \qquad (2)$$

where $x = 1$ for $CO(g)$ and $x = 2$ for $CO_2(g)$.

II. Desorption of adsorbed CO_x:

$$CO_x(ad) = CO_x(g, 1\ atm) \qquad (3)$$

The equation relating current density and anode potential for step I can be written as:

$$i = k^+ C^2 (1-\theta) \exp\left[\frac{2\alpha FE}{RT}\right] - k^- \theta \exp\left[\frac{-2(1-\alpha)FE}{RT}\right] \qquad (4)$$

where, C is the concentration of the oxygen-carrying complex LiO_xF^{-2}, k^+ and k^- are the rate constants for the anodic and cathodic reactions, θ is the surface coverage of $CO_x(ad)$, E the anode potential, α the transfer coefficient, R the gas constant, T the absolute temperature and F Faradays constant.

By substituting the standard anode potential E^0, exchange current density i_0 and $\eta = E-E^0$ in equation (4) and rearranging, we obtain equation (5).

$$i = i_0 \{ [\frac{1-\theta}{1-\theta_0}] \exp [\frac{2\alpha F\eta}{RT}] - \frac{\theta}{\theta_0} \exp [\frac{-2(1-\alpha)F\eta}{RT}]\} \qquad (5)$$

Assuming a surface coverage $\theta \approx \theta_0$ (i.e. no accumulation of produced CO_X) and for high anodic current densities in equation (5), the equation (6) can be written.

$$\eta = -\frac{2.303RT}{2\alpha F} \log i_0 + \frac{2.303RT}{2\alpha F} \log i$$

$$\text{or} \qquad \eta = a + b \log i \qquad (6)$$

Comparing equation (1) and (6), the Tafel constants **a** and **b** were deduced as 1.32 and 0.84 respectively.

At higher current densities, beyond the Tafel limit, a Langmuir adsorption of CO_X is assumed viz. step II. The non-linear relationship observed may be due to the slow desorption of absorbed CO_X on the anode. The rate of step II can be expressed by equation (7)

$$i = k_d \theta - k_a PCO_x (1-\theta) \qquad (7)$$

where K_d and K_a are rate constants for desorption and adsorption of CO_x, θ the surface coverage of CO_x(ad) and P_{COx} the partial pressure of CO_x gas. A limiting current phenomenon will occur when $\theta \rightarrow 1$. The value of the "exchange current density" (i_r) for Step II, at equilibrium, the equation reduces to Equations (8) and (9).

$$i_r = K_d \theta_o \qquad (8)$$

$$i_r = K_a PCO_x (1-\theta_o) \qquad (9)$$

Under the assumption of $\alpha = 1/2$ and solving for θ gives equation (10).

$$\theta = \frac{i}{i_r} \theta_0(1-\theta_0) + \theta_0 \qquad (10)$$

Substituting equations (8),(9) and (10) in equations (7) and (5), and neglecting the cathodic term, the equation (11) can be obtained .

$$\frac{1}{i} = \frac{1}{i_0} \exp [- \frac{F\eta}{RT}] + \frac{\theta_0}{i_r} \qquad (11)$$

The term $\exp[-F\eta/RT]$ in equation (11) was calculated using the experimental data from Figure 2. Figure 3 shows the plot of $1/i$ as a function of $\exp[-F\eta/RT]$. From this plot the following relationship was obtained.

$$\frac{1}{i} = 1.45 \times 10^{-6} \exp\left(\frac{-F\eta}{RT}\right) + 1.94 \qquad (12)$$

By comparison of equation (11) and (12), θ/i_r and i_0 were determined to be 1.94 and 1.45×10^{-6} respectively.

By substituting the θ/i_r value in equation in (10), when $\theta \rightarrow 1$ (limiting current phenomenon occurs), the limiting current i_L was calculated to be 0.55 A/cm^2. This value is within the range of experimentally observed limiting current density of 0.5 to 0.71 A/cm^2. The experiments showed that the limiting current density is independent of the stirring rate. From the results, it is concluded that the limiting current phenomenon is predominantly due to a blockage effect caused by adsorption of CO on the anode surface.

CONCLUSIONS

The anodic overvoltage measurements were made with the steady state current density method. A value of $\eta = 1.32 + 0.84 \log i$ is obtained for the straight line region for the melt 4 $LiF.CaF_2 + Li_2O$ (sat) at 1093 K. A two-electron controlled charge transfer reaction for the reaction between the oxyfluoride melt and the graphite anode is proposed. The limiting current density of 0.55 A/cm^2 in the melt is deduced. From the knowledge of stirring rate on the limiting current density, a limiting current phenomenon due to absorption of CO on the anode surface is deduced.

ACKNOWLEDGEMENTS

The authors are pleased to acknowledge the financial support of this research by National Science Foundation (Grant No: DDM-9022127).

REFERENCES

1. Reddy, R.G. and Narayan, A.R.: Mat. Sci. Forum, Vol. 73-75, 1991, p. 521.
2. Bratland, D. and Grojtheim, K.: Revue Roum. Chim., Vol. 17, 1972, p. 41.
3. Boe, G.: Ph.D. Thesis, Univ. of Trondheim, Norway, 1976.
4. Vetter, K.J.: Electrochemical Kinetics, Academic Press, N.Y., 1967.

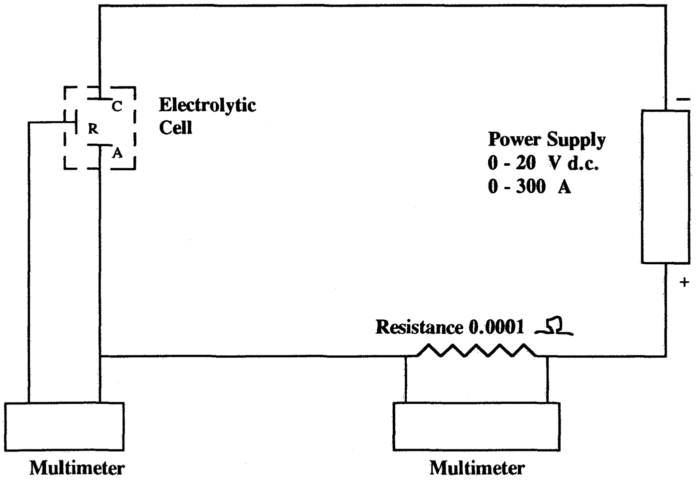

Figure 1. Anode overvoltage measuring experimental setup

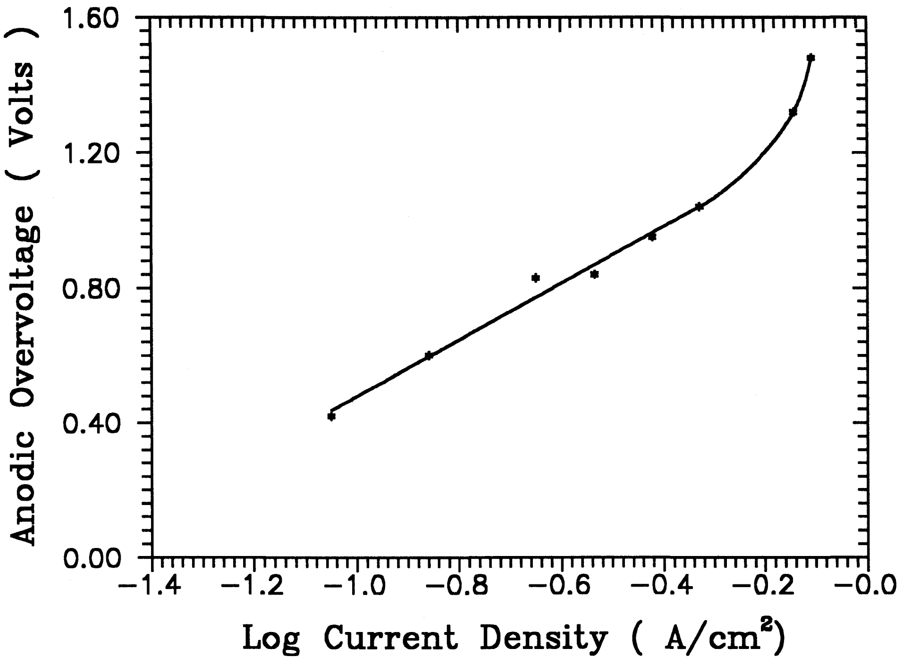

Figure 2. Log current density as a function of overvoltage on graphite during electrolysis of $LiF+CaF_2+Li_2O$ (sat.) melt at 1093 K

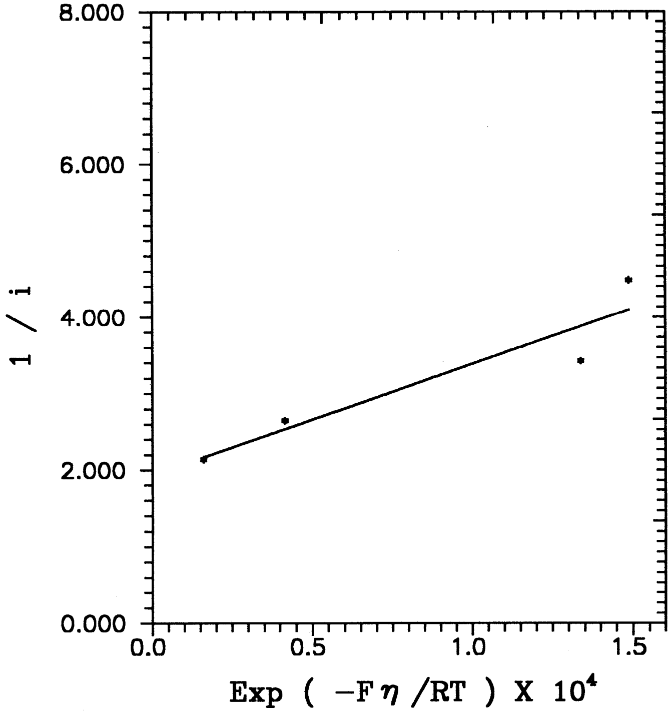

Figure 3. Current density as a function of Exp(-Fη / RT) at 1093 K

DOI: 10.1149/199413.0392PV

LITHIUM INTERCALATION INTO GRAPHITE FROM AMBIENT-TEMPERATURE MOLTEN SALTS

Michael J. Lysaght and Michael Hedenskoog
Department of Chemistry
United States Air Force Academy, Colorado 80840-6272

Richard T. Carlin and Joan Fuller
The Frank J. Seiler Research Laboratory
2354 Vandenberg Drive, Suite 2A35
United States Air Force Academy, Colorado 80840-6272

ABSTRACT

The cycling efficiency of lithium intercalation into graphite using the $AlCl_3$:EMICl:LiCl (EMICl = 1-ethyl-3-methylimidazolium chloride) molten salt was studied using staircase cyclic voltammetry and chronopotentiometry. The cycling efficiency of the Li^--graphite electrode ranges from 80 to 90% for current densities of 0.2 to 1 mA cm^{-2}. At 50 mV s^{-1}, the oxidation process occurs at a potential approximately 1 V positive of the reduction process. However, employing slower scans ($\leq$ 10 mV s^{-1}), the separation of the reduction and oxidation process decreases to only ca. 0.6 V. The lithium intercalation process is essentially identical in the related room-temperature molten salt $AlCl_3$:DMPICl:LiCl (DMPICl = 1,2-dimethyl-3-propylimidazolium chloride). In addition to lithium ion, the organic cation and $AlCl_4^-$ can also be intercalated into graphite.

INTRODUCTION

The room-temperature molten salts composed of $AlCl_3$, 1-ethyl-3-methylimidazolium chloride (EMICl), and an alkali metal chloride, particularly LiCl and NaCl, have recently been employed as electrolytes for alkali metal electrochemical investigations (1-4). These melts have several unique properties which make them promising candidates for battery electrolytes, including a wide electrochemical window, high inherent conductivity, negligible vapor pressure, high thermal stability, high alkali metal cation concentration, and low alkali metal cation solvation energies. Although it is possible to reduce and anodize elemental lithium and sodium in these melts under certain conditions, their stability is very limited due to reaction with the organic cation (1).

To avoid the problems associated with elemental lithium anodes, we have employed a graphite intercalation anode in these room-temperature molten salts. The intercalation of lithium into a graphite matrix provides a more stable and safer means for lithium utilization (5). We wish to report here the investigation of lithium electrochemistry at a graphite intercalation electrode in the imidazolium-based molten salt electrolytes. In addition, we will present results for intercalation into graphite of the other melts components, i.e., the organic cation and $AlCl_4^-$.

EXPERIMENTAL

Lithium chloride melts, $AlCl_3$:EMICl:LiCl and $AlCl_3$:DMPICl:LiCl, were prepared as previously described (2). All voltammetric experiments were performed using an EG&G PARC model 273 Potentiostat/Galvanostat controlled with the EG&G PARC 270 software package. The graphite working electrode was a high purity, spectroscopic grade graphite rod with a 3 mm diameter (Union Carbide). The glassy carbon working electrode was a 3 mm disk sealed in Kel-F (Bioanalytical Systems). The graphite rod was pretreated by drying at 400 °C for several hours in air and cooling under vacuum in the dry box antechamber. The reference electrode consisted of an Al wire immersed in a 1.5:1.0 $AlCl_3$:EMICl melt contained in a separate fritted glass tube. The counter electrode was an Al wire dipped into a portion of the analyte melt contained in a 3 mm OD, D-porosity gas dispersion tube (Ace Glass). All experiments were performed in a Vacuum Atmosphere Dry Box under He with an $O_2 + H_2O$ concentration of < 5 ppm.

RESULTS AND DISCUSSION

Lithium Intercalation into Graphite.

To make certain the electrochemical response of the graphite electrode in the presence of Li^+ was due to graphite reduction with concurrent Li^+ intercalation, a 1:1 $AlCl_3$:EMICl melt ($[Li^+] = 0$ M) and a 1.1:1.0:0.1 $AlCl_3$:EMICl:LiCl melt ($[Li^+] = 0.45$ M) were prepared. Staircase cyclic voltammograms (50 mV s^{-1}) obtained at a graphite rod electrode in these two melts are shown in Figs. 1a and 1b. It is clear that the redox process centered at -1.4 V in Fig. 1b is due to Li^+ intercalation into the reduced graphite lattice. The reduction process initiated at -1.6 V in both voltammograms is due to intercalation of EMI^+ into the reduced graphite lattice; the -1.6 V reduction potential is well positive of the potential for EMI^+ reduction at glassy carbon at ca. -2.2 V.

Integration of the cathodic and anodic currents in Fig. 1b gives a lithium cycling efficiency (anode charge/cathodic charge) of only 34%. Efficiencies up to 50% are seen for this process at higher scan rates, while lower efficiencies are obtained at slower scan rates. When the reverse scan is extended to +1.0 V, a significant second oxidation process is observed starting at -0.4 V (Fig. 2a). Chemically irreversible lithium reduction at GC is shown in Fig. 2b for comparison. Integration of the anodic current and the total cathodic current in Fig. 2a gives a lithium cycling efficiency of 80%. Slowing the scan rate to < 10 mV s^{-1}, reduces the separation of the intercalation and deintercalation process to ca. 0.6 V, and the more negative oxidation process is completely absent. This lower potential separation and the presence of only the more positive oxidation process is in agreement with the chronopotentiometric experiments discussed below. Staircase cyclic voltammograms performed in 1.1:1.0:0.1 $AlCl_3$:DMPICl:LiCl (DMPICl = 1,2-dimethyl-3-propylimidazolium chloride) show essentially identical lithium intercalation behavior as the EMICl melt. The intercalation and deintercalation of lithium ions in $AlCl_3$:DMPICl:LiCl shown in Fig. 3 at 1 mV s^{-1} illustrates the effect slow scans have on the shape of the redox process. Integration of Fig. 3 gives a cycling efficiency of 84% for lithium in the DMPICl melt.

Battery-relevant cycling efficiencies of the Li-graphite anode were obtained by collecting charge/discharge curves at constant current (double-step chronopotentiometry). Typical charge/discharge chronopotentiograms obtained at a graphite rod electrode in a 1.1:1.0:0.1 $AlCl_3$:EMICl:LiCl melt are shown in Figs. 4a and 4b, using a current density of 0.5 mA cm^{-2} for both charging and discharging. The cycling efficiency for the data in Fig. 4 is 82%. In addition, the cycling efficiency at 0.5 mA cm^{-2} with a 10 min charge remained essentially unchanged when a delay time of 10 min at open-circuit was imposed prior to discharge. Other experiments gave cycling efficiencies from 80 to 90% with 10 min charging and current densities. Using a charge/discharge current density of 0.2 mA cm^{-2} and charging times of 10 min to 2 hrs, cycling efficiencies from 70 to 90% were obtained. Importantly, the discharge potential was relatively flat and was centered around -0.35 V for all discharge curves.

Organic Cation and Tetrachloroaluminate Intercalation into Graphite

Staircase cyclic voltammograms illustrating EMI^+ reductive intercalation and $AlCl_4^-$ oxidative intercalation into graphite in the 1:1 $AlCl_3$:EMICl (no LiCl) molten salt electrolyte are shown in Fig. 5. The graphite electrochemical intercalation processes occur well within the electrochemical limits of the melt which, at GC, are found at -2.2 V and +2.5 V and correspond to EMI^+ reduction and $AlCl_4^-$ oxidation, respectively. The electrochemical process at -1.5 V (Fig. 5a) involves the intercalation and deintercalation of EMI^+ into the graphite lattice. The electrochemical process at +1.8 (Fig. 5b) probably involves the intercalation and deintercalation of $AlCl_4^-$ into the graphite lattice. Although it has been proposed that graphite oxidation in this melt involves intercalation of Cl_2 (6), the potential of the oxidative intercalation (0.6 V negative of $AlCl_4^-$ oxidation to Cl_2) and the lack of known stable chlorine intercalates points towards the formation of an $AlCl_4^-$ intercalation compound instead (7). Numerous chloroaluminate and other metal halide intercalation compounds are known (8,9).

The relevant parameters for EMI^+ and $AlCl_4^-$ intercalation, studied with chronopotentiometry, are presented in Table I. The EMI^+ cycling efficiency decreases as the time delay between charging and discharging is increased. This instability of EMI^+ may involve reaction of the relatively acidic C-2 proton with the negatively charged graphite lattice (10). This is supported by the high cycling efficiencies observed for the reductive intercalation of the $DMPI^+$ cation in which the C-2 proton has been replaced by a methyl group (11).

Because both the cation and anion of the 1:1 $AlCl_3$:EMICl molten salt can be intercalating in the same system, a battery cell can be constructed by simply inserting two graphite electrode into the melt. Charging of this cell causes oxidative intercalation of the organic cation into the graphite anode and reductive intercalation of $AlCl_4^-$ into the graphite cathode. The molten salt electrolyte provides both intercalating species, and so, we have termed this cell a Dual Intercalating Molten Electrolyte (DIME) battery. The performance of such a cell using 1:1 $AlCl_3$:EMICl as the electrolyte is summarized in Table II. Based on a comparison of cycling efficiencies in Tables I and II, it appears the instability of EMI^+ limits the performance of this DIME battery configuration. As expected, better DIME battery performance can be achieved using the $AlCl_3$:DMPICl molten salt electrolyte instead (11).

ACKNOWLEDGMENTS

This work was supported by the Air Force Office of Scientific Research.

REFERENCES

1. R. T. Carlin and C. Scordilis-Kelley, Proceedings of the Ninth International Symposium on Molten Salts, The Electrochemical Society, Pennington, N. J., 1993.
2. C. Scordilis-Kelley and R. T. Carlin, *J. Electrochem. Soc.*, **140**, 1606 (1993).
3. T. L. Riechel and J. S. Wilkes, *J. Electrochem. Soc.*, **139**, 977 (1992).
4. C. Scordilis, J. Fuller, R. T. Carlin, and J. S. Wilkes, *J. Electrochem. Soc.*, **139,** 694 (1992).

5. J. M. Tarascon and D. Guyomard, *Electrochimica Acta*, **38,** 1221 (1992).

6. P. R. Gifford and J. B. Palmisano, *J. Electrochem. Soc.*, **135,** 650 (1988).

7. H. Selig and L. B. Ebert in *Advances in. Inorganic Chemistry and Radiochemistry*, Vol 23, H. J. Emeleus and A. G. Sharpe, Editors, p. 281, Academic, Orlando (1980).

8. R. Setton, in *Graphite Intercalation Compounds I: Structure and Dynamics*, H. Zabel and S. A. Solin, Editors, p. 305, Springer Verlag, Berlin, Heidelberg, New York (1990).

9. K. Kinoshita, *Carbon, Electrochemical and Physiochemical Properties*, John Wiley and Sons, Inc., New York (1988).

10. J. L. Wong and J. H. Keck, Jr., *J. Org. Chem.*, **39,** 2398 (1974).

11. See H. C. De Long and R. T. Carlin in this proceedings volume.

Table I. Chronopotentiometric studies of EMI^+ and $AlCl_4^-$ intercalation into graphite using 1:1 $AlCl_3$:EMICl. All runs conducted at 31°C with a charging time of 30 min.

Intercalating Ion	I_{charge} (mA cm^{-2})	E_{charge} (V)	$I_{discharge}$ (mA cm^{-2})	$E_{discharge}$ (V)	Time Delay	Efficiency %
$AlCl_4^-$	1	+2.01	1	+1.64	N/A	68
$AlCl_4^-$	1	+1.97	0.5	+1.64	N/A	79
$AlCl_4^-$	1	+1.95	0.25	+1.65	N/A	79
EMI^+	1	-1.72	1	-1.49	N/A	48
EMI^+	1	-1.72	0.5	-1.51	N/A	49
EMI^+	1	-1.73	0.25	-1.52	N/A	57
EMI^+	1	-1.73	0.25	-1.51	30 min	51
EMI^+	1	-1.73	0.25	-1.44	4 hr's	29
EMI^+	1	-1.73	0.25	-1.27	10.5 hr's	2

Table II. Performance parameters for a Dual Intercalating Molten Electrolyte (DIME) battery cell. All runs conducted at 31°C with a charging time of 30 min.

E_{open} (V)	I_{charge} (mAcm^{-2})	E_{charge} (V)	$I_{discharge}$ (mAcm^{-2})	$E_{discharge}$ (V)	Time Delay	Efficiency %
-3.14	1	-3.69	1	-3.15	N/A	63
-3.36	1	-3.76	0.5	-3.14	N/A	60
-3.23	1	-3.71	0.25	-3.25	N/A	61
-2.87	1	-3.70	1	-3.12	30 min	62
-2.62	1	-3.70	1	-2.80	4.3 hr's	27
-3.05	1	-3.71	1	-2.80	6.1 hr's	25
----	1	-3.70	1	-1.40	17.5 hr's	0

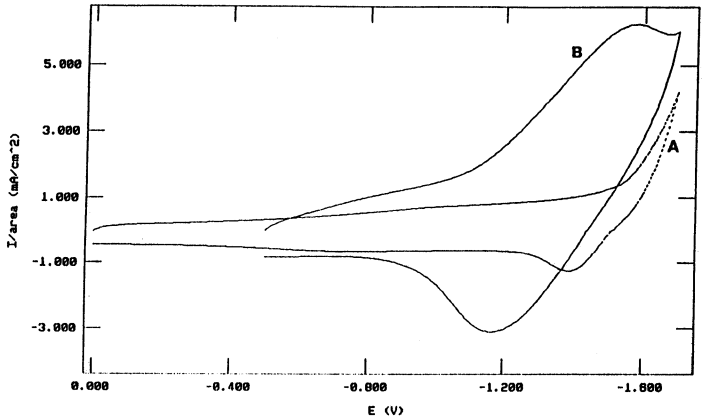

Fig. 1. Staircase cyclic voltammograms at a graphite rod in (a) 1:1 $AlCl_3$:EMICl melt an (b) 1.1:1.0:0.1 $AlCl_3$:EMICl:LiCl melt, $[Li^+]$ = 0.45 M. Scan rate = 50 mV s^{-1}.

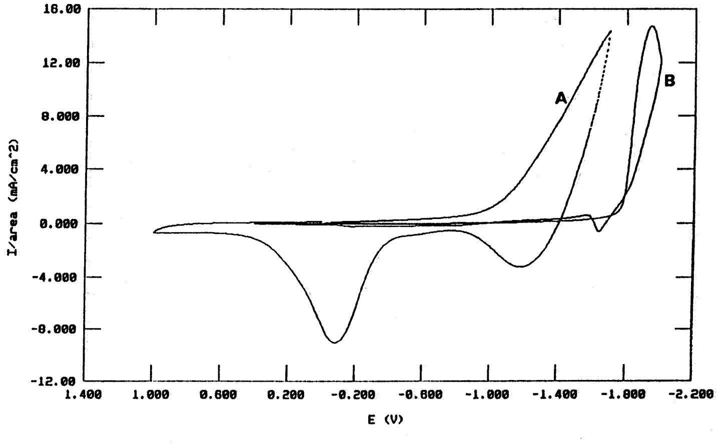

Fig. 2. Staircase cyclic voltammograms at (a) a graphite rod and (b) a glassy carbon disk in 1.1:1.0:0.1 $AlCl_3$:EMICl:LiCl melt. Scan rate = 50 mV s^{-1}.

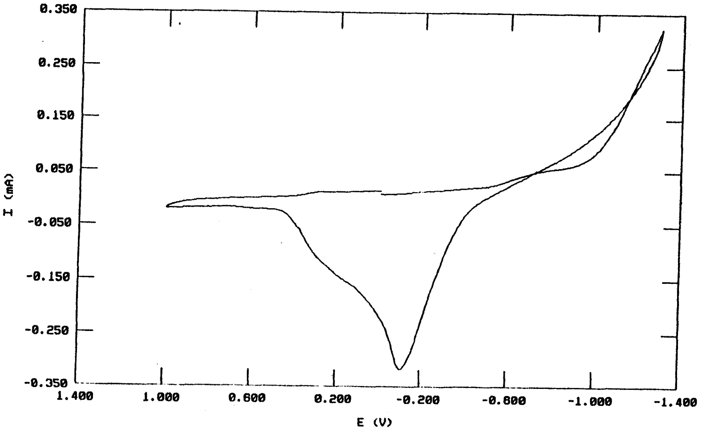

Fig. 3. Staircase cyclic voltammogram in 1.1:1.0:0.1 AlCl$_3$:DMPICl:LiCl showing lithium intercalation/deintercalation at 1 mV s^{-1}.

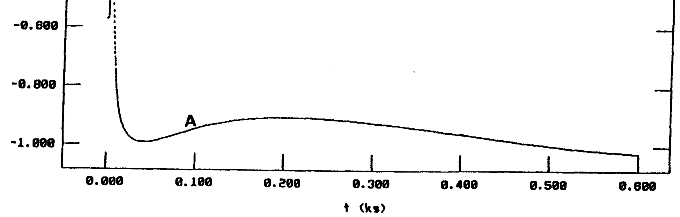

Fig. 4. Chronopotentiometric (a) charge and (b) discharge curves for a lithium-graphite rod electrode in 1.1:1.0:0.1 AlCl$_3$:EMICl:LiCl melt. Current density is 0.5 mA cm^{-2} for both charging and discharging.

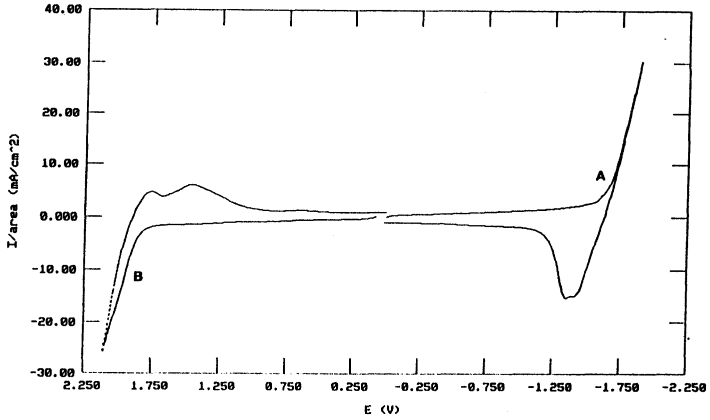

Fig. 5. Staircase cyclic voltammograms at graphite in 1:1 $AlCl_3$:EMICl showing (a) reductive intercalation of EMI^+ and (b) oxidative intercalation of $AlCl_4^-$; scan rate = 50 mV s^{-1}.

DOI: 10.1149/199413.0400PV

THE ELECTRODEPOSITION OF COPPER AND NICKEL IN THE ACIDIC ROOM-TEMPERATURE ALUMINUM CHLORIDE-1-METHYL-3-ETHYLIMIDAZOLIUM CHLORIDE MOLTEN SALT

William R. Pitner and Charles L. Hussey
Department of Chemistry
University of Mississippi
University, MS 38677

ABSTRACT

The electrodeposition of copper and nickel was investigated at polycrystalline platinum, gold, and tungsten and at glassy carbon electrodes in the acidic 66.7-33.3 mole percent aluminum chloride-1-methyl-3-ethylimidazolium chloride molten salt. The electrodeposition of these metals at platinum and gold is complicated by underpotential deposition phenomena whereas the electrodeposition of these metals at glassy carbon and tungsten requires a significant nucleation overpotential. Dimensionless experimental current-time transients recorded at glassy carbon and tungsten are in good agreement with theoretical models based on three-dimensional nucleation with diffusion-controlled growth of the nuclei. The reduction of nickel(II) on nickel in this molten salt appears to involve the concurrent formation of a soluble nickel species.

INTRODUCTION

A family of room-temperature melts is obtained when aluminum chloride is mixed with the quaternary ammonium chloride salt 1-methyl-3-ethylimidazolium chloride (MeEtimCl) (1). For a review of room-temperature chloroaluminate melts see ref. 2. The Lewis acidity of this molten salt system can be varied over a wide range by simply altering the ratio of $AlCl_3$ to MeEtimCl. Melts that contain a molar excess of aluminum chloride are acidic whereas melts that contain an excess of the organic salt are basic. In this article, the melt composition is expressed as the mole percent (m/o) of $AlCl_3$ present in the $AlCl_3$-MeEtimCl mixture.

The acidic $AlCl_3$-MeEtimCl molten salt possesses several chemical and physical properties that make it attractive for use as an electroplating bath and as an electrolyte for the electrochemical polishing and etching of metals: (*i.*) it is a good solvent for simple inorganic metal ions, and large concentrations of these ions can be introduced into the melt by anodic dissolution of the respective metal; (*ii.*) it exhibits good chemical stability, and it can be heated to ca. 150 °C for several hours without undergoing appreciable decomposition; (*iii.*) it exhibits negligible vapor pressure at elevated temperatures; (*iv.*) it is liquid at room temperature over a wide range of composition; (*v.*) it exhibits high intrinsic electrical conductivity; (*vi.*) it is miscible in large proportions with a variety of common organic solvents; (*vii.*) it can be rendered virtually proton-free, precluding the co-deposition of hydrogen during the metal deposition process; and (*viii.*) most M^{z+}/M electrochemical reactions are rapid in this melt.

The electrodeposition of copper (3,4) and nickel (5) from solutions of copper(I) and nickel(II) in the acidic room-temperature chloroaluminates has been reported. However, few details were given about the fundamental aspects of the electrodeposition of these metals such as the nucleation mechanism. In addition, these previous investigations were restricted to only a single substrate, namely glassy carbon. In this article, we describe recent results for the electrodeposition of copper and nickel on polycrystalline gold, platinum, and tungsten, and on glassy carbon.

EXPERIMENTAL

Apparatus

Electrochemical experiments were conducted with an EG & G PARC Model 173 potentiostat/galvanostat and Model 179 digital coulometer plug-in module. Voltammetric waveforms were supplied with a PARC Model 175 universal programmer. Data were recorded on a Linseis Model 1600 X-Y/Y-t recorder. A Pine Instruments model AFMSR electrode rotator was used during rotating disk electrode (RDE) voltammetry experiments. Electronic resistance compensation was employed during all experiments except controlled potential electrolysis.

The electrochemical cell for these experiments was a small Pyrex cup with a tapered bottom fitted with a Teflon lid. The reference and counter electrodes consisted of an aluminum-wire spiral immersed in pure 66.7 m/o $AlCl_3$-MeEtimCl melt contained inside a Pyrex tube that was sealed at one end with a fine-porosity fritted disk. These electrodes were inserted into the bulk melt through a hole in the Teflon cell cap. Teflon sheathed glassy carbon, gold, platinum, and tungsten rotating disk electrodes (geometrical area = 0.196 cm^2) were purchased from Pine Instruments, Grove City, PA. The former electrode was constructed from Tokai grade GC-20S glassy carbon, and the latter three were fabricated from the polycrystalline metals (Wilkinson, 99.9%+). Although these electrodes were received in a polished condition, they were polished further prior to each experiment with an aqueous slurry of 0.05 µm alumina using a Buehler Metaserv grinder/polisher. These electrodes were conditioned electrochemically before and after each voltammetric scan or current-time transient was recorded by holding the electrode potential at the positive potential limit of the melt for about one minute. This pretreatment procedure improved the reproducibility of these measurements. Copper and nickel electrodes were constructed from 1.0 mm diameter copper (Johnson-Matthey, 99.999%) and nickel (Johnson-Matthey, 99.9945%) wires. These wires were lightly polished with emery cloth, washed with copious amount of dry acetone, and dried in vacuo before use.

Due to the moisture-sensitive nature of the $AlCl_3$-MeEtimCl melt, all experiments were conducted in a dry N_2 atmosphere inside a Kewaunee Scientific Equipment Corp. glove box equipped with a 30 ft^3/min inert gas purifier. The quality of the glove-box atmosphere was monitored by observing the lifetime of a 25-W incandescent light bulb with an exposed filament (6).

Chemicals

The procedures used for the preparation and purification of the $AlCl_3$-MeEtimCl molten salt have been described previously (1); freshly distilled 1-methylimidazole (Aldrich, 99%+) is combined with excess of chloroethane (Linde Specialty Gases) in a glass pressure vessel and allowed to react for about 3 days at 60 °C. The resulting MeEtimCl was purified by precipitation from acetonitrile solutions with ethyl acetate. Aluminum(III) chloride (Fluka, >99%) was purified by vacuum sublimation. The purified $AlCl_3$ and MeEtimCl were then combined slowly to produce a melt with the desired molar ratio (66.7 m/o $AlCl_3$). The resulting melt was purified by electrolysis between two aluminum electrodes. In addition, the melt was evacuated to $< 1 \times 10^{-3}$ torr for 24 hr before use in order to remove protonic impurities.

RESULTS AND DISCUSSION

Copper

Copper(I) was introduced into the 66.7 m/o $AlCl_3$-MeEtimCl melt by the controlled potential coulometric oxidation of a copper wire electrode at an applied potential, E_{app}, of 0.71 V. To ensure that copper(I) was the anodization product, the weight loss of the copper electrode was determined after the passage of a known charge. These results confirmed that copper(I) is indeed the anodization product. A plot of the equilibrium potential, E_{eq}, of the Cu(I)/Cu couple versus the molar concentration of copper(I) indicated that the formal potential of this couple is 0.789 ± 0.003 V versus the Al(III)/Al couple in the 66.7 m/o melt at 40 °C.

Reduction of Copper(I) at Glassy Carbon and Tungsten. The electrodeposition of copper was studied at glassy carbon and tungsten in acidic melt containing various amounts of copper(I). Some examples of the cyclic voltammograms of copper(I) that were recorded at these electrodes are shown in Fig. 1. These voltammograms exhibit a current cross-over on the reverse scan, indicating a nucleation rate-controlled deposition process (7). In order to probe the nucleation mechanism taking place at these electrodes, chronoamperometric experiments were carried out by stepping the electrode potential from 1.0 V to a value sufficiently negative to initiate the formation of copper nuclei after a delay time of only a few seconds. The final potential was typically equal to or less than 0.30 V at glassy carbon and 0.65 V at tungsten. Examples of the current-time transients resulting from these potential-step experiments are shown in Fig. 2. Each transient exhibits a double layer charging current spike, which occurs as the potential step is applied. This current spike is followed by a rising current indicating the formation and growth of copper nuclei on the electrode surface. The rising current reaches a maximum, i_M, as the individual diffusion zones of the growing nuclei merge. The time at which the current maximum is observed, t_M, depends on the magnitude of the potential step; t_M decreases as the applied potential is made more negative.

Models involving three-dimensional (3-D) nucleation with hemispherical diffusion-controlled growth of the nuclei (8,9) were found to be appropriate to describe the nucleation process occurring during the electrodeposition of copper(I) at both glassy carbon and tungsten. The two limiting cases for 3-D nucleation with hemispherical diffusion-controlled growth correspond to instantaneous nucleation, i.e., rapid nucleation on a limited number of active sites, and progressive nucleation or slow nucleation on a large number of active sites. The best method for differentiating between these models is to compare the experimental current-time transients to the dimensionless theoretical transients for each nucleation mechanism. These theoretical transients can be generated from the following equation (10)

$$(i/i_M)^2 = (t/t_M)^{-1}\{1 - \exp[-xt/t_M + \alpha(1 - \exp(-xt/t_M\alpha))]\}^2/$$
$$\{1 - \exp[-x + \alpha(1 - \exp(-x/\alpha))]\}^2 \qquad [1]$$

In this expression, α and x are adjustable parameters that contain information concerning the number density of active sites for nucleation, N_o, and the nucleation rate constant per active site, A. For the limiting cases of instantaneous and progressive nucleation, α tends to 0 and ∞, respectively, while the x approaches 1.2564 and 2.3367, respectively (9,10). In this case, the limiting forms of Eq. [1] become

$$(i/i_M)^2 = 1.9542(t/t_M)^{-1}\{1 - \exp[-1.2564(t/t_M)]\}^2 \qquad [2]$$

$$(i/i_M)^2 = 1.2254(t/t_M)^{-1}\{1 - \exp[-2.3367(t/t_M)^2]\}^2 \qquad [3]$$

for instantaneous and progressive nucleation, respectively. In Fig. 3, plots of $(i/i_M)^2$ versus t/t_M generated from Eq. [2] and [3] are compared to the experimental current-time data shown in Fig. 2. It is clear from Fig. 3 that the electrodeposition of copper on both glassy carbon and tungsten involves a 3-D progressive nucleation process with hemispherical diffusion-controlled growth of the nuclei.

Reduction of Copper(I) at Platinum and Gold. - Cyclic voltammograms for the electrodeposition and stripping of copper at platinum and gold stationary electrodes from solutions of copper(I) in acidic melt are shown in Fig. 4. Prior to the bulk deposition wave, these voltammograms exhibit small "pre-waves" which have oxidation counterparts. These waves are most apparent when the voltammetric scan is reversed before the bulk reduction wave is traversed and are attributed to the underpotential deposition and stripping of copper on these electrodes.

Further investigations of the copper deposition process at these electrodes were carried out by recording voltammograms at gold and platinum rotating disk electrodes (RDE). These RDE voltammograms, shown in Fig. 5, display a well-defined limiting current. A Levich plot was constructed from a series of RDE voltammograms taken at different angular velocities. The slope of this plot yielded a diffusion coefficient for copper(I) of 7.25 ± 0.03 x 10^{-7} cm^2 sec^{-1}.

Nickel

Nickel(II) was introduced into the melt by anodic dissolution of a nickel wire electrode at E_{app} = 0.85 V. The weight lost by this electrode after the passage of a known charge confirmed that nickel(II) was the oxidation product. The intercept of a Nernst plot gave $E^{o\prime}$ = 0.910 ± 0.003 V versus Al(III)/Al in the 66.7 m/o melt at 40 °C.

Reduction of Nickel(II) at Glassy Carbon. The electrodeposition of nickel was studied at a glassy carbon electrode in acidic melt containing various amounts of nickel(II). Cyclic stationary and RDE voltammograms of nickel(II) at glassy carbon are shown in Fig. 6. These voltammograms exhibit a current cross-over on the reverse scan similar to that seen for copper at glassy carbon and tungsten electrodes. In order to investigate the nucleation mechanism associated with the electrodeposition of nickel on glassy carbon, a series of chronoamperometric experiments was carried out similar to those described above for copper. In these experiments, it was necessary to step the electrode potential from 1.0 V to less than 0.5 V in order to induce the nucleation of nickel. Examples of the experimental current-time transients resulting from these potential-step experiments are shown in Fig. 7a. In Fig. 7b, plots of $(i/i_M)^2$ versus t/t_M calculated from Eq. [2] and [3] are compared to the experimental current-time data shown in Fig 7a. It can be seen that the experimental data fall between the two limiting models. However, it is possible to fit the experimental data to Eq. [1] by adjusting α and x; the best fit is obtained for $\alpha = 0.55$ and $x = 2.22$. The applicability of Eq. [1] in this case indicates that the electrodeposition of nickel on glassy carbon involves progressive nucleation on a finite number of active sites (9,10).

Reduction of Nickel(II) at Platinum and Gold. Cyclic stationary and RDE voltammograms for the electrodeposition and stripping of nickel at gold and platinum electrodes from solutions of nickel(II) in acidic melt are shown in Figs. 8 and 9, respectively. From the appearance of these voltammograms, it is obvious that the electrodeposition of nickel on gold and platinum involves processes not found during the electrodeposition of this metal on glassy carbon (Fig. 6). For example, small UPD waves can be seen prior to the bulk deposition waves in these voltammograms. These small waves are similar to those seen during the electrodeposition of copper at these same electrodes (Fig. 4). In addition, three oxidation waves are associated with the stripping of the nickel deposit from gold and platinum as opposed to two waves at glassy carbon.

An unusual feature of the stationary electrode voltammograms shown in Fig. 8 is the oxidation wave appearing at ca. 0.60 V at gold and 0.55 V at platinum. Although somewhat less distinct, this wave can also be seen at about 0.65 V at glassy carbon (Fig. 6a). This wave is only present if the electrode potential is scanned more negative than ca. 0.35 V. A similar wave was noted by Gale *et al.* (5) during the electrodeposition of nickel on glassy carbon, and it was attributed to the stripping of a co-deposited nickel-aluminum alloy. However, this explanation seems unlikely because this wave is absent if the electrode is rotated (Figs. 6b and 9), indicating that this wave arises from the oxidation of a soluble species produced in the electrode diffusion layer during the reduction of nickel(II) and not from the stripping of an insoluble electrode deposit. Controlled potential electrolysis experiments were carried out in which nickel was electrodeposited on a small platinum flag at $E_{app} = 0.10$ V. The resulting nickel deposit adhered strongly to the platinum surface. From these experiments, it was found that the weight of the deposited nickel was only 65 % of the expected weight based on the charge passed during the experiment. Similar experiments at the same E_{app} with the same batch of molten salt without nickel(II) did not produce a significant reduction current. In addition, experiments involving the electrodeposition of copper always produced a deposit with the expected mass. Therefore, we conclude that the reduction of nickel(II) involves the concurrent formation of a soluble nickel species. Furthermore, it appears that this nickel species is only produced in detectable amounts after the electrode surface is covered with electrodeposited nickel metal. The identity of this species has not been established; however, numerous nickel(I) species are known, especially complexes containing phosphine ligands (11). Further investigations into the identity of this soluble species as well as the deposition and stripping of copper and nickel are in progress.

ACKNOWLEDGEMENT

This research was sponsored by the National Science Foundation through Grant No. CHE-9016632.

REFERENCES

1. J. S. Wilkes, J. A. Levisky, R. A. Wilson, and C. L. Hussey, *Inorg. Chem.*, **21**, 1263 (1982).

2. R. A. Osteryoung in *Molten Salt Chemistry: An Introduction and Selected Applications*, NATO ASI Series C: Mathematical and Physical Sciences, Vol. 202, G. Mamantov and R. Marassi, Editors, p. 329, Reidel, Dordrecht (1987).

3. C. L. Hussey, L. A. King, and R. A. Carpio, *J. Electrochem. Soc.*, **126**, 1029 (1979).

4. C. Nanjundiah and R. A. Osteryoung, *J. Electrochem. Soc.*, **130**, 1312 (1983).

5. R. J. Gale, B. Gilbert, and R. Osteryoung, *Inorg. Chem.*, **18**, 2723 (1979).

6. I. D. Eubanks and F. J. Abbott, *Anal. Chem.*, **41**, 1708 (1969).

7. R. Greef, R. Peat, L. M. Peter, D. Pletcher, and J. Robinson, *Instrumental Methods in Electrochemistry*, p. 211, Ellis Horwood, Chichester (1985).

8. B. Scharifker and G. Hills, *Electrochim. Acta*, **28**, 879 (1983).

9. B. R. Scharifker and J. Mostany, *J. Electroanal. Chem.*, **177**, 13 (1984).

10. V. Tsakova and A. Milchev, *J. Electroanal. Chem.*, **235**, 237 (1987).

11. F. A. Cotton and G. Wilkinson, *Advanced Inorganic Chemistry*, 5th Edition, p. 754, Wiley, New York (1988).

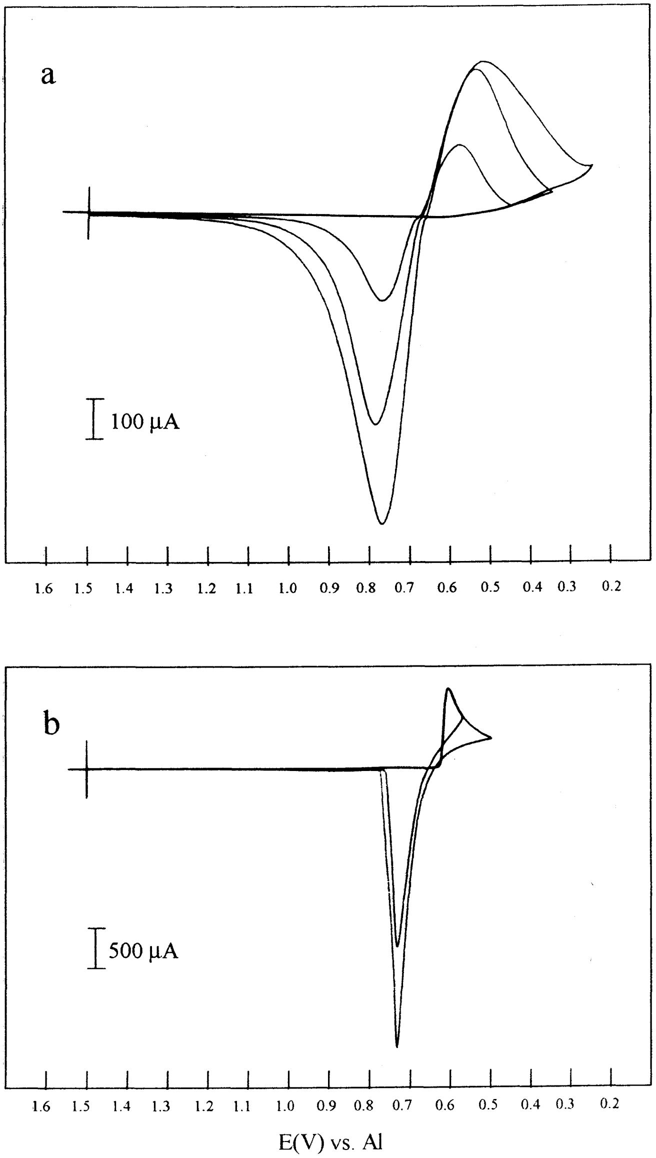

Fig. 1. Cyclic voltammograms of a 15.0 mM solution of Cu(I) in the 66.7 m/o melt at different switching potentials: (a) glassy carbon and (b) tungsten electrodes. The sweep rates were 0.050 V s^{-1}, and the temperatures were 40 °C.

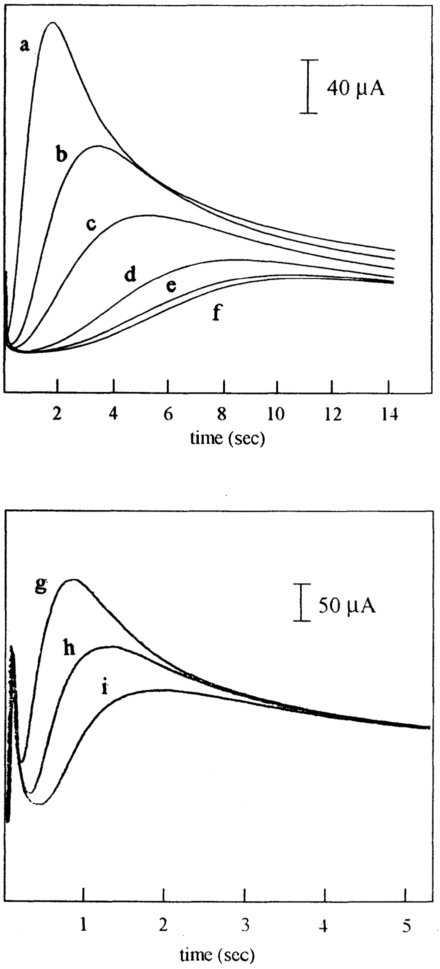

Fig. 2. Current-time transients for the deposition of Cu from a 15.0 mM solution of Cu(I) in the 66.7 m/o melt on glassy carbon (a-f) and tungsten (g-i) electrodes at 40 °C recorded at these potentials: (a) 0.180, (b) 0.200, (c) 0.220, (d) 0.240, (3) 0.260, (f) 0.300, (g) 0.580, (h) 0.600, and (i) 0.610 V.

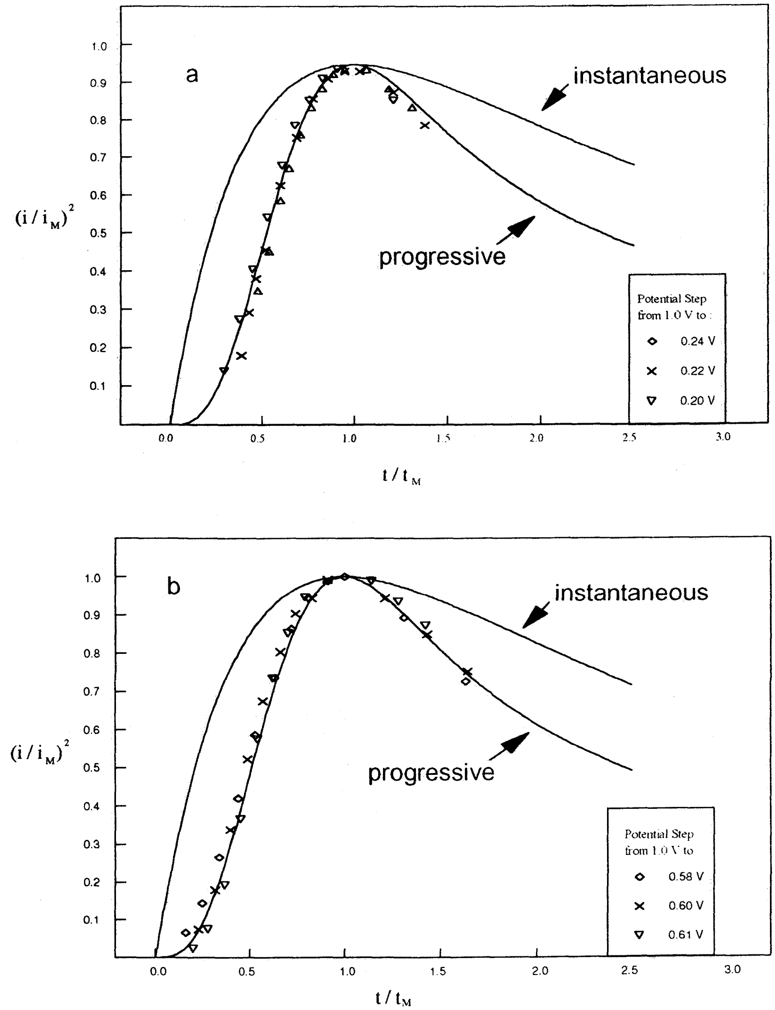

Fig. 3. Comparison of the theoretical models for three-dimensional instantaneous and progressive nucleation having hemispherical diffusion-controlled growth (solid lines) with the dimensionless experimental data derived from the current-time transients shown in Fig. 2: (a) glassy carbon and (b) tungsten electrodes.

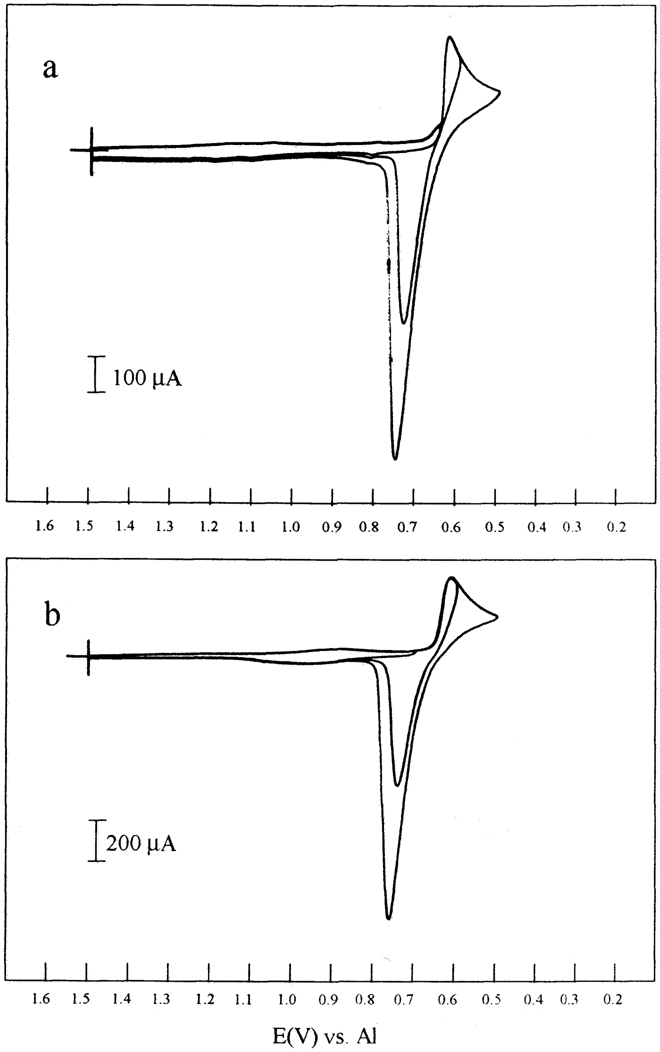

Fig. 4. Cyclic voltammograms of a 15.0 mM solution of Cu(I) in the 66.7 m/o melt at different switching potentials: (a) gold and (b) platinum electrodes. The sweep rates were 0.050 V s^{-1}, and the temperatures were 40 °C.

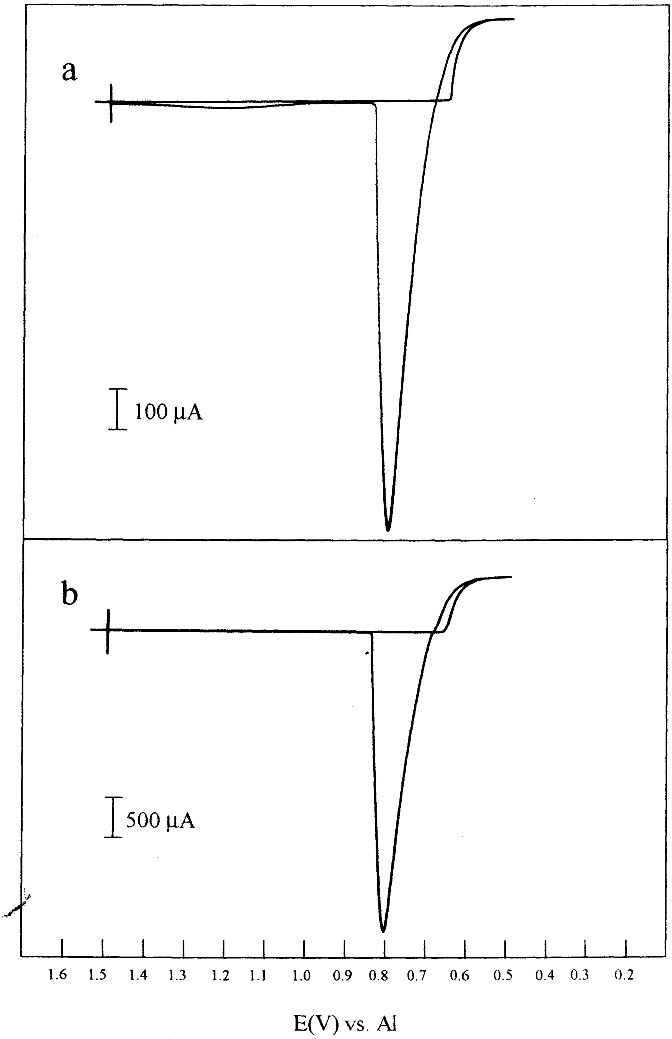

Fig. 5. Rotating disk electrode voltammograms of a 15.0 mM solution of Cu(I) in the 66.7 m/o melt: (a) gold and (b) platinum electrodes. The sweep rates were 0.005 V s^{-1}, the electrode rotation rates were 210 rad s^{-1}, and the temperatures were 40 °C.

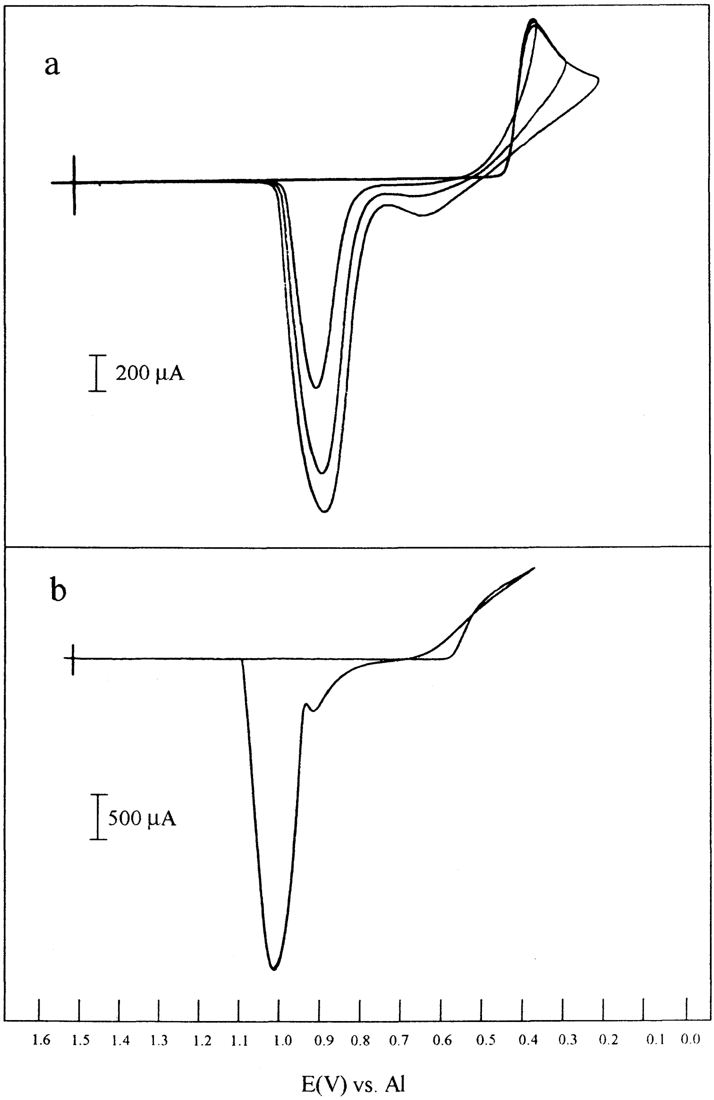

Fig. 6. Voltammograms of solutions of 15.0 mM Ni(II) in the 66.7 m/o melt recorded at glassy carbon electrodes: (a) Stationary electrode at a sweep rate of 0.050 V s^{-1} and different switching potentials and (b) RDE at a sweep rate of 0.005 V s^{-1} and a rotation rate of 210 rad s^{-1}. The temperatures were 40 °C.

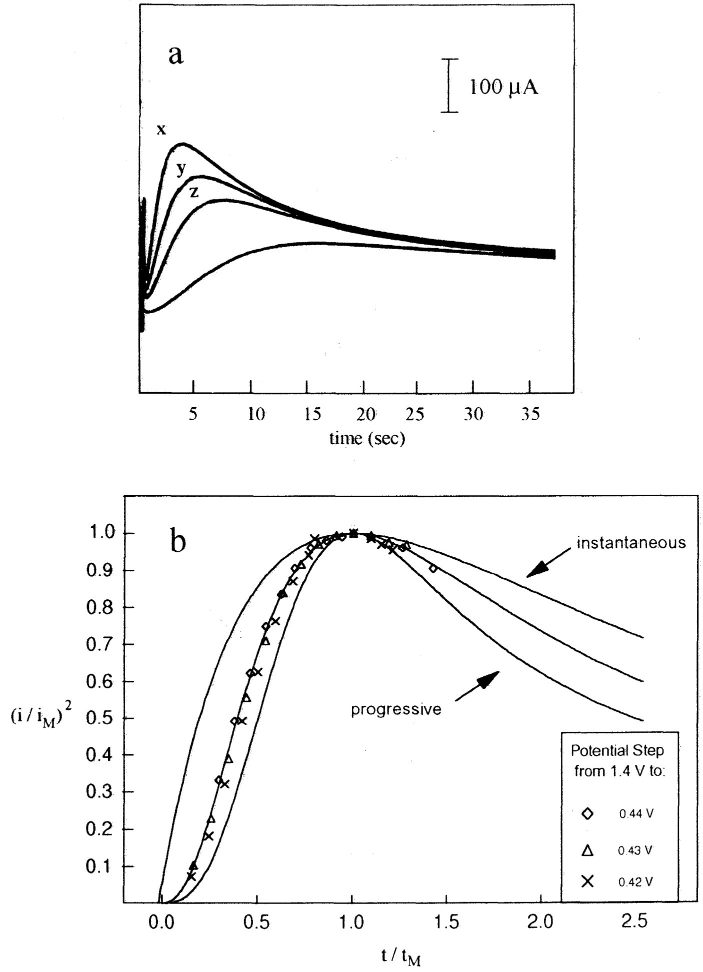

Fig. 7. (a) Current-time transients for the deposition Ni from a 15.0 mM solution of Ni(II) in the 66.7 m/o melt on glassy carbon electrodes at 40 °C recorded at these potentials: x = 0.420 V, y = 0.430 V, and z = 0.440 V. (b) Comparison of the theoretical models for nucleation with the dimensionless experimental data derived from the current-time transients in (a). The line through the data in (b) was calculated from Eq. 1 with $\alpha = 0.55$ and $x = 2.22$.

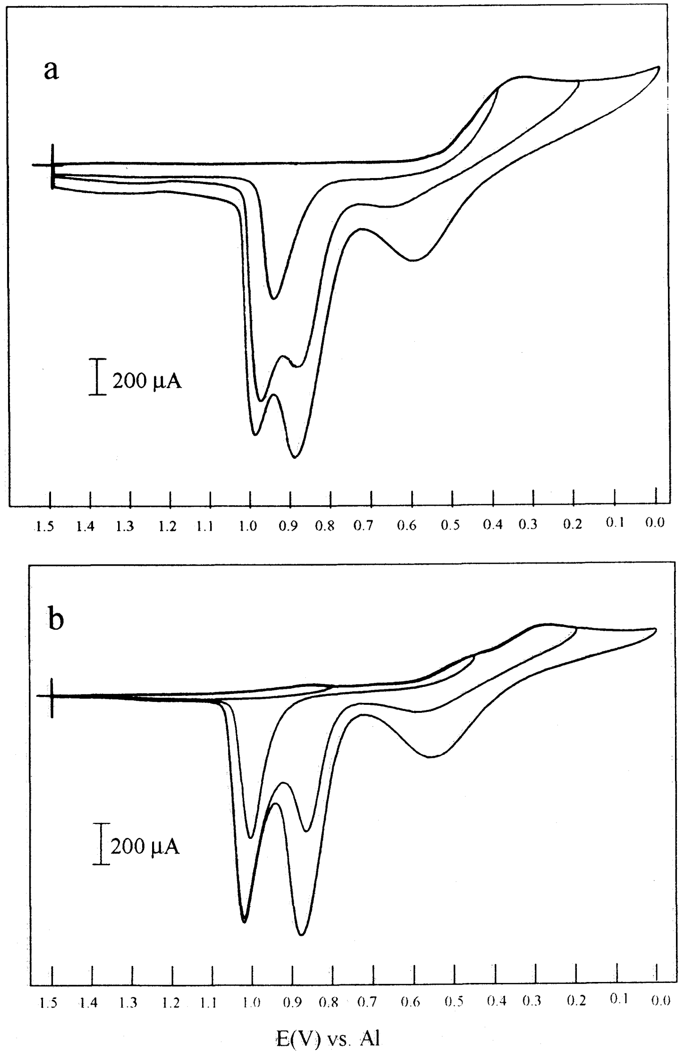

Fig. 8. Cyclic voltammograms of a 15.0 mM solution of Ni(II) in the 66.7 m/o melt at different switching potentials: (a) gold and (b) platinum electrodes. The sweep rates were 0.050 V s^{-1}, and the temperatures were 40 °C.

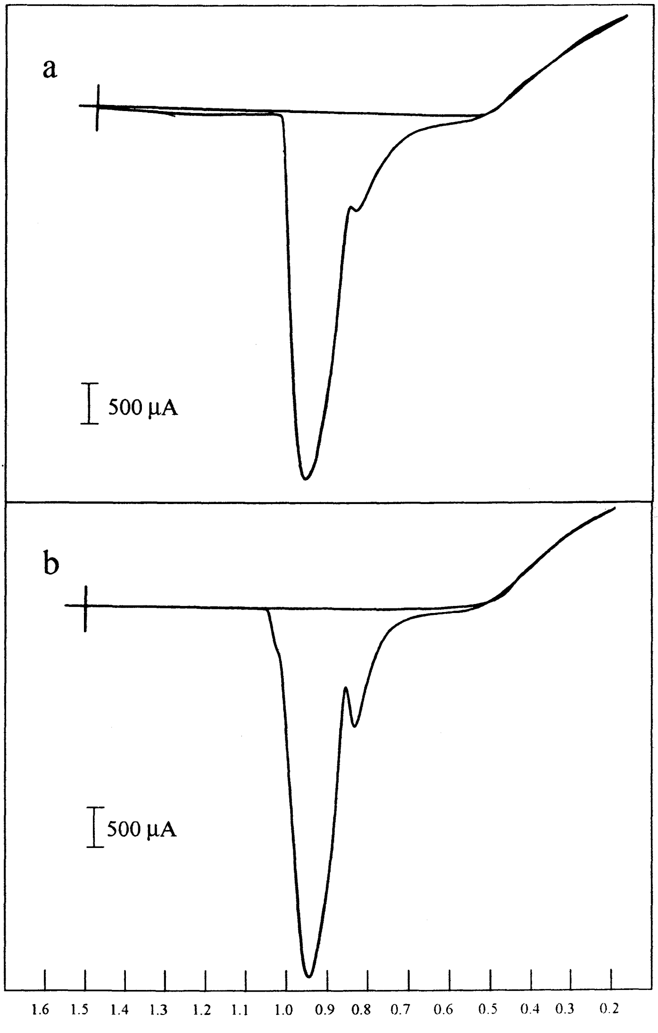

Fig. 9. Rotating disk electrode voltammograms of a 15.0 mM solution of Ni(II) in the 66.7 m/o melt: (a) gold and (b) platinum electrodes. The sweep rates were 0.005 V s^{-1}, the electrode rotation rates were 210 rad s^{-1}, and the temperatures were 40 °C.

DOI: 10.1149/199413.0415PV

ELECTROCHEMISTRY OF LITHIUM IN ROOM TEMPERATURE MOLTEN SALT ELECTROLYTES

Bernard J. Piersma
Houghton College
Houghton, New York 14744

ABSTRACT

The demonstration of a stable reversible lithium anode is an important step in the development of practical secondary batteries using room temperature chloroaluminate melts as electrolytes. Riechel and Wilkes found that proton added to a sodium chloride buffered melt as ethylmethylimidazolium hydrogen dichloride provides a more negative voltage window and nearly reversible deposition-stripping behavior for sodium when proper proton concentration is maintained. While $EMIHCl_2$ is a proven proton source and is also effective for lithium deposition-stripping behavior, its stability in the melt is limited with HCl being lost relatively rapidly into the vapor phase. We have explored many possible alternatives and have found triethanolamine•hydrogen chloride to be an effective proton source with good stability in the melt. This paper presents our studies of lithium deposited on tungsten in proton rich lithium chloride buffered neutral melts.

INTRODUCTION

Room temperature molten salts formed by mixing 1—ethyl—3—methylimidazolium chloride (EMIC) with aluminum chloride have been intensively studied, particularly by Wilkes and coworkers at FJSRL, for more than a decade with the goal of developing high energy density batteries. Alkali metals have high oxidation-reduction potentials and relatively low atomic masses making them very attractive candidates as battery anodes. Lithium is of particular interest because it has the highest electricity storage density of the active metals.

The Lewis acid-base behavior of these melts has a substantial influence on their physical and electrochemical properties. Melt acidity is easily ascertained electrochemically since Al deposition only occurs from acidic melts and the melt window is significantly greater in neutral melts than in either basic or acidic melts. Because of the wide electrochemical window it is desirable to work with a melt which is exactly neutral but, as with most acid-base systems, maintaining neutrality is not easily achieved unless the system is buffered. The use of sodium chloride to buffer the melt to neutral composition has been demonstrated by Wilkes, et.al.(1) More recently it was found that proton added to the melt as 1—ethyl—3—methylimidazolium hydrogen dichloride

($EMIHCl_2$) provides a more negative voltage window and nearly reversible deposition-stripping behavior of sodium when proper proton concentration is maintained.(2) We initially studied lithium chloride-buffered neutral melts by first removing protonic impurity (resulting from contamination by H_2O during synthesis and purification of EMIC) with ethylaluminum dichloride. By adding proper amounts of $EMIHCl_2$ nearly reversible deposition-stripping behavior of lithium could be observed at tungsten electrodes.

While $EMIHCl_2$ is a proven proton source, its stability in the melt is limited with HCl being lost into the vapor phase relatively rapidly in an open system. We investigated many possible alternative proton sources and found triethanolamine • hydrogen chloride (TEOA • HCl) to be an effective source. TEOA • HCl is electrochemically stable within the melt window, except for proton reduction which is expected, and maintains a stable proton concentration in the neutral melt for times two orders of magnitude greater than that obtained with $EMIHCl_2$. Proton enrichment of the melt with TEOA • HCl has been very successful in bringing a lithium chloride buffered melt to exactly neutral acidity which prevents aluminum deposition and stripping and in extending the cathodic limit of the melt but has not provided the desired stability of deposited Li in the melt. We have made some attempts to understand the role of added protons (or HCl) in the observed electrochemistry of lithium in the melt. In addition we have initiated a study of LiAl alloys in these melts and this is being continued.

EXPERIMENTAL

All experimental work was performed with materials and electrochemical cell contained a Vacuum Atmospheres dry box system with a helium atmosphere. Electrochemical measurements were accomplished with an EG & G Princeton Applied Research (PAR) Model 263 Potentiostat/Galvanostat interfaced with an IBM 486 personal computer using EG & G PAR 270 software and a Hewlett Packard plotter model HP 7475A. A three-electrode arrangement in a single compartment cell used a molybdenum foil counter electrode and Bioanalytical System (BAS) working electrodes of platinum, tungsten, or glassy carbon. Most of the work reported here was obtained with tungsten working electrodes. The reference electrode was an Al wire in 0.60 EMIC/$AlCl_3$ melt contained in a pyrex glass tube constructed with an asbestos tip to provide solution contact.

Components for the melt were synthesized and purified following the procedures developed by Wilkes and coworkers at FJSRL. LiCl was dried for a minimum of 10 days in a vacuum oven at 130°C. The many compounds tested for improving proton stability in the melts were used as obtained from Johnson-Matthey or Aldrich. These included in addition to the triethanolamine • hydrogen chloride, a number of mono —, di — and tri — substituted amine • hydrogen chlorides, LiH and $LiAlH_4$. In general the purity of melt components and additives were tested by preparing exactly neutral melts and observing the melt window using cyclic voltammetry.

An acidic melt (0.55 mole fraction of $AlCl_3$) was prepared by adding the amount of $AlCl_3$ calculated to give the desired composition to an exactly neutral melt which had been treated with ethylaluminum dichloride. Then LiCl was added (with a calculated 25% excess) to buffer the melt back to neutral. LiCl was found to dissolve much more slowly than NaCl, requiring several days with occasional heating to 50°C for attainment of a neutral melt. Neutrality of this melt was demonstrated by the absence of Al deposition and stripping during a cyclic voltammetric scan. In a slightly acidic melt Al deposition could be observed at a cathodic potential approximately one volt more negative than in 0.55 melt. This Al deposition and stripping could be observed in buffered melts even after several days (up to 5 days) of stirring with LiCl in the melt. As with NaCl, LiCl was found to be insoluble in basic melt and all attempts to buffer a melt to neutral from the basic side with LiCl were unsuccessful.

RESULTS AND DISCUSSION

The buffered melt remained slightly acidic even after seven days of stirring with excess LiCl, similar to the observed behavior of NaCl buffered melts reported by Riechel and Wilkes.(3) The cyclic voltammograms presented in this report were recorded at a sweep rate of 100 mV/sec using a W working electrode. Al deposition occurs at about -0.90 V and stripping at about -0.191 V (depending on melt acidity). The potential for Al deposition in this melt is more cathodic than the potential for the same process in more acidic melts by almost one volt. The Al stripping in this melt occurred at a potential that was reported for a corresponding NaCl buffered melt having an $AlCl_3$ mole fraction of 0.5002,(3) suggesting that the LiCl buffered melt has a composition between 0.501 and exactly neutral. The deposition of Li at -1.6 V, significantly changes the Al stripping behavior.

In the search for a stable proton source three criteria were used:

1) the electrochemical stability of the proton source, no redox reaction within the electrochemical window of the melt, except for the desired proton reduction.
2) essentially reversible deposition-stripping behavior of lithium (nearly 100% cycling efficiency) which is reproducible without cleaning the electrode.
3) relatively constant proton content of the melt over a period of several days.

Of the ten compounds selected and tested as potential proton sources, only triethanolamine•hydrogen chloride satisfied our three criteria.

As background for our discussion, Fig. 1a shows CV behavior, at a W working electrode, for an exactly neutral melt and Fig. 1b for LiCl-buffered melt, representing typical CV behavior and showing the melt limits with a window of about 4.0 volts. Behavior in a LiCl-buffered melt which is near to but not exactly neutral is further seen in Fig. 2 with cathodic sweep limits of -1.80 V (Fig. 2a) and -2.7 V (Fig. 2b). Al deposition is clearly evident at about -1.0 V but the stripping, clearly seen in curve b at about 0.0V is significantly altered by Li deposition which occurs at about -1.7 V.

Figure 3 presents representative CV data for the addition of triethanolamine•hydrogen chloride to LiCl-buffered melt. Fig. 3a is for 0.10 M TEOA•HCl showing the deposition of Li but very little stripping. The cathodic sweep limit is -2.5 V. Figs. 3 b-d are for 0.20 M TEOA•HCl added to LiCl buffered melt showing essentially reversible deposition-stripping behavior for Li as a function of cathodic sweep limit, which are respectively (Fig. 3b), -2.20 V, (Fig. 3c) -2.5O V, and (Fig. 3d) -2.80 V. This series of CV curves shows clearly that when the proton concentration is maintained at the proper level (in this case 0.20 M) the Li deposition-stripping behavior or cycle efficiency is not dependent on the cathodic sweep limit. We also note that no Al deposition is observed indicating that the melt composition is exactly neutral.

The following summarizes the important cyclic voltammetric characteristics for 0.2 M TEOA•HCl in LiCl buffered melt:

For sweep rates from 10 mV/sec to 1 V/sec and cathodic sweep limits from 2.40 V to -2.90 V:
Li deposition begins at -2.15 ± 0.02 V
Li deposition peak at -2.40 ± 0.15 V
Li stripping peak at -1.85 ± 0.15 V
Cycle efficiency 0.74 ± 0.10

These results are comparable with those obtained using $EMIHCl_2$ as a proton source in LiCl-buffered neutral melt.

CONCLUSIONS

1. We have found that triethanolamine•hydrogen chloride provides a better proton source than ethylmethylimidazolium hydrogen dichloride with stability in the melts studied measured in weeks rather than hours.

2. Nearly reversible deposition-stripping of lithium is obtained in LiCl-buffered melts when the TEOA•HCl concentration is between about 0.20 and 0.225 M. It does not appear however, that the Li deposit on W is stable in this system.

3. The protective film which has been reported to form on Li does not form on the Li deposits under conditions in our melts where reversible deposition-stripping behavior is observed. The brown films which we observe with proton concentrations below the minimum concentration of 0.20 M may possibly be identified with the lithium oxide or lithium hydroxide films reported by other groups. The increased proton concentration appears to be related to the lack of this film formation and to the reversible deposition-stripping behavior.

4. The white precipitate formed when sufficient $EMIHCl_2$ or TEOA•HCl is added to provide reversible deposition-stripping behavior has been identified as $LiAlCl_4$.

REFERENCES

1. Melton, T.J., Joyce, J., Maloy, J.T., Boon, J.A. and Wilkes, J.S., J. Electrochem. Soc. 137, 3865 (1990)

2. Riechel, T.L. and Wilkes, J.S., J. Electrochem. Soc. 139, 977 (1992)

3. Riechel, T.L. and Wilkes, J.S., J. Electrochem. Soc. 140, 3104 (1993)

ACKNOWLEDGEMENT

We are pleased to acknowledge support of this work by the Air Force Office of Scientific Research, Bolling AFB, D.C.

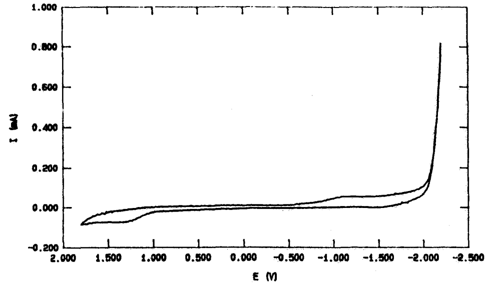

Fig. 1a Neutral Melt

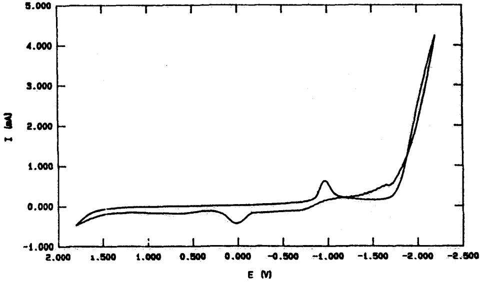

Fig. 1b LiCl-buffered melt

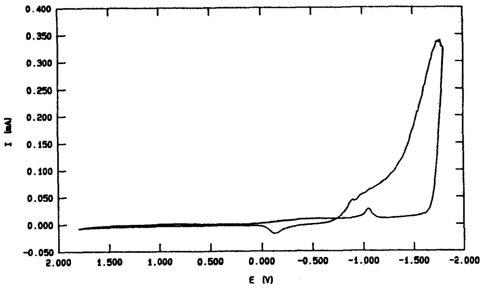

Fig. 2a LiCl-buffered melt, sweep to -1.8 V

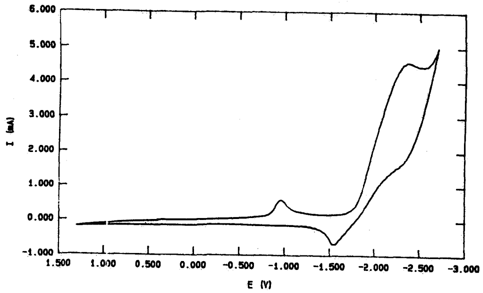

Fig. 2b LiCl-buffered melt, sweep to -2.7 V

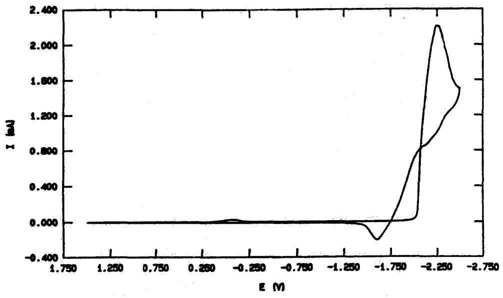

Fig. 3a 0.1 M TEOA • HCl, sweep to -2.5 V

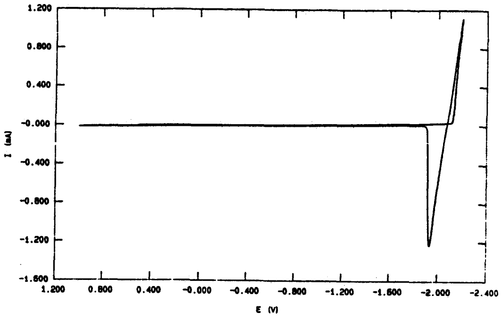

Fig. 3b 0.2 M TEOA • HCl, sweep to -2.2 V

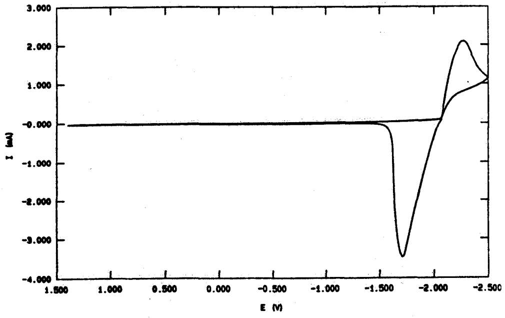

Fig. 3c 0.2 M TEOA • HCl, sweep to -2.5 V

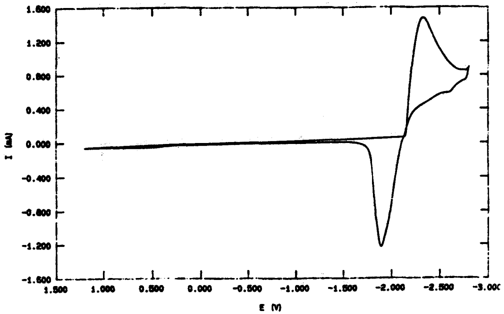

Fig. 3d 0.2 M TEOA • HCl, sweep to -2.8 V

DOI: 10.1149/199413.0422PV

ELECTRODEPOSITION OF ALUMINUM-CHROMIUM ALLOY FROM AMBIENT TEMPERATURE MELT

M. Matsunaga, T. Kitazaki, and K. Hosokawa
Department of Applied Chemistry, Faculty of Engineering,
Kyushu Institute of Technology,
1-1 Sensui-cho, Tobata, Kitakyushu 804, Japan

S. Hirano and M. Yoshida
Yawata R & D Laboratory, Nippon Steel Corp.
1-1 Tobihata-cho, Tobata-ku, Kitakyushu 804, Japan

ABSTRACT

The electrodeposition of aluminum-chromium alloy has been studied in the $AlCl_3$-EMICl (1-ethyl-3-methylimidazolium chloride) melt containing $CrCl_2$. No clear wave for the deposition of pure chromium is observed by voltammetric methods. The deposits always contain both aluminum and chromium, while the chromium deposition is preferred at low overpotential. The chromium content in the deposit increases by the use of the rotating disk electrode.

INTRODUCTION

The mixtures of aluminum chloride ($AlCl_3$) and 1-ethyl-3-methylimidazolium chloride (EMICl) are promising ambient temperature molten salts, since their wide electrochemical window suggests high potential for several applications such as electroplating, high energy density batteries and the medium for chemical reactions. Among them the ambient temperature melts are good solvents for the electroplating of aluminum (1,2) and its alloy such as Al-Ti (3).

Since aluminum and chromium have corrosion resistance, there is a possibility that the alloy of these metals will possess the high resistance to corrosion. It is, however, quite difficult to electroplate this alloy at room temperature. In the present study we discuss the electroplating of aluminum-chromium alloys to develop the new corrosion-resisting coating on the steel surface.

EXPERIMENTAL

The $AlCl_3$ was sublimed through a glass frit after melted with 1 wt% sodium chloride with 5N pure aluminum metal for one day at 478 K. The EMICl was recrystallized three times from a mixture of acetonitrile and ethylacetate, and washed with anhydrous ethylacetate. The purified EMICl was dried under vacuum for one day at 343 K before the mixing with $AlCl_3$. The mixture of purified $AlCl_3$ and EMICl was digested for a few days with the aluminum metal. The 3N pure $CrCl_2$ was used as received.

Vitreous carbon rod was used as working electrodes for the voltammetric studies. Nickel flag and steel flag electrodes were used to determine the composition of deposits. A nickel rotating disk electrode was also used to study the influence of the melt flow. The counter electrode was 5N pure aluminum foil. The reference electrode was a 5N pure aluminum wire which was separated from the main compartment by a fine glass frit.

The Al–Cr alloy was deposited by galvanostatic and potentiostatic methods with commercially available electrochemical instrumentation (Hokuto Denko Models HA-501 and HB–105). The films of deposited alloys were dissolved in hydrochloric acid to determine the composition by the inductively coupled plasma and atomic absorption spectroscopies. The current efficiency was determined by comparing the amount of each component in the deposits with the charge passed during the deposition. The deposits were also analyzed by X–ray photoelectron spectroscopy (XPS) with JEOL JPX–90SX. All measurements were done in a glove box filled with nitrogen of high purity.

RESULTS AND DISCUSSION

Figure 1 shows the differential pulse polarography measured in a 2/1 $AlCl_3$–EMICl melt with 8.1 mmol/kg $CrCl_2$. No clear cathodic wave for the deposition of pure chromium is observed in the potential range nobler than the aluminum deposition. The addition of $CrCl_2$ causes only the cathodic shift of the deposition potential of aluminum. The shift of deposition potential is also observed by other voltammetric methods.

Figure 2 depicts the composition of the alloy film obtained by potentiostatic method. The deposits always contain both aluminum and chromium. At the potentials more positive than –50 mV, the chromium content in deposits is higher than that of aluminum, which indicates the deposition of chromium is preferred. the coulombic efficiency for the alloy deposition is quite low at this potential region, which is caused by the poor adherence of deposits or the reduction of impurities. The question then arises about the deposition potential of aluminum and chromium. Although no clear current of the chromium deposition is observed in voltammetric curves as shown in Fig. 1, chromium can mainly deposit at low overpotential. What has to be noticed is the shift of the deposition potential of aluminum by the addition of $CrCl_2$ into the melt, even if its concentration is quite low. This potential shift may be important to demonstrate the mechanism on the Al–Cr alloy deposition, while we have little clear information by now.

The coulombic efficiency for the deposition of the alloy approaches 100% with cathodic overpotential, where the chromium content in the deposits becomes quite low. As shown in Fig. 3, the partial current density for the chromium deposition becomes the diffusion limited values with current density. Because of the low concentration of $CrCl_2$ in the melt, the diffusion limited current density is low, which results in low chromium content in the deposits. Therefore, the rotating disk electrode was used to increase the content of chromium in deposits. In Fig. 3 typical composition of the deposits obtained with the rotating disk electrode are also shown. By comparing these results with the deposits without the electrolyte flow, it is clear that the partial current densities for the chromium deposition becomes high with rotating the electrode. On the other hand, the partial current densities for aluminum deposition vary little, because of the high concentration of $Al_2Cl_7^-$ ion in the acidic melt. We may, therefore, reasonably conclude that the composition of the Al–Cr deposit can be controlled by the flow rate of the melt. Moreover, the use of the rotating disk electrode improves the surface morphology of deposits. The effect of the chromium content in the deposit on the corrosion-resistance is now studied.

CONCLUSION

The aluminum–chromium alloy can be electroplated from the $AlCl_3$–EMICl melt containing $CrCl_2$, although no pure chromium can be obtained. The deposition of chromium is preferred at low overpotential, which relates to the cathodic shift of the deposition potential of aluminum. The chromium content in the deposit can be controlled by an increase in the flow rate of the melt.

REFERENCES

1. S. Takahashi, *Denki Kagaku*, **59**, 14 (1991)
2. S. Takahashi, I. Saeki, and K. Akimoto, *J. Surf. Finish. Soc. Japan,* **40**, 548 (1989)
3. T. Takenaka, A. Hoshikawa, and M. Kawakami, in "Proceedings of the International Symposium on Molten Salt Chemistry and Technology 1993," M.-L. Saboungi and

H. Kojima, Editors, PV 93-9, pp. 184-192, The Electrochemical Society, Pennington, NJ (1993)

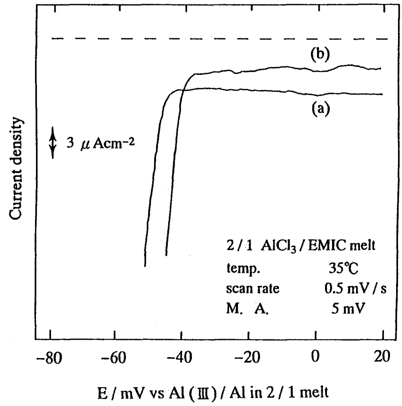

Fig. 1 Differential pulse polarograms on a vitreous carbon electrode (0.07 cm^2) at 308 K for the melt (a) with 8.1 mmol/kg $CrCl_2$ and (b) without $CrCl_2$.

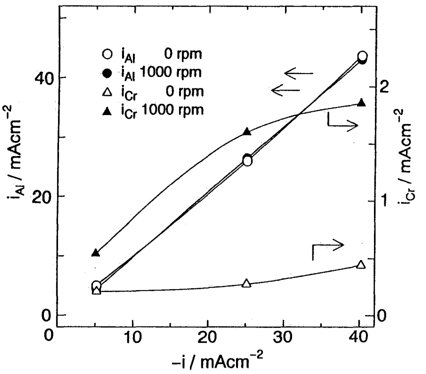

Fig. 3 Effects of electrolyte flow on the partial current densities.

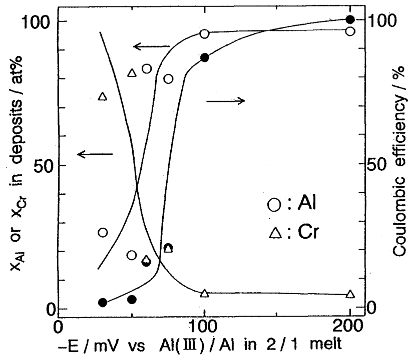

Fig. 2 Composition of the deposits and coulumbic efficiency by potentiostatic method.

DOI: 10.1149/199413.0426PV

PROTON DONOR CHARACTERISTICS OF A ROOM-TEMPERATURE MOLTEN SALT

Graham T. Cheek
Julie A. Spencer

Chemistry Department, Stop 9b
United States Naval Academy
572 Holloway Road
Annapolis MD 21402-5026

ABSTRACT

Evidence has been obtained that the ring protons of 1-ethyl-3-methylimidazolium chloride (EMIC) can act as proton donors towards electrochemically generated bases in the aluminum chloride : EMIC molten salt. Reduction of benzophenone in the deuterated (2 position of EMIC) basic melt yields benzhydrol deuterated at the carbinol carbon, showing that the intermediate carbanion is basic enough to be protonated by the EMI cation. Anthracene undergoes a two-electron reduction in the basic melt, giving dideuterioanthracene. Considering that both benzophenone and anthracene can be reversibly reduced in one-electron processes in acetonitrile, these results indicate that the $AlCl_3$: EMIC melt environment is considerably more acidic than are conventional solvents such as acetonitrile.

INTRODUCTION

The aluminum chloride : 1-ethyl-3-methylimidazolium chloride (EMIC) molten salt system has proved to be a useful medium in which to carry out electrochemical reductions of organic compounds (1,2,3). In the basic melt, which is composed of a molar excess of EMIC, the melt species are the EMI cation and chloride and tetrachloroaluminate anions. The attractive feature of this melt regime is that the negative potential limit, determined by EMI cation reduction (-2.3 V vs 2:1 $AlCl_3$: EMIC reference electrode), is sufficiently negative to allow the reduction of aromatic ketones (1,2). Upon studying the reduction of several ketones in this melt, it has become evident that the reduction products are often protonated as they are generated in the melt. The chemistry of protons resulting from trace amounts of water in the melt components has been thoroughly explored, and methods are available for virtually complete removal of these protons (4). The protonation of the reduction products must, then, be due to the EMI cation. Considering that the imidazolium ring system is known to possess ring protons of considerable acidity (5), it was decided to investigate the proton-donating ability of the melt system towards several representative electrogenerated bases.

EXPERIMENTAL

Molten salt components were prepared according to standard procedures (4), all operations being carried out in a Vacuum Atmospheres glovebox. Protonic impurities in the basic melts, in which most of the present work was carried out, were removed by placing the melt under high vacuum at 65-70°C. The proton level was assessed by voltammetry at a platinum electrode and was found to be in the 0.3 - 0.5 mM range. Deuterated EMIC (2 position; 2-d-EMIC) was prepared by dissolving EMIC in D_2O for three days (5). Melts prepared from 2-d-EMIC were purified by the same vacuum treatment as used for EMIC-based melts.

Voltammetric experiments were carried out using a PAR 174A Voltammetric Analyzer, with a Bioanalytical Systems CV-27 unit for potential scan waveforms. Voltammograms were taken at vitreous carbon electrodes (Tokai GC-30, 3 mm diameter, sealed in Pyrex). Preparative scale electrolyses were carried out in vitreous carbon crucibles (Atomergic Chemetals Corp.) with a PARC 273 Electrochemical Analyzer.

Following preparative electrolysis, the melt was generally extracted with hexane (previously distilled over sodium) to obtain neutral products, after which the melt was hydrolyzed over ice and extracted with benzene to remove other products. Product determination was carried out primarily by GC/MS (HP 5988A and HP 5890/5971A) and HPLC (C18 column, methanol/water eluent) methods.

RESULTS AND DISCUSSION

Benzophenone

Benzophenone was chosen as a system for investigation because of the variety of possible anionic products formed during its reduction. Acid/base interactions between these anions and the EMI ring were expected to be manifested by the formation of protonated products. In the basic melt, benzophenone is reduced in a single process (Figure 1), giving tetraphenyloxirane (10-15%, isolated in the hexane extract) and benzhydrol (85-90%, from hydrolysis/benzene extract). The coulometric value of 1.7 - 1.8 agrees with the product yields, considering that these products are formed in one and two-electron processes, respectively. The nature of these products suggests the initial formation of the ketyl (anion radical) which, as in the acidic melt, very quickly undergoes complexation of the oxygen by chloroaluminate (Figure 2). Further reactions of this species are very rapid, the anodic process for ketyl oxidation back to benzophenone being observed only at scan rates above 10 V/s. Coupling of two ketyl species leads to oxirane formation, whereas further reduction produces the alcohol (benzhydrol) which exists in the melt as the complexed anion (Figure 2) and must be isolated after melt hydrolysis.

The isolation of benzhydrol from the basic melt poses the question of whether the protonation (uptake of 2 protons) occurs in the melt during reduction or during the workup procedure. The O-H bond is evidently formed during workup because the product exists as the complexed anion in the melt and is therefore not extracted into hexane, gaining the proton during addition of water to the melt. The carbanion, however, is much more basic than the oxygen anion, suggesting the possibility that the proton is donated in the melt by the EMI cation. This is entirely reasonable given the rather great acidity of the proton on the 2 position of the EMI ring (5). When the reduction of benzophenone is carried out in a basic melt composed of 2-d-EMIC, the mass spectrum (Figure 3) contains a peak one mass unit higher (185) than that seen for benzhydrol (184), showing conclusively that the carbanion in this system abstracts hydrogen from the EMI cation. A close look at the spectra reveals that there appears to be a considerable amount of benzhydrol in the product from the deuterated melt, judging from the sizeable signal at 184. This peak could arise from a M-1 process from the deuterated product; however, the corresponding process for benzydrol (upper spectrum) seems to be a rather minor one. Assuming that the fragmentation pathways of the protio and deuterio analogs of benzyhdrol are the same, this finding indicates that the EMI cation also supplies protons from the 4 and 5 positions. These positions, although not as acidic as that in the 2 position, are still acidic enough to exchange with D_2O at elevated temperatures (5) and probably play a minor role in protonating the benzhydrol carbanion.

Anthracene

The reduction of anthracene has also been extensively studied in nonaqueous systems, providing another system (aromatic anions) for comparison of proton-accepting ability.

In acetonitrile/0.1 M TEAP, anthracene undergoes a reversible one-electron reduction; however, the two-electron reduction (dianion) is irreversible due to protonation of the dianion formed in the second step. In the EMIC-based melt, anthracene reduction occurs in a single step, two-electron process (Figure 4). This behavior implies that the anion radical undergoes protonation by the melt, leading to ECEC behavior in which the chemical steps are protonations. The product isolated from a preparative electrolysis of 20 mM anthracene (hexane extraction) is dihydroanthracene in good yield. This level of product formation, in the absence of protonic impurities, is by itself good evidence for protonation of reduction products by the EMI cation. In addition, the reduction product isolated from the deuterated melt (2-d-EMIC) gives dideuterioanthracene as seen by mass spectrometry.

Triphenylmethyl chloride

Reduction of triphenylmethyl chloride (trityl chloride) in the basic melt produces triphenylmethane in a two-electron process. The process involves the cleavage of the C-Cl bond to form the trityl radical, which is then reduced to the trityl anion. Once again, carrying out the reduction in the deuterated melt gave the deuterated analog (m/z 245). As in the case of benzophenone, there was an appreciable response for the protio analog at m/z 244, again suggesting that protons in the 4 and 5 EMI ring positions are capable of some proton donation under these conditions.

CONCLUSIONS

Generation of carbanionic species in the $AlCl_3$: EMIC molten salt has demonstrated that the EMIC ring system is capable of donating protons to these species. An estimate for the pK_a of the proton on the 2 position of the EMIC ring can be made considering its facile exchange with D_2O. It appears that the pK_a for the EMIC proton is similar to the value of 15.7 for the H_2O/OH^- system (6). Complete exchange occurs in an environment containing somewhat more than a ten-fold molar excess of D_2O, producing an estimate (upper limit) of 17 for the pK_a of the 2 proton of EMIC. This value is given some support by the fact that protonation of the anthracene anion radical occurs in the melt, whereas this species is not protonated in anthracene, which has a pK_a of 25 [aqueous scale, (6)]. The trityl anion is much more basic [pK_a 32, (6)] and is expected to be protonated in the melt.

REFERENCES

1. G.T. Cheek, in Seventh International Symposium on Molten Salts, C.L. Hussey, J.S. Wilkes, S.N. Flengas, and Y. Ito, Editors, PV 90-17, p. 325, The Electrochemical Society Softbound Proceedings Series, Pennington, NJ (1990).

2. G.T. Cheek, in Eighth Internation Symposium on Molten Salts, R.J. Gale, G. Blomgren, and H. Kojima, PV 92-16, p. 426, The Electrochemical Society Softbound Prodeedings Series, Pennington, NJ (1992).

3. J.E. Coffield, G. Mamantov, S.P. Zingg, G.P. Smith, and A.C. Buchanan, III, J. Electrochem. Soc., 139, 355 (1992).

4. M.A.M. Noel, P.C. Trulove, and R.A. Osteryoung, Anal. Chem., 63, 2892 (1991).

5. K.M. Dieter, C.J. Dymek, Jr., N.E. Heimer, J.W. Rovang, and J.S. Wilkes, J. Am. Chem. Soc., 110, 2722 (1988).

6. J. March, Advanced Organic Chemistry, Fourth Edition, Chapter 8, Wiley-Interscience, New York, (1992).

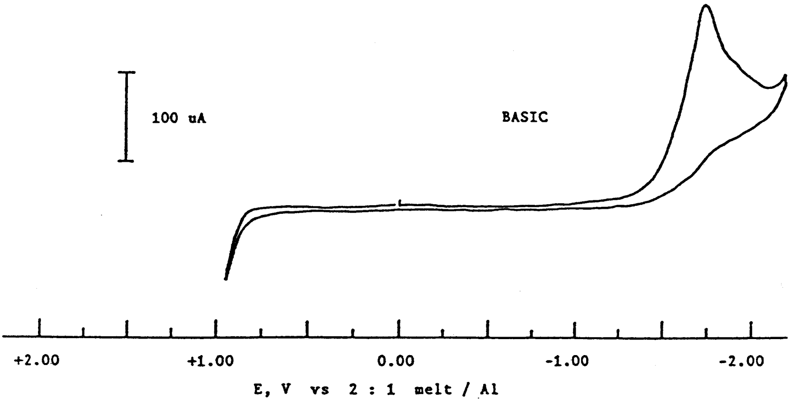

Figure 1. Cyclic voltammogram of benzophenone in basic melt (0.8 : 1.0)
Conditions: 31 mM, 100 mV/s, temperature = 40°C

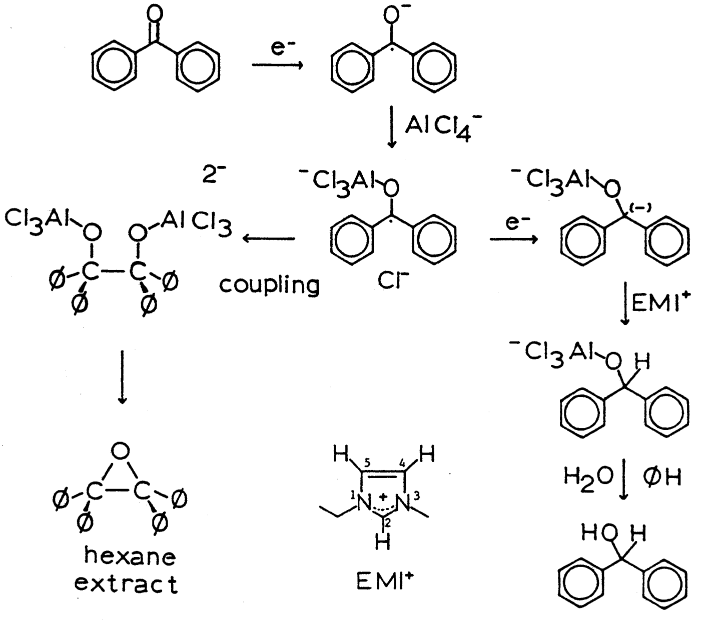

Figure 2. Mechanistic pathway for benzophenone reduction in basic melt

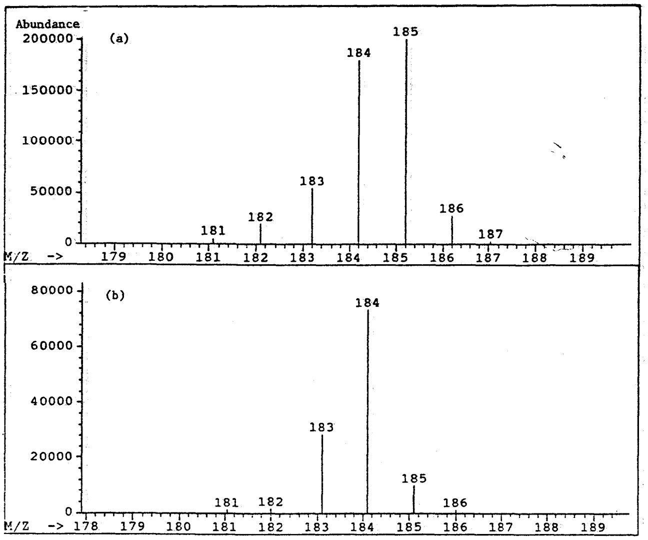

Figure 3. Mass spectra in the molecular ion region for
(a) benzophenone reduction product in 2-d-EMIC-based melt
(b) benzhydrol

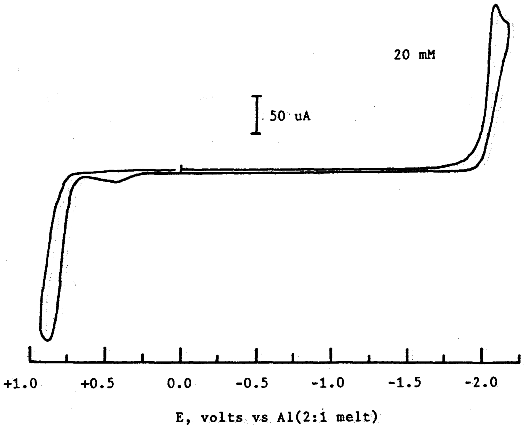

Figure 4. Cyclic voltammogram of anthracene in basic melt (0.8 : 1.0)
Conditions: 20 mM, 100 mV/s, temperature = 40°C

DOI: 10.1149/199413.0433PV

ANODIC BEHAVIOR IN THE PRODUCTION OF Al-Li ALLOY USING Li_2CO_3 IN LiCl MELT

Yuzuru Sato, *Sakae Saito, Hongmin Zhu, Mamoru Endo
and Tsutomu Yamamura
Department of Metallurgy, Faculty of Engineering,
Tohoku University, Sendai 980, Japan.
*Institute for Materials Research, Tohoku University, Sendai 980, Japan.

ABSTRACT

Al-Li alloy is a promising structural material due to its low density and high strength. For producing the alloy, a new molten salt electrolysis process was adopted. Since the cathodic reaction, which is lithium deposition into molten aluminum, had already been studied, the anodic reaction was studied by using Li_2CO_3, which is relatively inexpensive and non-hygroscopic, as a source of lithium and a graphite anode. Carbonate is confined to the anode compartment made of porous Al_2O_3 to avoid the reaction of CO_3^{2-} with the alloy. Using Li_2CO_3 does not affect the cathodic behavior and the anodic potential decreases almost 1V. The principal anodic exhaust is preferably CO_2. It was found that CO_3^{2-} also reacted with carbon non-electrochemically if excess Cl_2 was near the anode. In this work, it was confirmed that Li_2CO_3 has many advantages in the electrolytic production of Al-Li alloy.

INTRODUCTION

Aluminum alloy containing lithium is a very promising material in the field of metallurgy due to its lightness and strength. Therefore, the use of Al-Li alloy as a practical structural material is being developed. However, it is not so easy to produce the alloy by using conventional metallurgically mixing processes because lithium is very active chemically and its density is only one fifth that of aluminum. Several of us have introduced a new production process, molten salt electrolysis, and found that it is very effective in producing the alloy$^{1)}$. In the earlier study, the cathodic behavior of Al-Li alloy was studied in chloride melts containing LiCl. The effects of impurities, such as NaCl and KCl, on the contamination of the alloy by sodium and potassium and current efficiencies of the electrolysis were studied. Those results showed that lithium is cathodically deposited into molten aluminum in molten LiCl with a high current efficiency and the alloy obtained is very clean metallurgically. Addition of NaCl into the electrolyte causes a slight decrease in the current efficiency and some contamination by sodium of the alloy obtained. The effect of KCl is only to decrease current efficiency; no contamination by potassium was found. These effects are only observed when large amounts of NaCl and KCl are added to the electrolyte. Therefore, pure industrial grade LiCl is satisfactory as the electrolyte for producing metallurgically acceptable Al-Li alloy.

In this work, we planned to use Li_2CO_3 as a source of lithium. The reasons why Li_2CO_3 was chosen as a source of lithium were as follows. Li_2CO_3 is inexpensive and if it is the only source of lithium used, then the cost for producing Al-Li alloy is expected to be reduced. Li_2CO_3 is very pure in general and easily handled because it is non-hygroscopic. The potential needed for electrowinning lithium is also expected to be reduced by using a carbon anode. Therefore, using Li_2CO_3 as a source of lithium is considered to be very attractive for producing Al-Li alloy.

When using Li_2CO_3, the process is more complex compared with using LiCl for producing the Al-Li alloy. Fortunately, Li_2CO_3 is expected to dissolve into LiCl easily according to the phase diagram$^{2)}$, and CO_3^{2-} oxidizes the Al-Li alloy very easily and decreases the current efficiency due to its strong oxidative property if it reaches the molten alloy. The refore, Li_2CO_3 should be limited to the area around the anode. In this work, an anode compartment was set up to separate Li_2CO_3 from the cathode compartment and the anodic behavior of CO_3^{2-} was studied electrochemically. Furthermore, the current efficiency was determined in order to know how well this process worked.

EXPERIMENTAL

The apparatus used is shown in Fig. 1. This apparatus contains separate anode and cathode compartments. The molten aluminum cathode is put into a porous MgO crucible which is immersed in the molten LiCl electrolyte which is contained in a highly sintered 99.5%Al_2O_3 crucible. Lead wire from the cathode is tungsten covered with a 99.%Al_2O_3 tube. Cathodic deposition of lithium occurs at not only the upper surface, but also on the side and bottom surfaces of the molten aluminum because the LiCl electrolyte soaks through the porous MgO crucible. The anode compartment, made of a 99.5%Al_2O_3 crucible with microporous walls whose average pore size is about 10^{-4}mm, is also immersed in the LiCl electrolyte. This crucible acts as a diaphragm to separate the anode and cathode and to prevent mixing of anolyte and catholyte. Therefore, it is expected that CO_3^{2-} remains in the anode compartment and only Li^+ goes to the cathode through the diaphragm in the electric field. The anode is a graphite rod immersed in the anolyte and is expected to react with CO_3^{2-} anodically. A quartz tube for feeding Li_2CO_3 is inserted into the anode compartment. A reference electrode shown, in Fig. 2, is a mullite protection tube containing silver wire immersed in LiCl-5mol%AgCl melt. The mullite tube prevents the mixing of inner and outer electrolytes completely. The electrode shows a very stable potential in molten chlorides at high temperatures.

The final lithium concentration in the alloy was found to be 5mass%(17at%) to confirm the performance of the electrolysis, although the concentration of lithium in practical Al-Li alloys is regarded as 2.5~3mass%(9.1~10.7at%). Electrolysis is carried out under constant current by using a galvanostat. Anodic and cathodic equilibrium potentials are measure by a transient memory recorder using a short time-current interruption method. The interruption time is typically 5ms. Experimental temperature is 973K. The atmosphere is replaced with dry argon before the experiments began. Since Li_2CO_3 may diffuse out from the anode compartment if no current is applied through the diaphragm, electrolysis is carried out for the LiCl electrolyte without Li_2CO_3 at the first stage of the experiment. Next, small pieces of crystalline Li_2CO_3 are carefully fed into the anode compartment through the quartz feeding tube during electrolysis and the potential changes caused by adding Li_2CO_3 are measured.

After the electrolysis, the lithium content in the alloy is analyzed by using atomic absorption to determine the current efficiency. Anodic exhaust gas, which is carried by argon, is corrected and analyzed for the total amount of Cl_2, CO_2 and CO to determine the anodic reaction.

The LiCl and Li_2CO_3 used were anhydrous transparent large crystals which were purified by bubbling HCl and CO_2 into the melts at temperatures somewhat higher than their respective melting temperatures. The aluminum used is 99.99% pure.

RESULTS AND DISCUSSION

Figure 3 shows the potentials during the electrolysis. The cathodic reaction is the deposition of lithium given in eq.(1). The cathodic potential moved in a less noble direction during the progress of electrolysis due to increasing activity of lithium in the Al-Li alloy.

$$Li^+ + e = Li(\text{in alloy}) \qquad (1)$$

However, the cathodic potential was kept still more noble than the potential shown by the dotted line, which is the potential for pure lithium deposition. More noble cathodic potentials have many advantages. Not only is the deposition potential of lithium reduced, but also impurity deposition is prevented. This behavior is the same as the results[1)] reported previously, and no effect on feeding Li_2CO_3 into the anolyte was found, at least on the cathodic reaction. Therefore, only the anodic reaction should be taken into account when studying the effects of Li_2CO_3 under the stipulation that Li_2CO_3 is confined to the anode compartment, as mentioned above.

The anodic potential showed a constant value at the initial stage of the electrolysis when the electrolyte was pure LiCl. The initial anodic potential corresponds to Cl_2 evolution. Just after feeding Li_2CO_3 into the anolyte, the anodic potential moved in a less noble direction, and then remained constant. After maintaining this anodic potential, it returned to its initial value. This suggests that Li_2CO_3 dissolves in the LiCl electrolyte and reacts with the graphite anode rapidly. The decrease in anodic potential reaches almost 1V. The decreasing potential is considered to be due to the two following reactions.

$$CO_3^{2-} + 0.5\,C = 1.5\,CO_2 + 2\,e \qquad (2)$$

$$CO_3^{2-} + 2\,C = 3\,CO + 2\,e \qquad (3)$$

Of course, reaction (2) is desirable because the carbon consumption is only one forth that of reaction (3) and CO_2 is not harmful. However, it is not clear which reaction is predominant because the difference between the anodic potentials of Eq. (2) and (3) at 973K is estimated to be very small from the thermodynamic calculation based on Barin's table[2)]. The dotted line near -0.5V indicates an anodic potential calculated assuming that the activity of CO_3^{2-} is unity and P_{co_2} or P_{co} is also unity.

Differences between the measured and calculated potentials may be caused by the very low activity of CO_3^{2-} because only small pieces of Li_2CO_3 were fed into large amounts of anolyte.

The anodic exhaust was passed through a KI solution, $Ba(OH)_2$ solution, I_2O_5 column and again the $Ba(OH)_2$ solution to analyze the total amounts of Cl_2, CO_2 and CO, respectively. The amount of Cl_2 is equal to the difference between the amount of electricity and the number of equivalents of Li_2CO_3. The ratio of CO_2 and CO was about 98% and 2%, respectively. Consumption of graphite was also measured after the experiment. It was about one half of the Li_2CO_3 using a mol ratio. These results suggest that the predominant anodic reaction is CO_2 evolution shown in eq(2). It is difficult to explain the result by thermodynamic considerations. Probably, the reaction rate is higher in reaction(2) than in reaction(3). It is like the Hall-Heroult aluminum smelting process. Kruesi and Fray also reported similar results4) that CO_2 evolution is predominant in the electrowinning of metallic lithium using a LiCl-KCl eutectic electrolyte. Chemical analysis of the alloy obtained has indicated that the current efficiencies for lithium deposition are slightly higher than 95% in spite of the high content of lithium in the alloy. These values are almost the same as previous results using LiCl only as the electrolyte1).

The period showing less noble anodic potentials shown in Fig.3 was found to be variable. The periods were always shorter than the times calculated from the amount of Li_2CO_3 fed, as shown in Fig.4. Here, R means the ratio of the quantity of electricity passed between the points, S and E to equivalents of Li_2CO_3. R decreases as the Cl_2 evolution time becomes longer. The reason for this phenomenon is considered to be the non-electrochemical reactions of CO_3^{2-} with Cl_2, as indicated in Eq.(4) and (5).

$$CO_3^{2-} + Cl_2 + 0.5\,C = 1.5\,CO_2 + 2Cl^- \qquad (4)$$

$$CO_3^{2-} + Cl_2 + 2\,C = 3\,CO + 2Cl^- \qquad (5)$$

These reactions occur when excess Cl_2 is dissolved in the anolyte or in the gas near the anolyte. Although this phenomenon has no effect on the amount of Li_2CO_3 consumed, the potential required for the electrolytic production of Al-Li alloy increases and this is undesirable. Therefore, it is recommended that Li_2CO_3 be fed in continuously.

CONCLUSION

The anodic reaction of CO_3^{2-} with carbon in LiCl melt has been studied for use in the electrolytic production of Al-Li alloys. The anode compartment was separated from the cathode compartment to prevent the mixing of catholyte with anolyte which contained oxidative Li_2CO_3. Results obtained indicate that Li_2CO_3 is very useful compared with LiCl as the source of lithium. That is, the anodic potential decreased almost 1V, the current efficiency did not decrease, and the main exhaust gas is CO_2 which is easily disposed of. It was found that Li_2CO_3 reacted with carbon not only electrochemically but also non-electrochemically if excess Cl_2 was present in the anolyte.

REFERENCES

1) Y. Sato, T. Yamamura, E. Araike, T. Suzuki, H. Zhu, M. Endo and T. Sugimoto: Proceedings of International Symposium on Molten Salt Chemistry and Technology, (1993), 480-489.
2) E.M. Levin, C.R. Robbins and H.F. McMurdie: "Phase Diagram for Ceramists", The American Ceramic Society, (1964).
3) I. Barin: "Thermochemical Data of Pure Substances", VCH, (1989)
4) W.H. Kruesi and D.J. Fray: Met. Trans. B, **24B** (1993), 605.

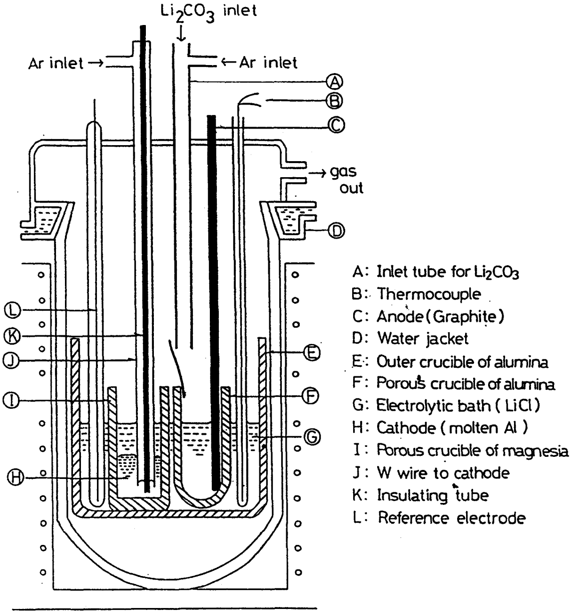

Fig.1 Apparatus used for the electrolytic production of Al-Li alloy by using Li_2CO_3 as a source of lithium.

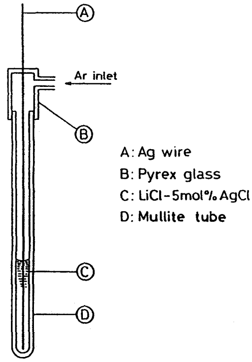

Fig.2 Ag/AgCl reference electrode.

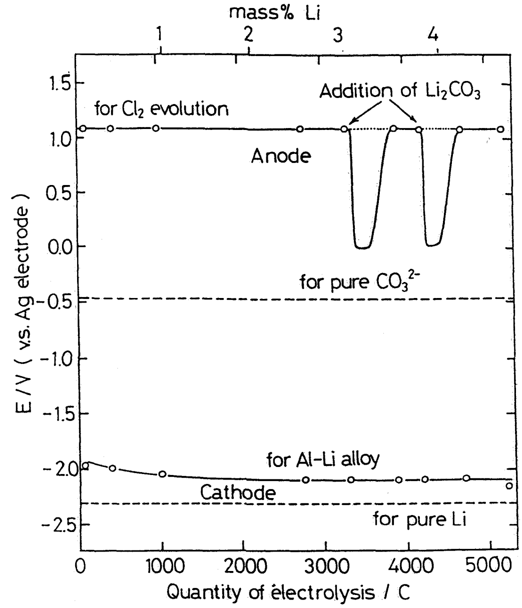

Fig.3 Variations of the electrode potentials for Li_2CO_3 addition into LiCl electrolyte.

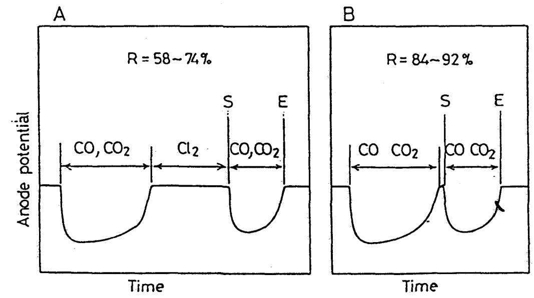

Fig.4 Relation between the quantity of electricity and the amount of Li_2CO_3 fed

DOI: 10.1149/199413.0441PV

ELECTROPLATING OF NICKEL-ALUMINUM ALLOYS FROM ROOM TEMPERATURE MOLTEN CHLOROALUMINATES

L. Heerman and W. D'Olieslager

Laboratorium voor Radiochemie, Katholieke Universiteit Leuven
Celestijnenlaan 200G, B-3001 Heverlee (Belgium)

ABSTRACT

This paper demonstrates the feasibility of the electrochemical deposition of Ni-Al phases from room temperature molten chloroaluminates using either DC or pulsed current electrolysis. Occlusion of the molten salt in the deposits, in many cases followed by rapid degradation in contact with the air, is the main problem to overcome before the process has any real application potential for the preparation of HER-electrodes.

INTRODUCTION

Room temperature molten haloaluminates were introduced by Hurley and Wier (1) in 1951 for practical use as aluminum plating baths. A 2:1 molar ratio mixture of aluminum chloride and N-ethylpyridinium bromide was found to be liquid at room temperature (although the liquidus temperature steeply increases for other compositions) and smooth, adherent aluminum plates were obtained from this composition (2-6).

The subject of room temperature haloaluminates did not receive much more attention until Robinson and Osteryoung (7) combined aluminum chloride and N-(n-butyl)pyridinium chloride (BuPyCl) and obtained an ambient molten salt with low liquidus temperature: these melts are ionic liquids at temperatures only slightly greater than 27°C for all melt compositions in the range 2:1 - 0.75:1 molar ratios $AlCl_3$ - BuPyCl and acidic, i.e. $AlCl_3$ - rich, melts remain liquid even at temperatures far below ambient. Later, Wilkes et al. (8) formulated another series of ambient molten salts by combining aluminum chloride and dialkylimidazolium chlorides, typically 1-ethyl-3-methylimidazolium chloride (ImCl). These molten salts exhibit adjustable Lewis acid-base properties and have been used extensively as media for fundamental electrochemical and spectroscopic studies of inorganic and organic solutes (9,10). Furthermore, these molten salts have a technological potential for use as battery electrolytes and as media for electroplating, electrochemical polishing and electrochemical etching. The electrodeposition of aluminum was investigated by several groups (11-15) and the practical electroplating of this metal (including continuous plating) (16, 17) and of aluminum-manganese alloys (18) were successfully demonstrated. Data on the electrochemistry of several other metals in these melts, such as copper (19-21), nickel (22, 23), cobalt (24), bismuth (25), lead (26), silver (27), gold (28) and tin (29) have been reported.

In general most of these studies were conducted with rather low concentrations of the electroactive species (10-20 mM at maximum) while evidently the successfull application of these molten salts as electrolytes for electroplating baths requires operation at much higher concentrations of metal ions. Furthermore, there are virtually no data available on the anodic behaviour of metals in these melts, although recently anodic passivation has been reported for lead electrodes (26). This paper investigates the posssibility of electroplating nickel-aluminum alloys from acidic $AlCl_3$ - BuPyCl melts and reports some results on the anodic behavior of nickel.

One possible application of this research is to make a contribution to the development of durable and efficient electrode materials for the hydrogen evolution reaction (HER) in alkaline solution. High surface nickel electrode materials have received much attention as they represent a good balance between cost and efficiency. For this reason, Raney-type nickel materials have received much attention (30). Usually, powdered Raney-type nickel-aluminum alloys are used as the starting material for the preparation of HER-electrodes by leaching of aluminum but the direct electrodeposition of thin layers of the alloy may be an interesting alternative worthwhile to explore.

EXPERIMENTAL

The synthesis and purification of BuPyCl, the sublimation of $AlCl_3$ (Fluka) and the preparation of the melts was described previously (28). Dilute solutions of Ni(II)-ion, up to ~ 10^{-2} are easily prepared by constant current anodisation of nickel in well-stirred acidic melts. However, this method was not convenient for the preparation of more concentrated solutions. Since anhydrous $NiCl_2$ does not dissolve well in acidic melts, the metal chloride was dissolved in a basic melt which was then rapidly mixed with an excess of 2:1 $AlCl_3$ - BuPyCl melt, eventually precipitated chloride was filtered off and the acidity was adjusted by addition of solid aluminum chloride (31): this way, solutions containing up to 0.12 M Ni(II)-ion could be prepared (preparation of solid $Ni(AlCl_4)_2$ (32) eventually may be a nicer way to arrive at the same result).

All experiments were carried out under a purified nitrogen atmosphere (VAC dry box ; HE-493 Dri Train) at ambient temperature. Nickel and tungsten wires (eventually rotating) were used as the working electrodes for voltammetric experiments. Plating experiments were performed with a cylindrical rotating copper electrode with an exchangeable sample holder (height = 10 mm ; diameter = 3 mm) or with 1x1 cm^2 plane stainless steel electrodes (simply using a magnetic stirring bar). A large concentric nickel wire spiral was used as the counter electrode. The reference electrode, an aluminum wire immersed in a 2:1 $AlCl_3$ - BuPyCl melt, was provided with a Luggin capillary to minimize ohmic drop.

Electrochemical experiments were performed with a EG&G Princeton Applied Research Corporation (PARC) Model 174 potentiostat, a PARC Model 175 universal programmer, a PARC Model 379 digital coulometer and a Houston Instrument Omnigraphic 2000 XY-recorder. Part of the experiments was performed with a Tacussel PJT 24-1 potentiostat/galvanostat coupled with a computer controlled Tacussel IMT-1 interface for electrolysis experiments with pulsed current.

RESULTS AND DISCUSSION

The absorption spectrum of Ni(II) in acidic $AlCl_3$-BuPyCl melts (fig.1) indicates that the metal ion has an octahedral coordination in this medium and can be represented either as $Ni(Al_2Cl_7)_2$ or $Ni(AlCl_4)_2$. The spectrum does not change with the melt composition whereas the potential of the Ni-Ni(II)-couple decreases by several hundred millivolt in going from a 2:1 melt to less acidic compositions (23, fig.4). Such a change of potential, which has been observed for many other metal/metal-ion couples in these melts (20,21,27) evidently must be accounted for by the variation in anion speciation with melt acidity. The observation that the absorption spectrum does not change with the melt acidity suggests that the first coordination sphere is not affected and that the metal ion remains coordinated by the same species for all acidic melt compositions (this is tantamount to saying that $Al_2Cl_7^-$ and $AlCl_4^-$ have very different coordinating strenghts!).

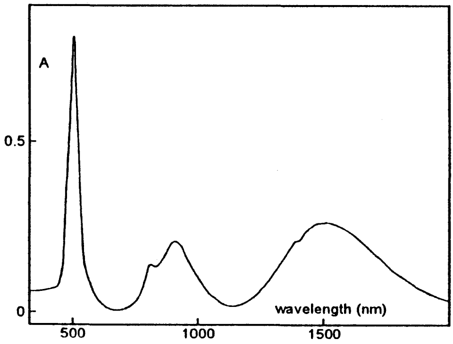

Figure 1 Absorption spectrum of Ni(II) in acidic $AlCl_3$-BuPyCl melts

Cyclic voltammograms of a Ni(II) solution in 2:1 melts on a tungsten electrode (fig.2a) show that the deposition of nickel starts at about 0.4 V but the current does not really decay after the peak maximum and develops into a broad region where nickel and aluminum are codeposited, as has been reported previously(22). The anodic portion of the voltammograms show the peak expected for the dissolution of bulk aluminum, a broad current region which is attributed to the dissolution of aluminum from the Ni-Al phase and finally a peak for the dissolution of the electrodeposited nickel. Cyclic voltammograms recorded on nickel wire electrode (fig. 2b) exhibit an additional anodic peak at more positive potentials which corresponds to the dissolution of the base metal. Codeposition of nickel and aluminum is also evident from experiments with rotating tungsten wire electrodes (fig. 3): the voltammograms do not exhibit a well defined limiting current and instead the current increases steadily until the potential is reached where deposition of bulk aluminum starts.

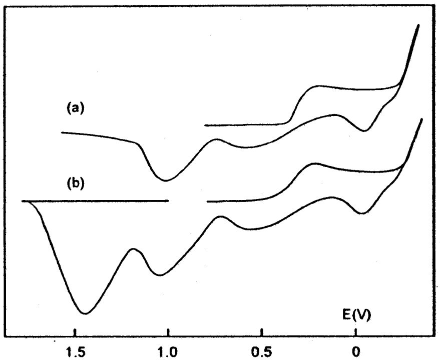

Figure 2 Cyclic voltammetry of Ni(II) in 2:1 $AlCl_3$-BuPyCl melts (a) tungsten electrode (b) nickel wire electrode

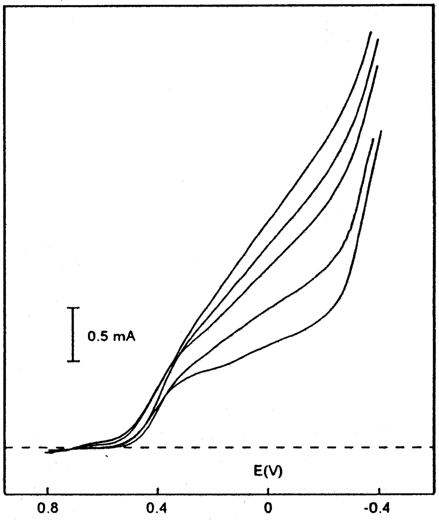

Figure 3 Voltammograms of nickel(II)-ion reduction on rotating wire tungsten electrodes at different rotation rates (500, 1000, 1250, 1500 and 2000 rpm)

A series of electrolysis experiments using DC or pulsed current was carried out to confirm directly the results of the voltammetric experiments and to investigate the composition of the electrodeposited layers (in DC experiments the applied current was maximum 30% of the estimated limiting current for nickel deposition; in pulsed current experiments the rotation rate was kept rather low, maximum 100 rpm, so that relatively long pulse times (0.5 - 2 s) could be applied). The results of some 60 electrodeposition experiments can be summarized as follows:

1. using flat cathodes, it is evident that the current distribution was far from ideal as evidenced by irregular coverage, specially near the edges of the electrode: this may be a more general problem if one tries to use this kind of room temperature molten salts as a medium for electrodeposition since the conductivity is rather low, i.e. as compared with aqueous plating solutions but this difficulty probably can be overcome with a better cell design and eventually by raising the temperature.

2. some typical results of SEM analysis of the electrodeposits are given in table 1: The aluminum content increases with increasing current density but the increase is far from linear: in this study deposits containing up to 14 atom% aluminum were obtained using pulsed current if the pulse duration was adjusted so that the potential of the electrode was in a region just before the onset of bulk aluminum deposition. Furthermore it was found that the deposits contained a few atom% of aluminum even at relatively low current densities, i.e. almost at the foot of the nickel wave: this suggests that the codeposition of aluminum actually starts much earlier than is evident from the voltammetric results.

Table 1 Some typical results of SEM analysis of electrodeposited Ni-Al phase

			atom% Ni	atom% Al	atom% Cl
DC	3 mA	180 min	88	8.5	3.5
PC	3 mA	180 min	88	8.5	3.5
PC	6 mA	90 min	84	11	5
PC	9 mA	60 min	80	14	6

3. the most striking fact in this table is the fact that all the deposits contain a considerable amount of chloride which evidently points to occlusion of the molten salt, probably caused by the rather high viscosity of the electrolyte (i.e., the molten salt sticks almost like a syrup to the electrode). If this explanation is true, one could consider the use of a cosolvent like toluene to lower the viscosity and to increase the conductivity which would have a beneficiary effect also on current distribution, although the use of aromatic solvents could cause other, e.g. ecological, problems. Another possibility is that occlusion of the molten salt could be prevented by the use of much more stringent procedures for the pretreatment of the electrodes than have been used in the present study (polishing, degreasing with acetone, drying with alcohol).

4. most of the deposits were bright and well-adhering to the cathode substrate when they were removed from the electrolysis cell and washed with toluene to remove the adhering molten salt. For example, in DC experiments, surface roughening and internal stressses seems to be no problem as long as the current is lower than 30 % of the limiting current

and the thickness of the deposits does not exceed 3-4 microns. The deposits did not visibly change as long as they were kept in the dry box used for the electrolysis experiments. However, once out of the dry box about 50 % of the deposits degraded rapidly: black spots developped on the surface of the specimens (the deposits became almost "pock-pitted") and the electrodeposited layer was pulverized (in most cases this process did not take more than a few hours): it is believed that reaction of the occluded molten salt with moisture in the air is responsible for this rapid degradation of the deposits.

5. the electrodeposition of Ni-Al phases from a room temperature molten salt is thus demonstrated in principle but occlusion of the molten salt, followed by rapid degradation in contact with the air, is the main problem to overcome before this process can have any real application potential.

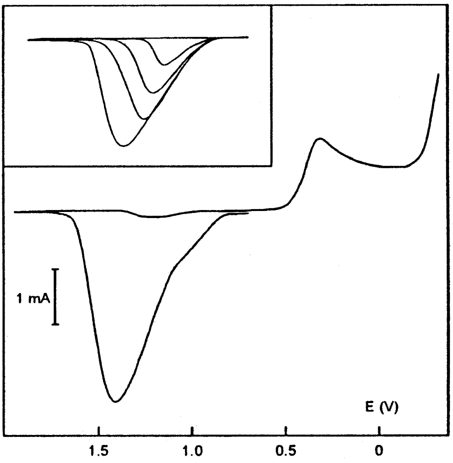

Figure 4 Cyclic voltammogram of nickel in a pure $AlCl_3$-BuPyCl melt: the scan was started from 0.7 V in the anodic direction (20 mV/s). Inset: influence of scan rate: 5, 20, 50, 100 mV/s (different potential scale)

A cyclic voltammogram of nickel in a pure $AlCl_3$-BuPyCl melt, started in the anodic direction (fig.4), exhibits a large peak which corresponds to the anodic dissolution and passivation of the metal (such a peak is also present in fig.2b), as was reported also for lead electrodes (26). The cathodic portion of the voltammogram exhibits a large peak for the deposition of nickel from the saturated solution, at least in the vicinity of the electrode (the solubility of Ni(II)-ion in a 2:1 $AlCl_3$-BuPyCl melt is estimated as 0.15 M); thus the layer formed on the electrode during the anodic scan is either very porous or does not well adhere to the electrode. Application of a constant current results in well defined transition times for the passivation of the metal. A plot of $i\tau^{1/2}$ vs. i obtained from such experiments (fig.5) yields an almost horizontal line, suggesting that the process can be described by a simple dissolution-passivation mechanism. However, the scatter of the points is rather large: this may indicate that nucleation of the solid precipitate plays an important role and that the solution at the electrode surface is actually supersatured before the onset of precipitation. This is confirmed by the fact that $C(x=0,\tau)$, the concentration of Ni(II)-ion at the electrode surface at time τ, calculted from the Sand equation with $D = 8.5.10^{-7}$ cm^2/s, is slightly more than 0.5 M, i.e. more than three times the estimated value of the solubility. From a practical viewpoint these experiments merely indicate that electroplating experiments from these molten salts require anodes with a much larger area than the area of the cathode to permit the use of rather concentrated solutions (close to saturation).

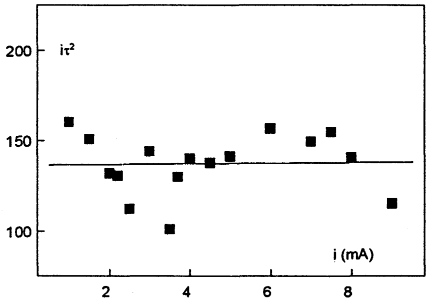

Figure5 Plot of $i\tau^{1/2}$ vs. i for constant current anodization of nickel metal in pure 2:1 $AlCl_3$-BuPyCl melts

ACKNOWLEDGEMENT

This work was supported by a grant of the I.I.K.W. (Brussels, Belgium).

REFERENCES

1. F.H. Hurley and T.P. Wier, J. Electrochem. Soc., **98**, 203 (1951)
2. F.H. Hurley, U.S. Pat. 2.446.331 (1948)
3. T.P. Wier and F.H. Hurley, U.S. Pat. 2.446.349 (1948)
4. T.P. Wier, U.S. Pat. 2.446.350 (1948)
5. F.H. Hurley and T.P. Wier, J. Electrochem. Soc., **98**, 207 (1951)
6. W.H. Safranek, W.C. Schickner and C.L. Faust, J. Electrochem. Soc., **99**, 53 (1952)
7. J. Robinson and R.A. Osteryoung, J. Am. Chem. Soc., **101**, 323 (1979)

8. J.S. Wilkes, J.A. Levisky, R.A. Wilson and C.L. Hussey, Inorg. Chem., **21**, 1263 (1982)
9. C.L. Hussey, ***Advances in Molten Salt Chemistry. Vol. 5***, G. Mamantov, Editor, p. 185, Elsevier, New York (1983)
10. C.L. Hussey, Pure Appl. Chem., **60**, 1763 (1988)
11. J. Robinson and R.A. Osteryoung, J. Electrochem. Soc., **127**, 122 (1980)
12. P.K. Lai and M. Skyllas-Kazacos, Electrochim. Acta, **32**, 1443 (1987)
13. Y. Chryssoulakis, J.C. Poignet and G. Manoli, J. Appl. Electrochem., **17**, 857 (1987)
14. P.K. Lai and M. Skyllas-Kazacos, J. Electroanal. Chem., **248**, 431 (1988)
15. R.T. Carlin and R.A. Osteryoung, J. Electrochem. Soc., **136**, 1409 (1989)
16. S. Takahashi and I. Saeki, Molten Salts, **33**, 195 (1990)
17. S. Takahashi, K. Ida and S. Mori, ***Proceedings of the Seventh International Symposium on Molten Salts***, C.L. Hussey, J.S. Wilkes, S.N. Flengas and Y. Ito, Editors, p. 661, The Electrochemical Society Softbound Proceedings Series, Pennington, NJ (1990)
18. A. Shibuya, T. Tsuda, Y. Yamamoto, T. Uchida and H. Seto, Molten Salts, **33**, 129 (1990)
19. C.L. Hussey, L.A. King and R.A. Carpio, J. Electrochem. Soc., **126**, 1029 (1979)
20. Chenniah Nanjundiah and R.A. Osteryoung, J. Electrochem. Soc., **130**, 1312 (1983)
21. T.M. Laher and C.L. Hussey, Inorg. Chem., **22**, 3247 (1983)
22. R.J. Gale, B. Gilbert and R.A. Osteryoung, Inorg. Chem., **18**, 2723 (1979)
23. T.M. Laher and C.L. Hussey, Inorg. Chem., **21**, 4079 (1982)
24. C.L. Hussey and T.M. Laher, Inorg. Chem., **20**, 4201 (1981)
25. L. Heerman and W. D'Olieslager, J. Electrochem. Soc., **138**, 1372 (1991)
26. C.L. Hussey and Xiao-HongXu, J. Electrochem. Soc., **138**, 1886 (1991)
27. Xiao-HongXu and C.L. Hussey, J. Electrochem. Soc., **139**, 1295 (1992)
28. Xiao-HongXu and C.L. Hussey, J. Electrochem. Soc., **139**, 3103 (1992)
29. Xiao-HongXu and C.L. Hussey, J. Electrochem. Soc., **140**, 618 (1993)
30. L. Chen and A. Lasia, J. Electrochem. Soc., **140**, 2464 (1993) and other references cited in this paper
31. This method was suggested to us by B. Gilbert, University of Liège (Belgium)
32. J. Brynestad, H.L. Yakel and G.P. Smith, Inorg. Chem., **9**, 686 (1970)

DOI: 10.1149/199413.0449PV

INFLUENCE OF THE MELT STRUCTURE ON THE ELECTRODEPOSITION OF MOLYBDENUM, TITANIUM AND ALUMINIUM

M. Makyta, P. Zatko, and V. Daněk

Institute of Inorganic Chemistry
Slovak Academy of Sciences
Dúbravská cesta 9, 842 36 Bratislava,
Slovakia

ABSTRACT

The influence of ionic structure of molten salts used as electrolytes in electrodeposition of molybdenum, titanium and aluminium has been studied by voltametric method. It was found that in all the investigated systems the electrodeposition process is significantly facilitated by the formation of complex anions with lowered symmetry of coordination sphere. In the case of molybdenum, complex heteropolyanions are created in the melt by the addition of B_2O_3 and SiO_2 to K_2MoO_4. The electrodeposition of titanium from K_2TiF_6 is enhanced by formation of TiF_7^{3-} or TiF_6Cl^{3-} which are present in the molten KF–K_2TiF_6 and KCl–K_2TiF_6, respectively. The formation of complex aluminium oxyfluoride species is responsible for electrodeposition of aluminium from cryolite - alumina melts.

INTRODUCTION

Electrodeposition of metals from molten salts has been extensively studied over the last decades. From an analysis of the literature data it follows, that several types of molten systems were tested as electrolytes. On the basis of the electroactive species used they can be divided into two principal groups:

- systems containing halo-complexes of deposited metals,
- systems containing oxides or oxy-complexes of deposited metals.

In all of the investigated systems one of the most important tasks solved is the composition of the electrolyte with regard to both the suitable physicochemical properties of the electrolyte and the desired character of the electrodeposited product. Both problems are close related to the actual structure, i.e. the ionic composition of the melt.

Quite recently the attention to the role of oxides, either as electroactive species, as impurities or as additives in the electrodeposition of metals was paid. This may be demonstrated e.g. on the case of electrodeposition of molybdenum (1, 2), where the electrolysis of neither pure K_2MoO_4, nor the KF–K_2MoO_4 mixture does not yield molybdenum deposit. However, introducing small amounts of boron oxide, or silicon dioxide to the basic melts smooth and adherent molybdenum deposits may be obtained (2, 3).

In the present work the influence of different additives to the pure molten compound containing the deposited metal on the mechanism of the cathodic process in the electrodeposition of molybdenum, titanium and aluminium was studied using the voltametric method. Conclusions on the possible structure of electroactive species present in the electrolyte and their electrochemical stability were made.

EXPERIMENTAL

The voltametric experiments were performed in an electric resistance tube furnace. The shaft was made of a special refractory steel and was protected by an internal nickel anti-corrosive lining. The shaft was closed by an air-tight water-cooled head. The head was provided with inlets for the working and reference electrodes and for contact to the counter electrode, an inlet for argon, passages for introducing the electrochemical active components and for sampling of the electrolyte, a window for visual observation and a thermocouple holder. All the experiments were carried out in the argon atmosphere at the temperature 20 K over the melting temperature of the pure investigated salt. The design of the head allowed sampling and exchange of the electrodes while preserving the inert atmosphere in the shaft.

The electrolytic cell consisted of a platinum crucible which was also used as the counter electrode. The working electrode alternatively consisted of platinum wire, molybdenum wire and glassy carbon rod which was dipped into the melt by means of a micrometric screw so that the active surface area was approx. 0.2 cm^2. To avoid a possible pollution of the tested melt by a construction material a platinum wire was also used as quasi-reference electrode. The potentiostat TACUSSEL 20–2 PRT was used as the source of potential. The observed voltametric curves were recorded by means of a data acquisition system using a DAS-A0 ADDA card.

The analytical grade K_2TiF_6, Merck, K_2MoO_4, B_2O_3, KF, KCl, Al_2O_3, all of Fluka and hand-picked Greenland natural Na_3AlF_6 were used for the preparation of the electrolytes. Before use the chemicals were dried at room temperature in vacuum in the presence of P_2O_5 for a week and subsequently at 500 K for two days. All handling of the chemicals were done in glove box to avoid moisture contamination.

RESULTS AND DISCUSSION

Electrodeposition of molybdenum

The influence of B_2O_3 and SiO_2 additions on the electrodeposition of molybdenum from the molten K_2MoO_4 and KF–K_2MoO_4 systems was studied. Fig. 1 shows the voltametric curves recorded in pure potassium molybdate melt and in the K_2MoO_4–B_2O_3 system with different boron oxide additions. It can be seen from the figure that on the voltametric curve recorded in pure K_2MoO_4 (curve 1) only one electrochemical process is observed at potential approximately -1 V. This process represents electrodeposition of potassium on the cathode. The addition of small amount of boron oxide to the basic melt causes significant changes in the shape of voltametric curves. A new expressive current peak starting at approx. –0.2 V appeared on the curve (curves 2, 3). The current value of the peak depends on the B_2O_3 content in the melt. The similar behaviour was observed using KF–K_2MoO_4 system as a basic melt and also with SiO_2 additions to the both basic melts.

On the basis of the above presented results it can be assumed that the addition of oxides causes most probably changes in the ionic composition of the electrolyte, i.e. the kind of the electroactive species, which enable molybdenum can be reduced. From the physicochemical and thermodynamic analysis of the molten system KF–K_2MoO_4–B_2O_3 (4–6) it follows that the formation of heteropolymolybdates containing boron ($[BMo_6O_{24}]^{9-}$) or silicon ($[SiMo_{12}O_{40}]^{4-}$) (7) as a central atom is responsible for the easy molybdenum deposition. Moreover, the entrance of fluoride atoms into the co-ordination sphere of molybdenum in the heteropolyanions lowers the electrochemical stability of such electroactive species as well.

Electrodeposition of titanium

The influence of the ionic structure of the melt on titanium electrodeposition is clearly demonstrated in Fig. 2 where a remarkable changes are observed on cathodic part of voltametric curves recorded in the melts with various KCl content in basic K_2TiF_6 melt. According to (8–10) reduction of Ti(IV) to titanium metal proceeds in two electrochemical consecutive reduction steps, Ti(IV) → Ti(III) and Ti(III) → Ti(0). These two electrochemical reduction steps are clearly visible in all recorded curves, first one starting approximately at –0.2 V and second one starting at approximately –1.5 V. It can be seen from the figure that the current values of the peaks representing the above mentioned reduction steps of titanium increase with increasing content of potassium chloride in the melt. The similar changes were observed on voltametric curves also by the KF addition to the molten K_2TiF_6.

In both $KF–K_2TiF_6$ and $KCl–K_2TiF_6$ systems congrurently melting additive compounds K_3TiF_7 and K_3TiF_6Cl, respectively, are formed (11). In spite of the thermal dissociation at melting, these compounds affects the actual ionic composition in favour of the presence of less symmetrical and thus less electrochemical stable anions TiF_7^{3-} and TiF_6Cl^{3-}. From the comparison of the voltametric curves obtained in the pure K_2TiF_6 (curve 1) and those obtained in the $KF–K_2TiF_6$ and $KCl–K_2TiF_6$ mixtures (curves 2 – 4) it follows that substantial changes occur when KF or KCl is added to the pure K_2TiF_6. Even when titanium may be deposited also from pure K_2TiF_6, most probably due to the presence of KF impurities, expressed peaks corresponding to the titanium reduction have been observed with addition of either KF or KCl. This observation indicates the positive role of the less symmetrical titanium species on the electrodeposition of titanium.

Electrodeposition of aluminium

Aluminium is generally produced by the electrolysis of the cryolite - alumina melts. Dissolution of alumina in cryolite leads to the formation of various aluminium oxyfluoride species such as $AlOF_3^{2-}$, $AlOF_5^{4-}$, $AlOF_2^{2-}$, $Al_2O_2F_4^{2-}$ and $Al_2OF_6^{2-}$ (12). These species undergo reduction on the cathode surface. The lower symmetry of oxyfluoride anions is most probably responsible for the easy deposition of aluminium. This phenomenon is confirmed by the voltametric measurements in the system $Na_3AlF_6–Al_2O_3$. Fig. 3 shows cathodic part of voltametric curves recorded in pure cryolite (curve 1) and in the melt containing 2 mole % of Al_2O_3 (curve 2). Comparing the curves shown in the figure confirms that the introduction of oxygen containing species to the molten cryolite favourably influences the deposition of aluminium. The electrodeposition potential is shifted to the more positive values and the peak current, which represents the amount of electrochemical active aluminium in the melt, increased.

However, it is very difficult to prepare oxygen free pure cryolite. Even the Greenland hand-picked natural cryolite or synthetic cryolite prepared from sublimated AlF_3 may content a small amount of alumina. Contamination of cryolite by moisture may happen also during the preparation of samples despite of careful treatment in the glove box. The problem of oxygen free cryolite preparation and the electrochemical study of the possibility of the aluminium deposition from oxygen free cryolite will be the objective of further work.

CONCLUSION

It can be concluded on the basis of presented results that the ionic structure has a key role in the mechanism of electrodeposition of metals from molten salts. It is clearly demonstrated in the above presented examples that the creation of species with lowered symmetry containing electrodeposited metal enables its deposition (molybdenum) or enhances the rate of deposition (titanium, aluminium).

Molybdenum is electrodeposited from B_2O_3–K_2MoO_4 and KF–B_2O_3–K_2MoO_4 systems due to the presence of complex heteropolyanions in the melt. The electrodeposition of titanium from K_2TiF_6 is enhanced by formation of TiF_7^{3-} or TiF_6Cl^{3-} which are present in the molten KF–K_2TiF_6 and KCl–K_2TiF_6 melts, respectively. The formation of complex aluminium oxyfluoride species is responsible for electrodeposition of aluminium from cryolite - alumina melts.

REFERENCES

1. K. Koyama, Y. Hashimoto, S. Omori, and K. Terawaki, J. Less-Common Met. **132**, 57 (1987).
2. M. Makyta, P. Zatko, and P. Bezdička, Chem. Papers **47**, 28 (1993).
3. P. Zatko, M. Makyta, J. Sýkorová, and A. Silný, Chem. Papers, in press.
4. O. Patarák, Z. Jantáková, and V. Daněk, Chem. Papers **47**, 342 (1993).
5. M. Chrenková, V. Daněk, and A. Silný, Z. Anorg. Allg. Chemie **620**, (1994).
6. A. Silný, V. Daněk, and M. Chrenková, Ber. Bunsenges. Phys. Chem., in press.
7. A. Silný, P. Zatko, M. Makyta and J. Sýkorová, *Molten Salts Forum*, Vol. 1-2, Ed. C.A.C. Sequeira and G.S. Picard, Trans Tech Publications, Switzerland, 1993, pp. 155–160.
8. J. de Lepinay, and P. Paillere, Electrochim. Acta **29**, 1243 (1984).
9. M. Makyta, M. Matiašovský, and V.I. Taranenko, Electrochim. Acta **34**, 861 (1989).
10. V.I. Taranenko, I.V. Zarutskii, V.I. Shapoval, M. Makyta, and K. Matiašovský, Electrochim. Acta **37**, 263 (1991).
11. R.V. Chernov, P.M. Ermolenko, Zh. neorg. khim. **18**, 1372 (1973).
12. K. Grjotheim, and B.J. Welch, *Aluminium Smelter Technology*, Aluminium-Verlag, Düsseldorf, 1988, p. 46.

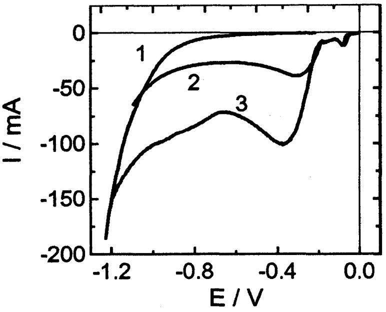

Fig. 1. Voltametric curves recorded in the system K_2MoO_4–B_2O_3 using platinum as a working electrode, polarization rate 0.5 V/s.

Curve 1 – K_2MoO_4

Curve 2 – K_2MoO_4 + 2 mole % B_2O_3

Curve 3 – K_2MoO_4 + 5 mole % B_2O_3

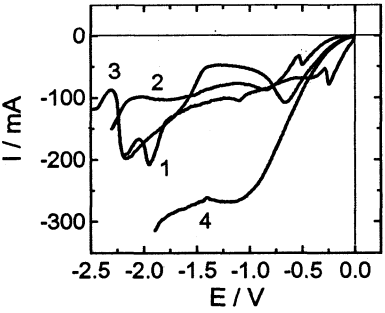

Fig. 2. Voltametric curves recorded in the system K_2TiF_6–KCl using glassy carbon as a working electrode, polarization rate 0.5 V/s.

Curve 1 – K_2TiF_6

Curve 2 – K_2TiF_6 + 5 mole % KCl

Curve 3 – K_2TiF_6 + 50 mole % KCl

Curve 4 – K2TiF6 + 90 mole % KCl

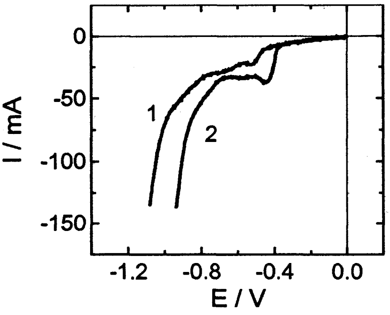

Fig.3. Voltametric curves recorded in the system Na_3AlF_6–Al_2O_3 using molybdenum as a working electrode, polerization rate 0.5 V.s^{-1}

Curve 1 – Na_3AlF_6

Curve 2 – Na_3AlF_6 + 2 mole % Al_2O_3

DOI: 10.1149/199413.0455PV

CATHODIC DISCHARGE OF Mg(II)-SPECIES AND NUCLEATION OF Mg METAL FROM MOLTEN MAGNESIUM CHLORIDE

B. Børresen, G.M. Haarberg, R. Tunold and O. Wallevik*

Department of Electrochemistry,
The Norwegian Institute of Technology
University of Trondheim
N-7034 Trondheim, Norway

*Norsk Hydro A/S
Research Center
N-3900 Porsgrunn, Norway

ABSTRACT

The cathodic discharge of Mg(II)-species and nucleation of Mg metal from molten magnesium chloride on glassy carbon, molybdenum and iron have been studied using electrochemical techniques. At potentials more positive than the deposition potential the reaction is mainly controlled by diffusion of dissolved magnesium away from the electrode interface. The standard rate constant for the charge transfer process was determined to be 10^{-4} to 10^{-3} cm/s on the different electrode materials in the temperature range investigated (725°C-780°C). Determination of the electrode capacitance on an iron electrode using galvanostatic pulses gave values in the range 10-50 μF/cm^2. The nucleation overvoltage was determined by linear potential sweep to be 16 ± 4 mV. A model for the total cathode process is discussed.

INTRODUCTION

The deposition of magnesium from molten chlorides on different electrode substrates, such as glassy carbon and iron, has mainly been studied in solutions with small amounts of $MgCl_2$. The reaction is found to be controlled by diffusion of Mg(II)-species toward the electrode surface [1,2]. In recent studies electrochemical techniques have been applied to study the cathode reaction in pure molten magnesium chloride [3]. Measurements by AC impedance spectroscopy combined with a galvanostatic relaxation technique have shown that the discharge of Mg(II) species on a reversible Mg electrode is a two step process, and that the discharge from divalent to monovalent Mg species probably is the rate determining step [4].

In the pure $MgCl_2$ system a remarkable unstability of the nuclei formed on glassy carbon electrodes was observed. The unstability was detected using both cyclic voltammetry and potential step chronoamperometry. This unstability, which was observed even at rather low potentials (high negative overpotentials) is proposed to be due to a sudden homogeneous nucleation in the electrolyte, reducing the supersaturation of dissolved reduced magnesium species (metal). This homogeneous nucleation probably creates socalled "metal fog" observed during deposition of metals from molten salts.

On the basis of the previously mentioned observations a model of the total cathode process during discharge of Mg(II) species and deposition of magnesium metal is proposed. A schematic drawing of the model is given in Fig.1.

As part of the investigation of the total process we have studied the charge transfer reaction of Mg(II)-species and the diffusion process in pure molten $MgCl_2$ on glassy carbon, iron and molybdenum.

EXPERIMENTAL

Magnesium Chloride-Hexahydrate (p.a. Merck) was predried under HCl atmosphere up to 450°C and subsequently distilled under vacuum.

The working electrodes were rods of iron (Johnson Matthey, specpure), glassy carbon (Tokai, GC30S) and molybdenum (99.97%). The active electrode area was determined by visual inspection of the wetted area after each experiment. The reference electrode was liquid Mg cathodically deposited on a molybdenum wire placed in an MgO tube. The presence of oxide material in the melt is a source of oxide contamination. Samples taken from the melt during experiments were analyzed by iodometric titration to contain approximately 1500 ppm magnesium oxide, which corresponds to saturation of the chloride melt.

The system was studied by linear sweep voltammetry, chronoamperometry and galvanostatic pulses.

RESULTS AND DISCUSSION

A typical voltammogram obtained on iron in this system is shown in Fig.2. One should notice the considerable cathodic current at potentials more positive than the Mg reference potential. This cathodic current is probably due to formation of dissolved Mg species.

Previously reported measurements on glassy carbon, using a platinum reference electrode, has shown an unstable behaviour of the formed Mg nuclei [3]. In the reported measurements, where the melt was saturated with oxide, this unstability was not observed on any of the electrode materials. The overvoltage associated with the deposition of Mg on the three substrates was determined by linear sweep voltammetry at 0.1 mV/s. The nucleation overpotential was found to be 16±4 mV on all the electrode materials. It is surprising that the nucleation overvoltage on glassy carbon is not considerably higher than on iron and molybdenum. This can probably be explained by the presence of the oxide tube in the melt that saturates the melt with oxide. As a result the dissolved oxide may stabilize the nuclei formed on the electrode which favours growth of the nuclei instead of dissolution.

The standard rate constants for the discharge of Mg(II)-species on glassy carbon, iron and molybdenum were determined by extrapolation of current transients at different potentials. The logarithm of the rate constants as a function of potential should be linear. From the slope of this line the product of the cathodic charge transfer coefficient and number of electrons in the rate determining step, $z \cdot \alpha_c$, can be calculated. The activation energy of the electrode process, $\Delta E^\#$, can then be calculated from the temperature dependency of the standard rate constants. The values for the standard rate constant, charge transfer coefficient and activation energy for the three electrode materials are given in Table 1. Unpublished work using an AC impedance technique has shown that the rate determining step is a one electron transfer, probably from Mg(II) to Mg(I) [4]. The number of electrons in the rate determining step, z, is therefore taken to be one.

Table 1 Kinetic parameters obtained on glassy carbon (GC), molybdenum (Mo) and iron (Fe) in pure molten $MgCl_2$ [standard deviation for $\Delta E^\#$ is given]

Temp (°C)	GC			Mo			Fe		
	$k^o \cdot 10^4$ (cm/s)	α_c	$\Delta E^\#$ (kJ/mol)	$k^o \cdot 10^4$ (cm/s)	α_c	$\Delta E^\#$ (kJ/mol)	$k^o \cdot 10^4$ (cm/s)	α_c	$\Delta E^\#$ (kJ/mol)
725	4	0.2	85±4	7	0.7	150 ± 40	13	0.6	83±6
735	-	-		8	0.5		13	0.5	
750	5	0.3		14	0.2		18	0.2	
780	7	0.2		17	0.6		21	0.1	

As can be read from Table 1 the value of the standard rate constant for the discharge process on the different electrode substrates vary between 10^{-4} and 10^{-3} cm/s in the temperature range studied. If the electrodes were only a source of electrons one should expect the rate of the discharge process to be independent of the substrate. The standard rate constant is about three times higher on iron than on glassy carbon. The differences found on the three substrates might be due to unequal number of active sites on the materials or an influence of oxide layers on the metal electrodes. One may also notice that the values for the charge transfer coefficient vary considerably. However, the standard rate constants and the activation energy determined on glassy carbon and iron has nearly the same value as found by AC impedance measurements on a molten Mg electrode[4]. On Mo the value of the activation energy is nearly two times the values obtained on GC and Fe. This value shows also a high degree of uncertainty which might be due to special difficulties in determining the active electrode area on this material.

Fig.3 shows typical current transients obtained on iron. From the figure a hump is easily observed, which could be caused by a monolayer formation. The charge associated with this peak is approximately 0.4 mC/cm^2. The charge required to form a dense monolayer of Mg atoms can be calculated to be $\sim$ 0.8 mC/cm^2

The electrode capacitance for the iron electrode has been calculated from potential transients obtained by galvanostatic pulses after 2-3 μs. It was found that the capacitance increases with time, which could be explained by the formation of a monolayer. The electrode capacitance (recorded after 2-3 μs) was found to vary between 10 μF/cm^2 and 50 μF/cm^2.

From current transients it has been found that at potentials positive to the nucleation potential the process seems to be mainly diffusion controlled. A plot of current density versus $t^{-1/2}$ gives a straight line in an intermediate region, but the intercept for $t^{-1/2} = 0$ is not equal to zero. This deviation is probably caused by convection, playing a role at longer times ($t > 1$s.). Plots of i versus $t^{-1/2}$ obtained on molybdenum and glassy carbon are given in Fig.4. From the slope of the straight lines the product of the concentration gradient and the square root of the diffusion coefficient can be determined. The interfacial concentration of the diffusing species may then be calculated assuming that the diffusion coefficient is known and that the bulk concentration is taken to be zero. From the two lines given in Fig.4 the concentration at the interface was calculated to be $6 \cdot 10^{-5}$ mol/cm^3 and $5 \cdot 10^{-5}$ mol/cm^3 for molybdenum and glassy carbon respectively, using the diffusion coefficient given by van Norman and Egan [5]. This shows that the process occurring at this potential (0 mV vs Mg) probably is independent of the electrode material. Assuming that the process is reversible the interfacial concentration of dissolved metal, at the standard reversible potential, should be equal to the solubility of dissolved metal found by Wypartowicz et al [6], which is $2.5 \cdot 10^{-5}$ mol/cm^3. This indicates that our values are somewhat high. An alternative method for determining the concentration of the diffusing species was also applied. The electrode was polarized to a given potential (-20 mV) for a certain time (2s.). After the polarization period the potential was swept anodically with varying sweep rates. As can be observed from Fig.5 the i_p versus $\nu^{1/2}$ is close to linear for both glassy carbon and molybdenum. From the slope of these lines the concentration at the interface can be calculated to be $3 \cdot 10^{-5}$ mol/cm^3 and $7 \cdot 10^{-5}$ mol/cm^3 on glassy carbon and molybdenum respectively. The reason for the higher value found on Mo is not clear, but could be caused by nucleation on Mo which would tend to increase the peak current. The theoretical value at this potential assuming a reversible process is $4 \cdot 10^{-5}$ mol/cm^3.

Finally, a qualitative discussion of the proposed model is appropriate. The initial step is a two step charge transfer reaction. The rates of the following parallel paths are determined by the applied potential and the electrode materials. At potentials positive to the nucleation potential, the magnesium formed at the electrode dissolves in the melt independently of the electrode material. The dissolved metal diffuses away from the electrode to the melt. At more negative potentials, the concentration of dissolved metal is high enough for Mg nuclei to form. This critical nucleation potential is determined by the interfacial properties. The different wetting properties of Mg on the electrode materials are of decisive importance when it comes to the stability of the nuclei formed on the electrode. If Mg wets the electrode poorly, the concentration of dissolved metal at the electrode interface has to be high to facilitate the nucleation. The small nuclei would, if the concentration of dissolved metal decreases (ie homogeneous nucleation in the melt), tend to dissolve. However, if the nuclei are covered by a protective oxide layer, the dissolution would be hindered and the nuclei are stabilized.

ACKNOWLEDGMENTS

This work has been supported by Norsk Hydro A/S and the Norwegian Research Council (NFR).

REFERENCES

1) R. Tunold, Light Metals,AIME, 949 (1980)

2) G.M. Haarberg, S.R. Johansen, J. Melaas and R. Tunold, Proc.Seventh Int.Symp.Molten Salts, The Electrochem.Soc.,Inc.,NJ, Vol.90-19,p.449,1990.

3) B. Børresen, G.M. Haarberg, R. Tunold and O. Wallevik, J.Electrochem. Soc.,**140**,6,L99 (1993)

4) A. Kisza, J. Kazmierczak, B. Børresen, G.M. Haarberg and R. Tunold. " The kinetics and mechanism of the magnesium electrode reaction in pure molten magnesium chloride." To be published.

5) J.D. van Norman and J.J. Egan, J.Phys.Chem., **67**,2460 (1963)

6) J. Wypartowicz, T. Østvold and H. Øye, Electrochim.Acta, **25**,151 (1980)

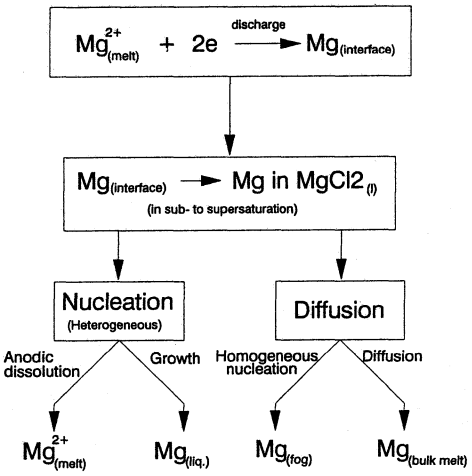

Fig.1 A model of the total process for cathodic discharge of Mg(II) species

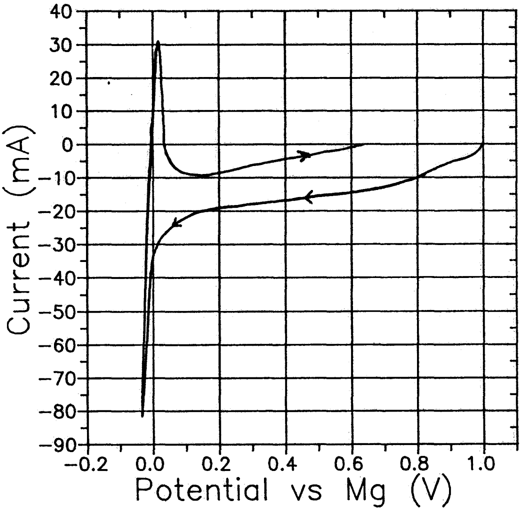

Fig.2 Cyclic voltammogram obtained on iron in pure $MgCl_2$ at 735°C. Sweep rate: 100 mVs^{-1}. Electrode area: 0.32 cm^2.

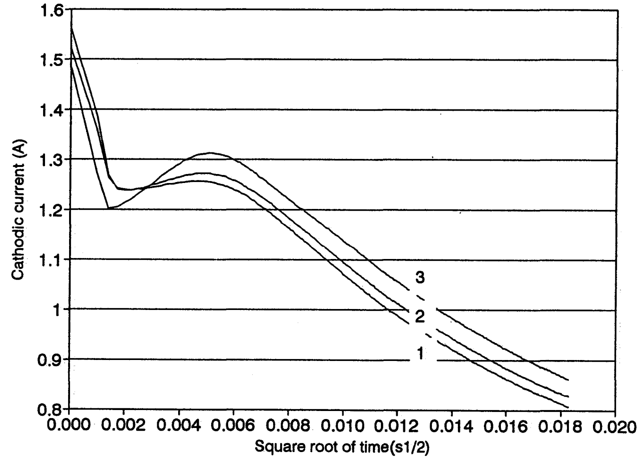

Fig.3 Cathodic current transients obtained on iron in pure $MgCl_2$ at 780 °C. Applied potential: 1) +50 mV, 2) +40 mV and 3) +20 mV versus the Mg reference electrode. Electrode area: 0.22 cm^2.

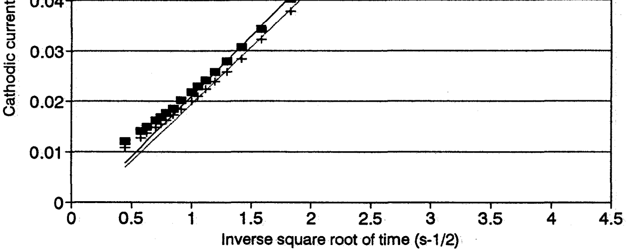

Fig.4 Cathodic current density as a function of $t^{-1/2}$ obtained on glassy carbon (crosses) and molybdenum (filled squares)in pure $MgCl_2$ at 725°C. The applied potentials was 0 mV versus the Mg reference electrode.

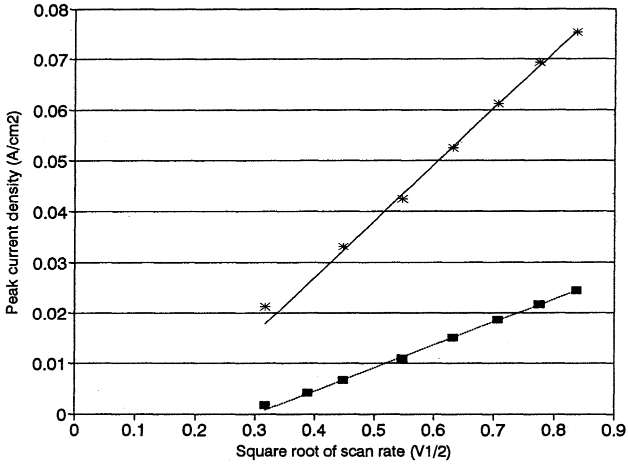

Fig.5 Peak current density versus the square root of scan rate obtained on glassy carbon (filled squares) and molybdenum (asterisks). Temperature: 725 °C. Applied potential was -20 mV vs Mg reference with a residence time of 2s.

DOI: 10.1149/199413.0463PV

ELECTROCHEMICAL STUDIES OF LEAD DEPOSITION FROM PURE MOLTEN LEAD CHLORIDE

G.M. Haarberg, T. Støre, B. Børresen, and R. Tunold

Department of Electrochemistry
The Norwegian Institute of Technology
7034 Trondheim, Norway

ABSTRACT

The cathodic deposition of lead from pure molten lead chloride was studied by electrochemical techniques. The cathode substrate plays an important role for the rate of the cathode process, which involves the discharge of Pb(II) species and the subsequent nucleation and growth of Pb. The formation of a liquid Pb phase on the cathode was found to be more easily achieved on tungsten than glassy carbon. The use of a single molten salt apparently gives rise to a strong increase of the overvoltage compared with metal deposition reactions in multicomponent molten salts. A reproducible linear steady state current density versus potential dependency was observed using both glassy carbon and tungsten substrates. The kinetics of the charge transfer reaction was studied by analysis of potentiostatic current transients.

INTRODUCTION

Metal deposition processes from mixtures of molten salts are generally considered to be comprised of fast electron transfer reactions and diffusion of dissolved species on the reactant side. Phase formation and dissolved metal may also influence the rate and efficiency of metal deposition processes. Very limited information is available from electrochemical studies in single molten salts. Cathodic discharge of Mg(II) species from pure molten $MgCl_2$ was studied by Børresen et. al. [1]. The wetting properties of the substrate were found to influence the phase formation. Heterogeneous nucleation was facilitated on iron, whereas on glassy carbon homogeneous nucleation (formation of metal fog) is as likely to take place.

EXPERIMENTAL

Dry $PbCl_2$ was contained in a pyrex crucible, which was placed inside a transparent furnace with argon atmosphere. The working electrodes were tungsten rods (1 mm and 3 mm diameter) sealed with pyrex and rods of glassy carbon (Tokai, GC-20). A rod of pure graphite served as the counter electrode. The reference electrode, which was made of a tungsten rod in contact with Pb placed inside an alumina tube with a hole, was found to give a stable potential throughout the measurements. Linear sweep voltammetry and potential step chronoamperometry were used to study the cathodic discharge of Pb(II) species from pure molten $PbCl_2$ at 585°C.

RESULTS AND DISCUSSION

Pure molten $PbCl_2$ was yellowish transparent. During potentiostatic electrolysis the melt near the cathode became coloured; transparent red to opaque black as the deposition of lead progressed. This is due to formation of dissolved lead, which is known to be present as a Pb_2^{2+} species [2]. Socalled metal fog was visually observed at the cathode during deposition of lead. However, metal fog was only observed at glassy carbon electrodes. The metal fog was found to spread in the electrolyte near the cathode, disappearing when electrolysis was interrupted.

Figures 1 and 2 show cyclic voltammograms obtained with glassy carbon and tungsten respectively. An anodic wave (Fig. 1) in the potential region ~0.5-1.2 V is believed to be due to oxidation of dissolved oxide complexes. Using glassy carbon a significant cathodic current was observed at potentials approaching the reversible potential for Pb deposition. Potentiostatic current transients indicate that the corresponding reaction is diffusion controlled. No concentration gradients may develop in a single molten salt, and diffusion of dissolved Pb formed in the process may account for the observed behaviour. Similar observations were made during deposition of Mg from pure molten $MgCl_2$ [1]. The cathodic background current detected with a tungsten electrode was insignificant.

The role of the substrate on the cathode process was also studied by coulometric measurements during cyclic voltammetry and reversed potential step chronoamperometry. The ratio of the anodic to the cathodic charge was always less than one and decreased with overpotential and time. The ratio was found to be significantly lower with glassy carbon than tungsten, which shows that the phase formation is facilitated on tungsten. Homogeneous nucleation, i.e. formation of metal fog, at glassy carbon probably accounts for the major difference between the two materials. During long time deposition (seconds) also detachment of deposited Pb causes anodic deficiency.

Potential step chronoamperometry was applied to determine steady state current versus potential curves. A reproducible linear current density versus potential dependency was observed using both substrates. The corresponding overvoltage was significantly higher than expected for a charge transfer controlled reaction. Figure 3 shows a plot of current density versus potential obtained with a tungsten cathode. The linear relationship corresponds to an apparent charge transfer resistance of ~0.009 ohm cm^2. The overvoltage was found to be higher with glassy carbon cathode. Such linear i vs E behaviour has only been reported in cases where the electrolyte resistance is important. In this study the resistance between the cathode and the reference electrode was corrected for by positive feedback. The applied IR compensation was varied over a wide range (0-110% of the actual resistance). Linear i vs E curves were measured over the entire region under study, i.e. up to ~100 A cm^{-2}. The high overvoltages and the linear i vs E dependencies may be due to problems related with the transport of Pb(II) species by migration in pure $PbCl_2$. Experiments with the use of a tungsten microelectrode are under way to eliminate inaccuracies due to the IR drop.

Potential step chronoamperometry at short times (microseconds) was applied to study the kinetics of the charge transfer reaction. The potential dependent rate constant was determined from extrapolating the measured current transient to zero time. Figure 4 shows a plot of the logarithm of the rate constant versus potential from measurements with tungsten. The standard rate constant was determined from the linear relationship to be ~$6.6 \cdot 10^{-4}$ cm s^{-1}, which corresponds to an exchange current density of ~1.7 A cm^{-2}. The results indicate that the charge transfer reaction takes place in one step.

REFERENCES

1. B. Børresen, G.M. Haarberg, R. Tunold, O. Wallevik, J. Electrochem. Soc., **140,** L99 (1993).

2. J.J. Egan, J. Phys. Chem., **65C**, 2222 (1961).

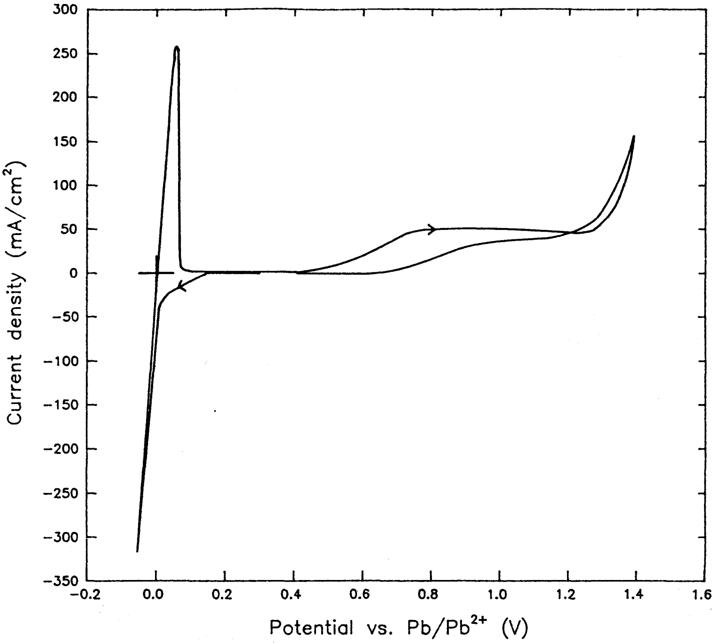

Figure 1. Cyclic voltammogram (100 mV s^{-1}) obtained at a glassy carbon electrode in molten $PbCl_2$ at 585°C.

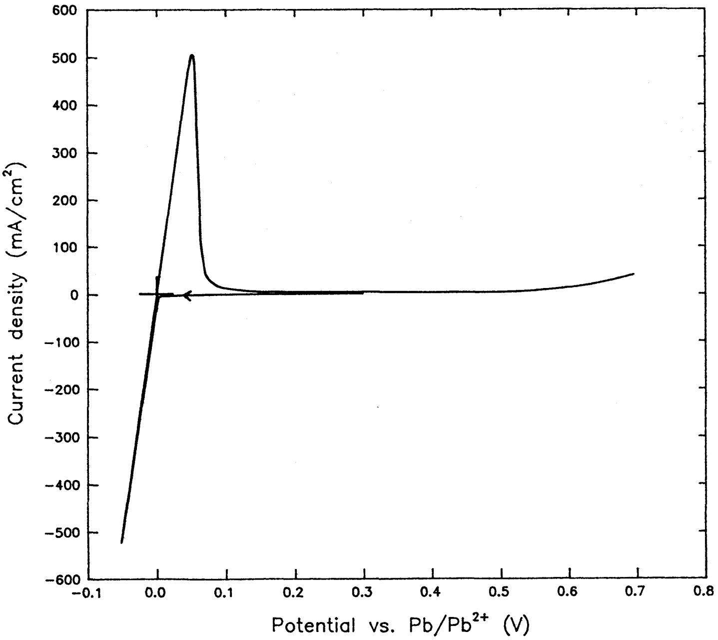

Figure 2. Cyclic voltammogram (100 mV s^{-1}) obtained at a tungsten electrode in molten $PbCl_2$ at 585°C.

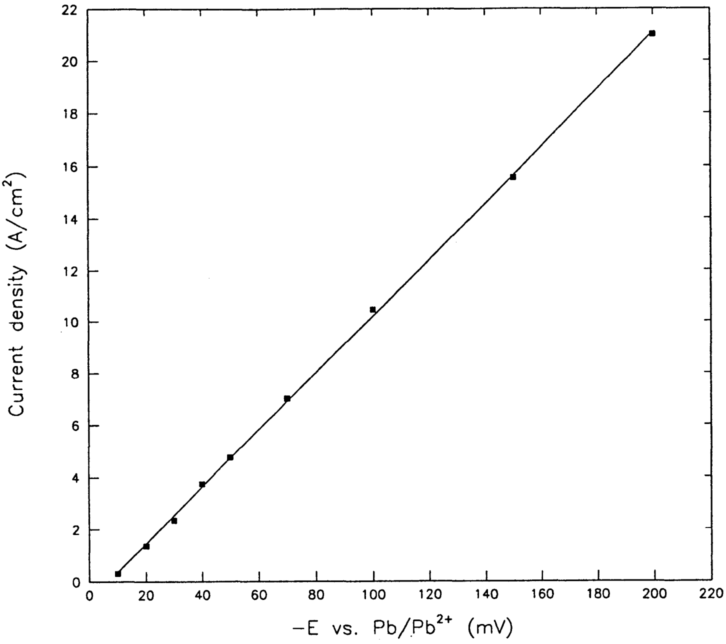

Figure 3. Current density versus potential from potential step measurements at a tungsten electrode in molten $PbCl_2$ at 585°C.

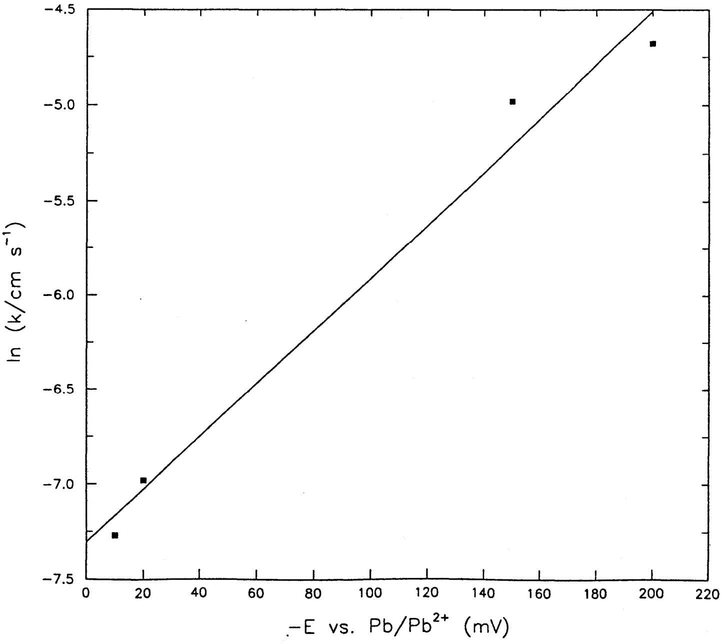

Figure 4. The logarithm of the rate constant versus potential from potential step measurements at a tungsten electrode in molten $PbCl_2$ at 585°C.

DOI: 10.1149/199413.0468PV

REMOVAL OF LEAD AND SILVER FROM CRUDE BISMUTH BY ANODE REFINING.

Zhang Yongjian, Ren Hongyan and Xie Zhong

Central South University of Technology,
Changsha, Hunan 410083. P.R. China

ABSTRACT

The anode refining process of crude bismuth to remove lead and silver was studied. The study was carried out with chloride melts at 400°C in a crucible-in-crucible type pyrex glass electrolyzer. The kinetic regularity of lead and silver removal was found to be in accordance with the equation: $\ln C = b - kt$. Values of the constant k were determined for different current densities. The relationship between the purity of refined bismuth and its direct yield was also determined. A two-stage anode refining method was designed. The first stage was to remove most of the lead (~90%) at higher current density; whereas the second stage was used for removing silver and the remaining lead at lower current density. Under appropriate conditions, high purity (Pb<0.001%, Ag<0.004%) bismuth could be obtained from crude bismuth with the direct yield of bismuth up to 98%.

INTRODUCTION

Impurities in bismuth are removed by fire refining in most bismuth production plants of the world. For removal of impurities such as Sb, As, Se, Te, Fe and Cu, fire refining is highly efficient, but the refining process on the whole is very complicated with a large amount of byproducts and residues, resulting in a very low direct yield of bismuth, great consumption of materials and labor, and poor working conditions. These drawbacks are mainly attributed to the removal of impurity silver with zinc and impurity lead with chlorine, the two most uneconomical and inefficient steps in the process. One better alternative is anode refining in molten slats. Extensive studies in this field have been made by the scholars of the former Soviet Union (1). By the use of anode refining, lead and bismuth in bismuth containing lead, or lead containing bismuth, can be successfully separated from each other (2). The purposes of this study are to investigate methods and conditions for the separation of lead and silver from commercial crude bismuth with emphases on the possibility of attainment of high direct yields of bismuth on the basis of high purity.

EXPERIMENTAL

The study was carried out with $PbCl_2$ - $ZnCl_2$ - KCl - NaCl and $PbCl_2$ - $ZnCl_2$ - NaCl melts at 400°C. A crucible-in-crucible type pyrex glass electrolyzer was used and located in a inconel wire resistance furnace with a silica window to enable one to see inside during electrolysis. The temperature was controlled to ±0.5 C by a TWK - 702 precise temperature control system. Crude bismuth was placed in the inner crucible and served as the anode. A molybdenum wire encapsulated with pyrex glass with the end exposed was used as the electrical contact lead. A circular molybdenum wire surrounding the inner crucible was employed as the cathode. Direct current was supplied by DH 1720 - 1 DC power supply. Electrochemical measurements were carried out by use of a PAR M173 Potentiolstat/Galvanostat and M175 Universal Programmer. Chemical reagents were AR grade and were treated prior to use according to the usual procedure for molten salts. Content of lead and silver in crude bismuth is 2.01% and 0.018% respectively. Some 150g crude bismuth was sued for each run of electrolysis. Lead and silver were analyzed by atomic absorption spectrometry and the result was sometimes checked against spectrographic analysis.

RESULTS AND DISCUSSION

Kinetic Regularity

Fig. 1 shows the voltammograms of anode process of crude bismuth dissolution (lead reference electrode). The electrolyte used in the study was 39% $PbCl_2$ - 31%$ZnCl_2$ - 30%KCl. A slight peak (curve 1) and a plateau (curve 2) in the transient shows that the dissolution of lead is diffusion controlled. There is no indication of silver dissolution, probably due to its content in crude bismuth being too low. According to the figure, the diffusion limiting current of lead dissolution is 1.63 (C_{Pb}=2.01%) and 0.81 (C_{Pb}=1.02%) A • cm^{-2} respectively. Under diffusion control conditions, the variation of dissolving species contained in crude bismuth with electrolysis time can be expressed as:

$$\frac{dC}{d\tau} = - \frac{DS}{V\delta}C \tag{1}$$

Where C is the concentration of dissolving species in crude bismuth ($mol.cm^{-3}$), V the volume of electrolyte, and others have their usual significance. When τ=), C=C_0.Integration of Eq. (1) gives

$$ln(C/C_0) = - \frac{DS}{V\delta}\tau \tag{2}$$

Hence

$$\begin{aligned} lnC &= lnC_0 - \frac{DS}{V\delta}\tau \\ &= b - k\tau \end{aligned} \tag{3}$$

The variation of the concentration of Pb in refined bismuth with electrolysis time at varied current density is shown in Fig. 2. Each plot in Fig. 2 consists of two sections. The first is a straight line, which is in accordance with the equation:

$$C_\tau = C_0 - \frac{a\eta I\tau}{V} \tag{4}$$

Where C_0 and C_τ are the concentrations of lead at the beginning and at the time τ, a the electrochemical equivalent of lead, I current intensity, and V is the volume of crude bismuth (considered as a constant). The second section is in conformity with equation (3) as shown in Fig. 3 The intersection of the two parts represents a critical concentration (C_c), below which the dissolution proceeds under diffusion control. Fig. 4 shows the logarithm of silver concentration in refined bismuth as a function of τ. The dissolution of silver occurs some time after electrolysis begins and is controlled by diffusion from the beginning of dissolution.

Some parameters for anode dissolution of lead and silver are given in Table I

Table I. Parameters for anode dissolution of lead and silver.

$d, A.cm^{-2}$	0.059	0.12	0.24	0.47	0.71	0.94
k, for lead	0.12	0.20	0.30	0.60	0.90	1.20
C_c, for lead	0.012	0.023	0.039	0.059	0.065	0.078
k, for silver	0.0018	0.0030	0.0050	0.0083	0.0095	0.012

Figs. 5 and 6 show the relationship between the direct yield (η_{Bi}) of bismuth and the logarithm of concentration of Pb (C_{Pb}) and Ag(C_{Ag}) in refined bismuth at different current density. In the case of lead, when the concentration is less than the critical one, the following relation applies:

$$lgC_{b} = m + n\eta_{Bi} \qquad (5)$$

This relation can also be de duced from equation (3). The lgC_{Ag} - η_{Bi} relationship also follows equation (5). The direct yield of bismuth at different current density at C_{Pb}=0.001% and C_{Ag}=0.004% is shown in Table II.

Table Ⅱ. Direct yield of bismuth at different current density

d / η / C	0.059		0.12		0.24		0.41		0.71		0.94	
C_{Pb} 0.001%	m	n	m	n	m	n	m	n	m	n	m	n
	77.51	75.62	74.23	72.47	63.11	61.45	49.88	46.48	35.40	34.14	34.14	30.72
	97.2		96.9		96.2		94.4		92.0		90.7	
C_{Ag} 0.004%	m	n	m	n	m	n	m	n	m	n	m	n
	14.08	11.34	12.21	9.45	10.59	7.88	9.31	6.54	7.76	4.99	7.50	4.73
	94.2		93.2		91.3		90.4		87.5		86.7	

Two-Stage Refining Test

It can be seen from the preceding study that it is unreasonable from the viewpoint of high direct yield to use the same current density to remove lead and silver in a single electrolysis run. The current density should be diminished at low concentration of lead and for the removal of silver, which, in crude bismuth, is in very low concentration. A two-stage refining process was therefore considered. The first stage was designed to remove most of the lead in crude bismuth and the second state to remove the remaining lead and silver. To reduce the volatility a melt composition of 60% $PbCl_2$ - 20% $ZnCl_2$ - 15% KCl - 5% NaCl was used as the electrolyte.

Various tests were performed for the first stage of the electrolysis. Tests indicated that when current density increased from 0.1 to 1.0 $A \bullet cm^{-2}$ with the same quantity of electricity, the content of lead in refined bismuth increased from 0.12% to 0.78%, the lead removing rate decreased from 94% to 60% and the direct yield of bismuth dropped down from 100% to 99.36%. It was noted that content of silver in this stage was unchanged.

The second stage refining at lower current density started with first-stage-refined bismuth (or so called intermediate bismuth) obtained at a different current density. Results indicated that the quantity of remaining lead in intermediate bismuth strongly influenced the bismuth yield at the second stage. When the second stage electrolysis was carried out at a current density less than 0.025 $a \bullet cm^{-2}$ (lead removing rate ~90%, bismuth yield more than 99.9%) the direct bismuth yield (from crude bismuth to finished bismuth) would e more than 98% with the content of lead and silver in it less than 0.001% and 0.004% respectively.

REFERENCE

1. U.K. Delimarskii, Chemistry of ionic melts: Electrolysis of Ionic melts (Chinese version, p. 269), Navkova Dymka, Moscow. 1980.

2. O.G. Zarvbitskii, Colored Metalls, No. 6, Vol. 41, 1990.

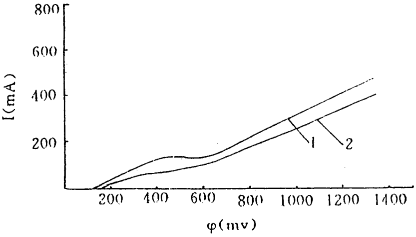

Fig. 1 Voltammograms of anodic dissolution of lead. lead concentration (wt%): 1—2.01%; 2—1.02%

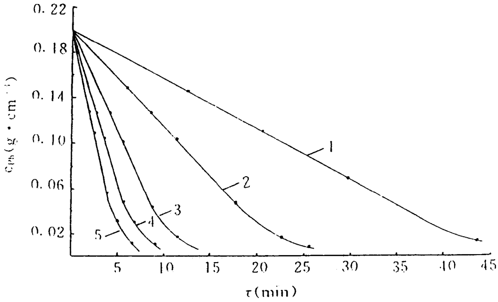

Fig. 2 Variation of lead concentration in bismuth with time. current density (A · cm^{-2}): 1—0.12; 2—0.24; 3—0.47; 4—0.71; 5—0.94;

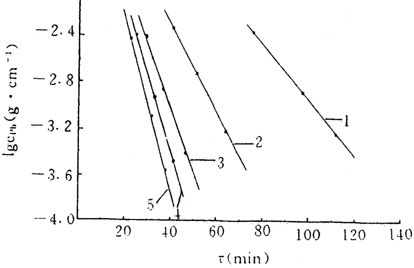

Fig. 3 lgc_{Pb}~τ plot. current density (A · cm^{-2}): 1—0.12; 2—0.24; 3—0.47; 4—0.71; 5—0.94;

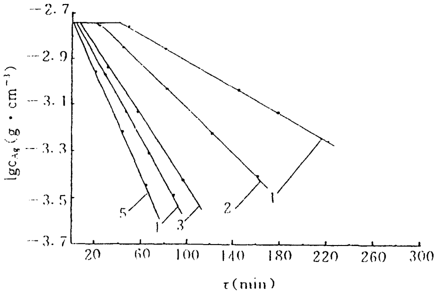

Fig. 4 Variation of silver concentration in bismuth with time. current density (A · cm⁻²): 1—0.12; 2—0.24; 3—0.47; 4—0.71; 5—0.94;

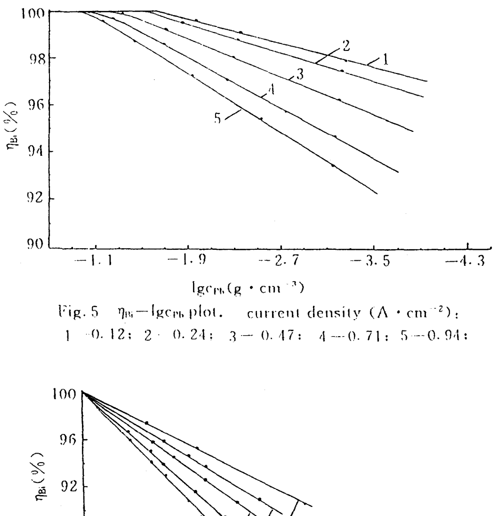

Fig. 5 η_{Bi}—$\lg c_{Pb}$ plot. current density (A · cm⁻²): 1—0.12; 2—0.24; 3—0.47; 4—0.71; 5—0.94;

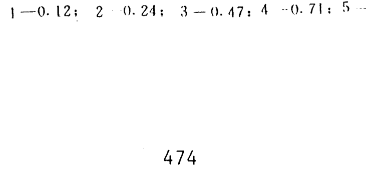

Fig. 6 η_{Bi}—$\lg c_{Ag}$ plot. current density (A · cm⁻²): 1—0.12; 2—0.24; 3—0.47; 4—0.71; 5—0.94;

DOI: 10.1149/199413.0475PV

A STUDY OF LITHIUM DEPOSITION AND STRIPPING FROM AN ALUMINIUM ELECTRODE IN 1-METHYL-3-ETHYLIMIDAZOLIUM CHLORIDE/ $AlCl_3$/LiCl MELTS

Y.S. Fung and S.M. Chau

Department of Chemistry
Hong Kong University
Pokfulam Road
Hong Kong

ABSTRACT

The electrochemical kinetics of the deposition and stripping of lithium from an aluminium electrode in the low melting 1-methyl-3-ethylimidazolium chloride/$AlCl_3$/LiCl system was studied using cyclic voltammetry, chronoamperometry and chronopotentiometry. The effect of the variation of the melt composition on the electrode kinetics was studied and the results were correlated with the structure of the melt as shown by FTIR and NMR techniques. The effect of acidity of the melt and the addition of organic solvents on the kinetics of lithium deposition and stripping were also investigated.

INTRODUCTION

The lithium chloride/ambient-temperature 1-methyl-3-ethylimidazolium chloride(MeEtImCl)-aluminium chloride ionic liquid system has been shown recently to provide a promising medium for advanced lithium battery applications because of its inertness towards lithium and satisfactory conductivity (1-6). LiCl is also quite soluble in this melt. However, rather large changes in the physical properties of melts with high lithium content have been observed [1]. This has important implications for battery applications and is the principal reason for initiating the current investigation. The current investigation is a detailed study of the electrochemical kinetics and the correlations between the kinetics and the changes in MeEtImCl-$AlCl_3$ melt structure as a function of LiCl content up to the saturation of the melt at about a 1.5 mole percent.

The addition of large amounts of LiCl to the MeEtImCl forms a basic melt and gives rise to a high viscosity. Therefore, the LiCl saturated melt has to be neutralized with $AlCl_3$, which influences the melt's structure and physical properties. Therefore, the present work will focus on how LiCl will interact with the melt when it is added progressively up to high LiCl concentrations.

EXPERIMENTAL

The preparation of the lithium chloride enriched 1-methyl-3-ethyl-imidazolium chloride/aluminium chloride melt has been described elsewhere [2,6]. The experiments for electrochemical studies were conducted in an argon filled glove box and the NMR and FTIR studies were performed in a sealed cell filled with melt of the required composition in the glove box. Experiments were conducted immediately after the sealed cell was taken out of the glove box.

RESULTS AND DISCUSSION

The electrochemical kinetics of the deposition and stripping of lithium from aluminium electrode in the low melting MeEtImCl/$AlCl_3$/LiCl system was studied using cyclic voltammetry, chronoamperometry and chronopotentiometry. The effect of the variation of the melt composition on the electrode kinetics was studied and the results were correlated with the structure of the melt as shown by FTIR and NMR techniques.

The effect of the acidity of the melt was shown in Fig. 1 in which the presence of excess amounts of $AlCl_3$ led to reduction of nucleation polarization. This is attributed to the co-deposition of the LiAl alloy at the aluminium electrode as a function of increasing the amount of $AlCl_3$ added to the saturated melt, which led to the decrease in the nucleation potential is indicated by the trend shown in Fig 1 A to C.

The nucleation of the LiAl alloy at the aluminium electrode was shown to be affected by stirring the melt, as indicated in Fig. 2. Increasing the stirring rate led to the reduction in the nucleation potential as shown by the trend revealed in Fig. 2 A to F. This shows that the nucleation rate is the same order as the mass diffusion polarization and thus it will contribute significantly to increasing the current when the system is used for lithium battery applications.

The presence of excessive amounts of $AlCl_3$ in the melt was shown to be detrimental to the cycling performance of the LiAl alloy as shown by the results given in Fig. 3. The presence of more $AlCl_3$ led to the decrease in the cycling efficiency as shown by the trend given in Fig. 3 A to C.

The addition of organic solvents such as benzene and toluene was shown to break up the cation-anion interaction by solvating the ions. This is shown in Fig. 4, which is the ^{27}Al NMR spectra of solvent mixtures with the addition of benzene and toluene. Only a single resonance was obtained with reduction in the linewidth when the organic solvent was added as compared to the lithium enriched ambient melt.

In summary, the acidity of the melt and the presence of organic additives were found to affect the nucleation and the deposition of the LiAl phase at the aluminium electrode. The effect of excessive amounts of $AlCl_3$ was shown to degrade the cycling efficiency of the LiAl. The effect of the organic solvent is attributed to the reduction in viscosity and the break up of the ionic interaction between lithium and the tetrachloro aluminate anion in the highly concentrated lithium enriched ambient melt.

ACKNOWLEDGMENT

The authors would like to acknowledge the support of the Research Grants Council and the Hong Kong University Research Grants Committee for the above work.

REFERENCES

1. Y.S. Fung and S. M. Chau, Mater. Sc. Forum 73-75, 677 (1991).
2. Y.S.. Fung and S.M. Chau, J. Appl. Electrochem., 1992, in press.
3. R. J. Gale, B. Gilbert and R. A. Osteryoung, Inorg. Chem. 17, 2728 (1978).
4. R. J. Gale and R. A. Osteryoung, Inorg. Chem. 19, 2240 (1980).
5. J. S. Wilkes, J. S. Frye, and G. F. Reynolds, Inorg. Chem. 22, 3870 (1983).
6. A. A. Fannin, Jr., L. A. King, J. A. Levisky, and J. S. Wilkes, J. Phys. Chem. 88, 2609 (1984).

FIGURE 1 The chronoamperograms of lithium deposition from the melts with various acidities. A, excess $AlCl_3$ = 4.44 %, B, excess $AlCl_3$ = 2.44 % and C, no excess $AlCl_3$. Stepping potential = -1.65 V, $[LiAlCl_4]$ = 0.84 mole/kg, working electrode = Al 0.79 mm^2.

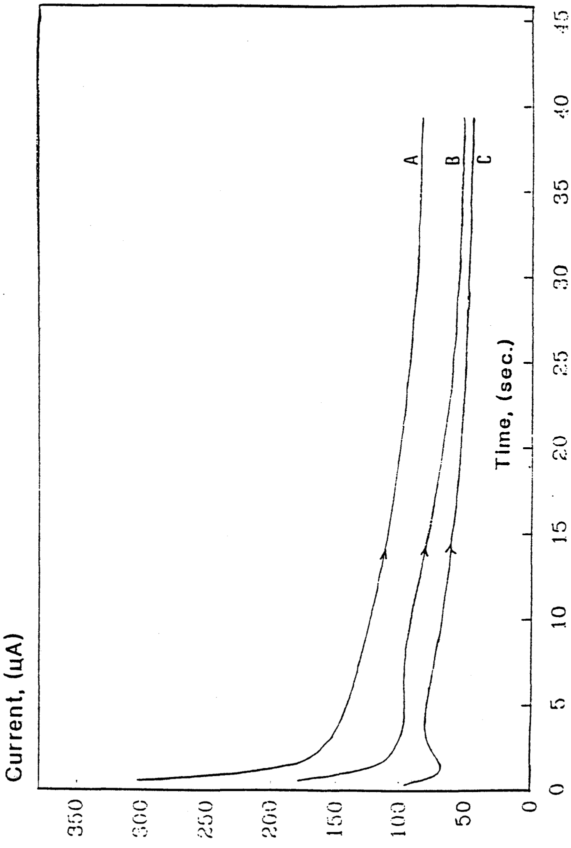

FIGURE 2 The chronoamperograms of lithium deposition from the melts with various stirring rates. Stepping potential = -0.65 V, [$LiAlCl_4$] = 0.84 mole/kg, stirring rate A, 0 r/min; B, 105 r/min; C, 375r/min; D, 600 r/min; E, 840 r/min and F, 1020r/min.

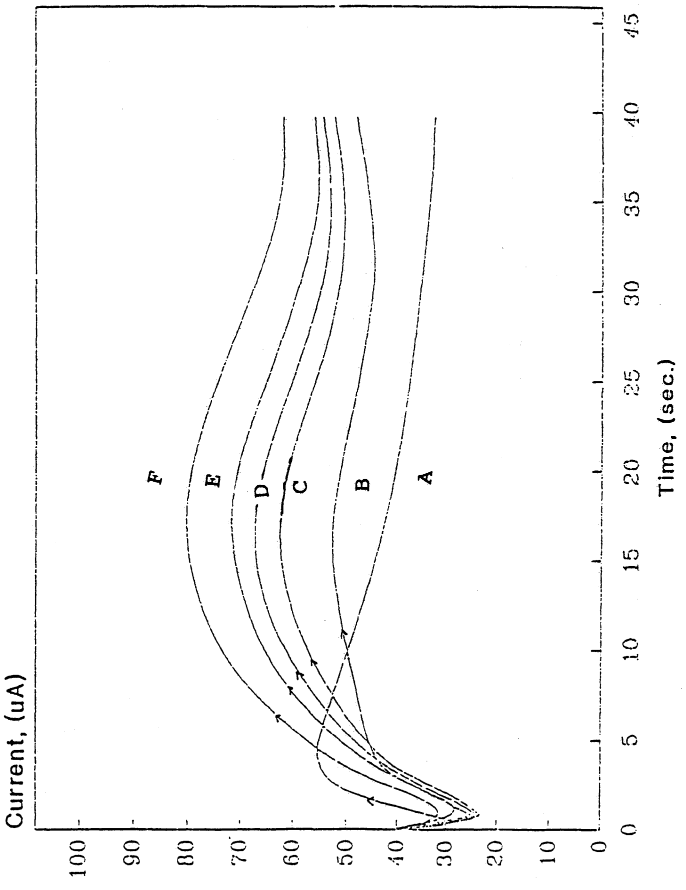

FIGURE 3 The chronopotentiograms of lithium deposition from the melts with various acidities. A, excess $AlCl_3$ = 9.4 % ; B, excess $AlCl_3$ = 2.4 % and C, no excess $AlCl_3$. $[LiAlCl_4]$ = 0.85 mole/kg, working electrode : Al 0.16 cm^2. Stepping current = 0.6 mA.

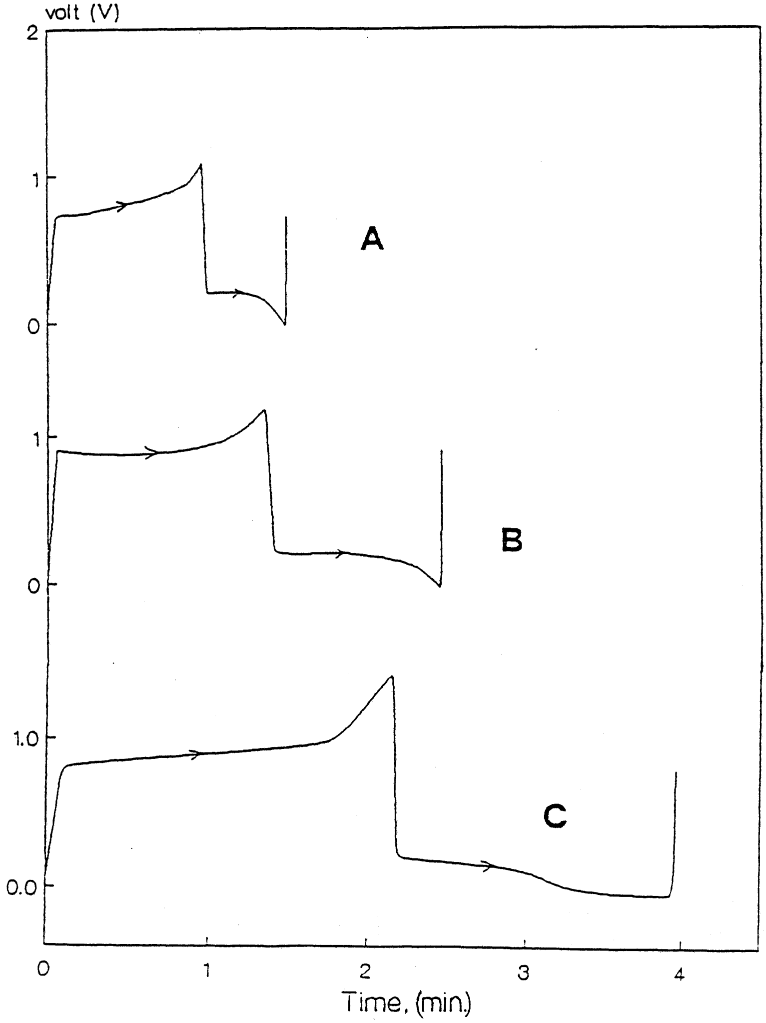

FIGURE 4 ^{27}Al NMR spectra of melt-toluene (A) and melt-benzene (B) mixtures.

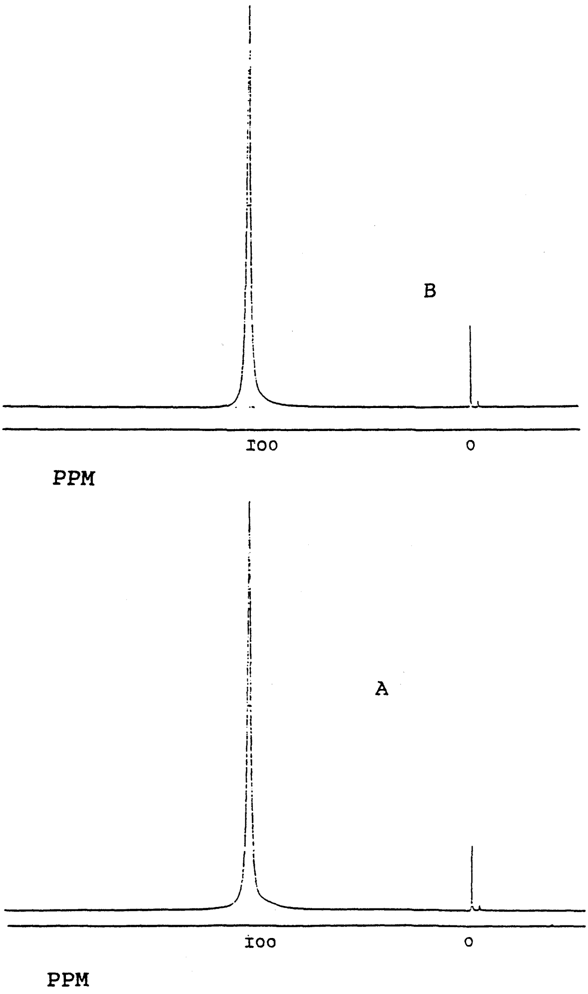

DOI: 10.1149/199413.0483PV

LATENT ACIDITY IN BUFFERED CHLOROALUMINATE IONIC LIQUIDS

I. C. Quarmby, R. A. Mantz, L. M. Goldenberg, and R. A. Osteryoung*

Department of Chemistry
North Carolina State University
Raleigh, NC 27695-8204

ABSTRACT

Buffered chloroaluminate ionic liquids are prepared by taking the ambient temperature molten salt, 1-ethyl-3-methylimidazolium chloride (ImCl)-$AlCl_3$, containing an excess of $AlCl_3$, and adding NaCl. The reaction $NaCl(s) + Al_2Cl_7^- \rightleftharpoons 2\ AlCl_4^- + Na^+(l)$ takes place and the melt is driven towards neutrality. NaCl is insoluble in the resultant neutral melt; the liquid then consists of Im^+, Na^+, and $AlCl_4^-$ ions, with $[Im^+] + [Na^+] = [AlCl_4^-]$. The electrochemical window that results is essentially that of the unbuffered neutral melt and shows no Al(III) reduction wave.

We have found that these buffered melts possess what we term "latent acidity". A weak Lewis base, B, such as acetylferrocene, is uncomplexed by $AlCl_3$ in an unbuffered neutral melt. In a neutral buffered melt, the $AlCl_3$ adduct forms. This takes place as a result of the reaction $B + AlCl_4^- + Na^+ \rightleftharpoons B{:}\ AlCl_3 + NaCl(s)$, the reaction being driven by the precipitation of NaCl(s). Experiments justifying these statements are presented.

INTRODUCTION

Chloroaluminate ionic liquids formed from aluminum chloride and an organic chloride, typically 1-ethyl-3-methylimidazolium chloride (ImCl) or N-(butyl)-pyridinium chloride (BuPyCl), are liquid at room temperature (1,2). These molten salts exhibit Lewis acid-base chemistry governed by the equilibrium :

$$2\ AlCl_4^-(l) \rightleftharpoons Cl^-(l) + Al_2Cl_7^-(l) \qquad K \approx 10^{-18} \qquad [1]$$

The concentrations of Lewis acidic species ($Al_2Cl_7^-$) and basic species (Cl^-) define the chloroacidity of the melt. The melts are termed acidic, basic, or neutral if the mole ratio of $AlCl_3$ to the organic chloride is greater than, less than, or equal to 1.00. In a neutral melt, prepared by adjusting a slightly acidic or basic melt until the desired electrochemical window is obtained, the principle anionic species is $AlCl_4^-$; neutral melts obtained in this manner have an electrochemical window of approximately 4.4 V (3). This window is reduced if Lewis acidic or basic species are generated *in situ,* even in small concentrations.

A method of producing and maintaining buffered neutral melts, which are of considerable interest as potential battery electrolytes, is to add NaCl(s) or LiCl(s) to an acidic melt (4,5). The reaction:

$$MCl(s) + Al_2Cl_7^-(l) \rightleftharpoons 2\ AlCl_4^-(l) + M^+(l) \quad K >> 1 \qquad [2]$$

takes place, where M^+ is an alkali metal cation.

The addition of MCl to an acidic melt results in the dissolution of MCl equivalent to the moles of $Al_2Cl_7^-$ initially present and buffers the melt. If $Al_2Cl_7^-$ is generated, neutrality is maintained by dissolution of excess MCl(s) or, if chloride is generated, by precipitation of MCl(s). Recent work in our laboratory, however, has revealed an unexpected consequence of these buffered melts. These melts show a chemical behavior that we term "latent acidity". We report on the use of acetylferrocene and other Lewis bases as probes of this behavior in NaCl-buffered melts.

RESULTS AND DISCUSSION

Acetylferrocene

The chemistry of acetylferrocene in non-buffered $AlCl_3$:BuPyCl melts was reported by Slocum *et al.* (6). In basic melts the behavior of acetylferrocene is similarly to that observed in conventional solvents. In acidic melts an $AlCl_3$ adduct was formed at the carbonyl group:

$$Fc(COMe) + Al_2Cl_7^- \rightleftharpoons Fc(C(O{:}AlCl_3)Me) + AlCl_4^- \qquad [3]$$

where Fc = $(C_5H_5)Fe(C_5H_4-)$. Formation of such adducts has been reported for carbonyl, cyanide, and ferrocyanide groups in acidic melts (7-9). The adduct undergoes a 1-electron oxidation at a potential 350 mV positive of acetylferrocene itself.

In slightly acidic or basic $AlCl_3$:ImCl melts we observed virtually identical behavior to that reported in the literature. In unbuffered neutral melts we have found that a mixture of adduct and free acetylferrocene is formed although the ratio of species varied from batch to batch of melt. However, the concentration of adduct was always less than 2 mM and occasionally only free acetylferrocene was observed. The formation of the adduct in unbuffered neutral melts most probably arises from the presence of small amounts of $Al_2Cl_7^-$ which are present simply as a result of the difficulty of preparing an "exactly" neutral melt (3). "Neutral" melts may, in fact, be several millimolar in Cl^- or $Al_2Cl_7^-$ which cannot be detected electrochemically (10).

In contrast, addition of acetylferrocene to a neutral buffered melt, $[Na^+] = 0.36M$, prepared by the addition of NaCl(s) to an initially acidic melt, i.e., one containing excess $AlCl_3$, resulted solely in the formation of the acetylferrocene-$AlCl_3$ adduct even at high concentrations of acetylferrocene (20 mM). The formation of the adduct in a buffered melt suggests that there is a source of $AlCl_3$ present. No aluminum deposition wave is observed in the buffered neutral melt at either platinum or glassy carbon electrodes which implies that the concentration of $Al_2Cl_7^-$ is very low. A possible source of $AlCl_3$, however, is $AlCl_4^-$, a very weak Lewis acid.

In an unbuffered neutral melt the equilibrium:

$$Fc(COMe) + AlCl_4^- \rightleftharpoons Fc(C(O{:}AlCl_3)Me) + Cl^- \qquad [4]$$

lies far to the left. The $AlCl_4^-$ is not a sufficiently strong Lewis acid for the reaction to occur. In a buffered melt, however, the reaction:

$$Fc(COMe) + AlCl_4^- + Na^+(l) \rightleftharpoons Fc(C(O{:}AlCl_3)Me) + NaCl(s) \qquad [5]$$

can take place; the generation of chloride ion results in the precipitation of Na^+ to yield NaCl(s), thus providing a driving force to pull the equilibrium to the right.

Accordingly we prepared an acidic melt which was ~80 mM in $AlCl_3$ (Al deposition evident) and added NaCl(s). A neutral melt electrochemical window was observed. Acetylferrocene was then added to the melt and its electrochemistry examined. RDE voltammograms were run over a range of rotation rates and acetylferrocene concentrations. The adduct was the only species present at concentrations under 80 millimolar. On increasing the concentration of acetylferrocene a second wave, due to uncomplexed acetylferrocene appeared. Limiting currents were measured for each species (Figure 1). Plots of limiting current against $\omega^{1/2}$ were linear for both waves throughout the concentration range. From the Levich equation:

$$I_{lim} = KC^{o}\omega^{1/2}, \quad \text{where } K = 0.62nFAD^{2/3}\upsilon^{-1/6} \qquad [6]$$

the slope of the I_{lim} *vs.* $\omega^{1/2}$ plot is proportional to the concentration (C^{o}) of the electroactive species in the bulk of the solution. A plot of the slopes against total acetylferrocene concentration is shown in Figure 2. It clearly illustrates that below 75 millimolar the adduct is the sole species present and at higher concentrations the adduct concentration is constant and equal to the initial concentration of sodium ions in the buffered melt. The concentration of the free species increases linearly with total acetylferrocene concentration above 80 millimolar, as predicted by equation 5. That is, once all the sodium ions precipitated, no adduct could form (equation 4).

The equilibrium was also characterized by UV-Visible spectroscopy. The adduct and free acetylferrocene exhibit markedly different spectra (Table I), both species obeying Beer's law. At 580 nm the molar absorptivity of the adduct is two orders of magnitude greater than the free species and thus absorbance at 580 nm gives, to a first approximation, a measure of adduct concentration. The absorbance at 580 nm *vs.* acetylferrocene concentration (Figure 3) rises linearly to a maximum at 80 millimolar and remains constant above this concentration. The molar absorptivities determined from the experimental data agree with those obtained from a Beer's law plot of acetylferrocene in a buffered melt ($[Na^{+}] = 0.5$ M). This is in good agreement with the electrochemical data above. However a Beer's law plot of acetylferrocene in an acidic melt ($[Al_2Cl_7^{-}] = 0.5$ M) gave much smaller molar absorptivities (*ca.* 60%) although the peak shape was identical. Sodium chloride particulates do not appear to be responsible for the difference. Buffered solutions of acetylferrocene showed similar spectra before and after filtration through a 0.2 micron filter. Further work is planned in this area.

Dimethylaniline (DMA) and Pyrrole

DMA, a stronger Lewis base than acetylferrocene, has been shown to form an aluminum chloride adduct in an acidic room temperature molten salt (11) according to equation 7:

$$DMA + Al_2Cl_7^{-} \rightleftharpoons DMA{:}AlCl_3 + AlCl_4^{-} \qquad [7]$$

The equilibrium lies far to the right when $Al_2Cl_7^{-}$ is in excess over DMA. When DMA is in excess a mixture of adduct and free DMA results. The ^{1}H nmr spectrum of the methyl region shows a single line that is the population weighted average of the spectrum of the adduct and the free DMA. This is the result of a fast exchange process on the nmr timescale between DMA and $DMA{:}AlCl_3$. Similarly the chemical shift of the methyl protons in a buffered melt also depends on the population weighted average of the adduct and the free DMA (Figure 4). When the stoichiometry of [DMA]/[Na^+] is less than 1 the chemical shift is that of the adduct. Above this the chemical shift decreases linearly with mole fraction of free DMA in exactly the same fashion as in an acidic melt.

The electropolymerisation of pyrrole is very sensitive to adduct formation (12). In unbuffered neutral melts pyrrole is easily polymerized at potentials close to 1V. A chronoamperometric curve (Figure 5a) shows the typical nucleation loop and a thin film is observed on a platinum electrode. In contrast no polymerization is observed in either an acidic or a buffered neutral melt where pyrrole forms an adduct. No nucleation loop (Figure 5b) or polymer peak are observed. As the [pyrrole]/[Na^+] stoichiometry becomes greater than 1 waves for polypyrrole appear. A white solid precipitated following addition of both DMA and pyrrole to a buffered melt, presumably NaCl.

All our observations are in agreement with equation 8, a general description of the chemistry of a Lewis base in a buffered melt:

$$B{:} + AlCl_4^- + Na^+(l) \rightleftharpoons B{:}AlCl_3 + NaCl(s) \qquad [8]$$

where B: is a Lewis base.

CONCLUSION

NaCl-buffered melts exhibit latent acidity in the presence of a Lewis base. The precipitation of NaCl provides the driving force for the formation of aluminum chloride adducts. These melts are an excellent medium in which to study $AlCl_3$ complexation, allowing precise control of the amount of $AlCl_3$ available for complexation and possessing a very large electrochemical window in which to observe complexed species. Additionally, one might anticipate that proton may be superacidic in buffered neutral melts as it is in acidic melts. In the latter system it is proposed that $Al_2Cl_7^-$ acts as a sink for Cl^- (13). Likewise, Na^+ acts as a sink for Cl^- in buffered melts. Work to investigate the acidity of proton is in progress (14).

ACKNOWLEDGMENT

This work was supported by theAir Force Office of Scientific Research.

REFERENCES

1. J. S. Wilkes, J. A. Levisky, R. A. Wilson, and C. L. Hussey, *Inorg. Chem* **1982,** *21,* 1263.
2. J. Robinson and R. A. Osteryoung, *J. Am. Chem. Soc.* **1979,** *101,* 323.
3. M. Lipsztajn and R. A. Osteryoung, *J. Electrochem. Soc.* **1983,** *130,* 1968,
4. T. J. Melton, J. Joyce, J. T. Maloy, J. A. Boon, and J. S. Wilkes, J. *Electrochem. Soc.,* **1990**, *137,* 3865.
5. C. Scordilis-Kelley, J. Fuller, R. T. Carlin, and J. S. Wilkes, J. *Electrochem. Soc.*, **1992**, *139*, 694.
6. D. W. Slocum, A. L. Edgecombe, J. S. Fowler, H. F. Gibbard, and J. Phillips, *Organometallics*, **1990**, *9*, 307.
7. G. Cheek and R. A. Osteryoung, *J. Electrochem. Soc.*, **1982**, *129*, 2488; **1982**, *12*, 2739.
8. C. Woodcock and D. F. Shriver, *Inorg. Chem.* **1986**, *25*, 2137
9. B. Das, R. T. Carlin, and R. A. Osteryoung, *Inorg. Chem.*, **1989**, *28*, 421 .
10. Z. J. Karpinski and R. A. Osteryoung, *Inorg. Chem.* **1984**, *23*, 4561.
11. P. C. Trulove, R. T. Carlin, and R. A. Osteryoung, *J. Am. Chem. Soc.* **1990,** *112, 4567.*
12. T. A. Zawodzinski, Jr., L. Janiszewska, and R. A. Osteryoung, *J. Electroanal. Chem.,* **1988**, *255*, 111 and references therein.
13. G. P. Smith, A. S. Dworkin, R. M. Pagni, and S. P. Zingg, *J. Am. Chem. Soc.*, **1989**, *111*, 525; **1989**, *111*, 5075.
14. R. A. Mantz, I. C. Quarmby, and R. A. Osteryoung, work in progress.

Table I Molar absorptivity of Acetylferrocene in $AlCl_3$:ImCl Melts

		ε (± 5%) / $dm^3\ mol^{-1}\ cm^{-1}$		
Melt	Species	454 nm	518 nm	580 nm
Basic	Free	426	140	12
Acidic	Adduct	468	1170	589
Buffered	Adduct	822	2180	1106

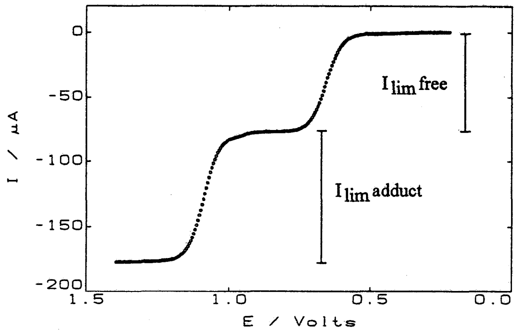

Figure 1 RDE voltammogram of acetylferrocene (120mM) in a NaCl-buffered melt; [Na^+] = 80mM; 2000rpm; Pt disk electrode (area = 0.020 cm^2)

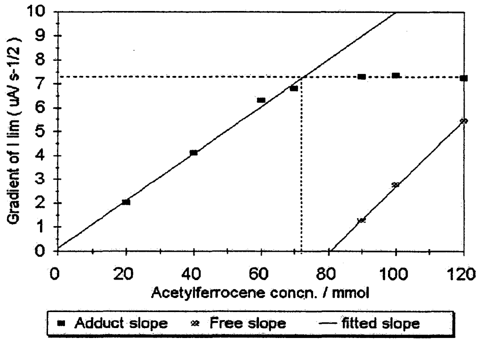

Figure 2 Plot of the slopes of I lim *vs.* $\omega^{1/2}$ plots for acetylferrocene and the $AlCl_3$ adduct *vs.* concentration of acetylferrocene

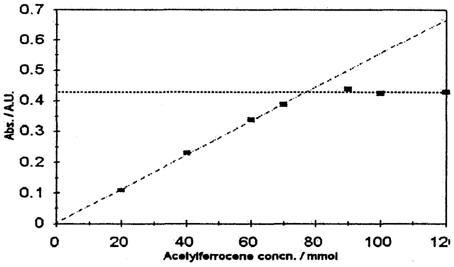

Figure 3 A plot of absorbance at 580 nm *vs.* acetylferrocene concentration in a 0.05 mm path length cell

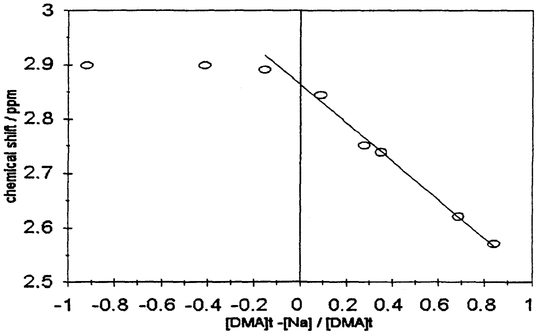

Figure 4 Chemical shift of DMA Methyl protons *vs.* $[DMA]_t$ - $[Na^+]$ / $[DMA]_t$

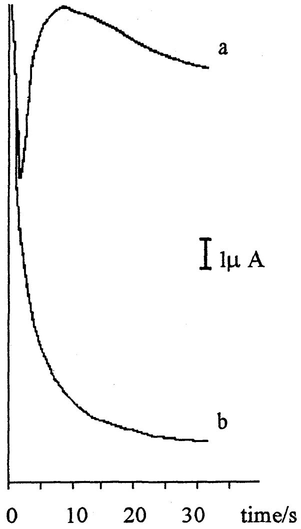

Figure 5 Chronoamperometric response of a Pt disk electrode, [pyrrole] = 0.5M, Epol = 1.0V *vs.* Al wire in 1.5:1 melt, a) neutral unbuffered melt; b) NaCl-buffered melt, $[Na^+]$ = 0.5M.

DOI: 10.1149/199413.0491PV

STUDIES OF THE CATHODIC LIMIT OF PROTON-MODIFIED ROOM TEMPERATURE CHLOROALUMINATE MOLTEN SALT ELECTROLYTES

Thomas L. Riechel, Michael J. Miedler,
and Eric R. Schumacher

Department of Chemistry
Miami University
Oxford, OH 45056

ABSTRACT

When protons in the form of HCl_2^- are added to a 1-methyl-3-ethylimidazolium chloride/$AlCl_3$ melt, buffered with sodium chloride, the negative voltage limit shifts farther negative from −2100 mV to −2400 mV (vs. a reference of Al in an N = 0.6 melt). When protons are added to a similar neutral melt without NaCl present, no such shift occurs. It has previously been shown that in the proton-modified melts sodium is plated on Pt electrodes, and it is believed that the limiting reduction process is for the methylethylimidazolium cation (MEI^+). Thus, both added protons and a sodium surface are necessary to shift the reduction of MEI^+ and widen the voltage limit. FTIR studies are underway to try to identify the product of MEI^+ reduction.

INTRODUCTION

Sodium chloride buffered room temperature chloroaluminate molten salts made by mixing 1-methyl-3-ethylimidazolium chloride (MEICl) and $AlCl_3$ are being evaluated as possible battery electrolytes. These buffered melts provide a stable 4V window and a water-free environment needed for the use of alkali metal anodes. In spite of this wide voltage window (approximately +2.2V to −2.2V vs a reference electrode of Al in an N=0.6 melt) the window does not extend to negative enough voltages to observe the reversible reduction of Na^+. Riechel and Wilkes [1] have shown that the voltage window can be extended about 200 mV more negative by the addition of a proton-rich melt, 1-methyl-3-ethylimidazolium hydrogen dichloride ($MEIHCl_2$) [2]. The resulting proton-modified melt allows the reversible plating and stripping of sodium at Pt and W electrodes [1].

To be useful in a rechargeable battery the sodium deposited on these inert electrodes must be stable, but also easily stripped. Riechel and Wilkes showed that the plated surface was stable for over five hours, but the stripping process often exhibited two peaks. It was suggested that the product of MEI^+ reduction is plated and stripped along with sodium, and that the resulting organic film protects the sodium metal from reacting directly with the melt.

In this paper we explore the redox chemistry of MEI^+ and its relationship to plated sodium. Electrochemical studies will be reported concerning the cathodic voltage limit change as $MEIHCl_2$ is added to the buffered melt. FTIR studies are underway to help identify the MEI^+ reduction product that coats the electrodes.

EXPERIMENTAL

Cyclic voltammetry and controlled potential electrolysis were performed using a Bioanalytical Systems (BAS) Model 100A Electrochemical Analyzer. A three electrode cell was used with a BAS Pt working electrode, a Pt flag auxiliary electrode, and a reference electrode consisting of an Al wire in an N=0.6 $MEICl/AlCl_3$ melt. All electrochemical experiments were carried out in a Vacuum Atmospheres glove box under a dry nitrogen atmosphere.

Preparation of the sodium chloride buffered $MEICl/AlCl_3$ melt and the $MEIHCl_2$ melt have been described previously [1-3] and are straightforward. The formation of the protonic melt with the extended voltage window requires the dropwise addition of $MEIHCl_2$ to the NaCl buffered $MEICl/AlCl_3$ melt until the melt becomes thick and cloudy in appearance. This physical change corresponds to the observation of sodium plating and stripping via cyclic voltammetry [1].

For FTIR examination of coated electrodes an air tight electrode cap has been made and fitted with a 13x2 mm KCl window. FTIR spectra will be recorded using a Perkin Elmer Model 1800 spectrometer integrated with a Spectra Tech IRPLAN microscope.

RESULTS AND DISCUSSION

Gray, Winnick, and Kohl [4] have also investigated the proton-modified melt by bubbling HCl(g) directly through the neutral, NaCl buffered melt. They found that an HCl partial pressure of at least 6mm Hg was necessary to shift the voltage limit and observe sodium plating. But the sodium reduction peak was difficult to resolve from the MEI^+ reduction peak and the product of MEI^+ reduction has not been identified. Scordilis-Kelley and Carlin [5] used a similar melt modification ($MEIHCl_2$ added to a LiCl buffered melt) to separate the reduction peak for Li^+ from the solvent window and measure the standard reduction potential for lithium. To avoid overlap and measure the standard reduction potential for sodium they modified a 1,2-dimethyl-3-

propylimidazolium chloride/$AlCl_3$ melt, which has a more negative potential window. These workers concluded that HCl_2^- causes the reduction potential of MEI^+ to shift negatively, and may slow down the oxidation of Li(s) and Na(s) by organic cations. Since the stability of Na(s) and its reversible plating and stripping are critical for its use in such electrolytes, we are attempting to characterize the process occurring near the voltage limit and to identify the MEI^+ reduction product that sometimes coats the electrode.

As seen in Figure 1, for the proton-modified NaCl buffered melt, sharp plating and stripping peaks for sodium are observed if the potential is not scanned too far negatively. When a scan proceeds too far into the limiting voltage process, the sodium reduction peak appears as only a shoulder, and no stripping peak is observed (Fig. 2). Following controlled potential electrolysis to plate sodium, two peaks are often observed when anodic stripping is subsequently performed (Fig. 3). These data show that it is difficult to separate the reduction of Na^+ from that of MEI^+.

In order to optimize the separation of these two reduction processes we have attempted to correlate the shift in the potential window limit to the amount of HCl present in the melt. Since the definition of the voltage limit depends on the amount of current deemed allowable, we have carried out preliminary experiments monitoring the decrease in current at a fixed potential on the leading edge of the limiting reduction process. The data given in Table 1 clearly indicate that as the Wt.% HCl in the melt increases, the potential of the limiting reduction process shifts negatively, and the current at −2.10V drops by a factor of ten. This means that the reduction of MEI^+ becomes progressively more difficult as the presence of HCl_2^- impedes that process.

From another series of experiments, we have plotted the potential corresponding to a current of 10 μA, representing the negative voltage limit, when various amounts of $MEIHCl_2$ have been added. Figure 4 shows that the limiting voltage changes linearly from about −2100 mV to −2400 mV. This represents a 300 mV shift in the reduction potential of MEI^+.

A similar experiment was carried out adding $MEIHCl_2$ to a neutral, unbuffered (no NaCl) melt. In this case (Figure 5) the background currents rose significantly and chloride oxidation was apparent at 1.3V (because the melt was not buffered), but there was no shift in the negative voltage limit. This means that the sodium surface on the plated electrode is required for the shift in the MEI^+ reduction potential observed in proton-modified buffered melts.

In efforts to identify the MEI^+ reduction product by FTIR spectroscopy, we are examining neutral, neutral buffered, and neutral buffered proton-modified melts. Lewis basic, neutral, and acidic melts have been examined previously and their IR spectra reported [6]. We are recording spectra of the melts between KCl windows and have constructed an air-tight electrode cap for use with plated electrodes. If reduction of MEI^+ leads to significant structural changes, this should be observable in the IR spectra.

From the above studies we hope to learn how to stabilize the sodium plated on inert electrodes in the proton-modified melts.

ACKNOWLEDGEMENTS

We wish to thank the Frank J. Seiler Research Laboratory for supplying some of the melt components, and Dr. Andy Sommer of the Molecular Microspectroscopy Laboratory (Miami University) for assistance in obtaining the FTIR spectra.

REFERENCES

1. T.L. Riechel and J.S. Wilkes *J. Electrochem. Soc.* **139**, *977* (1992).

2. T.A. Zawodzinski, Jr. and R.A. Osteryoung *Inorg. Chem.*, **27**, *4383* (1988).

3. T.J. Melton, J. Joyce, J.T. Maloy, J.A. Boon, and J.S. Wilkes, *J. Electrochem. Soc.*, **137**, *3865* (1990).

4. G.E. Gray, J. Winnick, and P.A. Kohl "A Room Temperature Molten Salt Electrolyte for the Sodium/Iron Chloride Battery", Paper No. 10, 183rd Meeting of the Electrochemical Society, May 16-21, 1993, Honolulu Hawaii.

5. C. Scordilis-Kelley and R.T. Carlin *J. Electrochem. Soc.*, **140**, *1606* (1993).

6. K.M. Dieter, C.J. Dymek, Jr., N.E. Heimer, J.W. Rovang, and J.S. Wilkes, *J. Amer. Chem. Soc.*, **110**, *2722* (1988).

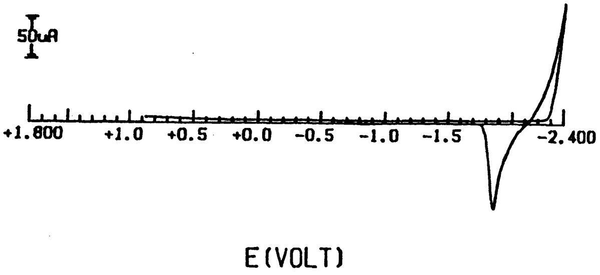

Fig. 1 Cathodic scan cyclic voltammogram of a Lewis neutral, NaCl buffered, MEICl/AlCl$_3$ melt after the addition of MEIHCl$_2$, at a Pt working electrode. Scan rate: 100mV/sec.

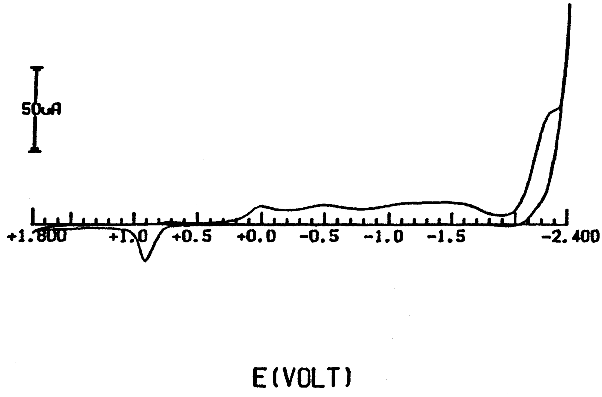

Fig. 2. Cathodic scan cyclic voltammogram of the melt described in Fig. 1. (Scan rate: 100mV/sec.) The scan proceeds beyond the negative potential limit of the electrolyte.

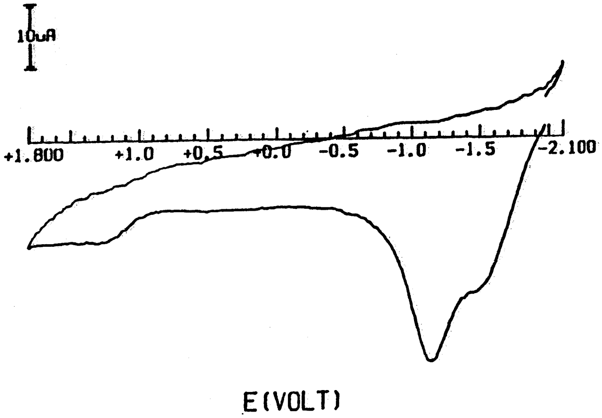

Fig. 3. Anodic scan cyclic voltammogram of the melt described in Fig. 1 after plating for 1 min. at −2.5V. Scan rate: 100mV/sec.

Table 1
Current for the Cathodic Solvent Peak at −2.10V

Wt. % HCl in Melt	Current (amps)
0	1.05×10^{-5}
0.014	1.02×10^{-5}
0.055	9.66×10^{-6}
0.137	7.73×10^{-6}
0.259	4.83×10^{-6}
0.299	3.95×10^{-6}
0.406	9.88×10^{-7}

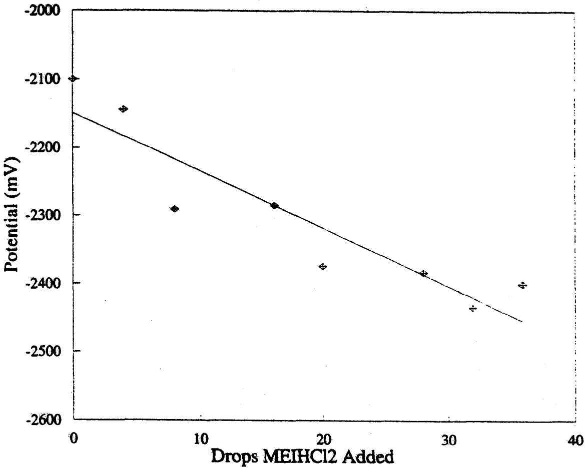

Fig. 4. Plot of the limiting potential corresponding to a 10 μA current in cyclic voltammograms of a Lewis neutral, NaCl buffered, MEICl/AlCl$_3$ melt as a function of the amount of MEIHCl$_2$ added.

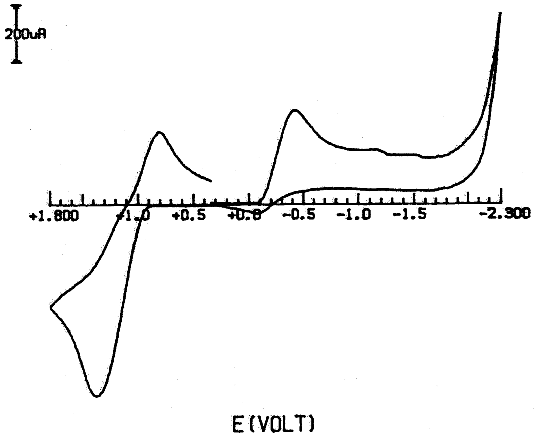

Fig. 5. Cathodic scan cyclic voltammogram of a Lewis neutral, unbuffered, MEICl/AlCl$_3$ melt after the addition of MEIHCl$_2$, at a Pt working electrode. Scan rate: 100 mV/sec.

DOI: 10.1149/199413.0498PV

ELECTROCHEMICAL STUDY ON THE REDUCTION OF Gd(III) IN MOLTEN CHLORIDES

Qiqun Yang, Guankun Liu, Yanbing Ao
Department of Chemistry, Zhongshan University,
Guangzhou 510275, China

Abstract

The electrode processes of Gd(III) reduced on Mo and Ni electrodes in molten NaCl-KCl-$GdCl_3$ and KCl-$GdCl_3$ have been investigated by cyclic voltammetry, potential-time curves after potentiostatic electrolysis and current-time curves at varying potential steps. The free energy of formation of intermetallic compounds, the diffusion coefficients of Gd(III) in the melt and in the alloyed cathode were determined.

INTRODUCTION

Gadolinium is one of the important rare earth elements. The alloys of gadolinium with ferrous metals received much attention because of their magnetic and magneto-optical properties. These alloys, for example, the Gd-Ni and Gd-Co alloys, have been used to manufacture useful materials. It is necessary to investigate the electrochemical behavior of Gd(III) in molten salt in order to prepare gadolinium and its alloys by electrolysis. Electrodeposition of gadolinium in molten fluorides had been studied(1-3). In this paper, the electroreduction of Gd(III) on molybdenum and on nickel electrodes in molten NaCl-KCl-$GdCl_3$ and KCl-$GdCl_3$ were investigated.

EXPERIMENTAL

Equimolar NaCl-KCl and KCl were dehydrated in vacuum at 400°C respectively. Dehydrated $GdCl_3$ was obtained by the reaction of Gd_2O_3($\geq$99.5%) with an excess of NH_4Cl. All reagents used here were A.R. or C.P..

Mo and Ni were used as the working electrodes. Spectrally pure graphite was used as the counter electrode. The reference electrode was Ag/AgCl(10 mol%), NaCl-KCl. The electrode potentials measured were given versus the chlorine electrode according to Ref. 4. The electrochemical measurements were made with a quartz cell under agron atmosphere. The DCD-3 low and superlow frequency functional generator, HDV-7B potentiostat and 3086 X-Y recorder were used to measure the cyclic voltammograms, potential-time curves after potentiostatic electrolysis and current-time curves at stepped potentials. The temperature was controlled by a WT-722 regulator and a KG-GA silicon controlled power unit.

The $GdCl_3$ concentration in the melt was analyzed by complexometric titration. The phases of the surface alloy layers were analyzed by x-ray diffraction.

RESULTS AND DISCUSSION

The electrode process of Gd(III) reduced on a molybdenum electrode

Fig. 1a shows the cyclic voltammogram of a Mo electrode in molten NaCl-KCl-$GdCl_3$(2.72 mol%) at 730°C. Two cathodic waves started at -3.01, and -3.19 V. The deposition potential of sodium on the Mo electrode in this melt was determined to be -3.17 V. Hence, the cathodic wave started at -3.01 V is due to the reduction of Gd(III) to Gd(0) in one step. When the potential was swept back before the deposition of sodium occurred and measured at a higher concentration of Gd(III), a narrow anodic stripping peak was observed and the line crossed the zero current axis with a very steep slope (Fib. 1b). These features indicate that the reduction of Gd(III) to gadolinium is reversible. A plot of I_p-$\upsilon^{1/2}$ is linear (Fig. 1c). From equation(5):

$$I_p = 0.611(nF)^{3/2}(D\upsilon/RT)^{1/2}AC$$

and the slope of the line, the diffusion coefficient of Gd(III) was calculated as 2.5 x 10^{-5} cm^2 s^{-1} in NaCl-KCl-$GdCl_3$ at 730°C. The D of Gd(III) in KCl-$GdCl_3$ at 800°C was determined to be 3.6 x 10^{-5} cm^2s^{-1}.

The electrode processes for Gd(III) reduced on ClNi electrode

The cyclic voltammogram of Ni in NaCl-KCl--$GdCl_3$ at 730°C is shown in Fig. 2a. Six cathodic waves starting at -2.55, -2.75, -2.81, -2.84, -2.89, -2.93 V appear. Another cathodic wave appears when the potential is swept to -3.08 V. The deposition potential of sodium on the Ni electrode in this melt was determined as

-3.1 V. Therefore, the last cathodic wave in Fig. 2a corresponds to deposition of gadolinium.

The difference between the peak potential and the half peak potential for the 1st cathodic wave is 0.057 V and the electron transfer number calculated is 3.0 according to $| E_p-E_{p/z} | = 2.2RT/nF$. A plot of $E - \log[(I_p-I)/I]$ is linear (Fig. 1b) for the 1st cathodic wave. The n calculated from the slope, $m = 1.72RT/nF$(6) is 3.2. The potentiostatic electrolysis in this melt was done with a Ni electrode at -2.63 V. After removing the salt, the surface phase of the electrode was determined to be $GdNi_5$ by x-ray diffraction. The starting potential of this peak is positive with respect to the deposition potential of gadolinium, i.e. the existence of depolarization which is caused by alloy formation. It can be assumed that the 1st through the 5th cathodic waves in Fig. 2a are due to formation of GdNi alloys and that the charge transfer reactions are reversible.

Free energy of formation of intermetallic compounds (Gd-Ni)

The potentiostatic electrolysis was done with a Ni electrode in molten NaCl-KCl-$GdCl_3$ at the potential of which metallic gadolinium deposited. The potential-time curve after potentiostatic electrolysis is shown in Fig. 3. Seven plateaus appeared. The 1st plateau is due to the metallic gadolinium and the others correspond to the Gd-Ni alloys. The plateaus at -2.48, -2.58 V correspond to Gd_zNi_{17} and $GdNi_5$ can be calculated using the e-t curve method (7).

The potential difference between the 1st plateau and the 7th plateau corresponds to the emf(E_1^0) of the cell: Gd | $GdCl_3$, NaCl-KCl | Gd_2Ni_{17}, Ni. The cell reaction is

$$Gd(s) + 17/2\ Ni(s) = GdNi_{17/2}(s) \qquad (1)$$

The variation of free energy for reaction (1): $\Delta G_1° = -3FE_1°$, where $\Delta G_1°$ is the standard free energy of formation of $GdNi_{17/2}$.

The potential difference between the 1st plateau and the 6th plateau corresponds to the emf ($E_2°$) of the cell: Gd | $GdCl_3$, NaCl-KCl | $GdNi_5$, Gd_zNi_{17}. The cell reaction is

$$7/17\ Gd(s) + 10/17\ GdNi_{17/2}(s) = GdNi_5(s) \qquad (2)$$

From the ΔG_1° and $\Delta G_z^\circ = -3FE_z^\circ$, the standard free energy of formation of $GdNi_5$ was calculated. At 730°C, $\Delta G_f^\circ(GdNi_{17/2}) = -124.5$ kJ/mol, $\Delta G_f(GdNi_5) = -112.5$ kJ/mol.

Diffusion of Gd in its alloy phase

The diffusion coefficient of a metallic atom in the alloying cathode can be calcualted from the following equation (8):

$$D = (Q_e M/xnFA\rho)^2/2\tau$$

Where M and P are the molecular weight and density of the intermetallic compound respectively; x and n are the coefficients in the chemical equation of $xm_1^{n+} + ym_z + xne = m_{1x}m_{zy}$. For the $GdNi_5$ phase $x = 1$, $n = 3$, $M = 450.7$, $p = 8.65$ g cm^{-3}. Qe is the quantity of electricity needed to form the intermetallic compound at the potential where the current reached a steady state, T is the time required to reach the steady state and A is the area of electrode. Fig. 4 is the current-time curve for the Ni electrode in the KCl-$GdCl_3$ melt at -2.6 V. The product formed on the electrode at -2.6 V was determined to be $GdNi_5$. Q_e and T were obtained from Fig. 4. The diffusion coefficient of gadolinium into the $GdNi_5$ phase was calculated as 8.1×10^{-11} cm^z s^{-1} (820°C) which is much smaller than the D of Gd(III) in the melt. Diffusion of gadolinium into the alloying cathode is so slow that this step may be the rate-determining step of the electrode process.

CONCLUDING REMARKS

1. Reduction of Gd(III) to metallic gadolinium on a molybdenum electrode in molten chlorides is reversible in one step.
2. The Gd-Ni alloys are formed first and then the metallic gadolinium is deposited when Gd(III) is reduced on the nickel electrode.
3. The diffusion coefficient of Gd(III) in molten chlorides is $(2\sim4) \times 10^{-5}$ cm^{2}s^{-1}(700 800°C) and that of Gd in the Gd-Ni alloy phase is $10^{-11}\sim10^{-10}$ cm^2 s^{-1}.
4. ΔG_f° of intermetallic compounds of Gd with Ni can be calculated using an E-t curve after potentiostatic-electrolysis.

ACKNOWLEDGMENTS

The project was supported by the National Natural Science Foundation of China.

References

1. D. Brantland and K. A. Gschneidner, Jr., Electrochim. Acta 27, 1233 (1982)
2. D. Brantland and K. A. Gschneidner. Jr., Electrochim. Acta 25, 145 (1980)
3. Gunter Zwilling, Z. Metallkunde, Bd. 71, H. 11, 752 (1980)
4. S. N. Flengas and T. R. Ingraham, J. Electrochem. Soc. 106, 714 (1959)
5. T. Berzins and P. Delahay, J. Am. Chem. Soc. 75, 555 (1953)
6. F. R. Clayton, G. Mamantov and D. L. Manning, J. Electrochem. Soc. 120, 1193 (1973)
7. Qiqin Yang, Guankun Liu and Zejin Liu, Acta Metallurgica Sinica, Series B, 3(1), 28(1990)
8. Qiqin Yang, Guankun Liu, Weiwen Cai and Zejin Liu, Rare Metals (in Chinese) 16(1), 18(1992)

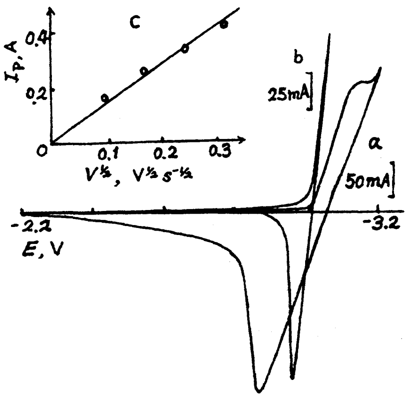

Fig 1 Cyclic voltammogram of Mo(0.4cm^2) in NaCl-KCl-GdCl$_3$ (a: 2.72 mol%, b: 3.81mol%) at 730°C, 60 mV/s and plot of I_p-$v^{1/2}$(c)

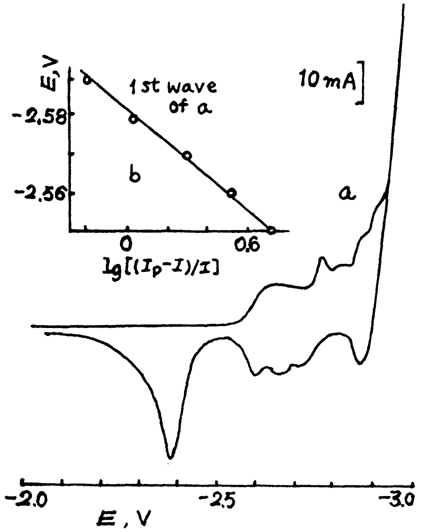

Fig 2 (a) Cyclic voltammogram of Ni(0.35cm^2) in NaCl-KCl-GdCl$_3$(2.9 mol%),730°C, 30 mV/s
(b) plot of E-lg $(I_p-I)/I$

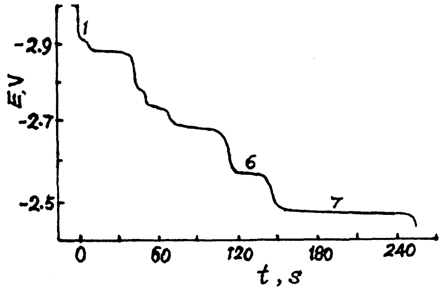

Fig 3 E-t curve of Ni in NaCl-KCl-GdCl$_3$ after electrolysis at -3.0 V, 730°C

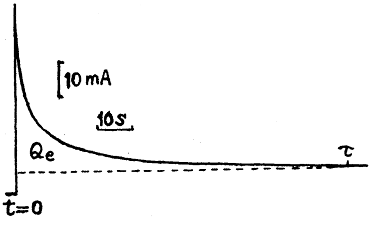

Fig 4 I-t curve of Ni(0.47cm^2) in KCl-GdCl$_3$ at -2.6 V, 820°C

DOI: 10.1149/199413.0504PV

THE MECHANISM OF THE DISSOLUTION OF Nd AND THE ELECTRODE REACTION IN EUTECTIC LiCl-KCl, $NdCl_3$ MELTS

Icheng Wu, Hongmin Zhu, Yuzuru Sato, Tsutomu Yamamura and Katsuhisa Sugimoto
Department of Metallurgy, Faculty of Engineering, Tohoku University.
Sendai 980, Japan.

ABSTRACT

The dissolution of neodymium into LiCl-KCl-$NdCl_3$ melts and the electrode reaction of Nd^{3+} have been studied. Neodymium metal scarcely dissolved into the eutectic LiCl-KCl. However, the presence of Nd^{3+} accelerates the dissolution of neodymium into the melts. The reaction for the dissolution of neodymium can be given by the following equation. $2NdCl_3 + Nd \rightarrow 2NdCl_2$. The electrode reaction for the electrolysis of Nd^{3+} has been studied by cyclic voltammetry. It was found that Nd^{3+} was reduced to neodymium according to the following reaction. $Nd^{3+} + 3e \rightarrow Nd$. The reversibility of the electrode reaction and the effects of the electrode materials on the reaction have been discussed.

INTRODUCTION

Recently, there has been a wide interest in the development of a process for producing high purity neodymium, because it can be utilized as an important component of high performance magnets[1]. An electrowinning process using molten salts can usually be applied even to the production of reactive metals, such as rare earths, by the use of a molten alkali halide bath. However, it is known that the current efficiency of the electrowinning of neodymium is very low[2][3] using dehydrated neodymium chlorides dissolved in alkali or alkaline-earth chloride melts. Moreover, the electrode reaction has not been clarified yet. It was pointed out that the low current efficiency was due to the dissolution of Nd metal into the melt. As for dissolution mechanisms of deposited rare earths in molten salts, a shuttle reaction and a direct dissolution of metal etc., have been reported[3][4][5] for the rare earths other than neodymium, but studies of the dissolution mechanism of neodymium were rare until now.

In this study, the dissolution of neodymium metal into the solvent and the electrochemical behavior of Nd^{3+} ion have been investigated using a eutectic LiCl-KCl melt as the solvent. The dissolution of neodymium metal into the molten salt was studied under vacuum and at high pressures. LiCl-KCl-$NdCl_3$ melts were used as the solvents, and quartz or Pyrex tubes were used as the cell materials. The amount of neodymium metal dissolved in the molten salts was determined. After the experiments, the samples were investigated by X-ray diffraction and electron diffraction. The electrochemical behavior was studied by cyclic voltammetry at 670, 770, 870 K to understand the electrode reactions. The reversibility of the electrode reaction and the effects of the electrode materials such as Pt or Au on the reaction have been discussed.

EXPERIMENTAL

The LiCl-KCl binary eutectic salt was used as the solvent and $NdCl_3$ was used as the solute. All the chemicals were dehydrated by heating in argon up to the melting temperatures of the salts. After the salts were melted, dried HCl was bubbled into the melts and then argon was bubbled into the melts to remove the residual HCl.

The dissolution experiments of neodymium into LiCl-KCl-$NdCl_3$ or eutectic LiCl-KCl melts were done at 770K. The ampoules made of quartz or Pyrex containing the solvent and neodymium metal were heated for fixed times and were cooled down to room temperature. After all experiments were completed, the samples were analyzed by ICP, SEM and XPS to investigate the reaction products. Figure 1 shows the cells used for the dissolution experiments. For the case of the LiCl-KCl, Nd system, the purified salts and the neodymium specimen were sealed under vacuum and under moderately pressurized argon and were used in the dissolution experiments. In order to know the amount of Nd^{3+}present in the melt, the cell shown in Fig. 1(a) was used. The cell was heated for the specified amount of time and then turned upside down so that the residue remained on the upper surface of the quartz frit and the filtrate, which contained Nd^{+3} dropped to the bottom of the cell. In order to gain some insight into the mechanism of the dissolution, the melting process was visually observed from the outside of the see-through oven.

The electrochemical experimental equipment consists of a potentiostat, a function generator, an X-Y recorder, an intelligent recorder and a personal computer. Triangular waves, were set up and produced by the function generator. The current and voltage responses were recorded at the X-Y recorder by way of the potentiostat. The data were stored at the intelligent recorder once, then taken out and processed by the personal computer. The high frequency noises involved in the current supply were cut off by a low-pass filter. The electrochemical experiment was done by using a three electrode system. Flag type electrodes, made of Pt and Au with a 1 cm^2 surface area were used as the working electrode. A graphite rod was used as the counter electrode and a Ag wire immersed in LiCl-KCl-5mol%AgCl was used as the reference electrode. The concentrations of $NdCl_3$ were 3.4×10^{-5} mol•cm^{-3}. The sweep rate was varied from 50 to 1000 mV•s^{-1}.

RESULTS AND DISCUSSION

Dissolution of neodymium metal

The amount of neodymium dissolved in the molten eutectic LiCl-KCl melts was plotted against time and shown in Fig. 2. As shown in Fig. 2, the amount of neodymium dissolved is constant, as low as 10^{-3} mol% over the time range of 18 to 320ks. By visually observing the sample after the experiment, it was found that the surface of the neodymium strip in contact with salt became dark colored. Therefore, an X-ray diffraction was carried out on the dark colored parts of the neodymium strip and the bulk salts. However, peaks other than the peaks assigned to the solvent salts could not be observed. Based on the results obtained, it is concluded that neodymium hardly dissolves into the LiCl-KCl eutectic melts. The solubility of neodymium is less than 10^{-3} mol%. The tiny amount of neodymium metal dissolved into the molten eutectic LiCl-KCl can be considered to be the dark reactant which could be seen at the interface of the melt and the neodymium metal. The amount of reactant was too little to be detected by X-ray diffraction. It was, however, assumed to be neodymium oxide.

Dissolution of neodymium metal into the eutectic LiCl-KCl salt containing 3.85 wt% $NdCl_3$ was studied by using the cell shown in Fig. 1(a). Photo 1 shows the effect of the surrounding atmosphere on the dissolution of neodymium for 150s. In the case of the sample sealed under vacuum, when the solvent melted, metal fog rose rapidly and spread out all around from the surface of neodymium metal, and the evaluation of a small number of bubbles were observed. A similar neodymium fog was also reported earlier[6][7]. For samples sealed under vacuum, it took 150s for the melt to be filled by the dark metal fog. On the other hand, in the case of the sample sealed with argon, it took 10ks for the malt to be filled by the dark metal fog and the bubble formation was not observed. The spread of the metal fog in the samples sealed under argon was much slower than in the samples sealed under vacuum.

The time dependence of the dissolution of neodymium in LiCl-KCl with 0.85mol% $NdCl_3$ is shown in Fig. 3. The dissolution ratio of the weight of dissolved metal, ΔW, to the initial weight of $NdCl_3$, W_i, $\Delta W/W_i$, increases almost linearly with an increase in time for both samples. The dissolution ratio of the sample sealed under vacuum is smaller than that of the sample sealed under argon. It should be noted that the ratio $\Delta W/W_i$ exceeds 50% at the dissolution time of 105ks for the vacuum sealed samples, and at 180ks for the argon sealed samples. If it is assumed that the dissolution of neodymium proceeds according to the shuttle reaction given by eq.(1), the maximum value of the dissolution ratio $\Delta W/W_i$ should be 50%. Therefore, present results indicate that the mechanism of the dissolution of neodymium would be more complicated than the simple shuttle reaction.

$$2\,NdCl_3 + Nd \rightarrow 3\,NdCl_2 \qquad [1]$$

When the melts, after a dissolution experiment, were filtered using a quartz filter at the elevated temperatures, the filtrate was clear. The content of neodymium in the filtrate was quantitatively analyzed. The time dependence of the neodymium content in the filtrate is shown in Fig. 4. The ratio $\Delta W/W_i$, ΔW being the decrease of Nd^{3+} content in filtrate, shows an increase until 1800s, and then decreases gradually to an almost constant value. The value of the equilibrium constant calculated from the chemical analyses was about 2×10^{-4}. Therefore, the equilibrium reaction given by eq. [1] prefers the left direction.

In order to identify the reaction products after dissolution experiments, the samples were examined by the scanning electron microscope and X-ray photoelectron spectroscopy. Photo 2 shows the scanning electron microscopy image of the residue at the upper side of the quartz frit after a 600ks neodymium dissolution experiment. Two kinds of structure an be seen in this photo. One is the plate-like structure, and the other is the fine particle structure. The plate-like structure was identified as the chloride compound of neodymium and alkaline metal by X-ray diffraction. By tentative X-ray diffraction and fluorescence analyses, the fine particle structure was considered to be neodymium powder. According to the results obtained above, it can be thought that neodymium metal and $NdCl_3$ reacted according to eq.[1], and then $NdCl_2$ moves in the electrolyte, and forms the neodymium metal and $NdCl_3$ according to the left direction of eq.[1].

Electrochemical behavior of $NdCl_3$

Figure 5 shows the cyclic voltammogram at 670K, using a Au working electrode. The cathodic peak nearby -1.57V is considered to be the reduction of Nd^{3+} to neodymium. The anodic peak near -1.25V corresponds to the oxidation of Nd to Nd^{3+}. The anodic peak near 0V corresponds to the cathodic peak near -1.57V since the anodic peak near 0V was not observed unless the electrode was swept to -1.57V. Therefore, the anodic peak near 0V can be considered to correspond to the oxidation of the Nd-Au alloy.

In order to confirm the electrode reaction of $NdCl_3$, the relationship between the peak current density and concentration of $NdCl_3$ was considered. The dependence of peak current density with sweep rates of 100, 400 and 800 $mV \bullet s^{-1}$ on concentration of neodymium ion for reduction of $NdCl_3$ at 770K is shown in Fig. 6. It shows that the peak current density is in proportion to the concentration of neodymium ion. Therefore, it is obvious that the cathodic peak near -1.57V shown in Fig. 5 is due to the reduction of $NdCl_3$.

Figure 7 shows the relation between peak current density and the square root of sweep rate for reduction of $NdCl_3$. The peak current density increased with increasing sweep rate, but the increasing rate became smaller with increasing peak current density. The electrode reaction of the cathodic peak shown in Fig. 5 is considered to be a quasi-reversible process[8][9]. For a Nd^{3+} concentration of 3.4×10^{-5} $mol \bullet cm^{-3}$ and a sweep rate less than $50 mV \bullet s^{-1}$, the electrode reaction was a reversible process. The electron number n which participates in the reaction was calculated to be 2.8. Therefore, the electrode reaction can be expressed as follows.

$$Nd^{3+} + 3e \rightarrow Nd \qquad [2]$$

SUMMARY

The dissolution of neodymium metal into LiCl-KCl melt and the electrode reaction of Nd^{3+} have been studied. The results obtained are summarized as follows:

1. Neodymium metal scarcely dissolves in eutectic LiCl-KCl without $NdCl_3$.
2. During the dissolution of neodymium in the LiCl-KCl-$NdCl_3$ system, when the solvent melted, a metal fog rose rapidly and spread out all around from the neodymium metal surface, and the evolution of bubbles were observed.
3. The dissolution rate of neodymium metal into LiCl-KCl-$NdCl_3$ system, via the shuttle reaction is suppressed under pressurized argon.
4. When Au is used as the working electrode, the electrode reaction is reversible at a sweep rate less than $50mV \bullet s^{-1}$, and the reaction was determined to be the reduction of Nd^{3+} to neodymium metal.

REFERENCE

1. K.A. Gschneidner, Jr.: J. Less-Common Met., **100** (1984), p.1.
2. J. Shiogawa and T. Ishino: Denki Kagaku, **32** (1964) p. 116.
3. R.A. Sharma: J. Met., **39** (1987) p. 33.
4. L.F. Druding and J.D. Corbett: J. Amer. Chem. Soc., **83** (1061) p. 2462.
5. L.R. Morss and M.C. McCue: Inorganic Chemistry, **14**, 7 (1975) p. 1624.
6. F. Li, G. Chantai, L. Jie, and T. Dingziang: Journal of Rare Earths, **9**, 1 (1991) p. 20.
7. I. Wu, H. Zhu, Y. Sato, T. Yamamaura and K. Sugimoto: Proceedings of the fourth Japan-China bilateral conference on molten salt chemistry and technology, Nov. (1992)), p. 67.
8. A.J. Bard and L.R. Faulkner: "Electrochemical methods - fundamentals and Applications", Ed. by J. Wiley and Sons, New York, New York, (1980).
9. H. Matsuda and Y. Ayabe: Z. Elektrochem., **59** (1955), p. 494.

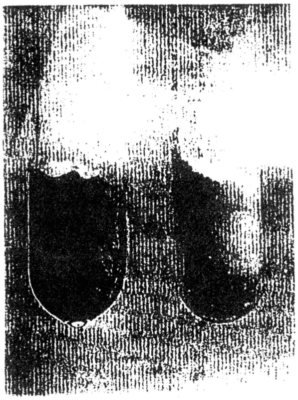

Photo.1 The effect of atmospheres on dissolution of Nd for 150s.
Left : Vacuum
Right : Argon
Solvent : LiCl-KCl-$NdCl_3$

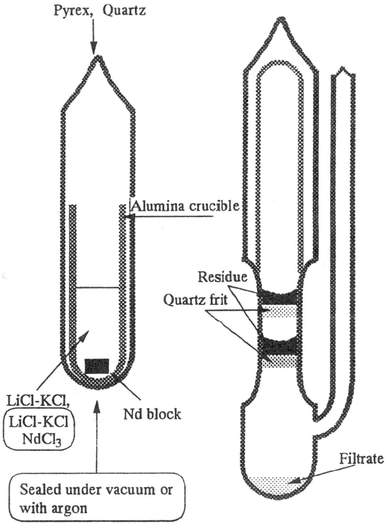

Fig.1 Cells used for dissolution experiment.

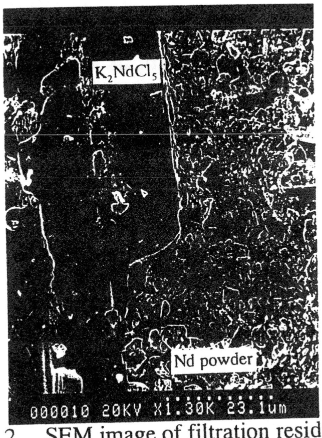

Photo.2 SEM image of filtration residue of LiCl-KCl-$NdCl_3$ after dissolution experiment of Nd for 600 ks.

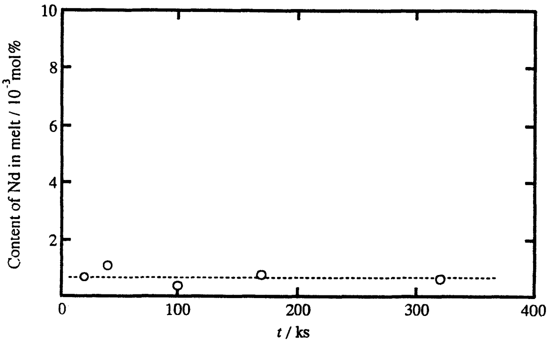

Fig.2 Time dependence of dissolution of Nd in eutectic LiCl-KCl.

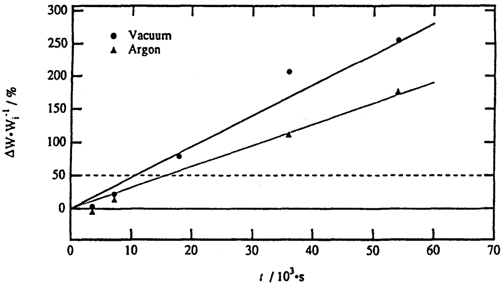

Fig.3 Time dependence of dissolution of Nd in LiCl-KCl with 0.85 mol% $NdCl_3$.

ΔW is the difference between final and initial contents in molten salts.

$2NdCl_3 + Nd \rightarrow 3NdCl_2$ • • • • •[1]

The dotted line refers to the maximum content if the dissolution proceeds according to the reaction shown above.

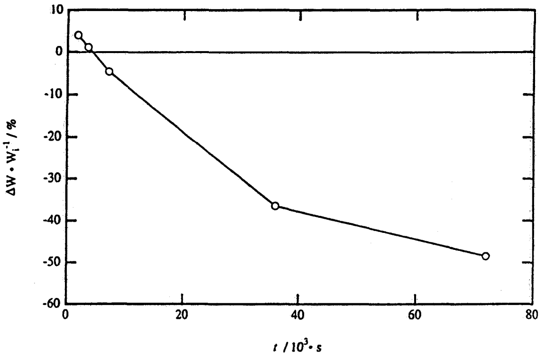

Fig.4 Time dependence of dissolution of Nd in LiCl-KCl with 0.56 mol% $NdCl_3$.

ΔW is the difference between final and initial contents of Nd in molten salts.

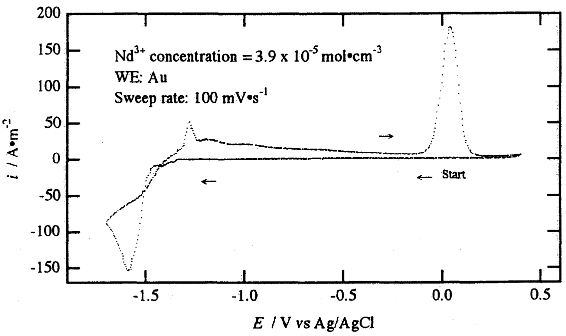

Fig.5 Cyclic voltammogram of Nd^{3+} ion in molten LiCl-KCl at 670K.

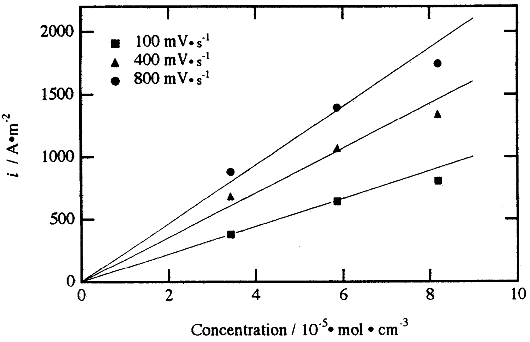

Fig.6 Dependence of peak current density on Nd ion concentration for reduction of $NdCl_3$ at 770K. WE: Au

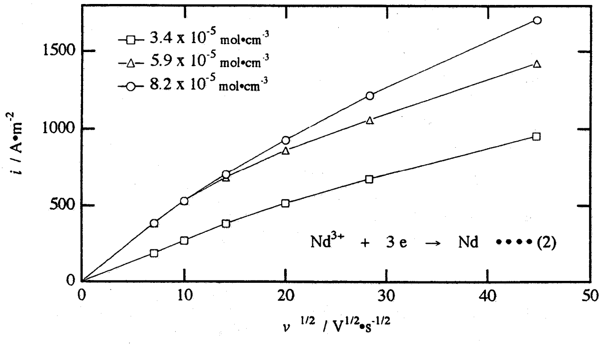

Fig.7 Relation between peak current density and sweep rate v for reduction of $NdCl_3$.
Temp.: 670K; WE: Au

DOI: 10.1149/199413.0514PV

ELECTROCHEMISTRY OF NIOBIUM IN MOLTEN ALKALI CHLORIDES AND THE INFLUENCE OF DISSOLVED FLUORIDE IONS

M. Chemla, F. Lantelme and Y. Berghoute
Laboratoire d'Electrochimie, URA 430 CNRS, U. P. M. C, Case 51
4 Place Jussieu, 75252 PARIS CEDEX 05, France

ABSTRACT

The electrochemical properties of the solutions of niobium chlorides in fused NaCl-KCl were determined by transient electrochemical techniques at temperatures ranging from 670° to 870°C. It is shown that the stable oxidation states of niobium ions are Nb(V), Nb(IV) and Nb(III). The reduction of Nb(III) gives rise to metallic niobium. At higher temperature (T>750°C) Nb(V) tends to decompose into Nb(IV) with chlorine evolution. Introducing fluoride ions stabilizes the higher oxidation states. For a molar ratio F/Nb greater than 2, the direct reduction Nb(IV) → Nb is obtained, the Nb(III) species being no longer stable. The standard potentials of the redox reactions are given for various concentrations of fluoride ions.

INTRODUCTION

Recently research works (1, 2) have been undertaken to obtain niobium deposit in fused alkali chlorides which are less corrosive and toxic than fluorides (3). The chemistry of niobium salts in these liquids is rather complicated and some controversy existed about the stable oxidation states of niobium (4). Indeed the chemical properties of the solutions depend on various factors such as the melt composition, temperature and also the presence of impurity (traces of oxide ions in the bath (5)). The determination of the redox properties is perturbed by reaction with the material of the working electrode, such as formation of alloys or carbides (6). In a recent paper (7) the electrochemical properties of niobium chlorides in the eutectic mixture LiCl-KCl have been studied at temperatures ranging from 380° to 620°C. It has been shown that the oxidation states II, III, IV and V are stable. The redox reactions Nb(V)/Nb(IV) and Nb(IV)/Nb(III) are rapid.

The aim of the present paper is to study the niobium deposition in alkali metal chlorides at higher temperature (T>670°C) using the mixture NaCl-KCl. The mechanism of the redox reaction was studied by electrochemical techniques, mainly cyclic voltammetry. Digital simulation was used to interpret the experiments in the frame of electrochemical models. The standard potentials of the redox couples were determined at temperatures ranging from 670° to 900°C. The complexing effect of fluoride ions was studied by addition of sodium fluoride.

EXPERIMENTAL

The equimolar NaCl-KCl mixture was purified by applying a high vacuum, chlorine bubbling and argon flushing. The salt container was a vitreous carbon crucible placed in an Hastelloy tube. The components of the apparatus were selected to achieve a vacuum-tight cell at elevated temperature (8). The niobium ions were generated by oxidation of a plate of pure niobium (Johnson Matthey) by anhydrous nickel chloride (Merck Reagent).

The reference electrode was a Ni^{2+}/Ni (1 mol % Ni^{2+}) electrode with a boron nitride diaphragm [9]. Internal reference systems, such as Pt^{2+}/Pt, were used to re-standardize the electrode, the standard potential of the couple Ni^{2+}/Ni is -0.858 V vs Pt^{2+}/Pt and -1.105 V vs Cl_2/Cl^- at 720°C (10). A rod of pure graphite (208, Carbone Lorraine), dia. 6 mm, formed the counter electrode. The working electrode was either a rod of vitreous carbon (V25, Le Carbone Lorraine), dia. 3 mm, or a rod of metal (tungsten, platinum, or niobium).

RESULTS AND DISCUSSION

Upper oxidation states, fluoride-free electrolyte

Two redox systems Nb(V)/Nb(IV) and Nb(IV)/Nb(III) were detected by cyclic voltammetry and gave rise to associated peaks (Fig. 1). The reactions are reversible. $NbCl_5$ has a strong oxidizing power (11), i. e. the two redox reactions Nb(V)/Nb(IV) and Cl_2/Cl^- overlapped, and it was hard to determine their respective contribution to the i/V curves. At temperature higher than 750°C the peaks for the reaction Nb(V)/Nb(IV) were hardly visible. The method of digital simulation (12) was used to obtain a calculated curve. The standard potential, E^o_{54}, for the Nb(V)/Nb(IV) couple was adjusted to obtain the best fit with the experimental curves. At 720°C it was found

$$E^o_{54} = -0.09 \text{ V} \pm 0.01 \text{ vs } Cl_2/Cl^- \qquad [1]$$

The standard potential, E^o_{43}, is calculated either from voltammetry or chronopotentiometry. At temperatures ranging from 670° to 800°C it is found

$$E^o_{43} = -0.988 \text{ V} \pm 0.005 \text{ vs } Cl_2/Cl^- \qquad [2]$$

The value of the diffusion coefficient, D_{NbIII}, calculated from chronopotentiometry, is

$$D_{NbIII} = 1.18 \times 10^{-2} \exp(-5910/T) \quad \text{in cm}^2 \text{ s}^{-1} \qquad [3]$$

Upper oxidation states in melts containing fluoride ions

Introducing fluoride ions into the bath induced a negative shift in the peak potentials. Now, the Nb(V)/Nb(IV) couple became well separated from Cl_2/Cl^- (Fig. 2). The standard potentials, E^0_{54}, are shown in Table I.

Table I - Standard potential, E^0_{54}(Volt) vs Pt^{2+}/Pt (molar scale), for the couple Nb(V)/Nb(IV). Influence of the molar ratio r_F = F/Nb. T = 670°C. Concentration of niobium ions: 0.196 mol l^{-1}.

r_F	0	0,38	0,75	1,0	1,13	1,5	3,0	4,5	7,0	10
E^0_{54}/V	0,121	0,128	0,052	0,060	-0,037	-0,416	-0,713	-0,851	-0,904	-0,964

A similar shift in the potential E^0_{43} was observed (Table II). This negative shift caused the Nb(IV)/Nb(III) peaks to disappear, for a molar ratio, r_F = F/Nb>2, Nb(III) was no longer stable, and Nb(IV) reduced directly to metallic niobium.

Table II - Standard potential, E^0_{43}(Volt) vs Pt^{2+}/Pt (molar scale), for the couple Nb(IV)/Nb(III). Influence of r_F. Concentration of niobium ions: 0.196 mol l^{-1}.

r_F	0	0,38	0,75	1,0
E^0_{43}/V	-0,741	-0,776	-0,801	-0,811

Increasing temperature induced a positive shift in the standard potential E^0_{54} (Table III). This behavior was already observed for the fluoride-free bath. However now, for r_F>1.5, Nb(V) remained stable even at high temperatures.

Lower oxidation states

The steep anodic peak (Fig. 3) indicates the formation of an insoluble product at the electrode surface. X ray diffraction analysis showed that the deposit formed during electrolysis at constant potential (foot of the reduction peak) was made of metallic niobium. In the fluoride-free electrolyte the last step of the electroreduction of niobium ions was Nb(III) → Nb (Table IV). As pointed out in the previous paragraph, when the concentration of fluoride ions increased, the direct reduction Nb(IV) → Nb was obtained (Table V).

Table III - Standard potential, E^0_{54}(Volt) vs Pt^{2+}/Pt (molar scale), for the couple Nb(V)/Nb(IV). Influence of the temperature (Kelvin) and r_F. Concentration of niobium ions: 0.196 mol l^{-1}.

r_F / T	1,5	3,0	4,5	7,0	10
943	-0,416	-0,713	-0,851	-0,904	-0,964
993	-0,399	-0,661	-0,802	-0,880	-0,938
1043	-0,372	-0,638	-0,754	-0,857	-0,911
1093	-0,345	-0,605	-0,706	-0,833	-0,885
1143	-0,324	-0,585	-0,657	-0,810	-0,858

Table IV - Parameters for the reactions Nb(III) ⇔ $Nb(II)_{clusters}$ ⇔ Nb; standard potentials (vs Pt^{2+}/Pt, molar scale) and kinetic constants. Concentration of niobium ions: 0.196 mol l^{-1}.

r_F	T K	E^0_{30} V	E^0_{20} V	$10^3 \times k^0_{32}$ cm s^{-1}	$10^4 \times k^0_{20}$ cm s^{-1}
0	949	-1,048	-1,104	0,8	1,1
0	993	-1,030	-1,077	1,6	1,7
0	1073	-1,024	-1,055	3,2	2,8
1,0	1078	-1,043	-1,093	0,9	1,3

The experimental results indicated that a thin layer of niobium subhalides (cluster compounds) formed at the metal surface (11, 13). According to that observation the successive steps of the reduction of Nb(V) are

$$Nb(V) \Leftrightarrow Nb(IV) \Leftrightarrow Nb(III) \overset{k^0_{32}}{\Leftrightarrow} Nb(II)_{clusters} \overset{k^0_{20}}{\Leftrightarrow} Nb \qquad [4]$$

Table V - Parameters for the reactions Nb(IV) ⇔ Nb(III) ⇔ $\mathrm{Nb(II)_{clusters}}$ ⇔ Nb; standard potentials (vs Pt^{2+}/Pt, molar scale) and kinetic constants. Concentration of niobium ions: 0.190 mol l^{-1}.

r_F	T K	E^0_{40} V	E^0_{43} V	E^0_{20} V	$10^3 \times k^0_{32}$ cm s^{-1}	$10^4 \times k^0_{20}$ cm s^{-1}
3,0	1078	-1,213	-1,403	-1,225	2,5	1,0
7,0	973	-1,329	-1,570	-1,289	1,3	3,6
10,0	950	-1,485	-1,813	-1,425	2,7	4,0

To go deeper into the mechanism of the electroreduction it was assumed that the two last steps obeyed the intensity-overpotential equation taking into consideration the formation of the cluster layer (14).

The parameters involved in the calculation (standard potentials, rate constants...) are varied for obtaining computed curves fitting the experimental voltammograms. Calculated and experimental curves are shown in Figs 1-3. The following comments are drawn from the results: i) A higher temperature resulted in a small positive shift in the standard potentials and an increase in the value of the rate constants. ii) The rate constant, k^0_{20}, for the reaction $\mathrm{Nb(II)_{cluster}}$ ⇔ Nb(0), is about ten times lower than k^0_{32} (reaction Nb(III) ⇔ $\mathrm{Nb(II)_{cluster}}$). iii) Increasing amounts of fluoride ions induce a negative shift in the standard potentials. For E^0_{54} and E^0_{43} the shift is very large around the value $r_F = 1.5$.

CONCLUSION

In fluoride-free baths, it was shown that Nb(IV) and Nb(III) ions were stable. The presence of fluoride ions stabilizes the upper oxidation states Nb(V) and Nb(IV). In fluoride-free baths the metal deposition comes from the reaction

$$\mathrm{Nb(III)} + 3e \rightarrow \mathrm{Nb} \qquad [5]$$

While, as soon as $r_F > 1.5$, the reduction process becomes

$$\mathrm{Nb(IV)} + 4e \rightarrow \mathrm{Nb} \qquad [6]$$

These previous equations represent an overall process. The intimate mechanism obeys the scheme [4]. This is in agreement with the statement that for an electrochemical reaction a single four or three electron step is highly improbable. Voltammograms involving the reactions [5] or [6] were correctly described by the model deduced from the reaction scheme [4]. The standard potentials of the reactions [5] and [6] are linked to the potentials of the intermediate couples by: $E^0_{30} = (E^0_{32} + 2E^0_{20})/3$ and $E^0_{40} = (E^0_{43} + E^0_{32} + 2E^0_{20})/4$.

Metallic niobium can be prepared by electrolysis at constant potential either in fluoride-free bath or in bath containing NaF. Electron scanning micrography shows that the deposit carried out in a fluoride-free bath has a coarse structure with large crystals which tend to form dendrites. A more coherent layer is obtained in a bath containing NaF.

ACKNOWLEDGEMENTS

We gratefully acknowledge the financial support of CNRS and AFME under contract A. R. C. "Procédés de métallurgie extractive utilisant les sels fondus", N° 8780 N 2030 of PIRSEM.

REFERENCES

1. A. Barhoun, F. Lantelme, M. E. de Roy and J. P. Besse, in *Third International Symposium on Molten Salt Chemistry and Technology*, Materials Science Forum, **73-75**, 313 (1991).
2. G. S. Picard and P. Bocage, in *Molten Salts*, PV 92-16, Electrochemical Society Softbound Proceedings Series, Pennington, NJ, p. 622 (1992).
3. G. W. Mellors and S. Senderoff, *J. Electrochem. Soc.*, **112**, 266 (1965).
4. V. I. Konstantinov, E. G. Polyakov, and P. T. Stangrit, *Electrochim. Acta*, **26**, 4455 (1981).
5. M. Chemla and V. Grinevitch, *Bull. Soc. Chim. France*, n°3, 853 (1973).
6. A. Barhoun, Y. Berghoute, and F. Lantelme, *J. Alloys and Compounds*, **179**, 241 (1992).
7. F. Lantelme, A. Barhoun, J. Chevalet, *J. Electrochem. Soc.*, **140**, 324 (1993).
8. F. Lantelme, D. Inman, and D. G. Lovering, Electrochemistry, in *Molten Salt Technology*, R. J. Gale and D. G. Lovering, Editors, Vol. I, Plenum Press, New-York (1976).
9. H. W. Jenkins, G. Mamantov and D. L. Manning, *J. Electroanal. Chem.*, **19**, 385 (1968).
10. Y. Berghoute, A. Salmi and F. Lantelme, *J. Electroanal. Chem.*, in press.
11. L. Arurault, J. Bouteillon, J. de Lépinay, A. Khalidi and J. C. Poignet, in *Third International Symposium on Molten Salt Chemistry and Technology*, Materials Science Forum, **73-75**, 305 (1991).
12. D. Britz, *Digital Simulation in Electrochemistry*, Springer, Berlin (1988).
13. K. D. Sienerth and G. Mamantov, in PV 93-9, *Molten Salt Chemistry and Technology*, Electrochemical Society Softbound Proceedings Series, Pennington, NJ, p. 365 (1993).
14. F. Lantelme, Y. Berghoute and A. Salmi, *J. Appl. Electrochem.*, in press.

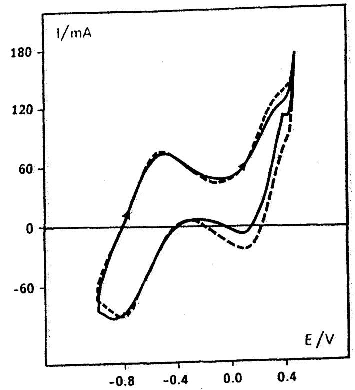

Fig. 1. Voltammogram for the reactions Nb(V) + e ⇔ Nb(IV) and Nb(IV) + e ⇔ Nb(III) at a glassy carbon electrode (Electrode area = 1.037 cm^2), solution of niobium ions at the concentration, 0.129 mol l^{-1}, in NaCl-KCl. T = 690°C. Sweep rate: 1 V s^{-1}. Reference electrode: Pt^{2+} (molar)/Pt. Full line: experimental. Dashed line: simulated.

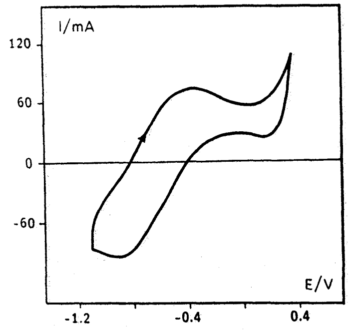

Fig. 2. Voltammogram for the reaction Nb(V) + e ⇔ Nb(IV), solution of Nb(IV) at the concentration, 0.129 mol l^{-1}, in NaCl-KCl containing 0.387 mol NaF l^{-1}. T = 672°C. Reference electrode: Pt^{2+} (molar)/ Pt. Working electrode: glassy carbon electrode (electrode area = 1.037 cm^2), sweep rate: 5 V s^{-1}.

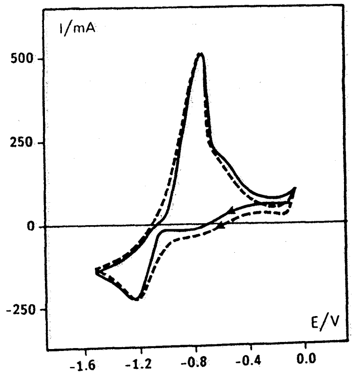

Fig. 3. Voltammogram at a platinum electrode (Electrode area = 0.345 cm^2), solution of Nb(III) at the concentration, 0.412 mol l^{-1}, in NaCl-KCl. T = 720°C. Sweep rate: 0.2 V s^{-1}. Reference electrode: Pt^{2+}(molar)/Pt. Full line: experimental. Dashed line: simulated.

DOI: 10.1149/199413.0521PV

ELECTROCHEMICAL AND SPECTROELECTROCHEMICAL INVESTIGATION OF K_2ReCl_6 AND $[Bu_4N]_2Re_2Cl_8$ IN THE $AlCl_3$-$NaCl_{sat}$ MELT

E.M. Hondrogiannis and G. Mamantov

Department of Chemistry
University of Tennessee
Knoxville, TN 37996-1600

ABSTRACT

The electrochemical and UV-visible spectroelectrochemical studies of the $[ReCl_6]^{2-}$ and $[Re_2Cl_8]^{2-}$ ions in the sodium chloride saturated $AlCl_3$-NaCl melt at 180°C are reported. Both species are stable in the melt on the voltammetric time-scale to yield an equilibrium cyclic voltammogram, consisting of three reduction and two oxidation waves. Electrochemical reduction of $[ReCl_6]^{2-}$ proceeds through the $[Re_2Cl_8]^{2-}$ and $[Re_2Cl_8]^{3-}$ ions to an insoluble product. Some details of this complicated process are reported.

INTRODUCTION

Molten chlorides are well suited for stabilizing transition metal chloride complexes, since the hydration and hydrolysis reactions occurring with such complexes in aqueous solutions cannot take place in these ionic liquids. Recent results by Hussey and co-workers(1,2) involved such an application of the room temperature $AlCl_3$/1-methyl-3-ethylimidazolium chloride ($AlCl_3$-MEIC) melt to the study of various rhenium chloride complexes. It was found that in the basic melt (49 mol% $AlCl_3$) $[ReCl_6]^{2-}$ is stable and can be reversibly reduced voltammetrically to $[ReCl_6]^{3-}$. $[Re_2Cl_9]^-$ can also be reversibly reduced voltammetrically to $[Re_2Cl_9]^{2-}$; however, the $[Re_2Cl_9]^-$ is not stable and is slowly converted to $[ReCl_6]^{2-}$. $[Re_2Cl_9]^{2-}$ is reduced electrochemically to $[Re_2Cl_8]^{2-}$ in an irreversible process. The $[Re_2Cl_9]^{2-}$ is also unstable; it is converted to $[ReCl_6]^{2-}$ and $[Re_2Cl_8]^{2-}$. $[Re_2Cl_8]^{2-}$ can be reversibly reduced to $[Re_2Cl_8]^{3-}$.

The chemistry of K_2ReCl_6 in the LiCl-KCl eutectic at 450°C has been reported by Bailey and Nobile(3). According to them Re(IV) is stable in the melt, but addition of K_2ReCl_6 to the melt involves some decomposition to the metal during the dissolution process. They further report that Re(III) disproportionates to Re(IV) and Re(0) in the melt.

It was our goal to compare the behavior of rhenium chlorides in the $AlCl_3$-$NaCl_{sat}$ melt with that observed in the $AlCl_3$-MEIC and LiCl-KCl melts.

EXPERIMENTAL

The $AlCl_3$-$NaCl_{sat}$ melt was prepared from purified aluminum chloride and vacuum dried sodium chloride. Any remaining base metal impurities in the melts were removed by adding aluminum metal (AESAR, 99.999%) in the process of preparing the melt.

The K_2ReCl_6 (Aesar Co., 99.9%) and $[Bu_4N]_2Re_2Cl_8$ were used without further purification. Use of K_2ReCl_6 synthesized in this laboratory or CCl_4 treated melts, to remove oxides(4), yielded the same results. All manipulations were carried out in a nitrogen filled dry box (moisture level <2ppm), and all electrochemical and spectroelectrochemical measurements involved solutions contained in sealed Pyrex cells.

An EG&G Princeton Applied Research (PAR) potentiostat/galvanostat (Model 273) connected to an IBM computer (PS/2 Model 70 386) utilizing the PAR M270 software package was used to obtain the electrochemical information. Ultraviolet-visible absorption spectra were recorded using a Hewlett Packard 8452A diode array spectrophotometer.

RESULTS AND DISCUSSION

We have studied the electrochemistry, UV-visible spectroscopy, and UV-visible spectroelectrochemistry of K_2ReCl_6 and $[Bu_4N]_2Re_2Cl_8$ in the $AlCl_3$-$NaCl_{sat}$ melt at 180°C. It has been found that $[ReCl_6]^{2-}$ is stable in this melt; it is reduced in two steps to an insoluble product. The reduction involves the formation of $[Re_2Cl_8]^{2-}$, $[Re_3Cl_{12}]^{3-}$, and $[Re_2Cl_8]^{3-}$. $[Re_2Cl_8]^{2-}$ appears to react with $[ReCl_6]^{2-}$ to form $[Re_2Cl_9]^{2-}$. This is evidenced by a voltammetric wave at potentials more positive than the $[ReCl_6]^{2-}$ reduction which grows in after several scans in solutions containing $[ReCl_6]^{2-}$ and with time in solutions containing $[Re_2Cl_8]^{2-}$. This new wave is believed to result from the $[Re_2Cl_9]^{2-}/[Re_2Cl_8]^{2-}$ couple. After this new wave grows in, the equilibrium cyclic voltammogram for a solution of $[ReCl_6]^{2-}$ consisting of three reduction and two oxidation waves, does not change (Fig.1). As stated above, the first reduction and corresponding oxidation waves are attributed to the $[Re_2Cl_9]^{2-}/[Re_2Cl_8]^{2-}$ couple. Further support that the first wave results from the chemical, or electrochemical, product of the second reduction comes from the significant increase in peak height for the first reduction wave following bulk electrolysis after the second reduction wave.

The second broad reduction wave is attributed to the reduction of both $[Re_2Cl_8]^{2-}$ and $[ReCl_6]^{2-}$ both of which are regenerated by the disproportionation of the $[Re_2Cl_9]^{2-}$. The increase of the current function for this second wave with scan rate shows a concentration dependence supporting the disproportionation in this step. The $[ReCl_6]^{2-}$ is believed to produce very unstable $[ReCl_6]^{3-}$ which readily forms $[Re_3Cl_{12}]^{3-}$, $[Re_2Cl_8]^{2-}$, $[ReCl_6]^{2-}$, and possibly other products.

The third reduction and corresponding oxidation appear to involve a surface reaction. This large wave does not decrease even after 24 hours of electrolysis at a potential corresponding to this wave. This electrolysis further resulted in the generation of another species that is irreversibly reduced at potentials slightly more negative than the third reduction. A significant increase in the baseline indicated that a large amount of insoluble product was formed. UV-visible spectroscopy revealed that a small amount of a rhenium species with a weak absorbance at 314 nm still remained in solution, indicating that not all of the rhenium is reduced in this step. No x-ray evidence for the formation of rhenium metal was found in this step.

In conclusion, our studies to date point to many similarities with the results obtained in the $AlCl_3$-MEIC melt.

ACKNOWLEDGMENTS

The authors wish to thank Professor C.L. Hussey for the sample of $[Bu_4N]_2Re_2Cl_8$ as well as acknowledge C.L. Hu for her preliminary studies of various rhenium chloride species in the $AlCl_3$-$NaCl_{sat}$ melt.

This work was supported by the Air Force Office of Scientific Research, Grants No. 88-0307 and No. F49620-93-0129.

REFERENCES

1. S.K.D. Strubinger, I.W. Sun, W.E. Cleland, Jr., and C.L. Hussey, Inorg. Chem., 29, 4246 (1990).

2. S.K.D. Strubinger, C.L. Hussey, and W.E. Cleland, Inorg. Chem., 30, 4276 (1991).

3. R.A. Bailey and A.A. Nobile, Electrochim. Acta, 17, 1139 (1972).

4. G.S. Chen, I.W. Sun, K.D. Sienerth, A.G. Edwards and G. Mamantov, J. Electrochem. Soc., 140, 1523 (1993).

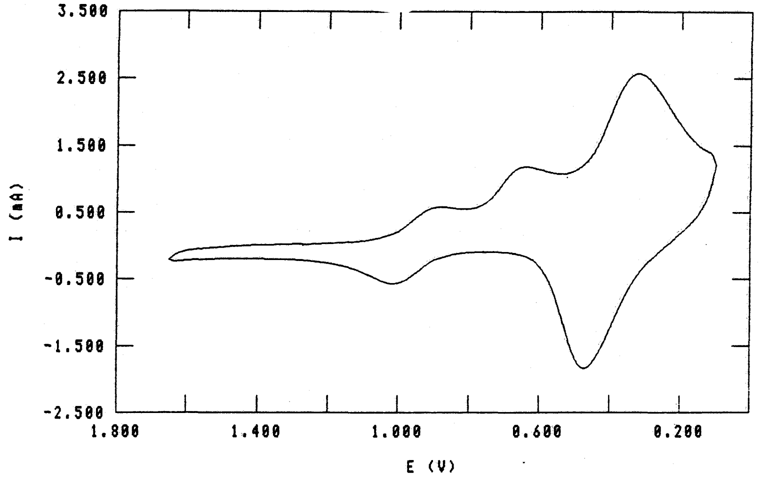

Figure 1. First scan cyclic voltammogram obtained after several scans for a solution of 4.4 m$\underline{M}$ K_2ReCl_6 in $AlCl_3$-$NaCl_{sat}$ melt at 180°C. Initial potential = 1.279 V (vs. Al(III)/Al in $AlCl_3$-$NaCl_{sat}$ melt); scan rate = 100 mV/sec. Tungsten working electrode (same results obtained at a glassy carbon electrode).

DOI: 10.1149/199413.0525PV

ELECTROCHEMICAL STUDIES ON SELENIUM SPECIES IN A BASIC $AlCl_3$-NaCl MELT

M. Morimitsu, M. Matsunaga, and K. Hosokawa
Department of Applied Chemistry, Faculty of Engineering,
Kyushu Institute of Technology,
1-1 Sensui, Tobata, Kitakyushu 804, Japan

ABSTRACT

The electrochemistry of selenium species in a basic $AlCl_3$–NaCl melt has been studied by cyclic, differential pulse, sampling voltammetries as well as emf measurements of a Na/$SeCl_4$ battery. The reaction of selenium tetrachloride with elemental selenium forms the low oxidation states of selenium compounds even in the basic melt. The oxidation of selenium proceeds from elemental selenium to tetravalent selenium through four electrochemical steps and involves intermediates Se_8^{2+}, Se_4^{2+} and Se(II). From the results of emf measurements, it is possible that Se(I) participates in the reaction mechanism.

INTRODUCTION

In recent years we have been interested in developing a sodium/selenium(IV) molten salt battery for load leveling and electric vehicle applications (1–5). The chemistry and electrochemistry of selenium species in $AlCl_3$–NaCl melts were studied by the electrochemical and spectroscopic analyses (6–10), which suggested the existence of tetravalent selenium and several low oxidation states of selenium. The mechanism for the reduction of tetravalent selenium was proposed as follows,

$$2\ SeCl_n^{(n-4)-} + 8\ e^- \rightarrow Se_2 + 2n\ Cl^- \qquad [1]$$

where n is 5 in an acidic melt and 6 in a basic melt (7). Potentiometric and spectroscopic studies, however, suggested that the reactions in acidic melts were more complex, because of the existence of low oxidation states such as Se_{16}^{2+}, Se_{12}^{2+}, Se_8^{2+}, Se_4^{2+} and Se_2^{2+} (8–10). While the electrochemical reactions of selenium species in acidic melts have been widely studied, there was few reports on the detailed discussion in basic melts. Previous studies on the performance of the

Na/SeCl$_4$ battery utilizing a basic AlCl$_3$–NaCl melt by us (4, 5) indicated that the reaction mechanism between Se(0) and Se(IV) is quite complex and the low oxidation state species are stable even in NaCl–saturated melts. In this paper we have demonstrated the reaction mechanism of selenium species in the basic melt.

EXPERIMENTAL

Melt preparation and several other experimental procedures have been described previously (3–5). 99.999% pure selenium and 99.9% pure selenium tetrachloride were used as received.

The electrochemical cells made of Pyrex glass were equipped with vitreous carbon (Tokai Carbon, GC–20SS) and tungsten working electrodes, a coiled tungsten wire counter electrode and a tungsten quasi–reference electrode. The reference electrode (99.999% pure aluminum wire in a NaCl–saturated melt) was separated from the main compartment by a thin glass membrane. The electrochemical reactions of selenium were studied for the solutions of several formal oxidation sates (FOXS) of selenium. The FOXS was changed by adding known amounts of either SeCl$_4$ or Se to the basic melt. Commercially available electrochemical instrumentation (Hokuto Denko Models HA–501G, HB–105, and Yanako P–1100) was used for all voltammetric (cyclic, sampling, and differential pulse) studies.

Na/SeCl$_4$ cells for emf measurements were composed of a Pyrex compartment filled with the mixture of a basic melt and elemental selenium which was separated from a sodium electrode by means of a β"–alumina tube (NGK Spark Plug, 13mm ID, 15mm OD, 100mm length). The FOXS was changed by either charging or discharging with coiled tungsten wire electrodes in the negative and positive compartments. The positive compartment was also equipped with a tungsten microelectrode for potentiometric measurements. The melt composition was kept basic even at a fully charged state.

RESULTS AND DISCUSSION

Figure 1 shows the dependence of emf of a Na/SeCl$_4$ battery on the FOXS of selenium. It can be seen in Fig. 1 that there are several points of inflection at the FOXS close to +1/4, +1/2, +1 and +2. Because the activity of chloride ion is constant in a basic AlCl$_3$–NaCl melt (11), the emf in Fig. 1 depends on only the activity of selenium compounds, even if those are chlorocomplexes as previously proposed (7). The results on the emf suggest that the electrochemical reactions of selenium species in the basic melt are quite complex and involve several intermediates.

No well-defined voltammetric wave was observed, when the elemental selenium was dissolved in a NaCl-saturated melt. The reason seems to be that the solubility of elemental selenium in NaCl-saturated melts is quite low (7,9). While the basic melt containing selenium is colorless, $SeCl_4$ dissolves in this melt to give a light orange solution. The dissolved $SeCl_4$ reacts slowly with elemental selenium and the color of the solution changes to be dark violet, when the FOXS is 0.23. Figure 2 depicts the typical cyclic voltammogram obtained with the vitreous carbon electrode at 473 K in the basic melt, in which the FOXS of selenium is 0.23. Similar cyclic voltammograms were obtained at a tungsten electrode. Four oxidation waves (A, B, C, H) and four reduction waves (D, E, F, G) are present in Fig. 2. Comparing the voltammograms in the different ranges of potential, the shape of voltammetric curves indicates that the waves A–F, B–E, C–D and H–G each correspond to a different redox couple. These results support the complex reaction mechanism of selenium indicated from the emf curve.

Some additional quantitative information about the waves A–F have been obtained by differential pulse voltammetry and sampling voltammetry. Figures 3a and 3b show the typical differential polarogram and the voltammogram constructed from current–time curves at 1 sec. Four individual waves for the oxidation and reduction of selenium species can be observed in Fig. 3a. The peak potential for the wave A is 1856±3 mV and the width of this peak at half height is 74 mV. This peak width agrees well with the theoretical value for a reversible two-electron process (72 mV at 473 K). In order to deduce the stoichiometry involved in this electrochemical step, the wave A in Fig. 3b was analyzed. The potential *vs.* log $\{i^2/(i_d - i)\}$ is linear with the slope of 42.4 mV, which is close to the theoretical value for the two-electron transfer (46.9 mV at 473 K). Considering that the wave A corresponds to the first oxidation step of selenium species with the FOXS near +1/4, a possible over-all reaction for the wave A–F is,

$$2\ Se_4^{2+} + 2\ e^- \rightleftarrows Se_8^{2+}. \qquad [2]$$

Equation [2] is also supported by the emf curve, which shows the points of inflection at the FOXS of +1/4 and +1/2. Similar analysis for the voltammetric results for the melt with the FOXS of 0.23 gives no stoichiometric conclusions for other three steps. Further electrochemical study for the selenium solutions with different FOXS, for example +1/2, +1 and +2, is now in progress.

The reaction mechanism for the waves B–E and C–D have been discussed from Nernst plots constructed from the emf data. While the voltammetric results suggested that the oxidation of Se_4^{2+} to Se(IV) may consist of two clear steps, the emf curve indicated more complex reaction sequence between the FOXS of +1/2 and +4. We, therefore, have discussed the final oxidation step, a redox couple C–D, at first. If the following reaction is assumed for the waves C–D,

$$Se^{4+} + 2\ e^{-} \rightleftarrows Se^{2+}, \qquad [3]$$

the emf *vs.* log $\{m(Se^{4+}) / m(Se^{2+})\}$ should show the linear relation between the FOXS of +2 and +4 with the slope of 46.9 mV at 473 K. The plot constructed from the emf values was successfully linear with the slope of 44.5 mV. In addition, the emf values are in good agreement with the Nernst equation for the reaction [3] as shown in Fig. 4, as the half wave potential is estimated from the peak potential of the wave C in the differential pulse voltammogram.

Based on the above discussion, it may be reasonable to consider that Se_4^{2+} and Se^{2+} participate in the reaction of the waves B–E. The relation between the emf and log $\{m^4(Se^{2+}) / m(Se_4^{2+})\}$, however, was not linear in the whole range between the FOXS of +1/2 and +2. The linearity is obtained only within the FOXS of +1 to +2 with the slope of 14.2 mV. Considering that the theoretical value is 15.6 mV for the six–electron step at 473 K, the following reaction may correspond to the waves B–E,

$$4\ Se^{2+} + 6\ e^{-} \rightleftarrows Se_4^{2+}. \qquad [4]$$

The deviation from the linearity in the FOXS range between +1/2 and +1 may be caused by the slow chemical reaction following the electrochemical reaction, although we have obtained no clear evidence for the EC mechanism by voltammetric studies. If Se_2^{2+} forms slowly by chemical reaction of Se_4^{2+} with Se^{2+} and is stable even in basic melts, the Nernst plot will show a break at the FOXS of +1. In order to prove this assumption and to demonstrate the total reaction mechanism of selenium species, the spectroscopic study will be necessary as well as further electrochemical analysis.

CONCLUSION

The electrochemical reactions of selenium species in basic $AlCl_3$–NaCl melts have been investigated by voltammetric techniques and emf measurements of Na/$SeCl_4$ batteries. The reaction mechanism during the oxidation and reduction between Se(0) and Se(IV) is quite complex and involves intermediates as Se_8^{2+}, Se_4^{2+} and S(II). S(I) may participate in the selenium reactions.

ACKNOWLEDGEMENTS

The present work was carried out under a cooperative program supported by Kyushu Electric Power Ltd. and Ministry of Education, Science and Culture, Japan.

REFERENCES

1. M. Matsunaga, K. Kitagawa, and K. Hosokawa, *Denki Kagaku*, **51**, 847 (1983).
2. M. Matsunaga and K. Hosokawa, *Yoyuen (Molten Salts)*, **30**, 83 (1987).
3. M. Matsunaga, T. Gouda, R. Otogawa, and K. Hosokawa, *Nippon Kagaku Kaishi*, **8**, 1466 (1988).
4. M. Matsunaga, M. Morimitsu, and K. Hosokawa, in "Proceedings of International Symposium on Molten Salt," C. L. Hussey, J. S. Wilkes, S. N. Flengas, and Y. Ito, Editors, PV 90-17, pp. 753-760, The Electrochemical Society Softbound Proceedings Series, Pennington, NJ (1990).
5. M. Morimitsu, M. Matsunaga, and K. Hosokawa, in "Proceedings of International Symposium on Molten Salt Chemistry and Technology 1993," M.-L. Saboungi and H. Kojima, Editors, PV 93-9, pp. 403-412, The Electrochemical Society Soft -bound Proceedings Series, Pennington, NJ (1993).
6. R. Marassi, G. Mamantov, and J. Q. Chambers, *Inorg. Nucl. Chem. Lett.*, **11**, 245 (1975).
7. J. Robinson and R. A. Osteryoung, *J. Electrochem. Soc.*, **125**, 1454 (1978).
8. D. J. Prince, J. D. Corbett, and B. Garbisch, *Inorg. Chem.*, **9**, 2731 (1970).
9. R. Fehrmann, N. J. Bjerrum, and H. A. Andreasen, *ibid.*, **14**, 2259 (1975).
10. R. Fehrmann and N. J. Bjerrum, *ibid.*, **16**, 2089 (1977).
11. D. E. Bartak and R. A. Osteryoung, *J. Electrochem. Soc.*, **122**, 600 (1975).

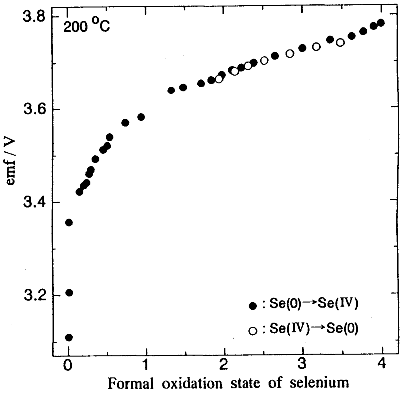

Fig. 1 Electromotive force of a Na/SeCl$_4$ battery with various FOXS at 473 K.

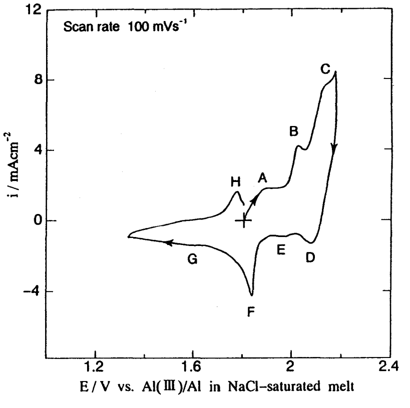

Fig. 2 Cyclic voltammogram for the selenium species in a AlCl$_3$-NaCl melt at 473 K. VC electrode area: 0.07 cm^2. Scan rate: 0.1 V/s. FOXS of Se: 0.23.

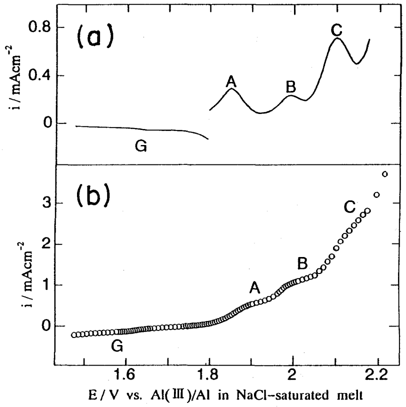

Fig. 3(a) Differential pulse voltammogram (scan rate: 0.5 mV/s, pulse width: 50 ms, modulation amplitude: 5 mV) and (b) voltammogram constructed from current-time curve at 1 sec. VC electrode area: 0.07 cm^2. FOXS of Se: 0.23. Temperature 473 K.

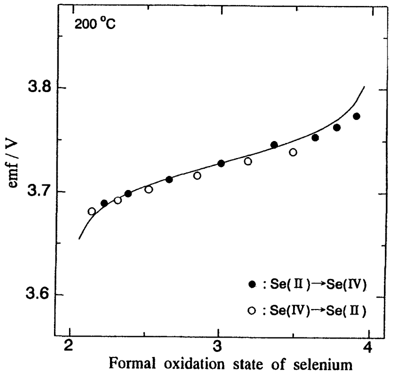

Fig. 4 Experimental(○, ●) and theoretical (—) emf of a Na/SeCl$_4$ battery between the FOXS of +2 and +4.

DOI: 10.1149/199413.0531PV

ELECTROCHEMISTRY OF THE DIMERIC COMPLEX $K_3W_2Cl_9$ IN MOLTEN ALKALI CHLORIDES

C.A.C. Sequeira
Instituto Superior Técnico
Av. Rovisco Pais
1096 Lisboa Codex, Portugal

ABSTRACT

The mechanism of the reduction of $K_3W_2Cl_9$ in molten LiCl-KCl eutectic was studied using cyclic voltammetry, chronopotentiometry, and controlled potential coulometry over a temperature range of 400 to 500°C and a $W_2Cl_9^{3-}$ concentration of 0.0005 to 0.005 mol/liter. The reduction occurred in two steps, complicated by the presence of a W_2^{6+}/W^{3+} disproportionation reaction. Diffusion coefficients, transfer coefficients, and the number of electrons involved in the rate-determining steps were also determined.

INTRODUCTION

The electrochemistry of tungsten and related investigations have been performed by several researchers, using different kinds of molten salts (1-15). Johnson and MacKenzie (4), Zuckerbrod and Bailey (12), and Sequeira (14, 15) investigated chemistry and electrochemistry of some tungsten species in molten LiCl-KCl. A striking feature of tungsten halide chemistry is the assortment of structures obtained, ranging from the simple monomeric WCl_6, WF_6 to the polymeric W_6Cl_{12} containing M-M bonding. Unlike the Mo and Cr analogues, tungsten does not form monomeric trivalent anions of the form WCl_6^{3-}. The dimeric $W_2Cl_9^{3-}$ anion is formed containing W^{3+}. This reflects the increasing tendency of tungsten to form metal-metal bonded compounds. This green anion may be prepared either by the reduction of W^{6+} in concentrated HCl with metallic Sn (16) or electrolytically (17).

The aim of this paper is to help elucidate the solution chemistry and electrochemistry of tungsten halide species in molten alkali halides. In particular, to characterise the dimeric chloride complex $K_3W_2Cl_9$ in the LiCl-KCl eutectic melt by cyclic voltammetry, chronopotentiometry and controlled potential coulometry over a temperature range of 400 to 500°C and a $W_2Cl_9^{3-}$ concentration of 0.0005 to 0.005 mol/liter, thus providing an overall view of its electrochemistry.

EXPERIMENTAL

LiCl + KCl eutectic mixture [57.8 + 42.2 mole percent (m/o)] prepared from Analar grade was used after treatment by the anhydrous hydrogen chloride technique (18). $K_3W_2Cl_9$ was prepared by the method of Saillant et al. (16), involving the controlled reduction of W^{6+} with metallic tin in concentrated HCl. At the end of the reduction process, freshly recrystallized $K_3W_2Cl_9$ was dissolved in concentrated HCl and characterised by UV-visible spectroscopy, as reported by Lingane and Small (19).

Voltammetric, chronopotentiometric and coulometric measurements were made using the equipment and procedure described elsewhere (15).

Pellets of $K_3W_2Cl_9$ were added to the fused LiCl + KCl eutectic mixture via a long Pyrex tube which had a funnel attached at the top. Complete dissolution of the pellets under prolonged sparging with Ar gas took about 1 hour, leading to a blue/green solution. Usually an electrochemical measurement was performed once completed dissolution occurred, or, about 1 hour after each halide addition. Background currents of the LiCl-KCl melt were less than 200μA/cm², so the IR drop has been ignored. Transition times were evaluated according to Kuwana's method (20).

RESULTS AND DISCUSSION

Voltammetric Measurements

Cyclic voltammetry was performed in LiCl-KCl-$K_3W_2Cl_9$ blue-green coloured melts. A black deposit was always noticed at the cooler portion of the cell, indicating that some tungsten species evaporated. The morphology of the voltammograms was relatively similar, although in several cases the positioning and magnitude of the peaks on the potential axis was dependent upon concentration, temperature, and potential sweep rate.

Typical cyclic voltammograms show a broad cathodic peak at approximately -0.24V corresponding to an irreversible step, since no anodic peak is seen on the reverse scan. On scanning to more negative potentials an additional reduction process occurs at a peak potential of around -0.56V, with a corresponding stripping wave at -0.47V.

The relationship between the measurable parameters and increasing sweep rate is given in Table I. The influence of increasing sweep rate, v, on the first peak potential, E_{cp1}, is difficult to determine because of the very broad nature of the wave, although slight cathodic shifts of about 10-20 mV for eight times increases in sweep rate are noted. The second reduction peak, E_{cp2}, remained practically constant with increasing sweep rate. The cathodic peak currents, i_{cp1} and i_{cp2}, increased linearly with increasing (sweep rate)$^{1/2}$ with a zero intercept, but some scatter in the results is noted for the second peak current, particularly at 400°C. The current function $i_p/v^{1/2}$ remains virtually constant with increasing sweep rate (Table I). These results clearly indicate that the process is diffusion controlled.

The half-peak width E_{cp1}-$E_{cp1/2}$ remains constant at about 60 mV; the logarithmic plot of E vs. log $[(i_{cp1}-i)/i]$ over the range $(0.5\text{-}0.9)i_p$ is linear with a slope of 19.95 at 450 °C. These results evidence an irreversible electroreduction process, for which it is possible to calculate $\alpha n=2.87$, where α is the charge transfer coefficient of the reduction step, and n is the number of electrons involved in the electrode step.

The half peak width E_{cp2}-$E_{cp2/2}$ increased with increasing sweep rate from a value of 60 mV at v=50 mV/s to 120 mV at v=800 mV/s. The logarithmic plot of E vs. log $[(i_{cp2} - i)/i]$ over the range $(0.5\text{-}0.9)i_p$ is linear with a slope of 14.95 at 450 °C. The corresponding anodic peak potential, E_{ap2} showed an anodic shift with increasing sweep rate of 45 mV for eight times increases in sweep rate.

The ratio of the two cathodic peak currents i_{cp2}/i_{cp1} remains approximately constant with an average value of about 0.67-0.57 with

Table I . Voltammetric results for the reduction of $K_3W_2Cl_9$ in the LiCl-KCl eutectic melt

V (Vs^{-1})	i_{cp1} ($mAcm^{-2}$)	$\frac{i_{cp1}}{v^{1/2}}$	i_{cp2} ($mAcm^{-2}$)	$\frac{i_{cp2}}{v^{1/2}}$	$\frac{i_{ap2}}{i_{cp2}}$	$\frac{i_{cp2}}{i_{cp1}}$	E_{cp1} (V)	$E_{cp1} - E_{cp1/2}$ (mV)	E_{cp2} (V)	$E_{cp2} - E_{cp2/2}$ (mV)	E_{ap2} (V)	E_{cp2} - E_{ap2} (mV)	E_{cp2} - E_{cp1} (mV)
400 °C; [$K_3W_2Cl_9$] = 10^{-3} mol/liter													
0.05	**0.63**	**2.80**	**0.50**	**2.23**	**0.95**	**0.79**	**-0.23**	**50**	**-0.57**	**60**	**-0.48**	**90**	**340**
0.10	**0.90**	**2.85**	**0.60**	**1.90**	**1.05**	**0.67**	**-0.24**	**55**	**-0.56**	**80**	**-0.47**	**90**	**320**
0.20	**1.30**	**2.91**	**0.70**	**1.57**	**1.25**	**0.54**	**-0.24**	**50**	**-0.57**	**90**	**-0.45**	**120**	**330**
0.40	**1.70**	**2.69**	**1.13**	**1.79**	**1.35**	**0.67**	**-0.25**	**60**	**-0.56**	**110**	**-0.43**	**130**	**310**
0.80	**2.60**	**2.90**	**1.75**	**1.96**	**1.40**	**0.67**	**-0.25**	**55**	**-0.56**	**115**	**-0.42**	**140**	**310**
500 °C; [$K_3W_2Cl_9$] = 5 x 10^{-3} mol/liter													
0.05	**2.9**	**12.9**	**1.60**	**7.20**	**1.05**	**0.55**	**-0.15**	**55**	**-0.51**	**65**	**-0.40**	**110**	**360**
0.10	**4.2**	**13.3**	**2.40**	**7.59**	**1.10**	**0.57**	**-0.16**	**60**	**-0.51**	**80**	**-0.37**	**140**	**350**
0.20	**6.0**	**13.4**	**3.30**	**7.38**	**1.20**	**0.55**	**-0.16**	**65**	**-0.52**	**95**	**-0.36**	**160**	**360**
0.40	**7.9**	**12.5**	**5.00**	**7.90**	**1.35**	**0.63**	**-0.17**	**60**	**-0.51**	**110**	**-0.36**	**150**	**340**
0.80	**12.1**	**13.5**	**6.60**	**7.38**	**1.35**	**0.55**	**-0.17**	**65**	**-0.52**	**120**	**-0.32**	**200**	**350**

increasing sweep rate and temperature (Table I). The ratio i_{ap2}/i_{cp2} is greater than unity and increases with an average value of about 1.0-1.4 with increasing sweep rate .

Voltammetric results of decreasing concentration of $K_3W_2Cl_9$ over the range 10^{-3}-$5x10^{-4}$M for a sweep rate of 0.1 Vs^{-1}, showed that i_{cp2}/i_{cp1} increases with decreasing concentration, the greater increase being noted at the more diluted melt. Voltammetric results of increasing concentration of $K_3W_2Cl_9$ over the range 10^{-3}-$5x10^{-3}$M for a sweep rate of 0.1 Vs^{-1}, showed that i_{cp2}/i_{cp1} decreases with increasing concentration, the greater decrease being noted at the higher $K_3W_2Cl_9$ concentration. This indicates that at low concentration of $K_3W_2Cl_9$ the second step is prominent, whether at high concentration it predominates the first charge transfer step.

Chronopotentiometric Measurements

Chronopotentiometric curves were run at current densities between 2.0 and 24 mA/cm^2. At low current densities (less than 5 mA/cm^2) no transition other than the first could be defined. At higher current densities, a well-defined second transition became noticeable. The Sand equation $i\tau^{1/2} = 1/2\ \pi^{1/2}\ n\ FAD^{1/2}C$ is obeyed for the first step process, and from the obtained data the diffusion coefficient of $W_2Cl_9^{3-}$ was calculated to be $1.1(\pm\ 0.3) \times 10^{-5}$ cm^2 s^{-1}, at 450°C.

The potential-time curve for the first reduction step was found to agree with the relationship (21)

$$E = (2.3RT / \alpha nF)\log(nFCK / i) + (2.3RT / \alpha nF)\log\left[\left(\tau^{1/2} - \tau^{1/2}\right) / \tau^{1/2}\right]$$

where K is the formal heterogeneous rate constant of the reduction process at E equal to zero, vs. the platinum reference electrode. From the slope of the resulting E-log$[(\tau^{1/2} - t^{1/2})/\tau^{1/2}]$ straight line, at 400°C, $\alpha n = 3.15$ was calculated. This value is compared with the αn value evaluated from the voltammetric data. From the E-τ equation, at t equal to zero

$$E = (2.3RT / \alpha nF)\log(nFCK / i)$$

The rate constant at 400°C, $K=3.5\times10^{-5}$ cm s^{-1}, was then calculated from this equation since all of the required factors were available.

It has been shown by Berzins and Delahay (22) that the Sand equation for a second transition is given by

$$(\tau_1 + \tau_2)^{1/2} - \tau_1^{1/2} = \pi^{1/2} nFAD^{1/2} C / 2i$$

A plot of 1/i vs. $(\tau_1+\tau_2)^{1/2} - \tau_1^{1/2}$ was made for the second transition, and since a linear relationship existed it can be concluded that the occurring electrode process is diffusion-controlled.

Transition times measured for $K_3W_2Cl_9$ concentrations ranging from 5×10^{-4} to 5×10^{-3} mol/liter, showed that the τ_1/τ_2 ratio increases with increasing concentration. This behaviour of the transition times is compared with the behaviour of the peak current densities obtained by the voltammetric study.

Controlled Potential Electrolysis

Controlled potential electrolysis (using a large Pt electrode) was attempted at -400 mV, and at -700 mV vs. Ag^+/Ag, for a 10^{-3}M $K_3W_2Cl_9$ melt at 450°C.

Metallic tungsten deposited at -700 mV, whereas a black deposit was obtained at -400 mV which exhibited a distinct X-ray diffraction pattern different from that of tungsten metal. This black deposit, unlike the tungsten deposition, did not adhere to the Pt electrode and could be easily knocked off.

The results obtained at -400 mV indicate that the first reduction step consumes about 2.9 moles of electrons per mole of $K_3W_2Cl_9$; the overall reduction process (electrolysis at -700 mV) consumes about 6.1 moles of electrons per mole of $K_3W_2Cl_9$.

With continued electrolysis and when prolonged periods of time were taken to run the chronopotentiograms, the melts changed their colour from blue-green to yellow-green, indicating the occurrence of a disproportionation process as postulated for molybdenum-containing chloride melts (23, 24).

CONCLUSION

The present results for the cathodic discharge of $K_3W_2Cl_9$ in molten LiCl-KCl, at 400-500°C, are consistent with the two-step process

$$W_2^{6+} + 3e^- \rightarrow W^{3+} + W$$

$$W^{3+} + 3e^- \Leftrightarrow W$$

The first three-electron transfer step is an irreversible diffusion-controlled process. The second step is most probably a quasi-reversible diffusion-controlled process. Experimental data indicate that $W_2Cl_9^{3-}$ ions react slowly with Cl^- ions to form WCl_6^{3-} monomer ions in accordance with the equilibrium reaction

$$W_2Cl_9^{3-} + 3Cl^- \Leftrightarrow 2WCl_6^{3-}$$

This disproportionation reaction may explain some lack of reproducibility observed during the running of the electrochemical experiments.

ACKNOWLEDGMENT

The author is grateful to ITEC, Lisbon, for support of this research through contract PEDIP2/F0004/1026.

REFERENCES

1. S. Senderoff and G.W. Mellors, J. Electrochem. Soc., 114, 586 (1967).
2. D. Inman and S.H. White, J. Appl. Electrochem., 8, 375 (1978).
3. S.H. White and U.M. Twardoch, J. Appl. Electrochem., 17, 225 (1987).
4. K.E. Johnson and J.R. MacKenzie, Anal. Chem., 41, 1483 (1969).
5. L. Sabbatini, P.M.A. Sherwood and P.G. Zambonin, J. Electrochem. Soc., 130, 2199 (1983).
6. T.B. Scheffler and C.L. Hussey, Inorg. Chem., 23, 1926 (1984).

7. A.G. Cavinato, G. Mamantov and X.B. Cox III, J. Electrochem. Soc., 132, 1136 (1985).
8. J.-P. Schoebrechts, P.A. Flowers, G.W. Hance and G. Mamantov, J. Electrochem. Soc., 135, 3057 (1988).
9. A. Katagiri, M. Suzuki and Z. Takehara, J. Electrochem. Soc., 138, 767 (1991).
10. K. Tanemoto, G. Mamantov and G.M. Begun, Inorg. Chim. Acta, 76, L79 (1983).
11. H. Hayashi, K. Uno, N. Hayashi, A. Katagiri and Z. Takehara, Denki Kagaku, 56, 40 (1988).
12. D. Zuckerbrod and R.A. Bailey, in "Proceedings of the Fourth International Symposium on Molten Salts", M. Blander, D.S. Newman, G. Mamantov, M.-L. Saboungi and K. Johnson, Editors, PV84-2, p.571, The Electrochemical Society Softbound Proceedings Series, Pennington, NJ (1984).
13. A. Katagiri, Materials Science Forum, 73-75, 415 (1991).
14. C.A.C. Sequeira, Materials Science Forum, 73-75, 569 (1991).
15. C.A.C. Sequeira, J. Electrochem. Soc., 140, 2526 (1993).
16. R. Saillant, J.L. Hayden and A.D. Wentworth, Inorg. Chem., 6, 1497 (1967).
17. H.B. Jonassen, in Inorganic Synthesis, vol.5, T. Moeller, Editor, p.139, McGraw-Hill Book Co. Ltd., New York (1970).
18. C.R.Boston and G.P. Smith, J. Amer. Chem. Soc., 80, 409 (1958).
19. J.J. Lingane and L.Y. Small, J. Amer. Chem. Soc., 71, 973 (1949).
20. R.N. Adams, Electrochemistry at Solid Electrodes, Marcel Dekker, New York (1969).
21. J.A. Lely, Ber. Deut. Keram. Ger., 32, 229 (1955).
22. T. Berzins and P. Delahay, J. Am. Chem. Soc., 75, 4205 (1953).
23. S. Senderoff and G.W. Mellors, J. Electrochem. Soc., 114, 556 (1967).
24. D. Inman, R.S.Sethi and R. Spencer, J. Electroanal. Chem., 29, 137 (1971).

DOI: 10.1149/199413.0539PV

ELECTRODE PROCESSES IN THE ELECTROCHEMICAL SYNTHESIS OF TiB2 IN MOLTEN FLUORIDES ①

Shuzhen Duan, Qingrong Shi and Xindong Wang

University of Science and Technology Beijing
Beijing 100083, P.R.China

ABSTRACT

The mechanism of the cathode process in the electrochemical synthesis of TiB_2 in molten $LiF-NaF-K_2TiF_6-KBF_4$ system has been investigated by means of cyclic voltammetry and convolution technique. It is found that the reduction of Ti(Ⅳ) proceeds in three steps: Ti(Ⅳ)→Ti(Ⅲ)→Ti(Ⅱ)→Ti(0). The first step is accompanied by the chemical disproportionation reaction: 2Ti(Ⅲ)→Ti(Ⅳ)+Ti(Ⅱ), and the second step is followed by the reduction of B(Ⅲ) to elementary boron. The reaction of boron with titanium reduced subsequently causes the formation of TiB_2. The codeposition of titanium and boron as well as the synthesis of TiB_2 is facilitated by polarization from B(Ⅲ) and depolarization from Ti(Ⅱ) owing to the high negative value of the free energy of formation of TiB_2.

INTROUCTION

Titanium diboride exhibits a number of specific properties, namely a high melting point, extreme hardness, wettability by molten aluminium and a general chemical inertness characterized by high resistance to oxidation at elevated temperatures and high corrosion resistance to molten metals and salts, good electrical conductivity and thermal conductivity etc., which make it a most promising construction material for various advanced technologies. It is evident that the study on mechanism of the cathode process in the electrochemical synthesis of TiB_2 in molten salts is of great importance to the preparation of titanium diboride and its coatings on substrates by molten salt electrolysis.

Makyta and Taranenko et al. [1,2] investigated the mechanism of the cathode process in the electrochemical synthesis of TiB_2 in molten $LiF-KF-k_2TiF_6-KBF_4$ and $NaCl-KCl-NaF-NaBF_4-TiCl_3$ systems by means of linear and cyclic voltammetry. The results showed that the reduction of Ti(Ⅳ) in the system $LiF-KF-K_2TiF_6-KBF_4$ proceeds in two steps:Ti(Ⅳ)→

---

① This Project is supported by National Nature Science Fundation of China.

Ti(Ⅲ)→Ti. The first step is followed by the reduction of B(Ⅲ) to elementary boron which reacts with titanium reduced with depolarization from Ti(Ⅲ) under formation of TiB_2. The electrochemical synthesis of TiB_2 in NaCl–KCl–NaF–$NaBF_4$–$TiCl_3$ proceeds in one step.

In this paper, the reactive electron number of each step and the mechanism of the electrochemical reduction of Ti(Ⅳ) and B(Ⅲ) from K_2TiF_6 and KBF_4, respectively dissolved in the LiF–NaF eutectic, have been determined and the investigation on the mechanism of the cathode process in the synthesis of TiB_2 in the system LiF–NaF–K_2TiF_6–KBF_4 has been carried out by means of cyclic voltammetry and convolution technique.

EXPERIMENTAL

Chemicals and Electrodes

The eutectic LiF–NaF mixture (60.9–39.1 moles%, $T_f = 652$℃) was used as solvent, into which the electrochemically active components, K_2TiF_6 and KBF_4, were added. All the chemicals used were analytical–reagent grade and K_2TiF_6 as well as KBF_4 were still recrystallied. The working electrode consisted of a platinum wire (d=0.5mm). A platinum wire was also used as the reference electrode. The counter electrode was a spectroscopic pure graphite rod.

Molten Salt Purification

The LiF–NaF mixture as solvent was purified by evacuating and pre–electrolysis in order to dehydrate and remove a small quantity of metallic impurities. The electrochemical cell, which is made of a stainless steel, consisted of a high–pure graphite crucible. Firstly, the mixture of LiF and NaF was contained in the crucible and dehydrated by evacuating and heating. Whenever the pressure inside the cell was below 5Pa, the temperature was raised by 50℃ time and again until 600℃. Subsequently, the high–pure argon gas was bubbled through the melt and the temperature was controlled at 750℃. The purification of the molten salts with pre–electrolysis as the final step was carried out for 36h using graphite anode and cathode until the residual current was less than 1mA. The efficiency of purification in this step was tested by voltammetric measurements.

Instrumentation

The experiments were performed in an electric resistance furnace and the temperature of the furnace was controlled by means of a DWT–702 precise temperature controller. The actual temperature of the melt was monitored using a thermocouple connecting with a digital multimeter. The electrochemical cell could be operated under either a vacuum or an inert atmosphere. A potentiostat (MODEL LB 81M) controlled by a function singal generator (TYPE GSTP3) was used as a source of potential and current. The observed curves were recorded by means of an X–Y recorder (TYPE 3033).

RESULTS AND DISCUSSION

Reductive Features of Ti(IV) in the LiF–NaF–K_2TiF_6System

The experimental results show that all the recorded voltammograms exhibite the same character. The typical cyclic voltammograms at various scan rates are shown in Fig.1 and three reduction waves as well as three oxidation waves are observed. Based on the analysis of the first reduction wave in Fig.1, It is found that the peak current function $i_p / v^{1/2}$ for the first reduction wave descends with increasing the scan rates v and the descending rate is slow more and more. Fig.2 shows the variations of $i_p / v^{1/2}$ for the first reduction wave with v at different concentrations of K_2TiF_6. It would indicate that the electrochemical reduction of Ti(IV) couples the homogeneous chemical reaction[3](disproportionation reaction).

For a electrochemical reduction corresponding to the first reduction wave taking place at a plane electrode

$$O + n_1 e \rightarrow R \tag{1}$$

the homogeneous chemical reaction is coupled

$$R \xrightarrow{k_1} O + Y \tag{2}$$

the current is given by [4]

$$i = \frac{n_1 FA(Dk_1)^{1/2} C_o^*}{1 + exp[\frac{n_1 F}{RT}(E - E_{1/2})]} \tag{3}$$

at sufficiently negative potentials, the i–E curves tend to a limiting value of current i_∞, given by:

$$i_\infty = n_1 FA(Dk_1)^{1/2} C_o^* \tag{4}$$

from (3) and (4)

$$E = E_{1/2} + \frac{RT}{n_1 F} ln \frac{i_\infty - i}{i} \tag{5}$$

Fig.3 shows the first reduction waves on the voltammetric curves at different concentrations of K_2TiF_6 and the limiting current $i_\infty$is obtained. The linear relations between E and $\ln[(i_\infty - i)/i]$ corresponding to Fig.3 are shown in Fig.4. The electron number n_1 can be calculated to be 1.2 ± 0.1 according to the slope of RT/n_1F. It indicates that the first step reduction of Ti(Ⅳ) is a one–electron reaction: $\mathrm{Ti(IV)} + e \rightleftharpoons \mathrm{Ti(III)}$, accompanized by the chemical disproportionation reaction: $2\mathrm{Ti(III)} \rightarrow \mathrm{Ti(IV)} + \mathrm{Ti(II)}$.

The convolution technique has been applied to transform and analyse the third reduction wave on the cyclic voltammogram (curve 1 in Fig.5).

A simple reaction corresponding to the third reduction wave is assumed:

$$O' + n_3 e \rightleftharpoons R' \tag{6}$$

If the electron transfer reaction is nernstian and the product is soluble, the expression of the potential E is given by [4]

$$E = E_{1/2} + \frac{RT}{n_3 F} ln[(I_l - I(t))/I(t)] \tag{7}$$

where

$$I_l = n_3 F D_o^{1/2} C_o'^* \tag{8}$$

$$I(t) = \frac{1}{\sqrt{\pi}} \int_t^0 \frac{i(u)}{(t-u)} du \tag{9}$$

I_l is the limiting value of I(t). I(t) is obtained by the numerical intgeration:

$$I(t) = \frac{1}{2} \sqrt{\frac{\triangle t}{\pi}} \sum_{j=1}^{k} \frac{i_j + i_{j-1}}{\sqrt{k - j + \frac{1}{2})}} \tag{10}$$

So the voltammetric i–E curve (curve 1 in Fig.5) can be transformed into I(t)–E curve (curve 2 in Fig.5), closely resembling a S–shape steady–state voltammetric curve. A plot of E vs. $\ln[(I_l - I(t))/I(t)]$ shown in Fig.6 is a straight line with the slope of RT/n_3F. The electron number n_3 corresponding to the third reduction wave is approximately 2. It is inferred that the electron number n_2 corresponding to the second–step reduction is 1.

It can be concluded that the electrochemical reduction of Ti(Ⅳ) at a platinum electrode in molten LiF–NaF at 750℃ proceeds in three steps: Ti(Ⅳ)→Ti(Ⅲ)→ Ti(Ⅱ)→ Ti(0). The first step is accompanied by the chemical disproportionation reaction: $2\mathrm{Ti(III)} \rightarrow \mathrm{Ti(IV)} + \mathrm{Ti(II)}$. The cathodic product is soluble and possibly forms alloy with platinum[5].

Electrochemical Reduction of B(Ⅲ) in the LiF–NaF–KBF_4 System

Fig.7 shows the cyclic voltammograms at various scan rates. It is found that on all curves only one cathodic reduction wave is observed and the cathodic peak potential slightly moves towards negative direction with increasing the scan rate. It indicates that the cathodic reduction of B(Ⅲ) is very close to a reversible process. According to the characteristic data of voltammetric curves, the peak potential E_p and the half–peak potential $E_{p/2}$, the electron number n is calculated to be 3.0 ± 0.2 using the equation[4] as follows:

$$E_p - E_{p/2} = -2.2RT/nF \tag{11}$$

so the electrochemical reduction of B(Ⅲ) to elementary boron is a simple three–electron process and the product is soluble, which accords with the analytical result of the convolution technique[6]. The variations of the peak current i_p with the square root of the scan rate $v^{1/2}$ shown in Fig.8 are straight lines through the coordinate origin, indicating that the process is diffusion–controlled.

Electrochemical Synthesis of TiB_2 in the $LiF–NaF–K_2TiF_6–KBF_4$ System.

Fig.9 shows the voltammetric curves recorded in the systems $LiF–NaF–K_2TiF_6$ (curve 1), $LiF–NaF–KBF_4$ (curve 2) and $LiF–NaF–K_2TiF_6–KBF_4$ (curve 3). From this comparison it follows that waves Ⅰ and Ⅱ on the curve 3 correspond to the reduction processes Ti(Ⅳ)→ Ti(Ⅲ)→Ti(Ⅱ). The two steps are followed by the reduction of B(Ⅲ) to elementary boron (wave Ⅲ), then the reduction of Ti(Ⅱ) to elementary titanium (wave Ⅳ). However, the molar ratio of K_2TiF_6 and KBF_4 exhibits a strong influence on the reduction potential of B(Ⅲ) and Ti(Ⅱ) as well as the shape of the voltammetric curves. Fig.10 shows voltammograms recorded in the system $LiF–NaF–K_2TiF_6–KBF_4$ at a constant concentration of K_2TiF_6 and various concentration of KBF_4 at the same scan rates. It can be seen from curves 1 and 2 that the current values of the third wave increase obviously with increasing concentration of KBF_4 and the third wave corresponding to the reduction of B(Ⅲ) to elementary boron is supported by this experimental result. At molar ratio $B/Ti > 2$ (curve 3), the reduction potential of B(Ⅲ) shifts about –0.15V towards more negative direction and the reduction potential of Ti(Ⅱ) shifts 0.10V towards more positive direction, which indicate that reductions of B(Ⅲ) and Ti(Ⅱ) can take place at the same potential. The observed shift of the potential corresponding to the codeposition of titanium and boron can be interpreted in relation to the reaction $Ti+2B=TiB_2$. Owing to the high negative value of the free energy of formation of TiB_2($\Delta G^0_{f,1000k} = -264KJ/mol$[7]), the reduction of Ti(Ⅱ) is facilitated by depolarization in the presence of elementary boron. The reduction potential of B(Ⅲ) is shifted towards more negative volues by polarization, which results from the reduction of B(Ⅲ) and the formation of stable TiB_2 leading up to the consuming of the concentration of BF_4^- near to the electrode surface.

CONCLUSIONS

1. The reduction of Ti(Ⅳ) in the LiF–NaF–K_2TiF_6 system proceeds in three steps: Ti(Ⅳ)→Ti(Ⅲ)→Ti(Ⅱ)→Ti(0). The first step is accompanied by the chemical disproportionation reaction 2Ti(Ⅲ)→Ti(Ⅳ)+Ti(Ⅱ).

2. The reduction of B(Ⅲ) in the LiF–NaF–KBF_4 system is a simple three–electron process: B(Ⅲ) + 3e = B. The cathodic process is very nearly reversible and is controlled by the diffusion of BF_4^- in the melt.

3. The mechanism of the electrochemical synthesis of TiB_2 in the LiF–NaF–K_2TiF_6–KBF_4 system can be described by following sequence of electrode reactions:

$$TiF_6^{2-} + e \rightarrow TiF_6^{3-}$$

$$TiF_6^{3-} + e \rightarrow TiF_6^{4-}$$

$$BF_4^- + e \rightarrow B + 4F^-$$

$$TiF_6^{4-} + 2e \rightarrow Ti + 6F^-$$

accompanied by the chemical reaction:

$$Ti + 2B = TiB_2 \qquad \triangle G^0_{f,1000k} = -264 KJ/mol$$

The codeposition of titanium and boron as well as the synthesis of titanium diboride can be ascribed to the polarization from B(Ⅲ) and the depolarization from Ti(Ⅱ), depending on the composition of the electrochemically active components.

REFERENCES

1. M.Matyta, K.Matiasovsky and V.T.Taranenko, Electrochim. Acta, 34, 861(1989)
2. V.I.Taranenko, I.V.Zarutskii, V.I.Shapoval, M.Makyta and K.Matiasovsky, Electrochim. Acta, 37, 263(1992)
3. R.S.Nicholson and I.Shain, Anal. Chem., 36, 706(1964)
4. A.J.Bard and L.R.Faulkner, Electrochemical Methods: Fundamentals and Applications, John Wiley & Sons, New York (1980)
5. H.Nishimura and T.Hiramatsu, Nippon Kinzoku Gakkaishi, 21, 469(1957)
6. Q.Shi, S.Duan and S.Wu, Journal of University of Science and Technology Beijing(Chin), to be published
7. JANAF Thermochemical Tables (2nd ed.), NSRDS, Washington (1971)

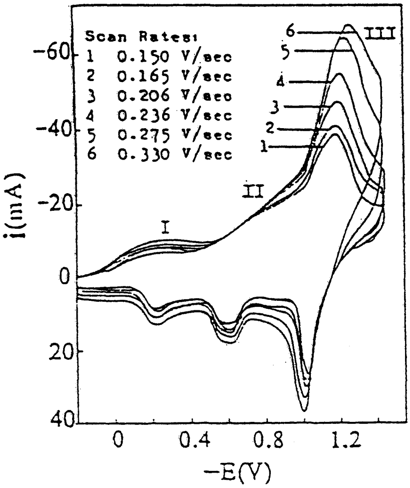

Fig.1 Voltammograms recorded at platinum electrode in the LiF −NaF −K_2TiF_6 system at various scan rates. T= 1023K, c(K_2TiF_6) = 0.119 mol / l.

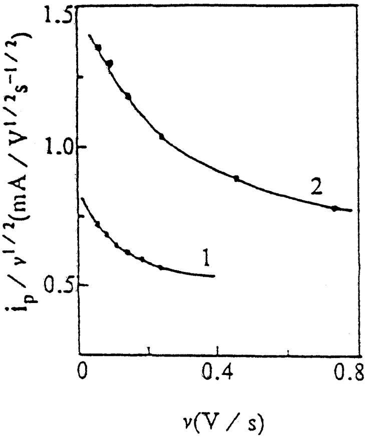

Fig.2 Variation of $i_p / \nu^{1/2}$ for wave I with ν. The same system as Fig.1. Curve 1: c (K_2TiF_6) = 0.119 mol / l; Curve 2: c (K_2TiF_6) = 0.167 mol / l.

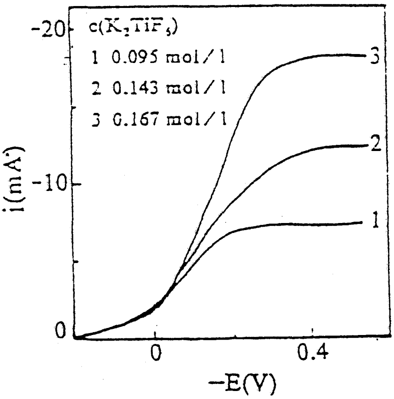

Fig.3 Voltammgrams for the reduction of Ti(IV) to Ti(III) in the LiF −NaF −K_2TiF_6 system at various concentrations of K_2TiF_6. ν= 0.165 V / s, T= 1023K.

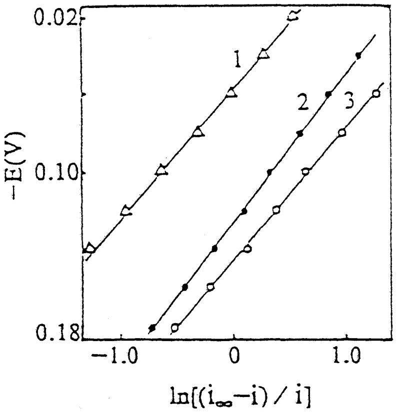

Fig.4 Relation between E and $\ln[(i_\infty - i) / i]$ for the voltammograms of Fig.3.

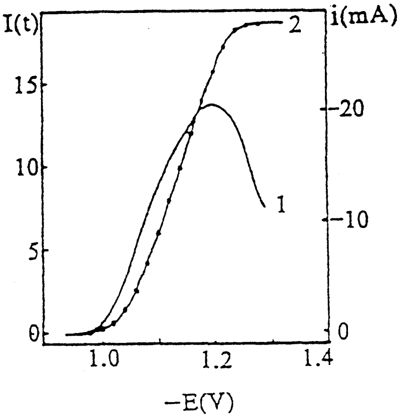

Fig.5 Voltammogram (Curve 1) and convolution (Curve 2) of the reduction of Ti(Ⅱ) to Ti in the LiF−NaF−K_2TiF_6 system.

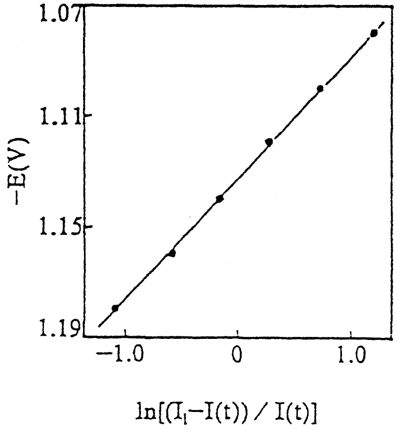

Fig.6 Relation between E and ln[(I$_l$−I(t)) / I(t)] for the curve 2 of Fig.5.

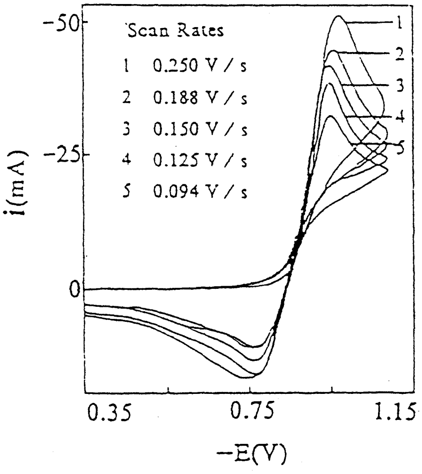

Fig.7 Voltammograms recorded at platinum electrode in the LiF−NaF−KBF_4 system at various scan rates. T = 1023K, c(KBF_4) = 0.381mol / l.

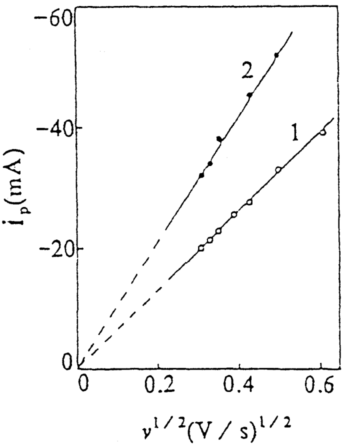

Fig.8 Dependence of the i_p on $\nu^{1/2}$ in the same system as Fig.7. Curve 1: c(KBF_4) = 0.286 mol / l; Curve 2: c(KBF_4) = 0.381 mol / l.

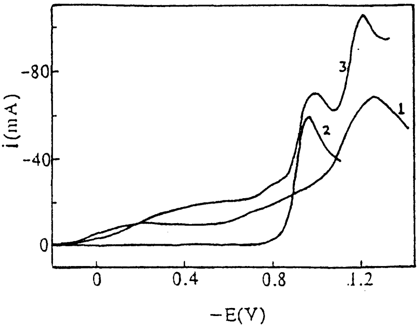

Fig.9 Voltammograms recorded at platinum electrode in various systems at 1023K. $v = 0.250$ V / s.
Curve 1: LiF–NaF–0.167mol / l K_2TiF_6
Curve 2: LiF–NaF–0.286mol / l KBF_4
Curve 3: LiF–NaF–0.214mol / l K_2TiF_6
–0.286mol / l KBF_4

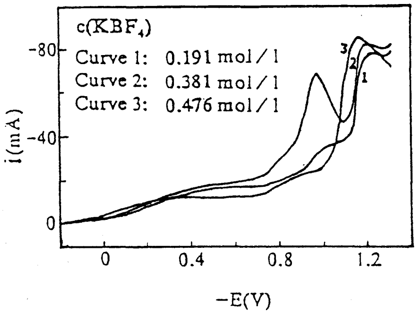

Fig.10 Voltammograms recorded in the LiF–NaF–K_2TiF_6–KBF_4 system at various concentrations of KBF_4 and constant concentration of K_2TiF_6. c (K_2TiF_6) = 0.214 mol / l, $v = 0.183$ V / s.

DOI: 10.1149/199413.0548PV

HIGH-TEMPERATURE ELECTROCHEMICAL SYNTHESIS OF TiB_2 FROM CRYOLITE-ALUMINA MELTS CONTAINING OXIDES OF BORON AND TITANIUM

S.V. Deviatkin, G. Kaptay, and E. Berecz

The University of Miskolc, Department of Physical Chemistry
Miskolc, 3515 Hungary

First, thermodynamic estimation of the possibility of electrochemical synthesis of TiB_2 from cryolite-alumina melts containing oxides of titanium and boron has been carried out. Then, the possibility of synthesis of TiB_2 was studied by linear voltammetric measurements with 0.01-0.1 V/s scan rates at 1273 K. Finally, electrolysis experiments were performed on cathodes made of graphite, Mo, and Nb in graphite crucibles, from Na_3AlF_6-Al_2O_3-TiO_2-B_2O_3 melt, at 1273 K. Eventually it was concluded that TiB_2 layers can be deposited from cryolite-alumina melts containing oxides of titanium and boron under certain circumstances.

INTRODUCTION

Electrochemical synthesis of TiB_2 from molten salts was studied by different researchers (1-7). L. Andrieux (1,2), G.A. Meerson, and M.P. Smirnov (3) were studying electrochemical synthesis of TiB_2 on graphite cathodes from B_2O_3-CaO-CaF_2($CaCl_2$)-TiO_2 and B_2O_3-MgO-MgF_2($MgCl_2$)-TiO_2 systems at 1173 - 1273 K. C.W. Mellors, and S. Senderoff (4), D. Schlain, F.X. Mecawley, and C. Wiche (5), H. Wendt, K., Reuhl, and V. Schwarz (6) were studying the possibility of electrochemical synthesis of TiB_2 from FLiNaK melts containing KBF_4 and K_2TiF_6 at 973 K. The main problem arising at depositing TiB_2 from FLiNaK melts is connected with losses of boron due to high partial pressure of BF_3. The same problem raised during electrochemical synthesis of TiB_2 from chloro-fluoride melts carried out by V.I. Taranenko et al. (7). In the present paper we are studying the possibility of electrochemical synthesis of TiB_2 from cryolite-alumina melts containing oxides of boron and titanium.

MELTS TO BE USED FOR SYNTHESIS

For depositing TiB_2 layers from cryolite-alumina melts sufficient quantities of both B(III) and Ti(IV) should be first dissolved in the melt. TiO_2 and B_2O_3 seem to be convenient compounds to be used for entering ions Ti(IV) and B(III) into the cryolite-alumina melt. There are two criteria for that :

i. TiO_2 and B_2O_3 should form stable solutions with cryolite-alumina melt ;

ii. solubility of both TiO_2 and B_2O_3 should be high enough for carrying the process of synthesis at economical (relatively high) current density.

First, reactions between the components of the melt, and between the oxides of Boron and Titanium have been considered. Results of calculation supposing exchange reactions only between fluorides and oxides are given in Table 1. Thermodynamic properties of pure compounds are generally taken from (8). For liquid BF_3 data taken from (9), while for liquid AlF_3 data taken from (10). From Table 1. one can see that reactions with AlF_3 can provide some amount of TiF_4, and especially BF_3 in the melt. However, in real cryolite melt activity of AlF_3 is low, and so the only products of the possible exchange reactions with considerable concentration can be BF_3 and Al_2O_3. However, BF_3 obviously has very high partial pressure, thus its formation would lead to losses of Boron. To prevent that, alumina should be added to cryolite melt. Consequently, B_2O_3 and TiO_2 will form stable solutions with a cryolite-alumina melt saturated by alumina.

Table 1. Change of standard Gibbs free energies of exchange reactions between oxides of Boron and Titanium, and between components of the melt at 1273 K

Reactions	ΔG_R^0 kJ
$TiO_2(c)+4NaF(l)=TiF_4(l)+2Na_2O(c)$	698.6
$3TiO_2(c)+4AlF_3=3TiF_4(l)+2Al_2O_3(c)$	79.0
$B_2O_3(l)+6NaF(l)=2BF_3(l)+3Na_2O(c)$	914.0
$B_2O_3(l)+2AlF_3=2BF_3(l)+Al_2O_3(c)$	-49.6

According to (11), B_2O_3 can be dissolved in cryolite melt with no limit at 1273 K. According to different authors solubility of TiO_2 in cryolite melt at 1273 K varies from 3 w% (12) to 6.7 w% (13). Solubility of both B_2O_3, and TiO_2 in the cryolite melt is obviously due to the following two mechanisms :

i. exchange reactions between the oxides and AlF_3 (see Table 1);

ii. formation of oxo-fluoride compounds between the oxides and NaF (14, 15).

Addition of Al_2O_3 to cryolite melt will obviously lower solubility of both B_2O_3 and TiO_2 by the both mechanisms given above. Actually, in presence of B_2O_3 and TiO_2 even the solubility of Al_2O_3 will be lower than that in pure cryolite. Hence the working electrolyte for synthesis of TiB_2 at 1273 K should be:

i. saturated by alumina ;

ii. saturated by TiO_2;

iii. consist of about 5 w% of B_2O_3. This value - being probably lower than the solubility level of B_2O_3 in cryolite melt saturated both by Al_2O_3 and TiO_2 at 1273 K - will provide the desired ratio of concentrations between Ti(IV) and B(III) in the melt for TiB_2 synthesis.

In the resulting melt, all the oxides (Al_2O_3, TiO_2, and B_2O_3) will present in the form of oxo-fluoride complexes.

THERMODYNAMIC CALCULATION

Principle of the Calculation

Thermodynamic estimation of the possibility of electrochemical synthesis of TiB_2 from cryolite-alumina melt has been carried out using our general equation (16):

$$\Delta E_{Me^{l+},A^{k+}/Me_nA_m} = -\frac{\Delta G_R^0}{(nl+mk)F} + \frac{nl}{nl+mk}\Delta E_{Me^{l+}/Me} + \frac{mk}{nl+mk}\Delta E_{A^{k+}/A} \qquad [1]$$

where: ΔE - equilibrium potential of deposition of the given compound our element; Me - metallic element; A - nonmetallic element (or another metallic element in case of intermetallic compound formation); n, m - stochiometric coefficients of Me and A in the compound Me_nA_m; l, k - charges of ions of Me and A in the melt; ΔG_R^0 - change of standard free energy of reaction [2].

$$nMe + mA = Me_nA_m \qquad [2]$$

Values of Parameters for the Calculation

Thermodynamic properties of substances in their standard state are taken from handbooks (8,17). For calculations, equilibrium potentials of deposition of Aluminum, Titanium and Boron is requested at 1273 K, from the cryolite melt being saturated by Aluminum oxide, and Titanium oxide, consisting 5 w% of Boron Oxide (see above). Hence activity of both Al_2O_3 and TiO_2 can be taken as 1 (if standard state is pure solid oxide), and decomposition potentials of these oxides can be calculated from thermodynamic properties of pure compounds. Thus, equilibrium potentials of Aluminum and Titanium (reference electrode Pt/O_2) equal (8, 17) : $\Delta E_{Al^{3+}/Al}$ = -2.196±0.002 V; $\Delta E_{Ti^{4+}/Ti}$ = -1.848±0.004 V. Standard equilibrium potential for Boron can be found in the same way (8, 17): $\Delta E^0_{B^{3+}/B}$ = -1.660 ±0.005 V. Using Nernst equation for B_2O_3 dissolved in the cryolite melt, and having concentration 5 w% (supposing ideality) one can obtain: $\Delta E_{B^{3+}/B}$ = -1.696 ± 0.005 V.

For a real solution of B_2O_3 in a cryolite melt some correction for non-ideality should be taken into account. In order to judge about the value of this correction experimental values on deposition potentials of Boron from cryolite-Al_2O_3(1 w%)-B_2O_3(0,2 w%) melt at 1323 K can be used (18). According to Fig.1. of this paper (18) the potential difference between the peaks corresponding to dissolution of Aluminum and Boron is about - 0.525± 0.025 V. As known from the literature (8, 19-23) equilibrium potential of Aluminum (reference electrode Pt/O_2) in a cryolite melt containing 1 w% of alumina at 1323 K equals : $\Delta E_{Al^{3+}/Al}$ (1 w%, 1323 K) = -2.292±0.008 V. Thus, equilibrium potential of Boron (reference electrode Pt/O_2) in a cryolite melt containing 0.2 w% of Boron oxide at 1323 K should be $\Delta E_{B^{3+}/B}$ = -1.767±0.033 V. In fact, in the experiments of (18) deposition of Boron, and then Aluminum was performed on a graphite cathode. Consequently, in calculation of the real equilibrium potential of Boron on inert cathode depolarization of about 0.05 V (see last row of Table 2) should be taken into account. Thus : $\Delta E_{B^{3+}/B}$ = -1.817±0.033 V. Comparing this value with the standard equilibrium potential of Boron at the same temperature (being -1.642±0.004 V (8, 17)), and using the Nernst equation for the melt containing 0.2 w% of Boron oxide, one can finally obtain the possible range of values for the activity coefficient of B_2O_3 in the melt : γ = 0.0024 - 0.12. This result is in full accordance with our previous statement, saying that "in the resulting melt ... B_2O_3 will present in the form of oxo-fluoride complexes". Extrapolating the values for the activity coefficient to our melt saturated by Al_2O_3 and TiO_2, and consisting 5 w% of B_2O_3 at 1273 K, the final possible range of the equilibrium potential of Boron on the inert cathode becomes: $\Delta E_{B^{3+}/B}$ = -1.77 ± 0.04 V. Because of higher concentration of B_2O_3 itself, and higher total oxide content of the melt, the real value of equilibrium potential of Boron is obviously closer to the positive end of the given range, i.e. is about -1.73 V.

Finally, the following potentials have been chosen for the calculations :

$$\Delta E_{Al^{3+}/Al} = -2.196 \pm 0.002 \text{ V}$$
$$\Delta E_{Ti^{4+}/Ti} = -1.848 \pm 0.004 \text{ V}$$
$$\Delta E_{B^{3+}/B} = -1.77 \text{ V} \pm 0.04 \text{ V}$$

Results of the Calculation

Results of the calculation are given in Table 2. for all the possible compounds, which can be formed as a result of chemical interaction between Boron, Titanium and Aluminum to be deposited on an inert cathode. As follows from Table 2., first TiB_2 will be deposited from the melt. This process is taking place at potential -1.49 ± 0.03 V, which is more positive by 270 mV, than the following possible cathode process , i.e. deposition of Boron (possibly with formation of Aluminum boride). In Table 2. compounds, which can be formed between the material of a graphite cathode and the metals to be deposited are given, as well (carbides of aluminum, boron and titanium). As follows from the Table 2., in case of electrolysis on the graphite cathode Titanium carbide is the first cathodic product, having potential by 80 mV more positive than that for Titanium diboride. Consequently, the first layer deposited on graphite cathode will be TiC, which probably will increase cohesion between the material of cathode and between further TiB_2 layers to be deposited on its top. As all the above proves, TiB_2 layers can be deposited from cryolite-alumina melts at 1273 K both on inert and graphite cathodes.

Table 2. Calculation of equilibrium deposition potentials of possible compounds from cryolite-Al_2O_3(sat)-TiO_2(sat)-B_2O_3(5%) melt at 1273 K on inert and graphite cathode (reference electrode : Pt/O_2)

Electrode	Reactions	n	l	m	k	ΔG_R^0 kJ	$-\dfrac{\Delta G_R^0}{(nl+mk)F}$ V	$\Delta E_{Me^{l+},A^{k+}/Me_nA_m}$ V
inert	$Ti+2B=TiB_2$	1	4	2	3	-303	0.314	-1.49 .± 0.03
	$Al+2B=AlB_2$	1	3	2	3	-54.9	0.063	-1.85 ± 0.03
	$Al+12B=AlB_{12}$	1	3	12	2	-174	0.046	-1.76 ± 0.04
	$Ti+Al=TiAl$	1	4	1	3	-65.3	0.097	-1.90 ± 0.01
	$3Ti+Al=Ti_3Al$	3	4	1	3	-84.1	0.058	-1.86 ± 0.01
	$Ti+3Al=TiAl_3$	1	4	3	3	-118	0.094	-2.00 ± 0.01
graphite	$Ti+C=TiC$	1	4	1	-	-170	0.440	-1.41 ± 0.01
	$4Al+3C=Al_4C_3$	4	3	3	-	-149	0.129	-2.07 ± 0.01
	$4B+C=B_4C$	4	3	1	-	-58.1	0.050	-1.72 ± 0.04

VOLTAMMETRIC EXPERIMENTS

Experimental

The possibility of synthesis of TiB_2 from Na_3AlF_6-Al_2O_3-B_2O_3-TiO_2 was studied by linear voltammetric measurements with 0.01-0.1 V/s scan rates at 1273 K in the atmosphere of air. The electrolyte was in glassy carbon crucibles, acting at the same time as a counter electrode. Glassy carbon and W were used as working electrodes. Reference electrode was Pt.

Results and Discussions

On the voltammetric curve obtained in a Na_3AlF_6-Al_2O_3 melt (Fig.1) a stable wave of the deposition of Al(III) to its metal appears in one step. That corresponds to the results of (11, 18). On the voltammetric curve obtained in a Na_3AlF_6-Al_2O_3-TiO_2 melt (Fig.2) a stable wave of the deposition of Ti(IV) complex to its metal appears in one step, which corresponds to results (18). On the voltammetric curve obtained in a Na_3AlF_6-Al_2O_3-B_2O_3 melt (Fig.3) a stable wave of the deposition of B(III) complex to boron appears in one step, as well, which is in agreement with results (18). Comparing Figures 1-3 the following conclusions can be drawn :

i. potential of deposition wave of Aluminum is much more negative than that for Titanium, and Boron.

ii. potential of deposition wave of Boron is more positive than that for Titanium by about 100 mV, which is in good agreement with the results of our calculations (78 ± 44 mV).

On the voltammetric curve obtained in a Na_3AlF_6-Al_2O_3-TiO_2-B_2O_3 melt (Fig.4) one additional wave was found at a more electropositive potential than those obtained from ternary melts. This potential was more positive by about 300 mV than the potential of deposition wave of Boron from a ternary melt (see Fig. 3), and by about 400 mV than that for Titanium (see Fig.2). Comparing this potential differences with our results of calculation (see Table 2) one can suppose, that the curve obtained in Fig.4 corresponds to joint deposition of Boron and Titanium with a formation of a compound TiB_2. Further electrolysis experiments were carried out at this positive potential in order to obtain and identify the macroscopic cathodic product.

Electrolysis Experiments

Electrolysis experiments were performed on cathodes made of graphite, Mo and Nb in graphite crucibles, from Na_3AlF_6-Al_2O_3(sat)-TiO_2(sat)-B_2O_3(5 %w) melt, at 1273 K in atmosphere of air. Macroscopic cathodic product has been obtained in potentiostatic way at the above mentioned potential (corresponding to deposition wave in Fig.4). It should be mentioned, that X-ray diffraction analysis of the cathodic product could be hardly performed, as Al_2O_3 (i.e. traces of electrolyte from the top of the cathodic layer) can not be dissolved in water, while in boiling NaOH solution (the only possibility to remove Al_2O_3) TiB_2 (the supposed cathodic product) dissolves more rapidly than Al_2O_3. Anyway, certain peaks of TiB_2 have been found during X-ray diffraction analysis of the cathodic product.

CONCLUSIONS

As both theoretically and experimentally has been previously proved, finally we can state that TiB_2 layers can be deposited from cryolite-alumina melts using TiO_2 and B_2O_3 additives.

ACKNOWLEDGMENTS

This work has been supported by "Foundation for Hungarian Higher Education and Research" and by "Hungarian Scientific Research Foundation" (OTKA-2395/91).

REFERENCES

1. L. Andrieux, Chim. et. ind., **25**, 1053 (1931).
2. L. Andrieux, Chim. et. ind., **27**, 411 (1932).
3. G.A. Meerson, and M.P. Smirnov, Chemistry of Rare Elements (in Russian), **2**, 130 (1955).
4. C.W. Mellors, and S. Senderoff, J. Electrochem., **113**, 60 (1966).
5. D. Schlain, F.X. Mecawley, and Ch. Wiche, J. Electrochem., **116**, 1227 (1969).
6. H. Wendt, K. Reuhl, and V. Schwarz, Electrochimica Acta, **37**, 237 (1992).
7. V.I. Taranenko, I.V. Zarutskii, V.I. Schapoval, M. Makyta, and K. Matiasovsky, Electrochimica Acta, **37**, 263 (1992).
8. M.W. Chase, and al. "JANAF Termochemical Tables (Third Edition)", J.Phys.Chem.Data, **14**, Suppl.1 (1985).
9. A.I. Efimov : Properties of Inorganic Compounds (in Russian), Leningrad (1983).
10. G. Kaptay, Euchem Conference on Molten Salts, De Haan, Belgium, Book of Abstracts, P-36 (1992).

11. A.I Beliaev, M.B. Rapoport, and L.A. Firsanova : Electrometallurgy of Aluminium (in Russian), Moscow (1953).
12. E.I. Hazanov, Light Metals (in Russian), **12**, 16 (1936).
13. Y. Hayakawa, and H. Kido, J.Electrochem. Soc. (Japan), **20**, 263, (1953).
14. V.N. Pavlikov, and al., Russ.J.Inorg.Chem., **20**, 3075 (1975).
15. V.N. Pavlikov ,and al., Russ.J.Inorg.Chem., **19**, 1597 (1974).
16. S.V. Deviatkin, G. Kaptay, V.I. Shapoval, and E. Berecz, Proceedings of the Int.Symp. on Molten Salt Chemistry and Technology, **93-9**, 584 (1993).
17. V.P.Glushko, et al : Therodynamic Properties of Individual Substances (in Russian) - Moscow, "Nauka", in 8 books (1978)
18. S.C. Raj, and M. Skyllas-Kazakos, Electrochimica Acta, **37**, 1787 -96 (1992).
19. M.Rolin, A.Ducouret, Bull. Soc. Chim. France, pp. 794-797 (1964)
20. M.M.Vetyukov, N.Van-Ban, Tsvetnie Metali, .**8**., pp. 31-32 (1971)
21. N.Van-Ban, Ph.D. Thesis, Leningrad, 126 p. (1971)
22. S.Chen, Journal of Northeast Institute of Technology, **37,** N.4., pp. 37-44 (1983)
23. I.Bader, E.Berecz, Acta Technica Acad. Sci. Hung. **101**, N.2., pp. 113-127 (1988)

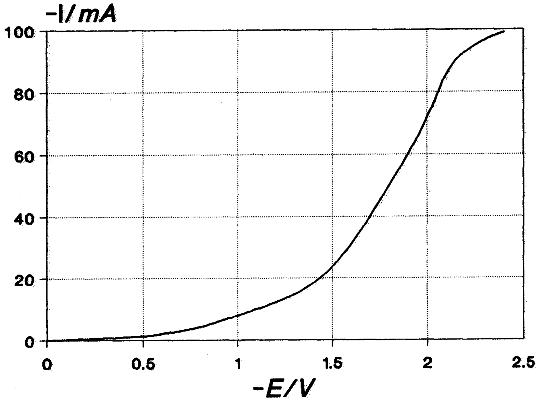

Fig.1. Voltammetric curve in the system Na_3AlF_6-Al_2O_3(3.9×10^{-4} $mol\times cm^{-3}$) at the scan rate of 0.1 V/s at 1273 K.

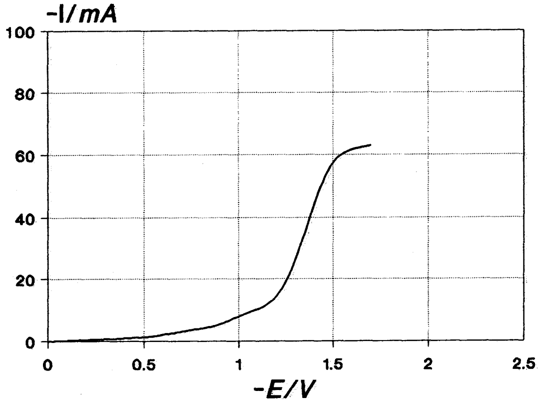

Fig.2. Voltammetric curve in the system Na_3AlF_6-Al_2O_3(3.7×10^{-4} $mol\times cm^{-3}$)-TiO_2(2.5×10^{-4} $mol\times cm^{-3}$) at the scan rate of 0.1 V/s at 1273 K.

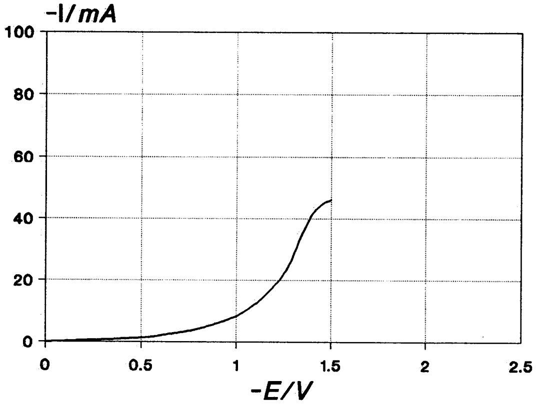

Fig.3. Voltammetric curve in the system Na_3AlF_6-Al_2O_3(3.6×10^{-4} $mol \times cm^{-3}$)-B_2O_3(2.8×10^{-4} $mol \times cm^{-3}$) at the scan rate of 0.1 V/s at 1273 K.

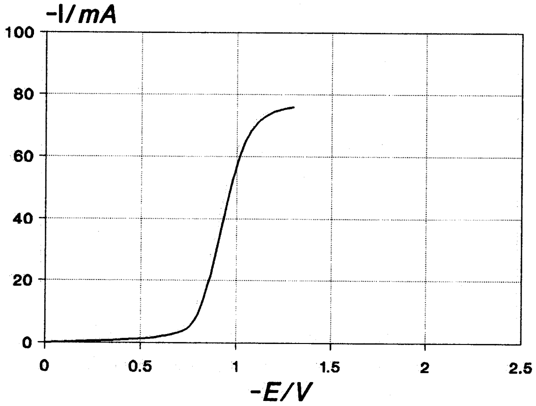

Fig.4. Voltammetric curve in the system Na_3AlF_6-Al_2O_3(3.4×10^{-4} $mol \times cm^{-3}$)-TiO_2(2.5×10^{-4} $mol \times cm^{-3}$)-B_2O_3(2.8×10^{-4} $mol \times cm^{-3}$) at the scan rate of 0.1 V/s at 1273 K.

DOI: 10.1149/199413.0558PV

ELECTROCHEMICAL SURFACE NITRIDING OF TITANIUM IN MOLTEN SALT SYSTEM

Yasuhiko Ito, Masayuki Tada and Takuya Goto
Department of Nuclear Engineering, Faculty of Engineering, Kyoto University,
Sakyo, Kyoto 606, Japan

ABSTRACT

A new electrochemical process for the surface nitriding of titanium has been developed. A LiCl-KCl eutectic melt is used at 450℃ as a model solvent. When KNO_3 or KNO_2 is dissolved in the solvent and the titanium electrode is cathodically polarized in the melt, surface nitriding of titanium can be achieved. On the other hand, when Li_3N is dissolved in the solvent and the titanium electrode is anodically polarized in the melt, it can also be achieved.

In both cases, adsorbed nitrogen atoms react with the outer most surface and diffuse into the bulk of titanium electrode to form a nitride layer. This principle has been successfully confirmed by the experiments.

INTRODUCTION

Several surface nitriding processes have been developed so far in order to obtain the surface functions of materials such as super hardness, corrosion resistance, friction resistance, and so on [1-10]. These processes are all practically available, however, some of them have still some disadvantages from an engineering viewpoint. From this background, new molten salt electrochmical process has been developed by the authors, which details will be described in the followings. This new process does not need complicated and expensive apparatus. Furthermore, by this electrochemical process, the thickness, composition and structure of the nitride layer can be controlled easily by controlling the electrolytic conditions.

PRINCIPLE

Let us use LiCl-KCl eutectic melt at 450℃ as a model solvent[11,12]. When KNO_3 or KNO_2 is dissolved in the solvent and titanium electrode is cathodically polarized in the melt, surface nitriding of titanium can be achieved according to the following reaction steps:

$$NO_3^- + 2e^- = NO_2^- + O^{2-}$$

$$NO_2^- + 2e^- = NO^- + O^{2-}$$

$$NO^- + e^- = N_{ads} + O^{2-}$$

and

$$Ti + N_{ads} = TiN$$

On the other hand, when Li_3N is dissolved in the solvent and titanium electrode is anodically polarized in the melt, it can also be achieved according to the following reaction step :

$$N^{3-} = N_{ads} + 3e^-.$$

and

$$Ti + N_{ads} = TiN.$$

In both cases, adsorbed nitrogen atoms react with the outer most surface and diffuse into the bulk of titanium electrode to form nitride layer. This principle has been successfully confirmed by the experiments.

EXPERIMENTAL

Figure 1 shows experimental setup for voltammetric investigations and surface nitriding of titanium. Purging was performed by a pure dry argon inside the holder. The counter electrode was suspended just at the center of the electrolyte in an alumina crucible. Other electrodes and alumina tubes were set in the same distance from the counter electrode. Chromel-Alumel thermocouple was used as an indicator of temperature. The top of the thermocouple covered by an alumina tube was immersed at the same depth as the center of the working electrode. Temperature was controlled by a thermostat with monitoring temperature of another thermocouple mounted near the heater in the furnace. All experiments were performed at 450℃. Titanium electrode was used as a substrate for the surface nitriding. And nickel was used as an indicative electrode for the analysis of the reaction process since it has a wider electrochemical window than that of titanium in molten LiCl-KCl eutectic melt. The working electrodes were mechanically polished with a fine grained emery paper followed with 0.3 μm alumina-water suspension to obtain a mirror surface. After this treatment, the electrodes were washed with distilled water and finally rinsed with ethanol. In order to remove the air-formed surface oxide, a pretreatment of nickel working electrode before experiment was performed by potential sweep reduction method to obtain reproducibility of data. Reference electrode was a Ag wire immersed in LiCl-KCl containing 1mol% AgCl, contained in a pyrex glass tube with thinner bottom. A dynamic reference electrode using electrochemically deposited lithium[13] was used to correct the potential measured by Ag/AgCl reference electrode and all potentials are refered to this potential and shown as [V (vs. Li^+/Li)] in this report. Counter electrode was glassy carbon.The electrolyte consisted of LiCl-KCl eutectic melt (59mol% LiCl, 41mol% KCl) that was prepared under an argon atmosphere. All chemicals were of reagent grade (Wako Chemical Co., Ltd.) and were dried in vacuum for more than 72 hours at 200℃ to remove water. Salts were melted in an alumina crucible set in a pyrex glass holder flowed with pure dry argon at 450℃. Nitrate ion source was KNO_3 (99.9%, Wako Pure Chemical Co., Ltd.) and nitrite ion source was KNO_2 (99.9%, Wako Pure Chemical Co., Ltd.). Nitride ion source was Li_3N powder (99.9%, Rare Metal Co., Ltd.). As this Li_3N powder easily reacts with water in the air, it was handled in a dry box with very low water concentration(<0.5ppm).

After melting the salt, potassium nitrate, potassium nitrite or lithium nitride was added with various concentrations.Cyclic voltammetric investigations were carried out to analyze the reaction process of the nitriding ion source. Surface analysis was conducted by XPS (JEOL, Co.,Ltd.:JPS-90SX). Mg K α line was used as an X-ray source. Sputtering was performed with an argon ion gun at 400V and 6mA. XPS signals of Ti_{2p} and those of N_{1s} were analyzed respectively, to identify chemical state and measure the quantity of each element.

RESULTS AND DISCUSSION

1. Cathodic surface nitriding

Electrochemical behavior of nitrate and nitrite ion

Figure 2 shows typical continuously recorded cyclic voltammograms of nickel after they achieved their steady state in the melt containing 0.3mol% KNO_3 or 0.3mol% KNO_2. Five cathodic peaks from A to E and one anodic peak F are observed in Fig.2. Both peaks A and B are observed in case of KNO_3 addition, while peak B is mainly observed in case of KNO_2 addition. Cathodic peak current at A and B increased with the increase of the amount of KNO_3 and KNO_2, respectively. Speculating from the above results together with the electrochemical behavior of nitrate ion and nitrite ion in molten nitrate and molten nitrite reported by Marchiano and Arvia[14], peaks A, B are considered to correspond to following reactions, respectively:

$$NO_3^- + 2e^- = NO_2^- + O^{2-} \qquad (1)$$

$$NO_2^- + 2e^- = NO^- + O^{2-} \qquad (2)$$

Anodic peak F and cathodic peaks C, D are due to oxide ion oxidation and reduction on nickel[15], respectively and these are not associated with the electrochemical reaction of nitrate ion and nitrite ion. Therefore, cathodic peak E which appears at less noble potential than cathodic peaks A and B is considered to correspond to further reduction as:

$$NO^{-} + e^{-} = N_{ads} + O^{2-} \qquad (3)$$

Thus, nitrate ion and nitrite ion in the melt are considered to be cathodically reduced to adsorbed nitrogen atom according to eqns.1,2 and 3.

Cathodic surface nitriding of titanium

Taking into account the above fundamental study, adsorbed nitrogen atoms produced by the cathodic reduction of nitrate ion and nitrite ion can be expected to be a surface nitriding source of titanium. In order to confirm this, potentiostatic cathodic reduction was performed at two typical potentials ; (a) at 0.4V (vs.Li^{+}/Li) where potential is considered to be negative enough to form adsorbed nitrogen as surface nitriding source according to eqn. 3, (b) at 1.6V (vs.Li^{+}/Li) where potential is considered to be not negative enough to form adsorbed nitrogen.

The titanium electrode surface obtained after potentiostatic cathodic reduction at 0.4V turned to golden. XPS analysis was performed in order to investigate titanium electrode surface change caused by cathodic reduction. Figure 3 shows XPS spectra for the outer most part of the surface of titanium electrode after potentiostatic cathodic reduction at 0.4V for 3h. It was characteristic that $Ti_{2p1/2}$, $Ti_{2p3/2}$ and N_{1s} peaks indicative of titanium nitride were observed[16]. Figure 4 shows atomic ratio profiles of nitrogen for titanium electrode after potentiostatic cathodic reduction at 0.4V and 1.6V, respectively. In the profile obtained after cathodic reduction at 0.4V, the concentration gradient of nitrogen is observed from the outer most part of the surface to the bulk. Maximum nitrogen ratio approaches 43% at the outer most part of the surface and the ratio decreases gradually across the layer. It was remarkable that N_{1s} peak energy value was indicative of titanium nitride (397.2eV) for the outer most surface and this value shifted gradually towards 399.7eV, indicative of solid solution of nitrogen in titanium across the layer. In contrast, in the profile obtained after cathodic reduction at 1.6V, the atomic ratio of nitrogen is staying low, at the same ratio of nitrogen included in titanium specimens before electrolysis. In addition, N_{1s} peak energy value kept almost the same as that indicative of solid solution of nitrogen in titanium.

Thus, it is concluded that surface nitriding can be achieved by cathodic reduction of nitrate ion or nitrite ion and that nitriding reaction can be easily controlled by the applied potential.

2. Anodic surface nitriding

Electrochemical behavior of nitride ion

Figure 5 shows typical continuously recorded cyclic voltammograms of nickel after they achieved their steady state in the melt before and after 0.1mol% Li_3N addition. Anodic peak G, cathodic peak H and anodic current I are observed in the solid line in the figure. It should be noticeable that anodic current I is obviously observed both in the anodic and cathodic scans comparing with the background anodic current. Since there are only two anion species of nitride ion and chloride ion in the melt and chloride ion can not be discharged at such negative potential region[11], it should be reasonable that the anodic current I corresponds to discharge of nitride ion as:

$$N^{3-} = N_{ads} + 3e^- \qquad (4)$$

Thus, the nitride ion in the melt is considered to be anodically oxidized to adsorbed nitrogen atom according to eqn.4.

Concerning the anodic peak G and cathodic peak H, the reaction is not so clear yet, but it may be associated with the synergetic electrochemical reaction of alkali metal and nitrogen.

Anodic surface nitriding of titanium

Taking into account the above fundamental study, adsorbed nitrogen atoms produced by the anodic oxidation of nitride ion can be expected to the source of surface nitriding of titanium. In order to confirm this, potentiostatic anodic oxidation was performed at two typical potentials ; (a) at 0.8V (vs.Li^+/Li) where potential is considered to be positive enough to form adsorbed nitrogen as surface nitriding source according to eqn.5, (b) at 0.4V (vs.Li^+/Li) where potential is considered to be not positive enough to form adsorbed nitrogen.

Figure 6 shows XPS spectra for the outer most part of the surface of titanium electrode after potentiostatic anodic oxidation at 0.8V for 4h . The $Ti_{2p1/2}$, $Ti_{2p3/2}$ and N_{1s} peaks indicative of titanium nitride were observed. Figure 7 shows atomic ratio profiles of nitrogen for titanium electrode after oxidation at 0.8V and 0.4V, respectively. In the profile obtained after anodic oxidation at 0.8V, concentration gradient of nitrogen is observed from the outer most part of the surface to the bulk. Maximum nitrogen ratio approaches 45% at the outer most part of the surface and the ratio decreases gradually across the layer. It was remarkable that N_{1s} peak energy value indicative of titanium nitride for the outer most surface shifted gradually towards that indicative of solid solution of nitrogen in titanium across the layer. In contrast, in the profile obtained after potentiostatic anodic oxidation at 0.4V, the atomic ratio of nitrogen was staying low, and N_{1s} peak energy value kept almost the same value as that indicative of solid solution of nitrogen in titanium.

Thus, it is concluded that surface nitriding can be achieved by anodic oxidation of nitride ion and that this nitriding reaction can be easily controlled by the applied potential .

CONCLUSION

A new electrochemical process for the surface nitriding of titanium has been developed. The results from the above experiments are summarized as follows:

(1) When KNO_3 or KNO_2 is dissolved in LiCl-KCl eutectic melt at 450℃ and titanium electrode is cathodically polarized in the melt, electrochemical surface nitriding of titanium can be achieved.

(2) This surface nitriding is considered to proceed according to the following reaction steps :

1) $NO_3^- + 2e^- = NO_2^- + O^{2-}$,
2) $NO_2^- + 2e^- = NO^- + O^{2-}$,
3) $NO^- + e^- = N_{ads} + O^{2-}$,

4) Reaction of adsorbed nitrogen with the surface and its diffusion into the bulk of titanium electrode.

(3) when Li_3N is dissolved in LiCl-KCl eutectic melt and titanium electrode is anodically polarized in the melt, surface nitriding can also be achieved.

(4) This surface nitriding is considered to proceed according to the following reaction steps :

1) $N^{3-} = N_{ads} + 3e^-$,
2) Reaction of adsorbed nitrogen with the surface and its diffusion into the bulk of titanium electrode

REFERENCES

1. J. L. Witton, G. T. Ewan and M. M. Ferguson, Mater. Sci. Eng., 69, 111(1985)
2. K. H. Habig, Surface and Coatings Technology, 42, 133 (1992)
3. B. Edenhofer, Heat Treat. Metals, 1, 23 (1973), ibid., 2, 59 (1974)
4. F.El-Hossary, F. Mohammed, A. Hendry, D.J. Fabian and Z. Szasan-Csih, Surface Engineering, 4, 150 (1988)
5. R. Buhl, H. K. Pulker and E. Moll, Thin Solid Films, 80, 265 (1981)

6. W. Lengauer, J. Cryst. Growth, 87, 295 (1988)
7. A. J. Perry, M. Georgson and W.D. Sprout, Thin Solid Films, 157, 255 (1988)
8. R. D. Singh and R.D. Doherty, Mater. Letter, 9, 87 (1990)
9. T.J. O'keefe and W.J. James, Mater. Sci. Eng.B, Solid-State Mater. Adv. Technol.,15, 203 (1992)
10. W.D. Munz and D. Hofman, Metal, 37, 279 (1983)
11. A.J. Bard, Ed., Encyclopedia of Electrochemistry of the Elements,vol.10, Marcel Dekker (1976)
12. G.J. Janz, Ed., Molten Salt Handbook, Academic press (1967)
13. T. Takenaka, Y. Ito and J. Oishi, Denki Kagaku, 53, 476 (1985)
14. S.L. Marchiano and A.J. Arvia, Electrochim. Acta, 17, 25 (1972)
15. M. Tada and Y. Ito, Denki Kagaku, 60, 615 (1992)
16. H. Hochst, R. D. Bringans, P. Steiner and Th Wolf, Physical Review B, 25, 7183 (1982)

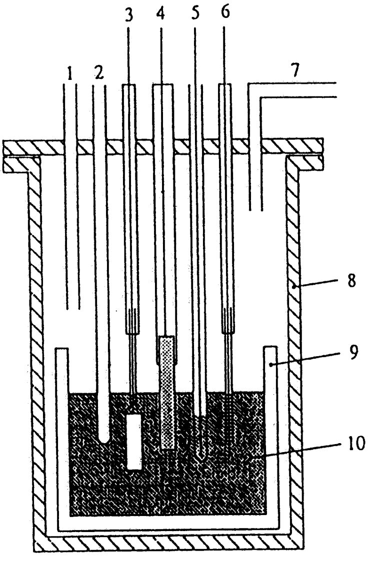

Fig. 1. Schematic of experimental setup for voltammetric investigation and surface nitriding of titanium; (1) argon gas inlet, (2) thermocouple, (3) working electrode, (4) counter electrode, (5) reference electrode, (6) dynamic reference electrode, (7) argon gas outlet, (8) pyrex holder, (9) alumina crucible and (10) electrolyte.

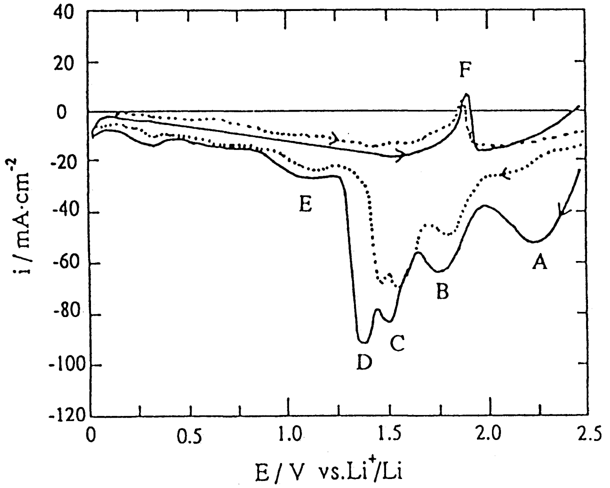

Fig. 2. Continuously cycled cyclic voltammograms for nickel in LiCl-KCl eutectic melt containing; (—) 0.3mol% KNO_3 and (----) 0.3mol% KNO_2 at 450℃, scan rate 100mVs^{-1}!

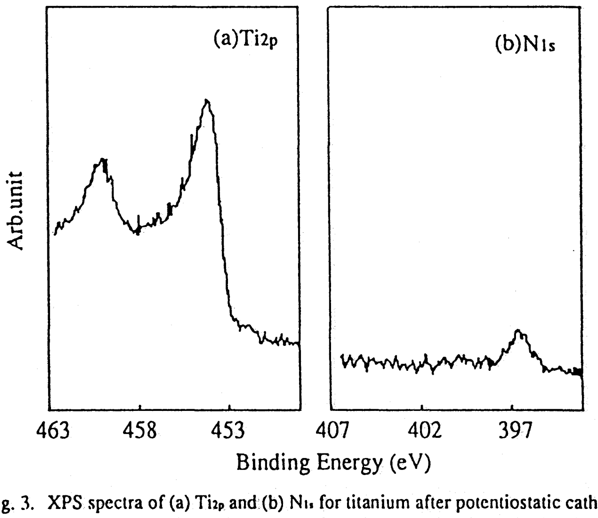

Fig. 3. XPS spectra of (a) Ti_{2p} and (b) N_{1s} for titanium after potentiostatic cathodic redution at 0.4V for 3h in LiCl-KCl eutectic melt containing 0.5mol% KNO_3 at 450℃.

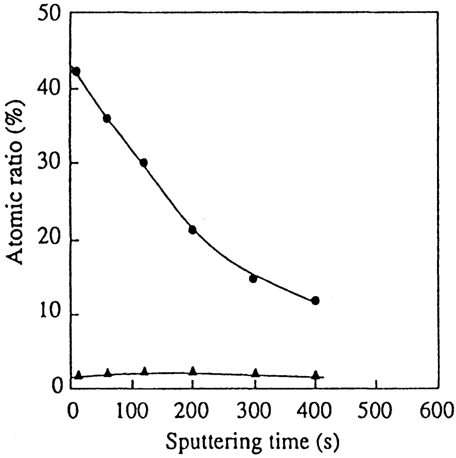

Fig.4. . Atomic ratio profiles of nitrogen for titanium after potentiostatic cathodic reduction; (●) at 0.4V for 3h and (▲) at 1.6V for 6h in LiCl-KCl eutectic melt containing 0.5mol% KNO_3 at 450℃.

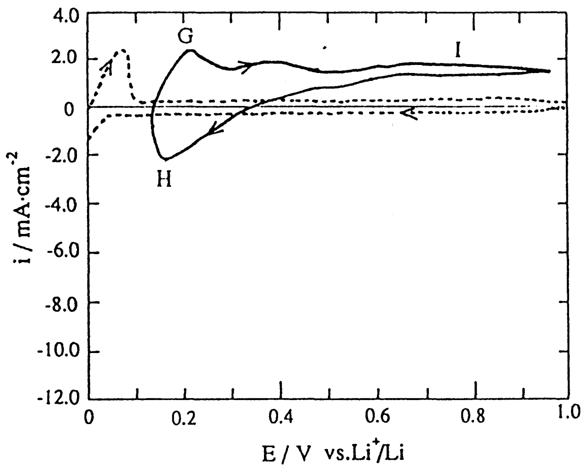

Fig. 5. Continuously cycled cyclic voltammograms for nickel in LiCl-KCl eutectic melt; (---) before and (—) after 0.1mol% Li_3N addition at 450℃, scan rate $100mVs^{-1}$.

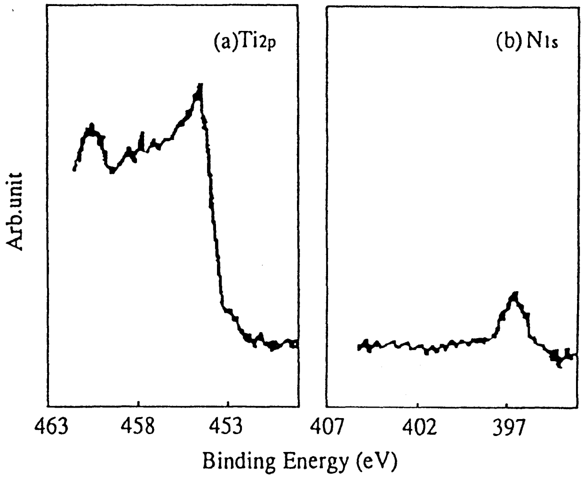

Fig. 6. XPS spectra of (a) Ti_{2p} and (b) N_{1s} for titanium after potentiostatic anodic oxidation at 0.8V for 4h in LiCl-KCl eutectic melt containing 0.1mol% Li_3N at 450℃.

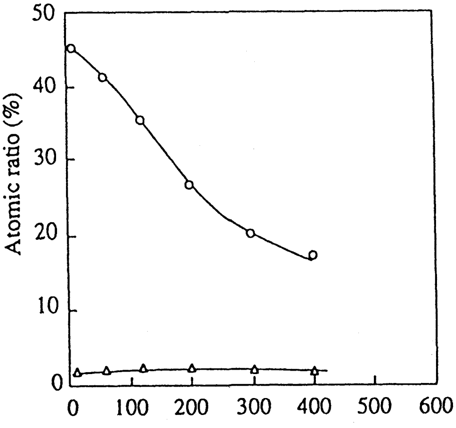

Fig.7. Atomic ratio profiles of nitrogen for titanium after potentiostatic anodic oxidation; (o) at 0.8V for 4h and (▵) at 0.4V for 6h in LiCl-KCl eutectic melt containing 0.1mol% Li_3N at 450℃.

DOI: 10.1149/199413.0568PV

THE INTERACTION BETWEEN TIN OXIDE AND CRYOLITE-ALUMINA MELTS

Liuoba Issaeva[1], Geir Martin Haarberg, Haiming Xiao[2] and Jomar Thonstad.

Department of Electrochemistry, Norwegian Institute of Technology,
7034 Trondheim, Norway.

ABSTRACT

Solubility data for SnO_2 in Na_3AlF_6 - Al_2O_3 melts are briefly reviewed. Cyclic voltammetry measurements were performed on glassy carbon and platinum electrodes in pure cryolite and cryolite-alumina melts containing tin salts. The voltammograms showed several peaks which were attributed to the presence of different oxidation states of tin in the melt, i.e. Sn(I), Sn(II), Sn(IV). In pure cryolite the oxidation waves were accompanied by current oscillations due to the formation of the volatile species SnF_2 and SnF_4. These oscillations were absent in the presence of alumina, which stabilized the tin species. The voltammograms gave indications of anodic precipitation of SnO_2 on the anode.

INTRODUCTION

Tin oxide is a candidate material for inert anodes, i.e. oxygen-evolving anodes, for aluminum electrolysis. Tin oxide has a certain solubility in the electrolyte, and the dissolved species can be reduced to metallic tin at the aluminium cathode, thus contaminating the metal produced. The behavior of the tin-containing species in the electrolyte is of interest in order to understand the mechanism of the corrosion of the anode and the transfer of tin to the cathode.

As shown in the following the solubility of tin oxide in the $NaF-AlF_3-Al_2O_3$ electrolyte varies in the range 0.08-0.01 wt.% SnO_2, depending on the concentration of alumina, the NaF/AlF_3 ratio and the temperature (1,2). The solubility increases under reducing conditions, indicating the formation of divalent tin species.

Information about the behavior of divalent tin in fluoride melts was not found in the literature, whereas this subject has been studied in chloride melts. Castrillejo et al. (3)

---

[1] Permanent addresses : Department of Light Metallurgy, Institute of Non-Ferrous Metals, Krasnoyarsk, Russia. [2] Department of Metallurgy Central South University of Technology, Changsha, China.

investigated the behavior of tin chloride in $ZnCl_2$-NaCl melts, and observed a wide stability range of $SnCl_2$. Voltammograms showed an anodic wave of formation of $SnCl_4$, which was volatilized. Among the oxides SnO was found to be unstable, while SnO_2 was stable at oxygen partial pressures above 10^{-10} atm. In a subsequent work Garcia et al. (4) determined the activity coefficients of $SnCl_2$ and $SnCl_4$, and the solubility product of SnO_2 was found to vary from 10^{-23} in LiCl-KCl to 10^{-17} in $ZnCl_2$-NaCl.

Elizarov and Novichkov (5) studied the behavior of tin salts in NaCl-KCl melts. The concentration decreased with time due to volatilization of $SnCl_2$ and $SnCl_4$. Voltammograms showed peaks corresponding to the Sn/Sn^{2+} and Sn^{2+}/Sn^{4+} pairs. It was found that $SnCl_2$ decomposed slowly into tin and $SnCl_4$. Delimarskii and Zarubitski (6) found that by anodic dissolution of tin into a chloride melt the current efficiency with respect to divalent tin varied from 116 to 103%, indicating co-formation of monovalent tin.

In the present work a voltammetric study was made of the behavior of tin salts dissolved in cryolite-alumina (Na_3AlF_6 - Al_2O_3) melts. Solubility data for SnO_2in these melts are reported.

Thermodynamic Data

Relevant thermodynamic data for tin fluorides and tin oxides were collected from the literature. Tin forms several fluorides and oxides: SnF, SnF_2, SnF_3, SnF_4, SnO, Sn_3O_4 SnO_2, (7,8). Tin monofluoride and tin trifluoride are gaseous over a wide range of temperatures. The temperatures of melting and boiling of SnF_2 are 190°C and 756°C respectively. Solid SnF_4 sublimates at 705°C (7). SnO is thermodynamically stable only up to 300-400°C, and at higher temperature it decomposes (8),

$$2\,SnO = Sn + SnO_2 \tag{1}$$
$$4\,SnO = Sn + Sn_3O_4 \tag{2}$$

Thermodynamic data of possible reactions were calculated (8,9) and are presented in Table 1 (8,9).

Table 1. Gibbs energies and standard potentials of possible reactions referred to aluminium.

Reaction	$-\Delta G$ kJ	$E^{\circ}_{1300\,K}$ V
$SnF_{2(g)} + 2/3\ Al_{(l)} = Sn_{(l)} + 2/3\ AlF_{3(s)}$ (3)	279.9	1.45
$SnF_{4(g)} + 4/3\ Al_{(l)} = Sn_{(l)} + 4/3\ AlF_{3(s)}$ (4)	729.5	1.89
$SnF_{4(g)} + 2/3\ Al_{(l)} = SnF_{2(g)} + 2/3\ AlF_{3(s)}$ (5)	449.7	2.33
$SnO_{(l)} + 2/3\ Al_{(l)} = Sn_{(l)} + 1/3\ Al_2O_{3(s)}$ (6)	256.7	1.33
$SnO_{2(s)} + 4/3\ Al_{(l)} = Sn_{(l)} + 2/3\ Al_2O_{3(s)}$ (7)	525.0	1.36
$SnO_{2(s)} + 2\ Al_{(l)} = SnO_{(l)} + Al_2O_{3(s)}$ (8)	268.3	1.39

If we correct for the AlF_3 activity in cryolite ($4 \cdot 10^{-4}$ (10)), the given potentials may be brought down by 0.29 V for reactions (3 - 5).

Solubility of SnO_2

Due to limited space the data on the solubility of tin oxide in cryolite melt must be limited to a short summary, with reference to one recent publication (1) and one forthcoming (2). In pure cryolite at 1035 °C the solubility of tin oxide was found to be 0.08 wt%, but it decreased rapidly with increasing alumina concentration, reaching a value of 0.02 wt% at high contents. When the NaF/AlF_3 ratio was varied, the solubility showed a maximum at molar ratio 3 (i.e. cryolite), and this maximum was observed in the pure fluorides as well as in alumina saturated melts. The solubility increased with increasing temperature, and an Arrhenius plot yielded an enthalpy of dissolution of 129 kJ/mole.

A logarithmic plot of solubility versus alumina concentration showed two straight segments, which were interpreted as different species being dominant at high and low contents of alumina. Model fitting of the data indicated that the associated species $SnO_2AlF_6^{3-}$ is presentat all alumina concentrations, while at low alumina concentrations (< 1wt.%) the species $SnOF_4^{2-}$ and $Sn_2O_2F_8^{4-}$ predominate.

The solubility of SnO_2 increased under reducing condition, when the composition of the reducing atmosphere (CO_2/CO) was adjusted so as to avoid the formation of metallic tin. Presumably the increased solubility was due to the presence of divalent or even monovalent tin.

EXPERIMENTAL

The electrolyte which was based on hand-picked Greenland cryolite, was contained in a graphite crucible, which also served as the counter electrode. The anodes consisted of a 3 mm rod of glassy carbon or of a 1 mm platinum wire, dipping 5-10 mm into the melt. The measurements on glassy carbon and Pt anodes were performed in the same electrolytes. The reference electrode was aluminum, protected by a closed end boron nitride tube. The cell was placed in a furnace under argon atmosphere. The temperature of the melt was 1020±1°C.

Pre-electrolysis was conducted in order to purify the melt, according to a previously reported procedure (11). A graphite anode of 3 mm diameter was used, and the graphite crucible served as cathode. At a constant voltage of 1.6 V the initial current density was 0.2 A cm^{-2}, but it decreased rapidly to 0.06 A cm^{-2} and then more slowly to a value of less than 0.01 A cm^{-2} after 20 hours. The voltammetric measurements were performed using a potentiostat (PAR Model 179) a programmer (PAR Model 175) and an x-y recorder. The sweep rate was normally varied from 1 to 1000 mV/s in the potential range of 0.5-3.0 V referred to aluminum.

The additives SnF_2, SnO and SnO_2 were added to the melt through an alumina tube, or alternatively tin species were introduced by anodic dissolution of tin. In that case tin was added to the crucible which then served as anode, using an auxiliary graphite cathode. Anodic dissolution of tin was carried out at 100 mA for 10 minutes, corresponding to a maximum concentration of 3.66 10^{-6} mol Sn(II) cm^{-3}, or 0.021 wt.% Sn. The concentration of Al_2O_3 was varied from 0.5 to 10 wt.%. The quantity of the additives, SnF_2, SnO_2 and SnO, was always 2 g of additive to 170 g of melt.

RESULTS AND DISCUSSION

Measurements in Pure Cryolite.

In cryolite melts which had been pre-electrolyzed, the voltammograms obtained with glassy carbon and platinum electrodes were smooth in the potential range of interest. On platinum a large anodic current was observed at potentials above 2.5 V, which was possibly due to anodic dissolution of platinum (12). Current oscillations observed on glassy carbon at above 2.5 V, were attributed to the evolution of CF_4 gas (10).

Voltammograms recorded with a glassy carbon electrode in a cryolite melt containing tin species which was generated by anodic dissolution, are presented in Fig. 1. Three peaks, accompanied by oscillations of the current, started at 0.6-0.7 V, 1.4-1.5 V and 2.2-2.3 V respectively. The oscillations diminished and disappeared with the start of a reduction peak at 0.7-0.8 V. The beginning of the first increase in anodic current at 0.6-

0.7 V probably corresponds to anodic dissolution of Sn with formation of SnF_2 according to reaction (3). The second peak starting at 1.4-1.5 V could be due to oxidation of the dissolved tin, which could exist in the form of monovalent tin. As mentioned above Delimarskii and Zarubitski (6) found indications of the formation of monovalent tin (Sn^+) in chloride melts.

The third peak in Fig. 1 could be due to oxidation of Sn(II) to Sn(IV),

$$Sn(II) = Sn(IV) + 2e \qquad (9)$$

At potentials higher than 2.5 V, CF_4 may be evolved (10),

$$AlF_3 + 3/4\ C = Al + 3/4\ CF_{4(g)} \qquad (10)$$

Reactions (5) and (9) and the oxidation of dissolved tin are accompanied by evolution of the gaseous compounds $SnF_{2(g)}$, $SnF_{4(g)}$, since the vapor pressures of these species may reach one atmosphere near the anode, as indicated by the ripples on the curve. This conclusion is further confirmed by the absence of corresponding cathodic waves and by the gradual decrease with time of the first cathodic wave starting at 0.8 V.

The peak currents decreased during subsequent cyclic voltammograms due to volatilization of the tin salts. Even without running voltammograms the height of the peaks decreased with time, e.g. the height of the second peak was lowered by 80% within 30 minutes after the first voltammogram. The peak height increased again after a new sequence of anodic dissolution of tin.

Four anodic peaks were observed in voltammograms with a Pt electrode in cryolite where tin species were introduced by anodic dissolution of tin, as shown in Fig. 2. The first oxidation wave at 0.5 V probably represents the dissolution of aluminum from an Al-Pt-Sn alloy (13). The corresponding reduction wave for deposition of aluminium with alloy formation started at 0.5 V. The second peak at 1 V was probably due to the oxidation of tin from the alloy with the formation of Sn(II). A corresponding reduction peak was observed starting at 0.8 V. The explanation for the third and fourth anodic waves starting at 1.5 and 2.2 V is the same as for the second and third peaks obtained with glassy carbon. Voltammograms obtained in cryolite with SnF_2 as additive were similar to those obtained when tin species were introduced by anodic dissolution of tin.

Measurements in Cryolite-Alumina Melts.

In the presence of alumina oxygen evolution was observed on platinum at around 2.2 V, and on glassy carbon CO_2 evolution occurred at around 1.3 V. Voltammograms obtained with a Pt electrode in cryolite-alumina melts after additions of SnO or anodic dissolution of tin, are shown in Figs. 3 and 4. Four anodic peaks starting at 0.3 V, 0.6 V, 1.1 V and 1.4 V respectively were observed. None of the peaks at potentials higher than 0.3 V were observed in the absence of tin compounds in the melt. The peaks starting at 0.3 V were probably due to deposition and dissolution of Al from an Al-Sn-Pt alloy. The peak starting at 1.1 V was high shortly after additions, as shown in Fig. 5, but it decreased with time and became very small in voltammograms obtained some time (3 hours) after addition of the various compounds, as shown in Figure 6.

The appearance of a loop at the far end of the voltammograms in Figs. 3 and 6 will be discussed later. A dependence between the peak heights at 0.9 and 1.4 V and the sweep rate could not be established since these peaks changed with time. The height of the peak at 1.8 V increased with increasing sweep rate, as shown in Fig. 7. A plot of the peak current versus the square root of sweep rate gave a straight line. The areas under the anodic and cathodic peaks agreed within 10-15 %.

The oxidation wave starting at 0.5 V in Figures 3 and 4 probably corresponded to the dissolution of Sn from a Sn-Al alloy with the formation of Sn(1l) species in the melt. A corresponding reduction wave was observed for the deposition of tin. The height of this peak decreased with time, and it increased again after a new addition of SnO or a new anodic dissolution of tin. The decreasing current might be connected with reactions of the type (1) and (2). Metallic tin was found on the bottom of the crucible after the experiments when SnO and SnO_2 were used as additives. The current density of this peak could approach 1 A cm^{-2}. Therefore, one can assume that the solubility of Sn(1l) is higher than for Sn(1V), in agreement with the solubility data reported above.

The peak starting at 1.1-1.2 V in Figures 3-6 might possibly be due to oxidation of dissolved tin in the form of monovalent tin (Sn^+), and the reduction wave at 1.2-1.3 V could be due to reduction of monovalent tin. New additions of the various compounds or new anodic dissolution of tin or stirring of the melt with a Mo wire made this peak increase, because of increasing rate of mass transfer. The peak at 1.4-1.5 V always appeared when tin species were present in the melt. The current density did not change with time for a given sweep rate. This peak was probably due to the reaction,

$$Sn(1l) = Sn(1V) + 2e \qquad (11)$$

The presence of alumina apparently stabilizes the tin species in the melt, and as pointed out above the likely tin species present in cryolite-alumina melts all contain Sn-O bonds.

In the first sweep with a newly polished Pt electrode a loop was observed on the voltammograms, as shown in Figs. 3 and 5. Such a loop where the current continues to increase after the sweep has been reversed, is typical for nucleation phenomena with deposition at a solid surface, i.e. it represented the deposition of solid SnO_2 on the electrode, because the melt became supersaturated with SnO_2.

Fig. 8 shows a voltammogram obtained with a glassy carbon electrode in cryolite-8 wt.% alumina and with tin species added by anodic dissolution of tin. Oxidation and reduction waves starting at 0.6 V were probably due to dissolution and deposition of tin. Different heights of the oxidation and the reduction waves could be due to the presence of metallic tin on the surface of the glassy carbon, caused by reactions (1) and (2). The ripples appearing above 1.3 V were due to CO_2 evolution.

ACKNOWLEDGEMENT

Financial support from the Norwegian Research Council and the Norwegian aluminum industry is gratefully acknowledged. The voltammetric studies were carried out by Prof. Issaeva during a stay as visiting scientist at The Norwegian Institute of Technology.

REFERENCES

1. H. Xiao, J. Thonstad and S. Rolseth, in Electrochemical Technology of Molten Salts, ed.C.A.C. Sequeira and G.S. Picard, editors, Molten Salt Forum, Vol. 1 & 2,pp. 215-229, Trans. Tech. Publ., Switzerland (1993).

2. H. Xiao, J. Thonstad and S. Rolseth, Submitted for publication in Acta Chem. Scand.

3. Y. Castrillejo, D. Ferry, A. Garcia, R. Pardo, and P. Sanchez Batanero, Material Science Forum, Vol. 73-75, 341-348 (1991).

4. M. Garcia, Y. Castrillejo, P. Pasquier, and G. Picard, in Electrochemical Technology of Molten Salts, ed.C.A.C. Sequeira and G.S. Picard, editors, Molten Salt Forum, Vol. 1 & 2, 47-56, Trans. Tech. Publ., Switzerland.

5. D. V. Elizarov, and V. Y. Novichkov, Rasplavy, 4, 93-96 (1992).

6. I. K. Delimarskii and O. G. Zarubitski, Electochemical purification of refractory metals in fused salts, p.74, Metallurgia, Moscow (1975).

7. Handbook of Chemistry and Physics. 70th edition, CRC Press, (1989-1990).

8. L. V. Gurvich and I. V. Veyts, Thermodynamic Properties of Individual Substances. V. 2, part 2, pp. 306-315, part 1, pp.349-370, Hemisphere Publishing Corporation (1991).

9. O. Knacke, O. Kubaschewski, and K. Hesselmann, Thermodynamical Properties of Inorganic Substances, Second Edition, Part 2, Springer-Verlag (1991).

10. K. Grjotheim, C. Krohn, M. Malinovsky, K. Matiasovsky, J. Thonstad, Aluminium Electrolysis, 2nd, ed. Aluminium-Verlag, Dusseldorf (1982).

11. J. Thonstad, F. Nordmo and J. K. Rødseth, Electrochim. Acta, 19, 761-769 (1974).

12. H. Xiao, R. Hovland, S. Rolseth and J. Thonstad, Light Metals, 1992, p.p.389 - 399 (1992).

13. H. Okamoto, P. R. Subramian, and L. Kacprzak, Binary Alloy Phase Diagrams. V. 1,3, Second Edition, ASM International (1990).

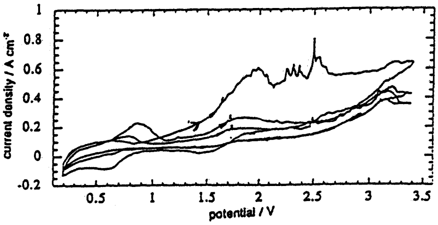

Fig. 1. Cyclic voltammogram for a glassy carbon anode in cryolite with tin species introduced by anodic dissolution of tin. Scan rate: 500 mV/s.

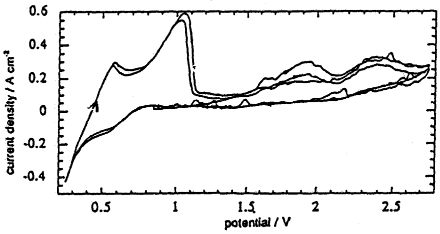

Fig. 2. Cyclic voltammogram for Pt electrode in cryolite with tin species introduced by anodic dissolution of tin. Scan rate: 200 mV/s.

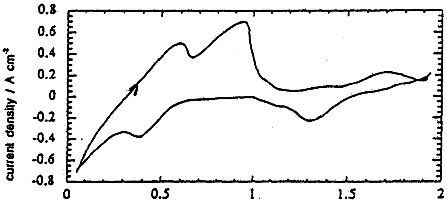

Fig. 3. Voltammogram for Pt electrode in cryolite - 1 wt.% Al_2O_3 after addition of SnO. Scan rate: 100 mV/s.

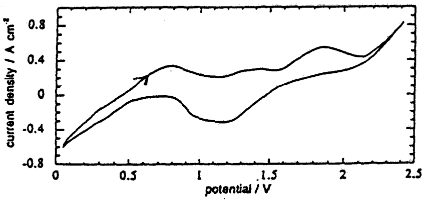

Fig. 4. Voltammogram for Pt electrode in cryolite - 1 wt.% Al_2O_3 with tin species introduced by anodic dissolution of tin. Scan rate: 500 mV/s.

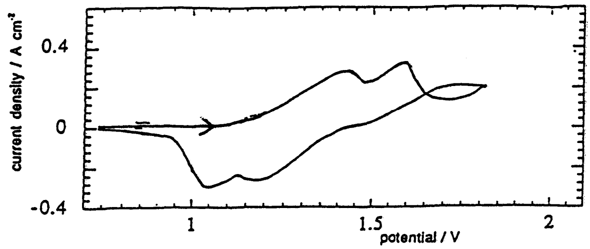

Fig.5. Voltammogram for Pt electrode in cryolite - 1 wt. % Al_2O_3 recorded 30 minutes after the addition of SnO. Scan rate: 100 mV/s.

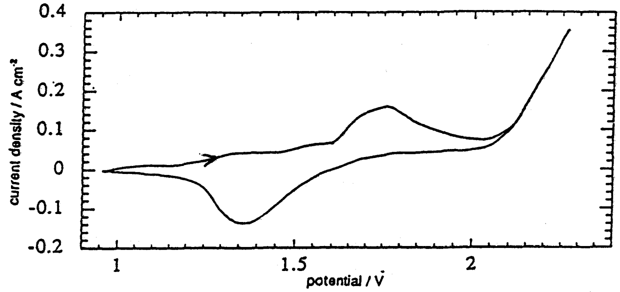

Fig. 6. Voltammogram for Pt electrode in cryolite - 5 wt. % Al_2O_3 recorded 3 hours after the addition of SnO. Scan rate: 200 mV/s.

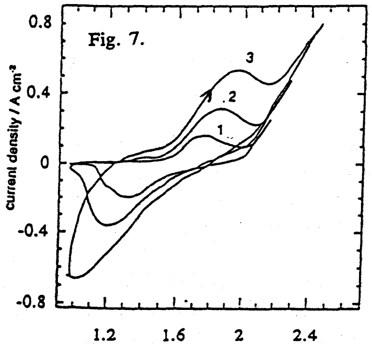

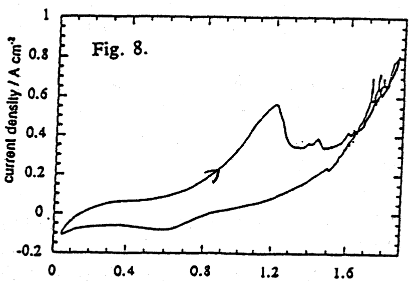

Fig. 7. Voltammograms for Pt electrode in cryolite - 0.5 wt. % Al_2O_3 at three different scan rates, recorded 3 hours after the addition of SnO. 1 - 100 mV/s, 2 - 500 mV/s, 3 - 1000 mV/s.

Fig. 8. Voltammogram for a glassy carbon electrode in cryolite - 8 wt. % Al_2O_3 with tin species introduced by anodic dissolution of tin. Scan rate: 200 mV/s.

DOI: 10.1149/199413.0578PV

IMPROVEMENTS IN FLUORINE GENERATION: AMORPHOUS CARBON ANODES WITH VERTICAL CHANNELS

W. V. Childs and G. L. Bauer

3M Fluorochemical and Process Technology Center
St. Paul, MN 55144-1000

Abstract

We have operated fluorine cells with YBD amorphous carbon anodes for over 2000 hours and at current densities over 200 ma.cm^{-2} practically free of polarization. Vertical channels facilitate the movement of fluorine up the face of the anode. Current efficiency estimates for hydrogen generation and for fluorine generation were near 100%.

Introduction

Within a few minutes of being made anodic the voltage required to pass 25 ma.cm^{-2} from molten KF.2HF into a fresh piece of carbon increased from about 3 volts to over 5 volts (Figure 1) and the carbon surface became highly non-wetting. This is consistent with the reports of Bai and Conway (1), Rudge (2), and Brown et al (3) that a very high contact angle leads to the formation of strongly adherent lenticular bubbles of fluorine that cover most of the anode surface. This behavior is ascribed to the formation of a layer of fluorinated carbon, CF_x which makes it difficult for current to pass from the electrolyte into the anode surface and leads to what Rudge (2) called polarization.

Bai and Conway (1a) concluded that "the formation and detachment of F_2 bubbles is the current-controlling factor for the fluorine evolution reaction ...". Presumably wherever the current can work into the anode surface the local current density will be very high, and the local anode will become even more non-wetting and polarize more frequently. In their third paper (1c) they reported extensively on a treatment that had been previously described by Rüdorf (4) and by Childs (5,6,7). Bai and Conway (1c) conclude that "[t]he improvements ... are believed to be associated mainly with facilitation of the detachment of the fluorine gas bubble/film..."

We believe that the improvements are due to facilitated movement of bubbles up the surface and have tested a design with vertical channels to enhance this movement. This design, in combination with the high voltage treatment, has allowed us to operate an anode in KF.2HF for well over 2000 hours at 226 ma.cm^{-2}. A similar anode was operated at 226 ma.cm^{-2} for over 1000 hours and then at 338 ma.cm^{-2} for 132 hours without subsequent polarization. Both anodes were in excellent condition when the runs were ended. A control anode without channels polarized at 50 hours and at 200 hours at 226 ma.cm^{-2}.

We also describe a simple method for estimating the current efficiencies for hydrogen generation and for fluorine generation.

Making Fluorine

Caution: The procedures described in this paper pose the risk of exposure to hydrogen fluoride and to elemental fluorine and should only be carried out by or under the direction of qualified professionals. Hydrogen fluoride and fluorine are dangerous materials. Qualified first aid treatment and professional medical resources must be established prior to working with them. Material Safety Data Sheets are available from HF and fluorine suppliers. The recommendations contained therein should be followed scrupulously.

The system is computer controlled.

Figure 2 is a section view of the cell. The cell body is of Monel^{TM} and is 60 cm tall, 30 cm wide, and 15 cm front to back. Kel-F^{TM} polymer windows permit viewing the cathode compartment. The lid is 1 cm Kel-F polymer. A 20 watt halogen reflector lamp illuminates the interior through the translucent lid. The electrolyte is contained in a loop consisting of a cathode tube, upper horizontal conduit, downcomer tube, and lower horizontal conduit. The tubes are jacketed and baffled for circulation of a tempered mixture of water and ethylene glycol for temperature control. This mixture also passes through a coil of copper tubing fastened to the bottom of the cell. The cathode and downcomer tubes are 7.80 cm inside diameter and 30 cm tall. The upper and lower conduits are 15 cm by 15 cm in cross section. Hydrogen from the cathode drives circulation up the cathode tube. When the hydrogen disengages in the upper conduit the denser electrolyte returns through the downcomer tube and the lower conduit.

The electrolyte is nominally KF.2HF (20.85±0.10 meq HF per gram). Low concentrations of HF lead to a polarization that is not amenable to the "high voltage treatment" and to stalactites of electrolyte on the cell lid and plugged effluent lines. At moderately higher concentrations the HF vapor pressure increases, and at much higher concentrations anodes will disintegrate.

Sixty 60 ml.min^{-1} of nitrogen is introduced through the FEP tube shown in the downcomer tube as a reference flow for analytical purposes and to prevent electrolyte from rising in the tube when HF is not being added.

HF is added on demand to keep the electrolyte level constant. Four nickel wire probes (not shown) (minus 110 volts to the case through 12,000 ohms) pass through the lid over the downcomer tube. The control probe ends one cm above the bottom of the upper conduit and controls, through the computer and a solenoid valve an air-powered bellows valve with a Kel-F polymer seat which controls HF addition through the FEP tube shown in the downcomer. The HF is taken as vapor from a 45 kg cylinder maintained at 35°C to 40°C. High (+1cm) and low (-1cm) probes generate signals that shut down the electrolysis power and HF (control and backup valves) on error. The fourth probe (+ 2 cm) shuts down operation independently of the computer.

Figure 3 shows some anode and hanger details. The anode is 3.5 cm in diameter and 35 cm long with. It is fabricated from Union Carbide YBD carbon. The upper 4 cm of the anode is coated with plasma sprayed nickel (10). The channels are 0.2 mm wide and 2 mm deep. They extend from the bottom of the anode to about 3 mm above the electrolyte level. Other spacings work well. Fluorine moves up the anode and mixes with nitrogen in the vapor space. The nitrogen serves as a reference gas for estimating the anodic current efficiency. The mixture leaves the cell through the hanger as shown. (Except for a stream drawn off for analysis the fluorine is destroyed in a fuel-rich natural gas flame.)

The anode is connected to the hanger (Monel) with a split sleeve of nickel which is kept under compression with three mild steel bands. The bands are firmly, but carefully, tightened with a banding tool.

The skirt is Monel and is not in electronic contact with either the anode or the cathode. It is insulated from the hanger, which is at anode potential, with a Fluorel™ gasket. The skirt extends 2.5 cm into the electrolyte. The anode extends 21.6 cm below the skirt. The current density is based on the lateral geometric area of the carbon below the skirt. The cell is operated at constant current with a hardware voltage limit. At 226 ma.cm^{-2} the current is 53.6 amperes (two faradays per hour). The voltage limit is set at 15 volts.

Polarization and Depolarization (High Voltage Treatment)

The time from first startup to first polarization depends on the rate of current increase, the electrolyte composition, the choice of carbon, and the presence or absence of channels. Polarization is manifested by the inability to pass the desired current at a normal voltage.

Depolarization is performed by allowing the power supply voltage to rise to a value that will allow the normal current to pass. At 226 $ma.cm^{-2}$ this voltage will be in the range of 24 to 30 volts. Our experience has been that after a minute or so the voltage will drop rapidly and the cell will operate at a normal voltage. It is thought that depolarization works by burning off some of the outer layer of the anode.

One anode ran well for over 2000 hours at 226 $ma.cm^{-2}$. A similar anode was operated at 226 $ma.cm^{-2}$ for over 1000 hours and then at 338 $ma.cm^{-2}$ for 132 hours without trouble. Both anodes were found to be in excellent condition when the runs were stopped.

Estimating the Rates of Production of Hydrogen and Fluorine

Please refer to Figure 4. An air-powered ejector is used to draw five to ten ml per minute of the effluent stream from the cathode compartment through a bed of activated alumina pellets at ambient temperature to remove HF. The hydrogen/nitrogen mixture is then analyzed It is straightforward to calculate the current efficiency for hydrogen generation from the current level, the hydrogen/nitrogen ratio, and the nitrogen flow rate to the cathode compartment. Similarly a sample of the effluent stream from the anode compartment is drawn through a bed of activated alumina at 100°C to 115°C. The alumina removes HF and reacts with fluorine quantitatively to produce oxygen. The oxygen/nitrogen mixture is then analyzed and the current efficiency is calculated. The gas mixtures are analyzed with a TCD detector with an argon carrier using a 5A molecular sieve column at 60°C. Current efficiencies for the anode and cathode reactions are usually about 100%. Standard deviations are about 2%.

Conclusion

Carbon anodes with vertical channels on their face and that have been depolarized or activated with a "high voltage treatment" will produce elemental fluorine for at least 2000 hours at high current densities and with excellent current efficiencies.

The use of reference gas flows provides a simple means to estimate the current efficiencies for gas generating electrochemical processes.

References

1. (a) Lijun Bai and B. E. Conway, J. Applied Electrochem. **18** (1988) 839;
   (b) Lijun Bai and B. E. Conway, J. Applied Electrochem. **20** (1990) 916;
   (c) Lijun Bai and B. E. Conway, J. Applied Electrochem. **20** (1990) 925.

2. (a) A. J. Rudge "Production of Elemental Fluorine by Electrolysis", in Industrial Electrochemical Processes, (A. T. Kuhn, Ed.), Elsevier (New York) 1971, Chapter 1;
   (b) A. J. Rudge, The Manufacture and Use of Fluorine and Its Compounds, Oxford (London) 1962).

3. O. R. Brown, B. M. Ikeda and M. J. Wilmot, Electrochimica Acta **32**(1987) 1163.

4. W. Rüdorf, U. Hoffman, G. Rüdorf, J. Endell and G. Ruess, Z. Anorg. Allgem. Chem **256** (1948) 125.

5. W. V. Childs, "The Phillips Electrochemical Fluorination Process", in Techniques of Electroorganic Synthesis (N. L. Weinberg and B. V. Tilak, Eds.) Wiley (New York) 1982, Chapter VII.

6. W. V. Childs, U. S. Patent 3616315 (1971).

7. W. V. Childs and F. N. Ruehlen, U. S. Patent 3616336 (1971)

8. W. V. Childs, "Behavior of Carbon Anodes in the CAVE/Phillips KF.2HF Electrolyte System with Applications", in Proceedings of Fifth International Forum on Electrolysis in the Chemical Industry, Fort Lauderdale, FL, Electrosynthesis Company (East Amherst, N. Y.) 1991.

9. Alan Marshall, U. K. Patent 2135335(1984)

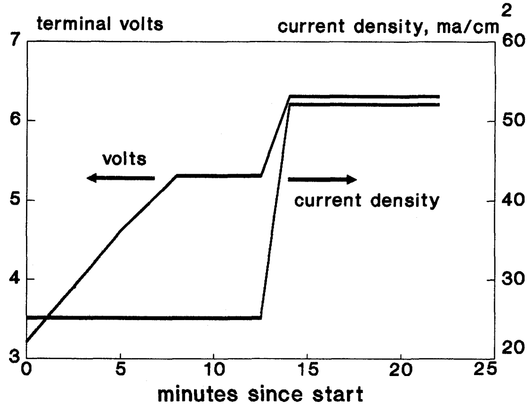

Figure 1. Effect of current passage on terminal voltage starting with new carbon.

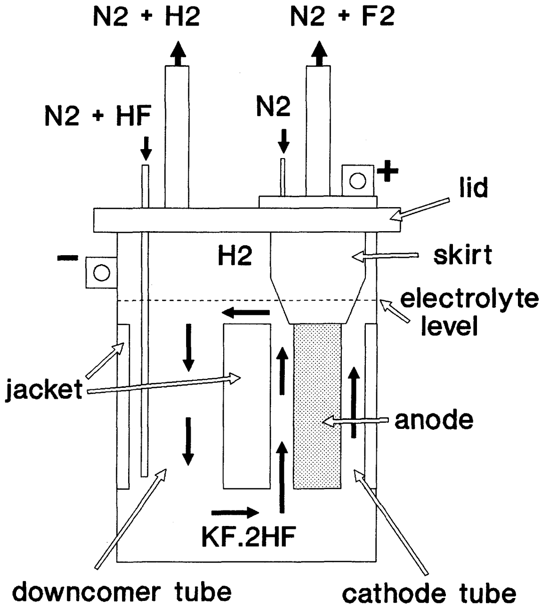

Figure 2 Section view of cell.

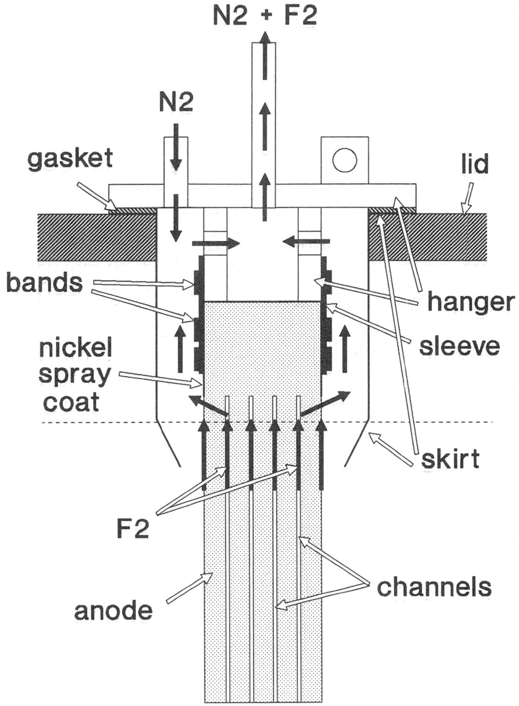

Figure 3. Anode and hanger details

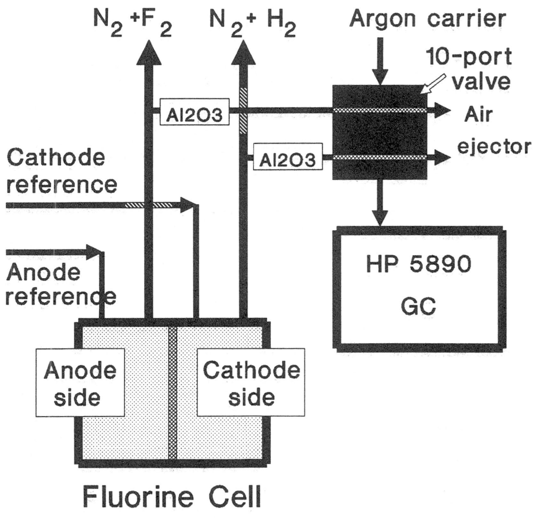

Figure 4. Block diagram of analytical layout and flows.

DOI: 10.1149/199413.0585PV

BASIC DATA AND ENGINEERING FOR ELECTROLYTIC RAFFINATION OF ALUMINUM SCRAP FROM CHLORIDE MELTS

Hartmut Wendt, Volker Schwarz
Institut für Chemische Technologie, TH Darmstadt
Petersenstraße 20, D-64287 Darmstadt

ABSTRACT

Primary aluminium production in Europe is steadily decreasing. Therefore the production of aluminium of primary quality from scrap by electrorefining may become an option of stratetic importance.
The precondition is: (i) substantial energy savings compared to electrowinning, (ii) easy recycling of alloying elements and electrolyte without ecological hazards. The use of molten chloride electrolytes instead of fluoride electrolytes seems to be the method of choice as emissions are low, work up in aqueous electrolyte is easy and alumina can be used for cells and diaphragms .

According to formal potentials of alloying elements (Mg,Mn,Zn,Si,Fe and Cu: -0.89 V, + 0.22 V, + 0.4 V, + 0.45 V,+ 0,54 V, + 1.09 V vs Al/$AlCl_3$) only mangenese could cause trouble in separating it from aluminium. Batch raffination experiments show, that all alloying metals, even Mn can be easily separated. Results with cells divided by alumina diaphragms demonstrate, that energy consumptions can be kept below 5 kWh/kg Al.

INTRODUCTION

According to recently published data on aluminium production in Germany, primary aluminium production in Europe declines steadily (1991: consumption 1.9 Mio tons, 1.295 Mio tons being primary aluminium, half of which is imported: 0.566 Mio tons). The recycling of aluminium scrap, amounting to 30% of the total consumption increases slowly but steadily. Because of this tendency the fundamentals of electrolytic scrap refining are worthwhile to elaborate as only electrolytic refining - in contrast to recycling by remelting - produces aluminium of primary quality and offers the possibility to the aluminium industry to increase the amount of recycled scrap in the total consumption of aluminium to any desired degree between 30 and 100%. Electrorefining of aluminium with solid metal in low temperature melts seems to be technically not feasible although it had been demonstated by Pemsler and Dempson /1/, to work on laboratory scale. It is however, severely hampered by the formation of dendritic deposits.

Electrorefining of aluminium producing metal of 99.99% quality and better is performed today with liquid aluminium cathodes and anodes according to the three layer process of Hoope`s, which using a fluoride electrolyte has too high energy consumptions of between 10 to 15kWh per kg.

T.A. Sullivan and coworkers /2/ have recently shown that highly contaminated aluminium alloys containing only 70% Al can be electrolytically refined enhancing the contaminant concentration in the anode by a factor of 3 obtaining purities of the refined aluminium of 99.6%, matching that of primary aluminium quality. They used mixed fluoride/chloride melts and a chloride melt in a divided cell with a diaphragm and a three layer cell according to Hoope`s principles. But in both cells energy consumption was too high.

Aims of and means for electrolytic refining of aluminium scrap

It is obvious that energy consumption below 5kWh per kg for aluminium scrap refining at current densities of more than 0.1Acm^{-2}, which would be a necessity for scrap electrorefining, can only be achieved, if the cell would have an interelectrodic gap of a few millimeters and cell resistances of less than 0,5 Ω cm^2. Conductivities of the usual melts (alkali fluorides and chlorides) at 700°C (i.e. 40° above the melting point of aluminium) are between 0,2 and 0,6 Ω^{-1}cm^{-1}.

Cell resistances as low may therefore only be obtained by using an electrolyte-flooded diaphragm seperating the two electrodes of molten metal. Such diaphragm also has to allow easy exchange of the electrolyte which fills the interelectric gap, for instance by gravity flow. Fray`s proposal /3/ of the so-called recessed channel cell using as diaphragm a fabric of oxide ceramic fibres or a porous sintered material offers a second possibility of narrow interelectrodic gaps with easy exchange of electrolyte and molten metal. If both liquid electrode metals touch the diaphragm, electronically conducting diaphragms are excluded. Alumina is an insulating diaphragm material most consistent with the aim to exclude any contamination of the refined metal by construction materials. Chloride melts are ideal in this respect since the solubility of Al_2O_3 in chloride melts is almost nil. Chloride melts are also easier to work up and to recycle than fluoride melts by dissolving the electrolyte in water and recovering it again from aqueous solutions.

It is the aim of this paper to report on (i) the determination of the voltage series of the alloying metals of aluminium in chloride melts and (ii) to investigate electrolytic raffination of model alloys in divided laboratory scale cells equipped with sintered porous alumina diaphragms.

EXPERIMENTAL

All experiments reported in this paper refer to a temperature of 700°C although raffination experiments had also been performed at temperatures below the melting point of aluminium (660°C) which showed, that electrodissolving and depositing solid instead of liquid aluminium is not a reasonable option for electroraffination.
Three different types of experiments had been performed:

(i) cyclic voltametry of deposition/dissolution of alloying elements from chloride melts at different electrode materials.
(ii) measurements of equilibrium potentials
(iii) electrolytic refining of exemplary alloys in divided cells from chloride melts in closed steel vessels containing an Al_2O_3-crucible with the chloride melt and protected in a quartz cylinder situated within the steel vessel.

All chemicals used were of p.A. (Merck) grade. The investigations were performed in a semitransparent gold-covered tubular quartz furnace in which a stainless steel tube was inserted containing the electrolyte cell. The stainless steel tube whose upper part was water-cooled was closed by a graphite lid. Cylindrical Al_2O_3-crucibles, forming the electrolysis cells proper, were of 4cm diameter and 15cm height with a wall thickness of 2mm.

An aluminium reference electrode was constructed from an alumina-vessel equipped with a Luggin capillary also of Al_2O_3 which contained a pool of liquid aluminium. A tungsten-wire served for connecting the Al-pool to the lead which was connected to the voltmeter. As the diameter of the Luggin "capillary" was much wider than the usual capillary tips (2 mm) its tip could not be fixed at a distance of closer than 2 mm in front of the electrode. Therefore the IR-potential drop could not be neglected. Current voltage curves in the cyclic voltametric measurements had been corrected by the interrupture technique using an interrupture unit UP2 of Meinsberg. All experiments were performed at 700°C - this temperature being the anticipated temperature of a scrap electrorefining process.
Metal electrodes made of liquid Mg, Mn, liquid Zn, Fe and Cu which had been used to measure equilibrium potential were all at least 99% pure. Graphite rods at which cyclic voltametric measurements were performed were of PT-2114 quality, supplied by Deutsche Carbone company. The alumina diaphragms were of quality AL25, from Fa. Friedrichsfeld, Mannheim; Al_2O_3 contents: 99.7%, porosity 25%, pore radius: between 10 and 20µm, thickness 2.5 and 5mm. The $AlCl_3$ of pA grade (Merck) contained more than 5000 atppM $FeCl_3$ which could not be removed be resublimation. Therefore $AlCl_3$ always introduced seizeable amounts of iron into the electrorefining experiment.

Analysis Thanks to Vereinigte Aluminiumwerke, VAW Bonn, immpurities in the purified metal had been determined be spark spectroscopy.

RESULTS

Definition of model alloys

Table 2, first row, collects a typical composition of a cast aluminium alloy (a 1:1 mixture of GB-AlSi9Cu3 and AlMg2.3,) which had been used in this investigation for electroraffination experiments. The wrought alloy was standard alloy AlMg4.5 containing magnesium in 4.5 wt% and all other metals in less than 1 wt% .

Definition of the electrolyte

The ALCOA-electrolyte seems to be a suitable choice containing a mixture of LiCl/NaCl in a molar ratio of 4:5 and $AlCl_3$ in variable concentrations ranging from 5 to 15 mole %. At 700°C this mixed electrolyte exhibits $AlCl_3$ pressures from 37 to 55 Torr only and relatively high conductivities of 3.53 (5 mole %) and 2.81 $\Omega^{-1}cm^{-1}$ (15 mole %)/4/,/5/. For raffination experiments 15 mole % $AlCl_3$ were used in the electrolyte in order to avoid safely mass transport limitations at the cathode. Melts containing 15 mole % of $AlCl_3$ refer to a volume related concentrations of approximately 3.9 moles aluminium cloride per liter.

Voltametric investigations

Current voltage curves of aluminium The IR-corrected current voltage curve of cathodic aluminium deposition on an aluminium pool under the condition of free thermal convection measured in a melt containing 10 mole % of $AlCl_3$ obeys the equation calculated for mass transport limited current densities and compares well with the theoretical curve according to equ. (1):

$$i = i_l\{1-\exp(-\nu_e F/RT)\} \qquad (1)$$

The deviations between observed and predicted potentials do not surmount 15mV and might be due to incorrect IR-compensation. The cathodic curve and the respective curve for anodic aluminium dissolution confirm reports in the literature that cathodic Al-deposition and dissolution in chloride melts is a fast, kinetically unhindered process /6/.

Cyclic voltametry of alloying metals Gold, tungsten and grafite had been used as electrodes for cyclic voltametry. The aim was to find for each metal a substrate which did not influence the respective voltamogram by alloy formation. Fig.1 depicts the voltamograms of four different metals. Table 1 collects the equilibrium potentials (geometric mean of anodic and cathodic peak potentials) together with the respective concentrations of the salt and the predicted concentration dependence dE/dlgc of respective metals. Silicon is an exception because its concentration due to the volatility of $SiCl_4$ is not well defined. For four-valent silicon, however, the equilibrium potential is least sensible to concentration changes as it changes with concentration by less than 50mV per decade at 700°C, so that the inaccuracy in determining the formal potential is comparable to that of the two-valent metals.

Measurement of the equilibrium potentials of the alloying elements

Rod or pool electrodes of the alloying elements Mg, Mn, Zn, Fe and Cu had been used to measure their equilibrium potentials in NaCl/LiCl melts containing the respective metal chlorides in six different concentrations ranging from $2*10^{-5}$ to $5*10^{-4}$ moles cm^{-3}. Fig. 2 depicts the least square linear log concentration/potential correlation and compares them with the theoretical slope. Repeated readings are reproducible within ± 30 mV. These experiments allow to obtain the formal potentials of the respective metal/metal chloride couple. The formal potential - different from the mormal convention in melts which refers to the pure metal salt - refers in our case to a volumetric concentration of the dissolved salt of 10^{-3} moles/l or 10^{-6} moles cm^{-3} resp. Table 1 collects the formal potentials measured vs. an aluminium electrode in LiCl/NaCl melts containing 10^{-3} mole cm^{-3} of $AlCl_3$.

ELECTRORAFFINATION EXPERIMENTS

The electroraffination experiments had two different aims:

(i) Finding a cell design, with sufficiently low cell resistances

(ii) Investigating the effective purification effect achieved in long term raffination processes in which nine tenth of the metal had been dissolved anodically and recovered cathodically.

Different cell designs Three different cell designs had been compared:

(1) Divided cell with Al_2O_3 diaphragm, soaked with electrolyte,

(2) Three-partitioned cell containing a bipolar aluminium electrode between the anode and the cathode - all three electrodes separated from each other by electrolyte flooded alumina diaphragms

(3) Cell with EDE-(electrode/diaphragm/electrode)geometry established by backing the brittle electrolyte-flooded diaphragm from both sides by porous, metal flooded carbon plates.

The different cells had the specific reistances: 1.8 Ωcm^2, 3.6 Ωcm^2 and 3.6 Ωcm^2. Obviously the simple, divided cell is at an advantage and had therefore been used for all further experiments. Cells of this design are operated at current densities of 0.5 Acm^{-2} with cell voltages around 1 V. The anode contained initially up to 80g alloy and its oxidation consumed sufficient current to oxidize 90% of the initially present non noble metals aluminium and mangnesium. The anode metal dissolved and cathode metal deposisited was determined gravimetrically and the metal contents of the anode and cathode were analyzed after termination of the experiment.

Table 2 shows the results of three typical experiments with cast alloy which allow to gain a judgement of the precision and reprocubility of such laboratory scale raffinations. The raffination yields from 89% aluminium cast alloy a purified metal of 99.88% - a quality better than primary aluminiums, (99.7% purity). The results with wrought alloy are similar. During anodic dissolution of the alloy the dissolution of magnesium which is less noble than aluminium proceeds almost to completion and $MgCl_2$ accumulates in the electrolyte without deposition in the cathode metal.

Discussion

A critical survey of the data of Table 2 reveals that the purification factor, c/c_0, for iron is particularly poor. Iron, next to copper is the noblest metal and should have a depletion factor comparable at least to that of silicon. The reason is obvious: Iron is imported by the electrolyte because the aluminium chloride used contains more than 5000 at.ppM iron and as a contaminant of the construction maerials.

It is unexpected that manganese, being in its formal potential closest to that of the aluminium electrode has a remarkably high depletion factor of 1/33. This is certainly caused by strong reduction of the activity of this metal in aluminium, as the binary phase diagram of Mn/Al reveals that several aluminium rich compounds are formed as e.g. $MnAl_6$ and $MnAl_4$. Magnesium as the least noble metal, as expected, is reliably separated by the raffination process and is accumulating in the electrolyte, as it is shown that the anode contains almost no magnesium after the experiment.

Assuming, that the depletion factor of iron would be at least that of silicon, one would obtain a cathode quality of 99.97 - a value which would promise, that it could be possible to obtain 99.99% or even higher grade aluminium by primary aluminium raffiniation in chloride melts. Initial experiments with the aim to obtain high purity aluminium from primary aluminium showed, however, that the depletion factor for all metals decreases at low metal concentrations, yielding only 99.94% aluminium. Therefore further efforts would have to be expended to achieve this target.

ACKNOWLEDGEMENT

The authors are indebted to the Commission of the European Communities for financialsupport

REFERENCES

/1/ J.P.Pemsler,M.Dempsey, Electrorefining of aluminium, Gouv. Rep. Announce,, NSF/CPE- 81012, B.P. 81 - 243693, 1981

/2/ T.A. Sullivan, R.L. De Beauchamp, Recovery of aluminium, base and precious metal from electronic scrap, Bu. Mines, RI - 7617, BP - 2090, 1971.

/3/ D.J.Fray, Brit.Pat. Appl. 130821, 1986.

/4/ H.Linga, H.Øye ,K.Motzfeld, Ber.Bunsenges.physik. Chemie,85,1132(1981)

/5/ B.Knapstadt, Ber. Bunsenges. physik.Chemie, 75 1132 (1981)

/6/ R.Odegard, A.Bjorgum, A. Sterten, J.Thonstad, R.Thunold, Electrochim. Acta, 27 1595 (1982)

Table 1

Equilibrium and formal potentials (convention: c($MeCl_n$)= 1.10^{-3} moles cm^{-3}) of different metal/metal chloride couples measured in LiCl/NaCl (35/45 mole/mole) melts at 700^{o}C.(Reference Al/$AlCl_3$,10^{-3} moles cm^{-3}).

metal/metal chloride	equil.pot. E/mV*	conc. c/moles cm^{-3}	electrode material	formal pot. E/mV	dE/lgc mV/dec
Mg/$MgCl_2$	-950±30	$1.03*10^{-4}$	W	-880±20	97
Mn/$MnCl_2$	+180±20	$4.06*10^{-5}$	Au	+220±20	97
Zn/$ZnCl_2$	+350±30	$2.44*10^{-5}$	C	+400±20	97
Si/K_2SiF_6**	+450±50	10^{-5}to10^{-4}**	Au	+450±30	48
Fe/$FeCl_3$	+450±50	$2.86*10^{-5}$	Au	+540±20	65
Cu/$CuCl_2$	+850±30	$1.11*10^{-5}$	C	1090±20	97

* All potentials vs. $AlCl_{3v}10^{-3}$ moles cm^{-3} in LiCl/NaCl melt

** K_2SiF_6 decomposes in the chloride melt forming mixed $SiF_xCl_{(1-x)}$-complexes followed by release of $SiCl_4$

Table 2

Comparison of anode and cathode composition (weight %),raffination of wrought alloy.

	anode (initially)	cathode 1	cathode 2	cathode 3	average	c/c_0
Si	4.7	0.00361	0.0315	0.0374	0.025	1/140
Fe	0.3	0.0908	0.1032	0.0800	0.091	1/3.3
Cu	4.1	0.0002	0.0013	0.0017	0.001	1/4100
Mn	0.4	0.0061	0.0198	0.0098	0.012	1/33
Mg	0.9	0.0008	0.0010	0.0010	0.0010	1/900
Cr	0.01	0.0007	0.0006	0.0007	0.0007	1/14
Zn	0.6	0.0061	0..198	0.0089	0.012	1/50

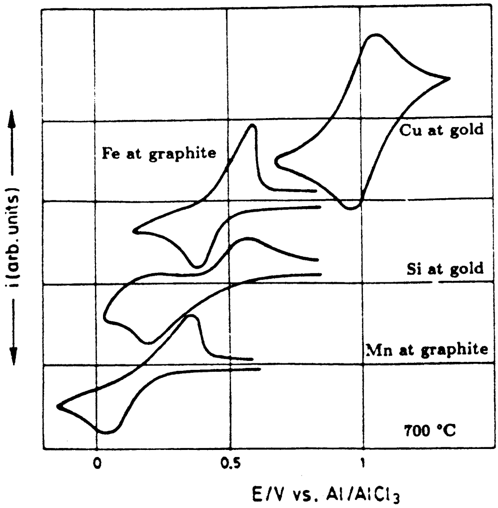

Fig.1 Cyclic voltamograms of deposition/dissolution of four alloying elements from LiCl/NaCl-melts.

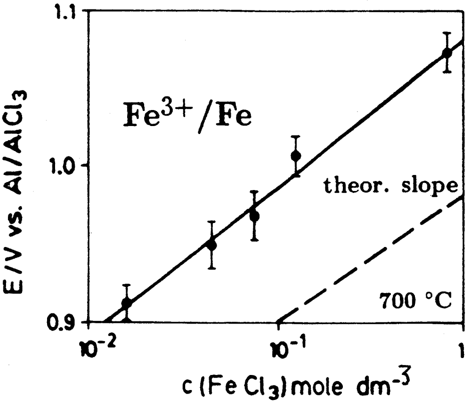

Fig.2 Least square evaluation of the concentration dependence of the equilibrium potential of Fe/Fe^{3+}

DOI: 10.1149/199413.0593PV

PHYSICAL CHEMISTRY IN MOLTEN SALT ELECTROLYSIS OF ALUMINIUM

Qiu Zhuxian, Wei Qingbin, Yu Yaxin, and Fan Liman

Northeastern University, Shenyang 110006, China

ABSTRACT

This paper deals with studies on the wettability of carbon anode and carbon cathode by molten salts, the reason of initiation of anode effect and the metal fog formation in molten electrolyte. Some new investigations of lithium salt–containing anode in relation to critical current density (CCD) are also reported.

WETTABILITY OF CARBON ANODE AND CARBON CATHODE BY MOLTEN ELECTROLYTE

The wettability of carbon electrodes by molten salts is quite different when the electrodes are polarized than when they are not, because of the variation of the surface state of the electrodes, as well as the ionic concentration of the liquid layer adjacent to the electrodes during the electrolysis process of cryolite–alumina melts. The laboratory microelectrolysis cell is shown in Fig.1.

When the carbon plate was given a cathodic polarization, the molten drop gradually spread out on the carbon plate after several minutes of electrolysis, and tended to separate from the anode. This caused an interruption in electrolysis. However, the spread molten drops often collected together automatically and touched the anode again, then electrolysis resumed.

As the carbon plate was anodically polarized, good wettability of the carbon rod (now it was cathode) by the molten drop was observed. The wettability of the carbon anode by the melt was good at the beginning of electrolysis, but it became poor later, and the electrolyte even coalesced into a globe. At this moment, the current decreased suddenly and the voltage increased and an anode effect occurred (Fig.2). Sometimes, most of the melt adhered to the cathode (carbon rod) and separated from the carbon plate anode. These phenomena were consistent with those mentioned above.

When the polarities of the electrodes were changed, the back EMF of the electrolysis cell changed significantly. Hence it is possible to decrease the overvoltage during the normal electrolysis process by periodically reversing the polarities of electrodes.

When a platinum wire loop was used instead of carbon as an anode or a cathode, similar phenomena were observed. The wettability of platinum by the molten cryolite–alumina electrolyte was originally very good, but when it was used as anode and a carbon plate as cathode, after a D. C. was applied, the molten electrolyte would be repulsed by the anode and separated from it. After

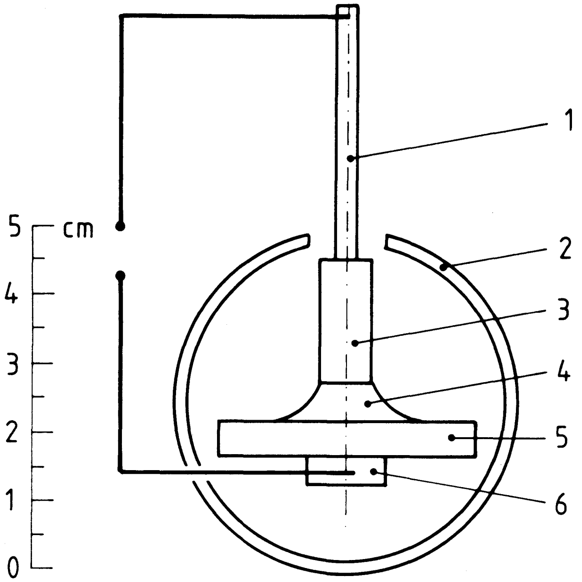

Fig.1 Schematic diagram of the microelectrolysis cell; 1—Ni–Cr wire conductor, 2—stainless steel tube (45 mm dia., L.600 mm), 3—carbon rod (8 mm dia.), 4—molten electrolyte, 5—carbon plate($\gamma = 5$ mm), 6—steel support.

a while the electrolyte would touch the anode again. Thus appeared a cyclic process of electrolysis–repulsion–electrolysis. When the platinum wire loop was used as cathode and the carbon plate as anode, the electrolyte would be attracted by the cathode, and an anode effect was observed on the anode carbon plate. The Pt loop would be vibrated vigorously.

So both carbon and platinum electrodes showed the same behaviour of repulsing the electrolyte when anodically polarized, this phenomenon is called ″Anodic Repulsion″, and of attracting the electrolyte when cathodically polarized–this phenomenon is called ″Cathodic Attraction″.

ANODE EFFECT

Some characteristics of the anode effect in aluminium electrolysis may be described briefly as follows:

(1) When an anode effect occurs in one cell, the cell voltage is with high frequency (about 10000 to 20000 Hz, Fig.3). This corresponds to the appearance of electric sparking on the carbon anode. The carbon anode and aluminium bus–bar vibrate.

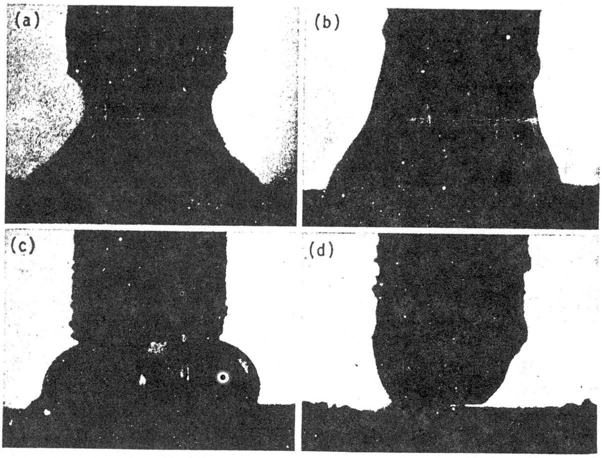

Fig.2 Aluminium electrolysis in cryolite–alumina melts. (a) when the carbon electrode was served as anode and the carbon plate as cathode, (b) when the carbon electrode was served as cathode and the carbon plate as anode, (c) and (d) when anode effect occurred.

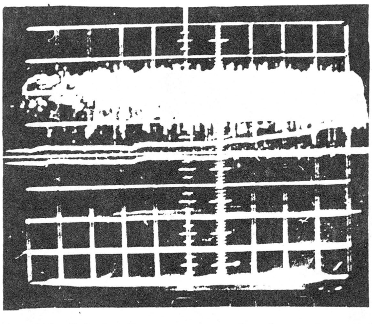

Fig.3 Cell voltage with high frequency during the anode effect in industrial aluminium electrolysis cell.

(2) During the anode effect, on the part of anode surface submerged in molten salt there appears electric sparking. The electric sparks are twinkling, and they appear first at some places, then at other places.

(3) The anode gas composition changes suddenly when an anode effect occurs. During normal electrolysis the anode gas usually consists of 75%

CO_2 and 25% CO. When an anode effect occurs, the gas composition may be changed to CO_2 25%, CO 50%, CF_4 22.5 and C_2F_6 2.5%. This fact implies that there happens a change in anodic reaction from the discharge of oxygen ions to codischarge of oxygen and fluorine ions.

(4) During the anode effect, there is a jet action from the anode bottom surface when the cell voltage is over 20 V. From jet actions it was observed that there are minute gas bubbles injecting from the carbon anode into the molten bath, causing a violent stirring in the interpolar space. The jet action from the carbon anode was found in molten $PbCl_2$ as well as in molten cryolite–alumina salts. The reason for the jet action may be due to an expansion of anode gases at high temperature during anode effect. However, this jet action is harmful to current efficiency because the stirring action of these gas bubbles would cause much metal on the cathode to be reoxidized (see Fig.4).

It was found in a see-through cell that during normal electrolysis in cryolite–alumina melts the anode gas bubbles could leave the carbon anode freely, but when the electric current density was raised to the critical value, the gas bubbles on the anode would be tightly pulled up and stuck on the whole anode surface to form a thin continuous film, at that time an anode effect occurred. The anode gases were already ionized and attracted electrostatically by the carbon anode. When the current was cut off, the gas film contracted all at once to form a single bubble which stayed on the undersurface of the anode.

From the above facts we can infer that the direct reason of anode effect may be related to the electrostatic attraction of ionized gas bubbles by the anode. This is due to the newly formed gases, such as CF_4, C_2F_6 and CO, being

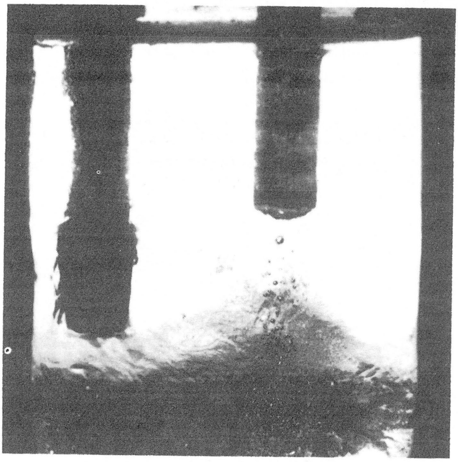

Fig.4 Jet action from carbon anode during the anode effect in cryolite–alumina melts.

more easily polarized, they can be attracted electrostatically by the anode at high potential. This gas film sticks firmly to the anode surface and penetrates into the pores and fissures of the carbon anode.

The above viewpoint may be confirmed by the appearance of electric sparks on the anode during the anode effect. On industrial cell, the carbon anode is very big. It may be 12 m^2 in one piece. During the anode effect, the gas film is not actually continuous, which may be in shape of a network. At the boundaries of gas bubbles there are some electrolyte. The electric sparks first appear at some localities, then they move to other places. So the electric sparks are twinkling. The occurrence of electric sparks means ionization of gas bubbles. When the electric charges of gas bubbles are neutralized in some places, there the electric sparks will disappear.

In industrial aluminium electrolysis cells, for quenching the anode effect we usually make the anode and cathode short-circuited for a short time, i.e., by splashing the negatively charged liquid aluminium in the cell to the anode, so that the electric charges on the gas bubbles can be neutralized. This is a support for the electrostatic attraction theory.

Therefore, the primary reason for the initiation of anode effect may be the anodic repulsion by gases exerted to the molten electrolyte, and the direct reason may be due to an electrostatic attraction of gases by the anode at high anodic potential.

INFLUENCE OF LITHIUM SALT ADDITION TO CARBON ANODE ON ANODE EFFECT

The result of lithium salt addition to carbon anode on anode effect was investigated by critical current density measurements.

In the experiments spectroscopic graphite electrode of ϕ 6 mm was used as anode. The electrode was impregnated in molten LiF at 900℃ for 2 hours. The results of CCD$\sim$ Al_2O_3 concentration measurements are plotted in Fig.5.

It was seen that the CCD values increased with Al_2O_3-content in the melts. It was very interesting to say that the lithium salt-containing anodes are usually with higher CCD values than those without. The reason is that the lithium salt-containing carbon anode may be much better wetted by the molten bath, and the gas bubbles on the anode may be expelled more easily by the molten electrolyte. So this kind of carbon anode is very useful in preventing the frequent occurrence of anode effect in aluminium electrolysis cells, and it can decrease the cell voltage by decreasing the ohmic overvoltage of gas film on the carbon anode.

For preparing the lithium salt-containing carbon anode there are two methods: (1) by impregnation in molten LiF, (2) by adding Li_2Co_3 to the carbon paste and forming the anode. The second method has been used in Söderberg cells for over 3 years with good operational results.

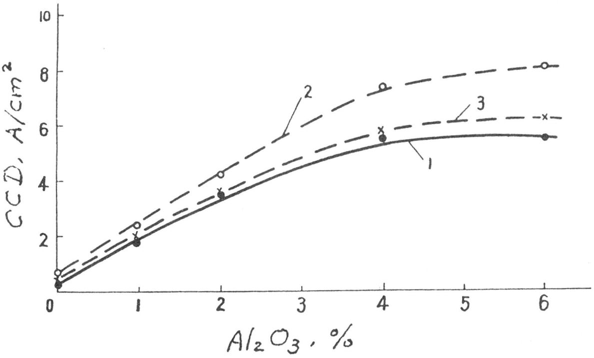

Fig.5 CCD~ Al_2O_3 concentration curve. 1—without LiF impregnation, 2—with LiF impregnation, 3—with cryolite impregnation.

FORMATION OF METAL FOG IN MOLTEN SALTS

Visual observations of several molten salt electrolysis processes were made in a two-compartment see through quartz cell. The electrolysis of aluminium, magnesium, lead, zinc, sodium and potassium were studied. The colour of the melt in the anode compartment was pale yellow for fluoride-chloride melts and red for chloride melts, caused by the presence of dispersed anode gases during electrolysis. In the cathode compartment, streamer of metal fog were formed. The colours of the metal fog were purple for aluminium, grey for magnesium, lead and zinc, blue for sodium and green for potassium (Table 1).

The metal fog tended to sink to the bottom of the cell, which indicated that it had a higher density than that of the melt (Fig.6). The metal fog also penetrated into the anode compartment, probably due to convection and diffusion in the melt. The most probable explanation of the nature of the metal fog

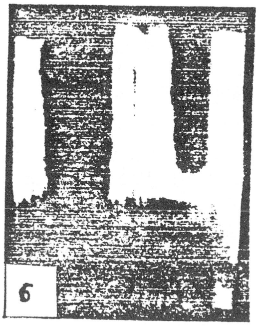

Fig.6 Aluminium electrolysis in a two-compartment, see-through cell. Left, cathode; right, anode. (a) At the beginning of the electrolysis (4.0 A). (b) Metal fog has reached into the anode compartment. The upper surface of the metal fog was located about 5 mm below the bottom surface of the anode.

Table 1. Colours of molten salts before and after electrolysis in a two–compartment, see–through cell

Metal	Molten salt composition	Bath temperature (℃)	Colours		
			Before electrolysis —both compartments	After electrolysis	
				Anode compartment	Cathode compartment
Al	$NaF–AlF_3–Al_2O_3–NaCl$	800	White transparent	Pale yellow	Purple
Mg	$NaCl–KCl–MgCl_2$	800	White transparent	Red	Grey
Pb	$NaCl–KCl–PbCl_2$	800	White transparent	Red	Grey
Zn	$NaCl–KCl–ZnCl_2$	800	White transparent	Red	Grey
Na	NaCl	800	White transparent	Red	Blue
K	KCl	800	White transparent	Red	Green

is that it consisted of dispersed metal particles. This chemically unstable phase dissolved easily in the melt and was oxidized quickly by the anode gases.

Key words: wettability, anode effect, Li-salt containing carbon electrode.

REFERENCES

1. Qiu Zhuxian, Wei Qingbin and Yuo Kwantsung, ALUMINIUM, Vol.59 (1983) 9, pp.670/673 and 10, pp.753/756.
2. Qiu Zhuxian, Chinese Journal of Metal Science and Technology, No.1, pp.15-19 (1992).
3. Qiu Zhuxian, Fan Liman, K. Grjotheim, H. Kvande, J. Applied Electrochemistry, No.7, pp.707-714 (1987).

Acknowledgement: Thanks for the financial support from the Natural Scientific Funds of the Government.

DOI: 10.1149/199413.0601PV

EFFECT OF METAL IMPURITIES ON ANODIC REACTION OF NICKEL ELECTRODE IN A MOLTEN NH_4F-HF SYSTEM

Akimasa Tasaka*, Mitsuhiro Negami, Kishio Nagasaki,
Toshiharu Ozaki and Toshinori Osada

Department of Applied Chemistry, Doshisha University
Imadegawa, Karasuma, Kamigyo-ku, Kyoto 602, Japan

ABSTRACT

The effects of metal impurities added and dissolved from a cell on both the anodic dissolution of a nickel electrode and the current efficiencies of NF_3-formation and total anode gas were studied in molten $NH_4F \cdot 2HF$ at 120°C by galvanostatic electrolysis. The current loss caused by anodic dissolution of nickel in a copper cell (3.5%) was larger than those in a steel cell (1.5%) and a nickel cell (2.5%). Mixed gas composed of N_2, O_2, N_2O, NF_3, N_2F_4 and N_2F_2 was liberated at the nickel anode during electrolysis at 25 mA/cm^2. Copper ion almost unaffected the current efficiencies of NF_3-formation (60%) and total anode gas (90%), while iron and nickel ions decreased them. The existence of water in the melt lowered the anodic dissolution of nickel electrode. The addition of complexes such as NH_4NiF_3 and $(NH_4)_3FeF_6$ in the melt was also effective for prevention of the anodic dissolution of nickel, but it decreased the current efficiencies of NF_3-formation and total anode gas. Therefore, it is concluded that heavy metal impurities, especially Ni and Fe compounds, in the electrolyte are detrimental to the reaction proposed.

INTRODUCTION

Highly pure nitrogen trifluoride (NF_3, 99.99%) free from carbon tetrafluoride (CF_4) is mainly produced by electrolysis of molten $NH_4F \cdot 2HF$ with a nickel anode. However, the high consumption of nickel anode is troublesome for this process. The corrosion of nickel anode results in electrolytic current losses of 3∿5% at 120°C, resulting in deposition of nickel compounds such as NH_4NiF_3 and NiF_2 on the cell bottom and increases operating cost. Also, the corrosion rate is unaffected by the addition of LiF into the melt (1).

The objective of this work is to analyze the metal impurities in the melt dissolved from cells made of copper, steel and nickel and to investigate the effects of metal impurities on both the anodic dissolution of nickel and the current efficiencies of NF_3-formation and total anode gas.

EXPERIMENTAL

Three kinds of cylinder-type cells made of copper, steel and nickel (ca. 1.5 dm^3 volume) were provided for production of nitrogen trifluoride. Another H-type cell made of PTFE (ca. 1 dm^3 volume) was also provided for investigation of the effect of the additives such as NH_4NiF_3 and $(NH_4)_3FeF_6$ on the current efficiencies of NF_3-formation and total anode gas. The cell configuration was described in the previous papers (2, 3) in detail. A nickel sheet anode having the effective area of 24 cm^2 was located at the center of each cell through the cell cover. The inside wall of each cell was used as the cathode in a metal cell and a large-area nickel cathode was also used in a PTFE cell. Anode gas was separated by a skirt made of each metal or PTFE from hydrogen evolved at a cathode. The cell bottom was insulated by PTFE sheet to avoid mixture of anode gas with hydrogen formed on the bottom due to the corrosion of metal during shutdown. The anode gas was treated with sodium fluoride (NaF) to eliminate HF. Its sample gas was fractionated by means of gas chromatography, and analyzed by infrared spectroscopy. The current efficiencies with respect to these constituents were evaluated from the results of gas analysis and overall flow rate of anode gas.

A Ni working electrode of 2 cm^2 effective area through a cover of box-type cell made of PTFE (ca. 2 dm^3 volume) was separated by a PTFE skirt from a large-area nickel cathode at which electrolytic hydrogen was evolved. Although the electrode potential was measured against the static potential of platinum wire or a new type of the reference electrode immersed in the same molten electrolyte, it was calibrated to the hydrogen potential in V vs. H_2. The cell positioned in a chamber filled with dry nitrogen to avoid moisture, and was warmed with a heater to 120°C.

Pre- electrolysis at low current densities with a carbon anode was conducted for many hours until NF_3 was generated and the electrolytic cell was stabilized before the polarization measurement and/or corrosion testing. A nickel working electrode washed with water was rinsed with methanol to remove trace water prior to weighing. The anode was weighed before and after electrolysis to evaluate weight loss and the corresponding current loss. In this case, the concentration of water in the electrolyte could not be determined, but it might be less than 0.02 wt% (about 21 mmol/dm^3) (4).

In experiments with the production cell, the electrolyte of $NH_4F\cdot 2HF$ was prepared with highly pure HF (99.99%) and $NH_4F\cdot HF$ (purity of 99.7%), but the cell was positioned in the atmosphere. Electrolysis was conducted at 120°C soon after the electrolyte was charged in the cell. However, in our experiments it was not possible to determine the concentration of water in the melt.

RESULTS AND DISCUSSION

Fig. 1 illustrates the change of the current efficiencies of NF_3-formation (curves 1, 2 and 3) and total anode gas (curves 4, 5 and 6) during electrolysis at 25 mA/cm^2 using copper, steel and nickel cells as a function of time, respectively. Using copper cell, the best current efficiencies of NF_3-formation (60%) and total anode gas (90%) were obtained. The current efficiency of hydrogen evolved at a cathode was 70 ∿ 75% in every cell. The current losses caused by the anodic dissolution of nickel in copper cell (3.5%) was larger than those in a steel cell (1.5%) and in a nickel cell (2.5%). The results obtained were given in Table 1 together with that in a steel cell having a nickel skirt.

Fig. 2 shows the change of the concentrations of nickel, iron and copper ions in each cell with a course of time. The concentration of nickel ion was the lowest in a copper cell (0.060 mol%), while it was the highest in a nickel cell (0.100 mol%). In a steel cell, iron ion of 0.010 mol% was also present in addition to the almost same concentration of nickel ion (0.065 mol%) as that in a copper cell. The concentration of copper ion was only 0.001 mol% and copper deposited was observed on the cell bottom in a copper cell.

The effect of metal complex salts such as NH_4NiF_3 and $(NH_4)_3FeF_6$ on the current efficiencies of NF_3-formation, total anode gas and cathode gas were investigated in a H-type PTFE cell without and with a diaphragm made of PTFE filter, and the results were given in Table 2 and 3, respectively. Electrolysis with a carbon anode was conducted in the same melt, as reference to the result obtained in electrolysis with a nickel anode. When a carbon (FE-5, Toyo Tanso Co. Ltd.) anode was used, the current efficiencies of both total anode gas and hydrogen evolution reached to about 96% and 97%, respectively. In the PTFE cell without the diaphragm, they were decreased by some 6% when the carbon anode was substituted by a nickel anode. The addition of metal complex salts decreased them by a further 16 to 26%. In contrast, in the PTFE cell with the diaphragm, they were not almost decreased by the addition of same complex salts and using a nickel anode, in comparison with those using a carbon anode. It is therefore concluded that heavy metal impurities, especially Ni and Fe compounds, in the electrolyte are harmful to the production of NF_3.

Fig. 3 shows the effect of the additives and impurities on the current loss caused by the anodic dissolution of nickel (Q_a/Q_t; %) during electrolysis at the current density of 25 mA/cm^2. Open circle (curve 1) and closed circle (curve 2) designate the Q_a/Q_t obtained in the electrolyte with and without the treatment of pre-electrolysis for the purpose of elimination of water in the fluoride melt, respectively. In Fig. 3, the nickel anode was prevented from corrosion when a small amount of nickel ions exists in the electrolyte. Also, the value of Q_a/Q_t obtained in a well dehydrated melt of $NH_4F \cdot 2HF$ was higher than that in molten fluoride containing water. Since it is reported that the solubility of α-NiF_2 is dependent upon the concentration of water in liquid HF (5), the behavior in molten $NH_4F \cdot 2HF$ may be caused by the same reason as that in liquid HF.

From these results, it is concluded that nickel ions such as Ni^{2+} and NiF_3^- exhibit both the positive and negative behaviors for the process proposed, considered with the effect as described in the current efficiencies for NF_3-formation, total anode gas and hydrogen evolution (see Tables 1, 2 and 3) and that the concentration of nickel ions in molten $NH_4F \cdot 2HF$ may be decided by the concentration of water in the electrolyte. Consequently, we estimate the optimum concentration of total nickel ions some 0.06 mol% to keep the current efficiency of NF_3-formation high.

REFERENCES

1) A. Tasaka, K. Miki, T. Ohashi, S. Yamaguchi, M. Kanemura, N. Iwanaga and H. Aritsuka; Proceedings of The International Symposium on Molten Salt Chemistry and Technology 1993, p. 306 (1993).
2) A. Tasaka, H. Itoh, T. Isogai, H. Aio and T. Tojo; J. Electrochem. Soc., 138, 421 (1991).
3) A. Tasaka, K. Mizuno, A. Kamata and K. Miki; J. Fluorine Chem., 57, 121 (1992).

4) T. Nakajima, T. Ogawa and N. Watanabe; J. Electrochem. Soc., 134, 8 (1987).

5) A. F. Clifford and A. C. Tulumello; J. Chem. Eng. Data, 8, 425 (1963).

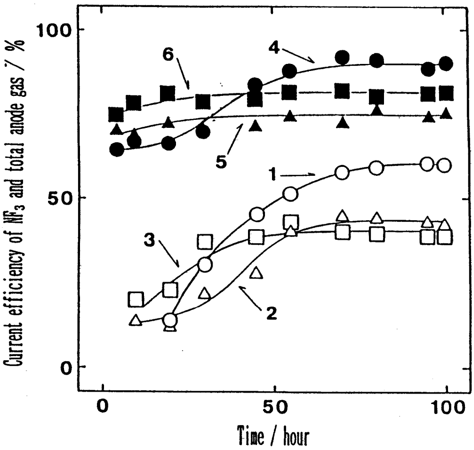

Fig. 1 The change of the current efficiencies of NF$_3$-formation and total anode gas during electrolysis at 25 mA/cm^2 using copper, steel and nickel cells as a function of time.

1(○) NF$_3$(in Copper cell) 4(●) total anode gas(in Copper cell)
2(△) NF$_3$(in Iron cell) 5(▲) total anode gas(in Iron cell)
3(□) NF$_3$(in Nickel cell) 6(■) total anode gas(in Nickel cell)

Table 1 Effects of cell material on both current loss caused by anodic dissolution of nickel (Q_a/Q_t) and current efficiencies of each product in anode gas, total anode gas and hydrogen evolution in electrolysis at 25 mA/cm^2 and 120°C for 70 hours in molten $NH_4F \cdot 2HF$.

Cell	Skirt	Current efficiency of anode, cathode gas products (%) NF_3	N_2	O_2	N_2F_4	N_2F_2	N_2O	Total	H_2	Q_a/Q_t (%)
Copper	Copper	58.1	20.8	2.33	3.58	0.19	7.33	92.3	67.7	3.53
Iron	Iron	44.9	13.6	5.47	2.11	0.55	5.96	72.5	73.6	1.46
Nickel	Nickel	40.4	28.5	2.70	4.35	0.15	5.65	82.4	77.5	2.65
Iron	Nickel	44.6	24.6	3.53	3.82	0.36	5.19	82.1	82.9	2.02

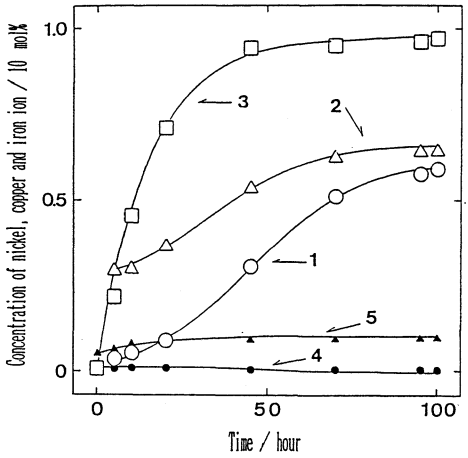

Fig. 2 The change of the concentrations of nickel, iron and copper ions in each cell with a course of time.

1(○) : Nickel ion(copper cell) 4(●) : Copper ion(copper cell)
2(△) : Nickel ion(iron cell) 5(▲) : Iron ion(iron cell)
3(□) : Nickel ion(nickel cell)

Table 2 Effects of NH_4NiF_3 and $(NH_4)_3FeF_6$ added in molten $NH_4F \cdot 2HF$ on both current loss caused by anodic sollution of nickel (Q_a/Q_t) and current efficiencies of each product in anode gas, total anode gas and hydrogen evolution in electrolysis at 25 mA/cm^2 and 120°C in a PTFE cell without a diaphragm.

Anode material	Additive (mol%)	Current efficiencies of anode and cathode gas							(%)	Q_a/Q_t (%)
		NF_3	N_2	O_2	N_2F_4	N_2F_2	N_2O	Total	H_2	
Carbon	–	35.3	52.0	5.00	0.47	1.30	1.58	95.7	97.1	–
Nickel	–	31.4	45.2	4.13	0.59	2.69	5.83	89.8	90.9	3.24
Nickel	NH_4NiF_3 0.076	27.7	40.7	4.28	0.95	1.67	4.40	79.6	80.1	2.76
Nickel	$(NH_4)_3FeF_6$ 0.033	24.2	38.1	3.81	0.73	1.79	1.48	70.1	74.0	2.60

Table 3 Effects of NH_4NiF_3 and $(NH_4)_3FeF_6$ added in molten $NH_4F \cdot 2HF$ on both current loss caused by anodic dissolution of nickel (Q_a/Q_t) and current efficiencies of each product in anode gas, total anode gas and hydrogen evolution in electrolysis at 25 mA/cm^2 and 120°C in a PTFE cell with the diaphragm made of PTFE filter.

Anode material	Additive (mol%)	Current efficiencies of anode and cathode gas							(%)	Q_a/Q_t (%)
		NF_3	N_2	O_2	N_2F_4	N_2F_2	N_2O	Total	H_2	
Nickel	NH_4NiF_3 0.076	31.2	54.1	3.58	1.06	1.91	1.41	93.3	94.9	2.34
Nickel	$(NH_4)_3FeF_6$ 0.033	29.3	53.4	4.76	0.76	1.92	2.24	92.4	94.5	2.11

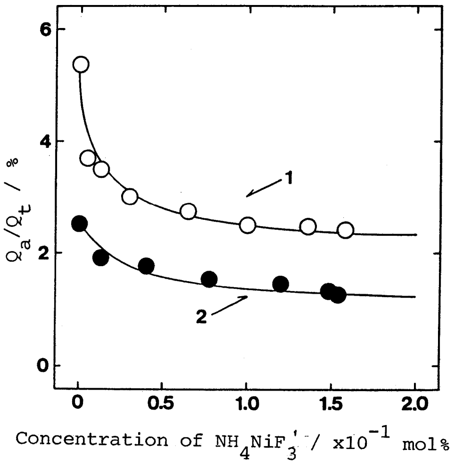

Fig. 3 Relationship between current loss caused by anodic dissolution of nickel (Q_a/Q_t) and the concentration of NH_4NiF_3.

1 (o) ; In a well dehydrated melt of $NH_4F \cdot 2HF$,

2 (●) ; In molten $NH_4F \cdot 2HF$ containing water.

DOI: 10.1149/199413.0609PV

CATALYTIC ACTIVITY OF Na_2CO_3-K_2CO_3 EUTECTIC SUPPORTED BY $LiAlO_2$ TOWARDS THE OXIDATIVE DIMERIZATION OF METHANE

V. TASHJIAN, M. CASSIR* and J. DEVYNCK

Ecole Nationale Supérieure de Chimie de Paris,
Laboratoire d'Electrochimie (URA 216 du CNRS)
11, rue Pierre et Marie Curie,
75231 PARIS CEDEX 05 (FRANCE)

ABSTRACT

Catalytic properties of Na_2CO_3-K_2CO_3 molten eutectic supported by lithium aluminate, towards the selective transformation of methane into C_2 hydrocarbons are investigated at 800-850°C. C_2 yields of 12% and methane conversion of 21.5% are reached at 850°C. A correlation is established between catalytic performance and existence of peroxide species, which are stabilized in oxobasic media. Lithium aluminate support greatly enhances gas-liquid contact and, therefore, catalytic activity of the molten carbonate.

INTRODUCTION

Oxidative dimerization of methane into ethane and ethene has recently been studied in alkali molten carbonate eutectics at high temperature [1-3]. Reduced oxygen species, stabilized in such media in oxobasic conditions are involved in the catalytic process. Their stability has been systematically investigated in different carbonate melts [4]. Potential-oxoacidity diagram of molten Na_2CO_3-K_2CO_3 eutectic presented in Fig. 1 shows that, in the usual catalytic conditions, both peroxide and superoxide species can be stabilized in this melt. Oxygen species are stabilized in oxoacidic media (low carbon dioxide partial pressures), superoxide in intermediate oxoacidity media and peroxide species in oxobasic media. These results were confirmed by electrochemical experiments. Voltammograms in Fig. 2 were recorded at two oxoacidity levels: 2a- intermediate oxoacidity and 2b- oxobasic melt obtained after extended decarbonation. In Fig. 2a, no significant currents were observed. In Fig. 2b, two reduction currents appeared corresponding to superoxide and peroxide species and an oxidation current corresponding to oxide ions. This confirms that reduced oxygen species are mainly stabilized in oxobasic media.

Nevertheless, in bulk molten carbonate, such as Na-K, low values of methane and oxygen conversion were obtained, indicating a bad gas-liquid contact. Improvement of the catalytic behavior of these melts can be attempted by the use of a chemically stable solid in order to immobilize the molten phase, i. e. $LiAlO_2$ matrix, generally used in the electrolytic part of molten carbonate fuel cell MCFC [5]. Interesting results have been reached in supported Li-Na at different temperatures [3]. In view of the similarities of this melt with Na-K eutectic and the greater stability of the last one, it is worthy of analysing its catalytic properties.

The purpose of this work was to study Na_2CO_3-K_2CO_3 supported by $LiAlO_2$ at different oxoacidity levels and temperature and compare it with that of Na-K eutectic in solution. Correlation of the catalytic activity with the stability of peroxide species was established.

EXPERIMENTAL

Immobilization of Na_2CO_3-K_2CO_3 within lithium aluminate was carried out at 750°C under a 80% CO_2-20% H_2O atmosphere. The morphology of samples before and after catalytic reaction was studied by scanning electron microscopy (SEM) and Xray probe microanalysis, as shown in Fig. 3. Carbonate melt form a thin layer of about 200 nm at the surface of $LiAlO_2$ particles. Before catalytic reaction the sample has a regular structure formed by particles of 0.1 μm. After extended use, a microstructural change occurs: particles coalesce into aggregates from 0.5 to 5 μm.

Catalytic reaction was carried out in a vertical tubular reactor described elsewhere [3]. The reactant gas was a mixture of methane and oxygen with helium as diluent. Gases after the catalytic transformation were analysed in a gas chromatograph (Delsi Instrument DI 700) equipped with TCD and FID detectors. Separation was realized in a Carbosphere column (3m, 80-100 mesh).

CATALYTIC PERFORMANCE

The oxidative transformation of methane by molecular oxygen was realized at 800 and 850°C. Table 1 shows the evolution of the catalytic performance at 850°C with the oxoacidic properties of the melt. The melt becomes more oxoacidic when a known carbon dioxide partial pressure, higher than that relative to a "neutral" solution ($P(CO_2) = 10^{-3.7}$ atm. at 850°C), is set above the melt. On the contrary, the oxobasicity increases with the slow decarbonation of the melt (formation of oxide species). At 850°C, a small increase in C_2 selectivity (53.1 to 55.8%) and C_2 yield (10.9 to 11.8%) was observed after heating the melt under helium during 72 hours (assay 1 to 2). When CO_2 was set over the melt the catalytic activity fell from 11.8% to 10.2%. This moderate oxoacidity effect was limited because of the low solubility of CO_2 (around 5×10^{-4} mol.Kg^{-1}) [6], which means that low amounts of O_2^{2-} are still present in the melt. When the reaction time increased, provoking an increase in the oxobasicity, C_2 yield became progressively higher (12.1% at 850°C).

The effect of the oxoacidity of the melt is shown in Fig. 4 where the evolution of C_2 yield is given as a function of the reaction time with the presence or the absence of a CO_2 atmosphere. Catalytic activity increased with decarbonation, but after 250 h, it slightly fell (C_2 yield of 11.5% instead of 12.1%). This loss of efficiency could be explained by the morphology of the catalyst, where particles coalesce into aggregates, as observed in Fig. 3b, leading to a smaller contact area. This can also be due to the formation of solid sodium oxide (presence of whiskers with high Na_2O content identified by Xray probe microanalysis); the increase in the oxobasicity being compensated for by a less efficient gas-liquid contact due to a more viscous molten phase containing solid particles.

Results achieved at 800°C were compared to those obtained with Na-K bulk or Na-K dispersed on alumina beads, as observed in Fig. 5. A significant increase of catalytic performance can be noted in the case of Na-K immobilized on $LiAlO_2$.

Table 1- Influence of the acidity on the oxidative dimerization of methane in Na_2CO_3-K_2CO_3 at 850°C.

General conditions: 7.6 mol% of Na_2CO_3-K_2CO_3 *in 0.393 g of* $LiAlO_2$*; initial pressures of 138.5 Torr* CH_4*, 47.0 Torr* O_2*, 574.5 Torr He, total flow rate of 58.2 ml/min. t is the time during which the catalyst is maintained at 800°C under the reactant gas mixture (during the different assays), carbon dioxide at atmospheric pressure (during 10 hours between assays 2 and 3) or helium at atmospheric pressure (between assays 1-2, 3-4 and 4-5).*

Assay	t	Selectivity %				O_2	CH_4	C_2	C_2
	(h:min)	CO_2	CO	C_2H_4	C_2H_6	conv.%	conv.%	select%	yield %
1	28:00	41.4	5.5	32.6	20.5	78.3	20.6	53.1	10.9
2	100:00	38.8	5.4	34.0	21.6	77.3	21.1	55.8	11.8
CO_2	1 atm.	from 102h to 112h							
3	123:00	39.6	4.8	32.1	23.5	69.0.	18.4	55.6	10.2
4	147:00	39.1	5.0	32.7	23.7	68.2	18.2	55.9	10.2
5	195:00	39.2	4.8	33.4	22.7	73.6	21.5	56.1	12.1

CONCLUSION

Experimental evidence was given for the influence of the oxobasicity of Na_2CO_3-K_2CO_3 on its catalytic properties. Catalytic transformation increased with melt decarbonation until precipitation of Na_2O was reached. The importance of a solid support to immobilize molten carbonate and improve gas-liquid contact was outlined. Two aspects should be considered to optimize catalytic performance: - the proportion of molten carbonate in Na_2CO_3-K_2CO_3/$LiAlO_2$ system and - a deeper understanding of morphology changes during catalytic operations.

ACKNOWLEDGMENTS

The authors wish to acknowledge Professor H. Wendt (Intitut für Chemische Technologie, Darmstadt, Germany) for interesting advices and W. Rummel (Siemens, Germany) for his help in samples preparation.

REFERENCES

1. M. Cassir, G. Moutiers, C. Moneuse, J. Devynck and B. Trémillon, Material Science Forum, 73-75, 331 (1991).
2. C. Moneuse, M. Cassir, G. Martin and J. Devynck, Applied Catalysis, 85, 147 (1992).
3. V. Tashjian, M. Cassir, J. Devynck and W. Rummel, Applied Catalysis (1994) in press.
4. M. Cassir, G. Moutiers and J. Devynck, J. Electrochem. Soc., 11, 3114 (1993).
5. H. A. Liebhafsky and E. J. Cairns, in *"Fuel Cells and Fuel Batteries"*, John Wiley and Sons, New York (1968).
6. A. J. Appleby and C. Van Drunen, J. Electrochem. Soc., 127, 1655 (1980).

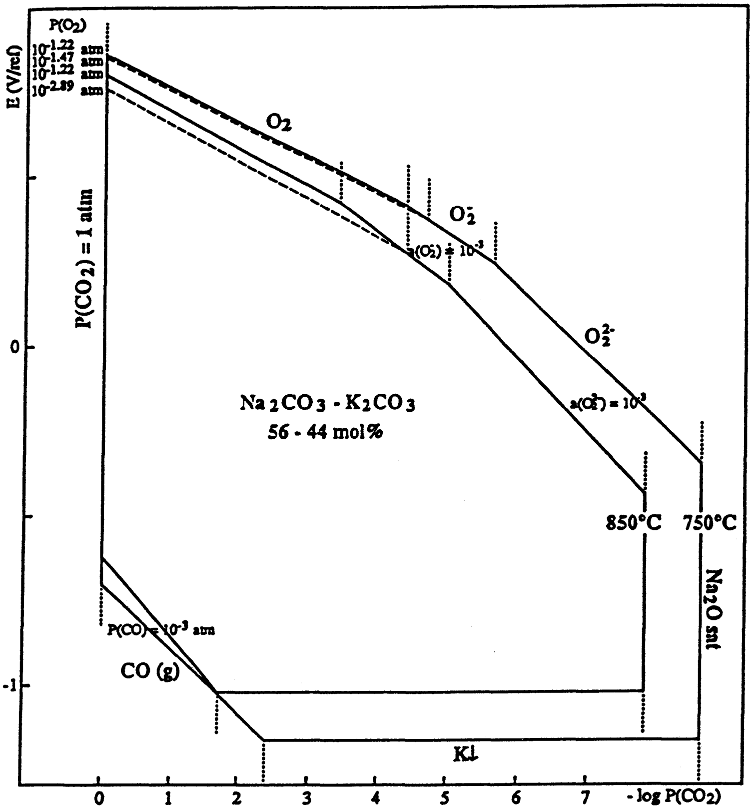

Fig. 1. Potential-oxoacidity diagram of Na_2CO_3-K_2CO_3 eutectic

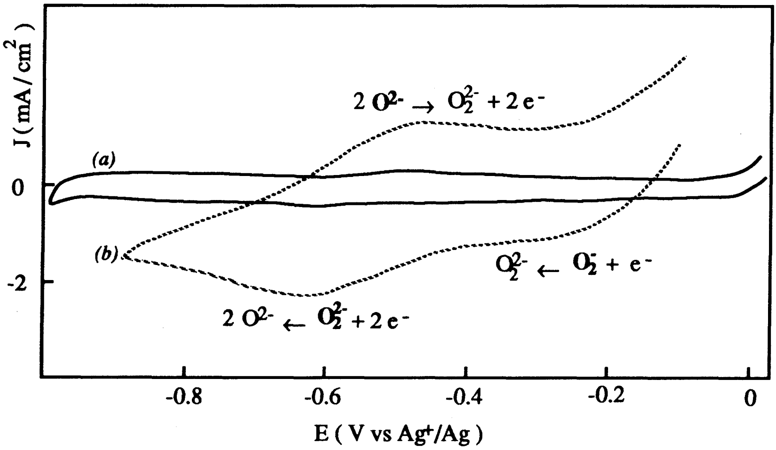

Fig. 2. Cyclic voltammograms of Na_2CO_3-K_2CO_3 at a gold electrode at 750 °C: v = 0.1 V/s; $P(O_2)$ = 1atm; (a) t = 24 hours (b) t = 7 days

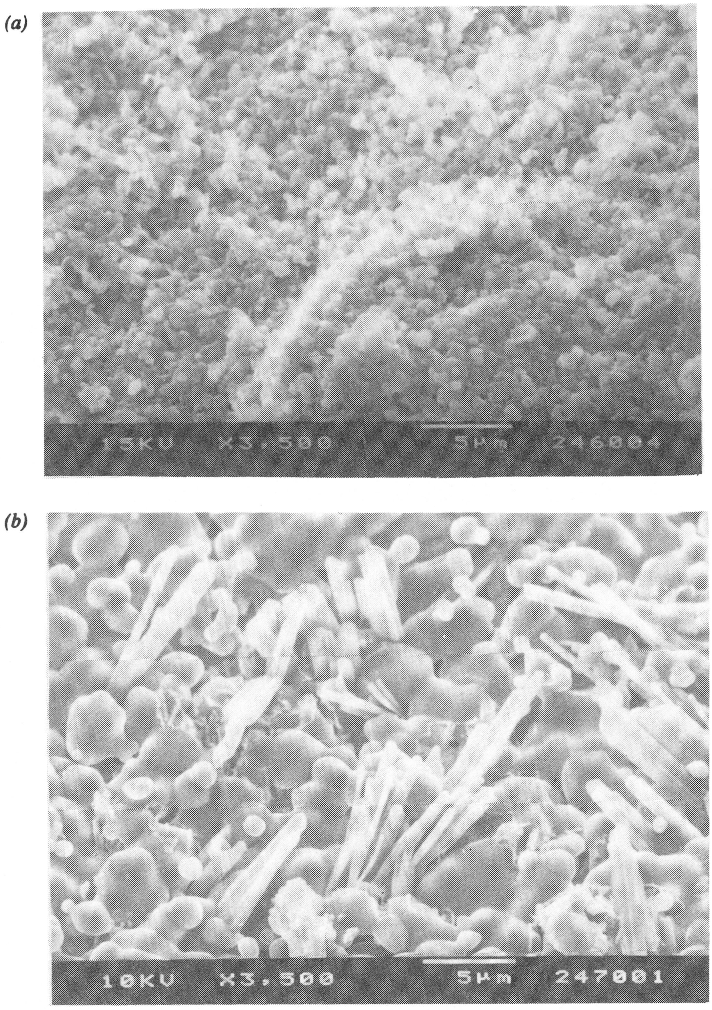

Fig. 3. SEM micrographs of carbonate/$LiAlO_2$ samples: (a) before catalytic reaction (b) Na_2CO_3-K_2CO_3 after extended catalytic reaction

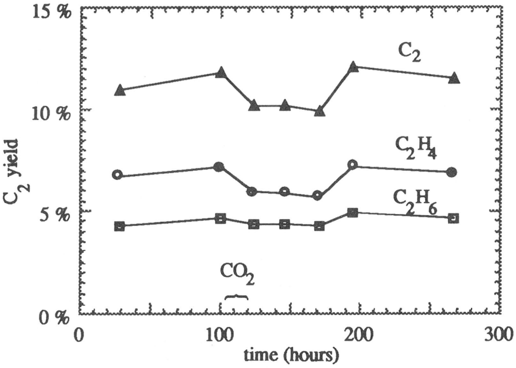

Fig. 4. Evolution of C_2 yields as a function of the reaction time with the presence or the absence of CO_2 at 850°C

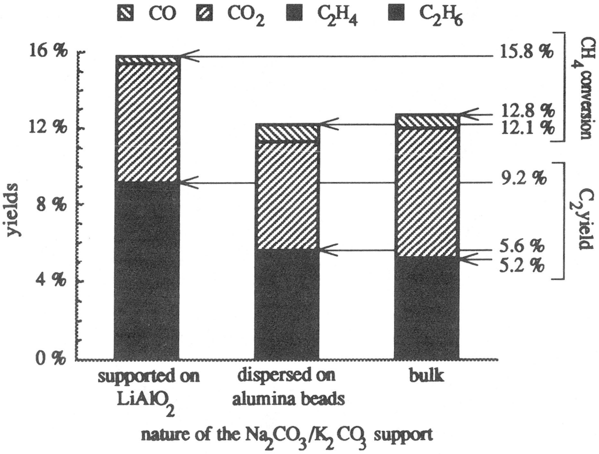

Fig. 5. Results of methane coupling obtained with different Na-K melts at 800°C

DOI: 10.1149/199413.0617PV

TRANSITION-METAL CATALYSIS IN ROOM TEMPERATURE CHLOROALUMINATE MOLTEN SALTS: DIMERIZATION OF PROPYLENE CATALYZED BY NICKEL COMPLEXES AND METATHESIS OF OLEFINS CATALYZED BY TUNGSTEN COMPLEXES.

Yves Chauvin, Françoise Di Marco, and Hélène Olivier
Institut Français du Pétrole
BP 311, 92506 Rueil-Malmaison, France.

Bernard Gilbert
Université de Liège, Laboratoire de Chimie Analytique B6
Sart Tilman, B-4000 Liège, Belgium.

ABSTRACT

Room temperature molten salts based on aluminum chloride or ethylaluminum dichloride and 3-butyl-1-methyl imidazolium chloride have been used as solvents for the catalytic dimerization of propylene by nickel complexes and for the metathesis of olefins by tungsten complexes. Both these reactions were performed in a two-phase system. The role of the composition of the salt and the effect of the ligands coordinated on the metal have been studied. The existence of equilibria between the molten salt phase and the hydrocarbon phase was described.

INTRODUCTION

Two-phase catalysis is an attractive alternative to homogeneous and heterogeneous catalysis. Several reactions have tentatively been studied using this technique, and at least two of them have received industrial applications: the propylene hydroformylation reaction catalyzed by rhodium complexes dissolved in an aqueous phase (1) and the ethylene oligomerization catalyzed by nickel complexes dissolved in butanediol polar phase (2). Both these applications use protic coordination phases as catalyst solvents. However, such media could not be considered for the organometallic catalysts that are highly sensitive to protons or bases. For such catalysts, acidic room temperature molten salts based on aluminum trichloride or ethylaluminum dichloride ($EtAlCl_2$) and 3-butyl-1-methyl imidazolium chloride (BMIC) proved to be particularly suitable. They are good, noncoordinating solvents for many transition-metal complexes and do not dissolve aliphatic hydrocarbons. In addition, their acidity can be adjusted by varying their composition.

In this paper, we describe two reactions of petrochemical interest: the dimerization of propylene into isohexenes catalyzed by nickel complexes, and the metathesis of 2-pentene catalyzed by tungsten complexes.

EXPERIMENTAL

Air-sensitive compounds were manipulated in a glove box. Molten salts were prepared as previously described (3). Catalysis experiments were performed in a 100 mL double-walled glass reactor containing a stirring bar. The reactor was purged of air and moisture. The transition-metal complex (0.1 mmole), heptane (2 to 4 mL), molten salt (3 to 4 mL) and olefin were introduced successively into the reactor.

Dimerization. It was conducted in semi-batch experiments. An atmospheric pressure of propylene was maintained as the vapor phase. When the reactor was nearly full of liquid, the upper hydrocarbon phase was decanted and withdrawn and the experiment was started again up to 10 times with the same molten salt.

Metathesis. It was investigated in batch experiments. 2-Pentene (10 mL) was introduced under argon. 2-Pentene conversion was determinated by the analysis (VPC) of the olefinic upper phase. After hydrocarbon phase withdrawals, the molten salt was reused several times.

The products were analyzed by conventional VPC techniques using an internal standard.

PROPYLENE DIMERIZATION

Dimerization of propylene was performed with $NiCl_2$,2L complexes (L=trialkylphosphine). It is generally assumed that the formation of dimers results from a series of insertions into Ni-H and Ni-C bonds, thus affording various structures: n-hexenes, 2-methylpentenes, 2,3-dimethylbutenes. The presence of sterically demanding phosphines can modify the distribution of dimers by increasing the 2,3-dimethylbutene content.

Two types of molten salts were used: those based on $EtAlCl_2$ and those based on the $AlCl_3/EtAlCl_2$ mixture. Catalytic activity was observed only in melts where the total aluminum molar fraction was higher than 0.5. In both these systems, $(EtAlCl_2)_2$ contained in the melt acted not only as a component of the ionic solvent but also for the formation of a nickel-carbon bond. The results are given in Table 1. The presence of sterically demanding phosphine (P*i*-Pr_3) led to high selectivity in 2,3-dimethylbutenes, thus demonstrating the effectiveness, in molten salts, of the "phosphine effect", already observed in organic media (4, 5).

$EtAlCl_2$:BMIC (1.2:1) melts. In these molten salts, deactivation of the catalyst was observed, and the amount of dimers produced before the catalyst was deactivated was 45 kg/g Ni. This catalyst deactivation can be ascribed to the fact that, when contacted with a hydrocarbon phase, the $Et_2Al_2Cl_5^-$ polynuclear anions, present in the initial melt (6), disproportionate (Raman spectroscopy) (7), $(Et_2AlCl)_2$ being soluble in the hydrocarbon phase:

$$Et_2Al_2Cl_5^- \rightleftharpoons AlCl_4^- + 0.5\ (Et_2AlCl)_2 \qquad [1]$$

Thus, after extensive extraction, the melt was essentially composed of the $AlCl_4^-$ anions.

$AlCl_3$:$EtAlCl_2$:BMIC (1.2:0.1:1) melts. As shown by Raman spectroscopy (7), such melts contained the mixture of the $Al_2Cl_7^-$, $EtAl_2Cl_6^-$ and $Et_2Al_2Cl_5^-$ polynuclear anions and the $AlCl_4^-$ anions. However, extensive extraction of this melt by a hydrocarbon phase, led to a new melt which contained only the $Al_2Cl_7^-$ and the $AlCl_4^-$ anions. The $AlCl_4^-$ anions, already present in the initial melt, were also formed by the disproportionation reaction of the $EtAl_2Cl_6^-$ anions, $(EtAlCl_2)_2$ being soluble in the hydrocarbon phase:

$$EtAl_2Cl_6^- \rightleftharpoons AlCl_4^- + 0.5\ (EtAlCl_2)_2 \qquad [2]$$

In such melts, the 2,3-dimethylbutene content and catalyst activities were enhanced (entries 1 and 2, Table 1). Such an enhancement can be ascribed to the change in the anion associated with the active cationic nickel catalyst.

By using $NiCl_2,2PBu_3$ complexes as catalyst precursor, a constant dimer distribution was obtained throughout the reaction time (entry 4, Table 1). On the contrary, with $NiCl_2,2Pi\text{-}Pr_3$ complexes, the high yield in 2,3-dimethylbutenes found at the beginning, decreased rapidly (entry 2) suggesting that the "phosphine effect" gradually disappeared. It could be assumed that there is competition, for the phosphine, between "soft" nickel active catalyst and "hard" aluminum chloride:

$$RNiPR_3^+ + Al_2Cl_7^- \rightleftharpoons RNi^+ + AlCl_3, PR_3 + AlCl_4^- \qquad [3]$$

The formation of a phosphine-aluminum chloride complex was also supported by the ^{31}P NMR spectrum of the $NiCl_2,2PCy_3$ (Cy=cyclohexyl) complex in $AlCl_3$:BMIC (1.2:1) molten salts which showed the presence of a species with a ^{31}P-^{27}Al coupling. On the other hand, no ^{31}P-^{27}Al coupling was observed when the $NiCl_2,2PBu_3$ complex was dissolved in $AlCl_3$:BMIC (1.2:1) molten salts suggesting that, in that case, the equilibrium [3] was strongly displaced to the left.

We have anticipated that the best way to prevent such an interaction was to add a "soft" competitive base which does not interfer with the cationic nickel active species. It is known that aromatic hydrocarbons (ArH) interact with acidic melts (8) to give colored species:

$$Al_2Cl_7^- + ArH \rightleftharpoons ArH, AlCl_3 + AlCl_4^- \qquad [4]$$

Thus, we have performed the reaction with $NiCl_2,2Pi\text{-}Pr_3$ complex in molten salts in which different aromatic hydrocarbons were added (1 molar equivalent per $Al_2Cl_7^-$ anion present in the melt). As shown in Figure 1, in the presence of tetramethylbenzene or pentamethylbenzene, the 2,3-dimethylbutene content decreased very slowly thus indicating that the interaction between the aromatic hydrocarbon and $AlCl_3$ can be strong enough to prevent the decoordination of the phosphine from the nickel. On the contrary, the 2,3-dimethylbutene content decreased much more rapidly when methylnaphtalene or toluene

were added to the melt suggesting that the interaction is all the weaker as the aromatic hydrocarbon is less basic. The effect of hexamethylbenzene, the most basic of the hydrocarbons studied, is limited due to its insolubility in the melt.
However, aromatic hydrocarbons tend to be extracted by the reaction products. Thus, toluene (0.5 equivalent per $Al_2Cl_7^-$ anion present in the melt) was added to the melt after each withdrawal of the reaction product phase. In that way, the 2,3-dimethylbutene content remained constant as long as toluene was added but decreased when the addition was suppressed.

OLEFIN METATHESIS

The reaction is usually described by the following equilibrated disproportionation of olefins:

$$\underset{\text{2-pentene 50\%}}{2\,CH_3CH{=}CHCH_2CH_3} \rightleftharpoons \underset{\text{2-butene 25\%}}{CH_3CH{=}CHCH_3} + \underset{\text{3-hexene 25\%}}{CH_3CH_2CH{=}CHCH_2CH_3}$$

In an organic solution, tungsten hexachloride (WCl_6) and tungsten oxytetrachloride ($WOCl_4$) associated with an organometallic compound, such as $(EtAlCl_2)_2$, are the classical olefin metathesis catalysts.

In room-temperature chloroaluminate molten salts, these complexes proved to be inactive, which could be ascribed to their well-known reduction to tungsten V and IV by the chloride anions (9). However, it has been demonstrated by cyclic voltammetric measurements (10) that the $W(OAr)_xCl_{6-x}$ complexes, in which some chloride were replaced by aryloxide ligand were harder to reduce. Thus, we have investigated the efficiency of these complexes in $AlCl_3/EtAlCl_2$ based molten salts for 2-pentene metathesis. As shown in Table 2, the most efficient catalyst are the $W(OAr)_2Cl_4$ complexes (ArOH=2,6-diphenylphenol or 2,4,6-triphenylphenol). These results differ from those described for the catalysis in organic hydrocarbon solvents in which the most active catalysts are formed when aryloxide is substitued in ortho, ortho' by a chlorine atom (11). The activity of the $W(OAr)_2Cl_4$ (ArOH=diphenylphenol or triphenylphenol) complexes, in molten salts could be ascribed to the steric and electronic influence of the diphenylphenoxide ligand on the metal (12).

CONCLUDING REMARKS

Room-temperature acidic haloaluminate molten salts containing ethylaluminum dichloride proved to be good solvents for coordination catalysts, mainly to perform dimerization and metathesis of olefins. They make possible the extension of two-phase catalysis to noncoordinating and nonproton active solvents.

REFERENCES

1. E. G. Kuntz, Chemtech, 570, (1987).
2. E. R. Freitas and C. R. Gum, Chem. Eng. Prog., 73, (1979).

3. J. S. Wilkes, J. A. Levisky, R. A. Wilson and C. C. Hussey, Inorg. Chem., 21, 1263, (1982).
4. B. Bogdanovic, B. Henc, H. G. Karmann, H. N. Nüssel, D. Water and G. Wilke, Ind. Eng. Chem., 62, 34, (1970).
5. Y. Chauvin, B. Gilbert and I. Guibard, J. Chem. Soc., Chem. Commun., 1716, (1990).
6. Y. Chauvin, B. Gilbert and I. Guibard, Vibrational Spectroscopy, 1, 299, (1991).
7. B. Gilbert, Y. Chauvin and F. Di Marco, submitted to Inorg. Chem..
8. J. Robinson and R. A. Osteryoung, J. Am. Chem. Soc., 101, 323, (1979).
9. T. B. Scheffler and C. L. Hussey, Inorg. Chem., 23, 1926, (1984).
10. A. Bell, Polymeric Material Science and Engineering, 67, 39, (1992).
11. F. Quignard, M. Leconte and J. M. Basset, J. Mol. Catal., 36, 13, (1986).
12. L. M. Atagi and J. M. Mayer, Angew. Int. Ed., Engl., 32, 439, (1993).

Table 1. Dimerization of Propylene Catalyzed by $NiCl_2$,2L Complexes in Molten Salts[a].

Entry	Molten Salt		Nature of L	Additive	Temp	Reaction Time	Yield	Dimer distribution (weight %)		
	Composition	Molar Ratio			(°C)	(hours)	(kg/gNi)	DMB[b]	MP[c]	*n*-H[d]
1	$EtAlCl_2$:BMIC	1.2:1	P*i*-Pr_3	no	-15	18	45	70	27	3
2	$AlCl_3$:$EtAlCl_2$:BMIC	1.2:0.1:1	P*i*-Pr_3	no	-15	8	100	83 to 11	14 to 50	2 to 16
3	$AlCl_3$:$EtAlCl_2$:BMIC	1.2:0.1:1	P*i*-Pr_3	yes[e]	-15	8	73	84 to 80	15 to 18	1
4	$AlCl_3$:$EtAlCl_2$:BMIC	1.2:0.1:1	PBu_3	no	5	12	100	34	63	3

[a] $NiCl_2$, $2PR_3$ (R=P*i*-Pr_3 or PBu_3) gave red solutions in heptane; when acidic molten salts were added, the heptane phase turned colorless and the molten salt turned yellow.

[b] DMB=2,3-dimethylbutenes, [c] MP=2-methylpentenes, [d] *n*-H=*n*-hexenes, [e] tetramethylbenzene (aromatic hydrocarbon:$Al_2Cl_7^-$ molar ratio=1).

Table 2. Metathesis of 2-Pentene Catalyzed by Tungsten Complexes in Acidic $AlCl_3$:$EtAlCl_2$:BMIC (0.9:0.2:1) Molten Salts[a].

Entry	Tungsten complex		Reaction time (hours)	2-Pentene conversion (molar %)
	Type	Nature of the aryloxide ligand (OAr)		
1	$W(OAr)_2Cl_4$	2, 6-diphenylphenoxide	4	50[b]
2	$W(OAr)_2Cl_4$	2, 6-dichlorophenoxide	>4	7
3	$W(OAr)_2Cl_4$	2, 4, 6-triphenylphenoxide	4	50[b]
4	$W(OAr)_2Cl_4$	2, 6 -di-*tert*-butyl 4-methylphenoxide	>4	40
5	$W(OAr)_2Cl_4$	2-phenylphenoxide	>4	<1
6	$W(OAr)Cl_5$	2, 6-diphenylphenoxide	>4	33
7	$W(OAr)_4Cl_2$	phenoxide	>4	no activity
8	$W(OAr)_3Cl_3$	2, 4, 6-trimethylphenoxide	>4	no activity

[a] Tungsten complexes dissolved in basic $AlCl_3$ based salts giving black solutions which turned brown upon addition of a heptane solution of $(EtAlCl_2)_2$

[b] Maximum of 2-pentene conversion (50% mole) was obtained when the reaction equilibrium was reached (25% 2-butene, 25% 3-hexene). The upper hydrocarbon phase was withdrawn, and 10 mL 2-pentene were again added in the melt containing the used catalyst.

Figure 1. Dimerization of Propylene Catalyzed by NiCl2,2PiPr3 Complexes (0.1mmole). Effect of the Addition of Aromatic Hydrocarbons on the 2,3-Dimethylbutene Selectivity.

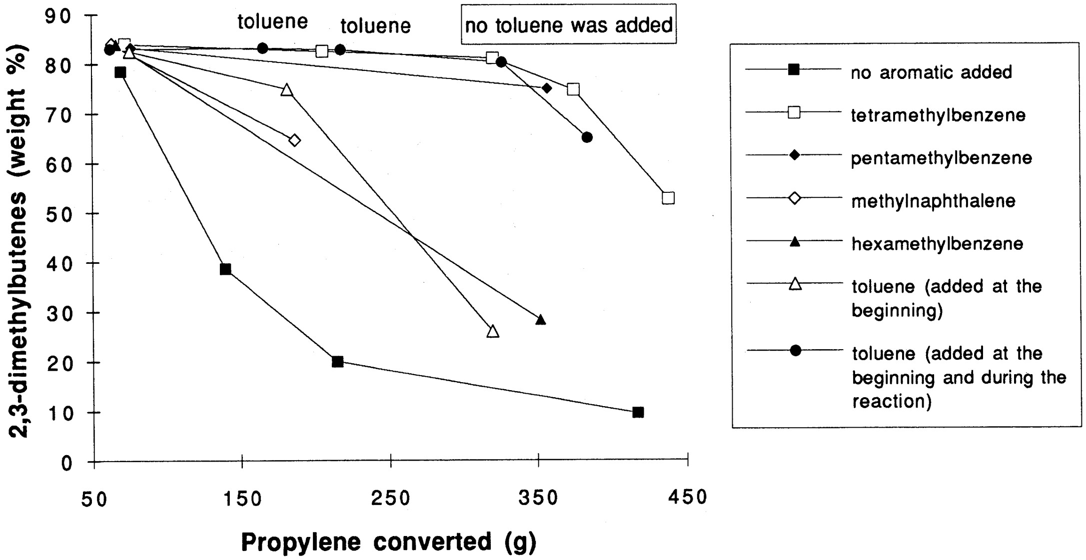

DOI: 10.1149/199413.0625PV

Activity and Deactivation of Molten Salt Catalyst During SO_2 Oxidation and SO_2 Removal from flue gasses.

S. Boghosian[1], *A. Chrissanthopoulos*[1], *D. A. Karydis*[1],
S. G. Masters[2], *K. M. Eriksen*[2] *and R. Fehrmann*[2]

[1] Institute of Chemical Engineering and High Temperature Processes, University of Patras,
P.O. Box 1414, GR-26500 Patras, Greece.

[2] Chemistry Department A, The Technical University of Denmark, DK-2800 Lyngby, Denmark.

Abstract

Catalytic activity of commercial SO_2 oxidation catalysts have been measured in a simulated flue gas from coal fired power plants, both with and without the typical water vapour content. This shows that usual sulfuric acid catalysts are not affected by the the water content, but a specially adapted catalyst with a different pore size is. An ESR investigation of the catalyst suggests, that it deactivates due to precipitation of a V(III) compound and not V(IV) as usual for sulfuric acid catalysts.

Introduction

The industrial catalyst for SO_2 oxidation, which is the key step in the production of sulfuric acid can, at operating conditions, be described by the melt-gas system $M_2S_2O_7/V_2O_5$-$SO_2/O_2/SO_3/N_2$, where M = Na, K or Cs or mixtures of these. While the catalyst works well at rather high temperatures (> ca. 440 °C), it deactivates below this temperature and thus limits the degree of conversion for the exothermic oxidation. This results in SO_2 emission to the environment. Therefore, but also from a process design point of view, an active 'low temperature' catalyst has been needed for many years, but so far it has not appeared.

This need has been further increased during the last decade where attention has been drawn to abatement of industrial flue gasses, including those from coal fired power plants. Several methods exist to remove SO_2 from off-gases, but all of them, except converting it into sulfuric acid, creates new types of waste (e.g. gypsum). The catalyst used for oxidizing SO_2 in flue gasses into sulfuric acid is essentially identical to the usual catalyst used for production of sulfuric acid. However, due to a lower SO_2 concentration in flue gasses, the deactivation occurs at a slightly lower temperature. It is evident, that an active 'low temperature' catalyst is highly desirable for this purpose.

The operation conditions of the catalyst during flue gas purification is very different from the ones in sulfuric acid production. Not only the SO_2 concentration is much lower, but the 'wet' gas probably influences the chemical composition of the catalyst too, by transforming pyrosulfate into hydrogensulfate:

$$S_2O_7^{2-} + H_2O \rightleftarrows 2HSO_4^- \qquad [1]$$

The flue gas from a typical coal fired power plant is approximately 0.2% SO_2, 4% O_2, 7% H_2O, 14% CO_2 and 75% N_2.

The results presented here are a part of our continuous investigation of the sulfuric acid catalyst and its chemistry by a multiinstrumental research strategy - see e.g. ref. 1-6. By using both real industrial catalysts and well defined model melts and comparing the results, we can increase the knowledge of the catalytic system. Here we have measured the activity and recorded ESR spectra of commercial catalysts in flue gas with and without water vapor in order to investigate the influence of this component. We have also isolated compounds from catalyst model melts in the two feed gasses at the conditions of industrial operation.

Experimental

The flue gas was premixed in gas bottles using dry SO_2, O_2, CO_2 and N_2 to the desired composition. Wetting of gasses was done by bobbling the gas through water containing flasks heated to the appropriate temperature, e.g. 40 °C for a water content of 7% (saturation). The SO_2 concentration was monitored by UV spectrophotometry using a gas cuvette with an optical path of 50 mm. The concentration of CO_2, O_2 and N_2 was found by gas chromatography (Supelco Chromosorb 102 and Molecular Sieve 5A). The H_2O concentration was measured by a Jenway 5075 Humidity meter.

For the activity measurements and compound isolation the gas was led to a molten salt reactor cell of Pyrex as shown in Figure 1. The crushed catalyst or model melt is supported by the porous glass filter disk through which the gas bobbles.The conversion of SO_2 was monitored spectrophotometrically (on line) and was always below 20%. The reactor cell was placed in a double walled kanthal wire wound quartz furnace. This setup allowed direct visual inspection of the crystal formation at high temperature.

For the ESR measurements, the gas was led to a quartz cell as shown in Figure 2. This cell fits into a Bruker ER4114HT high temperature X-band cavity mounted in a slightly modified JEOL JES-ME-1X instrument. The temperature was measured by a non-magnetic chromel-constantan thermocouple positioned on top of the catalyst.

The industrial catalyst samples were delivered by the manufacturer, Haldor Topsøe A/S, Denmark. Chemicals for the model melts were commercial grade V_2O_5 (Cerac, > 99.9%) and alkali pyrosulfates made by thermal decomposition of the corresponding alkali peroxodisulfate (> 99.8% by gravimetric analysis)[1].

Results and Discussion

Catalyst Activity

The activity of three industrial catalysts with the approximate compositions given in Table 1 has been measured in the temperature range around 350 - 500 °C. All catalysts have a total vanadium content of around 6% V_2O_5 in the solid support of kieselguhr. VK38 is the widespread K and Na promoted type used for conversion of gasses with high SO_2 content (~10%), i.e. in sulfuric acid plants. VK/WSA is used for flue gas conversion with low SO_2 content (~0.2%) and it has the same chemical composition as VK38 but a different poresize of the solid support. VK58 has a modified chemical composition - it includes Cs in addition to K and Na as promoter. It is considered to have a higher low-temperature activity. The measured catalytic activity of these catalysts in 'dry' and 'wet' flue gasses are displayed in Figure 3 and 4, respectively. In both type of gasses all catalysts show a marked decrease in the activity at a certain temperature - the break point temperature T_b as given in Table 1. The trend in T_b for the different catalysts are in accordance with the industrial experience. However, it seems curious that

VK/WSA in 'dry' gas deactivates at a higher temperature that both VK38 and VK58.

None of the catalysts meet the desire of a T_b of 350 °C or lower. Therefore we have decided to undertake investigations that could explain the catalyst deactivation in flue gasses.

In situ ESR-spectroscopy

Series of ESR-spectra of the three catalysts converting both 'dry' and 'wet' flue gasses have been measured in the approximate temperature range 450 - 300 °C. The spectra obtained on VK/WSA are shown in Figure 5A and 5B for 'dry' and 'wet' flue gas, respectively. At higher temperatures the spectra shows a broad rather weak unresolved line which is attributed to polymer (or dimer) V(IV)-complexes in solution. By lowering of the temperature in the 'dry' gas a sharp almost isotropic line appears around 439 °C, i.e. at the temperature of deactivation as observed in Figure 3. By lowering the temperature further, a g-value of 1,972 can be found for the line. The spectrum is identical to the ESR-spectrum of the compound $K_4(VO)_3(SO_4)_5$ which has been isolated from model melts[4] and earlier[3] been shown - by in situ ESR spectroscopy - to deactivate VK38 in sulfuric acid synthesis gas. In 'wet' flue gas the ESR-spectrum shows the broad line at higher temperatures too, but no sharp isotropic line is observed at lower temperatures, not even far below the breakpoint temperature of 386 °C (Table 1). A double integration of the spectra shows that the V(IV) amount increases with decreasing temperature down to ca. 380 °C. Below this temperature, the V(IV) amount decreases. This behavior indicates that the catalyst is deactivated by ESR silent V(III) compounds: below T_b vanadium is removed from the liquid phase into solid V(III) compounds, which causes the decrease of the V(IV) concentration. Further work is in progress to identify this V(III) compound by isolating it from a model melt at the same conditions in the reactor cell. Earlier the V(III) compound $KV(SO_4)_2$ has been isolated and characterized[7] from similar catalyst melts, but at much higher SO_2 partial pressure. It is interesting that in this 'wet' gas both VK38, which is chemical identical to VK/WSA, and VK58 deactivates due to precipitation of the V(IV) compound $K_4(VO)_3(SO_4)_5$. This indicates that the support has an important role for the nucleation of the compounds.

Key words: ESR-spectroscopy, vanadium compounds, wet sulfuric acid process.

References

1 Hansen, N.H.; Fehrmann, R; Bjerrum, N.J. *Inorg. Chem.* **1982,** *21,* 744.

2 Boghosian, S; Fehrmann, R; Bjerrum, N.J; Papatheodorou, G.N. *J. Catal.* **1989,** *119,* 121.

3 Eriksen, K.M; Fehrmann, R; Bjerrum, N.J. *J. Catal,* **1991,** *132,* 263.

4 Fehrmann, R; Boghosian, S; Papatheodorou, G.N; Nielsen, K; Berg, R.W; Bjerrum, N.J. *Inorg. Chem.* **1989,** *28,* 1847.

5 Folkmann, G.E; Hatem, G; Fehrmann, R; Gaune-Escard, M; Bjerrum, N.J. *Inorg. Chem.* **1991,** *30,* 4057.

6 Nielsen, K; Fehrmann, R; Eriksen, K.M. *Inorg. Chem.* **1993,** *32,* 4825.

7 Fehrmann, R; Krebs, B; Papatheodorou, G.N; Berg, R.W; Bjerrum, N.J. *Inorg. Chem.,* **1986,** *25,* 1571.

Table 1: Temperature of the Activity Drop in Industrial Molten Salt Catalysts and Compound Formation in Catalyst Model Melts.

Industrial Catalyst	Composition of model melt (molar ratio)	T_b (°C) [a]	Colour of Crystalline Precipitate
VK38 [b]	K/Na/V = 3/0.8/1	421	
VK58 [b]	K/Cs/Na/V = 3/1/0.25/1	380	
VK/WSA [b]	K/Na/V = 3/0.8/1	436	
VK38 [c]	K/Na/V = 3/0.8/1	420	green and pale blue crystals
VK58 [c]	K/Cs/Na/V = 3/1/0.25/1	381	bright blue crystals
VK/WSA [c]	K/Na/V = 3/0.8/1	386	green and pale blue crystals

[a] T_b is the temperature at which the break point in the Arrhenius plots and the compound precipitation occur simultaneously.

[b] Feed gas : 0.2% SO_2, 4.5% O_2, 15.1% CO_2 and 80.2% N_2.

[c] Feed gas : 0.2% SO_2, 4% O_2, 7% H_2O, 14% CO_2 and 75% N_2.

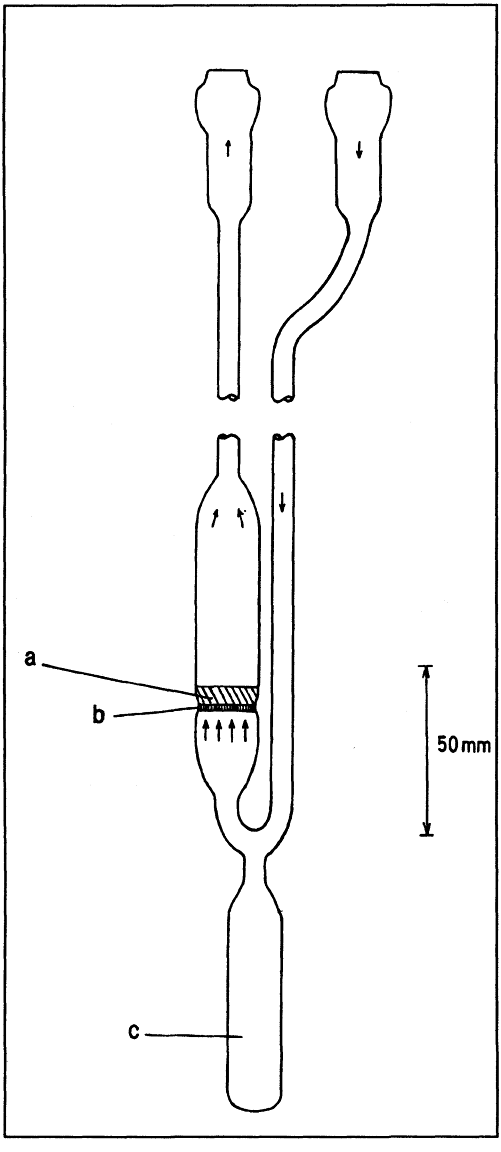

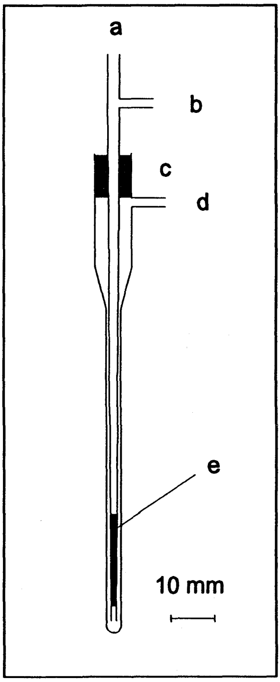

⇧ *Figure 2*. ESR-reactor cell. (a) Thermocouple inlet, (b) Gas outlet, (c) Teflon stopper, (d) Gas inlet, (e) Catalyst bed

⇦ *Figure 1*. Molten-salt reactor cell. (a) Catalyst melt, (b) sintered glass-filter disk, (c) bottom ampule for filtrate collection. Arrows indicate direction of flow during catalyst operation. The flow direction is reversed for filtering the melts and isolating the crystalline precipitates

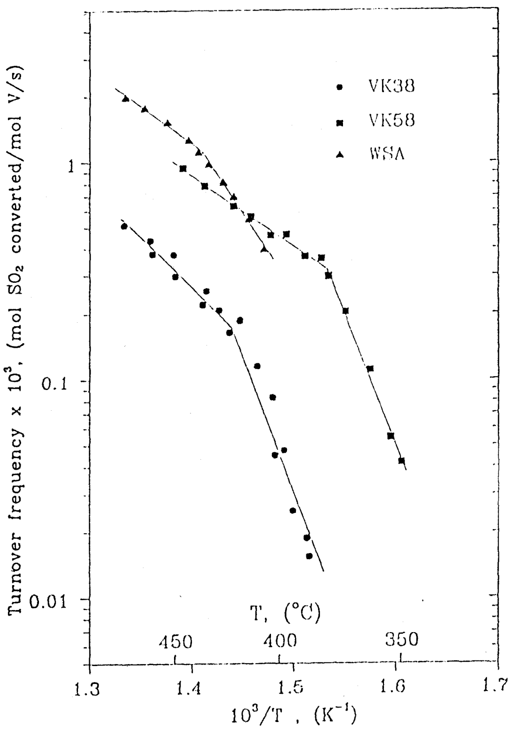

Figure 3: Arrhenius plots of the industrial catalysts in a 'dry' flue gas consisting of 0.2% SO_2, 4.5% O_2, 15.1% CO_2 and 80,2% N_2.

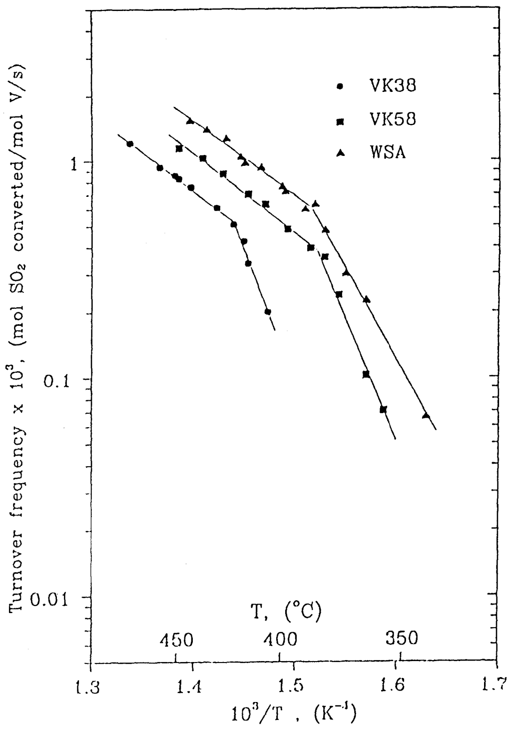

Figure 4: Arrhenius plots of the catalysts in 'wet' flue gas, e.g.0.2% SO_2, 4.0% O_2, 7.0% H_2O, 14.1% CO_2 and 74.8% N_2.

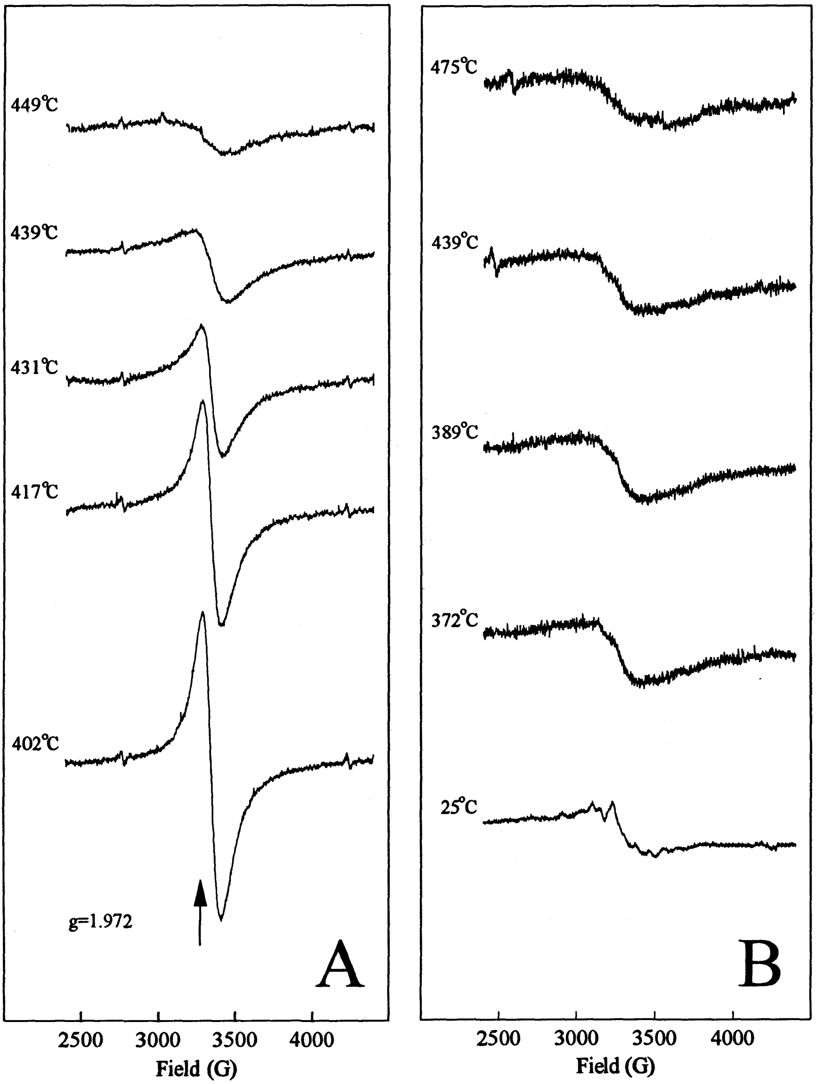

Figure 5: ESR spectra of WK/WSA catalyst at various temperatures in (A) 0.2% SO_2, 4.5% O_2,15.1% $CO_2$and 80.2% N_2or (B) 0.2% SO_2,4% O_2,7% H_2O, 14% $CO_2$and 75% N_2.

DOI: 10.1149/199413.0633PV

THE KINETICS OF THE SOLID STATE REACTIONS BETWEEN PYRIDINIUM CHLORIDE AND ALUMINUM CHLORIDE

David S. Newman and Jennifer Rosinski
Department of Chemistry
Bowling Green State University
Bowling Green, OH 43403

ABSTRACT

The kinetics of the solid state reactions:

$$C_5H_6NCl + AlCl_3 = C_5H_6NAlCl_4$$

and

$$C_5H_6NCl + 2AlCl_3 = C_5H_6NAl_2Cl_7$$

were studied using differential scanning calorimetry. Both reactions were exothermic, unusually rapid for solid state reactions, and probably diffusion controlled. In the neutralization reaction, the degree of transformation, α, as a function of time, was found to exhibit the type of behavior characteristic of reactions that proceed evenly on the entire surface of all reactant particles. The specific rate constant, k, for this reaction showed perfect Arrhenius dependence on the temperature. Preliminary results seem to indicate that the second reaction is also highly exothermic, but less so than the first and at 35 ^{o}C proceeds at about the same rate as the first reaction does at 50 ^{o}C.

INTRODUCTION

During the last two decades, or so, molten salt research has shifted from predominantly high melting salts (used in nuclear reactors, aluminum and magnesium production and carbonate fuel cells) to predominantly low melting salts and chloroaluminates. There are many reasons for this emphasis shift, but perhaps the principal one is that in low temperature melts, interesting and potentially useful reactions can occur whereas in high melting salts, such as cryolyte and NaCl, relatively few interesting reactions occur. The chloroaluminates receiving most attention are $M^+AlCl_4^-$ and $M^+Al_2Cl_7^-$, where the M^+ can be a methylethylimidazolium ion, a pyridinium ion or an alkali metal ion. $MAlCl_4$ can be considered the product of the neutralization reaction between the Lewis acid $AlCl_3$ and the base MCl.:

$$MCl + AlCl_3 = MAlCl_4 \qquad [1]$$

MAl_2Cl_7 is formed when a molecule of MCl reacts with two molecules of $AlCl_3$ (or when a molecule of $MAlCl_4$ reacts with a molecule of $AlCl_3$):

$$MCl + 2AlCl_3 = MAl_2Cl_7 \qquad [2]$$

These reactions tend to be highly exothermic and relatively rapid even though both reactants are solids at the usual temperatures of interest so that their rates can be measured using differential scanning calorimetry as the experimental technique. Although not the most widely used method for measuring reactions rates, energies of activation, and reaction order, all of these quantities are theoretically measurable using a differential scanning calorimeter (DSC) (1). A preliminary investigation of the reactions between pyridinium chloride and aluminum chloride was initiated in order to explore the feasibility of using calorimetry to explore the kinetics of these reactions.

THEORETICAL BACKGROUND

A DSC can be used to measure both isothermal and adiabatic processes and in the present study, an isothermal mode was used. This means changes as a function of time, keeping temperature constant were recorded. Since the DSC is designed, in effect, to maintain a zero temperature differential between a standard and a test sample, any heat evolved (or absorbed) during the reaction (the test sample) will be supplied by the instrument and is therefore easily measured. Since the heat begins to evolve at the beginning of the reaction, $\zeta = 0$, and stops when the system equilibrates at $\zeta = 1$, where ζ is the degree of transformation, the rate at which the heat is evolved is proportional to the rate of the reaction and can be measured by the DSC. In the neutralization reaction, since the stoichiometric coefficients are all unity, $N_o(d\zeta/dt)$, where N_o is the number of moles of either reactant at the start of the reaction, is the true rate of the reaction, dN/dt.

For the solid state reaction,

$$A = C + \Delta H \qquad [3]$$

where A is the solid at the start of the reaction, C is the material after the reaction has equilibrated, and ΔH is the heat evolved during the reaction, in general, $\zeta = \Delta H_{(partial)}/\Delta H_{(reaction)}$. The temperature dependence of the reaction rate is given by the familiar Arrhenius equation so that the rate law for the neutralization reaction becomes

$$d\zeta/dt = k(1-\zeta)^n = A_o[\exp - E_a/RT](1-\zeta)^n \qquad [4]$$

In linear form, this equation becomes

$$\ln(d\zeta/dt) = \ln A_o - E_a/RT + n\ln(1-\zeta). \qquad [5]$$

A_o, E_a, n and k are obtained from experimental values of $d\zeta/dt$, 1/T, and $(1-\zeta)$.(2) That is, the entire area under the experimental Q vs. time curve gives ΔH for the reaction and an area corresponding to a particular time less than $t_{reaction}$,(ΔQ/Δt) x Δt, gives $\Delta H_{(partial.)}$. for that elapsed time. Dividing $\Delta H_{(partial)}$ by $\Delta H_{(reaction)}$ yields the value of ζ corresponding to that rate. The process is repeated for several times at each of several temperatures.

EXPERIMENTAL DETAILS

The experiments were performed on a Perkin-Elmer DSC-4 with a thermal analysis data station(TADS). Data were collected in the isothermal mode using a special isothermal program. Because the reactions between C_5H_6NCl and $AlCl_3$ were fairly rapid, even at room temperature, both reactants were cooled on dry ice in a nitrogen filled glove box (moisture content less than 10 ppm). The proper mole fractions of the reactants were prepared by weighing approximately 0.0001 moles of each reactant in the glove box. The mixtures were placed in large stainless steel pans and sealed. The temperature of the sealed pans was further reduced before removing them from the glove box. The cold pans were quickly removed, placed in the DSC and brought to temperature. Since the reactions occurred quickly, the heat evolved could be easily measured.

The melting and freezing point of the products were obtained by switching to the normal temperature mode of the machine. This was done to ensure a true product was actually produced because sublimation, decomposition, and vaporization would all produce thermograms similar to a melting point. None of these processes would produce exotherms. Since all reactants are very hygroscopic, all transfer reactions were done in a controlled atmosphere glove box in which the boil-off from liquid nitrogen was the atmosphere and the moisture content was less than 10 ppm.

RESULTS AND DISCUSSION

Figure 1,2,and 3 are thermograms for the reaction between 0.0001 mole of C_5H_6NCl and 0.0001 mole at 100 °C, 80 °C, and 50 °C respectively. Fig. 4 shows the thermogram for the reaction between 0.0001mol pyridinium chloride and 0.0002 mol $AlCl_3$. In these figures, the temperature axis is actually the time axis with a "heating rate" of 10 °C/min. This means that a ten degree temperature rise is, in reality, a sixty second time interval.

The thermal data obtained for Eq. [1] are listed in Table I and the kinetic data are listed in Table II. A plot of ln k vs 1/T gave a perfectly straight line with an energy of activation of 10.4 kJ/mol. k is, of course, $d\zeta/dt$ at $t = 0$. Although the data in Table I and in Table II are given to three significant figures, the results are considerably less precise because of the errors in estimating the start and end of the reaction, differences in particle size, and the fact that small amounts of reactants may have begun to react in the steel pan before the reaction temperature was reached. Nevertheless, the results are internally self consistent in so far as the lowest temperature gives the slowest reaction and the highest temperature the fastest reaction. In addition the enthalpies of reaction are all more or less the same, as they should be, and lnk vs 1/T is perfectly linear.

A plot of $-\ln(1 - \zeta)$ vs t was not perfectly linear for any of the experiments indicating that the reaction was not first order. A plot of $(1 - \zeta)^{-1}$ vs t gave an even worse fit indicating that the reaction is not second order. The plot of ζ vs t at all three temperatures gave a "text book" kinetic curve for the case where reactions proceed evenly on all surfaces. (3) That is, ζ initially changed rapidly with time, but gradually slowed down as the reaction proceeded. The heat of the reaction, approximately 50 kJ/mol, is typical of ionic reactions, but the low energy of activation indicates diffusion control. That is, 10 kJ/mol is typical of the energy required to move a Cl^- ion from one site to an adjacent site at the crystal surface or in a melt. This means the chemical reaction's activation energy is being supplied by the heat of the reaction and is, in effect, an autocatalytic process.

The likely mechanism that fits all of the data is that the basic Cl^- from a pyridinium chloride molecule "hops" or "jumps" to an acidic $AlCl_3$ to form $AlCl_4^-$ and the $AlCl_4^-$ reacts with a $C_5H_6N^+$ to form $C_5H_6NAlCl_4$. The hopping or jumping of the Cl^- ion to the $AlCl_3$ evolves heat which becomes the activation energy for another ion to react.

This sort of switching mechanism is not unlike the way a proton would move through water and would account for diffusion control, but at the same time a very fast reaction.

The kinetics of Eq. [2] were also studied, but the results are more ambiguous; especially the fact that the apparent heat of the reaction is slightly lower than the heat of reaction for Eq. [1]. Pyridinium heptachloroaluminate is a liquid at the reaction temperature so that its heat of fusion, which is opposite in sign to the heat of the reaction, may be interfering with the measurement. On the other hand, if the reaction is run at a low enough temperature to prevent melting, it takes place more slowly so that the experimental error is greater and the data are less reproducible. Nevertheless, this reaction is still being studied and will be reported on at a later date.

LIST OF REFERENCES

1. B. Cassel, M.P. DiVito, *American Laboratory,* **14**, 29 (1994)

2. W.W. Wendlandt, *Thermal Analysis,* Third Edition, J. Wiley & Sons, New York, 1986,
pp 282-293

3. V.V. Boldyrev, V.V., M. Bulens, B. Delmon, *The Control of the Reactivity of Solids,* Elsievier Scientific Publishing Co. Amsterdam, 1979, p 21

ACKNOWLEDGMENT

We wish to thank the NSF REU program for its support.

Table I Thermal Data for the reaction of $AlCl_3$ with C_5H_6NCl

T ^oC	**ΔH(react.),J**	**time (sec)**	**ΔH(partial),J**	**α**
100	4.66	54	4.66	1
		30	4.15	0.882
		15	2.37	0.508
		6	0.98	0.21
80	5.00	64	5.00	1
		30	3.98	0.796
		15	0.219	0.438
		6	0.624	0.125
50	4.78	120	4.78	1
		60	3.91	0.810
		30	2.71	0.57
		15	1.42	0.29

Table II. Kinetic data for the reaction between $AlCl_3$ and C_5H_6NCl

T (^oC)	**T (K)**	**k (sec^{-1})**	**lnk**	**1000/T**
100	373	0.044	-3.12	2.68
80	353	0.036	-3.32	2.83
50	323	0.026	-3.64	3.09

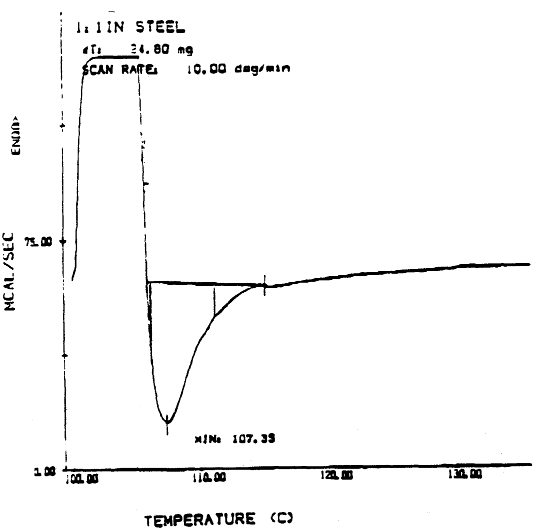

Fig. 1 Thermogram for Eq.[1] at 100°C

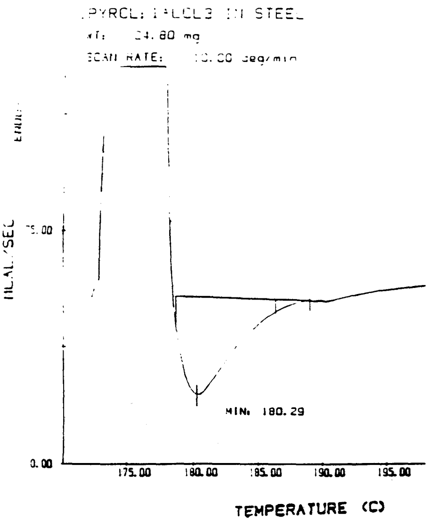

Fig. 2 Thermogram for Eq.[1] at 80

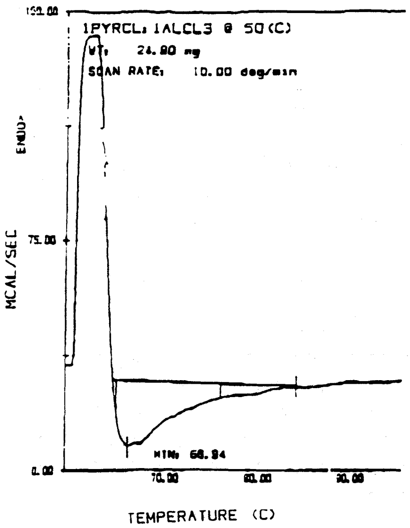

Fig. 3 Thermogram for Eq.[1] at 50°C

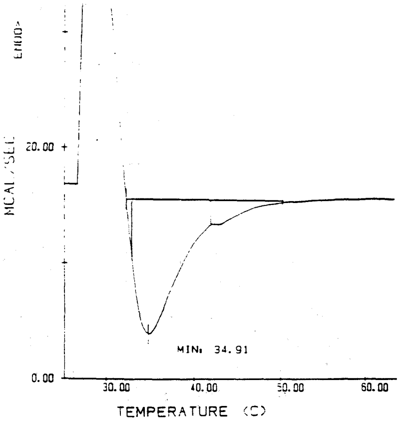

Fig. 4 Thermogram for Eq.[2] at 35°C

DOI: 10.1149/199413.0638PV

THE PHOTOCHEMISTRY OF ANTHRACENE AND ITS DERIVATIVES IN ROOM TEMPERATURE MOLTEN SALTS

Richard M. Pagni, Gleb Mamantov, Carlos W. Lee, and George Hondrogiannis
Department of Chemistry
University of Tennessee
Knoxville, Tennessee 37996-1600

ABSTRACT

The photochemistry of anthracene (An) has been examined in the room temperature molten salt: aluminum chloride/1-ethyl-3-methylimidazolium chloride. In deoxygenated basic melt, the reaction affords the normal (4+4) dimer. In deoxygenated acidic melt the reaction takes a different course, yielding a variety of monomeric and dimeric, oxidized, neutral and reduced products. This unusual photoreaction is initiated by electron transfer from the excited state of An to protonated anthracene (AnH^+), which is generated in low concentration by the reaction of An with trace amounts of HCl, a strong acid in acidic medium. Identical results are obtained when An is photolyzed in a solution of 2% CF_3SO_3H in CF_3COOH (w:w), a medium which also contains both An and AnH^+. Photolysis of An in oxygenated basic melt also occurs in part by electron transfer, this time from the excited state of An to O_2. Photolysis of the more easily oxidized 9-methylanthracene (9-MeAn) in deoxygenated basic melt also occurs in part by photoinduced electron transfer. In this instance the electron acceptor is probably the 1-ethyl-3-methylimidazolium ion.

INTRODUCTION

The photochemistry of anthracene (**1a**) in solution has been studied extensively for more than one hundred years.[1] Until recently the photochemistry could be characterized simply in two ways. When the reaction was run in the absence of oxygen, a (4+4) dimer (**2a**) was generated. Mechanistic studies showed that this product arose from an excimer (excited dimer) formed by the reaction of the singlet excited state of **1a** with ground state **1a**.

$$\mathbf{1a} \xrightarrow{h\nu} \mathbf{1a}^{*1}$$

$$\mathbf{1a}^{*1} + \mathbf{1a} \rightarrow \text{Excimer} \rightarrow \mathbf{2a}$$

When the reaction was run in the presence of oxygen, on the other hand, an endo-peroxide (**3**) was produced exclusively. Studies showed that **3** arose from the reaction of **1a** with singlet oxygen, which was generated by the reaction of the triplet excited state of **1a** with ground state oxygen, a triplet species.

$$\mathbf{1a} \xrightarrow{h\nu} \mathbf{1a}^{*1} \rightarrow \mathbf{1a}^{*3}$$

$$\mathbf{1a}^{*3} + O_2 \rightarrow \mathbf{1a} + O_2^{*1} \rightarrow \mathbf{3}$$

The photochemistry of **1a** in water was completely different than that described above.[2] The reaction in deoxygenated water afforded largely three diastereomeric dimer diols (and no **2a**), which arose in a sequence of steps initiated by electron transfer from the excited state of **1a** to the solvent itself, to form the radical cation of **1a** ($\mathbf{1a}^{+\cdot}$) and the solvated electron. This ionic reaction is undoubtedly a consequence of the fact that water has a very large dielectric constant and is a good medium for ions and ionic reactions. In oxygenated water, on the other hand, **3** and anthraquinone (**4**) were the major photoproducts. Although complete mechanistic details have not been worked out for this reaction, it is known that the formation of **3** arose, at least in part, from the reaction of **1a** with singlet oxygen. The origin of **4** is unknown but it did not arise from **3**.

Until recently photochemical reactions in molten salts, including the room temperature molten salt: aluminum chloride/1-ethyl-3-methyl-imidazolium chloride ($AlCl_3$/EMIC), were unknown. This is unfortunate because $AlCl_3$/EMIC in particular should be an interesting and unusual medium for photochemistry. Its composition can be varied from basic (EMIC in excess; Cl^- = base) to acidic ($AlCl_3$ in excess; $Al_2Cl_7^-$ = acid),[3] and it contains a possible electron acceptor, EMI^+,[4] which is common to both basic and acidic melts, in high concentrations.

We report herein the results of photochemical studies of **1a** and 9-methylanthracene (**1b**) in $AlCl_3$/EMIC and selected strong acids and show that under some circumstances the chemistry is dominated by photoinduced electron transfer.

EXPERIMENTAL

^1H NMR spectra were recorded on Brucker 250 MHz and 400 MHz instruments. HPLC (analytical and semi-prep) was carried out on a Varian Model 5000 HPLC, and GC/MS on a Hewlett-Packard 5890 gas chromatograph with a 5970 series mass selective detector using a crossbonded 100% polysiloxane column. Uv/vis spectra were recorded using a Hewlett-Packard 8452A diode-array spectrophotometer. Photochemical reactions were performed in a Rayonet Type RS reactor in Pyrex vessels using 350-nm lamps.

Anthracene, 9-methylanthracene, dimer (**2a**), trifluoroacetic acid, and trifluoromethanesulfonic acid were commercial materials of highest quality. The preparation and purification of the molten salts are described elsewhere.[5]

The products arising from the photolysis of anthracene in degassed acidic $AlCl_3$/EMIC were separated and characterized as described elsewhere.[6] The same products were obtained when anthracene was irradiated in degassed 2% CF_3SO_3H in CF_3COOH (w:w).[7] The products arising from the photolysis of anthracene in oxygenated basic EMIC/$AlCl_3$ were separated and characterized by GC/MS and compared to known compounds.

Several products were formed in the photoreaction of 9-methylanthracene in degassed basic $AlCl_3$/EMIC of which four have been characterized: **7** by ^{1}H NMR, MS, and independent synthesis;[8] **8a** by ^{1}H NMR, MS, and independent synthesis;[9] **8b** by ^{1}H NMR and MS; and dimer **2b** by independent synthesis (photolysis of **1b** in deoxygenated acetonitrile).

RESULTS AND DISCUSSION

As described elsewhere,[6] the photoreaction of **1a** in degassed basic $AlCl_3$/EMIC afforded the (4+4) dimer (**2a**) exclusively. As **2a** arises from an excimer, it is clear that no electron transfer had occurred between the excited state of **1a** and EMI^+. For such an electron transfer to have occurred between an excited state donor D* and a ground state acceptor A, the reaction must be exothermic.

The free energy of the electron transfer between D* and A is given by the Rehm-Weller equation,[10] which is $\Delta G = E(D/D^+) - E(A^-/A) - \Delta E(D) - C$, where $E(D/D^+)$ and $E(A^-/A)$ are, respectively, the oxidation potential of D and the reduction potential of A, $\Delta E(D)$ is the excitation energy of D, and C is a coulombic term between $D^{+\cdot}$ and $A^{-\cdot}$ which will be zero if one of the reactants such as EMI^+ is ionic. Unfortunately, one can not apply this equation in the case of **1a** in the basic melt because the oxidation of the donor **1a** in basic $AlCl_3$/EMIC is irreversible[11] and the reduction potential of the acceptor EMI^+ represents the cathodic limit of the molten salt. Nonetheless, the results infer that ΔG is endothermic in this case.

When O_2 is present in the basic molten salt, it can function as the electron acceptor. When **1a** was photolyzed in oxygenated basic $AlCl_3$/EMIC (55 mol% EMIC) for 6 hours, five products were generated: anthraquinone (**4**) (41% yield based on consumed **1a**), anthrone (**5**) (trace), dimer **2a** (5%), 9-chloroanthracene (**6a**) (1-2%), and 9,10-dichloroanthracene (**6b**) (trace). Although **6a** was only formed in low yield, its presence in the product mixture is indicative of an electron transfer reaction. It most likely arose by the reaction of the radical cation of **1a** with Cl^-, a prominent component of the basic melt, followed by the loss of H to another species.

Because $\mathbf{1a}^{+\cdot}$ cannot be generated by electron transfer from $\mathbf{1a}^{*}$ to EMI^{+}, another species, namely O_2, must serve this function.

$$O_2 + \mathbf{1a}^{*} \rightarrow O_2^{-\cdot} \text{ (superoxide) } + \mathbf{1a}^{+\cdot} \xrightarrow{\quad Cl^- \quad} \rightarrow \mathbf{6a}$$

Two other points about this reaction need to be made. (1) The origin of the major product, anthraquinone (**4**), is unclear at present, but may involve the endo-peroxide (**3**), singlet oxygen or superoxide. Additional experiments will be required before the source of **4** is known. (2) Because dimer **2a** was formed in this reaction, excimer formation, i.e., $\mathbf{1a}^{*} + \mathbf{1a} \rightarrow$ excimer, competes with electron transfer chemistry, namely, $\mathbf{1a}^{*} + O_2 \rightarrow \mathbf{1a}^{+\cdot} + O_2^{-\cdot}$.

One might conclude from the studies on **1a** in degassed and oxygenated basic $AlCl_3$/EMIC that EMI^{+} cannot serve as an electron acceptor. This is not true. If one uses another substrate whose excitation energy is similar to that of anthracene (**1a**) but whose oxidation potential is less than that of anthracene (**1a**), ΔG in the Rehm-Weller equation will become negative, implying a fast electron transfer between donor and acceptor. 9-Methylanthracene (**1b**) possesses these properties. It has a similar excitation energy to that of **1a** but is electrochemically oxidized more easily than is **1a** in the basic melt.[12]

Photolysis of **1b** ($AnCH_3$) in degassed basic $AlCl_3$/EMIC afforded at least six products (HPLC), four of which have been isolated and characterized to date: dimer (**2b**) (anti), 9-methyl-9,10-dihydroanthracene (**7**), 9-(9-anthrylmethyl)-9-methyl-9,10-dihydroanthracene (**8a**), and 9-methyl-10-(9-anthrylmethyl)-9,10-dihydroanthracene (**8b**); yields of these products have not yet been determined. The formation of **8a** and **8b**, both of which contain the 9-anthrylmethyl group, provides good evidence that some of the photoreaction occurred by electron transfer. If the radical cation of **1b** were formed by electron transfer from the excited state of **1b** to EMI^{+}, as expected, it should have appreciable acidity based on the behavior of similar radical cations[13] and be deprotonated by Cl^{-} in the solvent to yield the 9-anthrylmethyl radical (and HCl), which is contained in both **8a** and **8b**.

$$AnCH_3^{*} + EMI^{+} \rightarrow AnCH_3^{+\cdot} + EMI^{\cdot}$$

$$Cl^{-} + AnCH_3^{+\cdot} \rightarrow HCl + AnCH_2^{\cdot} \xrightarrow{\quad AnCH_3 \quad} \rightarrow \mathbf{8a} + \mathbf{8b}$$

The formation of dimer **2b**, on the other hand, clearly shows that not all of the photoreaction occurred by electron transfer.

$$AnCH_3^{*} + AnCH_3 \rightarrow \text{Excimer} \rightarrow \text{Dimer } \mathbf{2b}$$

In addition to O_2 and EMI^+, protonated anthracene (**15**$^+$) will function as an electron acceptor in $AlCl_3$/EMIC. In a recent publication[6] it was reported that photolysis of **1a** in deoxygenated, acidic $AlCl_3$/EMIC (55 mol % $AlCl_3$) afforded, in addition to the (4+4) dimer **2a**, a series of monomeric and dimeric, oxidized, neutral, and reduced hydrocarbons (**9-14**) (**14** is an unknown hydrocarbon similar in structure to **13**). Detailed experiments demonstrated that the chemistry was initiated by electron transfer from the excited state of **1a** to protonated anthracene (**15**$^+$). The protonated anthracene (**15**$^+$) arose by protonation of **1a** by traces of HCl, a very strong acid in the acidic melt.[5] Because there were no components in the acidic melt with which **1a**$^{+\cdot}$ (and **15**$^\cdot$) can react, due to the very low basicity of the medium, **1a**$^{+\cdot}$ and **15**$^\cdot$ underwent a complex series of coupling, electron transfer, and hydrogen transfer reactions to form the ultimate products, **9-14** and **2a**.

$$\mathbf{1a} + HCl \rightleftharpoons \mathbf{15}^+ + Cl^-$$

$$\mathbf{1a} + \mathbf{15}^+ \xrightarrow{h\nu} \mathbf{1a}^{+\cdot} + \mathbf{15}^\cdot \rightarrow \rightarrow \mathbf{9\text{-}14}$$

It is reasonable to believe that any medium which can sustain both **1a** and **15**$^+$ and is also poorly basic, will yield similar photochemistry of **1a** as that observed in acidic $AlCl_3$/EMIC. A mixture of trifluoromethanesulfonic acid (CF_3SO_3H) and trifluoroacetic acid (CF_3COOH) has these requirements.

When **1a** was photolyzed in deoxygenated CF_3COOH, which is a moderately strong acid (H_0 = -2.7[14]), the (4+4) dimer was generated exclusively.[7] This is not surprising because ^1H NMR and Uv-vis studies showed that **1a** is completely unprotonated in CF_3COOH. When **1a** was photolyzed in CF_3SO_3H, a very strong acid (H_0 = -13.7[14]), no photoreaction occurred; **1a** was recovered quantitatively on workup. **1a** is completely protonated in CF_3SO_3H (^1H NMR) and the resulting **15**$^+$ is photoinert.

$$\mathbf{1a} \underset{CF_3COOH}{\xrightarrow{h\nu}} \mathbf{2a} \qquad\qquad \mathbf{1a} \underset{CF_3SO_3H}{\rightarrow} \mathbf{15}^+ \xrightarrow{h\nu} \text{No Reaction}$$

It is clear from the H_0 values of the two pure acids, and the behavior of **1a** in them, that a mixture of the two acids with an intermediate H_0 will sustain an equilibrium mixture of **1a** and **15**$^+$. 2% of CF_3SO_3H in CF_3COOH (w:w; H_0 = -8.1[14]) is such a mixture. When **1a** was photolyzed in this acid mixture in the absence of oxygen, a complex mixture of hydrocarbons, reminiscent of that formed in acidic $AlCl_3$/EMIC, was generated. As can be seen in Table I, not only were the same products generated in the acid mixture and molten salt, but in approximately the same yields for reactions run for comparable times. It is reasonable to conclude that the photoreaction in CF_3SO_3H/CF_3COOH was initiated by electron transfer from **1a** to **15**$^+$.

$$\mathbf{1a} \underset{\text{acid}}{\overset{\text{mixed}}{\rightleftharpoons}} \mathbf{15}^+ \xrightarrow{h\nu} \mathbf{9\text{-}14} + \mathbf{2a}$$

Table I. Product Distribution from the Photolysis of Anthracene in CF_3SO_3H/CF_3COOH^a and $AlCl_3/EMIC.^b$

entry	% Product yield						
	9	**10**	**11**	**12**	**13**	**14**^{c}	**2a**
CF_3SO_3H/CF_3COOH^d	9.3	6.0	1.4	3.0	0.4	3.8	1.8
$AlCl_3/EMIC$	7.3	6.8	2.3	1.5	1.0	1.8	2.0

(a) Reaction time = 28 hr.; 52% of **1a** was consumed. 24% material balance was attained. (b) Reaction time = 24 hr.; 60.4% of **1a** was consumed. 22.7% material balance was attained. (c) An unknown condensed product similar in structure to **13**. (d) 9,9′-Bianthracene and two other unknown dimeric products were also formed in the reaction.

CONCLUSIONS

Photoinduced electron transfer is a common, but not exclusive, reaction for **1a** and **1b** in $AlCl_3/EMIC$. Under the appropriate circumstances O_2, EMI^+, and protonated anthracene (**15**$^+$) serve as electron acceptors. CF_3SO_3H/CF_3COOH is a good mimic for HCl in acidic $AlCl_3/EMIC$, at least as far as the photochemical behavior of anthracene (**1a**) is concerned.

ACKNOWLEDGMENT

This research was supported by the Air Force Office of Scientific Research.

REFERENCES AND NOTES

1. D. O. Cowan, Elements of Organic Photochemistry, Chapter 2, Plenum, New York (1976).

2. M. E. Sigman, S. P. Zingg, R. M. Pagni, and J. H. Burns, Tetrahedron Lett., 5737 (1991).
3. J. S. Wilkes, J. A. Levisky, R. A. Wilson, and C. L. Hussey, Inorg. Chem., **21**, 1263 (1982).
4. P. S. Mariano, Acc. Chem. Res., **16**, 130 (1983).
5. (a) G. P. Smith, A. S. Dworkin, R. M. Pagni, and S. P. Zingg, J. Am. Chem. Soc., **111**, 525 (1990). (b) G. P. Smith, A. S. Dworkin, R. M. Pagni, S. P. Zingg, J. Am. Chem. Soc., **111**, 5075 (1990).
6. G. Hondrogiannis, C. W. Lee, R. M. Pagni, and G. Mamantov, J. Am. Chem. Soc., **115**, 9828 (1993).
7. G. Hondrogiannis, R. M. Pagni, and G. Mamantov, submitted to Tetrahedron Lett.
8. R. G. Harvey, L. Arzadon, J. Grant, and K. Urberg, J. Am. Chem. Soc., **91**, 4535 (1969).
9. M. Takagi, T. Hirabe, M. Nojima, and S. Kusabayashi, J. Chem. Soc., Perkin Trans., I, 1311 (1983).
10. D. Rehm, A. Weller, Isr. J. Chem., **8**, 259 (1970).
11. R. T. Carlin, P. C. Truelove, and R. A. Osteryoung, Electrochimica Acta, **37**, 2615 (1992).
12. Unpublished results.
13. F. G. Bordwell and J.-P. Cheng, J. Am. Chem. Soc., **111**, 1792 (1989).
14. S. Saito, S. Saito, T. Ohwada, and K Shudo, Chem. Pharm. Bull., **39**, 2718 (1991).

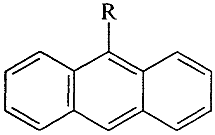

1 a : R=H
b : R=CH_3

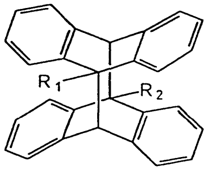

2 a : R_1=R_2=H
b : R_1=R_2=CH_3

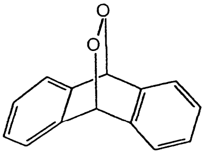

3

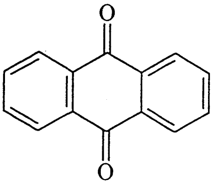

4

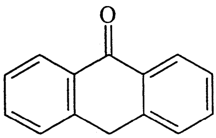

5

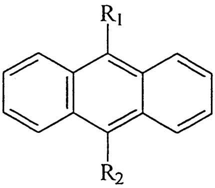

6 a : R_1=Cl , R_2=H
b : R_1=R_2=Cl

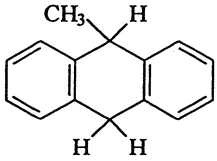

7

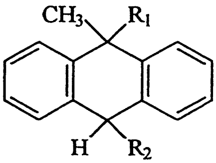

8 a : R_1=9-anthrylmethyl, R_2=H
b : R_1=H , R_2=9-anthrylmethyl

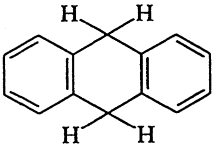

9

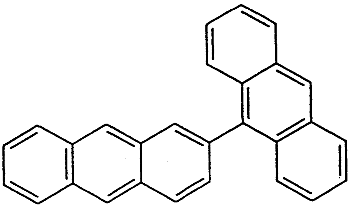

10

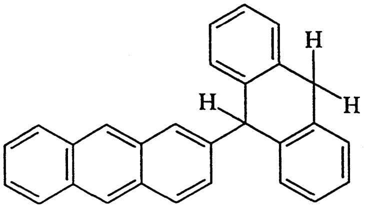

11

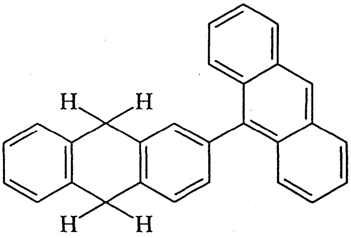

12

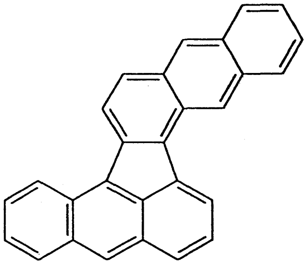

13

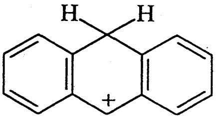

15^+

DOI: 10.1149/199413.0646PV

THE ELIMINATION OF COMPONENT MATERIALS FROM ALUMINUM MATRIX COMPOSITES BY A MOLTEN SALT PROCESS AND THE MECHANISM OF THIS PROCESS

Tetsuo INOUE and Hideyuki KANEMATSU
Department of Materials Science and Engineering
Suzuka College of Technology, Suzuka, 501-02, JAPAN

Takeo OKI
Department of Materials Science and Engineering
Faculty of Engineering, Nagoya University, Nagoya,
464-01, JAPAN

ABSTRACT

The elimination process using a molten KCl-NaCl system and the mechanism of this process were investigated experimentally. The specimens were Si_3N_4/2024(No. 1), SiC/6061(No. 2) and K_2TiO_3, Al_2O_3 and SiC/Al-Si alloy (No. 3) system composites. These aluminum matrix composites were treated in the molten salts at 1033K and the extent of the elimination of various components was measured by X-ray diffraction(XRD), X-ray photoelectron spectroscopy(XPS) and electron probe microanalysis(EPMA) respectively. The results indicated that various components of the composit specimens were eliminated from these composites by being transferred into molten salts. The extent of elimination of carbide and nitride components was different from oxide components, such as Al_2O_3, due to the difference in wettability of the component materials by the molten salt.

INTRODUCTION

Practical techniques for recycling and reclamation of metal matrix composite materials are required for the commercialization of these advanced materials (2)-(4). Particularly, the development of aluminum matrix composite materials is dependent on utilizing aluminum metal sources more efficiently and in an environmentally safe manner since the production cost of secondary aluminum from these sources has to be much lower than from any other process. However, a useful recycling process for aluminum from composite materials has not been established as of yet. Therefore, the elimination process of ceramic components from aluminum matrix composite materials by molten KCl-NaCl salts and the mechanism of this elimination process were investigated. In this process, materials were immersed in the molten salts without electrolysis. If the effectiveness of the process is verified by our experiments, it is possible for aluminum alloys to be recovered from composite materials using less energy than is now required.

EXPERIMENTAL

The specimens used were Si_3N_4/2024(No. 1), SiC/6061(No. 2) and K_2TiO_3, Al_2O_3 and SiC/Al-Si alloy (No. 3) systems. Table 1 shows the chemical composition of each specimen, their ceramic components and volume fractions. The salts used consist of NaCl and KCl basically, with the addition of small quantities of fluorides such as LiF, NaF and KF to remove the surface oxide films on the specimens. Prior to treating, the mixed salts were heated to 1033K, and held at that temperature for about an hour in order to reduce the amount of moisture.

At first, specimens(15g) were immersed in molten salts at 1033K for 0.6ks-3.6ks. The molten salt, in a mullite crucible, was agitated intermittently during the treatment in the electric furnace. After immersion and agitation, the crucible was slowly cooled to room temperature in the furnace, and then the specimen and salt was separated mechanically. During the operation, the atmosphere in the furnace was not especially regulated, since the molten salt itself plays an effective role as a defense against the ambient atmosphere. The salts and specimens, after separation, were examined by X-ray diffraction(XRD), X-ray photoelectronspectroscopy(XPS) and electron probe microanalysis(EPMA) respectively, and the extent of the elimination of ceramic components was confirmed.

RESULTS AND DISCUSSION

Fig. 1 shows some X-ray diffraction spectra for Specimen No. 1. For the non-treated specimen, not only were aluminum peaks observed, but also those of the SiC ceramic component (Fig.1-(a)). However, there were no peaks of the ceramic component in the specimen treated for 3.6ks in molten salts containing 5% NaF (Fig. 1-(b)). For the specimen treated in molten salts with 10% NaF for 3.61 sec, the same result as with 5% NaF was obtained (Fig. 1-(c). These XRD results seem to suggest that the SiC component was almost completely eliminated, but the details were further investigated with XPS and EPMA. Fig. 2 shows some XPS spectra for Specimen No. 1 treated for 3.6ks by various molten salts. The remarkable peak of Si2p at about 100eV for the non-treated specimen which corresponds to the presence of SiC (Fig. 2-(a)) was not observed in treated specimens (Fig. 2-(b) ~ (e)). Instead of SiC, all results of experiments with treated specimens indicate the presence of SiO_2 except that treated by molten salts containing 10% NaF (fig. 2-(c)). This SiO_2 is formed by the reaction between the SiC component and oxygen in the surface oxide film on the specimen. Therefore, the amount of SiO_2 will represent the inadequacy of the SiC elimination process. From the results shown in Fig. 1 and 2, the following conclusion can be drawn: The SiC component can be eliminated by the treatment, but the extent of elimination relates to oxide films removed by molten salts. Oxide films can be removed more easily for the salts containing 10% NaF than those containing 5% NaF. In terms of fluoride species, the removing capability increases in the following order: LiF, KF, NaF.

Fig. 3 shows the X-ray diffraction spectra for Specimen No. 2. For a non-treated specimen, several peaks due to Si_3N_4 components, as well as those due to the aluminum matrix, were observed (Fig. 3-(a)). On the other hand, there were no Si_3N_4 peaks in specimens treated by molten salts containing 10% NaF (Fig. 3-(b)). The possibility that the Si_3N_4 component was eliminated, as indicated by the XRD results, was also confirmed by XPS. Fig. 4 shows the XPS spectra for treated and non-treated specimens compared to the sintered Si_3N_4 ceramic as a reference. The spectrum for the non-treated specimen contains two Si_3N_4 peaks between 100 and 200eV (Fig. 4-(b)). However those peaks disappeared in the spectrum of the treated specimen (Fig. 4-(c)). These results indicate that the Si_3N_4 component can be also eliminated from aluminum composite materials by the molten salts.

Fig. 5 shows the X-ray diffraction spectra for Specimen No. 3 and their change with immersion treating time. The spectrum of the non-treated specimen contains the peaks of all the ceramic components such as K_2TiO_3, Al_2O_3 and SiC as well as those of the aluminum matrix (Fig. 5-(a)). The silicon peaks in the figure belong to

Si in the aluminum alloy matrix. In these experiments, the molten salts were agitated immediately after the specimens were immersed and cooled after the passage of a certain amount of time. Fig. 5-(b) shows the results of XRD for the specimen cooled immediately after agitation. In this spectrum, the peaks of K_2TiO_3 and SiC have already disappeared, which suggests that the elimination rates of both components from composites are very high. On the other hand, the peak due to Al_2O_3 at about 43° (2θ /deg) was observed, although its intensity decreased in (b) less than in (a). However, the peak could not be seen for specimens treated for more than 0.9ks(Fig. 5-(c) ~ (e)). Therefore, it should be concluded that the elimination rate of Al_2O_3 from composites is much lower than those of other components such as SiC and K_2TiO_3. The two silicon peaks at about 48 and 56° were also observed with treated specimens. These peaks indicate the presence of silicon as one of the alloyed elements in treated specimens. This result suggests that the recovery of the alloy itself from composites will also be possible using this process.

These salts, without immersion treatment, are inherently white. However, the salts cooled after the immersion treatment of composites look gray, which suggests the presence of some ceramic components that were transferred from the composites. Fig. 6 shows the results of XRD for the salts which were cooled and filtered after being used to heat Specimen No. 3. The salts cooled just after agitation contain several peaks due to ceramic components such as Al_2O_3, K_2TiO_3 (Fig. 6-(a)). The intensity of these peaks increased with increased treatment time, and the tendency was the most remarkable for Al_2O_3. From all these results, it can be concluded that the elimination rate of Al_2O_3 is much lower than that of K_2TiO_3. In these spectra, there are no SiC peaks. The reason for this has not been clarified in detail yet. Perhaps this component was removed during the filtration operation.

All these results confirm that some representative ceramic components can be eliminated from composites by the molten salts. However, it is not clear why those components transfer from the composites to the molten salt phase. Part of the explanation can be deduced from earlier experiments (1,5).

The ability of the molten salt solution to wet the aluminum matrix is much lower than the melt's ability to wet the ceramic components. Therefore, the ceramic components in the composites in contact with the molten salts will transfer continuously into the molten salt phase and, as a result, the elimination will be completed. The low elimination rate of Al_2O_3 is attributed to its low wettability in the melt. The surface oxide films must also be removed by the addition of various fluorides, since their presence prevents the direct contact between ceramic components and molten salts.

CONCLUSIONS

The elimination of ceramic components from composites in molten NaCl-KCl solutions was investigated and the following results were obtained.

(1) Various ceramic components such as SiC, Si_3N_4, K_2TiO_3, and Al_2O_3 were removed from the composites and transferred to the molten salt phase by the immersion treatment.

(2) The addition of fluorides such as Lif, KF, Naf etc. is indispensable for the elimination process, since they remove the surface oxide films on the specimen that would otherwise present the transfer of ceramic components.

(3) The capability of removing oxides was the highest for NaF, and it decreased in this order: NaF, KF, LiF. The extent of elimination of ceramic components increased with fluoride content and immersion time.

(4) The transfer of ceramic components to molten salts is probably caused by the difference in wettability of aluminum alloy matrices and the component materials.

(5) The aluminum alloy matrix, itself, could be recovered from composites by the elimination process, which can lead to the development of an effective low energy recycling process for industry.

ACKNOWLEDGMENT

The major part of this work was supported by the Mechanical Industry Development & Assistance Foundation (Tokyo).

REFERENCES

(1) T. Inoue, H. Kanematsu and T. Oki: "SEPARATION AND RECOVERY OF ALUMINUM FROM ALUMINUM COMPOSITE MATERIALS BY MOLTEN SALT PROCESS", Proc. Intern. Conf. on Processing Materials and Properties, p755-758, TMS & MMIF, 1993.

(2) T. Nakamura, "RECYCLING PROCESSES OF METALS", Molten salts, 35(1992), p 81-94.
(3) M. Nanjoh and N. Sato, "RECYCLING OF MATERIALS", Jour. Min. Mat. Proc. Inst. Jpn., 105 (1989), p17-22
(4) R. Yamamoto: "THE PRESENT AND FUTURE PROSPECT ON ALUMINUM RECYCLING", Jour. of Min. Proc. Inst. Jpn. 107(1991)p95-102
(5) T. Choh and T. Oki, "WETTABILITY FOR FABRICATION OF METAL MATRIX COMPOSITE", Bull. of Jpn. Inst. of Metals, 28(1989), p285-293

Table 1 Chemical Composition of Materials (wt%)

spec.	①	②	③
Si	0.4~0.8	<0.5	6.5~7.5
Cu	0.15~0.40	3.8~4.9	0.2
Mg	0.8~1.2	1.2~1.8	0.2~0.4
Cr	0.04.~0.35	<0.1	
comp. (vf)	Si_3N_4 (20%)	SiC (30%)	K_2TiO_3, Al_2O_3, SiC, (30%)

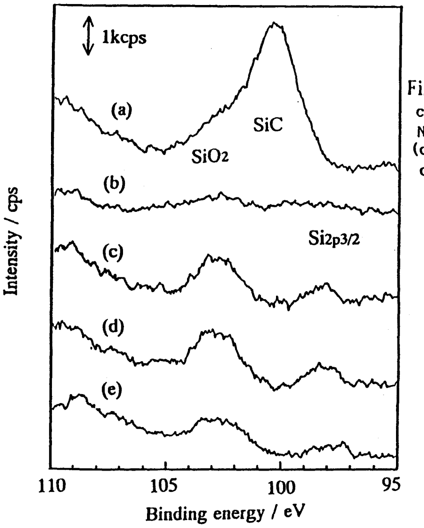

Fig. 2 ESCA spectra for SiC/6061 specimen after treated in molten salt:(a)non- treated (b)salt containing 10%NaF (c)salt containing 5% NaF (d)salt containing 10% LiF (e)salt containing 10% KF

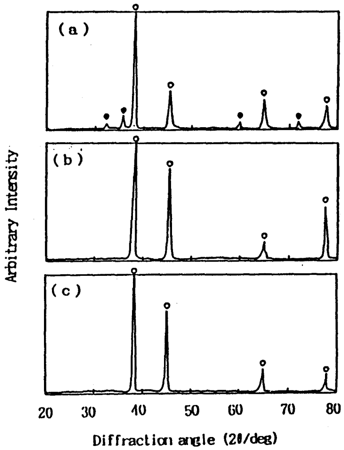

Fig. 1 X-ray diffraction spectra for SiC/6061 composite:(a)non-treated, (b)treated by KCl-NaCl molten salts containing 5% NaF, (c)treated by KCl-NaCl molten salts containing 10% NaF ○ aluminium ● SiC

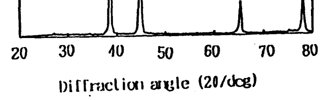

Fig. 3 X-ray diffraction spectra for Si_3N_4/2024 composite:(a)non-treated (b)treated by KCl-NaCl molten salts containing NaF in 3.6ks

○aluminium ●Si_3N_4

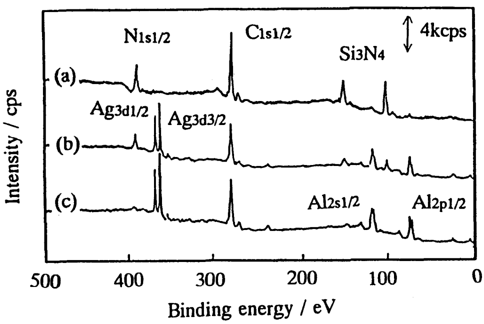

Fig. 4 ESCA spectra for Si_3N_4 and Si_3N_4/2024 specimen after treated in molten salt:(a)Si_3N_4 (b)non-treated (c)salt containing 10%NaF

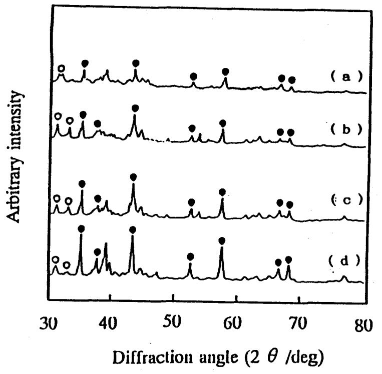

Fig. 6 X-ray diffraction spectra for involved materials in salts after treated (a)cooled after agitation (b)0.9ks agitaition (c)3.6ks agitation (d)9ks after agitation

● Al_2O_3 ○ K_2TiO_3

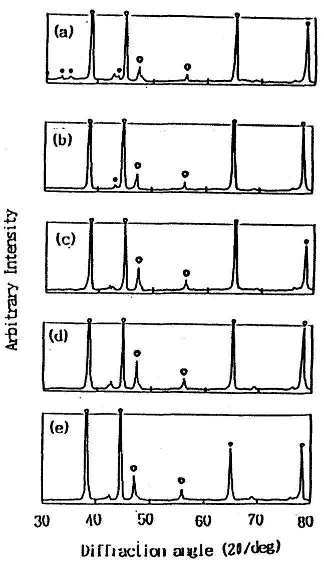

Fig. 5 X-ray diffraction spectra for Al_2O_3, K_2TiO_3, SiC/AC4C composite: (a)non-treated(b)cooled just after agitation(c)0.9ks after agitation (d)9ks after agitation ○aluminium ●K_2TiO_3 ◐Al_2O_3 ◎Si

DOI: 10.1149/199413.0654PV

A STUDY OF PRODUCTION PROCESS OF URANIUM METAL BY MOLTEN SALT ELECTROLYSIS USING ZINC CATHODE

K. Nakamura, H. Ikeda, H. Kubota
Y. Kijima* and S. Yamasaki*

Metal Mining Agency of Japan
1-24-14, Toranomon, Minato-ku, Tokyo 105, Japan

* Sumitomo Metal Mining Co., Ltd.
5-11-3, Shimbashi, Minato-ku, Tokyo 105, Japan

ABSTRACT

A molten salt electrolysis of uranium tetrachloride was investigated applying KCl - LiCl - NaCl - UCl_4 molten eutectic salts. This process is aimed at the production of high purity uranium metal for the ^{235}U isotopic enrichment process by Atomic Vapor Laser Isotope Separation (AVLIS). High current efficiency has been confirmed in the salt electrowinning process by applying a liquid zinc cathode. A series of purification processes have also been demonstrated to produce high purity uranium metal by filtration, distillation and final vacuum refining treatments of Zn - U cathode products. Optimal operating conditions are discussed in terms of each unit process.

INTRODUCTION

The AVLIS isotopic separation technology for the enrichment of ^{235}U has been studied intensively in Japan, the USA and European countries. The magnesium thermite method had been widely adopted to produce the uranium metal which is the starting material for AVLIS process. However, this resulted in a large amount of magnesium fluoride slag solid waste containing trace amounts of uranium. Hence the treatment and disposal of this radioactive waste should be required.

The molten salt electrolysis method has been developed for uranium metal production in Japan to avoid the waste problem. [1]-[3] We have been studying the electrolysis of UCl_4 (m. p. 590°C) using molten zinc as cathode. In the present paper, the experimental results on the effects of fundamental process parameters, i. e. anode geometry, current density, operating temperature, electrolyte salt composition, and the construction materials of electrolytic cells will be reported. The separation characteristics of uranium from zinc in the cathode products are also reported. [4]-[8] Figure 1 illustrates the overall flowsheet of the present process.

This work was funded by the Ministry of International Trade and Industry of Japan.

EXPERIMENT

Molten Salt Electrolysis

Prior to electrolysis experiments, uranium tetrachloride UCl_4 green powder was produced by a single reaction of UO_2 reduction with Cl_2 gas in the presence of carbon as a reductant. This operation was conducted efficiently by a vertical fixed bed reactor loaded with 1 kg/batch under the flow rate of 0.8 l/min Cl_2 at 900 °C.

$$UO_2 + 2\,Cl_2 + C \rightarrow UCl_4 + CO_2\uparrow \qquad [1]$$

Liquid zinc was selected not only to maximize the solubility of uranium in the cathode but also to facilitate the discharge of the product. Approximately 10 kg of fused zinc was charged as the cathode.

The geometry of the electrolytic cell and the two types of anodes, i. e. multi-hole and double-cylindrical ones, used in the present study is shown in Figs. 2 and 3. The cell and anode were covered by alumina or quartz cylinder to avoid the direct contact of molten salt and liquid cathode with graphite crucible. Multi-hole and double-cylindrical types of anode geometry were attempted: both types of anode geometry were aimed at facilitating the removal of electrolytic Cl_2 gas evolved during operations. The anode was set 5 cm above the surface of liquid cathode. Two component KCl - NaCl (m.p. 658 °C) and three component KCl - LiCl - NaCl (m.p. 346 °C) eutectic systems have been selected as the supporting molten salts for electrolysis. High purity guaranteed-grade salts were used in all experiments.

The operating temperatures were fixed to 800 °C with alumina insulator and 700 °C with quartz insulater respectively for the KCl - NaCl and KCl - LiCl - NaCl eutectic salts. All the experiments were carried out to maintain the concentration of uranium at constant by adding UCl_4 regularly during electrolysis.

The electrowinning of uranium was carried out at a constant current mode by monitoring the potential difference between the electrodes and that of the cathode with reference to an Ag/AgCl electrode:

$$UCl_4 \rightarrow U^{4+} + 4\,Cl^- \qquad [2]$$

$$U^{4+} + 4\,e^- \rightarrow U\,(s) \qquad [3]$$

$$4\,Cl^- \rightarrow 2\,Cl_2\,(g)\uparrow + 4\,e^- \qquad [4]$$

As shown in Table 1, all the electrolytic reduction experiments were performed to confirm the effects of anode geometry, operating temperature, the concentration of uranium in the molten salt system, and the behavior of insulating crucible between the electrodes. The experiments were performed in a mode of constant electrical current to maintain the anodic current density at either 1.14 A/cm^2 or 2.41 A/cm^2: the total electrical current of either 45 A or 70 Awas selected.

The experimental equipment was installed in a glove-box of argon atmosphere (>99.999 %) in order to avoid the effects of atmospheric moisture and oxygen, since they have deleterious effects in fused salt experiments.

Zinc Separation

To separate U/Zn alloys from metallic zinc and other impurities, three steps were performed: (1) the filtration of U - Zn cathode products to separate solid U/Zn alloys from zinc, (2) the distillation of filtered cake alloys to obtain sponge uranium, and finally (3) the vacuum refining of uranium. The outline of the distillation equipment is shown schematically in Fig. 4.

After the electrolysis process, solid intermetallic alloy compounds, i. e. UZn_{12} and U_2Zn_{17}, were formed in the cathode melt by decreasing the temperature, and these solid alloys were sedimented by the difference of specific gravities from the metallic zinc which contains a very low amount of uranium. Thus, these intermetallic alloys were separated mechanically by either graphite or alumina ceramic filter elements at about 500 °C in argon atmosphere.

In the distillation step, the filtered cakes were then heated up to 900 °C to 950 °C in argon atmosphere to remove residual zinc and other impurities from the filtered cake. In this treatment calcia, magnesia and yttria were examined as the construction material for the crucibles.

The final finishing vacuum purification step was performed at 1250 °C, and the reactivity of the yttria, high-purity magnesia, and yttria-coated graphite crucibles with uranium were also studied.

RESULTS AND DISCUSSION

Molten Salt Electrolysis

The experimental results are summaried in Table 1. Maximum current efficiency of 87 % was attained in Run E1. The uranium content in the bath was maintained constant by adding UCl_4 regularly. This was attained by monitoring the potential between the electrodes during electrolysis as shown in Fig. 5. Current efficiency of 77 % was obtained in Run E2 when the content of UCl_4 was 20 wt % in the electrolytes. The current efficiency tends to decrease with the increase of UCl_4 contents in the molten salts. This might be explained by the increase of the counteracting effects of the reverse reactions. After electrolysis, the salts attached to the cathode products were removed easily, because the surface of the alloy was flat. Besides, it was confirmed that the deposited uranium was distributed homogeneously in the cathode (Fig. 6).

Although it was confirmed from the phase diagram that operation under high temperature will favor the solubility of uranium into the cathode, the operation should be made at 700 °C rather than 800 °C to mitigate the corrosion of construction materials. The selection of the material for the crucible should be important. In the operations at 800 °C, alumina was adopted instead of quartz, since the quartz crucible was attacked by the deposited metal uranium and it caused to promote the side-reactions to decrease the current efficiency. Hence, it is confirmed that the selection of crucible materials is important.

Stable electrolysis was attained with maximum total current of 70 A by applying double-cylindrical anode in Run E3, while it was reduced to 45 A with multi-hole anode. It has been confirmed that the effective removal of Cl_2 gas is also an important factor for electrolysis. This was confirmed by visual observation that the double-cylindrical geometry is superior to the multi-hole geometry for gas removal .

Zinc Separation

The experimental results are summarised in Tables 2 to 4. The uranium concentrations of 7 wt % to 8 wt % in the cathode zinc were further increased up to 14 wt % to18 wt % by the filtration step. The filtration was conducted easily by 140 µm and 400 µm of pore sizes. The separation performance is dependent on the distribution of uranium in the cathode: both the operational temperature and pore size of the filter had no significant effects. The residual uranium concentrations in the zinc filtrate were limited to less than 0.12 wt %.

The filtered cake was then distilled to remove zinc from uranium at 900 °C to 950 °C in argon atmosphere. It has been confirmed that pure uranium sponge can be produced free from carbon by applying either calsia, yttria, or magnesia crucible, and caution should be paid to the handling of the uranium, because of its ignition behavior even at room temperature.

The uranium sponge was further refined under 10^{-3} Torr vacuum at 1250 °C to produce about 850 g of purified uranium. Magnesia crucible can be applied for this vacuum refining, because magnesium can easily be removed in the vacuum refining step. As can be seen from Table 5, the final concentrations of various impurities, such as Zn, Mg, Na and K, were reduced to trace levels of several 10 ppm. This level of contamination is compatible to the preliminary specifications for the starting material in the AVLIS process. On the other hand, the metallic zinc recovered by these steps can be returned to the electrolysis process as the cathode.

CONCLUSIONS

The molten salt electrowinning of uranium tetrachloride applying liquid zinc as the cathode was investigated experimentally, and sufficient current efficiency has been attained. Moreover, high purity uranium has been obtained by separating uranium in the

U/Zn alloys from zinc and other impurities by filtration, distillation and vacuum refining steps. The process developed in the present study has demonstrated that the product uranium metal is applicable to the AVLIS isotopic enrichment process as the starting material. Further studies on the production process are under way. This study was conducted by Sumitomo Metal Mining Co., Ltd. under contract with the Metal Mining Agency of Japan.

REFERENCES

1. T. Kuroda: Electrochemistry Handbook, 2nd Edition, Maruzen, 1055(1964).
2. T. Kuroda: Denki Kagaku, 33, 116(1965).
3. T. Mukaibo and M. Kanno: J. Atomic Energy Society Japan, 7[8], 410(1965).
4. Knighton, J. B. Burris et al.: ANL-6223(1961).
5. S. Lawroski: ANL-5789, 90(1957).
6. P. Chiotti, H. H. Klepfer et al.: J. Metals, 9, 51(1957).
7. S. Lawroski: ANL-5730, 114(1957).
8. S. Lawroski: ANL-5820, 127(1957).

Table 1 Summary of Molten Salt Electrolysis Operations

Test No.		**Run E1**	**Run E2**	**Run E3**
Support electrolyte	-	KCl - NaCl - LiCl	KCl - NaCl - LiCl	KCl - NaCl
Charged salt	kg	1.66	1.66	1.68
Charged Zn	kg	9.86	10.0	9.86
UCl_4 content	wt %	10	20	10
Temperature	°C	700	700	800
Total current	A	45	45	70
Current density$^{1)}$	A/cm^2	1.14	1.14	2.41
Current density$^{2)}$	A/cm^2	0.28	0.28	0.45
Anode type	-	Multi-hole	Multi-hole	Double-cylindrical
Voltage	V	4.5 - 5.1	3.7 - 4.8	4.7 - 6.6
Deposited U	g	896	791	827
Current efficiency	%	87	77	83

Electrode distance is fixed at 5 cm, 1) anode, 2) cathode.

Table 2 Summary of Cathode Filtration Operations

Test No.		**Run F1**	**Run F2**	**Run F3**
Temperature	°C	550	500	500
Filter material	-	Graphite	Graphite	Alumina
Pore size	μm	10	120	400
Charged ingot	kg	10.22	9.83	8.86
Filtercake	kg	5.18	5.43	4.72
U content	wt %	18.6	13.8	15.3
Filtrate zinc	kg	4.87	4.31	4.14
U content	wt %	-	0.06	0.12

Table 3 Summary of Distillation Operations

Test No.		**Run D1**	**Run D2**	**Run D3**
Crucible material	-	Calcia	Yttria	Magnesia
Charged cake	kg	7.36	8.04	6.99
Recovered U	g	471	857	796

Temperature was fixed at 920 °C.

Table 4 Summary of Vacuum Refining Operations

Test No.		**Run R1**	**Run R2**	**Run R3**
Crucible material	-	Yttria	High purity Magnesia	Graphite coated with Yttria
Charged U	g	852	791	828
Purified U	g	852	791	827

Temperature and vacuum were fixed at 1250 °C and ~ 10^{-3} Torr, respectively.

Table 5 Analytical Results of Impurities in Uranium Products

	Al	**C**	**K**	**Mg**	**Na**	**Si**	**Y**	**Zn**
Filtercake	480-880	220-680	<100	<2	<160	<50	<10	-
Distilled U	510-950	120-600	<55	<12	<110	30-300	6-600	46-202
Purified U	460-700	160-600	<10	<3	<40	40-200	<1-200	<22-43

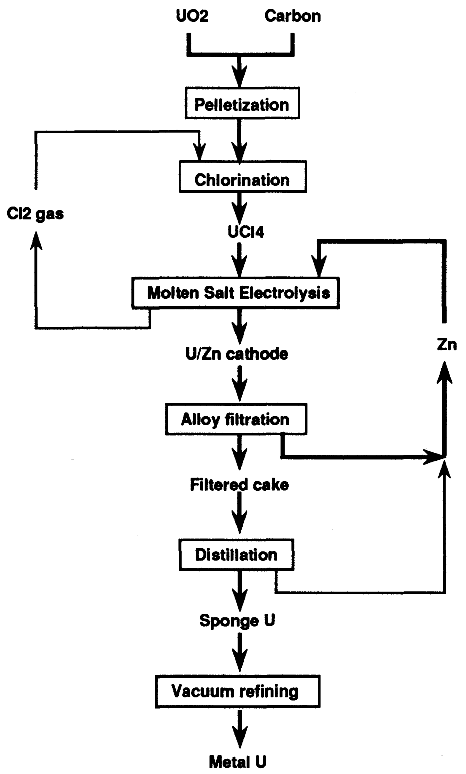

Fig. 1 Flowsheet for high purity uranium metal production.

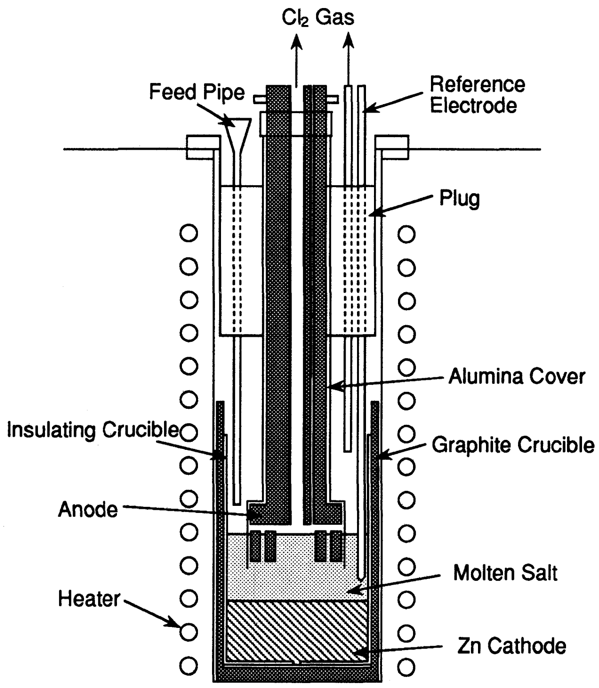

Fig.2 Schematics of Electrolytic Cell

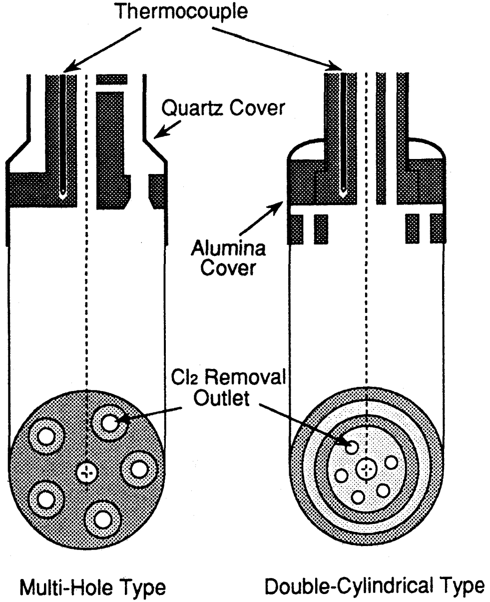

Fig.3 Anode Geometry

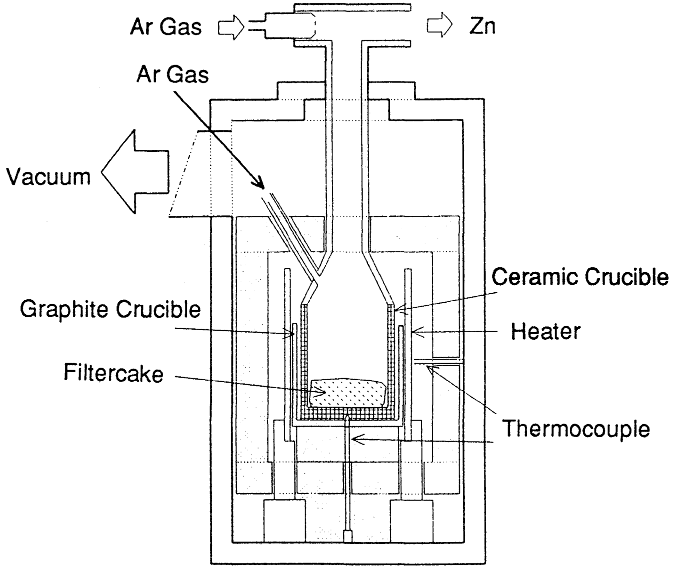

Fig.4 Distillation Furnace

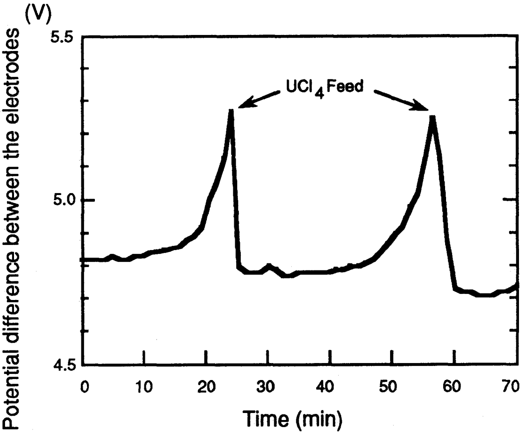

Fig.5 Potential difference between the electrodes vs. Time

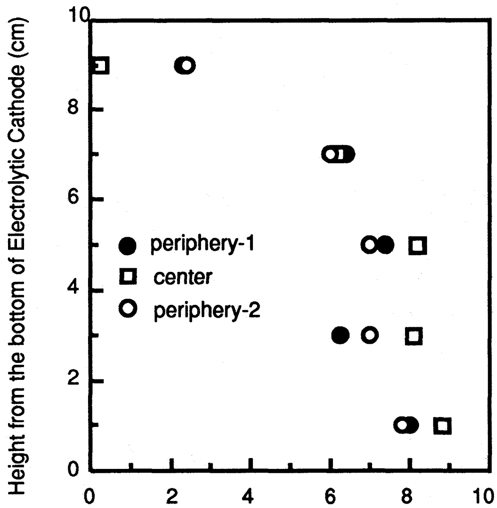

Fig.6 Uranium Concentration in the Electrolytic Cathode

DOI: 10.1149/199413.0665PV

A PRELIMINARY STUDY ON REDUCING URANIUM OXIDE (UO_2,U_3O_8,UO_3) BY FLUORIDE MOLTEN SALT ELECTROLYSIS

Yutaka Takasawa, Kazuaki Ota, Takeshi Onoue, Sumio Yamagami
Naka Nuclear Development Center, Mitsubishi Materials Corporation
1002-14 Mukoyama, Nakamachi, Nakagun, Ibaraki 311-01, Japan

Hajime Ikeda, Hiroshi Kubota, Katsutoshi Nakamura
Metal Mining Agency of Japan
Tokiwa Bldg. 1-24-14 Toranomon, Minato-ku, Tokyo 105, Japan

Kazuhiro Endo
Nuclear Engineering Center, Mitsubishi Materials Corporation
1-38-9 Kakigaracho, Nihonbashi, Chuo-ku, Tokyo 103, Japan

ABSTRACT

Atomic vapor laser isotope separation (AVLIS), which is a promising uranium enrichment technology for the next generation, needs uranium metal for feed material. Commercial production of uranium metal in the world is done by thermite reduction of UF_4 with magnesium. Considering economical performance, minimization of waste production and the continuous process concept, an electrolytic process for producing uranium metal directly from uranium oxide will offer potential advantages over the existing commercial process. Electrolytic reduction of UO_2, U_3O_8 and UO_3 in molten fluoride salt mixture BaF_2-LiF-UF_4 at 1200 ℃ was carried out to examine electrolytic behavior. Polarization curves, off gas analysis by mass spectrometer and ΔGs of formation of UO_2 from U_3O_8 with carbon monooxide or carbon, indicate that part of highly oxidized uraniums are reduced to UO_2 and electrolyzed into uranium metal.

INTRODUCTION

In the uranium enrichment of the nuclear fuel cycle, atomic vapor laser isotope separation (AVLIS) will be a promising uranium enrichment technology for the next generation because of its cost performance and high enrichment efficiency. In this AVLIS enrichment process, uranium metal or uranium metal alloy will be used as feed material.

Today, commercial production of uranium metal in the world is done by thermite reduction of uranium tetra fluorides with magnesium(1). In this thermite process, magnesium fluoride is produced as a byproduct. This byproduct needs to be treated to reduce its uranium contamination for disposing of it or selling it on the market.

Considering economical performance, minimization of waste production and the continuous process concept, an electrolytic process for producing uranium metal directly from uranium oxide will offer potential advantages over the existing commercial process(2).

In the uranium metal production plant for AVLIS we are now considering, yellow cake will be the starting material, and this yellow cake will be dissolved in nitric acid, purified by solvent extraction, denitrated, calcinated and reduced to produce uranium dioxide. Thus uranium oxides such as UO_3, U_3O_8 and UO_2 are intermediate or final row materials for metal conversion by electrolysis. Availabilities of these oxides may enable its simplification of the plant pre-treatment process such as calcination and reduction of uranium tri-oxide.

In this study, electrolytic reduction of these uranium oxides was carried out to examine their reduction process and to evaluate their availabilities for electrolysis.

This work was funded by the Ministry of International Trade and Industry of Japan.

EXPERIMENT

Materials

Barium fluoride, lithium fluoride and uranium fluoride salts mixture was used as electrolysis. Its composition was 74wt.%BaF_2-11wt.%LiF-15wt.%UF_4. Uranium tetra-fluoride acts as solvent for uranium oxide in this electrolysis. BaF_2 and LiF were regent grade chemicals. Uranium tetra-fluoride was produced by the reaction of UO_2 with HF at about 400 ℃. These fluorides were mixed and premelted before experiment. In most cases, uranium tri-oxide produced by fluidized bed denitration was used as a starting material. UO_3 was also treated in a vacuum furnace to remove remaining acidic moisture at 450 ℃. U_3O_8 was prepared by calcination of UO_3 in the N_2 atmosphere at 650 ℃. UO_2 was prepared by reduction of UO_3 with hydrogen at 600 ℃. Uranium dioxide was used as standard material, and other uranium oxides were use in a parametric examination.

Apparatus

The schematic diagram of the experimental apparatus is shown in Figure 1. And the outline of the electrolysis apparatus is listed in Table 1. The electrolytic cell has a size of 200mm inner diameter and 350mm height and is made of graphite. The anode is made of graphite which has a cylindrical shape with slit as a standard case. The cathode rod is made of tungsten and its size is 22mm in diameter. It is considered to act as an uranium electrode under electrolysis because the tungsten surface is covered with liquid uranium. A graphite uranium metal receiver covered with boron nitride had a capacity for 3 kg uranium metal and was set just below the cathode.The electrolytic cell was enclosed in a quartz tube with steel flanges so that a gas tight enclosure was achieved. High purity argon gas (>99.999%) was used as purge gas in the cell. Off gas was introduced to gas mass spectrometry. This spectrometer can provide the spectrum scanning any continuous range of masses between 1 and 300 amu (atomic mass unit) and the monitoring of time-dependent data of selected channels such as CO, CO_2 and CF_4 gases. Direct current for electrolysis had a capacity of 0～20V and 0 ～500A. Induction heating which had a maximum heating capacity of 1400 ℃ was used to bring the cell to the experiment temperature of about 1200 ℃ and maintain it during the experiment.

Experimental Procedure

Mixture of LiF, BaF_2 and UF_4 was pretreated in a vacuum at 400 ℃ and in Ar at 800 ℃ for 30 minutes in order to evacuate volatile species and moisture, then heated up to about 1200 ℃, which is well over the melting point of LiF-BaF_2-UF_4 electrolyte. The cathode and anode electrodes assembly, and uranium receiver were immersed slowly into the electrolyte to the desired depth and a brief pre-electrolysis was conducted to evacuate still remaining volatile impurities. The pre-electrolysis time was decided by measuring the off-gas composition such as CO, CO_2 and CF_4. After pre-electrolysis, polarization curves before and after uranium oxides feed were measured in the range of 0 to 2.4 A/cm^2 at anode. All of the experiments were carried out by constant current mode. During the experiments, uranium oxides were fed periodically into the cell and off-gas composition was analyzed continuously with electrolysis. Direct current, cell voltage, temperature, and induction heating power were also recorded continuously. After electrolysis, cathode and anode electrodes assembly, and uranium metal receiver were removed upward in order to minimize back-reaction of the metal with the electrolyte. After cooling, uranium metal was removed from the receiver and was weighed. Current efficiencies were calculated by off gas volume of CO, CO_2 and CF_4, and by the metal produced.

RESULTS AND DISCUSSION

Polarization Curves

Polarization curves obtained after uranium oxides (UO_2, U_3O_8 and UO_3) addition are shown in Figure 2. These curves were obtained by the anode current density gradually increasing up to 2.4 A/cm^2. There are two decomposition voltages at about 1.5V and 2.7V and small shoulders between 3 and 4 volts. These voltages are responsible for UO_2 and UF_4 decomposition voltages, respectively. These three curves show that there are no difference. The result shows that electrolytic reductions of these UO_2, U_3O_8 and UO_3 seem to progress in the same way.

Off-Gas Analysis

Figure 3 shows the typical gas mass spectrum from 1 to 80 amu (atomic mass unit) during electrolysis. The peaks at 20, 36, 38, and 40 amu are due to Ar gas, 12, 14, 28 and 29 are CO, 16 and 44 are CO_2 and 69 is CF_4. From this result, no gases are generated except for CO, CO_2 and CF_4. During electrolysis the concentrations of CO, CO_2 and CF_4 gases in the off-gas were monitored. And Figure 4 shows the off-gas (CO, CO_2 and CF_4) analysis by gas spectrometry during electrolysis. The major components of off-gas were CO and CO_2. CF_4 gas was not detected when uranium oxides were periodically fed, but without feeding uranium oxides CF_4 gas was gradually generated. After feeding UO2, the concentration of oxide ion in the electrolyte was getting lower, so that UF_4 in the electrolyte decompose by the following reaction [1].

$$UF_4 + C \rightarrow CF_4 + U \quad \cdots\cdots\cdots\cdots [1]$$

Figures 5 and 6 show the off-gas (CO, CO_2 and CF_4) analysis by gas spectrometry during electrolysis of U_3O_8 and UO_3, respectively. They show that the higher the oxidation state of uranium oxides that were fed periodically, the higher the CO_2 concentration peak in off-gas was observed. Its peak appearance was so rapid. Figure 7 shows the relation between O/U ratio of the uranium oxides and the peak area of CO2 gas. Its increase of CO_2 peak area had a tendency to increase with its higher O/U ratio.

ΔGs of Formation of UO_2 From U_3O_8 by Reaction CO and C

At a high temperature such as 1200 ℃, UO_3 is not so stable that it could be reduced into U_3O_8 in the electrolytic cell atmosphere [2].

$$3UO_3 \rightarrow U_3O_8 + (1/2)O_2 \quad \cdots\cdots\cdots\cdots[2]$$

As far as U_3O_8 is concerned, CO gas and C, which are dissolved in the electrolyte, could react to reduce U_3O_8 into UO_2. According to thermodynamic calculations, ΔGs of formation of UO_2 from U_3O_8 by reaction CO and C at 1200 ℃ are below zero as follows(3).

$$U_3O_8 + 2CO \rightarrow 2CO_2 + 3UO_2 \qquad \Delta G_T^o = -59200+7.5T \text{ cal/mol} \quad \cdots\cdots\cdots\cdots[3]$$
$$U_3O_8 + 2C \rightarrow 2CO + 3UO_2 \qquad \Delta G_T^o = 22400-75.9T \text{ cal/mol} \quad \cdots\cdots\cdots\cdots[4]$$
$$U_3O_8 + C \rightarrow CO_2 + 3UO_2 \qquad \Delta G_T^o = -18400-34.2T \text{ cal/mol} \quad \cdots\cdots\cdots\cdots[5]$$

Thus, U_3O_8 will be thermodynamically reduced to UO_2 under this condition.

Current Efficiency

Current efficiency was calculated by obtained uranium metal or the volume of generated gas. They are shown in Table 1. This indicates that higher current efficiency can be obtained by feeding higher oxidation states of oxides. However, it is necessary to pay some attention to the evaluation of current efficiency by off-gas data, when U_3O_8 and UO_3 are used as feed materials, and the reactions are discussed above.

Two chemical and electrochemical processes can be considered as the reduction processes of U_3O_8 and UO_3. They are shown in Figure 8. The first case is that U(Ⅵ) and (V) are directly reduced to U(0) electrochemically. The second case is that U_3O_8 and UO_3 are not directly reduced to uranium metal by electrolysis. They are chemically reduced to UO_2 by the reaction with carbon in the cell, and then UO_2 was electrically reduced into uranium metal. The off-gas data include the volumes of CO and CO_2 gas generated by the reactions of [2], [3], [4] and [5]. So we have to estimate these volume, and subtract it from the volumes of off-gas data. Current efficiency was calculated on the assumption that U(Ⅳ) is reduced to U(0) by the reactions [6] and [7].

$$U^{4+} + 2O^{2-} + 2C = U + 2CO \quad \cdots\cdots\cdots\cdots[6]$$
$$U^{4+} + 2O^{2-} + C = U + CO_2 \quad \cdots\cdots\cdots\cdots[7]$$

Taking into account the off-gas analysis and the thermodynamic approach, the second consideration may be more reasonable. To confirm the reduction behavior of UO_2, U_3O_8 and UO_3 in BaF_2-LiF-UF_4 at 1200 ℃ in detail, it is necessary to study the processes by voltammetory, chronopotentiometry and so forth.

CONCLUSION

Electrolytic reduction of UO_2, U_3O_8, and UO_3 was examined by polarization curves, off-gas analysis by mass spectrometry, and ΔGs of formation of UO_2 from U_3O_8 with CO and C. Any of the uranium oxides can be available for feed materials and can be reduced to uranium metal. The current efficiency, which can be obtained in this study, is from 22 to 52 % (based on recovered metal) or from 32 to 48 % (based on generated gas). Highly oxidized uraniums such as U_3O_8 and UO_3 are reduced to UO_2 by CO gas and C. And then UO_2 is reduced to uranium metal.

REFERENCES

1. C.D.Harrington and A.E.Ruehle, "Uranium Production Technology", D.Van Nostrand Co., Inc., Princeton (1959).
2. K.O.Laughon, "Uranium Processing for the AVLIS Enrichment Process", Uranium Seminar '89, (1989).
3. O.Kubaschewski, E.Ll.Evans and C.B.Alcock in *Metallurgical Thermochemistry,* 4th ed., Pergamon Press, England (1967).

Table 1 Current Efficiency.

Feed Oxides		UO_2	U_3O_8	UO_3
Case 1	Gas	50 %	69 %	86 %
	Metal Uranium	53 %	59 %	49 %
Case 2	Gas	48 %	32 %	41 %
	Metal Uranium	52 %	44 %	32 %

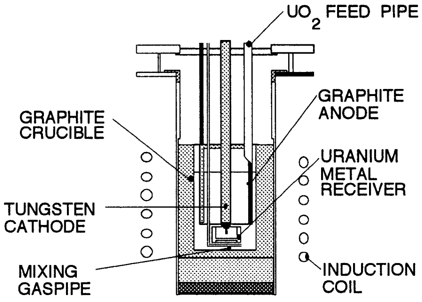

Fig.1 Schematic Diagram of Experimental Apparatus.

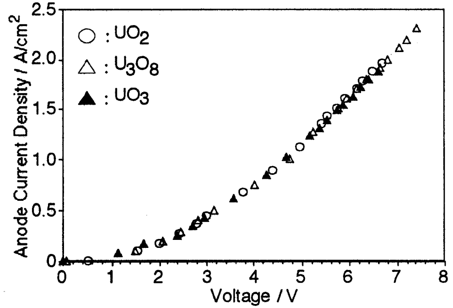

Fig.2 Polarization Curves in Molten BaF_2-LiF-UF_4 at 1200℃ after Uranium Oxides Addition.

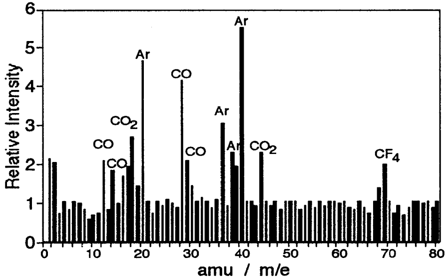

Fig.3 Gas Mass Spectrum Scanning between 1 and 80 amu.

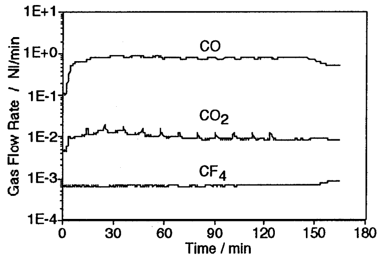

Fig.4 Gas Flow Rate during Electrolysis of UO_2.

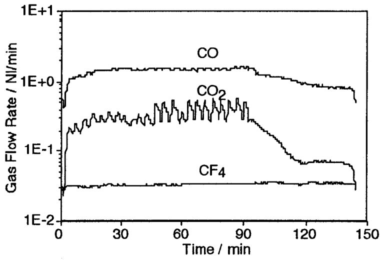

Fig.5 Gas Flow Rate during Electrolysis of U_3O_8.

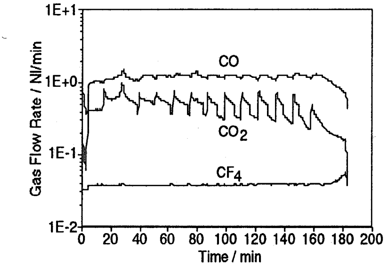

Fig.6 Gas Flow Rate during Electrolysis of UO_3.

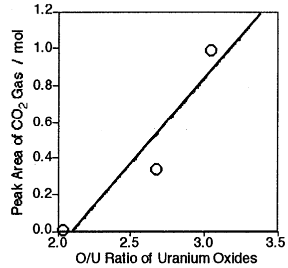

Fig.7 Relation between O/U Ratio of Uranium Oxides and Peak Area of CO_2 Gas.

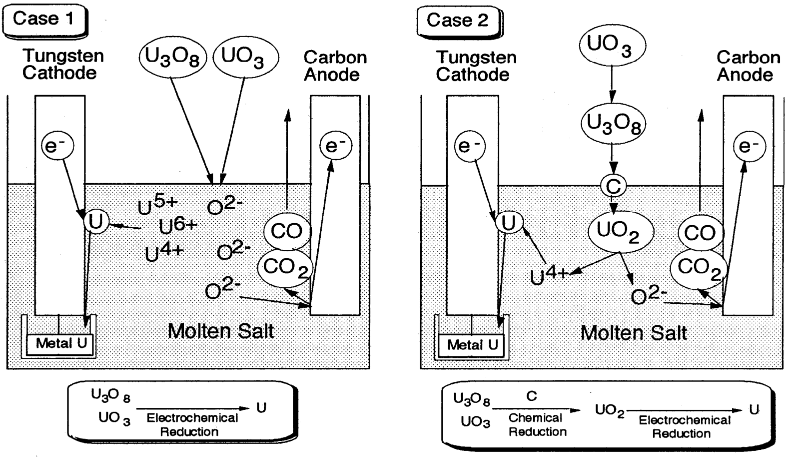

Fig.8 Reduction Processes of U_3O_8 and UO_3 to Metal Uranium

DOI: 10.1149/199413.0673PV

A PARAMETRIC STUDY ON REDUCTION OF URANIUM OXIDE BY FLUORIDE MOLTEN SALT ELECTROLYSIS FOR SCALE-UP

Hajime Ikeda, Hiroshi Kubota, Katsutoshi Nakamura
Metal Mining Agency of Japan
Tokiwa Bldg. 1-24-14 Toranomon, Minato-ku, Tokyo 105, Japan

Kazuaki Ota, Yutaka Takasawa, Takeshi Onoue, Sumio Yamagami
Naka Nuclear Development Center, Mitsubishi Materials Corporation
1002-14 Mukoyama, Nakamachi, Nakagun, Ibaraki 311-01, Japan

Kazuhiro Endo
Nuclear Engineering Center, Mitsubishi Materials Corporation
1-38-9 Kakigaracho, Nihonbashi, Chuo-ku, Tokyo 103, Japan

ABSTRACT

Uranium metal production from uranium oxide by molten salt electrolysis has been examined to get basic characteristics of electrolysis and design data for scale-up. Current efficiency obtained was around 50%, which was higher value than reported in early experiments. Lower concentration of UF_4, higher current density, adequate agitation, and lower temperature improved current efficiency. UO_2, U_3O_8 and UO_3 were all available as feed material, and adequate feed condition enabled the UF_4 salt not to decompose and to control its product nature.

INTRODUCTION

In the nuclear fuel cycle processes such as uranium enrichment, fuel fabrication, nuclear reactor, spent fuel management and waste management, bringing down the cost of each process to be acceptable to the public as well as safe is a never-ending theme. And there are many activities in all fields in order to improve its cost performance and safety. The uranium enrichment area is no exception. In this uranium enrichment, commercial production processes now in operation in the world are the gaseous diffusion process or the centrifugal process of uranium hexa-fluoride. And these cost performances are well achieved by operating deduced plants. However, it is considered to be more expensive if these plants will be dismantled and rebuilt applying the same process concepts. On the other hand, atomic vapor laser isotope separation (AVLIS) will be a promising uranium enrichment technology for the next generation because of its high cost performance and high enrichment efficiency. In this AVLIS enrichment process, uranium metal or uranium metal alloy will be used as feed material. Today, commercial production of uranium metal in the world is done by thermite reduction of uranium tetra-fluoride with magnesium[1]. In this thermite process, magnesium fluoride is produced as a byproduct. This byproduct needs to be treated to reduce its uranium contamination for disposing of it or selling it on the market. Considering cost performance, minimization of waste production and continuous process concept, an electrolytic process for producing uranium metal directly from uranium oxide will offer potential advantages over the existing commercial process[2].

Metal Mining Agency of Japan has carried out a feasibility study on metallic uranium production systems for AVLIS feed materials since fiscal 1989[3]. In this study, parametric experiments were carried out to get basic characteristics of electrolysis and design data for a scale-up of electrolytic apparatus.

This work was funded by the Ministry of International Trade and Industry of Japan.

EXPERIMENT

Materials

Barium fluoride, lithium fluoride and uranium fluoride salts mixture was used as electrolyte. Its composition was 74wt%BaF_2-11wt%LiF-15wt%UF_4. Uranium tetra-fluoride acts as solvent for uranium oxide in this electrolysis. LiF and BaF_2 will act to lower the melting point of electrolyte and reduce vaporization of LiF respectively. And these salts were regent grade chemicals. Uranium tetra-fluoride was produced by the reaction of UO_2 with HF at about 400℃. These fluorides were mixed and premelted before experiment. In most cases, uranium tri-oxide produced by fluidized bed denitration was used as starting material. UO_3 was also treated in a vacuum furnace to remove remaining acidic moisture at 450℃. U_3O_8 was prepared by calcination of UO_3 in the N_2 atmosphere at 650 ℃. UO_2 was prepared by reduction of UO_3 with hydrogen at 600 ℃. Uranium dioxide was used as standard material, and other uranium oxides were used in a parametric examination.

Apparatus

The schematic feature of the apparatus and the outline of the electrolysis apparatus are described in the former presentation. The electrolytic cell made of graphite has a size of 200mm inner diameter and 350mm height. The anode is made of graphite which has a cylindrical shape with slits as a standard case. The cathode rod is made of tungsten. It is considered to act as uranium electrode under electrolysis because the tungsten surface is covered with liquid uranium. A graphite uranium metal receiver covered with boron nitride has a capacity for 3 kg uranium metal and is set just below the cathode. The electrolytic cell is enclosed in a quartz tube with steel flanges so that a gas tight enclosure was achieved. High purity argon is used as purge gas in the cell. Off gas is introduced to gas mass spectrometer, for the measurement of gas composition such as CO, CO_2 and CF_4 with electrolysis. Direct currency for electrolysis has a capacity of 0~20V and 0 ~500A. Induction heating which has a maximum heating capacity of 1400℃ is used to bring the cell to the experiment temperature of about 1200℃ and maintain it during the experiment.

Experimental Procedure

Mixture of LiF, BaF_2 and UF_4 was pretreated in a vacuum at 400℃ and in Ar at 800 ℃ for 30 minutes in order to evacuate volatile species and moisture, then heated up to about 1200℃, which is well over the melting point of LiF-BaF_2-UF_4 electrolyte and the melting point of uranium metal(1130℃). The cathode and anode electrodes assembly, and uranium receiver were immersed slowly into the electrolyte to the desired depth and a brief pre-electrolysis was conducted to evacuate still remaining volatile impurities. Pre-electrolysis time was decided by measuring the off-gas composition such as CO, CO_2, CF_4. After pre-electrolysis, polarization curves before and after uranium oxides feed were measured in the range of 0 to 2.4 A/cm^2 at anode. All of the experiments were carried out by constant current mode. During the experiments, uranium oxides were fed periodically into the cell and off-gas composition was analyzed continuously with electrolysis. Direct currency, impressed voltage, temperature, and induction heating power were also recorded continuously.After electrolysis, cathode and anode electrodes assembly, and uranium metal receiver were removed upward in order to minimize back-reaction of the metal with the electrolyte. After cooling, uranium metal was removed from the receiver and was weighed. Current efficiencies were calculated by off gas volume of C0, CO_2 and CF_4, and by weight of uranium metal produced.

RESULTS AND DISCUSSION

UF_4 Concentration of The Salt

The effect of uranium tetra-fluoride concentration of the LiF-BaF_2-UF_4 salt was examined in the range of 10~20 wt % without changing its LiF to BaF_2 molar ratio. A summary result of calculated current efficiency was shown in Figure 1. Current efficiency had a tendency to increase with decrease of UF_4 concentration. This is a similar to the behavior which was reported by Piper[4] using a different type of electrolytic cell called the Hall process. The lower current efficiency at higher UF_4 concentration results from the formation of UF_3 by the reaction of uranium at the cathode with UF_4 in the salt($U + 3UF_4 \rightarrow 4UF_3$)[5]. Current efficiency is one of the important factors for electrolysis performance. However decrease of UF_4 in the salt will result in decreasing the solubility of uranium oxide in the salt. Considering a scale up of the electrolytic cell, optimization of current efficiency and uranium oxide solubility should be achieved. At present, 15 wt % of UF_4 is selected as a standard operational condition and a range of 10 to 20 wt % of UF_4 is treated as an operational deviation of UF_4 concentration of the salt.

Oxidation States of Uranium Oxides

Uranium oxides such as UO_2, U_3O_8 and UO_3 are typical products of the nuclear fuel cycle. And in the uranium metal production plant for AVLIS we are now considering, these uranium oxides are intermediate or final material for metal conversion. Thus availabilities of these oxides may enable its simplification of the plant pretreatment process such as calcination and reduction of uranium tri-oxide. The experimental results showed a possibility that any of the uranium oxides was available without any operational trouble. Figure 2 shows the results of obtained current efficiency. It shows that the higher the oxidation state of uranium oxide was fed, the higher the current efficiency calculated by off gas analysis was. In this calculation, UO_2, U_3O_8 and UO_3 were considered to be dissolved in their oxidation states and reduced electrolytically. On the other hand, off gas analysis results indicated that higher CO_2 concentration was obtained by feed of higher oxides, and that the CO_2 gas peak appeared immediately after the feed of oxide. Thus a part of excess oxygen in the oxides may be reduced chemically with carbon mono-oxide or carbon in the cell. Details of this evaluation will be discussed in another presentation at this meeting.

Current Density

Increase of current density can lead to the increase of electrolysis capacity or the contribute to cell compactness. However increase of current density on anode may cause the undesired anode effect. In this present work, more than 50 experimental runs have been conducted in the range of $0.242 \sim 1.74$ A/cm^2 on anode. Electrolysis was successfully carried out without any decomposition of uranium tetra fluoride. And there were not any features of anode effect such as overvoltage during these experiments. As for cathode, Figure 3 shows a relation between cathode current density and current efficiency. Current efficiency had a slight tendency to increase with the increase of cathode current density. This is the similar to the behavior which was reported by Piper[4], too. From this result, one of the considerations for large scale apparatus is to keep the ratio of anode area to cathode area as high as possible.

Temperature

Electrolysis temperature was controlled by induction heating power. And a temperature range from 1150 to 1300 ℃ was examined. Uranium metal melting point is 1130℃ so that produced uranium metal could be treated in liquid condition and recovered in receiver. A summary result of current efficiency is shown in Figure 4. Current efficiency had a tendency to decrease with the increase of temperature. This is also the same behavior which was reported by Piper. However, higher temperature reduced the impressed voltage of the electrode so that energy consumption was less at higher temperature. Besides these results, the solubility of UO_2 in the electrolyte and the limiting anode current density generally increase with temperature[4]. And carbon contamination and corrosion of the cell materials increase with temperature. Thus in a design of large scale apparatus, consideration of these relations with temperature becomes important.

Agitation

Uniform distribution of dissolved uranium oxide in the salt may be desired for stable electrolysis. Uniformity of dissolved uranium oxide may cause the decomposition of uranium tetra-fluoride or the overvoltage of electrodes. Argon bubbling and/or superposition of alternating current were examined for their agitation effects. As for argon bubbling, argon gas tube was introduced under the uranium metal receiver, and flow rates of 0, 0.05 and 1 Nl/min were tested. At any condition, degradation of uranium tetra-fluoride was not observed, and current efficiencies calculated by off gas showed almost same values. However at 1 Nl/min flow rate, uranium metal produced seemed to be mechanically dispersed out of the receiver so that current efficiency calculated by uranium metal showed less value. Generally higher agitation will result in better electrolysis. However, in this experimental system with uranium metal receiver, adequate gas flow agitation seems to exist. On the other hand, the effect of alternating current addition to direct current on electrolysis was examined by changing its ripple factor from 1～44 % which is defined as:

$$\text{Ripple value} = \Delta V^{AC}_{\text{peak-peak}} / V^{DC}_{\text{mean}} / \sqrt{2} \times 100 \ (\%)$$

The result of current efficiency is shown in Figure 5. In this range, current efficiency didn't seem to be affected by superposition of alternating current component. Figure 6 shows its electrolysis energy for production of 1 kg uranium metal(energy cost kWh/kg-U). The result indicates that superposition of alternating current seems to improve its energy cost. Chemla et al[6] reported the reduction of the formation of a passivating layer of CFx on the carbon anode by superposition of pulsed current in their HF-KF molten salt electrolysis. Thus in this present work, a similar effect may occur to reduce the overvoltage on the anode.

Graphite Anode Shapes

Graphite anode is consumed with electrolysis to produce CO and CO_2 so that its design and cost have to be as simple and cheap as possible. In the standard experiments, cylindrical type anode with vertical slits was used, which will be expensive if it is used for a large scale apparatus. Thus rod and plate type anode were examined which seem to be more realistic shapes. A result of current efficiencies obtained by different anode shapes is shown in Figure 7. The current efficiencies obtained showed there were no difference between these anodes types. Thus rod and plate types are promising anode shapes for large scale apparatus.

CONCLUSION

Uranium metal production from uranium oxides by molten salt electrolysis was examined to get basic characteristic effects on UF_4 concentration, oxidation states of uranium oxides, current density and temperature. Higher current efficiency could be achieved by:

- Lower UF_4 concentration
- Higher cathode current density
- Lower electrolysis temperature

And any of the uranium oxides is available as a feed material for electrolysis. Agitation effect by argon is not so clear but it could support stable electrolysis and reduce the decomposition of UF_4. Agitation by alternating currency did not seem to effect current efficiency but seemed slightly effective in lowering the energy cost. Anode shapes such as rod or plate seem to be promising for large scale apparatus.

REFERENCES

[1] C.D.Harrington and A.E.Ruehle, "Uranium Production Technology", D.Van Nostrand Co., Inc., Princeton (1959).

[2] K.O.Laughon, "Uranium Processing for the AVLIS Enrichment Process", Uranium Seminar '89, 1989

[3] Y.Hosoi and H.Ikeda, "Feasibility Study on Metallic Uranium Production System - Test of Reduction of Uranium by Molten Salt Electrolysis", Proceedings of the 24th Youyuuen Kagaku Touronkai held at Kyoto Japan, November, 1992.

[4] R.D.Piper, "Production of Uranium Metal from Uranium Oxide by Fused Salt Electrolysis", Electrochem. Technol., Vol.5, pp147-151, 1967

[5] D.S.Poa et al.,"Laboratory-Scale Study of Electrolytic Reduction of Uranium Oxides", ANL 88-29, 1988

[6] M.Chemla et al., "Production of Fluorine by Pulsed Current Electrolysis of Molten 2 HF-KF Salt", Proceedings of the Fourth Japan-China Bilateral Conference on Molten Salt Chemistry and Technology, Kyoto, Japan, pp107-110, 1992

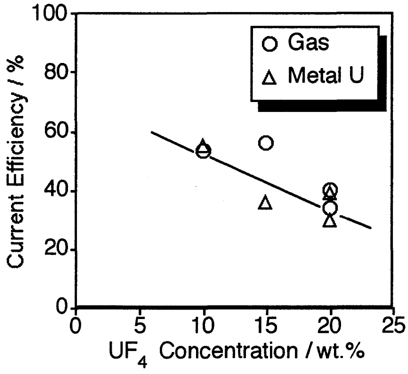

Fig 1 Current Efficiency vs. UF_4 Concentration in the Salt.

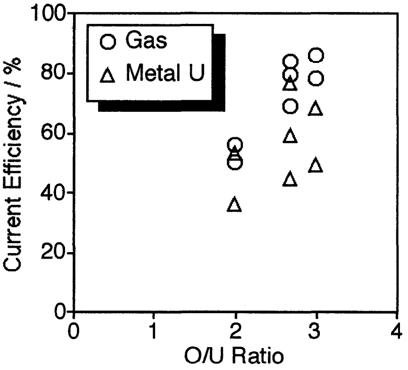

Fig 2 Current Efficiency vs. Oxidation State of Uranium Oxides.

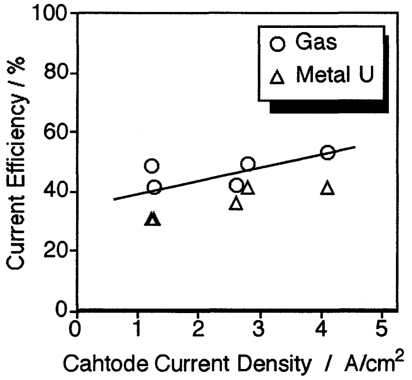

Fig 3 Current Efficiency vs. Cathode Current Density.

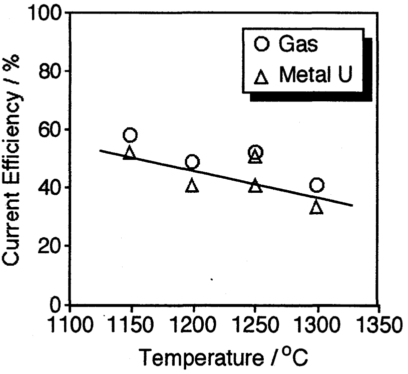

Fig 4 Current Efficiency vs. Temperature.

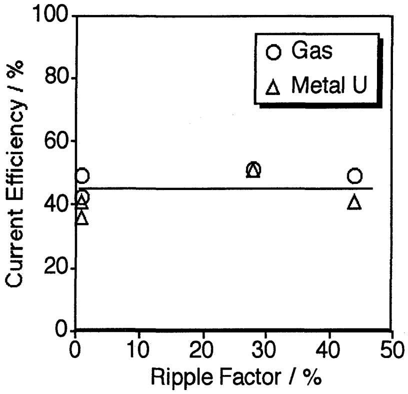

Fig 5 Current Efficiency vs. Ripple Factor.

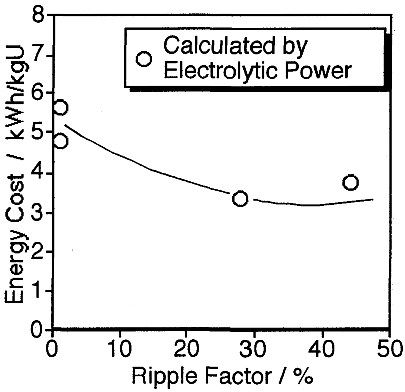

Fig 6 Electrolysis Energy vs. Ripple Factor.

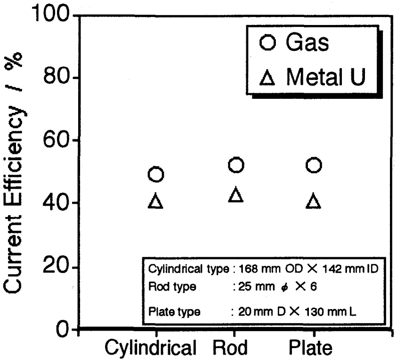

Fig 7 Current Efficiency vs. Anode Shapes.

DOI: 10.1149/199413.0681PV

SEPARATION OF ACTINIDES (U, Np, Pu) FROM LANTHANIDES (Gd, Nd) UTILIZING ELECTRODEPOSITION IN MOLTEN LiCl/KCl EUTECTIC

S.P.Fusselman, C.L.Krueger, T.S.Storvick, P.R.Sharp, D.A.Sorrell, P.S.Stith, and J.W.Cooper
University of Missouri-Columbia and
Missouri University Research Reactor (MURR)

D.L.Grimmett, J.J.Roy, and L.F.Grantham
Rockwell International/Rocketdyne Division, Canoga Park, CA 91309-7922

Tadashi Inoue and Takatoshi Hijikata
Central Research Institute of Electric Power Industry (CRIEPI)
Komae Research Laboratory, Tokyo, Japan

Noriaki Takahashi
Kawasaki Heavy Industries, Ltd. (KHI)
Nuclear Systems Division, Tokyo, Japan

ABSTRACT

In order to evaluate the feasibility of using electrodeposition for separation of actinides from rare earths in PUREX waste, studies of deposition of U, Np, and Pu individually in the presence of $GdCl_3$ and $NdCl_3$ in molten LiCl/KCl eutectic at 450C were carried out. Deposition onto tantalum cathodes resulted in actinide/lanthanide separation ratios in the order U>Np>Pu. Separation ratios were potential dependent and decreased as the actinide concentration decreased.

INTRODUCTION

Processing for treatment and disposal of spent nuclear fuel has been the subject of developmental work in a variety of groups (1,2). Separation and recovery of long lived transuranics from rare earth fission products would result in improved nuclear waste management and would be an essential prerequisite for actinide disposal through transmutation. The TRUMP-S process (TRansUranic Management by Pyropartitioning Separation) proposes the conversion of PUREX waste, through a series of processing steps to a final electrolytic separation of actinides from rare earths at a solid cathode in a molten LiCl/KCl eutectic solution. Molten salt electrolytes with their radiation resistance and stability with actinide and rare earth chlorides have advantages over organic and aqueous solutions. In addition, the high temperatures of molten salt solutions result in enhanced kinetics.

This work is part of a larger effort to examine electrochemistry in molten LiCl/KCl and cadmium relevant to separation of actinides and rare earths in PUREX waste. The work described here is part of a continuing study and involves use of electrodeposition at a solid cathode to separate actinides (U, Np, Pu) from rare earths in molten LiCl/KCl eutectic at 450C. Removal of actinides from solution as well as separation ratios and cathode current efficiencies during the deposition and as a function of deposition potential are reported.

EXPERIMENTAL

Anhydrous lanthanide chlorides of 99.99% purity were used as purchased and were supplied in glass ampoules under argon. High purity, anhydrous LiCl/KCl eutectic was supplied in glass ampoules from APL engineering and was used as received. Solutions of actinide chlorides in LiCl/KCl eutectic were prepared by $CdCl_2$ oxidation of actinide metals (supplied by DOE) out of a stirred cadmium solution at 450 to 550C. Eutectic solutions for separation studies were prepared by mixing the actinide chloride solution, lanthanide chlorides and LiCl/KCl eutectic. Initial concentrations of actinide and lanthanide chlorides measured in the mixed solution at 450C were always somewhat less than that based on the materials weighed out, possibly due to diffusion between the main and secondary compartments of the two compartment cell.

Depositions were carried out at 450C in a thermal well which extended from the floor of an argon glovebox (<0.3ppm O_2, <0.01ppm H_2O, <1ppm H_2). A clamshell furnace surrounding the thermal well was controlled by proportional controllers with type K, tantalum sheathed thermocouples. Depositions were carried out with an EG&G PAR 273 potentiostat/galvanostat. Several depositions were carried out during the course of each separation experiment. After each deposition a sample of the molten salt solution was taken and the cathode was pulled from the melt for later analysis. Sampling of the salt was accomplished by briefly dipping a metal wire into the melt and collecting the frozen adhering salt. Cathode deposits were generally rough in appearance and contained at least 70% adhering salt by weight. Typical depositions took place at 1 to 5 mA/cm^2 for 2 to 5 Coulombs. For Np and Pu a series of short depositions at nominally 0.5 Coulombs were performed over a range of current densities. Ag/AgCl reference electrodes with a AgCl mole fraction of 0.00477 were used.

Compositional analysis of salt and of cathode deposits was accomplished by dissolution in water or nitric acid respectively followed by elemental analysis with a Baird PSX inductively coupled plasma spectrometer. For salt analyses in Np and Pu separation tests, correction for salt matrix effects were made by matrix matching standard and sample solutions. For ICP analyses during the U separation experiments and for all cathode analyses, the attenuation factors due to the presence of dissolved LiCl/KCl were applied to the calculation of U, Gd, and Nd concentration. The potassium content of deposits was used to determine the amount of salt which adhered to the cathode deposits.

RESULTS

UCl_3, $NpCl_3$, and $PuCl_3$ individually were separated by electrodeposition from $GdCl_3$ and $NdCl_3$. These two lanthanides were chosen since they are the rare earths present in significant amounts in PUREX waste (Nd has fission yields of about 15%) which have potentials in molten LiCl/KCl eutectic closest to the actinides (3,4,5) and hence are the most difficult to separate.

Initial and final concentrations of actinide, Gd, and Nd, shown in Table I indicate that depletion of about 99% of actinides in the presence of lanthanides is possible through electrodeposition to a solid cathode. Concentrations of actinides and lanthanides as a function of actinide removal are shown in Figure 1. For Np and Pu, removal of the last few percent of actinides is accompanied by some lanthanide codeposition. This codeposition of lanthanides near the end of the separation experiments is also reflected in the measured separation ratios shown in Figure 2. Throughout most of the electrolysis, the ratio of U to Gd or Nd on the cathode was 100 or greater while separation ratios of Np and Pu were progressively less. This ordering of separation ratios $Pu < Np < U$ is qualitatively consistent with the ordering of their potentials in molten LiCl/KCl (4,5,6). The largest difference in deposition potentials between actinides and lanthanides studied here is for U and hence its larger separation ratio. Conversely, Pu with deposition potentials closer to the lanthanides has smaller separation ratios. For U, Np, and Pu, in the latter stages of the separation when the actinide was depleted from solution, deposition potentials became closer to the lanthanides and separation ratios decreased.

Deposits tended to be rough in appearance. Analysis of deposits indicated that less deposited metal was present than would be expected based on the coulombs passed, presumably due to nonadherent deposits. This total cathodic current efficiency, usually significantly less than 100%, is depicted in Figure 3 as a function of actinide removal. Although current efficiencies are variable, U deposition exhibits current efficiencies which never exceed about 60%. Cathodic current efficiencies significantly less than 100% for U have been reported by others (7). One clear trend evident from Figure 3 is a lowering of current efficiencies near actinide depletion. This may be due to reequilibration of small amounts of divalent Nd with deposited metallic Nd ($2Nd^{3+} + Nd = 3Nd^{2+}$). This corrosion of the initial amounts of deposited Nd or direct reduction of Nd^{3+} to Nd^{2+} may lower measured current efficiencies.

Table I. Initial and Final Concentrations in Separation Experiments.

	Initial Mole fractions x10^4				Final Mole Fractions x10^4		
	Ac	Gd	Nd	Coulombs	Ac	Gd	Nd
U	5.67	6.8	6.1	21.9	.05	9.2	8.7
U	5.2	8.7	8.2	18.2	ND	8.7	8.5
Np	4.9	8.0	7.5	31.0	.05	4.6	4.1
Np	5.5	7.8	7.2	36.7	.08	2.3	2.2
Pu	4.4	8.3	7.4	37.1	.07	5.5	4.5
Pu	3.8	7.7	7.3	41.5	.04	5.3	4.8

Separation ratios of Np and Pu vs deposition potential, shown in Figures 4 and 5 respectively, indicate a maximum in separation ratio is reached. Cathodic current efficiencies generally increased with more cathodic deposition potentials for Np (Figure 6), but no clear trend is evident for Pu (Figure 7).

ACKNOWLEDGEMENTS

This project was made possible by the cooperation of the MURR staff. Financial and technical support from CRIEPI, KHI, and DOE are greatly appreciated.

REFERENCES

1. J. P. Ackerman, Ind. Eng. Chem. Res., **30**, 141 (1991).
2. M. S. Coops and D. H. Sisson, Radioactive Waste Management, Actinide Recovery of Waste, (1982) p. 333.
3. J.J. Roy, L.F. Grantham, L.R. McCoy, C.L. Krueger, T.S. Storvick, T. Inoue, H. Miyashiro, and N. Takahashi in *Molten Salt Chemistry and Technology*, Eds. M. Chemla and D. Devilliers, Trans Tech, Switzerland (1991) p. 547.
4. J. A. Plambeck, J. Chem. Engr. Data, **12** #1, 77 (1967).
5. C.L.Krueger, T.S.Storvick, J.J.Roy, L.F.Grantham, L.R.McCoy, T.Inoue, H.Miyashiro, and N.Takahashi, J. Electrochem. Soc., **138**, 1186 (1991).
6. G.M.Campbell and J.A.Leary, USAEC Report LA-3399, (1966).
7. J.L. Willit, W.E. Miller and J.E. Battles, J. Nuclear Materials, **195**, 229 (1992).

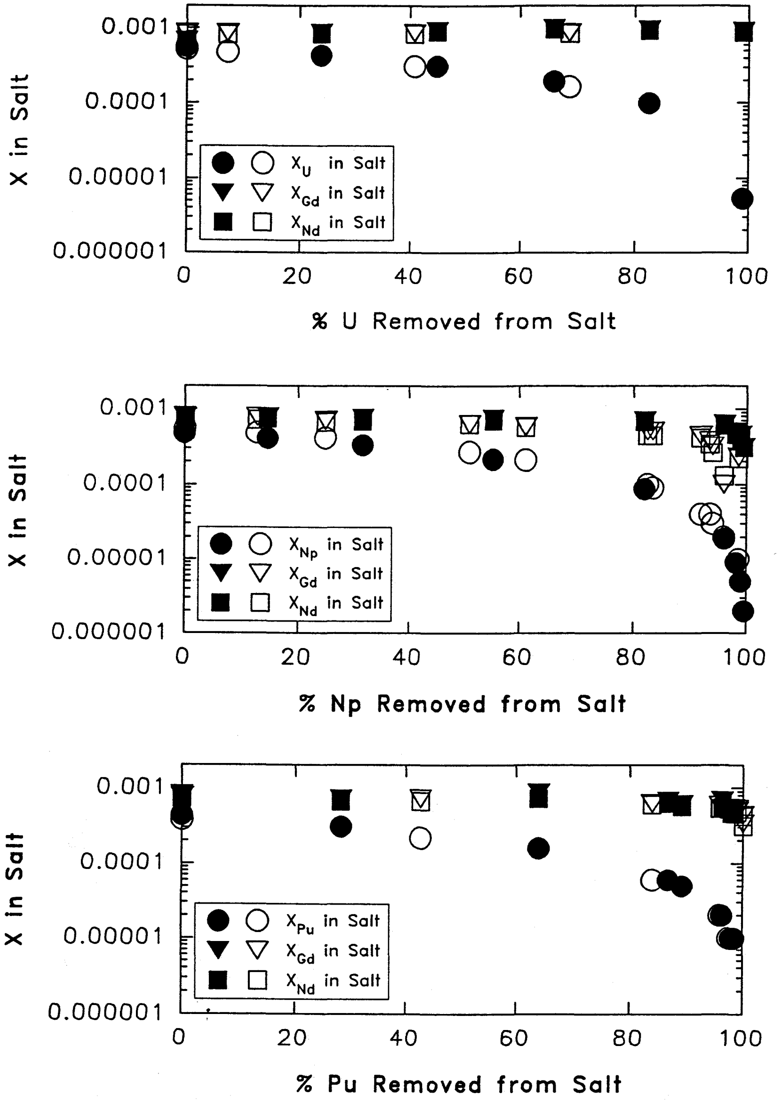

Figure 1. Mole Fraction in Salt During Electrolysis
Closed symbols trial 1, Open symbols trial 2.

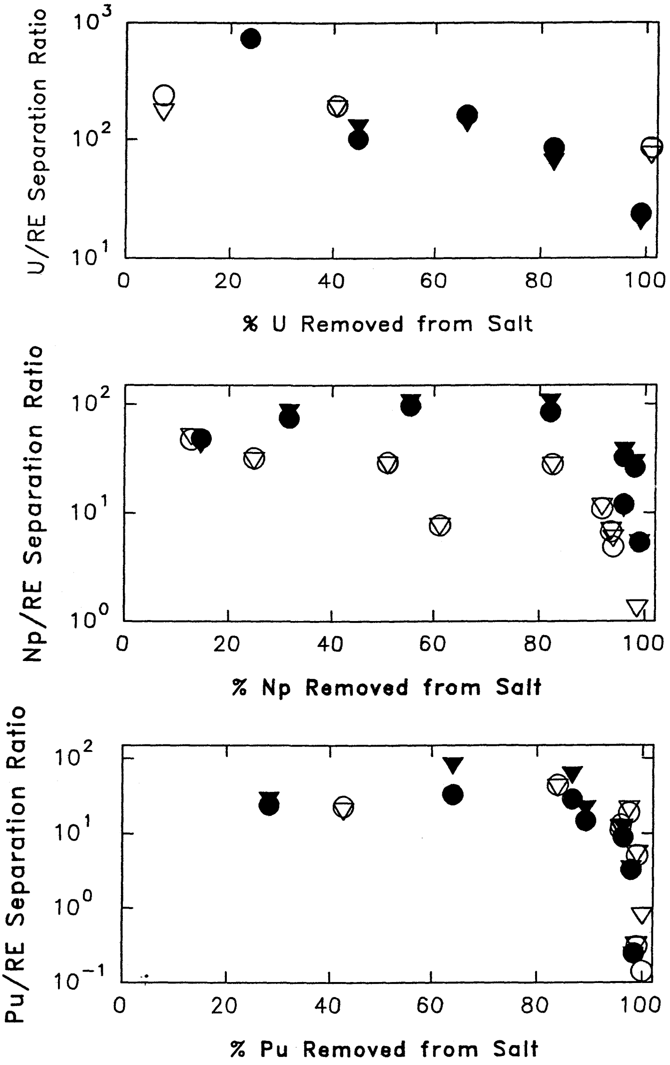

Figure 2. Separation Ratio on Cathode for depositions > 1 Coulomb. ● Ac/Gd trial 1, ○ Ac/Gd trial 2, ▼ Ac/Nd trial 1, ▽ Ac/Nd trial 2.

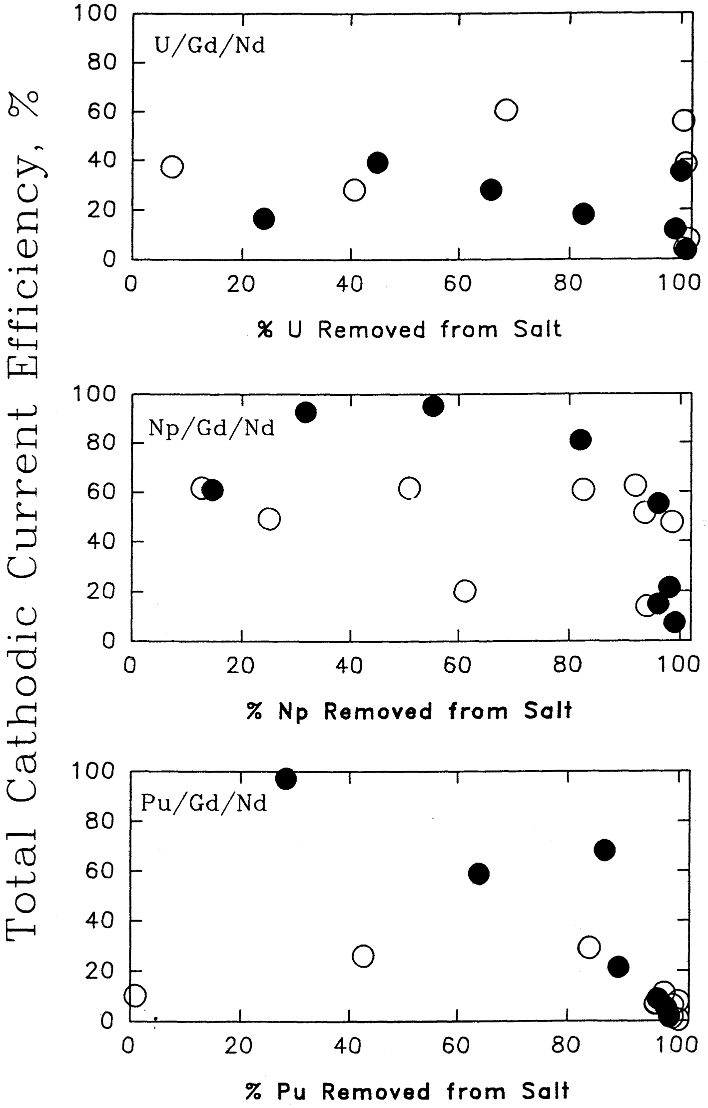

Figure 3. Total Cathodic Current Efficiency for. depositions > 1 Coulomb ● trial 1, ○ trial 2.

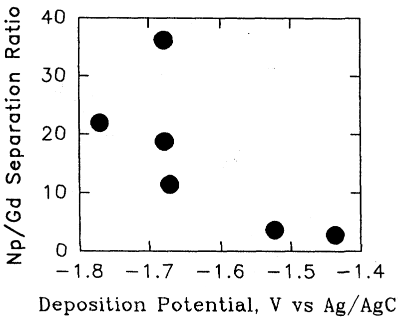

Figure 4. Dependence of Np/Gd separation ratio on deposition potential. 0.5 Coulomb deposits.

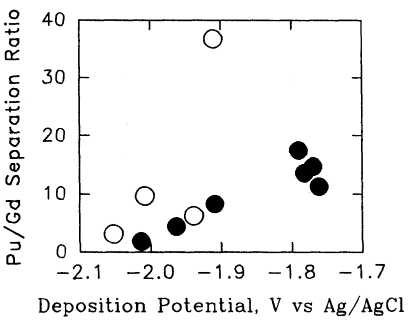

Figure 5. Dependence of Pu/Gd separation ratio on deposition potential. 0.5 Coulomb deposits.

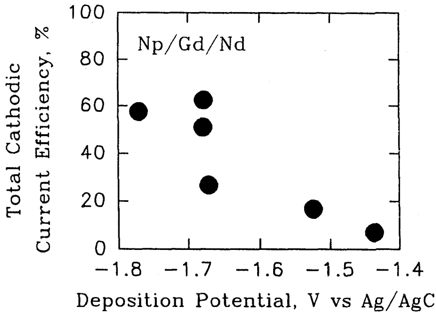

Figure 6. Dependence of total cathodic current efficiency on deposition potential. 0.5 Coulomb deposits.

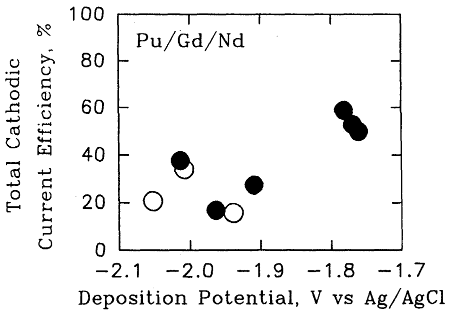

Figure 7. Dependence of total cathodic current efficiency on deposition potential. 0.5 Coulomb deposits.

DOI: 10.1149/199413.0689PV

THE ROLE OF CHROMIUM IN OXYGEN SPARGING OF CONTAMINATED MOLTEN SALTS

B. Mishra and W.A. Averill*

Kroll Institute for Extractive Metallurgy
Colorado School of Mines
Golden, Colorado 80401

* Residue Treatment Technology
EG&G Rocky Flats Plant, Golden, Colorado 80402

ABSTRACT

Oxygen Sparging is an effective method for the remediation of radioactively-contaminated-waste salt generated during the pyrochemical processing of plutonium metal. However, the discardable portion of the salt having below EDL plutonium can not be disposed as such, if it contains chromium, lead, cadmium, mercury, etc. - elements that are hazardous in the salt, as per the Resource Conservation and Recovery Act [RCRA]. The role of chromium has been studied during the oxygen sparging of contaminated waste salt and the efficiency of oxygen sparging process has been optimized using $CeCl_3$ as the surrogate for $PuCl_3$. The efficiency of cerium and chromium removal from the salt has been measured as a function of the time of sparging at varying flow rates of an Ar-O_2 gas-mix and the amount of RCRA constituent. The results show that chromium entirely transfers to the product phase of oxides/oxychlorides and that the residual salt is completely devoid of chromium.

INTRODUCTION

The production technology of foundry-grade plutonium metal involves several pyrochemical processes which use molten halides as the processing media (1). Molten Salt Extraction [MSE] Process is used to separate americium and plutonium in molten calcium chloride salt medium using di-cesium-hexa-chloro-plutonate [DCHP] as the reagent. The americium-rich fraction also contains significant amount of plutonium (approximately twenty-five weight percent as Pu, $PuCl_3$ and PuO_2) which must be recovered (2). Electrorefining [ER] of the non-foundry grade metal is carried out through a molten calcium chloride or equi-molar potassium chloride and sodium chloride salt mixture with magnesium chloride addition (3,4). Typically, one third of the refining process products by weight end up as a residue salt waste that must be treated for the recovery of plutonium and for the recycling/ discarding of the process salt. The spent ER salt also has free plutonium metal in addition to the chloride and oxychloride as some of the refined metal is trapped by the salt forming a 'metal-fog' (5). The formation of oxychloride in these systems essentially occurs due to the practice of using magnesia or alumina components as the molten salt container, stirrer or sheaths for metallic components (6). Americium is also picked up from the impure anode by the salt as a chloride due to the relative thermodynamic stability with respect to plutonium chloride (7). The typical amount of plutonium in one kilogram of the spent ER and MSE salt is 0.9 to 1.0 gram-atom, or 200 to 250 grams, depending on the efficiencies of MSE and ER processes. Thus, the processing of the MSE and ER process waste salts performs an important function in the over-all waste minimization strategy and recovery technology in plutonium metal production.

Oxygen Sparging Technique has been studied and optimized to treat the waste salt. In the Oxygen Sparging Technique, a mixture of argon and oxygen gas is bubbled through the molten salt which converts the soluble plutonium and americium chloride in to their respective insoluble oxides that can, hence be precipitated (8). Americium oxide precipitates at a much slower rate than the plutonium oxide and, thus provides additional separation from plutonium. Also, the metallic plutonium and the plutonium oxychloride can convert into plutonium oxide and precipitate out. Approximately 97 wt. pct. of the total plutonium is recovered as an oxide and metal globules, mixed with a significant quantity of salt. The stoichiometric reaction can be represented by Equations [1 and 2]:

$$2\,PuCl_3 + 2\,O_2 \rightarrow 2\,PuO_2\downarrow + 3\,Cl_2\uparrow \qquad [1]$$

$$2\,PuOCl + O_2 \rightarrow 2\,PuO_2\downarrow + Cl_2\uparrow \qquad [2]$$

Recently, it has been mandated through the Resource Conservation and Recovery Act [RCRA] that the so-called 'discardable' salt fractions from these waste reduction and metal recovery processes can not be thrown away if they contain RCRA regulated elements, such as chromium, cadmium, lead, mercury, etc. Therefore, understanding the behavior of these RCRA elements during oxygen sparging is necessary to be able to label the waste-salt 'discardable'. The transfer of RCRA constituents to the product phase would be desired during the waste treatments. This work has been conducted to evaluate the behavior of chromium in the oxygen sparging process. The actinide chloride has been surrogated with cerium (III) chloride owing to its excellent chemical similarity and chromium has been added as a chromium (III) chloride in a equimolar sodium chloride-potassium chloride salt matrix. The role of chromium during the sparging and the efficiency of cerium recovery have been measured. The results are useful in obtaining proper certification for the mixed waste handling and disposal.

EXPERIMENTAL PROCEDURE

The schematic diagram of the experimental set-up is shown in Figure 1. 500 g of equi-molar potassium and sodium chloride salt-mix was taken in a dense magnesia crucible (100 mm ID x 250 mm height) and mixed thoroughly with the required quantities of cerium (III) chloride and chromium (III) chloride. The crucible was introduced in a resistance heated furnace enclosed in an inert atmosphere glove-box. The furnace gas was scrubbed through a sodium carbonate scrubber to remove chlorine gas and was subsequently vented off.

The furnace lid-assembly consists of two ports. A K-type thermocouple was placed inside a closed-end mullite tube (9.5 mm OD x 6.4 mm ID x 450 mm length) and inserted into the furnace through the off-centered port. An open-ended alumina tube (9.5 mm OD x 6.4 mm ID x 450 mm length) was inserted through the central port. A pre-mixed argon and oxygen gas source, at a pre-determined volume ratio, was introduced through the central alumina tube. The flow-rate of the gas-mix was monitored with a gas flow-meter.

The salt temperature was brought to the desired level and melted by controlling the furnace temperature. Once the salt-mix was molten, the central alumina tube was lowered to the desired level and the thermocouple tube was lowered to a level 50 mm above the crucible bottom. The Ar/O_2 gas-mix was turned on at the desired flow-rate for the required length of time. At the end of the required time-period, the gas was turned off. The furnace was cooled at a rate of 100°C/hr to an inside temperature of 200°C, and the furnace was subsequently turned off.

The crucible was then broken within the glove-box and the product was separated from the clean salt mass and the ceramic pieces. The dark-green oxide/oxychloride product layer has a sharp interface and distinct separation line from the yellow salt cake and is easily separated along the line. The initial salt weight, final total product weight and weights of the individual product layers were recorded for each experimental run to carry out a mass balance and to measure the process efficiency at the end. The amounts of sodium, potassium, calcium, cerium, chromium and chlorine in both the layers were semi-quantitatively measured by SEM-EDS. The phases in the dark-green product layer were identified by XRD and the level of chromium in both the layers was precisely determined by AAS, since removal of chromium from the clean yellow salt phase is of utmost importance in this work.

The base parameters for the experimental verification of chromium behavior were chosen as 500 g of KCl/NaCl salt + 1 mole of cerium chloride/kg salt + 10 g $CrCl_3$, sparged with a gas mix of Ar-20 vol. pct. O_2, at a flow rate of 1 liter/min, at 973 K temperature for a length of time corresponding to 100 percent excess, ie. twice the required amount, of oxygen over stoichiometry. No formation of oxychloride was assumed in the initial determination of oxygen requirement. Also, no free metal was added in the salt. The stoichiometric reactions are given as follows:

$$2\,CeCl_3 + 2\,O_2 \rightarrow 2\,CeO_2\downarrow + 3\,Cl_2\uparrow \qquad [3]$$

$$4\,CrCl_3 + 3\,O_2 \rightarrow 2\,CrO_2\downarrow + 6\,Cl_2\uparrow \qquad [4]$$

Table I lists the variables being optimized and their range of values. The results and discussion presented in this work describe the oxygen quantity optimization. If the reactions go to completion, as predicted by Equations [3] and [4], then a 6.5 percent weight loss should be recorded. Also, if no salt is carried over to the product oxide/oxychloride phase, then the process efficiency can be defined as 100 percent. When the salt is carried over or a complete conversion does not occur, the process efficiency is given by the following equation:

$$\eta = \left(\frac{(3.05 x Cr + 1.76 x Ce)_{oxide\text{-}product}}{(CeCl_3 + CrCl_3)_{init.\ salt}} - \frac{(KCl + NaCl)_{oxide\text{-}product}}{(KCl + NaCl)_{init.\ salt}} \right) x\ 100 \qquad [5]$$

It is evident from the above efficiency relationship, that if a large quantity of salt is carried over to the dark-green product phase, the second term within the parenthesis increases and the efficiency is lowered. However, if the conversion of cerium and chromium chlorides to oxides/oxychlorides is high, the first term increases, resulting in an increase in the efficiency. Therefore, the process efficiency is a combination of these two factors.

RESULTS AND DISCUSSION

The results from fifteen experiments have been tabulated in Table II. The effect of flow rate, amount of excess oxygen over stoichiometry, concentration of oxygen gas in the gas mix and the effect of the amount of chromium chloride have been studied in these experiments. Two aspects have been addressed, (i) the conversion of chromium and cerium into their oxides/oxychlorides and (ii) the identification of the products. Table II shows the data on the study of conversion of chlorides to oxides. This work has an underlying objective of maximizing the discardable portion of the salt. This can be achieved by defining a maximum allowable level of cerium and chromium in the discardable salt portion, since the fraction of salt carried over to the product phase increases as one attempts to convert over 90 pct. of the cerium present in the starting salt, as indicated by the low process efficiencies in Experiment Nos. 6 and 10-12, which show high conversion efficiencies for both cerium and chromium. The data in Table II show that chromium chloride is almost entirely converted to the product phase, irrespective of the flow rate, oxygen concentration, chromium chloride concentration or the time of sparging (excess oxygen). At a high flow rate of 2 l/min and only 100 percent excess oxygen, there is an incomplete conversion of chromium chloride. This can be explained on the basis of a slower kinetics of conversion for $CrCl_3$. A high flow rate essentially lowers the available conversion time for the same amount of oxygen sparged.

The conversion of cerium chloride to cerium oxide (reaction 3) is thermodynamically more favored than the conversion of chromium chloride to chromium oxide (reaction 4). However, the mass effect is strongly in favor of chromium chloride conversion, due to the presence of a very small quantity of $CrCl_3$. Figure 2 shows that for a fixed quantity of total oxygen sparged the conversion of cerium chloride increases with an increase in flow rate. Kinetically, this observation can only be explained by the fact that the pressure of oxygen gas during the sparging increases as the flow rate increases, since the bore diameter of the sparge tube is constant. Increasing the pressure of oxygen gas in the system improves the kinetics considerably, as evidenced by an improved conversion efficiency for $CeCl_3$. Sparging experiments with a richer gas (Ar/O_2 vol ratio = 1.5) at a moderate flow rate of 1.5 l/min show that the cerium chloride conversion efficiency increases with an increase in excess oxygen used. However, the process efficiency does not show a large increase, if over-sparging is done to lower the contents of cerium and chromium.

Optimally, if a cerium chloride conversion of 95 pct. is accepted as the threshold limit and 80 percent of the salt matrix is recovered as the top layer of clean salt, a level of 8 g of cerium/kg of discardable salt will remain. In a recent work (9), where the level of plutonium in the discardable salt was defined at 6 g Pu/kg of salt, only 55-60 pct. of the salt was recovered after sparging with a 50:50 Ar/O_2 gas mix for 3 hours at a flow rate of 1 l/min. Hence, to optimize the salt recovery at an acceptable purity (< 6 g actinide/kg of salt), a rich gas mix (50-60 vol. pct. O_2) at a moderately high flow rate of 1.25-1.50 l/min. is desired.

The sparge time should be kept moderately high by providing up to 300 percent excess oxygen over the stoichiometric requirement. This flow condition has been experimentally verified. It should be noted that the effect of flow rate on the kinetics is directly linked with the height of molten salt pool in the crucible. If the height of the salt pool is increased in the crucible, a higher flow rate will be required to provide the same kinetic effect for a fixed diameter of the sparge tube.

The second aspect of this study deals with the identification of product phases. Table III shows the analytical data for five of the experiments. The amount of cerium and chromium in the top layer have been obtained by SEM-EDS and AAS, respectively. It was found that approximately 33-36 wt. pct. of the consolidated bottom dark-green layer is insoluble in all of the common solvent acids, such as hydrochloric, sulphuric, nitric and hydrofluoric acids, aqua-regia, etc. However, the amount of chromium in the water-soluble fraction of the bottom product was analyzed by AAS. The amount of cerium and chromium in the insoluble portion were determined by SEM-EDS and the phases were identified by XRD.

CeO_2 and CrO_2 were the only two major phases identified by XRD in the insoluble product. The amounts of chromium and cerium in the same insoluble part of the product, as determined by SEM-EDS, are 6-8 wt. pct. and 92-94 wt. pct., respectively. Based on these levels of cerium and chromium, the mixed insoluble oxide is found to be $4\ CeO_2 \bullet CrO_2$. This kind of complex chromate has also been found with other actinides and lanthanides and has been reported to be completely insoluble in most of the strong acid solvents (10). Thus, it is the complexing reaction with chromium oxide which makes the product insoluble. No evidence of oxychloride formation was found, even in the undersparged condition. Oxychloride formation is likely to occur when free metal is also present in the salt (11).

It has been shown in this study that above 79 wt. pct. of the spent ER and MSE salt can be discarded by a proper oxygen sparging of the salt and only 20 wt. pct. of the salt needs to be stored as the radioactively contaminated product. It has also been shown that the discardable salt should be acceptable under RCRA regulations.

CONCLUSIONS

Oxygen sparging tests have been conducted to evaluate the behavior of chromium [RCRA regulated element] and cerium (surrogate for plutonium) in the clean-up of spent ER and MSE salts produced during the production of plutonium. Approximately 20 wt. pct. of the salt is mixed with the product phase of oxides. A flow rate of 1.25 l/min. for Ar-40 vol. pct. oxygen gas mix is adequate for 95 percent conversion of cerium chloride. 250-300 percent excess oxygen over the stoichiometric level is found to be required.

$4\ CeO_2 \bullet CrO_2$ complex oxide has been identified as the product. The discardable portion of the sparged salt is acceptable under RCRA regulations.

REFERENCES

1. D.C. Christensen, J.D. Williams, J.A. McNeese and K.W. Fife, "Plutonium Metal Preparation and Purification at Los Alamos - 1984, Actinide/Lanthanide Separation, Ed. G.R. Choppin, J.D. Navratil and W.W. Schulz, (World Scientific Publishing Co., Singapore, 1984), 238-266.

2. A.M. Murray, Private communication with author, EG&G Rocky Flats Plant, August 1992.

3. L.J. Mullins and A.N. Morgan, "A review of operating experience at the Los Alamos Electrorefining Facility, 1963-1977", LANL Report No. LA-8943, (1981).

4. L.J. Mullins and J.A. Leary, "Fused salt electrorefining of molten plutonium and its alloys by the LAMEX Process", Industrial and Engineering Chemistry, Process Design and Development, 4(4), (1965), 394.

5. D.C. Christensen and L.J. Mullins, "Salt Stripping, A Pyrochemical approach to the recovery of plutonium electrorefining salt residues, "LANL Report No. LA-9464-MS (1982).

6. L.E. McCurry and G-M. M. Moy, " Electrochemical investigation into the mechanism of plutonium reduction in electrorefining", Trans. Am. Nucl. Soc., 55, (1987), 248.

7. K.W. Fife, D.C. Christensen and J.D. Williams, "Plutonium and americium separation from molten salt extraction waste salts", Actinide/Lanthanide Separation, Ed. G.R. Choppin, J.D. Navratil and W.W. Schulz, (World Scientific Publishing Co., Singapore, 1984), 313-325.

8. L.J. Mullins and J.A. Leary, "Molten salt method of separation of americium from plutonium", US Patent No. 3,420,639, January 1969.

9. M.H. West, G.D. Bird and J.E. Valdez, "Oxygen Sparging of Spent Electrorefining Salts for Plutonium Recovery", LANL Report No. LA-12092 (1991).

10. A. Roy and K. Nag, "Studies on rare earth trisoxalatochromates (III), rare earth chromates (V) and rare earth chromites (III)", J. Inorg Nucl. Chem., Vol. 40. (1978), 1501-1505.

11. C.W. Koch, "Thermodynamics of the trichlorides and oxychlorides of some of the lanthanide and actinide elements", Report No. UCRL-2286, Office of Tech. Services, Washington, DC, (1983), 61-65.

TABLE I: RANGE OF VARIABLES IN OXYGEN SPARGING EXPERIMENTS

No.	Parameter	Range
1.	Amount of chromium (III) chloride/500 g salt	0-30 g
2.	Ar/O_2 gas ratio; vol % / vol %	4, 1.5
3.	Amount of excess O_2 over stoichiometry, %	100 - 350
4.	Gas-mix flow rate, l/min.	0.75-2.00
5.	Sparging temperature, K	923-1023

TABLE II: RESULTS OF THE OXYGEN SPARGING EXPERIMENTS TO OPTIMIZE THE QUANTITY OF OXYGEN

Expt. No.	Flow Rate of O_2, l/min.	Amount of excess O_2, %	Amount of $CrCl_3$, g	Ar/O_2 ratio vol/vol	Percent Conversion of $CrCl_3$	Percent Conversion of $CeCl_3$	Process efficiency, % (η)
1.	0.75	100	10	4	99+	2	13.6
2.	1.00	100	10	4	99+	20	28.7
3.	1.25	100	10	4	99+	26	37.3
4.	1.50	100	10	4	99	52	53.4
5.	2.00	100	10	4	94	76	72.7
6.	1.00	200	0	4	----	95	78.4
7.	1.00	100	20	4	99+	51	51.4
8.	1.00	100	30	4	99+	54	55.1
9.	1.50	150	10	1.5	99+	84	73.2
10.	1.50	250	10	1.5	99	91	75.4
11.	1.50	300	10	1.5	99+	96	77.9
12.	1.50	350	10	1.5	99+	93	76.6
13.*	1.25	300	10	1.5	99	92	76.3
14.	1.25	300	10	1.5	99+	95	78.1
15.	1.25	300	10	1.5	99+	97	79.7

* Sparging performed at 1023 K.

TABLE III: IDENTIFICATION OF PHASES AND THE Cr AND Ce CONTENT IN THE PRODUCT

Measurement	**Expt. 3**	**Expt. 5**	**Expt. 6**	**Expt. 8**	**Expt. 9**
Pct. insoluble in bottom layer	**33.8 %**	**36.9 %**	**16.7 %**	**35.6 %**	**36.6 %**
Chromium in insoluble bottom layer [SEM]	**6.2 %**	**8.6 %**	____	**7.4 %**	**5.9 %**
Cerium in insoluble bottom layer [SEM]	**93.8 %**	**91.3 %**	**99.3 %**	**92.5 %**	**94.1 %**
Phases in insoluble bottom layer [XRD]	**CrO_2+ CeO_2**	**CrO_2+ CeO_2**	**CeO_2**	**CrO_2+ CeO_2**	**CrO_2+ CeO_2**
Chromium in soluble bottom layer [AAS]	291 ppm	638 ppm	____	487 ppm	411 ppm
Chromium in soluble top layer [AAS]	12.7 ppm	1390 ppm	____	24.6 ppm	17.9 ppm
Cerium in soluble top layer [SEM]	23.58 %	10.85 %	0.68 %	16.43 %	6.04 %

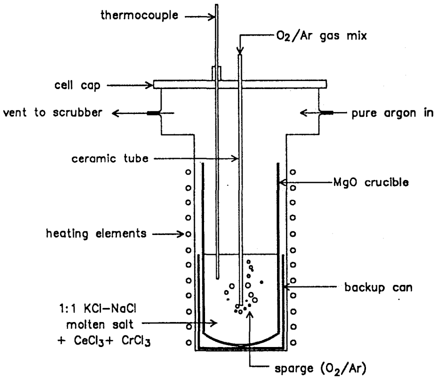

Figure 1: Schematic diagram of the oxygen sparging set-up

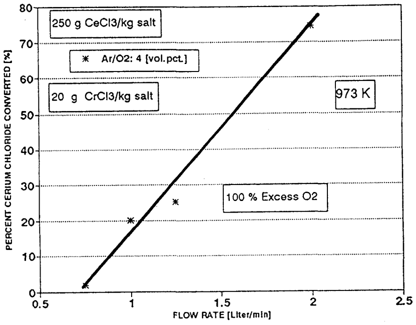

Figure 2: Effect of flow rate of oxygen on the conversion of $CeCl_3$ to CeO_2

DOI: 10.1149/199413.0697PV

DIFFUSION COEFFICIENT OF OXYGEN IONS IN MOLTEN CALCIUM CHLORIDE

B. Mishra, P.D. Ferro and D.L. Olson

Kroll Institute for Extractive Metallurgy
Colorado School of Mines
Golden, Colorado 80401

ABSTRACT

Calciothermic reduction of metal oxides in a molten salt media is a commercial process for the production of certain actinides and lanthanides which produces a calcium oxide saturated calcium chloride salt mix as the process waste. Electrolytic reduction of calcium oxide (CaO) has been carried out in a molten calcium chloride ($CaCl_2$) medium to produce calcium metal cathodically and to regenerate the chloride. A porous ceramic anodic sheath has been used which allows the diffusion of ions from the catholyte into the anolyte. Diffusion of oxygen ions has been found to be the rate controlling step in the electrowinning of calcium metal. The diffusion coefficient of oxygen ions in molten $CaCl_2$ has been measured in the temperature range of 800 - 900°C. The data has been used to design the cell for optimizing the cell efficiency.

INTRODUCTION

Industrial processes must strive to mitigate wastes where the wastes are generated. Reactive metal production using molten salt electrolysis is an example of an industrial process which has progressed towards achieving value-recovery through hazardous waste mitigation. CaO saturated $CaCl_2$ salts are a by-product of the calciothermic reduction of plutonium oxide in the presence of $CaCl_2$, referred to as the Direct Oxide Reduction [DOR] process (Reaction [1]).

$$PuO_2 + 2Ca \rightleftharpoons Pu + 2CaO \qquad [1]$$

The effluent salt is radioactively contaminated and can not be discarded as such. This investigation was aimed at the electroreduction of CaO component of the salt to cathodically produce calcium metal for subsequent reduction of reactive metal oxides and an oxide free $CaCl_2$ for recycling in the DOR process. A summary of the previous work in this area and the results of the extensive investigations have been comprehensively discussed (1,2).

Conclusions regarding the feasibility of electrowinning calcium suggest that (i) atmosphere control is essential to the recovery of calcium, due to its highly reactive nature and strong thermodynamic tendency to form stable compounds, (ii) a net gain of calcium is possible if the rate at which calcium is electrowon is greater than the rate at which calcium is 'lost' due to chemical reactions, (iii) porous ceramic diaphragms must be used to separate anode and cathode products, and thus improve the overall efficiency of the cell and (iv) the transport rate coefficients of ionic species in the molten salt needs to be determined if the kinetics of winning calcium is to be modeled and the processes, which include cell configuration and materials, are to be optimized (3,4). This study has identified the controlling factors for enhancing the calcium deposition rate by placing a ceramic diaphragm between the electrodes which provides the ionic conductivity but keeps the reaction products separated.

The porous sheath requires sufficient porosity to allow transport of specific ionic species, sufficient mechanical integrity to withstand the thermal shock and agitation in the molten salt and sufficient corrosion resistance in the aggressive, high-temperature molten salt environment. The sheath must not react with the ionic species to a degree which causes ionic transport to cease.

An investigation which has relevance to the present study was concerned with the measurement of effective diffusion coefficient in porous media (5) where the effect of path-tortuosity of the porous media on diffusion has been shown. Bouhroum et al.(6) have studied the effect of concentration and viscosity on the effective ionic diffusion. Some of the techniques which have been used to determine diffusion coefficients for particular species include radiotracer methods, chronopotentiometry, and diaphragm cell methods. In this work, the electrolytic recovery rate of calcium was found to depend on the ionic diffusion through the porous membrane. Therefore, measurement of the diffusion coefficient of oxygen ions has been made as a function of cell temperature and membrane porosity. Suggestions for the modification of cell design have also been made to enhance the rate of metal deposition.

EXPERIMENTAL PROCEDURE

The objective of these trials was to demonstrate the process of depositing calcium on the cathode by dissociating CaO, to determine the operating parameters (temperature, voltage, current densities, electrolyte composition) necessary and to investigate the problem areas in calcium recovery. The arrangement of the cell components in a typical cell is shown in Figure 1 and Table I lists the various process parameters used in the experiments.

The furnace and the cell were contained within an argon atmosphere glovebox with a slightly positive argon pressure. The atmosphere was circulated and kept within acceptable purity limits ($O_2 < 50$ ppb). 5.0 wt. pct. CaO was dissolved in $CaCl_2$ at 900°C in a magnesia crucible. A stainless steel backup liner was used to protect the furnace well in the event of a crucible failure. A thermocouple was immersed in the salt bath and contained within an alumina sheath. Consumable graphite anodes and a stainless steel cathode were used for electrolysis. Magnesia porous sheaths (52 mm diameter and 2 mm wall thickness) were used to protect the anode, with a porosity ranging between 20 and 32 percent which allowed the ionic infiltration into the sheath. The porous sheath worked as the anolyte compartment. The initial level of oxygen concentration (calculated from the measured CaO content) was measured. A known weight of salt-mix is dissolved in water and titrated against hydrochloric acid. The dc current was applied to the cell and the anodic gas composition was monitored. The current was interrupted once an appreciable level of chlorine was detected in the anodic gas. Intermediate and final levels of oxygen were recorded by the titration method as a function of time. The cell was held at a set temperature and oxygen ions were allowed to diffuse in and replenish the anolyte. The replenishment was also monitored as a function of time at a given temperature. Once the concentration of oxygen levelled off, current was reapplied and calcium was won at a different temperature . This sequence was continued for four more times at 875, 850, 825 and 800 °C for a given sheath porosity. Equivalent amount of calcium was dissolved in the catholyte and samples from different regions of the solidified catholyte salt were analyzed. Analytical method, based on hydrogen evolution upon water dissolution, was used as the technique to establish the amount of calcium. The collected data is in the form of a concentration measurement in the anolyte chamber as a function of time along with the physical characteristics data of the cell components and the diaphragm. The data was analyzed to obtain a diffusion coefficient of oxygen ions in molten $CaCl_2$-CaO system as a function of temperature.

RESULTS AND DISCUSSION

It was determined that the primary difficulty in obtaining a cathodic calcium deposit is due to the use of graphite anode and the evolution of carbonaceous anodic gases. These gases encourage various back-reactions in the cell through which the deposited calcium is lost (2). Therefore, in this work a porous ceramic anode-sheath was incorporated. Electrowinning under non-steady state conditions (until the point of chlorine gas generation) is performed to achieve a concentration gradient between the anolyte and catholyte. The concentration gradient which is established allows for quantifying the transport rate coefficient across the porous diaphragm. A model was used on the basis of Fick's 1st Law which relates the measured flux of oxygen into the anolyte with the diffusion coefficient:

$$D_{eng} = \frac{C_t - C_{min}}{C_B - \frac{1}{2}(C_t + C_{min})} \cdot \frac{V\,\delta}{A\,t} \qquad [2]$$

where, D_{eng} is the engineering diffusion coefficient for oxygen ions in $CaCl_2$ diffusing through a porous sheath in $m^2 \bullet s^{-1}$, C_B, C_t and C_{min} are the bulk composition of electrolyte, the changing anolyte composition as a function of time, t (sec) and the minimum oxide concentration of anolyte (concentration at the start of diffusion), respectively, in $mol \bullet m^{-3}$, δ is the sheath wall thickness in m, A is the active area of inside wall of porous cylinder in contact with the salt in m^2 and V is the volume of cylinder that is filled with salt in m^3. In the present investigation, the effective or engineering diffusion coefficient is related to the diffusion coefficient for oxygen ions (D_{O2-}) as:

$$D_{eng} = D_{O2-} \frac{f\,\phi}{q}\,\beta \qquad [3]$$

where ϕ is the void fraction of the porous medium calculated by subtracting from unity the ratio of the measured density of the sheath and the theoretical density for magnesia [$3.58 \times 10^3\ kg \bullet m^{-3}$ (7)], q is the tortuosity factor, β takes into consideration possible chemical interactions between diffusing ionic species and the porous media and f is the open porosity fraction. Typical values of tortuosity factor range between unity and two for various media (8). For a perfectly inert media, β would have a value of unity. Because the possible chemical interactions are dependent on the amount of surface area available in the porous microstructure, β is a function of porosity fraction (ϕ), tortuosity factor (q) and sheath wall thickness (δ). The chemical interaction parameter, β, is an adsorption dependent quantity. The open porosity fraction (f) is the fraction of the voids fraction that are open. The open porosity fraction is dependent on the ceramic manufacturing process. In equation (3), D_{O2-} represents the diffusion coefficient for oxygen ions in liquid calcium chloride which is a fundamental property and is only a function of the temperature and the partial pressure of oxygen.

Figure 2 shows a plot of $[C_t-C_{min}]/C_f$ versus time, where $C_f = [(C_t+C_{min})/2 - C_B]$, and the slope of the line is used to calculate the engineering diffusion coefficient at different temperatures. The diffusion coefficients, as a function of temperature have been plotted in Figure 3. The use of Fick's first law is valid only as a first approximation as the driving force changes constantly with time. The measurement of C_t is made in the bulk anolyte which is assumed to be same as the concentration at the inner sheath surface, i.e. $C_{-x,t} = C_{-\delta,t}$.

The purpose of this work is to determine a rate at which calcium may be electrowon from the present experimental system. The model uses Faraday's law modified for the rate limiting process in the system, which is diffusion of oxygen ions into the anolyte. The constraint that oxygen is the rate limiting species in the system is based upon the facts that there is a relatively small quantity (3.3 atom pct.) of oxygen present in the system, the anolyte volume is relatively small (1.28×10^{-4} m^3 compared with 4.5×10^{-3} m^3 for the catholyte) and the cell is operated at an applied potential such that oxygen, carbon monoxide or carbon dioxide gases are evolved, and chlorine gas is not evolved at the anode. The rates of ionic diffusion and electrowinning are linked by:

$$R_{max} = -D_{O2-} \cdot \frac{1.789}{0.0254 - r} \cdot [2\pi r l + \pi r^2] \cdot \frac{f\phi}{q} \cdot \beta \qquad [4]$$

where R_{max} is the maximum rate of winning in kg-moles of calcium per second, r is the inside radius of the sheath and l is the salt height in the anolyte. Thus, the maximum rate of electrowinning can be simulated using Equation (4). Figure 4 shows the relationship of R_{max} and sheath porosity for a given void fraction, ϕ and tortuosity, q. Knowing the maximum rate of electrowinning, the limiting current density can be estimated, using Faraday's law. Assuming favorable conditions for a high rate of calcium electrowinning, a cell can be designed, as shown in Figure 5. The optimization of porosity is essential since large porosity adversely affects the mechanical integrity of the sheath. However, small porosity levels of the sheath make the transport extremely difficult. Since one has to wait for oxygen transport, the transport through the sheath is the rate controlling process. The sheath size, geometry and porosity must be optimized to achieve a calcium winning electrolytic cell. The favorable conditions for a higher flux of oxygen ions into the anolyte are (i) thin walled porous membrane, (ii) high surface area, (iii) high open porosity and (iv) small anolyte volume. Open porosity and wall thickness are factors that, in general, compromise with the mechanical strength of the sheath. A high flux of oxygen ion allows a high current density, thereby increasing the metal recovery efficiency.

Cell Temperature

A high cell temperature in excess of 900°C is desired due to the following factors associated with the cell operation:

[i] High diffusion coefficient for ionic migration.
[ii] High dissolution kinetics for calcium oxide in calcium chloride.
[iii] High fluidity for salt and calcium metal.
[iv] Low dissociation potential for calcium oxide and chloride.
[v] Unstability of calcium carbonate - a possible back-reaction product.

The results show that calcium can be cathodically electrowon by effectively shielding the anode with a porous membrane and by optimizing the sheath parameters to enhance the dissociation rate. The process will be most effective when the electrowon calcium will be used ***insitu,*** to reduce another metal oxide, which will, in turn, maintain a low desired activity of calcium in the cell. These investigations offer potential improvements in waste management in the reactive metal production and provide an accurate mechanistic understanding of the electrolytic calcium metal production process.

CONCLUSIONS

Calcium can be electrowon from calcium oxide-calcium chloride salt mixture by the dissociation of calcium oxide. However, the recovery as a mass requires the use of a proous anodic sheath with over 30 vol. pct. porosity.

Ionic diffusion through the sheath is the rate controlling step. A diffusion coefficient in the range of $10^{-4.6}$ to $10^{-5.6}$ cm^2/sec is obtained for a thirty percent porous magnesia sheath for cell temperatures between 800° and 900°C.

Acknowledgement: The authors acknowledge the material and financial support received from the EG&G Rocky Flats Plant of the US Department of Energy.

REFERENCES

1. P.D. Ferro, B. Mishra, D.L. Olson, J.J. Moore & W.A. Averill, "Recovery of calcium from the effluent of direct oxide reduction process", Residues and Effluents: Processing & Environmental Considerations, Ed. Reddy et al., p 539-550, TMS Publication, Warrendale, PA, [1992].

2. B. Mishra. D.L. Olson and W.A. Averill, "Application of molten salts in pyrochemical processing of reactive metals", Molten Salts, ed. R.J. Gale et al., Electrochem. Soc., Vol. 92-16, (1992), 184-203.

3. P.D. Ferro, B. Mishra, D.L. Olson & W.A. Averill, "Process Optimization for Electrowinning of Calcium", Light Metals 1993, Ed. Das, S.K., p 1129-1136, TMS Publication, Warrendale, PA, [1993].

4. B. Mishra, D.L. Olson & W.A. Averill, "Applications of Molten Salts in Reactive Metals Processing", Emerging Separation Technologies for Metals and Fuels, Ed. Lakshmanan, et al., p 317-328, TMS Publication, Warrendale, PA, [1993].

5. H.L. Weissberg, "Effective Diffusion Coefficient in Porous Media", J. Appl. Phys., 34, 9, 2636-2639 (1963).

6. V.A. Bouhroum, "Investigation on the Determination of Diffusion Coefficients in Porous Media", DGM 33, H 3/4 (1989), pp. 76-81.

7. Handbook of Chemistry and Physics, R.C. Weast, M.J. Astle, W.H. Beyer, eds., 64th Edition., CRC Press, Inc., Boca Raton, FL, (1984).

8. P.C. Carman, Flow of Gases through Porous Media, Academic Press, Inc., London, (1956), pp. 46-49.

TABLE I: CELL OPERATING DATA FOR CALCIUM ELECTROWINNING

Electrolyte	$CaCl_2$, 0-5 wt. pct. CaO
Cell Parameter Figure (1)	
atmosphere:	argon
crucible:	MgO
operating temp.:	800-900°C
current:	15 A
voltage:	5-15 V
time:	variable
Anode	
material:	graphite
size:	12.7 mm ϕ x 305 mm
active area:	11.4-26.6 cm^2
current density:	2.3-8.8 $KA.m^{-2}$
Cathode	
material:	high purity iron
size,:	273 x 152 mm
active area:	0.0173-0.0312m^2
current density:	0.40-1.44$KA.m^{-2}$

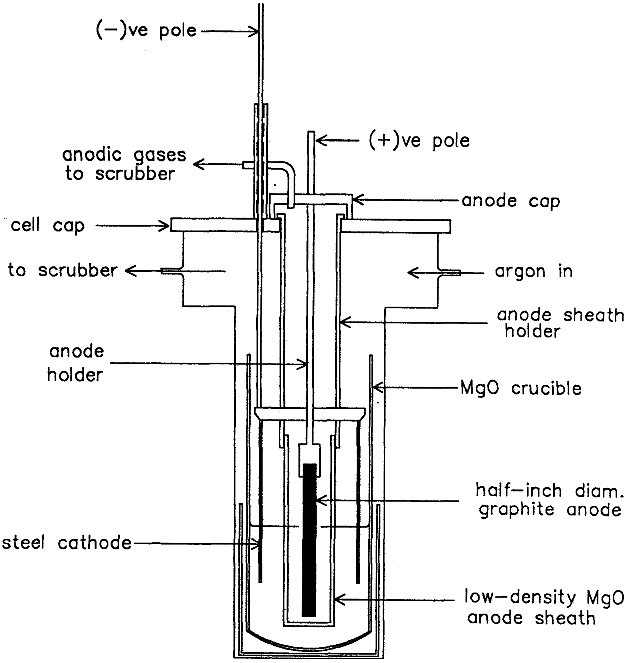

Figure 1: Schematic diagram of the cell showing the 50 mm diameter ceramic sheath around the 13 mm diameter graphite anode-rod.

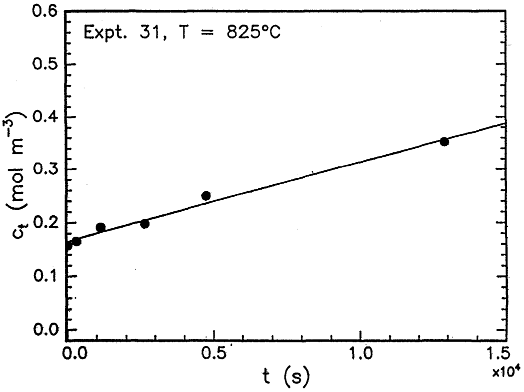

Figure 2: Oxygen ion concentration in the anolyte as a function of time

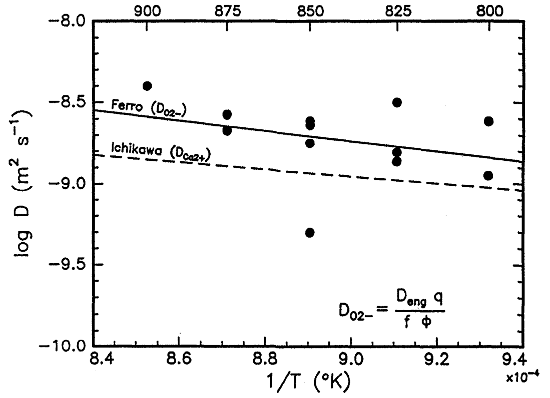

Figure 3: Diffusion coefficient as a function of temperature

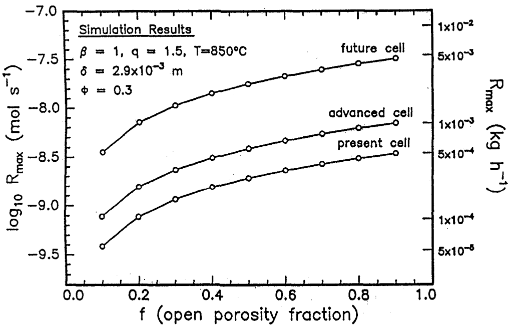

Figure 4: Simulation studies to predict the maximum rate of calcium electrowinning as a function of the sheath porosity

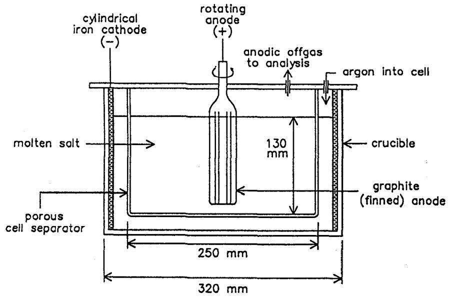

Figure 5: Schematic Diagram of an advanced cell designed to enhance the rate of calcium electrowinning.

DOI: 10.1149/199413.0705PV

COLD CRUCIBLE MELTING: A MULTIPURPOSE TECHNIQUE

Claude G. Sombret

Commissariat à l'Energie Atomique
Rhône Valley Research Center
BP 171, 30207 Bagnols-sur-Cèze, France

ABSTRACT

French research in the area of radioactive waste conditioning has led to the development of a number of promising techniques, some of which have already been implemented at industrial scale. One such technique, cold-crucible melting, in which an electric current is induced in the process material inside a cooled vessel, is of particular interest for certain waste forms, notably clean or contaminated metallic waste, irradiated fuel clads, and low or high-level radioactive solutions. Non-nuclear applications are also feasible, including metal melting or remelting and oxide reduction, notably calciothermic reduction.

INTRODUCTION

The use of induction-heated cold crucible melters by the French *Commissariat à l'Energie Atomique* (CEA) began with the vitrification of a high-level radioactive waste form: concentrated fission product solutions produced in fuel reprocessing plants. A vitrification technique based on an induction-heated crucible was developed and implemented in the vitrification units at the three French reprocessing plants; one such unit has now been operating for over 15 years [1][2].

The limited capacity of this process is sufficient for existing needs. However, to meet the demand for vitrifying large volumes, notably of low-level radioactive wastes, a new development program was undertaken. Preliminary studies had demonstrated the possibility of induction heating of the glass itself, first in an uncooled crucible [3] and subsequently in a cold crucible [4]. Moreover, the inherent advantages of this technique have spurred additional nuclear and non-nuclear applications.

PRINCIPLE

The process uses the transparency to electric fields of a cooled metal structure to create induced currents in the material contained inside the structure. The material may be in a molten state at the core, and partially solidified in contact with the cooled structural wall, hence the frequently used term of *skull melting*.

The cold crucible may be designed to allow continuous casting, for example for metal remelting or for metal processing by direct calciothermic reduction, mainly of metallic oxides or halides. Vitreous materials or molten salts may be cast from the bottom of the melter through nozzles or calibrated orifices, or from the top by overflow or pouring.

A cold crucible induction melter is generally a cylindrical assembly of water-cooled copper tubes separated by a thin layer of insulating material. The peripheral heating inductor is supplied at a suitable voltage and frequency by a motor generator, an inverter or a vacuum tube oscillator, depending on the desired frequency.

APPLICATIONS

Nuclear applications primarily include vitrification of low- or high-level radioactive waste and melting of metal cladding waste after the removal of irradiated fuel. Non-nuclear applications include the glassmaking and metallurgical industries.

Vitrification

The glass is fabricated and melted in a cylindrical, water-cooled metal crucible. The glass in contact with the cooled wall solidifies to a depth of a few millimeters, as the wall temperature does not exceed 200°C. The bottom of the crucible is also a water-cooled metal plate, so the glass is fully contained in a solid glass "crust".

The crucible is surrounded by the coils of an inductor supplied with a high-frequency alternating current, which induces currents in the molten glass that dissipate heat by Joule effect (the resistivity of molten glass is a few Ω·cm). In order to ensure suitable electrical efficiency when transferring power from the inductor to the melt, the frequency must be determined so the penetration depth of the induced currents in the glass is less than the crucible radius. The penetration is given by the following relation:

$$p = \sqrt{\frac{\rho}{\pi \mu_0 \mu_r F}}$$

where p is the penetration depth in meters, ρ the glass resistivity in Ω·m, μ_0 the magnetic permeability of empty space ($4\pi \times 10^{-7}$ H·m^{-1}), μ_r the relative magnetic permeability of the glass and F the inductor frequency in Hz. The following simplified formula is generally used:

$$p = 503\sqrt{\frac{\rho}{F}}\ .$$

The metal crucible containing the glass must be sectorized to ensure relative transparency to the electromagnetic field generated by the inductor; otherwise, it would constitute a Faraday cage, preventing the formation of induction currents to heat the glass. The power density transmitted to the glass decreases to zero from the wall to the center of the melt; this gradient provides for convective stirring within the molten glass. The glass level rises along the wall and diminishes in the center of the crucible. There is no electromagnetic stirring effect, since the electromagnetic forces are one or two orders of magnitude lower than those generated by the thermal gradient.

The melting facility comprises four subsystems: a water-cooled sectorized cold crucible; a crucible bottom structure supporting the glass casting nozzle; a high-frequency generator, inductor and trimming capacitors; and a glass preheating system required on startup, since cold glass is a poor conductor and must be preheated until the energy transmitted by induction exceeds the thermal losses.

The crucible (Figure 1) is an assembly of stainless steel sectors forming a cylindrical structure. Typical crucibles are 0.55 m in diameter and 0.70 m high, although the actual dimensions may be smaller or larger (e.g. 1.50 m diameter). A three-dimensional computer model is used to optimize the dimensions and ensure better than 80% electrical efficiency. Each sector has a rectangular cross section, and includes water ports mating with the inlet and outlet manifolds. The sectors are separated from one another by electrically insulating material. The structure is maintained externally by strapping with refractory fabric.

The cold crucible is supported by a bottom structure comprising a water-cooled stainless steel center plate and a refractory cement outer ring. The refractory assembly is molded to allow handling. Water cooling of the center plate and crucible walls is sufficient to solidify the glass in contact with the refractory ring, forming a continuous layer around the melt. The center plate supports the following elements:

- a casting nozzle extending into the melt, designed to retain a sufficient glass heel to allow continued induction after casting; it comprises either a glass freeze valve controlled by a medium-frequency inductor, or a separate mechanical shutter;
- a drain nozzle with an induction-heated freeze valve at the bottom of the crucible to empty the glass heel;
- air or argon injectors extending into the melt to ensure thermal and chemical homogeneity by stirring if necessary.

A vacuum tube generator with three shunted triodes supplies 240 kW at 12 000 V at a frequency of 335 kHz for a crucible 0.55 m in diameter. A high-frequency line consisting of two water-cooled copper sections connects the generator to a multiple-winding inductor placed around the cold crucible. The geometry of the oscillating circuit and the distribution of the trimming capacitors ensure a null potential between the cold crucible and earth, making additional insulation unnecessary between the crucible and its supporting structure.

A microwave preheating system was adopted because it allows energy to be transmitted to the cold glass without contact, and without requiring placement of the generator in the shielded cell containing the melter: no mechanical or electronic components of unproven reliability are therefore located inside the cell.

Most of the cold crucibles implemented to date have used a 25 kW microwave generator operating at a frequency of 915 MHz, transmitting energy to the melter via a rectangular waveguide with inside dimensions of 124 × 248 mm. The waveguide is connected to the tapered upper junction; a quartz window on the melter end ensures a leaktight seal.

Not only does this process prevent corrosion and allow higher capacities than a system in which the current is induced in the crucible itself, it also allows higher melting temperatures to be obtained without difficulty. The glass melting temperature may easily be raised above 1200°C since the energy input to the glass is unlimited (this type of crucible has successfully been used to melt UO_2 at 2500°C).

Several thousand hours of tests have been conducted to date with melters 0.35, 0.55 and 1.20 m in diameter, supplied with ground glass or with simulated waste at temperatures ranging from 1150 to 1380°C. The maximum capacity has been about 25 $kg \cdot h^{-1}$ for the 0.35 m diameter melter, and 50 $kg \cdot h^{-1}$ for the 0.55 m diameter melter. The actual throughput depends not only on the melter diameter, but also on the temperature. At 1300°C, a melter 1 meter in diameter can produce 200 kg of glass per hour when supplied with dry material. Testing with liquid feed resulted in a lower capacity, and raised some technological problems.

The process is perfectly suitable for producing conventional glass materials with high added value such as "crystal" glass: from an energy standpoint, the power transmission efficiency from the inductor to the melt ranges from 70 to 90%, allowing a specific power consumption of 1.5 to 10 $kWh \cdot kg^{-1}$ depending on the melter size and material (larger melters consume less power).

Metal Melting

Metal melting applications mainly involve metal waste consisting of irradiated fuel cladding "hulls", produced by reprocessing spent fuel from different types of reactors. After the subassemblies are cut up and the fuel is dissolved in a nitric acid solution, the waste consists primarily of short cladding tube scraps made of zircaloy in pressurized water reactors, or of stainless steel in fast breeder reactors. The hulls are both alpha and high-level beta-gamma wastes, as they may contain transuranic nuclides in residual undissolved fuel as well as high-level fission or activation products.

Such wastes are currently embedded in cement at the reprocessing complex. Melting would produce a better quality final waste form in a much smaller volume. The cold crucible process has therefore been adapted for this purpose, generally using a current frequency of 10 kHz produced by a motor generator.

Melting occurs in the presence of oxide or fluoride flux which fills the gap formed by magnetic striction between the molten metal and the cold crucible. The flux is important in digesting the oxides formed during melting, as well as any residual (e.g. uranium and plutonium) oxides still contaminating the hulls after fuel dissolution. This process is facilitated by vigorous electromagnetic stirring of the molten bath. The crucible includes a sealed cover assembly for controlled atmosphere melting. The cover also includes metered inlets for cladding hulls and flux, together with the argon inlet and off-gas outlet ports.

At the beginning of the melting process, a water-cooled mobile furnace bed is positioned so that its top face is level with the bottom of the inductor. The cold crucible is then continuously fed with metal scraps and a suitable percentage of slag. When the molten metal bath reaches a predetermined level, the bed begins to move downward continuously to maintain a constant level in the crucible. The metal solidifies as it exits the inductor, allowing the extraction of an ingot with the diameter of the crucible and with any desired length, surrounded by a thin layer of solidified slag. Most of the slag detaches naturally from the ingot during cooling and is suitable for further treatment.

A full-scale prototype unit (Figure 2) implementing this process has been built by the CEA. The facility includes the following major components:

- the melter assembly comprising a 20 mm I.D. cold crucible surrounded by an inductor supplied with 10 kHz current from a motor generator rated at 300 kW. A conical manifold above the crucible provides for process inlet and outlet flows (hulls, flux, argon, off-gas); the complete assembly is cooled with demineralized water;
- the hull feed system, including a feed hopper and a rotating disk distributor;
- the flux feed system installed in a glove box and connected to the cold crucible via a series of shutoff valves;
- the off-gas treatment system, comprising a particle separator, scrubbing column and HEPA filter stage;
- the ingot drawing machine.

Melting is performed automatically using a centralized control system to produce ingots 200 mm in diameter and 1000 mm long. Tens of metric tons of nonradioactive zircaloy and stainless steel hulls have been melted in this prototype unit.

A similar facility has been built in a hot cell at the CEA's Marcoule pilot reprocessing plant, and will soon begin operation. A unit of this type can handle 150 tons of hulls on the basis of 250 working days a year. Two units will be required for a facility such as UP3, one of the reprocessing plants located at La Hague, which produces 250 tons of hulls per year. A small-scale device producing ingots 0.57 m in diameter weighing about 3 kg each has also been set up in a hot cell for material investigation purposes. Ingots cast from actual radioactive zircaloy or stainless steel hulls are routinely produced in this cell.

Other Applications

Uranium metal is generally produced by metallothermic reactions between UF_4 or U_3O_8 and reactant metals such as calcium, magnesium or aluminum. A cold crucible reaction process would present a number of advantages:

- high-frequency induction melting of raw materials creates suitable reaction conditions;
- magnetodynamic phenomena created by the electric fields may favor coalescence of the metal and improve the uranium ingot quality;
- the cold structure is capable of removing the heat generated by the exothermic reaction, and thus shortening the fabrication cycles;
- the process is well suited to continuous production runs.

The validity of the method has been demonstrated by calciothermic tests with UF_4 and U_3O_8.

Cold crucible induction calciothermy may also be applied to other metals. Tests with neodymium fluoride to produce Nd-Fe alloys have yielded promising results.

Finally, cold crucible induction melting is ideal for use with highly corrosive materials. Melting tests with monopotassium phosphate and sodium polypentaphosphate have shown no corrosion of the crucible.

CONCLUSION

Cold crucible induction melting is a very promising technique for the nuclear industry, for melting low or high-level radioactive metallic or nonmetallic waste. In conventional industrial applications, it could replace widely used processes when the resulting improvements offset potentially higher fabrication costs.

REFERENCES

1. C. Sombret, *Nuclear Energy*, 24/2, 85-98 (April 1985).
2. J.P. Moncouyoux and C. Sombret, "French High-Level Waste Management Research and Development Program", International High-Level Radioactive Waste Management Conference, Las Vegas (1982).
3. J. Moulin, J. Reboux, R. Bonniaud and C. Sombret, *Verres et Réfractaires*, 26/4 (1972).
4. J.P. Moncouyoux, R. Boen, M. Puyou and A. Jouan, RECOD '91, Sendai, Japan, *Proceedings of the Atomic Energy Society of Japan and Japan Atomic Industrial Forum*, I, 307-311 (1991).

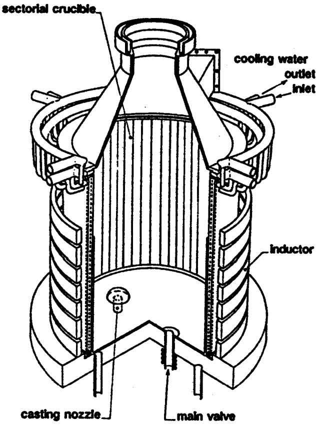

Fig. 1 : COLD-CRUCIBLE MELTER FOR GLASS MELTING

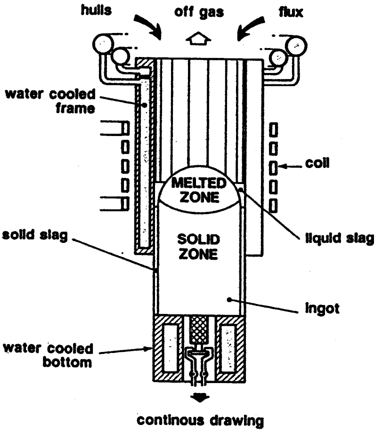

Fig. 2 : INDUCTION MELTING PROCESS FOR HULLS

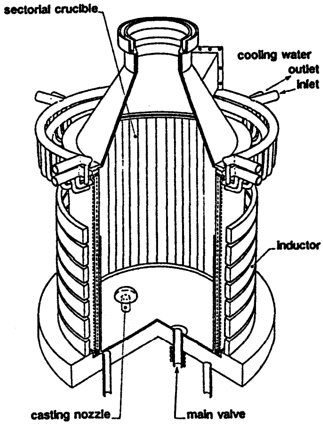

Figure 1. Cold Crucible Melter for Glass Melting

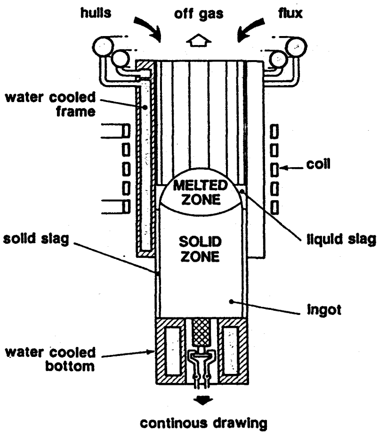

Figure 2. Induction Melting Process for Cladding Hulls

DOI: 10.1149/199413.0713PV

Ion Replacement Electrorefining

J. L. Willit, Z. Tomczuk, W. E. Miller, and J. J. Laidler

Argonne National Laboratory
Chemical Technology Division
Argonne, Illinois 60439

ABSTRACT

At Argonne National Laboratory we are developing a two-step electrochemical process for purifying and separating metals called *ion replacement electrorefining*. In each step, metal cations formed by oxidation at an electrode replace other metal cations that are reduced at another electrode. Using this approach, we have separated or purified uranium, dysprosium, and lanthanum on a laboratory scale. This paper explains the ion replacement concept and presents the results of these demonstration experiments.

INTRODUCTION

Background

The concept of ion replacement electrorefining grew out of our work in pyroprocessing spent metal fuel for the Integral Fast Reactor under development at Argonne National Laboratory. In that program conventional electrorefining[1] of the spent fuel is used to separate the actinides from the rare earths and fission products in a molten chloride salt. In conventional electrorefining, impure metal is oxidized at the anode and pure metal is deposited at the cathode. These two processes are referred to, respectively, as anodic dissolution and cathodic deposition. With careful control of the cell potential, more-noble impurities, such as ruthenium, remain in the anode and less-noble impurities, such as the rare earths, remain dissolved in the electrolyte. Deposition of pure metal at the cathode and oxidation of impure metal at the anode occur simultaneously. Several batches of impure metal can be processed in succession. Eventually, however, it is impossible to obtain a pure deposit because the less-noble impurities that accumulate in the electrolyte contaminate the product. The electrolyte must be replaced or processed to remove the impurities. We conceive ion replacement electrorefining as an alternative to conventional electrorefining. As in conventional electrorefining, the more-noble impurities are left behind in the anode. However, in ion replacement electrorefining, the pure metal is removed first, *followed by* the less-noble impurities. In ion replacement electrorefining, the less-noble impurities do not accumulate in the electrolyte.

We also conceive ion replacement electrorefining as an alternative to electrowinning. Electrowinning begins with the metal being processed already oxidized and dissolved in the electrolyte. A potential is applied between two electrodes, and metal deposits at the cathode. Oxidation of the most easily oxidized species occurs at the anode. Typically this results in the formation of corrosive gases such as chlorine or oxygen. The greatest challenge in most electrowinning schemes is the selection of a suitable anode that is not corroded or consumed by oxidation. Ion replacement electrorefining addresses this problem as well.

In ion replacement electrorefining, anodic dissolution and cathodic deposition are conducted in two separate steps. This approach allows one to remove the impurities after each process cycle by use of an ion replacement electrode. Figure 1 shows anodic dissolution, the first step in ion replacement electrorefining. Alkali metal cations from the molten electrolyte are reduced to the metallic state at the ion replacement electrode. At the anode, replacement cations are formed as the metal being processed is oxidized into the electrolyte. This first step is analogous to re-charging a discharged battery. The second step, shown in Fig. 2, is analogous to discharging a battery. Metal cations formed in the first step are deposited sequentially at the cathode. Replacement alkali metal cations are formed by oxidation of alkali metal at the ion replacement electrode. The system is consequently restored to its initial "discharged" state.

If two different metals are anodically dissolved in the first step, the degree of separation achievable in the second step is a function of ΔE_{dep}, the difference deposition potentials of the two metals. For ΔE_{dep} values of 0.010 V, 0.10 V, and 0.30 V, the theoretical purity of the metal deposits (assuming a three-electron reduction at 728 K) is 61.73%, 99.17%, and 99.9999%.

This technology has several potential applications in nuclear and non-nuclear areas. In nuclear areas, ion replacement electrorefining could be used to recover actinides from a variety of pyrochemcial process wastes. Non-nuclear applications include separation of transition metals and rare earths and the removal of trace sodium from the molten salt baths used in lithium production. Ion replacement electrorefining also simplifies the electrochemical determination of activity coefficients of species in solution because it affords a simple way to add or remove select species.

Approach

We are developing two types of ion replacement electrodes. Type I consists of a molten alkali metal separated from the bulk electrolyte by an ion-conducting solid electrolyte. Type II consists of an alkali metal alloy in which the activity of the alkali metal is greatly suppressed. The majority of the 21 ion replacement experiments performed to date have focused on the Type I electrodes. However, as we discuss below, some success has been achieved with the Type II electrodes as well.

In our Type I electrodes, Na β"-alumina, a Na^+ ion conductor, separates the ion replacement metal, sodium, from a molten chloride electrolyte. Most metal chlorides are soluble in molten chloride salts, and molten salt electrolytes afford a much wider electrochemical potential working region than aqueous or organic systems. Sodium β"-alumina is a well-characterized, commercially available material that has been often used in molten salt applications, most notably the Na/S battery system. Sodium β"-alumina has a spinel structure and its general formula is $Na_{1+x}M_xAl_{1+x}O_{17.1}$, where the dopant species M is typically Li^+, Mg^{2+}, Ni^{2+}, or Zn^{2+}. In our case, the dopant was Li^+. Although Na β"-alumina is a sodium ion conductor, other cations will exchange with Na^+ and transport through the material. For example, Ag^+, K^+, and Tl^+ undergo good exchange with Na^+, whereas Li^+ and Cs^+ do not. Therefore, to minimize this exchange process, we selected a ternary chloride salt, CsCl-LiCl-NaCl, for our initial tests.

Our main objectives for this work were to identify a suitable Na β"-alumina/electrolyte system capable of operation at 575 to 775 K, to conduct tests on the anodic-dissolution and cathodic-deposition behavior of selected materials using the Na β"-alumina ion replacement electrode, and to identify possible alloys for use in a Type II electrode.

EXPERIMENTAL

Reagents

All experiments used a CsCl (77.7 wt%)-LiCl (13.7 wt%)-NaCl (8.6 wt%) salt. These salts, along with $LaCl_3$ and $DyCl_3$. were obtained from APL Engineered Materials (Urbana, IL) and were >99.99% pure as analyzed by the manufacturer.. Sodium (99.95% pure) was obtained from Aldrich Chemical Co. (Milwaukee, WI) as ingots sealed under nitrogen in glass ampoules. Uranium metal rods were obtained from the Special Materials Division at Argonne National Laboratory.

Two sizes of Na β"-alumina tubes, each closed at one end, were obtained from Ceramatec (Salt Lake City, UT) for these experiments. The "small" tubes measured 1.0 cm O.D. x 10 cm long x 0.09 cm thick, and the "large" tubes measured 1.5 cm O.D. x 20 cm long x 0.1 cm thick. Ceramatec reports a Na^+ ion resistivity of 3.5 Ω·cm at 628 K for their β"-alumina tubes.

Equipment

The experiments were conducted with an electrochemical cell placed in a furnace well suspended from the floor of a glove box. Stacked stainless steel heat shields were placed at the top of the furnace well. Holes in the heat shields allowed two electrodes, a thermocouple, and a stirrer to be placed in the cell. The furnace well was heated by a resistance furnace. Oxygen and water levels in the glovebox were maintained at <4 ppm and <0.1 ppm, respectively, by a Vacuum Atmospheres Dri-Train purification system. The electrochemical cell included a stainless steel crucible placed in a MgO secondary crucible to isolate the cell from earth ground. The nested crucible pair was placed inside a third crucible to catch the cell contents in the event of leakage or breakage of the primary or secondary crucibles. All experiments used a two-electrode configuration. A metal electrode (uranium or mild steel) was attached to a stainless steel rod using a Swagelock® fitting. An alumina tube insulated the rod as it passed through holes in the heat shields. The ion replacement electrode consisted of a sodium-filled Na β"-alumina tube supported by a stainless steel shroud. The molten salt contacted the Na β"-alumina tube through holes drilled in the shroud. A Swagelock® connector joined the shroud to an alumina-insulating tube. Electrical contact with the sodium inside the β"-alumina was made by placing a steel rod down through the alumina tube. All experiments were conducted at 728 K. The cell temperature was monitored to within ± 0.2 K with a calibrated chromel-alumel thermocouple.

Cell potential and current were controlled using an EG&G PAR Model 173 potentiostat or a Fluke Model 382A voltage/current calibrator. Current, potential, and temperature data were acquired every 60 seconds using a National Instruments AT-MIO-16H A/D converter installed in an IBM-PC compatible computer. Commercial data acquisition software (Labview® or Labtech Notebook®) was used to process and store the data for later analysis.

Experimental procedures

The Na β"-alumina tubes were loaded with sodium by pipetting liquid sodium metal into the heated Na β"-alumina tube. Once the tubes were loaded, the temperature was increased slowly until the sodium wet the tube, which typically occurred at ~578 K. The sodium-loaded β"-alumina tube was then slowly cooled to room temperature and placed in the stainless steel shroud. The entire cell was then assembled, lowered into the furnace well, and heated at 2 K/min to 728 K with the electrodes suspended slightly above the surface of the molten electrolyte, which contained small concentrations of the rare earth chlorides or uranium chloride. The electrodes were then lowered into the melt. Wires were connected to the electrodes using alligator clips. The molten electrolyte was stirred to minimize concentration polarization at the electrodes. Cell currents typically ranged from 5 to 50 mA. These currents correspond to current densities of 1 to 3 mA/cm^2 at the sodium ion replacement electrode and 20 to 65 mA/cm^2 at the counter electrode. Current densities were low because the concentrations of La^{3+}, Dy^{3+}, or U^{3+} in the molten electrolyte were low. Conductivity of the Na β"-alumina did not limit the current.

Filtered salt samples were taken using tantalum tubes fitted with a tantalum frit. The details of this sampling procedure have been described previously.[2] Inductively coupled plasma/atomic emission spectroscopy (ICP-AES) analyses of the molten salt and the cathode deposits were performed by the Analytical Chemistry Group of the Chemical Technology Division at Argonne National Laboratory. The analytical results were reported to be accurate to ± 10%.

RESULTS AND DISCUSSION

Rare earth studies

We chose dysprosium and lanthanum for our initial rare earth investigations because the ΔG°_{f} values for $DyCl_3$ and $LaCl_3$ are separated by 83 kJ/mol (0.286 V). As discussed above, this degree of separation is sufficient to give a >99.99% theoretical separation of the two metals by ion replacement if the potential is controlled. For the initial experiment our goal was to deposit both metals from the melt onto a cathode, making no attempt to separate dysprosium from lanthanum. We began with 0.156 wt% $DyCl_3$ and 0.134 wt% $LaCl_3$ in the CsCl-LiCl-NaCl electrolyte. Initially, setting the potential at 1.0 V (cathode vs. sodium ion replacement electrode) gave a current of 0.8 mA. After 2.5 hours, we decreased the applied potential to 0.05 V, and the current increased to 16.8 mA. We then decreased the applied potential further to -0.35 V and the current rose to 40 mA.

Because our applied potentials were referenced to the sodium ion replacement electrode, at negative potentials we expected sodium to deposit as well as lanthanum and dysprosium. In spite of the expected sodium co-deposition, we continued at -0.35 V and passed an amount of charge exceeding the amount required to deposit all the dysprosium and lanthanum from the electrolyte. We assumed that any sodium that deposited on the cathode would re-oxidize as long as $DyCl_3$ or $LaCl_3$ were available in solution. However, upon removing the $DyCl_3$ or $LaCl_3$ from the melt, the only possible reaction left was the electrotransport of sodium from the sodium ion replacement electrode to the cathode. The experiment gave the expected results. Lanthanum and dysprosium deposited as metals on the cathode. There was also clear evidence of sodium electrotransport. As we examined the cell at the end of the experiment, we found that sodium metal had deposited at the cathode, vaporized, and condensed in the cooler regions of the cell.

We were also surprised to find that the cathode deposit was coherent, not dendritic. (See Fig. 3.) It appears that sodium co-deposition has a leveling effect on rare earth metal deposition. Chemical analysis of the deposit revealed that it consisted of dysprosium, lanthanum, and sodium metal as well as the CsCl-LiCl-NaCl salt. Analysis of the electrolyte confirmed that we had lowered the Dy^{3+} and La^{3+} concentrations to 180 ppm and 390 ppm, repectively.

Next, we attempted to separate dysprosium and lanthanum by sequential deposition under controlled current conditions. Calculations predict that dysprosium deposition occurs at

0.75 V to 0.55 V, and that lanthanum deposition occurs at 0.45 V to 0.3 V. We operated the next experiment under controlled current conditions, intending to use the potential as an indicator of which species, dysprosium or lanthanum, was being deposited at the cathode. We set the cell current at 30 mA and passed 0.048 equivalents of charge. This should have deposited ~90% of the dysprosium from the melt. Analysis of the salt revealed that the dysprosium concentration decreased 77%, from 0.156 wt% to 0.036 wt%, while the lanthanum concentration decreased only 8.5%, from 0.133 wt% to 0.122 wt%. The coulombic efficiency to this point was ~100% based on the amount of charge passed and the concentration change measured in the melt. With the current set at 30 mA, the cell potential decreased to <0.4 V towards the end of the experiment. Evidently 30 mA exceeded the diffusion-limited current for dysprosium deposition and some lanthanum deposited as well. Therefore the potential vs time plot did not show two plateau regions, one for dysprosium deposition and one for lanthanum deposition. Better separation should occur by using controlled potential deposition or by decreasing the current to maintain the desired voltage.

We continued this experiment and passed a total of 5.7×10^{-3} equivalents. Analysis of the salt revealed that the lanthanum and dysprosium concentrations in the melt had decreased to 0.004 wt% and 0.008 wt%, respectively. The coulombic efficiency remained at ~100%. We expect that even lower concentrations could have been achieved by passing additional current.

We have also removed La^{3+} and Dy^{3+} from the CsCl-LiCl-NaCl electrolyte using a Type II ion replacement electrode of Li_2Sb alloy. Alloying lithium with antimony shifts the lithium redox potential ~0.7 V.[3] This alloy will not spontaneously reduce La^{3+} and Dy^{3+} from the electrolyte and thus can be used as an ion replacement electrode. Using the Li_xSb ion replacement electrode in the Fig. 2 configuration, we decreased the La^{3+} concentration from 0.32 wt% to 56 ppm, and the Dy^{3+} concentration from 0.39 wt% to 44 ppm.

Uranium studies

Because the rare earth studies did not demonstrate the anodic dissolution step, we began our uranium study with the anodic dissolution of a uranium rod. The cell was configured as in Fig. 1. We visually inspected the salt after passing 1.0×10^{-3} equivalents and found that it was pink--an unmistakable indicator of the presence of UCl_3. We reversed the polarity and passed another 1.0×10^{-3} equivalents and the pink color disappeared. When the experiment was repeated by passing 1.6×10^{-3} equivalents, the salt was a slightly darker pink, and analysis showed it to contain 0.043 wt% uranium. We also observed a decrease in diameter for the submerged portion of the uranium rod shown in Fig. 4. The Na β''-alumina tube ruptured in the course of re-depositing the uranium back onto the uranium rod.

Concluding remarks

This work demonstrates the feasibility of ion replacement electrorefining of rare earth and actinide metals. Using a sodium ion replacement electrode, we anodically dissolved and re-deposited actinide metals, demonstrated deposition and separation of two rare earth metals, and showed that ion replacement can reduce $LaCl_3$ and $DyCl_3$ concentrations to <0.008 wt%. We expect that even lower concentrations can be achieved with this approach. However, to do so will require more time and lower current densities. The Li_2Sb alloy used in our Type II ion replacement electrode also behaved as we expected. This electrode decreased the La^{3+} and Dy^{3+} concentrations to <60 ppm.

In the Type I ion replacement electrodes, the Na β''-alumina behaved as expected, isolating the ion replacement metal, sodium, from the bulk electrolyte while providing ionic conductivity. The CsCl-LiCl-NaCl salt was also compatible with this ionic conductor. In future experiments we will evaluate diagnostic tools such as dc resistance and ac impedance for assessing changes in the performance of Na β''-alumina in the Type I electrodes. Microscopic examination as well as dc resistance and ac impedance measurements will be performed.

We will continue to study ion replacement electrorefining of rare earths and actinides using Type I and Type II electrodes. In the next phase of this work we will conduct larger-scale experiments using higher concentrations of rare earths and actinides and will explore the application of ion replacement electrorefining to transition metals such as titanium and zirconium.

ACKNOWLEDGMENTS

This work is being funded by the United States Department of Energy, Office of Basic Energy Sciences, Division of Advanced Energy Projects.

REFERENCES

1. J. L. Willit, W. E. Miller, and J. E. Battles, J. Nucl. Mat., 195, 229 (1992).

2. D. S. Poa, Z. Tomczuk, and R. K. Steunenberg, J. Electrochem. Soc., 135, 1161 (1988).

3. R. A. Huggins in "Fast Ionic Transport in Solids--Electrodes and Electrolytes, P. Vashishta, J. N. Mundy, and G. K. Shenoy, Eds., North Holland, New York, pp. 53 (1979).

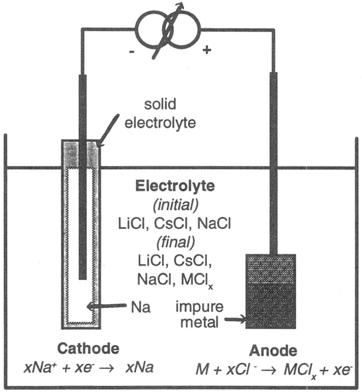

Fig. 1. Diagram of Anodic Dissolution Step in Ion Replacement Electrorefining.

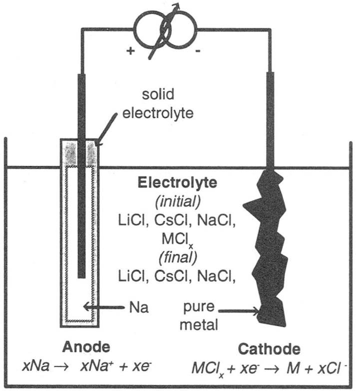

Fig. 2. Diagram of Cathodic Deposition Step in Ion Replacement Electrorefining.

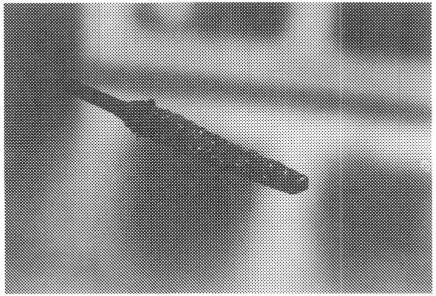

Fig. 3 Codeposited dysprosium and lanthanum metals.

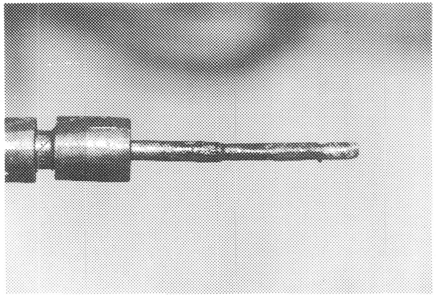

Fig. 4. Uranium rod after anodic dissolution.

DOI: 10.1149/199413.0721PV

METHOD FOR REMOVAL OF HEAVY METAL FROM MOLTEN SALT

E. C. Gay, W. E. Miller, and J. J. Laidler
Argonne National Laboratory
Chemical Technology Division
9700 South Cass Avenue
Argonne, Illinois 60439-4837 U.S.A.

ABSTRACT

The pyrometallurgical process for recycling spent metal fuels from the Integral Fast Reactor (IFR) involves electrorefining spent fuel in a molten salt electrolyte (LiCl-KCl-U/$PuCl_3$) at 500°C. At some point, the concentrations of alkali, alkaline earth, and rare earth fission products in the salt must be reduced to lower the amount of heat generated in the electrorefiner. The heavy metal concentration in the salt must be reduced before removing fission products from the salt. The operation uses a lithium-cadmium alloy anode that is solid at 500°C and a solid mandrel cathode. In tests conducted in an engineering-scale electrorefiner (10 kg uranium per cathode), good separation was achieved while removing uranium and rare earths from the salt. Only 13% of the rare earths was removed, while 99.9 % of the uranium in the salt was removed; subsequently, the rare earths were also reduced to low concentrations.

INTRODUCTION

Electrorefining is a key step in the pyrometallurgical process that was developed to recover uranium, plutonium, and minor actinides from spent metal fuel (1,2) from the Integral Fast Reactor (IFR). The IFR is an advanced reactor concept that was developed at Argonne National Laboratory. It has these distinguishing features: It is a sodium-cooled, pool-type reactor; that is, all the major components, reactor core, pumps, and heat exchangers are in a large sodium-filled pot) (3). It employs a metallic fuel, a U-Pu-Zr alloy clad with a stainless steel alloy. It has an integral fuel cycle, whereby discharged core and blanket materials are processed and refabricated in an on-site facility.

We previously have reported experiments using an engineering-scale electrorefiner (4). The electrorefiner consisted of a cadmium anode or anodic dissolution baskets, solid and liquid cathodes, and a molten salt electrolyte (LiCl-KCl) at 500°C. A dual cathode approach was adopted where uranium is recovered on a solid cathode mandrel and uranium-plutonium is recovered in a liquid cadmium cathode. In the engineering-scale electrorefiner, we have demonstrated the following: electrotransport of uranium from the cadmium anode to a solid cathode in 10-kg batches; anodic dissolution of 10-kg batches of chopped fuel (U-10 wt % Zr); and recovery of 4 kg of heavy metal using the liquid cadmium cathode.

EXPERIMENTAL EQUIPMENT

Electrorefiner Assembly

An engineering-scale electrorefining facility that can support 10 kg of uranium on a single solid cathode was constructed to demonstrate the electrolytic transport of uranium at plant-scale levels and to measure the dissolution rate of clad segments of uranium-zirconium alloy. The electrorefiner assembly is enclosed by a 42-cubic-meter, argon-filled glovebox (with ovens, transfer locks, wells, and lifting systems), that is equipped to control gas pressure, temperature, and gas purity.

Schematic of Drawdown Operation

A schematic representation of the drawdown operation is shown in Fig. 1. A lithium-cadmium alloy (5.8 wt % lithium) that is solid at 500°C is loaded into the anodic dissolution baskets and rotated at 75 rpm; current is driven from the anodic dissolution baskets to a solid mandrel cathode, that has a ceramic catch crucible below to collect product that falls off of the solid cathode. Salt and cadmium mixers are operated at 150 and 50 rpm, respectively. The possible drawdown reactions include (1) electrotransport of lithium to the solid cathode and lithium reduction of the uranium and rare earth chlorides at the solid cathode and (2) lithium reduction of the uranium and rare earth chlorides at the anode and electrotransport of the uranium and rare earths to the solid cathode. The design criteria that had to be met for the drawdown equipment include the following: (1) control of the reduction rate by lithium, (2) good separation between uranium and rare earths, and (3) the capability to collect uranium and rare earths over a wide range of salt concentrations.

EXPERIMENTAL RESULTS

The concentrations of uranium in the cathode deposits from the drawdown runs were found to fall into three ranges: low (<0.1 wt %), medium (31.8-39.2 wt %) and high (70-89.3 wt %). The results are summarized in Table I.

Table I. Summary of Data from Drawdown Operations in the Engineering-Scale Electrorefiner

U in Cathode Deposit, wt %	U in Salt, wt %	Run	Rare Earths in Cathode Deposit, wt %
High			
89.3	4.33	65	<0.01
79.5	1.75	71	1.2
73.2	6.68	58	<0.01
70.0	2.98	70	1.1
Medium			
39.2	0.72	75	1.8
32.4	0.14	76	2.7
31.8	1.3	72	2.8
Low			
<0.1	0.015	77	31.8

High Uranium Concentration

The average uranium concentrations in the salt during drawdown Runs 58, 65, 70, and 71 ranged from 6.68 to 1.75 wt %, while the concentrations of uranium in the cathode deposits from these runs ranged from 70.0 to 89.3 wt %. These data are plotted in Fig. 2. The concentrations of rare earths (cerium, neodymium, and yttrium) in the cathode deposits were low (1.2 wt % or less). These results are shown in Fig. 3.

Medium Uranium Concentration

The range of average uranium concentrations in the salt during drawdown Runs 72, 75, and 76 was 0.14 to 1.30 wt %. The range of uranium concentrations in the cathode deposits from these runs was 31.8 to 39.2 wt %. These results are plotted in Fig. 2. The concentrations of rare earths in the cathode deposits from Runs 72, 75, and 76 were 2.8, 1.8, and 2.7 wt %, respectively. These results are shown in Fig. 3. Over this range of uranium concentration in the salt, the concentrations of rare earths in the cathode deposits were still low (1.8 to 2.8 wt %, as shown in Fig. 3).

Low Uranium Concentration

The average concentration of uranium in the salt during drawdown Run 77 was 0.015 wt %, and the concentration of uranium in the cathode deposit from this run was <0.1 wt %. This result is also plotted in Fig. 2. The concentration of rare earths in the deposit was 31.8 wt %, which is shown in Fig. 3.

CONCLUSIONS

Good separation can be achieved while removing uranium and rare earths in the salt from the engineering-scale electrorefiner. Only 13% of the rare earths were removed, while 99.9% of the uranium in the salt was removed. The uranium and rare earth concentrations in the salt were reduced to <0.01 wt %, using the in-situ drawdown techniques described in this paper.

ACKNOWLEDGMENTS

This work was supported by the U.S. Department of Energy, Nuclear Energy Research & Development Program, under Contract W-31-109-Eng-38 at Argonne National Laboratory (ANL). The authors also wish to acknowledge the contributions of the staff and support groups in the Chemical Technology and Reactor Engineering Divisions at ANL. We also appreciate the managerial support of Dr. Yoon Chang and Dr. James E. Battles.

REFERENCES

1. L. Burris, R. Steunenberg, and W. E. Miller, AIChE Symposium Series, No. 254, 83, pp. 135-142 (1987).

2. L. Burris, Chemical Engineering Progress, 82(2), pp. 35-39 (February 1986).

3. C. Till and Y. Chang, "Evolution of the Liquid Metal Reactor: The Integral Fast Reactor (IFR) Concept," in Proceedings of the American Power Conference, Illinois Institute of Technology: Chicago, April 24-26, 1989.

4. J. E. Battles, W. E. Miller, and E. C. Gay, "Pyrometallurgical Processing of Integral Fast Reactor Metal Fuels," in Proceedings of the Third International Conference on Nuclear Fuel Reprocessing and Waste Management, RECOD '91, Sendai, Japan, April 14-18, 1991.

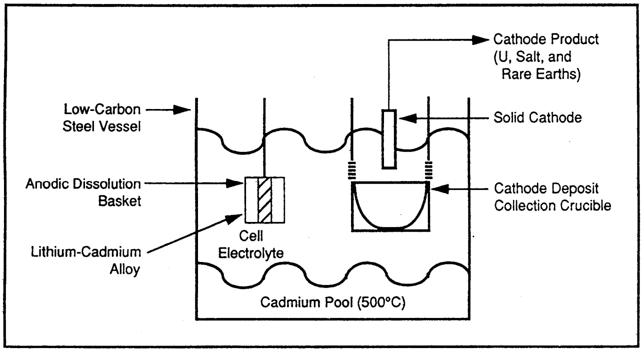

Fig. 1. Schematic of Electrorefiner Drawdown

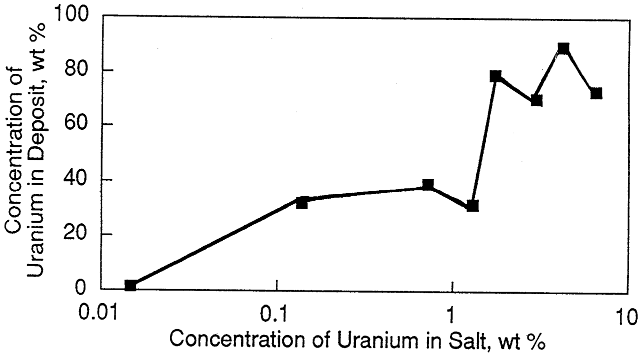

Fig. 2. Uranium Concentration in the Salt vs. Uranium Concentration in the Cathode Product

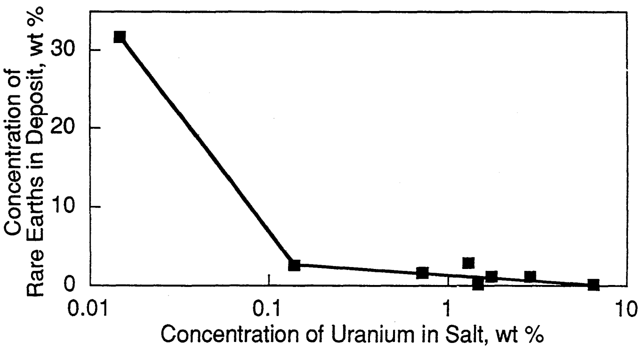

Fig. 3. Concentration of Uranium in the Salt vs. Concentration of Rare Earths in the Product

DOI: 10.1149/199413.0728PV

ALUMINUM CHLORIDE-1-BUTYLPYRIDINIUM CHLORIDE MELTS AS AN ELECTROLYTE FOR ALUMINUM / POLYANILINE CELLS

N. Koura and K. Takeishi
Faculty of Science and Technology, Tokyo University of Science,
2641 Yamazaki, Noda 278, Japan

S. Takahashi,* L. A. Curtiss, K. Suzuya, Marie- Louise Saboungi, and D. L. Price
Argonne National Laboratory, Argonne, Illinois 60439-4814, U.S.A.

ABSTRACT

The electrolyte properties and the cell performances of a new type of secondary cell, i.e., Al/$AlCl_3$-BPC/PAn are studied as a function of the $AlCl_3$ composition in the electrolyte. Significant changes are reported as the $AlCl_3$ composition varies from 54 mol% to 66.7 mol% which can be explained in terms of the formation of ionic species in the melts: $Al_2Cl_7^-$ and $AlCl_4^-$, for the solutions with 66.7 mol% and 61.5 mol% $AlCl_3$, and $AlCl_4^-$ for the 54.5 mol% $AlCl_3$. Recent studies of the structure of these melts by neutron diffraction techniques support the above assumptions. *Ab initio* molecular orbital calculations are carried out to determine the equilibrium structure of the anionic species and the BP^+ (1-butylpyridinium) cation.

INTRODUCTION

A dense and smooth Al deposit can be obtained at room temperature using an ambient temperature molten salt electrolyte (1,2), i.e., $AlCl_3$-1-butylpyridinium chloride (BPC) melt. On the other hand, polyaniline (PAn) has a high doping level per polymer unit and a large discharge capacity. Highly electroactive PAn can be synthesized from the

---

* Present address: Nisshin Steel Co., Ltd. 7-1Koya-shinmachi, Ichikawa 272, Japan

nonaqueous $AlCl_3$-BPC melt bath (3). We have therefore investigated this new type of Al/$AlCl_3$-BPC/PAn secondary cell operated at room temperature (4).

Variations in the electrolyte property were observed accompanying changes in composition. The changes were attributed to various ionic species present in the melt (5,6). The electrochemical behavior of PAn is expected to vary with the electrolyte composition, since the oxidation-reduction (i.e., charge-discharge) reaction of PAn is performed by anionic doping and undoping in the electrolyte. The electrochemical behavior of the PAn electrode was investigated for various compositions of the electrolyte.

These changes were characterized by neutron diffraction techniques and analyzed using structure factor S(Q), total correlation function T(r), and average pair distribution function g(r). *Ab initio* molecular orbital calculations were performed to determine the equilibrium structures of ionic species in the melt.

EXPERIMENTAL

The Al/PAn cell electrolyte was prepared from anhydrous $AlCl_3$ and BPC. The melt was purified by the substitution method with Al (99.99 %) wire at 80 °C. The PAn film was electrolytically deposited on a Pt substrate from a 66.7 mol% $AlCl_3$-BPC + 50 vol% benzene + 0.5 M aniline bath. Cyclic voltammograms for a PAn film and a Al substrate were performed using Al (99.99 %) as a reference electrode immersed in a 66.7 mol% $AlCl_3$-BPC melt. PAn films were synthesized at a constant current of 1 $mA\cdot cm^{-2}$. The Al/PAn cell with a PAn film (20 $C\cdot cm^{-2}$) synthesized on a Pt substrate as the positive electrode and with a spiral Al wire as the negative electrode was assembled. All cells were operated under a dry N_2 atmosphere. After the anions were doped into the PAn from various $AlCl_3$-BPC acidic melts at constant current of 0.1 $mA\cdot cm^{-2}$, the dopants in the PAn were determined by the analysis of Al in the PAn using Inductively Coupled Plasma Atomic Emission Spectroscopy (SEIKO SPS7000).

Neutron scattering measurements were made on the GLAD instrument at the Intense Pulsed Neutron Source at Argonne National Laboratory. The samples were prepared by mixing highly anhydrous $AlCl_3$ with fully deuterated BPC in a glove box, where the H_2O and O_2 levels were maintained at less than 2 ppm. Deuterated BPC was purchased from Isotech. Co. The melts were sealed under vacuum in quartz tubes of 1 mm wall thickness and 3 mm ID. Four compositions, 46, 50, 60, and 66.7 mol% of $AlCl_3$, were chosen for study at 298 K. Measurements were made on each sample, a set of empty tubes and a vanadium reference. The measured differential cross section per atom was reduced to the neutron-weighted average structure factor S(Q).

Ab initio molecular orbital calculations (7,8) were carried out to determine the equilibrium structures of the ionic species. Two basis sets were used: the minimal STO-3G basis and the polarized split valence 6-31G* basis. All of the *ab initio* molecular orbital calculations were done at the Hartree Fock (HF) level of theory. Computations were also carried out using the MNDO (modified neglect of differential overlap) semiempirical molecular orbital method.

RESULTS

Changes in the electrolyte characteristics were observed accompanying changes in the composition. Figures 1 and 2 show the variations of the specific conductivity and the viscosity with the $AlCl_3$ composition in the $AlCl_3$-BPC melts. The specific conductivity exhibits a maximum at the 50 mol% $AlCl_3$. Figure 3 shows cyclic voltammograms for the PAn electrode. The results imply that the redox reaction changes with the melt composition, and suggest that the ionic species formed upon doping and undoping vary with the composition. The doped ions were studied by determining the amount of doped Al in PAn as shown in Fig. 4. In the case of the 66.7 mol% and 54.5 mol% $AlCl_3$ melts, the dopant are assumed to be $Al_2Cl_7^-$ and $AlCl_4^-$, respectively, while, in the case of the 61.5 mol% $AlCl_3$ melt, the dopant was $AlCl_4^-$ at early charging state and $Al_2Cl_7^-$ at late charging state. Changes of the ionic species affected the life of the PAn electrode. In the case of a flexible PAn powder electrode, the cycle life was nearly the same for the various compositions of the electrolyte as shown in Fig. 5; in the case of a non-flexible PAn electrode pressed strongly, the cycle life was significantly affected by changing the composition. Consequently, a charge-discharge reaction is proposed as schematically shown in Fig. 6 .

Fig. 7 shows the measured structure factors S(Q) for the three melts (46, 60 and 66.7 mol% $AlCl_3$). The 50.0 mol% composition was not shown because the sample was solid at room temperature. These are rather similar over the range $Q > 5Å^{-1}$. However, they show differences at relatively low Q, in the range of 1 - 5 $Å^{-1}$, which must be due to the interactions between the anions (Cl^-, $AlCl_4^-$, or $Al_2Cl_7^-$) and the cation (BP^+). The neutron-weighted total correlation function T(r) and the average pair distribution function g(r) are shown in Figs. 8 and 9, respectively. Some information on interatomic distances can be obtained from these plots. The change of ionic species with composition was supported by these results. However, it is difficult to make a detailed interpretation because of the complex nature of the systems. A better understanding of the structure of these melts can be achieved by combining *ab initio* calculations with the neutron diffraction data.

Ab initio calculations were carried out to study the equilibrium structure of the ionic species in the melt, i.e., $AlCl_4^-$, $Al_2Cl_7^-$, and BP^+ (1-butylpyridinium cation). The optimized structures of $AlCl_4^-$, $Al_2Cl_7^-$, and BP^+ are shown in Fig. 10. The *ab initio* calculations for $AlCl_4^-$ and $Al_2Cl_7^-$ were described earlier (9). No previous theoretical study of the BP^+ cation has been reported to our knowledge. At all three levels the fully optimized cation has a structure with C_1 symmetry. The HF/6-31G* structure is shown in Fig. 10(c). The calculated structure factors for each of these ionic species will be compared with the measurements in future work.

ACKNOWLEDGMENTS

Work at ANL was supported by U.S. DOE under contact No. W-31-109-ENG-38. We thank the staff of IPNS, K.J. Volin, and A.J.G. Ellison for assistance in the neutron experiments.

REFERENCES

1. S. Takahashi, N. Koura, and R. Nakajima, Denki Kagaku, **54**, 257(1986).
2. S. Takahashi, N. Koura, and R. Nakajima, Denki Kagaku, **54**, 263(1986).
3. N. Koura, H. Ejiri, and K. Takeishi, Denki Kagaku, **59**, 74(1991).
4. N. Koura, H. Ejiri, and K. Takeishi, J. Electrochem. Soc., **140**, 602(1993).
5. S. Takahashi, N. Koura, and N. Yoneda, Denki Kagaku, **52**, 244(1984).
6. N. Koura, and M. Murase, J. Jpn. Inst. Light Met., **39**, 333(1989).
7. W. J. Hebre, L. Rodom, P .V. R. Schleyer, and J. A. Pople, *Ab initio* Molecular Orbital Theory, Wiley, New York, (1986).
8. M. J. Frisch, *et al*, Gaussian 90 (Gaussian, Inc., Pittsburgh, PA, 1990).
9. S. Takahashi, L. A. Curtiss, D. Gozstola, N. Koura, and M. L. Saboungi, "Molecular Orbital Calculations and Raman Measurements for 1-Ethyl-3-Methylimidazolium Chloroaluminates, submitted.

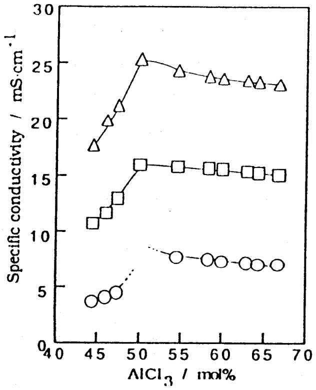

Fig.1 Variations of the specific conductivity with $AlCl_3$ composition in the $AlCl_3$-BPC melts at various temperatures.
○: 30°C, □: 60°C, △: 80°C

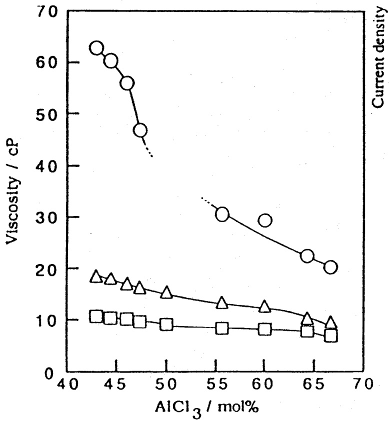

Fig.2 Variations of the specific viscosity with $AlCl_3$ composition in the $AlCl_3$-BPC melts at various temperatures.
○: 30°C, △: 60°C, □: 80°C

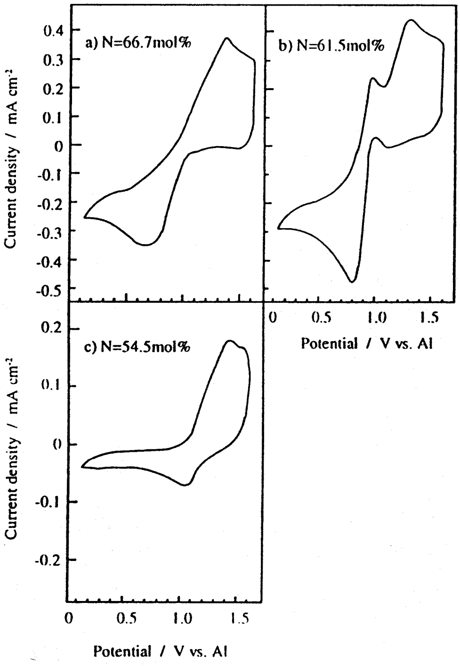

Fig.3 Cyclic voltammograms for PAn electrode in various $AlCl_3$-BPC melts.
Sweep rate : 10 mV s^{-1}

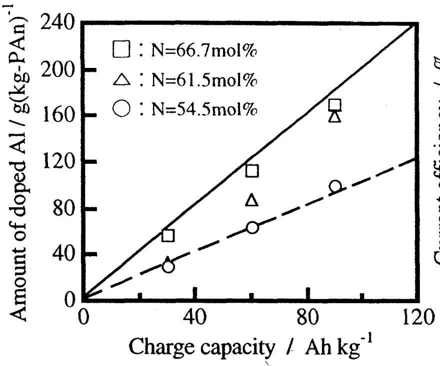

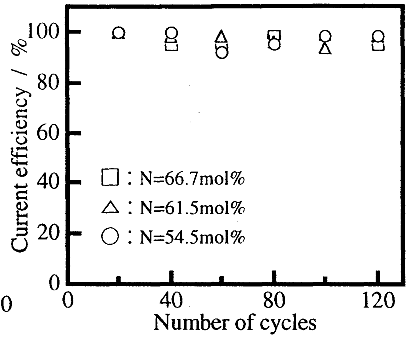

Fig.4 Variations of the amount of doped Al in PAn with charge capacity in various $AlCl_3$-BPC melts.

Charged current density: 0.1mA cm^{-2}

——— : theoretical line for $Al_2Cl_7^-$

— — — : theoretical line for $AlCl_4^-$

Fig.5 Characteristic cycle (Discharge/ charge efficiency) of the Al/PAn powder secondary cell in various $AlCl_3$-BPC electrolytes.

Current density : 0.5mA cm^{-2}

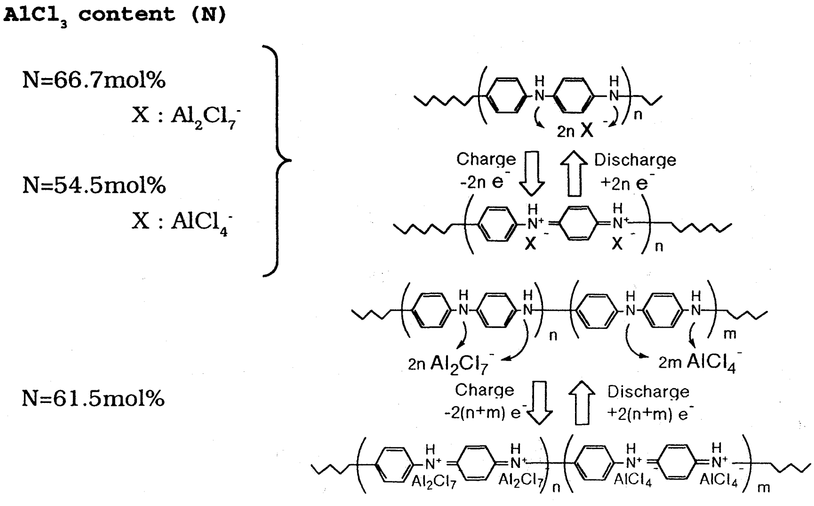

Fig.6 Charge and discharge reaction schemes for PAn in various $AlCl_3$-BPC melts.

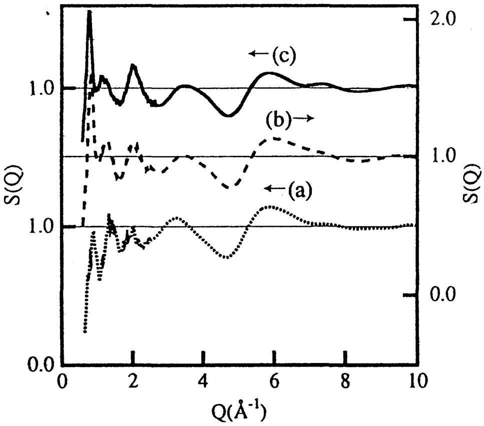

Fig.7 Measured structure factors S(Q) for $AlCl_3$-BPC melts at room temperature.
(a): 46 mol%$AlCl_3$, (b): 60 mol%$AlCl_3$, (c): 66.7mol%$AlCl_3$

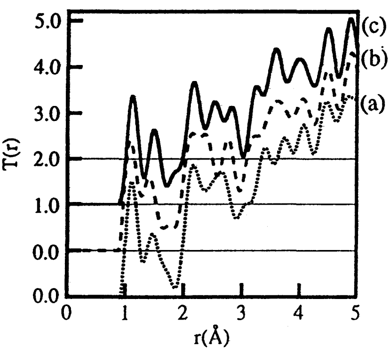

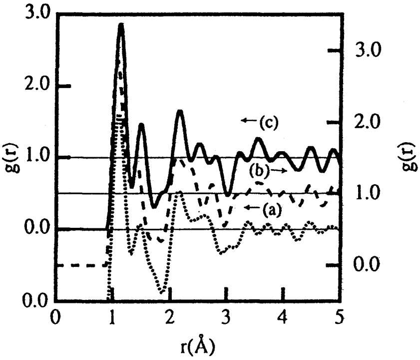

Fig.8 Measured total correlation functions T(r) for $AlCl_3$-BPC melts at room temperature.

(a): 46 mol%$AlCl_3$
(b): 60 mol%$AlCl_3$
(c): 66.7mol%$AlCl_3$

Fig.9 Measured average pair distribution functions g(r) for $AlCl_3$-BPC melts at room temperature.

(a): 46 mol%$AlCl_3$
(b): 60 mol%$AlCl_3$
(c): 66.7mol%$AlCl_3$

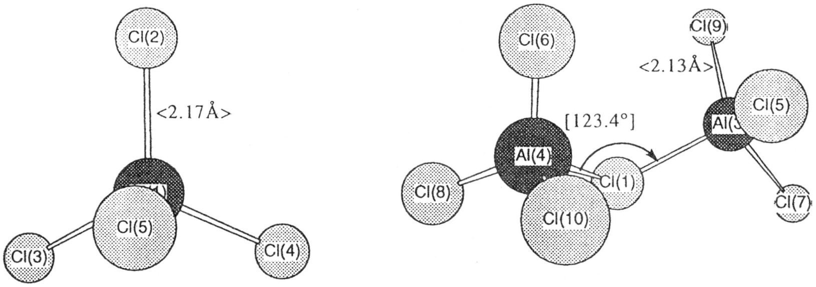

{Al(4)-Cl(1)-Al(3)-Cl(5)}=37.6°
{Al(3)-Cl(1)-Al(4)-Cl(6)}=37.6°

(a) $AlCl_4^-$

(b) $Al_2Cl_7^-$

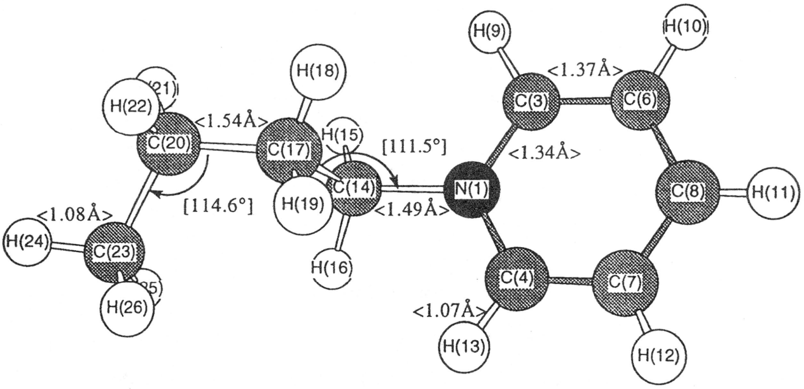

{N(1)-C(14)-C(17)-C(20)}=177.6°
{C(14)-C(17)-C(20)-C(23)}=66.0°

(c) BP^+

Fig.10 Structures of $AlCl_4^-$, $Al_2Cl_7^-$, and BP^+.
Number: Z-matrix number
< >: Typical bond length
[ ]: Typical bond angle
{ }: Typical dihedral angle

DOI: 10.1149/199413.0736PV

Ionic Liquid Battery Electrolytes as Sources for Reversible Graphite Intercalation Anodes for Battery Applications

Hugh C. De Long and Richard T. Carlin

Frank J. Seiler Research Laboratory
Division of Electrochemical Sciences
2354 Vandenberg Drive Suite 2A35
U.S. Air Force Academy, Colorado 80840-6272

An examination of the intercalation of various cations (1,2-dimethyl-3-propylimidazolium (DMPI), 1-ethyl-3-methylimidazolium (EMI), or 1-ethyl-2,3-dimethylimidazolium (EDMI)) into graphite electrodes, in room temperature $AlCl_3$ molten salts, was undertaken. The reduction process involves making the graphite anionic, which allows for the above cations to incorporate into the graphite matrix. By using the cations of the electrolyte itself, this eliminates the need for separate intercalation compounds. A cell employing a (DMPI)($AlCl_4$) electrolyte and two graphite rod electrodes achieved an open-circuit voltage of 3.5 V and a cycling efficiency of 85%.

Introduction

The determination of the behavior of materials in room temperature molten salts is an important step in assessing their suitability for use as electrodes in follow-on battery development. Lithium's use as an intercalation compound in graphite electrodes is known throughout the world.[1] The many improvements (reliability, safety, environmental, and economic) offered by the rocking chair battery over other rechargeable batteries comes primarily from the use of a carbon or graphite anode. The cathodes in these batteries still utilize transition metal oxides of manganese, nickel, or cobalt which are more expensive, less desirable environmentally, and more synthetically demanding than the carbon anode. In addition, the liquid electrolytes in these batteries consist of lithium salts dissolved in a mixture of organic carbonates or ethers, which require rigorous purification. Therefore, the rocking chair battery requires the synthesis, purification, and assemblage of multiple active components.

What makes this work unique is that no additional compound is used for intercalation in the graphite except the electrolyte itself. The systems discussed in this paper utilize room-temperature or low-melting molten salts composed of a substituted imidazolium cation and an inorganic anion. The molten salt serves in a multifunctional capacity leading to a battery configuration requiring only two active materials - the molten salt and graphite. This would greatly simplify the construction of a battery cell. Therefore, we wish to report here the initial investigation of reversible ionic electrolyte cation insertion into graphite electrodes as a part of what we term is a Dual Intercalating Molten Electrolyte (DIME) batteries.

Experimental

Purification of melt components has been previously described[2,3]. The room-temperature 1:1 chloroaluminate molten salts were prepared by combining equal molar quantities of sublimed $AlCl_3$ with the appropriate organic chloride inside a Vacuum Atmosphere dry box under He with an O_2 + H_2O concentration of < 5 ppm. Polycrystalline platinum metal and glassy carbon electrodes were purchased from Bioanalytical Systems. Polishing was accomplished using a Struers DAP-V grinder-polisher producing a highly polished disk electrode. The geometric areas of the platinum electrode were $2.011 \times 10^{-2} cm^2$ and the glassy carbon electrode was $7.068 \times 10^{-2} cm^2$. The pretreated, high purity, spectroscopic grade graphite working electrode (Union Carbide) has a geometric area of $1.2 cm^2$.

All experiments were performed in a UHP helium atmosphere using a Vacuum Atmospheres dry box at room temperature. The counter electrode was an aluminum wire immersed into a portion of the analyte melt contained in a 3 mm OD, E-porosity gas dispersion tube (Ace Glass). The reference electrode consisted of an Al wire immersed in N=0.60 with either a $AlCl_3$-DMPIC, $AlCl_3$-EMIC, or $AlCl_3$-EDMIC melt contained in separate fritted glass or asbestos fiber compartments. Cyclic voltammetry was performed on an EG&G PAR model 273 potentiostat/galvanostat using the M270 version 4 software environment with a Tangent 486DX/33MHz computer.

Protonic impurities in the melts were removed by vacuum treatment at 1×10^{-5} Torr for several days. Neutral melts of the three cationic species (DMPI, EMI, DMEI) were prepared slightly basic (extra organic salt) to make sure no aluminum would be plating out.

Results and Discussion

DMPI

Staircase cyclic voltammograms for the reductive and oxidative intercalation of graphite in the room-temperature molten salt (DMPI)($AlCl_4$) are shown in Fig. 1. The graphite electrochemical intercalation processes occur well within the electrochemical limits of the melt which, at GC, are found at -2.2 V and +2.5 V and correspond to $DMPI^+$ reduction and $AlCl_4^-$ oxidation, respectively. The electrochemical process at -1.5 V in Fig. 1a involves the intercalation (forward scan) and de-intercalation (reverse scan) of $DMPI^+$ into the graphite lattice. The electrochemical window of the melt is large (>4 volts). Using Cyclic Staircase Voltammetry (CSV) gives a reduction process (see Fig. 1) initiating at -1.6 V, which results in intercalation of the cationic species. This intercalation is reversible with 80 to 90 % efficiency for DMPI. Scan rate studies indicate an increasing charge density with decreasing scan rate. This is due to loading more of the cation into the graphite. The electrochemical process at +1.8 probably involves the intercalation and de-intercalation of $AlCl_4^-$ into the graphite lattice. Although it has been proposed that graphite oxidation in this melt involves intercalation of Cl_2,[4] the potential of the oxidative intercalation (0.6 V negative of $AlCl_4^-$ oxidation to Cl_2) and the lack of known stable chlorine intercalates points towards the formation of an $AlCl_4^-$ intercalation compound instead.[5] Numerous chloroaluminate and other metal halide intercalation compounds are known.[6,7] Therefore, the proposed electrochemical processes in Fig. 1 can be written

$$DMPI^+ + x\,C + e^- \Leftrightarrow (DMPI)C_x \qquad (1)$$

$$AlCl_4^- + y\,C \Leftrightarrow C_y(AlCl_4) + e^- \qquad (2)$$

Chronopotentiometric charging and discharging curves for graphite in (DMPI)($AlCl_4$) are shown in Figs. 2a and 2b, respectively. The de-intercalation process for $DMPI^+$ has a high efficiency, 94%, and a flat potential profile. The charging was done at 1.0 mA and discharge was done at 0.25 mA. Table 1 shows data for charging at 1.0mA and discharging 1.0-0.25mA to demonstrate the effect of varying the discharge rate at a different constant currents. The data indicates that reducing the discharge current and running at longer times increases the cycling efficiency. From the discharge potentials for the two couples, it should be possible to construct a battery with a voltage of approximately 3 V utilizing only two graphite electrodes. Such a cell was constructed by inserting two 3 mm graphite rod electrodes into the melt. Using the potentiostat in a two-electrode configuration, charge and discharge curves for this cell were collected. The resulting curves are shown in Fig. 2c, and the cell performance parameter are summarized in Table II. The small spikes on the discharge curve are current interrupts used to measure the open-circuit potential at various times during discharge. The net cell reaction can be written

$$\mathrm{DMPI^+ + AlCl_4^- + (x+y)\,C \Leftrightarrow (DMPI)C_x + C_y(AlCl_4)} \qquad (3)$$

EMI

The intercalation processes of (EMI)($AlCl_4$) substituted into reactions 1 and 2 were also studied using chronopotentiometry, and results for the (EMI)($AlCl_4$) melt are presented as the second set of entries in Table I. Average charge (intercalation) and discharge (de-intercalation) potentials at various current densities are also provided. The cycling efficiencies, defined as % efficiency = discharge coulombs/charge coulombs x 100, are only approximately 60% for both graphite intercalation processes in this melt. In fact, the EMI^+ intercalate is unstable and decomposes in a few minutes upon standing at open-circuit. The decomposition may involve reaction of the relatively acidic C-2 proton with the negatively charged graphite lattice.[8] This is supported by the high cycling efficiencies observed for the reductive intercalation of the $DMPI^+$ cation (second set of entries in Table I) in which the C-2 proton has been replaced by a methyl group.

A similar cell configuration was tested for the (EMI)($AlCl_4$) melt, and these results are also presented in Table II. Both cells exhibit similar potential behavior including an open-circuit potential of 3.5 V immediately after charging; however, the (EMI)($AlCl_4$) cycling efficiency is much lower due to the instability of the EMI^+ intercalate. In reaction 3, the cations and anions for both electrochemical intercalation reactions are provided by the molten salt electrolyte, i.e., the cell operates as a DIME battery.

EDMI

Finally, the intercalation process using (EDMI)($AlCl_4$) was studied with chronopotentiometry (see Table I). The data was collected at 100°C using an aluminum block heater. (EDMI)($AlCl_4$) is a solid at room temperature and melts at 70-72°C. The charge and discharge data were better for the $EDMI^+$ ion, than for EMI^+ ion, but the anion charge and discharge were unobtainable due to its instability in this melt. Using a different anion which is more stable at these temperatures or one that lowers the temperature of the resulting $EDMI^+$ melt are being researched.

We are also currently investigating the reversibility, capacity, and structure of the graphite intercalates formed in these molten salts as a function of several parameters. In particular, it is well known that the type of graphite or carbon used plays a significant role in the formation of the intercalation compound.[6,7,9] The rate and capacity of the intercalation processes will be dependent on numerous parameters including carbon structure, temperature, and electrode history.

Conclusion

A single room-temperature or low-temperature molten salt electrolyte can be used to provide the intercalating ions for a rechargeable electrochemical cell utilizing a graphite anode and cathode. This Dual Intercalating Molten Electrolyte (DIME) battery has many practical advantages including (1) inexpensive graphite electrodes are used, (2) only a single molten salt needs to be synthesized and purified, (3) no organic solvents are required, (4) the battery can be assembled in the discharged state, and (5) all components have low toxicity. DMPI ended up having the best overall performance of the cations studied in this report. It demonstrated much higher cycling efficiencies than either of the other cations. This should demonstrate the utility of using the electrolyte itself as the intercalation compound for use in graphite intercalation electrodes.

Acknowledgments

This work was supported by the Air Force Office of Scientific Research.

References

1. J. M. Tarascon and D. Guyomard, *Electrochimica Acta*, **38,** 1221 (1992).
2. P. R. Gifford and J. B. Palimisano *J. Electrochem. Soc.*, **134,** 610. (1987).
3. J. S. Wilkes, L. A. Levinsky, R. A. Wilson, and C. L. Hussey, *Inorg. Chem.*, **21,** 1263 (1982).
4. P. R. Gifford and J. B. Palmisano, *J. Electrochem. Soc.*, **135,** 650 (1988).
5. H. Selig and L. B. Ebert in *Advances in. Inorganic Chemistry and Radiochemistry*, Vol. 23, H. J. Emeleus and A. G. Sharpe, Editors, p. 281, Academic, Orlando (1980).
6. R. Setton, in *Graphite Intercalation Compounds I: Structure and Dynamics*, H. Zabel and S. A. Solin, Editors, p. 305, Springer Verlag, Berlin, Heidelberg, New York (1990).
7. K. Kinoshita, *Carbon, Electrochemical and Physiochemical Properties*, John Wiley and Sons, Inc., New York (1988).
8. J. L. Wong and J. H. Keck, Jr., *J. Org. Chem.*, **39,** 2398 (1974).
9. J. R. Dahn, A. K. Sleigh, H. Shi, J. N. Reimers, Q. Zhong, and B. M. Way, *Electrochim. Acta*, **38,** 1191 (1993).

Table I. Anion and cation intercalation into graphite using molten salt electrolytes. Charging time is 30 min. unless stated otherwise.

Molten Salt Electrolyte	Intercalate Ion	T (°C)	I_{charge} (mA cm^{-2})	E_{charge} (V)	$I_{discharge}$ (mA cm^{-2})	$E_{discharge}$ (V)	Cycle Eff %
(DMPI)(AlCl$_4$)	DMPI$^+$	30	1	-1.70	1	-1.25	60
	DMPI$^+$	30	1	-1.70	0.5	-1.36	100
	DMPI$^+$	30	1	-1.70	0.25	-1.35	94
	AlCl$_4^-$	30	1	+2.15	1	+1.50	64
	AlCl$_4^-$	30	1	+2.15	0.5	+1.60	86
	AlCl$_4^-$	30	1	+2.15	0.25	+1.60	76
(EMI)(AlCl$_4$)	EMI$^+$	24	1	-1.64	1	-1.47	59
	EMI$^+$[a]	24	2	-1.69	2	-1.50	65
	AlCl$_4^-$	24	1	+1.93	1	+1.6	41
	AlCl$_4^-$	24	2	+2.01	2	+1.6	64
(EDMI)(AlCl$_4$)[b]	EDMI$^+$	100	1	-1.63	0.25	-1.50	62
	AlCl$_4^-$	100	1	+2.25	1	----[c]	----[c]

[a] Charging time = 60 min.; [b] Solid at room temperature; [c] AlCl$_4^-$ is unstable in graphite at this temperature.

Table II. Performance parameters for Dual Intercalating Molten Electrolyte (DIME) cells.

Molten Salt Electrolyte	T (°C)	E_{open} (V)	t_{charge} (min.)	I_{charge} (mA cm^{-2})	E_{charge} (V)	$I_{discharge}$ (mA cm^{-2})	$E_{discharge}$ (V)	Cycle Eff %
(DMPI)(AlCl$_4$)	30	3.52	60	1	3.72	1	2.92	85
(EMI)(AlCl$_4$)	24	3.54	20	1	3.67	0.5	3.22	44

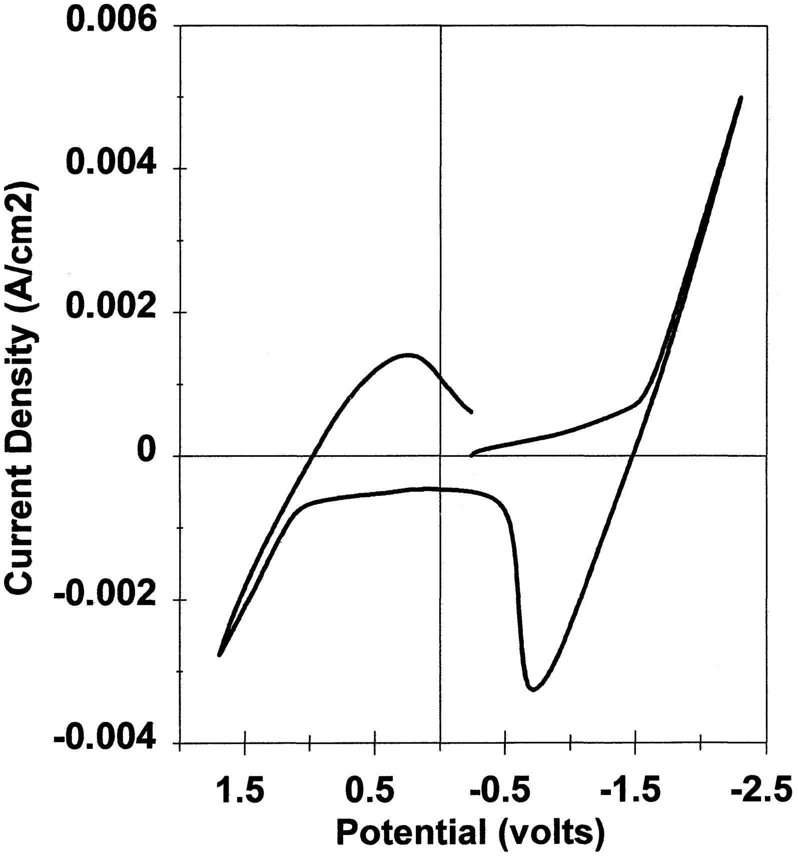

Fig. 1. Staircase cyclic voltammograms at graphite in (DMPI)($AlCl_4$) showing (a) reductive intercalation of $DMPI^+$ and (b) oxidative intercalation of $AlCl_4^-$; scan rate = 50 mV s^{-1}.

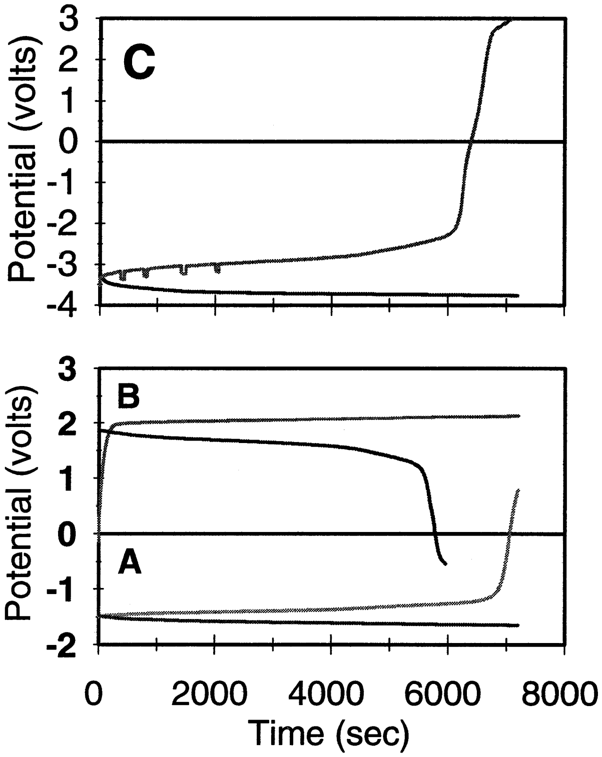

Fig. 2. Chronopotentiometric curves at graphite in (DMPI)(AlCl4) showing (a) $DMPI^+$ intercalation (1 mA cm^{-2}) and de-intercalation (0.25 mA cm^{-2}), (b) $AlCl_4^-$ intercalation (1 mA cm^{-2}) and de-intercalation (0.25 mA cm^{-2}), and (c) cell charging and discharging (both 1 mA cm^{-2}).

DOI: 10.1149/199413.0744PV

A SILANE-IMIDAZOLE ELECTROACTIVE FILM FOR BATTERY CATHODES

Richard T. Carlin
Frank J. Seiler Research Laboratory
2354 Vandenberg Drive, Suite 2A35
USAF Academy, Colorado 80840-6272

Robert A. Osteryoung
Department of Chemistry
North Carolina State University
Raleigh, North Carolina 27695

ABSTRACT

Electrochemical oxidation of $ClSiPh_3$ (Ph = phenyl) in the room-temperature molten salt $AlCl_3$:EMICl (EMICl = 1-ethyl-3-methylimidazolium chloride) results in the formation of an adherent electroactive film on the surface of solid electrodes which is reversibly oxidized and reduced in the molten salt. Based on XPS analysis, the film consists of both a silane and an imidazole component, and the charge storage properties of the film are localized on the heterocyclic rings. This electroactive film compares favorably to other conducting polymers currently being investigated as positive electrodes in room-temperature molten salt batteries.

INTRODUCTION

The room-temperature chloroaluminate molten salt $AlCl_3$:EMICl (EMICl = 1-ethyl-3-methylimidazolium chloride) is an interesting electrolyte for battery development. It has a substantial liquid temperature range, a wide adjustable electrochemical window, a high thermal stability, an inherently high ionic conductivity, and a negligible vapor pressure even at elevated temperatures (1-3). To achieve the highest possible voltages for battery applications, recent research has focused on the use of reversible alkali metal negative electrodes in these neutral buffered melts; however, it is not certain the stability of the alkali metals is sufficient to produce a reliable secondary battery (4-6). Also, the current densities achievable with the alkali metal electrodes may not be sufficient for some applications (4). In acidic melts ($AlCl_3$:EMICl > 1), it has been established that aluminum serves as an excellent reversible negative electrode with high anodic current densities

(7,8). The aluminum reduction sets the anodic limit of the acidic melt at 0 V, while the cathodic limit is set by $AlCl_4^-$ oxidation at +2.5 V, giving an electrochemical window of 2.5 V. Therefore, combined with high $Al_2Cl_7^-$ concentrations (3.4 M for $AlCl_3$:EMICl = 2:1), the acidic melt is a promising electrolyte for secondary batteries assuming an appropriate reversible positive electrode can be identified.

From the perspective of reversibility, stability, ease of preparation, charge/discharge rates, and cost, conducting polymers such as polypyrrole (9), polythiophene (10), polyfluorene (11), and polyaniline (12,13) are excellent candidates for battery positive electrodes in the ambient-temperature $AlCl_3$:EMICl molten salts. Polypyrrole and polythiophene are electroactive only in melts with the neutral composition, while polyaniline and polyfluorene are electroactive in acidic and neutral melts. Therefore, secondary batteries with an acidic $AlCl_3$:EMICl electrolyte can be envisioned using a polyaniline or polyfluorene positive electrode and an aluminum negative electrode. Despite their promise, it is not certain the polymeric positive electrodes already identified will stand the test of time; therefore, it is desirable to have other polymeric positive electrodes available.

We wish to report here a new electroactive material produced by electrochemical oxidation of Ph_3SiCl (Ph = phenyl) in acidic $AlCl_3$:EMICl. During its synthesis, this new material forms as an adherent electroactive film on the surface of the solid working electrode. The film is reversibly oxidized and reduced in acidic melts, and so, may serve as a positive electrode for secondary room-temperature molten salt batteries.

EXPERIMENTAL

EMICl was synthesized as previously described (2). Melts were prepared by gradual addition of small quantities of sublimed $AlCl_3$ (Fluka) to EMICl with stirring until the desired ratio was obtained. All experiments were performed under a purified He atmosphere in a Vacuum Atmosphere dry box with $O_2 + H_2O < 5$ ppm.

Glassy carbon (GC, area = 0.071 cm^2) and platinum (area = 0.020 cm^2) working electrodes were purchased from Bioanalytical Systems. The reference and counter electrodes consisted either of Al wires dipped directly into the 1.5:1.0 $AlCl_3$:EMICl analyte melt or of Al wires immersed in acidic 1.5:1.0 $AlCl_3$:EMICl melts contained in separate fritted tubes isolated from the analyte solution. Both choices of reference and counter electrodes gave essentially identical results. Cyclic staircase voltammetry, chronopotentiometry, and pulse experiments were performed using an EG&G PARC Model 273 Potentiostat/Galvanostat controlled with in-house software or with the EG&G PARC Model 270 software.

X-ray photoelectron spectra were obtained with a Perkin Elmer Model 5100 instrument. A magnesium Kα source at 300 watts was used. Base pressure was 5 x 10^{-9} torr, and the operating pressure was less than 1 x 10^{-8} torr. All data were analyzed with sensitivity factors provided by Perkin Elmer. Binding energies are referenced to carbon 1s, which was set at 285.0 eV.

RESULTS AND DISCUSSION

Film Preparation and Electrochemical Behavior.

All films were oxidatively prepared using 0.1 M or 0.2 M solutions of Ph_3SiCl in acidic 1.5:1.0 $AlCl_3$:EMICl melts. The method of film preparation varied depending upon the electrode used. Voltammograms recorded for films in pure 1.5:1.0 $AlCl_3$:EMICl melts (no Ph_3SiCl present) showed the same redox behavior as voltammograms recorded in acidic melts containing Ph_3SiCl. Exposure of the film to air did not appear to be deleterious to the film's performance.

At a GC electrode, a single irreversible oxidation wave at +2.5 V is observed for Ph_3SiCl near the anodic limit of the acidic melt as shown in Fig. 1a. This irreversible oxidation is the film-producing oxidation wave. On GC, it is possible to prepare films using repetitive cyclic voltammetric scans to +2.6 V to +2.75 V. The redox behavior of the film is shown in Fig. 1b.

At a Pt electrode, the anodic limit of an acidic melt is at ca. +2.0 V; therefore, it was not possible to observe the Ph_3SiCl oxidation wave at +2.5 V. Using cyclic voltammetry, repetitive scans to +2.5 V (well beyond the anodic limit of the melt) did not produce a film on a clean Pt electrode; however, holding the potential at +2.5 V for several seconds initiated film formation. After the film formation was initiated, continued film growth was achieved employing repetitive voltammetric scans to +2.5 V without the need to hold the potential at +2.5 V. Scanning the potential only to +2.0 V oxidized and reduced the deposited film without depositing additional material. A representative staircase cyclic voltammogram of the film's electrochemical behavior on Pt is compared to that on GC in Fig. 2. Films formed on Pt were not as uniform as those prepared on GC. This is not surprising since the films on Pt are formed concurrently with Cl_2 evolution resulting from oxidation of $AlCl_4^-$ at the anodic limit of the acidic melt.

Galvanostatic experiments were performed to evaluate the charge/discharge performance of the film. The film was prepared at GC by oxidation of 0.1 M Ph_3SiCl in 1.5:1.0 $AlCl_3$:EMICl and then transferred to a a 1.5:1.0 $AlCl_3$:EMICl melt containing no Ph_3SiCl. Typical charging (to +2.0 V) and discharging (to +0.4 V) curves are shown in

Fig. 3; the charging and discharging currents are both 2.8 mA cm^{-2}. The time for a complete charge/discharge cycle remains constant at 150 s for numerous cycles, emphasizing the film's reversible redox behavior and high cycling efficiency (ca. 100%). Also, the shape of the curves remained constant with most of the charge introduced and recovered between +1 and +2 V. Following charging to +2.0 V, the open circuit of the film is stable at +1.65 V, in agreement with the average discharge voltage of +1.5 V seen in Fig. 3.

X-ray Photoelectron Spectroscopy (XPS) Analysis.

Reverse pulse voltammetry was used to prepare films on Pt foils for XPS analysis (14). The film was formed during 5 s generation pulses at a potential between +2.4 V and +2.45 V. Following each generation pulse, the potential was stepped to more negative potentials in 25 mV steps, and an analysis pulse of 100 ms was applied. This allowed monitoring of the film formation. The potential range of the reverse pulse voltammograms was from the generation pulse potential to +0.3 V. Following electrochemical preparation, excess melt was washed from the films with ethanol in the air.

XPS results for two of the samples are summarized in Tables I and II. The oxidized and reduced states were generated by holding the potential of the films at +2.0 V and +0.4 V, respectively, for several seconds. The most important difference in the oxidized and reduced films is found for the N 1s electron binding energy which undergoes a significant shift from 399.8 eV to 401.7 eV upon oxidation of the film. Also, in the oxidized film's N 1s spectrum, a shoulder is observed at the energy for the peak in the reduced film's N 1s spectrum and visa versa. This shift in the N 1s binding energy implies that the formal charge on the nitrogens in the film is more positive following film oxidation. In fact, the shift corresponds to an increase of ca. +0.5 in the nitrogen's formal charge (15). Therefore, oxidation of the film results in removal of electrons from the film which are, at least in part, localized on the nitrogens.

In addition to this shift in the N 1s binding energy, oxidation of the film causes the Cl 2p binding energy to broaden and to shift to lower energy. Based on the Cl 2p binding energy, the chlorine in the reduced film appears to be covalently bound probably as chloroaluminate species (16). Upon oxidation of the film, the covalently bound chlorine remains in the film, while a new chlorine having a lower Cl 2p binding energy is incorporated into the film. This chlorine of lower binding energy may be free chloride anions introduced into the film as counterions to maintain electrical neutrality during film oxidation.

The Si 2p electron binding energies for both films are appropriate for silicon bound to phenyl groups and an electronegative atom such as oxygen or nitrogen, such as Ph_3Si-O- or Ph_3Si-N- (17).

Table II summarizes the atomic percentages determined from XPS of the elements in the oxidized and reduced films. Although the film samples were prepared separately, the relative quantities of the elements in each of the films are similar. The most significant numbers are those for silicon and nitrogen which indicate a N:Si atomic ratio of 1.1:1 to 1.6:1. Because the atomic percentages in Table II were not obtained from standard curves, caution must be employed to avoid putting too great a significance on this quantitative data.

The XPS results are compatible with a postulated film formation mechanism involving reaction of the EMI^+ cation with an oxidized Ph_3SiCl intermediate. Attack at the nitrogen atom on EMI^+ could led to a polymeric materials such as -(Ph_2Si-NC_3H_3N)$_n$- with N:Si = 2:1 and a repeat unit molecular weight of 249.4 g or to a molecular species such as Ph_3Si-NC_3H_3N-$SiPh_3$ with N:Si = 1:1 and a molecular weight of 585.9 g. These formulae probably constitute the lower and upper molecular weights for the film; molecular alkylated imidazole species such as Ph_3Si-NC_3H_3N-R (R = Me, Et) with intermediate molecular weights are also possible film formulations. The film may be a mixture of the above formulations.

Comparison of the Silane-Imidazole Film to Other Conducting Polymers.

The XPS results can be used to predict performance values for the silane-imidazole film. The N 1s binding energy indicate the transfer of 0.5 e^- per nitrogen, or 1.0 e^- per imidazole unit, in the film during the reversible redox process; therefore, the weight per electron for the film falls in the range of 249.4 g to 585.9 g per mole e^-. From this, the electricity storage capacity can be calculated and combined with the open circuit potential of the charged film (+1.65 V vs. Al) to obtain an energy storage capacity for a cell employing a silane-imidazole film positive electrode and an aluminum negative electrode. Corresponding values for polyaniline and polyfluorene positive electrodes with the same cell configuration can be obtained from the literature (9-13). Table III summarizes the results of these calculations. Although the values for the silane-imidazole film are based on several assumptions, they clearly indicate that further investigations of this novel material as a battery positive electrode are warranted.

ACKNOWLEDGMENTS

We wish to thank SDIO/IST managed by ONR, and the Air Force Office of Scientific Research for supporting this work. We are also grateful to Prof. J. Gardella and Dr. M. Clark of the SUNY/AB Surface Science Center for performing the XPS analyses.

REFERENCES

1. R. A. Osteryoung, in G. Mamantov and R. Marrasi (eds.), "Molten Salt Chemistry," ASI Series C, Vol. 202, Reidel, Dordrecht, The Netherlands, 1987, p. 329.
2. J. S. Wilkes, J. A. Levisky, R. A. Wilson, C. L. Hussey, *Inorg. Chem.*, **21**, 1263 (1982).
3. C. J. Dymek, Jr., G. F. Reynolds, and J. S. Wilkes, *J. Electrochem. Soc.*, **134**, 1658 (1987).
4. R. T. Carlin and C. Scordilis-Kelley, Proceedings of the Ninth International Symposium on Molten Salts, The Electrochemical Society, Pennington, N. J., 1993.
5. C. Scordilis-Kelley and R. T. Carlin, *J. Electrochem. Soc.*, **140**, 1606 (1993).
6. T. L. Riechel and J. S. Wilkes, *J. Electrochem. Soc.*, **139**, 977 (1992).
7. J. J. Auborn and Y. L. Barberio, *J. Electrochem. Soc.*, **132**, 598 (1985) 598.
8. R. T. Carlin and R. A. Osteryoung, *J. Electrochem. Soc.*, 136, 1409 (1989).
9. P. G. Pickup and R. A. Osteryoung, *J. Electroanal. Chem.*, **195**, 271 (1985).
10. L. Janiszewski and R. A. Osteryoung, *J. Electrochem. Soc.*, **135**, 116 (1988).
11. L. Janiszewski and R. A. Osteryoung, *J. Electrochem. Soc.*, **135**, 116 (1988).
12. J. Tang and R. A. Osteryoung, *Synthetic Metals*, **45**, 1 (1991).
13. N. Koura, H. Ejira, and K. Takeishi, *J. Electrochem. Soc.*, **140**, 602 (1993).
14. J. Osteryoung and E. Kirower-Eisner, *Anal. Chem.*, **52**, 62 (1980).
15. D. N. Hendrickson, J. M. Hollander, and W. L. Jolly, *Inorg. Chem.*, *8*, 2642 (1969).
16. J. R. Ebner, D. L. McFadden, D. R. Tyler, and R. A. Walton, *Inorg. Chem.*, **15**, 3014 (1976).
17. C. D. Wagner, W. M. Riggs, L. E. Davis, and J. F. Moulder in G. E. Muilenberg (ed.), "Handbook of X-Ray Photoelectron Spectroscopy," Perkin Elmer, Eden Praire, MN, 1979.

Table I. XPS results for films prepared on Pt Foils; binding energies (eV) with FWHM (eV) are given in parentheses.

Element and Orbital	Oxidized Film	Reduced Film
N 1s	399.8(sh) 401.7(2.0)	399.8(2.0) 402.0(sh)
Cl 2p[a]	198.8(4.0)	200.7(3.4) 199.0(sh)
Si 2p[a]	102.0(2.1)	102.1(2.0)

[a] No spin-orbit splitting was discernible.

Table II. Atomic percentages determined by XPS.

Element	Oxidized Film	Reduced Film
C	59.5	72.8
Si	2.4	1.8
N	3.9	1.95
Cl	4.1	2.6
Al	5.0	2.12
O	23.6	17.1

Table III. Comparison of polymer electricity storage capacities and of cell performance characteristics using a polymer positive electrode and an Al negative electrode.

Polymer	Polyaniline	Polyfluorene	Silane-imidazole
Capacity, Ah kg^{-1}	68 (37 - 133)	54 - 82	46 - 107
E_{cell}, V	1.60	1.4 - 1.6	1.65
Energy Storage, Wh kg^{-1}	108	74 - 129	75 - 172

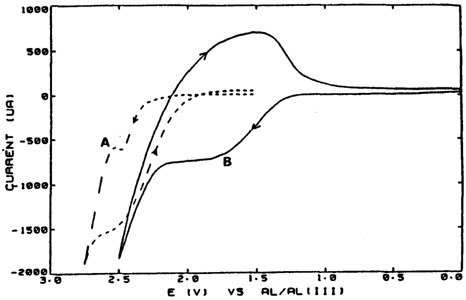

Figure 1. Staircase cyclic voltammograms at GC showing (a) the oxidation of 0.2 M Ph_3SiC at +2.5 V in 1.5:1.0 $AlCl_3$:EMICl (scan rate = 12.5 mV s^{-1}), and (b) the redox behavior of the resulting film (scan rate = 200 mV s^{-1})

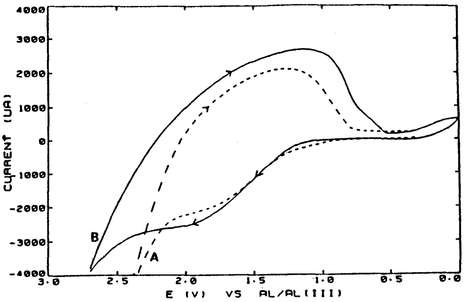

Figure 2. Staircase cyclic voltammograms at (a) Pt and (b) GC showing the redox behavior of films prepared by oxidation of 0.2 M Ph_3SiCl in 1.5:1.0 $AlCl_3$:EMICl.

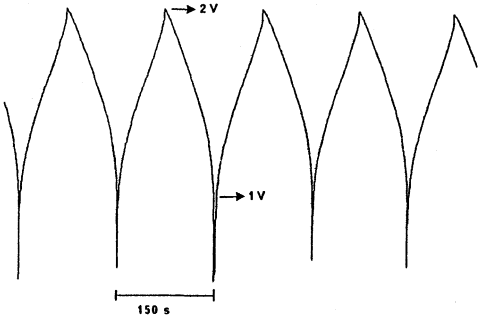

Figure 3. Galvanostatic charge/discharge study of a film produced by oxidation of 0.1 M Ph_3SiCl in 1.5:1.0 $AlCl_3$:EMICl at GC. The charging and discharge current densities are both 2.8 mA cm^{-2}.

DOI: 10.1149/199413.0752PV

A NOVEL LOW TEMPERATURE MOLTEN SALT SYSTEM CONTAINING FLUOROPYRAZOLIUM SALT

J. Čaja, A. A. Gakh, T. D. J. Dunstan,
J. L. Adcock, and G. Mamantov
Department of Chemistry
University of Tennesssee
Knoxville, TN 37996-1600

ABSTRACT

Development of a novel low temperature chloroaluminate melt more resistant towards oxidation is presented. The stability towards oxidation was obtained by substituting hydrogen on the pyrazolium cation with fluorine. The compound 1,2-dimethyl-4-fluoropyrazolium chloride (DMFP) was synthesized and a 65/35 mole% $AlCl_3$/DMFP melt was prepared. The conductivity of 5 mS/cm was obtained at 30°C. The width of the electrochemical window measured for this melt is about the same as the one obtained for the 65/35 mole% $AlCl_3$/MEIC melt. Initial observations suggest that this melt may be stable towards oxidation by the SCl_3^+ cation. It was previously determined that the $AlCl_3$/MEIC melt reacts with the SCl_3^+ cation.

INTRODUCTION

Ambient temperature chloroaluminate melts for use as solvents in high energy rechargeable cells have been under development for over ten years (1,2). These melts are made of aluminum chloride and compounds such as N-(n-butyl)pyridinium chloride (BPC), 1-methyl-3-ethylimidazolium chloride (MEIC), trimethylphenylammonium chloride (TMPAC), and trimethylsulfonium chloride (TMSC) (1-3).

Unfortunately, these melts show some disadvantages. Thus, the melt $AlCl_3$/BPC has a relatively narrow electrochemical window due to the reduction of the butylpyridinium cation. The melts containing MEIC have a much wider potential window; however, the synthesis of MEIC is fairly involved. The conductivity of the TMPAC-containing melts is lower than those for the other melts. Although TMSC is readily available, the $AlCl_3$/TMSC melts have lower conductivities than MEIC-containing melts. Recently, the 1,4-dimethyl-1,2,4-triazolium chloride(DMTC)-$AlCl_3$ melt was described (4). This melt can be used as an electrolyte for batteries with an aluminum electrode.

In order to develop improved ambient temperature melts for high voltage cells, their stability towards oxidation should be improved. This paper presents the development of a novel low temperature chloroaluminate melt to be used as a solvent in high voltage ambient temperature rechargeable cells containing strong oxidants.

EXPERIMENTAL

All chemicals used were of the highest available purity. $AlCl_3$ (Fluka) was purified according to standard procedure (5). The compound 1,2-dimethyl-4-fluoropyrazolium chloride (DMFP) was synthesized by the direct fluorination of pyrazole using elemental fluorine followed by alkylation (dimethylsulfate) and anion exchange (6). The composition and purity of DMFP as well as of $AlCl_3$/DMFP melts were established by proton, ^{19}F and ^{13}C NMR and by elemental analysis. Elemental analysis of the DMFP showed the following results: 39.92% C, 18.57% N, 5.20% H, 23.58% Cl, 12.69 % F (theoretical values are: 39.88 % C, 18.61 % N, 5.32% H, 23.56% Cl, 12.63% F). MEIC was synthesized according to the procedure described by Smith et al. (7).

The melts were prepared and tested in a custom made dry box equipped with a Photohelic automatic pressure control and a Dri-Train which kept the combined concentration of oxygen and moisture less than 1 ppm.

Conductivities were measured using an YSI Model 35 Conductance Meter and a custom made conductivity cell. Bright platinum foil electrodes were used. The conductance cell was calibrated by using 0.1 demal KCl (8). The density was determined by weighing 0.1ml of the melt.

For cyclic voltammetry (CV) measurements a PAR Model 173 Potentiostat/ Galvanostat and a PAR Model 175 Universal Programmer were used. The CV measurements were performed in a Pyrex glass cell which contained working and counter electrodes made of tungsten. A glass frit separated the counter electrode from the cathode compartment. The reference electrode was an Al wire immersed in a 65/35 mole % $AlCl_3$/DMFP solution separated from the cathode compartment by a fine glass frit.

All of the above measurements were performed in the dry box at approximately 30°C.

RESULTS AND DISCUSSION

Imidazoles and their salts are very reactive towards oxidation and towards electrophilic agents (9). To obtain higher stability towards oxidation, hydrogen on the aromatic ring can be replaced by an electron withdrawing group, or another, more stable heterocycle can be used. The fluoropyrazolium salt was, therefore, selected, since pyrazole is more stable towards oxidation than imidazole, and fluorine being an electron withdrawing group could provide additional stability (10).

To prepare a 65/35 mole % $AlCl_3$/DMFP melt, the reagents DMFP and $AlCl_3$ were mixed and heated to 80°C. A brown liquid was slowly formed which upon cooling to ambient temperature became more viscous. The density of 1.5 g/cm^3 was obtained for the 65/35 mole% $AlCl_3$/DMFP melt. The conductivity of 5 mS/cm at 30°C for the 65/35 mole% $AlCl_3$/DMFP melt was measured. Wilkes et al. (11) obtained the conductivity of 15.4 mS/cm for the 67/33 mole% $AlCl_3$/MEIC melt at 32.2°C.

The electrochemical window for this melt was determined by cyclic voltammetry; it was compared to that obtained for the 65/35 mole % $AlCl_3$/MEIC melt. The cyclic voltammograms of the $AlCl_3$/DMFP melt and the $AlCl_3$/MEIC melt are given in Fig.1. It can be seen that the potential limit is somewhat more positive for the former melt than for the latter.

Stability of the 65/35 mole% $AlCl_3$/DMFP melt towards oxidation was determined from the observation of the reactivity of SCl_3AlCl_4 in this melt. Initial observations, based on NMR spectra, suggest that the melt may be stable towards SCl_3AlCl_4. It was determined previously that SCl_3AlCl_4 reacts with the 65/35 mole% $AlCl_3$/MEIC melt.

Electrochemistry of sulfur in the 65/35 mole % $AlCl_3$/DMFP melt is under investigation.

ACKNOWLEDGMENT

This work was supported by the Air Force Office of Scientific Research.

REFERENCES

1. C. L. Hussey, in Advances in Molten Salt Chemistry, Vol. 5, G. Mamantov and C. B. Mamantov, eds., Elsevier, Amsterdam, 1983, pp. 185-230.
2. C. L. Hussey, in Chemistry of Nonaqueous Solutions-Current Progress, G. Mamantov and A. Popov, eds., VCH Publishers (in press).

3. S. D. Jones and G. E. Blomgren, in Proceedings of the Seventh International Symposium on Molten Salts , C. L. Hussey, J. S. Wilkes, S. N. Flengas, and Y. Ito, eds., The Electrochemical Society, Pennington, NJ, 1990, pp. 273-280.
4. B. Vestergaard, N. J. Bjerrum, I. Petrushina, H. A. Hjuler, R. W. Berg, and M. Begtrup, J. Electrochem. Soc., 140, 3108 (1993).
5. R. Marassi, J. Q. Chambers, and G. Mamantov, J. Electroanal. Chem., 69 , 345 (1976).
6. A. A. Gakh, K. G. Nikishin, N. D. Kagramanov, and V. V. Semenov, Izv. AN USSR, Ser. Khim., 1991, p. 2403.
7. G. P. Smith, A. S. Dworkin, R. M. Pagni, and S. P. Zingg, J. Am. Chem. Soc., 111, 525 (1989).
8. G. Jones and B. C. Bradshaw, J. Am. Chem. Soc., 55, 1780 (1933).
9. A. R. Katritzky, in Comprehensive Heterocyclic Chemistry, A. R. Katritzky and C. W. Rees, eds., Pergamon Press, Oxford, 1984, pp. 56, 58.
10. M. E. Niyazymbetov, V. A. Petrosyan, A. A. Gakh , and A. A. Fainzil'berg, Izv. AN USSR, Ser. Khim., 1987, p. 2390, and ref. cited therein.
11. J. S. Wilkes, J. A. Levisky, R. A. Wilson, and C. L. Hussey, Inorg. Chem., 21, 1263 (1982).

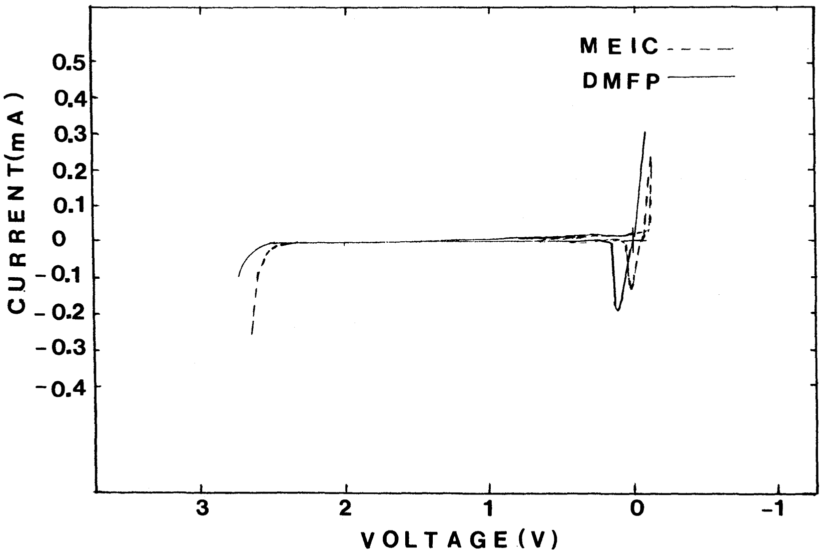

Fig 1. Cyclic voltammograms for the 65/35 mole% $AlCl_3$/DMFP melt (–) and for the 65/35 mole% $AlCl_3$/MEIC melt (--) at ambient temperature. Sweep rate 20 mV/sec.

DOI: 10.1149/199413.0757PV

SOLUBILITY AND CORROSION OF COBALT IN MOLTEN CARBONATES

Baek-un KIM, Yasuhiro TAKEISHI, Hideaki YOSHITAKE, Nobuyuki KAMIYA, and
Ken-ichiro OTA
Department of Energy Engineering, Yokohama National University
156 Tokiwadai, Hodogaya-ku, Yokohama 240, Japan

ABSTRACT

The solubility of Co oxide and the corrosion of Co in the presence of $(Li_{0.62}K_{0.38})_2CO_3$ melt have been studied in CO_2-O_2 atmosphere at 873 ~ 1073 K. The stable phase of Co oxide in the melt was $LiCoO_2$ coexisting with O_2 and CO_2 and the solubility of was proportional to $Pco_2^{1.5}$ and $Po_2^{-2.5}$. The dissolution reaction is estimated to be

$$LiCoO_2 + 3/2CO_2 \rightarrow Li^+ + Co^{2+} + 3/2CO_3^{2-} + 1/4O_2.$$

In spite of the low solubility of the Co oxide in the carbonate melt, the hot corrosion of Co metal occurred when the thin film of the melt was present on the metal. The weight gain curve could be divided into two regions : (1) the first stage of severe corrosion and (2) the second stage of slow corrosion rate. The corrosion products at the first stage were CoO and Co_3O_4, and those of the second stage were Co_3O_4 and $LiCoO_2$. The low solubility of $LiCoO_2$ might affected the corrosion reaction and suppressed the corrosion rate.

INTRODUCTION

The molten carbonate fuel cell(MCFC) is expected to be one of the most promising power generation systems for the coming century owing to the high efficiency, the excellent characteristics to the environment and the ability of utilization of wide variety fuels.

In this system, the durability is quite important for the long time operation. Especially, the solubility of the cathode material under the cathodic condition and the metallic corrosion in the presence of molten carbonate are thought to be very important factors for the commercialization. Recently, Veldhuis reported that the solubility of

$LiCoO_2$ is very low compared to NiO[1]). In this paper the solubility of Co oxide was measured and the result was compared with that of NiO[2]). If the solubility of Co oxide is low, Co metal might be stable with the carbonate melt. In this paper the corrosion of Co has also been studied in the presence of molten carbonate.

EXPERIMENTAL

(1) Solubility measurement

The solubility of $LiCoO_2$ was measured in the binary eutectic melt of $(Li_{0.62}K_{0.38})_2CO_3$. High purity $LiCoO_2$ powder was pressed to a pellet and sintered at 1073 K for 12 h. The sintered pellet was crushed to small particles and the particles whose size were about 1 mm were selected for the solubility measurement to ensure a large surface area. The particles of $LiCoO_2$ were immersed in the carbonate melt and the solubility measurement was started. The gaseous atmosphere was $Ar\text{-}CO_2\text{-}O_2$ mixture, where Pco_2 was varied from 0.1 to 0.7 atm (Po_2 is fixed with 0.3 atm) in order to measure the effect of Pco_2 and Po_2 was varied from 0.1 to 0.7 atm (Pco_2 is fixed with 0.3 atm) to check the effect of Po_2. The cell temperature was varied from 873 K to 1023 K. A small portion of the melt (0.2~0.5 g) was taken out periodically by means of a pure alumina tube and weighed. The melt sample was dissolved in HCl solution and the content of Co was measured by atomic absorption spectroscopy.

(2) Corrosion study

99.9% Co sheet (thickness=1 mm) was cut to a rectangular size (6x12mm) and used for the corrosion test. Two types of corrosion test were carried out in a gold cell. One is the corrosion in the melt(immersed) and the other is the corrosion with carbonate melt coating. For the test of coated sample, the carbonates were put on the surface of the specimen by dipping the carbonate-ethanol mixture and dried. The amount of carbonate on the metal was determined by the weight change before and after the coating process. The corrosion tests were carried out at 923 K in $CO_2\text{-}O_2$ atmosphere with $(Li_{0.62}K_{0.38})_2CO_3$ melt. The weight gain of the specimen was monitored continuously by TGA (Shimazu DT-40). And after the corrosion test, the corrosion products were analyzed by X-ray diffraction.

RESULTS AND DISCUSSION

(1) Solubility of $LiCoO_2$

Figure 1 shows the dissolution curves of $LiCoO_2$ under Pco_2=1 atm(without O_2) and Pco_2=0.7 atm (Po_2 was 0.3 atm) at 923 K. The concentrations are expressed in mole fraction. The Co content in the melt increased immediately after the start in both cases. Under Pco_2=0.7 atm, the Co content in the melt reached a steady state after 150 h, and then kept constant for three weeks. The solubility was determined from this steady state concentration. The value was 1/3 of the NiO solubility at the same condition. Thus, from the point of the solubility under this condition, $LiCoO_2$ is more stable than NiO. However, under Pco_2=1 atm and without O_2, the Co content in the melt did not reach a steady state even at 250 h. The content went up more than 70 ppm (mole fraction) at 250 h and still increased. Therefore, $LiCoO_2$ is considered to be unstable without O_2 gas.

Figure 2 shows the solubility of $LiCoO_2$ in $(Li_{0.62}K_{0.38})_2CO_3$ as a function of Po_2 at 923 K (Pco_2 is fixed with 0.3 atm). The result of Veldhuis'1) and the solubility of NiO2) are also shown for comparison. Although the NiO solubility was independent of Po_2, the $LiCoO_2$ solubility decreased with increasing of Po_2. This means that the difference of the solubilities of $LiCoO_2$ and NiO becomes smaller at low pressure of O_2. Although the tendency was similar, our results are smaller than that of Veldhuis. The slope of the line was -0.22 and this number is close to -0.25. Thus, the solubility of $LiCoO_2$ is considered to be proportional to $Po_2^{-0.25}$.

Figure 3 shows the solubility of $LiCoO_2$ in $(Li_{0.62}K_{0.38})_2CO_3$ at 923 K as a function of Pco_2 (Po_2 is fixed at 0.3 atm). The results of Veldhuis1) and the solubility of NiO2) at Po_2=0.3 atm are also plotted. Our results are different from those of Veldhuis as of Fig.2. This might be caused by the difference in the analytical method of Co in the melt. Veldhuis used the electrochemical reaction in the melt that is indirect method. In this study the Co content in the melt was obtained directly by the atomic adsorption spectroscopy. The solubility of $LiCoO_2$ increased with Pco_2. The solubility is proportional to $Pco_2^{1.5}$. The dependence of the solubility on Pco_2 is larger than that of NiO, since the solubility of NiO was proportional to Pco_2. Although the solubility of $LiCoO_2$ was lower than that of NiO in the low pressure range of CO_2., the difference becomes smaller at high pressure of CO_2.

Considering the dependences of the solubility of $LiCoO_2$ on Pco_2 and Po_2, the dissolution reaction in this study is considered as follows.

$$LiCoO_2 + 3/2CO_2 \rightarrow Li^+ + Co^{2+} + 3/2CO_3^{2-} + 1/4O_2 \quad (1)$$

Figure 4 shows the temperature dependence of the $LiCoO_2$ solubility under Pco_2=0.7 atm and Po_2=0.3 atm. The NiO solubility decreased with the increase of temperature, but the $LiCoO_2$ solubility increased with the increase of temperature. The effect of temperature on the solubility of $LiCoO_2$ was smaller than that of NiO. And the solubility of $LiCoO_2$ above 1023 K was larger than that of NiO

From these results the solubility can be expressed as follows.

For $LiCoO_2$

$$X=621\times10^{-6} \cdot Pco_2^{1.5} \cdot Po_2^{-0.25} \cdot e^{-3061/T}$$

For NiO

$$X=0.187\times10^{-6} \cdot Pco_2 \cdot e^{5163/T}$$

where X is the solubility(mole fraction) of metal oxide and T is absolute temperature. Using these equations, the solubilities of metal oxides can be calculated at the actual MCFC cathode inlet or outlet conditions at 923 K. Followings are calculated results.

a) solubility under 1 atm (Air/CO_2=70/30, gas utility:30%)
    $LiCoO_2$: $X_{in}=17\times10^{-6}$, $X_{out}=11\times10^{-6}$
    NiO:$X_{in}=34\times10^{-6}$, $X_{out}=24\times10^{-6}$
b) solubility under 8 atm (Air/CO_2=70/30, gas utility:30%)
    $LiCoO_2$: $X_{in}=227\times10^{-6}$, $X_{out}=146\times10^{-6}$
    NiO: $X_{in}=274\times10^{-6}$, $X_{out}=192\times10^{-6}$

X_{in} means the solubility of the metal oxide(mole fraction) at the inlet condition of MCFC cathode and X_{out} means that of outlet condition. At 1 atm, the solubility of $LiCoO_2$ is half of NiO. However, at higher pressure system, the difference is almost negligible. In order to apply $LiCoO_2$ to the cathode of MCFC, this point should be considered.

(2) Corrosion study

Figure 5 shows the weight gain curves for the corrosion of Co under $33\%O_2$-$67\%CO_2$ at 923 K. The amounts of corrosion were large with the presence of carbonate melt, either immersed or coated. The effect of the melt coating is larger than that in the melt. When Co was immersed in the melt, the weight gain after 50 h was 38.5 mg/cm^2 and the amount was 1/3 of that with coating. The reaction products in the melt after 50 h were $LiCoO_2$ and CoO. With 41 mg/cm^2 coating the weight gain curve divided into two regions : (1) the first stage of severe corrosion, where the so-called hot corrosion occurred and (2) the second stage of slow corrosion rate. The high corrosion rate in the initial period is surprising, considering the small solubility of $LiCoO_2$. The reaction products were CoO after 30 min, $LiCoO_2$ and Co_3O_4 after 15 h, and $LiCoO_2$ and Co_3O_4 after 50 h.

The formation of CoO and Co_3O_4 occurred mainly in the first stage of the corrosion. However, after 15 and 50 h CoO could not be detected. This is because the formation of CoO was very limited compare to other oxides and CoO could not be detected by the XRD. Once the formation of $LiCoO_2$ started, the corrosion rate decreased. The low solubility of $LiCoO_2$ might affect the corrosion reaction.

Figure 6 shows the effect of the coated amount on the corrosion of Co coated with $(Li_{0.62}K_{0.38})_2CO_3$ at 923 K under $33\%O_2$-$67\%CO_2$. The detected product after 50 h were $LiCoO_2$ and Co_3O_4 in any case. The more the coated amount increased, the longer the first stage continued. The amount of corrosion until the turning point of the first stage to the second stage increased owing to the coating amount. This is the other reason why the turning point was affected by the solubility of Co oxide that was formed during the corrosion reaction. The initial corrosion rate decreased with the increase of the coated amount up to 27 mg/cm^2. The increase of coating amount caused the increase of the thickness of the melt on the metal. Since the diffusion of O_2 from gas phase to scale became smaller owing to the increase of the film thickness, the corrosion rate decreased during the first stage.

REFERENCES

1) J.B.J. Veldhuis, F.C. Eckes, and L. Plomp, J. Electrochem. Soc., **139**, L6 (1992).
2) K.Ota et al, ibid, **139**, 667 (1992)

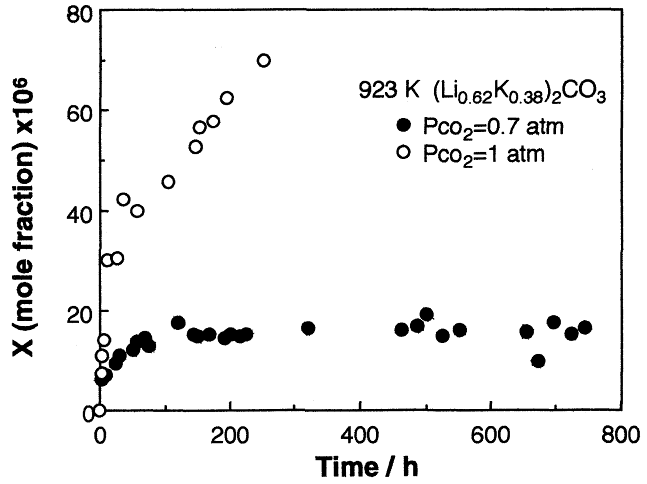

Fig. 1 Solubilities of $LiCoO_2$ in $(Li_{0.62}K_{0.38})_2CO_3$ under Pco_2=1 and 0.7 atm at 923 K.

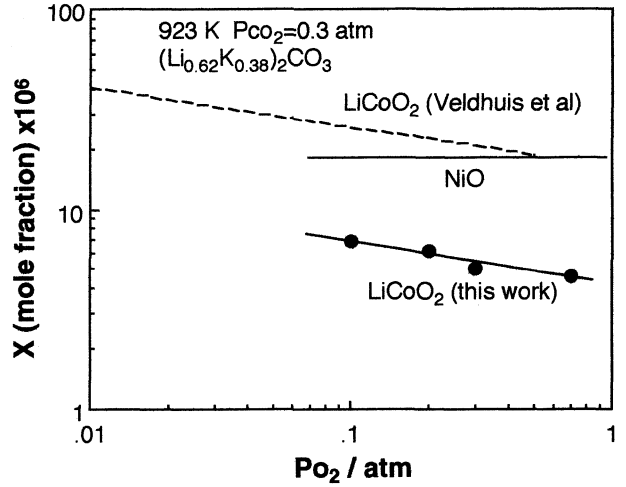

Fig. 2 Solubilities of $LiCoO_2$ and NiO in $(Li_{0.62}K_{0.38})_2CO_3$ as a funtion of Po_2 under Pco_2=0.3 atm at 923 K.

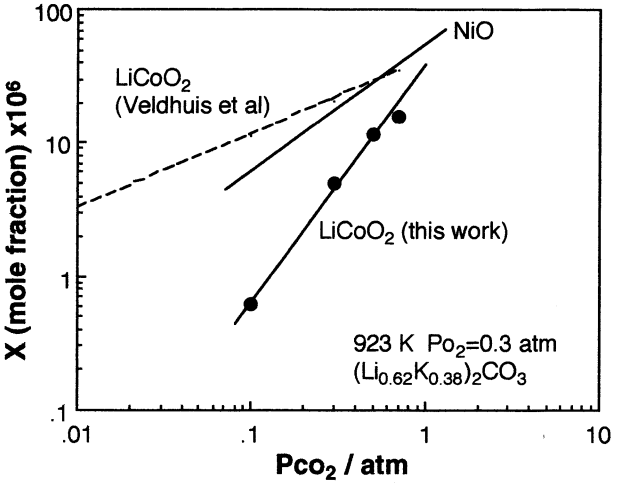

Fig. 3 Solubilities of $LiCoO_2$ and NiO in $(Li_{0.62}K_{0.38})_2CO_3$ as a funtion of Pco_2 under Po_2=0.3 atm at 923 K.

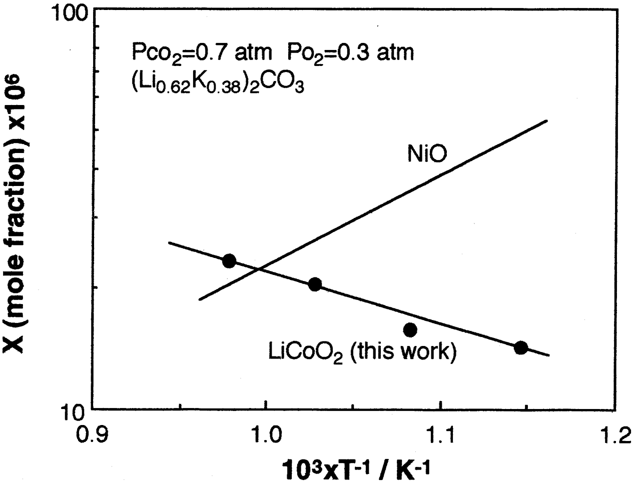

Fig. 4 Temperature dependence of solubilities of $LiCoO_2$ and NiO in $(Li_{0.62}K_{0.38})_2CO_3$ under Pco_2=0.7 atm and Po_2=0.3 atm.

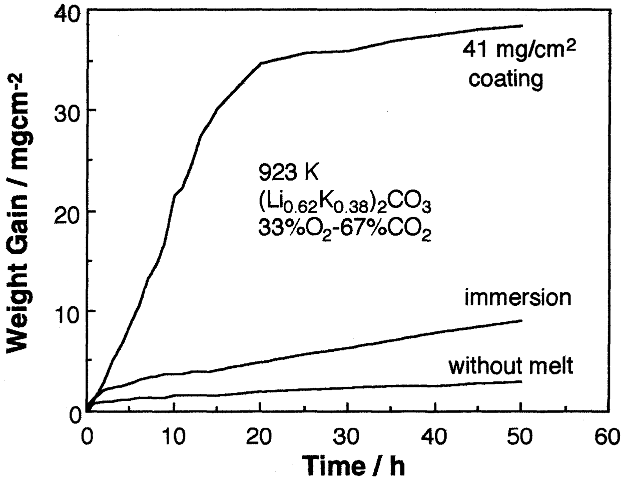

Fig. 5 Weight gain curves for the corrosion of Co at 923 K under $33\%O_2$-$67\%CO_2$.

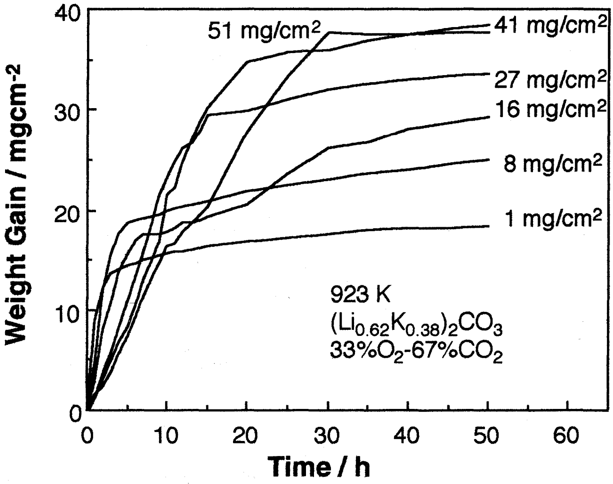

Fig. 6 Weight gain curves for the corrosion of Co coated with 1~51 mg/cm^2 of $(Li_{0.62}K_{0.38})_2CO_3$ at 923 K under $33\%O_2$-$67\%CO_2$.

DOI: 10.1149/199413.0765PV

ELECTROCHEMICAL AND THERMODYNAMIC BEHAVIOR OF NICKEL SPECIES IN MOLTEN Li_2CO_3-Na_2CO_3-K_2CO_3 AT 650°C

B. MALINOWSKA, M. CASSIR* and J. DEVYNCK

Ecole Nationale Supérieure de Chimie de Paris,
Laboratoire d'Electrochimie (URA 216 du CNRS)
11 rue Pierre et Marie Curie,
75231 PARIS CEDEX 05 (FRANCE)

ABSTRACT

The behavior of nickel species is investigated in Li_2CO_3-Na_2CO_3-K_2CO_3 molten eutectic at 650°C by the means of thermodynamic data and electrochemical experiments at nickel and gold microelectrodes. Potential-oxoacidity diagrams allows to predict the stability domains of Ni, Ni(II) and Ni(III) species. NiO species can be dissolved in oxoacidic media by the formation of $NiCO_3$, and in oxobasic media by the formation of NiO_2^{2-}. NiO/Ni, Ni^{2+}/Ni and Ni(III)/Ni(II) systems are characterized by voltammetric techniques.

INTRODUCTION

One of the major difficulties to improve molten carbonate fuel cell MCFC lifetime, in order to commercialize this kind of electrical generator, is the problem of cathodic material stability. The material generally used is nickel recovered by lithiated NiO, which can slowly be dissolved either in oxoacidic media (formation of $NiCO_3$), in the conditions commonly employed in MCFC, or in oxobasic media (formation of M_2NiO_2. M: alkali metal) [1-4].

In this study, thermodynamic and electrochemical behavior of Li_2CO_3-Na_2CO_3-K_2CO_3 ternary eutectic, which has been relatively neglected in the literature, was investigated at different oxoacidity levels in the absence or in presence of carbon dioxide, argon and oxygen. Thermodynamic data were compared to electrochemical experiments performed at conventional nickel and gold electrodes, as well as at a 200 µm diameter gold microelectrode, which has been fully described in a previous paper [5].

THERMODYNAMIC STUDY

Stability ranges of nickel species were established as a function of the oxoacidity of the ternary eutectic. Thermochemical data of oxygen and nickel species were extracted from the literature [6-9]. In the case of nickel-alkali metal species, no data was found concerning lithium-nickel and potassium-nickel compounds and only nickel-sodium compounds were considered for thermodynamic calculations.

A general description of the electrochemical stability of Li-Na-K eutectic was developed elsewhere [10]. The following nickel redox systems were considered: NiO/Ni, $NiCO_3$/Ni,Ni_2O_3/NiO, Ni_2O_3/$NiCO_3$, NiO_2^{2-}/Ni, NiO_2^-/NiO, NiO_2^-/NiO_2^{2-}, NiO_2^-/$NiCO_3$, Ni_2O_3/NiO_2^{2-}. Standard potentials of these systems were referred to $Li_2O(a=1)/O_2(1\text{ atm})$ reference system, previously described. Table I shows these potentials at 650°C.

Table I- Standard potentials E*(V) of nickel species at 650°C, calculated from thermochemical data [6-9]. Reference Li_2O/O_2.

	NiO/Ni	$NiCO_3$/Ni	Ni_2O_3/NiO	Ni_2O_3 /$NiCO_3$	Na_2NiO_2 /Ni
E* (V)	-0.807	-0.338	0.188	-0.749	-1.295

	$NaNiO_2$ /NiO	$NaNiO_2$ /Na_2NiO_2	$NaNiO_2$ /$NiCO_3$	Ni_2O_3 /Na_2NiO_2
E*(V)	-1.071	-1.187	-2.006	-0.473

Figure 1 shows a potential-oxoacidity diagram of the ternary eutectic at 650°C* and, in particular, the stability domains of nickel species. Nickel can be stabilized under three oxidation numbers: Ni(0), Ni(II) and Ni(III). NiO species is stable whatever the oxoacidity level. Nevertheless, a partial dissolution can be observed either in oxoacidic melts, transformation into Ni^{2+} ($NiCO_3$ at an activity of about 10^{-5}), or in oxobasic melts, transformation into NiO_2^{2-} (calculations were developed considering the formation of $NaNiO_2$ at an activity of 10^{-7}). Ni(III) can only be stabilized under a soluble form NiO_2^- (calculations made for a $NaNiO_2$ compound at an activity of 10^{-3}).

EXPERIMENTAL

Lithium-sodium-potassium molten carbonate (43.5-31.5-25.0 mol.%) and sodium oxide, were prepared from Merck reagents of analytical purity (>98%). All the gases, of high purity grade, were dried before bubbling through the melt. Electrochemical experiments were performed with an ELECTROKEMAT (EK. E390 model) potentiostatic system. The cell and conventional electrodes were described in a previous

---

* Oxoacidity limit: formation of CO_2, set at one atmosphere; oxobasicity limit: formation of Li_2O; oxidation limit: formation of O_2 or O_2^{2-} and reduction limit: formation of K or CO.

article [10]. Fabrication of gold microelectrodes of 200µm diameter was described elsewhere [5].

ELECTROCHEMICAL CHARACTERIZATION

Electrochemical behavior of Ni in the ternary eutectic has been investigated at 650°C at different oxoacidity levels: oxoacidic media, $P(CO_2) = 1$atm. or $P(CO_2) = 0.1$ atm. + $P(O_2) = 0.9$ atm. (conditions generally used in MCFC); neutral media: $P(Ar) = 1$atm.; oxobasic media: $P(Ar) = 1$ atm. + Na_2O.

Fig. 2 shows voltammograms obtained in Li_2CO_3-Na_2CO_3-K_2CO_3 at 650°C at a conventional gold electrode. Curve shown in Fig. 2a was observed in the absence of nickel salt in the melt. After adding Ni(II) salt in the melt, a complex reduction current appeared at -1200, -1300 mV, associated with an oxidation current at -1000 mV, as it can be seen in Fig. 2b. These currents increased when increasing the oxobasicity of the melt, as shown in Fig. 2c. The same system was observed under an argon pressure of 1 atm (Fig. 3). On the one hand, evolution of this system with v (scan rate) showed that anodic and cathodic peak currents were directly proportional to v and not to $\sqrt{v}$., which significates that both species are in a solid form, adsorbed at the electrode surface. On the other hand peak potentials were shifted towards more negative potentials (reduction currents), as observed in Fig. 4, or more positive potentials (oxidation currents), when increasing v, which is characteristic of a non-reversible system. According to our thermodynamic study and the fact that Janz et al [11] showed that the corrosion potential of Ni into NiO in Li-Na-K eutectic at 600°C was -1166 mV with respect to Ag^+/Ag reference system; this system can be expressed as NiO/Ni . Reduction of NiO is in fact more complex and might involve a structural change due to lithiated NiO [12]. In oxobasic conditions, under argon atmosphere and addition of sodium oxide, as shown in Fig. 5, oxidation of nickel probably occurs in two steps:

$$Ni + 2O^{2-} \Leftrightarrow NiO_2^{2-} + 2e^-$$

$$Ni + NiO_2^{2-} \Leftrightarrow 2NiO + 2e^-$$

After dipping a nickel electrode in an oxoacidic melt: $P(CO_2) = 1$atm., a second system was observed at higher potentials. Addition of Ni(II) salt in the same melt increased both reduction and oxidation currents of this system. In oxobasic media this system disappeared. Analysis of the voltammogram relative to this system showed a two-electron process and, in particular, a reduction current diffusion-controlled. It can be deduced that this system is Ni^{2+}/Ni, Ni^{2+} being formed by the partial dissolution of NiO, according to: $NiO + CO_2 \Leftrightarrow Ni^{2+} + CO_3^{2-}$. This is in accordance with the results of other authors [4,13] on nickel solubility in Li-K melt. Fig. 6 shows the evolution of Ni^{2+}/Ni system with v at a 200 µm diameter gold microelectrode. Steady-state voltammograms were obtained at all the mentioned scan rates, which is an important characteristic of this kind of electrode, allowing an easier quantitative analysis of voltammograms.

The third nickel system corresponds to Ni(III)/Ni(II), as identified by other authors in Li-K melt [14-16], and was observed in all the mentioned media, with a peak evolution towards negative potentials with the increase in the oxobasicity of the melt. Fig. 7 shows this sytem in an oxoacidic medium. Analysis of this system indicated that both Ni(II) and Ni(III) species were under a solid form. In the case of Ni(III) this is in contradiction with thermodynamic predictions, mentioning the presence of a soluble species. The influence of lithiation on this system will be presented in a future work.

CONCLUDING REMARKS

Behavior of nickel species has been briefly described in Li-Na-K ternary eutectic. Three systems have been identified NiO/Ni, Ni^{2+}/Ni and Ni(III)/Ni(II). Thermodynamic data are generally in agreement with electrochemical experiments, but a contradiction has been pointed out concerning the form under which Ni(III) species is stabilized. Thus, a more detailed study, including spectroscopic data and lithiation aspects, is necessary.

ACKNOWLEDGMENTS

Professor B. Trémillon is gratefully acknowledged for helpful discussions.

REFERENCES

1. M. L. Orfield and D. A. Shores, J. Electrochem. Soc., 135, 1662 (1988).
2. M. L. Orfield and D. A. Shores, ibid, 136, 2862 (1989).
3. C. E. Baumgartner, J. Am. Ceram. Soc., 67, 460 (1984).
4. K. Ota, S. Mitsushima, S. Kato, S. Asano, H. Yoshitake and K. Kamiya, ibid, 139, 667 (1992).
5. B. Malinowska, M. Cassir and J. Devynck, submitted at J. of Electrochem. Soc. (1993).
6. Janaf Thermochemical Tables, 3rd ed., US Department of Commerce, Washington, DC (1986).
7. Bulletin 542, US Bureau of Mines (1954), in CRC *Handbook of Chemistry and Physics*, 65th ed., D36, CRC Press, Boca Raton, FL (1988-1989).
8. D. Mehandjiev, Comptes Rendus de l'Académie Bulgare des Sciences, 22, 11, 1253 (1969).
9. B. J. Shaiu, P. C. S. Wu and P. Chiotti, J. of Nuclear Materials 67,13 (1977).
10. M. Cassir, G. Moutiers and J. Devynck, J. of Electrochem. Soc., 140, 3114 (1993) .
11. G. I. Janz and A. Conte, Electrochimica Acta, 9, 1269 (1964).
12. I. J. Pickering, P. J. Maddox and J. M. Thomas, Chem. Mater., 4, 994 (1992).
13 T. D. Kaun, in *"Molten Carbonate Fuel Cell Technology"*, J. R. Selman and J. D. Claar, Editors, PV 84-13, p.489, The Electrochemical Society Softbound Proceedings Series, Pennington, NJ (1984).
14. T. Nishina, K. Takizawa and I. Uchida, J. Electroanal. Chem., 263, 87 (1989).
15. G. Xie, Y. Sakamura, K. Ema and Y. Ito, J. of Power Sources, 32, 125 (1990).
16. G. Xie, Y. Sakamura, K. Ema and Y. Ito, J. of Power Sources, 32, 135 (1990).

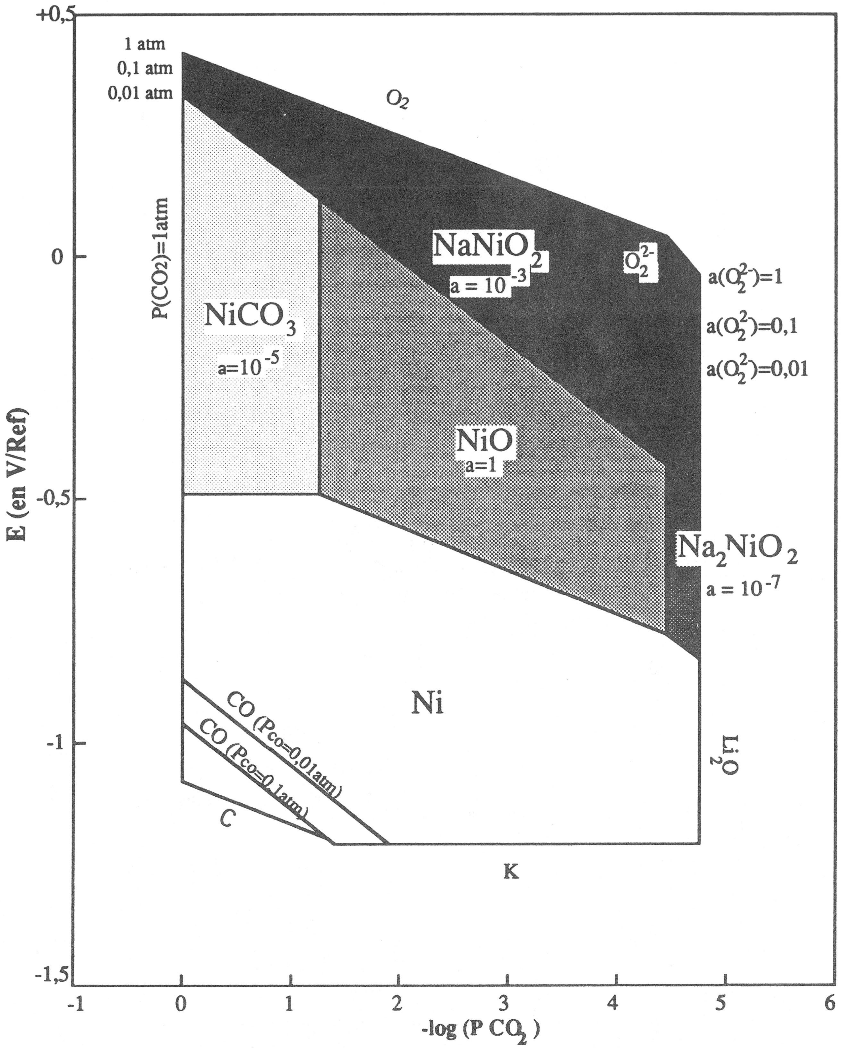

Fig.1. Potential - oxoacidity diagram of Li_2CO_3 - Na_2CO_3 - K_2CO_3 eutectic at 650°C

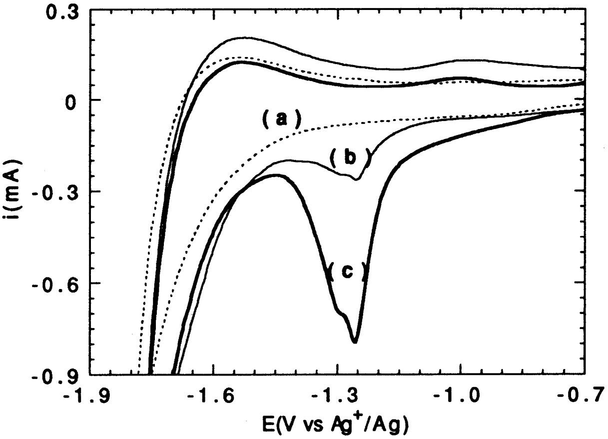

Fig. 2. Cyclic voltammograms of Li_2CO_3-Na_2CO_3-K_2CO_3 at a gold electrode(1.6 mm diameter) at 650°C:(a) v = 0.1 V/s; P(CO_2) = 1atm (b) v = 0.2 V/s; P(CO_2) = 1atm; addition of Ni (II) salt (m = 208 mg); (c) v = 0.2 V/s; P(CO_2) = 0.1 atm+P(O_2 = 0.9 atm;addition of Ni(II) salt (m = 208 mg)

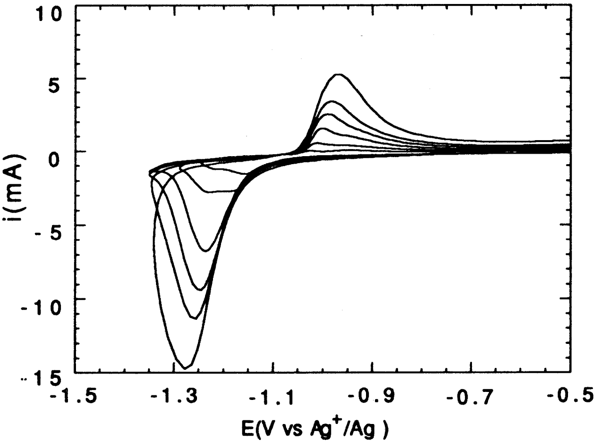

Fig. 3. Cyclic voltammograms of Li_2CO_3 - Na_2CO_3 - K_2CO_3 after adding a nickel (II) salt (m = 86.5 mg) at different scan rates: 1) 0.2 V/s; 2) 0.5 V/s; 3) 1V/s; 4) 1.5 V/s; 5) 2 V/s; 6) 3 V/s. Gold electrode (1.6 mm diameter); T = 650°C; P(Ar) = 1 atm

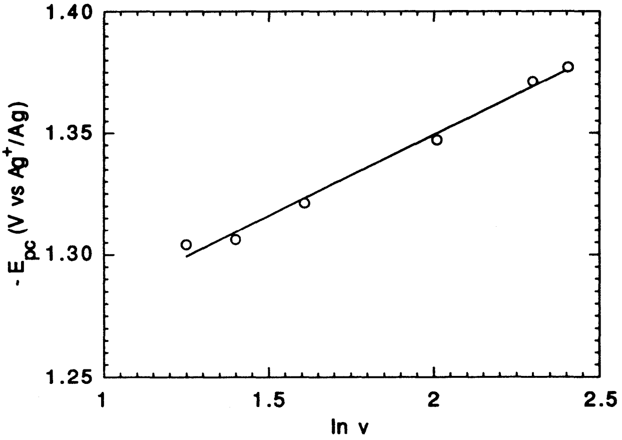

Fig. 4. Plot of cathodic peak potential vs ln v (v: scan rate) in the conditions given in Fig. 3.

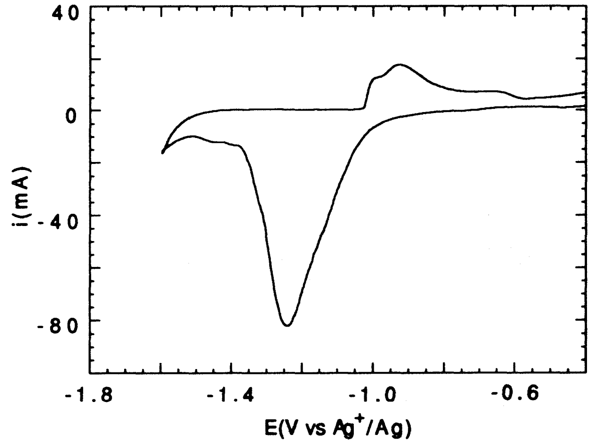

Fig. 5. Voltammogram of Li_2CO_3 - Na_2CO_3 - K_2CO_3 *at a nickel electrode, at 650°C.[* Na_2O *] = 1.46* 10^{-1} *mol/kg; addition of Ni (II) salt = 66.5mg; P(Ar) = 1 atm; v = 0.2 V/s.*

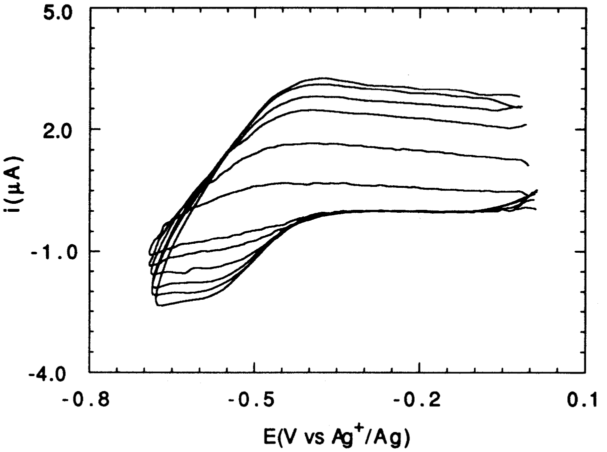

Fig. 6. Voltammograms of Li_2CO_3 - Na_2CO_3 - K_2CO_3, after adding a nickel (II) salt (m = 83.1 mg) at different scan rates : 0.1 V/s; 0.4 V/s; 1.0 V/s; 1.5 V/s; 2.0 V/s; 2.5 V/s. Gold microelectrode (200 μm diameter). $P(CO_2) = 1$ atm.

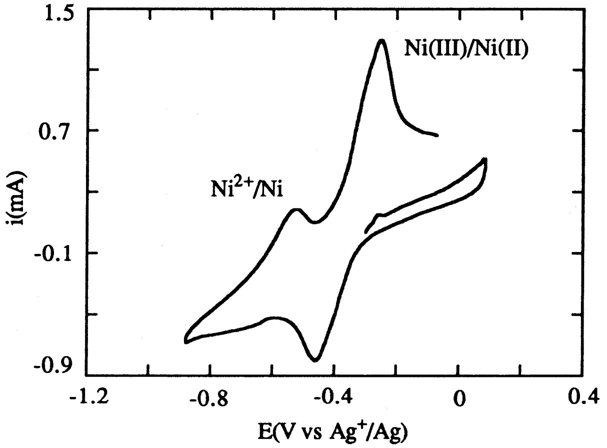

Fig. 7. Voltammogram obtained at a nickel electrode in molten Li_2CO_3 - Na_2CO_3 - - K_2CO_3 eutectic at 650°C under the following conditions: $P(CO_2) = 1$ atm; $v = 0.1$ V/s; addition of 10^{-2} $mol.kg^{-1}$ of $NiCO_3$

DOI: 10.1149/199413.0773PV

SUPPORTED MOLTEN-SALT ELECTROCATALYST FOR CO-GENERATION OF ACETALDEHYDE AND ELECTRICITY FROM ETHANOL IN A FUEL CELL

Sanjiv Malhotra and Ravindra Datta*

Department of Chemical and Biochemical Engineering
The University of Iowa, Iowa City, IA 52242.

ABSTRACT

A novel fuel cell has been developed for simultaneously generating electricity and acetaldehyde from ethanol, that is based on supported molten-salt electro-catalysts (SMSEC). The SMSEC used the Wacker homogenous catalyst, namely $PdCl_2/CuCl_2$, dissolved in a low-melting molten salt. Current denisities of up to 3.5 mA/cm^2 with good selectivity (85%) to acetaldehyde were obtained in the tetra-n-butylammonium trichlorostannate as the molten salt. Preliminary results for different molten salt catalysts and electrolytes are presented here.

INTRODUCTION

The utilization of the favorable free energy of reaction to drive fuel cells to produce desired chemicals and cogenerate electricity is an attractive idea (1). In cogeneration fuel cell systems, selective electrocatalysis is employed to produce value-added chemicals, in contrast to fuel cells where complete combustion of the reactants and energy production is the usual goal. Further, attention being attributed to biomass-based chemical feedstocks has generated an interest in the usage of ethanol for producing other basic chemicals and for alternative energy generation.

Acetaldehyde is an important large scale industrial intermediate chemical. It is an intermediate in the production of a number of chemicals such as acetic acid, acetic anhydride, ethyl acetate, 1,3-butylene glycol, and peracetic acid, etc. There are several commercial routes for acetaldehyde production: 1) partial oxidation of ethylene, 2) oxidation or dehydrogenation of ethanol, 3) hydration of ethylene, now obsolete, and 4) partial oxidation of low molecular weight paraffin hydrocarbons. While more than 80% of the acetaldehyde is produced by the Wacker-Hoechst process involving partial oxidation of ethylene, some of it is also produced by the oxidation or, less commonly, by the dehydrogenation of ethanol. This work is concerned with the feasibility of a novel prototype fuel cell designed to simultaneously produce value-added acetaldehyde and electricity from renewable ethanol.

The fuel cell is based on the novel electro-catalytic usage of *homogenous* (liquid phase) catalysis to achieve high selectivity and reactivity at relatively low temperatures (~150°C). This has been made possible by the development of the technique of supported molten-salt catalysis (SMSC) (2). The fuel cell system described here possesses the following novel features:

---

*Author to whom correspondence may be addressed.

- A homogenous supported molten salt electrocatalyst (SMSEC) for the cogeneration of acetaldehyde and electricity from ethanol.

- An electrolyte comprising of a low melting point molten salt supported on a Nafion® membrane.

- New chemistry for producing acetaldehye from ethanol, which combines the chemistries of the Veba-Chemie method for producing acetaldehyde from ethanol and the Wacker process which is used for producing acetaldehyde from ethanol.

DESCRIPTION

Supported Molted-Salt Catalyst:

In the homogeneously catalyzed Wacker process for acetaldehyde synthesis there are some engineering problems: inefficient catalyst utilization, limited gas-liquid surface area, corrosion, and the required separation of the catalyst from the product. In fact, many of these problems are inherent to homogeneous catalysis, which have thus limited its industrial application, even though there are now many major industrial processes that employ soluble transition metal complexes as catalysts (3-4). Due to the dwindling raw material supplies, higher energy costs, and more stringent environmental standards, the use of the more efficient homogeneous catalysis is expected to continue to grow because of its high selectivity, high activity, mild operating conditions, molecular dispersion of the catalyst, and better control of the nature of the catalytic species.

Several hybrid techniques (5) have been developed that seek to combine the attractive features of homogeneous catalysis with those of heterogeneous catalysis such as large interfacial area, use of conventional reactors such as packed-bed and fluidized-bed reactors, and ease of separation of catalyst from products. These techniques include polymer heterogenized metal complexes (5-6), zeolite entrapped complexes, supported liquid-phase catalysis (SLPC) (7), and supported molten-salt catalysis (2). At the present time none of these approaches have yielded a commercially viable catalyst. However, the SMSC approach, described below, offers some promise in this regard.

In the SMSC technique (2), a molten-salt containing the dissolved or dispersed transition metal complex catalyst is coated on the walls of a porous support so as to occupy a fraction of the pore space, much like a chromatographic packing supporting a liquid phase. The gaseous or vapor phase reactants diffuse through the residual gas pore space, as well as through the liquid, and react within the liquid catalyst film. The catalyst retains a dry external appearance and, thus, effectively combines the attractive features of homogeneous catalysis with those of heterogeneous catalysis. It virtually eliminates liquid-diffusion limitations, since the liquid is coated as a very thin film and the interfacial area is extremely large. The SMSC technique is a very powerful one since a large variety of molten salts is available for practically any temperature range. Co-catalysts or promoters can also be easily incorporated in the liquid. Further, molten salts have excellent solvent properties and can dissolve a wide variety of substances such as ionic substances, organic substances, gases, water, metal oxides, non-metallic elements and even metals (8-9). Thus, SMSC can be developed not only for homogeneous catalysts but also for "heterogeneous" catalysts by dispersing crystallites of metals and inorganic metal compounds in supported molten salts (10).

Rao and Datta (2) have developed a SMSC Wacker catalyst by replacing the aqueous solvent ($H_2O + HCl$) with a eutectic melt of CuCl and KCl (m.p. 150 °C), which is highly active, affording almost complete utilization of the expensive Pd catalyst, has high selectivity, is extremely stable, and virtually eliminates the corrosion problems encountered in the industrial process. This catalyst forms the basis of the proposed SMSEC.

Novel Catalysis for the Reaction:

The reaction system chosen here is the Veba-Chemie process, i.e., the oxidative dehydrogenation of ethanol to form acetaldehyde. However, the traditional Veba-Chemie process oxidizes ethanol by passing ethanol vapors and air over a silver catalyst at a high temperature (~500 °C). We conduct this reaction by combining the chemistries of the Veba-Chemie and the Wacker-Hoechst processes in order to produce acetaldehyde from ethanol at a relatively mild temperature (~100-190°C) in a fuel cell. Experiments in our laboratory have indicated that this catalysis is feasible. The anticipated overall reaction mechanism, analogous to the Wacker process, is:

$$PdCl_4^{2-} + C_2H_5OH \longrightarrow CH_3CHO + Pd^0 + 2HCl + 2Cl^-$$

$$2Cl^- + Pd^0 + 2CuCl_2 \longrightarrow PdCl_4^{2-} + 2CuCl$$

$$2CuCl + 2HCl + \frac{1}{2}O_2 \longrightarrow 2CuCl_2 + H_2O$$

$$C_2H_5OH + \frac{1}{2}O_2 \longrightarrow CH_3CHO + H_2O$$

Supported Molted-Salt Electrocatalytic Fuel Cell:

The new supported molten-salt electro-catalyst (SMSEC) design is shown schematically in Figure 1. A molten-salt containing the dissolved catalyst, is coated on the walls of porous carbon, which on account of its excellent corrosion resistance, electronic conductivity and cost, is a popular porous electrocatalyst support. The gaseous or vapor phase reactants diffuse through the residual gas pore space as well as through the molten-salt phase, and react within the catalyst layer. The anode and cathode are separated by a thin layer of supported electrolyte for the conduction of ions. The electrolyte used is either an appropriate acid which provide excellent ionic conductivities, or a supported molten-salt electrolyte. The electrolyte support material must be nonconducting.

Different molten salts as follows were employed as solvents for electrocatalysts:

Catalyst Type A had the Wacker homogeneous catalyst ($PdCl_2 + CuCl_2$) dissolved in a eutectic melt of 35 mol% KCl-65 mol% CuCl (m.p. = 150 °C) (Janz, 1969). The catalyst preparation procedure is described by Rao and Datta (2). It involves dissolving the above substances in a dilute aqeous solution of HCl in a volumetric ratio corresponding to the desired liquid loading. The mixture is gently stirred for about 24 hrs. Meanwhile the porous supports are kept in vacuum overnight to remove air from the pores. Then the vacuum pump is shut off and the catalyst solution is added to the porous supports. The supports are thus immersed for 24 hrs and then the supports are removed from the solution and placed in a vacuum oven at 110°C for about 12 hrs to evaporate the hydrochloric acid and water from the pores. The weight gain of support provides the amount of catalyst-salt mixture remaining in the pore space. The solvent loading (CuCl +KCl) was about 30% and the palladium chloride and copper(II) chloride concentration was 10.5mmol/L and 0.13mol/L respectively.

Catalyst Type B had the Wacker homogenous catalyst ($PdCl_2$ + $CuCl_2$) dissolved in an organic eutectic melt namely tetra-n-butylammonium trichlorostannate. The crystals of the melt were prepared by adding 100 ml of aqueous 1 M tetra-n-butylammonium chloride to a solution of 0.1 mol of $SnCl_2.2H_2O$ at room temperature. The solution was stirred for about 15 minutes. A colorless oil separated. The residual oil crystallized on cooling. Recrystallization of the tetra-n-butylammonium trichlorostannate from ethanol gave white crystals with a melting point of around 60°C. The catalyst and the molten salt were mixed at around 90°C in a vacuum oven and spread uniformly on a graphite support thus allowing direct impregnation for a period of 24 hrs. The amount of the molten salt impregnated was 2.5 gms and the catalyst concentration was the same as that used in catalyst Type A.

Catalyst Type C had the Wacker homogenous catalyst dissolved in ethylene glycol. The volumetric solvent loading was around 24% with the same catalyst concentrations as in catalyst type A.

Catalyst Type D had Platinum catalyst supported on graphite discs. The method of preparation was the same as used for the Cathode, described in the next section. The platinum loading was around 1.2 mg/cm^2.

Anode:

The different electrocatalysts used at anode are listed in Table 1.

The anticipated half-cell reactions at the anode are:

$$PdCl_4^{2-} + C_2H_5OH \longrightarrow CH_3CHO + Pd^0 + 2HCl + 2Cl^-$$

$$2Cl^- + Pd^0 + 2CuCl_2 \longrightarrow PdCl_4^{2-} + 2CuCl$$

$$2CuCl + 2HCl \longrightarrow 2CuCl_2 + 2H^+ + 2e^-$$

$$C_2H_5OH \longrightarrow CH_3CHO + 2H^+ + 2e^-$$

Cathode:

The cathode has platinum catalyst supported on graphite discs (Catalyst Type D). The graphite discs are immersed in a solution of chloroplatinic acid for a period of 5 days. The discs are then placed in a vacuum oven (85°C) for 12 hours. Then the catalyst is reduced with flowing hydrogen at 450°C for 6-7 hours. The half-cell reaction is:

$$\frac{1}{2}O_2 + \ + 2H^+ + 2e^- \rightarrow H_2O$$

Electrolyte:

The different electrolytes tried include phosphoric acid, Nafion® membranes and a molten-salt eutectic (CuCl-KCl). Since the Nafion membrane is dehydrated and exhibits a loss in ionic conductivity at temperatures above 80°C, we saturated the membrane with phosphoric acid for 24 hrs in order to have it operational even at temperatures above 100°C. Alternatively, the Nafion membrane was impregnated with low melting molten salts possessing protonic conductivity. The different inert supports tried for the molten salt eutectic (CuCl-KCl) and phosphoric acid include porous vycor glass (40 Å pore size), alumina disc (0.125" thick and 5μm pore size), and aluminium nitride (0.125 " thick and 5 μm pore size) disc. A thin film of phosphoric acid was contained between two Nafion® membranes and nafion gel along with phosphoric acid was applied to the faces of the electrodes which were in contact with the nafion membranes. In another set of experiments, a thin disc of glass wool (1mm thick) was saturated with phosphoric acid and contained between two Nafion® membranes which had been impregnated with the acid for 24 hours. This reduced the possibility of the acid evaporating during the fuel cell operation.

Experimental Apparatus and Test Procedure:

Ethanol was supplied by means of a liquid pump (Eldex, Model No. A-60-S) and, upon evaporation in a vaporizer with controlled temperature, was carried by He into the anode compartment. Air (or O_2) was supplied to the cathode compartment. The fuel cell is made of stainless steel. The reactant inlet and product outlet connections from each half cell have the shell-and-tube exchanger design, with the tubes (1/8" and 1/4" O.D) placed concentrically in each opening. This minimizes the number of connections to the fuel cell and hence the possibility of leaks. The temperature of the vaporizer was controlled using a Omega temperature controller (CN9100A). The flow rates were controlled by needle valves and measured with mass flow meters (Omega, FMA 1700/1800 series). The pressure in the reactant gas line and in the fuel cell was measured by means of a Matheson pressure gage. Two three way valves allowed the feed stream as well as the product stream to be analyzed on a continous basis by means of an on-line gas chromatograph (Gow-Mac, Series 580) utilizing a Porapak-Q column. Another set of three-way valves allowed the monitoring of products and reactants in the two electrode compartments (anode and cathode) separately. Heating tape was used for the gas lines to avoid condensation of product stream leading from the fuel cell to the G.C. The temperature of the fuel cell was controlled with a temperature controller (Omega, CN9000A) and heating tapes.

The rate of formation of the product on the basis of ethanol converted, the selectivity to acetaldehyde and the current efficiencies for the products were studied. The current efficiency can be calculated by measuring the total electric charge passed with the help of the coulometer, and dividing this by the amount of electric charge that should be stoichiometrically produced with the measured amount of the products produced.

RESULTS AND DISCUSSION

Different combinations of the electro-catalysts at the anode and the cathode along with different electrolytes were studied for carrying out initial feasibility studies (Table 1). Initially, Catalyst Type A was studied both at the anode and the cathode with CuCl-KCl eutectic supported on porous vycor glass as the electrolyte medium. The current density obtained was only around 0.05mA/cm^2 with a low conversion at around 180°C. Catalyst Type A was discarded for the cathode since it was found that the Pt catalyst supported on graphite discs was far more suitable for the reduction reaction (Catalyst Type D). In order to improve the ionic contact and to circumvent the problem due to the fragility of the porous vycor glass, a nafion membrane with a thin film of phosporic acid was used as the electrlolyte. Current densities of around 1mA/cm^2 were obtained with acetaldehyde selectivity of around 75%. However, this was not reproducible due to the fact that phoshoric acid evaporated at 180°C. Then ethanol was fed along with 5% phosporic acid - 5% water to the anode side. In different experimental runs carried out with the above solution as the anode feed, the current densities obtained were around 1-1.3 mA/cm^2 but substantial amount of ethylene was also formed due to the acidic nature of the anode, thus reducing the selectivity to acetaldehyde.

Since, Nafion® membrane is dehydrated above 100°C, a liquid solvent such as ethylene glycol was used for the wacker catalyst at the anode (Catalyst C). Platinum on graphite was used at the cathode and a nafion membrane impregnated with phosphoric acid with a thin film of ethylene glycol on the electrode surface in contact with the Nafion® membrane was used as the electrolyte. Current densities of around 0.3mA/cm^2 with 65% selectivity to acetaldehyde were obtained, but the catalyst deactivated after an initial run of 5 hrs at around 90°C due to the evaporation of the liquid solvent.

Next, an organic molten salt (tetra-n-butylammonium trichlorostannate) was used as the melt for dissolving the catalyst for two primary reasons:

- To have a low melting point molten salt so that the low operating temperatures reduce the rate of evaporation of the phosporic acid contained between the nafion membranes.

- To have a molten salt with a good protonic conductivity, thus facilitating protonic conduction from the catalytic site to the electrolyte interface.

The reason for the relatively low current densities compared to the circuit voltages obtained from the various set of experiments is probably due to the thickness (0.125") of the electrodes. The high resistance to diffusional transfer provides the overpotential losses. To avoid this loss, we plan on next employing very fine weave carbon cloth electrodes (0.4 mm thick) obtained from Electrosynthesis Corp. The electrode will be characterized using cyclic voltammogram and SEM techniques in order to study the active catalyst layer.

ACKNOWLEDGEMENT

This work was performed under the auspices of the Iowa Energy Center under award No. 9301A-07.

REFERENCES

1. Langer, S.H., and Skellaropoulos, G., Ind. Eng. Chem. Process Des. Dev., **18**, 567 (1979).
2. Rao, V., and Datta, R., J. Catal., **114**, 377-387 (1988).
3. Parshall, G. W., *Homogeneous Catalysis*, John Wiley, New York (1990).
4. Parshall, G. W. and Putscher, R. E., J. Chem. Edu., **63**, 189-191 (1986).
5. Hartley, F. R., *Supported Metal Complexes*, D. Reidel Pub. Co., Dordrecht, Holland (1985).
6. Raje, A. P. and Datta, R., J. Mol. Catal., **72**, 97-116 (1992).
7. Datta, R., and Rinker, R. G., J. Catal., **95**, 202 (1985).
8. Janz, G. J., *Molten Salts Handbook*, Academic Press, New York (1969).
9. Inman, D., and Lovering, D. G., in Conway, B. E., Bockis, J. O. M., Yeager, E., Khan, S. U. M., and White, R. E., *Comprehensive Treatise of Electrochemistry*, Vol. 7., Plenum Press, New York (1983).
10. Datta, R., and Eyman, D. P., U.S. Patent No. 4,898,845, February 6 (1990).

Anode	Cathode	Electrolyte	Temperature (°C)	Current Density (mA/cm^2)	Voltage (V)	Current Efficiency (%)	Selectivity (%)
Type A	Type A	CuCl-KCl	180	0.05	0.15	45	65
Type A	Type D	Nafion 1*	180	1.0	0.25	82	75
Type A	Type D	Nafion 2$^{\$}$	180	1.3	0.27	47	41
Type B	Type D	Nafion 1*	90	3.5	0.53	87	83
Type C	Type D	Nafion 1*	90	0.3	0.36	67	65
Type D	Type D	Nafion	70	1.6	0.45	81	72
Type D	Type B	Nafion 1*	90	0.9	0.46	73	70

* Nafion 1: Phosphoric acid contained between two Nafion membranes.

\$ Nafion 2: 5% Phosphoric acid fed along with ethanol to the anode.

Table 1: Results of Feasibility Study of Supported Molten-Salt Electrocatalysts.

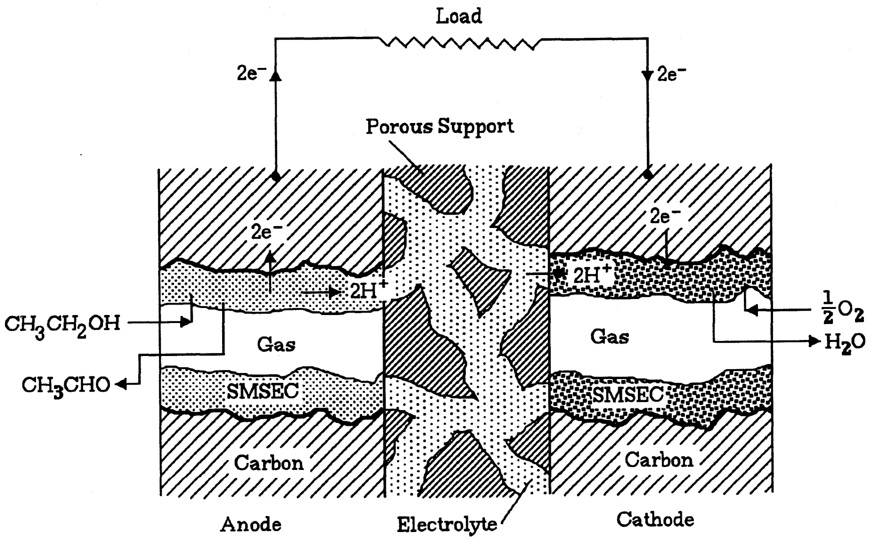

Figure 1: Schematic of SMSEC Fuel Cell for Co-Generation of Acetaldehyde and Electricity from Ethanol.

DOI: 10.1149/199413.0781PV

MECHANISM OF LOW-CO_2 PERFORMANCE OF THE MCFC CATHODE

Yong Hwan Kim and J. Robert Selman
Department of Chemical Engineering
Illinois Institute of Technology
Chicago, IL 60616

ABSTRACT

From data obtained on $3cm^2$ lab-scale Molten Carbonate Fuel Cells (MCFC) at low CO_2 partial pressure of the oxidant, is appears that cathode dissolution decreases and the cell life-time is increased. However, operating MCFCs at very low CO_2 partial pressure (below 0.05 atm) lowers the cell performance; the cell mechanism seems to be changed seriously and performance recovers extremely slowly after returning oxidant composition to normal CO_2 level. The effective cathode polarization for the low-CO_2 range is not fitted by available correlations based on rate control by O_2^- and CO_2 diffusion, and it is very high. These effects must be accounted for in the estimation of optimum CO_2 partial pressure for maximum cell life-time and cell performance, and the estimation of optimum electrolyte filling of the cathode.

Key words : cathode polarization, electrolyte filling, AC Impedance

INTRODUCTION

In the last stage before commercialization of the Molten Carbonate Fuel Cell(MCFC), some issues concerning cell life time such as cathode dissolution, separator plate corrosion, and electrolyte distribution must be satisfactorily resolved. The key to the improvement of long-term MCFC performance seems to be the mechanism of the electrochemical processes which cause the cell performance decay. A correlation of the time-to-short of MCFC cells presented by Kunz and Pandolfo(1) suggests that cell operation at low CO_2 partial pressure lowers cathode dissolution and, therefore, increase cell life-time. In a previous study(2), the effective cathode polarization was expressed as a simple correlation involving P_{O2}, P_{CO2} and cell temperature. In Lee and Selman's recent study(3), AC/DC Impedance characteristics of MCFC porous electrodes were analyzed to obtain kinetic and mass transfer information. A mechanism controlled by O_2^- and CO_2 was inferred. The overall objectives of the present study are: (a) to observe the cell performance at low CO_2 partial pressure of the oxidant, (b) to understand the relationship between cathode polarization of

MCFC electrodes and current density at low CO_2 partial pressure, (c) to understand the effect of electrolyte filling ratio on cell performance.

EXPERIMENTAL SET UP AND CELL COMPONENTS

The experimental instruments employed in this research included an EG&G Model 173 Potentiostat/Galvanostat with Model 176 compartment for IR compensation, an EG&G Model 273 Potentiostat/Galvanostat, an EG&G Model 175 Universal programmer, a Nicolet Model 206 Digital Oscilloscope, a Fisher Series 5000 recorder, a specially designed current interrupter with very short working time at speed of 2μs, Matheson 600 Series flowmeter, Omega Chromel-Alumel thermocouples, a Simpson digital D.C. millivoltmeter, a Newport digital D.C. milliammeter, and an EG&G Model 5208 Two-Phase Lock-In Analyzer.

3 cm^2 lab-scale MCFCs were assembled using the configuration which has been previously applied to the 3 cm^2 lab-scale cells at the Institute of Gas Technology(4), and employed for stationary polarization, AC Impedance, and potential relaxation measurements. The cell consisted of porous electrodes, electrolyte matrix, reference electrodes, and current collectors (Figure 1).

The composition of the oxidant gas supplied to the cathode was a mixture of 30 vol% of CO_2 and 70 vol% of air. Its flow rate was kept constant at 102 ml/min. The analyzed oxidant gas supplied to the cathode was saturated by passing it through a water container which was maintained at a temperature close to room temperature. The composition of the fuel gas supplied to the anode was 75 vol% of H_2 and 25 vol% of CO_2. Its flow rate was kept constant at 102 ml/min. The analyzed fuel gas fed to the anode was saturated by passing it through a water container which was maintained at a constant temperature of 60°C degrees. Flow rate and composition of the anode gas were always maintained at constant values for this research work. The reference gas was a dry mixture of 67 vol% CO_2 and 33 vol% O_2, and its composition was maintained constant during this research work. Its flow-rate was also maintained constant, at 10 ml/min.

The cell temperature was maintained at 650°C degrees, and the cell was usually loaded at 480 mA. The cell was observed by checking the daily performance corresponding to ordinary condition. This explained if the cell is running at steady state. The IR value was also measured using the current interruption method, and to ensure that its value did not vary.

All cell components were supplied by the Institute of Gas Technology. These components were assembled together in a high-purity alumina housing. Porous Ni-10% Cr was used as the anode electrode. Porous lithiated nickel oxide was used as the cathode. Gold wire was used for the reference electrodes. Novamet Ni on the anode side and SS 316 on the cathode side were used as current collectors. Molten carbonate (eutectic mixture of 62 mol% Li_2CO_3 and 38 mol% K_2CO_3) in a ceramic tile ($LiAl_2O_3$ matrix) was used as the electrolyte layer.

The electrolyte filling ratio (ratio of electrolyte volumes to the void volume of cathode and anode electrodes) was usually 25% at the start of a cell. Sometimes, a lower than 25% of electrolyte filling ratio of both electrodes was applied at the start and the value increased to more than 25% by adding electrolyte.

Cathode gas composition for this research work was varied from 0.9 atm to 0.02 atm of CO_2 and from 0.9 atm to 0.02 atm of O_2. Nitrogen gas was used for balancing all gases. Some experimental data were obtained at higher than standard temperature (698°C) and some at lower than standard temperature (608°C).

EXPERIMENTAL RESULTS AND DISCUSSION

1. Stationary polarization

The correlation between the cathode polarization and current density is linear at high CO_2 partial pressure (above 0.1 atm). As CO_2 partial pressure decreases, the relationship becomes non-linear (Figure 2). As Fig. 2 shows, at or below 0.02 atm CO_2 partial pressure, the polarization becomes very large, and cell performance extremely poor.

The correlation between the cathode polarization and current density is also linear at high O_2 partial pressure (above 0.1 atm). As in the case of CO_2, as O_2 partial pressure decreases, the relationship becomes non-linear. However, the effect of O_2 on the relationship between the cathode polarization and current density seems to be less significant than that of CO_2.

Cathode polarization is also affected by electrolyte filling. Minima in cathode polarization were observed in the range of 20% - 30% electrolyte filling ratio (Figure 3). As current density increases, the deviation from linearity becomes obvious. In the low range of current density, the correlation between cathode polarization and current density is clearly linear.

2. AC/DC Impedance

AC/DC impedance data were obtained under various conditions. At constant O_2 partial pressure (0.3 and 0.1 atm) of oxidant, a weak effect of CO_2 on the charge transfer resistance and a strong effect of CO_2 on the mass transfer resistance were observed. Two semi-circles (kinetic loop and diffusion loop) were clearly observed as the CO_2 concentration was decreased. At constant CO_2 partial pressure (0.3, 0.1, and 0.02 atm) of oxidant, strong effect of O_2 on mass transfer resistance were observed. Also, two distinct semi-circles (kinetic loop and diffusion loop) were observed at high O_2.

At very low CO_2 pressure (e.g. 0.02 atm), results under current load and under OCV were significantly different. Under these conditions, AC/DC Impedance data for different electrolyte filling ratios were also significantly different. The mechanism of oxygen reduction under low CO_2 conditions is changed by current load much more than under standard gas conditions. Therefore, kinetic information obtained from AC/DC impedance measurements at OCV may not be applicable to operation under load.

3. Potential relaxation

The potential relaxation upon switching the oxidant gas from one concentration to another was systematically measured at 650°C. The time required to reach steady state upon switching to lower CO_2 oxidant was longer than that to higher CO_2 oxidant. Especially, switching to 0.02 atm CO_2 oxidant showed significantly slower transition. Under load condition, steady state seemed to be reached within 1 hour after switching gas. However, cathode polarization still was increased significantly after about 2 hours (Figure 4). Cell performance hardly recovered, even if gas was switched to at, or above, normal CO_2 levels.

DISCUSSION AND CONCLUSION

Operating a MCFC using very-low-CO_2 oxidant lowers the cell performance drastically. The cell mechanism seems to be changed seriously and to be more complex than the mechanism at or above 0.1 atm of CO_2 partial pressure. The cell performance recovers extremely slowly after return to normal CO_2 levels (e.g. 0.147 atm). The effective cathode polarization for this low range of CO_2 was not predicted correctly by correlations such as those of Yuh (Figure 5).

The present study is helpful in estimating optimum CO_2 partial pressure for maximum cell life-time and cell performance. It is also relevant for the estimation of optimum electrolyte filling. Even though AC/DC Impedance has been considered a useful tool for electrochemical application, a more accurate technique and less external noise in AC Impedance measurements seems to be required to provide sufficiently accurate information for the kinetics and mass transfer resistance of the cell in the low-CO_2 range.

ACKNOWLEDGEMENTS

This work has been carried out at the Institute of Gas Technology. We acknowledge technical assistance of the staff at Institute of Gas Technology to obtain experimental evidence.

REFERENCES

1. H.R. Kunz and J.W. Pandolfo, J. Electrochem. Soc., 139, 1549 (1992)
2. a). C.Y. Yuh and J.R. Selman, J. Electrochem. Soc., 138, 3642 (1991)
   b). C.Y. Yuh and J.R. Selman, J. Electrochem. Soc., 138, 3649 (1991)
3. G.L. Lee, Ph.D. Dissertation, IIT, Chicago, IL (1992)
4. E.S. Argano and J. Levitan, J. Electrochem. Soc., 116, 153 (1969)

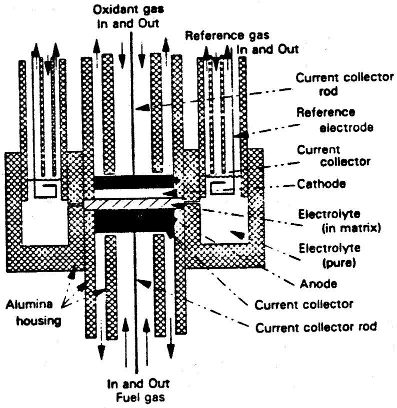

Fig. 1. Schematic of 3 cm^2 lab-scale cell

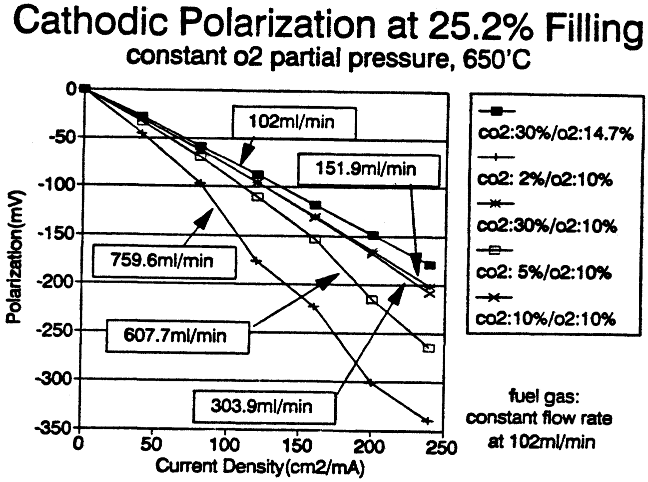

Fig. 2. Cathode polarization vs current density as CO_2 varies.

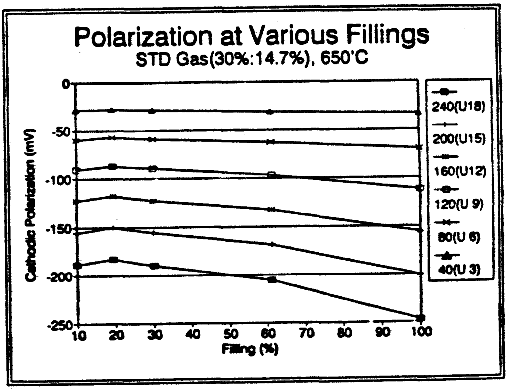

Fig. 3. Cathode polarization vs electrolyte filling (Symbols indicate current density in mA/cm^2. U indicates utilization of oxidant in %.)

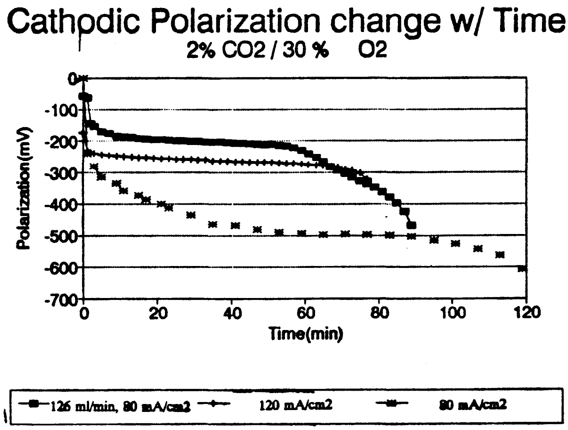

Fig. 4. Cathodic polarization vs time for very low CO_2 gas

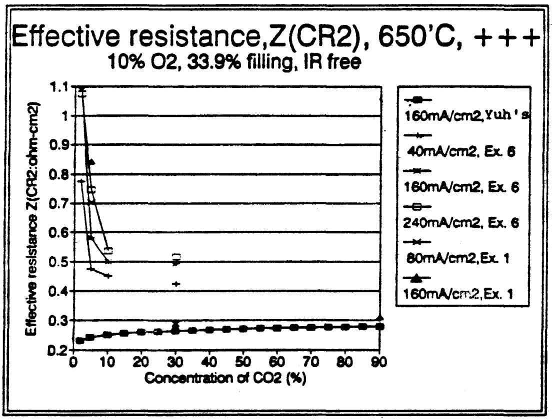

Fig. 5. Cathodic polarization from experimental data and Yuh's correlation

DOI: 10.1149/199413.0788PV

WATER EFFECT ON OXYGEN REDUCTION IN MOLTEN CARBONATES

Isamu Uchida, Tatsuo Nishina, Shinji Ohuchi, and Kohta Yamada
Department of Molecular Chemistry and Engineering, Faculty of Engineering, Tohoku University
Aramaki-Aoba, Aoba-Ku, Sendai 980, Japan

ABSTRACT

The effect of water on electrode kinetics and mechanism of the oxygen reduction at the fully immersed flag type Au electrode in (62+38)mol% (Li+K)CO_3 melt at 650°C have been investigated using cyclic voltammetry (CV), electrochemical impedance spectroscopy (EIS) and the digital simulation of the single scan voltammograms. The cyclic voltammograms of the oxygen reduction under P_{O_2}:P_{CO_2} = 0.9:0.1 atm with 2.9~15.4 mmHg H_2O vapor showed more reversible waves than that obtained under a dry atmosphere. The EIS spectra at the open circuit potential for the oxygen reduction also showed distinctly reduced impedance values by the presence of water. From the analysis of both data, it was found that the apparent mass transfer parameter $C\sqrt{D}$ was increased by the presence of water, indicating that water can act as an acid species in the neutralization reaction of the oxide ion according to the reaction $H_2O + O^{2-} \rightleftarrows 2OH^-$.

INTRODUCTION

The molten carbonate fuel cell (MCFC) is expected to be a one of the most promising power generation systems for the coming century due to the high energy conversion efficiency, the excellent characteristics to the environment and the ability to utilize a wide variety of fuels. In the MCFC power generation plant, CO_2 from the anode exhaust is recycled to the cathode gas inlet, and this may introduce certain amount of H_2O to the cathode gas stream.

The overall oxygen reduction in the carbonate melt is

$$\frac{1}{2}O_2 + CO_2 + 2e \rightarrow CO_3^{2-} \qquad [1]$$

For the past 20 years, many efforts have been made to elucidate the oxygen electrode reaction in molten alkali carbonates (1-19). Recently, Nishina *et al.* (12,13) have investigated the reaction order of the oxygen reduction with respect to the partial pressures of O_2 and

CO_2 using the Warburg coefficients. They concluded that the process proceeds via the mixed diffusion of superoxide ion O_2^- and CO_2 in Li/K carbonate melts at 888-1027K at the moderate O_2 and CO_2 partial pressures (0.9-0.1 atm):

$$\frac{3}{4}O_2 + \frac{1}{2}CO_3^{2-} \overset{K_1^{-1}}{\rightleftarrows} O_2^- + \frac{1}{2}CO_2 \qquad [2]$$

$$\left[O_2^-\right] = K_1 P_{O_2}^{0.75} P_{CO_2}^{-0.5} \qquad [3]$$

$$[CO_2] = K_h P_{CO_2} \qquad [4]$$

$$O_2^- + 3e \rightarrow 2O^{2-} \qquad [5]$$

$$O^{2-} + CO_2 \overset{K_d^{-1}}{\rightleftarrows} CO_3^{2-} \qquad [6]$$

where the recombination reaction [6] of the oxide ion with CO_2 is the reverse reaction of the dissociation reaction of carbonate ion CO_3^{2-}, which controls the acid–base property in molten salts of the Lux-Flood type, where the oxide ion acceptor CO_2 is an acid, and the oxide ion donor CO_3^{2-} is a base (20).

However, all the studies mentioned above were carried out under the dry atmospheres, and the effect of H_2O impurity on the electrode kinetics and mechanisms of the oxygen reduction have not been well understood despite of the probable existence of certain amount of H_2O impurity gas in the cathode gas stream. This paper reports the effect of H_2O in O_2+CO_2 mixed gases on the electrode kinetics and mechanisms of the oxygen reduction at gold electrodes.

EXPERIMENTAL

Figure 1 shows the schematics of the electrochemical cell assembly. An alumina crucible containing (62+38)mol% (Li+K)CO_3 was placed in the gas-tight quartz vessel. The working electrode was fully immersed flag type electrode of gold (0.39 cm^2). All the potentials were referred vs (0.33+0.67)atm (O_2+CO_2)/Au reference electrode which is denoted as (1:2 O_2/CO_2)/Au in this paper. The experimental temperature was fixed at 650°C.

The mixed gases of O_2:CO_2=9:1, 5:5, and 1:9 were supplied to the cell via a humidifier as shown in figure 2. The water vapor pressures applied in this work were 2.9, 6.2 and 15.4 mmHg. They were obtained by controlling the concentration of H_2SO_4 aqueous solution and the temperature of the humidifier (21,22). The electrode kinetic data were measured using cyclic voltammetry (CV), AC impedance (or electrochemical impedance spectroscopy (EIS). The experimental techniques, melt purification, apparatus and cell assembly were similar as described in a previous paper (6).

RESULTS AND DISCUSSION

Cyclic Voltammetry

Figure 3 shows the effect of water vapor pressures on single scan voltammograms for the oxygen reduction at P_{O_2}:P_{CO_2}=0.9:0.1 atm. The single peak which resembles the constant activity case (23) was observed. The peak potential E_p was independent of the scan rate up to 10 V/s, and the peak current density i_p was proportional to the square root of the scan rate as shown in figure 4, indicating that the reaction is reversible and diffusion controlled. The increase in the water vapor pressure appeared not only in increasing i_p but also in the peak shape which becomes sharper.

According to the voltammetric theory of the constant activity case for a single redox species (23), the following equations were derived.

$$i_p = 0.6105 \frac{n^{1.5}F^{1.5}}{R^{0.5}T^{0.5}} C_{ox}\sqrt{D_{ox}}\,\sqrt{v} \qquad [7]$$

$$|E_p - E_i| = 0.8540 \frac{RT}{nF} \qquad [8]$$

The equation [7] predicts that the slope of the ip–$\sqrt{v}$ plot is proportional to the apparent value $C_{app}\sqrt{D_{app}}$ of the electrochemically active species. Thus, the apparent electron number n_{app} transferred through the reaction and $C_{app}\sqrt{D_{app}}$ values were calculated and shown in table 1. The n_{app} increased with increasing water content, and the $C_{app}\sqrt{D_{app}}$ values, which were calculated using n_{app}, were decreased with increasing water content. This results is inconsistent because the peak current increased with increasing water content. This means that the equations [7] and [8] are not applicable directly to this case. As discussed later, in the "digital simulation of single scan voltammograms" section, the oxygen reduction path is complicated by "mixed" diffusion of O_2^- and CO_2.

Generally, the slope of the i_p–$\sqrt{v}$ plot is proportional to the apparent value $C_{app}\sqrt{D_{app}}$ of the electrochemically active species and this enables us to perform the reaction order analysis vs the water vapor pressure. Unfortunately, it is impossible to analyze the true reaction order on the water vapor pressure in this case because the n_{app} varies as discussed above. However, the slope $i_p/\sqrt{v}$ is an experimental parameter related to the mass transfer, and we tried to construct the reaction order plot as shown in figure 5. In this figure, we showed the similar reaction order plot using the Warburg coefficients obtained from the EIS data as discussed later. Two plots gives similar dependency on P_{H_2O}.

According to our earlier works (12,13), the oxygen reduction process in this melt proceeds via the mixed diffusion of superoxide ion O_2^- and CO_2 under the dry condition as follows:

$$O_2^- + 3e \rightarrow 2O^{2-} \qquad [5]$$

$$O^{2-} + CO_2 \overset{K_d^{-1}}{\rightleftarrows} CO_3^{2-} \qquad [6]$$

When P_{O_2}:P_{CO_2}=0.9:0.1 atm, CO_2 diffusion dominates the overall reaction process of the oxygen reduction, CO_2 being depleted in the electrode surface. If the water vapor exists in the cathode gas, it may act as an additional oxide ion acceptor (24):

$$O^{2-} + H_2O \rightleftarrows 2OH^- \qquad [9]$$

When reaction [9] is relatively fast than reaction [6], part of O^{2-} ion can be consumed by H_2O in a reaction layer adjacent to the electrode surface. The recovery of H_2O may occur outside the reaction layer according to reaction [10] as follows (20):

$$2OH^- + CO_2 \overset{K_H^{-1}}{\rightleftarrows} CO_3^{2-} + H_2O \qquad [10]$$

Thus, the apparent diffusion resistance of CO_2 can be decreased by coexistence of the additional acid-base reaction [9] and reaction [6].

In this context, the water effect may disappear if the CO_2 concentration in the melt is larger than the O_2^- concentration, *i.e.*, under high CO_2 partial pressures. To confirm this, we performed single scan voltammetric experiments as shown in figure 6 for P_{CO_2}=0.5 atm and figure 7 for P_{CO_2}=0.9 atm. Clearly, the water effect disappeared even when the 15.4 mmHg of the water vapor was introduced to the cathode gas of the P_{O_2}:P_{CO_2}=0.5:0.5 and 0.1:0.9 atm. Therefore, it can be concluded that the water impurity in the cathode gas stream of MCFC has no negative effect on the oxygen reduction kinetics.

Electrochemical Impedance Spectroscopy

Figure 8 shows the effect of water vapor pressure on the EIS data of oxygen reduction at the rest potential. The frequency range was 6 kHz to 1 Hz. The absence of a semicircular arc indicates a fast charge transfer process. These plots show linear behavior with a slope close to 45 degrees, indicating a mass transfer limited process, that is, the diffusion (Warburg) impedance prevails over the entire frequency range used in this study. Again, the diffusion impedances at lower frequency region were reduced with increasing water vapor pressure, which is similar to the CV behavior.

These EIS data were analyzed using the Randles–Ershler equivalent circuit shown in figure 8, where R_{ct} is the charge transfer resistance, C_d is the double layer capacitance, the R_Ω is the solution resistance and σ is the Warburg coefficient.

$$\sigma_{app} = \frac{RT}{n_{app}^2 F^2 \sqrt{2} C_{app} \sqrt{D_{app}}} \qquad [11]$$

These parameters were determined by the non-linear parameter fitting (Simplex method) over the whole frequency range. The results are listed in table 2. In this table, we neglected R_{ct} because it was such small that it was difficult to obtain its reliable values. Clearly, the σ values decreased with increasing water vapor pressure.

According to the theory of EIS (25), the apparent value of the Warburg coefficient σ_{app} for the reactions [5], [6] and [9] under the semi-infinite diffusion condition may be expressed as following:

$$\sigma_{app} = \frac{RT}{3^2 F^2 \sqrt{2} C_{O_2^-} \sqrt{D_{O_2^-}}} + \frac{RT}{1.5^2 F^2 \sqrt{2}} \left(\frac{1}{C_{CO_2}\sqrt{D_{CO_2}} + C_{H_2O}\sqrt{D_{H_2O}}} \right) \qquad [12]$$

In this equation, σ_{H_2O} and σ_{CO_2} are connected in parallel, because the water effect appears as an additional oxide ion acceptor according to the reaction scheme [5], [6] and [9]. Thus, it can be explained that the presence of water vapor in the cathode gas decreases the σ_{app} according to the equation [12]. In addition, this equation may be used to explain the water effect which disappears at high CO_2 concentration as shown in figures 6 and 7. In such the extreme case, we can assume that $C_{CO_2} \rangle\rangle C_{O_2^-}$ so that the second term of the right hand side of equation [12] is negligibly small compared to the first term, *i.e.*, only the O_2^- diffusion dominates the diffusion impedance.

Digital Simulation of Single Scan Voltammograms

To elucidate the above reaction schemes, the digital simulation of the single scan voltammograms was carried out. Since there are no data for the solubility and diffusivity of H_2O in molten carbonates, we applied the following simplified reaction scheme.

$$O_2^- + 3e \rightarrow 2O^{2-} \qquad [5]$$

$$O^{2-} + CO_2 \underset{k_b}{\overset{k_f}{\rightleftarrows}} CO_3^{2-} \qquad [6']$$

where

$$K_d = \frac{k_b}{k_f} \qquad [13]$$

According to the equation [12], the effect of water vapor in the cathode gas appears as an similar effect for increasing CO_2 concentration. Therefore, It may be possible to simulate the water effect using the reaction scheme [5] and [6'] with an increased CO_2 concentration, and the following simultaneous partial differential equations have been solved with the appropriate boundary conditions and initial conditions.

$$\frac{\partial C_{O_2^-}}{\partial t} = D_{O_2^-} \frac{\partial^2 C_{O_2^-}}{\partial x^2} \qquad [14]$$

$$\frac{\partial C_{O^{2-}}}{\partial t} = D_{O^{2-}} \frac{\partial^2 C_{O^{2-}}}{\partial x^2} - k_f C_{O^{2-}} C_{CO_2} + k_b C_{CO_3^{2-}} \qquad [15]$$

$$\frac{\partial C_{CO_2}}{\partial t} = D_{CO_2} \frac{\partial^2 C_{CO_2}}{\partial x^2} - k_f C_{O^{2-}} C_{CO_2} + k_b C_{CO_3^{2-}} \qquad [16]$$

where $C_{CO_3^{2-}}$ is constant ($C_{CO_3^{2-}} \gg C_{O_2^-}$, $C_{CO_3^{2-}} \gg C_{O^{2-}}$ and $C_{CO_3^{2-}} \gg C_{CO_2}$). To solve the above simultaneous partial differential equations, equations [14]-[16] were converted to the finite difference equations and then calculated numerically using the explicit calculation method (26). In the numerical calculation, we assumed the followings:

i) $D_{O_2^-} = D_{O^{2-}} = D_{CO_2} = D_{H_2O} = 7.8 \times 10^{-6}$ cm^2/s (27) to simplify the calculation according to the Feldbergh's notation (26),

ii) Reaction [5] (charge transfer process) is very rapid and reversible so that the Nernst equation for reaction [5] is always fulfilled.

The actual calculations were carried out for the following three cases.

Under Dry Pure O_2 Atmosphere In this procedure, we fitted the experimental single scan voltammograms with calculated one to obtain the $C_{O_2^-}$ and $C_{O^{2-}}$ as shown in figure 9 and to calculate K_d and K_1 values. In this case, we supplied pure oxygen gas to the cell, but small amount of CO_2 exists due to the decomposition of carbonate ion according to the reaction [6]. At first, we estimate the dissociation pressure of CO_2 from the equilibrium potential as $P_{CO_2}=0.0012$ atm and $P_{O_2}=0.9988$ atm. Since P_{CO_2} was very small, we can neglect the reaction [6'], and only the O_2^- and O^{2-} diffusions were considered with taking k_f and k_b as zero. Thus determined values were $C_{O_2^-} = C_{O^{2-}} = 1.9 \times 10^{-6}$ mol/cm^3, $K_d = P_{CO_2}C_{O^{2-}} / C_{CO_3^{2-}} = 1.1 \times 10^{-7}$ atm, and $K_1 = 6.6 \times 10^{-8}$ mol$\cdot$ cm$^{-3}\cdot$ atm$^{-0.25}$. These values were used in the following simulations.

Under Dry P_{O_2}:P_{CO_2}=0.9:0.1 Atm Using the above estimated values, the concentrations of diffusing species were calculated as $C_{O_2^-} = 1.93 \times 10^{-7}$ and $C_{O^{2-}} = 2.15 \times 10^{-8}$ mol/cm^3 respectively, and C_{CO_2} was calculated as $C_{CO_2} = 7.16 \times 10^{-7}$ mol/cm^3 by using the data from the literature (27) of the Henry's constant of CO_2 dissolution ($K_{h,\ CO_2} = 7.16 \times 10^{-6}$ mol$\cdot$ cm$^{-3}\cdot$ atm^{-1}). Then, the single scan voltammograms were simulated for the following three cases as shown in figure 10.

a) Assuming the polarographic case, only the reaction [5] was considered with taking $k_f = 0$ cm$^3\cdot$ mol$^{-1}\cdot$ s^{-1}.
b) Assuming the mixed diffusion of O_2^- and CO_2, the reaction [5] and [6'] were considered where k_f was the fitting parameter.
c) Assuming the constant activity case which corresponds to the direct reduction of O_2^- to CO_3^{2-}, *i.e.*, the case of $C_{CO_2} \rangle\rangle C_{O_2^-}$, only the diffusion of O_2^- was taken into account in the calculation.

As seen in the figure 10, the measured single scan voltammograms was well simulated only in case the mixed diffusion of O_2^- and CO_2 was assumed (case b) with taking $k_f = 10^{10}$ cm$^3\cdot$ mol$^{-1}\cdot$ s^{-1}, i.e., the reaction [6'] is very rapid. Some difference in peak current between the calculated value and the measured value is noted in the figure 10. Since there are some uncertainties in literature values, and also the diffusion coefficients of all species are assumed to be equal in this calculations, it is reasonable to conclude that the simulated single scan voltammograms agree well with the measured one.

Under P_{O_2}:P_{CO_2}=0.9:0.1 Atm With 15.4 mmHg H_2O Using the above estimated values, the single scan voltammograms with and without 15.4 mmHg H_2O were simulated as shown in figure 11, where C_{CO_2} was the fitting parameter in this case to examine the water effect and the Y axis was normalized by the peak current under the dry conditions. As shown in figure 11, the simulated voltammograms fit well with the measured one, indicating that the constant activity case could not be applied to the oxygen reduction at these conditions. The obtained values for C_{CO_2} were $C_{CO_2} = 7.16 \times 10^{-7}$ mol/cm^3 at dry condition under $P_{CO_2} = 0.1$ atm, and $C_{CO_2} = 3.5 \times 10^{-6}$ mol/cm^3 under 15.4 mmHg H_2O. It was found that $C_{CO_2,\ wet}/C_{CO_2,\ dry} \approx 5$, that is, the effective concentration of CO_2 increased by a factor of 5 in the presence of water (P_{H_2O}=15.4 mmHg). If we may assume the followings:

i) the water dissolves into the carbonate melt physically;
ii) the equation [12] can be applied;
iii) $D_{H_2O} = D_{O_2^-} = D_{O^{2-}} = D_{CO_2} = 7.8 \times 10^{-6}$ cm^2/s can be applied.

Then the Henry's coefficients for CO_2 and H_2O is estimated. The estimated values were $K_{h,\ CO_2} = 7.16 \times 10^{-6}$ mol· cm^{-3}· atm^{-1} and $K_{h,\ H_2O} = 1.37 \times 10^{-4}$ mol· cm^{-3}· atm^{-1}. Using these parameters, the σ_{app} values were calculated using the equation [12] and the results were shown in table 2. Although the calculated σ_{app} were a little bit smaller than that of the experimental values, the data showed fair agreement.

CONCLUSIONS

The effect of water on electrode kinetics and mechanisms of oxygen reduction at the fully immersed flag type Au electrode in (62+38)mol% $(Li+K)CO_3$ melt at 650°C have been investigated using cyclic voltammetry (CV), electrochemical impedance spectroscopy (EIS) and the digital simulation of the single scan voltammograms, and the following conclusions were obtained.

i) The presence of 2.9~15.4 mmHg H_2O vapor to the $P_{O_2}:P_{CO_2}$ = 0.9:0.1 atm gas lowered the apparent diffusion resistance of oxygen reduction.
ii) The apparent mass transfer parameters, $i_p/\sqrt{v}$ and $1/\sigma_{app} \propto C_{app}\sqrt{D_{app}}$, were increased by the presence of water, indicating that water can act as an acid species in the neutralization reaction of oxide ion, $H_2O + O^{2-} \rightleftarrows 2OH^-$.
iii) Single scan voltammograms of oxygen reduction in this melt was simulated using finite difference method with assuming the reaction path as the mixed diffusion of O_2^- and CO_2. Also the condition $D_{H_2O} = D_{O_2^-} = D_{O^{2-}} = D_{CO_2} = 7.8 \times 10^{-6}$ cm^2/s was assumed in the numerical calculations. The simulated voltammograms agreed well with the observed ones, and the following parameters were obtained with the above assumptions: $K_1 = 6.6 \times 10^{-8}$ mol· cm^{-3}· atm$^{-0.25}$, $K_d = P_{CO_2}C_{O^{2-}} / C_{CO_3^{2-}} = 1.1 \times 10^{-7}$ atm, $k_f = 10^{10}$ cm^3· mol^{-1}· s^{-1}, $K_{h,\ CO_2} = 7.16 \times 10^{-6}$ mol· cm^{-3}· atm^{-1} and $K_{h,\ H_2O} = 1.37 \times 10^{-4}$ mol· cm^{-3}· atm^{-1}.
iv) The water impurity in the cathode gas stream of MCFC has no negative effect on the oxygen reduction kinetics.

ACKNOWLEDGMENT

This work was supported by a Grant-in-Aid for Scientific Research of the Ministry of Education, Science, and Culture of Japan.

REFERENCES

1. A.J. Appleby and S.B. Nicholson, *J. Electroanal. Chem.*, **53**, 105(1974).
2. A.J. Appleby and S.B. Nicholson, *J. Electroanal. Chem.*, **83**, 309(1977).
3. A.J. Appleby and S.B. Nicholson, *J. Electroanal. Chem.*, **112**, 71(1980).
4. W.M. Vogel, S.W. Smith, and L.J. Bregoli, *J. Electrochem. Soc.*, **130**, 575(1983).
5. S.H. White and U.M. Twardoch, *Electrochim. Acta*, **27**, 1599(1982).
6. I. Uchida, T. Nishina, Y. Mugikura and K. Itaya, *J. Electroanal. Chem.*, **206**, 229(1986).
7. I. Uchida, Y. Mugikura, T. Nishina and K. Itaya, *J. Electroanal. Chem.*, **206**, 241(1986).
8. I. Uchida, T. Nishina, Y. Mugikura and K. Itaya, *J. Electroanal. Chem.*, **209**, 125(1986).
9. T. Nishina and I. Uchida, *Denki Kagaku*, **56**, 111(1988).
10. T. Nishina and I. Uchida, *Denki Kagaku*, **56**, 419(1988).
11. I. Uchida and T. Nishina, *Nippon Kagaku Kaishi*, **1988(8)**, 1297(1988).
12. T. Nishina and I. Uchida, *Proceedings of the 2nd symposium on Molten Carbonate Fuel Cell Technology*, **PV90-16**, The Electrochem. Soc., Pennington, 1990, p.438-453.
13. K. Yamada, T. Nishina and I. Uchida, *Proceedings of the 3rd symposium on Carbonate Fuel Cell Technology*, **PV93-3**, The Electrochem. Soc., Pennington, 1993, p.368-384.
14. M. Takahashi, *Extended Abstract of 21st Symposium on Molten Salt Chemistry*, Yamanashi, JAPAN, 1989, p.51.
15. G.B. Dunks and D. Stelman, *Inorg. Chem.*, **22**, 2168(1983).
16. D.A. Tryk and E.B. Yeager, *Proceedings of the Second Symposium on Molten Carbonate Fuel Cell Technology*, **PV90-16**, The Electrochemical Society, Inc., 1990, p.395-404.
17. S.H. Lu and J.R. Selman, *J. Electrochem. Soc.*, **137**, 1125(1990).
18. S.H. Lu and J.R. Selman, *J. Electroanal. Chem.*, **333**, 257(1992).

19. P. Tomczyk and L.K. Bieniasz, *J. Electroanal. Chem.*, **304**, 111(1991).

20. B.K. Andersen, *Doctorate Thesis*, Tech. Univ. of Denmark, Lyngby, Denmark, 1975.

21. F.C. Blake and C.H. Greenewalt, *International Critical Tables*, **Vol.3**, McGraw-Hill, New York, 1928, p.302.

22. J.H. Perry, *Chemical Engineers' Handbook*, McGraw-Hill, New York, 1963, p.3-65.

23. T. Berzins and P. Delahay, *J. Am. Chem. Soc.*, **75**, 555(1953).

24. J.R. Selman and H.C. Maru in G. Mamantov and J. Braunstein (Eds.), *Advances in Molten Salt Chemistry*, **Vol.4**, Plenum Press, New York, 1981, p.231-218.

25. M. Sluyters-Rehbach and J.H. Sluyters in A.J. Bard (Ed.), *Electroanalytical Chemistry*, **Vol.4**, Marcel Dekker, New York, 1970, p.16.

26. S.W. Feldberg in A.J. Bard (Ed.), *Electroanalytical Chemistry*, **Vol.3**, Macel Dekker, New York, 1969, p.199.

27. T. Nishina, Y. Masuda and I. Uchida, *Proceedings of the International Symposium on Molten Salt Chemistry and Technology*, **PV93-9**, The Electrochemical Society, Inc., 1993, p.424-435.

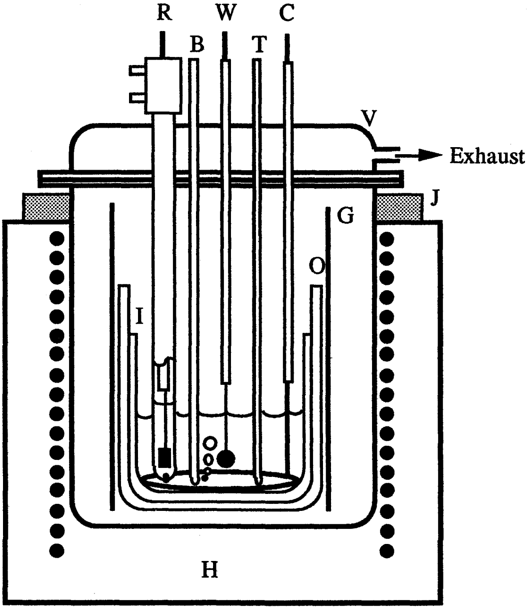

Figure 1 Schematics of the electrochemical cell assembly used in the experiment. R; reference electrode, W; working electrode, C; counter electrode, B; gas bubbler, T; thermocouple, V; quartz vessel and Pyrex™ top lid, J; cooling jacket, G; splash guard, O; outer alumina crucible, I; inner alumina crucible, H; electrical furnace.

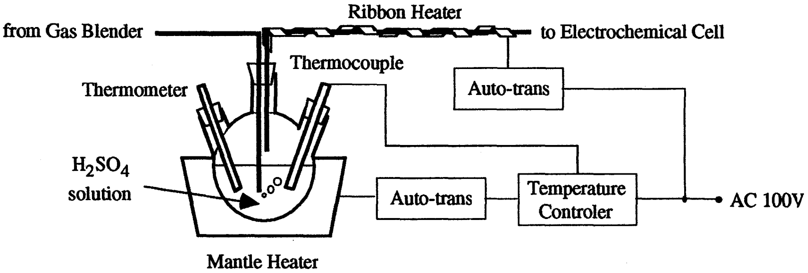

Figure 2 Schematics of gas humidifier.

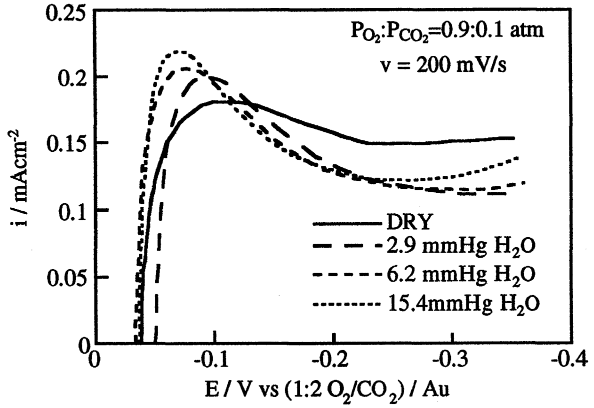

Figure 3 Single scan voltammograms of oxygen reduction as a function of water vapor pressures at a gold electrode in (62+38)mol% (Li+K)CO_3 melt at 650°C.

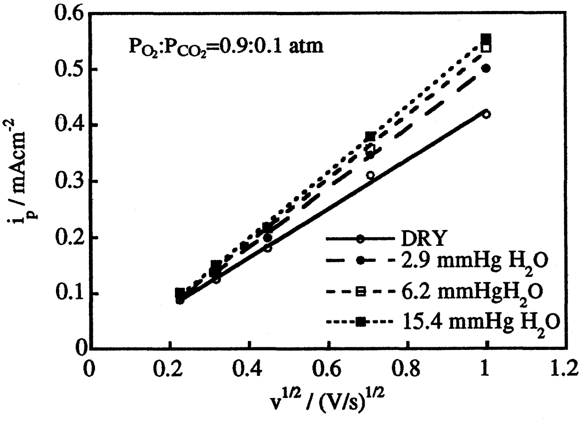

Figure 4 $i_p - \sqrt{v}$ plots obtained from the single scan voltammograms of oxygen reduction as a function of water vapor pressures at a gold electrode in (62+38)mol% (Li+K)CO_3 melt at 650°C.

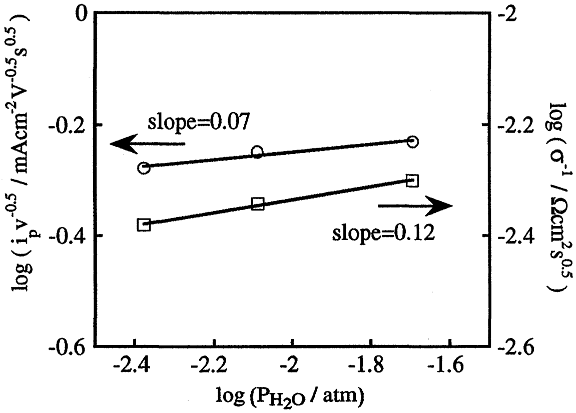

Figure 5 Reaction order plots of water vapor pressure to the slope of ip–√v plots (O) and the inverse of the Warburg coefficients (□) of oxygen reduction at a gold electrode under P_{O_2}:P_{CO_2} = 0.9:0.1 atm in (62+38)mol% (Li+K)CO_3 melt at 650°C.

Table 1 The effect of water vapor in the cathode gas stream to the kinetic parameters of oxygen reduction at a gold electrode under P_{O_2}:P_{CO_2} = 0.9:0.1 atm in (62+38)mol% (Li+K)CO_3 melt at 650°C obtained from the single scan voltammetry.

P_{H_2O} mmHg	n_{app}	$i_p / \sqrt{v}$ $mA\cdot cm^{-2}\cdot V^{-0.5}\cdot s^{0.5}$	$C_{app}\sqrt{D_{app}}$ using n_{app} $mol\cdot cm^{-2}\cdot s^{-0.5}$
0	0.89	0.434	2.49×10^{-9}
2.9	1.57	0.526	1.27×10^{-9}
6.2	1.60	0.563	1.33×10^{-9}
15.4	2.00	0.587	9.94×10^{-10}

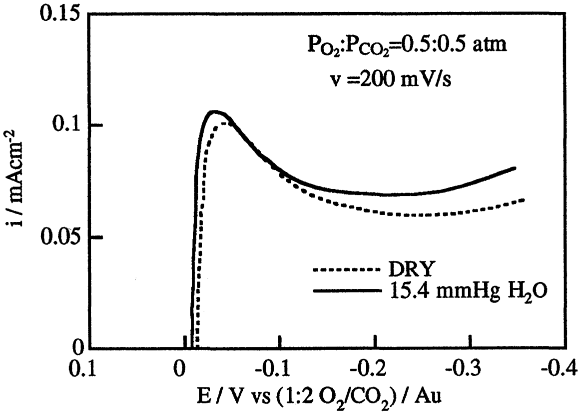

Figure 6 The effect of water vapor pressures at a low P_{O_2}/P_{CO_2} ratio (0.5/0.5) on cyclic voltammograms of oxygen reduction at a gold electrode in (62+38)mol% $(Li+K)CO_3$ melt at 650°C.

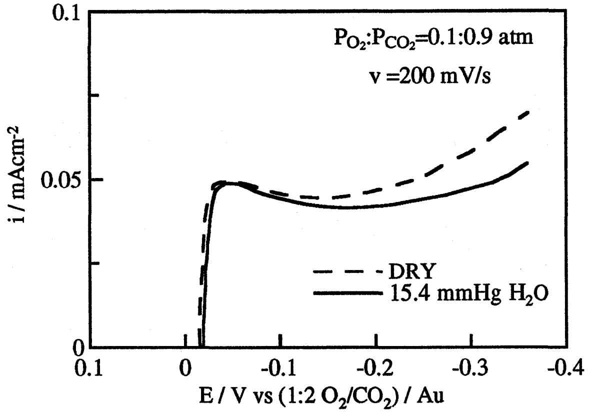

Figure 7 The effect of water vapor pressures at a low P_{O_2}/P_{CO_2} ratio (0.1/0.9) on cyclic voltammograms of oxygen reduction at a gold electrode in (62+38)mol% $(Li+K)CO_3$ melt at 650°C.

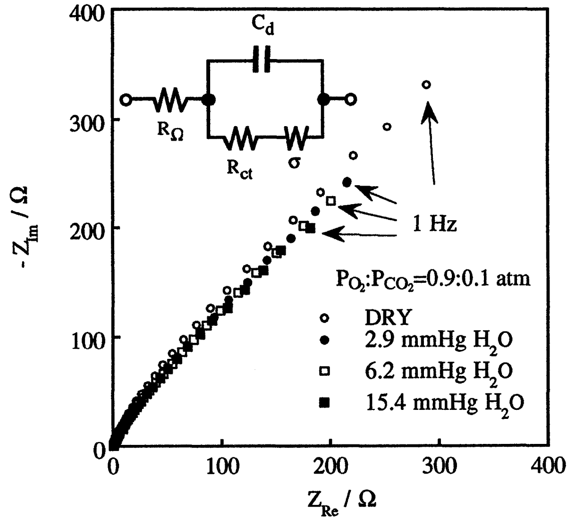

Figure 8 The EIS spectra (6kHz – 1Hz) at an open-circuit potential of oxygen electrode reaction at an gold electrode as a function of water vapor pressures in (62+38)mol% $(Li+K)CO_3$ melt at 650°C.

Table 2 The effect of water vapor in the cathode gas stream to the kinetic parameters of oxygen reduction at a gold electrode under P_{O_2}:P_{CO_2} = 0.9:0.1 atm in (62+38)mol% $(Li+K)CO_3$ melt at 650°C obtained from the EIS analysis.

P_{H_2O} mmHg	Experimental σ_{app} $\Omega\cdot cm^2\cdot s^{0.5}$	Calculated σ_{app}[a)] $\Omega\cdot cm^2\cdot s^{0.5}$	C_d $\mu F\cdot cm^{-2}$
0	330	250	96
2.9	230	195	111
6.2	220	171	122
15.4	200	147	131

a) these values were calculated with equation [12] using the parameters obtained by the digital simulation of the single scan voltammograms.

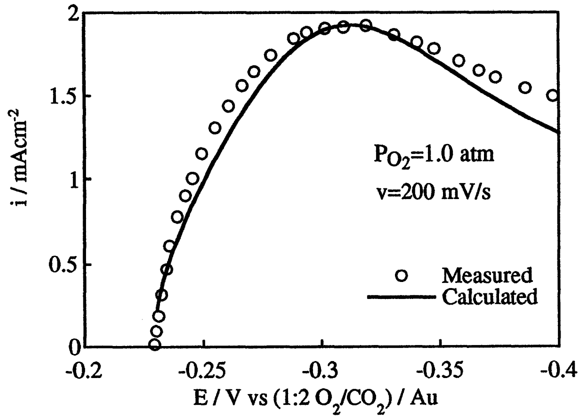

Figure 9 Simulated single scan voltammograms of the oxygen reduction at a gold electrode under pure oxygen atmosphere without water traces at 650°C.

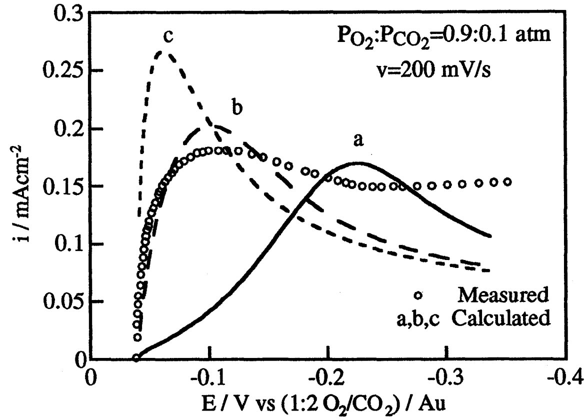

Figure 10 Simulated single scan voltammograms of the oxygen reduction at a gold electrode under P_{O_2}:P_{CO_2} = 0.9:0.1 atm without water traces at 650°C.

a) Polarographic case

b) Mixed diffusion of O_2^- and CO_2 case

c) Constant activity case

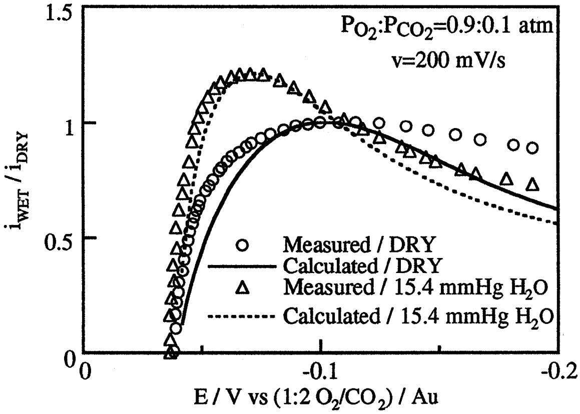

Figure 11 Simulated single scan voltammograms of the oxygen reduction at a gold electrode under $P_{O_2}:P_{CO_2}$ = 0.9:0.1 atm with and without 15.4 mmHg H_2O at 650°C. Y axis was normalized by the peak current of the dry condition.

DOI: 10.1149/199413.0805PV

THERMAL ASYMMETRY IN HIGH TEMPERATURE CELLS.

Brian Cleaver and Viktor S. Sharivker

Chemistry Department
The University
Southampton SO9 5NH, UK.

ABSTRACT

The sodium - nickel chloride battery (the ZEBRA cell) contains ß"-alumina as solid electrolyte. When the cell is charged or discharged, heat is absorbed or released; some of the heat comes from dissipative effects such as Joule heating and electrode irreversibility, and some from the reversible reactions at the electrodes. If these effects are non-uniform within the cell, thermal stresses could be produced in the electrolyte. In this paper we apply irreversible thermodynamics to quantify these effects.

INTRODUCTION

The term 'ZEBRA cell' covers a family of high temperature electrochemical cells in which one electrode is liquid sodium, the electrolyte is ß"-alumina and the other electrode is a transition metal chloride suspended in molten sodium tetrachloroaluminate, $NaAlCl_4$ (1,2). Such cells are serious contenders for applications such as vehicle traction (2). Favoured versions of the cell are those containing $NiCl_2$ or $FeCl_2$ as the metal chloride (3). The former version is considered in this paper:

$$\mathrm{Na(liq)} \mid \beta''\text{-alumina} \mid \mathrm{NaAlCl_4(liq),\ NiCl_2(s),\ Ni(s)}.$$

The cell discharge reaction is

$$\mathrm{2Na(liq) + NiCl_2(s) \rightarrow 2NaCl(s) + Ni(s)}. \qquad [1]$$

In considering thermal effects which accompany charging and discharging of the cell, we have to distinguish between dissipative and reversible effects. The dissipative effects include Joule heating and heating arising from overpotentials at the electrodes, both of which would cause heat evolution in the cell both on charge and on discharge. The magnitude of these effects depends on the design of the cell and also on the current density; for a given charge passed, they fall to zero as the current density is reduced. In contrast, the reversible heat changes sign with the direction of current flow; it is equal to $-T\Delta S$, where ΔS is the entropy change for the cell reaction. The reversible heat depends on the total charge passed, and not on the current density. ΔS can be found by measuring the ocv, E, of the cell as a function of temperature; it is easily shown that $-T\Delta S = T(d\Delta G/dT) = -nFT(dE/dT)$.

In batteries made from cells containing the solid electrolyte ß"-alumina, fracture of the electrolyte would result in mixing of the anode and cathode materials, i.e. cell failure. One possible cause of electrolyte breakage is thermal stress, arising from generation or absorption of different amounts of heat in different parts of the cell. A knowledge of ΔS is not enough to allow this effect to be investigated; we also need to know the Peltier heat involved in each electrode reaction. It is possible to derive this information by measuring Seebeck coefficients in cells with two electrodes of the same kind, between which a temperature difference is established. These measurements are outlined in the next Section.

THEORY.

Consider a system in which there are two forces, X_1 and X_2, with conjugate fluxes J_1 and J_2. The thermodynamic equations of motion are (4):

$$J_1 = L_{11}X_1 + L_{12}X_2 \qquad [2]$$

$$J_2 = L_{21}X_1 + L_{22}X_2, \qquad [3]$$

where $L_{12} = L_{21}$ by the Onsager reciprocal relation.
If the forces are those arising from gradients in temperature, T, and electric potential, ϕ, then

$$X_1 = -\text{grad} (\ln T) \qquad [4]$$

and

$$X_2 = -F \text{ grad } \phi \qquad [5]$$

J_1 and J_2 are then the heat flux, J_q, and the current density I, so equations [2] and [3] become:

$$J_q = -L_{11} \text{ grad } (\ln T) - L_{12} F \text{ grad } \phi \qquad [6]$$

and

$$I = -L_{21} \text{ grad } (\ln T) - L_{22} F \text{ grad } \phi \qquad [7].$$

These equations will now be applied to a cell of the type

$$\underset{T}{\text{Na(liq)}} \mid \text{ß"-alumina} \mid \underset{T + \Delta T}{\text{Na(liq)}}$$

The Peltier heat, π_T, is defined as the heat transferred from the left to the right electrode by passage of one faraday of charge in the same direction at constant temperature. Using [6] and [7],

$$\pi_T = (J_q/I)_{\Delta T=0} = (L_{12}/L_{22}) = (L_{21}/L_{22}) \qquad [8].$$

The Seebeck coefficient is defined as the potential difference between the two sodium reservoirs of the above cell per unit difference in temperature when the current is zero, i.e. $(\text{grad } \phi / \text{ grad } T)_{I=0}$. Since grad (ln T) = (grad T)/T, application of [7] gives for the Seebeck coefficient:

$$\begin{aligned}(\text{grad } \phi/\text{grad } T)_{I=0} &= -L_{21}/(L_{22}FT) \\ &= -L_{12}/(L_{22}FT) \\ &= -\pi_T/FT \qquad [9].\end{aligned}$$

[9] can now be used to calculate the Peltier heat from a measured value of the Seebeck coefficient.

EXPERIMENTAL

Reversible heat.

A ZEBRA cell of 30 Ah nameplate capacity was placed in a tube furnace and brought to 20 Ah discharge. The ocv of the cell was measured between 250°C and 315°C. The results are displayed in Figure 1. The value of dE/dT was found to be -0.221 mV K^{-1}, from which we conclude that the reversible heat, $-T\Delta S$, released in the cell on passage of two faradays of charge is 23.6 kJ (equivalent to 13.2 kJ for the 30 Ah cell).

Seebeck coefficients and Peltier heats.

Seebeck coefficients have been measured for the cells

$$\text{Na(liq)} \mid \beta''\text{-alumina} \mid \text{Na(liq)}, \qquad \text{and}$$

$$\text{Ni, NiCl}_2\text{, NaAlCl}_4\text{(liq)} \mid \beta'' \mid \text{Ni, NiCl}_2\text{, NaAlCl}_4\text{(liq)}.$$

Figure 2 shows the construction of the first of these cells. Liquid sodium was contained in two small alumina crucibles, with a bridge of ß"-alumina between them. One electrode was fitted with a small nichrome heater, wound directly onto the outside of the crucible. Dipping into each sodium pool was a stainless-steel sheathed, type K thermocouple. The sheaths were used to measure the potential difference between the sodium pools, and the temperatures were measured by recording the emf from each thermocouple. The entire cell was mounted inside a Pyrex jacket, sealed to the atmosphere and filled with dry nitrogen, and place inside a tube furnace. The second cell was of similar construction, except that the sodium was replaced by a mixture of nickel powder, nickel chloride and sodium tetrachloraluminate.

RESULTS

Figure 3 shows the combined results for the two cells, at 280°C (553 K). In both cases, two heating and two cooling cycles were made. It is seen that the Seebeck coefficients for the two cells have opposite signs. The coefficients are: for the sodium cell, +0.220 mV K^{-1}; for the nickel - nickel chloride cell, -0.443 mV K^{-1}.

Applying [9], we find that the Peltier heats for the two cells are -13.2 kJ and +26.5 kJ, referring to the passage of 30 Ah of charge. The sum of these figures, +13.3 kJ, is in satisfactory agreement with the value for the reversible heat (13.2 kJ) for the 30 Ah ZEBRA cell quoted above.

CONCLUSIONS

It is clear that the value of the reversible heat alone gives no clue as to the considerable asymmetry of the reversible heat effect in this cell. In fact, when the cell is discharged, heat is absorbed in the sodium electrode and the heat liberated in the nickel chloride electrode is equal approximately to twice the reversible heat for the cell as a whole. The effect of this asymmetry is likely to be accentuated by the superposition of the dissipative heat effects mentioned in the introduction. If the cell impedance is 20 mΩ, the total heat dissipated during passage of 30 Ah of charge is 2.2 kJ at 1A, 10.8 kJ at 5A, 21.6 kJ at 10A and 64.8 kJ at 30A. Most of this heat is likely to be evolved in the ß"-alumina electrolyte and the nickel chloride electrode, since there is relatively little resistance associated with the liquid sodium electrode. Thus, substantial amounts of heat would have to pass from the nickel chloride electrode to the sodium electrode, by conduction through the solid electrolyte, to maintain constant temperature within the cell. In extreme cases this heat flux, and the associated temperature gradient, could give rise to significant thermal stresses. Stresses would be greatest upon discharge, at a given current density; upon charge, the reversible heat and the Peltier heats change sign, but the dissipative heat is still generated mainly in the solid electrolyte and the nickel chloride electrode, so that the Peltier heat removed from the nickel chloride is compensated by the dissipative heat liberated in the same part of the cell.

If details of the cell dimensions are available, it would be possible to derive temperature distributions and stress values for cells under working conditions (5). It must be emphasised that endurance trials with the above 30 Ah cells have now entered their fourth year, and that very few cell failures have occurred, none of which are attributable to thermal stress in the electrolyte (6). However, this is a matter of which the designer should be aware.

ACKNOWLEDGMENTS

We are grateful to Beta Research and Development, Derby, England for supplies of cells, ß"- alumina, and to The Royal Society, London, for a Visiting Fellowship for V.S.S.

REFERENCES

1. J. Coetzer, J. Power Sources, **18**, 377 (1986).

2. A.R. Tilley and R.J. Wedlake, Electric Vehicle Developments, **6**, 119 (1987).

3. R.J. Bones, J. Coetzer, R.C. Galloway and D.A. Teagle, J. Electrochem. Soc., **134**, 2379 (1987).

4. K.S. Forland, T. Forland and S.K. Ratkje, *Irreversible Thermodynamics: Theory and Applications*, John Wiley & Sons, Chichester (1988).

5. Y. Ito, H. Hayashi, N. Hayafuji and S. Yoshizawa, Electrochim. Acta, **30**, 701 (1985).

6. Personal communication, Dr. R. Galloway, Beta Research and Development, Sinfin, Derby, UK.

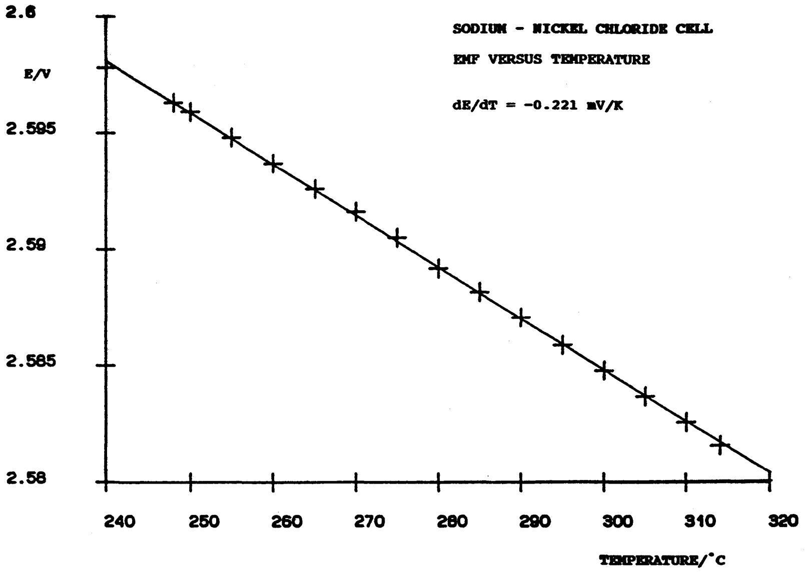

FIGURE 1: plot of emf versus temperature for a sodium - nickel chloride cell on open circuit.

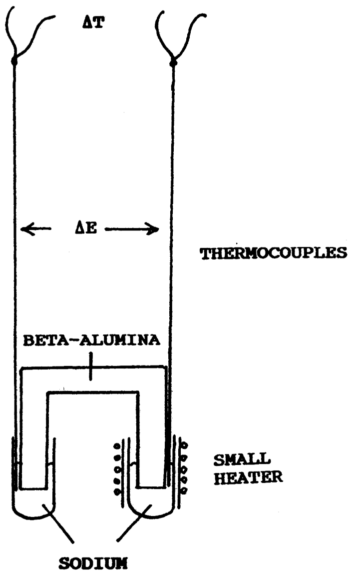

FIGURE 2: diagram showing construction of the cell used for Seebeck coefficient measurement.

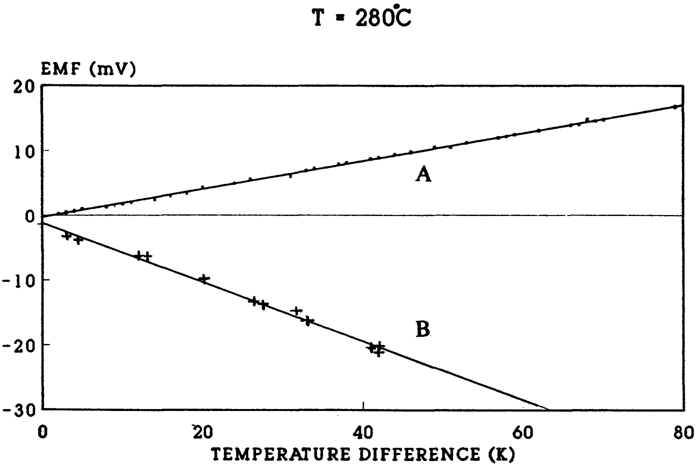

FIGURE 3: Seebeck effect measurements for symmetrical thermocells; A, Na | ß"-alumina | Na; B, Ni. $NiCl_2$, $NaAlCl_4$ | ß"-alumina | $NaAlCl_4$, $NiCl_2$, Ni.

DOI: 10.1149/199413.0812PV

AN INTERPRETATION OF THE ASYMMETRIC POLARIZATION AT THE β-ALUMINA/LIQUID ELECTROLYTE INTERFACE

Akira Katagiri

Chemistry Laboratory, Faculty of Integrated Human
Studies, Kyoto University, Sakyo-ku, Kyoto 606,
JAPAN

ABSTRACT

Asymmetric polarization at the sodium β-alumina/liquid electrolyte interface is interpreted by the assumed existence of a surface layer in which the transference number of Na^+ ion is less than unity. When a current flows in the direction from the liquid electrolyte to β-alumina, the Na^+ concentration in the layer decreases with time, and polarization increases. When a current flows in the opposite direction, the reverse situation occurs. A model calculation is presented using diffusion-migration equations of ions in the surface layer.

INTRODUCTION

Sodium β- and β"-aluminas are good sodium ion conductors which can be used as a separator in energy storage batteries (1,2) and for other applications. Although the bulk conductivities of these materials are sufficiently large, occurrence of significant resistance has been reported in some cases. Thus, Breiter et al.(3) and Demott (4) have observed an asymmetric polarization at the sodium /β"-alumina interface. Formation of a thin passivating film of Na_2O has been suggested(3).

Voinov and Tannenberger (5) and Farrington (6) have observed non-ohmic resistance at the β-alumina/ propylene carbonate interface. The interfacial resistance increases when Na^+ ions enter β-alumina from the propylene carbonate solution. Influence of adsorbed water has been discussed. Non-ohmic resistance has also been encountered sometimes in Na/ β"-alumina/molten chloroaluminate cells. A previous study (7) has shown that the polarization arises mainly at the β"-alumina/molten salt interface. In order to eliminate such resistance, it is important to reveal the mechanism of polarization. The present paper describes the characteristics of polarization and presents a model and interpretation of the phenomena.

POLARIZATION AT THE β-ALUMINA/MOLTEN SALT INTERFACE

Figure 1, which is reproduced from the previous report (7), shows the polarization observed at the interface between β-alumina and slightly acidic $AlCl_3$/NaCl melt. Current was passed through the cell, Na/β"-alumina disk/molten salt/tungsten current collector. The ordinate of Fig. 1 represents the potential difference between two aluminum electrodes (aluminum wire in $AlCl_3$-$NaCl_{sat}$), one placed in the molten salt side of the β"-alumina disk, the other placed in the outer $AlCl_3$-$NaCl_{sat}$ bath which was in contact with the peripheral area of the β"-alumina disk. When the current was forced to flow in the direction from β"-alumina to molten salt,* polarization decreased with time. When the direction of current was reversed,** the polarization increased. It is noticeable that the polarization vanished almost instantaneously when the current was interrupted. The polarization is essentially resistive, although it is not ohmic.

Figure 2 shows polarization characteristics at the β"-alumina/$AlCl_3$-NaCl (51.0-49.0 m/o) interface after the passage of current (10 mA, 1 hr) in the direction from the molten salt to β"-alumina. The polarization is larger when Na^+ ions flow from molten salt into β"-alumina.

MODELING OF THE POLARIZATION

The transient behavior (Fig. 1) suggests that the polarization is not due to a simple charge transfer resistance as observed at a metal/electrolyte interface. It is not a kind of concentration polarization, either, because no gradual change of potential is observed on the interruption of current. Farrington (6) has considered the adsorbed H_2O and exchanged H_3O^+ as the cause of polarization. However, H_2O may not be stable in chloroaluminate melts at 200°C. Vallet and Braunstein (8) have discussed the concentration gradient in molten salts which is induced by high current density. When their treatment is applied to the present case, the magnitude of predicted polarization is much smaller than the observed one.

It is rather probable that a surface region of β-alumina reacts with moisture, forming a partially blocking layer. It is posssible that the Na^+ ion transfer is hindered and other ions have finite mobility in that surface layer. Then non-ohmic polarization can arise due to the accumulation or depletion of ions. For example, assume that the surface layer contains A^- ions which have finite mobility (Fig. 3). When a current is applied in the direction from β-alumina to the liquid electrolyte, the Na^+ ion concentration in the surface layer increases with time, and therefore the polarization decreases, because the transference number of Na^+ is less than unity in the surface layer.

When an ionic species i moves in a surface layer of thickness d under potential and concentration gradients, the flux j_i of species i can be expressed as (9)

---

*The current is designated as 'anodic current.'

**The current is designated as 'cathodic current.'

$$j_i = -z_i u_i F c_i \, \partial\phi/\partial x - D_i \partial c_i/\partial x \tag{1}$$

where c_i, u_i, and D_i are the concentration, mobility, and diffusion coefficient of species i, respectively, ϕ is the electric potential, F is Faraday's constant, and x is the distance from the boundary between the β-alumina and the surface layer. As an approximation, the electroneutrality condition can be applied:

$$\sum_j z_j c_j + c_0 = 0 \tag{2}$$

where c_0 is the net charge density of fixed ions composing the surface layer. The current density is related to the total flow of charge as

$$\begin{aligned} i &= F\sum_j z_j j_j \\ &= -F^2\Big(\sum_j z_j^2 u_j c_j\Big)\partial\phi/\partial x - F\sum_j z_j D_j \partial c_j/\partial x \end{aligned} \tag{3}$$

Under a constant current condition, it is convenient to use i as a parameter. Rearranging Eq. 3 yields

$$\partial\phi/\partial x = -i\Big(F^2\sum_j z_j^2 u_j c_j\Big)^{-1} - \Big(F\sum_j z_j^2 u_j c_j\Big)^{-1}\sum_j (z_j D_j \partial c_j/\partial x) \tag{4}$$

Substitution of Eq. 4 for $\partial\phi/\partial x$ in Eq. 1 gives

$$j_i = \frac{z_i u_i c_i}{F\Big(\sum\limits_j z_j^2 u_j c_j\Big)} i + \frac{z_i u_i c_i}{\sum\limits_j z_j^2 u_j c_j} \sum_j \Big(z_j D_j \frac{\partial c_j}{\partial x}\Big) - D_i \frac{\partial c_i}{\partial x} \tag{5}$$

Introducing the transference number t_i of species i

$$t_i = z_i^2 u_i c_i / \sum_j z_j^2 u_j c_j \tag{6}$$

into Eq. 5 yields

$$j_i = t_i i / z_i F + (t_i/z_i)\sum_j z_j D_j \partial c_j/\partial x - D_i \partial c_i/\partial x \tag{7}$$

The rate of change of concentration c_i is obtained from mass balance of species i:

$$\begin{aligned} \partial c_i/\partial t &= -\partial j_i/\partial x \\ &= -(i/z_i F)\partial t_i/\partial x - (1/z_i)(\partial/\partial x)\Big(t_i \sum_j z_j D_j \partial c_j/\partial x\Big) + D_i \partial^2 c_i/\partial x^2 \end{aligned} \tag{8}$$

If appropriate initial and boundary conditions are given, Eqs. 2, 6, and 8 determine concentration distributions of all species, and then integration of Eq. 4 gives potential distribution in the surface layer.

The following is a model calculation in the case in which Na^+ ions and A^- ions (for example, Cl^-) are movable ions in the surface layer. In this case Eq. 2 becomes

$$c_{Na} - c_A + c_0 = 0 \qquad [9]$$

Since A^- ions can not enter the β-alumina, the flux of A^- at x=0 must be zero:

$$j_A = -z_A u_A F c_A \partial\Phi/\partial x - D_A \partial c_A/\partial x = 0 \quad \text{at } x = 0 \qquad [10]$$

Assuming a quasi-equilibrium at the interface between the liquid electrolyte and the outermost region of surface layer, concentrations c_{Na} and c_A are considered to be constant at x = d.

$$c_{Na} = c_{Na}^0 \quad \text{at } x = d \qquad [11]$$

$$c_A = c_A^0 \quad \text{at } x = d \qquad [12]$$

Equations 10-12 serve as boundary conditions. For numerical calculations it is convenient to use dimensionless variables and parameters:

$$X = x/d, \quad \Theta = D_{Na}t/d^2, \quad \Phi = F\phi/RT, \quad C_{Na} = c_{Na}/c_{Na}^0, \quad C_A = c_A/c_{Na}^0, \quad I = id/FD_{Na}c_{Na}^0 \qquad [13]$$

Finite difference method can be used for numerical solution of the partial differential equation Eq. 8.

EXAMPLE OF CALCULATION

A model calculation was performed for $c_0=0$ and $D_A/D_{Na}=0.5$. Figure 4 shows concentration profiles of Na^+ (A^-) ions in the surface layer at different times after applying a constant anodic current (I=2) and a constant cathodic current (I=-2). When the anodic current is applied, the concentration of Na^+ (A^-) ions near the interface X=0 increases with time. The opposite change occurs on applying the cathodic current. The current of I=-2 is the limiting current at which the concentration of C_{Na} (and therefore C_A) approaches zero at X=0. Figure 5 shows the variation of potential distribution in the surface layer. The decrease in potential gradient near X=0 on applying the anodic current reflects the accumulation of Na^+ (A^-) ions. On applying the anodic current, on the other hand, the potential gradient decreases with time according to the depletion of Na^+ (A^-) ions. Figure 6 shows the variation of potential drop $V=\Phi_{X=1}-\Phi_{X=0}$ across the whole thickness of surface layer on applying different currents. The magnitude of V decreases with time for an anodic current and increases with time for a cathodic current.

Such asymmetric behavior is in qualitative agreement with the observed polarization at β-alumina mentioned above.

For quantitative discussion, more information is necessary regarding the nature of the surface layer.

REFERENCES

1. J. L. Sudworth and A. R. Tilley, "The Sodium Sulfur Battery," Chapman and Hall (1985).
2. G. Mamantov, R. Marassi, M. Matsunaga, Y. Ogata, J. P. Wiaux, and E. J. Frazer, J. Electrochem. Soc., **127**, 2319 (1980).
3. M. W. Breiter, B. Dunn, R. W. Powers, Electrochim. Acta, **25**, 613 (1980).
4. D. S. Demott, J. Electrochem. Soc., **127**, 2312 (1980).
5. M. Voinov and H. Tannenberger, Electrochim. Acta **19**, 959 (1974).
6. G. C. Farrington, J. Electrochem. Soc., **123**, 591 (1976).
7. A. Katagiri, J. Hvistendahl, K. Shimakage, and G. Mamantov, J. Electrochem. Soc., **133**, 1281 (1986).
8. C. E. Vallet and J. Braunstein, J. Electrochem. Soc., **125**, 1193 (1978).
9. J. Newman, "Electrochemical Systems," 2nd Ed., Prentice Hall, Englewood Cliffs, NJ (1991).

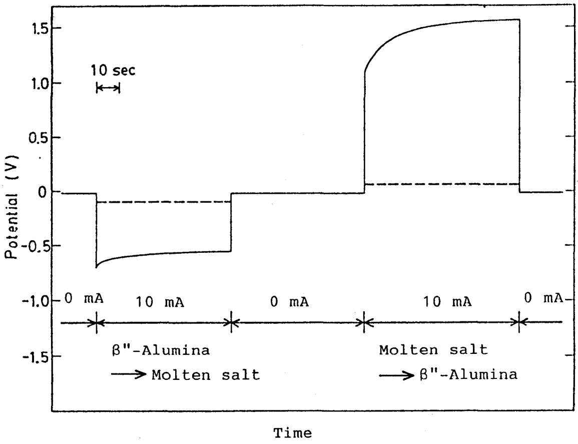

Fig. 1 Interfacial polarization at β"-alumina/$AlCl_3$-NaCl (51.9-48.1 m/o) melt (7).
Temperature, 200°C; thickness and effective area of the β"-alumina disk, 3 mm and 0.95 cm^2.

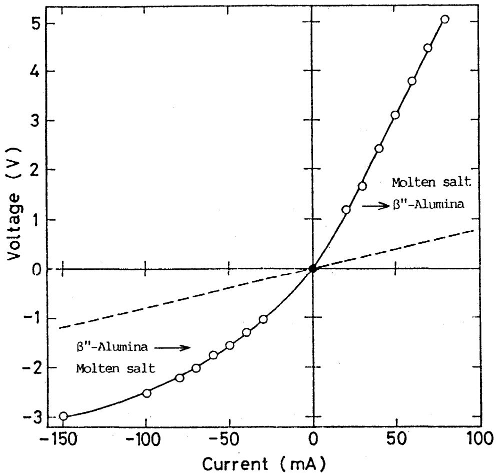

Fig. 2 Polarization curve obtained at the β"-alumina/ $AlCl_3$-NaCl(51.0-49.0 m/o) melt (7).
Temperature, 205°C.

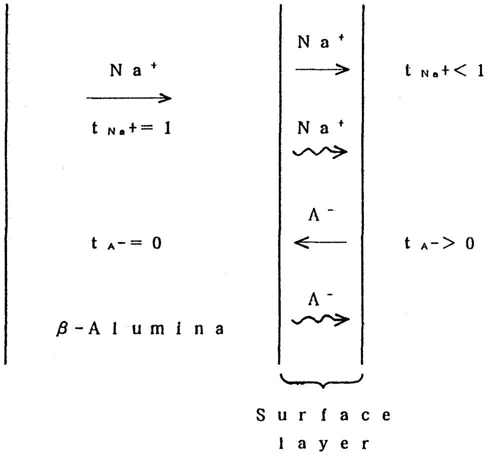

Fig. 3 A model of a surface layer in which A$^-$ ions have finite mobility; the transference number of Na$^+$ ions is less than unity.

⟶ indicates the direction of migration.
⇝ indicates the direction of diffusion.

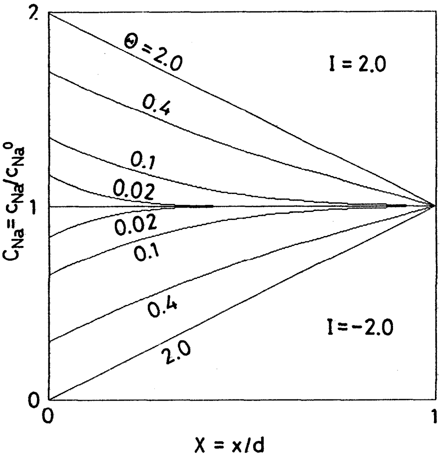

Fig. 4 Concentration profiles of Na$^+$ (A$^-$) in the surface layer.
$c_0/c_{Na}{}^0 = 0$; $D_A/D_{Na} = 1$; dimensionless current $I = id/FD_{Na}c_{Na}{}^0$; dimensionless time $\Theta = D_{Na}t/d^2$.

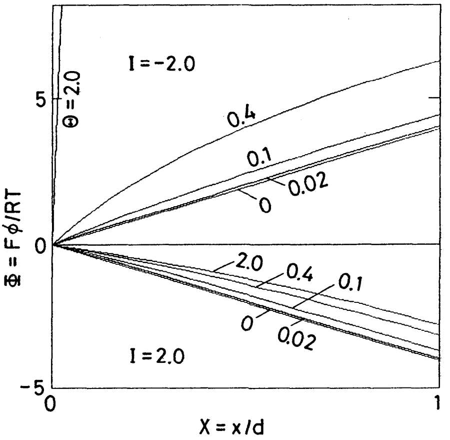

Fig. 5 Potential distributions in the surface layer. $c_0/c_{Na}^0 = 0$; $D_A/D_{Na} = 1$; dimensionless current $I = id/FD_{Na}c_{Na}^0$; dimensionless time $\Theta = D_{Na}t/d^2$.

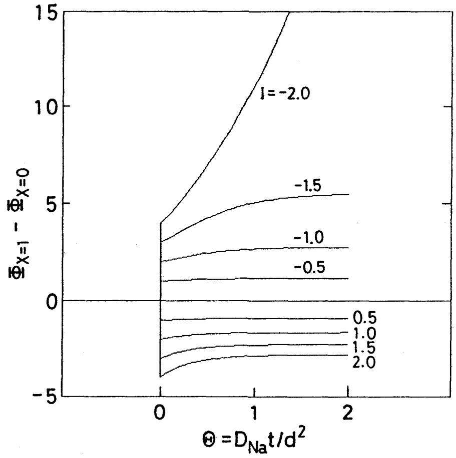

Fig. 6 Variation of potential difference $\Phi_{X=1} - \Phi_{X=0}$ on applying different currents. $c_0/c_{Na}^0 = 0$; $D_A/D_{Na} = 1$; dimensionless current $I = id/FD_{Na}c_{Na}^0$.

DOI: 10.1149/199413.0820PV

THE RELATIVE PERFORMANCE OF FeS_2 AND CoS_2 IN LONG-LIFE THERMAL-BATTERY APPLICATIONS

Ronald A. Guidotti and Frederick W. Reinhardt
Battery Development Department
Sandia National Laboratories
P.O. Box 5800
Albuquerque, NM 87185-0614

ABSTRACT

The relative performance of FeS_2 and CoS_2 was measured in single cells based on the LiBr-KBr-LiF eutectic electrolyte over a temperature range of 400° to 550°C using both standard (dry) and flooded anodes . This electrolyte is designed to be used in long-life (>1 h) thermal-battery applications because it has a lower melting point (313°C) and a higher electrical conductivity than the standard LiCl-KCl eutectic (m.p.=352°C). The cells were continuously pulsed for 1 ms every 10 ms from a background current density of 190 mA/sq cm to 1,130 mA/sq cm until end of life.

INTRODUCTION

The Li(Si)/FeS_2 electrochemical system has been used extensively by Sandia National Laboratories in the design of thermally activated ("thermal") batteries for nuclear-weapons applications. The batteries function only when the electrolyte becomes molten, which occurs at 352°C for the LiCl-KCl eutectic typically used. The first-generation thermal batteries utilized the Ca/$CaCrO_4$ couple. This system suffered from a number of shortcomings, however, such as lot-to-lot variability in Ca (1) or the cathode mixes (2,3) and liquid Ca-Li alloy formation which tended to result in shorting when not properly controlled. In contrast, the Li-alloy/FeS_2 couple has functioned quite well for almost all of its intended applications and, from a design perspective, is a much easier system to engineer than the Ca/$CaCrO_4$ system.

Thermal batteries utilize a molten salt immobilized in a MgO matrix as the separator between the Li-alloy anode and FeS_2 cathode. Normal operating temperatures for a thermal battery are generally between 550°C and the melting point of the electrolyte. By use of the LiBr-KBr-LiF eutectic, a much greater liquid range is possible. This makes this electrolyte ideally suited for thermal-battery applications where lifetimes in excess of one hour are needed.

The main limitation of the use of FeS_2 as the cathode in long-life thermal batteries is its thermal stability. The FeS_2 thermally decomposes to FeS and elemental sulfur vapor when held at temperatures above 550°C for prolonged periods. The evolved sulfur can then migrate to the anode and chemically react with it generating considerable heat which in turn causes even more thermal decomposition of the FeS_2.

In contrast, CoS_2 is much more thermally stable than FeS_2 and has excellent kinetics for high-temperature secondary-battery applications, as reported by researchers at Westinghouse (4,5). These results indicate that CoS_2 should perform equally as well in primary (thermal) batteries. The greater thermal stability of CoS_2 relative to FeS_2 makes this material attractive for long-life (>1 h) thermal batteries, as it allows a much higher initial temperature to be sustained without degradation of the cathode.

This report describes the relative electrochemical performance of Li(Si)/FeS_2 and Li(Si)/CoS_2 thermal cells under high-rate conditions when formulated with the low-melting LiBr-KBr-LiF eutectic, which was adapted at Sandia for thermal-battery applications (6). Single cells were discharged isothermally over a temperature range of 400° to 550°C using standard (dry or unflooded) Li(Si) anodes as well as flooded anodes--anodes containing free electrolyte.

The cells were subjected to a continuous cycle of pulsing during discharge. The performance parameters for characterization included the maximum time for sustaining the pulse current, the steady-state voltage prior to pulsing, the minimum voltage during pulsing, and the polarization (voltage loss) that occurred during pulsing.

EXPERIMENTAL PROCEDURES

Equipment

Li(Si)/FeS_2 and Li(Si)/CoS_2 single cells (3.2 cm dia.) were discharged between heated platens in a glove box under high-purity argon. The moisture and oxygen contents were maintained at <10 ppm each. An HP6060B programmable electronic load was used to step the background current from 1.5 A (~ 190 mA/sq cm) to 9 A (~1,130 mA/sq cm) during a 1 ms pulse. A duty cycle of 10% was used for pulsing, i.e., a pulse duration of 1 ms followed by 9 ms at the steady state or background current. The cell was subjected to this cycle continuously for five minutes until the cathode capacity was exhausted . The current through the cell and the voltage across the cell during the a pulse was periodically monitored during discharge using HP3458A high-speed DVMs. The experiment was under the control of a HP9000 Series 200 computer.

Materials and Processing

The catholytes contained 73.5% FeS_2 or CoS_2, 25% electrolyte-binder (EB) mix, and 1.5% Li_2O as a lithiation agent (in the case of FeS_2) or as a wetting agent (in the case of CoS_2). (Unless otherwise stated, all compositions are in weight percent.) The CoS_2 was obtained from Cerac (Milwaukee, WI) and was used as received after vacuum drying at 80° to 100°C overnight. The -325 mesh FeS_2 was obtained from American Mineral and was purified by leaching with 1:1 v/v HCl and then concentrated HF. After treatment, the nominal FeS_2 purity was 98.6% or better.

The catholyte mixes were fused under argon at 400°C for 16 hours and were then granulated and cold pressed into pellets using a graphite paper backing. The FeS_2-based cathode was 0.581 g and the CoS_2-based cathode was 0.636 g, so as to have comparable capacities.

The low-melting (313°C) LiBr-KBr-LiF eutectic electrolyte used in the EB was prepared by fusing the appropriate amounts of reagent-grade halides 57.33% LiBr, 42% KBr, and 0.67% LiF together in a fused-quartz crucible at 600°C for three hours in a dry room where the relative humidity was maintained at <3%. The EB used in the catholyte was also used as the separator for the cell. It was prepared by blending the electrolyte with 25% Maglite S MgO (Calgon, Pittsburgh, PA) that had been calcined at 600°C for four hours. The mixture was then fused at 400°C for 16 hours in a dry room. The calcined EB mix was then granulated and cold pressed into 0.38-mm thick separator pellets or blended into the catholyte mix.

The Li(Si) anode material was -100+325 mesh in size and contained 44% Li by weight. This material was cold pressed as is (0.3 g pellet) for unflooded anodes and 25% electrolyte was added before pressing for the flooded anodes (0.41 g pellet).

The single cells consisted of a separator pellet sandwiched between an anode and cathode pellet. The cells were assembled between 0.25 mm stainless steel current collectors and held together by stapling between two mica sheets.

RESULTS

Pulse Current

The CoS_2 was able to sustain the pulse current for a longer period of time relative to FeS_2. As shown in Figure 1 for a temperature of 400°C, a current density of 1,130 mA/sq cm was maintained for ~156 s for CoS_2 compared to only 78 s for FeS_2. (The run time has been corrected for the time required for data acquisition and data transfer.) At higher temperatures, this time increased to 234 s for both cathodes after which the peak current density dropped. The drop was greater for the FeS_2 cathode in all cases.

When flooded anodes were used, the pulse current density could be sustained for 234 s at 400°C for the CoS_2 cells. For the corresponding FeS_2 cells, the pulse current density could be sustained for about the same time as for cells with unflooded anodes (about 78 s). However, the relative rate of decrease in the maximum sustained pulse current density after 78 s was reduced.

Cell Resistance

The apparent cell resistance was determined by dividing the voltage drop by the current change during pulsing. It includes both ohmic as well as concentration polarization. The cell resistances at 400°C are compared in Figure 2 for unflooded anodes. The resistance did not increase very much with depth of discharge for the CoS_2 cells. In contrast, the cell resistance of the FeS_2 cells rose dramatically near the end of life. The same trends were observed at the higher temperatures, except that the absolute magnitude of the resistance was reduced. The use of flooded anodes reduced the differences in resistance between the CoS_2 and FeS_2 cells at all temperatures as well as the absolute values of cell resistance.

Minimum Pulse Voltage

The open-circuit voltage for the Li(Si)/FeS_2 cell at 500°C is 1.99 V which is higher than that of 1.85 V for Li(Si)/CoS_2. Thus, at the beginning of discharge, the CoS_2 cells showed a slightly lower minimum voltage during pulsing. However, since the CoS_2 cells had a lower resistance, they outperformed the FeS_2 cells later in life. As shown in Figure 3, this crossover occurred at ~25 s at 400°C, where polarization losses were greatest. As the temperature was increased, the time for crossover lengthened. Similar trends occurred when flooded anodes were used, except that the time for crossover was markedly increased. At 500°C, for example, crossover took place at 75 s for cells with unflooded anodes and 175 s for cells with flooded anodes.

DISCUSSION

The relative differences in performance of CoS_2 and FeS_2 are related to differences in discharge mechanism. In the case of FeS_2, the first discharge step is:

$$FeS_2 + 3/2\ Li^+ + 3/2\ e^- \longrightarrow 1/2\ Li_3Fe_2S_4 \qquad [1]$$

The $Li_3Fe_2S_4$ is further reduced to Li_2FeS_2 according to Eq. 2:

$$Li_3Fe_2S_4 + Li^+ + e^- \dashrightarrow 2\ Li_2FeS_2 \qquad [2]$$

In the case of CoS_2, the first discharge step is:

$$CoS_2 + 4/3\ e^- \dashrightarrow 1/3\ Co_3S_4 + 2/3\ S^{-2} \qquad [3]$$

This material can be further discharged according to Eq. 4:

$$Co_3S_4 + 8/3\ e^- \dashrightarrow 1/3\ Co_8S_9 + 4/3\ S^{-2} \qquad [4]$$

The reactions of Eqns. 1 and 3 were used to calculate the capacities of the cathodes in this study. (On a weight basis, this corresponds to 1,206 coulombs/g FeS_2 and 1,046 coulombs/g CoS_2; on a volume basis, this corresponds to 6,030 and 4,465 coulombs/cc, respectively.)

Compared to FeS_2, the $Li_3Fe_2S_4$ phase is more resistive by several orders of magnitude at 400°C, while Li_2FeS_2 is only four times more resistive (7). This accounts for the shape of the resistance-discharge time curves for the FeS_2 cells. While comparable data do not exist for the discharge phases for the Li(alloy)/CoS_2 system, the resistance data for the CoS_2 cells (Fig. 3) suggest that they are as good or better conductors than the parent CoS_2.

Note that the discharge phases of CoS_2 do not depend upon the presence of Li^+ as do those of FeS_2. Thus, Li^+ concentration gradients at the cathode in the case of FeS_2 can severely limit the discharge rate. CoS_2 also has negligible solubility in the molten electrolyte when compared to FeS_2.

The presence of electrolyte in the anode improves the performance by providing a larger reservoir (relative to dry anodes) for assimilation of Li^+ generated during discharge. It also prevents wicking of electrolyte from the separator which results in a higher separator resistance. The use of flooded anodes results in a lower cell resistance because it reduces the anodic contribution to the overall cell polarization. As a consequence, the time that the maximum pulse current density can be sustained is increased.

For a long-life thermal battery, the performance at the end of life becomes critical, relative to short-duration (e.g., 5 min) applications. Since the temperature will be at its lowest at this time, the relative performance of FeS_2 and CoS_2 at the lower temperatures becomes increasingly important. The relative performance data at 400°C indicates that CoS_2 should outperform FeS_2 for such applications. To test this theory, single cells were subjected to a ramped-temperature profile comparable to that of a long-life battery during discharge. The cells were discharged under a resistive background load of 15.7 ohms and a pulse load of 1 ohm for 5 s at 500 s and 3,580 s into discharge. The test results are shown in Figure 4.

The FeS_2 cell performed better initially but was surpassed by the CoS_2 cell after ~30 min. The discharge curve for the CoS_2 cell was also much flatter. The minimum pulse voltage at the first pulse was slightly higher for the FeS_2 cell but was much lower than the CoS_2 cell at the second pulse near the end of life. The substantial drop in voltage after 55 min for the FeS_2 cell is a consequence of thermal decomposition of the FeS_2 to sulfur vapor and FeS which has a much lower open-circuit potential. Clearly, CoS_2 is the preferred cathode choice for long-life thermal batteries. These data have since been corroborated in tests with full-sized thermal batteries (8).

CONCLUSIONS

CoS_2 shows superior performance to FeS_2 in single-cell tests with Li(Si) anodes at temperatures of 400° to 550°C with the low-melting LiBr-KBr-LiF eutectic electrolyte. The CoS_2 cells show a higher rate capability and a lower voltage loss during heavy-current pulses as a result of their lower internal resistance, even though the FeS_2 cells have a higher open-circuit voltage. The use of flooded anodes improves the performance of both types of cells relative to the use of dry (unflooded) anodes. Because of its superior discharge characteristics and higher thermal stability, CoS_2 is preferred to FeS_2 for use in thermal batteries with lifetimes of 60 min or more.

ACKNOWLEDGEMENT

This work was supported by the U. S. Department of Energy under contract DE-AC04-94AL85000.

REFERENCES

1. R. A. Guidotti, F. W. Reinhardt, and G. C. Nelson, "Characterization of Sheet Calcium for $Ca/CaCrO_4$ Thermal Batteries," *SAND83-2269* (1985).
2. R. A. Guidotti and F. W. Reinhardt, "Characterization of DEB Powders and Pellets for $Ca/CaCrO_4$ Thermal Batteries," *SAND83-2270* (1985).
3. R. A. Guidotti, F. W. Reinhardt, D. R. Tallant, and K. L. Higgins, "Dissolution of $CaCrO_4$ in Molten LiCl-KCl Eutectic," *SAND83-2272* (June, 1984).
4. H. N. Sieger, "Lithium/Cobalt Sulfide Pulse Power Battery," *Proc. 34th Power Sources Symp.*, pp. 334-338 (1990).
5. N. Papadakis, "Development of a Bipolar Lithium/Cobalt Disulfide

Battery for Pulse Power", *Ibid.*, pp. 339-342 (1990).

6. R. A. Guidotti and F. W. Reinhardt, "Evaluation of Alternate Electrolytes for Use in Li(Si)/FeS$_2$ Thermal Batteries," *Proc. 33rd Power Sources Symp.*, pp. 369-376 (1988).
7. S. P. S. Badwal and R. J. Thorn, *J. Sol. St. Chem.*, 43, 163 (1982).
8. R. A. Guidotti and A. R. Baldwin, "Development of a Two-Hour Hour Thermal Battery," to be presented at *36th Power Sources Symposium*, June 6-9, 1994, Cherry Hill, NJ.

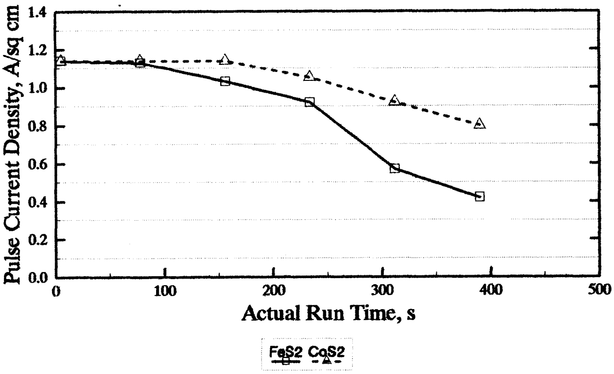

Figure 1. Maximum Pulse Current Density as a Function of Time of Li(Si)/FeS$_2$ and Li(Si)/CoS$_2$ Thermal Cells During Continuous Pulsing at 400°C.

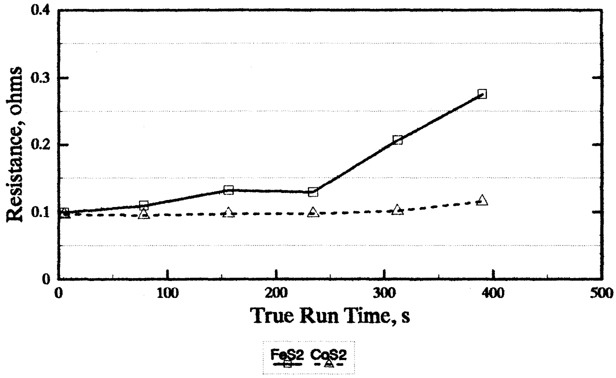

Figure 2. Apparent Cell Resistance as a Function of Time of Li(Si)/FeS$_2$ and Li(Si)/CoS$_2$ Thermal Cells During Continuous Pulsing at 400°C.

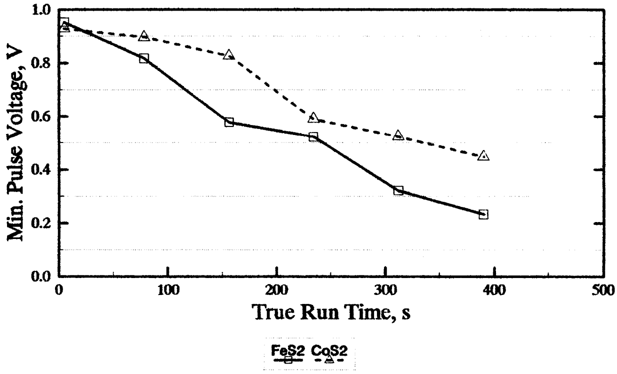

Figure 3. Minimum Pulse Voltage as a Function of Time of Li(Si)/FeS_2 and Li(Si)/CoS_2 Thermal Cells During Continuous Pulsing at 400°C.

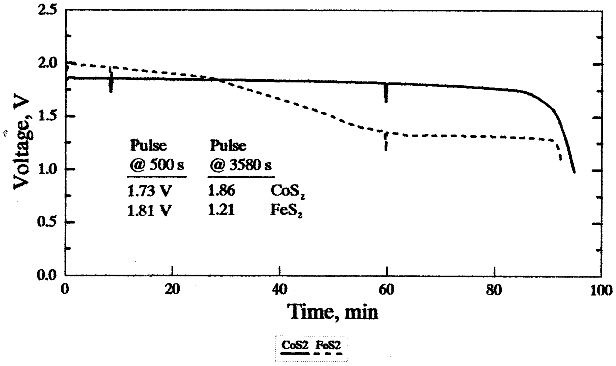

Figure 4. Voltage as a Function of Time of Li(Si)/FeS_2 and Li(Si)/CoS_2 Thermal Cells Under a 15.7 Ohms Steady-State/1 Ohm Pulse Load While Subjected to a Temperature Profile of a Long-Life Thermal Battery.

DOI: 10.1149/199413.0828PV

THERMODYNAMICS AND KINETICS OF ELECTRODE PROCESSES IN SODIUM AND POTASSIUM POLYSULPHIDES

V. S. Sharivker

Department of Chemistry, University
of Southampton SO9 5NH, UK

A. G. Morachevskii

Technical Academy, St. Petersburg, Russia

ABSTRACT

Investigations of electrode processes in molten polysulphides have been made by an EMF method and by studying the potentiodynamic, potentiostatic and pulse-galvanostatic polarisation curves. It was shown that there is no specific influence on the values of the potentials at the phase boundary: solid electrolyte-polysulphide melt. The ions of alkali metals take part in the processes of alloy formation during the cathodic polarisation of Sb, Te, Bi in the molten polysulphides. They also participate in the reduction of the metals from their sulphides.

Keywords: alkali metals, solid electrolyte, cathodic polarisation

INTRODUCTION

At present the problem of the medium-temperature rechargeable battery is quite important. The sodium-sulphur battery is one of the most interesting of such batteries. It is being developed for electric vehicle propulsion and offpeak energy storage (1). The potassium-sulphur battery also has high energy storage capability (2). But now there is not agreement about the mechanism of the cathodic processes in molten polysulphides and about the nature of the polysulphide melts. There is now full information for electrochemical characteristics of the different materials in these molten media. Investigation of the electrode reactions in sodium and potassium polysulphide melts at 250-350C have been made, especially with regard to a better understanding of the behaviour of sodium- or potassium-sulphur cells.

Experimental

Sodium and potassium were used in the work, not containing measurable quantities of foreign metals, ultrapure sulphur, and analytical-grade sodium and potassium sulphide were dehydrated by the previously described method (3). The dehydrated alkali sulphides were mixed with sulphur to obtain the polysulphides with the required composition. The mixture was remelted in argon atmosphere and kept at 350C for 2 h. After cooling the solid polysulphide was transferred to the cell. In individual cases the sulphur-rich polysulphide melts were prepared by direct fusion of the components. The alkali metal content of the mixture with sulphur was determined by flame photometry. Solid glass and ceramic electrolytes were used for the construction of the cells. The solid electrolyte was prepared by ion exchange replacing the sodium ions in the lattice of sodium polyaluminate with potassium ions by treatment with potassium chloride vapour and molten potassium nitrate (4).For the determination of the thermodynamic characteristics of the processes occurring during cathodic polarization of solid metals in a molten sodium and potassium polysulphide we used a galvanostatic pulse technique where square current pulses of increasing amplitude were applied to the electrode at certain time intervals and the potential was recorded at the points where the current was turned off. Potential decay curves were also recorded after the electrode had been polarized with currents of certain current density. The time of polarization of the electrode and the pause between current pulses were 15 sec each. The working surface of the test electrode was the polished end face of rod (0.3 mm diameter) of metal; the sides of the rod were protected with corundum-coated tubing. The auxiliary electrode was a rod of spectroscopically pure graphite placed into a glass test tube with small hole. A sodium microelectrode served as the reference electrode (5). Liquid potassium in a test tube made of potassium polyaluminate (a ceramic solid electrolyte) was used as the reference electrode during the cathodic polarization of solid electrodes in molten potassium polysulphide. The experiment were performed in glass equipment under argon.

Potentiometry

The EMF's of the different cells [1] to [8] have been measured.

(-) Mo, Na ¦ glass ¦ Na_2S_n ¦ C (+) [1]

(-) Mo, K ¦ solid electrolyte ¦ K_2S_n ¦ C (+) [2]

(-) Mo, Na ¦ glass ¦ (Na+Pb), Mo (+) [3]

(-) Mo, Na ¦ glass ¦ Na_2S_n ¦ glass ¦ (Na+Pb), Mo (+) [4]

(-) C ¦ Na_2S_{n1} ¦ glass ¦ Na_2S_{n2} ¦ C (+) [5]

(-)C ¦ Na_2S_{n1} ¦ glass ¦NaCl,$ZnCl_2$¦ glass ¦ Na_2S_{n2} ¦ C(+) [6]

(-) Mo, Na ¦glass¦Na_2S_{n1}¦glass¦Na_2S_{n2}¦glass¦ Na, Mo (+) [7]

(-)Mo,Na¦glass¦NaCl,$PbCl_2^{(1)}$¦glass¦NaCl,$PbCl_2^{(2)}$¦Na,Mo(+) [8]

Experimental EMF values of cell [1] and [3] have a good correlation with date from literature. It is interesting that the addition of fused sodium polysulphide as an intermediate electrolyte in cell [3] does not influence the EMF of this cell: the value of the EMF of cells [3] and [4] are equal. The EMF value of cell [5] is equal to the difference between the EMF of two cells of type [1] with different compositions of the polysulphide melts. The EMF values of cells [5] and [6] were equal; the addition of the salt intermediate electrolyte does not influence the EMF values of these cells. The EMF values of cell [7] were independent of the composition of the molten polysulphide and were equal to zero. This has been connected with the compensation of the potential differences at the phase-boundary: glass - polysulphide melt. We observed such an effect not only for molten polysulphide. The EMF value of cell [8] was zero.

The results obtained in the measurement of the EMF of the cell [2] with the use of glass and ceramic solid electrolytes are in satisfactory agreement. On the curve of EMF vs. composition a clear region of phase separation appears where the EMF remains constant. The thermodynamic characteristics of the system potassium-sulphur at 325C were calculated. As expected, the system potassium-sulphur is characterized by clearly pronounced negative deviations from the ideal behaviour as well as system sodium-sulphur. In the investigated region of compositions the temperature coefficient of EMF for this systems is negative, the partial molar entropies of potassium and sodium are negative, and the integral entropies and enthalpies of mixing are negative. All this is characteristic for systems with a strong interaction between the components in the appearance of ionic bonds.

Cathodic polarisation of the indifferent electrode

A sharp change in the potential of the vitreous carbon electrode has been observed on the polarisation curves which were obtained by the pulse-galvanostatic method. A value of the shift of potential is approximately 1.67V relative to the sodium reference electrode. This coincides with the EMF value of the concentration cell [1] for the composition of the polysulphide melt which corresponds to the composition on the liquidus on the phase diagram for system sodium-sulphur at the experimental temperature. It has been correlated with the crystallization of the solid phase Na_2S_2 on the surface of the inert electrode. That is why the continuation of the polarisation gives a sharp change of potential into the region of pure sodium.

Polarisation curves in the melts of the polysulphide Na_2S_3 and Na_2S_4 were obtained with the help of a rotating disc electrode made from vitreous carbon for the determination of the nature of the rate-determining step. Rotation velocities were: 6.7, 10, 15, 22.5, 33.5 s^{-1}. Liner $i\text{-}\omega^{1/2}$ plots were obtained by the traditional treatment of the experimental data. These plots pass through the origin. Therefore we can suppose that cathodic processes proceed into the diffusion region. We supposed that the diffusion of Na_2S_2 from the electrode into the melt is the limiting stage of the cathodic process in the limiting current region. In this instance the values of the experimental limiting current have good correlation with the values of current calculated with help of the Levich equation for the rotating disc electrode:

$$i = 0.62\ n\ F\ D^{2/3}\ \nu^{-1/6}\ \Delta c\ \omega^{1/2} \qquad [9]$$

Investigation of alloy formation processes

The value of the initial potential of Sb and Te on the polarisation curves coincides with the potential of the indifferent electrode in the polysulphide melt with this composition at the operating temperature. Increasing the current density stimulates the change of the concentration in the layer near the electrode and as a result the potential is displaced to more negative values. We observed sections on the polarisation curves in the region of formation of alloys, where potentials are constant. This is connected with the formation of the two-phase systems on the surface of the cathode. The activities of the components in this system have a constant value. Two-phase regions are formed one after another on the surface of antimony: Sb+NaSb, NaSb+Na_3Sb and of tellurium: Te+$NaTe_3$, $NaTe_3$+NaTe, NaTe+Na_2Te. Potentials of these two-phase regions had been measured in different electrolytes. Their values have a good conformity one with another. In summary, the process on the initial section of the polarisation curve can be described by reaction

$$2Na + (n-1)Na_2S_n = nNa_2S_{n-1} \qquad [10]$$

Apparently ions of sodium take part in reaction during polarisation of the electrode. The act of their discharge has been accompanied by depolarisation of the electrode owing to chemical interaction with polysulphide melt.

In addition, we observed that the process of formation of alloys on the tellurium precedes the crystallization of the film of Na_2S_2 on the surface of the inert electrode. This effect can be used to indicate the end of the discharge for the sodium-sulphur battery. Tellurium addition on the inert electrode gives the possibility to have a signal before the formation of the film of solid Na_2S_2, which is undesirable as it inhibits recharge. In this case there is electrochemical oxidation of the sodium and formation of Na^+ at the anode during the discharge. Na_2S_n has been reduced at the surface of the cathode. The cathodic potential has been changed from 2.07V. When the potential becomes 1.775V, the Na^+ has been discharged on the surface of the tellurium and two-phase region $Te+NaTe_3$ has been formed. The cathodic potential is constant during this process. Constant potential is the signal to stop the discharge of the cell. The intermetallic compound $NaTe_3$ is oxidized when the cell is charged. There is formation of Te and Na^+ in this case. The continuation of the charge gives the formation of the metal sodium at the sodium electrode and electrochemical oxidation of the polysulphide in the catholyte.

Cathodic polarisation of metal electrodes

The cathodic polarisation of tungsten, molybdenum, aluminium, copper and nickel in fused sodium polysulphide has been studied. When we submerged these metals into the fused polysulphide the surface of the metal electrodes became coated with the respective sulphides. The initial potential of these metals in the molten polysulphide are not distinguishable from the potential of an indifferent electrode. Therefore the initial sections of the polarisation curves can be attributed to reaction [10]. The sulphides of these metals are reduced during cathodic polarisation. Thermodynamic calculations show that the standard potentials of the reduction reactions of Cu, Ni and Al sulphides by sodium coincide with the constant potential sections of the polarisation curves. The form of the polarisation curves which have been obtained on the Mo and W electrodes is similar to the form of the curves which have been obtained for the indifferent vitreous carbon electrode. This can be connected with the fact that the rate of formation of the sulphides of these metals in fused polysulphide at 350C is very slow. Mo and W are more stable under these conditions than another metals.

We obtained results analogous with results for sodium-sulphur melts, when we carried out the cathodic polarisation of Sb and Bi in fused potassium polysulphide.

CONCLUDING REMARKS

Our conclusion is the ions of the alkali metals take part in the processes of alloy formation during the cathodic polarisation of Sb, Te, Bi in the molten polysulphide of Na and K. They also participate in the reduction of the metals from their sulphides.

ACKNOWLEDGMENTS

We acknowledge Dr. A.I. Demidov, Dr. E.B. Klebanov and Dr. E.A. Mayorova for their collaboration during the course of this investigation. We thank Prof. Brian Cleaver for his kindly help to present this paper.

REFERENCES

1. J. L. Sadworth and A. R. Tilley, The Sodium-Sulfur Battery, p. 447, University Press, Cambridge (1985).

2. G. M. Crosbie, J. Electrochem. Soc., 129, 2707 (1982).

3. N. I. Kopylov, Zh. Neorg. Khim., 13, 529 (1968).

4. G. M. Crosbie and G. J. Tennenhouse, J. Amer. Ceram. Soc., 65, 187 (1982).

5. A. G. Morachevskii, E. B. Klebanov, V. S. Sharivker, and A.I. Demidov, Elektrokhimiya, 23, 698 (1985).

AUTHOR INDEX

SUBJECT INDEX